Lecture Notes in Mechanical Engineering

M.K. Singh
B.S. Kushvah
G.S. Seth
J. Prakash *Editors*

Applications of Fluid Dynamics

Proceedings of ICAFD 2016

Springer

Lecture Notes in Mechanical Engineering

About this Series

Lecture Notes in Mechanical Engineering (LNME) publishes the latest developments in Mechanical Engineering—quickly, informally and with high quality. Original research reported in proceedings and post-proceedings represents the core of LNME. Also considered for publication are monographs, contributed volumes and lecture notes of exceptionally high quality and interest. Volumes published in LNME embrace all aspects, subfields and new challenges of mechanical engineering. Topics in the series include:

- Engineering Design
- Machinery and Machine Elements
- Mechanical Structures and Stress Analysis
- Automotive Engineering
- Engine Technology
- Aerospace Technology and Astronautics
- Nanotechnology and Microengineering
- Control, Robotics, Mechatronics
- MEMS
- Theoretical and Applied Mechanics
- Dynamical Systems, Control
- Fluid Mechanics
- Engineering Thermodynamics, Heat and Mass Transfer
- Manufacturing
- Precision Engineering, Instrumentation, Measurement
- Materials Engineering
- Tribology and Surface Technology

More information about this series at http://www.springer.com/series/11236

M.K. Singh · B.S. Kushvah
G.S. Seth · J. Prakash
Editors

Applications of Fluid Dynamics

Proceedings of ICAFD 2016

Springer

Editors
M.K. Singh
Indian Institute of Technology (Indian School of Mines)
Dhanbad, Jharkhand
India

G.S. Seth
Indian Institute of Technology (Indian School of Mines)
Dhanbad, Jharkhand
India

B.S. Kushvah
Indian Institute of Technology (Indian School of Mines)
Dhanbad, Jharkhand
India

J. Prakash
University of Botswana
Gaborone
Botswana

ISSN 2195-4356 ISSN 2195-4364 (electronic)
Lecture Notes in Mechanical Engineering
ISBN 978-981-10-5328-3 ISBN 978-981-10-5329-0 (eBook)
https://doi.org/10.1007/978-981-10-5329-0

Library of Congress Control Number: 2017943830

Printed on acid-free paper

This Springer imprint is published by Springer Nature
The registered company is Springer Nature Singapore Pte Ltd.
The registered company address is: 152 Beach Road, #21-01/04 Gateway East, Singapore 189721, Singapore

Preface

International conference on Applications of Fluid Dynamics (ICAFD 2016) was organized by Department of Applied Mathematics, Indian Institute of Technology (Indian School of Mines), Dhanbad, Jharkhand, India, in association with Fluid Mechanics Group, Department of Mathematics, Faculty of Science, University of Botswana, Gaborone, Botswana. ICAFD 2016 at IIT(ISM) Dhanbad was third in continuation following the first ICAFD 2012 in University of Botswana and second ICAFD 2014 in S.V. University, Tirupati.

The aim of the conference was to provide a platform for academicians, experts, and researchers in various disciplines of mathematics and its allied areas exclusively in applications of fluid dynamics. This international platform provided opportunities for eminent personnel to interact and suggest various corrective measures for advancement of the subject and its applications in industry, science, engineering and technology, research and development, etc. The deliberations made by an eminent mathematicians, engineers, scientists, and young researchers published in the form of conference proceeding entitled "Applications of Fluid Dynamics" by Springer in Lecture Notes in Mechanical Engineering. This international conference received overwhelming response from academicians, scientists, engineers, researchers, and most importantly research scholars of various institutions of our country such as IITs, IISc Bangalore, R&D Center, IOL, HPCL Mumbai, NITs, Central and State Universities, and foreign countries as well such as USA, New Zealand, West Indies, Botswana, Ostrava, South Africa, Russia. The financial support for organizing this international conference was extended by Jharkhand Council of Science and Technology (JCST), Ranchi, Jharkhand; Department of Science and Technology (DST-SERB), New Delhi; Defense Research Development Organization (DRDO), New Delhi; and Society of Applied Mathematics (SAM) and IIT(ISM), Dhanbad.

We are thankful, rather grateful, to the Key Speakers like Sri C.K. Asnani, Chairman and Managing Director, UCIL Jaduguda and Chief Guest of inaugural function; Prof. Dhanush Dhari Misra, Chairman, Board of Governors, Indian Institute of Technology (Indian School of Mines), Dhanbad; Prof. D.C. Panigrahi, Director, Indian Institute of Technology (Indian School of Mines), Dhanbad; Prof.

Vijay P. Singh, Guest of Honor of inaugural function and University Distinguished Professor and Caroline and William N. Lehrer Distinguished Chair in Water Engineering at Texas A&M University, USA; Prof. R. Panneer Selvam, James T. Womble Professor of Computational Mechanics and Nanotechnology Modeling, University Professor of Civil Engineering and Director of Computational Mechanics Laboratory, University of Arkansas, USA; Prof. Venkatesh Uddameri, Director, Water Resources Center, Texas Tech University, USA; Prof. Lakshmi Narasimhan, University of Botswana, Botswana; Prof. Elma Annette Hernandez Uddameri, Department of Civil, Environmental, and Construction Engineering, Texas Tech University, USA; Dr. Raj Das, Group Leader, 'Simulation and Modeling', Mechanical Engineering Department, University of Auckland, New Zealand; Dr. Sreedhara Rao Gunakala, Lecturer (Tenure track), Department of Mathematics, The University of the West Indies, St. Augustine, West Indies; Prof. J. Prakash, Head, Department of Mathematics, Faculty of Science, University of Botswana, Botswana; Prof. Sergej Hloch, Technical University of Košice in Slovakia; Prof. Alok K. Gupta, Emeritus Professor, National Center of Experimental Mineralogy and Petrology, University of Allahabad; Prof. B.V. Rathish Kumar, Department of Mathematics and Statistics at Indian Institute of Technology, Kanpur; Prof. Mridula Kanoria, Department of Applied Mathematics, University of Calcutta, Kolkata; Prof. Naveen Kumar, Department of Mathematics, Institute of Science, BHU, Varanasi; Dr. Shivendra Nath Rai, Chief Scientist, (CSIR-National Geophysical Research Institute (NGRI)), Hyderabad; Prof. Ashok Mishra, Director, "Center for Fluid Dynamics Research," CUTM, Paralakhemundi, Odisha; Prof. S.V.K. Varma, S.V. University, Tirupati; Dr. Sachin Saw, School of Mathematics and Statistical Science, Botswana International University of Science and Technology, Botswana.

On behalf of organizing committee, we express our sincere gratitude to Prof. D. D. Misra, Chairman, BoG, IIT(ISM) and Chief Patron, ICAFD-2016 for their encouragement. We express our sincere thanks to Prof. D.C. Panigrahi, Director, IIT(ISM), Prof. Thabo T. Fako, Vice-Chancellor, University of Botswana, Botswana and Patrons, ICAFD 2016 for their guidance and source of inspiration. We also express our thanks to IIT(ISM) and University of Botswana administrations for providing infrastructural support to organize an international event at such a large scale smoothly and successfully. We acknowledge the support and motivation received from each one of them who have directly or indirectly helped us to organize this international event in a grand way. We also put on record about the contribution of Research Associate and Scholars namely Dr. Pintu Das, Sultana Begam, Ayan Chatterjee, Chandan Kumar Thakur, Affreen Akhter, Rakesh Kumar Singh, Rohit Kumar, Animesh Samanta, and Manish Chaudhary for helping us to organize an international event apart from preparing and formatting the manuscript. Finally, the execution of international event is possible with support of one and all.

Dhanbad, India — Dr. M.K. Singh
Dhanbad, India — Dr. B.S. Kushvah
Dhanbad, India — Prof. G.S. Seth
Gaborone, Botswana — Prof. J. Prakash

Committee Members

Chief Patron
Prof. Dhanush Dhari Misra, Chairman, BOG, IIT(ISM), Dhanbad, India

Patrons
Prof. D.C. Panigrahi, Director, IIT(ISM), Dhanbad, India
Prof. Thabo T. Fako, Vice-Chancellor, University of Botswana, Botswana
Prof. Edward M. Lungu, University of Botswana, Botswana

International Advisory Board
Prof. Paneer Selvam, University of Arkansas, USA and President, IAFM, Botswana
Prof. Vijay P. Singh, A&M University, Texas, USA
Prof. K. Vajravelu, University of Central Florida, USA
Prof. Graham R. Thorpe, Victoria University, Australia
Prof. Girija Jayaraman, The University of the Westindies, Jamaica
Prof. W. Malalasekera, Loughborough, UK
Dr. M.M. Hantush, US EPA National Risk Management Laboratory, USA
Prof. Walter Dragoni, Perugia University, Italy
Prof. F.C. Tsai, Lousiana State University, USA
Prof. Martin Bees, University of York
Prof. Wayne M. Getz, University of California, USA
Prof. Ravi V. Gomatam, Bhakti Vedanta Institute, Berkeley, USA
Prof. Aliakbar Montazer Haghighi, A&M University, Prairie View, Texas, USA
Prof. Balswaroop Bhatt, University of the West Indies, West Indies
Prof. Bruce-van Brunt, Institute of Fundamental Sciences, Massey University, New Zealand
Prof. Ali J. Chamkha, Applied Education and Training Shuwaikh, Kuwait
Dr. N. Chaturvedi, University of Botswana, Botswana
Prof. Dr.-Ing. Verdiana Grace Masanja, University of Rwanda, Rwanda
Prof. James McKenzie, University of Kwazulu Natal, Durban, South Africa
Prof. Robert McKibbin, Massey University, Albany Campus, New Zealand
Prof. Kh.S. Mekheimer, Al-Azhar University, Egypt

Prof. Josua P. Meyer, School of Engineering, University of Pretoria, South Africa
Mr. Manhar Mooney, Overseas Development Enterprises, Trans Africa, Botswana
Prof. V. Lakshmi Narasimhan, East Carolina University, USA
Prof. S.N. Pandey, Papua New Guinea University of Technology, Papua New Guinea
Prof. Kailash C. Patidar, University of the Western Cape, South Africa
Prof. V.C.C. Raju, University of Botswana, Botswana
Prof. Matti Hellio, Lappeenranta University of Technology, Finland
Prof. Bernardine R. Wong Cheng Kiat, Institute of Mathematical Sciences, Malaysia
Dr. G. Sreedhara Rao, University of the West Indies, West Indies
Prof. Sergej Hloch, Technical University of Košice, Slovakia
Dr. Sharidan Shafie, University Teknologi, Malaysia
Prof. Nitin Kumar Tripathi, School of Engineering and Technology, Pathumthani, Thailand
Prof. Bhadra Man Tuladhar, President, Nepal Mathematical Society, Nepal
Prof. Daya Reddy, University of Cape Town, South Africa
Prof. P. Sibanda, University of KwaZulu-Natal, South Africa
Prof. Karan P. Singh, University of North Texas, USA
Prof. Graeme C. Wake, Massey University, New Zealand
Prof. Ebrahim Shirani, IUT, Iran
Prof. Ioan Pop, University of Cluj, Romania
Prof. Lokanath Debnath, The University of Texas, USA
Prof. Kambiz Vafai, University of California, USA
Prof. I-Chung Liu, National Chi Nan University, Taiwan
Prof. Otlogetswe Totolo, Deputy Vice-Chancellor (Academic Affairs), University of Botswana, Botswana
Prof. Julius R. Atlhopheng, Dean, Faculty of Science University of Botswana, Botswana
Prof. Arjun Kumar Gupta, Distinguished Professor, Bowling Green State University, Ohio, USA
Prof. M. Sambandham, Morehouse College, Atlanta, USA
Dr. Josef Foldyna, Head of the Department; Institute of Geonics, Ostrava
Dr. Grzegorz Krolczyk, Faculty of Production Engineering and Logistics, Opole University of Technology, Poland
Prof. Sc. Drazan Kozak, Mechanical Engineering Faculty in Slavonski Brod, University of Osijek, Croatia
Prof. Aleksander Sedmark, Director of Innovation Center, University of Belgrade, Serbia

National Advisory Board
Prof. A. Chattopadhyay, IIT(ISM), Dhanbad
Prof. S. Mohanty, Dean (Academic), IIT(ISM), Dhanbad
Prof. J. Manam, Dean (SW), IIT(ISM), Dhanbad
Prof. S.K. Paul, Dean (Faculty), IIT(ISM), Dhanbad

Prof. V. Priye, Dean (R&D), IIT(ISM), Dhanbad
Prof. V.M.S.R. Murthy, Dean (IRAA), IIT(ISM), Dhanbad
Prof. J.K. Pattanayak, Dean (Infrastructure), IIT(ISM), Dhanbad
Prof. G. Udaybhanu, ASD (A&R), IIT(ISM), Dhanbad
Prof. A.K. Verma, ASD (SW), IIT(ISM), Dhanbad
Prof. G.N. Singh, ASD (HM), IIT(ISM), Dhanbad
Prof. S.K. Sinha, PCE, IIT(ISM), Dhanbad
Prof. A.S. Venkatesh, PIC, IIT(ISM), Dhanbad
Col. M.K. Singh, Registrar, IIT(ISM), Dhanbad
Prof. B.C. Sarkar, IIT(ISM), Dhanbad
Prof. Shalivahan, IIT(ISM), Dhanbad
Prof. Phoolan Prasad, IISc, Banglore
Prof. Dinesh Singh, Delhi University
Prof. Vishnu Dutt Sharma, IIT Bombay
Prof. H.S. Dhami, Kumaun University
Prof. Rama Bhargava, IIT Roorkee
Prof. P. Chandra, IIT, Kanpur
Prof. Y.V.S. Sanyasiraju, IIT Madras
Prof. D.K. Gupta, IIT Kharagpur
Prof. B. Rai, University of Allahabad
Dr. Ashok Kr. Singh, CIMFR, Digwadih Campus
Prof. Naveen Kumar, BHU, Varanasi
Prof. L.P. Singh, IIT, BHU, Varanasi
Prof. S. Bhattacharya, IIT Kharagpur
Prof. P. Kandaswamy, Bartihar University
Prof. P.V.S.N. Murthy, IIT Kharagpur
Prof. B.V. Rathish Kumar, IIT Kanpur
Prof. B.S. Dandapat, SMIT, Sikkim
Prof. J.P. Vishwakarma, DDU, Gorakhpur
Prof. B.N. Mandal, ISI Kolkata
Prof. P.R. Sharma, University of Rajasthan, Jaipur
Prof. A.K. Singh, BHU, Varanasi
Prof. G. Radhakrishnamacharya, NIT, Warangal
Prof. S.V.K. Varma, S.V. University, Tirupati
Prof. R.R. Yadav, Lucknow University, Lucknow
Prof. B.S. Bhadauriya, BBAU, Lucknow
Prof. Reeta Chaudhury, Gauhati University, Gauhati
Prof. Ashok Mishra, Centurian University, Orissa
Prof. Dulal Pal, Vishwa Bharti, Santiniketan
Prof. N. Ahamad, Gauhati University, Gauhati
Prof. P.G. Sidheshwar, Bangalore University, Bangalore
Dr. Swati Mukhopadhyay, The University of Burdwan
Dr. K.R. Murali Mohan, DST, Government of India
Dr. A.K. Singh, DST, Government of India
Dr. Peyush Pal Roy, CIMFR, Dhanbad

Dr. D.D. Tripathi, CIMFR, Dhanbad
Dr. Ajay Kr. Singh, CIMFR, Dhanbad
Dr. Arvind Kr. Singh, CIMFR, Dhanbad

Contents

About the Editors

Dr. M.K. Singh is an Associate Professor in the Department of Applied Mathematics at the IIT(ISM), Dhanbad, Jharkhand, India. Dr. Singh has published more than 50 research papers in National and International journals and conferences of repute. He has edited three books and published three chapters in his area of expertise. Dr. Singh has guided more than five M.Phil. and Ph.D. students. Dr. Singh has more than fifteen years of teaching and research experience in Applied Mathematics. His research interest is in the field of Solute Transport Modeling. He has executed three Minor and Major Research Projects successfully. Dr. Singh is the life member/member of various professional bodies. Dr. Singh has organized various national and international events, i.e., workshops, training programmes, conferences, etc. Dr. Singh is the panel examiner of Ph.D. in Central Universities/Institutes of our country and abroad.

Dr. B.S. Kushvah is an Associate Professor of Applied Mathematics at the IIT(ISM), Dhanbad. He is also a Visiting Associate of IUCAA Pune since 2011. He is a sectional Recorder of Mathematical Sciences Section (including Statistics), Indian Science Congress for 2016–17 and 2017–18. His research interest includes celestial mechanics, dynamical astronomy, orbital mechanics, and high-performance computing. He has published more than 27 research papers in National and International journals and conferences of repute. He is a reviewer of many peer-reviewed

journals. He is the recipient of Best Poster Presentation Award of 93rd Indian Science Congress for year 2005–06 and Canara Bank Research Publication Award of 2015 of IIT(ISM), Dhanbad. He is a member of various academic bodies. He has co-organized workshops, short-term courses, etc. He has executed three research projects as a principal investigator successfully.

Dr. G.S. Seth is a Professor in Department of Applied Mathematics at the Indian Institute of Technology (Indian School of Mines), Dhanbad, Jharkhand, India. Dr. Seth has more than 35 years of teaching and research experience. He has guided more than 10 Ph.D. students and published more than 100 research papers in National and International journals and conferences of repute. Dr. Seth is the life member/member of various professional bodies. He is the editorial board member and reviewer of national and international peer-reviewed journals in the areas of his expertise. His area of specialization is numerical methods, fluid dynamics, magnetohydrodynamics, and heat and mass transfer.

Dr. J. Prakash is working as a Professor in the Department of Mathematics, Faculty of Science, University of Botswana, Botswana. He is having more than forty years of teaching experience in various countries such as India, Iraq, Zambia, New Zealand, and Botswana at university levels. He is having research interest in bio-fluid dynamics, fluid mechanics, computational fluid dynamics (CFD), mathematical modeling, mathematical methods, etc., with more than 175 research publications in various International journals. He has organized international conferences at India and abroad. Dr. Prakash has received C.V. Raman International Fellowship Award for African Researchers under Visiting Fellowship Program from FICCI Science and Technology, International Cooperation Division, Government of India. He has also received Global Visionary Award on January 13, 2014, by Vision Foundation, Ahmedabad, India.

Applications of Fluid Dynamics: An Introduction

Mritunjay Kumar Singh

Locke has said "Mathematics is a way to settle in the mind a habit of reasoning." Basically, two types of reasoning exist in mathematics such as inductive and deductive. Inductive reasoning in which statement or propositions are made on general observation and experience while deductive reasoning based on self-evident truth in which statements are the product of mind. Mathematics in widest sense is the development of all types of deductive reasoning. A true lover of MATHEMATICS should be Methodical, Analytical, Technical, Humble, Ethical, Meritorious, Assertive and Attentive, Thoughtful and Tenacious, Introspective and Indigenous, Cautious and Curious, Studious. Subsequently, mathematics enhances mind power, apprehension, talent, honesty, enthusiasm, memory, ambition, thirst of knowledge, intelligence and intricacy, confidence and clarity, and self-realization. A genuine learner of mathematics is certainly interested in finding out the answers of some of the questions which are as follows: Why should everybody learn mathematics? What is the place of mathematics in any scheme of education? What are the aims and objectives of teaching mathematics to everybody? How does it make contribution in the development of an individual? Mathematics must contribute toward the acquirement of the values like knowledge and skill, intellectual habits and power, desirable attitude, and ideals. Moreover, it also possesses practical value, disciplinary value and cultural value, etc., as well. As per Hamilton, the study of mathematics cures the vice of mental distraction and cultivates the habit of continuous attention. As we all know, mathematics demands hard work from the learner and hardworking people are very much needed in any developing society. We can establish the very good relation of mathematics with the other subject such as Physics, Chemistry, Biology, Agriculture, Engineering, Social Science, Economics, Logic. Some of the views of mathematics regarding relationship with

M.K. Singh
Department of Applied Mathematics, Indian Institute of Technology (Indian School of Mines), Dhanbad-826004, Jharkhand
e-mail: drmks20@rediffmail.com

the other subject were quoted as follows: Mathematics gives the final shape to the rules of physics. Mathematical nature of the chemical equation can be explored. The claim of any particular branch of natural philosophy to be considered as a science can be assessed only on the basis of the amount of mathematics employed in it. The proportions of human body are strictly mathematical. A human being's beauty and attractive form depends on his/her proportionate buildup. The whole figure is six times the length of the foot which holds well for the form either is slender or plump. For example, the Greek made all their statues according to this rule. The hand, from the wrist to the middle finger, is one tenth of the whole stature. The scientific calculation about the normal weight in pounds is double the height in inches. Mathematics in engineering deals with surveying, leveling, designing, estimating constructions, computing, etc. Applied mathematics includes fluid mechanics in detail and explores their applications extensively in science, engineering and technology as well.

Fluid mechanics is defined as the science that deals with the behavior of fluids at rest (fluid statics) or in motion (fluid dynamics). Fluid mechanics is also referred to as fluid dynamics by considering fluids at rest as a special case of motion with zero velocity. Fluid dynamics has several subdisciplines itself, including aerodynamics (the study of air and other gases in motion) and hydrodynamics (the study of liquids in motion). Fluid dynamics has a wide range of applications, including calculating forces and moments on aircraft, determining the mass flow rate of petroleum through pipelines, predicting weather patterns, understanding nebulae in interstellar space, and modeling fission weapon detonation. Some of its principles are even used in traffic engineering, where traffic is treated as a continuous fluid, and crowd dynamics. Fluid mechanics is encountered in almost every area of our physical lives. Blood flows through our veins and arteries, a ship moves through water and water flows through rivers, airplanes fly in the air and air flows around wind machines, air is compressed in a compressor and steam expands around turbine blades, a dam holds backwater, air is heated and cooled in our homes, and computers require air to cool components. All engineering disciplines require some expertise in the area of fluid mechanics. Fluid mechanics, especially fluid dynamics, is an active field of research with many unsolved or partly solved problems. Fluid mechanics can be mathematically complex, and can best be solved by numerical methods, typically using computers. A modern discipline, called computational fluid dynamics (CFD), is devoted to this approach to solving fluid mechanics problems. The solution to a fluid dynamics problem typically involves calculating various properties of the fluid, such as flow velocity, pressure, density, and temperature, as functions of space and time. Before the twentieth century, hydrodynamics was synonymous with fluid dynamics. This is still reflected in names of some fluid dynamics topics, like magnetohydrodynamics and hydrodynamic stability, both of which can also be applied to gases (Munson et al. 1990; Yunus and Cimbala 2006; Potter and Wiggert 2008).

Magnetohydrodynamics is also known as MHD or magneto-fluid dynamics or hydromagnetics which is the study of the magnetic properties of electrically conducting fluids. Examples of such magneto-fluids include plasmas (electrically

conducting gas), liquid metals, and salt water or electrolytes. The word MHD is derived from magneto—meaning magnetic field, hydro—meaning water, and dynamics—meaning movement. One of the most famous scholars associated with MHD was the Swedish Physicist Hannes Alfvén (1908–1995), who received the Nobel Prize in Physics (1970) for fundamental work and discoveries in magneto-hydrodynamics with fruitful applications in different parts of plasma physics. The fundamental concept behind MHD is that magnetic fields can induce currents in a moving conductive fluid, which in turn polarizes the fluid and reciprocally changes the magnetic field itself. The set of equations that describe MHD are a combination of the Navier-Stokes equations of fluid dynamics and Maxwell's equations of electromagnetism. These differential equations must be solved simultaneously, either analytically or numerically.

A nanofluid is a fluid containing nanometer-sized particles, called nanoparticles. These fluids are engineered colloidal suspensions of nanoparticles in a base fluid. The nanoparticles used in nanofluids are typically made of metals, oxides, carbides, or carbon nanotubes. Common base fluids include water, ethylene glycol, and oil. Nanotechnology is being used or considered for use in many applications targeted to provide cleaner, more efficient energy supplies and uses. While many of these applications may not affect energy transmission directly, each has the potential to reduce the need for the electricity, petroleum distillate fuel, or natural gas that would otherwise be moved through energy transmission system. More efficient energy generation and use may decrease the amount of construction, maintenance, repair, and decommissioning activities. Examples of how nanotechnology may be integrated into each of these technological areas are: engine cooling, engine transmission oil, in diesel electric generator as jacket water coolant, boiler exhaust flue gas recovery, heating and cooling of buildings, cooling of electronics, cooling of welding, nanofluids in transformer cooling oil, nuclear systems cooling, solar water heating, nanofluids in drilling, refrigeration (domestic refrigerator, chillers), defense, space, high-power lasers, microwave tubes, biomedical applications, drilling, lubrications, thermal storage, drag reductions. Nanofluids in solar collectors are another application where nanofluids are employed for their tunable optical properties.

In analysis such as computational fluid dynamics (CFD), nanofluids can be assumed to be single-phase fluids. However, almost all of new academic papers use two-phase assumption. Classical theory of single-phase fluids can be applied, where physical properties of nanofluid are taken as a function of properties of both constituents and their concentrations. An alternative approach simulates nanofluids using a two-component model (Saidur et al. 2011).

The spreading of a nanofluid droplet is enhanced by the solid-like ordering structure of nanoparticles assembled near the contact line by diffusion, which gives rise to a structural disjoining pressure in the vicinity of the contact line. However, such enhancement is not observed for small droplets with diameter of nanometer scale, because the wetting time scale is much smaller than the diffusion time scale.

The problem of solute transport in porous media has become a major research area in hydrology over the last five decades. Two fundamental worldwide issues are

directly concerned (1) the selection of repository sites for radioactive waste in deep geological formations, and (2) groundwater pollution in fractured/unfractured reservoirs. The objective of this section is to investigate the roles of pore-water velocity, water content, and soil textural properties on solute dispersion in saturated/unsaturated porous media. There are many authors who have examined the process of dispersion in fully saturated porous media. Their finding suggested a linear relationship between the longitudinal dispersion coefficient and the pore-water velocity. In this section, seepage of water through earth dams, underneath hydraulic structures and problems related the supply of drinking water, a mathematical models are employed to predict the fate of hazardous chemicals environmental problems. Waterjet is a generic term used to describe equipment that uses a high-pressure stream of water for cutting or cleaning purposes. Abrasive jet is a subcategory of waterjet in which abrasive is introduced to accelerate the process. In other words, abrasive jets and pure waterjet are kinds of waterjet which is a kind of machinery. We can find the various applications in geophysics, earthquakes, astrophysics, sensors, engineering, magnetic drug targeting, etc.

References

Munson BR, Young DF, Okiishi TH, Huebsch WW (1990) Fundamentals of fluid mechanics, 6th edn. Wiley
Potter MC, Wiggert DC (2008) Fluid mechanics. Schaum's outline series. McGraw-Hill, USA
Saidur R, Leong KY, Mohammad HA (2011) A review on applications and challenges of nanofluids. Renew Sustain Energy Rev 15(3):1646–1668
Yunus AC, Cimbala JM (2006) Fluid mechanics: fundamentals and applications. International Edition, McGraw Hill Publication
https://en.wikipedia.org/wiki/Fluid_dynamics
https://en.wikibooks.org/wiki/Fluid_Mechanics_Applications
https://en.wikipedia.org/wiki/Magnetohydrodynamics
http://www.scholarpedia.org/article/Magnetohydrodynamics
https://en.wikipedia.org/wiki/Nanofluid

Part I
Fluid Dynamics

Unsteady MHD Nanobioconvective Stagnation Slip Flow in a Porous Medium Due to Exponentially Stretching Sheet Containing Microorganisms

R. Kumar and S. Sood

Abstract This communication deals with the numerical investigation of bioconvection induced by an unsteady MHD stagnation point flow of a nanoliquid containing suspension of microorganisms over a stretching sheet. The sheet is stretched in an exponential fashion and set at the right side of porous medium saturated with nanofluid, and permeability of porous medium is considered to have a specified form. The setup deals with the velocity slip and thermal slip at the sheet surface. Here, water is considered as the carrier liquid. Similarity transformations are used to convert the governing coupled nonlinear partial differential equations into ordinary differential equations and solved numerically by employing implicit finite difference scheme known as Keller box method. The effects of nanofluid parameters and bioconvection parameters on non-dimensional velocity, temperature, nanoparticle concentration, and motile microorganism concentration are presented through graphs. The effects of related parameters on local skin friction, Nusselt number, Sherwood number, and density number of microorganisms are exhibited through tables. The substantial influence of bioconvection parameters is noticed on the profiles of velocity, temperature, nanoparticle volume fraction, and density of microorganisms.

1 Introduction

Bioconvection caused by the suppression of self-driven microorganisms in a base fluid is an area in fluid mechanics which have attracted the attention of several scientists and engineers due to its various applications in industry, technology, and environmental sciences. It is a mesoscale phenomenon, in which the motion of

R. Kumar · S. Sood (✉)
Department of Mathematics, Central University of Himachal Pradesh, Dharamsala, India
e-mail: shilpasilvi99@gmail.com

R. Kumar
e-mail: rakesh.lect@gmail.com

M.K. Singh et al. (eds.), *Applications of Fluid Dynamics*, Lecture Notes in Mechanical Engineering, https://doi.org/10.1007/978-981-10-5329-0_1

motile microorganisms induces a macroscopic motion in the fluid. These microrganisms have active response to external stimuli such as light, gravity, chemical reactions and oxygen, and the responses are termed as 'taxes'. The pioneering work of Pedley et al. (1988) on the bioconvection growth patterns due to suspension of gyrotactic microorganisms framed the basis for its detailed analysis. Later on, the paper of Bees and Hill (1997, 1999) and Ghorai and Hill (2000) on the wavelength of bioconvection patterns appeared in the literature. Very recently, in linear stability analysis, Hwang and Pedley (2014) showed that uniform shear can significantly alter the gravitaxis microorganisms. Simultaneously, the work on heat transfer analysis of nanofluid (coined by Choi 1995) also developed to a great extent. The suspension of metallic oxides including copper, aluminum, titanium as nanoparticles in base fluid is known to enhance the thermal conductivity of the base fluid tremendously. Moreover, nanoparticles like silver have hygiene features, and can also be utilized in wound treatment (Lee et al. 2007) and can be used as an anti-bacterial agent (Lee et al. 2003). The concept of bioconvection in nanofluid was introduced by Kuznetsov (2010), in which he claimed that the self-driven microorganisms enhance mixing and prevent nanoparticles from agglomeration in nanofluids. The suspension of nanoparticles and motile microorganisms in base fluid will not only be helpful in enhancing the thermal performances but would also be useful in producing next-generation biofuels with green and sustainable features (Chiu et al. 2011). Mutuku and Makinde (2014) presented a numerical solution on the hydromagnetic bioconvection flow of nanofluid along a vertical permeable plate due to gyrotactic microorganisms. Further, the introduction of porous medium into a flow field plays a vital role in dampening the convective effects caused by bioconvection. New developments in bioconvection in porous medium can be found in Vadasz (2008). In this sequence, Aziz et al. (2012) investigated the effects of free convection on the boundary layer flow of a nanofluid over a horizontal flat plate embedded in porous medium which is filled by nanoparticles and gyrotactic microorganisms. Shaw et al. (2014) extended this problem by analyzing the magnetohydrodynamics and soret effects and considering the flow across an inclined plate to justify the influence of gravity. Their study further demonstrates the substantial effect of magnetic field on the microorganisms behavior.

In the above cited investigations, emphasis has been given on the steady-state problem, which relies on no-slip conditions. But in certain situations, velocity may slip on a stretching boundary when the fluid contains particulates in the form of suspensions, polymer solutions, and emulsions. Due to this, the Navier slip model has been employed by various researchers to depict the jump in velocity and temperature on the surface of the wall. Navier slip effects on the MHD boundary layer flow of a nanofluid containing gyrotactic microorganisms over a vertical plate have been discussed by Khan et al. (2014). Very recently, Uddin et al. (2016) investigated the Stefan blowing and multiple slip effects on the bioconvection nanofluid flow. This study revealed that microorganisms' propulsion can be enhanced, higher flow velocity can be achieved, and nanoparticle distributions can

be improved by the introduction of Stefan blowing through the stretching/shrinking surface. On the other hand, the flow can turn out to be time dependent due to the impulsive stretching of surface or when there is step change in the temperature of the surface. Raees et al. (2015) analyzed unsteady mixed nanobioconvection flow in a horizontal channel and found monotonic decrease in velocity components and continuous decrease in temperature with increasing time. The influence of magnetic field and bioconvection on the stagnation point flow of nanofluid over a stretching surface has been presented by Ahmed et al. (2015).

Though many research paper can be found in literature on the nanofluid bioconvection concepts but many characteristics of these latest fluids are yet to be explored at fundamental level. Hence, an attempt has been made to reveal the effects of velocity and thermal slip on the unsteady mass stagnation flow of nanofluid over a vertical exponentially stretching sheet embedded in a porous medium which is filled with nanoparticles and microorganisms.

2 Mathematical Formulation of the Problem

We considered an unsteady boundary layer stagnation point flow of a water-based nanofluid having a suspension of gyrotactic microorganisms over a vertical sheet embedded in a porous medium. The porous medium is filled with nanoparticles and microorganisms. A Cartesian coordinate system is considered, in which x-axis is measured along the surface and y-axis normal to it. The flow is induced by the exponential stretching of the surface and slip effects under the following assumptions: (i) suspension of nanoparticles is stable and dilute; (ii) nanoparticles do not alter the direction and velocity of swimming microorganisms; (iii) shape of microorganisms is uniform and no extra cellular polymers are produced on the surface of microorganisms; (iv) pore size of porous medium is significantly larger so that microorganisms can penetrate freely through the pores; and (v) porous matrix does not absorb microorganisms. Under above said assumptions, the boundary layer equations utilizing Boussinesq approximation and extended Darcy model for porous medium are as follows:

$$\frac{\partial u}{\partial x} + \frac{\partial v}{\partial y} = 0, \tag{1}$$

$$\begin{aligned} \frac{\partial u}{\partial t} + u\frac{\partial u}{\partial x} + v\frac{\partial u}{\partial y} &= \frac{\partial U_e}{\partial x} + \frac{1}{\rho_f}\left[(1-C_\infty)\beta g(T-T_\infty)\right. \\ &\left. -(\rho_p - \rho_f)g(C-C_\infty) - (n-n_\infty)g\gamma(\rho_m - \rho_f)\right] \\ &+ U_e\frac{\partial U_e}{\partial x} + \vartheta\frac{\partial^2 u}{\partial y^2} + \frac{\vartheta}{k_0}(U_e - u) + \frac{\sigma B_0^2}{\rho}(U_e - u), \end{aligned} \tag{2}$$

$$\frac{\partial T}{\partial t}+u\frac{\partial T}{\partial x}+v\frac{\partial T}{\partial y}=\alpha\frac{\partial^2 T}{\partial y^2}+\tau\left\{D_B\frac{\partial T}{\partial y}\frac{\partial C}{\partial y}+\frac{D_T}{T_\infty}\frac{\partial^2 T}{\partial y^2}\right\}, \tag{3}$$

$$\frac{\partial C}{\partial t}+u\frac{\partial C}{\partial x}+v\frac{\partial C}{\partial y}=D_B\frac{\partial^2 C}{\partial y^2}+\frac{D_T}{T_\infty}\frac{\partial^2 T}{\partial y^2}, \tag{4}$$

$$\frac{\partial n}{\partial t}+u\frac{\partial n}{\partial x}+v\frac{\partial n}{\partial y}=D_B\frac{\partial^2 n}{\partial y^2}-\frac{b_1 W_c}{(C_w-C_\infty)}\left[\frac{\partial}{\partial y}\left(n\frac{\partial C}{\partial y}\right)\right], \tag{5}$$

where u and v are the respective components of velocity along x and y directions. Here, $\nu, \mu, k_0, \sigma, \rho_f, g, T, \alpha, \tau=\frac{(\rho C)_p}{(\rho C)_f}, D_B, D_T, D_m, C, n, b_1$ and W_c are kinematic viscosity, dynamic viscosity, permeability, electrical conductivity, density of the base fluid, gravity, volume expansion coefficient, average volume of microorganisms, temperature, thermal diffusivity, volumetric heat capacitance ratio of nanoparticle to base fluid, coefficients of Brownian diffusion, thermophoretic diffusion, microorganisms diffusion, nanoparticle volume fraction, concentration of motile microorganisms, chemotaxis constant, and maximum swimming speed of microorganisms, respectively.

The relevant boundary conditions are as follows:

$$\begin{aligned} &u=v=0, \quad T=T_\infty, \quad C=C_\infty, \quad n=n_\infty \quad \text{at} \quad t\le 0,\\ &v=0, \quad u=U_w(x,t)+\vartheta N_1\frac{\partial u}{\partial y}, \quad T=T_w+D_1\frac{\partial T}{\partial y},\\ &C=C_w(x,t), \quad n=n_w(x,t) \quad \text{at} \quad y=0, (t>0) \end{aligned} \tag{6}$$

$$u=U_e(x,t), \quad T=T_\infty, \quad C=C_\infty, \quad n=n_\infty \quad \text{at} \quad y\to\infty, \ (t>0), \tag{7}$$

where N_1 and D_1 are the velocity and thermal slip respectively. The velocity, temperature and concentration at the surface of the sheet are considered in the following syntax: $U_w(x,t)=\frac{b\exp(x/l)}{1-ct}$, $T_w=T_\infty+\frac{T_0\exp(x/2l)}{1-ct}$, $C_w=C_\infty+\frac{C_0\exp(x/2l)}{1-ct}$, $n_w=n_\infty+\frac{n_0\exp(x/2l)}{1-ct}$, respectively. $U_w(x,t)=\frac{a\exp(x/l)}{1-ct}$ is external flow velocity. The following similarity transformations have been introduced to reduce the set of Eqs. (1)–(7) into self-similar form:

$$\begin{aligned} &\eta=\sqrt{\frac{a\exp(x/l)}{2\vartheta L(1-ct)}}y, \quad \psi=\sqrt{\frac{2\vartheta La\exp\left(\frac{x}{l}\right)}{(1-ct)}}f(\eta), \quad \theta(\eta)=\frac{(T-T_\infty)}{(T_w-T_\infty)},\\ &\phi(\eta)=\frac{(C-C_\infty)}{(C_w-C_\infty)}, \quad \xi(\eta)=\frac{(n-n_\infty)}{(n_w-n_\infty)}, \quad u=\frac{\partial\psi}{\partial y}, \quad v=-\frac{\partial\psi}{\partial x}. \end{aligned} \tag{8}$$

In above similarity transformations, we assumed that $(1-ct)>0$, and hence, the similarity transformation is valid only for $t<\frac{1}{c}$.

The following set of modified equations is obtained after the application of above transformations:

$$\begin{aligned} f''' + ff'' - 2f'^2 + 2 + M(1-f') + K(1-f') \\ - A(\eta f'' + 2f' - 2) + \lambda(\theta - Nr\phi - Rb\xi) = 0 \end{aligned} \tag{9}$$

$$\theta'' - APr(\eta\theta' + 2\theta) + \Pr(\theta' f - f'\theta) + Nb\phi'\theta' + Nt\theta'^2 = 0, \tag{10}$$

$$\phi'' - ASc(\eta\phi' + 2\phi) + Sc(\phi' f - f'\phi) + \frac{Nt}{Nb}\theta'' = 0, \tag{11}$$

$$\xi'' - ALb(\eta\xi' + 2\xi) + Lb(\xi' f - f'\xi) - Pe[\phi''(\xi + \omega) + \xi'\phi'] = 0. \tag{12}$$

The boundary conditions will take the following altered form:

$$\begin{aligned} &f(0) = 0, \quad f'(0) = \frac{b}{a} + Nf''(0), \\ &\theta(0) = 1 + D\theta'^{(0)}, \quad \phi(0) = 1, \quad \xi(0) = 1. \end{aligned} \tag{13}$$

$$f'(\infty) = 1, \quad \theta(\infty) = 0, \quad \phi(\infty) = 0, \quad \xi(\infty) = 0, \tag{14}$$

where prime signifies differentiation with respect to h, and in the meanwhile, following dimensionless parameters are ensued: $A = \frac{Lc}{U_e}, M = \frac{2\sigma B_0^2 L}{U_e \rho_f}$, $K = \frac{2\vartheta L}{kU_e}$, $\lambda = \frac{2L(1-C_\infty)\beta g(T_w - T_\infty)}{U_e^2}$, $Nr = \frac{(\rho_p - \rho_f)(\phi_w - \phi_\infty)}{\rho_f \beta(1-C_\infty)(T_w - T_\infty)}$, $Rb = \frac{(\rho_m - \rho_f)(n_w - n_\infty)}{\rho_f \beta(1-C_\infty)(T_w - T_\infty)}$, $Pr = \frac{\vartheta}{\alpha}$, $Nb = \frac{\tau D_B(\phi_w - \phi_\infty)}{\alpha}$, $Nt = \frac{\tau D_B(T_w - T_\infty)}{T_\infty \alpha}$, $Sc = \frac{\vartheta}{D_B}$, $Lb = \frac{\vartheta}{D_m}$, $Pe = \frac{bW_c}{D_m}$, $\omega = \frac{n_\infty}{(n_w - n_\infty)}$, $\varepsilon = \frac{b}{a}$, $N = N_1\sqrt{\frac{\vartheta U_e}{2L}}$, $D = D_1\sqrt{\frac{U_e}{2\vartheta L}}$ which represent unsteady parameter, magnetic parameter, permeability parameter, mixed convection parameter, buoyancy ratio parameter, bioconvection Rayleigh number, Prandtl Number, Brownian motion parameters, thermophoresis parameter, Schmidt number, bioconvection Lewis number, bioconvection Peclet number, microorganisms concentration difference parameter, velocity ratio parameter, velocity slip parameter, and thermal slip parameter, respectively. In this study, the quantities of engineering interest are c_f, Nu, Sh, and Nn, which are termed as coefficient of skin friction, Nusselt number, Sherwood number, and density number of motile microorganisms, respectively. These physical quantities are defined mathematically as follows:

$$\begin{aligned} c_f &= \frac{\mu}{\rho_f U_e^2}\left(\frac{\partial u}{\partial y}\right)_{y=0}, \quad Nu = -\frac{Lk}{k(T_w - T_\infty)}\left(\frac{\partial T}{\partial y}\right)_{y=0}, \\ Sh &= -\frac{L}{(C_w - C_\infty)}\left(\frac{\partial C}{\partial y}\right)_{y=0}, \quad Nn = -\frac{L}{(n_w - n_\infty)}\left(\frac{\partial n}{\partial y}\right)_{y=0} \end{aligned} \tag{15}$$

After substituting Eq. (8) in (15), we reckoned that

$$c_{fx} = \sqrt{2Re_x}c_f, \quad Nu_x = \frac{Nu}{Re_x} = -\sqrt{\frac{x}{2L}}\theta'(0),$$
$$Sh_x = \frac{Sh}{Re_x} == -\sqrt{\frac{x}{2L}}\phi'(0), \quad Nn_x = \frac{Nn}{Re_x} = -\sqrt{\frac{x}{2L}}\xi'(0) \tag{16}$$

Here, k is thermal conductivity of nanofluid. Above stated quantities are the local skin friction which specifies the wall shear stress, local Nusselt number which connotes the heat transfer rate, local Sherwood number which indicates the mass transfer rate, and local density number of motile microorganisms which represents the microorganisms transfer rate respectively.

3 Results and Discussion

In order to gain physical insight into the flow problem, rigorous numerical computations have been performed for different values of pertinent parameters that describe the flow features. Implicit finite difference method (IFDM) also known as Keller box method (KBM) has been employed for the numerical solutions of strongly coupled boundary layer equations due to the limitations of closed-form solutions. The maximum values for η_∞ have been chosen as $\eta_\infty = 2$ to $\eta_\infty = 7$, which lies well outside the boundary layers and provides the mesh-independent numerical results. By choosing a grid size $\Delta\eta = 0.005$, the whole computational procedure is administered with the aid of computational language MATLAB. The numerical computations are accomplished for various values of parameters, which have been displayed through figures and tables. During the whole computational process, the values to related parameters are assigned as $D = 0.1$, $A = M = K = \lambda = Sc = Pe = Lb = 1$, $N = \varepsilon = 0.5$, $Pr = 6.2$, $Nr = Nb = Nt = Rb = \omega = 0.1$, unless otherwise stated.

The variations of local skin friction coefficient $f''(0)$, heat transfer coefficient, $-\theta'(0)$, mass transfer coefficient $-\phi'(0)$, and local density number of motile microorganisms $-\xi'(0)$ with respect to nanofluid, and bioconvection parameters have been shown in Tables 1 and 2. It is noticed that coefficient of local skin friction $f''(0)$ and wall heat transfer rate $-\theta'(0)$ are decreased with increasing values of $N = D = K = M = \lambda = Nr = Rb = Nt = Sc = Pe$ and Lb, whereas an enhancing influence of unsteadiness parameter A is observed on $f''(0)$ and $-\theta'(0)$. On the other hand, augmentation in wall mass transfer rate $-\phi'(0)$ and local density number of motile microorganisms $-\xi'(0)$ is observed with an increment in the values of parameters like $A = N = D = K = M = \lambda = Nr = Rb = Sc = Pe$

Table 1 Values of $f''(0), -\theta'(0), -\phi'(0)$ and $-\xi'(0)$ for $Pr = 6.2, \epsilon = 0.5, \omega = 0.1$

A	N	D	K	M	λ	$f''(0)$	$-\theta'(0)$	$-\phi'(0)$	$-\xi'(0)$
0						0.180599	−1.251593	−0.351064	−1.345503
1	0.5	0.1	1	1	1	0.184604	−1.691026	−0.521726	−1.877642
2						0.186737	−2.010296	−0.693214	−2.348334
	0.0					1.355115	−1.576390	−0.514971	−1.770079
1	0.1	0.1	1	1	1	0.583455	−1.670693	−0.507650	−1.831366
	1.0					0.103086	−1.666725	−0.544509	−1.906117
		0.0				0.262521	−4.147615	1.206921	−0.225112
1	0.5	0.5	1	1	1	0.143727	−0.502031	−1.361957	−2.695745
		1.0				0.131642	−0.267268	−1.528455	−2.859221
			0.5			0.185232	−1.724980	−0.497114	−1.853184
1	0.5	0.1	1.5	1	1	0.183832	−1.658360	−0.545380	−1.901132
			3.0			0.180919	−1.567415	−0.611120	−1.966347
				2.0		0.182946	−1.626912	−0.568130	−1.923711
1	0.5	0.1	1.0	3.0	1	0.180919	−1.567415	−0.611120	−1.966347
				5.0		0.176268	−1.460450	−0.688262	−2.042765
					2.0	0.182700	−1.626614	−0.567342	−1.922392
1	0.5	0.1	1	1	5.0	0.162550	−1.459187	−0.685097	−2.037310
					10	0.092166	−1.244191	−0.834066	−2.181045

and *Lb*, while on the contrary, $-\phi'(0)$ and $-\xi'(0)$ are depressed with increasing thermophoresis parameter *Nt*. The substantial effects of nanofluid and bioconvection parameters on $f''(0), -\theta'(0), -\phi'(0)$, and $-\xi'(0)$ have been noticed due to coupling of momentum, thermal, nanoparticle species and motile microorganism species fields through conservation equations. The well-known influence of velocity and thermal slips has also been observed for the flow problem (Uddin et al. 2016). Schmidt number, Sc, greater than unity depicts that momentum diffusivity is higher than the nanoparticles' species diffusivity, and this serves to enhance the nanoparticles mass transfer rate in the neighborhood of the sheet. In similar manner, *Lb* characterizes the ratio of momentum diffusivity to microorganisms' species diffusivity, and for $Lb > 1$, momentum diffusivity dominates the microorganisms' species diffusivity, and this leads to increment in microorganisms transfer rate at the surface. Also for higher values of bioconvection Peclet number *Pe*, species diffusivity of microorganisms is dominated by their swimming motion and this leads to enhance the rate of microorganism transfer at the wall. This is true because *Pe* is the ratio of maximum swimming speed of microorganism to its rate of diffusion. The influence of remaining pertinent parameters has already been explained repeatedly by many researchers such as Mutuku and Makinde (2014), Shaw et al. (2014), Khan et al. (2014), and Uddin et al. (2016).

Table 2 Values of $f''(0), -\theta'(0), -\phi'(0)$ and $-\xi'(0)$ for $Pr = 6.2, \epsilon = 0.5, \omega = 0.1$

Nr	*Rb*	*Nb*	*Nt*	*Sc*	*Pe*	*Lb*	$f''(0)$	$-\theta'(0)$	$-\phi'(0)$	$-\xi'(0)$
0.5							0.076207	−1.661378	−0.536873	−1.888408
0.8	0.1	0.1	0.1	1	1	1	−0.005006	−1.639724	−0.547799	−1.896040
1.2							−0.113221	−1.611594	−0.561809	−1.905642
	0.4						0.121138	−1.669461	−0.534350	−1.888033
0.1	0.7	0.1	0.1	1	1	1	0.057776	−1.648387	−0.546618	−1.898070
	1.0						−0.005494	−1.627787	−0.558540	−1.907762
		0.4					0.186544	−1.589726	−1.442298	−2.776769
0.1	0.1	0.7	0.1	1	1	1	0.184816	−1.494729	−1.573194	−2.905544
		1.0					0.182799	−1.405847	−1.625142	−2.956813
			0.5				0.156032	−1.628604	4.008728	2.359567
0.1	0.1	0.1	1.0	1	1	1	0.116734	−1.556152	9.144095	6.655163
			1.5				0.072326	−1.489247	13.763331	9.827329
				2			0.178275	−1.616124	−1.412482	−2.706805
0.1	0.1	0.1	0.1	3	1	1	0.170820	−1.550161	−2.077787	−3.356267
				5			0.156275	−1.435730	−3.106659	−4.393188
					2		0.174764	−1.626720	−0.568007	−2.219948
0.1	0.1	0.1	0.1	1	3	1	0.166053	−1.567086	−0.610895	−2.725753
					5		0.151050	−1.459943	−0.687864	−4.136866
						2	0.174937	−1.626723	−0.568001	−2.606828
0.1	0.1	0.1	0.1	1	1	3	0.165647	−1.567064	−0.610847	−3.182837
						5	0.149021	−1.459869	−0.687736	−4.110475

3.1 Velocity Profiles

Figures 1, 2, 3, 4, 5, and 6 have been plotted to observe the influence of associated parameters like unsteady parameter (A), bioconvection Rayleigh number (Rb), velocity slip (N), buoyancy ratio parameter (Nr), mixed convection parameter (λ), velocity ratio parameter (ϵ), magnetic field parameter (M), porous medium

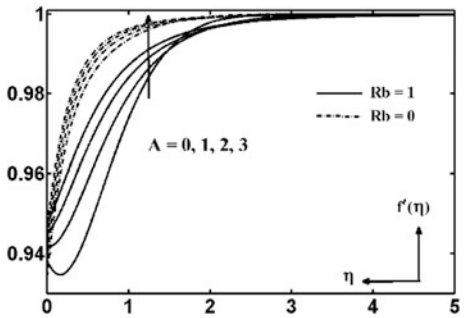

Fig. 1 Dimensionless velocity profiles for A and Rb

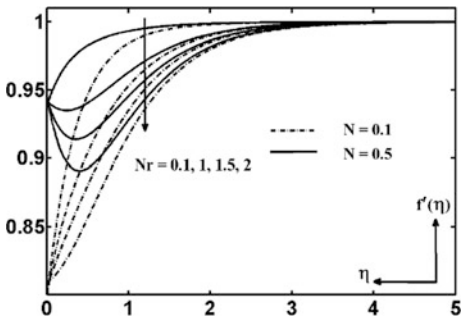

Fig. 2 Dimensionless velocity profiles for N and Nr

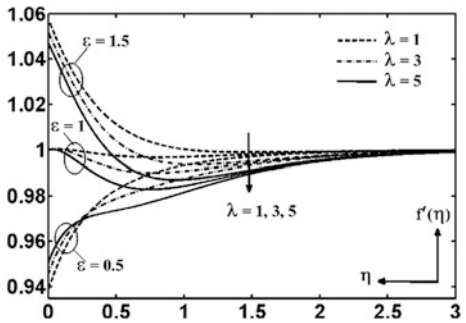

Fig. 3 Dimensionless velocity profiles for λ and ϵ

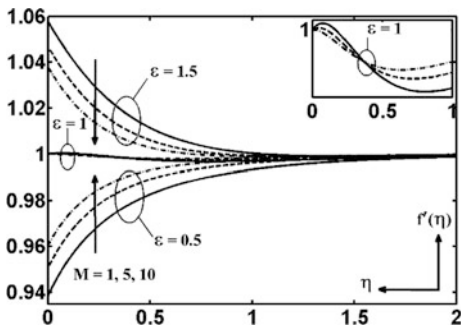

Fig. 4 Dimensionless velocity profiles for ϵ and M

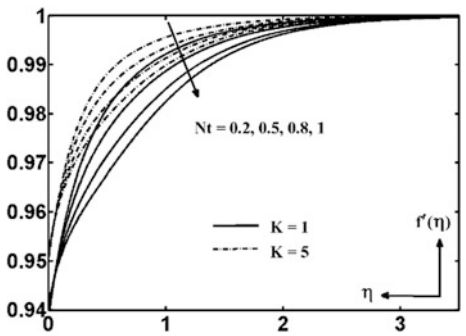

Fig. 5 Dimensionless velocity profiles for Nt and K

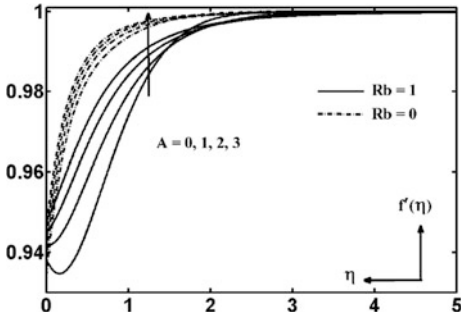

Fig. 6 Dimensionless velocity profiles for A and Rb

permeability parameter (K), thermophoresis parameter (Nt), Brownian motion parameter (Nb), and bioconvection Peclet number (Pe) on the distribution of velocity in the flow field. It is clear from these figures that velocity profiles are reduced with the increasing Rb, Nr, λ, Nt and Pe, whereas increasing values of A, N, ε, K, M and Nb enhance the velocity profiles. Since the upward motion of the nanofluid is resisted due to buoyancy by the bioconvection plumes, therefore, an increase in Rb leads to a decrease in velocity. Also increasing porous medium permeability provides larger space for fluid particles to flow and becomes a responsible factor in the expansion of velocity profiles.

3.2 Temperature Profiles

Figures 7, 8, 9, and 10 illustrate the influences of unsteady parameter (A), thermal slip (D), mixed convection parameter (λ), magnetic field parameter (M), Brownian motion parameter (Nb), thermophoresis parameter (Nt), and bioconvection Rayleigh number (Rb) on temperature profiles $(\theta(\eta))$ of nanofluid. It is observed from these figures that profiles of temperature and thermal boundary layer thickness are reduced with the increase of A, D, λ, M and Rb. The nanofluid thermal boundary

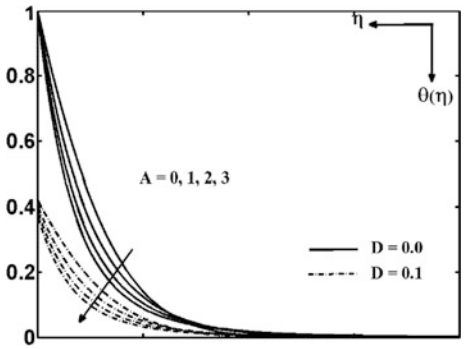

Fig. 7 Dimensionless temperature profiles for A and D

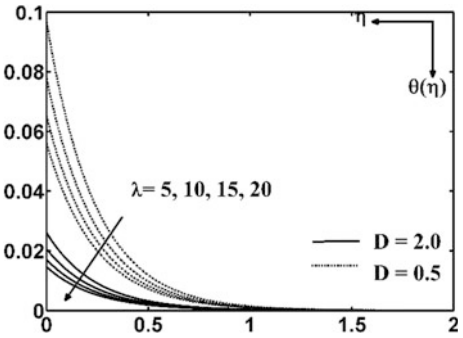

Fig. 8 Dimensionless temperature profiles for λ and D

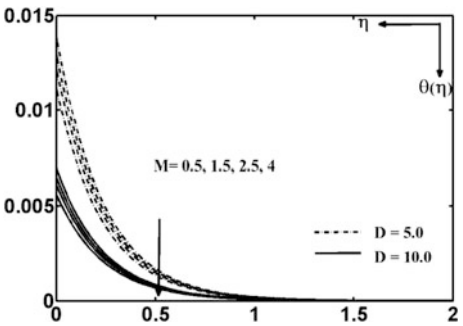

Fig. 9 Dimensionless temperature profiles for M and D

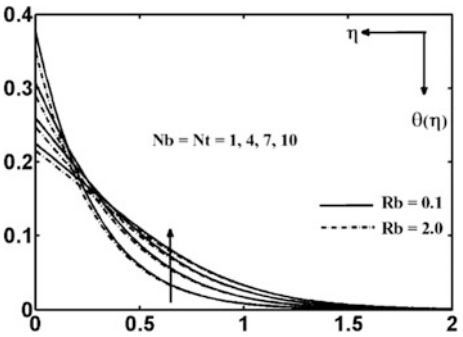

Fig. 10 Dimensionless temperature profiles for Nb and Rb

layer is strongly suppressed near the sheet by thermal slip for different values of A and D, and weakly dampened by λ and Rb. A significant fall in temperature in the vicinity of sheet presents an increase in thermal slip, and hence, thermal slip has a cooling effect on thermal boundary layers. However, Nb and Nt have a reversed effect on the temperature of nanofluid inside the thermal boundary layer, i.e., temperature is raised with Nb and Nt. It is true because Nb and Nt enhance the thermal conductivity of base fluid and is responsible for raising the boundary layer thickness and temperature.

3.3 Nanoparticle Concentration Profiles

Figures 11 and 12 demonstrate the effects of Brownian motion parameter (*Nb*), thermophoresis parameter (*Nt*), unsteady parameter (*A*), and Schmidt number (*Sc*) on the concentration profiles of nanoparticles $(\phi(\eta))$. Concentration profiles are reduced with the enhancement of A, Sc, and *Nb*, whereas profiles are increased with *Nt*. An increase in *Sc* significantly reduces the thickness of concentration boundary layer. The shape of nanoparticle mass fraction profiles dramatically changes from parabolic distribution to monotonic decay near the stretching surface when *Nt* obtains the critical value $Nt = 0.01$.

3.4 Motile Microorganisms Density Profiles

Figures 13 and 14 exhibit the impact of bioconvection Lewis number (*Lb*), bioconvection Peclet number (*Pe*), unsteady parameter (*A*), and microorganisms concentration difference parameter (ω) on the motile microorganisms density profiles. The density of motile microorganisms is diminished with the raise of Lb, Pe, A and ω. It is true because larger values of *Lb* present larger motile

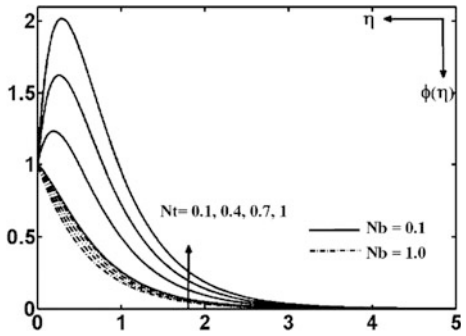

Fig. 11 Nanoparticles concentration profiles for *Nt* and *Nb*

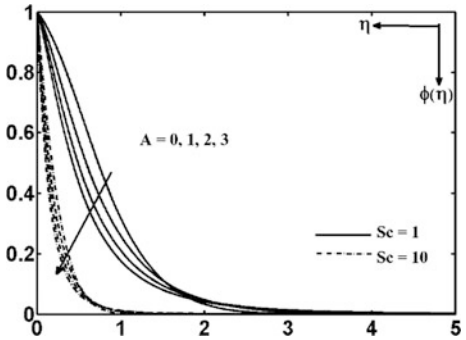

Fig. 12 Nanoparticles concentration profiles for *A* and *Sc*

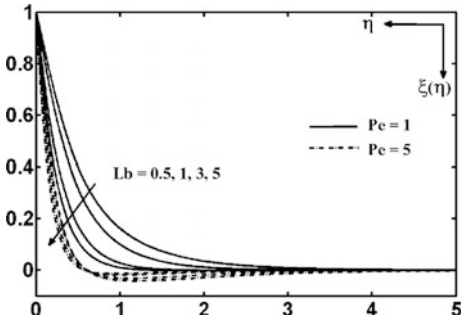

Fig. 13 Microorganisms concentration profiles for *Pe* and *Lb*

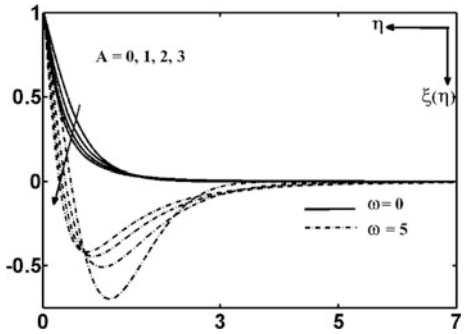

Fig. 14 Microorganisms Concentration profiles for A and ω

microorganisms diffusion rate in comparison with viscous diffusion rate. Similarly, higher values of *Pe* account for higher microorganisms swimming speed than diffusivity of microorganisms in nanofluid.

4 Conclusions

A numerical investigation for an unsteady stagnation point flow of a water-based hydromagnetic nanofluid containing gyrotactic microorganisms over a vertical stretching surface through porous medium was presented. Following conclusions are derived on the basis of numerical results:

(i) Unsteady parameter diminishes temperature, concentration volume fraction, microorganism density boundary layers, whereas velocity boundary layers are prolonged.
(ii) Magnetic field and thermal slip diminish thermal boundary layer.
(iii) Porous medium permeability and velocity slip accelerate the velocity distribution, whereas buoyancy ratio has a reversed effect.

(iv) Local skin friction, local Nusselt number, local Sherwood number, and local density number of motile microorganisms are enhanced with A.
(v) Local Sherwood number and local density number of motile microorganisms fall with thermophoresis parameter.

References

Ahmed SE, Aly AM, Mansour MA (2015) MHD mixed bioconvection stagnation point flow of nanofluids towards a stretching surface. J Nanofluids 4(4):528–535
Aziz A, Khan WA, Pop I (2012) Free convection boundary layer flow past a horizontal flat plate embedded in porous medium filled by nanofluid containing gyrotactic microorganisms. Int J Therm Sci 56:48–57
Bees M, Hill NA (1997) Wavelengths of bioconvection patterns. J Exp Biol 200(10):1515–1526
Bees M, Hill NA (1999) Non-linear bioconvection in a deep suspension of gyrotactic swimming micro-organisms. J Math Biol 38:135–168
Chiu SY, Kao CY, Huang TT, Lin CJ, Ong SC, Chen CD, Lin CS (2011) Microalgal biomass production and on-site bioremediation of carbon dioxide, nitrogen oxide and sulfur dioxide from flue gas using Chlorella sp. cultures. Biores Technol 102(19):9135–9142
Choi SUS (1995) Enhancing thermal conductivity of fluids with nanoparticles, development and applications of non-Newtonian flow. ASME Fluid Eng Div USA 66:99–105
Ghorai S, Hill NA (2000) Wavelengths of gyrotactic plumes in bioconvection. Bull Math Biol 62:429–450
Hwang Y, Pedley TJ (2014) Bioconvection under uniform shear: linear stability analysis. J Fluid Mech 738:522–562
Khan WA, Makinde OD, Khan ZH (2014) MHD boundary layer flow of a nanofluid containing gyrotactic microorganisms past a vertical plate with Navier slip. Int J Heat Mass Transfer 74:285–291
Kuznetsov AV (2010) The onset of nanofluid bioconvection in a suspension containing both nanoparticles and gyrotactic microorgan-isms. Int Commun Heat Mass Transfer 37(10):1421–1425
Lee HJ, Yeo SY, Jeong SH (2003) Antibacterial effect of nanosized silver colloidal solution on textile fabrics. J Mater Sci 38(10):2199–2204
Lee HY, Park HK, Lee YM, Park SB (2007) A practical procedure for producing silver nanocoated fabric and its antibacterial evaluation for biomedical applications. Chem Commun 28:2959–2961
Mutuku WN, Makinde OD (2014) Hydromagnetic bioconvection of nanofluid over a permeable vertical plate due to gyrotactic microorganisms. Comput Fluids 95:88–97
Pedley TJ, Hill NA, Kessler JO (1988) The growth of bioconvection patterns in a uniform suspension of gyrotactic micro-organisms. J Fluid Mech 195:223–237
Raees A, Xu H, Liao SJ (2015) Unsteady mixed nano-bioconvection flow in a horizontal channel with its upper plate expanding or contracting. Int J Heat Mass Transfer 86:174–182
Shaw S, Sibanda P, Sutradhar A, Murthy PVSN (2014) Magnetohydrodynamics and soret effects on bioconvection in a porous medium saturated with a nanofluid containing gyrotactic microorganisms. J Heat Transfer 136(5):052601
Uddin MJ, Kabir MN, Beg OA (2016) Computational investigation of Stefan blowing and multiple-slip effects on buoyancy-driven bioconvection nanofluid flow with microorganisms. Int J Heat Mass Transfer 95:116–130
Vadasz P (ed) (2008) Emerging topics in heat and mass transfer in porous media: from bioengineering and microelectronics to nano-technology. Springer Science & Business Media

MHD Free Convection Flow Past an Exponentially Accelerated Inclined Plate Embedded in Porous Medium

R. Swetha, J. Prakash, G. Viswanatha Reddy and S. Vijaya Kumar Varma

Abstract The consequences of radiation absorption and chemical reaction in the presence of heat generation on a MHD unsteady laminar flow with mass and heat transfer of an electrically conducting, incompressible, and viscous fluid over an accelerated exponentially inclined vertical moving porous plate in a porous medium are analyzed in closed form. A perfect solution for this flow problem was obtained by resolving the resulting governing equations by the technique of Laplace transforms. The exact solutions for profiles of concentration, temperature, velocity, and the gradient of velocity are presented, and the effects of these profiles for several values of various arguments are discussed through graphs.

1 Introduction

In recent years, flows through porous media have the considerable research activities such as the filtration of solids from liquids, the extraction of geothermal energy, flow of liquids through ion exchange beds, chemical reactor for purification of mixtures or economical separation and so on. These flows are also having many applications in engineering. Many engineering applications are susceptible to MHD analysis. In technological point of view, magnetohydrodynamic flow finds application in the fields of aeronautics, planetary and stellar magnetospheres, solar physics, cosmic fluid dynamics, electronics, chemical engineering, MHD generators, MHD accelerators, construction of turbines, and other centrifugal machines.

R. Swetha (✉)
Department of Mathematics, Gudalvalleru Engineering College, Gudlavalleru 521356, AP, India
e-mail: swetha.salini@gmail.com

J. Prakash
Department of Mathematics, University of Botswana, Private Bag 0022, Gaborone, Botswana

G. Viswanatha Reddy · S. Vijaya Kumar Varma
Department of Mathematics, S.V. University, Tirupati, AP, India

M.K. Singh et al. (eds.), *Applications of Fluid Dynamics*, Lecture Notes in Mechanical Engineering, https://doi.org/10.1007/978-981-10-5329-0_2

The consequence of chemical reaction on MHD convective transient free flow past a vertical moving plate was studied by Al-Odat and Al-Azab (2007).

Chamkha (2004) investigated the MHD unsteady convective mass and heat transfer with heat absorption over a permeable semi-transfinite vertical moving plate. Kafousias and Raptis (1981) continued this problem containing the leads of mass transfer corresponding to the varying suction or injection. Magnetohydrodynamic convective mixed flow, mass, and heat transfer with constant wall suction in porous medium past a vertical plate was presented by Makinde and Sibanda (2008). Muthucumaraswamy and Subramanian (2010) discussed the heat transfer consequences with mass flux and varying temperature on vertical accelerated plate. Raptis and Massalas (1998) identified the consequences of radiation in the presence of induced magnetic field on the oscillatory flow. Raptis and Perdikis (1985) numerically analyzed the convective free flow through porous medium bounded by a semi-transfinite vertical porous plate. Convective heat transfer with uniform free stream in a fluid which is electrically conducting at an extending surface was discussed by Vajravelu and Hadjinicolaou (1997).

The main intension of this flow problem is to discuss the consequences of heat source parameter, mass diffusion, chemical reaction, and radiation absorption with the constant temperature in the presence of applied uniform magnetic field on a magnetohydrodynamic unsteady convective free flow with mass and heat transfer past an inclined vertical porous plate which is accelerated exponentially in a porous medium.

2 Mathematical Analysis

For this flow problem, consider a transient mass and heat transfer flow of incompressible, natural, electrically conducting, radiation absorption, and viscous fluid with constant heat source past an inclined vertically moving porous plate which is accelerated exponentially in a porous medium in the presence of magnetic field and a chemical reaction. Presuming at all the points, initially in the stationary state, fluid and the plate are maintained the equal temperature T'_{∞} with level of concentration C'_{∞}. The y' axis is chosen normal to the vertical plate, and x' axis is considered along the vertical plate. At time $t' > 0$, in its own plane, the vertical plate is accelerated exponentially with a velocity $u_0 e^{a't'}$. And at the same time, the vertical plate temperature raises to T'_w, and the level of concentration is also raises to C'_w near the plate. Also assuming that, a transverse magnetic field B_0 is applied normal to the vertical plate. Hence, the physical arguments are functions of coordinates t' and y' only because of the fluid flow is assumed to be in the direction of x' axis.

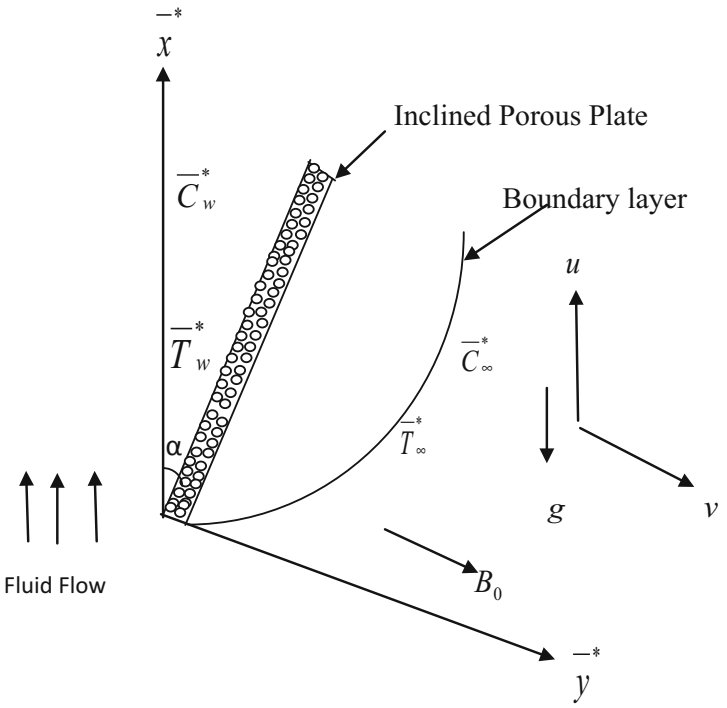

FLOW CONFIGURATION

By the usual approximation of Boussenique's, the governing equations in Cartesian frame of reference for this unsteady flow are

$$\frac{\partial \bar{u}^*}{\partial \bar{t}^*} = g\beta\cos\alpha\left(\overline{T}^* - \overline{T}_\infty^*\right) + g\overline{\beta}\cos\alpha\left(\overline{C}^* - \overline{C}_\infty^*\right) + \nu\frac{\partial^2 \overline{u}^*}{\partial \overline{y}^{*2}} - \frac{\sigma B_0^2 \overline{u}^*}{\rho} - \frac{\nu}{\kappa}\overline{u}^* \quad (1)$$

$$\frac{\partial \overline{T}^*}{\partial \bar{t}^*} = \frac{\kappa}{\rho C_p}\frac{\partial^2 \overline{T}^*}{\partial \overline{y}^{*2}} - \frac{Q_0}{\rho C_p}\left(\overline{T}^* - \overline{T}_\infty^*\right) + \overline{Q}_1^*\left(\overline{C}^* - \overline{C}_\infty^*\right) \quad (2)$$

$$\frac{\partial \overline{C}^*}{\partial \bar{t}^*} = D\frac{\partial^2 \overline{C}^*}{\partial \overline{y}^{*2}} - K_r\left(\overline{C}^* - \overline{C}_\infty^*\right) \quad (3)$$

with the conditions

$$\left.\begin{array}{cccc} \bar{t}^* > 0\text{: } \bar{u}^* = u_0 e^{a^* \bar{t}^*}, & \overline{T}^* = \overline{T}_w^*, & \overline{C}^* = \overline{C}_w^* & \text{at } \bar{y}^* = 0 \\ \bar{u}^* = 0, & \overline{T}^* \to \overline{T}_\infty^*, & \overline{C}^* \to \overline{C}_\infty^* & \text{as } \bar{y}^* \to \infty \\ \bar{t}^* \le 0\text{: } \bar{u}^* = 0, & \overline{T}^* = \overline{T}_\infty^*, & \overline{C}^* = \overline{C}_\infty^* & \forall\ \bar{y}^* \end{array}\right\} \quad (4)$$

And the introduced dimensionless quantities are

$$\left.\begin{array}{llll} U=\dfrac{\bar{u}^*}{u_0}, & t=\dfrac{\bar{t}^* u_0^2}{v}, & y=\dfrac{\bar{y}^* u_0}{v}, & Pr=\dfrac{\mu C_p}{\kappa}, \quad a=\dfrac{\bar{a}^* v}{u_0^2} \\ Gr=\dfrac{g\beta v\left(\overline{T}_w^*-\overline{T}_\infty^*\right)}{u_0^3}, & \theta=\dfrac{\overline{T}^*-\overline{T}_\infty^*}{\overline{T}_w^*-\overline{T}_\infty^*}, & Gm=\dfrac{g\overline{\beta} v\left(\overline{C}_w^*-\overline{C}_\infty^*\right)}{u_0^3} & \\ C=\dfrac{\overline{C}^*-\overline{C}_\infty^*}{\overline{C}_w^*-\overline{C}_\infty^*}, & K=\dfrac{K_r v}{u_0^2}, & Sc=\dfrac{v}{D}, & Q_1=\dfrac{v\overline{Q}_1^*\left(\overline{C}_w^*-\overline{C}_\infty^*\right)}{u_0^2\left(\overline{T}_w^*-\overline{T}_\infty^*\right)} \\ M=\dfrac{\sigma B_0^2 v}{\rho u_0^2}, & k_p=\dfrac{\kappa u_0^2}{v^2}, & \phi=\dfrac{Q_0 v}{\rho C_p u_0^2} & \end{array}\right\} \tag{5}$$

Using (5), the ruled equations (1)–(3) are reduced into the following dimensionless form:

$$\frac{\partial U}{\partial t}=Gr\theta\cos\alpha+GmC\cos\alpha+\frac{\partial^2 U}{\partial y^2}-\left(M+\frac{1}{k_p}\right)U \tag{6}$$

$$\frac{\partial \theta}{\partial t}=\left(\frac{1}{Pr}\right)\frac{\partial^2\theta}{\partial y^2}-\phi\theta+Q_1 C \tag{7}$$

$$\frac{\partial C}{\partial t}=\left(\frac{1}{Sc}\right)\frac{\partial^2 C}{\partial y^2}-KC \tag{8}$$

And the corresponding conditions are

$$\left.\begin{array}{cccc} \text{at } t>0\text{: } U=\mathrm{e}^{at}, & \theta=1, & C=1 & \text{at } y=0 \\ U\to 0, & \theta\to 0, & C\to 0 & \text{as } y\to\infty \\ \text{at } t\le 0\text{: } U=0, & \theta=0, & C=0 & \forall\, y \end{array}\right\} \tag{9}$$

3 Solution of the Problem

With the conditions (9), these non-dimensional ruled equations (6)–(8) are solved by the technique of Laplace transforms in closed form, and hence, the exact solutions for profiles of concentration, temperature, velocity, and the gradient of velocity are given by

$$C(y,t)=A_4 \tag{10}$$

$$\theta(y,t)=A_1+\frac{b}{c}(A_2-A_1)-\frac{b}{c}(A_3-A_4) \tag{11}$$

$$U(y,t) = D_1 + \frac{N_1}{p}(D_2 - D_3 - D_6 + D_7) + \frac{bN_1}{pc}(D_3 - D_7) + \frac{bN_1}{c(c-p)}(D_4 - D_8) + \frac{bN_1}{p(p-c)}(D_2 - D_6) + \frac{bN_2}{cw}(D_9 - D_3) + \frac{bN_2}{c(c-w)}(D_{10} - D_4) + \frac{bN_2}{w(w-c)}(D_{11} - D_5) + \frac{N_3}{w}(D_5 - D_3 - D_{11} + D_9) \tag{12}$$

4 Velocity Gradient

From the field of velocity, the gradient of velocity in terms of Skin friction in dimensionless form is

$$\tau = -\left(\frac{\partial U}{\partial y}\right)_{y=0} \tag{13}$$

From (12) and (13), we get

$$\tau = B_1 + \frac{N_1}{p}(B_3 - B_2 + B_6 - B_7) + \frac{bN_1}{pc}(B_7 - B_3) + \frac{bN_1}{c(c-p)}(B_8 - B_4) + \frac{bN_1}{p(p-c)}(B_6 - B_2) + \frac{bN_2}{cw}(B_3 - B_9) + \frac{bN_2}{c(c-w)}(B_4 - B_{10}) + \frac{bN_2}{w(w-c)}(B_5 - B_{11}) + \frac{N_3}{w}(B_3 - B_5 + B_{11} - B_9) \tag{14}$$

where

$$A_1 = \frac{1}{2}\left[\operatorname{erfc}\left(\frac{y\sqrt{Pr}}{2\sqrt{t}} - \sqrt{\phi t}\right)e^{-y\sqrt{Pr}\sqrt{\phi}} + \operatorname{erfc}\left(\frac{y\sqrt{Pr}}{2\sqrt{t}} + \sqrt{\phi t}\right)e^{y\sqrt{Pr}\sqrt{\phi}}\right]$$

$$A_2 = \frac{e^{ct}}{2}\left[\operatorname{erfc}\left(\frac{y\sqrt{Pr}}{2\sqrt{t}} - \sqrt{(\phi+c)t}\right)e^{-y\sqrt{Pr}\sqrt{\phi+c}} + \operatorname{erfc}\left(\frac{y\sqrt{Pr}}{2\sqrt{t}} + \sqrt{(\phi+c)t}\right)e^{y\sqrt{Pr}\sqrt{\phi+c}}\right]$$

$$A_3 = \frac{e^{ct}}{2}\left[\operatorname{erfc}\left(\frac{y\sqrt{Sc}}{2\sqrt{t}} - \sqrt{(K+c)t}\right)e^{-y\sqrt{Sc}\sqrt{K+c}} + \operatorname{erfc}\left(\frac{y\sqrt{Sc}}{2\sqrt{t}} + \sqrt{(K+c)t}\right)e^{y\sqrt{Sc}\sqrt{K+c}}\right]$$

$$A_4 = \frac{1}{2}\left[\operatorname{erfc}\left(\frac{y\sqrt{Sc}}{2\sqrt{t}} - \sqrt{Kt}\right)e^{-y\sqrt{Sc}\sqrt{K}} + \operatorname{erfc}\left(\frac{y\sqrt{Sc}}{2\sqrt{t}} + \sqrt{Kt}\right)e^{y\sqrt{Sc}\sqrt{K}}\right]$$

$$D_1 = \frac{e^{at}}{2}\left[e^{-y\sqrt{a+M+\frac{1}{k_p}}}\operatorname{erfc}\left(\frac{y}{2\sqrt{t}} - \sqrt{\left(a+M+\frac{1}{k_p}\right)t}\right) + e^{y\sqrt{a+M+\frac{1}{k_p}}}\operatorname{erfc}\left(\frac{y}{2\sqrt{t}} + \sqrt{\left(a+M+\frac{1}{k_p}\right)t}\right)\right]$$

$$D_2 = \frac{e^{pt}}{2}\left[e^{-y\sqrt{p+M+\frac{1}{k_p}}}\operatorname{erfc}\left(\frac{y}{2\sqrt{t}} - \sqrt{\left(p+M+\frac{1}{k_p}\right)t}\right) + e^{y\sqrt{p+M+\frac{1}{k_p}}}\operatorname{erfc}\left(\frac{y}{2\sqrt{t}} + \sqrt{\left(p+M+\frac{1}{k_p}\right)t}\right)\right]$$

$$D_3 = \frac{1}{2}\left[\operatorname{erfc}\left(\frac{y}{2\sqrt{t}} - \sqrt{\left(M+\frac{1}{k_p}\right)t}\right)e^{-y\sqrt{M+\frac{1}{k_p}}} + \operatorname{erfc}\left(\frac{y}{2\sqrt{t}} + \sqrt{\left(M+\frac{1}{k_p}\right)t}\right)e^{y\sqrt{M+\frac{1}{k_p}}}\right]$$

$$D_4 = \frac{e^{ct}}{2}\left[\operatorname{erfc}\left(\frac{y}{2\sqrt{t}} - \sqrt{\left(c+M+\frac{1}{k_p}\right)t}\right)e^{-y\sqrt{c+M+\frac{1}{k_p}}} + \operatorname{erfc}\left(\frac{y}{2\sqrt{t}} + \sqrt{\left(c+M+\frac{1}{k_p}\right)t}\right)e^{y\sqrt{c+M+\frac{1}{k_p}}}\right]$$

$$D_5 = \frac{e^{wt}}{2}\left[e^{-y\sqrt{w+M+\frac{1}{k_p}}}\operatorname{erfc}\left(\frac{y}{2\sqrt{t}} - \sqrt{\left(w+M+\frac{1}{k_p}\right)t}\right) + e^{y\sqrt{w+M+\frac{1}{k_p}}}\operatorname{erfc}\left(\frac{y}{2\sqrt{t}} + \sqrt{\left(w+M+\frac{1}{k_p}\right)t}\right)\right]$$

$$D_6 = \frac{e^{pt}}{2}\left[e^{-y\sqrt{Pr}\sqrt{p+\phi}}\operatorname{erfc}\left(\frac{y\sqrt{Pr}}{2\sqrt{t}} - \sqrt{(p+\phi)t}\right) + e^{y\sqrt{Pr}\sqrt{p+\phi}}\operatorname{erfc}\left(\frac{y\sqrt{Pr}}{2\sqrt{t}} + \sqrt{(p+\phi)t}\right)\right]$$

$$D_7 = \frac{1}{2}\left[\operatorname{erfc}\left(\frac{y\sqrt{Pr}}{2\sqrt{t}} - \sqrt{\phi t}\right)e^{-y\sqrt{Pr}\sqrt{\phi}} + \operatorname{erfc}\left(\frac{y\sqrt{Pr}}{2\sqrt{t}} + \sqrt{\phi t}\right)e^{y\sqrt{Pr}\sqrt{\phi}}\right]$$

$$D_8 = \frac{e^{ct}}{2}\left[\operatorname{erfc}\left(\frac{y\sqrt{Pr}}{2\sqrt{t}} - \sqrt{(c+\phi)t}\right)e^{-y\sqrt{Pr}\sqrt{c+\phi}} + \operatorname{erfc}\left(\frac{y\sqrt{Pr}}{2\sqrt{t}} + \sqrt{(c+\phi)t}\right)e^{y\sqrt{Pr}\sqrt{c+\phi}}\right]$$

$$D_9 = \frac{1}{2}\left[e^{-y\sqrt{Sc}\sqrt{K}}\operatorname{erfc}\left(\frac{y\sqrt{Sc}}{2\sqrt{t}} - \sqrt{Kt}\right) + e^{y\sqrt{Sc}\sqrt{K}}\operatorname{erfc}\left(\frac{y\sqrt{Sc}}{2\sqrt{t}} + \sqrt{Kt}\right)\right]$$

$$D_{10} = \frac{e^{ct}}{2}\left[e^{-y\sqrt{Sc}\sqrt{c+K}}\operatorname{erfc}\left(\frac{y\sqrt{Sc}}{2\sqrt{t}} - \sqrt{(c+K)t}\right) + e^{y\sqrt{Sc}\sqrt{c+K}}\operatorname{erfc}\left(\frac{y\sqrt{Sc}}{2\sqrt{t}} + \sqrt{(c+K)t}\right)\right]$$

$$D_{11} = \frac{e^{wt}}{2}\left[\operatorname{erfc}\left(\frac{y\sqrt{Sc}}{2\sqrt{t}} - \sqrt{(w+K)t}\right)e^{-y\sqrt{Sc}\sqrt{w+K}} + \operatorname{erfc}\left(\frac{y\sqrt{Sc}}{2\sqrt{t}} + \sqrt{(w+K)t}\right)e^{y\sqrt{Sc}\sqrt{w+K}}\right]$$

$$B_1 = e^{at}\left[\operatorname{erf}\left(\sqrt{\left(a+M+\frac{1}{k_p}\right)t}\right)\sqrt{\left(a+M+\frac{1}{k_p}\right)} + \frac{1}{\sqrt{\pi t}}e^{-\left(a+M+\frac{1}{k_p}\right)t}\right]$$

$$B_2 = e^{pt}\left[-\sqrt{\left(p+M+\frac{1}{k_p}\right)}\operatorname{erf}\left(\sqrt{\left(p+M+\frac{1}{k_p}\right)t}\right) - \frac{1}{\sqrt{\pi t}}e^{-\left(p+M+\frac{1}{k_p}\right)t}\right]$$

$$B_3 = \left[\operatorname{erf}\left(\sqrt{\left(M+\frac{1}{k_p}\right)t}\right)\sqrt{\left(M+\frac{1}{k_p}\right)} - \frac{1}{\sqrt{\pi t}}\mathrm{e}^{-\left(M+\frac{1}{k_p}\right)t}\right]$$

$$B_4 = \mathrm{e}^{ct}\left[-\sqrt{\left(c+M+\frac{1}{k_p}\right)}\operatorname{erf}\left(\sqrt{\left(c+M+\frac{1}{k_p}\right)t}\right) - \frac{1}{\sqrt{\pi t}}\mathrm{e}^{-\left(c+M+\frac{1}{k_p}\right)t}\right]$$

$$B_5 = \mathrm{e}^{wt}\left[-\operatorname{erf}\left(\sqrt{\left(w+M+\frac{1}{k_p}\right)t}\right)\sqrt{\left(w+M+\frac{1}{k_p}\right)} - \frac{1}{\sqrt{\pi t}}\mathrm{e}^{-\left(w+M+\frac{1}{k_p}\right)t}\right]$$

$$B_6 = \mathrm{e}^{pt}\left[-\operatorname{erf}\left(\sqrt{(p+\phi)t}\right)\sqrt{Pr(p+\phi)} - \frac{\sqrt{Pr}}{\sqrt{\pi t}}\mathrm{e}^{-(p+\phi)t}\right]$$

$$B_7 = \left[-\operatorname{erf}\left(\sqrt{\phi t}\right)\sqrt{\phi Pr} - \frac{\sqrt{Pr}}{\sqrt{\pi t}}\mathrm{e}^{-\phi t}\right]$$

$$B_8 = \mathrm{e}^{ct}\left[-\operatorname{erf}\left(\sqrt{(c+\phi)t}\right)\sqrt{Pr(c+\phi)} - \frac{\sqrt{Pr}}{\sqrt{\pi t}}\mathrm{e}^{-(c+\phi)t}\right]$$

$$B_9 = \left[-\operatorname{erf}\left(\sqrt{Kt}\right)\sqrt{KSc} - \frac{\sqrt{Sc}}{\sqrt{\pi t}}\mathrm{e}^{-Kt}\right]$$

$$p = \frac{M-\phi Pr+\frac{1}{k_p}}{Pr-1}, \quad w = \frac{M-KSc+\frac{1}{k_p}}{Sc-1}$$

$$B_{10} = \mathrm{e}^{ct}\left[-\sqrt{Sc(c+K)}\operatorname{erf}\left(\sqrt{(c+K)t}\right) - \frac{\sqrt{Sc}}{\sqrt{\pi t}}\mathrm{e}^{-(c+K)t}\right], \quad N_1 = \frac{Gr_1}{Pr-1}$$

$$B_{11} = \mathrm{e}^{wt}\left[-\operatorname{erf}\left(\sqrt{(w+K)t}\right)\sqrt{Sc(w+K)} - \frac{\sqrt{Sc}}{\sqrt{\pi t}}\mathrm{e}^{-(w+K)t}\right],$$

$$N_2 = \frac{Gr_1}{Sc-1}, N_3 = \frac{Gm_1}{Sc-1}$$

$$b = \frac{Q_1 Pr}{Sc-Pr}, \quad c = \frac{\phi Pr - KSc}{Sc-Pr}, \quad Gr_1 = Gr\cos\alpha, \quad Gm_1 = Gm\cos\alpha$$

5 Results and Discussion

In this flow problem, the consequences of the different profiles are discussed through graphs in Figs. 1, 2, 3, 4, 5, 6, 7, 8, 9, 10, 11, and 12 for both heating and cooling of the plates. These leads are identified to illustrate the results of several

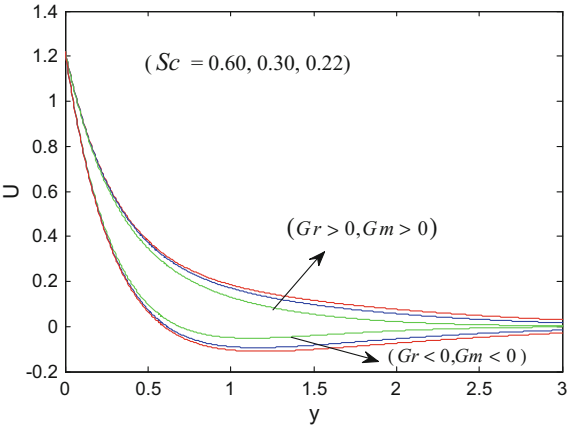

Fig. 1 Velocity results for several values of Sc and $Pr = 0.71$, $K_p = 0.1$, $Q_1 = 5$, $k = 0.5$, $M = 1$, $t = 0.4$, $a = 0.5$, $\phi = 5, \alpha = \pi/3$

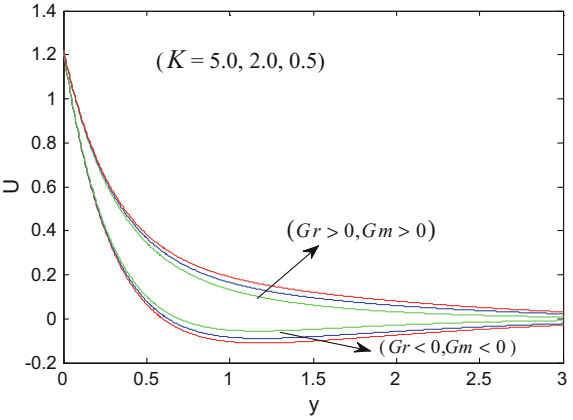

Fig. 2 Effect of k on velocity for different values of k and $Sc = 0.22$, $K_p = 0.1$, $Q_1 = 5$, $M = 1$, $Pr = 0.71$, $t = 0.4$, $a = 0.5$, $\phi = 5, \alpha = \pi/3$

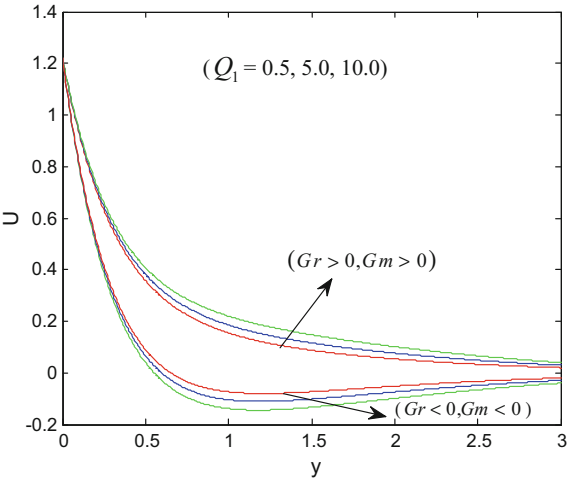

Fig. 3 Results of Q_1 on velocity for various values of Q_1 and $Sc = 0.22$, $k = 0.5$, $K_p = 0.1$, $Pr = 0.71$, $M = 1$, $t = 0.4$, $a = 0.5$, $\phi = 5, \alpha = \pi/3$

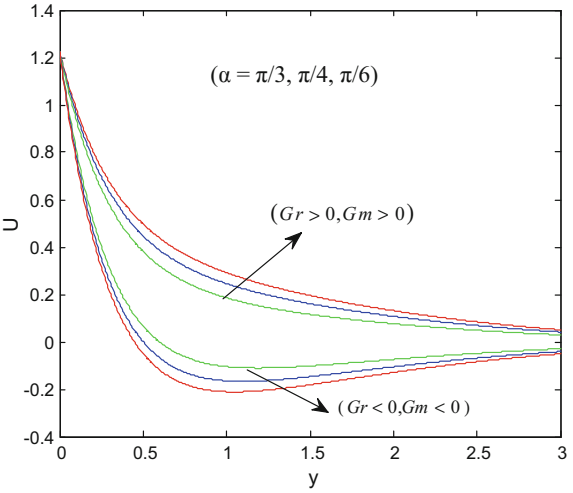

Fig. 4 Velocity effects for several values of α and $Sc = 0.22$, $K_p = 0.1$, $k = 0.5$, $Q_1 = 5$, $Pr = 0.71$, $t = 0.4$, $M = 1$, $a = 0.5$, $\phi = 5$

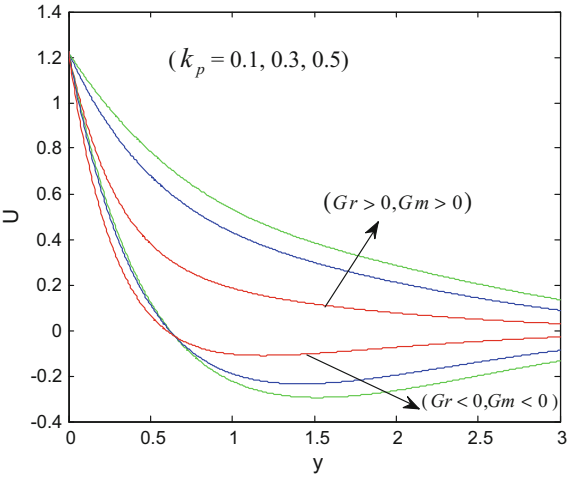

Fig. 5 Effects of K_p on velocity for various values of K_p and $k = 0.5$, $Sc = 0.22$, $Q_1 = 5, M = 1, Pr = 0.71$, $t = 0.4$, $a = 0.5$, $\phi = 5, \alpha = \pi/3$

physical arguments involved in this flow problem such as angle of inclination (α), magnetic parameter (M), parameter of heat absorption (ϕ), parameter of radiation absorption (), Schmidt number (Sc), parameter of chemical reaction (k), Prandtl number (Pr), mass Grashof number (Gm), thermal Grashof number (Gr), time (t) on profiles of velocity, temperature, concentration, and the velocity gradient.

The consequences of velocity for several values of various arguments are studied and presented in Figs. 1, 2, 3, 4, 5, and 6 for the both heating ($Gr = -2$, $Gm = -4$) and cooling ($Gr = 2$, $Gm = 4$) plates. Figures 1, 2, 3, and 4 depict the results of velocity due to variation in Sc, k, Q_1, and α. It is identified that the velocity raise for the cooling plate, and it falls decreases for the heating plate with the fall of Sc, k, α and with the raise of Q_1. The profile of velocity for various values of K_p and M is

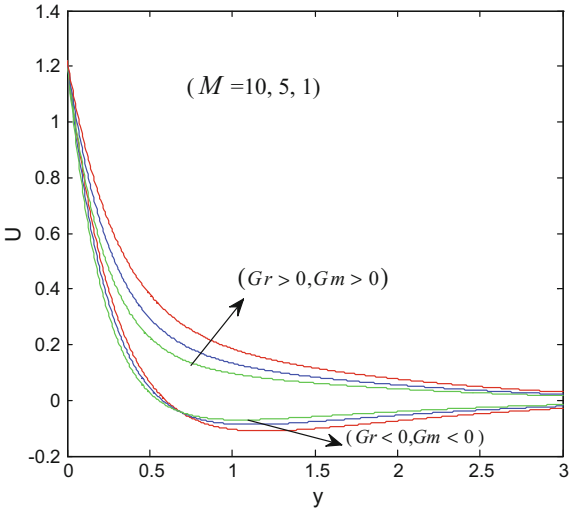

Fig. 6 Velocity results for various values of M and $Sc = 0.22$, $k = 0.5$, $K_p = 0.1$, $Q_1 = 0.5, Pr = 0.71$, $\phi = 5$, $t = 0.4$, $a = 0.5$, $\alpha = \pi/3$

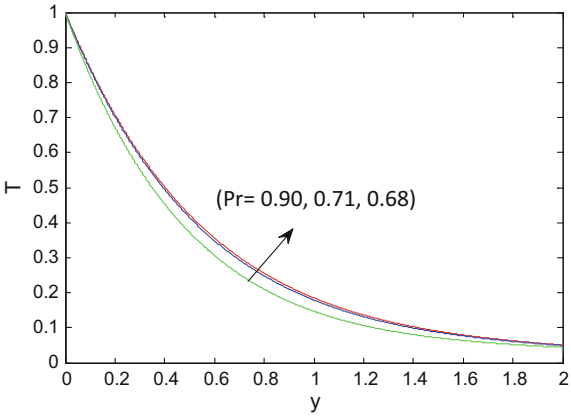

Fig. 7 Temperature results for several values of Pr and $k = 0.5$, $t = 0.4$, $Q_1 = 0.5$, $\phi = 5$, $Sc = 0.22$

discussed in Figs. 5 and 6 at $t = 0.4$. From Fig. 5, it is found that the velocity raises for cooling plate, whereas it raises near the plate and falls with a point of separation moving away from the plate for heating plate with the increase of K_p. Figure 6 describes the effect of M at t = 0.4; it is noticed that the velocity raises for cooling plate, whereas it falls near the plate and raises with a point of separation moving away from the plate for heating plate with the fall of M.

The leads of profiles of temperature for several values of various parameters are studied and discussed in Figs. 7, 8, 9, and 10. From these figures, it is identified that there is a raise in temperature with the fall of Pr, ϕ and with the raise of $Q1$, t.

The consequences of concentration profile for several values of various arguments are studied and presented in Figs. 11 and 12. Figures 11 and 12 reveal that there is a raise in concentration with the fall of Sc, k.

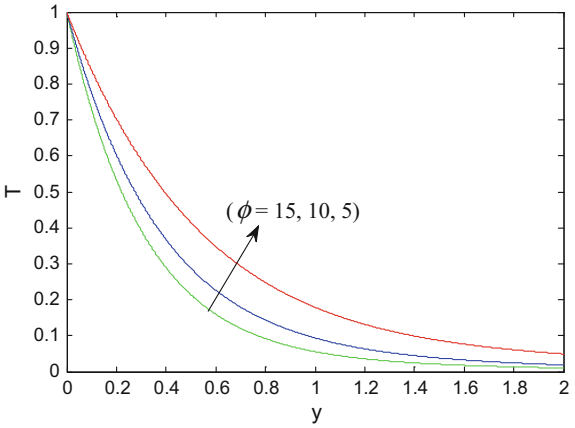

Fig. 8 Effects of temperature for different values of ϕ and $Sc = 0.22$, $t = 0.4$, $k = 0.5$, $Q_1 = 0.5, Pr = 0.71$

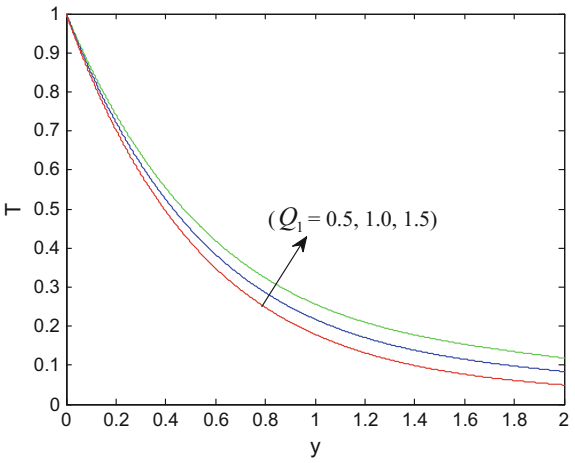

Fig. 9 Temperature effects for different values of Q_1 and $Sc = 0.22$, $t = 0.4$, $k = 0.5$, $\phi = 5$, $Pr = 0.71$

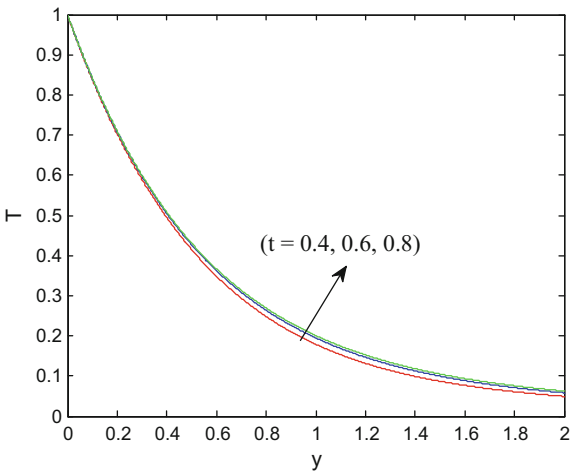

Fig. 10 Temperature leads for several values t and $Sc = 0.22$, $k = 0.5$, $\phi = 5$, $Q_1 = 0.5$, $Pr = 0.71$

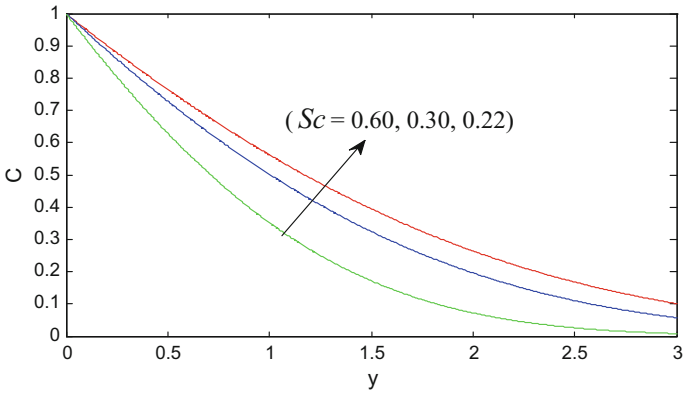

Fig. 11 Concentration effects for several values of *Sc* and $t = 0.4$, $k = 0.5$

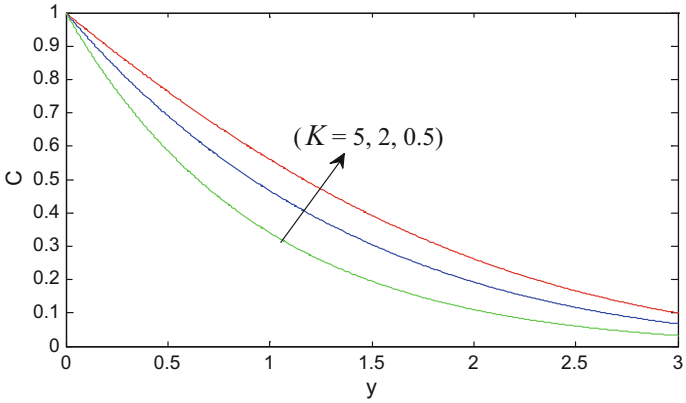

Fig. 12 Results of *k* on concentration for different values of *k* and $Sc = 0.22$

The gradient of velocity in terms of skin friction for several values of various arguments is discussed and is presented in Tables 1 and 2 for both heating ($Gr = -2$, $Gm = -4$) and cooling ($Gr = 2$, $Gm = 4$) plates. From Table 1, it is identified that there is a raise in skin friction with the raise of *Pr*, *Sc*, Q_1; also it decreases with raise of ϕ, *K*, *M* for cooling plate, and an opposite phenomenon was observed for heating plate and is shown in Table 2.

The same above results are noticed for both the cases in the absence of angle of inclination and parameter of the permeability of the porous medium. Hence, the results are in good agreement with the results of Vijaykumar et al. (2013).

Table 1 Cooling plates

Pr	Sc	ϕ	K	Q_1	M	A	Skin friction (for cooling plate) $\alpha = \pi/3$, $k_p = 0.1$	Skin friction (for cooling plate) $\alpha = 0$, $k_p \approx 0$
0.68	0.22	10	0.1	0.1	3	0.5	6.918657993	6.349229616
0.71	0.22	10	0.1	0.1	3	0.5	7.140507574	7.792928778
0.9	0.22	10	0.1	0.1	3	0.5	7.845391345	8.115749037
0.68	0.3	10	0.1	0.1	3	0.5	13.18412857	12.88017077
0.68	0.6	10	0.1	0.1	3	0.5	21.68903451	20.63490472
0.68	0.22	11	0.1	0.1	3	0.5	6.774587688	6.061089007
0.68	0.22	12	0.1	0.1	3	0.5	6.749025004	6.009963639
0.68	0.22	10	0.2	0.1	3	0.5	6.878243197	6.268400025
0.68	0.22	10	0.3	0.1	3	0.5	6.838386267	6.188686165
0.68	0.22	10	0.1	0.2	3	0.5	7.347101708	7.206117046
0.68	0.22	10	0.1	0.3	3	0.5	7.775545423	8.063004476
0.68	0.22	10	0.1	0.1	4	0.5	6.530715543	6.010236618
0.68	0.22	10	0.1	0.1	5	0.5	6.486863883	5.864913622

Table 2 Heating plates

Pr	Sc	ϕ	K	Q_1	M	A	Skin friction (for heating plate) $\alpha = \pi/3$, $k_p = 0.1$	Skin friction (for heating plate) $\alpha = 0$, $k_p \approx 0$
0.68	0.22	10	0.1	0.1	3	0.5	2.057514746	2.373056877
0.71	0.22	10	0.1	0.1	3	0.5	1.835665165	1.816756039
0.9	0.22	10	0.1	0.1	3	0.5	1.358104638	1.205914537
0.68	0.3	10	0.1	0.1	3	0.5	−4.20795583	−4.90399803
0.68	0.6	10	0.1	0.1	3	0.5	−5.015729484	−5.93614952
0.68	0.22	11	0.1	0.1	3	0.5	2.201585051	2.684916268
0.68	0.22	12	0.1	0.1	3	0.5	2.227147735	2.7137909
0.68	0.22	10	0.2	0.1	3	0.5	2.097929542	2.412227286
0.68	0.22	10	0.3	0.1	3	0.5	2.137786471	2.512513427
0.68	0.22	10	0.1	0.2	3	0.5	1.629071031	1.229944307
0.68	0.22	10	0.1	0.3	3	0.5	1.200627316	1.086831737
0.68	0.22	10	0.1	0.1	4	0.5	2.771673392	2.892152317
0.68	0.22	10	0.1	0.1	5	0.5	3.130764406	3.452714668

6 Conclusion

For this flow problem, the consequences of heat source parameter, mass diffusion, chemical reaction, and radiation absorption with the constant temperature are discussed in the presence of applied uniform magnetic field on a magnetohydrodynamic unsteady convective free flow with mass and heat transfer past an inclined

vertical porous plate which is accelerated exponentially in a porous medium. The dimensionless governing equations for velocity, temperature, and concentration are solved by the Laplace transform technique. The effects of velocity, temperature, concentration, and skin friction are discussed for both ammonia and water vapor, and the conclusions are as follows:

- Velocity raises for the cooling plate, and it falls for the heating plate with the fall of chemical reaction parameter (K) and with the raise of radiation absorption parameter (Q_1).
- Temperature raises with the fall in heat absorption parameter (ϕ), and the concentration raises with the raise in time (t).
- Skin friction increases for cooling plate and decreases for heating plate with the increase in Sc and Q_1.

The same results are observed in the absence of inclined plate and permeability of the porous medium. Hence, these results are in good agreement with results of Vijaykumar (2013).

References

Al-Odat MQ, Al-Azab TA (2007) Chemical reaction influence on transient MHD free convection over a moving vertical plate. Emirates J Eng Res 12:15–21

Chamkha AJ (2004) Unsteady MHD convective heat and mass transfer past a semi-infinite vertical permeable moving plate with heat absorption. Int J Eng Sci 42:217–230

Kafousias NG, Raptis AA (1981) Mass transfer and free convection effects on the flow past an accelerated vertical infinite plate with variable suction or injection. Revue Roummaine Science des Techniques – Mecanique Appliquee 26:11–22

Makinde OD, Sibanda P (2008) Magnetohydrodynamic mixed convective flow and heat and mass transfer past a vertical plate in a porous medium with constant wall suction. ASME J Heat Transfer 130(11260):1–8

Muthucumaraswamy R, Raj MS, Subramanian VSA (2010) Heat transfer consequences on vertical accelerated plate with varying temperature and mass flux. ACTA Tech Conviniensis Bull Eng 3:31–34

Raptis A, Perdikis C (1985) Unsteady flow through a porous medium in the presence of free convection. Int Commun Heat Mass Transfer 12(6):697–704

Raptis A, Massalas CV (1998) Magnetohydrodynamic flow past a plate by the presence of radiation. Heat Mass Transf 34:107–109

Vajravelu K, Hadjinicolaou A (1997) Convective heat transfer in an electrically conducting fluid at a stretching surface with uniform free stream. Int J Eng Sci 35:1237–1244

Vijaykumar AG, Bhanumathi D, Vijaykumar Varma S, Rajesh Yadav Y (2013) Effect of the heat source, radiation absorption and chemical reaction on the unsteady MHD free convective flow past an exponentially accelerated vertical moving plate. Adv Appl Fluid Mech 14:147–167

Radiation Effect on MHD Convective Flow of Nanofluids over an Exponentially Accelerated Moving Ramped Temperature Plate

S.M. Hussain, H.J. Joshi and G.S. Seth

Abstract The effect of thermal radiation on magnetohydrodynamic free convective flow of incompressible and viscous nanofluids, which is electrically conducting, over an exponentially accelerated moving ramped temperature plate is studied. The water-based nanofluids which contain the nanoparticles of copper, alumina, and titanium oxide are taken into consideration. The mathematical model of the problem is formulated by applying the nanoparticle volume fraction model. The governing equations for the flow, subjected to the associated conditions, have been solved analytically by Laplace transform method. Expressions of nanofluid velocity, temperature, shear stress, and Nusselt number have been obtained in compact form. Effects of controlling physical parameters on nanofluid velocity and temperature have been displayed using various graphs, whereas, for the engineering perspective, numerical values of shear stress are presented in table.

1 Introduction

Due to the widespread applications in industry and public endeavor, the study of nanofluids has engrossed enormous attention of several investigators engaged in the area of nanotechnology. Initially, the term nanofluid was coined by Choi (1995), referring to a base fluid embedded with particles of diameter less than 100 nm. The conventional fluids, i.e., water, polymer solutions, ethylene glycol, oils, and other

S.M. Hussain (✉)
Department of Mathematics, OP Jindal University, Raigarh 496109, India
e-mail: hussain.modassir@yahoo.com

H.J. Joshi
Department of Physics, OP Jindal University, Raigarh 496109, India
e-mail: hitesh.joshi@opju.ac.in

G.S. Seth
Department of Applied Mathematics, Indian Institute of Technology (Indian School of Mines), Dhanbad 826004, Jharkhand, India
e-mail: gsseth_ism@yahoo.com

M.K. Singh et al. (eds.), *Applications of Fluid Dynamics*, Lecture Notes in Mechanical Engineering, https://doi.org/10.1007/978-981-10-5329-0_3

lubricants, have feeble heat transfer characteristics because of their feeble thermal conductivity. Moreover, thermal conductivity of the base fluid can be enhanced by mixing small-size metallic particles in the fluid, as the thermal conductivity of the metals is typically higher than the fluid. Nanofluid being a mixture of nanoparticles and the base fluid is an innovative type of energy transport fluid, and their novel property makes them tremendously useful in different processes of heat transfer including microelectronics, automobiles, hybrid-powered engines, fuel cells, domestic refrigerator, nuclear reactor coolant, pharmaceutical processes. Choi (1995) was the first who pointed out that "base fluid's thermal conductivity may be improved radically by the uniform dispersion of nanosized particles into a fluid." This concept prompted many researchers toward nanofluids, and abundant studies, analyzing the thermal properties of nanofluids, have been carried out. Notable research studies reporting the improvement in the thermal conductivity of fluids due to suspension of nanoparticles and its frequent applications have been presented by Eastman et al. (1997), Kang Ki and Choi (2004), and Jang and Choi (2007).

The hydromagnetic nanofluids possess both the liquid and magnetic characteristics and are known to have enthralling relevance to magneto-optical wavelength filters, ink float separation, optical switches, optical gratings, nonlinear optical materials, etc. The magnetonanofluids have wide range of applications in drug delivery for cancer treatment. Following this, several researchers, namely Hamad and Pop (2011), Chamkha and Aly (2011), and Hayat et al. (2016), reported their investigation on the problems of MHD convective flow of nanofluids considering different geometries and configurations.

Various engineering processes such as gas turbines, various propulsion devices for aircraft, nuclear power plants, missile's reentry, space vehicles, rocket combustion, satellites, gas-cooled nuclear reactors take place at high temperatures where the role of thermal radiation in the overall surface heat transfer is of utmost importance. This fact has encouraged many researchers to undertake the effect of thermal radiation on hydromagnetic convective flow of nanofluids under different geometries and configurations. Notable research studies are due to Rashidi et al. (2014), Haq et al. (2015), and Das et al. (2015).

In all the aforementioned investigations, numerical/analytical solutions were obtained by considering no discontinuity in thermal conditions. But, majority of the problems of practical interest require the velocity and temperature to satisfy discontinuous or arbitrary conditions at the boundary. Few relevant studies are due to Chandran et al. (2005), Seth et al. (2011, 2013, 2014), and Khalid et al. (2015).

Intent of present paper is to analyze the influence of thermal radiation on MHD free convective flow of electrically conducting, incompressible, and viscous nanofluids near a ramped temperature plate which is moving with an exponential velocity.

2 Problem Formulation and Its Solution

Consider unsteady MHD free convection flow of optically thick radiating nanofluids over an exponentially accelerated vertical plate having ramped temperature profile as shown in Fig. 1. The x'-axis is along the flow, and y'-axis is perpendicular to it. A uniform magnetic field of intensity B_0 is applied, parallel to y'-axis. Initially, i.e., for $t' \leq 0$, there is no movement in fluid and plate, and both are kept as uniform temperature δ'_∞. Thereafter, the plate is provided with an exponential velocity $U_0 e^{a't'}$ in the x' direction aligned with the gravitational field.

The plate temperature is changed to $\delta'_\infty + (\delta'_w - \delta'_\infty)t'/t_0$. Subsequently, i.e., at time $t' > t_0$, plate is preserved at uniform temperature δ'_w. Cu–water, Al_2O_3–water, and TiO_2–water nanofluids are considered. The shape and size of nanoparticles are assumed to be uniform. We have also assumed the thermal equilibrium between base fluid and nanoparticles. Also, no slip mechanism is involved.

The properties of nanoparticles and base fluid are given in Table 1.

The plate is considered to be electrically non-conducting and of inestimable level in x' direction, so all quantities excluding pressure are the functions of only t' and y'. Since for the flows of liquid metals and partially ionized fluids, the value of magnetic Reynolds number is very small; consequently, the induced magnetic field can comfortably be ignored. Also, the effect of electric field, owing to polarization, is neglected because there is no electric field applied.

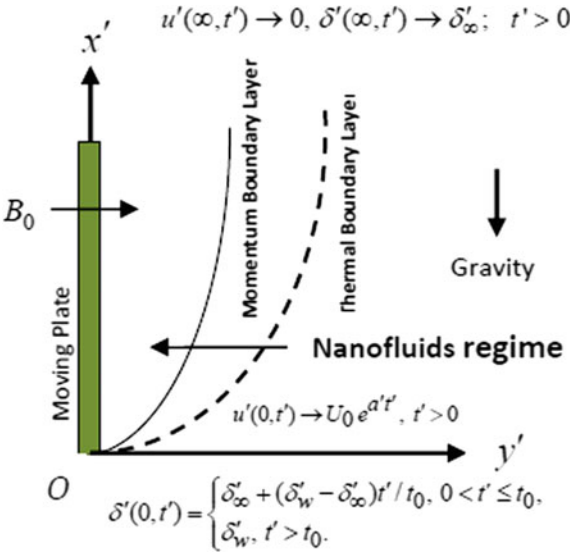

Fig. 1 Geometry of the problem

Table 1 Thermo-physical properties of water and nanoparticles (Oztop and Abu-Nada 2008)

	ρ (kg/m^3)	c_p (J/kg K)	k (W/m K)	$\beta \times 10^5$ (K^{-1})	ϕ	σ (S/m)
Water (base fluid)	997.1	4179	0.613	21	0.00	5.5×10^{-6}
Cu (copper)	8933	385	401	1.67	0.05	59.6×10^6
Al_2O_3 (alumina)	3970	765	40	0.85	0.15	35×10^6
TiO_2 (titanium oxide)	4250	686.2	8.9538	0.90	0.20	2.5×10^6

Under the conjecture made in this problem and Boussinesq approximation, the equations for unsteady MHD free convective flow of electrically conducting, viscous, and incompressible nanofluids taking into the consideration the effect of thermal radiation reduce to

$$\rho_{nf}\frac{\partial u'}{\partial t'} = \mu_{nf}\frac{\partial^2 u'}{\partial y'^2} - \sigma_{nf}B_0^2 u' + g(\rho\beta)_{nf}\left(\delta' - \delta'_\infty\right), \tag{1}$$

$$\left(\rho c_p\right)_{nf}\frac{\partial \delta'}{\partial t'} = k_{nf}\frac{\partial^2 \delta'}{\partial y'^2} - \frac{\partial q'_r}{\partial y'}, \tag{2}$$

where $u', \delta', \rho_{nf}, \sigma_{nf}, g, \mu_{nf}, \beta_{nf}, \left(\rho c_p\right)_{nf}, k_{nf}$ and q'_r are the component of nanofluid velocity in x' direction, temperature of nanofluid, density of nanofluid, electrical conductivity of nanofluid, acceleration due to gravity, dynamic viscosity of nanofluid, thermal expansion coefficient of nanofluid, heat capacitance of nanofluid, thermal conductivity of nanofluid, and radiative heat flux, respectively.

For the nanofluids, the expressions of $\rho_{nf}, \mu_{nf}, \sigma_{nf}, (\rho\beta)_{nf}$ and $\left(\rho c_p\right)_{nf}$ are given as (Khalid et al. 2015; Das et al. 2015)

$$\left.\begin{aligned} &\rho_{nf} = (1-\phi)\rho_f + \phi\rho_s, \quad \mu_{nf} = \mu_f(1-\phi)^{-2.5}, \\ &(\rho\beta)_{nf} = (1-\phi)(\rho\beta)_f + \phi(\rho\beta)_s, \\ &\left(\rho c_p\right)_{nf} = (1-\phi)\left(\rho c_p\right)_f + \phi\left(\rho c_p\right)_s, \\ &\sigma_{nf} = \sigma_f\left[1 + \frac{3(\sigma-1)\phi}{(\sigma+2)-(\sigma-1)\phi}\right], \quad \sigma = \frac{\sigma_s}{\sigma_f}, \end{aligned}\right\} \tag{3}$$

where $\phi, \rho_f, \rho_s, \mu_f, \beta_f, \beta_s, \left(\rho c_p\right)_f, \left(\rho c_p\right)_s, \sigma_f$ and σ_s are, respectively, the solid volume fraction of nanoparticle, density of base fluid, density of nanoparticle, viscosity of base fluid, thermal expansion coefficient of base fluid, thermal expansion coefficient of nanoparticle, heat capacitance of base fluid, heat capacitance of nanoparticle, electrical conductivity of base fluid, and electrical conductivity of nanoparticle. As pointed out by Oztop and Abu-Nada (2008), the expressions presented in Eq. (3) are limited to spherical nanoparticles, whereas it is not valid for other shape of nanoparticles. The model for effective thermal conductivity of the nanofluid, i.e., k_{nf} for the spherical nanoparticles given by Hamilton and Crosser model followed by Oztop and Abu-Nada (2008) is expressed as

$$k_{nf} = k_f \left[\frac{k_s + 2k_f - 2\phi(k_f - k_s)}{k_s + 2k_f + \phi(k_f - k_s)} \right], \tag{4}$$

where k_s and k_f are respectively, thermal conductivity of nanoparticles and the base fluid.

The associated conditions for the model are given by

$$\left.\begin{array}{l} u' = 0, \delta' = \delta'_\infty \quad \text{for } y' \geq 0 \text{ and } t' \leq 0, \\ u' = U_0 e^{a't'} \quad \text{at } y' = 0 \text{ for } t' > 0, \\ \delta' = \delta'_\infty + (\delta'_w - \delta'_\infty) t'/t_0 \quad \text{at } y' = 0 \text{ for } 0 < t' \leq t_0, \\ \delta' = \delta'_w \quad \text{at } y' = 0 \text{ for } t' > t_0, \\ u' \to 0, \delta' \to \delta'_\infty \quad \text{as } y' \to \infty \text{ for } t' > 0. \end{array}\right\} \tag{5}$$

The expression for radiative heat flux for an optically thick media adopting Rossel approximation is depicted as

$$q'_r = -\frac{4\sigma^*}{3k^*} \frac{\partial \delta'^4}{\partial y'}, \tag{6}$$

where k^* is the mean absorption coefficient, and σ^* is the Stefan–Boltzmann constant. The variation of fluid temperature δ' in the thermal boundary layer and fluid temperature δ'_∞ in the free stream is considered to be adequately small, so that Eq. (6) can be linearized by expressing δ'^4 in Taylor series about δ'_∞ which, after omitting out second- and higher-order terms, takes the following form

$$\delta'^4 \cong 4\delta'^3_\infty \delta' - 3\delta'^4_\infty, \tag{7}$$

Making use of Eqs. (6) and (7) in (2), we get

$$(\rho c_p)_{nf} \frac{\partial \delta'}{\partial t'} = \left(k_{nf} + \frac{16\sigma^* \delta'^3_\infty}{3k^*} \right) \frac{\partial^2 \delta'}{\partial y'^2}. \tag{8}$$

To convert Eqs. (1) and (8) into dimensionless form, following dimensionless variables and parameters are mentioned

$$y = \frac{y'}{U_0 t_0}, \quad u = \frac{u'}{U_0}, \quad t = \frac{t'}{t_0}, \quad \delta = \frac{(\delta' - \delta'_\infty)}{(\delta'_\omega - \delta'_\infty)}, \quad a = \frac{a' v_f}{U_0^2}. \tag{9}$$

Equations (1) and (8), in dimensionless form, become

$$\frac{\partial u}{\partial t} = a_1 \frac{\partial^2 u}{\partial y^2} - a_2 M^2 u + a_3 G_r \delta, \tag{10}$$

$$\frac{\partial \delta}{\partial t} = \frac{1}{\alpha_2}\frac{\partial^2 \delta}{\partial y^2}, \tag{11}$$

where

$$\left.\begin{aligned}
&\phi_1 = \left[(1-\phi) + \phi\left(\frac{\rho_s}{\rho_f}\right)\right], \quad \phi_2 = \left[1 + \frac{3(\sigma-1)\phi}{(\sigma+2)-(\sigma-1)\phi}\right], \quad \sigma = \frac{\sigma_s}{\sigma_f}, \\
&\phi_3 = \left[(1-\phi) + \phi\frac{(\rho\beta)_s}{(\rho\beta)_f}\right], \quad \phi_4 = \left[(1-\phi) + \phi\frac{\left(\rho c_p\right)_s}{\left(\rho c_p\right)_f}\right], \quad a_1 = \frac{1}{(1-\phi)^{2.5}\phi_1}, \\
&a_2 = \frac{\phi_2}{\phi_1}, \quad a_3 = \frac{\phi_3}{\phi_1}, \quad \alpha_1 = \frac{k_{nf}}{k_f}, \quad M^2 = \frac{\sigma_f B_0^2 \upsilon_f}{\rho_f U_0^2}, \quad P_r = \frac{\left(\rho \upsilon c_p\right)_f}{k_f}, \\
&Tr = \left(\frac{16\sigma^* \delta_\infty'^3}{3k^* k_f}\right), \quad G_r = \left[\frac{g\beta_f \upsilon_f \left(\delta_w' - \delta_\infty'\right)}{U_0^3}\right], \quad \alpha_2 = \left[\frac{P_r \phi_4}{\alpha_1 + T_r}\right],
\end{aligned}\right\} \tag{12}$$

where M^2, P_r, Tr and G_r are, respectively, the magnetic parameter, Prandtl number, thermal radiation parameter, and Grashof number, and ϕ_i $(i = 1, 2, 3, 4)$ are the functions which depend on the thermo-physical properties of nanoparticles and base fluid.

The characteristic time t_0 may be defined as $t_0 = \upsilon_f / U_0^2$, where U_0 is the uniform velocity.

The associated conditions (5) in dimensionless, reduce to

$$\left.\begin{aligned}
&u = 0, \quad \delta = 0 \quad \text{for } t \le 0, \text{ and } y \ge 0 \\
&u = \mathrm{e}^{at} \quad \text{at } y = 0 \text{ for } t > 0, \\
&\delta = t \quad \text{at } y = 0 \text{ for } 0 < t \le 1, \\
&\delta = 1 \quad \text{at } y = 0 \text{ for } t > 1, \\
&u \to 0, \delta \to 0 \quad \text{as } y \to \infty \text{ for } t > 0.
\end{aligned}\right\} \tag{13}$$

To find the exact solution, the set of dimensionless equations (10) and (11) together with associated conditions (13) is solved analytically employing the Laplace transform method, and solutions for the nanofluid velocity $u(y,t)$ and the nanofluid temperature $\delta(y,t)$ are obtained and are given as

$$\begin{aligned}
u(y,t) = &\frac{\mathrm{e}^{at}}{2} f_2(y, a_4, a_5, a, t) \\
&+ \frac{\alpha_3}{2\alpha_4}\{F_1(y,t) - H(t-1)F_1(y, t-1)\},
\end{aligned} \tag{14}$$

$$\delta(y,t) = \delta_1(y,t) - H(t-1)\delta(y, t-1), \tag{15}$$

where

$$a_4 = 1/a_1, \quad a_5 = M^2 a_2 \sin^2\theta, \quad \alpha_3 = G_r a_3 a_4/(\alpha_2 - a_4),$$
$$\alpha_4 = a_4 a_5/(\alpha_2 - a_4),$$
$$F_1(y,t) = \frac{e^{\alpha_4 t}}{\alpha_4}\{f_2(y,a_4,a_5,\alpha_4,t) - f_2(y,\alpha_2,0,\alpha_4,t)\}$$
$$- f_1(y,a_4,a_5,\alpha_4,t) - 2f_3(y,\alpha_2,\alpha_4,t), \delta_1(y,t)$$
$$= f_3(y,\alpha_2,0,t).$$

The expressions for $f_i(i = 1,2,3)$ are presented in Appendix.

3 Shear Stress and Nusselt Number

Expressions of shear stress τ and Nusselt number Nu are mentioned in the following forms

$$\tau = e^{at} f_5(a_4,a_5,a,t) + \frac{\alpha_3}{\alpha_4}\{F_2(t) - H(t-1)F_2(t-1)\}, \tag{16}$$

$$Nu = 2\sqrt{\frac{\alpha_2}{\pi}}\left\{\sqrt{t} - H(t-1)\sqrt{t-1}\right\}, \tag{17}$$

where

$$F_2(t) = \frac{e^{\alpha_4 t}}{\alpha_4}\{f_5(a_4,a_5,\alpha_4,t) - f_5(\alpha_2,0,\alpha_4,t)\}$$
$$- \frac{1}{2}\left\{f_4(a_4,a_5,t) + 4\sqrt{\frac{\alpha_2 t}{\pi}}\right\} - \frac{1}{\alpha_4}\left\{f_5(a_4,a_5,0,t) + \sqrt{\frac{\alpha_2}{t\pi}}\right\}.$$

Expressions for $f_i(i = 4,5)$ are given in Appendix.

4 Results and Discussion

To highlight the influence of various physical parameters on the flow field, the numerical computations are performed, and numerical results for the nanofluid velocity and nanofluid temperature are elucidated with the graphical illustrations, whereas, for engineering perspective, the numerical values of shear stress are given in the table. The numerical values of Cu–water-based nanofluid velocity $u(y,t)$, calculated from the solution (14), are presented by various graphs in Figs. 2, 3, 4, 5, and 6 against magnetic field parameter M^2, plate acceleration parameter a,

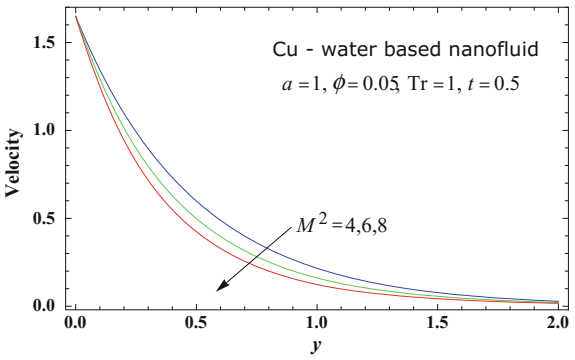

Fig. 2 Influence of M^2 on velocity profiles

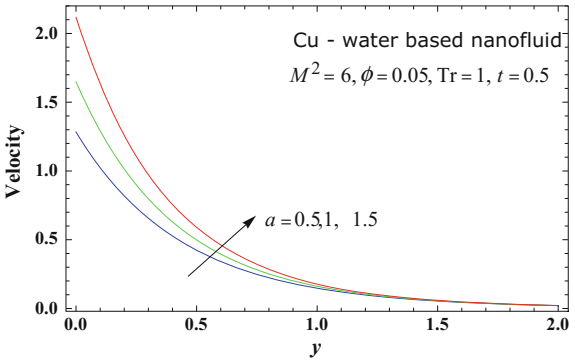

Fig. 3 Influence of a on velocity profiles

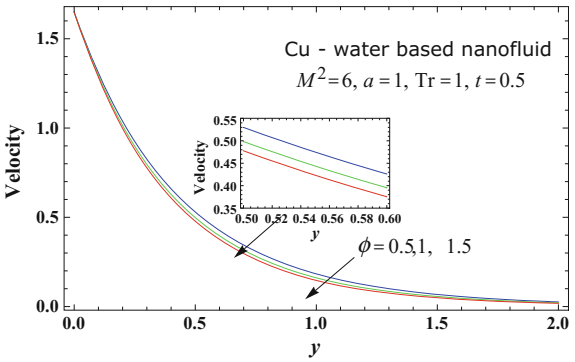

Fig. 4 Influence of ϕ on velocity profiles

nanoparticle volume fraction ϕ, radiation parameter Tr, and time t, by setting $P_r = 0.71$ and $G_r = 4$. As suggested by Das et al. (2015), the values of ϕ are considered in the range of $0 \leq \phi \leq 0.2$. In addition, the spherical nanoparticles with dynamic viscosity and thermal conductivity as mentioned in Table 1 are considered. It is detected from Fig. 2 that the nanofluid velocity decreases on increasing the values of M^2.

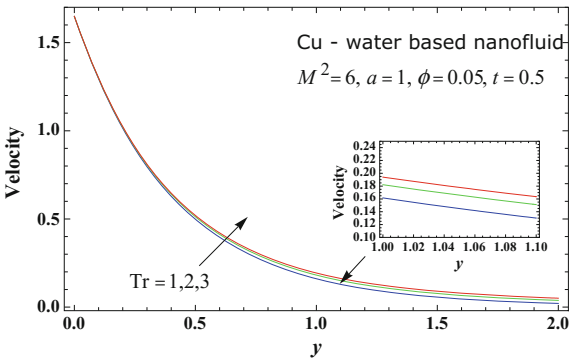

Fig. 5 Influence of *Tr* on velocity profiles

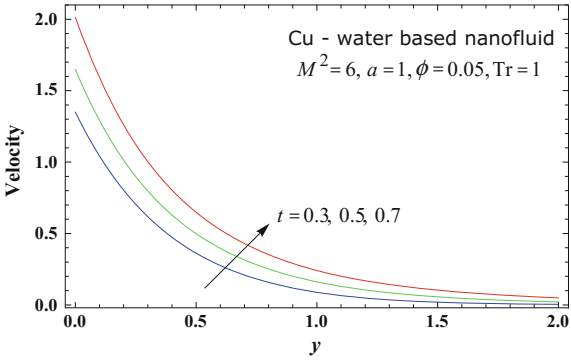

Fig. 6 Influence of *t* on velocity profiles

It is revealed from Fig. 3 that the nanofluid velocity gets accelerated due to the increasing values of a. This implies that the acceleration parameter of the plate has tendency to accelerate the nanofluid velocity. It is illustrated from Fig. 4 that as ϕ increases, the nanofluid velocity decreases. This infers that the nanoparticle volume fraction has a retarding effect on the nanofluid velocity. Physically, this trend is observed due to the fact that increase in the nanoparticle volume fraction tends to reduce the thermal conductivity of nanofluid, which in turn causes the thickness of boundary layer to reduce and the viscosity to increase, thereby decreasing the nanofluid velocity. It is grasped from Fig. 5 that the nanofluid velocity gets accelerated with rising value of radiation parameter *Tr*. This indicates that thermal radiation causes enrichment in the nanofluid velocity. It is revealed from Fig. 6 that there is an upsurge in the nanofluid velocity on increasing time t. This observation points out that the nanofluid velocity gets accelerated with the progress of time. Figure 7 shows the comparison of velocity profiles for different types of nanofluids containing the nanoparticles of copper (Cu), titanium oxide (TiO_2), and alumina (Al_2O_3). It is apparent from Fig. 7 that Cu–water-based nanofluid has highest velocity followed by Al_2O_3–water and TiO_2–water nanofluids. The influences of nanoparticle volume fraction ϕ and radiation parameter *Tr* considering $P_r = 0.71$ and $t = 0.5$ on Cu–water-based temperature profiles are presented in Figs. 8 and 9.

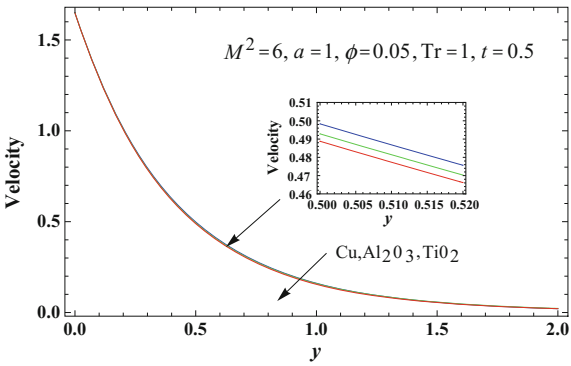

Fig. 7 Comparison of velocity profiles for different nanofluids

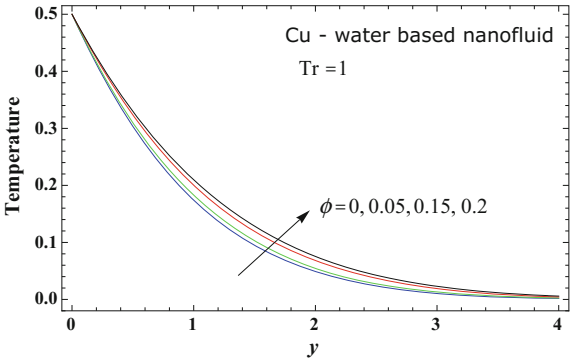

Fig. 8 Influence of ϕ on temperature profiles

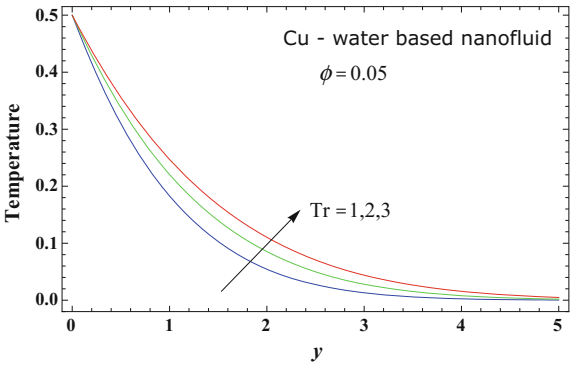

Fig. 9 Influence of Tr on temperature profiles

It is pervaded from Figs. 8 and 9 that an increase in either ϕ or Tr results in significant rise in the nanofluid fluid temperature $\delta(y, t)$. Physically, it is interpreted as the thermal radiation and nanoparticles volume fraction have tendency to increase the nanofluid temperature.

The numerical values shear stress τ of Cu–water-based nanofluid computed from Eq. (16) are mentioned in Table 2 for some values of M^2, ϕ, Tr and t by setting

Table 2 Skin friction τ for Cu–water-based nanofluid when $P_r = 0.71$

M^2	ϕ	Tr	t	τ
4	0.05	1	0.5	1.42944
6	0.05	1	0.5	1.10442
8	0.05	1	0.5	0.75043
6	0.00	1	0.5	0.76661
6	0.10	1	0.5	1.32735
6	0.05	2	0.5	1.07618
6	0.05	3	0.5	1.06015
6	0.05	1	0.3	1.88059
6	0.05	1	0.7	0.56077

$P_r = 0.71, G_r = 4$ and $a = 1$. It is perceived from this table that shear stress τ increases due to increase of ϕ, whereas it decreases due to increase of M^2, Tr and t. This infers that the nanoparticle volume fraction has tendency to enhance the shear stress, whereas magnetic field and radiation have adverse effects. As time increases, the shear stress gets reduced.

It is exhibited from Eqs. (12) and (17) that Nusselt number N_u decreases on increasing either nanoparticle volume fraction ϕ or radiation parameter Tr where it increases with the increase of t. This means that nanoparticle volume fraction and thermal radiation have propensity to squeeze the rate of heat transfer at the plate, and as time passes, the rate of heat transfer at plate gets improved.

5 Conclusions

Notable findings are summarized as under.

The acceleration parameter of the plate and thermal radiation lean to accelerate the nanofluid velocity while magnetic field and nanoparticle volume fraction have a reversal effect, and it gets speeded with the rise in time. The Cu–water-based nanofluid has highest velocity followed by Al_2O_3–water and TiO_2–water nanofluids. The nanoparticles' volume fraction and thermal radiation lead to augment the nanofluid temperature. The augmentation of nanoparticle volume fraction leads to raise the shear stress, while thermal radiation and magnetic field and have a reversal effect. The shear stress at the plate gets condensed with the progress of time. The nanoparticles' volume fraction and thermal radiation tend to diminish the rate of heat transfer at the boundary, whereas it gets improved with the progress of time.

Appendix

$$f_1(c_1,c_2,c_3,c_4,c_5) = \left\{\frac{1}{c_4} + \left(c_5 + \frac{c_1}{2}\sqrt{\frac{c_2}{c_3}}\right)\right\} e^{c_1\sqrt{c_2c_3}}\operatorname{erfc}\left(\frac{c_1}{2}\sqrt{\frac{c_2}{c_5}} + \sqrt{c_3c_5}\right) + \left\{\frac{1}{c_4} + \left(c_5 - \frac{c_1}{2}\sqrt{\frac{c_2}{c_3}}\right)\right\} e^{-c_1\sqrt{c_2c_3}}\operatorname{erfc}\left(\frac{c_1}{2}\sqrt{\frac{c_2}{c_5}} - \sqrt{c_3c_5}\right),$$

$$f_2(c_1,c_2,c_3,c_4,c_5) = e^{c_1\sqrt{c_2(c_3+c_4)}}\operatorname{erfc}\left(\frac{c_1}{2}\sqrt{\frac{c_2}{c_5}} + \sqrt{(c_3+c_4)c_5}\right) + e^{-c_1\sqrt{c_2(c_3+c_4)}}\operatorname{erfc}\left(\frac{c_1}{2}\sqrt{\frac{c_2}{c_5}} - \sqrt{(c_3+c_4)c_5}\right),$$

$$f_3(c_1,c_2,c_3,c_4) = \left\{\frac{1}{c_3} + \left(c_4 + \frac{c_2c_1^2}{2}\right)\right\}\operatorname{erfc}\left(\frac{c_1}{2}\sqrt{\frac{c_2}{c_4}}\right) - c_1\sqrt{\frac{c_2c_4}{\pi}}e^{-(c_2c_1^2)/(4c_4)},$$

$$f_4(c_1,c_2,c_3) = \left(\sqrt{\frac{c_1}{c_2}} + 2c_3\sqrt{c_1c_2}\right)\{\operatorname{erfc}(\sqrt{c_2c_3}) - 1\} - 2\sqrt{\frac{c_1c_3}{\pi}}e^{-c_2c_3},$$

$$f_5(c_1,c_2,c_3,c_4) = \sqrt{c_1(c_2+c_3)}\left\{\operatorname{erfc}\left(\sqrt{(c_2+c_3)c_4}\right) - 1\right\} - \sqrt{\frac{c_1}{\pi c_4}}e^{-(c_2+c_3)c_4}.$$

References

Chamkha AJ, Aly AM (2011) MHD free convection flow of a nanofluid past a vertical plate in the presence of heat generation or absorption effects. Chem Eng Comm 198:425–441

Chandran P, Sacheeti NC, Singh AK (2005) Natural convection near a vertical plate with ramped wall temperature. Heat Mass Transfer 41:459–464

Choi SUS (1995) Enhancing thermal conductivity of fluids with nanoparticles, developments and applications of non-Newtonian flows. ASME FED 231/MD 66:99–105

Das S, Jana RN, Chamkha AJ (2015) Magnetohydrodynamic free convective boundary layer flow of nanofluids past a porous plate in a rotating frame. J Nanofluids 4:176–186

Eastman JA, Choi SUS, Li S, Thompson LJ, Lee S (1997) Enhanced thermal conductivity through the development of nanofluids. In: Komarneni S, Parker JC, Wollenberger HJ (eds) Nanophase and nanocomposite materials II. Materials Research Society, Pittsburgh

Hamad MAA, Pop I (2011) Unsteady MHD free convection flow past a vertical permeable flat plate in a rotating frame of reference with constant heat source in a nanofluid. Heat Mass Transfer 47:1517–1524

Haq RU, Nadeem S, Khan ZH, Akbar NS (2015) Thermal radiation and slip effects on MHD stagnation point flow of nanofluid over a stretching sheet. Physica E 65:17–23

Hayat T, Muhammad T, Qayyum A, Alsaedi A, Mustafa M (2016) On squeezing flow of nanofluid in the presence of magnetic field effects. J Mol Liq 213:179–185

Jang SP, Choi SUS (2007) Effects of various parameters on nanofluid thermal conductivity. ASME J Heat Transfer 129:617–623

Kang Ki JYT, Choi CK (2004) Analysis of convective instability and heat transfer characteristics of nanofluids. Phys Fluids 16:2395–2401

Khalid A, Khan I, Shafie S (2015) Exact solutions for free convection flow of nanofluids with ramped wall temperature. Eur Phys J Plus 130:57

Oztop HF, Abu-Nada E (2008) Numerical study of natural convection in partially heated rectangular enclosures filled with nanofluids. Int J Heat Fluid Flow 29(5):1326–1336

Rashidi MM, Ganesh NV, Abdul Hakeem AK, Ganga B (2014) Buoyancy effect on MHD flow of nanofluid over a stretching sheet in the presence of thermal radiation. J Mol Liq 198:234–238

Seth GS, Ansari MS, Nandkeolyar R (2011) MHD natural convection flow with radiative heat transfer past an impulsively moving plate with ramped wall temperature. Heat Mass transfer 47:551–561

Seth GS, Nandkeolyar R, Ansari MS (2013) Effects of thermal radiation and rotation on unsteady hydromagnetic free convection flow past an impulsively moving vertical plate with ramped temperature in a porous medium. J Appl Fluid Mech 6(1):27–38

Seth GS, Hussain SM, Sarkar S (2014) Hydromagnetic natural convection flow with radiative heat transfer past an accelerated moving vertical plate with ramped temperature through a porous medium. J Porous Media 17(1):67–79

Free-Stream-Induced Unsteady MHD Flow with Hall Effect over Permeable Plate in a Rotating System

G.S. Seth, N. Mahto, R. Tripathi and R. Kumar

Abstract Analytical investigations of unsteady magnetohydrodynamic flow with Hall effect of a viscous, incompressible and electrically conducting fluid past a porous flat plate with impulsively moving free stream in a rotating frame of reference are carried out. Exact solution for the primary and secondary fluid velocities is obtained in closed form by Laplace transform technique. The expressions for skin frictions due to primary and secondary flows are also derived. The numerical values of the primary and secondary fluid velocities are displayed graphically, whereas those of skin frictions are presented in tabular form for various values of pertinent flow parameters. Asymptotic nature of the solution is also examined, for both small and large values of time T, to understand the physics of the flow.

1 Introduction

Lighthill (1954) initiated the study of unsteady flow of a viscous and incompressible fluid induced by time-dependent movement of free stream. In his classical paper, Lighthill (1954) investigated the response of skin friction in laminar flow due to fluctuations in the free-stream velocity. This research by Lighthill (1954) prompted several researchers to study the fluid flow problems induced by time-dependent movement of the free stream. Mention may be made of the relevant

G.S. Seth · R. Tripathi · R. Kumar (✉)
Department of Applied Mathematics, Indian Institute of Technology (Indian School of Mines), Dhanbad 826004, Jharkhand, India
e-mail: rajprsd.ismdhn1612@gmail.com

G.S. Seth
e-mail: gsseth_ism@yahoo.com

R. Tripathi
e-mail: rajat17mnnit@gmail.com

N. Mahto
RSP College, Jharia 828111, Jharkhand, India
e-mail: nmahto.rsp@gmail.com

M.K. Singh et al. (eds.), *Applications of Fluid Dynamics*, Lecture Notes in Mechanical Engineering, https://doi.org/10.1007/978-981-10-5329-0_4

research studies of Stuart (1955), Lin (1957), Watson (1958) and Messiha (1966). Gorla (1984) studied the effects of unsteady free-stream velocity and free-stream turbulence on stagnation point flow with heat transfer. Gorla (2003) analysed unsteady mixed convection flow from a horizontal cylinder due to time-dependent free-stream motion. Das et al. (2014) studied unsteady mixed convective flow of a viscous and incompressible fluid past an infinitely long vertical plate with Newtonian heating considering impulsive, accelerated and oscillatory movements of the free stream. Seth et al. (2014) extended the problem studied by Das et al. (2014) by including the effect of externally applied magnetic field. Shehzad et al. (2015) discussed the Soret and Dufour effects on hydrodynamic flow induced by time-dependent motion of free stream. Ganapathirao et al. (2015) considered time-dependent accelerating and decelerating free-stream flow over a vertical wedge with heat generation/absorption in the presence of uniform suction/injection and chemical reaction.

Investigation of magnetohydrodynamic flow in a rotating medium is of prime importance because it helps us in understanding various cosmical and geophysical problems such as maintenance and secular variations of Earth's magnetic field due to motion of Earth's liquid core, internal rotation rate of the Sun, structure of the rotating magnetic stars, and development of sunspots. The application of such studies is not limited only to the problems of geophysical and cosmical phenomenon, but also it has got a lot of modern-day engineering and industrial applications, viz. rotating MHD generators, rotating drum-type separators for liquid metal MHD applications, turbo machines, electromagnetic stirring of liquid metal in continuous-casting machines. Realizing the significance of such study, unsteady hydromagnetic flow past a plate in a rotating medium is investigated by several researchers. Noteworthy research studies on the topic are due to Singh (1984), Raptis and Singh (1985), Kythe and Puri (1988), Nanousis (1992), Singh et al. (2009), Seth et al. (2015) and Seth and Sarkar (2015). However in all the research studies made above for hydromagnetic rotating flow, the fluid flow is induced due to time-dependent movement of the plate. Seth et al. (1981) investigated unsteady hydromagnetic flow of a viscous, incompressible and electrically conducting fluid over a horizontal porous plate in a rotating medium with time-dependent movement of free stream. They consider two cases of physical interest, namely (i) impulsive movement of free stream and (ii) accelerated movement of free stream.

It is noticed that when the density of an electrically conducting fluid is low and/or applied magnetic field is strong, Hall current plays a vital role in determining flow features of the fluid flow problems because it induces secondary flow in the flow field. Lighthill (1960) highlighted the need to incorporate the effects of Hall current in magnetohydrodynamic flows. Sato (1961) indicated that Hall current induces secondary flow in the flow field whilst studying the effects of Hall current on magnetohydrodynamic boundary layer flows. It is noteworthy that Hall current induces secondary flow in the flow field which is also the characteristics of Coriolis force. Therefore, it is essential to compare and contrast the effects of these two agencies and also to study their combined effects on such fluid flow problems. Considering these two effects, Takhar et al. (2002) obtained numerical solution of

steady MHD flow over a moving plate in a rotating fluid in the presence of Hall currents and uniform free-stream velocity. Ahmed and Goswami (2011) employed Lighthill's (1954) principle to study the effects of Hall current on unsteady MHD forced convection flow from an infinite horizontal porous plate with dissipative heat in a rotating system. However, the very interesting and fundamental problem of unsteady MHD flow past a plate with time-dependent free-stream velocity (i.e. $u(\infty, t) = F(t)$) considering the dual effects of Hall current and rotation has not garnered much attention in recent past. Recently, Seth et al. (2016) considered combined effects of Hall current and rotation on unsteady hydromagnetic natural convection flow with exponentially accelerated free stream near a vertical plate in a fluid-saturated porous medium.

The objective of our present investigation is to study the effects of Hall current and rotation on unsteady hydromagnetic flow of a viscous, incompressible and electrically conducting fluid past a horizontal porous plate considering time-dependent movement of the free stream. Exact solution for fluid velocity is obtained using Laplace transform technique. In order to shed some light into the deeper aspects of the problem, asymptotic behaviour of the solution for fluid velocity is analysed for both small and large values of time T. Analytical solution to the problem presented is original in nature and may have bearings on several engineering problems, viz. aerodynamic heating, plasma confinement, geothermal energy extraction and many more.

2 Problem Formulation

Magnetohydrodynamic flow of an electrically conducting, viscous and incompressible fluid over an infinite horizontal permeable flat plate due to impulsive movement of free stream is considered. Plate lies in xy-plane, flow is directed along x-axis, and z-axis is normal to the plane of the plate. Initially, i.e. for time $t \leq 0$, fluid and plate are at rest. At time $t > 0$, free stream starts moving with time-dependent velocity $U(t)$ in x-direction. Fluid is permeated by a uniform transverse magnetic field H_0 acting in z-direction. It is assumed that the plate is infinite in x- and y-directions, so all physical quantities, except pressure, depend on z and t only. Figure 1 represents the geometry of the problem.

Keeping in view the assumptions made above, the equations of motion for unsteady magnetohydrodynamic flow of an electrically conducting, viscous and incompressible fluid in a rotating frame of reference are:

$$\frac{\partial u'}{\partial t} - w_0 \frac{\partial u'}{\partial z} - 2\Omega v' = \frac{\partial U}{\partial t} + \nu \frac{\partial^2 u'}{\partial z^2} + \frac{\sigma \mu_e^2 H_0^2}{\rho(1+m^2)}[mv' - u' + U], \tag{1}$$

$$\frac{\partial v'}{\partial t} - w_0 \frac{\partial v'}{\partial z} + 2\Omega(u' - U) = \nu \frac{\partial^2 u'}{\partial z^2} - \frac{\sigma \mu_e^2 H_0^2}{\rho(1+m^2)}[v' + mu' - mU], \tag{2}$$

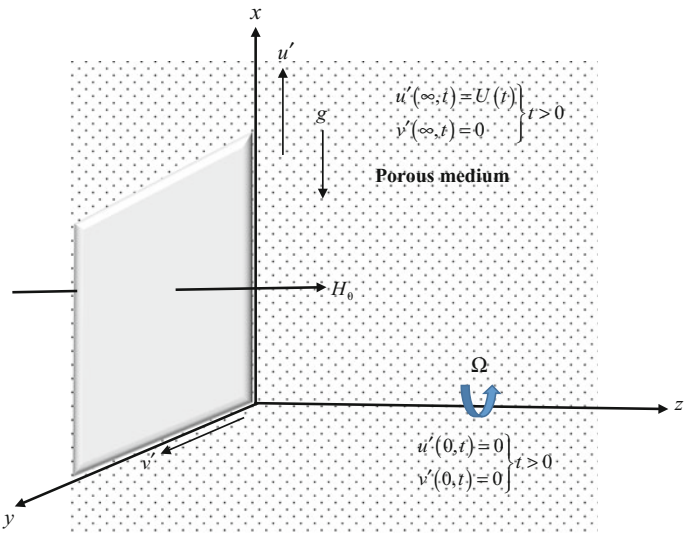

Fig. 1 Geometry of the problem

where $m = \omega_e \tau_e$ is Hall current parameter; $u, v, w_0, \rho, \nu, \sigma, \mu_e, \omega_e$ and τ_e are fluid velocity in x-direction, fluid velocity in y-direction, fluid velocity for suction/injection normal to the plate ($w_0 > 0$ for suction and $w_0 < 0$ for injection), fluid density, kinematic coefficient of viscosity, electrical conductivity, magnetic permeability, cyclotron frequency and electron collision time, respectively.

The initial and boundary conditions to be satisfied are:

$$u' = 0, \quad v' = 0 \ \text{ for } \ z \geq 0 \ \text{ and } \ t \leq 0, \tag{3a}$$

$$u' = 0, \quad v' = 0 \quad \text{at} \quad z = 0 \ \text{ for } \ t > 0, \tag{3b}$$

$$u' \to U(t), \quad v' \to 0 \ \text{ as } \ z \to \infty \ \text{ for } \ t > 0. \tag{3c}$$

Equations (1) and (2), in non-dimensional form, are given by:

$$\frac{\partial u}{\partial T} - S\frac{\partial u}{\partial \eta} - 2K^2 v = \frac{\mathrm{d}F}{\mathrm{d}T} + \frac{\partial^2 u}{\partial \eta^2} + \frac{M^2}{(1+m^2)}[mv - u + F], \tag{4}$$

$$\frac{\partial v}{\partial T} - S\frac{\partial v}{\partial \eta} - 2K^2(u - F) = \frac{\partial^2 v}{\partial \eta^2} - \frac{M^2}{(1+m^2)}[v + mu - mF], \tag{5}$$

where $\eta = U_0 z/\nu$, $u = u'/U_0$, $v = v'/U_0$, $T = U_0^2 t/\nu$, $S = \omega_0/U_0$ is the suction/injection parameter ($S > 0$ for suction and $S < 0$ for injection),

$M^2 = \frac{\mu_e H_0}{U_0}\left(\frac{\sigma v}{\rho}\right)^{1/2}$ is the magnetic field parameter, $K^2 = \left(v\Omega/U_0^2\right)^{1/2}$ is rotation parameter, and U_0 is the characteristic velocity.

The initial and boundary conditions (3a) to (3c), in non-dimensional form, reduce to:

$$u = 0, \quad v = 0 \text{ for } \eta \geq 0 \text{ and } T \leq 0, \tag{6a}$$

$$u = 0, \quad v = 0 \text{ at } \eta = 0 \text{ for } T > 0, \tag{6b}$$

$$u \to F(T), \quad v \to 0 \text{ as } \eta \to \infty \text{ for } T > 0, \tag{6c}$$

where $F(T) = U(t)/U_0$.

3 Exact Solution

Laplace transform technique is applied to solve Eqs. (4) and (5) together with initial and boundary conditions (6a) to (6c). Equations (4) and (5) together with initial and boundary conditions (6a) to (6c), by taking Laplace transform, reduce to

$$\begin{aligned} &\frac{\mathrm{d}^2 f}{\mathrm{d}\eta^2} + S\frac{\mathrm{d}f^*}{\mathrm{d}\eta} - \left\{\frac{M^2(1+im)}{1+m^2} + 2iK^2 + s\right\} f^* \\ &\quad = -\left\{\frac{M^2(1+im)}{(1+m^2)} + 2iK^2 + s\right\} F^*, \end{aligned} \tag{7}$$

$$\left.\begin{array}{lll} f^* = 0 & \text{at} & \eta = 0 \\ f^* = F^* & \text{as} & \eta \to 0 \end{array}\right\} \tag{8}$$

where

$$f = u + iv, \quad f^* = \int_0^\infty f(\eta, T)\mathrm{e}^{-sT}\mathrm{d}T \quad \text{and}$$

$$F^* = \int_0^\infty F(T)\mathrm{e}^{-sT}\mathrm{d}T, \ (s > 0).$$

Solution to Eq. (7) subject to the boundary conditions (8) is given by:

$$f^* = F^*\left[1 - \mathrm{e}^{-\left\{\frac{S}{2} + \left(\frac{S^2}{4} + \frac{M^2}{(1+m^2)}(1+im) + 2iK^2 + s\right)^{1/2}\right\}\eta}\right]. \tag{9}$$

Primary velocity $u(\eta, T)$ and secondary velocity $v(\eta, T)$ are obtained by taking inverse Laplace transform of Eq. (9) and are represented as:

$$u(\eta,T) = F(T) - \eta\frac{e^{-\left(\frac{S}{2}\right)\eta}}{4\sqrt{\pi}}\int_0^T F(T-\lambda)\left\{e^{-\left(a\lambda+\eta^2/4\lambda\right)} + e^{-\left(b\lambda+\eta^2/4\lambda\right)}\right\}\lambda^{-3/2}d\lambda, \tag{10}$$

$$v(\eta,T) = i\eta\frac{e^{-\left(\frac{S}{2}\right)\eta}}{4\sqrt{\pi}}\int_0^T F(T-\lambda)\left\{e^{-\left(a\lambda+\eta^2/4\lambda\right)} - e^{-\left(b\lambda+\eta^2/4\lambda\right)}\right\}\lambda^{-3/2}d\lambda, \tag{11}$$

where $a = (\alpha + i\beta)^2, b = (\alpha - i\beta)^2$,

$$\alpha = \frac{1}{\sqrt{2}}\left[\left\{\left(\frac{M^2}{1+m^2}+\frac{S^2}{4}\right)^2 + \left(\frac{mM^2}{1+m^2}+2K^2\right)^2\right\}^{1/2} + \left(\frac{M^2}{1+m^2}+\frac{S^2}{4}\right)\right]^{1/2}, \tag{12a}$$

$$\beta = \frac{1}{\sqrt{2}}\left[\left\{\left(\frac{M^2}{1+m^2}+\frac{S^2}{4}\right)^2 + \left(\frac{mM^2}{1+m^2}+2K^2\right)^2\right\}^{1/2} - \left(\frac{M^2}{1+m^2}+\frac{S^2}{4}\right)\right]^{1/2}. \tag{12b}$$

Solutions (10)–(12b) represents general solution to the problem considered when free stream moves with time-dependent velocity $F(T)$. We shall now discuss particular case of interest of the problem when there is impulsive movement of free stream.

For this purpose, we consider

$$F(T) = DH(T) \tag{13}$$

where D is a non-dimensional constant and $H(T)$ is Heaviside unit step function.

The general solutions (10) and (11) with the use of (13) assume the following form:

$$u(\eta,T) = DH(T) - \frac{1}{4}DH(T)e^{-\left(\frac{S}{2}\right)\eta}[f_1(\eta,a,T) + f_1(\eta,b,T)], \tag{14}$$

$$v(\eta,T) = \frac{i}{4}DH(T)e^{-\left(\frac{S}{2}\right)\eta}[f_1(\eta,a,T) - f_1(\eta,b,T)]. \tag{15}$$

The non-dimensional skin friction components, due to the primary and secondary flows, respectively, are given by:

$$\tau_{xi} = \frac{1}{2}DH(T)\left[S + f_2(a,T) + f_2(b,T) + \frac{1}{\sqrt{\pi T}}\left(\mathrm{e}^{-aT} + \mathrm{e}^{-bT}\right)\right], \tag{16}$$

$$\tau_{yi} = -\frac{i}{2}DH(T)\left[f_2(a,T) - f_2(b,T) + \frac{1}{\sqrt{\pi T}}\left(\mathrm{e}^{-aT} - \mathrm{e}^{-bT}\right)\right]. \tag{17}$$

The expressions for f_1 and f_2 are presented in Appendix.

The displacement thickness δ for impulsive movement in the free stream is given by:

$$\begin{aligned}\frac{U_0}{\upsilon D}\delta = \frac{1}{2}\mathrm{Real}\Bigg[&\left\{\frac{1}{\sqrt{a}}\left(1 + \frac{S^2}{4(a - S^2/4)}\right)\mathrm{erf}\left(\sqrt{aT}\right)\right\} \\ &+ \left\{\frac{1}{\sqrt{b}}\left(1 + \frac{S^2}{4(b - S^2/4)}\right)\mathrm{erf}\left(\sqrt{bT}\right)\right\} \\ &- \frac{S}{2(a - S^2/4)}\left\{1 - \mathrm{e}^{-\left(a - S^2/4\right)T}\mathrm{erfc}\left(\frac{S}{2}\sqrt{T}\right)\right\} \\ &- \frac{S}{2(b - S^2/4)}\left\{1 - \mathrm{e}^{-\left(b - S^2/4\right)T}\mathrm{erfc}\left(\frac{S}{2}\sqrt{T}\right)\right\}\Bigg].\end{aligned} \tag{18}$$

Equation (18) represents the measure of the depth of modified Rayleigh layer due to impulsive movement of the free stream which can be considered as classical Rayleigh layer modified by Hall current, rotation, magnetic field and suction/injection.

In the absence of Hall current and rotation (i.e. $m = 0$ and $K^2 = 0$), Eq. (18) reduces to

$$\begin{aligned}\frac{U_0\delta}{\upsilon D} = &\frac{1}{\sqrt{M^2 + \frac{S^2}{4}}}\left(1 + \frac{S^2}{4M^2}\right)\mathrm{erf}\left(\sqrt{\left(M^2 + \frac{S^2}{4}\right)T}\right) \\ &- \frac{S}{2M^2}\left\{1 - \mathrm{e}^{-M^2T}\,\mathrm{erfc}\left(\frac{S}{2}\sqrt{T}\right)\right\}.\end{aligned} \tag{19}$$

It presents the measure of the depth of modified Rayleigh layer and can be viewed as classical Rayleigh layer modified by rotation, magnetic field and suction/injection.

For impermeable plate (i.e. $S = 0$), Eq. (19) displays the measure of the depth of modified Rayleigh layer which can be viewed as classical Rayleigh layer modified by magnetic field. In this case, Eq. (19) reduces to:

$$\frac{U_0}{\upsilon D}\delta = \frac{1}{M}\mathrm{erf}\left(M\sqrt{T}\right), \tag{20}$$

In the absence of magnetic field (i.e. $M^2 = 0$), Eq. (20) represents the thickness of the classical Rayleigh layer given by $\delta\alpha\sqrt{\upsilon T}$.

When time $T \to \infty$, Eq. (19) represents the thickness of modified Hartmann layer which can be viewed as classical Hartmann layer modified by suction/injection and is given by:

$$\frac{U_0\delta}{\upsilon D} = \frac{1}{\sqrt{M^2 + \frac{S^2}{4}}}\left(1 + \frac{S^2}{4M^2}\right) - \frac{S^2}{2M^2}. \tag{21}$$

In the absence of suction/injection ($S = 0$), Eq. (21) represents the thickness of classical Hartmann layer which is given by:

$$\frac{U_0\delta}{\upsilon D} = \frac{1}{M}. \tag{22}$$

4 Asymptotic Solutions

We shall now obtain the asymptotic solutions, valid for small and large values of time T, from the solutions (14) and (15) to gain some physical insight into the flow pattern.

When T is small, the solutions (14) and (15) assume the following form:

$$\begin{aligned} u(\eta, T) = D\Bigg[1 - \mathrm{e}^{-\left(\frac{S}{2}\right)\eta}\Bigg\{\mathrm{erfc}\left(\eta/2\sqrt{T}\right) - \eta\left(\frac{M^2}{(1+m^2)} + \frac{S^2}{4}\right) \\ \times\Bigg\{\left(\frac{T}{\pi}\right)^{1/2}\mathrm{e}^{-\eta^2/4T} - \frac{1}{2}\eta\mathrm{erfc}\left(\eta/2\sqrt{T}\right)\Bigg\}\Bigg]\Bigg\} \end{aligned} \tag{23}$$

$$v(\eta, T) = D\left(\frac{mM^2}{(1+m^2)} + 2K^2\right)\eta\mathrm{e}^{\frac{S\eta}{2}} \times \left[\left(\frac{T}{\pi}\right)^{1/2}\mathrm{e}^{-\eta^2/4T} - \frac{1}{2}\eta\mathrm{erfc}\left(\eta/2\sqrt{T}\right)\right] \tag{24}$$

It is revealed from the solutions (23) and (24) that, for small time T, the primary fluid velocity $u(\eta, T)$ is independent of rotation whilst the secondary fluid velocity $v(\eta, T)$ has significant effects of Hall current, magnetic field and rotation. This is due to the fact that both Hall current and rotation generate secondary flow in the flow field. It is also noticed from (23) and (24) that both the primary and secondary fluid velocities have considerable effect of suction/injection. It may be noted from

(24) that in the absence of Hall current, secondary velocity $v(\eta, T)$ is unaffected by magnetic field. At initial stage, there arises a Rayleigh layer of thickness $O\left(2\sqrt{T}\right)$ near the plate and there are no inertial oscillations in the flow field.

For large time T, the solutions (14) and (15) reduce to

$$u(\eta,T) = D\Bigg[1 - \mathrm{e}^{-\left(\alpha+\frac{S}{2}\right)\eta}\cos\beta\eta + \frac{\eta}{2\zeta\sqrt{\pi T}}\mathrm{e}^{-\left\{\frac{\eta}{2}\times(S+\eta/2T)+\left(\frac{M^2}{1+m^2}+\frac{S^2}{4}\right)T\right\}} \times\left\{\left(\left(\frac{M^2}{1+m^2}+\frac{S^2}{4}\right)T-\frac{\eta^2}{4T}\right)\times\cos\left(\frac{mM^2}{1+m^2}+2K^2\right)T + \left(\frac{mM^2}{1+m^2}+2K^2\right)T\sin\left(\frac{mM^2}{1+m^2}+2K^2\right)T\Bigg]\right\} \tag{25}$$

$$v(\eta,T) = D\Bigg[\mathrm{e}^{-\left(\alpha+\frac{S}{2}\right)\eta}\sin\beta\eta - \frac{\eta}{2\zeta\sqrt{\pi T}}\mathrm{e}^{-\left\{\frac{\eta}{2}\times(S+\eta/2T)+\left(\frac{M^2}{1+m^2}+\frac{S^2}{4}\right)T\right\}} \times\left\{\left(\left(\frac{M^2}{1+m^2}+\frac{S^2}{4}\right)T-\frac{\eta^2}{4T}\right)\times\sin\left(\frac{mM^2}{1+m^2}+2K^2\right)T + \left(\frac{mM^2}{1+m^2}+2K^2\right)T\cos\left(\frac{mM^2}{1+m^2}+2K^2\right)T\Bigg\}\Bigg] \tag{26}$$

where

$$\zeta = \left\{\left(\frac{M^2}{1+m^2}+\frac{S^2}{4}\right)T-\frac{\eta^2}{4T}\right\}^2 + \left\{\left(\frac{mM^2}{1+m^2}+2K^2\right)T\right\}^2.$$

The expressions (25) and (26) reveal that the flow field is in a quasi-steady state. Steady-state flow is confined within a modified Ekman–Hartmann boundary layer which can be viewed as Ekman–Hartmann boundary layer modified by Hall current and suction/injection. The steady-state flow represents spatial oscillations in the flow field affected by Hall current, magnetic field, rotation and suction/injection. The unsteady-state flow represents inertial oscillations in the flow field which damp out effectively in a dimensionless time $O\left(1/\left(\frac{M^2}{1+m^2}+\frac{S^2}{4}\right)\right)$ when the final steady state is developed. The frequency of these oscillations is given by $(mM^2/(1+m^2)+2K^2)$.

In the absence of Hall current and rotation, there are no inertial oscillations in the flow field. Thus, we may conclude that Hall current and rotation are responsible for inducing inertial oscillations in the flow field. The time of decay of these oscillations is more in this case than the case in which either Hall current or suction/injection is absent or both Hall current and suction/injection are absent.

5 Results and Discussion

In order to gain a perspective of the physics of the flow regime, numerical computations are conducted from analytical solutions (14) and (15) for the primary and secondary velocity fields and from the analytical expressions (16) and (17) for the primary and secondary skin frictions for various values of the physical parameters that describe the flow characteristics.

The variation of primary velocity u and secondary velocity v, versus boundary layer coordinate η under the influence of Hall current parameter m, magnetic field parameter M^2, rotation parameter K^2 and suction/injection parameter S ($S > 0$ for suction and $S < 0$ for injection), taking $D = 1.0$ and $T = 0.3$, is depicted graphically in Figs. 2, 3, 4, 5 and 6.

It is observed from Fig. 2 that, on increasing m, u gets decelerated in the region $0 \leq \eta \leq 0.8$ and thereafter it changes its characteristics whilst v increases throughout the boundary layer. This observation suggests that Hall current tends to retard the primary flow in the region near the plate whereas it has a reverse effect on the secondary flow throughout the boundary layer. Figure 3 reveals that, with the increase in M^2, u increases throughout the boundary layer whereas there is almost no effect of M^2 on v in the region $0 \leq \eta < 0.18$ and thereafter, i.e. for $\eta \geq 0.18, v$ decreases on increasing M^2. This implies that magnetic field accelerates the primary flow throughout the boundary layer whereas it decelerates the secondary flow as we move away from the plate. These characteristics of flow with respect to the influence of magnetic field are in agreement with those of Seth et al. (1981). It is inferred from Fig. 4 that, on increasing K^2, u gets accelerated throughout the boundary layer whereas v increases in the region $0 \leq \eta < 0.35$ and then follows a reverse pattern in

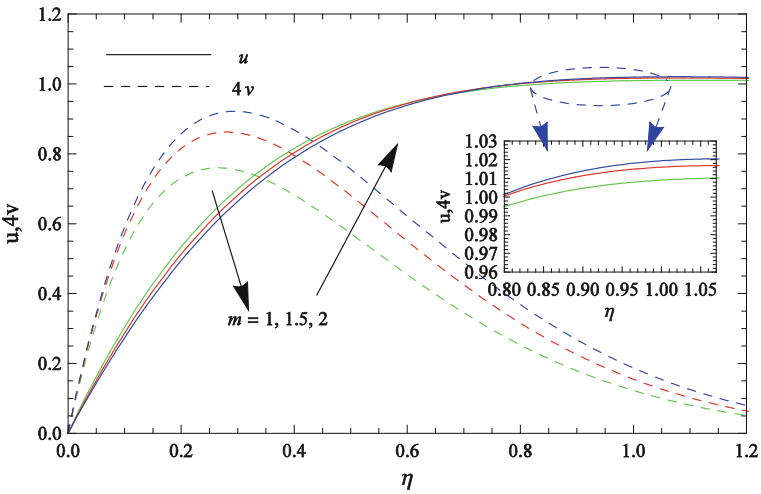

Fig. 2 Velocity profiles for $K^2 = 3, M^2 = 10$ and $S = 1$

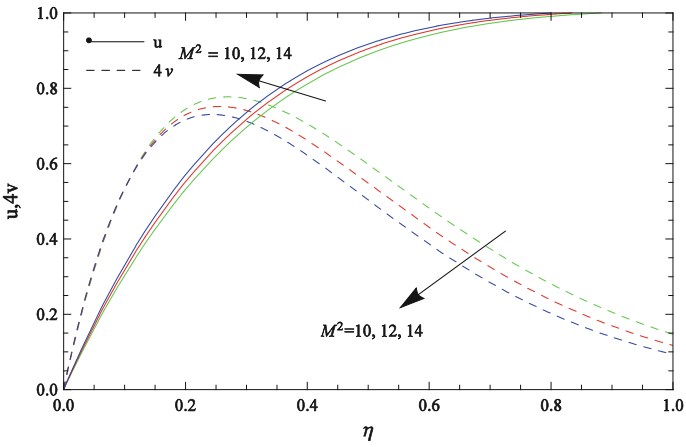

Fig. 3 Velocity profiles for $K^2 = 3, m = 1$ and $S = 1$

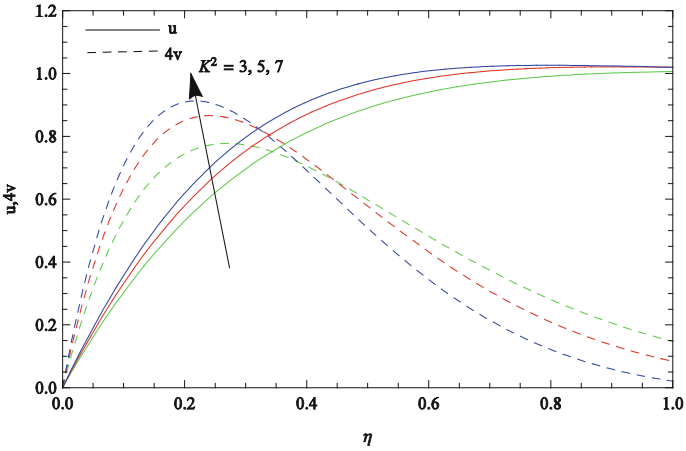

Fig. 4 Velocity profiles for $m = 1, M^2 = 10$ and $S = 1$

the rest of the boundary layer region. This suggests that rotation exerts accelerating influence on the primary flow throughout the boundary layer whereas it accelerates the secondary flow in the region near the plate. It is evident from Fig. 5 that, on increasing suction parameter S ($S > 0$), u gets accelerated whilst a reverse pattern occurs for v. This observation suggests that suction of fluid through the plate accelerates the primary fluid velocity whereas it has a reverse effect on the secondary fluid velocity. Figure 6 establishes that u gets decelerated whilst a reverse phenomenon is observed for v on increasing injection parameter S ($S < 0$). This implies that injection of the fluid from the plate retards the primary fluid velocity whereas it has a reverse effect on the secondary fluid velocity.

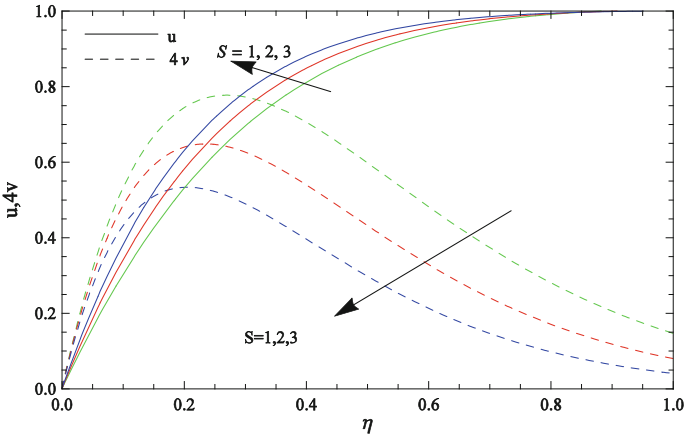

Fig. 5 Velocity profiles for $K^2 = 3, M^2 = 10$ and $m = 1$

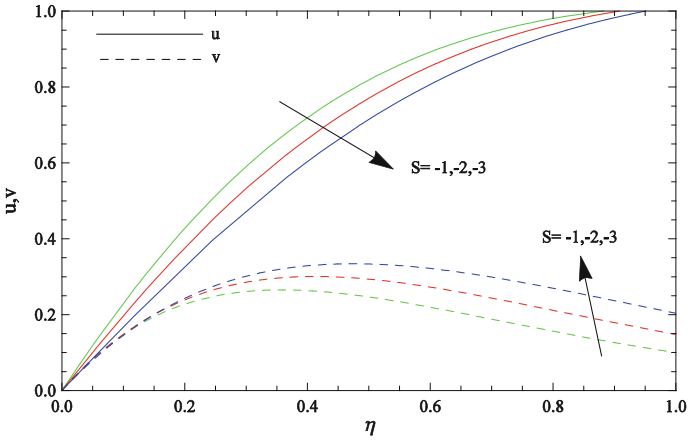

Fig. 6 Velocity profiles for $K^2 = 3, M^2 = 10$ and $m = 1$

The nature of primary skin friction τ_{xi} and secondary skin friction τ_{yi}, under the actions of Hall current parameter m, magnetic field parameter M^2, rotation parameter K^2 and suction/injection parameter S ($S > 0$ for suction and $S < 0$ for injection) taking $D = 1.0$ and $T = 0.3$, is presented in Table 1. It is revealed from Table 1 that τ_{xi} is getting reduced on increasing m and injection parameter S ($S < 0$) whereas it is getting enhanced on increasing M^2, K^2 and suction parameter S ($S > 0$). τ_{yi} is getting enhanced on increasing m, M^2 and K^2, whereas it is getting reduced on increasing either suction parameter S ($S > 0$) or injection parameter S ($S < 0$). These observations from Table 1 indicate that Hall current tends to reduce the primary skin friction whereas it has a reverse effect on the secondary skin

Table 1 Primary and secondary skin frictions

m	M^2	K^2	S	τ_{xa}	τ_{ya}
0.5	10	3	1	3.74929	1.53986
1.0	10	3	1	3.44079	1.88299
1.5	10	3	1	3.16363	2.01411
1.0	12	3	1	3.64094	1.92344
1.0	14	3	1	3.82727	1.96477
1.0	10	5	1	3.76520	2.32027
1.0	10	7	1	4.04695	2.68097
1.0	10	3	2	4.03390	1.82233
1.0	10	3	3	4.68857	1.73074
1.0	10	3	−1	2.44079	1.88299
1.0	10	3	−2	2.03390	1.82233
1.0	10	3	−3	1.68857	1.73074

friction. Intensification of magnetic field and enhancement in rotation result in the enhancement of both the primary and secondary skin frictions. Suction of fluid through the plate results in the enhancement of primary skin friction, whereas an opposite pattern is observed on the secondary skin friction. Fluid injection from the plate tends to diminish both the primary and secondary skin frictions.

6 Conclusion

Noteworthy results are summarized as follows:

- An intensification in magnetic field and suction of fluid through the plate tends to accelerate the primary flow in the boundary layer region, whereas these agencies have reverse effect on the secondary flow. Injection of fluid from the plate tends to decelerate the primary flow, whereas it has a reverse effect on the secondary flow. Primary velocity is getting retarded, on increasing the Hall current, in most of boundary layer region, whereas its effect on secondary velocity is of opposite nature throughout the boundary layer. Rotation exerts accelerating influence on the primary velocity throughout the boundary layer, whereas it accelerates the secondary flow in the region near the plate.
- Strengthening of magnetic field and enhancement in rotation result in enhancement of both the primary and secondary skin frictions. Hall current tends to reduce the primary skin friction, whereas it has a reverse effect on the secondary skin friction. Suction of fluid through plate enhances the primary skin friction, whereas its effect on the secondary skin friction is of opposite nature. Injection of fluid from the plate results in reduction of both the primary and secondary skin frictions.

Acknowledgements One of the Authors Mr. Rajan Kumar wishes to thank Indian Institute of Technology (Indian School of Mines) Dhanbad, India, for providing financial support to carry out this research work.

Appendix

$$f_1(c_1, c_2, c_3) = e^{c_1\sqrt{c_2}}\text{erfc}(c_1/2\sqrt{c_3} + \sqrt{c_2 c_3}) + e^{-c_1\sqrt{c_2}}\text{erfc}(c_1/2\sqrt{c_3} - \sqrt{c_2 c_3}),$$
$$f_2(c_1, c_2) = \sqrt{c_1}\text{erf}(\sqrt{c_1 c_2}).$$

References

Ahmed N, Goswami JK (2011) Hall effect on MHD forced convection form an infinite porous plate with dissipative heat in a rotating system. Turk J Phys 35(3):293–302

Das S, Mandal C, Jana RN (2014) Unsteady mixed convection flow past a vertical plate with newtonian heating. Int J Energy Tech 6(3):1–9

Ganapathirao M, Ravindran R, Momoniat E (2015) Effects of chemical reaction, heat and mass transfer on an unsteady mixed convection boundary layer flow over a wedge with heat generation/absorption in the presence of suction or injection. Heat Mass Transf 51(2):289–300

Gorla RSR (1984) Effects of unsteady free stream velocity and free stream turbulence on stagnation point heat transfer. NASA Contractor Report 3804. NASA-CR-3804 19840017875

Gorla RSR (2003) Unsteady mixed convection due to time-dependent free stream velocity. Heat Mass Transf 39(8–9):639–644

Kythe PK, Puri P (1988) Unsteady MHD free convection flows on a porous plate with time-dependent heating in a rotating medium. Astrophys Space Sci 143(1):51–62

Lighthill MJ (1960) Studies on MHD waves and other anisotropic wave motion. Phil Trans Roy Soc 252:397–430

Lighthill MJ (1954) The response of laminar skin friction and heat transfer to fluctuations in the stream velocity. Proc R Soc Lond A 224(1156):1–23

Lin CC (1957) Motion in the boundary layer with a rapidly oscillating external flow. In: Proceedings of 9th international congress of applied mechanics brussels, vol 4, pp 155–167

Messiha SAS (1966) Laminar boundary layers in oscillatory flow along an infinite flat plate with variable suction. Math Proc Camb Phil Soc 62:329–337

Nanousis N (1992) Thermal diffusion effects on MHD free convective and mass transfer flow a past a moving infinite vertical plate in a rotating fluid. Astrophys Space Sci 191(2):313–322

Raptis AA, Singh AK (1985) Rotation effects on MHD free-convection flow past an accelerated vertical plate. Mech Res Commun 12(1):31–40

Sato H (1961) The hall effect in the viscous flow of ionized gas between parallel plates under transverse magnetic field. J Phys Soc Jpn 16(7):1427–1435

Seth GS, Sarkar S (2015) MHD natural convection heat and mass transfer flow past a time dependent moving vertical plate with ramped temperature in a rotating medium with Hall effects, radiation and chemical reaction. J Mech 31(1):91–104

Seth GS, Jana RN, Maiti MK (1981) Unsteady hydromagnetic flow past a porous plate in a rotating medium with time-dependent free stream. Rev Roumaine Sci Technol Serie Mech Appl 26(3):383–400

Seth GS, Kumbhakar B, Sarkar S (2014) Unsteady hydromagnetic natural convection flow with heat and mass transfer of a thermally radiating and chemically reactive fluid past a vertical plate with newtonian heating and time dependent free-stream. Int J Heat Tech 32(1–2):87–94

Seth GS, Sharma R, Sarkar S (2015) Natural convection heat and mass transfer flow with Hall current, rotation, radiation and heat absorption past an accelerated moving vertical plate with ramped temperature. J. Appl. Fluid Mech. 8(1):7–20

Seth GS, Kumbhakar B, Sarkar S (2016) Unsteady MHD natural convection flow with exponentially accelerated free stream past a vertical plate in the presence of Hall current and rotation. Rendiconti del Circolo Matematico di Palermo (RCMP). doi:10.1007/s12215-016-0250-1

Shehzad SA, Hayat T, Alsaedi A, Asghar S (2015) Soret and Dufour effects in the time-dependent flow with variable free stream. Afr Mat 26:1095–1109

Singh AK (1984) MHD free convection flow past an accelerated vertical porous plate in a rotating fluid. Astrophys Space Sci 103:155–163

Singh AK, Singh NP, Singh U, Singh H (2009) Convective flow past an accelerated porous plate in rotating system in presence of magnetic field. Int J Heat Mass Transf 52:3390–3395

Stuart JT (1955) A solution of the Navier-Stokes and energy equations illustrating the response of skin friction and temperature of an infinite plate thermometer to fluctuations in the stream velocity. Proc R Soc Lond A 231(1184):116–130

Takhar HS, Chamkha AJ, Nath G (2002) MHD flow over a moving plate in a rotating fluid with magnetic field, Hall currents and free stream velocity. Int J Eng Sci 40:1511–1527

Watson J (1958) A solution of the Navier-Stokes equations illustrating the response of a laminar boundary layer to a given change in the external stream velocity. Quarterly J Mech Appl Math 11(3):302–325

Radiation Effect on MHD Williamson Fluid Flow over Stretching Cylinder Through Porous Medium with Heat Source

Shalini Jain and Amit Parmar

Abstract In this present paper, we have investigated radiation effects on MHD Williamson fluid flow past a stretching cylinder through porous medium. MHD with Hall and ion-slip currents impact is taken into consideration. The governing PDEs are transformed into BVPs by using appropriate transformations. Shooting technique with Runge–Kutta forth-order method is used to find the solution of the problem. The effect of various parameters such as curvature parameter γ, heat generation parameter β, Hall current parameter β_e, ion-slip parameter β_i magnetic parameter M, thermal conductivity ε, Weissenberg number λ, Eckert number Ec, radiation parameter K and Prandtl number Pr on momentum and thermal energy profiles are discussed and displayed graphically. Local Nusselt number and skin friction coefficient are tabulated.

1 Introduction

Several non-Newtonian models such as power law fluid model, Casson fluid model, Jeffery fluid model and Williamson fluid model have been predicted for the description of rheological behavior of fluid. Williamson fluid is a non-Newtonian fluid and holds viscoelastic property. In Williamson fluid model, maximum viscosity (μ_∞) as well as minimum viscosity (μ_0) both are taken into consideration. This model fits the experimental information of polymer solution and particle suspensions better than other Newtonian and non-Newtonian fluids models. Williamson fluid model has been studied by several researchers under various flow patterns. Malik et al. (2016a, b) studied Williamson fluid and thermal energy transfer past a stretching cylinder assuming that thermal

S. Jain · A. Parmar (✉)
Department of Mathematics and Statistics, Manipal University Jaipur, Jaipur 303007, Rajasthan, India
e-mail: amit.198631@gnail.com

S. Jain
e-mail: shalini.jain@jaipur.manipal.edu

M.K. Singh et al. (eds.), *Applications of Fluid Dynamics*, Lecture Notes in Mechanical Engineering, https://doi.org/10.1007/978-981-10-5329-0_5

conductivity varies linearly with temperature. Krishnamurthy et al. (2016) examined chemical reaction and radiative effects on the steady MHD Williamson fluid flow. Williamson fluid flow past a nonlinearly stretching sheet with thermal radiative effect has been investigated by Monica et al. (2016). Narayana et al. (2015) investigated the influence of viscous dissipation on thermal energy transfer of Magneto-Williamson nanofluid. Khan et al. (2014) studied Williamson fluid flow with chemically reactive species using scaling conversion and homotopy analysis method. Nadeem and Hussain (2014) analyzed Williamson fluid flow and thermal energy analysis over exponentially stretching surface, (PEST) and (PEHF) case.

The MHD boundary layer flow and thermal energy transfer over a stretching cylinder have many applications in manufacturing processes, plasma studies, petroleum industries, MHD power generator, boundary layer control in aerodynamics, chilling of nuclear reactors, crystal fiber production and paper production. Chauhan et al. (2012, 2014) investigated radiative effects on MHD flow and energy transfer in a permeable medium toward a stretching cylinder with or without slip effects. Salahuddin and Malik (2015) analyzed MHD Williamson fluid flow over a stretching cylinder. Jain et al. (2017), Jain and Parmar (2017a, b), Jain and Choudhary (2015, 2017) and Parmar (2017) investigated the Williamson fluid and other non-Newtonian and Newtonian flow through a various permeable and non-permeable surface. They have considered the steady and unsteady flow for MHD and Radiative non-Newtonian fluid through porous medium. Darji and Timol (2014) studied MHD boundary layer equations for non-Newtonian Williamson fluid. Slip boundary layer flow on MHD peristaltic transport of a Williamson fluid past a porous medium have been investigated by Jyothi and Rao (2013). Kumari et al. (2012) analyzed Williamson fluid flow in a vertical channel under the effect of a magnetic field. Osalusi et al. (2007) and Shateyi and Motsa (2010) examined Ohmic heating and viscous dissipation on unsteady MHD with Hall and ion-slip currents.

Heat source/sink chillers are used in renewable utilization and waste heat recovery. Few absorption technologies are generator absorber heat exchanger, compression absorber heat pump, discrete heating system. Sia et al. (2014) analyzed unsteady viscous flow and thermal energy transfer due to a porous expanding stretching cylinder. Mahdy and Chamkha (2015) investigated the thermal energy transfer and fluid flow of a non-Newtonian nanofluid toward an unsteady contracting cylinder employing Buongiorno's model. Rangi and Ahmad (2012) studied the influence of thermal energy transfer with variable thermal conductivity past a stretching cylinder. Thermal analysis of conducting dusty fluid flow in a porous medium over a stretching cylinder in the presence of non-uniform source/sink was investigated by Manjunatha et al. (2014). Mahapatra et al. (2013) have been investigated the influence of magnetic field with thermal radiative and thermal energy generation.

Thermal conductivity changes with the disparate in energy and depends on material. Chauhan and Sharma (2001) analyzed the heat transfer in a compressible

fluid flow with variable viscosity and thermal conductivity through a channel bounded by a highly porous medium. Mabood et al. (2015) have been investigated thermal radiative on Casson fluid flow heat and mass transfer around a circular cylinder in porous medium. Makinde et al. (2016) studied MHD variable viscosity reacting flow past a convective heated plate in porous medium with thermophoresis and radiative heat transfer. Hady et al. (2012) studied radiative effect on viscous nanofluid flow and thermal energy transfer over a nonlinearly stretching sheet. Kothandapania and Prakash (2015) examined thermal radiative and MHD on the peristaltic motion of Williamson nanofluid.

The present investigation aimed to study radiative effects on MHD Williamson fluid over a stretching cylinder through permeable medium with heat source. Hall current effect and ion-slip are also taken into account.

2 Problem Statement and Mathematical Formulation

The steady incompressible two-dimensional boundary layer flow of non-Newtonian Williamson fluid flow past a stretching cylinder is considered, as shown in Fig. 1. The axis of the cylinder is taken along the x-axis; r is taken along radial direction. Magnetic field is applied in radial direction, and effect of induced magnetic fluid is taken into consideration. Cylinder is immersed into a porous medium. Fluid and porous media are thermal equilibriums. Surface of stretching cylinder is at constant temperature T_w and ambient fluid temperature is T_∞. Under above assumptions, the continuity, momentum, and energy equations are

$$\frac{\partial(rv)}{\partial r} + \frac{\partial(ru)}{\partial x} = 0 \tag{1}$$

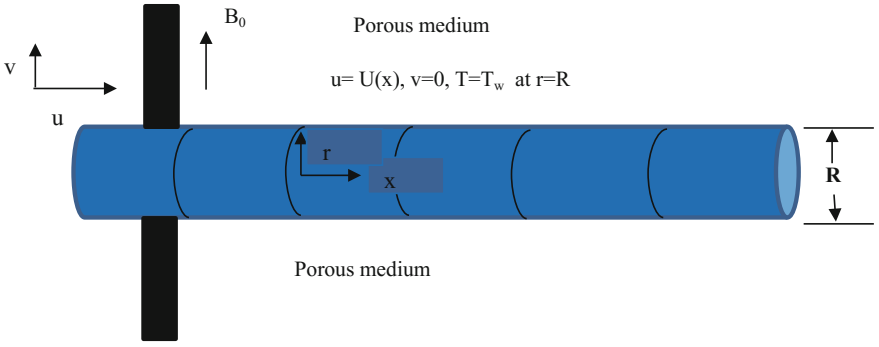

Fig. 1 Physical diagram of the problem

$$u\frac{\partial u}{\partial x}+v\frac{\partial u}{\partial r}=v\left[\frac{1}{r}\frac{\partial u}{\partial r}+\frac{\partial^2 u}{\partial r^2}+\frac{\Gamma}{\sqrt{2}r}\left(\frac{\partial u}{\partial r}\right)^2+\sqrt{2}\Gamma\frac{\partial u}{\partial r}\frac{\partial^2 u}{\partial r^2}\right] -\frac{1}{\rho}\frac{\sigma B_0^2(\alpha u)}{\alpha^2+\beta_e^2}-\frac{\mu}{k^*}u \tag{2}$$

$$u\frac{\partial T}{\partial x}+v\frac{\partial T}{\partial r}=\frac{1}{r}\frac{\partial}{\partial r}\left(\alpha r\frac{\partial T}{\partial r}\right)+\frac{\sigma B_0^2 u^2}{\alpha^2+\beta_e^2}\frac{1}{\rho c_p} -\frac{1}{\rho c_p}\frac{\partial q_r}{\partial r}+\frac{Q(T-T_\infty)}{\rho c_p} \tag{3}$$

Boundary conditions are following such as

$$\begin{aligned} &u=U(x),\quad v=0,\quad T=T_w,\ \text{ at }\ r=R\\ &u\to 0,\quad T\to T_\infty\ \text{ at }\ r\to\infty \end{aligned} \tag{4}$$

The stretching velocity is $U(x)=\frac{U_0 x}{l}$, and the U_0 is the reference velocity; l, T_∞, and T_W are the characteristic length, extrema temperature, and the wall temperature. On expanding T^4, in a Taylor series about T_∞, on neglecting higher order term, we get

$$\begin{aligned} T^4&\approx T_\infty^4+4T_\infty^3 T\\ \frac{\partial q_r}{\partial r}&=\frac{\partial}{\partial r}\left(\frac{-4\sigma^*}{3k}\frac{\partial T^4}{\partial r}\right)\\ &=\frac{\partial}{\partial r}\left(\frac{-4\sigma^*}{3k}\frac{\partial(T_\infty^4+4T_\infty^3 T-4T_\infty^3 T_\infty)}{\partial r}\right)\\ &=\frac{-16\sigma^* T_\infty^3}{3k}\frac{\partial^2 T}{\partial r^2} \end{aligned}$$

The stream function is introducing $u=\frac{1}{r}\frac{\partial\psi}{\partial r}, v=-\frac{1}{r}\frac{\partial\psi}{\partial x}$, and the similar transformation for the following momentum and temperature equation are defined as

$$\begin{aligned} &\eta=\frac{r^2-R^2}{2R}\sqrt{\frac{U}{vx}},\quad \psi=\sqrt{Uvx}Rf(\eta),\\ &\theta=\frac{T-T_W}{T_W-T_\infty}\quad\text{and}\quad \alpha=\alpha_\infty(1+\varepsilon\theta) \end{aligned} \tag{5}$$

where α_∞ is the thermal conductivity at a large distance away from the cylinder and ε is the small amount of thermal conductivity.

Equations (2)–(3) using Eq. (5) to make a non-dimension form such as

$$f'''\left((1+2\eta\gamma)+\lambda(1+2\eta\gamma)^{3/2}f''\right)+2\gamma f''+\frac{3}{2}\gamma\lambda(1+2\eta\gamma)^{1/2}f''^{2} -f'^{2}+ff''-\frac{\alpha Mf'}{\alpha^2+\beta_e^2}-Kf'=0 \tag{6}$$

$$\theta''(1+2\eta\gamma)\left(1+\varepsilon\theta+\frac{4R}{3}\right)+Prf\theta'+2\theta'\gamma\left(1+\varepsilon\theta+\frac{2}{3}R\right) +\beta\theta Pr+(1+2\eta\gamma)\varepsilon\theta'^{2}+\frac{MPrEcf'^{2}}{\alpha^2+\beta_e^2}=0 \tag{7}$$

And boundary condition is given below

$$\begin{aligned} &f=0 \quad f'=1, \quad \theta=1 \ \text{ at } \ \eta=0\\ &f'\to 0, \quad \theta\to 0 \ \text{ at } \ \eta=\infty \end{aligned} \tag{8}$$

The dimensionless number $Pr, \gamma, \lambda, M, R, K$ and β are the Prandtl number, curvature parameter, Weissenberg number, magnetic parameter, radiation parameter, Darcy permeability parameter, and heat generation parameter, defined as

$$\gamma=\frac{1}{R}\sqrt{\frac{xv}{U}}, \quad \lambda=\Gamma\sqrt{\frac{2U^3}{vx}}, \quad Pr=\frac{v}{\alpha_\infty}, \quad \beta=\frac{Qx}{\rho Uc_p},$$
$$M=\frac{lB_0^2}{U_0\rho}, \quad K=\frac{vl}{k^*U_0}, \quad R=\frac{4\sigma^*T_\infty^3}{3k_1\alpha_\infty\rho c_p}$$

where $\sigma=(e^2n_et_e)/m_e$: electrical conductivity; $\alpha=1+\beta_e\beta_i$, here $\beta_e=\omega_et_e$: the hall parameter; $\beta_i=en_eB_0/((1+n_e/n_a)k_{ai})$: the ion-slip parameter; $\omega_e=eB_0/m_e$: the electron frequency; e: the electron charge; n_e: the electron number density, t_e: the electron collision time; m_e: the mass of the electron; c_p: specific heat at constant pressure of the fluid; n_a is the neutral particle number density, and k_{ai} is the friction coefficient between ions and neutral particles.

3 Method of Solution

This system of equation has been solved using Runga–Kutta fourth-order method with shooting technique. In order to find solution of this problem using shooting method, equation (6)–(8) are converted into system of first-order differential equation as given below:

$$
\begin{aligned}
&f' = z, \quad z' = p,\\
&p' = \frac{1}{\left((1+2\eta\gamma)+\lambda(1+2\eta\gamma)^{3/2}p\right)}\left(z^2 - fp - 2\gamma p - \frac{3}{2}\gamma\lambda(1+2\eta\gamma)^{1/2}p^2 + \frac{\alpha M z}{\alpha^2+\beta_e^2} + zK\right)\\
&\theta' = q,\\
&q' = \frac{-1}{(1+2\eta\gamma)\left(1+\varepsilon\theta+\frac{4R}{3}\right)}\left(Prfq + 2q\gamma\left(1+\varepsilon\theta+\frac{2}{3}R\right) + \beta\theta Pr + (1+2\eta\gamma)\varepsilon q^2 + \frac{z^2 MPrEc}{\alpha^2+\beta_e^2}\right)
\end{aligned}
\tag{9}
$$

Subject to boundary conditions

$$
\begin{aligned}
&f = 0, \quad z = 1, \quad \theta = 1, \ \text{at} \ \eta = 0\\
&f' \to 0 \quad \theta \to 0 \ \text{at} \ \eta \to \infty
\end{aligned}
\tag{10}
$$

Now, the above system is solved by iterative shooting method. In order to solve Eq. (9) as an initial value problem, value of $f''(0)$ and $\theta'(0)$ is required which is not given in boundary conditions. For a set of certain physical parameters and η_∞, we choose some initial values. In current study, we have taken guesses for $f''(0)$, $\theta'(0)$, and $\phi'(0)$ from 1.1 to 1, 0.2 to 0.3. This procedure is repeated with some higher value of η_∞ until we obtain solution which satisfied given boundary conditions and correct up to the accuracy of 10^{-6}.

Skin friction coefficient and local Nusselt number

The skin friction coefficient is defined as

$$
C_f = \frac{\tau_W}{\frac{1}{2}\rho U^2} \quad \& \quad \tau_W = \mu\left[\frac{\partial u}{\partial r} + \Gamma\left(\frac{\partial u}{\partial r}\right)^2\right]_{r=R} \tag{11}
$$

In the above expression, τ_W represents the shear stress on the surface of cylinder. Shear stress is defined as using Eq. (11) we get

$$
\frac{1}{2}\left(C_f Re^{1/2}\right) = f''(0) + \frac{\lambda}{2}f''^2(0) \tag{12}
$$

Now, the local Nusselt number, q_W is the measure of thermal energy transfer on the surface of cylinder

$$
Nu_x = \frac{x q_W}{\alpha_\infty(T_W - T_\infty)} \quad \& \quad q_W = -\alpha_\infty\left(\frac{\partial T}{\partial r}\right)_{r=R} \tag{13}
$$

Using (13) in order to get the expression for local Nusselt number that is

$$
NuRe_x^{-1/2} = -\theta'(0), \quad Re_x = \frac{Ux}{v} \text{ is the Reynold number.} \tag{14}
$$

4 Results and Discussion

The effects of various flow parameters on velocity and temperature profiles are analyzed and depicted in Figs. 2, 3, 4, 5, 6, 7, 8, 9, 10, 11, 12, 13, 14, 15, 16, 17, and 18. It has been observed that results obtained are very well in agreement with the results obtained by Malik et al. (2016a, b) on reducing the present model into that model. This validates our observations and method of solution. Figure 2 shows that the velocity profile increases as curvature parameter γ increases. Because as curvature parameter increases, radius of curvature decreases as result resistance

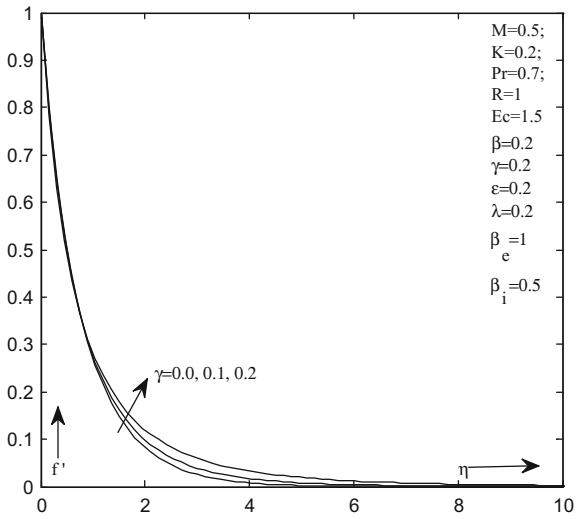

Fig. 2 Influence of curvature parameter on velocity profile

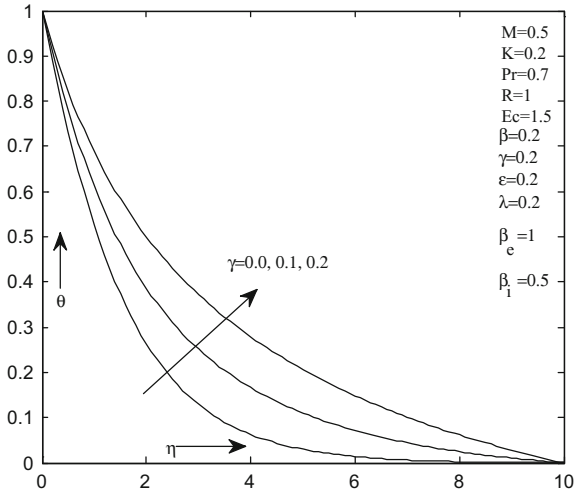

Fig. 3 Influence of curvature parameter on temperature profile

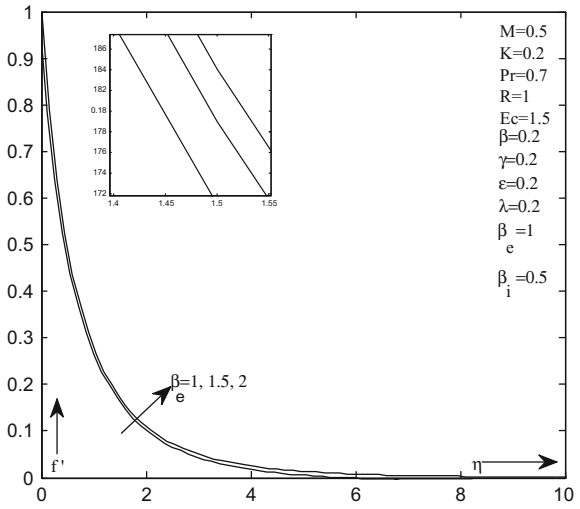

Fig. 4 Influence of hall current parameter on velocity profile

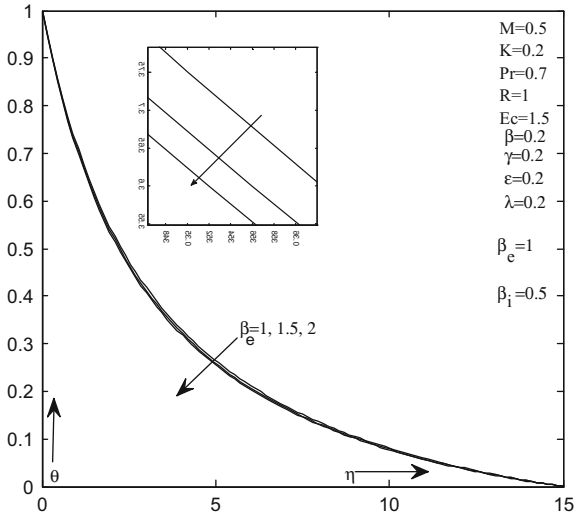

Fig. 5 Influence of hall current parameter on temperature profile

exert on flow decreases. It is observed from Fig. 3 that γ increase heat transfer rate accelerates and temperature increase. Figures 4 and 5 shows the influence of hall current parameter on velocity and temperature profiles. It is observed that as hall current parameter increases velocity increases, whereas temperature decreases. Figure 6 shows the effect of heat generation parameter β on temperature profile. It is observed that as β increases thermal boundary layer thickness increases. Figures 7 and 8 velocity profile whereas temperature profile the ion-slip parameter β_i increase. Figures 9 and 10 shows that increase in thermal conductivity parameter ε and Prandtl number Pr increases that temperature profile. Prandtl number Pr can

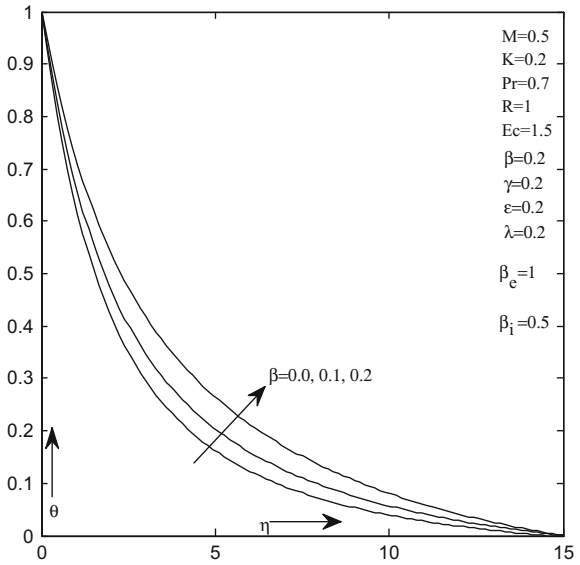

Fig. 6 Influence of heat generation parameter temperature profile

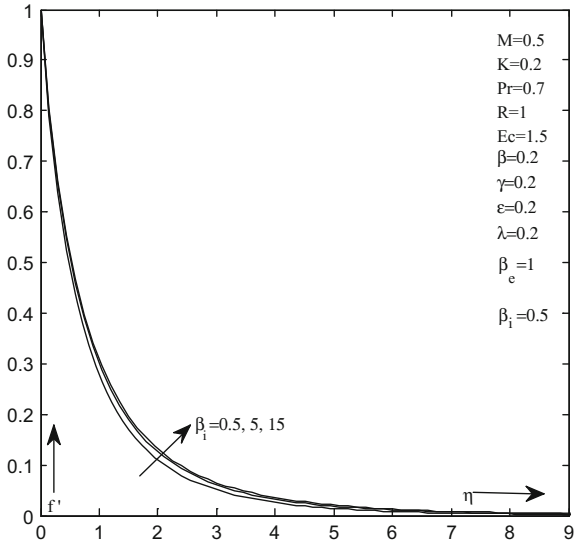

Fig. 7 Influence of ion-slip parameter on velocity profile

be used to control the cooling rate of conducting fluid. Since the Prandtl number is the rates of momentum diffusivity to thermal diffusivity, reduces thermal boundary layer thickness. Figures 11 and 12 shows the influence of magnetic field parameter on velocity and temperature profiles. It is observed that as magnetic field parameter increases velocity suppresses, whereas temperature enhances. Figures 13 and 14 shows the effect of Weissenberg number λ on velocity profile and temperature

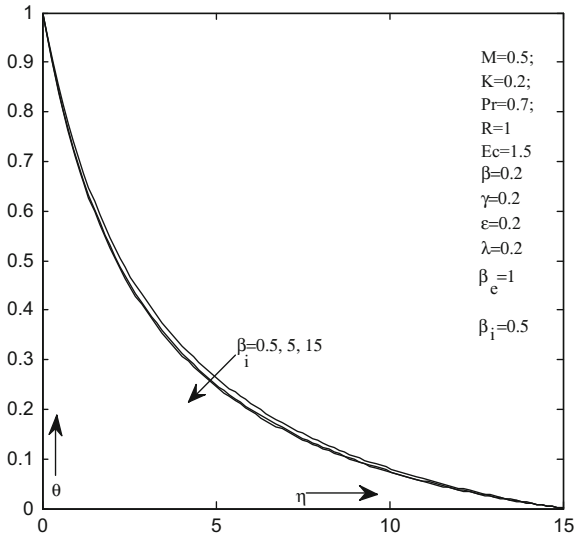

Fig. 8 Influence of ion-slip parameter on temperature profile

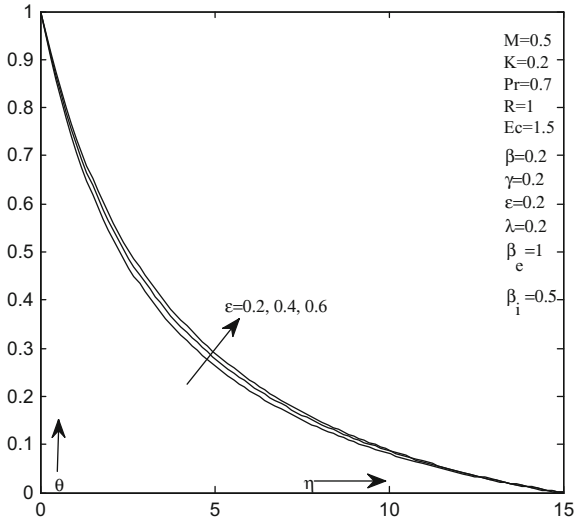

Fig. 9 Influence of small amount of thermal conductivity parameter on temperature profile

profile. Weissenberg number λ increases, boundary layer thickness decreases, whereas thermal boundary layer thickness increases. Figures 15 and 16 shows the influence of porosity parameter K on velocity profile and temperature profile. The porosity parameter K, velocity decreases whereas it enhances the temperature profile. Figure 17 shows the effect of radiation on temperature. The radiation parameter increases, the temperature profile decreases, whereas as shown in Fig. 18 an increment in Eckert number decreases the thermal boundary layer thickness.

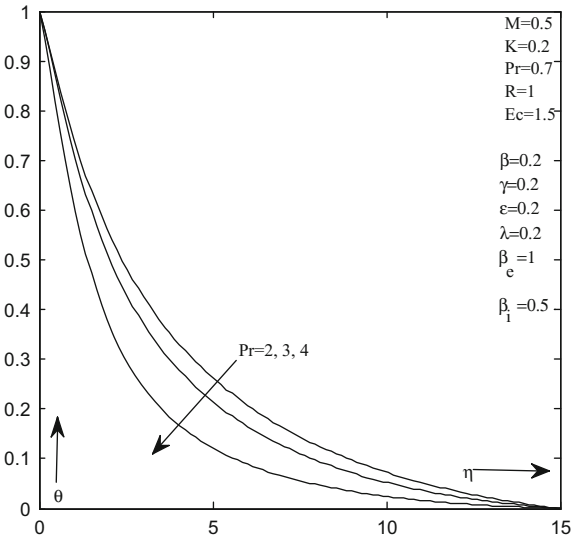

Fig. 10 Influence of Prandtl number on temperature profile

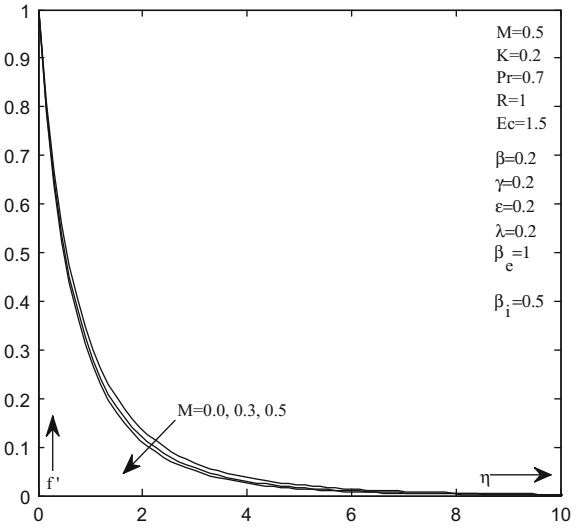

Fig. 11 Influence of magnetic field parameter on velocity profile

Tables 1.1 and 1.2 shows the effect of various physical parameters on skin friction coefficient and Nusselt number. It is observed that the data obtained are self-explanatory and well in agreement with the literature available.

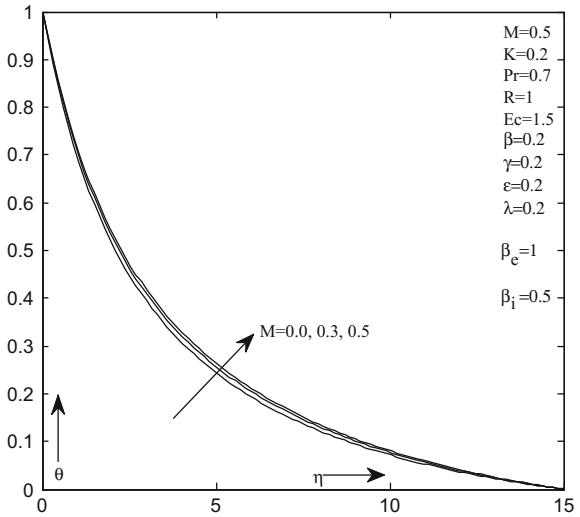

Fig. 12 Influence of magnetic field parameter on temperature profile

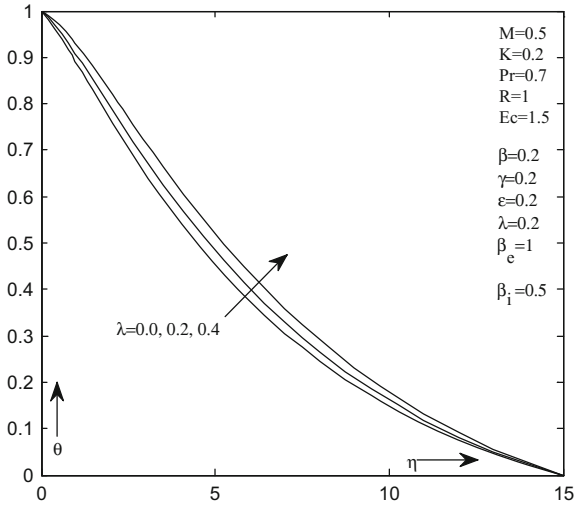

Fig. 13 Influence of Weissenberg number on temperature profile

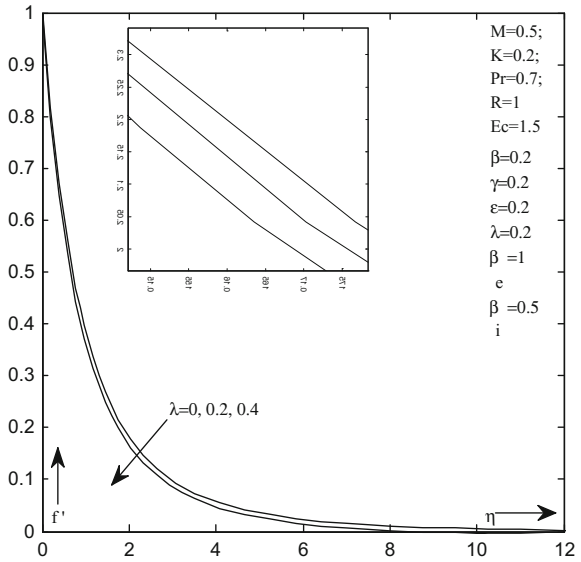

Fig. 14 Influence of Weissenberg number on velocity profile

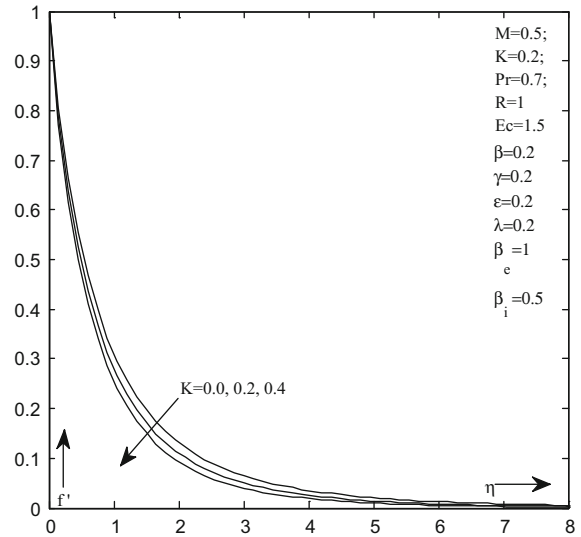

Fig. 15 Influence of porosity parameter on velocity profile

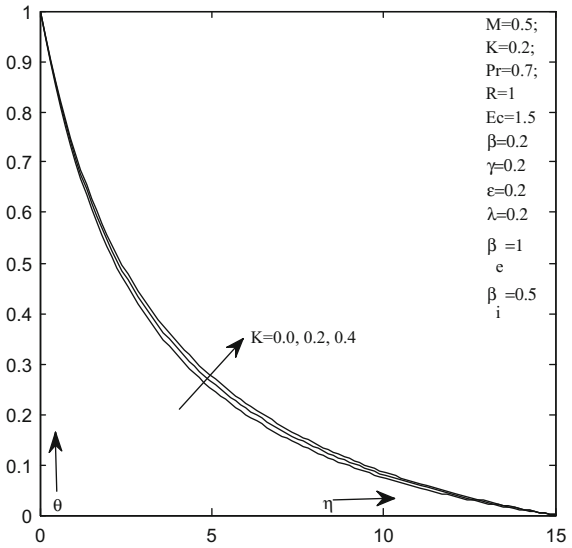

Fig. 16 Influence of porosity parameter on temperature profile

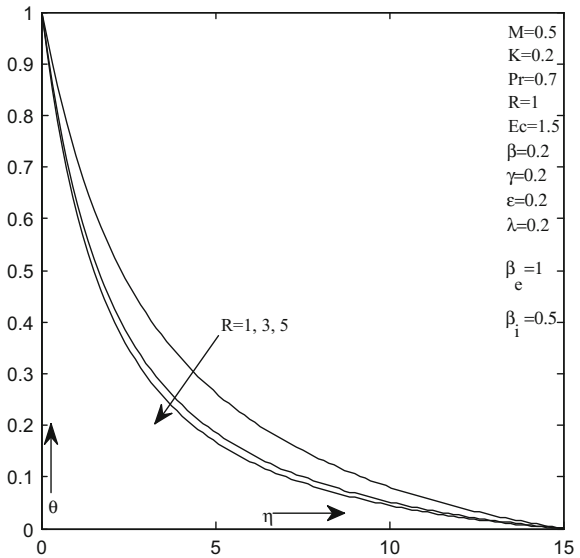

Fig. 17 Influence of radiation parameter on temperature profile

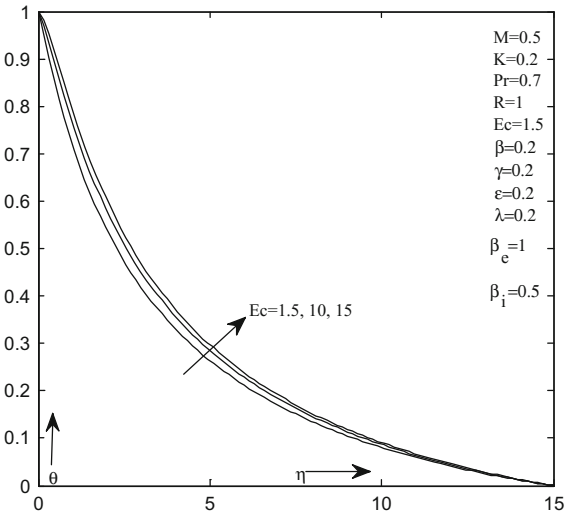

Fig. 18 Influence of Eckert number on temperature profile

Table 1 Skin friction coefficient and Nusselt number for the different values of physical parameters

$\gamma = 0.2, M = 0.5, \beta_2 = 1, \beta_3 = 0.5, K = 0.2$								
S. No.	γ	λ	M	β_e	β_i	K	$C_f \mathrm{Re}^{1/2}$	$Nu\mathrm{Re}_x^{-1/2}$
1	0						−2.57463	0.54890
2	0.1						−2.71662	0.42418
3	0.2						−2.87173	0.34407
4		0.0					−2.55748	0.35575
5		0.1					−2.64151	0.35063
6		0.2					−2.87173	0.34407
7			0.0				−2.57611	0.38975
8			0.3				−2.75172	0.36125
9			0.5				−2.87173	0.34407
10				1			−2.87173	0.34407
11				1.5			−2.78538	0.35933
12				2			−2.73454	0.36804
13					0.5		−2.87173	0.34407
14					5		−2.67877	0.38089
15					15		−2.61554	0.38693
16						0.0	−2.61509	0.35530
17						0.2	−2.87173	0.34407
18						0.4	−3.22303	0.33462

Table 2 Nusselt number for the different values of physical parameters

$Pr = 0.7, Ec = 1.5, R = 1, \varepsilon = 0.2, \beta_1$						
S. No.	Pr	R	Ec	ε	β_1	$NuRe_x^{-1/2}$
1	0.7					0.34407
2	1.5					0.27573
3	4					0.34196
4		1				0.34407
5		3				0.50922
6		5				0.55869
7			1.5			0.34407
8			10			0.17625
9			15			0.07753
10				0.2		0.34407
11				0.4		0.31917
12				0.6		0.29782
13					0.0	0.50343
14					0.1	0.42872
15					0.2	0.34407

5 Conclusion

The velocity and heat transfer effects have investigated the Williamson fluid flow with various conditions such as radiative effects, MHD in the attendance of Hall current, porous medium past a stretching cylinder, thermal energy transfer with variable thermal conductivity and heat generation. Our computations have indicated that:

- Increase in curvature parameter γ enhances both the momentum and the thermal energy profile.
- Increase in Weissenberg number λ reduces the velocity profile.
- Increase in thermal conductivity parameter ε increases the thermal energy profile.
- Rising in Prandtl number Pr reduces the thermal energy profile.
- Hall current parameter β_e and ion-slip parameter β_i enhances the velocity and thermal energy profile.
- Increase in magnetic field parameter M and porosity parameter K reduces the velocity profiles.
- Increase in magnetic field M parameter and porosity K parameter increases the temperature profiles.

Acknowledgements The authors wish to express gratitude to Prof. D.S. Chauhan, University of Rajasthan, for his guidance. Also, express sincere their thanks to anonymous reviewers for their valuable suggestions and comments.

Conflict of Interests The authors state that there is no strife of interests regarding the publication of this paper.

References

Chauhan DS, Sharma S (2001) MHD heat transfer in a compressible fluid flow with variable viscosity and thermal conductivity through a channel bounded by a highly porous medium. Ganita Sandesh 15(1):41–50

Chauhan DS, Agrawal R, Rastogi P (2012) Magnetohydrodynamic slip flow and heat transfer in a porous medium over a stretching cylinder: homotopy analysis method. Numer Heat Transf Part A: Appl 62(2):136–157

Chauhan DS, Agrawal R, Rastogi P (2014) Magnetohydrodynamic flow and heat transfer in a porous medium along a stretching cylinder with radiation: homotopy analysis method. Afrika Matematika. doi:10.1007/s13370-012-0102-x

Darji RM, Timol MG (2014) On invariance analysis of MHD boundary layer equations for non-Newtonian Williamson fluids. Int J Adv Appl Math Mech 1(4):10–19

Hady FM, Ibrahim FS, Gaied SMA, Eid MR (2012) Radiation effect on viscous flow of a nanofluid and heat transfer over a nonlinearly stretching sheet. Nanoscale Res Lett 7:229

Jain S, Choudhary R (2015) Effects of MHD on Boundary layer flow in porous medium due to exponentially shrinking sheet with slip. Procedia Eng 127:1203–1210

Jain S, Choudhary R (2017) Soret and Dufour effects on MHD fluid flow due to moving permeable cylinder with radiation. Glob Stochast Anal SI:75–84

Jain S, Kumar V and Bohra S (2017) Entropy generation for MHD radiative compressible fluid flow in a channel partially filled with porous medium. Glob Stochast Anal SI:13–31

Jain S, Parmar A (2017a) Study of radiative heat transfer of nano-Williamson fluid flow through a porous medium. Acta Technica 62(2):137–150

Jain S, Parmar A (2017b) Comparative study of flow and heat transfer behavior of Newtonian and non-Newtonian fluids over a permeable stretching surface. Glob Stochast Anal SI:41–50

Jyothi B, Rao PK (2013) Slip effects on MHD peristaltic transport of a Williamson fluid through a porous medium in a symmetric channel. J Math Comp Sci 3(5):1306–1324

Khan NA, Khan S, Riaz F (2014) Boundary layer flow of Williamson fluid with chemically reactive species using scaling transformation and homotropy analysis method. Math Sci Lett 3 (3):199–205

Kothandapania M, Prakash J (2015) Effects of thermal radiation parameter and magnetic field on the peristaltic motion of Williamson nanofluids in a tapered asymmetric channel. Int J Heat Mass Transf 81:234–245

Krishnamurthy MR, Prasannakumara BC, Gireesha BJ, Gorla RSR (2016) Effect of chemical reaction on MHD boundary layer flow and melting heat transfer of Williamson nanofluid in porous medium. Eng Sci Tech Int J 19:53–61

Kumari BA, Prasad KR, Kavitha K (2012) Fully developed free convective flow of a Williamson fluid in a vertical channel under the effect of a magnetic field. Adv Appl Sci Res 3(4): 2492–2499

Mabood F, Shateyi S, Khan WA (2015) Effects of thermal radiation on Casson flow heat and mass transfer around a circular cylinder in porous medium. Eur Phys J Plus 130:188

Mahapatraa TR, Pala D, Mondalb S (2013) Mixed convection flow in an inclined enclosure under magnetic field with thermal radiation and heat generation. Int Commun Heat Mass Transf 41:47–56

Mahdy A, Chamkha A (2015) Heat transfer and fluid flow of a non-Newtonian nanofluid over an unsteady contracting cylinder employing Buongiorno's model. Int J Numer Methods Heat Fluid Flow 25(4):703–723

Makinde OD, Khan WA, Culham JR (2016) MHD variable viscosity reacting flow over a convectively heated plate in a porous medium with thermophoresis and radiative heat transfer. Int J Heat Mass Transf 93:595–604

Malik MY, Uddin TS (2015) Numerical solution of MHD stagnation point flow of Williamson fluid model over a stretching cylinder. Int J Nonlinear Sci Numer Simul 16:161–164

Malik MY, Bibi M, Khan F, Salahuddin T (2016a) Numerical solution of Williamson fluid flow past a stretching cylinder and heat transfer with variable thermal conductivity and heat generation/absorption. AIP Adv 6:035101. doi:10.1063/1.4943398

Malik MY, Bibi M, Khan F, Salahuddin T (2016b) Numerical solution of Williamson fluid flow past a stretching cylinder and heat transfer with variable thermal conductivity and heat generation/absorption. AIP Adv 6:035101

Manjunatha PT, Gireesha BJ, Prasannakumara BC (2014) Thermal analysis of conducting dusty fluid flow in a porous medium over a stretching cylinder in the presence of non-uniform source/sink. Int J of Mech Mat Eng 1:13

Monica M, Sucharitha J, Kumar CK (2016) Stagnation point flow of a Williamson fluid over a nonlinearly stretching sheet with thermal radiation. Am Chem Sci J 13(4):1–8. Article no. ACSJ.25144. ISSN: 2249-0205

Nadeem S, Hussain ST (2014) Heat transfer analysis of Williamson fluid over exponentially stretching surface. Appl Math Mech Engl Ed. 35(4):489–502

Narayana KL, Gangadhar K, Subhakar MJ (2015) Effect of viscous dissipation on heat transfer of Magneto-Williamson nano fluid. IOSR J Math (IOSR-JM) 11(4):25–37

Osalusi E, Side J, Harris R (2007) The effects of Ohmic heating and viscous dissipation on unsteady MHD and slip flow over a porous rotating disk with variable properties in the presence of Hall and ion-slip currents. Int Commun Heat Mass Transf 34:1017–1029

Parmar A (2017) Unsteady convective boundary layer flow for MHD Williamson fluid over an inclined porous stretching sheet with non-linear radiation and heat source. Int J Appl Comput Math. doi:10.1007/s40819-017-0373-4

Rangi RR, Ahmad N (2012) Boundary layer flow past a stretching cylinder and heat transfer with variable thermal conductivity. Appl Math 3:205–209

Salahuddin T, Malik MY, Hussain A, Bilal S, Awais M (2015) Combined effects of variable thermal conductivity and MHD flow on pseudoplastic fluid over a stretching cylinder by using Keller box method. Nat Sci 5:11–19

Shateyi S, Motsa SS (2010) Variable viscosity on magnetohydrodynamic fluid flow and heat transfer over an unsteady stretching surface with hall effect. Boundary Value Probl 20 pages. Article ID 257568. doi:10.1155/2010/257568

Sia X, Lia L, Zhenga L, Zhangb X, Liua B (2014) The exterior unsteady viscous flow and heat transfer due to a porous expanding stretching cylinder. Comp Fluids 105:280–284

Part II
Nano-Fluid

Particle Size and Spacing Effects on Convective Heat and Mass Transfer of a Nanofluid in Wavy Annulus

V.P.N. Srikanth Gorti and Srinivas Gosukonda

Abstract In this paper, we attempted to study the heat and mass transfer of nanofluid flowing into a horizontal annulus whose outer cylinder is sinusoidal. Graham, Jang and Choi proposed expressions were considered. Various phenomena such as magnetic parameter (M), gap of the annulus from inner cylinder to mean position of outer wavy surface (s), heat source parameter (Q_H), and Darcy parameter ($1/D$) are considered. The governing equations are solved by R-K sixth order and shooting methods. The enhancement of temperature is observed for reduction in gap of the annulus.

1 Introduction

Many engineering applications such as cooling electronic components, solar energy collector designs, and several heat exchangers are based on convective heat and mass transfer. In many of these applications, the wavy surface study is required.

Flow around cylindrical structure has been widely investigated for over a large range of Reynolds numbers because of lot of their fundamental significance in flow physics. Among the physical phenomena of the flow past cylindrical structure, the generation and evolution of vortices in the wake region are important in practical application of engineering (Williamson 1989, 1996; Unal and Rockwell 1977). It produces a drag and fluctuating lift forces and vortex-induced vibration that affect aerodynamic performances such as the mean drag and fluctuating lift forces. Recently, Gosukonda and Gorti (2015) reported that particle spacing is directly

V.P.N. Srikanth Gorti (✉)
Department of Mathematics, VNR Vignana Jyothi Institute of Engineering and Technology, Hyderabad 500090, India
e-mail: srikanth.gorthi@gmail.com

S. Gosukonda
Department of Mathematics, Guru Nanak Institutions Technical Campus, Hyderabad 501506, India
e-mail: gn.nivas@gmail.com

M.K. Singh et al. (eds.), *Applications of Fluid Dynamics*, Lecture Notes in Mechanical Engineering, https://doi.org/10.1007/978-981-10-5329-0_6

proportional to flow and inversely proportional to heat distribution across the cylindrical annulus. Thus, a number of researchers for over a period took an effort to understand and to control the dynamics of the wake vortices with the aim of reducing the mean drag and fluctuating lift forces (Ahmed and Bays-Muchmore 1992; Lam et al. 2004; Lam and Lin 2008; Mittal and Balachandar 1994 and Lee and Nguyen 2007). One of some forms of three-dimensional (3-D) geometric disturbances for passive controlling is a wavy surface of cylinder. It has the sinusoidal variation in the cross-sectional area along the span-wise direction to consider its effect on the flow characteristics such as the wake vortices. Ahmed and Bays-Muchmore (1992) investigated experimentally the transverse flow over a wavy cylinder. They demonstrated that the sectional drag coefficient at the node was greater than that at the saddle and that the significant span-wise pressure gradients resulted in 3-D flow separation.

Motivated by the above, this paper describes heat and mass transfer of nanofluid through annulus formed due to circular cylinders whose outer cylinder is sinusoidal. Expressions derived by Graham (1981), Jang and Choi (2007) are used which suits the motive of the study. The transverse magnetic field is applied. The gap of the annulus from inner cylinder to mean position of outer wavy surface (s) is used for computational purpose. Heat source and porous medium are also taken into account.

2 Mathematical Formulation

The fully developed copper–water nanofluid flow in a porous medium in a wavy cylindrical annulus is considered. We consider the convective flow of nanofluid along z-axis. Both walls are assumed that they are separated by $a + s\varepsilon \sin(\lambda z + \psi)$ distance. The outer wall of the cylinder is assumed to be wavy wall. The inner and outer wall temperatures and concentration are assumed constant on both walls. The heat source is also considered. The physical properties of the fluid are assumed to be constant. The flow is due to buoyancy and of uniform axial pressure gradient. The Boussinesq approximation is also assumed. The geometry under consideration is as in Fig. 1.

Equations governing the flow are as follows:

$$\frac{\partial}{\partial r}(ru) = 0 \tag{1}$$

$$\mu_{nf}\left(\frac{\partial^2 w}{\partial r^2} + \frac{1}{r}\frac{\partial w}{\partial r}\right) - \frac{\mu_{nf}}{k}w + \frac{\sigma B_0^2}{r^2}w + g(\rho\beta_T)_{nf}(T - T_0) + g(\rho\beta_c)_{nf}(c - c_0) = 0 \tag{2}$$

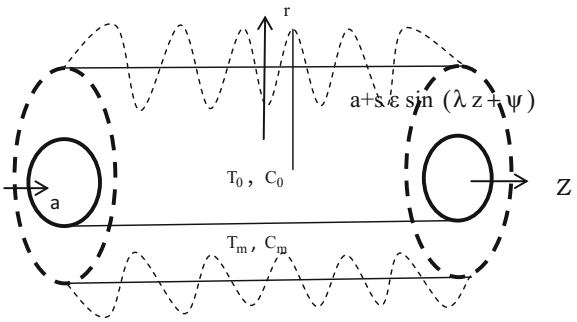

Fig. 1 Geometry under consideration

$$w\frac{\partial T}{\partial z}=\frac{\alpha_{nf}}{r}\frac{\partial}{\partial r}\left(r\frac{\partial T}{\partial r}\right)-\frac{Q}{(\rho c_p)_{nf}}(T-T_0) \tag{3}$$

$$w\frac{\partial c}{\partial z}=\frac{D_{nf}}{r}\frac{\partial}{\partial r}\left(r\frac{\partial c}{\partial r}\right)+k_l(c-c_0) \tag{4}$$

The appropriate initial and boundary conditions for the problem are given by

$$T=T_0,\quad c=c_0,\quad w=0\ \text{ on }\ r=a \tag{5}$$

$$T=T_m,\quad c=c_m,\quad w=0\ \text{ on }\ r=a+s\varepsilon\sin(\lambda z+\psi)$$

Thermo-physical properties are related as follows:

$$\begin{aligned}
&\rho_{nf}=(1-\phi)\rho_f+\phi\rho_s,\alpha_{nf}=\frac{k_{nf}}{(\rho c_p)_{nf}},\\
&(\rho c_p)_{nf}=(1-\phi)(\rho c_p)_f+\phi(\rho c_p)_s,\\
&(\rho\beta)_{nf}=(1-\phi)(\rho\beta)_f+\phi(\rho\beta)_s,\\
&k_{nf}=k_f(1-\phi)+\beta_1k_p\phi+c_1\frac{d_f}{d_p}k_f\mathrm{Re}^2d_p\,\mathrm{Pr}\,\phi\\
&\frac{\mu_{nf}}{\mu_f}=1+2.5\phi+4.5\left[\frac{h}{d_p}\left(2+\frac{h}{d_p}\right)\left(1+\frac{h}{d_p}\right)^2\right]^{-1}
\end{aligned} \tag{6}$$

We introduce the following dimensionless variables:

$$\begin{aligned}
&R=\frac{r}{a},\quad s^*=\frac{s}{a},\quad Z=\frac{z}{a},\quad W=\frac{w}{v_f},\quad U=\frac{u}{v_f},\\
&\theta=\frac{T-T_0}{T_m-T_0},\quad C=\frac{c-c_0}{c_m-c_0}
\end{aligned} \tag{7}$$

Using Eqs. (5)–(7), the Eqs. (2)–(4) can be written in the following dimensionless form:

$$1+2.5\phi+4.5\left[\frac{h}{d_p}\left(2+\frac{h}{d_p}\right)\left(1+\frac{h}{d_p}\right)^2\right]^{-1}\left(\frac{\partial^2 W}{\partial R^2}+\frac{1}{R}\frac{\partial W}{\partial R}\right)$$
$$\frac{1}{\left(1-\phi+\phi\left(\frac{\rho_s}{\rho_f}\right)\right)}-\frac{1}{\left(1-\phi+\phi\left(\frac{\rho_s}{\rho_f}\right)\right)}\mathrm{MW}$$
$$-\frac{1}{D}\left[1+2.5\phi+4.5\left[\frac{h}{d_p}\left(2+\frac{h}{d_p}\right)\left(1+\frac{h}{d_p}\right)^2\right]^{-1}\right]$$
$$\frac{1}{\left(1-\phi+\phi\left(\frac{\rho_s}{\rho_f}\right)\right)}W+\frac{1}{\left(1-\phi+\phi\left(\frac{\rho_s}{\rho_f}\right)\right)}Gr\theta+\frac{1}{\left(1-\phi+\phi\left(\frac{\rho_s}{\rho_f}\right)\right)}GcC=0$$

$$\left(1-\phi+0.01\phi\frac{k_p}{k_f}+\frac{k_p}{k_f^2}\phi\frac{\rho_f^2 c_{pf}}{d_p\mu_f^3}28632.9991\times10^{-52}\right)*\left[\left(1-\phi+\phi\frac{(\rho c_p)_s}{(\rho c_p)_f}\right)^{-1}\right]*\frac{1}{\mathrm{Pr}}\left[\frac{\partial^2\theta}{\partial R^2}+\frac{1}{R}\frac{\partial\theta}{\partial R}\right]$$
$$-\frac{1}{\mathrm{Pr}}Q_H\left[\left(1-\phi+\phi\frac{(\rho c_p)_s}{(\rho c_p)_f}\right)^{-1}\right]\theta=W\frac{\partial\theta}{\partial z}$$

$$W\frac{\partial C}{\partial z}=\frac{1}{Sc}\left[\frac{\partial^2 C}{\partial R^2}+\frac{1}{R}\frac{\partial C}{\partial R}\right]+KC$$

The corresponding boundary conditions (5) become:

$$W=0,\theta=0,C=0\quad\text{on}\quad R=1$$

$$W=0,\quad\theta=1,\quad C=1\quad on\quad R=1+s*\varepsilon\sin(\lambda z+\psi)$$

(We drop * in the later part)

Here Pr is the Prandtl number, M is the magnetic parameter (Hartmann number), Q_H is the heat source parameter, Sc is the Schmidt number, K is the chemical reaction parameter, D^{-1} is the Darcy number, Gr is the thermal Grashof number, Gc is the molecular Grashof number, which are defined as:

$$Pr=\frac{v_f}{\alpha_f},\quad M=\frac{\sigma B_0^2}{\mu_f}a,\quad Q_H=\frac{Q}{k_f}a,\quad Sc=\frac{v_f}{D_{nf}},\quad K=\frac{k_l}{v_f}a,\quad \frac{1}{D}=\frac{a}{k},$$
$$Gr=\frac{g(\rho\beta_T)(T_m-T_0)}{v_f^2},\quad Gc=\frac{g(\rho\beta_c)(c_m-c_0)}{v_f^2}$$

The nondimensional Nusselt number (Nu) is:

$$Nu = -\frac{k_{nf}}{k_f} \quad \theta'[1 + s\varepsilon \sin(\lambda z + \psi)]$$

The local Sherwood number Sh in dimensionless form:

$$Sh = -\frac{v_f}{D_{nf}} C'[1 + s\varepsilon \sin(\lambda z + \psi)]$$

3 Solution of the Problem

Cross section of the geometry is considered for numerical analysis. All the governing parameters are evaluated using shooting and R-K sixth order methods simultaneously using Mathematica package. The axial temperature gradient is assumed constant. The fixed values are φ: 0.02, s: 0.5, h: 4, d_p: 40, Gc: 5, Gr: 5, M: 5, Q_H: 5, Sc: 0.6, K: 0.5, $1/D$: 5, ε: 0.005.

4 Results and Discussion

The influence of various dimensionless numbers on the governing parameters is represented graphically. The Prandtl number (Pr) kept constant as 7 (for water) and $x = s\varepsilon \sin(\lambda z + \psi)$.

Figures 2, 3, 4, 5, 6, 7, 8, 9, and 10 represent the profiles of velocity w with various parameters mentioned above. All these profiles are bell shaped indicating the maximum flow in mean portion of the annulus. The significant variations are observed with φ, s, h, d_p, K, M, Sc, D^{-1}, and ε; for other parameters, the slight variation in w is observed. The absence of metal particles leads to the higher

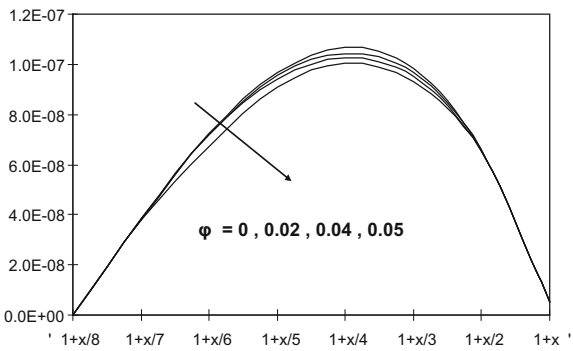

Fig. 2 Variation of W with ϕ

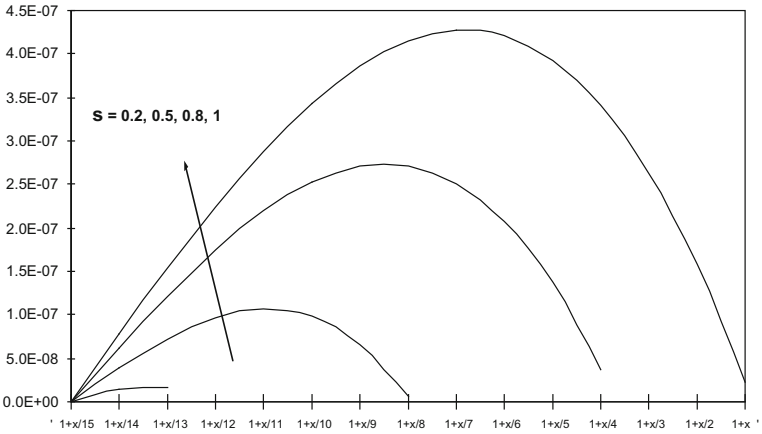

Fig. 3 Variation of W with s

Fig. 4 Variation of W with h

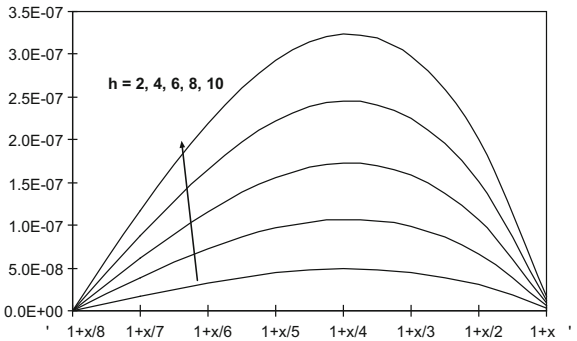

Fig. 5 Variation of W with d_p

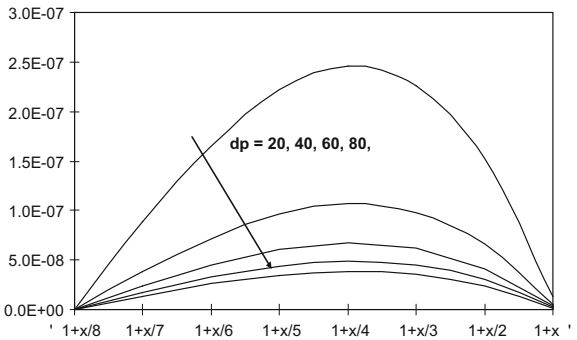

velocity, whereas the mixture of metal particles from 2 to 5% retards the flow (Fig. 2). This occurs due to clustering of the particles. Figure 3 represents the flow variation for gap of the annulus from inner cylinder to mean position of outer wavy

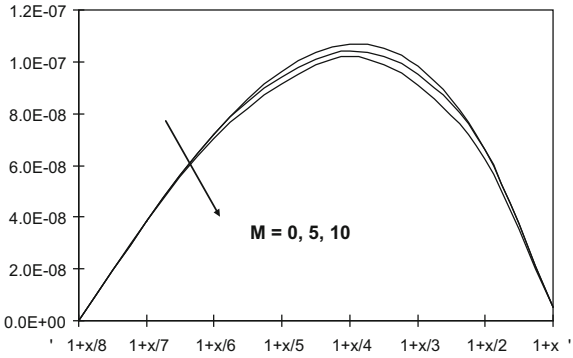

Fig. 6 Variation of W with M

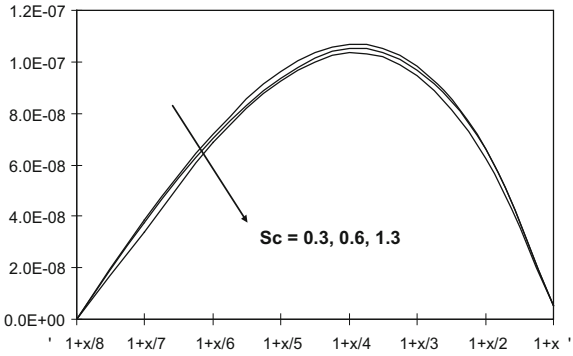

Fig. 7 Variation of W with Sc

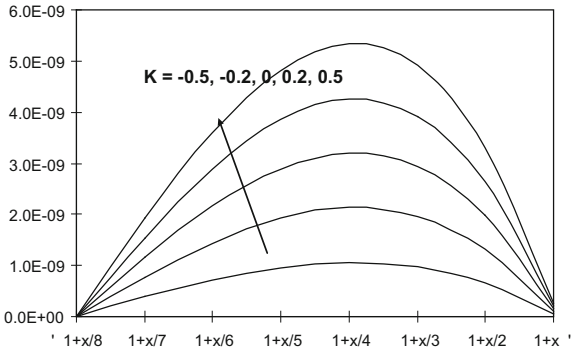

Fig. 8 Variation of W with K

surface (s). The flow increases with increase in gap from 20 to 100% compared with size of inner cylinder. The interparticle spacing is one of the parameters significantly enhancing the flow, and the Brownian motion may be the additional impact on the flow (Fig. 4). The effect of the size of the particle (d_{-p}) on flow has shown in Fig. 5. The significant enhancement of flow is noticed. But the flow has increased gradually. Figures 2, 4, and 5 show the significance of the presence of the Cu

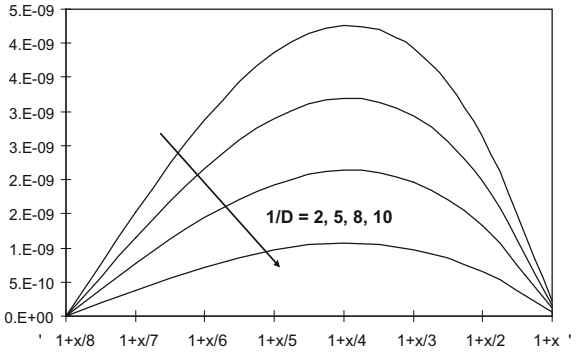

Fig. 9 Variation of W with D^{-1}

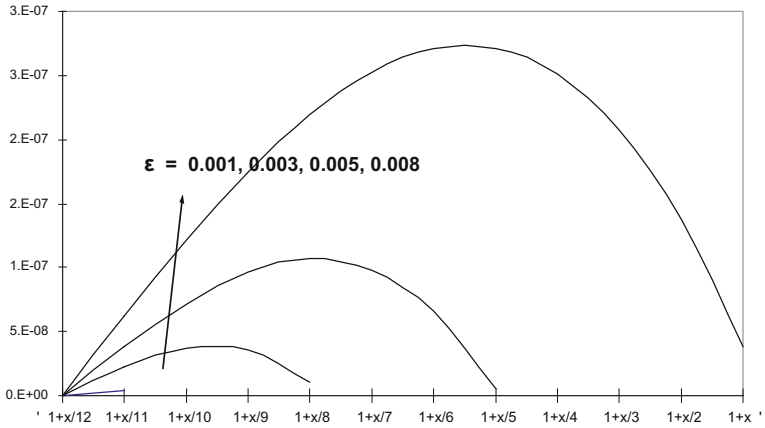

Fig. 10 Variation of W with ε

nanoparticles to enhance the flow. The flow is slightly reduced with magnetic parameter (M), indicates the Lorentz force has dominated/neutralized by viscous force (Fig. 6). Neither the absence nor the presence of magnetic field affect the flow. The increase in diffusivity (Sc) enhances the flow slightly (Fig. 7). The Fig. 8 depicts that destructive chemical reaction ($K > 0$) gives more velocity when compared with generative chemical reaction ($K < 0$). The uniform rate of increase of velocity is observed for $-0.5 < K < 0.5$. Figure 9 gives the velocity profile with Darcy parameter D^{-1}. The flow is more for the bigger pore. The variation of velocity with amplitude of the wave (ε) is given in Fig. 10. The flow is more for ε near 0.008 and retards from 0.008 to 0.001. So the wavy boundary shows the significant increase in flow.

Figures 11, 12, 13, 14, 15, and 16 represent the profiles of temperature with various parameters. The effect of φ, s, h, d_p, Sc, K and ε on temperature is more

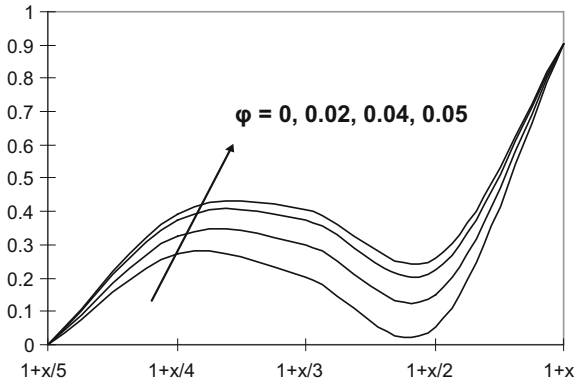

Fig. 11 Variation of θ with ϕ

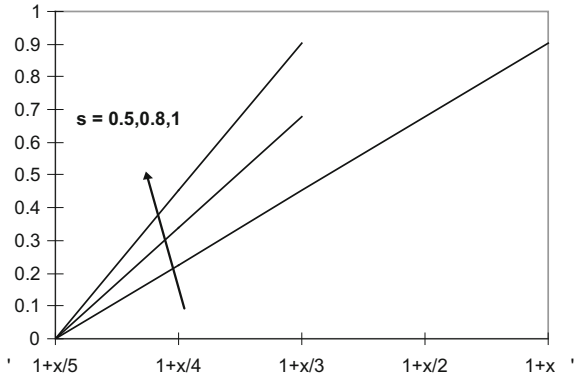

Fig. 12 Variation of θ with s

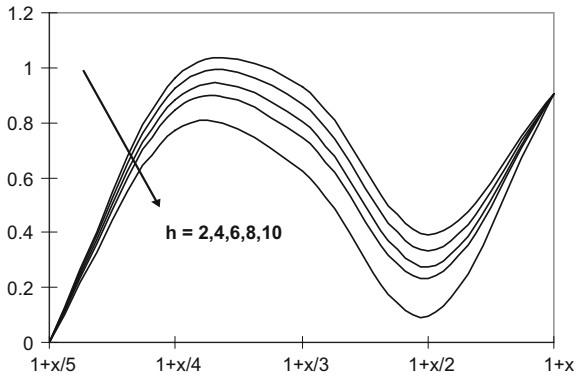

Fig. 13 Variation of θ with h

compared with effect of M. Except for s and ε, the temperature rises near the inner cylinder and falls, then rises near the outer cylinder to reach maximum temperature. On the other hand, the effect of s and ε on the temperature is linear. Figure 11 depicts the profile of temperature with φ. The increase in solid volume fraction

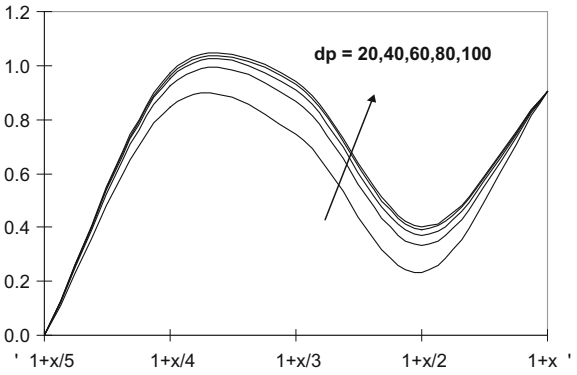

Fig. 14 Variation of θ with d_p

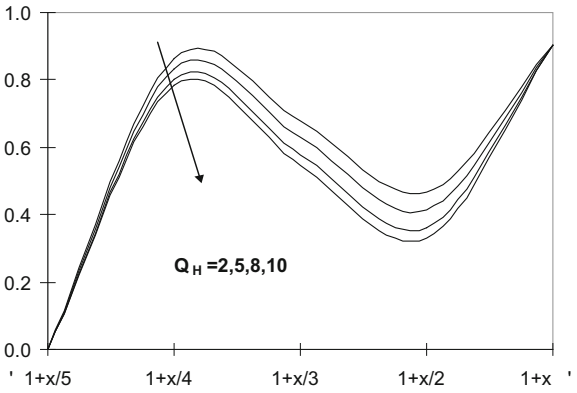

Fig. 15 Variation of θ with Q_H

increases the temperature due to the conductivity of Cu molecules. But the variation of temperature is not much for solid volume fraction $\geq 5\%$. This may be due to the clustering of the molecules. Figure 12 represents the effect of s on temperature. The enhancement of temperature is observed for reduction in gap of the annulus (s). This happens due to the Brownian motion of the particles. The increase in the interparticle spacing (h) reduces the temperature throughout the annulus. The cooling is observed from Fig. 13. From Fig. 14, the effect of d_p on temperature is observed. There is no much variation of temperature with increase in d_p. But the slight increase in temperature is noticed for d_p. From Fig. 15, the increase in heat source (Q_H) reduces the temperature in the mid-region of the annulus. However, no effect of heat source is observed near the inner cylinder. The increase in amplitude (ε) retards the temperature as shown in Fig. 16. But the variation of temperature is very linear with ε. The cooling effect may take place when the amplitude is more due to more disturbance of the flow along the outer cylinder.

Figures 17, 18, 19, 20, 21, 22, and 23 represent the profiles of diffusion (C) with various parameters. The effect of φ, s, h, d_p, Sc, K and ε. Except for s and ε, the diffusion rises and falls in the mid-region of the annulus, then rises near the outer

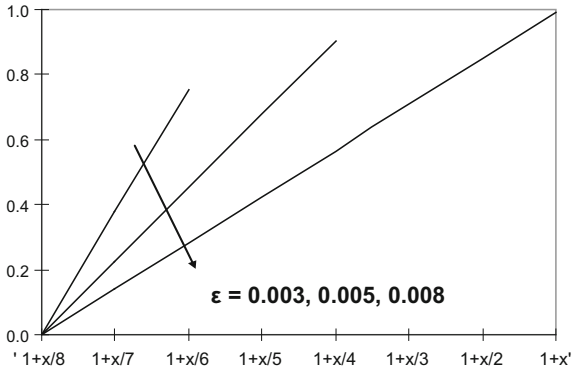

Fig. 16 Variation of θ with ε

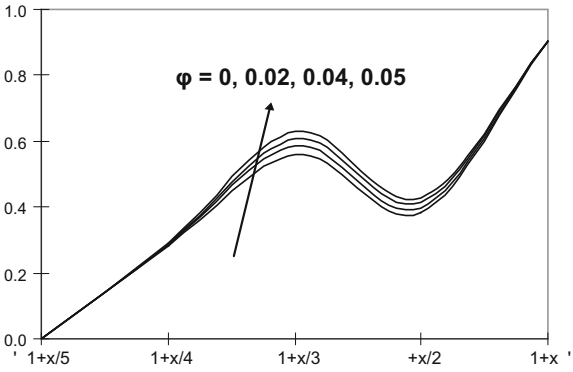

Fig. 17 Variation of C with ϕ

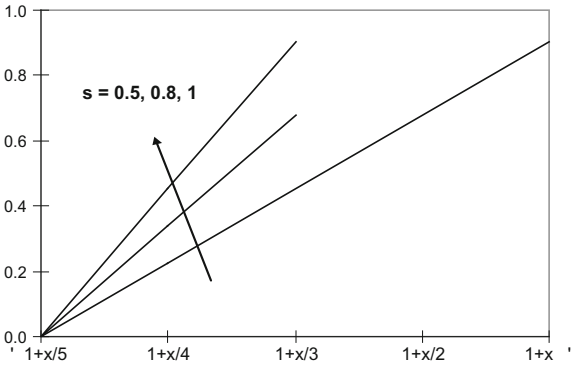

Fig. 18 Variation of C with s

cylinder to reach maximum diffusion. On the other hand, the effect of s and ε on the diffusion is very linear. Figure 17 represents the variation of C with φ. The impact of Brownian motion is clear on C, since C increases as φ increases ($0\% < \varphi < 5\%$ of Cu particles in water). From Fig. 18, the gap of the annulus should be moderate

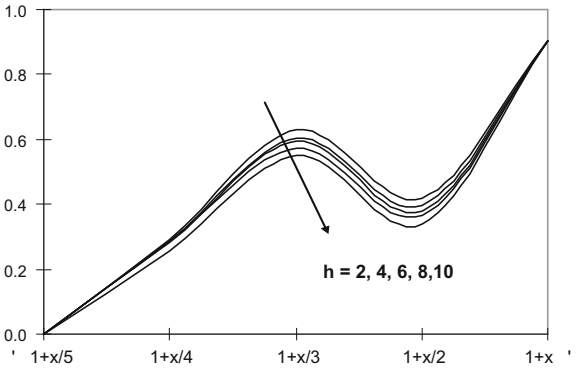

Fig. 19 Variation of C with h

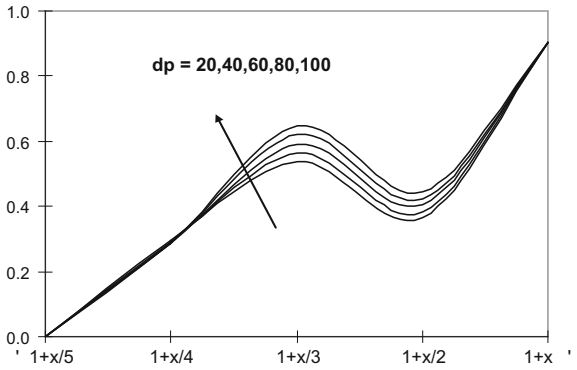

Fig. 20 Variation of C with d_p

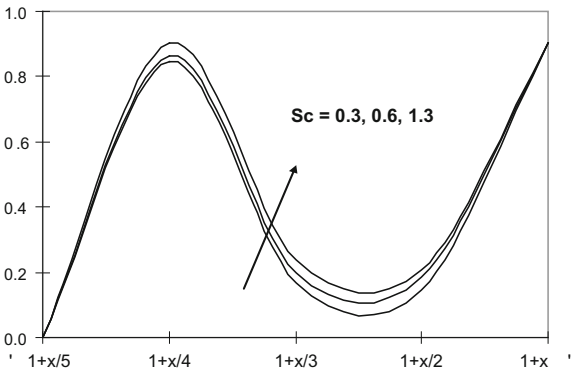

Fig. 21 Variation of C with Sc

to get effective diffusion. The gradual reduction of diffusion is observed for increase in interparticle spacing (h), from Fig. 19 this is due to the increase in flow. From Fig. 20, the increase in size of the Cu particle the diffusion enhances. This happens due to the reduction of flow. Interestingly, the increase in momentum enhances the diffusivity throughout the annulus. The significant rise and fall of diffusion is

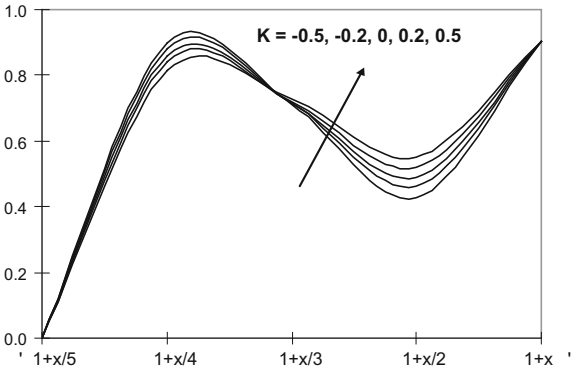

Fig. 22 Variation of C with K

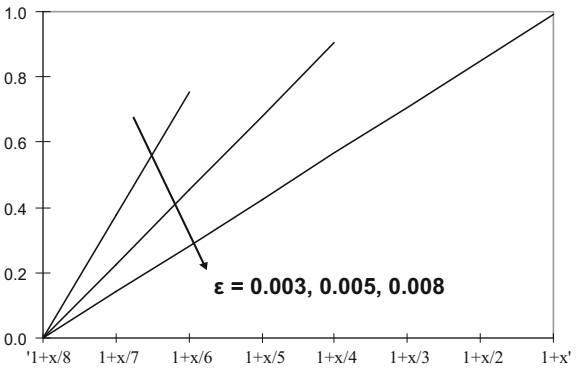

Fig. 23 Variation of C with ε

Table 1 Nusselt number

ϕ	$h = 2$, $dp = 40$, $Q_H = 5$	$h = 5$, $dp = 40$, $Q_H = 5$	$h = 10$, $dp = 40$, $Q_H = 5$	$h = 5$, $dp = 20$, $Q_H = 5$	$h = 5$, $dp = 80$, $Q_H = 5$	$h = 5$, $dp = 40$, $Q_H = 10$
0	5.5123	5.5125	5.5129	5.5129	5.5124	5.7985
0.05	5.449	5.4498	5.4501	5.4501	5.4497	5.6753
0.1	5.4091	5.4092	5.4095	5.4095	5.4092	5.5954

observed with Sc (Fig. 21). It is occurring due to the change of momentum at the outer wavy cylinder. Figure 22 exhibits the variation of diffusion with chemical reaction (K). The diffusion increases with increase in K near the inner cylinder, but the reversal effect is noticed near the outer wavy cylinder. The increase in amplitude (ε) retards the diffusion, from Fig. 23. But the diffusion profiles are very linear with ε, and the amplitude opposes the diffusion.

Table 1 displays the rate of heat transfer (Nusselt number) coefficient for various φ, h, d_p, and Q_H calculated on the outer wavy cylinder. The impact of nanofluid is very less in heat transfer, and the heat transfer coefficient decreases with increase in φ.

Table 2 Sherwood number

K	$dp = 20$, $Sc = 0.3$	$dp = 40$, $Sc = 0.3$	$dp = 80$, $Sc = 0.3$	$dp = 40$, $Sc = 0.6$	$dp = 40$, $Sc = 0.8$
−0.5	5.22931	5.2293	5.22929	5.23815	5.24405
0	5.22047	5.22045	5.22045	5.22047	5.22048
0.5	5.21162	5.21161	5.2116	5.20276	5.19687

It is due to the domination of amplitude over the momentum. The interparticle spacing is slightly enhancing the heat transfer rate. The size of the particle reduces the heat transfer due to the wavy surface as the movement of the particle is objected. The heat source enhances the heat transfer naturally.

Table 2 displays the mass transfer coefficient (Sherwood number) calculated for various K, $d_{p,}$ and Sc on the outer wavy cylinder. The mass transfer is more for generative ($K < 0$) and less for destructive ($K > 0$) chemical reactions. The increase in size of the particle is resisting the mass transfer in both chemical reactions. Sc improves the mass transfer for generative chemical reaction and retards the mass transfer for destructive chemical reaction. The absence of chemical reaction leads mass transfer to be a constant almost.

Acknowledgements Second author gratefully acknowledges UGC-SERO, Hyderabad, India, for the financial support in carrying out this work.

References

Ahmed A, Bays-Muchmore B (1992) Transverse flow over a wavy cylinder. Phys Fluids A 9 (4):1959–1967

Gosukonda S, Gorti VPN, Baluguri SB, Sakam SR (2015) Particle spacing and chemical reaction effects on convective heat transfer through a nano-fluid in cylindrical annulus. Procedia Eng 127(2015):263–270

Graham AL (1981) On the viscosity of suspension of solid spheres. Appl Sci Res 37(3):275–286

Jang SP, Choi SUS (2007) Effects of various parameters on nano-fluid thermal conductivity. J Heat Transf 129(5):617–623

Lam K, Lin YF (2008) Large eddy simulation of flow around wavy cylinders at a subcritical reynolds number. Int J Heat Fluid Flow 29:1071–1088

Lam K, Wang FH, Li JYRMC (2004) So, Experimental investigation of the mean and fluctuating forces of wavy (varicose) cylinders in a cross-flow. J Fluids Struct 19:321–334

Lee S, Nguyen AT (2007) Experimental investigation on wake behind a wavy cylinder having sinusoidal cross-sectional area variation. Fluid Dyn Res 39:292–304

Mittal R, Balachandar S (1994) Direct numerical simulation of flow past elliptic cylinders. J Comput Phys 124:351–367

Unal MF, Rockwell D (1977) On vortex formation from a cylinder, Part 1. The initial instability. J Fluid Mech 190:491–512

Williamson CHK (1989) Oblique and parallel modes of vortex shedding in the wake of a circular cylinder at low reynolds numbers. J Fluid Mech 206:579–628

Williamson CHK (1996) Vortex dynamics in the cylinder wake. Ann Rev Fluid Mech 28:477–539

Hydrodynamics of Non-Newtonian Spriggs Fluid Flow Past an Impulsively Moving Plate

Atul Kumar Ray and B. Vasu

Abstract One of the fundamental problems in unsteady viscous flows is that of impulsively started motion of a body in an infinite fluid medium which is referred as Stokes's first problem. On the basis of the fundamental understanding, we have developed a mechanistic modelling and thereby to improve existing technical applications. In this study, one of the particular non-Newtonian Spriggs fluid has considered that it is a truncated power law type of fluid. Flow of non-Newtonian Spriggs fluid caused by the unsteady impulsively moving plate is investigated using a similarity transformation. The use of similarity transformation reduces the unsteady boundary layer equations to linear and nonlinear ordinary differential equations governed by a non-dimensional material parameter. The effect of material parameter on velocity boundary layer is explained by an efficient and robust Homotopy Analysis Method. Variations of the velocity profile are presented graphically for distinct values of material constant. A physical interpretation is also provided. The flow past a plate has received much attention because of its major significance role in numerous disciplines which include the chemical engineering, manufacturing industry, heat conduction problems and geophysical flows (such as in earthquakes and fracture of ice sheets).

1 Introduction

Stokes's first problem is very famous unsteady viscous fluid flow problem in fluid mechanics which represents one of the few exact solutions to Navier–Stokes equation (which are governing equation in fluid mechanics). First problem of Stokes (1851) is also named as Rayleigh problem Tanner (1962), Soundalgekar

A.K. Ray (✉) · B. Vasu
Department of Mathematics, Motilal Nehru National Institute of Technology Allahabad, Allahabad 211004, India
e-mail: rma0215@mnnit.ac.in

B. Vasu
e-mail: bvasu@mnnit.ac.in

M.K. Singh et al. (eds.), *Applications of Fluid Dynamics*, Lecture Notes in Mechanical Engineering, https://doi.org/10.1007/978-981-10-5329-0_7

(1974), and is defined as the flow over flat plate which is initially at rest and impulsive set into motion with constant speed. Stokes's first problem has received much attention due to its theoretical and practical applications, particularly in field of polymer industries and in the manufacture of fibres in glass. Teipel (1981) and Puri (1984) studied impulsive motion of a flat plate in a viscoelastic fluid and in a Rivlin-Ericksen fluid, respectively. MHD flow near a wall suddenly sets in motion non-Newtonian viscoelastic fluid studied by Cuouusv (1985). Wenchang and Mingyu (2002) inspect Stokes's first problem for viscoelastic fluid with fractional Maxwell mode. Erdogan (2002) discussed some exact solution of equation of Navier–Stokes for flows which impulsively started from rest by application of sudden pressure gradient or by motion of a boundary. Sine transform was used for solving the Stokes's first problem for ordinary Oldroyd-B fluid by Fetecau and Fetecau (2003). Transverse magnetic field effect on the unsteady flow of a generalized second-grade fluid through a porous medium past an infinite flat plate was investigated by El-Shaded (2004). Tan and Masuoka (2005) explained first problem of Stokes for a second-grade fluid in a porous half space with heated boundary. Exact solution was obtained corresponding to the Stokes's first problem for Oldroyd-B fluid by Vieru et al. (2008). Hayat et al. (2008) has given numerical solution of first problem of Stokes, based on modified Darcy's law, for a third-grade fluid in a porous half space. Mistakes made in the literature of Stokes's first problem for some non-Newtonian fluid are identified by Christov (2010). Zaman and Sohail (2014) elaborate first problem of Stokes for an unsteady MHD third-grade fluid in a non-porous half space by taking hall currents into account. The flow for thermoelectric fluid for Stokes's first problem using the methodology of fractional calculus is examined by Ezzat et al. (2014).

Truncated power law fluid also known as Spriggs fluid was suggested by Spriggs (1965). Adusumilli and Hill (1984) investigated the transient laminar flow of Spriggs fluid in pipes in which they used truncated power law to exhibit the behaviour of real fluids undergoing the above pressure disturbance. Lavrov (2015) explores the hydraulic fracturing application of flow of Spriggs fluid between parallel walls and found that as compared to power law model, the truncated power law model upgrades precision of flow computations in small and large aperture parts of the fracture and so raising the overall accuracy and performance of hydraulic fracturing simulation.

Homotopy Analysis Method (HAM) is proposed by Liao (1992), based on the homotopy, a basic concept in topology. HAM is an analytic approximation technique and has been successfully applied widely to solve highly nonlinear problems in science and engineering. HAM has many advantages as compared to traditional analytic methods. HAM is independent on any small or large parameters, provides suitable way to control the convergence of series solution using parameter called convergence control parameter and also presents freedom to choose the operator called auxiliary linear operator so as to approximate a nonlinear problem more convincingly by means of choosing appropriate base function. Besides, it contains other non-perturbation techniques which are proved by Liao in his book Liao (2003).

The aim of this paper is to analyse flow of non-Newtonian Spriggs fluid caused by the unsteady impulsively moving plate. Similarity solution exists for flow over semi-infinite plates, so similarity transformation is used to investigate the flow. The transformed ordinary differential equation after using similarity transformation in partial differential equation is solved by the Homotopy Analysis Method (HAM) Liao (2012), (2004), (2003), (2013), Sajid and Hayat (2009). Variations of the velocity profile and local wall shear strain term to evaluate local friction coefficient are presented graphically for different values of material constant.

2 Mathematical Formulation

Consider a two-dimensional unsteady boundary layer flow of quiescent viscous incompressible non-Newtonian fluid past an impulsively started semi-infinite flat plate. A non-Newtonian Spriggs fluid is considered which is a truncated power-law type of fluid. The plate lies on x-axis at time $t = 0$ shown in Fig. 1a. For $t > 0$, instantaneously the plate moves with velocity U as shown in Fig. 1b. Let $U_w(x) = U$ denotes speed of flat plate.

Continuity and momentum equations are as follows:

$$\frac{\partial u}{\partial x} + \frac{\partial v}{\partial y} = 0 \tag{1}$$

$$\rho\left[\frac{\partial u}{\partial t} + u\frac{\partial u}{\partial x} + v\frac{\partial u}{\partial y}\right] = -\frac{\partial p}{\partial x} + \frac{\partial \tau_{xx}}{\partial x} + \frac{\partial \tau_{xy}}{\partial x} \tag{2}$$

$$\rho\left[\frac{\partial v}{\partial t} + u\frac{\partial v}{\partial x} + v\frac{\partial v}{\partial y}\right] = -\frac{\partial p}{\partial y} + \frac{\partial \tau_{yx}}{\partial y} + \frac{\partial \tau_{yy}}{\partial y} \tag{3}$$

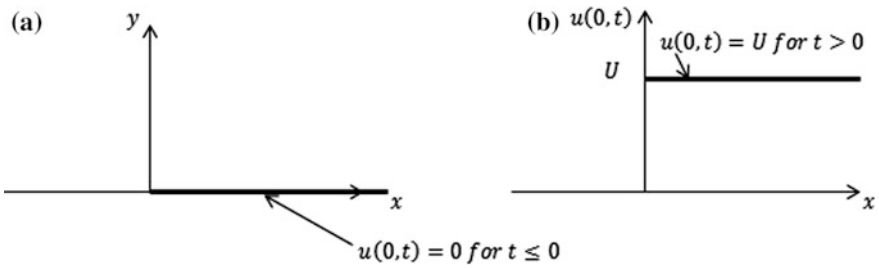

Fig. 1 Schematic diagram and coordinate system

Subject to boundary conditions,

$$v = 0, \quad \frac{\partial v}{\partial x} = 0 \tag{4}$$

Using (4) stress components reduced to,

$$\tau_{xx} = \tau_{yx} = \tau_{yy} = 0 \tag{5}$$

Using (4) and (5), (3) implies

$$\frac{\partial p}{\partial y} = 0 \tag{6}$$

As plate suddenly starts in motion and slides in its plane that is in x-direction with constant speed U, i.e. so velocity of plate is $(U, 0)$. Motion of fluid will also be in x-direction. So nonzero velocity component is only u. Under these conditions, flow velocity u at a given point depends only on its y-coordinate and time, i.e. $u = u(y, t), \quad v = 0$

The viscosity function of Spriggs fluid (Irgens 2014) is defined as

$$\eta = \begin{cases} \eta_0; & \dot{\gamma} \leq \dot{\gamma}_0 \text{ and } 0 < r < \delta_1 \\ \eta_0 \left(\frac{\dot{\gamma}}{\dot{\gamma}_0}\right)^{n-1}; & \dot{\gamma} \geq \dot{\gamma}_0 \text{ and } \delta_1 < r < \delta \end{cases} \tag{7}$$

where δ is boundary layer thickness, r is the distance away from the boundary of plate, Newtonian model is applied up to $r = \delta_1$ and $(\delta - \delta_1)$ is the region where power law model is applicable.

The interface is Newtonian flow,

$$\tau_{yx} = \eta_0 \dot{\gamma}_0$$

at $\delta = \delta_1$

And this is related to wall stress as

$$\frac{\tau_\delta}{\delta} = \frac{\tau_{yx}}{\delta_1} = \frac{\eta_0 \dot{\gamma}_0}{\delta_1}$$

therefore,

$$\delta_1 = \frac{\delta \eta_0 \dot{\gamma}_0}{\tau_\delta} \tag{8}$$

For non-Newtonian Spriggs fluid, the respective stress component is

$$\tau_{xy} = \begin{cases} \eta_0 \frac{\partial u}{\partial y}; & \dot{\gamma} \le \dot{\gamma}_0 \text{ and } 0 < r < \delta_1 \\ \eta_0 \left(\frac{\dot{\gamma}}{\dot{\gamma}_0}\right)^{n-1} \frac{\partial u}{\partial y}; & \dot{\gamma} \ge \dot{\gamma}_0 \text{ and } \delta_1 < r < \delta \end{cases} \tag{9}$$

where u and v are velocity component in direction of increasing x, y, respectively, and $\dot{\gamma} = \frac{\partial u}{\partial y}$ is the shear rate. As velocity u is independent of x, so pressure will be independent on x

$$\frac{\partial p}{\partial x} = 0 \tag{10}$$

Equations (7) and (10) yield pressure as constant.

Using Eqs. (4), (8), (9) and (10), by introducing the boundary layer approximation,x-momentum, Eq. (2) reduces to

$$\rho \frac{\partial u}{\partial t} = \eta_0 \begin{cases} \frac{\partial^2 u}{\partial y^2}; & \dot{\gamma} \le \dot{\gamma}_0 \text{ and } 0 < r < \delta_1 \\ \left(\frac{\dot{\gamma}}{\dot{\gamma}_0}\right)^{n-1} \frac{\partial^2 u}{\partial y^2}; & \dot{\gamma} \ge \dot{\gamma}_0 \text{ and } \delta_1 < r < \delta \end{cases} \tag{11}$$

Initial condition and boundary conditions are

$$u(y, 0) = 0 \quad \text{for} \quad y > 0 \tag{12}$$

$$u(0, t) = \begin{cases} 0; & t \le 0 \\ U; & t > 0 \end{cases} \tag{13}$$

$$u(y, t) \to 0 \quad \text{as} \quad y \to \infty \tag{14}$$

Introducing the similarity transformation,

$$f(\eta) = \frac{u}{U}, \quad \eta = \alpha \frac{y}{t^m} \tag{15}$$

From Eq. (11),

$$\rho m \eta U \frac{f'(\eta)}{t} = \eta_0 \begin{cases} \frac{\alpha^2 U}{t^{2m}} f''(\eta); & \dot{\gamma}\lambda \le 1 \text{ and } 0 < r < \delta_1 \\ \frac{n U^n \alpha^{n+1}}{\dot{\gamma}_0^{n-1}(n+1) t^{(n+1)m}} f'^{n-1}(\eta) f''(\eta); & \dot{\gamma}\lambda \ge 1 \text{ and } \delta_1 < r < \delta \end{cases} \tag{16}$$

Here, λ is relaxation time. Equation (16) is not ODE for arbitrary m.

We classified the two cases as follows:

Case 1: $\dot{\gamma}\lambda \le 1$ and $0 < r < \delta_1$. For $m = \frac{1}{2}$, using this value of m, respective equation reduced to

$$f'' + \frac{\rho\eta}{2\eta_0\alpha^2} f' = 0; \qquad \dot{\gamma}\lambda \leq 1 \text{ and } 0 < r < \delta_1, \quad m = \tfrac{1}{2} \tag{17}$$

Case 2: $\dot{\gamma}\lambda \geq 1$ and $\delta_1 < r < \delta$. For $m = \frac{1}{n+1}$, respective equation, we have

$$f'' f'^{n-1} + \frac{\rho}{2\eta_0(n+1)\alpha^{n+1}} \left(\frac{\dot{\gamma}_0}{U}\right)^{n-1} f' = 0; \quad \dot{\gamma}\lambda \geq 1 \text{ and } \delta_1 < r < \delta, \quad m = \frac{1}{n+1} \tag{18}$$

For simplicity, taking $\alpha = \sqrt{\frac{\rho}{2\eta_0}}$ for $\dot{\gamma}\lambda \leq 1$ *and* $0 < r < \delta_1$, $m = \frac{1}{2}$ and $\alpha = \left(\frac{\rho}{\eta_0(n+1)}\right)^{1/n+1}$ for $\dot{\gamma}\lambda \geq 1$ and $\delta_1 < r < \delta$, $m = \frac{1}{n+1}$ and $\beta_n = \left(\frac{\dot{\gamma}_0}{U}\right)^{n-1} = (\beta)^{n-1}$ is a non-dimensional parameter.

Now Eqs. (17) and (18) are reduced to

$$f'' + \eta f' = 0; \quad \dot{\gamma}\lambda \leq 1 \text{ and } 0 < r < \delta_1 \tag{19}$$

$$f'' f'^{n-1} + \eta_n \beta_n f' = 0; \quad \dot{\gamma}\lambda \geq 1 \text{ and } \delta_1 < r < \delta \tag{20}$$

which is reduced to ordinary differential equation.

For $n = 1$: $\beta_n = \beta$ and $\eta_n = \eta$ also, both Eqs. (19) and (20) are equal. This is the case of Newtonian fluid for impulsive start of flat plate which is also a well-known Stokes's problem.

Transformed boundary conditions are as follows:

$$f(0) = 1 \quad \text{and} \quad f(\infty) \to 0 \tag{21}$$

The local skin friction coefficient on the surface of moving plate is given by

$$C_f = \frac{2\tau_{xy}\big|_{y=0}}{\rho U^2}$$

Now using (9) and (15), we obtained

$$C_f = \begin{cases} \alpha_1 f'(0); & \dot{\gamma}\lambda \leq 1 \text{ and } 0 < r < \delta_1 \\ \alpha_n \beta^{n-1} f'(0)^n; & \dot{\gamma}\lambda \geq 1 \text{ and } \delta_1 < r < \delta \end{cases} \tag{22}$$

where $\alpha_1 = \frac{2\nu\alpha}{Ut^m}$ and $\alpha_n = \frac{2\nu}{U}\left(\frac{\alpha}{t^m}\right)^n$ depend on Reynolds number.

3 Analytic Approximation by HAM

In order to solve the transformed non-dimensional Eq. (20) under the condition (21), HAM has been employed. Liao (1998) used this technique for nonlinear problem. HAM converts a nonlinear problem into an infinite number of linear sub-problems, without any dependency on small or large physical parameters. HAM provides suitable way to ensure the convergence of series solution using convergence control parameter c_0. Region of this convergence control parameter is discussed and shown in Fig. 2.

Solutions for above two cases are as follows:

Case 1: For $\dot{\gamma}\lambda \leq 1$ and $0 < r < \delta_1$ and $m = \frac{1}{2}$,

exact solution for Eq. (19) with the boundary condition (21), which is a solution for Stokes's problem for a Navier–Stokes fluid (Currie 2012), is given by

$$u(y,t) = U\left[1 - \operatorname{erf}\left(\frac{y}{2\sqrt{tv}}\right)\right]$$

Case 2: For $\dot{\gamma}\lambda \geq 1$ and $\delta_1 < r < \delta$ and $m = \frac{1}{n+1}$,

to investigate the analytic solution of Eqs. (20) and (21) by using HAM, we select the appropriate initial approximation as

$$f_0(\eta) = e^{-\eta}$$

which satisfy the boundary condition (21), and we select auxiliary linear operator as

$$\mathcal{L}(f) = f'' - f$$

with the property that

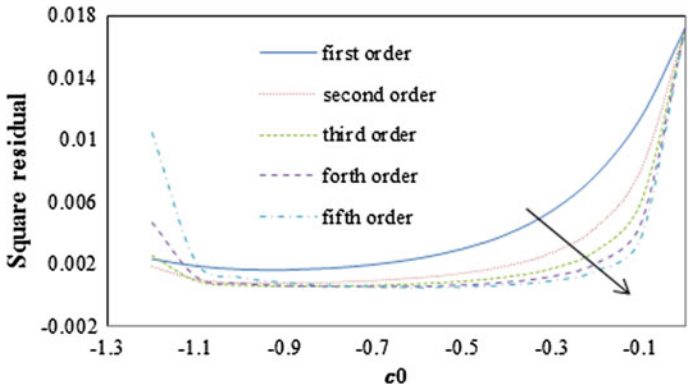

Fig. 2 Variation of square residual versus c_0 for different order

$$\mathcal{L}(a_1 e^{-\eta} + a_2 e^{\eta}) = 0$$

and define nonlinear operator as

$$\mathcal{N}[\phi(\eta; q)] = \phi''(\eta)(\phi'(\eta))^{n-1} + \eta_n \beta_n \phi'(\eta)$$

where $q \in [0, 1]$ is embedding parameter and ϕ is kind of mapping function for f.

Using these operators, zeroth order deformation equation can construct

$$(1 - q)\mathcal{L}[\phi(\eta; q) - f_0(\eta)] = c_0 q \mathcal{N}[(\phi(\eta; q))]$$

Subject to boundary condition,

$$\phi(0; q) = 1 \quad \text{and} \quad \phi(0; q) = 1$$

Homotopy series solution is as follows:

$$f(\eta) = f_0(\eta) + \sum_{m=1}^{+\infty} f_m(\eta)$$

where

$$f_m(\eta) = \frac{1}{m!} \frac{\mathrm{d}^m \phi(\eta; q)}{\mathrm{d}q^m}|_{q=0}$$

And $f_m(\xi)$ is governed by mth order deformation equation

$$\mathcal{L}[f_m(\eta) - \chi_m f_{m-1}(\eta)] = c_0 \mathcal{D}_{m-1}\{\mathcal{N}[\phi(\eta; q)]\}$$

where

$$\chi_m = \begin{cases} 0, & m \leq 1 \\ 1, & m > 1 \end{cases}$$

Subject to boundary condition,

$$f_m(0) = 1, \quad f_m(\infty) = 0$$

Now let $f_m^*(\eta)$ denotes the special solution of mth order deformation equation, $\mathcal{L}^{-1}$ is inverse of linear operator $\mathcal{L}$ and f_m^* is given by

$$f_m^*(\eta) = \sum_{k=0}^{m} \alpha_{m-k}^* f_k(\eta) + c_0 \sum_{k=0}^{m} \beta_k \mathcal{L}^{-1}[\mathcal{D}_{m-1}\{\mathcal{N}[\phi(\eta;q)]\}]$$

so that

$$f_m^*(\eta) = \chi_m f_{m-1}(\eta) + c_0 \mathcal{L}^{-1}[\mathcal{D}_{m-1}\{\mathcal{N}[\phi(\eta;q)]\}]$$

So general solution of mth order deformation equation is given by

$$f_m(\eta) = f_m^*(\eta) + B_0 + B_1 e^{-\eta} + B_2 e^{\eta}$$

Using boundary conditions of deformation equation, obtaining values of B_0, B_1 and B_2 and substituting these values in solution of deformation equation, we will have

$$f_m(\eta) = f_m^*(\eta) - f_m^*(\infty) + (1 - f_m^*(0) + f_m^*(\infty))e^{-\eta}$$

Thus, homotopy series solution of Eq. (20) subject to boundary conditions (21) is given by

$$\begin{aligned} f(\eta) &= f_0(\eta) + \sum_{m=1}^{\infty} f_m(\eta) \\ &= e^{-\eta} + \sum_{m=1}^{\infty} \{f_m^*(\eta) - f_m^*(\infty) + (1 - f_m^*(0) + f_m^*(\infty))e^{-\eta}\} \end{aligned} \tag{23}$$

4 Results and Discussion

After introducing similarity transformation, the partial differential equation (11) subject to boundary conditions (13) and (14) is reduce ordinary differential equations (19) and (20) subject to boundary conditions given in (21). Equation (19) is the case of Newtonian fluid for which Muzychka and Yovanovich (2010) have given analytic solution. It is worth mention that for $n = 1$, Eqs. (19) and (20) are same. The non-linear ordinary differential equation (20) subject to boundary conditions in (21) is solved via HAM, a semi-analytic method.

$$\beta \neq 1 \; \eta \neq 2$$

In the present study, n = 3 is considered. The effect of c_0 and β on f_η is shown by Figs. 3 and 4. The effect of c_0 and β on f'_η is shown by Figs. 5 and 6 respectively. Figure 2 depicts the variation of square residual error of different order over c_0 for finding the range of c_0 for convergence of series solution.

It is clear from the Fig. 2 that region of convergence of homotopy series solution is about $-1 \leq c_0 < 0$. We can easily get the value of c_0 from this range to ensure that the homotopy series solution is about all parameter in the whole domain $0 \leq \eta < \infty$ corresponding to $0 \leq y < \infty$, respectively.

The influence of parameters on the dimensionless velocity $f(\eta)$ is as follows:

Effect of Convergence Control Parameter c_0

The velocity profiles are shown in Fig. 3.

Figure 3 stipulates the variation of velocity $f(\eta)$ with η at various distances from the wall. It describes that as we move away from the moving wall, the velocity decreases. Further, it shows the effect of convergence control parameter c_0 on velocity profile. It is found that the decrease in convergence control parameter c_0 results in decrease in velocity profile.

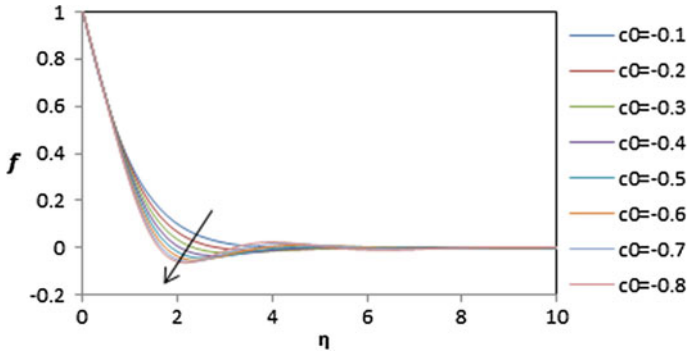

Fig. 3 Influence of c_0 on $f(\eta)$

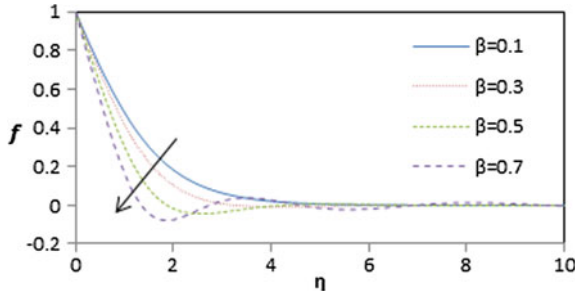

Fig. 4 Influence of c_0 on $f(\eta)$

Effect of Parameter β

The velocity profile for the solution (23) of (20) with boundary condition (21) is shown in Fig. 4 where the parametric values are $n = 3$ and $c_0 = -0.5$.

The discussion on effect of parameters on $f'(\eta)$ is as follows:

For $n = 3$, the local skin friction coefficient is

$$C_f = \begin{cases} \alpha_1 f'(0); & \dot{\gamma}\lambda \leq 1 \text{ and } 0 < r < \delta_1, \quad m = \frac{1}{2} \\ \alpha_3 \beta^2 (f'(0))^3; & \dot{\gamma}\lambda \geq 1 \text{ and } \delta_1 < r < \delta, \quad m = \frac{1}{n+1} \end{cases}$$

Influence of Convergence Control Parameter c_0

It is observed from Fig. 5 that velocity gradient f' changes its nature at $\eta = 1.6$.

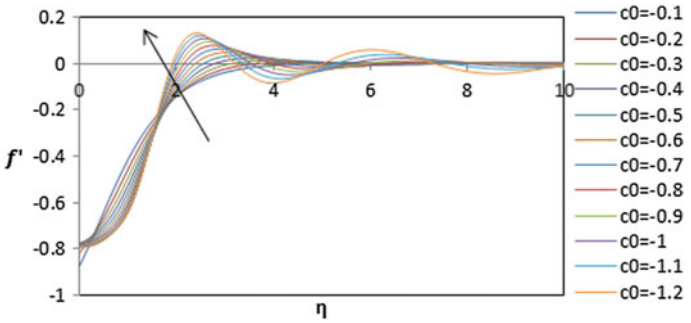

Fig. 5 Effect of c_0 on $f'(\eta)$

Fig. 6 Effect of β on $f'(\eta)$

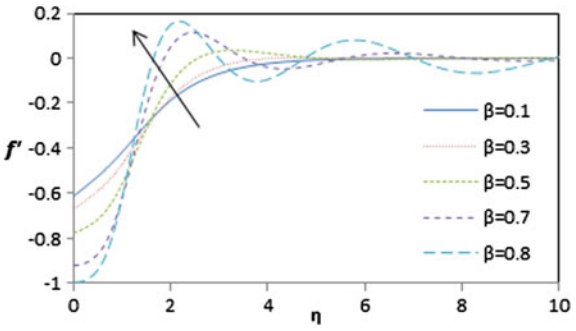

The parametric values are $n = 3$ and fixed $\beta = 0.5$

Eq. (22) contains $f'(0)$ that relates the local skin friction coefficient C_f and C_f has an important physical meaning. Figure 5 examines the influence of c_0 on $f'(\eta)$ with respect to η.

Influence of Parameter β

Figure 6 illustrates that with increase in β, the velocity gradient changes with the distance from the wall at $\eta = 1.4$. It shows that larger the value of β, more rapidly the velocity. Also it is remarked that $f'(\eta)$ is increasing with increase in values of β.

5 Conclusions

In this paper, we have resolute velocity field corresponding to the flow of non-Newtonian Spriggs fluid over impulsively started flat plate. Variations of the velocity profile $f(\eta)$ as well as for local skin friction coefficient $f'(\eta)$ are presented graphically for different values of material constant. The shear rate limit has influence on unsteady viscous flow state velocity profiles of an unsteady impulsive start of flat plate. Homotopy solution for the nonlinear problem is obtained, and convergence of the solution is discussed.

References

Adusumilli RS, Hill GA (1984) Transient laminar flows of truncated power law fluids in pipes. Can J Chem Eng 62(5):594–601

Christov IC (2010) Stokes's first problem for some non-Newtonian fluids: results and mistakes. Mech Res Commun 37(8):717–723

Cuouusv KR (1985) The impulsive motion of a flat plate in a viscoelastic fluid in the presence of a transverse magnetic field. Indian J Pure App Math, 19(8):931

Currie IG (2012) Fundamental mechanics of fluids, 4th edn. CRC Press

El-Shahed M (2004) On the impulsive motion of flat plate in a generalized second grade fluid. Zeitschrift für Naturforschung A 59(11):829–837

Erdoğan ME (2002) On the unsteady unidirectional flows generated by impulsive motion of a boundary or sudden application of a pressure gradient. Int J Non-Linear Mech 37(6): 1091–1106

Ezzat M, Sabbah AS, El-Bary AA, Ezzat S (2014) Stokes's first problem for a thermoelectric fluid with fractional-order heat transfer. Rep Math Phys 74(2):145–158

Fetecau C, Fetecau C (2003) The first problem of stokes for an Oldroyd-B fluid. Int J Non-Linear Mech 38(10):1539–1544

Hayat T, Shahzad F, Ayub M, Asghar S (2008) Stokes's first problem for a third grade fluid in a porous half space. Commun Nonlinear Sci Numer Simul 13(9):1801–1807

Irgens F (2014) Rheology and non-newtonian fluids. Springer International Publishing

Lavrov A (2015) Flow of truncated power-law fluid between parallel walls for hydraulic fracturing applications. J Nonnewton Fluid Mech 223:141–146

Liao S (1992) The proposed homotopy analysis technique for the solution of nonlinear problems, Ph.D. thesis, Shanghai Jiao Tong University
Liao S (1998) Homotopy analysis method: a new analytic method for nonlinear problems. Appl Math Mech 19(10):957–962
Liao S (2003) Beyond perturbation: introduction to the homotopy analysis method. CRC press
Liao S (2004) On the homotopy analysis method for nonlinear problems. Appl Math Comput 147(2):499–513
Liao S (2012) Homotopy analysis method in nonlinear differential equations, Beijing, Higher education press, pp 153–165
Liao S (ed) (2013) Advances in the homotopy analysis method. World Scientific
Muzychka YS, Yovanovich MM (2010) Unsteady viscous flows and stokes's first problem. Int J Therm Sci 49(5):820–828
Puri P (1984) Impulsive motion of a flat plate in a Rivlin-Ericksen fluid. Rheol Acta 23(4): 451–453
Sajid M, Hayat T (2009) Comparison of HAM and HPM solutions in heat radiation equations. Int Commun Heat Mass Transf 36(1):59–62
Soundalgekar VM (1974) Stokes's problem for elastico-viscous fluid. Rheol Acta 13(2):177–179
Spriggs TW (1965) A four-constant model for viscoelastic fluids. Chem Eng Sci 20(11):931–940
Stokes GG (1851) On the effect of the internal friction of fluids on the motion of pendulums, vol 9. Pitt Press, Cambridge
Tan W, Masuoka T (2005) Stokes's first problem for a second grade fluid in a porous half-space with heated boundary. Int J Non-Linear Mech 40(4):515–522
Tanner RI (1962) Note on the Rayleigh problem for a visco-elastic fluid. Zeitschrift fur angewandte Mathematik und Physik ZAMP 13(6):573–580
Teipel I (1981) The impulsive motion of a flat plate in a viscoelastic fluid. Acta Mech 39(3): 277–279
Vieru D, Nazar M, Fetecau C, Fetecau C (2008) New exact solutions corresponding to the first problem of stokes for Oldroyd-B fluids. Comput Math Appl 55(8):1644–1652
Wenchang T, Mingyu X (2002) Plane surface suddenly set in motion in a viscoelastic fluid with fractional Maxwell model. Acta Mech Sin 18(4):342–349
Zaman H, Sohail A (2014) Stokes's first problem for an unsteady MHD third-grade fluid in a non-porous half space with hall currents. Open J Appl Sci 4(03):85

Effects of Heat-Generating Component Size and Porous Layer Thickness on MHD Mixed Convection Flow of Ag-Water Nanofluid Through an L-Shaped Channel

Victor Job, Sreedhara Rao Gunakala, B. Rushi Kumar and R. Sivaraj

Abstract This paper focuses on the cooling of heat-generating components via MHD mixed convection flow of silver (Ag)-water nanofluid through an L-shaped channel with a porous inner layer. In this channel, four heat-generating components are located on the channel wall opposite to the porous layer. The governing equations with the given initial and boundary conditions are solved using the stabilized mixed finite element method based on the polynomial pressure projection technique. The effect of the thickness of the porous layer and size of the heat-generating components on fluid flow and heat transfer within the channel is investigated.

1 Introduction

The flow of fluids in channels with heated obstacles has been used as the canonical model for the cooling of electronic devices for many decades. The study of electronic cooling is necessary for improved thermal design of electronic components in order to reduce hot spots and to increase the reliability and durability of these devices (Young and Vafai 1998; Boutina and Bessaïh 2011). Young and Vafai (1998) examined the forced convective flow through a channel containing an array of heated obstacles. It was determined from this study that transfer of heat into the fluid is enhanced by a reduction in the size of the heated obstacles and an increase in the distance between obstacles. Boutina and Bessaïh (2011) considered the mixed convective air cooling of two isothermal electronic components in an inclined channel. In this connection, the authors found that the heat transfer

V. Job · S.R. Gunakala (✉)
Department of Mathematics and Statistics, The University of the West Indies, Saint Augustine, Trinidad and Tobago
e-mail: Sreedhara.Rao@sta.uwi.edu

B. Rushi Kumar · R. Sivaraj
Department of Mathematics, VIT University, Vellore, India

M.K. Singh et al. (eds.), *Applications of Fluid Dynamics*, Lecture Notes in Mechanical Engineering, https://doi.org/10.1007/978-981-10-5329-0_8

increases as the Reynolds number and the size of the electronic components increase.

The study of fluid flow and heat transfer at the interface between a porous medium and a free fluid is useful in a wide range of engineering applications. In particular, the use of high-porosity metal foams has potential applications in the cooling of electronic devices (Phanikumar and Mahajan 2002). In 2002, Phanikumar and Mahajan obtained numerical and experimental results for natural convection in high-porosity metal foams which are heated from below and surrounded by a fluid. These results revealed that the heat transfer rate increases as the foam porosity decreases. An increase in the Darcy number causes an enhancement in heat transfer rate. Hajipour et al. (2013) analysed the unsteady two-dimensional mixed convective flow of nanofluids in a vertical channel containing a porous inner layer. In this study, it was observed that an increase in the permeability of the porous medium results in an increase in flow velocity. Moreover, the velocity and temperature of the nanofluid increase with an increase in nanoparticle concentration.

The vast majority of the literature on the mixed convective cooling of heated obstacles pertains to straight channel flows. To the best of the author's knowledge, there is no existing study on the mixed convective nanofluid cooling of heat-generating obstacles within a bent channel containing a porous layer. In this chapter, the mixed convective cooling of four heat-generating components within an L-shaped channel with a porous inner layer using Ag-water nanofluid is considered. The effects of the relevant parameters on the thermal performance of this system are examined.

2 Mathematical Formulation

We consider the two-dimensional unsteady incompressible mixed convective flow of Ag-water nanofluid through an L-shaped channel as depicted in Fig. 1. This channel has width h, and the length of the inlet section and outlet section are both equal to $3h$. The porous layer has thickness h_1, porosity ε, and permeability K. There are four heat-generating components on the opposite side of the porous layer, each having area A_d and heat flux density q_c. The velocity and temperature at the channel inlet are U and T_0, respectively, while the channel walls are thermally insulated. The heat absorbed from these components by the nanofluid gives rise to free convection within the channel. Furthermore, the flow velocity is influenced by a magnetic field with strength B_0 in the negative x-direction. In this paper, the subscripts 'nf', 'm', '$c1$', '$c2$', '$c3$' and 'c4' refer to the nanofluid in the free-fluid region, the nanofluid in the porous layer and components 1, 2, 3 and 4, respectively. The nanofluid is assumed to be a single-phase Newtonian fluid with low nanoparticle concentration, and the nanoparticles have uniform size and are spherical in shape. The L-shaped domain Ω (Fig. 2) is comprised of the free-fluid region Ω_1, the saturated porous layer Ω_2 and the four heat-generating electronic components which are located at Ω_3, Ω_4, Ω_5 and Ω_6.

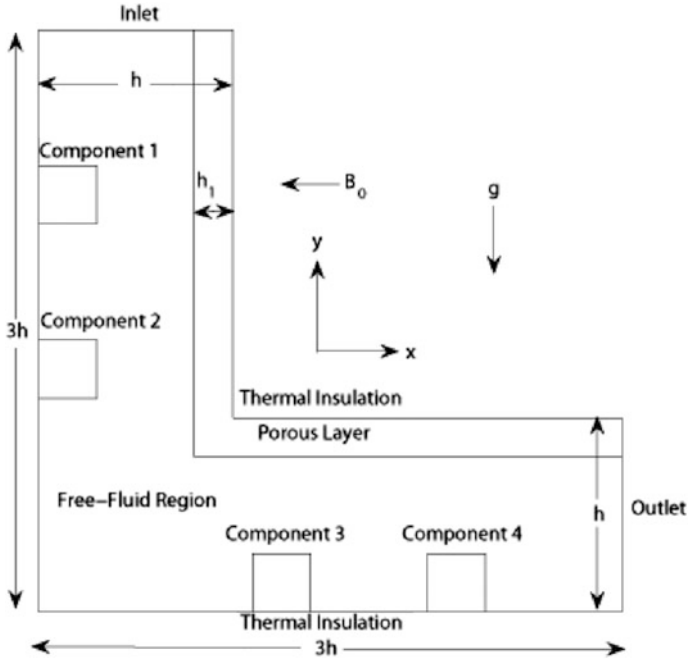

Fig. 1 Schematic diagram of the problem

The governing equations for the nanofluid flow under the Boussinesq approximation are given by:

Continuity Equation in the Free-Fluid Region:

$$\frac{\partial u_{nf}}{\partial x} + \frac{\partial v_{nf}}{\partial y} = 0 \tag{1}$$

X-Momentum Equation in the Free-Fluid Region:

$$\frac{\partial u_{nf}}{\partial t} + u_{nf}\frac{\partial u_{nf}}{\partial x} + v_{nf}\frac{\partial u_{nf}}{\partial y} = -\frac{\rho_f}{\rho_{nf}}\frac{\partial p_{nf}}{\partial x} + \frac{\mu_{nf}}{\mu_f}\frac{\rho_f}{\rho_{nf}}\frac{1}{Re}\left(\frac{\partial^2 u_{nf}}{\partial x^2} + \frac{\partial^2 u_{nf}}{\partial y^2}\right) \tag{2}$$

Y-Momentum Equation in the Free-Fluid Region:

$$\begin{aligned}\frac{\partial v_{nf}}{\partial t} + u_{nf}\frac{\partial v_{nf}}{\partial x} + v_{nf}\frac{\partial v_{nf}}{\partial y} &= -\frac{\rho_f}{\rho_{nf}}\frac{\partial p_{nf}}{\partial y} + \frac{\mu_{nf}}{\mu_f}\frac{\rho_f}{\rho_{nf}}\frac{1}{Re}\left(\frac{\partial^2 v_{nf}}{\partial x^2} + \frac{\partial^2 v_{nf}}{\partial y^2}\right) \\ &- \frac{\sigma_{nf}}{\sigma_f}\frac{\rho_f}{\rho_{nf}}\frac{Ha^2}{Re}v_{nf} + \frac{(\rho\beta)_{nf}}{(\rho\beta)_f}\frac{\rho_f}{\rho_{nf}}\frac{Gr}{\mathrm{Re}^2}T_{nf}\end{aligned} \tag{3}$$

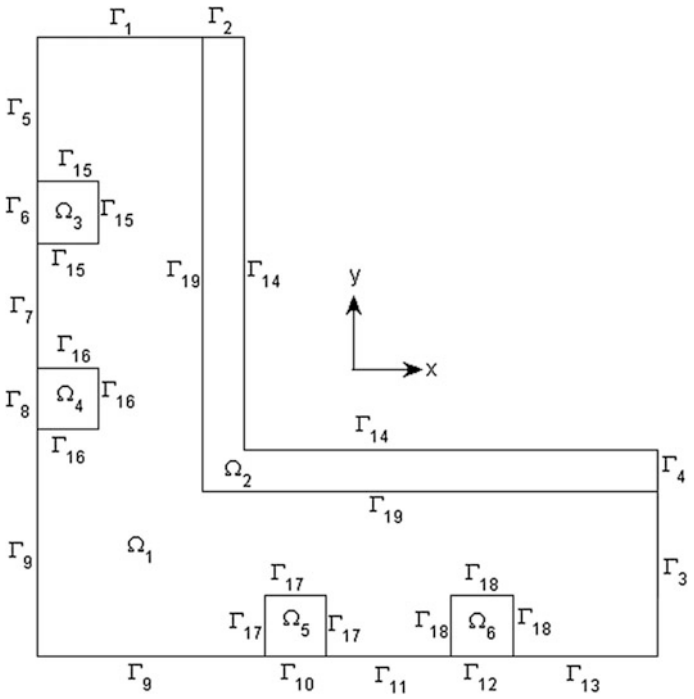

Fig. 2 Diagram of the domain

Energy Equation in the Free-Fluid Region:

$$\frac{\partial T_{nf}}{\partial t} + u_{nf}\frac{\partial T_{nf}}{\partial x} + v_{nf}\frac{\partial T_{nf}}{\partial y} = \frac{\kappa_{nf}}{\kappa_f}\frac{(\rho c_p)_f}{(\rho c_p)_{nf}}\frac{1}{RePr}\left(\frac{\partial^2 T_{nf}}{\partial x^2} + \frac{\partial^2 T_{nf}}{\partial y^2}\right) \tag{4}$$

Continuity Equation in the Porous Layer:

$$\frac{\partial u_m}{\partial x} + \frac{\partial v_m}{\partial y} = 0 \tag{5}$$

X-Momentum Equation in the Porous Layer:

$$\frac{1}{\varepsilon}\frac{\partial u_m}{\partial t} + \frac{1}{\varepsilon^2}\left(u_m\frac{\partial u_m}{\partial x} + v_m\frac{\partial u_m}{\partial y}\right) = -\frac{\rho_f}{\rho_{nf}}\frac{\partial p_m}{\partial x} + \frac{\mu_{nf}}{\mu_f}\frac{\rho_f}{\rho_{nf}}\frac{1}{\varepsilon Re}\left(\frac{\partial^2 u_m}{\partial x^2} + \frac{\partial^2 u_m}{\partial y^2}\right) - \frac{\mu_{nf}}{\mu_f}\frac{\rho_f}{\rho_{nf}}\frac{1}{ReDa}u_m - \frac{c_F}{\sqrt{Da}}\sqrt{u_m^2 + v_m^2}u_m \tag{6}$$

Y-Momentum Equation in the Porous Layer:

$$\frac{1}{\varepsilon}\frac{\partial v_m}{\partial t}+\frac{1}{\varepsilon^2}\left(u_m\frac{\partial v_m}{\partial x}+v_m\frac{\partial v_m}{\partial y}\right)=-\frac{\rho_f}{\rho_{nf}}\frac{\partial p_m}{\partial y}+\frac{\mu_{nf}}{\mu_f}\frac{\rho_f}{\rho_{nf}}\frac{1}{\varepsilon Re}\left(\frac{\partial^2 v_m}{\partial x^2}+\frac{\partial^2 v_m}{\partial y^2}\right)$$
$$-\frac{\mu_{nf}}{\mu_f}\frac{\rho_f}{\rho_{nf}}\frac{1}{ReDa}v_m-\frac{c_F}{\sqrt{Da}}\sqrt{u_m^2+v_m^2}v_m-\frac{\sigma_{nf}}{\sigma_f}\frac{\rho_f}{\rho_{nf}}\frac{Ha^2}{Re}v_m+\frac{(\rho\beta)_{nf}}{(\rho\beta)_f}\frac{\rho_f}{\rho_{nf}}\frac{Gr}{Re^2}T_m \tag{7}$$

Energy Equation in the Porous Layer:

$$\frac{\partial T_m}{\partial t}+\frac{(\rho c_p)_{nf}}{(\rho c_p)_{\text{eff}}}\left(u_m\frac{\partial T_m}{\partial x}+v_m\frac{\partial T_m}{\partial y}\right)=\frac{\kappa_{\text{eff}}}{\kappa_f}\frac{(\rho c_p)_f}{(\rho c_p)_{\text{eff}}}\frac{1}{RePr}\left(\frac{\partial^2 T_{nf}}{\partial x^2}+\frac{\partial^2 T_{nf}}{\partial y^2}\right) \tag{8}$$

Energy Equation in Components 1–4:

$$\frac{\partial T_{ck}}{\partial t}=\frac{\alpha_r}{RePr}\left(\frac{\partial^2 T_{ck}}{\partial x^2}+\frac{\partial^2 T_{ck}}{\partial y^2}+Q\right),\quad k=1,2,3,4 \tag{9}$$

where $Re=\frac{\rho_f U h}{\mu_f}$ is the Reynolds number, $Da=\frac{K}{h^2}$ is the Darcy number, $Ha=B_0 h\sqrt{\frac{\sigma_f}{\mu_f}}$ is the Hartmann number, $Gr=\frac{\rho_f^2\beta_f g T_0 h^3}{\mu_f^2}$ is the Grashof number, $Pr=\frac{\mu_f(c_p)_f}{\kappa_f}$ is the Prandtl number and $Q=\frac{q_c h^2}{\kappa_c T_0}$ is the heat-generation parameter.

The effective heat capacity $(\rho c_p)_{\text{eff}}$ and thermal conductivity κ_{eff} of the porous medium are given by

$$(\rho c_p)_{\text{eff}}=(1-\varepsilon)(\rho c_p)_{ps}+\varepsilon(\rho c_p)_{nf},$$
$$\kappa_{\text{eff}}=(1-\varepsilon)\kappa_{ps}+\varepsilon\kappa_{nf}$$

The above equations are non-dimensionalized using the following dimensionless variables:

$$\left(\widehat{x},\widehat{y},\widehat{h}_1\right)=\frac{(x,y,h_1)}{h},\left(\widehat{u}_{nf},\widehat{u}_m,\widehat{v}_{nf},\widehat{v}_m\right)$$
$$\widehat{t}=\frac{h}{U}t,\left(\widehat{p}_{nf},\widehat{p}_m\right)=\frac{(p_{nf},p_m)}{\rho_f U^2},$$

$$\widehat{T}_{nf}=\frac{T_{nf}-T_0}{T_0},\widehat{T}_m=\frac{T_m-T_0}{T_0},\widehat{T}_{ck}=\frac{T_{ck}-T_0}{T_0}\quad(k=1,2,3,4),$$
$$\alpha_r=\kappa_r\frac{(\rho c_p)_f}{(\rho c_p)_c},\kappa_r=\frac{\kappa_c}{\kappa_f}$$

The following equations are used in this chapter to describe the thermophysical properties of nanofluids (Minkowycz et al. 2013):

1. Viscosity (Brinkman):

$$\mu_{nf} = \frac{\mu_f}{(1-\phi)^{2.5}} \tag{10}$$

2. Density:

$$\rho_{nf} = (1-\phi)\rho_f + \phi\rho_s \tag{11}$$

3. Heat capacity:

$$(\rho c_p)_{nf} = (1-\phi)(\rho c_p)_f + \phi(\rho c_p)_s \tag{12}$$

4. Thermal expansion coefficient:

$$(\rho\beta)_{nf} = (1-\phi)(\rho\beta)_f + \phi(\rho\beta)_s \tag{13}$$

5. Thermal conductivity (Bruggerman):

$$\kappa_{nf} = \frac{(3\phi-1)\kappa_s/\kappa_f + 3(1-\phi) - 1 + \sqrt{\Delta}}{4}\kappa_f \tag{14}$$

where

$$\Delta = \left[(3\phi-1)\kappa_s/\kappa_f + 3(1-\phi) - 1\right]^2 + 8\kappa_s/\kappa_f$$

6. Electrical conductivity (Maxwell):

$$\sigma_{nf} = \sigma_f\left[1 + \frac{3(\sigma_s/\sigma_f - 1)\phi}{(\sigma_s/\sigma_f + 2) - (\sigma_s/\sigma_f - 1)\phi}\right] \tag{15}$$

The thermophysical properties of pure water and Ag (Mansour et al. 2010; Ganji and Kachapi 2015) at 52 °C are given in Table 1.

The no-slip condition is imposed at the walls of the channel and at the surface of the components. The temperature and normal heat flux are continuous at the surface

Table 1 Thermophysical properties of pure water and Ag at 25 °C

Quantity	Pure water	Ag
ρ (kg m^{-3})	997.1	10,500
c_p (J kg^{-1} K^{-1})	4179	235
κ (W m^{-1})	0.613	429
β (K^{-1})	21×10^{-5}	1.89×10^{-5}
σ (Ω^{-1} m^{-1})	0.05	6.3×10^{7}

of the heat-generating components and at the interface between the free-fluid region and porous layer (Nield and Bejan 2006). Continuity of the velocity and normal and tangential stresses at the interface between the free-fluid region and porous layer is imposed (Laptev 2003). Thus, the dimensionless initial conditions are

$$u_{nf} = v_{nf} = T_{nf} = 0 \quad \text{on } \Omega_1 \times \{0\} \tag{16}$$

$$u_m = v_m = T_m = 0 \quad \text{on } \Omega_2 \times \{0\} \tag{17}$$

$$T_{ck} = 0 \quad \text{on } \Omega_{k+2} \times \{0\}, \quad k = 1, 2, 3, 4 \tag{18}$$

and the dimensionless boundary conditions are

$$u_{nf} = 0, \quad v_{nf} = -1, \quad T_{nf} = 0 \ \text{ on } \ \Gamma_1 \times (0, t_{dm}] \tag{19}$$

$$u_m = 0, \quad v_m = -1, \quad T_m = 0 \ \text{ on } \ \Gamma_2 \times (0, t_{dm}] \tag{20}$$

$$\frac{\partial u_{nf}}{\partial \boldsymbol{n}} = \frac{\partial v_{nf}}{\partial \boldsymbol{n}} = \frac{\partial T_{nf}}{\partial \boldsymbol{n}} = 0 \quad \text{on } \Gamma_3 \times (0, t_{dm}] \tag{21}$$

$$\frac{\partial u_m}{\partial \boldsymbol{n}} = \frac{\partial v_m}{\partial \boldsymbol{n}} = \frac{\partial T_m}{\partial \boldsymbol{n}} = 0 \quad \text{on } \Gamma_4 \times (0, t_{dm}] \tag{22}$$

$$u_{nf} = v_{nf} = 0, \quad \frac{\partial T_{nf}}{\partial \boldsymbol{n}} = 0 \quad \text{on } (\Gamma_5 \cup \Gamma_7 \cup \Gamma_9 \cup \Gamma_{11} \cup \Gamma_{13}) \times (0, t_{dm}] \tag{23}$$

$$\frac{\partial T_{ck}}{\partial \boldsymbol{n}} = 0 \quad \text{on } \Gamma_{2k+4} \times (0, t_{dm}], \quad k = 1, 2, 3, 4 \tag{24}$$

$$u_m = v_m = 0, \quad \frac{\partial T_m}{\partial \boldsymbol{n}} = 0 \text{ on } \Gamma_{14} \times (0, t_{dm}] \tag{25}$$

$$\begin{aligned} &\text{On } \Gamma_{k+14} \times (0, t_{dm}] : u_{nf} = v_{nf} = 0, \\ &\kappa_r \frac{\kappa_f}{\kappa_{nf}} \frac{\partial T_{ck}}{\partial \boldsymbol{n}} = \frac{\partial T_{nf}}{\partial \boldsymbol{n}}, T_{nf} = T_{ck}, \quad k = 1, 2, 3, 4 \end{aligned} \tag{26}$$

$$\begin{aligned} &\text{On } \Gamma_{19} \times (0, t_{dm}] : u_{nf} = u_m, v_{nf} = v_m, \\ &-p_m n_x + \frac{\mu_{nf}}{\mu_f} \frac{1}{\varepsilon Re} \frac{\partial u_m}{\partial \boldsymbol{n}} = -p_{nf} n_x + \frac{\mu_{nf}}{\mu_f} \frac{1}{Re} \frac{\partial u_{nf}}{\partial \boldsymbol{n}}, \\ &-p_m n_y + \frac{\mu_{nf}}{\mu_f} \frac{1}{\varepsilon Re} \frac{\partial v_m}{\partial \boldsymbol{n}} = -p_{nf} n_y + \frac{\mu_{nf}}{\mu_f} \frac{1}{Re} \frac{\partial v_{nf}}{\partial \boldsymbol{n}}, \end{aligned}$$

$$T_{nf} = T_m, \quad \frac{\kappa_{eff}}{\kappa_{nf}} \frac{\partial T_m}{\partial \boldsymbol{n}} = \frac{\partial T_{nf}}{\partial \boldsymbol{n}} \tag{27}$$

where $t_{dm} > 0$ is the dimensionless length of the time interval and $n = (n_x, n_y)$ is the unit outward normal to Γ_{k+14}.

The removal of heat from the heat-generating components is described by

$$Nu_{av} = \frac{1}{4}\sum_{k=1}^{4} Nu_{av,k} \tag{28}$$

where

$$Nu_{av,k} = -\frac{\int_{\Gamma_{k+14}} \frac{\partial T_{ck}}{\partial n} \mathrm{d}l}{l(\Gamma_{k+14})} \tag{29}$$

is the dimensionless average Nusselt number at the fluid–solid interface of component k and $l(\Gamma_{k+14})$ is the length of Γ_{k+14}.

3 Finite Element Method

Equations (1)–(9) with the associated initial and boundary conditions (16)–(27) are solved numerically using the mixed finite element method with polynomial pressure projection stabilization (PPPS). The domain of the problem is first spatially discretized into three-noded linear triangular elements, and a stabilized mixed Galerkin formulation of the governing equations is constructed. The resulting system of ordinary differential equations is then time-discretized using the Crank-Nicholson scheme. This yields a system of nonlinear algebraic equations, which are solved iteratively using MATLAB with a relative error tolerance of 10^{-6}.

3.1 Grid-Independence Test

A grid-independence test was conducted for time $t_{dm} = 1$ with four different finite element meshes with 4942, 5596, 6466 and 6996 elements. The average Nusselt number Nu_{av} in the case of the Cu-water nanofluid for these meshes is shown in Table 2. It was determined from this test that a finite element mesh with 6466 elements is appropriate for the present problem.

Table 2 Grid independence test values at $t = 1$, $Pr = 6.2$, $\kappa_{ps} = 8$ W m^{-1}, $\rho_{ps} = 200$ kg m^{-3}, $(c_p)_{ps} = 900$ J kg^{-1} K^{-1}, $c_F = 0.06$, $Q = 100$, $\alpha_r = 10$, $\kappa_r = 4$, $Re = 1$, $Ha = 1$, $Gr = 1$, $\varepsilon = 0.95$, $Da = 10^{-5}$ and $\phi = 0.02$

Number of elements	Nu_{av}	Time (s)
4942	4.7725	8891
5596	4.7582	11,203
6466	4.7491	12,090
6996	4.7475	13,722

3.2 Code Validation

The present numerical scheme is validated by comparison against the work of Nithiarasu et al. (1998) on unsteady natural convective flow and heat transfer within an L-shaped cavity. Comparisons of the present results and those obtained by Nithiarasu et al. are given in Table 3 and Fig. 3. It was observed that there is good agreement between the compared results; hence, the present code may be used to accurately solve the problem under consideration.

Table 3 Comparison of Nu_{av} from the present code with the numerical solution of Nithiarasu et al. (1998)

L_2/H_2	Present work	Nithiarasu et al. (1998)	Error (%)
1	3.6169	3.58	1.03
0.65	3.7293	3.76	0.82
0.40	3.8270	3.80	0.71

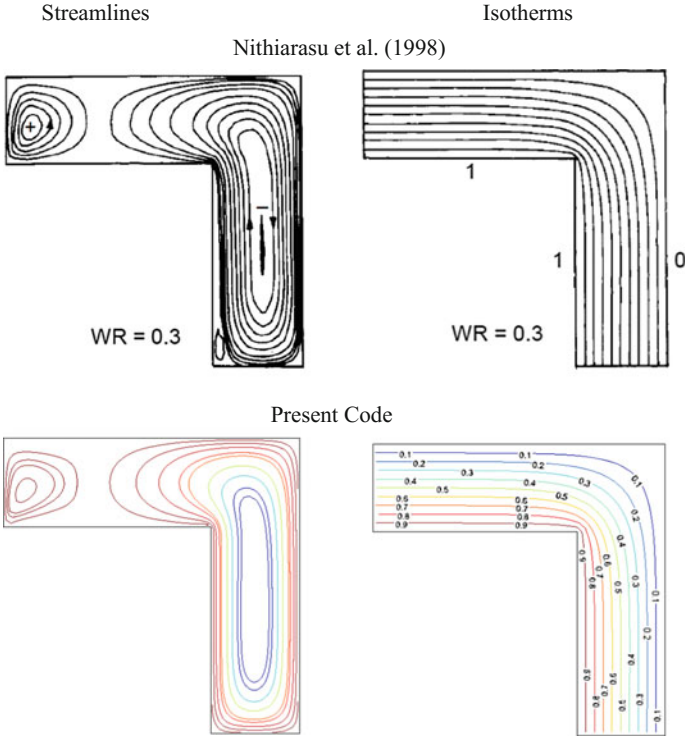

Fig. 3 Comparison between present code and that of Nithiarasu et al. (1998)

4 Results and Discussion

The porous medium used in this study is an ERG Aerospace Duocel® open-cell aluminium foam (ERM Aerospace Corporation 2011). This metal foam has thermal conductivity $\kappa_{ps} = 8$ W m^{-1} K^{-1}, density $\rho_{ps} = 200$ kg m^{-3}, specific heat capacity $(c_p)_{ps} = 900\,\mathrm{J kg^{-1}\,K^{-1}}$ and form drag coefficient $c_F = 0.06$ (Ashby et al. 2000; Dukhan and Minjeur 2011). Throughout the present study, the values $t = 1$, $Pr = 6.2$, $Q = 100$, $\alpha_r = 10$, $\kappa_r = 4$, $Re = 1$, $Ha = 1$, $Gr = 1$, $\varepsilon = 0.95$, $Da = 10^{-5}$ and $\phi = 0.02$ are assumed.

The effects of the thickness of the porous layer h_1 and size of the heat-generating components A_d are displayed in Figs. 4, 5, 6, 7, 8 and 9. These figures reveal that the size of the circulation zone decreases as the thickness of the porous layer h_1 increases. We also note that as A_d is increased, the streamlines become less concentrated between components 1 and 2 and between components 3 and 4. This is due to a reduction in the spacing of the components as the size of the components increases. The isotherm plots show that the temperature of the heat-generating components increases with increased A_d. An increase in A_d causes an increase in the heat generated within the components, which leads to the observed increase in temperature. We also observe that the temperature of the fluid near components 1 and 2 increases with increased h_1. The fluid temperature near components 3 and 4 is reduced when h_1 increases from 0.2 to 0.25; however, this trend is reversed when h_1 is increased from 0.25 to 0.3. This occurs as a result of the competing effects of enhanced thermal conductivity and reduced heat capacity within the porous layer, and a reduction in flow velocity within this layer as its thickness increases.

Table 4 displays the average Nusselt number Nu_{av} on the fluid–solid interface of the electronic components for different values of A_d and h_1. It is observed that an increase in the thickness h_1 of the porous layer results in a decrease in Nu_{av}. The average rate of heat transfer decreases with increased A_d when $0.09 \leq \leq 0.12$ and $0.135 \leq A_d \leq 0.15$, but increases as A_d increases when $0.12 \leq A_d \leq 0.135$. This may be explained by the competing effects of enhanced mixing within the fluid and an increase in the temperature within the components as A_d increases.

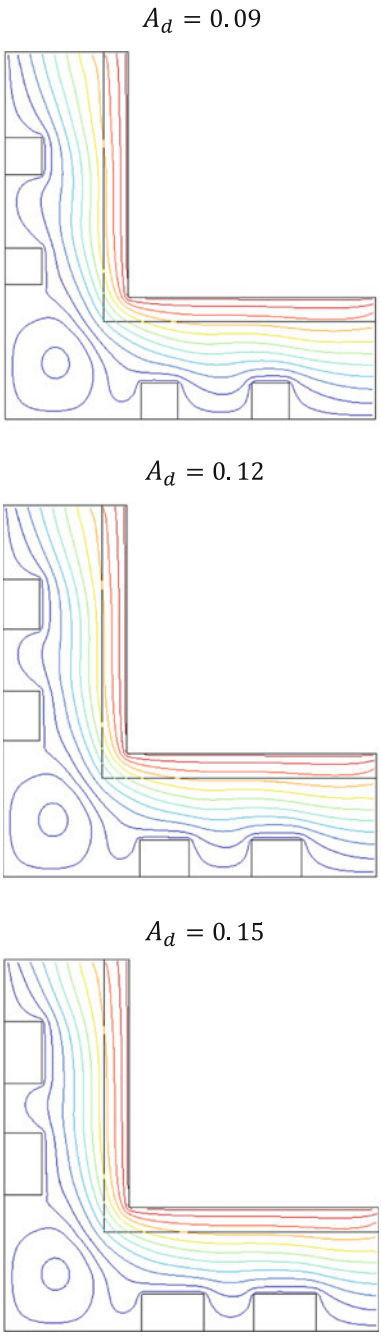

Fig. 4 Streamline plots for different values of A_d with $h_1 = 0.2$

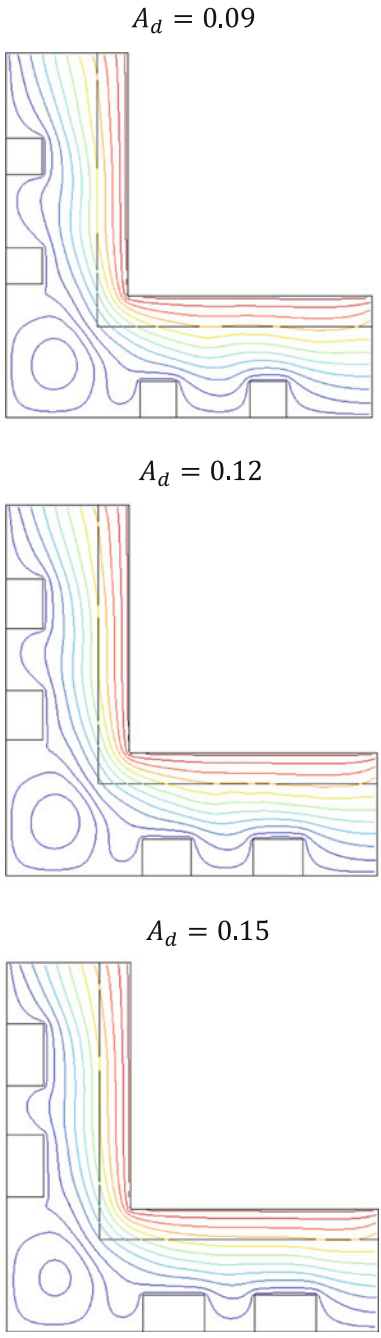

Fig. 5 Streamline plots for different values of A_d with $h_1 = 0.25$

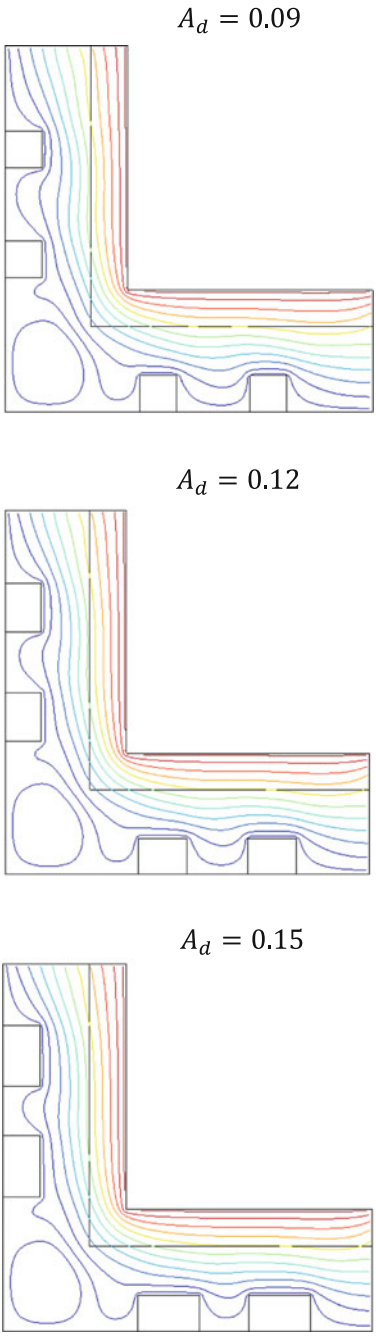

Fig. 6 Streamline plots for different values of A_d with $h_1 = 0.3$

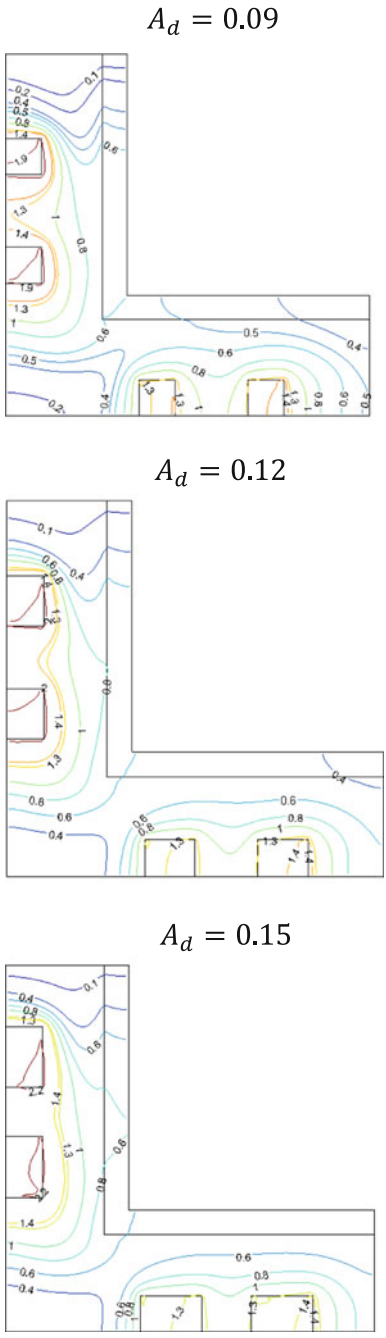

Fig. 7 Isotherm plots for different values of A_d with $h_1 = 0.2$

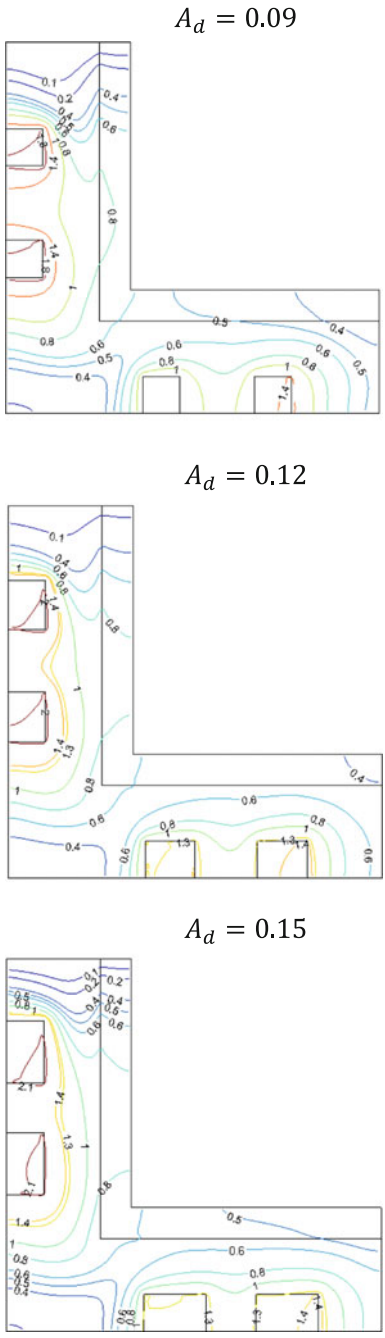

Fig. 8 Isotherm plots for different values of A_d with $h_1 = 0.25$

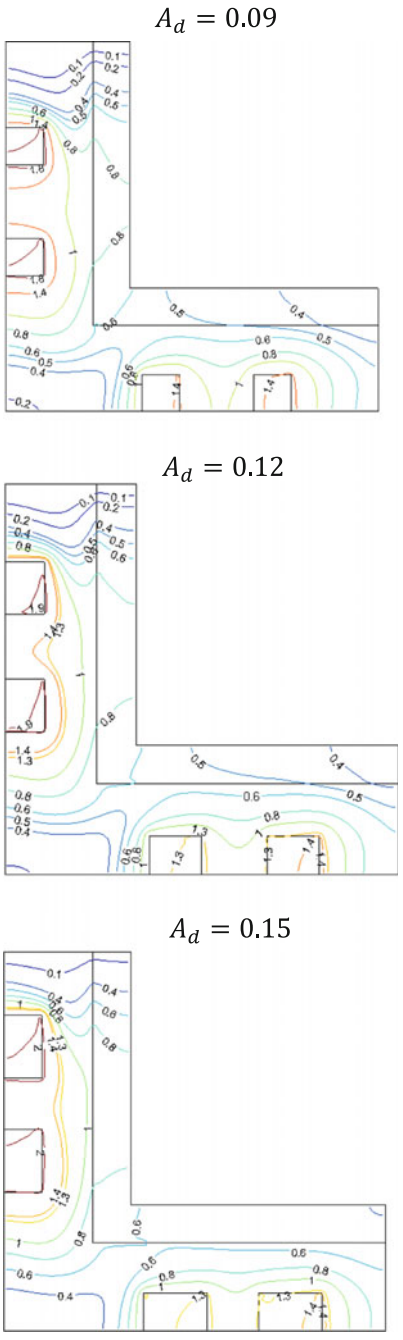

Fig. 9 Isotherm plots for different values of A_d with $h_1 = 0.3$

Table 4 Nu_{av} values for different values of A_d and h_1

	Nu_{av}		
A_d	$h_1 = 0.2$	$h_1 = 0.25$	$h_1 = 0.3$
0.090	4.7350	4.6980	4.3147
0.105	4.5908	4.5087	4.2827
0.120	4.5237	4.3440	4.1301
0.135	4.6062	4.4643	4.2936
0.150	4.6017	4.3386	4.1760

5 Conclusions

In this chapter, we studied the cooling of heat-generating electronic components via the mixed convective flow of nanofluids through an L-shaped channel with an inner porous layer. The effects of the thickness of the porous layer and the size of the heat-generating components on fluid flow and heat transfer within the channel were investigated. The results revealed that the size of the circulation zone near the outer corner of the channel decreases with increased porous layer thickness. Furthermore, an increase in the size of the components improves the heat transfer performance of the nanofluid when $0.09 \leq A_d \leq 0.12$ and $0.135 \leq A_d \leq 0.15$ and diminishes heat transfer performance when $0.12 \leq A_d \leq 0.135$. Finally, an increase in the thickness of the porous layer results in enhanced overall heat transfer performance within the L-shaped channel.

References

Ashby MF, Evans AG, Fleck NA, Gibson LJ, Hutchinson JW, Wadley HNG (2000) Metal foams: a design guide. Butterworth-Heinemann, USA

Boutina L, Bessaïh R (2011) Numerical simulation of mixed convection air-cooling of electronic components mounted in an inclined channel. Appl Therm Eng 31(11–12):2052–2062

Dukhan N, Minjeur CA II (2011) A two-permeability approach for assessing flow properties in metal foam. J Porous Mater 18(4):417–424

Ganji D, Kachapi S (2015) Application of nonlinear systems in nanomechanics and nanofluids: analytical methods and applications. Elsevier Inc, New York

Hajipour M, Dehkordi A, Jamshidi S (2013) Numerical investigation of nanofluid mixed-convection flow in the entrance region of a vertical channel partially filled with porous medium. Heat Transfer-Asian Res 43(7):607–627

Laptev V (2003) Numerical solution of coupled flow in plain and porous media. University of Kaiserslautern, Ph.D. Diss

Mansour MA, Mohamed RA, Abd-Elaziz MM, Ahmed SE (2010) Numerical simulation of mixed convection flows in a square lid-driven cavity partially heated from below using nanofluid. Int Comm Heat Mass Transf 37:1504–1512

Minkowycz WJ, Sparrow EM, Abraham JP (2013) Nanoparticle heat transfer and fluid flow. Vol 4 of advances in numerical heat transfer. CRC Press, USA

Nield D, Bejan A (2006) Convection in porous media, 3rd edn. Springer Science + Business Media Inc., New York

Nithiarasu P, Sundararajan T, Seetharamu KN (1998) Finite element analysis of transient natural convection in an odd-shaped enclosure. Int J Numer Meth Heat Fluid Flow 8(2):199–216

Phanikumar MS, Mahajan RL (2002) Non-darcy natural convection in high porosity metal foams. Int J Heat Mass Transfer 45(18):3781–3793

Young T, Vafai K (1998) Convective flow and heat transfer in a channel containing multiple heated obstacles. Int J Heat Mass Transf 41(21):3279–3298

Hall Current and Radiation Effects on Unsteady MHD Squeezing Nanofluid Flow in a Rotating Channel with Lower Stretching Permeable Wall

Shalini Jain and Shweta Bohra

Abstract In analysis of present model, we have analyzed the Hall current and radiative effects on unsteady MHD squeezing nanofluid in a rotating channel. The lower wall is permeable and linearly stretching, and the upper wall is squeezing downward in the presence of MHD. By introducing similarity transformation, we get the ordinary coupled differential equation. The transformed nonlinearly coupled differential equations are solved numerically by bvp4c solver using software MATLAB. We have taken nanoparticles of copper (Cu) and alumina (Al_2O_3) as base fluid (water). The effect of different parameters such as magnetic field parameter M, squeezing parameter Sq, rotational parameter ω, suction parameter w_0, nanofraction parameter ϕ, hall current parameter β_e, radiation parameter N on velocity profile, and temperature profile is displayed through tables and graphs.

1 Introduction

In a rotating medium, the hydromagnetic fluid flow study is highly significant due to its presence in various natural phenomena. It has vast number of applications in different technological situations, such as manufacture of insulating materials, thin plastic sheets, and paper fabrication. By considering various aspects of the problem, many researchers made an observation for steady hydromagnetic fluid flow of a viscous electrically conducting incompressible fluid due to channel which is rotating on its own plane. In the presence of uniform transverse magnetic field, Vidyaniti (1969) was the first who investigated the steady flow of rotating plate channel which is parallel. This work was extended by Nanda and Mohanty (1971) and Mazumder (1977); they investigated MHD flow in rotating channel. Datta and Jana (1977) investigated the Hall current effects on MHD fluid flow and heat transfer study in a rotating channel. Ghosh et al. (2009) studied characteristics of heat transfer for rotating system problem. Rao et al. (1982), Pop (2001), and Seth

S. Jain (✉) · S. Bohra
Department of Mathematics and Statistics, Manipal University Jaipur, Jaipur 303007, India
e-mail: shalini.jain@jaipur.manipal.edu

M.K. Singh et al. (eds.), *Applications of Fluid Dynamics*, Lecture Notes in Mechanical Engineering, https://doi.org/10.1007/978-981-10-5329-0_9

(2008, 2009) investigated free and forced convective fluid flow in a rotating channel under various flow patterns. Chauhan et al. (2009, 2010) investigated heat transfer effects on rotating channel which partially filled or filled with porous medium using continuity of velocity components and stress at the porous edge.

In recent past years, there has been a rising interest in the squeezing flow study between two rigid surfaces. These types of flow occurred in many engineering process such as compression and injection molding, lubrication theory, food industry, blood flow due to expansion and contraction of vessels. Squeezing flows are caused by the application of normal stresses to the running surfaces. Stefan (1874) was the pioneer of the squeezing fluid flow study. He investigated squeezed flow behavior of Newtonian fluid between two plates which are settled parallel and obtained an asymptotic solution. Bhattacharyya et al. (1997) examined squeezed flow of viscous MHD fluid between two disks which are rotating under different boundary conditions. The heat transfer characteristics in a squeezed Newtonian fluid flow between two horizontally parallel plates were observed by Duwairi et al. (2004). Munawar et al. (2012) studied the three-dimensional unsteady MHD fluid flow past a rotating channel with stretched lower wall and squeezing upper plate. Entropy generation effects have been observed by Butt and Ali (2015) on unsteady squeezing fluid flow past a rotating channel which has a lower stretching porous wall.

A liquid in which nanoscale particles are suspended in a base fluid, such as water, ethylene glycol, and propylene glycol, with low thermal conductivity is known as 'nanofluid.' Choi and Eastman (1995) were the first who have pointed out that nanofluid is a mixture of nanoparticles in base fluid. Later on, Xuan and Li (2003) examined the volume fraction and Reynolds number of nanoparticles' influences in turbulent flows for nanofluids in tubes experimentally. Buongiorno (2006) observed that due to Brownian diffusion and thermophoresis, there is enrichment in heat transfer for nanofluid. After that, Nield and Kuznetsov (2009) studied the behavior of natural convective boundary layer fluid flow of a nanofluid which employs Buongiorno model. Khan and Pop (2010) had been done the study of steady boundary layer flow of a nanofluid toward a sheet which is stretched. Makinde and Aziz (2011) analyzed fluid flow behavior for nanofluid due to a sheet which is linearly stretched by taking convective boundary condition. Mustafa et al. (2011) also have been given their contribution to the study of flow and heat transfer for nanofluid near a stagnation point. They considered stretching surface for their research. Rana and Bhargava (2012) investigated the laminar boundary layer flow for nanofluid due to the nonlinear stretching surface. Freidoonimehr et al. (2014) examined the three-dimensional nanofluid flow in a horizontally rotating parallel channel. They consider upper wall of the channel is squeezed downward and lower wall is stretched.

Pal and Mandal (2016) obtained MHD heat transfer characteristics of nanofluids over a nonlinearly stretching or shrinking sheet by considering the Hall current effect. Shit and Haldar (2012) illustrated the combined influences of thermal radiation and the Hall current effect on MHD free convective flow and mass transfer behavior over a stretching flat sheet by taking variable viscosity. Khidir (2013)

examined the viscous dissipation effect, radiative influence, and ohmic heating effect on MHD flow past a rotating disk which is embedded in a porous medium. He considered variable properties in his research. Recently, Mahanthesh et al. (2016) have been given the numerical solution for the problem of an unsteady three-dimensional squeezing flow of a nanofluid in rotating vertical channel of stretching left plane.

The purpose of the present study is to explore the combined influences of Hall current and radiation on unsteady MHD squeezing rotating channel with lower stretching permeable wall for nanofluid.

2 Mathematical Formulation

In this investigation, we consider unsteady, three-dimensional rotating, nanofluid flow of an incompressible, viscous fluid between two plane walls which are infinitely horizontal. Lower wall is stretched with the $U_w(t) = \frac{ax}{1-ct}$, dependent on time t, along x-direction, and is placed at $y = 0$. The upper plate is situated at variable distance $h(t) = \sqrt{\frac{\nu_f(1-ct)}{a}}$, and nanofluid is squeezed downward with velocity $V_h(t) = \frac{\mathrm{d}h}{\mathrm{d}t}$ which is dependent on time as shown in Fig. 1.

In the lower plate, suction with the velocity $V_w(t) = -\frac{V_0}{1-ct}$ is considered. The fluid and the channel are rotating around y-axis with an angular velocity $\omega^* = \frac{\omega_0}{1-ct}$. Magnetic field $B(t)$ with density $\frac{B_0}{\sqrt{1-ct}}$ is applied along the y-axis suggested by Khidir (2013). The lower stretching wall of the channel is kept on temperature T_w, and the squeezing wall has temperature T_h such that $T_w > T_h$

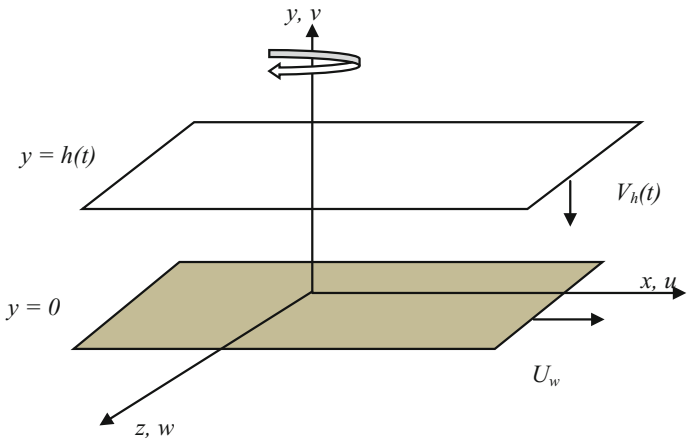

Fig. 1 Schematic diagram of the problem

The governing differential equations are followed by Butt and Ali (2015):

$$\frac{\partial u}{\partial x}+\frac{\partial u}{\partial y}=0, \tag{1}$$

$$\begin{aligned}&\rho_{nf}\left(\frac{\partial u}{\partial t}+u\frac{\partial u}{\partial x}+v\frac{\partial u}{\partial y}+2\frac{\omega_0}{1-ct}w\right)\\&=-\frac{\partial p}{\partial x}+\mu_{nf}\left(\frac{\partial^2 u}{\partial x^2}+\frac{\partial^2 u}{\partial y^2}\right)-\frac{\sigma_{nf}B_0^2}{(1-ct)\left(\alpha^2+\beta_e^2\right)}(\alpha u-\beta_e w),\end{aligned} \tag{2}$$

$$\rho_{nf}\left(\frac{\partial v}{\partial t}+u\frac{\partial v}{\partial x}+v\frac{\partial v}{\partial y}\right)=-\frac{\partial p}{\partial y}+\mu_{nf}\left(\frac{\partial^2 v}{\partial x^2}+\frac{\partial^2 v}{\partial y^2}\right), \tag{3}$$

$$\begin{aligned}&\rho_{nf}\left(\frac{\partial w}{\partial t}+u\frac{\partial w}{\partial x}+v\frac{\partial w}{\partial y}+2\frac{\omega_0}{1-ct}u\right)\\&=\mu_{nf}\left(\frac{\partial^2 w}{\partial x^2}+\frac{\partial^2 w}{\partial y^2}\right)-\frac{\sigma_{nf}B_0^2}{(1-ct)\left(\alpha^2+\beta_e^2\right)}(\alpha w+\beta_e u),\end{aligned} \tag{4}$$

$$\begin{aligned}&(\rho C_P)_{nf}\left(\frac{\partial T}{\partial t}+u\frac{\partial T}{\partial x}+v\frac{\partial T}{\partial y}\right)=k_{nf}\left(\frac{\partial^2 T}{\partial x^2}+\frac{\partial^2 T}{\partial y^2}\right)\\&+\mu_{nf}\left[4\left(\frac{\partial u}{\partial x}\right)^2+\left(\frac{\partial u}{\partial y}+\frac{\partial v}{\partial x}\right)^2+\left(\frac{\partial w}{\partial x}\right)^2+\left(\frac{\partial w}{\partial y}\right)^2\right]\\&-\frac{\partial q_r}{\partial y}+\frac{\sigma_{nf}B_0^2}{(1-ct)\left(\alpha^2+\beta_e^2\right)}\left(u^2+w^2\right),\end{aligned} \tag{5}$$

The appropriate boundary conditions are:
at

$$y=0 \qquad \begin{aligned}&u(x,y,t)=U_w(t)=\frac{ax}{1-ct},\\&v(x,y,t)=V_w(t)-\frac{V_0}{1-ct},\\&w(x,y,t)=0,\quad T(x,y,t)=T_w,\end{aligned}$$

at

$$y=h(t) \qquad \begin{aligned}&u(x,y,t)=0,\quad v(x,y,t)=V_h=\frac{\mathrm{d}h}{\mathrm{d}t}=\frac{-c}{2}\sqrt{\frac{\nu_f}{a(1-ct)}},\\&w(x,y,t)=0,\quad T(x,y,t)=T_h,\end{aligned} \tag{6}$$

where u, v, and w are components of fluid velocity along x-, y-, and z-directions, respectively. Here, the stretching rate of lower porous wall of the channel is represented by constant $a>0$, c is the parameter having dimensions of (time)$^{-1}$ and

$ct < 1$. T is the temperature of nanofluid, and σ is the electrical conductivity. $\alpha = 1 + \beta_i\beta_e$, where $\beta_e = \omega_e t_e$; the Hall current parameter, depends on the magnetic field's orientation which decides its positive or negative sign, and β_i is the ion slip parameter.

Further, μ_{nf}, ρ_{nf}, ν_{nf}, σ_{nf}, k_{nf}, and $(\rho C_P)_{nf}$ are effective dynamic viscosity, effective density, effective kinematic viscosity, electrical conductivity, thermal conductivity, and the heat capacitance of the nanofluid, which are defined as follows (Pal and Mandal (2016)):

$$\mu_{nf} = \frac{\mu_f}{(1-\phi)^{2.5}}, \quad \rho_{nf} = (1-\phi)\rho_f + \phi\rho_s, \quad \nu_{nf} = \frac{\mu_{nf}}{\rho_{nf}},$$

$$\begin{aligned} (\rho C_P)_{nf} &= (1-\phi)(\rho C_P)_f + \phi(\rho C_P)_s, \\ \sigma_{nf} &= \sigma_f\left[1 + \frac{3(\sigma-1)\phi}{(\sigma+2) - (\sigma-1)\phi}\right], \quad \sigma = \frac{\sigma_s}{\sigma_f} \\ \frac{k_{nf}}{k_f} &= \frac{(k_s + 2k_f) - 2\phi(k_f - k_s)}{(k_s + 2k_f) + \phi(k_f - k_s)}, \end{aligned} \tag{7}$$

where ϕ is the solid volume fraction of nanofluid, $\rho_f, \mu_f, \sigma_f, k_f, (\rho C_P)_f$ are reference density, dynamic viscosity, electrical conductivity, thermal conductivity, and heat capacitance of base fluid, respectively. $\rho_s, \mu_s, k_s, \sigma_s, (\rho C_P)_s$ are reference density, dynamic viscosity, thermal conductivity, electrical conductivity, and heat capacitance of solid fractions, respectively. The subscripts nf, f, and s denote the thermophysical properties of nanofluid, base fluid, and solid nanoparticles, respectively (Table 1).

For radiation effect, Rosseland approximation has been used:

$$q_r = -\frac{4\sigma_1}{3k_1}\frac{\partial T^4}{\partial y} \tag{8}$$

where σ_1 is the Stefan–Boltzmann constant and k_1 is the mean absorption coefficient. We consider that differences between the temperatures within the flow are such that the expression T^4 may be defined as a temperature's linear function. This is consummated by expanding T^4 in a Taylor series about T_h, and by avoiding second- and higher-order terms, we get:

Table 1 Thermophysical properties of fluid and nanoparticles (Pal and Mandal 2016)

Physical properties	Fluid phase	Cu (copper)	Al_2O_3 (alumina)
ρ (kg/m^3)	997.1	8933	3970
Cp (J/kg K)	4179	385	765
σ (S/m)	5.5×10^{-6}	59.5×10^{6}	35×10^{6}
κ (W/m K)	0.613	400	40

$$T^4 \cong 4T_h^3 T - 3T_h^4 \tag{9}$$

The following similarity transformations are used to reduce the above governing coupled equations with boundary conditions (1–6) in a non-dimensional form as Butt and Ali (2015):

$$\eta = \frac{y}{h(t)}, \quad u = U_w f'(\eta), \quad v = -\sqrt{\frac{av_f}{1-ct}} f(\eta), \quad w = U_w g(\eta),$$

$$\theta = \frac{T - T_w}{T_w - T_h}. \tag{10}$$

Substituting the similarity transformations (10) into (1–6) and using (8) and (9) in Eq. (5), the continuity equation is satisfied identically and we obtain the following system of nonlinear ordinary couple differential equations:

$$\begin{aligned} &f^{iv} - \phi_1\phi_2\left[\frac{Sq}{2}(3f'' + \eta f''') + f'f'' - ff''' + 2\omega g'\right] \\ &- \phi_1\phi_3 \frac{M^2}{(\alpha^2 + \beta_e^2)}(\alpha f'' - \beta_e g') = 0, \end{aligned} \tag{11}$$

$$\begin{aligned} &g'' + \phi_1\phi_2\left[fg' - f'g - Sq\left(g + \frac{\eta}{2}g'\right) + 2\omega f'\right] \\ &- \phi_1\phi_3 \frac{M^2}{(\alpha^2 + \beta_e^2)}(\alpha g + \beta_e f') = 0, \end{aligned} \tag{12}$$

$$\begin{aligned} &\left(\frac{k_{nf}}{k_f} + \frac{4N}{3}\right)\theta'' - \phi_4 Pr\left(\frac{Sq}{2}\eta\theta' - f\theta'\right) + \frac{Pr}{\phi_1}\left[Ec\left(4f'^2 + g^2\right) + Ec_x\left(f''^2 + g'^2\right)\right] \\ &+ \phi_3 \frac{M^2 PrEc_x}{(\alpha^2 + \beta_e^2)}\left(f'^2 + g^2\right) = 0, \end{aligned} \tag{13}$$

where,

$$\phi_1 = (1-\phi)^{2.5}, \quad \phi_2 = 1 - \phi + \phi\left(\frac{\rho_s}{\rho_f}\right),$$

$$\phi_3 = \left[1 + \frac{3(\sigma - 1)\phi}{(\sigma + 2) - (\sigma - 1)\phi}\right], \phi_4 = 1 - \phi + \phi\frac{(\rho C_P)_s}{(\rho C_P)_f}.$$

and the boundary conditions (6) in non-dimensional form at

$$\eta = 0\, f(0) = w_0, \quad f'(0) = 1, \quad g(0) = 0, \quad \theta(0) = 1,$$

at

$$\eta = 1\, f(1) = \frac{Sq}{2}, \quad f'(1) = 0, \quad g(1) = 0, \quad \theta(1) = 0. \tag{14}$$

where $\omega = \frac{\omega_0}{a}$ is the rotation parameter, $Sq = \frac{c}{a}$ is the squeezing parameter, $w_0 = \frac{V_0}{ah}$ is the suction parameter, $M^2 = \frac{\sigma_f B_0^2}{a\rho_f}$ is magnetic parameter, $Pr = \frac{\mu_f (C_P)_f}{k_f}$ is Prandtl number, $N = \frac{4\sigma_1 T_h^3}{k_1 k_f}$ is radiation parameter, $Ec = \frac{v_f^2}{h^2 (C_P)_f (T_w - T_h)}$ is Eckert number, and $Ec_x = \frac{U_w^2}{(C_P)_f (T_w - T_h)}$ is local Eckert number. In order to squeeze flow, we take $Sq > 0$, for which the upper wall is moving in downward direction with velocity $V_h < 0$. When $Sq < 0$, the upper wall moves away from the lower plate at $y = 0$. When $Sq = 0$, we arrive at the case where upper wall or plate is stationary and there is no squeezing effect or there is a steady state.

In this problem, the physical quantities of interest such as local skin friction coefficients C_f and C_g along and normal to stretching wall, respectively, and local Nusselt number Nu at the lower wall can be defined as follows:

$$C_f = \frac{\tau_{uy}}{\rho_f U_w^2}, \quad C_g = \frac{\tau_{wy}}{\rho_f U_w^2}, \quad Nu_x = \frac{q_w x}{k_f (T_w - T_h)} \tag{15}$$

where τ_{uy} and τ_{wy} are shear stresses along and normal to stretching wall and q_w is the wall heat flux. Here, we have:

$$C_f = \frac{\mu_{nf} (\partial u / \partial y)_{y=0}}{\rho_f U_w^2}, \quad C_g = \frac{\mu_{nf} (\partial w / \partial y)_{y=0}}{\rho_f U_w^2}, \quad q_w = \left[q_r - k_{nf} \left(\frac{\partial T}{\partial y} \right) \right]_{y=0} \tag{16}$$

Substituting Eqs. (10) and (16) into Eq. (15), we get:

$$C_f Re_x = \frac{f''(0)}{(1-\phi)^{2.5}}, \quad C_g Re_x = \frac{g'(0)}{(1-\phi)^{2.5}},$$
$$Nu_x = \frac{-x}{h} \left(\frac{k_{nf}}{k_f} + \frac{4N}{3} \right) \theta'(0)$$

where $Re_x = \frac{\rho_f U_w h}{\mu_f}$ is local Reynolds number.

3 Result and Discussion

The system of nonlinear ordinary coupled differential Eqs. (11)–(13) within the boundary conditions (14) is solved numerically by using bvp4c with MATLAB package. The effects of different parameters such as squeezing parameter (Sq), nanoparticle volume fraction (ϕ), rotation parameter (ω), suction parameter (w_0), magnetic field parameter (M), Hall current parameter (β_e), ion slip parameter (β_i), radiation parameter (N), Prandtl number (Pr), local Eckert number (Ec), Eckert number (Ec_x) on all velocity components and temperature profile, for two different types of nanofluids—Cu-*water* and Al_2O_3-*water*—have been investigated. As Cu nanoparticle possesses higher density than other nanoparticle, we can see that Cu-*water* nanofluids admit lower velocity profiles with the comparison of Al_2O_3–*water* and same effect shows for temperature profile also. The Prandtl number of base fluid (water) is kept 6.8. It is observed that the results obtained are very well in agreement with the literature present as shown in Table 2.

The effect of squeezing parameter Sq on normal, axial, and transverse velocity components is shown by Fig. 2a–c. We can see that with the increases in Sq, normal velocity $f(\eta)$ increases at the upper plate for both the nanofluids, which shows prominent effect on the upper plate. For both nanofluids, axial velocity $f'(\eta)$ and transverse velocity $g(\eta)$ also increase with increasing Sq and the increasing effect is prominent in the middle of the channel. When upper plate moves downward, a force exerted on fluid and fluid moves with more velocity. On comparing both the fluids observed that fluid with Cu attains more velocity than with Al_2O_3. Exactly reverse effect has shown when plate moves upward. Figure 3d shows the temperature profile for metal (Cu)-based nanofluid. As upper plate moves downward direction, more force exerted on fluid causes increase in temperature, and when plate moves upward, the temperature reduces.

Figure 3a–d shows the effect of volume fraction ϕ on all velocity components and temperature distribution. For both nanofluids, the normal velocity reduces by increasing value of ϕ as well as axial velocity decreases in lower half channel while increasing in upper half channel, and transverse velocity increases near the lower surface, but in rest of the channel, it deceases with increasing value of ϕ. It can be seen that temperature rises with the higher value of ϕ for both nanoparticle-based fluids.

Figure 4a–b displays the effect of rotation parameter ω on axial velocity components and temperature distribution. In Fig. 4a, we can see that axial velocity reduces in lower half channel while it shows reverse effect (approximately in the center of the channel, $\eta \cong 0.4$) in upper wall of the channel. Temperature increases with the increment of ω which is shown in Fig. 4b due to high convection rate as a consequence of large rotation of fluid and channel. This above result has been presented for both nanofluids.

The effect of Hall current parameter β_e on velocity and temperature distribution is plotted in Fig. 5a–d. When β_e increases, normal velocity increases for both nanofluids and axial velocity also increases in lower part of the channel while

Table 2 Comparison results of shear stresses $f''(0)$ and $g'(0)$ and heat transfer rate $-\theta'(0)$ at the lower surface with different values of Sq, w_0, ω parameters, when $Ec = Ec_x = 0.2$, $Pr = 1$, $\phi_e = M = N = 0$

ω	w_0	Sq	f″(0)		g′(0)		$-\theta'(0)$	
			Butt and Ali (2015)	Present result	Butt and Ali (2015)	Present result	Butt and Ali (2015)	Present result
0.5	0.5	2	−1.297045	−1.2970452	0.300313	0.3003129	0.906244	0.9062444
1			−1.291472	−1.2914716	0.600474	0.6004744	0.899782	0.89978149
3			−1.231657	−1.2316564	1.796681	1.79668101	0.831333	0.83133312
5			−1.110254	−1.1102543	2.979537	2.9795366	0.697004	0.69700358
	0.5		−1.297045	−1.2970452	0.300313	0.3003129	0.906244	0.9062444
	1		−4.814071	−4.8140715	0.072293	0.07229336	0.660729	0.66072942
	1.2		−6.311701	−6.3117016	−0.040879	−0.0408794	0.263867	0.26386685
		−1	−10.21413	−10.214133	−0.707731	−0.7077310	−3.138926	−3.1389260
		0	−7.419696	−7.4196962	−0.237555	−0.2375552	−0.833320	−0.8333195
		1	−4.445146	−4.4451460	0.075782	0.0757815	0.500581	0.5005808
		2	−1.297045	−1.2970452	0.300313	0.3003129	0.906244	0.9062444

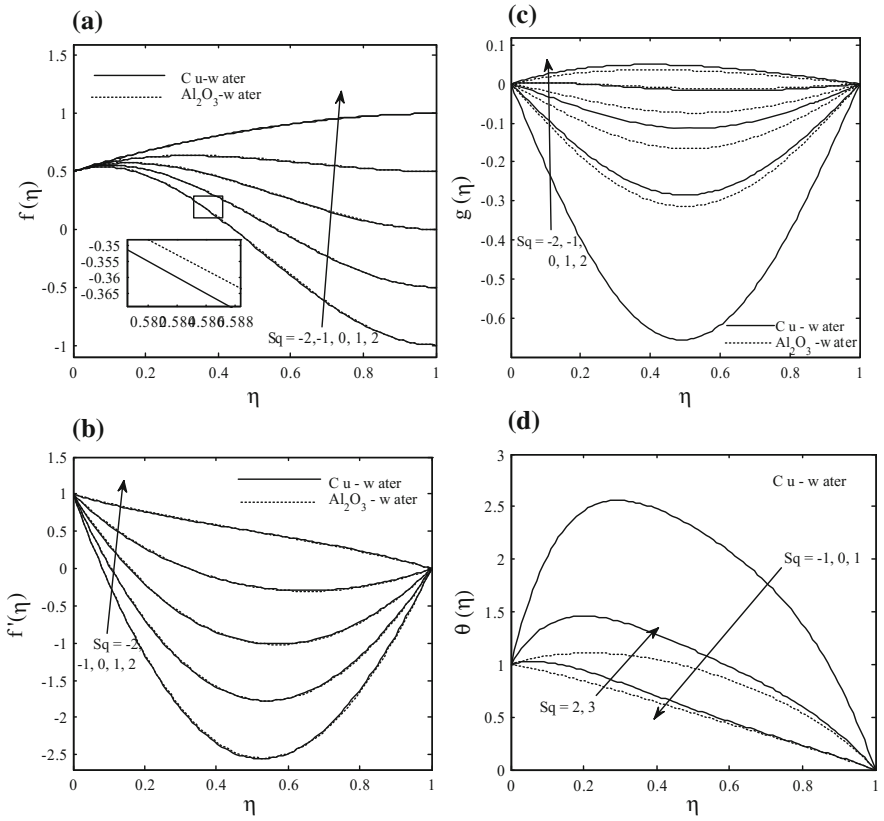

Fig. 2 Effect of variation in the squeezing parameter on the **a** normal, **b** axial, **c** transverse velocity, and **d** temperature profiles when $\phi = 0.1$, $\omega = 0.5$, $w_0 = 0.5$, $\beta_1 = \beta_e = 0.5$, $Ec = Ec_x = 0.2$, $M = N = 1$, $Pr = 6.8$

decreases in upper part of the channel. Transverse velocity component also increases near the lower wall, and after a point, it shows decrements in rest of the channel. Temperature rise with the increasing value of β_e.

In Fig. 6, we can see that for increasing value of radiation parameter *N,* temperature decreases for both nanofluids.

Table 3 displays the numerical value of shear stress $f''(0)$ and $g'(0)$ for variation $\phi, S_q, w_0, M, \beta_e$. It is observed that $f'(0)$ and $g'(0)$ increases with the increasing value of *Sq* while reduces when w_0, M, β_e decrease for both nanofluids, but when ϕ increases $f'(0)$ decreases while value of $g'(0)$ is increased for Cu-based nanofluid, and for Al_2O_3-based nanofluid, it shows reverse trend. In Table 4, we can see that numerical value of rate of heat transfer $\theta'(0)$ is increased with the increasing value of ϕ, w_0, and β_e, while it is decreased when *Sq*, *M,* and *N* increase for both nanofluids, Cu–*water* based and Al_2O_3–*water* based.

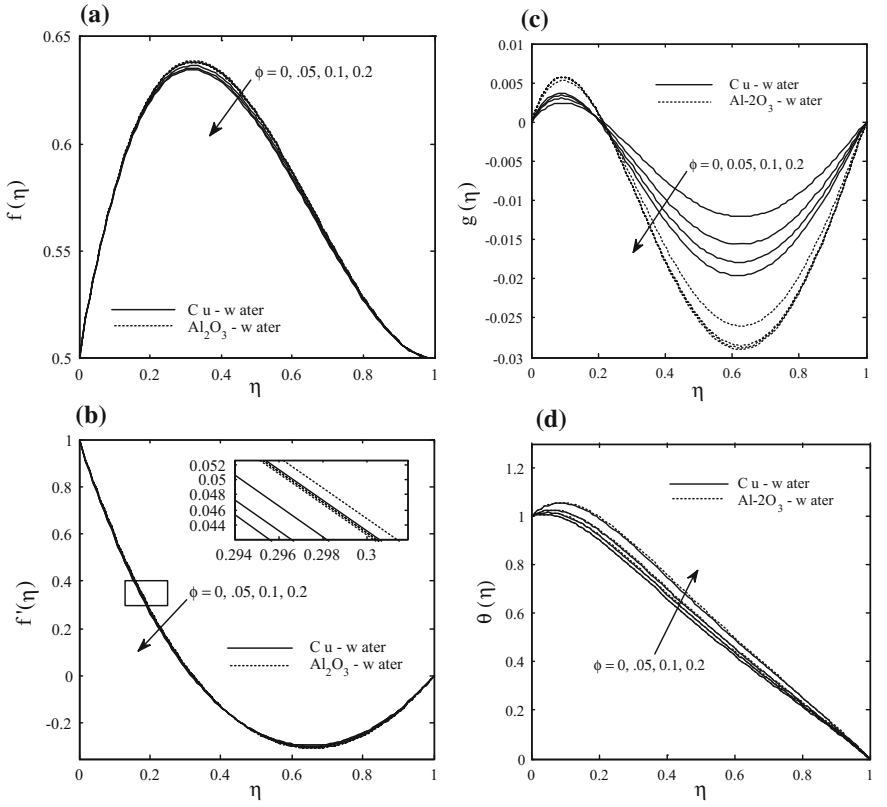

Fig. 3 Effect of variation in the nanoparticle fraction on the **a** normal, **b** axial, **c** transverse velocity, and **d** temperature profiles when, $Sq = 1$, $\omega = 0.5$, $w_0 = 0.5$, $\beta\imath = \beta_e = 0.5$, $Ec = Ec_x = 0.2$, $M = N = 1$, $Pr = 6.8$

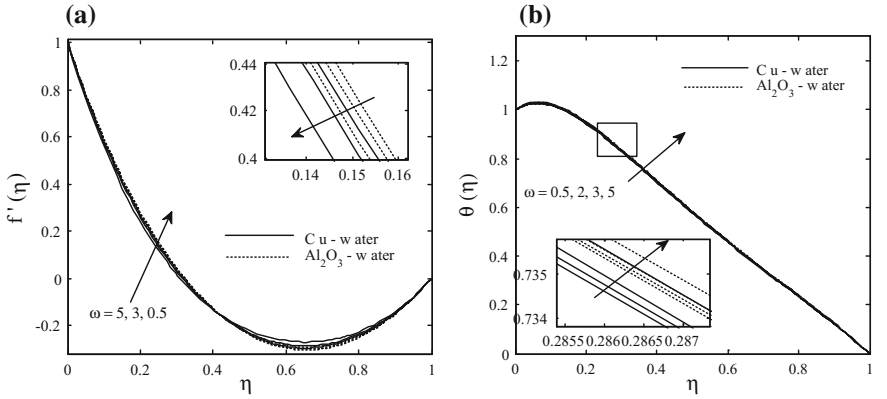

Fig. 4 Effect of variation in the rotation parameter on the **a** axial velocity, **b** temperature profiles when, $\phi = 0.1$, $Sq = 1$, $w_0 = 0.5$, $\beta\imath = \beta_e = 0.5$, $Ec = Ec_x = 0.2$, $M = N = 1$, $Pr = 6.8$

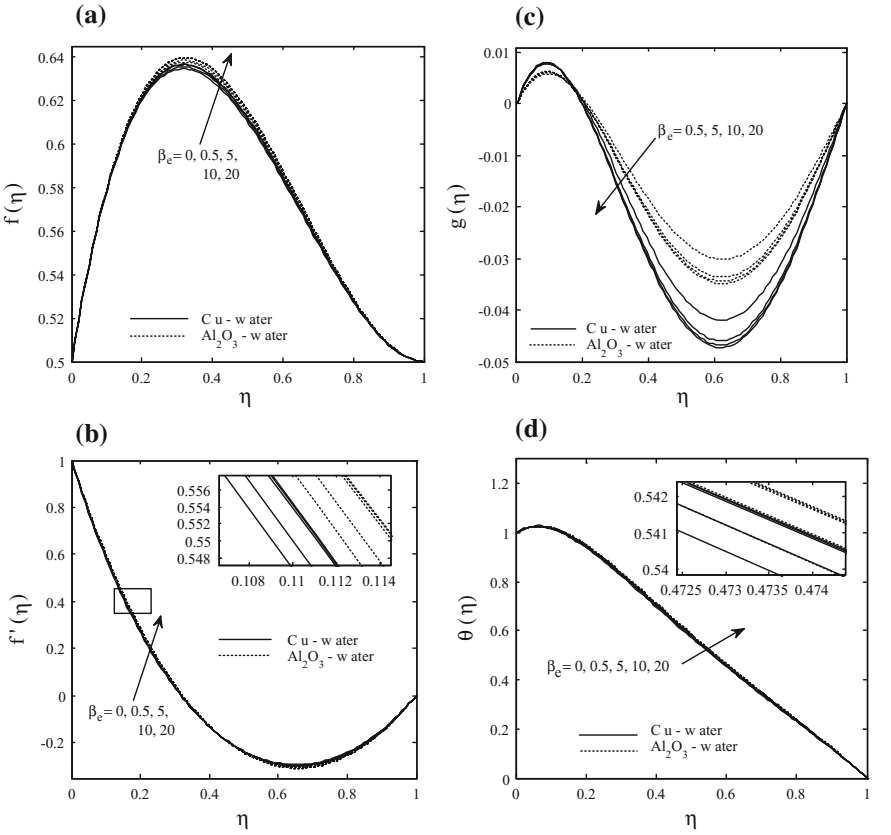

Fig. 5 Effect of variation in the Hall current parameter on the **a** normal, **b** axial velocity, **c** transverse, and **d** temperature profiles when $\phi = 0.1$, $\omega = 0.5$, $w_0 = 0.5$, $\beta\imath = 1$, $Ec = Ec_x = 0.2$, $M = Sq = N = 1$, $Pr = 6.8$

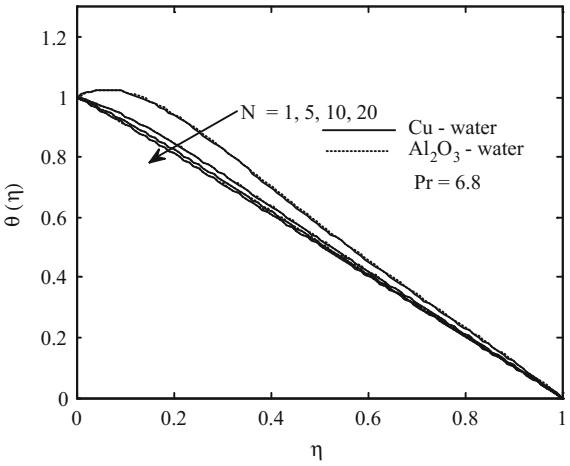

Fig. 6 Effect of variation in the radiation parameter $\phi = 0.1$, $Sq = 1$, $w_0 = 0.5$, $\beta\imath = \beta_e = 0.5$, $Ec = Ecx = 0.2$, $M = 1$, $\omega = 1$

Table 3 Variation of $f''(0)$ and $g'(0)$ at the lower surface with ϕ, Sq, w_0, M, and β_e parameters, when $Ec = Ec_x = 0.2$, $\omega = 1$, $Pr = 6.8$, $\beta_i = 0.5$

ϕ	Sq	w_0	M	β_e	$f''(0)$		$g'(0)$	
					Cu–water	Al_2O_3–water	Cu–water	Al_2O_3–water
0	1	0.5	1	0.5	−4.537783008	−4.537783008	0.132610617	0.132610617
0.1	1	0.5	1	0.5	−4.717174224	−4.538738789	0.184297173	0.131783922
0.2					−4.764288533	−4.498242267	0.198288175	0.120234334
	−1				−10.56718710	−10.41082563	−1.94501960	−1.080524248
	0				−7.754140578	−7.561212083	−0.59476075	−0.362843138
	1				−4.717174224	−4.538738789	0.184297173	0.131783922
	2				−1.456097243	−1.347909970	0.693595628	0.494623188
		0.1			−1.930999143	−1.860009037	0.607132137	0.430774139
		0.5			−4.717174224	−4.538738789	0.184297173	0.131783922
		1			−8.606721442	−8.166999935	−0.59461264	−0.366969368
			1		−4.717174224	−4.538738789	0.184297173	0.131783922
			2		−4.801433673	−4.625336497	0.165519912	0.111326820
			3		−4.884904719	−4.710999912	0.145653499	0.090057871
				0.5	−4.717174224	−4.538738789	0.184297173	0.131783922
				1	−4.687714422	−4.508873196	0.180907091	0.128674663
				5	−4.642567210	−4.462304808	0.192111423	0.141033464

Table 4 Variation of $\theta'(0)$ at the lower surface with ϕ, Sq, w_0, M, β_e, and N parameters, when $Ec = Ec_x = 0.2$, $\omega = 1$, $Pr = 6.8$, $\beta_i = 0.5$

ϕ	Sq	w_0	M	N	β_e	$\theta'(0)$	
						Cu-water	Al_2O_3-water
0	1	0.5	1	1	0.5	0.558213427	0.491997869
0.1	1	0.5	1	1	0.5	0.989707655	0.891142260
0.2						1.490564089	1.377132409
	−1					15.867700676	14.376900320
	0					6.139611121	5.766924071
	1					0.989707655	0.891142260
	2					−0.363586476	−0.588521552
		0.1				−0.049652606	−0.208843513
		0.5				0.989707655	0.891142260
		1				6.504295369	6.013741404
			1			0.989707655	0.891142260
			2			1.036967878	0.865046187
			3			1.083837312	0.840625575
				1		0.989707655	0.891142260
				5		−0.363685916	−0.398354966
				10		−0.656544714	−0.675655053
					0.5	0.989707655	0.891142260
					1	0.969133138	0.903961072
					5	0.944689354	0.918106971

4 Conclusion

In this paper, we have investigated three-dimensional flow of two types of nanoparicle, Cu–*water* based and Al_2O_3–*water* based, in a rotating channel on a lower permeable squeezing wall in the presence of Hall current and radiation. The upper wall is squeezed downward. The system of non-dimensional equations is solved numerically by bvp4c using MATLAB. It is observed that:

- Cu–*water* attains lower velocity and temperature profile than nanofluid Al_2O_3–*water* with the increasing value of all parameters except *Sq*. For upward squeezing Cu-*water*-based nanofluid admits maximum velocity and temperature compared to Al_2O_3-*water*.
- Normal velocity component decreases when volume fraction parameter ϕ and magnetic field parameter *M* increase, whereas reverse effect was observed with an increases in squeezing parameter *Sq* and Hall current parameter.
- An increase in volume fraction parameter ϕ and magnetic field parameter *M* axial velocity decreases in the lower half and increases in upper half portion of the channel, whereas increasing value of β_e shows reverse trend.
- An increase in radiation parameter causes decrease in temperature profile, whereas temperature rises as the Hall current parameter β_e increases.

Acknowledgements The authors express gratitude to Prof. D.S. Chauhan, University of Rajasthan for his guidance. Also wish to express sincere thanks to anonymous reviewers for their valuable suggestions and comments.

Conflict of Interests

The authors declare that there is no conffiict of interests regarding the publication of this paper.

References

Bhattacharyya S, Pal A (1997) Unsteady MHD squeezing flow between two parallel rotating discs. Mech Res Commun 24:615–623

Buongiorno J (2006) Convective transport in nanofluids. J Heat Transf 128(3):240–250

Butt AS, Ali A (2015) Analysis of entropy generation effects in unsteady squeezing flow in a rotating channel with lower stretching permeable wall. J Taiwan Inst Chem Eng 48:8–17

Chauhan DS, Rastogi P (2009) Hall current and heat transfer effects on mhd flow in a channel partially filled with a porous medium in a rotating system. Turk J Eng Environ Sci 33(3): 167–184

Chauhan DS, Agrawal R (2010) Effects of hall current on MHD flow in a rotating channel partially filled with a porous medium. Chem Eng Commun 197(6):830–845

Choi SUS, Eastman JA (1995) Enhancing thermal conductivity of fluids with nanoparticles. Mater Sci 231:99–105

Datta N, Jana RN (1977) Hall effects on hydromagnetic flow and heat transfer in a rotating channel. J Inst Math Appl 19:217–229
Duwairi HM, Tashtoush B, Damseh RA (2004) On heat transfer effects of a viscous fluid squeezed and extruded between two parallel plates. Heat Mass Transf 41:112–117
Freidoonimehr N, Rostami B, Rashidi MM, Momoniat E (2014) Analytical modelling of three-dimensional squeezing nanofluid flow in a rotating channel on a lower stretching porous wall. Math Prob Eng 1:1–14
Ghosh SK, Beg OA, Narahari M (2009) Hall effects on MHD flow in a rotating system with heat transfer characteristics. Mechanica 44:741–765
Khan WA, Pop I (2010) Boundary layer flow of a nanofluid past a stretching sheet. Int J Heat Mass Transf 53:2477–2488
Khidir AA (2013) Viscous dissipation, Ohmic heating and radiation effects on MHD flow past a rotating disk embedded in a porous medium with variable properties. Arab J Math 2:263–277
Mahanthesh B, Gireesha BJ, Gorla RSR (2016) Mixed convection squeezing three-dimensional flow in a rotating channel filled with nanofluid. Int J Numer Meth Heat Fluid Flow 26(5):1460–1485
Makinde OD, Aziz A (2011) Boundary layer flow of a nanofluid past a stretching sheet with a convective boundary condition. Int J Therm Sci 50(7):1326–1332
Mazumder BS (1977) Effect of wall conductances on hydromagnetic flow and heat transfer in a rotating channel. Acta Mech 28:85–99
Munawar S, Mehmood A, Ali A (2012) Three-dimensional squeezing flow in a rotating channel of lower stretching porous wall. Comput Math Appl 64:1575–1586
Mustafa M, Hayat T, Pop I, Asghar S, Obaidat S (2011) Stagnation-point flow of a nanofluid towards a stretching sheet. Int J Heat Mass Transf 54(25–26):5588–5594
Nanda RS, Mohanty HK (1971) Hydromagnetic flow in a rotating channel. Appl Sci Res 24:65–78
Nield D, Kuznetsov AV (2009) The cheng-minkowycz problem for natural convective boundary-layer flow in a porous medium saturated by a nanofluid. Int J Heat Mass Transf 52(25–26):5792–5795
Pal D, Mandal G (2016) Effects of hall current on magnetohydrodynamic heat transfer of nanofluids over a non-linear stretching/shrinking sheet. Int J Appl Comput Math 2016:1–18
Pop I, Ghosh SK, Nandi DK (2001) Effects of the hall current on free and forced convection flows in a rotating channel in the presence of an inclined magnetic field. Magnetohydrodynamics 37:348–359
Prasad Rao DRV, Krishna DV, Debnath L (1982) Combined effect of free and forced convection on MHD flow in a rotating porous channel. Int J Math Math Sci 5:165–182
Rana P, Bhargava R (2012) Flow and heat transfer of a nanofluid over a nonlinearly stretching sheet: a numerical study. Commun Nonlinear Sci Numer Simul 17(1):212–226
Seth GS, Singh MK (2008) Combined free and forced convection MHD flow in a rotating channel with perfectly conducting walls. Indian J Theo Phys 56:203–222
Seth GS, Ansari MS (2009) Magnetohydrodynamic convective flow in a rotating channel with Hall effects. Int J Theor Appl Mech 4:205–222
Shit GC, Haldar R (2012) Combined effects of thermal radiation and hall current on MHD free-convective flow and mass transfer over a stretching sheet with variable viscosity. J Appl Fluid Mech 5(2):113–121
Stefan MJ, Versuch U (1874) ber die scheinbareAdhäsion. SitzungsberAbt II. ÖsterrAkadWiss Math-Naturwiss Kl 69:713–721
Vidyanidhi V (1969) Secondary flow of a conducting liquid in a rotating channel. J Math Phys Sci 3:193–199
Xuan Y, Li Q, Wang J (2003) Investigation on convective heat transfer and flow features of nanofluids. J Heat Transf 125(1): 151–155

Part III
Heat and Mass Transfer

Natural Convection of a Micropolar Fluid Between Two Vertical Walls with Newtonian Heating/Cooling and Heat Source/Sink

Arun Kumar Singh and A.K. Singh

Abstract The aim of this paper is to investigate the natural convection of a micropolar fluid flow in two vertical walls with the Newtonian heating/cooling on one of its walls. The governing linear differential equations with their appropriate boundary conditions of the considered model are changed first into non-dimensional differential equations and boundary conditions by using the dimensionless parameters and variables. Analytic solutions of the non-dimensional differential equations have been obtained one by one for several cases of source or sink parameter. To obtain the influence of the Biot number and other physical parameters, the numerical results of the velocity, temperature, and microrotational velocity are finally shown in the graphs and table. It is found that the effect of the Newtonian heating is to increase the velocity, microrotational velocity, and rate of volume flow, while in the case of the Newtonian cooling, velocity, microrotational velocity, and rate of volume flow have decreasing tendency.

.

Nomenclature

S Dimensionless source/sink parameter
T Dimensionless temperature
K Vertex viscosity
w Angular viscosity
y Dimensionless transverse coordinate
y' Transverse coordinate
u Dimensionless streamwise velocity
u' Streamwise velocity
T' Temperature

A.K. Singh (✉) · A.K. Singh
Department of Mathematics, Institute of Science, Banaras Hindu University, Varanasi 221005, India
e-mail: arunsingh253@gmail.com

A.K. Singh
e-mail: ashok@bhu.ac.in

M.K. Singh et al. (eds.), *Applications of Fluid Dynamics*, Lecture Notes in Mechanical Engineering, https://doi.org/10.1007/978-981-10-5329-0_10

R Vertex viscosity parameter
Q Dimensionless volume flow rate
L Channel width
E Dimensionless total heat rate added to the fluid
G Gravitational acceleration
Gr Grashof number
w Dimensionless microrotational velocity
j Microinertia density
Bi Biot number

Greek Letters

ρ Density
β Coefficient of thermal expansion
γ Spin gradient viscosity
μ Dynamic viscosity

Subscripts

f Fluid layer
p Porous layer
c Cold wall

1 Introduction

The physical properties of many real fluids cannot be described by the Newtonian relationship in the current scenario, and therefore, many non-Newtonian fluid theories have been proposed to explain the property of real fluids by researchers. The physical description of such fluids demand a new idea which is different from the real fluids. To illustrate the complex nature of such fluids, additional balance laws are required. A new subclass of fluid is proposed by Erigen (1966, 1972) such as micropolar fluid which neglects the distortion of the microelements but permits to undergo rotation. The mathematical modeling of micropolar fluid can be used to the complex biological structures, certain polymer solutions, colloidal suspensions and lubricating fluids.

Aung (1972) described fully developed laminar-free convection flow in vertical parallel plate channel heated asymmetrically. Nelson and Wood (1973) obtained the solution for the combined influence of heat and mass transfer problem of natural convection in vertical channels. Miyatake and Fujii (1973) investigated the natural convection between vertical parallel plates, when they are at unequal uniform temperatures. Ravi et al. (2011) presented free convection of a micropolar fluid in

two vertical walls by considering into account the temperature-dependent source/sink. In some technological systems, the rate of the thermal energy transfer from the medium depends on the local surface temperature. The flow of this type is called as the conjugate convective flow, and the term Newtonian heating/cooling is used for proportional condition of the heat transfer to the local surface temperature. Using this condition, Merkin (1994) first studied the influence of Newtonian heating on the free convective boundary layer flow of a viscous fluid past vertical parallel flat plate. Then, several workers have used the Newtonian heating/cooling condition in view of its application in many engineering devices. Effects of induced magnetic field on natural convection with Newtonian heating/cooling in vertical annuli have been investigated by Kumar and Singh (2015).

Here, the purpose of this paper is to demonstrate the influence of Newtonian heating/cooling on the velocity and microrotation in the presence of parameters such as heat source/sink, vertex viscosity, material parameter. We have obtained the solution of linear simultaneous ordinary differential equations using the boundary condition for the velocity, microrotational velocity, and temperature.

2 Mathematical Formulation

We have considered steady-state one-dimensional, natural convection of a micropolar fluid between two vertical walls with the Newtonian heating/cooling and heat source or sink. The distance between the vertical walls is taken as L and having the Newtonian heating/cooling at the wall $y' = 0$, while the temperature of other wall is considered as T_1. One of the vertical walls is taken along x-axis and y-axis normal to x-axis. The length of the vertical wall is supposed to be infinitely long so that the dependent variables are free from the vertical coordinate. Using the Boussinesq approximation, the governing equation for natural convection of a micropolar fluid with temperature-dependent heat source or sink can be written in non-dimensional form as follows:

$$(1+R)\frac{\mathrm{d}^2u}{\mathrm{d}y^2} + \frac{\mathrm{d}w}{\mathrm{d}y} + T = 0, \tag{1}$$

$$(1+R)\frac{\mathrm{d}^2w}{\mathrm{d}y^2} - BR\left(2w + \frac{\mathrm{d}u}{\mathrm{d}y}\right) = 0, \tag{2}$$

$$\frac{\mathrm{d}^2T}{\mathrm{d}y^2} + sT = 0. \tag{3}$$

The boundary conditions in the non-dimension form are derived as follows:

$$u = 0, \quad w = 0, \quad \frac{dT}{dy} = BiT, \quad \text{at } y = 0;$$

$$u = 0, \quad w = 0, \quad T = 1, \quad \text{at } y = 1. \tag{4}$$

The dimensionless quantities used in the above equations are obtained as follows:

$$y = \frac{y'}{L}, \quad w = \frac{w'\mu}{\rho g \beta L\left(T_1' - T_0'\right)}, \quad B = \frac{L^2}{j}, \quad u = \frac{u'\mu}{\rho g \beta L^2\left(T_1' - T_0'\right)},$$

$$T = \frac{\left(T' - T_0'\right)}{\left(T_1' - T_0'\right)}, \quad s = \frac{s'L^2}{k}, \quad R = \frac{k}{\mu}, \quad Bi = \gamma L. \tag{5}$$

Here, velocity of the fluid along x-direction is u, the microrotational velocity is w, density of the fluid is ρ, the dynamic viscosity of the fluid is μ, the gravitational acceleration is g, and Biot number is Bi. The analytic solution of differential Eqs. (1)–(3) depends on the Biot number Bi and source/sink parameters. The values of s are taken as positive, negative, and zero for source, sink, and absence of source/sink parameters, respectively. The values of Bi are negative in the presence of the Newtonian heating and positive in the presence of the Newtonian cooling.

Case 1: When source ($s > 0$) is present

Analytic solutions for the velocity (u), microrotational velocity (w), and temperature (T) are derived as follows:

$$\begin{aligned} u = {} & k_{28}k_{14}\sinh\sqrt{k_5}y + k_{27}k_{14}\cosh\sqrt{k_5}y + k_{15}\cos\sqrt{s}y \\ & + k_{16}\sin\sqrt{s}y - 2k_{29}y + k_{30}, \end{aligned} \tag{6}$$

$$w = k_{29} + k_{28}\cosh\sqrt{k_5}y + k_{27}\sinh\sqrt{k_5}y - k_8\sin\sqrt{s}y - k_9\cos\sqrt{s}y, \tag{7}$$

$$T = k_3\cos\sqrt{s}y + k_4\sin\sqrt{s}y. \tag{8}$$

The rate of dimensionless volume flow is given by

$$Q = \int_0^1 u\,dy = k_{32}\sinh\sqrt{k_5} + k_{31}\cosh\sqrt{k_5} + k_{34}\sin\sqrt{s} + k_{33}\cos\sqrt{s} + k_{35}. \tag{9}$$

Case 2: When source/sink ($s = 0$) is absent

In this case, analytic solutions for the velocity (u), microrotational velocity (w), and temperature (T) are obtained as follows:

$$u = A_{23}A_{10}\sinh\sqrt{A_3}y + A_{22}A_{10}\cosh\sqrt{A_3}y + A_9 y - A_{11}y^3 - A_6 y^2 - 2A_{24}y + A_{25}, \tag{10}$$

$$w = A_{22}\sinh\sqrt{A_3}y + A_{23}\cosh\sqrt{A_3}y + A_5 y^2 + A_6 y + A_{24}, \tag{11}$$

$$T = A_1 y + A_2. \tag{12}$$

The rate of dimensionless volume flow is given by

$$Q = \int_0^1 u\mathrm{d}y = A_{27}\sinh\sqrt{k_5} + A_{26}\cosh\sqrt{k_5} + k_{30}. \tag{13}$$

Case 3: When sink ($s < 0$) is present

In this case, analytic solutions for the velocity (u), microrotational velocity (w), and temperature (T) are derived as ($s = -si$):

$$u = P_{30}P_{14}\sinh\sqrt{P_5}y + P_{29}P_{14}\cosh\sqrt{P_5}y + P_{15}\cosh\sqrt{siy} + P_{16}\sinh\sqrt{siy} - 2P_{31}y + P_{32}, \tag{14}$$

$$w = P_{31} + P_{30}\cosh\sqrt{P_5}y + P_{29}\sinh\sqrt{P_5}y + P_8\sinh\sqrt{siy} + P_9\cosh\sqrt{siy}, \tag{15}$$

$$T = P_3\cosh\sqrt{siy} + P_4\sinh\sqrt{siy}. \tag{16}$$

The rate of dimensionless volume flow is given by

$$Q = \int_0^1 u\mathrm{d}y = P_{33}\cosh\sqrt{P_5} + P_{34}\sinh\sqrt{P_5} + P_{36}\sinh\sqrt{si} + P_{35}\cosh\sqrt{si} + P_{37}, \tag{17}$$

3 Results and Discussion

In order to see the influence of physical parameters, such as the material, source/sink, and vertex viscosity as well as Biot number (Bi) on the free convective flow with the Newtonian heating/cooling between two vertical walls, the numerical calculations of velocity and microrotation are performed, and then, they are shown in the graphical forms.

Graphical representation in Fig. 1 shows that the influence of the material and source parameters on the velocity is to decrease it in case of the Newtonian cooling,

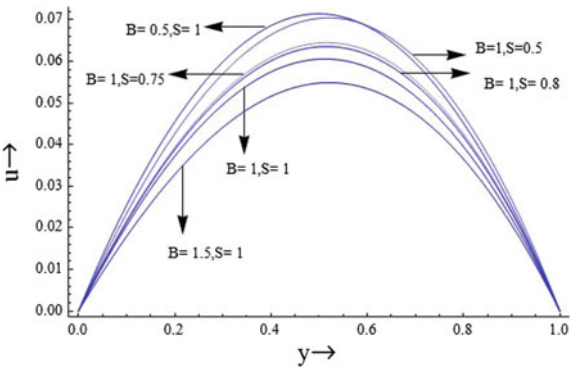

Fig. 1 Influence of material and source parameters on velocity for $R = 1$, $Bi = 0.5$

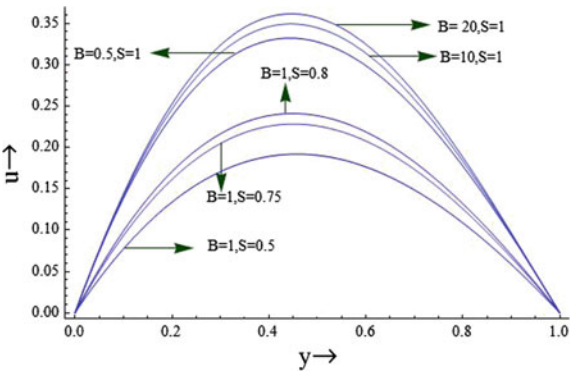

Fig. 2 Influence of material and source parameters on velocity for $R = 1$, $Bi = -0.5$

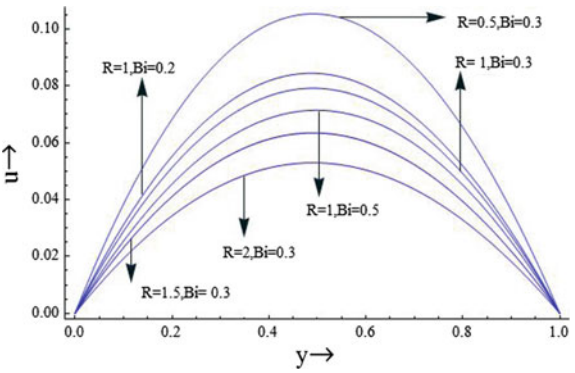

Fig. 3 velocity profile for $B = 0.5$, $S = 1$, and Newtonian cooling

while Fig. 2 indicates that the impact of the material and source parameters on the velocity is to increase it in case of the Newtonian heating. Next, Fig. 3 shows that the influence of the Newtonian cooling on the velocity is to decrease it, while Fig. 4 shows that the influence of the Newtonian heating on the velocity is to increase it.

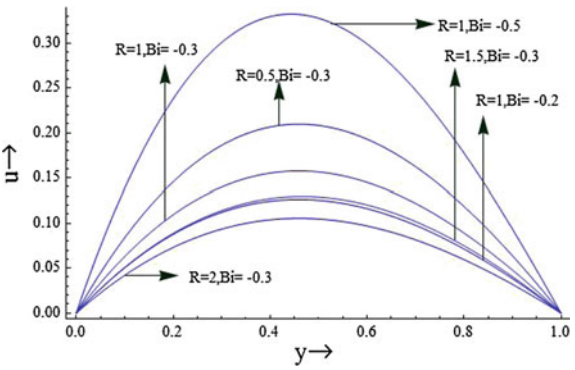

Fig. 4 velocity profile for $B = 0.5$, $S = 1$, and Newtonian heating

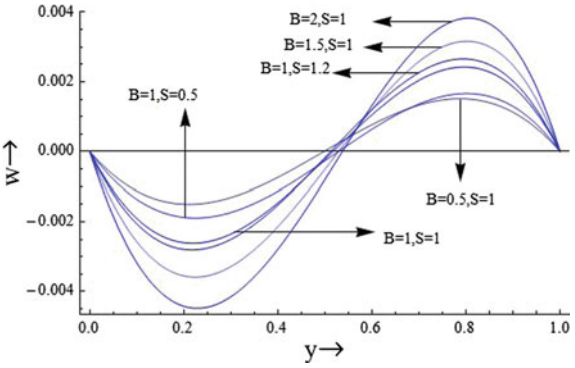

Fig. 5 Microrotational velocity profile for $R = 1$, $Bi = 0.5$

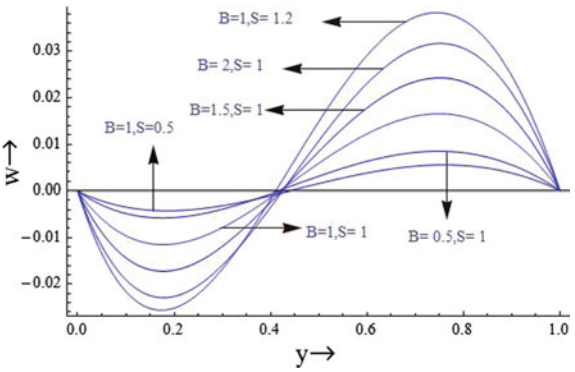

Fig. 6 Microrotational velocity profile for $R = 1$, $Bi = -0.5$

The vertex viscosity parameter has a decreasing effect on the velocity in both cases of the Newtonian heating and cooling.

Figures 5 and 6 clearly demonstrate that the impact of the material and source parameters on the microrotational velocity is to increase it in cases of the Newtonian heating/cooling. Figure 7 indicates an increase in the microrotational

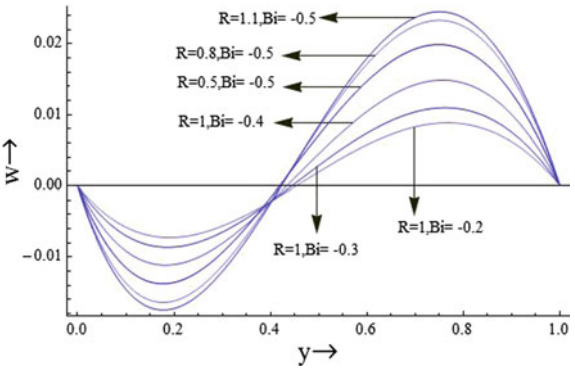

Fig. 7 Influence of vertex viscosity and Biot number on microrotational velocity in case of Newtonian heating

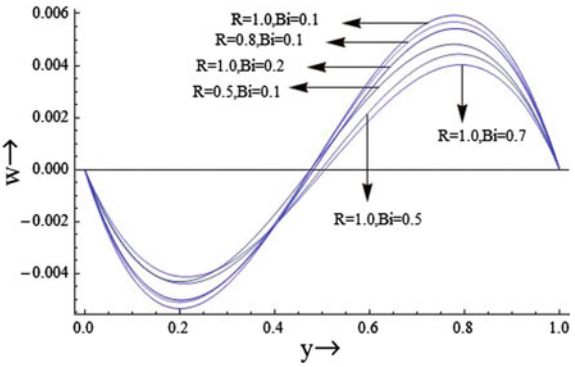

Fig. 8 Influence of Biot number and vertex viscosity on microrotational velocity in case of Newtonian cooling

velocity profiles with the Biot number in case of the Newtonian heating, while Fig. 8 reveals that the microrotational velocity decreases with the Biot number in case of the Newtonian cooling. The influence of vertex viscosity parameter is to increase the microrotational velocity in both cases of the Newtonian heating and cooling.

Figures 9 and 10 show that the velocity profile increases with the material parameter and decreases with the source parameter in cases of the Newtonian heating/cooling. Figures 11 and 12 indicate an increase in the microrotational velocity profiles with the material parameter and decrease in the microrotational velocity profiles with the source parameter in both cases of the Newtonian heating and cooling.

Table 1 clearly shows that in the presence of the Newtonian heating, the dimensionless volume flow rate has increasing tendency while decreasing tendency for the Newtonian cooling.

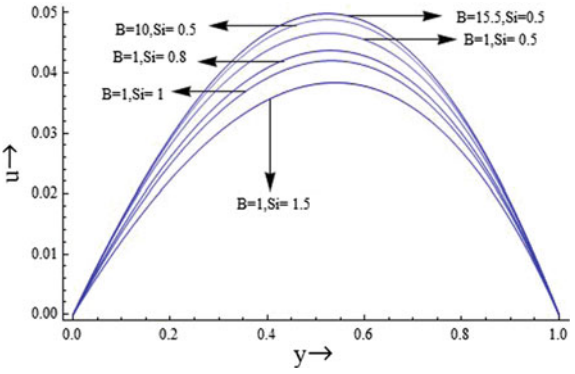

Fig. 9 Influence of source and material parameters on velocity for $R = 1$, $Bi = 0.5$

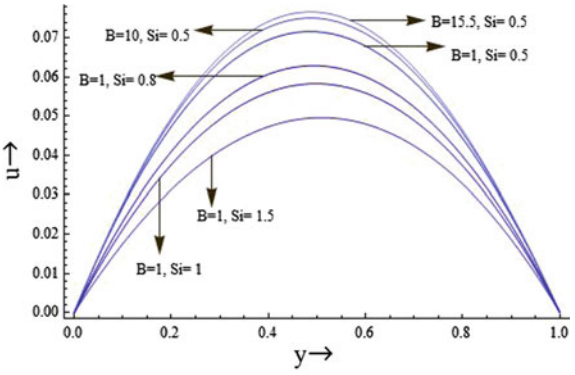

Fig. 10 Influence of source and material parameters on velocity for $R = 1$, $Bi = -0.5$

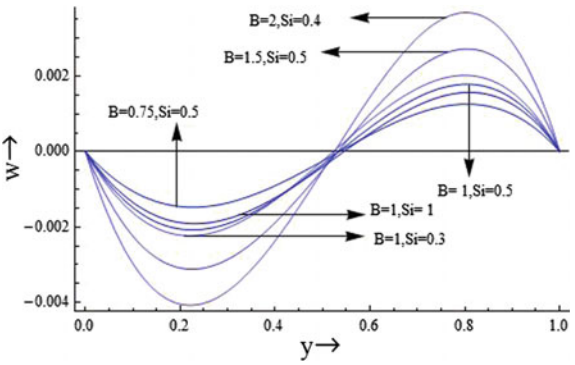

Fig. 11 Microrotational velocity profile for $Bi = 0.5$, $R = 1$

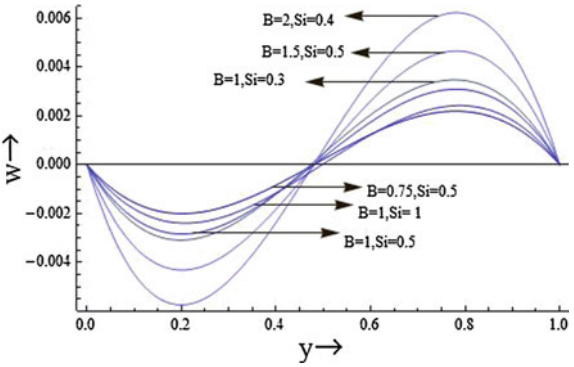

Fig. 12 Microrotational velocity profile for $Bi = -0.5$, $R = 1$

Table 1 Numerical values of the dimensionless volume flow rate (Q)

R	B	s	Bi	Q
0.75	1.0	1.0	−0.5	5.629427
0.75	1.0	1.0	−0.3	1.459802
0.75	1.0	4.0	0.5	0.026529
0.75	1.0	4.0	0.6	0.074489
0.75	1.0	−1.0	−0.5	−0.301138
0.75	1.0	−1.0	−0.3	−0.206970
0.75	1.0	−4.0	0.5	−0.138105
0.75	1.0	−4.0	0.3	−0.136560
0.75	2.0	1.0	−0.5	5.851975
0.75	2.0	1.0	−0.3	1.515474
0.75	2.0	4.0	0.5	0.032255
0.75	2.0	4.0	0.6	0.083662
0.75	2.0	−1.0	−0.5	0.384068
0.75	2.0	−1.0	−0.3	0.123054
0.75	2.0	−4.0	0.5	−0.137537
0.75	2.0	−4.0	0.3	−0.136161
1.5	1.0	1.0	−0.5	4.302331
1.5	1.0	1.0	−0.3	1.112192
1.5	1.0	4.0	0.5	0.024736
1.5	1.0	4.0	0.6	0.061993
1.5	1.0	−1.0	−0.5	0.623518
1.5	1.0	−1.0	−0.3	0.232780
1.5	1.0	−4.0	0.5	−0.142913
1.5	1.0	−4.0	0.3	−0.141932
1.5	2.0	1.0	−0.5	4.533721
1.5	2.0	1.0	−0.3	1.170173
1.5	2.0	4.0	0.5	0.031948
1.5	2.0	4.0	0.6	0.073577
1.5	2.0	−1.0	−0.5	0.239298
1.5	2.0	−1.0	−0.3	0.047863
1.5	2.0	−4.0	0.5	−0.141573
1.5	2.0	−4.0	0.3	−0.141020

4 Conclusion

The analytic solutions of the governing differential equations for the Newtonian heating/cooling and different cases of source/sink parameter have been obtained. The influence of Biot number parameter on the velocity and microrotational velocity is to increase them for the Newtonian heating, while in the case of the Newtonian cooling, the effect of Biot number is to decrease them. The dimensionless volume flow rate has increasing tendency in case of the Newtonian heating and decreasing tendency for the Newtonian cooling.

Acknowledgements Mr. Arun Kumar Singh is thankful for UGC, New Delhi, India, for the economical endorsement in the form of a Junior Research Fellowship to finish this work.

Appendix

$$k_1 = \cos\sqrt{s},\quad k_2 = \sin\sqrt{s},\quad k_3 = \frac{\sqrt{s}}{(k_2 Bi + \sqrt{s}k_1)},$$

$$k_4 = \frac{Bi}{(k_2 Bi + \sqrt{s}k_1)},\quad k_5 = \frac{2BR}{1+R},\quad k_6 = \frac{1}{2+R},\quad k_7 = k_5 k_6,$$

$$k_8 = -\frac{\sqrt{s}k_3 k_7}{s(s+k_5)},\quad k_9 = \frac{\sqrt{s}k_4 k_7}{s(s+k_5)},\quad k_{10} = \frac{2+R}{2BR},$$

$$k_{11} = k_{10}k_5 - 2,\quad k_{12} = 2k_8 + sk_{10}k_8,\quad k_{13} = 2k_9 + sk_{10}k_9,$$

$$k_{14} = \frac{k_{11}}{\sqrt{k_5}},\quad k_{15} = -\frac{k_{12}}{\sqrt{s}},\quad k_{16} = \frac{k_{13}}{\sqrt{s}},\quad k_{17} = \sinh\left(\sqrt{k_5}\right),$$

$$k_{18} = \cosh\left(\sqrt{k_5}\right),\quad k_{19} = k_{14}k_{17},\quad k_{20} = k_{14}k_{18},\quad k_{21} = k_{15}k_1 + k_{16}k_2,$$

$$k_{22} = -(k_8 k_2 + k_9 k_1),\quad k_{23} = -\frac{k_{22}+k_9}{k_{18}-1},\quad k_{24} = -\frac{k_{17}}{k_{18}-1},$$

$$k_{25} = k_{23}(k_{19}+2) + k_{21} - 2k_9),\quad k_{26} = k_{24}(k_{19}+2) + k_{20},$$

$$k_{27} = \frac{k_{15}-k_{25}}{k_{26}-k_{14}},\quad k_{28} = k_{23} + k_{27}k_{24},\quad k_{29} = k_9 - k_{28},$$

$$k_{30} = -k_{15} - k_{14}k_{27},\quad k_{31} = \frac{k_{14}k_{28}}{\sqrt{k_5}},\quad k_{32} = \frac{k_{14}k_{27}}{\sqrt{k_5}},\quad k_{33} = \frac{-k_{16}}{\sqrt{s}},$$

$$k_{34} = \frac{k_{15}}{\sqrt{s}},\quad k_{35} = -k_{29} + k_{30} - k_{31} + k_{33},$$

$$A_1 = \frac{Bi}{Bi+1},\ \ A_2 = \frac{1}{Bi+1},\ \ A_3 = \frac{2BR}{1+R},$$
$$A_4 = \frac{1}{2+R},\ \ A_5 = \frac{A_4 A_1}{2},\ \ A_6 = A_2 A_4,$$
$$A_7 = \frac{2+R}{2BR},\ \ A_8 = A_7 A_3 - 2,\ \ A_9 = 2A_5 A_7,$$
$$A_{10} = \frac{A_8}{\sqrt{A_3}},\ \ A_{11} = \frac{2}{3A_5},\ \ A_{12} = \sinh\sqrt{A_3},$$
$$A_{13} = \cosh\sqrt{A_3},\ \ A_{14} = A_9 - A_6 - A_{11},\ \ A_{15} = A_{10}A_{12},$$
$$A_{16} = A_{10}A_{13},\ \ A_{17} = A_5 + A_6,\ \ A_{18} = -\frac{A_{17}}{A_{13}-1},$$
$$A_{19} = -\frac{A_{12}}{A_{13}-1},\ \ A_{20} = A_{16} - A_{10} + (A_{15}+2)A_{19},$$
$$A_{21} = A_{14} + (A_{15}+2)A_{18},\ \ A_{22} = -\frac{A_{21}}{A_{20}},$$
$$A_{23} = A_{18} + A_{19}A_{22},\ \ A_{24} = -A_{23},\ \ A_{25} = -A_{10}A_{22},$$
$$A_{26} = \frac{A_{23}}{\sqrt{A_3}},\ \ A_{27} = \frac{A_{22}}{\sqrt{A_3}},\ \ A_{28} = A_{24} + \frac{A_5}{3} + \frac{A_6}{2} - \frac{A_{22}}{\sqrt{A_3}},$$

$$p_1 = \cosh\sqrt{si},\ \ p_2 = \sinh\sqrt{si},\ \ p_3 = \frac{\sqrt{si}}{(p_2 Bi + \sqrt{si}p_1)},$$
$$p_4 = \frac{Bi}{(p_2 Bi + \sqrt{si}p_1)},\ \ k_5 = \frac{2BR}{1+R} = p_5,\ \ p_6 = \frac{1}{2+R} = k_6,$$
$$p_7 = p_5 p_6,\ \ p_8 = -\frac{\sqrt{si}\,p_3 p_7}{si(si+p_5)},\ \ p_9 = \frac{\sqrt{si}\,p_4 p_7}{si(si+p_5)},$$
$$p_{10} = \frac{2+R}{2BR} = k_{10},\ \ p_{11} = p_{10}p_5 - 2,\ \ p_{12} = -2p_8 + si\,p_{10}p_8,$$
$$p_{13} = -2p_9 + si\,p_{10}p_9,\ \ p_{14} = \frac{p_{11}}{\sqrt{p_5}},\ \ p_{15} = \frac{p_{12}}{\sqrt{si}},$$
$$p_{16} = \frac{p_{13}}{\sqrt{si}},\ \ p_{17} = \sinh\left(\sqrt{p_5}\right),\ \ p_{18} = \cosh\left(\sqrt{p_5}\right),$$
$$p_{19} = p_{14}p_{17},\ \ p_{20} = p_{14}p_{18},\ \ p_{21} = p_{15}p_1 + p_{16}p_2,$$
$$p_{22} = (p_8 p_2 + p_9 p_1),\ \ p_{23} = \frac{-p_{22} + p_9}{p_{18} - 1},\ \ p_{24} = \frac{p_{17}}{1 - p_{18}},$$
$$p_{25} = p_{14}p_{17} + 2,\ \ p_{26} = p_{21} + 2p_9,\ \ p_{27} = p_{25}p_{24} + p_{20},$$
$$p_{28} = p_{26} + p_{23}p_{25},\ \ p_{29} = \frac{p_{15} - p_{28}}{p_{27} - p_{14}},\ \ p_{30} = p_{23} + p_{29}p_{24},$$
$$p_{31} = p_{30} - p_9,\ \ p_{33} = \frac{p_{14}p_{30}}{\sqrt{p_5}},\ \ p_{34} = \frac{p_{14}p_{29}}{\sqrt{p_5}},$$
$$p_{35} = \frac{p_{16}}{\sqrt{si}},\ \ p_{36} = \frac{p_{15}}{\sqrt{si}},\ \ p_{37} = -p_{31} + p_{32} - p_{33} + p_{35},$$

References

Aung W (1972) Fully developed laminar free convection between vertical plates heated asymmetrically. Int J Heat Mass Transf 15:1577–1580

Erigen AC (1966) Theory of micropolar fluids. J Math Mech 16:1–18

Erigen AC (1972) Theory of thermo-micropolar fluids. J Math Anal Appl 38:480–496

Kumar D, Singh AK (2015) Effects of induced magnetic field on natural convection with Newtonian heating/cooling in vertical annuli. Procedia Eng 127:568–574

Merkin JH (1994) Natural-convection boundary-layer flow on a vertical surface with Newtonian heating. Int J Heat Fluid Flow 15:392–398

Miyatake O, Fujii T (1973) Natural convection heat transfer between vertical parallel plates at unequal uniform temperatures. Heat Transf Jpn Res 2:79–88

Nelson DJ, Wood BD (1973) Combined heat and mass transfer natural convection between vertical parallel plates. Int J Heat Mass Transf 32:1779–1787

Ravi SK, Singh AK, Alawadhi KA (2011) Effects of temperature dependent heat source/sink on free convective flow of a micropolar fluid between two vertical walls. Inter J Energy Technol 3(27):1–8

Influence of Thermal Radiation and Heat Absorption of a Third-Grade Fluid in Wire Coating Analysis Through a Porous Medium

M.K. Nayak

Abstract In the present study, the influence of porous matrix, thermal radiation, and internal heat absorption on wire coating using third-grade fluid like melt polymer in the presence of constant as well as temperature-dependent viscosity has been analyzed. The governing equations are solved numerically by employing fourth-order Runge-Kutta method. Models such as third-grade fluid model, Reynolds model, and Vogel's model have been used. The results for the velocity and temperature are displayed and discussed in detail. Porous matrix has remarkable contributions in escalating the temperature whereas the effect of thermal radiation is diametrically opposite to that of porous matrix in the flow region within the die. Velocity profiles disparaged because of resistive force from medium porosity, and thereby, momentum boundary layer shrinks. Heat absorption in thermal boundary layer leads to decrease in temperature, and then, the associated thermal boundary layer thickness shrinks.

List of Symbols

R_w	Radius of the wire (m)
$\frac{D}{Dt}$	Substantial derivative
U_w	Wire velocity (m s^{-1})
p	Pressure (N m^{-2})
θ_w	Wire temperature (K)
F	Viscous force per unit volume (N m^{-3})
L	Length of die (m)
R_d	Radius of die (m)
k	Thermal conductivity (W m^{-1} K^{-1})
C_p	Specific heat at constant pressure (J kg^{-1} K^{-1})
q_r	Radiative heat flux (W m^{-2})
θ_d	Die temperature (K)

M.K. Nayak (✉)
Department of Physics, Radhakrishna Institute of Technology and Engineering, Biju Patnaik University of Technology, Rourkela, Odisha, India
e-mail: mkn2122@gmail.com

M.K. Singh et al. (eds.), *Applications of Fluid Dynamics*, Lecture Notes in Mechanical Engineering, https://doi.org/10.1007/978-981-10-5329-0_11

ϕ	Dissipation function (W m^{-2})
K_p	Non-dimensional permeability parameter
R	Radiation parameter
q	Velocity of fluid (m s^{-1})
S	Extra stress tensor
Q	Heat absorption parameter
θ	Fluid temperature (K)
β_0	Non-Newtonian parameter
B_r	Brinkman number
k_1	Mean absorption coefficient (m^{-1})
μ_0	Reference viscosity (N s m^{-2})
μ	Dynamic viscosity (N s m^{-2})
ρ	Density of the fluid (kg m^{-3})
σ_1	Stefan–Boltzmann constant (W m^{-2} K^{-4})
$\alpha_1, \alpha_2, \beta_1, \beta_2$	Material constants
m	Reynolds model viscosity parameter
Ω_1	Vogel's model viscosity parameter
Q_0	Rate of volumetric heat absorption

1 Introduction

Over the years, the boundary layer behavior of a viscoelastic fluid flowing over a continuously stretching surface is significant in view of its inevitable and important industrial applications include polymeric extrusion, petroleum drilling, hot rolling, and drawing of plastic films and wires. Such pristine applications in industrial and technological processes have led to deep interest in the study of viscoelastic fluid flow and heat transfer in the wire coating process. Wire coating process is nothing but an industrial process to coat a wire for primary insulation, mechanical strength, and environmental protection. Indeed, the most efficient process for wire coating is the coaxial extrusion process.

The co-extrusion process is an operation in which either the melt polymer is extruded on an axially traversing wire or the wire is dragged inside a die filled with molten polymer. In this process, the velocity of wire and the melt polymer produces high pressure that generates strong bonding between them and provides fast coating (Han and Rao 1978; Caswell and Tanner 1978; Nayak 2015).

Many researchers, namely Tadmor and Gogos (1979), Nayak et al. (2014), Ali and Javed (2016), have analyzed wire coating using third-grade fluid. Third-grade fluid is used because it exhibits the phenomena such as shear thickening and shear thinning. Also, many authors, namely Hayat et al. (2015), Daniel and Davé (2016), Chinyoka and Makinde (2012), have studied in the field of third-grade fluid.

The flow and heat transfer in association with a porous medium is prevalent in view of its numerous applications in diversified industries and contemporary

technologies. Porous materials can be used to enhance the heat transfer from the surface of the wire. The effect of porosity was examined by several authors (Jalaal and Ganji 2010; Rashidi and Hassan 2014; Nield and Bejan 2012; Rashidi et al. 2014a, b). The flow of fluids with internal heat absorption is important practically as well as theoretically. Because of the development of non-uniformity in the temperature field, fluid motion gets developed slowly. The volumetric heat absorption term influences strongly the flow and heat transfer with appreciably large temperature difference was investigated by Chen (2010). As far as cooling process is concerned, thermal radiation factor is a prospective candidate for consideration (Nayak et al. 2015; Kar et al. 2014).

Shah et al. (2011) have introduced third-grade fluid as coating material in wire coating analysis. However, they have not analyzed the influence of porous matrix, thermal radiation, and heat absorption in their study. The objective of the present study is to analyze the wire coating process where a coating material is modeled as third-grade fluid such as melt polymer having constant as well as temperature-dependent viscosities associated with Reynolds and Vogel's models.

The most fascinating aspects of the present study are as follows:

1. The porous matrix is included because it acts as an insulator due to which the flow and thermal processes restrain heat loss and accelerate the process of cooling/heating like a heat exchanger.
2. Thermal radiation is considered because the effect of radiation is of vital importance while investigating thermal effect in the processes dealing with high absolute temperatures. Also, thermal radiation plays an important role effectively in controlling the thermal boundary layers.
3. Heat absorption is included because it controls the heat transfer rates in the thermal boundary layer appreciably.

The fourth-order Runge-Kutta method in association with shooting technique is considered as method of solution. The influences of permeability parameter, radiation parameter, and heat absorption parameter on velocity as well as temperature profiles are well discussed and displayed diagrammatically.

2 Formulation of the Problem

Consider an incompressible flow of a third-grade fluid like polyvinyl chloride (PVC) inside a stationary pressure-type die of length L, radius R_d, and temperature θ_d. A wire of radius R_w at temperature θ_w is assumed to be dragged with velocity U_w along the axis of the die as shown in Fig. 1. Assume that the fluid is acted upon by a constant pressure gradient $\frac{dp}{dz}$ in the axial direction.

The wire and die are concentric where the center of the wire is considered as a coordinate system with z- and r-axes is taken along and perpendicular to the direction of flow, respectively.

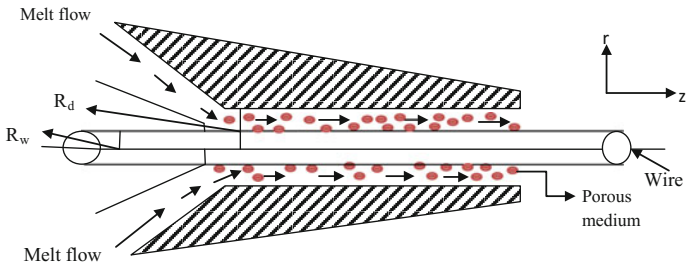

Fig. 1 Flow geometry

The design of wire coating dies greatly affects the quality of the final product. The pressure-type die is introduced because within this die the melt polymer meets the wire where a complex flow field prevails whose understanding is essential for the better die design with optimum performance. In order to prevent elongation and frequent breakage of the wire, excessive wall shear stresses at the wire are assumed to be avoided. Assume that no slip occurs at the moving wire as well as stationary die wall. With the aforesaid frame of reference and assumptions, the velocity field, extra stress tensor, and temperature field are considered, respectively,

$$\vec{q} = [0, 0, w(r)], \quad S = S(r) \text{ and } \theta = \theta(r) \tag{1}$$

The governing equations of continuity, momentum, and energy for the flow of an incompressible fluid are:

$$\vec{\nabla} \cdot \vec{q} = 0 \tag{2}$$

$$\rho \frac{\mathrm{D}\vec{q}}{\mathrm{D}t} = -\vec{\nabla} p + \vec{F} - \frac{\mu \vec{q}}{K_{\mathrm{p}}^*} \tag{3}$$

$$\rho C_{\mathrm{p}} \frac{\mathrm{D}\theta}{\mathrm{D}t} = k\nabla^2 \theta + \phi - q_{\mathrm{r}}' - Q_0(\theta - \theta_{\mathrm{w}}) \tag{4}$$

Boundary conditions are:

$$\left.\begin{aligned} w = U_{\mathrm{w}}, \quad \theta = \theta_{\mathrm{w}} \quad \text{at } r = R_{\mathrm{w}}, \\ w = 0, \quad \theta = \theta_{\mathrm{d}} \quad \text{at } r = R_{\mathrm{d}} \end{aligned}\right\} \tag{5}$$

For third-grade fluid, the extra stress tensor S is defined as

$$S = \mu A_1 + \alpha_1 A_2 + \alpha_2 A_1^2 + \beta_1 A_3 + \beta_2 (A_1 A_2 + A_2 A_1) + \beta_3 \left(tr\, A_1^2\right) A_1$$

where

$$A_1 = L^T + L \quad \text{and} \quad A_n = A_{n-1}L^T + LA_{n-1} + \frac{\mathrm{D}A_{n-1}}{\mathrm{D}t}, \quad n = 2, 3.$$

Here, T denotes the transpose of the matrix and $L = \operatorname{grad} q$.

The nonzero components of extra tensor S are

$$S_{rr} = (2\alpha_1 + \alpha_2)w'^2, \quad S_{zz} = \alpha_2 w'^2, \quad S_{rz} = \mu w' + 2(\beta_2 + \beta_3)w'^3$$

The velocity field (1) satisfies the continuity Eq. (2) and indicates that the fluid flow is possible. Using the nonzero components of S, Eqs. (1) and (5), and assuming that the pressure gradient in the axial direction is zero, the momentum Eq. (3) takes the form

$$\frac{2(\beta_2 + \beta_3)}{r} \cdot \frac{\mathrm{d}}{\mathrm{d}r}\left(rw'^3\right) + \frac{\mu}{r}\frac{\mathrm{d}}{\mathrm{d}r}(rw') - \frac{\mu w}{K_\mathrm{p}^*} = 0 \tag{6}$$

Using Rosseland approximation for thermal radiation (Brewster 1972), the radiative heat flux is modeled as

$$q_r = -\frac{4\sigma_1}{3k_1}\theta'^4$$

Expressing θ^4 as a linear combination of the temperature and expanding it in Taylor series about θ_∞ and neglecting higher order terms (Turkyilmazoglu 2011),

$$\theta^4 \simeq 4\theta_\infty^3\theta - 3\theta_\infty^4$$

and hence,

$$q_r' = -\frac{16\,\sigma_1\theta_\infty^3}{3k_1}\ \theta'' \tag{7}$$

Using Eq. (7), the energy equation (4) takes the form

$$k\left(\frac{\mathrm{d}^2}{\mathrm{d}r^2} + \frac{1}{r}\frac{\mathrm{d}}{\mathrm{d}r}\right)\theta + \mu w'^2 + 2(\beta_2 + \beta_3)w'^4 + \frac{16\sigma_1\theta_\infty^3}{3k_1} \cdot \theta'' - Q_0(\theta - \theta_\mathrm{w}) = 0 \tag{8}$$

where $'$ represents the differentiation with respect to r and $''$ denotes the differentiation two times with respect to r.

2.1 Constant Viscosity

Let us introduce the dimensionless parameters as

$$\left.\begin{array}{llllll} r^* = \frac{r}{R_w}, & w^* = \frac{w}{U_w}, & \theta^* = \frac{\theta-\theta_w}{\theta_d-\theta_w}, & \beta_0 = \beta_2 + \beta_3, & B_r = \frac{\mu U_w^2}{k(\theta_d-\theta_w)}, \\ \beta_0^* = \frac{\beta_0 U_w^2}{\mu R_w^2}, \frac{R_d}{R_w} = \delta > 1, & K_p = \frac{R_w^2}{K_p^*}, & R = \frac{16\sigma_1\theta_\infty^3}{3kk_1}, & Q = \frac{Q_0 R_w^2}{k} & & \end{array}\right\} \quad (9)$$

The system of Eqs. (5), (6), and (8) after dropping the asterisks becomes

$$rw'' + w' - K_p wr + 2\beta_0\left(3rw''w'^2 + w'^3\right) = 0 \quad (10)$$

$$w(1) = 1 \quad \text{and} \quad w(\delta) = 0 \quad (11)$$

$$(1+R)\theta'' + \frac{1}{r}\theta' + B_r w'^2 + 2B_r\beta_0 w'^4 - Q\theta = 0 \quad (12)$$

$$\theta(1) = 0 \quad \text{and} \quad \theta(\delta) = 1 \quad (13)$$

Numerical Scheme
Equations (10) and (12) have been solved with boundary conditions (11) and (13) using fourth-order Runge-Kutta method along with shooting technique. For computational purpose, we have taken $\delta = 2$.

2.2 Variable Viscosity

2.2.1 Reynolds Model

The non-dimensional temperature-dependent viscosity is

$$\mu = \mu_0 \exp(-\beta_0 m\theta) \approx \mu_0(1 - \beta_0 m\theta) \quad (14)$$

$$\left.\begin{array}{l} r^* = \frac{r}{R_w}, w^* = \frac{w}{U_w}, \theta^* = \frac{\theta-\theta_w}{\theta_d-\theta_w}, \beta_0 = \beta_2 + \beta_3, \frac{R_d}{R_w} = \delta > 1, K_p = \frac{R_w^2}{K_p^*}, \\ B_r = \frac{\mu_0 U_w^2}{k(\theta_d-\theta_w)}, \beta_0^* = \frac{\beta_0 U_w^2}{\mu_0 R_w^2}, R = \frac{16\sigma_1\theta_\infty^3}{3kk_1}, Q = \frac{Q_0 R_w^2}{k} \end{array}\right\} \quad (15)$$

Using Eqs. (14) and (15), the dimensionless momentum and temperature equations with boundary conditions become

$$(1 - \beta_0 m\theta)\left(rw'' + w' - K_p wr\right) + 2\beta_0\left[3rw''w'^2 + w'^3\right] - \beta_0 m\theta' w' = 0 \quad (16)$$

$$w(1) = 1 \quad \text{and} \quad w(2) = 0 \quad (17)$$

$$(1+R)\theta'' + \frac{1}{r}\theta' + (1-\beta_0 m\,\theta)B_r w'^2 + 2B_r\,\beta_0 w'^4 - Q\,\theta = 0 \tag{18}$$

$$\theta(1) = 0 \quad \text{and} \quad \theta(2) = 1 \tag{19}$$

Numerical Scheme
Equations (16) and (18) along with boundary conditions (17) and (19) have been solved by employing a numerical scheme named as fourth-order Runge-Kutta method along with shooting technique.

2.2.2 Vogel's Model

The non-dimensional temperature-dependent viscosity is

$$\mu = \mu_0 \mathrm{e}^{(DB_1+\theta)-\theta_w} \tag{20}$$

or

$$\mu = \Omega_1\left(1 - \frac{D}{B_1^2}\theta\right) \tag{21}$$

where $\Omega_1 = \mu_0 \mathrm{e}^{(D/B_1)-\theta_\mathrm{w}}$ and D, B_1 are viscosity parameters in connection with Vogel's model.

Using Eqs. (21) and (15), the non-dimensional momentum and energy equations are, respectively,

$$\Omega_1\left(1 - \frac{D}{B_1^2}\theta\right)\left(rw'' + w' - K_\mathrm{p} wr\right) + 2\beta_0\left[3rw''w'^2 + w'^3\right] - \left(\frac{\Omega_1 D}{B_1^2}\right)\theta' w' = 0 \tag{22}$$

$$w(1) = 1 \quad \text{and} \quad w(2) = 0 \tag{23}$$

$$(1+R)\theta' + \frac{1}{r}\theta' + \Omega_1\left(1 - \frac{D}{B_1^2}\theta\right)B_r w'^2 + 2B_r\,\beta_0\,w'^4 - Q\,\theta = 0 \tag{24}$$

$$\theta(1) = 0 \quad \text{and} \quad \theta(2) = 1 \tag{25}$$

Numerical Scheme
Applying fourth-order Runge-Kutta method along with shooting technique, the numerical solutions of Eqs. (22) and (24) with the boundary condition (23) and (25) have been obtained with $D = \beta_0 b$. During the numerical computation, we have taken the values of $B_1 = 1$ and $D = 2$.

3 Results and Discussion

The influence of several pertinent parameters such as permeability parameter (K_p), radiation parameter (R), and heat absorption parameter (Q) in case of constant and variable viscosities along with Reynolds and Vogel's models related to wire coating process using melt polymer satisfying third-grade fluid model in a pressure-type die has been divulged in the present study.

3.1 Case of Constant Viscosity

The effect of K_p on the velocity field is observed in Fig. 2. There is a decrease in the fluid velocities with increase in K_p for non-Newtonian fluids. This is due to the fact that the introduction of porous matrix has a tendency to offer a resistive force to oppose the flow. It complies with the discussion in Nield and Bejan (2012). Hence, the permeability parameter belittles the velocity throughout the flow domain.

The influence of K_p, R, and Q on temperature distribution of third-grade fluid is shown in Figs. 3, 4, and 5, respectively. Figure 3 displays, in rich detail, the fact that an increase in permeability parameter causes to increase the temperature in the region up to $r < 1.6$ but afterward the reverse effect is observed. This is because the resistive force offered by porous matrix is dominated by the boundary surface effects.

The behavior of temperature inspired by thermal radiation is depicted in Fig. 4. If we somehow increase R, then temperature decreases throughout the flow domain

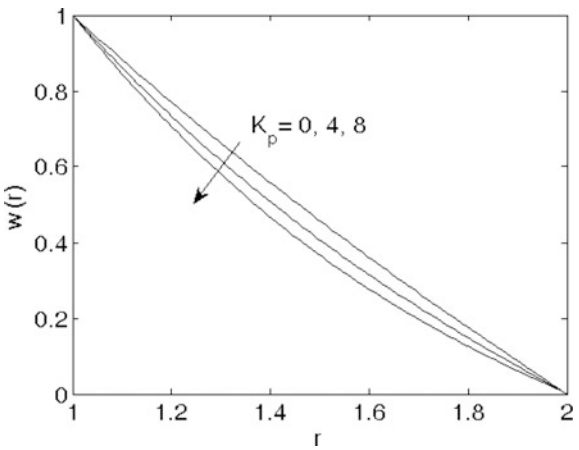

Fig. 2 Influence of K_p on velocity (constant viscosity case) for $\beta_0 = 0.5, B_r = 1, Q = 0.5, R = 0.2$

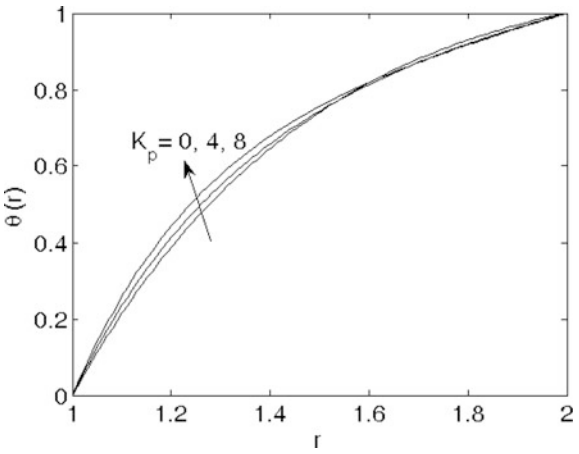

Fig. 3 Influence of K_p on temperature (constant viscosity case) for $\beta_0 = 0.5, B_r = 1, Q = 0.5$, $R = 0.2$

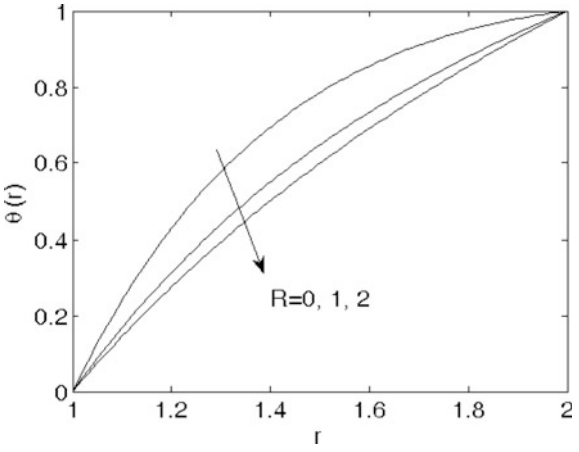

Fig. 4 Influence of R on temperature (constant viscosity case) for $\beta_0 = 0.5, B_r = 1, Q = 0.5$, $K_p = 0.5$

(Cortell 2014). This is probably due to the fact that the mean Rosseland absorption coefficient k_1 decreases (for small thermal conductivity k) with increase in R. It is a matter of interest to mention that temperature decreases with an increase of heat absorption parameter as sighted in Fig. 5.

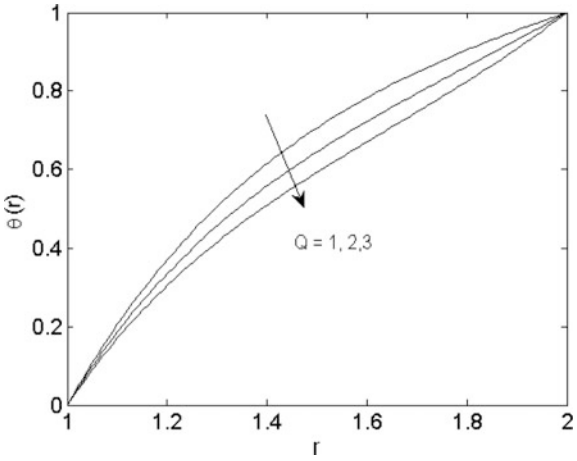

Fig. 5 Influence of Q on temperature (constant viscosity case) for $\beta_0 = 0.5, B_r = 1, R = 0.2$, $K_p = 0.5$

3.2 *Case of Variable Viscosity*

3.2.1 Reynolds Model

Figure 6 delineates that the presence of porous matrix and non-Newtonian property of the fluid favors to the enhancement of velocity of coating fluid associated with temperature-dependent variable viscosity. However, increase of K_p slows down the fluid motion throughout the die region. This diminution in velocity is by virtue of resistive force offered by the porous matrix. The effects of K_p, R, and Q on the temperature distributions of melt polymer used as coating fluid are shown in Figs. 7, 8, and 9, respectively. An increase in porous matrix results higher temperature within the layers $r < 1.6$; thereafter, no significant contribution of K_p is shown (Fig. 7). However, the fluid temperature gets enhanced for moderately large $K_p (K_p = 10)$. It is interesting to note that an increase in thermal radiation parameter decreases the temperature of the melt polymer in the presence of porous matrix as well as heat absorption indicating that the coating material gets cooled with moderately larger value of R (Fig. 8). So R should be kept minimum. It is to mention that heat absorption in thermal boundary layer causes the decrease in temperature and so reduces the thermal boundary layer thickness (Fig. 9).

3.2.2 Vogel's Model

Figures 10 and 11 illustrate, respectively, the velocity profiles of coating fluid influenced by K_p and Q. Velocity distributions, indicating retardation offered by the

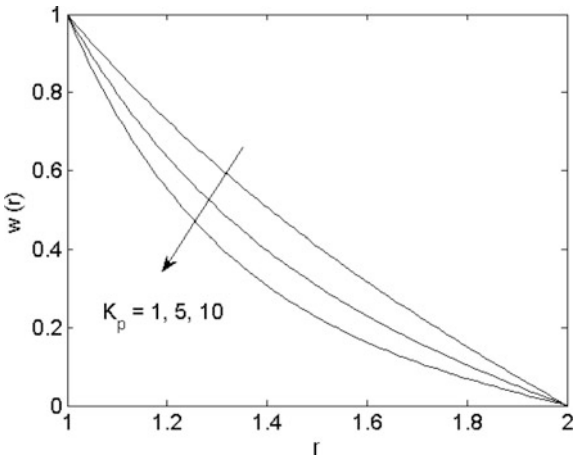

Fig. 6 Influence of K_p on velocity (Reynolds model) for $\beta_0 = 0.1, B_r = 1, R = 0.2, Q = 0.5, m = 1$

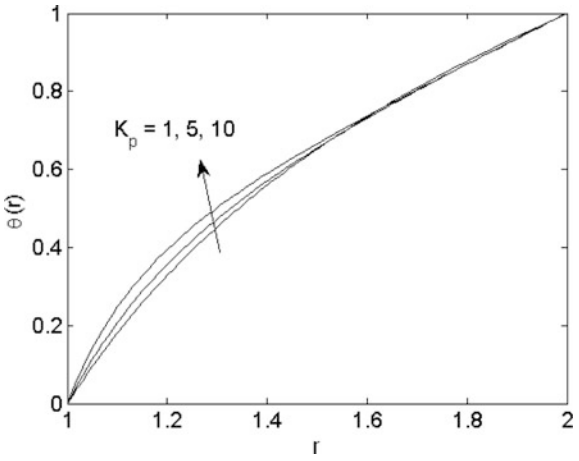

Fig. 7 Influence of K_p on temperature (Reynolds model) for $\beta_0 = 0.1, m = 1, B_r = 1, Q = 0.5, R = 0.2$

resistive force of porous matrix in the presence of thermal radiation and heat absorption, are observed (Fig. 10). Figure 11 portrays the significance of heat absorption in fluid motion where the velocity of the coating fluid gets reduced due to increase in Q. However, the fall is significant for higher Q. The effects of K_p, Q, and R on temperature distributions are obtained from Figs. 12, 13, and 14, respectively. The effect of porous matrix with viscous heating or variable viscosity enhances the temperature just immediate from the surface of the wire, but thereafter

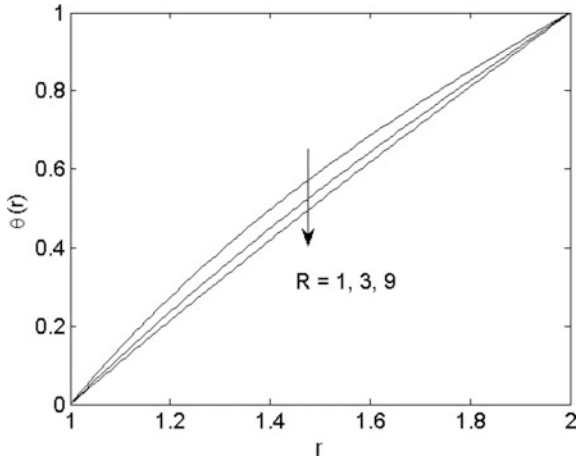

Fig. 8 Influence of R on temperature (Reynolds model) for $\beta_0 = 0.1, K_p = 0.2, B_r = 1, m = 1, Q = 0.5$

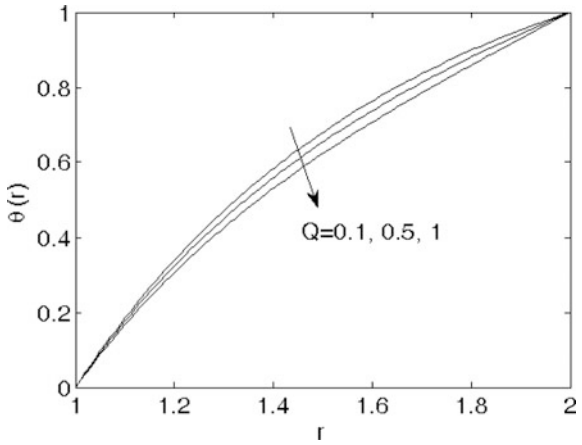

Fig. 9 Influence of Q on temperature (Reynolds model) for $\beta_0 = 0.1, K_p = 0.2, B_r = 1, m = 1, R = 0.2$

the reverse effect is visualized (Fig. 12). The effect of heat absorption parameter on temperature distribution by setting the fixed values of six parameters $\beta_0, K_p, B_r, \Omega_1, R, B_1$, and D is portrayed in Fig. 13. It shows that heat absorption causes the temperature to fall leading to enhancement in heat transfer rate and hence shrinks the thermal boundary layer. This is in good agreement with Nayak (2016). However, large value of Q (Q = 10) attributes to the nonlinearity and significant fall in temperature. A uniform decline in temperature due to increase in radiation

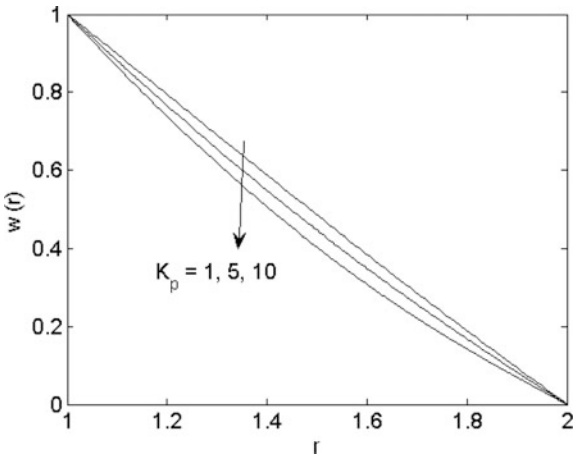

Fig. 10 Influence of K_p on velocity (Vogel's model) for $\beta_0 = 1.0, B_r = 1, R = 0.2, \Omega_1 = 1, Q = 0.5, D = 2, B_1 = 1$

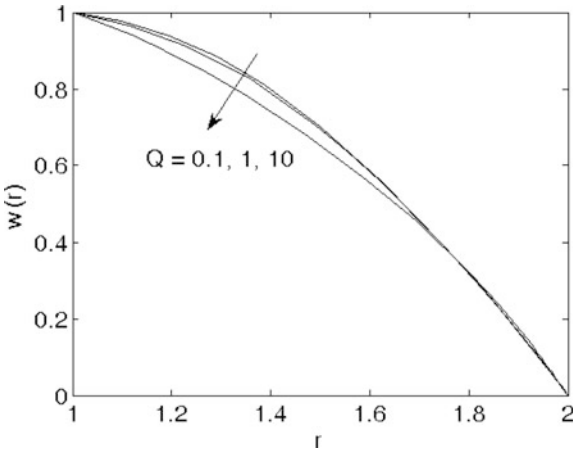

Fig. 11 Influence of Q on velocity (Vogel's model) for $\beta_0 = 0.1, K_p = 0.2, B_r = 1, \Omega_1 = 1, R = 0.2, B_1 = 1, D = 2$

parameter (R) indicates that thermal radiation is to be enhanced so as to make the cooling process faster in the presence of heat absorption (Fig. 14). It is in good agreement with Cortell (2014).

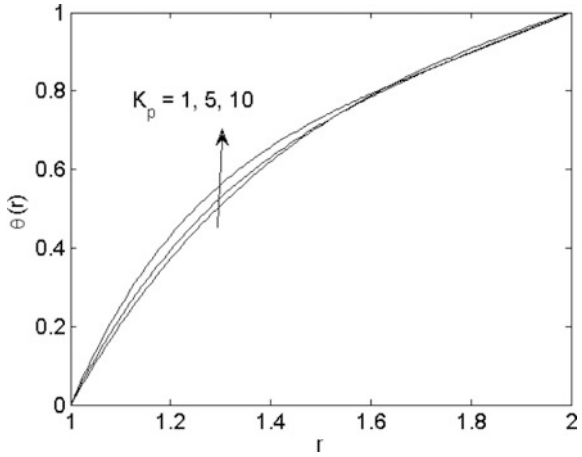

Fig. 12 Influence of K_p on temperature (Vogel's model) for $\beta_0 = 1.0, B_r = 1, \Omega_1 = 1, R = 0.2, B_1 = 1, D = 2, Q = 0.5$

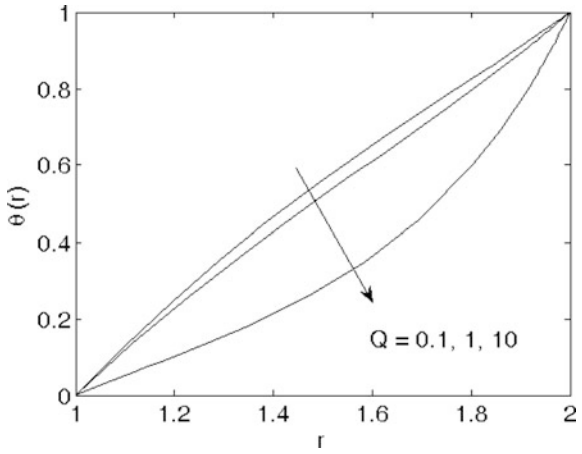

Fig. 13 Influence of Q on temperature (Vogel's model) for $\beta_0 = 0.1, K_p = 0.2, B_r = 1, \Omega_1 = 1, R = 0.2, B_1 = 1, D = 2$

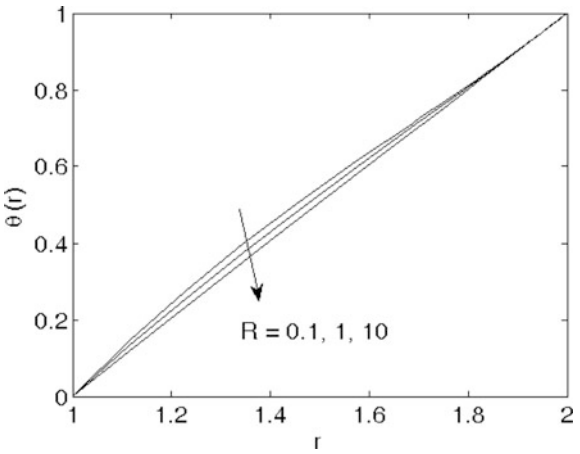

Fig. 14 Influence of R on temperature (Vogel's model) for $\beta_0 = 0.1, K_p = 0.2, B_r = 1, \Omega_1 = 1, B_1 = 1, D = 2, Q = 0.5$

4 Conclusion

An interesting consequence of the influence of thermal radiation as well as heat absorption in the presence of porous matrix is that they control the momentum and heat transfer rates in their respective ways so as to achieve a controlled cooling system which in turn determines the quality of the final products (such as coated wire) of wire coating process involved in industries. The major outcomes of the present study are mentioned below:

4.1 Case of Constant Viscosity

Porous matrix causes a reduction in the velocity of the coating fluid such as melt polymer.

4.2 Case of Variable Viscosity

Reynolds Model

- Temperature distribution in the flow region is enhanced by the effect of porosity.
- Increase in thermal radiation decreases the temperature profiles, and then, the thermal boundary layer thickness shrinks.

- Heat absorption in thermal boundary layer leads to decrease in temperature. This is in good agreement with Chen (2010) and Nayak (2016).

Vogel's Model

- Velocity distribution exhibits diminution on account of resistive force offered by porous matrix in constant viscosity as well as variable viscosity.
- Reynolds and Vogel's models provide the same behavior to porous matrix in the fashion that the temperature nearer to the wire surface enhances and possesses transition in the middle of the annular region.
- Temperature distribution in the flow region within the die gets reduced due to increase in radiation parameter (R). This investigation is in good agreement with Cortell (2014).
- Heat absorption causes the temperature to fall leading to diminution of thermal boundary layer thickness. This observation is compatible with the results as reported earlier by Chen (2010) and Nayak (2016).

References

Ali N, Javed MA (2016) Effects of temperature-dependent properties on wire-coating from a bath of FENE-P fluid. Int J Heat Mass Transf 103:401–410

Brewster MQ (1972) Thermal radiative transfer properties. Wiley, New York

Caswell B, Tanner RJ (1978) Wire coating die using finite element methods. Polym Eng Sci 18(5):417–421

Chen C-H (2010) On the analytic solution of MHD flow and heat transfer for two types of viscoelastic fluid over a stretching sheet with energy dissipation, internal heat source and thermal radiation. Int J Heat Mass Transf 53:4264–4273

Chinyoka T, Makinde OD (2012) Unsteady hydromagnetic flow of a reactive variable viscosity third-grade fluid in a channel with convective cooling. Int J Numer Meth Fluids 69(2):353–365

Cortell R (2014) Fluid flow and radiative non-linear heat transfer over a stretching sheet. J King Saud University-Sci 26:161–167

Daniel T, Davé RN (2016) Fluid bed film coating of fine ibuprofen particles. Powder Technol 290:102–113

Han CD, Rao D (1978) The rheology of wire coating extrusion. Polym Eng Sci 18(13):1019–1029

Hayat T, Shafiq A, Alsaedi A (2015) MHD axisymmetric flow of third grade fluid by a stretching cylinder. Alexandria Eng J 54(2):205–212

Jalaal M, Ganji DD (2010) An analytical study on motion of a sphere rolling down an inclined plane submerged in a Newtonian fluid. Powder Technol 198:82–92

Kar M, Sahoo SN, Rath PK, Dash GC (2014) Heat and mass transfer effects on a dissipative and radiative viscoelastic MHD flow over a stretching porous sheet. Arab J Sci Eng 39(5):3393–3401

Nayak MK (2015) Wire coating analysis, 2nd edn. India Tech, New Delhi

Nayak MK (2016) Chemical reaction effect on MHD viscoelastic fluid over a stretching sheet through porous medium. Meccanica 51:1699–1711

Nayak MK, Dash GC, Singh LP (2014) Steady MHD flow and heat transfer of a third grade fluid in wire coating analysis with temperature dependent viscosity. Int J Heat Mass Transf 79:1087–1095

Nayak MK, Dash GC, Singh LP (2015) Unsteady radiative MHD free convective flow and mass transfer of a viscoelastic fluid past an inclined porous plate. Arab J Sci Eng 40:3029–3039

Nield IA, Bejan A (2012) Convection in porous media, 4th edn. Springer, New York

Rashidi MM, Hassan H (2014) An analytic solution of micropolar flow in a porous channel with mass injection using homotopy analysis method. Int J Numer Meth Heat Fluid Flow 24(2):419–437

Rashidi MM, Ali M, Freidoonimehr N, Rostami B, Hossain MA (2014a) Mixed convective heat transfer for MHD viscoelastic fluid flow over a porous wedge with thermal radiation. Adv Mech Eng 6:735939

Rashidi MM, Momoniat E, Ferdows M, Basiriparsa A (2014b) Lie group solution for free convective flow of a nanofluid past a chemically reacting horizontal plate in a porous media. Math Probl Eng 2014:239082

Shah RA, Islam S, Ellahi M, Haroon T, Siddiqui AM (2011) Analytical solutions for heat transfer flows of a third grade fluid in post-treatment of wire coating. Int J Phys Sci 6(17):4213–4223

Tadmor Z, Gogos CG (1979) Principle of polymer processing. Wiley, New York

Turkyilmazoglu M (2011) Multiple solutions of heat and mass transfer of MHD slip flow for the viscoelastic fluid over a stretching sheet. Int J Therm Sci 50:2264–2276

Entropy Generation Analysis in a Vertical Porous Channel with Navier Slip and Viscous Dissipation

M. Sukumar, S.V.K. Varma, R. Swetha and R.V.M.S.S. Kiran Kumar

Abstract The intension of this paper is to investigate the effects of Navier slip and buoyancy force on the entropy in a vertical generation porous channel with suction/injection. This problem is solved analytically by perturbation technique. Closed form solutions are obtained for the fluid velocity and the temperature. The leads of slip parameter, injection/suction Reynolds number, Peclet number and Brinkmann number on the fluid velocity, temperature profiles, Bejan number, and rate of entropy generation are showed graphically and quantitatively discussed.

1 Introduction

Entropy generation has been studied several decades for ensuring optimal thermal systems in contemporary industrial and technological fields like heat exchangers, geothermal systems, and electronic cooling to name a few. All thermal systems confront with entropy generation. The entropy generation resulting from temperature differences has remained untreated by classical thermodynamics. Since entropy generation is the measure of the destruction of available work of the system, the determination of the active factors motivating the entropy generation is important in upgrading the system performances. Analysis of entropy generation in slip regime on thermal micro-Couette flows was reported by Chen and Tian (2010). Chauhan and Kumar (2009) described the slip conditions on entropy generation and forced convection in a circular channel occupied by a highly porous medium. Flow of entropy generation and thermal characteristics inside a porous channel with viscous dissipation was noticed by Mahmud and Fraser (2005). Heat transfer and entropy generation effects in a channel on a compressible fluid flow with porous medium were made by Chauhan and Kumar (2011).

M. Sukumar (✉) · S.V.K. Varma · R. Swetha · R.V.M.S.S.Kiran Kumar
Department of Mathematics, S.V. University, Tirupati 517502, AP, India
e-mail: sukumarphd@gmail.com

S.V.K. Varma
e-mail: svijayakumarvarma@yahoo.co.in

M.K. Singh et al. (eds.), *Applications of Fluid Dynamics*, Lecture Notes in Mechanical Engineering, https://doi.org/10.1007/978-981-10-5329-0_12

Moreover, Chauhan and Rastogi (2011) investigated the entropy generation and heat transfer in MHD flow past a stretching sheet through a porous medium. Chinyoka et al. (2013) have discussed the analysis of entropy on an unsteady MHD magnetic flow with buoyancy effects through a porous pipe. Hooman et al. (2007) have analyzed entropy generation optimization and heat transfer of forced convection in a porous-saturated duct of rectangular cross section. Makinde (2011) studied the analysis of second law for variable viscosity on MHD flow with Newtonian heating and thermal radiation. Chen (2011) and Chen and Du (2011) were discussed the entropy generation of double-diffusive convection in the presence of rotation and in rectangular cavity. Das and Jana (2014) presented the entropy generation in a porous channel due to MHD flow with Navier slip.

In this paper, our motto is to investigate the effects of Navier slip and buoyancy force on the entropy in a vertical generation porous channel with suction/injection under constant pressure gradient. A parametric study is carried out to see how the pertinent parameters of the problem affect the flow field and temperature field, and the entropy generation is studied by closed form and discussed graphically.

2 Mathematical Formulation

Consider the laminar viscous incompressible fluid bounded by a porous vertical channel with suction at the right wall, injection at the left wall, and nonuniform temperature under the effects of Navier slip, and buoyancy forces are considered. It is shown in Fig. 1.

The motion and energy equations are

$$V\frac{\mathrm{d}u}{\mathrm{d}y} = -\frac{1}{\rho}\frac{\mathrm{d}P}{\mathrm{d}x} + \frac{\mu}{\rho}\frac{\mathrm{d}^2u}{\mathrm{d}y^2} + g\beta(T - T_0) \tag{1}$$

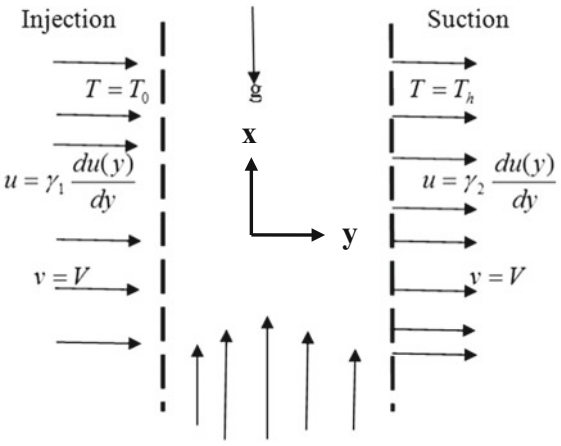

Fig. 1 Physical modal

$$V\frac{\mathrm{d}T}{\mathrm{d}y} = \alpha\frac{\mathrm{d}^2T}{\mathrm{d}y^2} + \frac{\mu}{\rho c_p}\left(\frac{\mathrm{d}u}{\mathrm{d}y}\right)^2 \tag{2}$$

The boundary conditions are

$$\left.\begin{aligned} v(0) = V, \quad u(0) = \gamma_1\frac{\mathrm{d}u(0)}{\mathrm{d}y}, \quad T(0) = T_0 \\ v(h) = V, \quad u(h) = \gamma_2\frac{\mathrm{d}u(h)}{\mathrm{d}y}, \quad T(h) = T_h \end{aligned}\right\} \tag{3}$$

Introducing dimensionless quantities are

$$\theta = \frac{T - T_0}{T_h - T_0}, \quad K = -\frac{\mathrm{d}\overline{\overline{P}}}{\mathrm{d}\bar{\bar{x}}}, \quad \bar{\bar{x}} = \frac{x}{h}, \quad \overline{\overline{P}} = \frac{Ph}{\mu V}, \quad W = \frac{u}{V}$$
$$\eta = \frac{y}{h}, \quad Re = \frac{V\rho h}{\mu}, \quad Pe = \frac{Vh}{\alpha}, \quad Br = \frac{V^2\mu}{\rho c_p\alpha(T_h - T_0)}$$
$$Gr = \frac{g\beta\rho h^2(T_h - T_0)}{\mu V}, \quad \beta_1 = \frac{\gamma_1}{h}, \quad \beta_2 = \frac{\gamma_2}{h}$$

Equations (1)–(3) become

$$\frac{\mathrm{d}^2W}{\mathrm{d}\eta^2} - Re\frac{\mathrm{d}W}{\mathrm{d}\eta} + K + Gr\theta = 0 \tag{4}$$

$$\frac{\mathrm{d}^2\theta}{\mathrm{d}\eta^2} - Pe\frac{\mathrm{d}\theta}{\mathrm{d}\eta} + Br\left(\frac{\mathrm{d}W}{\mathrm{d}\eta}\right)^2 = 0 \tag{5}$$

The boundary conditions are

$$\left.\begin{aligned} W(0) = \beta_1\frac{\mathrm{d}W(0)}{\mathrm{d}\eta}, \quad \theta(0) = 0 \\ W(1) = \beta_2\frac{\mathrm{d}W(1)}{\mathrm{d}\eta}, \quad \theta(1) = 1 \end{aligned}\right\} \tag{6}$$

Finally, Eqs. (4) and (5) are solved with the condition (6) by using perturbation technique:

$$W(\eta) = W_0(\eta) + BrW_1(\eta)$$
$$\theta(\eta) = \theta_0(\eta) + Br\theta_1(\eta)$$

on substituting these values in Eqs. (4)–(6), and on equating the corresponding coefficients on both sides, then we get the equations for velocity and temperature as follows:

$$W_0^{11} - ReW_0^1 + Gr\theta_0 + K = 0 \tag{7}$$

$$W_1^{11} - ReW_1^1 + Gr\theta_1 = 0 \tag{8}$$

$$\theta_0^{11} - Pe\,\theta_0^1 = 0 \tag{9}$$

$$\theta_1^{11} - Pe\,\theta_1^1 + W_0^{1^2} = 0 \tag{10}$$

And conditions are

$$\left.\begin{array}{llll} W_0(0) = \beta_1 W_0^1(0), & W_1(0) = \beta_1 W_1^1(0), & \theta_0(0) = 0, & \theta_1(0) = 0 \\ W_0(1) = \beta_2 W_0^1(1), & W_1(1) = \beta_2 W_1^1(1), & \theta_0(1) = 1, & \theta_1(1) = 0 \end{array}\right\} \tag{11}$$

With the help of condition (11), we get solutions for temperature and velocity of the ordinary differential equations (7)–(10) as follows:

$$\theta = \left(\frac{\exp(Pe\,\eta) - 1}{\exp(Pe) - 1}\right) + Br\left[\begin{array}{l} C_3 + C_4\exp(Pe\,\eta) + E_1\exp(Re\,\eta) \\ + E_2\,\eta\exp(Pe\,\eta) + E_3\exp(2Re\,\eta) + E_4\exp(2Pe\,\eta) \\ + E_5\exp((Re + Pe)\eta) + E_6\,\eta \end{array}\right]$$

$$\begin{aligned} W = {} & C_1 + C_2\exp(Re\,\eta) - Gr_2\exp(Pe\,\eta) - K_2\,\eta \\ & + Br\left[\begin{array}{l} C_5 + C_6\exp(Re\,\eta) - \dfrac{Gr\,E_2\exp(Pe\,\eta)}{Pe(Pe - Re)}\left(\eta - \dfrac{2Pe - Re}{Pe(Pe - Re)}\right) \\ + \dfrac{Gr\,C_3\,\eta}{Re} - \dfrac{Gr\,C_4\exp(Pe\,\eta)}{Pe(Pe - Re)} - \dfrac{Gr\,E_1\,\eta\exp(Re\,\eta)}{Re} - \dfrac{Gr\,E_3\exp(2Re\,\eta)}{2Re^2} \\ - \dfrac{Gr\,E_4\exp(2Pe\,\eta)}{2Pe(2Pe - Re)} - \dfrac{Gr\,E_5\exp((Re + Pe)\eta)}{(Pe(Pe + Re))} + \dfrac{GrE_6}{Re}\left(\dfrac{\eta^2}{2} + \dfrac{\eta}{Re}\right) \end{array}\right] \end{aligned}$$

The velocity gradient referring to skin friction at the channel walls is

$$S_f = \mu\left.\frac{\mathrm{d}u}{\mathrm{d}y}\right|_{y=0,h}$$

then, the skin friction coefficient by the nondimensional quantity (4) is

$$C_f = \frac{h}{V\mu} = \left.\frac{\mathrm{d}W}{\mathrm{d}\eta}\right|_{\eta=0,1}$$

and the heat transfer rate at the wall in nondimensional form is

$$N_u = -\left.\frac{\mathrm{d}\theta}{\mathrm{d}\eta}\right|_{\eta=0,1}$$

Entropy Generation

Entropy generation is associated with thermodynamic irreversibility. It is imperative to determine the rate of entropy generation in a system, in order to optimize energy for efficient operation in the system. The convection process in a channel is inherently irreversible, and this causes continuous entropy generation.

The volumetric entropy is

$$E_G = \frac{k}{T_0^2}\left(\left(\frac{\mathrm{d}T}{\mathrm{d}x}\right)^2 + \left(\frac{\mathrm{d}T}{\mathrm{d}y}\right)^2\right) + \frac{\mu}{T_0}\left[2\left\{\left(\frac{\mathrm{d}u}{\mathrm{d}x}\right)^2 + \left(\frac{\mathrm{d}v}{\mathrm{d}y}\right)^2\right\} + \left(\frac{\mathrm{d}u}{\mathrm{d}y} + \frac{\mathrm{d}v}{\mathrm{d}x}\right)^2\right]$$

The temperature and velocity distributions are simplified, then

$$E_G = \frac{k}{T_0^2}\left(\frac{\mathrm{d}T}{\mathrm{d}y}\right)^2 + \frac{\mu}{T_0}\left(\frac{\mathrm{d}u}{\mathrm{d}y}\right)^2 \tag{12}$$

Equations (4) and (12) reduces to

$$N_S = \frac{T_0^2 h^2 E_G}{k(T_h - T_0)^2} = \left(\frac{\mathrm{d}\theta}{\mathrm{d}\eta}\right)^2 + \frac{Br}{\Omega}\left(\frac{\mathrm{d}W}{\mathrm{d}\eta}\right)^2 \tag{13}$$

Here, $\Omega = \frac{T_h - T_0}{T_0}$ is the temperature difference parameter and

$$N_1 = \left(\frac{\mathrm{d}\theta}{\mathrm{d}\eta}\right)^2, \quad N_2 = \frac{Br}{\Omega}\left(\frac{\mathrm{d}W}{\mathrm{d}\eta}\right)^2 \tag{14}$$

where N_1 gives heat transfer irreversibility and N_2 represents entropy generation.

The irreversibility ratio is defined as

$$\varphi = \frac{N_2}{N_1} \tag{15}$$

If $\varphi > 1$, then the entropy generation due to viscous dissipation dominates and the irreversibility due to heat transfer dominates if $0 < \varphi < 1$, but both of them equally contribute for $\varphi = 1$.

Hence, the Bejan number is defined as

$$Be = \frac{N_1}{N_S} = \frac{1}{1+\varphi} \tag{16}$$

Irreversibility due to heat transfer dominates at the limit $Be = 1$, irreversibility due to fluid friction dominates at the limit $Be = 0$, and the limit $Be = 1/2$ implies that both of them equally contribute.

3 Results and Discussions

We studied the vertical lines at $\eta = 0$ as injection and at $\eta = 1$ as suction wall. The consequences of velocity profile for different values of various parameters are shown in Figs. 2, 3, 4, 5, and 6. In these, we consider nondimensional distance along X-axis and dimensionless velocity along *Y*-axis. From Figs. 4, 5, 6, and 7, it is observed that the velocity decreases at the suction wall and increases at the injection wall with the increase in Grashoff number and slip parameter β_1, and the other parameters are constant. The flow attains maximum velocity near to the central line. Figure 3 shows the effect velocity for various values of *Re*. The velocity decreases at both walls with increase of *Re*. The leads of velocity for different values of *Pe* are shown in Fig. 4. *Pe* rises the velocity falls at injection wall and raises at suction wall. Figure 6 shows the consequences of β_2. As β_2 increases, the velocity decreases more at suction wall and less at injection wall. The effect of temperature for several values of *Pe* is shown in Fig. 7. In this, dimensionless distance is taken along *X*-axis and nondimensional temperature is taken along *Y*-axis. The temperature increases at both suction and injection walls with the decrease in *Pe*.

The consequences of entropy generation for different values of various arguments are shown in Figs. 8, 9, 10, 11, and 12. In these, we consider nondimensional distance along *X*-axis and entropy generation along *Y*-axis. Figures 8, 9, and 10 depict the effect of entropy generation for several values of $Br\ \Omega^{-1}$, *Gr*, and *K*. It is identified that the entropy generation increases more at the suction wall and less at injection wall. It indicates that the there is more restrictive medium at the suction wall and less restrictive medium at injection wall. The effect slip parameters are

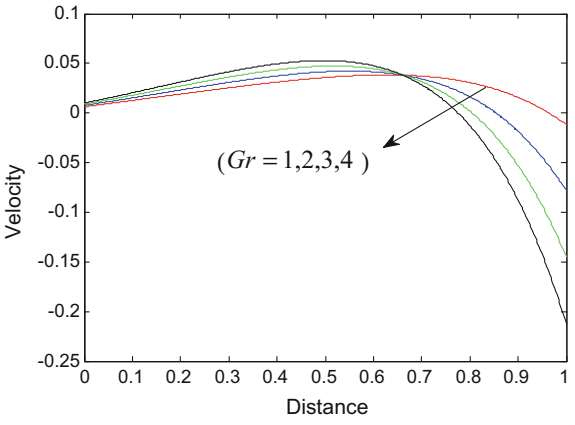

Fig. 2 Velocity leads for *Gr*, $Re = 2, Br = 0.1, Pe = 3$, $K = 0.1,\ \beta_1 = 0.1$, and $\beta_2 = 0.1$

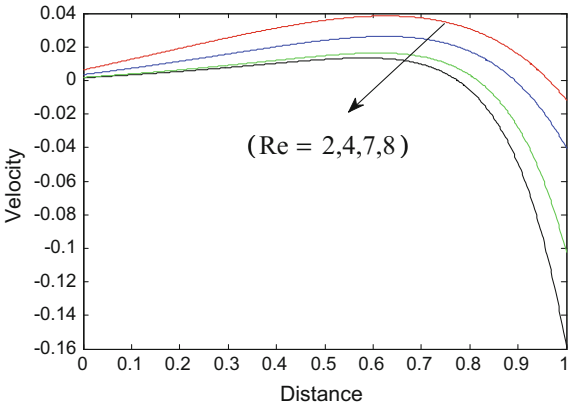

Fig. 3 Velocity leads for Re, $Gr = 1, Br = 0.1, Pe = 3$, $K = 0.1,\ \beta_1 = 0.1$, and $\beta_2 = 0.1$

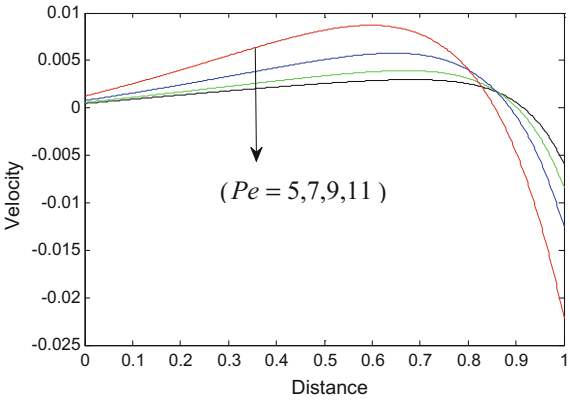

Fig. 4 Velocity leads for Pe, $Gr = 1, Br = 0.1, Re = 2$, $K = 0.1,\ \beta_1 = 0.1$, and $\beta_2 = 0.1$

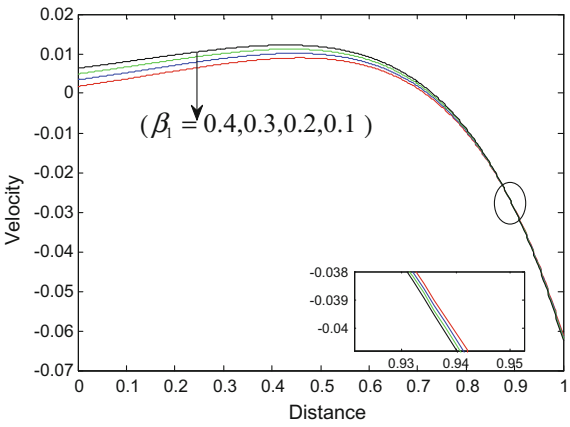

Fig. 5 Velocity leads for β_1 *with* $Gr = 1, Br = 0.1$, $Re = 2, K = 0.1,\ Pe = 3$, and $\beta_2 = 0.1$

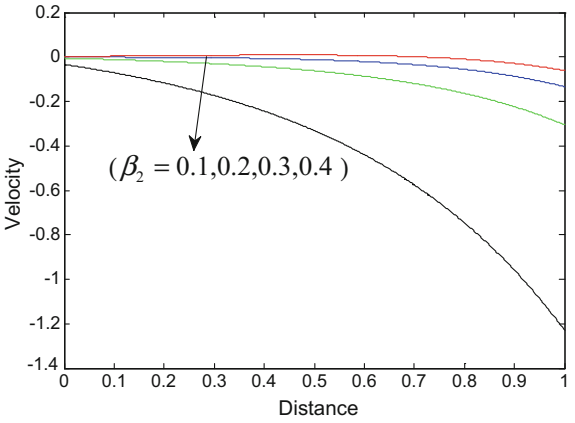

Fig. 6 Velocity leads for β_2, $Gr = 1, Br = 0.1, Re = 2$, $K = 0.1,\ Pe = 3$, and $\beta_1 = 0.1$

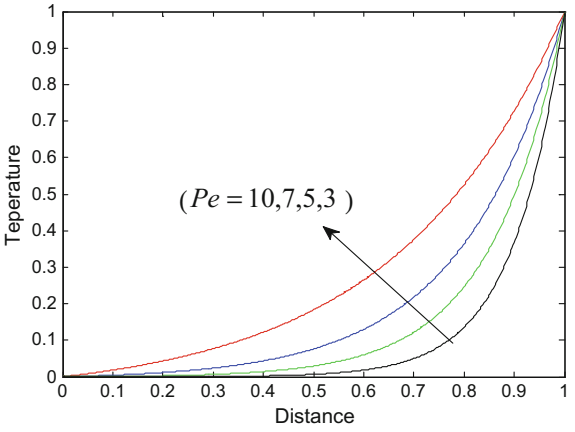

Fig. 7 Temperature effects for Pe, $Gr = 1, Br = 0.1$, $Re = 2$, $K = 0.1,\ \beta_1 = 0.1$, and $\beta_2 = 0.1$

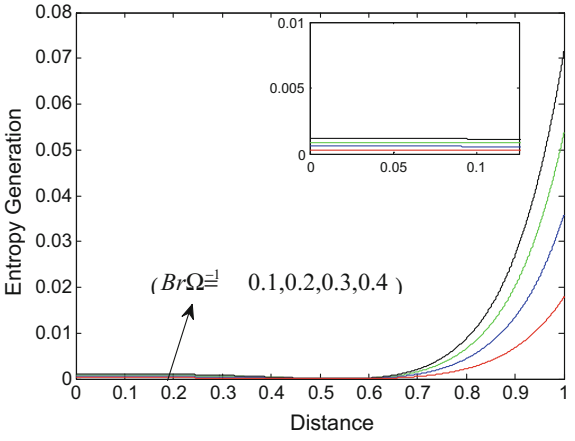

Fig. 8 Entropy generation effects for $Br\ \Omega^{-1}$, *with* $Gr = 1, Re = 2$, $K = 0.1,\ Pe = 3,\ \beta_1 = 0.1$, and $\beta_2 = 0.1$

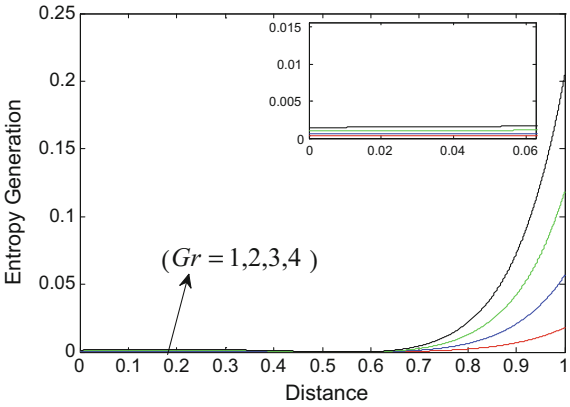

Fig. 9 Effects of entropy generation for Gr, with $Re = 2, Br = 0.1, Pe = 3,$ $\Omega = 1, K = 0.1, \beta_1 = 0.1,$ and $\beta_2 = 0.1$

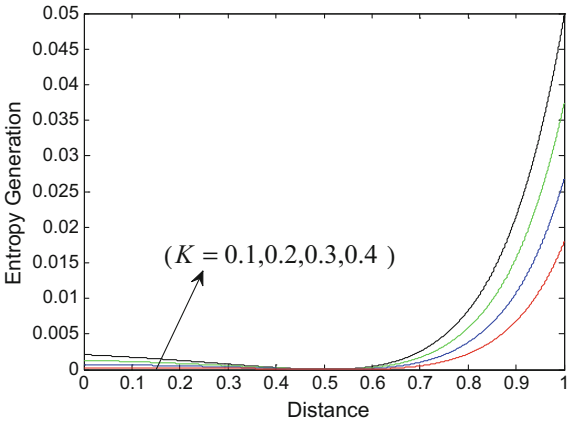

Fig. 10 Entropy generation effects for K, with $Re = 2, Br = 0.1, Pe = 3,$ $\Omega = 1,\ Gr = 1,\ \beta_1 = 0.1,$ and $\beta_2 = 0.1$

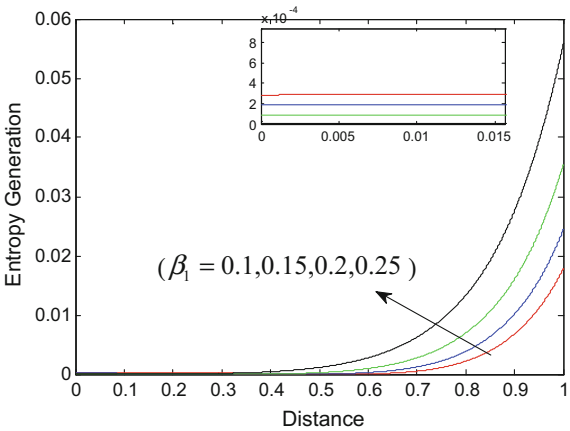

Fig. 11 Effects of entropy generation for β_1, with $Re = 2, Br = 0.1, Pe = 3,$ $Gr = 1,\ \Omega = 1,\ K = 0.1,$ and $\beta_2 = 0.1$

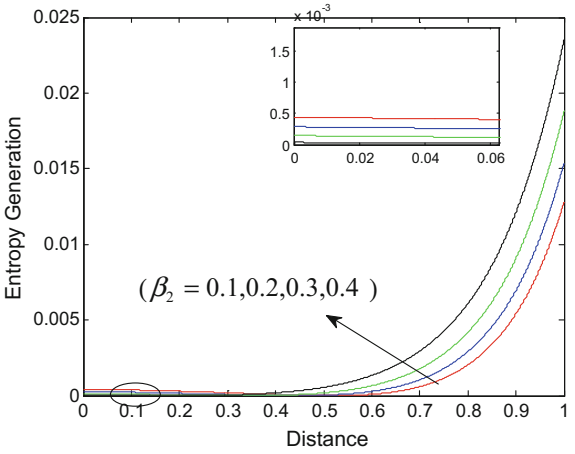

Fig. 12 Entropy generation effects for β_2, with $Re = 2, Br = 0.1, Pe = 3$, $Gr = 1$, $\Omega = 1$, $K = 0.1$, and $\beta_1 = 0.1$

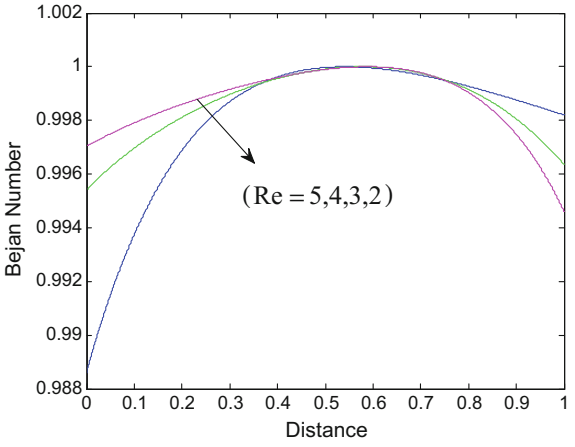

Fig. 13 Leads of Bejan number for Re, with $Br = 0.1$, $Pe = 3$, $Gr = 1$, $\Omega = 1$, $K = 0.1$, $\beta_1 = 0.1$, and $\beta_2 = 0.1$

shown in Figs. 11 and 12. From Fig. 11, it is noticed that there is a more restrictive medium at the suction wall and less restrictive medium at injection wall with increase of slip parameter β_1 and from Fig. 12, it is identified that as β_2 increases, the entropy generation also increases and more effect exists at suction wall.

The leads of Bejan number for several values of various parameters are shown in Figs. 13, 14, 15, 16, and 17. In these also, we consider nondimensional distance along X-axis and Bejan number along Y-axis. Figure 13 depicts the effect of entropy generation for several values of Re. As Re decreases, Bejan number Be also decreases at injection wall and increases at suction wall. From Figs. 14 and 15, it is identified that the decreases at both the walls with the increasing values of $Br\ \Omega^{-1}$, K, and more effect are noticed at injection wall and less effect is noticed at suction wall. The leads of slip parameters are shown in Figs. 16 and 17. It is observed that the Bejan number decreases at suction wall and increases at injection wall with the increase of slip parameters β_1 and β_2. Moreover, more effect is observed for β_1 and less effect is identified for β_2.

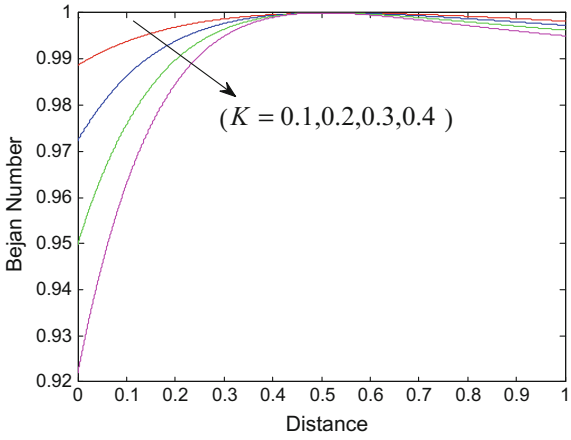

Fig. 14 Leads of Bejan number for K, $Re = 2, Br = 0.1, Pe = 3$, $\Omega = 1,\ Gr = 1,\ \beta_1 = 0.1$, and $\beta_2 = 0.1$

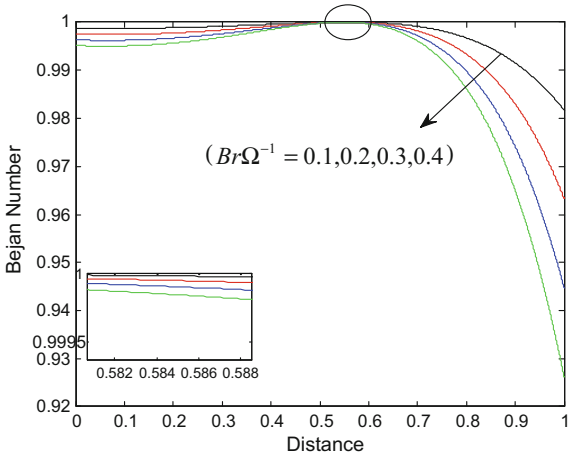

Fig. 15 Bejan number effects for $Br\ \Omega^{-1}$, with $Gr = 1, Re = 2$, $K = 0.1, Pe = 2, \beta_1 = 0.1$, and $\beta_2 = 0.1$

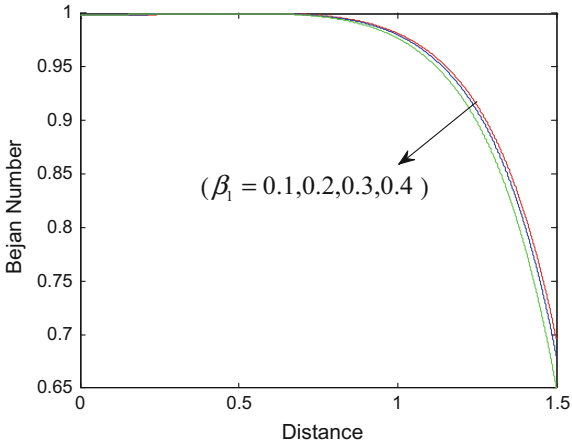

Fig. 16 Effects of Bejan number for β_1, with $Re = 2, Br = 0.1, Pe = 1$, $Gr = 1, \Omega = 1, K = 0.1$, and $\beta_2 = 0.1$

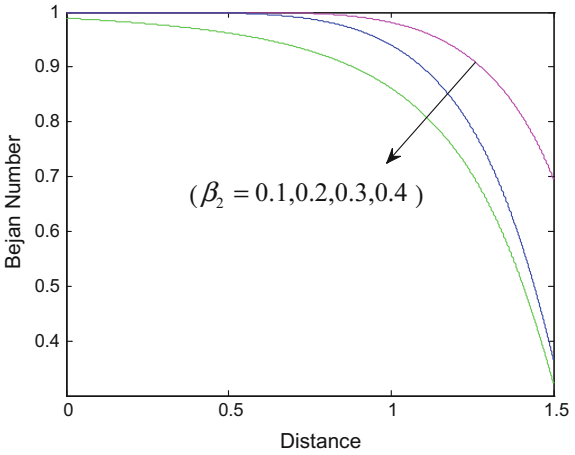

Fig. 17 Bejan number effects for β_2, with $Re = 2, Br = 0.1, Pe = 1, Gr = 1, \Omega = 1, K = 0.1$, and $\beta_1 = 0.1$

4 Conclusions

The combined effect of Navier slip and buoyancy force on the entropy generation rate through a vertical porous channel with injection/suction wall was analyzed. Bejan number also decreases at injection wall and increases at suction wall with the increasing values of *Re*. Also Bejan number decreases at suction wall and increases at injection wall with the increase of slip parameters β_1 and β_2. Moreover, more effect is observed for β_1 and less effect is identified for β_2. Theses analytical results obtained by using perturbation method are in good agreement with the results done by the authors (Ananthaswamy et al. 2016) by using homotopy perturbation method and are also in good agreement with the effects done by authors Eegunjobi and Makinde (2012) by using Runge–Kutta–Fehlberg method with shooting technique.

Appendix

$$K_2 = \frac{K_1}{Re}, \quad K_1 = Gr_1 - K, \quad Gr_1 = \frac{Gr}{(\exp(Pe) - 1)}, \quad Gr_2 = \frac{Gr_1}{Pe(Pe - Re)},$$
$$J = 1 - (\beta_2 Re), \quad a_1 = 1 - \beta_1 Re, \quad a_2 = \beta_1 K_2 + \beta_1 PeGr_2 - Gr_2,$$
$$b_1 = \exp(Re)(1 - (\beta_2 Re)),$$
$$b_2 = \beta_2 K_2 + \beta_2 PeGr_2 \exp(Pe) - Gr_2 \exp(Pe) - K_2,$$
$$d_1 = 2K_2 PeC_2, \quad d_2 = -2K_2 PeGr_2, \quad d_3 = -Re^2 C_2^2,$$
$$d_4 = -Pe^2 Gr_2^2, \quad d_5 = 2RePeGr_2 C_2, \quad d_6 = -K_2^2$$

$$E_1 = \frac{d_1}{Re(Re - Pe)}, \quad E_2 = \frac{d_2}{Pe}, \quad E_3 = \frac{d_3}{2Re(2Re - Pe)}, \quad E_4 = \frac{d_4}{2Pe^2},$$

$$E_5 = \frac{d_5}{Re(Re + Pe)}, \quad E_6 = -\frac{d_6}{Pe}, \quad F = E_1 + E_3 + E_4 + E_5, \quad H = 1 - (\beta_1 Re)$$

$$I = -\frac{GrC_3\beta_1}{Re} + \frac{GrC_4}{Pe(Pe - Re)}(Pe\beta_1 - 1) + \frac{GrE_1\beta_1}{Re} + \frac{GrE_3}{Re}\left(\beta_1 - \frac{1}{2Re}\right) + \frac{GrE_2}{Pe(Pe - Re)}\left[\beta_1 + \frac{2Pe - Re}{Pe(Pe - Re)} - \frac{\beta_1(2Pe - Re)}{Pe - Re}\right] + \frac{GrE_4}{2Pe(2Pe - Re)}(2Pe\beta_1 - 1) + \frac{GrE_5}{Pe(Pe + Re)}[\beta_1(Re + Pe) - 1] - \frac{GrE_6\beta_1}{Re^2}$$

$$K = \frac{GrC_3}{Re}(1 - \beta_2 Re) + \frac{GrC_4\exp(Pe)}{Pe(Pe - Re)}(Pe\beta_2 - 1) + \frac{GrE_1\exp(Re)}{Re}(\beta_2 + Re\beta_2 - 1) + \frac{GrE_3\exp(2Re)}{2Re^2}(2\beta_2 Re - 1) + \frac{GrE_4\exp(2Pe)}{2Pe(2Pe - Re)}(2Pe\beta_2 - 1) + \frac{GrE_2\exp(Pe)}{Pe(Pe - Re)}\left[\beta_2 + \beta_2 Pe - 1 + \frac{2Pe - Re}{Pe(Pe - Re)} - \frac{\beta_2(2Pe - Re)}{Pe - Re}\right] + \frac{GrE_5\exp(Re + Pe)}{Pe(Pe + Re)}[\beta_2(Re + Pe) - 1] + \frac{GrE_6}{Re}\left(\frac{1}{2} - \beta_2\right) + \frac{GrE_6}{Re^2}(1 - \beta_2)$$

$$G = E_1\exp(Re) + E_2\exp(Pe) + E_3\exp(2Re) + E_4\exp(2Pe) + E_5\exp(Re + Pe) + E_6$$

$$C_1 = \frac{a_1b_2 - a_2b_1}{b_1 - a_1}, \quad C_2 = \frac{a_2 - b_2}{b_1 - a_1}, \quad C_3 = \frac{G - F(\exp(Pe))}{\exp(Pe) - 1},$$

$$C_4 = \frac{F - G}{\exp(Pe) - 1}, \quad C_5 = \frac{HK - JI(\exp(Re))}{\exp(Re) - H}, \quad C_6\frac{I - K}{\exp(Re) - H}$$

References

Ananthaswamy V, Thenmozhi R, Seethalakshmi R (2016) Analytical expressions or combined effect of buoyancy force. Int J Mod Math Sci 14(1):77–99

Chauhan DS, Kumar V (2009) Effects of slip conditions on forced convection and entropy generation in a circular channel occupied by a highly porous medium: Darcy extended Brinkman-Forchheimer model. Turk J Eng Environ Sci 33:91–104

Chauhan DS, Kumar V (2011a) Heat transfer and entropy generation during compressible fluid flow in a channel partially filled with porous medium. Int J Energy Technol 3:1–10

Chauhan D, Rastogi P (2011b) Heat transfer and entropy generation in MHD flow through a porous medium past a stretching sheet. Int J Energy Technol 3:1–13

Chen S (2011) Entropy generation of double-diffusive convection in the presence of rotation. Appl Math Comput 217:8575–8597

Chen S, Du R (2011) Entropy generation of turbulent double-diffusive natural convection in a rectangle cavity. Energy 36:1721–1734

Chen S, Tian Z (2010) Entropy generation analysis of thermal micro-Couette flows in slip regime. Int J Therm Sci 49:2211–2221

Chinyoka T, Makinde OD, Eegunjobi AS (2013) Entropy analysis of unsteady magnetic flow through a porous pipe with buoyancy effects. J Porous Media 16:823–836

Das S, Jana RN (2014) Entropy generation due to MHD flow in a porous channel with Navier slip. Ain Shams Eng J 5:574–584

Eegunjobi AS, Makinde OD (2012) Combined effect of buoyancy force and navier slip on entropy generation in a vertical porous channel. Entropy 14:1028–1044

Hooman K, Gurgenci H, Merrikh AA (2007) Heat transfer and entropy generation optimization of forced convection in a porous-saturated duct of rectangular cross-section. Int J Heat Mass Tranf 50:2051–2059

Mahmud S, Fraser RA (2005) Flow, thermal and entropy generation characteristic inside a porous channel with viscous dissipation. Int J Therm Sci 44:21–32

Makinde OD (2011) Second law analysis for variable viscosity hydromagnetic boundary layer flow with thermal radiation and Newtonian heating. Entropy 13:1446–1464

Effect of Newtonian Heating/Cooling on Hydromagnetic Free Convection in Alternate Conducting Vertical Concentric Annuli

Dileep Kumar and A.K. Singh

Abstract This paper presents the effects of the Newtonian heating/cooling and the radial magnetic field on steady hydromagnetic free convective flow of a viscous and electrically conducting fluid between vertical concentric cylinders by neglecting compressibility effect. The derived governing equations of the model are first recast into the non-dimensional simultaneous ordinary differential equations using the suitable non-dimensional variables and parameters. By obtaining the exact solution of the simultaneous ordinary differential equations, the effects of the Hartmann number as well as the Biot number on the velocity, induced magnetic field, induced current density, Nusselt number, skin-friction and mass flux of the fluid are presented by the graphs and tables. The effect of the Biot number is to increase the velocity, induced magnetic field and induced current density in the case of the Newtonian heating and vice versa in the case of the Newtonian cooling, but the effect of Hartmann number is to decrease all above fields. Further, graphical representation shows that the velocity and induced magnetic field are rapidly decreasing, with increasing the Hartmann number, when one of the cylinders is conducting compared with when both the cylinders are non-conducting.

1 Introduction

The study of magnetohydrodynamic flow of an electrically conducting fluid with magnetic field has wide range of its applications in the technology, industries, geothermal power generation and metal-working processes. Such type of MHD flows have its attracted applications in design of magnetohydrodynamic power generators, plasma studies, nuclear reactor, the thermal recovery of oil, solar power

D. Kumar (✉) · A.K. Singh
Department of Mathematics, Institute of Science, Banaras Hindu University, Varanasi 221005, India
e-mail: dileepyadav02april@gmail.com

A.K. Singh
e-mail: ashok@bhu.ac.in

M.K. Singh et al. (eds.), *Applications of Fluid Dynamics*, Lecture Notes in Mechanical Engineering, https://doi.org/10.1007/978-981-10-5329-0_13

collector and geological formulation etc. Globe (1959) has obtained the analytical solution of an electrically conducting and fluid flowing between two infinite long concentric annular cylinders under the presence of a radial magnetic field. Ramamoorthy (1961) has analysed both classical and magnetohydrodynamic velocity between concentric annulus of rotating cylinders in the presence of a radial magnetic field. In the above references, authors have neglected the induced magnetic field in the problem. Keeping it mind, Arora and Gupta (1971) have extended the same problem with considering the impact of induced magnetic field. The natural convection in the vertical annular cylinders with one boundary isothermal and opposite adiabatic boundary has analysed by El-Shaarawi and Sarhan (1981). Further, Joshi (1987) has considered the isothermal boundaries in which the temperature of inner boundary is higher than the outer boundary.

Singh et al. (1997) have studied the free convective flow in vertical concentric annuli with more general thermal boundary conditions and radial magnetic field. Seong and Choung (2001) have analysed the electrically conducting fluid flow past a circular cylinder under continuous and pulsed electromagnetic forces. Fadzilah et al. (2011) have emphasised the importance of induced magnetic field and heat transfer on the steady, viscous and electrically conducting magnetohydrodynamic boundary-layer flow over a stretching sheet. Singh and Singh (2012) have investigated the influence of induced magnetic field on free convective flow between non-conducting vertical concentric annulus cylinders. Further, Kumar and Singh (2013) have extended the same problem by considering the concentric cylinders heated/cooled asymmetrically.

In many practical situations, such as if you turn off the breaker when you go on vacation, then it can tell us how fast a water heater cools down and the hot water in pipes cools off. In this case, the heat transfer from the surface of object is similar to the local surface temperature, and we use the term Newtonian heating/cooling for this condition. This type of flow is known as conjugate convective flow. In a pioneered work, the influence of the Newtonian heating on free convective boundary-layer flow over a vertical flat plate, which immersed in a viscous fluid, was studied by Merkin (1994). An analytical solution of natural convective flow past an oscillating vertical plate with the effects of heat and mass transfer, and the Newtonian heating has been obtained by Hussanan et al. (2013). Very recently, Kumar and Singh (2015) have investigated the impact of induced magnetic field on hydromagnetic natural convective flow with the Newtonian heating/cooling in vertical concentric annuli by obtaining the exact solution of the problem. Also, Kumar and Singh (2016) have performed the exact study of effects of heat source/sink and induced magnetic field on free convective flow between vertical concentric cylinders.

Motivated with excellent science of the authors, we intend here to investigate the effect of the Newtonian heating/cooling on hydromagnetic natural convection between alternate conducting vertical concentric annulus cylinders with radial magnetic field. We have analysed the model by taking three cases on the boundary conditions of the induced magnetic field. In case (A), both cylinders are considering as non-conducting, in case (B) the outer cylinder is conducting and inner is

non-conducting and finally in case (C) the inner is taking as conducting and outer is non-conducting. Here, we find the analytical solution for the temperature field and then fluid velocity and induced magnetic field by solving the non-dimensional governing linear simultaneous ordinary differential equations using the non-dimensional boundary condition. Also, we find the analytical solution for the governing differential equations at singular point $Ha = 2.0$. Finally, we focus on the effects of the Biot number (Newtonian heating/cooling parameter) and the Hartmann number on the velocity, induced magnetic, induced current density, Nusselt number, skin-friction and mass flux using graphics and tables.

2 Mathematical Formulation

We have taken here the steady and laminar flow of a viscous, incompressible and electrically conducting fluid in the fully developed region bounded by vertical concentric annuli of infinite length with radial magnetic field as shown in Fig. 1. Also, we have considered the temperature of fluid and both cylinders different to each other. The temperatures of fluid and outer cylinder have taken as T'_f and T'_b, respectively. Let z'- and r'-axes denote the axis of the co-axial cylinders taken in the vertical upward direction and the radial direction taken outward from the axis of the cylinder. Let a and b be the radius of inner and outer cylinders, respectively. The applied uniform magnetic field of strength $\left\{aB'_0/r'\right\}$ is taken as in the direction perpendicular to the direction of flow, and the Newtonian heating/cooling condition

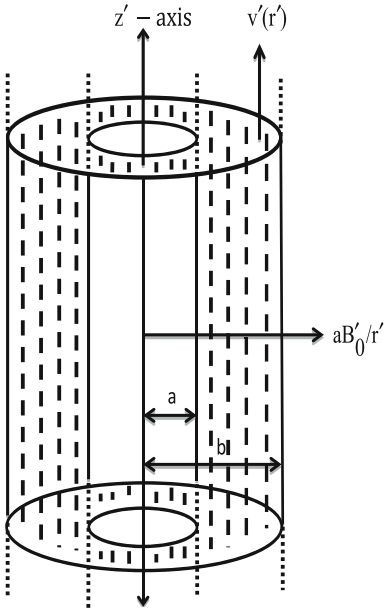

Fig. 1 Physical configuration

is applied at the inner cylinder of the annulus. Since z'-axis is the direction of fluid flow so the radial and tangential components of velocity are taken as zero. Due to axial symmetry and infinite length of cylinders, the transport phenomena will depend only on the variable r'. So, for the considered model the components of the velocity and applied uniform magnetic fields are taken as $\{0, 0, v'(r')\}$ and $\{aB_0'/r', 0, h'\}$, respectively.

Thus, the mathematical model equations for the present physical configuration with the usual Boussinesq approximation are as follows (Singh and Singh 2012):

$$\frac{\mathrm{d}^2 v'}{\mathrm{d}r'^2} + \frac{1}{r'}\frac{\mathrm{d}v'}{\mathrm{d}r'} + \frac{\mu_e}{\rho\nu}\frac{B_0' a}{r'}\frac{\mathrm{d}h'}{\mathrm{d}r'} + \frac{g\beta}{\nu}(T' - T_f') = 0, \tag{1}$$

$$\frac{\mathrm{d}^2 h'}{\mathrm{d}r'^2} + \frac{1}{r'}\frac{\mathrm{d}h'}{\mathrm{d}r'} + \frac{B_0' a}{\eta}\frac{1}{r}\frac{\mathrm{d}v'}{\mathrm{d}r'} = 0, \tag{2}$$

$$\frac{\mathrm{d}^2 T'}{\mathrm{d}r'^2} + \frac{1}{r'}\frac{\mathrm{d}T'}{\mathrm{d}r'} = 0. \tag{3}$$

In view of the considered model, the boundary conditions corresponding to the velocity, induced magnetic field and temperature field are obtained as:

$$v' = 0, \quad \frac{\mathrm{d}h'}{\mathrm{d}r'} = 0 \text{ or } h' = 0, \quad \frac{\mathrm{d}T'}{\mathrm{d}r'} = \alpha T', \text{ at } r' = a, \tag{4}$$

$$v' = 0, \quad \frac{\mathrm{d}h'}{\mathrm{d}r'} = 0 \text{ or } h' = 0, \quad T' = T_b', \text{ at } r' = b. \tag{5}$$

In above equations, ρ, μ_e, ν, g, η, σ and β are density of the fluid, magnetic permeability, kinematic viscosity, acceleration due to gravity, magnetic diffusivity, conductivity of the fluid and coefficient of thermal expansion, respectively.

To make above system of equations in non-dimensional form, we use some dimensionless quantities given as:

$$u = \frac{v'}{U}, \quad r = \frac{r'}{a}, \quad \lambda = \frac{b}{a}, \quad h = \frac{h'}{\sigma\mu_e H_0' U a}, \quad U = g\beta a^2 \frac{(T_b' - T_f')}{\nu}, \quad T = \frac{T'}{(T_b' - T_f')}. \tag{6}$$

Using Eq. (6), Eqs. (1)–(3) in the dimensionless form are obtained as follows:

$$\frac{\mathrm{d}^2 u}{\mathrm{d}r^2} + \frac{1}{r}\frac{\mathrm{d}u}{\mathrm{d}r} + \frac{Ha^2}{r}\frac{\mathrm{d}h}{\mathrm{d}r} + (T - R) = 0, \tag{7}$$

$$\frac{\mathrm{d}^2 h}{\mathrm{d}r^2} + \frac{1}{r}\frac{\mathrm{d}h}{\mathrm{d}r} + \frac{1}{r}\frac{\mathrm{d}u}{\mathrm{d}r} = 0, \tag{8}$$

$$\frac{\mathrm{d}^2 T}{\mathrm{d}r^2} + \frac{1}{r}\frac{\mathrm{d}T}{\mathrm{d}r} = 0. \tag{9}$$

The boundary conditions in non-dimensional form are obtained as:

$$u = 0, \quad \frac{\mathrm{d}h}{\mathrm{d}r} = 0 \ \text{ or } \ h = 0, \quad \frac{\mathrm{d}T}{\mathrm{d}r} = Bi\,T \ \text{ at } \ r = 1, \tag{10}$$

$$u = 0, \quad \frac{\mathrm{d}h}{\mathrm{d}r} = 0 \ \text{ or } \ h = 0, \quad T = (1+R) \ \text{ at } \ r = \lambda. \tag{11}$$

Some other dimensionless physical parameters Bi, Ha and R occurring in the above equations are the Biot number, Hartmann number and buoyancy force distribution parameter, respectively, and they are defined as:

$$Bi = a\,\alpha, \quad Ha = \mu_e H_0' a\sqrt{\frac{\sigma}{\mu}}, \quad R = \frac{T_f'}{(T_b' - T_f')}. \tag{12}$$

Here, the Biot number (Bi) and Hartmann number (Ha) have importance role on the flow of fluid between both the cylinders at $R = 1.0$, i.e. $2T_f' = T_b'$.

3 Analytical Solution

3.1 Solution for Hartmann Number (Ha) ≠ 2.0

The exact solution of Eqs. (7)–(9) using boundary conditions (10)–(11) is obtained as follows:

$$u = A_{k1} r^{Ha} + A_{k2} r^{-Ha} + A_{k3} + \frac{r^2(1+R)}{(Bi\log\lambda + 1)}(B_{k1}\log r + B_{k2}) + B_{k3} r^2 R, \tag{13}$$

$$h = A_{k4} - \frac{1}{Ha}(A_{k1} r^{Ha} - A_{k2} r^{-Ha}) + \frac{r^2(1+R)}{4(Bi\log\lambda + 1)}\{B_{k1}(1 - 2\log r) - 2B_{k2}\} - \frac{B_{k3} r^2 R}{2}, \tag{14}$$

$$T = (1+R)\frac{(Bi\log r + 1)}{(Bi\log\lambda + 1)}. \tag{15}$$

Here, $k = 1$ is for the case when both cylinders are non-conducting; $k = 2$, when outer cylindrical wall is non-conducting and inner cylindrical wall is conducting and finally $k = 3$, when inner cylindrical wall is non-conducting and outer cylindrical wall is conducting.

The skin-friction at outer surface of inner cylinder as well as inner surface of outer cylinder, Nusselt number at inner cylinder, induced current density and mass flux of fluid are obtained as:

$$\tau_1 = \left(\frac{\mathrm{d}u}{\mathrm{d}r}\right)_{r=1} = Ha(A_{k1} - A_{k2}) + \frac{(1+R)}{(Bi\,\log\lambda + 1)}(B_{k1} + 2B_{k2}) + 2B_{k3}R, \tag{16}$$

$$\begin{aligned}\tau_\lambda = \left(\frac{\mathrm{d}u}{\mathrm{d}r}\right)_{r=\lambda} &= Ha(A_{k1}\lambda^{Ha-1} - A_{k2}\lambda^{-Ha-1}) \\ &+ \frac{(1+R)}{(Bi\,\log\lambda + 1)}\{2\lambda\,(B_{k1}\log\lambda + B_{k2}) + B_{k1}\lambda\} + 2B_{k3}\lambda R,\end{aligned} \tag{17}$$

$$Nu_\lambda = -\left(\frac{\mathrm{d}T}{\mathrm{d}r}\right)_{r=\lambda} = \frac{Bi(1+R)}{\lambda(Bi\,\log\lambda + 1)}, \tag{18}$$

$$J_\theta = -\frac{\mathrm{d}h}{\mathrm{d}r} = A_{k1}r^{Ha-1} + A_{k2}r^{-Ha-1} + \frac{r(1+R)}{(Bi\,\log\lambda + 1)}(B_{k1}\log r + B_{k2}) + B_{k3}rR, \tag{19}$$

$$Q = 2\pi\left[\begin{array}{l}\dfrac{A_{k1}}{(Ha+2)}(\lambda^{Ha+2} - 1) + \dfrac{A_{k2}}{(-Ha+2)}(\lambda^{-Ha+2} - 1) + \dfrac{A_{k3}}{2}(\lambda^2 - 1) \\ \quad + \dfrac{(1+R)}{(Bi\,\log\lambda + 1)}\left\{\dfrac{\lambda^4}{16}(4B_{k1}\log\lambda + 4B_{k2} - B_{k1}) + \dfrac{B_{k1}}{16}\right\} + \dfrac{B_{k3}}{4}R(\lambda^4 - 1).\end{array}\right] \tag{20}$$

3.2 *Solution for Hartmann number (*Ha*) = 2.0*

Here, we have solved the governing differential equation for singular point $Ha = 2.0$ because the mathematical expressions $B_{k1} = -\left\{\frac{Bi}{(4-Ha^2)}\right\}$, $B_{k2} = \left\{\frac{4Bi}{(4-Ha^2)^2} - \frac{1}{(4-Ha^2)}\right\}$ and $B_{k3} = \frac{1}{(4-Ha^2)}$ present in the above Eqs. (13) and (14) clearly show that they have the singularity at $Ha = 2.0$. The velocity and induced magnetic field expressions are given by:

$$u = C_{k1}r^2 + C_{k2}r^{-2} + C_{k3} + \frac{(1+R)}{(Bi\,\log\lambda + 1)}\{r^2\log r(D_{k1}\log r + D_{k2})\} + \frac{Rr^2\log r}{4}, \tag{21}$$

$$h = C_{k4} - \frac{1}{2}(C_{k1}r^2 - C_{k2}r^{-2}) + \frac{R}{16}r^2(1 - 2\log r) - \frac{(1+R)}{(Bi\ \log\lambda + 1)}\{(D_{k3}\log r + D_{k4})r^2\log r + D_{k5}r^2\}. \tag{22}$$

In this case, the skin-friction at surface of cylinders, induced current density and mass flux of fluid are obtained as follows:

$$\tau_1 = 2(C_{k1} - C_{k2}) + \frac{(1+R)}{(Bi\ \log\lambda + 1)}D_{k2} + \frac{R}{4}, \tag{23}$$

$$\tau_\lambda = 2(C_{k1}\lambda - C_{k2}\lambda^{-3}) + D_{k2}\lambda\} + \frac{R}{4}\lambda(2\log\lambda + 1) + \frac{(1+R)}{(Bi\ \log\lambda + 1)}\{2\lambda\ \log\lambda\,(D_{k1}\log\lambda + D_{k1} + D_{k2}), \tag{24}$$

$$J_\theta = C_{k1}r + C_{k2}r^{-3} + \frac{(1+R)}{(Bi\ \log\lambda + 1)}\{r\log r(D_{k1}\log r + D_{k2})\} + \frac{R}{4}r\log r, \tag{25}$$

$$Q = 2\pi\left[\frac{C_{k1}}{4}(\lambda^4 - 1) + C_{k2}\log\lambda + \frac{C_{k3}}{2}(\lambda^2 - 1) + \frac{R}{64}\{4\lambda^4\log\lambda - (\lambda^4 - 1)\} + \frac{(1+R)}{(Bi\ \log\lambda + 1)}\left\{\frac{D_{k1}}{32}\{8\lambda^4(\log\lambda)^2 - 4\lambda^4\log\lambda + (\lambda^4 - 1)\} + \frac{D_{k2}}{16}\{4\lambda^4\log\lambda - (\lambda^4 - 1)\}\right\}\right] \tag{26}$$

The constants A_{k1}, A_{k2}, A_{k3}, A_{k4}, B_{k1}, B_{k2}, B_{k3}, C_{k1}, C_{k2}, C_{k3}, C_{k4} ,D_{k1}, D_{k2}, D_{k3}, D_{k4} and D_{k5} appearing in the above equations (for k = 1, 2 and 3) are defined in Appendix.

4 Results and Discussion

The main aim of the discussion is to bring out the impact of physical numbers such as Biot number and Hartmann number on the velocity field profiles, induced magnetic field profiles, induced current density field profiles, Nusselt number, sink friction and mass flux. The influence of these parameters (such as Biot number and Hartmann number) on the transport processes is illustrated by using the figures and tables. Here, we consider the case (A) when both cylindrical walls are non-conducting, case (B) when the outer cylindrical wall is conducting and inner is

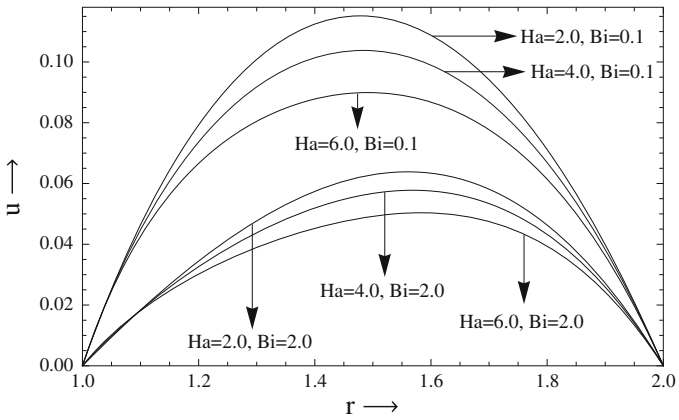

Fig. 2 Velocity profile in case one (A) for Bi = 0.1 and 2.0 at R = 1.0 and λ = 2.0

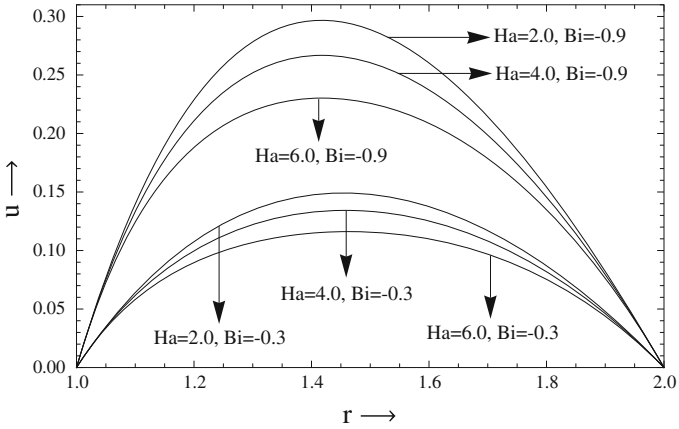

Fig. 3 Velocity profile in case one (A) for Bi = −0.3 and −0.9 at R = 1.0 and λ = 2.0

non-conducting and case (C) when the inner cylindrical wall is conducting and outer is non-conducting. As expected, it is found by numerical computations that the case (B) and case (C) have given almost same results. Therefore, we have discussed only two cases when both cylinders are non-conducting and when one is conducting and another is non-conducting. Figures 2, 3, 4 and 5 show the velocity profiles when both cylinders are non-conducting and when one cylinder is conducting and other is non-conducting, respectively. It is clear from these figures that the velocity profiles decrease with increasing values of the Hartmann number.

The influence of Biot number is to increase the velocity profiles for the Newtonian heating and decrease the velocity profiles for the Newtonian cooling. The region behind it is that as the Biot number increases the convective resistance

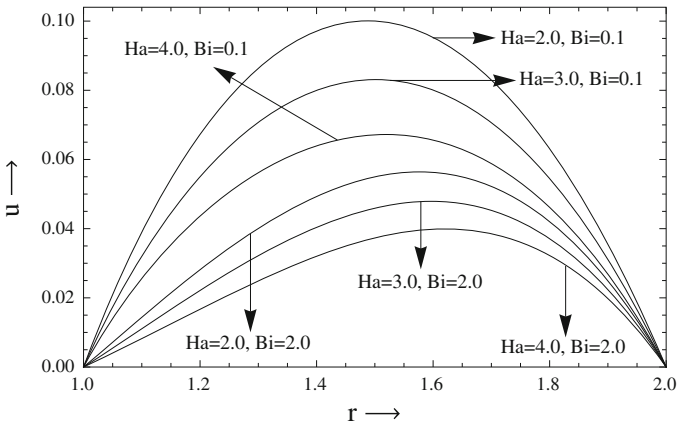

Fig. 4 Velocity profile in case two (B) for Bi = 0.1 and 2.0 at R = 1.0 and λ = 2.0

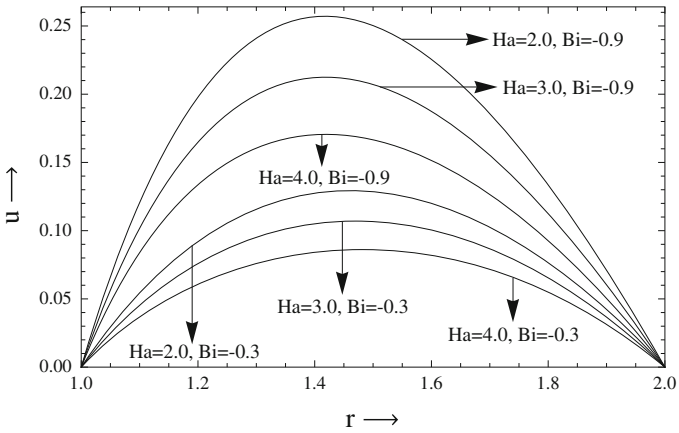

Fig. 5 Velocity profile in case two (B) for Bi = −0.3 and −0.9 at R = 1.0 and λ = 2.0

of wall reduces in the Newtonian heating while it increases in the Newtonian cooling. A comparative study of Figs. 2 and 3 with Figs. 4 and 5 shows that the velocity of the fluid is less when one of the cylindrical surface is conducting in comparison to non-conducting cylindrical surfaces in case of Newtonian heating while it is just reverse in the case of Newtonian cooling. The shape of velocity profile is of parabolic type in upward direction.

Further, from Figs. 6, 7, 8 and 9, we have observed the influence of the Hartmann number, the Newtonian heating/cooling parameter on the induced magnetic field. When both the cylinders are non-conducting and when inner is

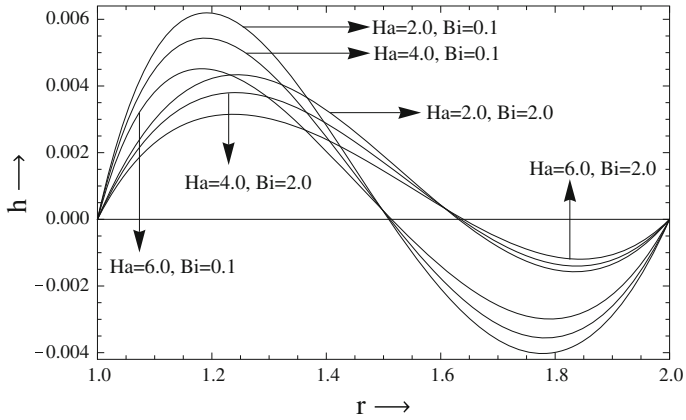

Fig. 6 Induced magnetic field profile in case one (A) for $Bi = 0.1$ and 2.0 at $R = 1.0$ and $\lambda = 2.0$

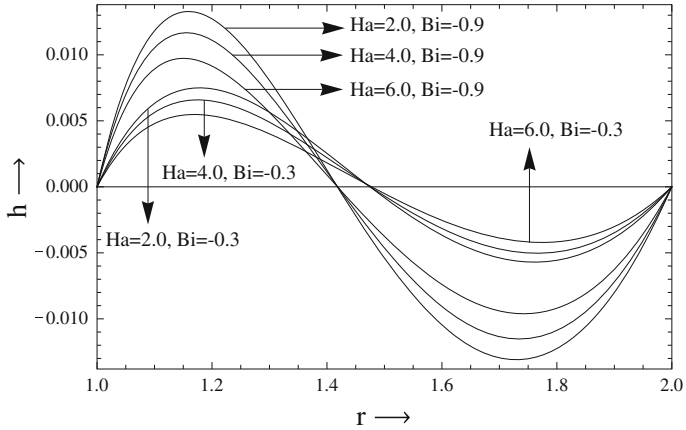

Fig. 7 Induced magnetic field profile in case one (A) for $Bi = -0.3$ & -0.9 at $R = 1.0$ and $\lambda = 2.0$

conducting and outer is non-conducting, the induced magnetic field increases as the values of Biot number increases in case of the Newtonian heating while decreases in the Newtonian cooling. The influence of the Hartmann number implies that the induced magnetic field decrease in the both cases, i.e. when both cylinders are non-conducting and when inner is conducting and outer is non-conducting since the Lorentz force acts opposite to the direction of induced magnetic field. From a comparative study of Figs. 6 with 8 and 7 with 9, we have observed that the magnitude of induced magnetic field is less than the case when both cylindrical walls are non-conducting compared to the case when one of the cylinders is conducting.

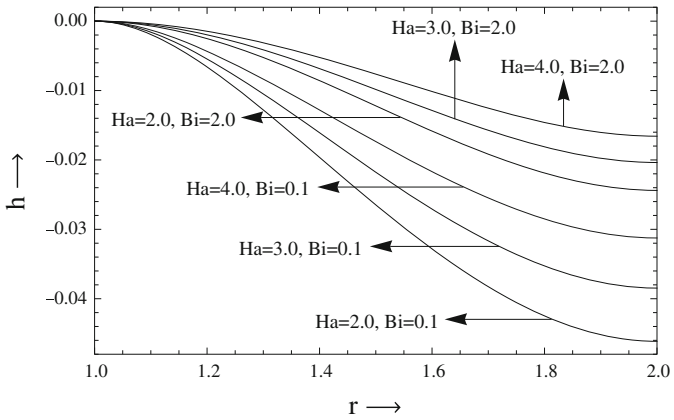

Fig. 8 Induced magnetic field profile in case two (B) for $Bi = 0.1$ & 2.0 at $R = 1.0$ and $\lambda = 2.0$

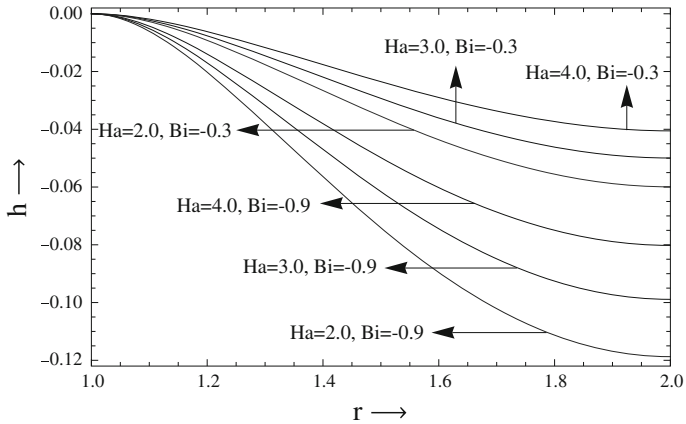

Fig. 9 Induced magnetic field profile in case two (B) for $Bi = -0.3$ & -0.9 at $R = 1.0$ and $\lambda = 2.0$

The behaviour of the induced current density is shown in Figs. 10, 11, 12 and 13 for various values of the Hartmann number and the Biot number. We find that for both cases, the induced current density profiles increase with increasing values of the Biot number (Bi) in case of the Newtonian heating; while in case of the Newtonian cooling, it reduces with improving the Biot number. From the given figures, it can be observed that the induced current density decreases in both cases when the value of the Hartmann number increases. Figures 10 and 11 show that the maximum induced current density is induced in the middle region while minimum current density near the both cylindrical walls. The modulus of current density at the surface of the inner cylindrical wall is greater than the outer wall. Also, Figs. 12 and 13 show that the maximum current density is induced in the middle region, and

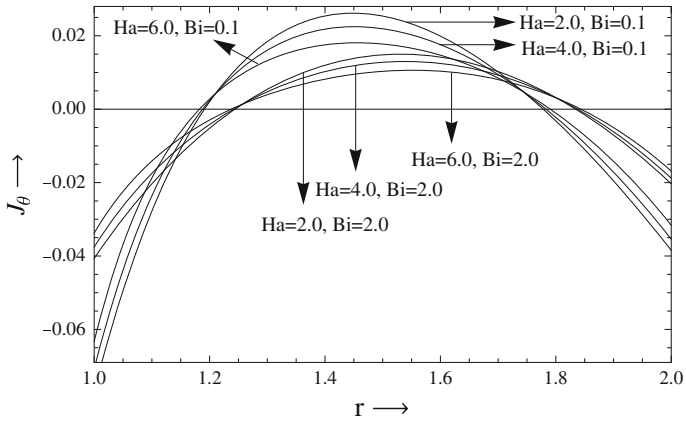

Fig. 10 Induced current density profile in case one (A) for Bi = 0.1 and 2.0 at R = 1.0 and λ = 2.0

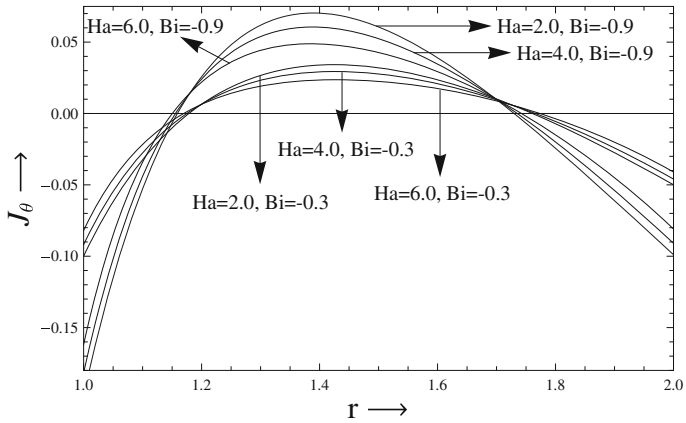

Fig. 11 Induced current density profile in case one (A) for Bi = −0.3 & −0.9 at R = 1.0 and λ = 2.0

then it has shifting tendency in direction of inner cylinder with increasing values of the heating/cooling parameter for the Newtonian heating while it has reverse effect in case of the Newtonian cooling. Comparing the induced current density profiles in Figs. 10 with 12 and 11 with 13, we observed that when one of the cylinders is conducting, the maximum value of induced current density is greater in comparison with if both cylindrical walls are non-conducting.

From Table 1, we can see the influence of the Hartmann number and the Biot number on the skin-friction, mass flux and Nusselt number at the surface of cylinders. It is observed that the skin-friction at outer surface of inlying cylindrical wall increases when both of the cylinders are non-conducting and vice versa when

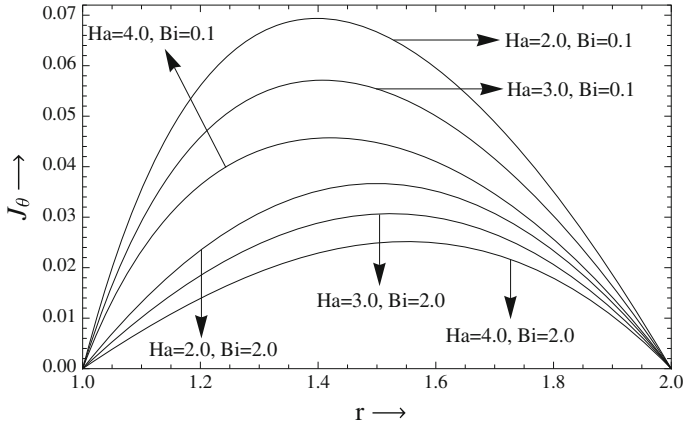

Fig. 12 Induced current density profile in case two (B) for Bi = 0.1 & 2.0 at R = 1.0 and λ = 2.0

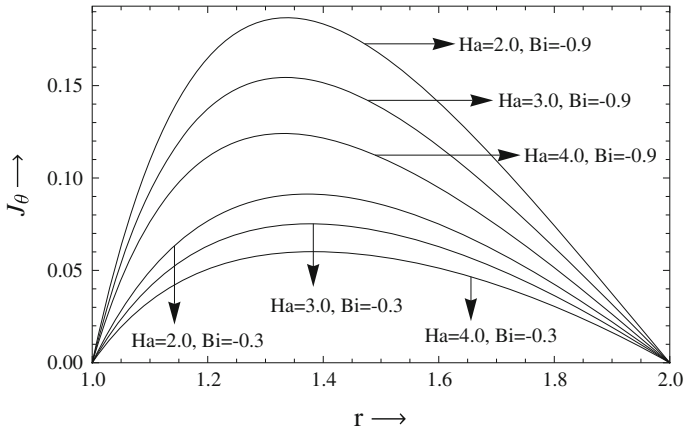

Fig. 13 Induced current density profile in case two (B) for Bi = −0.3 & −0.9 at R = 1.0 and λ = 2.0

one of the cylindrical wall is conducting. It is also clear that with improving of the Hartmann number, the skin-friction at interface of exterior cylinder decreases in both cases when both cylindrical surfaces are non-conducting and one of them is conducting.

The numerical values of the skin-friction at inner cylindrical wall increase by increasing the value of the Biot number for the Newtonian heating and conversely for the Newtonian cooling. Moreover, the skin-friction at outer cylinder surface decreases by increasing the value of the Biot number for the Newtonian heating and reverse for the Newtonian cooling. We observe that the impact of increasing the Hartmann number is to reduce the mass flux in the cases when both cylinders are

Table 1 Numerical values of dimensionless skin-frictions, mass flux and Nusselt number

Bi	Ha	τ_1		τ_λ		Q		Nu_λ
		Case-1	Case-2 & 3	Case-1	Case-2 and 3	Case-1	Case-2 & 3	
−0.7	1.0	1.2229	1.1726	−0.6870	−0.6618	1.3920	1.3392	1.4000
	2.0	1.2248	1.0476	−0.6861	−0.5975	1.3602	1.1789	1.3597
	3.0	1.2276	0.8955	−0.6847	−0.5187	1.3116	0.9838	2.0204
−0.3	1.0	0.7615	0.7274	−0.5220	−0.5050	0.9543	0.9186	0.6000
	2.0	0.7647	0.6448	−0.5204	−0.4605	0.9327	0.8100	0.3787
	3.0	0.7696	0.5449	−0.5179	−0.4055	0.8996	0.6776	0.2983
1.0	1.0	0.3055	0.2875	−0.3589	−0.3499	0.5219	0.5030	−2.0000
	2.0	0.3101	0.2468	−0.3566	−0.3250	0.5102	0.4455	−0.5906
	3.0	0.3171	0.1984	−0.3531	−0.2937	0.4924	0.3751	−0.3176
2.0	1.0	0.1890	0.1752	−0.3173	−0.3104	0.4114	0.3969	−4.0000
	2.0	0.1940	0.1452	−0.3148	−0.2904	0.4023	0.3524	−0.8381
	3.0	0.2016	0.1099	−0.3110	−0.2652	0.3884	0.2979	−0.4170

non-conducting and one of them is conducting. It is observed that the values of mass flux increase with improving the Biot number in the Newtonian heating and vice versa in the Newtonian cooling. Further, it is clear from the numerical calculation that the value of Nusselt number at inner and outer cylinders increases with increasing Biot number in case of Newtonian heating, and it is reverse in case of Newtonian cooling. Also, it is observed that the Nusselt number at cylindrical walls decreases with increasing ratio of outer radius to inner radius.

5 Conclusion

By obtaining analytical solution of the model, the effects of Newtonian heating/cooling and induced magnetic on hydromagnetic free convective flow between vertical concentric annular cylinders have been discussed. The influences of the various governing parameters such as the Hartmann number and the Biot number on the fluid velocity, induced magnetic field, induced current density, skin-friction, Nusselt number and mass flux have examined. The following conclusions have been drawn from the present analysis:

1. The fluid velocity, induced magnetic field and induced current density profiles have reducing tendency with increasing the Hartmann number.
2. Value of the velocity, induced magnetic field and induced current density increases for the Newtonian heating and vice versa for the Newtonian cooling.
3. The magnitude of the fluid velocity, induced magnetic field and induced current density profile is more if one of the cylindrical walls is conducting than if both walls are conducting.

4. The numerical values of Nusselt number at cylindrical walls increase in case of the Newtonian heating and vice versa in case of the Newtonian cooling with increasing values of the Biot number.
5. The skin-friction at inner cylinder decreases if one of the cylindrical walls is conducting and increases if both walls are non-conducting with increasing Hartmann number. Moreover, the skin-friction at outer cylinder increases in both cases with increasing Hartmann number.
6. The influence of Biot number is to increase/reduce the skin-friction in case of Newtonian heating/cooling at inlying cylinder and just reverse at outer cylinder.
7. The mass flux for the both cases has reducing nature with increasing Hartmann number. Further, values of mass flux increase with improve in value of Biot number in Newtonian heating and vice versa in Newtonian cooling.

Acknowledgements Mr. Dileep Kumar is grateful to the University Grants Commission, New Delhi, for financial assistance in the form of a Fellowship to carry out this work.

Appendix

$$A_{10} = \left\{\frac{(1+R)}{(Bi\log\lambda+1)}\right\}, A_{11} = \{A_{10}B_{16} + B_{17}\}, A_{21} = A_{31} = \{A_{10}B_{24} + B_{25}\},$$
$$A_{12} = \{A_{10}B_{18} + B_{19}\}, A_{23} = A_{33} = 0, A_{22} = A_{32} = \{A_{10}B_{26} + B_{27}\},$$
$$A_{13} = -\{A_{11} + A_{12} + A_{10}B_{12} + B_{13}R\}, B_{11} = B_{21} = B_{31} = -\left\{\frac{Bi}{(4-Ha^2)}\right\},$$
$$A_{14} = \left\{\frac{1}{Ha}(A_{11} - A_{12}) - \frac{A_{10}}{4}(B_{11} - 2B_{12}) + \frac{R}{2}B_{13}\right\}, B_{16} = \left\{\frac{(B_{14}+B_{15})}{2(1-\lambda^{Ha})}\right\},$$
$$A_{24} = \left\{\frac{1}{Ha}(A_{21} - A_{22}) - \frac{A_{10}}{4}(B_{11} - 2B_{12}) + \frac{R}{2}B_{13}\right\}, D_{27} = \left\{\frac{R\lambda^2\log\lambda}{4(\lambda^{-2}-\lambda^2)}\right\},$$
$$A_{34} = \left[\frac{1}{Ha}(A_{31}\lambda^{Ha} - A_{32}\lambda^{-Ha}) - \frac{A_{10}\lambda^2}{4}\{B_{11}(1 - 2\log\lambda) - 2B_{12}\} + B_{38}R\lambda^2\right],$$
$$B_{12} = B_{22} = B_{32} = \left\{\frac{4Bi}{(4-Ha^2)^2} - \frac{1}{(4-Ha^2)}\right\}, B_{13} = B_{23} = B_{33} = \left\{\frac{1}{(4-Ha^2)}\right\},$$
$$B_{14} = \left\{B_{11}\lambda^2\log\lambda + B_{12}(\lambda^2 - 1)\right\}, B_{24} = B_{34} = \left\{\frac{B_{11}\lambda^2\log\lambda + B_{12}(\lambda^2-\lambda^{-Ha})}{(\lambda^{-Ha}-\lambda^{Ha})}\right\},$$
$$B_{15} = \frac{M}{4}\left\{(2B_{12} - B_{11})(\lambda^2 - 1) + 2B_{11}\lambda^2\log\lambda\right\}, B_{25} = B_{35} = \left\{\frac{B_{13}R(\lambda^2-\lambda^{-Ha})}{(\lambda^{-Ha}-\lambda^{Ha})}\right\},$$
$$B_{26} = B_{36} = \left\{\frac{B_{11}\lambda^2\log\lambda + B_{12}(\lambda^2-\lambda^{Ha})}{(\lambda^{Ha}-\lambda^{-Ha})}\right\}, B_{17} = \left\{\frac{B_{13}R(\lambda^2-1)\left(1+\frac{Ha}{2}\right)}{2(1-\lambda^{Ha})}\right\},$$
$$B_{27} = B_{37} = \left\{\frac{B_{13}R(\lambda^2-\lambda^{Ha})}{(\lambda^{Ha}-\lambda^{-Ha})}\right\}, B_{18} = \left\{\frac{(B_{14}-B_{15})}{2(1-\lambda^{-Ha})}\right\}, B_{38} = \left(\frac{B_{13}}{2}\right),$$
$$B_{19} = \left\{\frac{B_{13}R(\lambda^2-1)\left(1-\frac{Ha}{2}\right)}{2(1-\lambda^{-Ha})}\right\}, C_{11} = \left\{\frac{A_{10}D_{17}}{2(1-\lambda^2)} + \frac{R(1-\lambda^2+4\lambda^2\log\lambda)}{16(1-\lambda^2)}\right\},$$

$$C_{12} = \left\{\frac{A_{10}D_{16}}{2(1-\lambda^{-2})} + \frac{R(\lambda^2-1)}{16(1-\lambda^{-2})}\right\}, C_{21} = (A_{10}D_{26} + D_{27}), C_{13} = -(C_{11} + C_{12}),$$
$$C_{14} = C_{24} = \left\{\frac{1}{2}(C_{11} - C_{12}) + A_{10}D_{15} - \frac{R}{16}\right\}, C_{22} = (A_{10}D_{28} + D_{29}),$$
$$C_{23} = C_{33} = 0, C_{31} = (A_{10}D_{36} + D_{37}), C_{32} = (A_{10}D_{38} + D_{39}),$$
$$C_{34} = \left[\frac{1}{2}(C_{11}\lambda^2 - C_{12}\lambda^{-2}) + A_{10}\lambda^2\left\{(D_{33}\log\lambda + D_{34})\log\lambda + D_{35}\right\} - \frac{R}{16}\lambda^2(1-\log\lambda)\right],$$
$$D_{11} = D_{21} = D_{31} = -\left(\frac{Bi}{8}\right), D_{29} = \left\{\frac{R\lambda^2\log\lambda}{4(\lambda^2-\lambda^{-2})}\right\}, D_{12} = D_{22} = D_{32} = \left(\frac{Bi}{16} - \frac{1}{4}\right),$$
$$D_{13} = D_{23} = D_{33} = \left(\frac{D_{11}}{2}\right), D_{14} = D_{24} = D_{34} = \left\{\frac{(D_{12}-D_{11})}{2}\right\},$$
$$D_{15} = D_{25} = D_{35} = \left\{\frac{(D_{11}-D_{12})}{4}\right\}, D_{28} = \left\{\frac{\lambda^2\log\lambda(D_{21}\log\lambda + D_{22})}{(\lambda^2-\lambda^{-2})}\right\},$$
$$D_{16} = \left\{D_{11}\lambda^2(\log\lambda)^2 + D_{12}\lambda^2\log\lambda - 2\lambda^2\log\lambda(D_{13}\log\lambda + D_{14}) - 2D_{15}(\lambda^2-1)\right\},$$
$$D_{17} = \left\{D_{11}\lambda^2(\log\lambda)^2 + D_{12}\lambda^2\log\lambda + 2\lambda^2\log\lambda(D_{13}\log\lambda + D_{14}) + 2D_{15}(\lambda^2-1)\right\},$$
$$D_{26} = \left\{\frac{\lambda^2\log\lambda(D_{21}\log\lambda + D_{22})}{(\lambda^{-2}-\lambda^2)}\right\}, D_{36} = \left\{\frac{\lambda^2\log\lambda}{(\lambda^{-2}-\lambda^2)}(D_{31}\log\lambda + D_{32})\right\},$$
$$D_{37} = \left\{\frac{R\lambda^2\log\lambda}{4(\lambda^{-2}-\lambda^2)}\right\}, D_{38} = \left\{\frac{\lambda^2\log\lambda}{(\lambda^2-\lambda^{-2})}(D_{31}\log\lambda + D_{32})\right\}, D_{39} = \left\{\frac{R\lambda^2\log\lambda}{4(\lambda^2-\lambda^{-2})}\right\}.$$

References

Arora KL, Gupta RP (1971) Magnetohydrodynamic flow between two rotating coaxial cylinders under radial magnetic field. Phys Fluid 15:1146–1148

El-Shaarawi MAI, Sarhan A (1981) Developing laminar free-convection in an open ended vertical annulus with rotating inner cylinder. ASME J Heat Transf 103:552–558

Fadzilah MA, Nazar R, Arifin M, Pop I (2011) MHD boundary-layer flow and heat transfer over a stretching sheet with induced magnetic field. J Heat Mass Transf 47:155–162

Globe S (1959) Laminar steady state magnetohydrodynamic flow in an annular channel. Phys Fluid 2:404–407

Hussanan A, Khan I, Shafie S (2013) An exact analysis of heat and mass transfer past a vertical plate with Newtonian heating. J Appl Math 2013:1–9

Joshi HM (1987) Fully developed natural convection in an isothermal vertical annular duct. Int Commun Heat Mass Transf 14:657–664

Kumar A, Singh AK (2013) Effect of induced magnetic field on natural convection in vertical concentric annuli heated/cooled asymmetrically. J Appl Fluid Mech 6:15–26

Kumar D, Singh AK (2015) Effect of induced magnetic field on natural convection with Newtonian heating/cooling in vertical concentric annuli. Procedia Eng 127:568–574

Kumar D, Singh AK (2016) Effects of heat source/sink and induced magnetic field on natural convective flow in vertical concentric annuli. Alexandria Eng J 55:3125–3133

Merkin JH (1994) Natural convection boundary layer flow on a vertical surface with Newtonian heating. Int J Heat Fluid Flow 15:392–398

Ramamoorthy P (1961) Flow between two concentric rotating cylinders with a radial magnetic field. Phys Fluid 4:1444–1445

Seong JK, Choung ML (2001) Control of flows around a circular cylinder suppression of oscillatory lift force. Fluid Dyn Res 29:47–63

Singh RK, Singh AK (2012) Effect of induced magnetic field on natural convection in vertical concentric annuli. Acta Mech Sin 28:315–323

Singh SK, Jha BK, Singh AK (1997) Natural convection in vertical concentric annuli under a radial magnetic field. Heat Mass Transf 32:399–401

Heat and Mass Transfer on Unsteady MHD Oscillatory Flow of Blood Through Porous Arteriole

M. Veera Krishna, B.V. Swarnalathamma and J. Prakash

Abstract We have considered the unsteady two-dimensional MHD oscillatory flow of blood in a porous arteriole under the influence of uniform transverse magnetic field in a planar channel. Heat and mass transfer during arterial blood flow through a porous medium are also studied. A mathematical model is developed for unsteady state situations using slip conditions. Analytical expressions for the velocity, temperature, and concentration profiles have been obtained and computationally discussed with respect to the non-dimensional parameters.

1 Introduction

Rates of many physiological functions, including the flow through blood vessels, are affected by drugs. The rates of different biochemical reactions that are responsible for the contraction muscles, secretion of different materials such as insulin, mucus, and stomach acid by the glands, and the transmission of messages by the nerves can be accelerated/decelerated by the action of drugs. The rate at which the kidney cells perform the regulation of the volume of water/salts in the body is affected by drugs. Several drugs (e.g. antacids) produce effects, where the function of a cell remains unchanged and a receptor does not have any cognition. Most of the antacids are bases that interact with stomach acid to neutralize it. Thus, stomach acid is reduced simply through chemical reactions. The strength (potency in medical terms) of a drug is the quantity that is required to be applied in order to have a visible effect

M. Veera Krishna (✉)
Department of Mathematics, Rayalaseema University, Kurnool 518007, AP, India
e-mail: veerakrishna_maths@yahoo.com

B.V. Swarnalathamma
Department of Science and Humanities, JB Institute of Engineering & Technology, Moinabad, Hyderabad 500075, Telangana, India

J. Prakash
Department of Mathematics, University of Botswana, Private Bag 0022, Gaborone, Botswana

M.K. Singh et al. (eds.), *Applications of Fluid Dynamics*, Lecture Notes in Mechanical Engineering, https://doi.org/10.1007/978-981-10-5329-0_14

(e.g., reduction of blood pressure, relief of pain); efficacy of a drug refers to its capacity to produce an effect (reduction in blood pressure, e.g.), while a drug's effectiveness is determined by how well a drug works in the medical treatment of a patient. It may so happen that a drug having higher efficacy (say, in reducing blood pressure) may be less effective. The reason behind this, the drug may have too many side effects and patient will be highly reluctant to take it. Such a drug is not at all suitable in real world life. Although oxygen binds with blood hemoglobin and does not react, the discussion on drug dynamics made above emphasizes the need for paying importance to the presence of chemical reactions during various physiological functions. Many researchers, including the present authors, have studied various aspects of blood flow in normal/diseased arteries. Misra et al. (2008) studied blood flow through an arterial segment having multiple stenoses. They presented a schematic diagram of the physical problem and developed an appropriate model. The effects of viscosity variation subject to the action of an external magnetic field were investigated by Sinha and Misra (2014a, b). In the realm of flow through porous media, in one of their recent studies dealing with MHD flow through a porous medium with stretching wall, Misra and Sinha (2013) made an important observation that both Hall current and thermal radiation play significant roles in controlling the temperature of blood. A fundamental problem concerning biomagnetic fluid flow through a porous medium was solved by Misra et al. (2010), by employing the principles of ferro-dynamics and biomagnetic fluid dynamics (BFD). The study shows that the presence of a magnetic dipole affects the characteristics of arterial blood flow significantly during electromagnetic hyperthermia. In a recent study, Adesanya et al. (2015) found that hyperviscosity of blood considerably affects the flow and pressure pulse wave propagation. The effect of viscous dissipation on the pulsating flow of a fluid was analyzed by Adesanya et al. (2015) by using a domain decomposition method, while the problem of heat transfer to MHD couple stress pulsatile flow between two parallel porous plates was investigated by Adesanya and Makinde (2012). By using advection–diffusion equations applicable for porous media, Ai and Vafai (2006) presented a mathematical model for the transport of macromolecules. Wade and Karino (2000) reported a computational study on LDL transfer from flowing blood to the wall tissues of arteries. The role of porous media in different studies of the mechanics of different biological organs and tissues is enormous. Khaled and Vafai (2003) in a review paper explained the role of porous media in studies related to the flow and heat transfer in biological tissues. The flow characteristics of a Casson fluid in a tube filled with a homogeneous porous medium were examined by Dash et al. (1996). On the basis of an experimental study, Beavers and Joseph (1967) proposed a theory according to which the effect of the boundary layer can be replaced by a slip velocity that is proportional to the exterior velocity gradient. Subsequently, Beavers et al. (1970) carried out experiments to study the laminar flow in a channel bounded by two parallel plates, one of whose bounding walls is a porous medium. They made an observation that owing to the presence of the porous wall, the mass flow increases. Further experiments were conducted by Beavers et al. (1974) with an aim to validate the slip boundary condition in the case of gas flows and to ascertain whether the fluid has a considerable influence on the

value of the slip parameter. Rivlin and Ericksen (1955) model of second-order fluids is one of several such fluid models that has drawn interest of fluid mechanics researchers. Oscillatory flow of a viscous fluid in a channel was studied by Makinde and Mhone (2005). Ram (1990) investigated the effect of Hall current and wall temperature oscillation in a plate where the fluid is rotating. Bastman (1982) considered low Reynolds number flow of blood in arteries of slowly varying cross section, treating blood as a second-order fluid. The unsteady flow of blood through vessels was studied by Misra and Sahu (1989) and Misra et al. (1998) by treating blood as a second-order viscoelastic fluid. Electrically conducting viscoelastic fluid flow and heat transfer in a parallel plate channel with stretching walls under the action of an external magnetic field were investigated by Misra and Shit (2008). Subsequently, Misra and Shit (2009) conducted another study on the flow of a biomagnetic viscoelastic fluid in the presence of a magnetic field generated by a magnetic dipole. In this study, the non-Newtonian character of blood was represented by Walter's liquid B model. Peristaltic motion of blood in the microcirculatory system was studied by Misra and Maiti (2012), by considering the arterioles to be of varying cross section. Sinha and Misra (2014b) developed a numerical model to perform a study on mixed convection hydromagnetic flow over an inclined nonlinear porous stretching sheet. Misra and Sinha (2013) also investigated the unsteady flow and temperature fields in a diseased capillary, its lumen being porous and wall permeable. Thermal radiation, velocity slip, and thermal slip were incorporated in the study. However, in none of the aforesaid studies mentioned above, the effect of chemical reaction has been incorporated. Xu et al. (2009) developed a theoretical model to study the impact of blood flow on rhombus growth, by considering the interaction between different constituents of blood and chemical reaction. Coulson and Hernandez (1983) carried out an experimental study that depicts the metabolic activities in the presence of chemical reactions. They made an important observation due to injection of certain drugs, hormones, and metabolites, and there occurs considerable increase in plasma concentration of reactants. Heat and mass transfer in magneto-micropolar fluid in a porous plate were studied by Chaudhary and Jain (2007). In their study, they considered the radiation term in the heat transfer equation. Das et al. (1994) considered the effects of a first-order chemical reaction on the flow past an impulsively started infinite vertical plate. Muthucumarswamy and Ganesan (2001) as well as Muthucumarswamy (2002) studied the first-order homogeneous chemical reactions. Recently, Kandasamy et al. (2005) discussed the heat and mass transfer effect along a wedge with a heat source. Chaudhary and Jain (2000) studied the effect of chemical reactions on MHD micropolar fluid flow past a vertical plate in slip-flow regime. Chemical physiology of Blood flow regulation by red cells was discussed by Singel and Stemler (2005). Recently, Veera Krishna and Swarnalathamma (2016c) discussed the peristaltic MHD flow of Williamson fluid. Swarnalathamma and Veera Krishna (2016) discussed the theoretical and computational study of peristaltic hemodynamic flow of couple stress fluids. Veera Krishna and Reddy (2016a) discussed MHD-free convective rotating flow. Veera Krishna and Reddy (2016b) discussed unsteady MHD convective flow of second-grade fluid.

The aim of the present investigation was to study the effect of chemical reaction, as well as heat and mass transfer on the oscillatory MHD flow of blood, under a single framework, treating blood as a second-grade fluid.

2 Formulation and Solution of the Problem

The circulatory system mainly consists of three-dimensional cylindrical vessels. However, in some cases, such as in microvessels of the lungs, motion of blood can be approximately considered as channel flow. With this consideration, as in many other similar theoretical studies the formulation analysis that follows, we use Cartesian co-ordinates. The flow is considered symmetric about the axis of the channel and driven by the stretching of the channel wall, such that the velocity of each wall is proportional to the axial coordinate. In order to study the second-order effects of unsteady MHD flow of blood, let us first consider the flow of a second-order fluid between two parallel plates at $z = 0$ and $z = h$, where the x-axis is taken parallel length to plates and z-axis along a direction perpendicular to the plates.

The physical sketch of the problem is as shown in Fig. 1. Taking into account the existence of sleep between the velocity of blood and the arterial wall tissues, the relative velocity between blood and the arterial wall is assumed to be proportional to the shear rate at the wall. Blood is considered as a suspension of erythrocytes and other micro-elements in plasma. It is assumed that in the segment under consideration, blood is uniformly dense. A magnetic field of constant intensity B_0 is considered to be applied in the y-direction.

The unsteady hydromagnetic equations of the momentum, heat transfer, and mass transfer for the MHD oscillatory flow of second-grade fluid through a porous arteriole in the parallel plate system are considered in the form

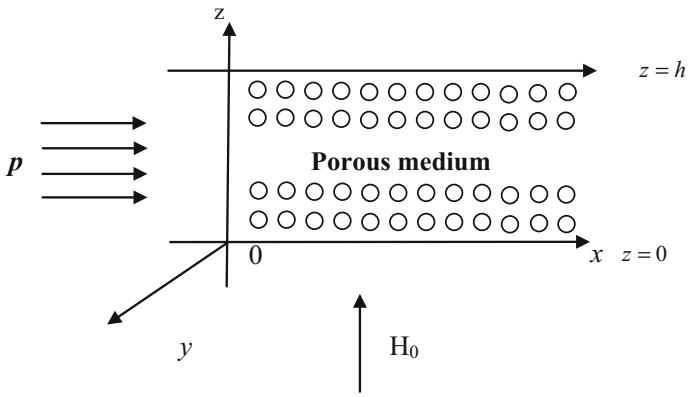

Fig. 1 Physical configuration of the problem

$$\frac{\partial u}{\partial t} = -\frac{1}{\rho}\frac{\partial p}{\partial x} + \nu\frac{\partial^2 u}{\partial z^2} + \frac{\alpha_1}{\rho}\frac{\partial^3 u}{\partial z^2 \partial t} - \frac{\sigma B_0^2}{\rho}u - \frac{\nu}{k}u + g\beta(T - T_\infty) + g\beta^*(C - C_\infty) \tag{1}$$

$$\frac{\partial v}{\partial t} = -\frac{1}{\rho}\frac{\partial p}{\partial y} + \nu\frac{\partial^2 v}{\partial z^2} + \frac{\alpha_1}{\rho}\frac{\partial^3 v}{\partial z^2 \partial t} - \frac{\sigma B_0^2}{\rho}v - \frac{\nu}{k}v \tag{2}$$

$$\frac{\partial T}{\partial t} = \frac{K_1}{\rho C_p}\frac{\partial^2 T}{\partial z^2} - \frac{1}{\rho C_p}\frac{\partial q_r}{\partial z} \tag{3}$$

$$\frac{\partial C}{\partial t} = D\frac{\partial^2 C}{\partial z^2} - K_c(C - C_0) \tag{4}$$

where the meanings of all the symbols appearing in the equations are listed in the nomenclature. The presence of red cell-slip at the boundary wall of the blood vessels reported by Brunn (1975) and Nubar (1971), the boundary conditions for the problem under consideration are given by

The corresponding boundary conditions are

$$u = \lambda\frac{\partial u}{\partial z}, \quad v = \lambda\frac{\partial v}{\partial z}, \quad T = T_0 + (T_w - T_0)e^{i\omega t}, \quad C = C_0 + (C_w - C_0)e^{i\omega t} \text{ at } z = h \tag{5}$$

$$u = \lambda\frac{\partial u}{\partial z}, \quad v = \lambda\frac{\partial v}{\partial z}, \quad T = T_0, \quad C = C_0 \text{ at } z = 0 \tag{6}$$

Using Rosseland approximation (Perdikis and Raptis 1996), the radiative transfer term q_r in Eq. (3) may be expressed as

$$q_r = -\frac{4\sigma^*}{3\alpha_r}\frac{\partial T^4}{\partial z} \tag{7}$$

We assume that the temperature differences within the flow are such that T^4 can be expressed as a linear function of the temperature T. This is accomplished by expanding T^4 in a Taylor series about T_0 (which is assumed to be independent of z) and neglecting powers of T higher than the first. Thus, we have

$$T^4 = 4T_0^3 T - 3T_0^4 \tag{8}$$

Then, the heat transfer equation becomes

$$\frac{\partial T}{\partial t} = \frac{K_1}{\rho C_p}\frac{\partial^2 T}{\partial z^2} - \frac{16\sigma^* T_0^3}{3\rho C_p \alpha_r}\frac{\partial^2 T}{\partial z^2} \tag{9}$$

Combining Eqs. (1) and (2), $q = u + iv$, and we obtain

$$\frac{\partial q}{\partial t} = -\frac{1}{\rho}\frac{\partial p}{\partial \xi} + \nu\frac{\partial^2 q}{\partial z^2} + \frac{\alpha_1}{\rho}\frac{\partial^3 q}{\partial z^2 \partial t} - \frac{\sigma B_0^2}{\rho}q - \frac{\nu}{k}q + g\beta(T - T_\infty) + g\beta^*(C - C_\infty) \tag{10}$$

We now introduce the following non-dimensional variables:

$$x^* = \frac{x}{h}, \quad y^* = \frac{y}{h}, \quad z^* = \frac{z}{h}, \quad q^* = \frac{q}{U_0}, \quad t^* = \frac{tU_0}{h}, \quad \theta = \frac{T - T_0}{T_w - T_0},$$
$$\phi = \frac{C - C_0}{C_w - C_0}, \quad \omega^* = \frac{\omega h}{U_0}, \quad t^* = \frac{tw_0^2}{\nu}, \quad \xi^* = \frac{\xi}{h}, \quad p^* = \frac{p}{\rho U_0^2}$$

Making use of non-dimensional quantities (dropping asterisks), the governing Eqs. (10), (2), and (3) can be written as

$$Re\frac{\partial q}{\partial t} = -\frac{\partial p}{\partial \xi} + \frac{\partial^2 q}{\partial z^2} + \alpha\frac{\partial^3 q}{\partial z^2 \partial t} - \left(M^2 + \frac{1}{K}\right)q + Gr\theta + Gc\phi \tag{11}$$

$$Pr\frac{\partial \theta}{\partial t} = (1 + R)\frac{\partial^2 \theta}{\partial z^2} \tag{12}$$

$$Sc\frac{\partial \phi}{\partial t} = \frac{\partial^2 \phi}{\partial z^2} - Kc\phi \tag{13}$$

The corresponding non-dimensional boundary conditions assume the form

$$q = \lambda\frac{\partial q}{\partial z}, \quad \theta = e^{i\omega t}, \quad \phi = e^{i\omega t} \text{ at } z = 1 \tag{14}$$

$$q = \lambda\frac{\partial q}{\partial z}, \quad \theta = 0, \quad \phi = 0 \text{ at } z = 0 \tag{15}$$

where $M^2 = \frac{\sigma B_0^2 h^2}{\rho \nu}$ is the Hartmann number (magnetic field parameter), $K = \frac{k}{h^2 \rho}$ is the permeability parameter, $\alpha = \frac{\alpha_1 U_0}{\nu h}$ is the second-grade fluid parameter, $Gr = \frac{g\beta(T_w - T_0)h^2}{\nu U_0}$ is the thermal Grashof number, $Gc = \frac{g\beta^*(C_w - C_0)h^2}{\nu U_0}$ is the mass Grashof number, $Pr = \frac{\rho C_p}{K_1}$ is Prandtl parameter, $R = \frac{16\sigma^* T_0^3}{3\alpha_r K_1}$ is the radiation parameter, $Kc = DK_c(C_w - C_0)$ is the chemical reaction parameter, and $Sc = \frac{\nu}{D}$ is the Schmidt number.

From Eq. (11), it follows that $\partial p/\partial \xi$ is a function of t only. We consider it to be of the form

$$\frac{\partial p}{\partial \xi} = P e^{i\omega t} \tag{16}$$

To solve Eqs. (11), (12), and (13) subject to the boundary conditions (14) and (15), we further write the velocity, temperature, and concentration as

$$q(z,t) = q_1 e^{i\omega t} \tag{17}$$

$$\theta(z,t) = \theta_1 e^{i\omega t} \tag{18}$$

$$\phi(z,t) = \phi_1 e^{i\omega t} \tag{19}$$

Substituting these expressions (17), (18), and (19) in (11), (12), and (13), respectively, and comparing the coefficient of like terms, we have the equations:

$$(1+\alpha i\omega)\frac{\partial^2 q_1}{\partial z^2} - \left(Rei\omega + M^2 + \frac{1}{K}\right)q_1 = -P - Gr\theta_1 - Gc\phi_1 \tag{20}$$

$$(1+R)\frac{\partial^2 \theta_1}{\partial z^2} - Pri\omega\theta_1 = 0 \tag{21}$$

$$\frac{\partial^2 \phi_1}{\partial z^2} - (Sci\omega + Kc)\phi_1 = 0 \tag{22}$$

With corresponding boundary conditions

$$q = \lambda\frac{\partial q_1}{\partial z}, \quad \theta_1 = 1, \quad \phi_1 = 1 \ \text{ at } \ z = 1 \tag{23}$$

$$q = \lambda\frac{\partial q_1}{\partial z}, \quad \theta_1 = 0, \quad \phi_1 = 0 \ \text{ at } \ z = 0 \tag{24}$$

Solving (20)–(22) subject to the conditions (23) and (24), we have velocity field, temperature, concentration, respectively, where the expressions for the constants $m_i (i = 1,2,\ldots,6)$ and $a_i (i = 1,2,\ldots,6)$ are given in Appendix.

$$\begin{aligned} q(z,t) = \Bigg(& a_1 e^{m_1 z} + a_2 e^{m_2 z} - \frac{P}{Rei\omega + M^2 + (1/K)} \\ & - \frac{Gr}{e^{m_3} - e^{m_4}}\left[\frac{e^{m_3 z}}{a_3} - \frac{e^{m_4 z}}{a_4}\right] - \frac{Gc}{e^{m_5} - e^{m_6}}\left[\frac{e^{m_5 z}}{a_5} - \frac{e^{m_6 z}}{a_6}\right]\Bigg) e^{i\omega t} \end{aligned} \tag{25}$$

$$\theta(z,t) = \frac{1}{e^{m_3} - e^{m_4}}(e^{m_3 z} - e^{m_4 z})e^{i\omega t} \tag{26}$$

$$\phi(z,t) = \frac{1}{e^{m_5} - e^{m_6}}(e^{m_5 z} - e^{m_6 z})e^{i\omega t} \tag{27}$$

where

$$m_1 = \sqrt{\frac{Rei\omega + M^2 + \frac{1}{K}}{1+\alpha i\omega}}, \quad m_2 = -\sqrt{\frac{Rei\omega + M^2 + \frac{1}{K}}{1+\alpha i\omega}}, \quad m_3 = \sqrt{\frac{Pri\omega}{1+R}},$$
$$m_4 = -\sqrt{\frac{Pri\omega}{1+R}}, \qquad m_5 = \sqrt{Sci\omega + Kc}, \qquad m_6 = -\sqrt{Sci\omega + Kc}$$

$$b_1 = \frac{P}{Rei\omega + M^2 + \frac{1}{K}} + \frac{Gr}{e^{m_3} - e^{m_4}}\left[\frac{1-\lambda m_3}{a_3} - \frac{1-\lambda m_4}{a_4}\right] + \frac{Gc}{e^{m_5} - e^{m_6}}\left[\frac{1-\lambda m_5}{a_5} - \frac{1-\lambda m_6}{a_6}\right]$$

$$b_2 = \frac{P}{Rei\omega + M^2 + \frac{1}{K}} + \frac{Gr}{e^{m_3} - e^{m_4}}\left[\frac{(1-\lambda m_3)e^{m_3}}{a_3} - \frac{(1-\lambda m_4)e^{m_4}}{a_4}\right] + \frac{Gc}{e^{m_5} - e^{m_6}}\left[\frac{(1-\lambda m_5)e^{m_5}}{a_5} - \frac{(1-\lambda m_6)e^{m_6}}{a_6}\right],$$

$$a_1 = \frac{b_2 - b_1 e^{m_2}}{(e^{m_1} - e^{m_2})(1-\lambda m_1)},$$

$$a_2 = \frac{b_2 - b_1 e^{m_1}}{(e^{m_1} - e^{m_2})(1-\lambda m_2)}$$

$$a_i = (1+\alpha i\omega)m_i^2 - \left(Rei\omega + M^2 + \frac{1}{K}\right), \quad i = 3,4,5,6$$

The volumetric flow rate is calculated as

$$Q = \int_0^1 q\,dz = \left(\frac{a_1}{m_1}(e^{m_1} - 1) + \frac{a_2}{m_2}(e^{m_2} - 1) - \frac{P}{Rei\omega + M^2 + (1/K)} - \frac{Gr}{e^{m_3} - e^{m_4}}\left[\frac{e^{m_3} - 1}{m_3 a_3} - \frac{e^{m_4} - 1}{m_4 a_4}\right] - \frac{Gc}{e^{m_5} - e^{m_6}}\left[\frac{e^{m_5} - 1}{m_5 a_5} - \frac{e^{m_6} - 1}{m_6 a_6}\right]\right)e^{i\omega t} \tag{28}$$

The wall shear stress at the wall of the upper plate representing the upper wall of the blood vessel is found as

$$\tau_w = \left[\frac{\partial q}{\partial z} + \alpha\frac{\partial^2 q}{\partial z \partial t}\right]_{z=1} = \left(a_1 m_1 e^{m_1} + a_2 m_2 e^{m_2} - \frac{Gr}{e^{m_3} - e^{m_4}}\left[\frac{m_3 e^{m_3}}{a_3} - \frac{m_4 e^{m_4}}{a_4}\right] - \frac{Gc}{e^{m_5} - e^{m_6}}\left[\frac{m_5 e^{m_5}}{a_5} - \frac{m_6 e^{m_6}}{a_6}\right]\right)(1+\alpha i\omega)e^{i\omega t} \tag{29}$$

The rates of heat and mass transfer across the upper plate (upper wall) are calculated as

$$Nu = \left[-\frac{\partial\theta}{\partial z}\right]_{z=1} = -\frac{1}{e^{m_3} - e^{m_4}}(m_3 e^{m_3} - m_4 e^{m_4})e^{i\omega t} \tag{30}$$

and

$$Sh = \left[-\frac{\partial\phi}{\partial z}\right]_{z=1} = -\frac{1}{e^{m_5} - e^{m_6}}(m_5 e^{m_5} - m_6 e^{m_6})e^{i\omega t} \tag{31}$$

3 Results and Discussion

A new mathematical model is accessible here to swat up the effects of chemical reaction as well as heat and mass transfer on the MHD oscillatory flow of blood through porous medium. Deliberation is made of the velocity slip of erythrocytes. It is significant to note that the pulsatility of blood flow owes its origin to the intermittent ejection of blood into the arterial network by the muscular pumping action (systolic and diastolic) of the heart. The analysis is applicable to pertinent problems of physiological fluids and fluid dynamical problems encountered in various industrial processes. However, the computational study has been carried out by using data which conform to those of blood flow in a diseased blood vessel. On the lower wall of the vessel, both the temperature and concentration of blood mass are maintained constant, while the variation of both of them is of oscillatory nature on the upper wall. These values/ranges of values of the parameters are mostly representative of blood flow, when a chemical reaction sets in. By using these values, the analytical expressions derived in the previous section have been computed by employing suitable software, viz. Mathematica. Variation in the distributions of velocity, temperature, concentration, and volumetric flow rate and wall shear stress has been investigated numerically, with respect to different governing parameters. Role of the same parameters in executing heat and mass transfer in the blood mass has also been investigated.

All the computational data have been presented in graphical/tabular form. The flow is governed by the non-dimensional parameters such as M Hartmann number, permeability parameter K, Re the Reynolds number, α viscoelastic parameter, R radiation parameter, Gr thermal Grashof number, Gc mass Grashof number, Sc Schmidt number, ω the frequency of oscillation, λ slip velocity parameter, Kc the chemical reaction parameter. The velocity, temperature, concentration, the shear stresses at the boundaries, Nusselt number (Nu), Sherwood number (Sh), and the volumetric flow rate (discharge) between the plates are evaluated analytically using regular perturbation technique and computationally discussed for different variations in the governing parameters. Figures 2, 3, 4, 5, 6, 7, 8, 9, 10, 11, and 12

represent the velocity profiles for u and v; Fig. 13 represents the temperature profiles for θ; Fig. 14 represents the concentration profiles for ϕ.

From Fig. 2, we noticed that both the velocity components u and v reduce with increasing the intensity of the magnetic field or Hartmann number M. Also, we have seen that the resultant velocity is experiencing retardation throughout the fluid region. The velocity component u increases and v reduces with increasing

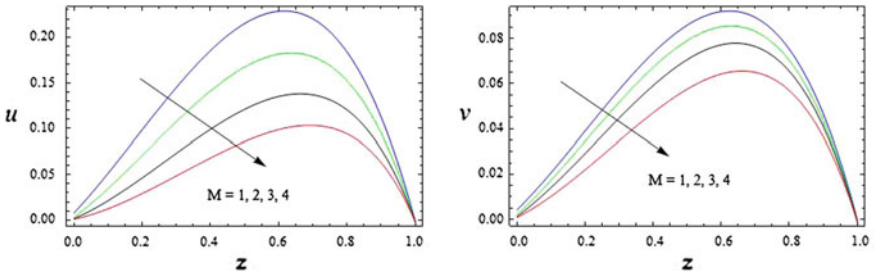

Fig. 2 Velocity profiles for u and v against M with $t = 1$, $Re = 1$, $K = 1$, $\alpha = 0.5$, $Pr = 0.71$, $Gr = 2$, $Gc = 5$, $R = 0.5$, $Sc = 0.22$, $\omega = \pi/4$, $\lambda = 0.002$, $Kc = 1$

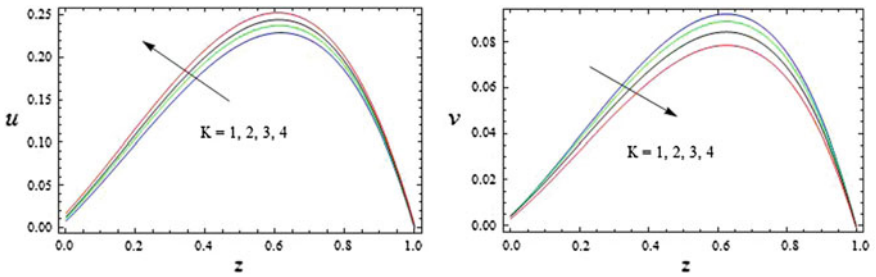

Fig. 3 Velocity profiles for u and v against K with $t = 1$, $Re = 1$, $M = 1$, $\alpha = 0.5$, $Pr = 0.71$, $Gr = 2$, $Gc = 5$, $R = 0.5$, $Sc = 0.22$, $\omega = \pi/4$, $\lambda = 0.002$, $Kc = 1$

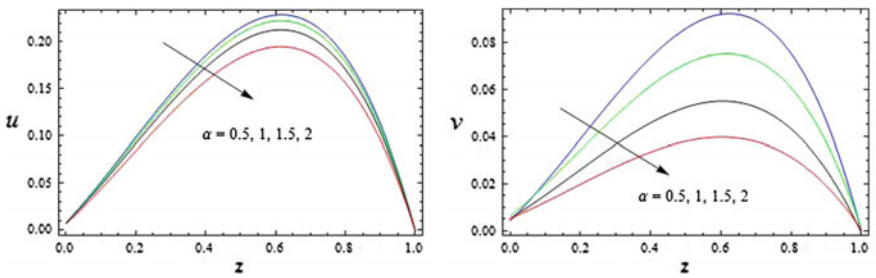

Fig. 4 Velocity profiles for u and v against α with $t = 1$, $Re = 1$, $K = 1$, $M = 1$, $Pr = 0.71$, $Gr = 2$, $Gc = 5$, $R = 0.5$, $Sc = 0.22$, $\omega = \pi/4$, $\lambda = 0.002$, $Kc = 1$

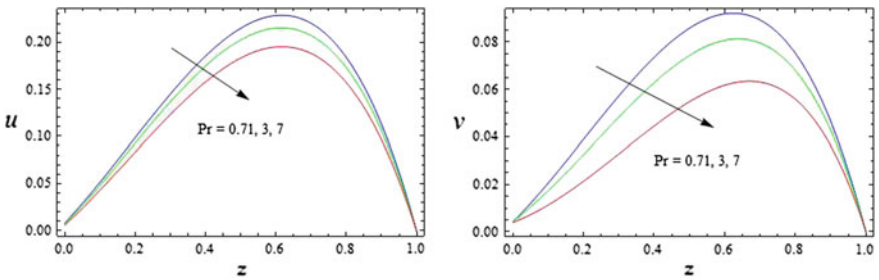

Fig. 5 Velocity profile for u and v against Pr with $t = 1$, $Re = 1$, $K = 1$, $\alpha = 0.5$, $Gr = 2$, $Gc = 5$, $R = 0.5$, $Sc = 0.22$, $\omega = \pi/4$, $\lambda = 0.002$, Kc=1

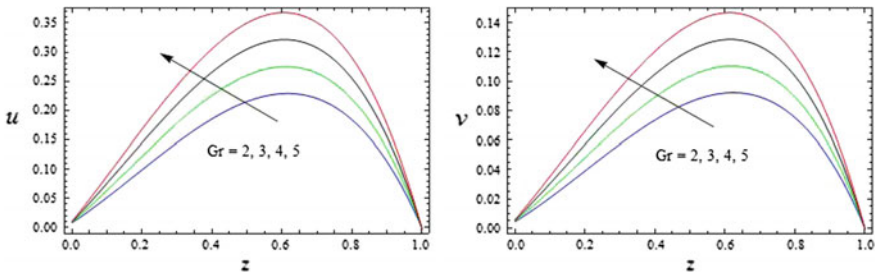

Fig. 6 Velocity profiles for u and v against Gr with $t = 1$, $Re = 1$, $K = 1$, $\alpha = 0.5$, $Pr = 0.71$, $M = 1$, Gc = 5, $R = 0.5$, $Sc = 0.22$, $\omega = \pi/4$, $\lambda = 0.002$, $Kc = 0.5$

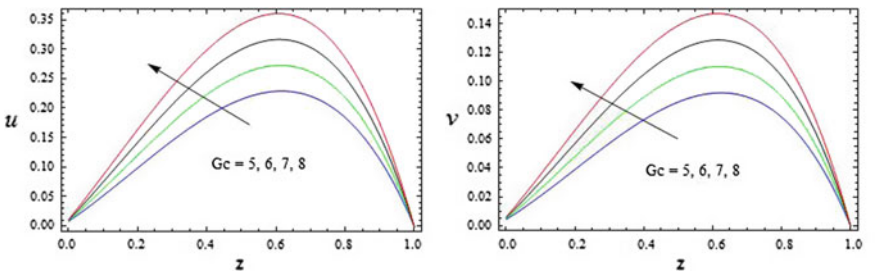

Fig. 7 Velocity profiles for u and v against Gc with $t = 1$, $Re = 1$, $K = 1$, $\alpha = 0.5$, $Pr = 0.71$, $Gr = 2$, $M = 1$, $R = 0.5$, $Sc = 0.22$, $\omega = \pi/4$, $\lambda = 0.002$, $Kc = 0.5$

permeability parameter K. The resultant velocity enhances with increasing K in the flow field. We also noticed that lower the permeability, lesser the fluid speed is observed the entire fluid region (Fig. 3). The similar behavior is observed for the velocity components with radiation parameter R (Fig. 8). This gives an idea of the influence of chemical reaction on the velocity distribution under identical condition of heat radiation. The magnitude of the velocity components u and v as well as

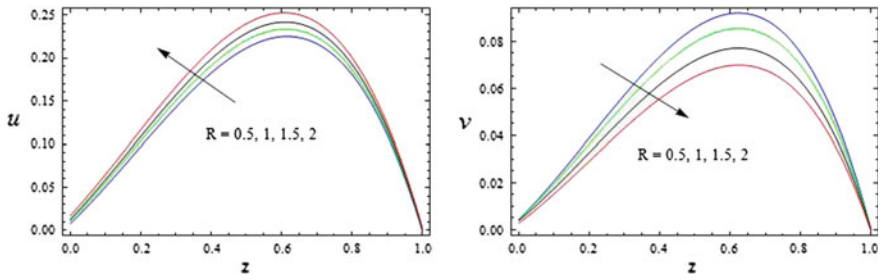

Fig. 8 Velocity profiles for u and v against R with $t = 1$, $Re = 1$, $K = 1$, $\alpha = 0.5$, $Pr = 0.71$, $Gr = 2$, $Gc = 5$, $M = 1$, $Sc = 0.22$, $\omega = \pi/4$, $\lambda = 0.002$, $Kc = 0.5$

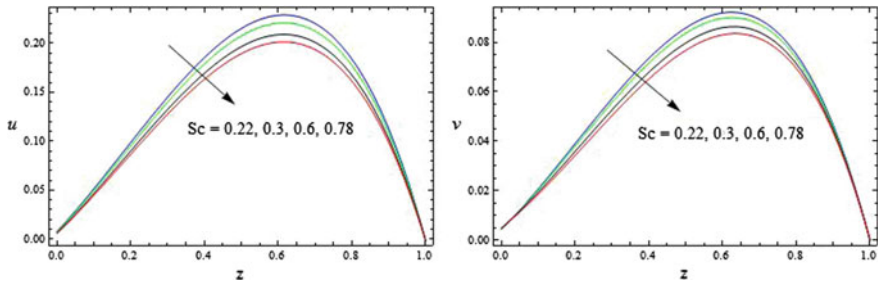

Fig. 9 Velocity profiles for u and v against Sc with $t = 1$, $Re = 1$, $K = 1$, $\alpha = 0.5$, $Pr = 0.71$, $Gr = 2$, $Gc = 5$, $R = 0.5$, M=1, $\omega = \pi/4$, $\lambda = 0.002$, $Kc = 0.5$

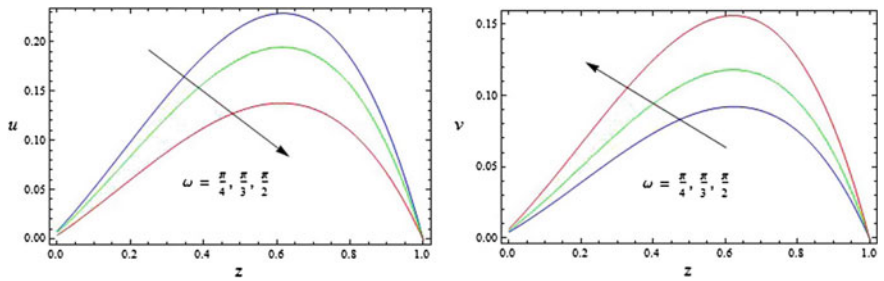

Fig. 10 Velocity profiles for u and v against ω with $t = 1$, $Re = 1$, $K = 1$, $\alpha = 0.5$, $Pr = 0.71$, $Gr = 2$, $Gc = 5$, $R = 0.5$, $Sc = 0.22$, $M = 1$, $\lambda = 0.002$, $Kc = 0.5$

resultant velocity reduces in the entire fluid region with increasing second-grade fluid parameter α, Pr, Sc, and Kc (Figs. 4, 5, 9, and 12). Also, it indicates that at a particular instant of time, blood velocity reduces as blood viscoelasticity (α) increases. From Figs. 6, 7, and 11, the velocity components u and v as well as resultant velocity increase with increasing thermal Grashof number Gr, mass Grashof number Gc, or λ. There is no indication of flow separation in the absence of

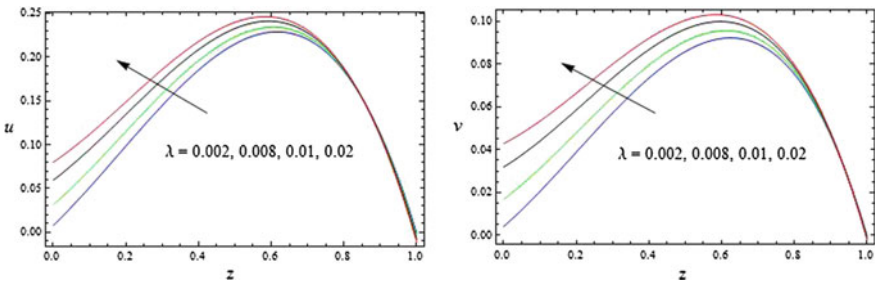

Fig. 11 Velocity profiles for u and v against λ with $t = 1$, $Re = 1$, $K = 1$, $\alpha = 0.5$, $Pr = 0.71$, $Gr = 2$, $Gc = 5$, $R = 0.5$, $Sc = 0.22$, $\omega = \pi/4$, M=1, $Kc = 0.5$

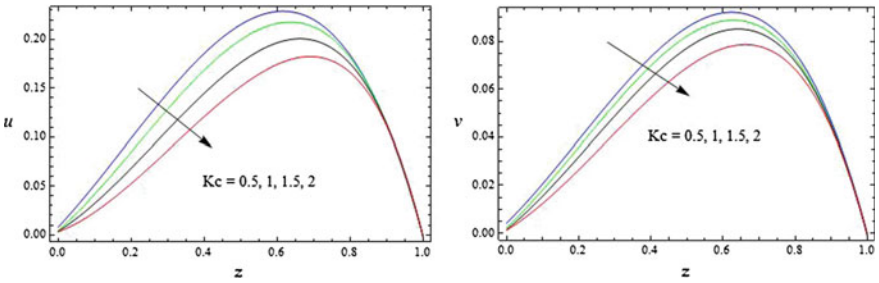

Fig. 12 Velocity profiles for u and v against Kc with $t = 1$, $Re = 1$, $K = 1$, $\alpha = 0.5$, $Pr = 0.71$, $Gr = 2$, $Gc = 5$, $R = 0.5$, $Sc = 0.22$, $\omega = \pi/4$, $\lambda = 0.002$, $M = 1$

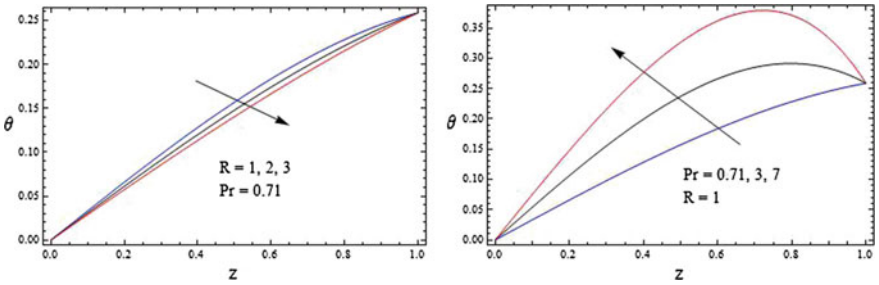

Fig. 13 Temperature profiles for θ against R and Pr with $\omega = 5\pi/12$, $t = 0.1$

slip velocity at the wall, but flow separation does take place whenever there is velocity slip at the boundary. It is important to note that the extent of flow separation increases with the increase in the slip velocity parameter λ. We also find that the magnitude of the velocity component u reduces and v enhances with increasing the frequency of oscillation ω. The resultant velocity reduces throughout the fluid region with increasing the frequency of oscillation (Fig 10).

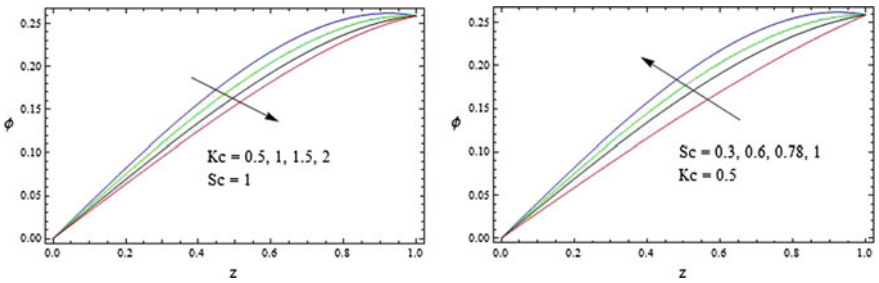

Fig. 14 Concentration profiles for ϕ against Kc and Sc with $\omega = 5\pi/12$, $t = 0.1$

We noticed that from Fig. 13, the magnitude of the temperature reduces with increasing radiation parameter R, whereas the reversal behavior is observed throughout the fluid region with increasing Prandtl number Pr. Also, we found that from Fig. 14, the magnitude of the concentration increases with increasing Schmidt number Sc, whereas the reversal behavior is observed throughout the fluid region with increasing chemical reaction parameter Kc. Finally, these reveal that under the purview of the present computational study, at any given distance the temperature/concentration reduces as the thermal radiation/chemical reaction parameter increases. Further, it reveals that for any particular values of thermal radiation/chemical reaction parameter, both the temperature and the concentration increase as we move further and further from the lower wall to the upper one.

The frictional force is determined at the upper wall and is presented in Table 1. This shows that in the absence of any magnetic field, the wall shear stress increases with increase in the value of the Reynolds number, and there occurs a sharp reduction in the wall shear stress, which changes its nature from tensile to compressive. A similar nature of the shear stress is observed, even in the presence of a magnetic field of unit strength (M); however, the change from tensile to compressive is somewhat smooth. The magnitude of the stress components τ_x and τ_y enhances with increasing K, Gr, Gc, and λ. The opposite nature is observed for the same components with increasing M and Kc. The magnitude of the stress component τ_x reduces and τ_y increases with increasing α, ω, and R. The reversal behavior is for the components τ_x and τ_y with increasing Pr and Sc. We also noticed that from Table 2 the Nusselt number Nu enhances with increasing Radiation parameter R and Prandtl number Pr. Likewise, the rate of mass transfer reduces with increasing Schmidt number Sc and increases with increasing chemical reaction parameter Kc (Table 3). From Table 4, we observed that volumetric flow rate enhances with increasing K, Gr, Gc, λ, and R as well as it reduces to M, Pr, Kc, Sc, α, and ω.

Table 1 Skin friction

M	K	α	R	Pr	Gr	Gc	Sc	ω	λ	Kc	τ_x	τ_y
1	**1**	**0.5**	**0.5**	**0.71**	**2**	**5**	**0.3**	$\pi/4$	**0.002**	**0.5**	−1.15824	−1.11049
2	1	0.5	0.5	0.71	2	5	0.3	$\pi/4$	0.002	0.5	−0.99349	−1.03204
3	1	0.5	0.5	0.71	2	5	0.3	$\pi/4$	0.002	0.5	−0.82503	−0.92514
1	**2**	0.5	0.5	0.71	2	5	0.3	$\pi/4$	0.002	0.5	−1.19415	−1.12444
1	**3**	0.5	0.5	0.71	2	5	0.3	$\pi/4$	0.002	0.5	−1.20699	−1.12914
1	1	**0.8**	0.5	0.71	2	5	0.3	$\pi/4$	0.002	0.5	−1.15094	−1.14180
1	1	**1**	0.5	0.71	2	5	0.3	$\pi/4$	0.002	0.5	−1.14122	−1.16036
1	1	0.5	**1**	0.71	2	5	0.3	$\pi/4$	0.002	0.5	−1.15595	−1.11309
1	1	0.5	**1.5**	0.71	2	5	0.3	$\pi/4$	0.002	0.5	−1.15456	−1.11464
1	1	0.5	0.5	**3**	2	5	0.3	$\pi/4$	0.002	0.5	−1.18323	−1.67388
1	1	0.5	0.5	**7**	2	5	0.3	$\pi/4$	0.002	0.5	−1.20522	−1.00436
1	1	0.5	0.5	0.71	**3**	5	0.3	$\pi/4$	0.002	0.5	−1.37321	−1.31567
1	1	0.5	0.5	0.71	**4**	5	0.3	$\pi/4$	0.002	0.5	−1.58818	−1.52084
1	1	0.5	0.5	0.71	2	**6**	0.3	$\pi/4$	0.002	0.5	−1.36496	−1.31158
1	1	0.5	0.5	0.71	2	**7**	0.3	$\pi/4$	0.002	0.5	−1.57168	−1.51267
1	1	0.5	0.5	0.71	2	5	**0.6**	$\pi/4$	0.002	0.5	−1.17133	−1.09545
1	1	0.5	0.5	0.71	2	5	**0.78**	$\pi/4$	0.002	0.5	−1.17886	−1.08614
1	1	0.5	0.5	0.71	2	5	0.3	$\pi/3$	0.002	0.5	−0.84071	−1.36616
1	1	0.5	0.5	0.71	2	5	0.3	$\pi/2$	0.002	0.5	−0.06741	−1.60135
1	1	0.5	0.5	0.71	2	5	0.3	$\pi/4$	**0.008**	0.5	−1.17648	−1.12958
1	1	0.5	0.5	0.71	2	5	0.3	$\pi/4$	**0.01**	0.5	−1.18263	−1.13601
1	1	0.5	0.5	0.71	2	5	0.3	$\pi/4$	0.002	**1**	−1.12842	−1.08348
1	1	0.5	0.5	0.71	2	5	0.3	$\pi/4$	0.002	**1.5**	−1.10104	−1.06013

Table 2 Nusselt number

R	Pr	ω	Nu
0.5	**0.71**	$5\pi/12$	−0.062010
1	0.71	$5\pi/12$	−0.110643
1.5	0.71	$5\pi/12$	−0.140021
2	0.71	$5\pi/12$	−0.159684
0.5	**3**	$5\pi/12$	0.512785
0.5	**7**	$5\pi/12$	1.209667

Table 3 Sherwood number

Sc	Kc	ω	Sh
0.3	**0.5**	$5\pi/12$	−0.182881
0.6	0.5	$5\pi/12$	−0.067315
0.78	0.5	$5\pi/12$	0.000764
1	0.5	$5\pi/12$	0.082496
0.3	**1**	$5\pi/12$	−0.228894
0.3	**1.5**	$5\pi/12$	−0.271903

Table 4 Volumetric flow rate

M	K	α	R	Pr	Gr	Gc	Sc	ω	λ	Kc	Q
1	**1**	**0.5**	**0.5**	**0.71**	**2**	**5**	**0.3**	$\pi/4$	**0.002**	**0.5**	6.483422
2	1	0.5	0.5	0.71	2	5	0.3	$\pi/4$	0.002	0.5	2.500108
3	1	0.5	0.5	0.71	2	5	0.3	$\pi/4$	0.002	0.5	1.254794
1	**2**	0.5	0.5	0.71	2	5	0.3	$\pi/4$	0.002	0.5	8.864866
1	**3**	0.5	0.5	0.71	2	5	0.3	$\pi/4$	0.002	0.5	10.07539
1	1	**0.8**	0.5	0.71	2	5	0.3	$\pi/4$	0.002	0.5	6.295777
1	1	**1**	0.5	0.71	2	5	0.3	$\pi/4$	0.002	0.5	6.142751
1	1	0.5	**1**	0.71	2	5	0.3	$\pi/4$	0.002	0.5	6.827244
1	1	0.5	**1.5**	0.71	2	5	0.3	$\pi/4$	0.002	0.5	7.166520
1	1	0.5	0.5	**3**	2	5	0.3	$\pi/4$	0.002	0.5	5.569850
1	1	0.5	0.5	**7**	2	5	0.3	$\pi/4$	0.002	0.5	5.321241
1	1	0.5	0.5	0.71	**3**	5	0.3	$\pi/4$	0.002	0.5	7.138641
1	1	0.5	0.5	0.71	**4**	5	0.3	$\pi/4$	0.002	0.5	7.793860
1	1	0.5	0.5	0.71	2	**6**	0.3	$\pi/4$	0.002	0.5	7.529665
1	1	0.5	0.5	0.71	2	**7**	0.3	$\pi/4$	0.002	0.5	8.575909
1	1	0.5	0.5	0.71	2	5	**0.6**	$\pi/4$	0.002	0.5	5.334855
1	1	0.5	0.5	0.71	2	5	**0.78**	$\pi/4$	0.002	0.5	4.679888
1	1	0.5	0.5	0.71	2	5	0.3	$\pi/3$	0.002	0.5	5.728721
1	1	0.5	0.5	0.71	2	5	0.3	$\pi/2$	0.002	0.5	4.099391
1	1	0.5	0.5	0.71	2	5	0.3	$\pi/4$	**0.008**	0.5	6.492027
1	1	0.5	0.5	0.71	2	5	0.3	$\pi/4$	**0.01**	0.5	6.494928
1	1	0.5	0.5	0.71	2	5	0.3	$\pi/4$	0.002	**1**	4.881600
1	1	0.5	0.5	0.71	2	5	0.3	$\pi/4$	0.002	**1.5**	4.836282

4 Conclusions

The analysis is applicable to pertinent problems of physiological fluids and fluid dynamical problems encountered in various industrial processes. However, the computational study has been carried out by using data which conform to those of blood flow in a diseased blood vessel. The study enables us to conclude the following:

1. The velocity reduces with increasing Hartmann number M and enhances with permeability parameter K.
2. Blood viscoelasticity lesser flow velocity significantly.
3. The resultant velocity enhances with increasing thermal Grashof number, mass Grashof number, and slip parameter.
4. The wall shear stress is strongly pretentious by the Reynolds number.
5. At any particular location as the thermal radiation increases, both heat transfer rate and temperature are reduced to an appreciable extent. However, the velocity is not significantly affected by thermal radiation.

6. The rate of heat transfer boosts with increasing Prandtl number.
7. Concentration and rate of mass transfer are abridged due to chemical reaction. Comparatively, the velocity distribution is less affected due to chemical reaction.
8. The rate of mass transfer is enhanced, as the mass diffusivity reduces (i.e., as the Schmidt number increases).

References

Adesanya SO, Makinde OD (2012) Heat transfer to magnetohydrodynamic non-Newtonian couple stress pulsatile flow between two parallel porous plates. Z Naturforsch 67(a):647–656

Adesanya SO, Eslami M, Mirzazadeh M, Biswas A (2015a) Shock wave development in couple stress fluid-filled thin elastic tubes. Eur Phys J Plus 130(6):1–21

Adesanya SO, Falade JA, Makinde OD (2015b) Pulsating flow through vertical porous channel with viscous dissipation effect. UPB Sci Bullitien Serv D 77(1):25–36

Bastman AR (1982) Low Reynolds number non-Newtonian flow in slowly varying axi-symmetric tubes. Acta Mech 44:107–119

Beavers GS, Joseph DD (1967) Boundary conditions at a naturally permeably wall. J Fluid Mech 30:197–207

Beavers GS, Sparrow EM, Magnuson RA (1970) Experiments on coupled parallel flows in a channel and a bounding medium. ASME J Basic Eng 92:843–848

Beavers GS, Sparrow EM, Masha BA (1974) Boundary conditions at a porous surface which bounds a fluid flow. Am Inst Chem Eng J 20:596–597

Brunn P (1975) The velocity slip of polar fluids. Rheological Acta 14:1039–1054

Chaudhary RC, Jain P (2000) Effects of chemical reactions on MHD micropolar fluid flow past a vertical plate in slip-flow regime. Appl Math Mech 29:1179–1194

Chaudhary RC, Jain P (2007) Combined heat and mass transfer in magneto-micropolar fluid flow from radiate surface with variable permeability in slip-flow regime. Z Angew Math Mech 87 (8–9):549–563

Coulson RA, Hernandez T (1983) Alligator metabolism studies on chemical reactions in vivo. Comp Biochem Physiol 74:i–182

Das UN, Deka RK, Soundalgekar VM (1994) Effects of mass transfer on flow past an impulsively started infinite vertical plate with constant heat flux and chemical reaction. Forsch Ingenieurwes 60:284–287

Dash RK, Metha KN, Jayaraman G (1996) Casson fluid in a pipe filled with a homogeneous porous medium. Int J Eng Sci 34(10):1145–1156

Kandasamy R, Periasamy K, Sivagnana KKP (2005) Effects of chemical reaction, heat and mass transfer along wedge with heat source and concentration in the presence of suction or injection. Int J Heat Mass Transf 48:1388–1394

Khaled ARA, Vafai K (2003) The role of porous media in modelling flow and heat transfer in biological tissues. Int J Heat Mass Transf 46:4989–5003

Makinde OD, Mhone PY (2005) Heat transfer to MHD oscillatory flow in a channel filled with porous medium. Rom J Phys 50:931–938

Misra JC, Sahu BK (1989) Unsteady flow of blood through arteries of non-uniform endothelial cross-section. Model Simul Contr 15:31–64

Misra JC, Shit GC (2008) Flow and heat transfer of a MHD viscoelastic fluid in a channel with stretching walls: some applications to haemodynamics. Comput Fluids 37:1–11

Misra JC, Shit GC (2009) Flow of a biomagnetic viscoelastic fluid in a channel with stretching walls. ASME J Appl Mech 76(6):061006
Misra JC, Maiti S (2012) Peristaltic pumping of blood in small vessels of varying cross-section. ASME J Appl Mech 79(061003):1–19
Misra JC, Sinha A (2013a) Effect of Hall current and heat radiation on flow of fluid through a porous medium subject to an external magnetic field. Spec Top Rev Porous Media Int J 4 (2):147–158
Misra JC, Sinha A (2013b) Effect of thermal radiation on MHD flow of blood and heat transfer in a permeable capillary in stretching motion. Heat Mass Transf 49(5):617–628
Misra JC, Paul B, Gupta AS (1998) Hydromagnetic flow of a second-grade fluid in a channel—some applications to the physiological systems. Math Models Methods Appl Sci 8(8):1323–1342
Misra JC, Sinha A, Shit GC (2008) Theoretical analysis of blood flow through an arterial segment having multiple stenosis. J Mech Med Biol 8:265–279
Misra JC, Sinha A, Shit GC (2010) Flow of a biomagnetic viscoelastic fluid: application to estimation of blood flow in arteries during electromagnetic hyperthermia, a therapeutic procedure for cancer treatment. Appl Math Mech 31:1405–1420
Muthucumarswamy R (2002) Effects of a chemical reaction on moving isothermal vertical surface with suction. Acta Mech 155:5–70
Muthucumarswamy R, Ganesan P (2001) First order chemical reaction on flow past an impulsively started vertical plate with uniform heat and mass flux. Acta Mech 147:45–57
Nubar Y (1971) Blood flow, slip and viscometry. Biophys J 11:252–264
Perdikis C, Raptis A (1996) Heat transfer of a micropolar fluid by the presence of radiation. Heat Mass Transf 31:381–382
Ram PC (1990) Effect of hall current and wall temperature oscillation on convective flow in a rotating fluid through porous medium. Heat Mass Transf 25:205–208
Rivlin RS, Ericksen JL (1955) Stress-deformation relations for isotropic materials. J Ratio Mech Anal 4:323–425
Singel DJ, Stemler JS (2005) Chemical physiology of flood flow regulation by red cells: the role of nitric oxide and S-nitrosohemoglobin. Annu Rev Physiol 67:99–145
Sinha A, Misra JC (2014a) MHD flow of blood through a dually stenosed artery: effects of viscosity variation, variable hematocrit and velocity-slip. Can J Chem Eng 92:23–31
Sinha A, JC Misra (2014b) Effect of induced magnetic field on magneto-hydrodynamic stragnation point flow and heat transfer on a stretching sheet. ASME J Heat Transf 136(11):112701
Swarnalathamma BV, Veera Krishna M (2016) Peristaltic hemodynamic flow of couple stress fluid through a porous medium under the influence of magnetic field with slip effect. AIP Conf Proc 1728:020603. doi:10.1063/1.4946654
Vafai Ai LK (2006) A Coupling model for macromolecular transport in a stenosed arterial wall. Int J Heat Mass Transf 49:1568–1591
Veera Krishna M, Gangadhar Reddy M (2016a) MHD free convective rotating flow of visco-elastic fluid past an infinite vertical oscillating porous plate with chemical reaction. IOP Conf Ser Mater Sci Eng 149:012217. doi:http://dx.doi.org/10.1088/1757-899X/149/1/012217
Veera Krishna M, Subba Reddy G (2016b) Unsteady MHD convective flow of Second grade fluid through a porous medium in a Rotating parallel plate channel with temperature dependent source. IOP Conf Ser Mater Sci Eng 149:012216. doi:http://dx.doi.org/10.1088/1757-899X/149/1/012216
Veera Krishna M, Swarnalathamma BV (2016c) Convective heat and mass transfer on MHD peristaltic flow of Williamson fluid with the effect of inclined magnetic field. AIP Conf Proc 1728:020461. doi:http://dx.doi.org/10.1063/1.4946512
Wada S, Karino T (2000) Computational study on LDL transfer from flowing blood to arterial wall. Clinical applications of computational mechanical model studies to the cardiovascular system, pp 157–173
Xu Z, Chen N, Shadden SC, Marsden JE, Kamocka MM, Rosen ED, Alber M (2009) Study of blood flow impact on growth thrombi using a multi-scale model. Soft Matter 5:769–779

Part IV
Numerical Simulation and Investigation of Fluid Dynamics

Numerical Simulation of Partially Covered Hartmann Whistle in a Sonic-Underexpanded Jet

Arnab Samanta, S. Narayanan, Ashish Narayan and Shailesh Kumar Jha

Abstract The current study provides numerical investigation into the use of "Hartmann whistle" as an effective passive flow control device by covering the major area between the nozzle exit and cavity inlet using a cylindrical shield. The passive control is accomplished by allowing the pulsating jet to exit through two small openings in the shield so that it can be utilized for various flow control applications such as mixing enhancement, drag reduction, noise mitigation. The current study numerically investigates the effect of partially covered cylindrical shield on the shock as well as regurgitant oscillation characteristics of a Hartmann whistle when the pulsating jet exits through the two small openings of the cylindrical shield. The relevant parameters that modify the flow/shock oscillations of the Hartmann whistle are the cavity standoff distance, nozzle pressure ratio, cavity length, cavity shield, etc. The studies were performed for various standoff distances values of 10, 20, and 30 mm to demonstrate the role of standoff distance in effective flow control. The modifications in the shock as well as regurgitant oscillation features of partially covered Hartmann whistles are systematically compared using transient velocity vectors, Mach number contours, etc. for various standoff distances. The velocity vectors indicate flow diversion features near the cavity mouth as well as inflow and outflow jet regurgitant phases. The Mach contours of partially shielded Hartmann whistles indicate shock structures, zones of flow deceleration and re-acceleration. It also clearly demonstrates that the resonant oscillations are primarily driven by jet regurgitance at smaller standoff distances, but at higher standoff distances they are primarily driven by the fluid column oscillations in the shock-cells, shield as well as in the cavity zones. Thus, the current study reveals that the standoff distance is a crucial parameter that controls the strength of shock, regurgitant as well as fluid column oscillations in a partially covered Hartmann whistle in order to achieve an effectual flow control.

A. Samanta · S. Narayanan (✉) · A. Narayan · S.K. Jha
Department of Mechanical Engineering, Indian Institute of Technology (Indian School of Mines), Dhanbad 826004, Jharkhand, India
e-mail: snarayan.1979@gmail.com

A. Samanta
e-mail: arnab.samanta91@gmail.com

M.K. Singh et al. (eds.), *Applications of Fluid Dynamics*, Lecture Notes in Mechanical Engineering, https://doi.org/10.1007/978-981-10-5329-0_15

List of Symbols

D_c Cavity diameter (m)
D_{fej} Fully expanded jet diameter (m)
D_j Jet exit diameter (m)
H Height of the cylindrical shield measured from the jet axis (m)
L Cavity length (m)
L_{shock} Length of shock-cell (m)
M_j Mach number at the nozzle exit
P_a Ambient pressure (pa)
P_o Stagnation pressure (pa)
R Nozzle pressure ratio (P_o/P_a)
S Standoff distance (m)
v_j Jet velocity at nozzle exit (m/s)

1 Introduction

The resonating air-jet devices such as Hartmann whistle have been found useful in flow and noise control applications and have assumed importance. "Hartmann whistle" is an open-closed cylindrical cavity, wherein high-speed jet impinges at its open end which is closed at the back end. When the cavity mouth is kept at certain regions (i.e., expansion, compression, and termination regions) of the underexpanded jet, intense flow/shock oscillations occur. The pertinent parameters that control the flow/shock oscillation features and its fundamental timbre frequency are its cavity standoff distance, cavity length, nozzle pressure ratio, etc. It is well known that Hartmann resonator can generate high intensity sonic as well as ultrasonic energy in a gaseous medium which finds immense applications in various industrial processes. The presence of complex flow patterns such as shock-cells, oscillations of flow/shock near the cavity inlet, other instabilities (i.e., shear-layer instabilities) in Hartmann resonator might be responsible for intensifying the energy of the gaseous medium and thus leading to the generation of sturdy and directed acoustic emissions from the cavity. In the field of flow controls, the most relevant part is the nature of the pulsating jet coming out of the Hartmann cavity. The pulsating jet is generally used to improve the performance of flight vehicles by reducing drag, delaying stall, suppressing acoustical disturbances, etc. In fact, there is hardly any literature which demonstrates the effect of partially covered cylindrical shield on the flow/shock oscillation features of a Hartmann whistle which forms the specific objective of the current work. Therefore, a detailed numerical simulation is carried out in the current study to predict the flow/shock oscillation characteristics of Hartmann whistle by partially covering the area between the jet exit and the cavity inlet. Some of the relevant literatures on Hartmann whistles are discussed below.

Gravitt (1959) investigated experimentally and theoretically the mechanism responsible for strong vibrations in the Hartmann tube. He found that the pressure instabilities were observed to act as the source of the forced oscillations of an air plug in the cavity. Theoretical results obtained agreed well with the experiments by incorporating viscous reaction and heat transfer during the plug oscillations.

Iwamoto (1990) studied the self-excited oscillation of a rectangular Hartmann-Sprenger (H-S) tube by flow visualization. It was found that the necessary conditions for commencing and sustaining a steady resonance in a Hartmann cavity were the existence of a positive pressure gradient in the vicinity of the open end of the cavity and a low-pressure region on the outside surface of the cavity wall.

Chang and Lee (2001) proposed a simplified model for the jet regurgitant mode of the Hartmann whistle and determined that its resonant behavior was mainly dependent on the wavelength of resonant wave and length of the tube. They studied numerically the effect of four most important parameters such as forcing frequency, oscillatory amplitude of the Mach number, separation distance between oscillatory position and tube inlet, and tube length on the regurgitant mode.

2 Computational Domain and Grid

The computational domain and boundary conditions for the jet flow impinging on a partially covered Hartmann whistle are shown in Fig. 1. The computational domain (Fig. 1) is limited to 20 D_j and 10 D_j in the axial and radial directions for simulating the Hartmann whistle, flow in order to capture the complex shock structures, flow oscillations, recirculation zones, spill-over features, etc. The computational grid with varying mesh size for is shown in Fig. 2. The grid was constructed using ANSYS CFD for predicting the flow features of the Hartmann cavity. The fine grids were used in the regions of shock-cells to resolve and capture the shocks without allowing it to diffuse, and coarse grids were used in those regions where flow effects were absent. A transient axisymmetric imitation was carried out with the help of commercial package ANSYS FLUENT 14 with a density-based implicit solver. The fluid was considered as compressible (i.e., ideal gas) for the present simulations with no slip boundary condition enforced at the walls. A total of about 1,36,521 cells were used in the present simulations. The simple one equation Spalart-Allmaras turbulence model with standard values of model constants (σ_v = 2/3, C_{b1} = 0.1355, C_{b2} = 0.622, k = 0.42, C_{w1} = 3.21, C_{w2} = 0.3, C_{w3} = 2.0, C_{v1} = 7.1) was used for modeling turbulence. The Spalart-Allmaras turbulence model is essentially intended for aerodynamic applications generally observed in high speed flows past airfoils, boundary layers, etc. Also, this one equation model has been observed to give good results with reduced computational time for problems involving wall-bounded flows as well as boundary layers subjected to adverse pressure gradients Spalart and Allmaras (1992).

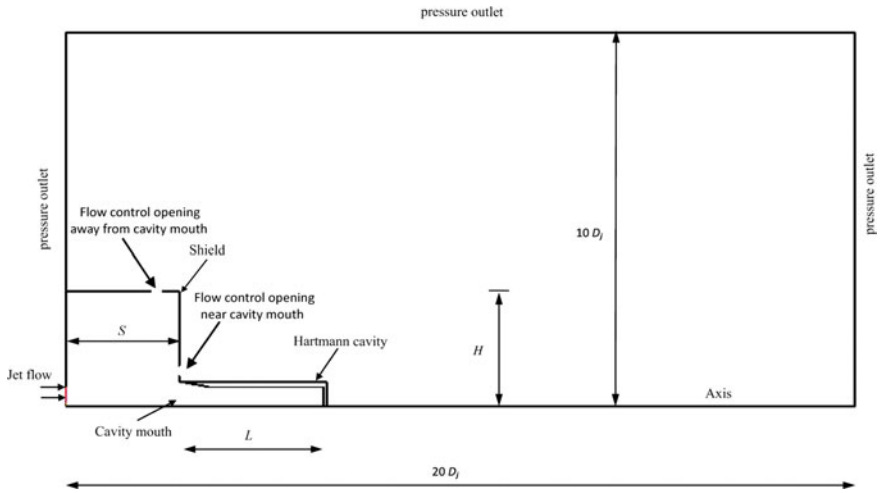

Fig. 1 Computational domain and boundary conditions

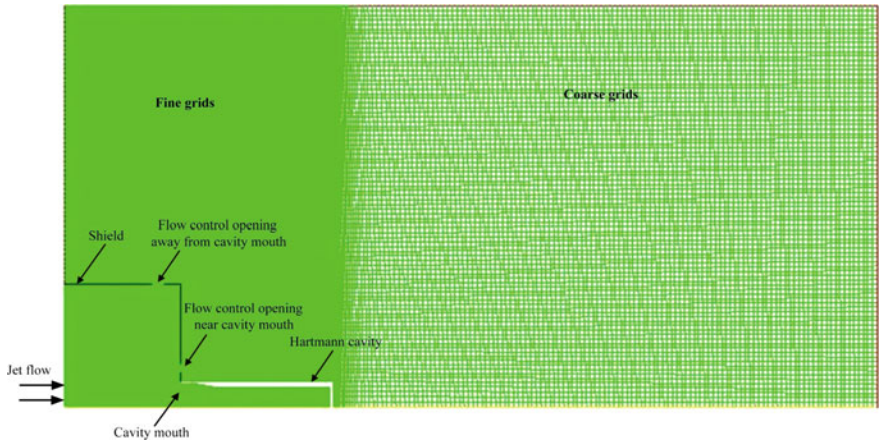

Fig. 2 Computational grid

2.1 Governing Equations

The 2D axisymmetric governing equations which control the occurrence of the physical phenomena when a sonic-underexpanded jet impinges a Hartmann whistle are given below.

2.1.1 Mass Conservation Equation

x is the axial coordinate, r is the radial coordinate, u_x is the axial velocity, and u_r is the radial velocity in the present simulation.

$$\frac{\partial}{\partial x}(\rho u_x) + \frac{\partial}{\partial r}(\rho u_r) + \frac{\rho u_r}{r} = 0. \tag{1}$$

2.1.2 Axial Momentum Conservation Equation

$$\frac{\partial}{\partial t}(\rho u_x) + \frac{1}{r}\frac{\partial}{\partial x}(r\rho u_x u_x) + \frac{1}{r}\frac{\partial}{\partial r}(r\rho u_r u_x) = -\frac{\partial p}{\partial x} + \frac{1}{r}\frac{\partial}{\partial x}\left[r\mu\left(2\frac{\partial u_x}{\partial x} - \frac{2}{3}(\nabla \cdot \vec{u})\right)\right] + \frac{1}{r}\frac{\partial}{\partial r}\left[r\mu\left(2\frac{\partial u_x}{\partial r} + \frac{\partial u_r}{\partial x}\right)\right] + F_x. \tag{2}$$

2.1.3 Radial Momentum Conservation Equation

$$\frac{\partial}{\partial t}(\rho u_r) + \frac{1}{r}\frac{\partial}{\partial x}(r\rho u_x u_r) + \frac{1}{r}\frac{\partial}{\partial r}(r\rho u_r u_r) = -\frac{\partial p}{\partial r} + \frac{1}{r}\frac{\partial}{\partial x}\left[r\mu\left(\frac{\partial u_r}{\partial x} + \frac{\partial u_x}{\partial r}\right)\right] + \frac{1}{r}\frac{\partial}{\partial r}\left[r\mu\left(2\frac{\partial u_r}{\partial r} - \frac{2}{3}(\nabla \cdot \vec{u})\right)\right] - 2\mu\frac{u_r}{r^2} + \frac{2}{3}\frac{u_r}{r}(\nabla \cdot \vec{u}) + \rho\frac{u_z^2}{r} + F_r \tag{3}$$

where

$$\nabla \cdot \vec{u} = \frac{\partial u_x}{\partial x} + \frac{\partial u_r}{\partial r} + \frac{u_r}{r}$$

F_x and F_r comprise external body forces, model-dependent sources terms as well as user-defined sources, and u_z is the swirl velocity.

2.1.4 Energy Conservation Equation

$$\frac{\partial}{\partial t}(\rho E) + \nabla \cdot \left(\vec{u}(\rho E + p)\right) = \nabla \cdot \left(k_{\text{eff}}\nabla T - \sum\nolimits_j h_j \vec{J}_j + (\bar{\bar{\tau}}_{\text{eff}} \cdot \vec{u})\right) \tag{4}$$

where k_{eff} is the effective thermal conductivity ($k_{\text{eff}} = k + k_t$), and k_t is the turbulent thermal conductivity defined based on the turbulence model. The first three terms on the right-hand side of Eq. (4) represent energy transfer due to conduction, species diffusion ($\vec{J}_j$ represents diffusion flux of species j), and viscous dissipation. In the current study, the first term and second term on the right-hand side are also zero due to the adiabatic boundary condition to the wall as well as no diffusion of species.

2.1.5 Equation of State

$$p = \rho R_c T \tag{5}$$

2.2 Grid-Sensitivity Study

The grid-sensitivity studies carried out by varying the number of cells 100,522, 136,521, and 164,778 revealed that the current results obtained with 136,521 cells for an S/D_j value of 2.86 are almost invariant to further grid refinement. The variation of static pressure with position along the axis for various grids is shown in Fig. 3.

2.3 Validation

In order to establish that the predictions are right, the length of the first shock-cell normalized with jet diameter ($L_{\text{shock-cell}}/D_j$) for $S/D_j = 2.86$, $L/D_j = 2.86$ for $R = 5$, obtained from the present computations is compared with the shock-cell length predicted by Edin et al. (2015) for a fully shielded Hartmann whistle as well as those estimated using Prandtl's expression Tam (1995) for a free jet, as shown in Table 1. The shock-cell length $L_{\text{shock-cell}}$ is determined using Eq. (6)

$$L_{\text{shock}-\text{cell}} = 3.14 \frac{\sqrt{M_e - 1}}{2.405} D_{\text{fej}} \tag{6}$$

The fully expanded jet diameter D_{fej} is estimated from using Eq. (7) proposed by Tam and Tanna (1982),

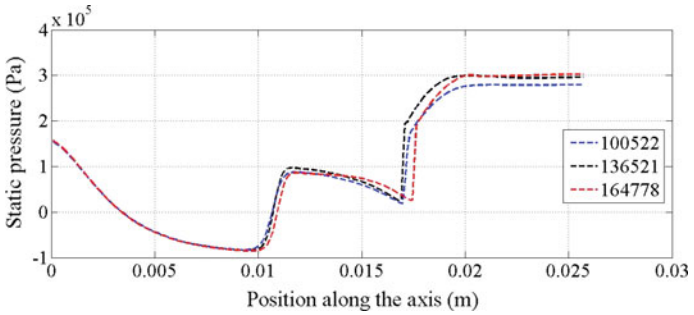

Fig. 3 Axial variation of static pressure of a partially covered Hartmann whistle ($L/D_j = 2.86$, $R = 5$, $S/D_j = 2.86$) for various grids showing grid sensitivity

$$D_{\text{fej}} = \left\{ \frac{1 + 0.5(\gamma - 1)M_e^2}{1 + 0.5(\gamma - 1)M_d^2} \right\}^{1.5} \left(\frac{M_d}{M_e} \right)^{1/2} D_j \tag{7}$$

The shock-cell length obtained from present computation show good agreement with the shock-cell length predicted by Edin et al. (2015) as well as those obtained using the analytical expression given by Tam (1995) within about 9%. The minor discrepancy observed between the frequency obtained from the present computation and those predicted by Edin et al. (2015) may be due to the difference in the two problems since Edin et al. (2015) simulated fully shielded Hartmann whistle, and the flow cannot exit out from the shield, whereas the present computation focuses in simulating the Hartmann whistle by covering it partially using a cylindrical shield so that the shield directs the flow to exit from the two controlled orifices (i) near the cavity mouth and (ii) away from the cavity mouth which can be used for effective flow control applications. The schematic of flow field around a cylindrical Hartmann whistle is shown in Fig. 4.

The Mach number contours obtained at $S/D_j = 2.86$, $L/D_j = 2.86$, $R = 5$ from predictions of a partially covered Hartmann whistle are compared with the corresponding shadowgraph image sequences of an un-shielded Hartmann whistle

Table 1 Comparison of length of the first shock-cell (L_{shock}/D_j) obtained from present simulation for a partially covered cavity ($S/D_j = 2.86$, $L/D_j = 2.86$ and $R = 5$) with shock-cell length predicted by Edin et al. (2015), and theory at the same parametric conditions

First shock-cell length (L_{shock}/D_j) from present computation at for partially covered cavity	First shock-cell length (L_{shock}/D_j) obtained for Edin et al. (2015) for fully shielded Hartmann	First shock-cell length (L_{shock}/D_j) from theory (Prandtl's expression)	% deviation between Edin et al. (2015) and present simulation	% deviation between theory and present simulation
1.91	1.84	2.09	3.8	8.61

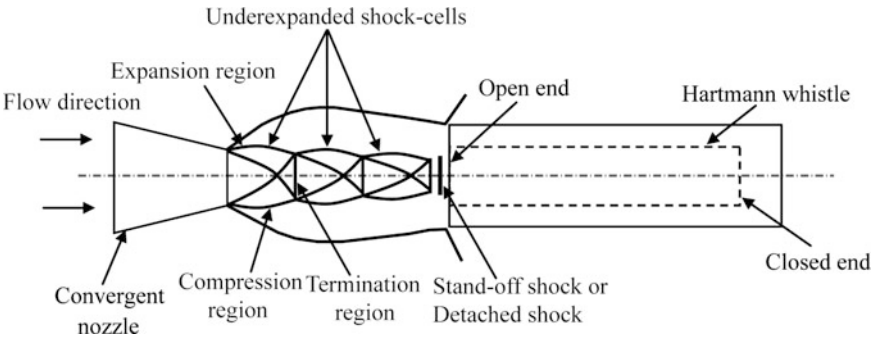

Fig. 4 Schematic of flow field around a cylindrical Hartmann whistle

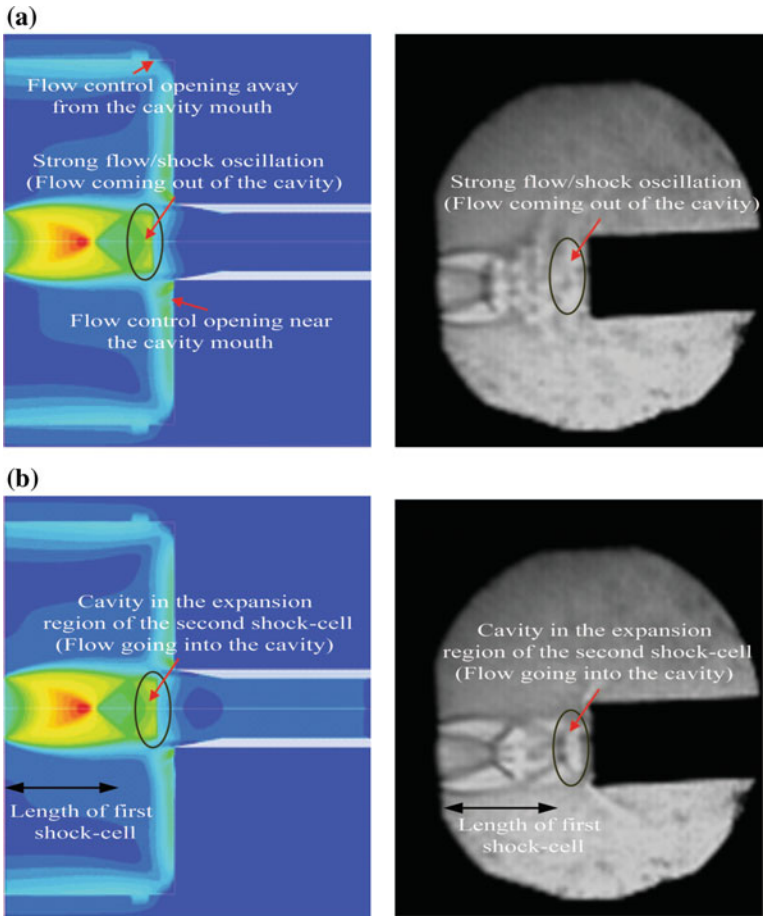

Fig. 5 Comparison Mach contours showing shock structures of a partially covered Hartmann whistle ($L/D_j = 2.86$, $R = 5$, $S/D_j = 2.86$) with the corresponding shadowgraph image sequences of un-shielded Hartmann whistle for the same relative time instances, **a** 6.45 ms, **b** 6.53 ms

roughly at the same relative time instances (Fig. 5). The flow/shock structures such as expansion, compression and termination regions of the underexpanded shock-cells as shown in Fig. 4, location of the Mach disk, regurgitant oscillations of the cavity etc. obtained from numerical predictions match very well with those observed in the shadowgraph image sequences, thus corroborates our numerical predictions.

3 Results and Discussions

3.1 Comparison of Mach Number Contours and Velocity Vectors for Different Standoff Distances

The comparison of Mach number contours and transient velocity vectors of a partially covered Hartmann whistle is shown in Fig. 6 in order to understand the modifications imparted to the flow/shock structure when cavity moves through different S/D_j values of 1.43, 2.86, and 4.28. When S/D_j is varied, the cavity passes through various zones (compression, expansion, and termination zones) of the underexpanded shock-cell structure. The compression and expansion regions of the shock-cell structure are clearly depicted in Fig. 6. The Mach number contour at small S/D_j value of 1.43 as shown in the left of Fig. 6a reveals the pattern of the shock structures in the flow field, where the cavity positions in the compression region of the first shock-cell. At this standoff distance, the complete expansion of the jet to form one full shock-cell is prevented by the cavity which makes the entire shock-cell formed to undergo severe oscillations thereby diverting most of the flow to exit through the control orifices positioned near and away from the cavity mouth thus eliminating the formation of conical oscillating shock near the cavity mouth. The velocity vector as shown in the right of the Fig. 6a depicts the corresponding flow direction patterns. Increase of S/D_j to 2.86 positions the cavity in the beginning of the expansion region of the second shock-cell (i.e., cavity mouth lies close to the termination region of the first shock-cell), thus permitting the formation of one full shock-cell as well as intense oscillating shock near the cavity mouth. The presents of oscillating shock may limit the pulsating flow through the control orifice thus providing an effective control. Further, increase of S/D_j to 4.28 puts the cavity in the expansion region of the third shock-cell, thus permitting the formation of one full shock-cell as mentioned earlier but reduces the strength of the oscillating shock near the cavity mouth thus providing weak regurgitant oscillations. The movement of cavity through various zones (i.e., compression, expansion and termination zones, etc.) of the shock-cells at different S/D_j's reveals the existence of resonant oscillations due to different operating modes of the cavity such as strong/weak regurgitant oscillations.

3.2 Effect of Standoff Distances on the Flow/Shock Characteristics of a Partially Covered Hartmann Whistle

The locations of shocks at different S/D_j values are shown in Mach number and static pressure plots (Fig. 7). The Mach number and static pressure plots as shown in Fig. 7a, b clearly show the absence of second oscillating shock at small S/D_j of 1.43 as compared to higher S/D_j's of 2.86 and 4.28 which exhibits an oscillating

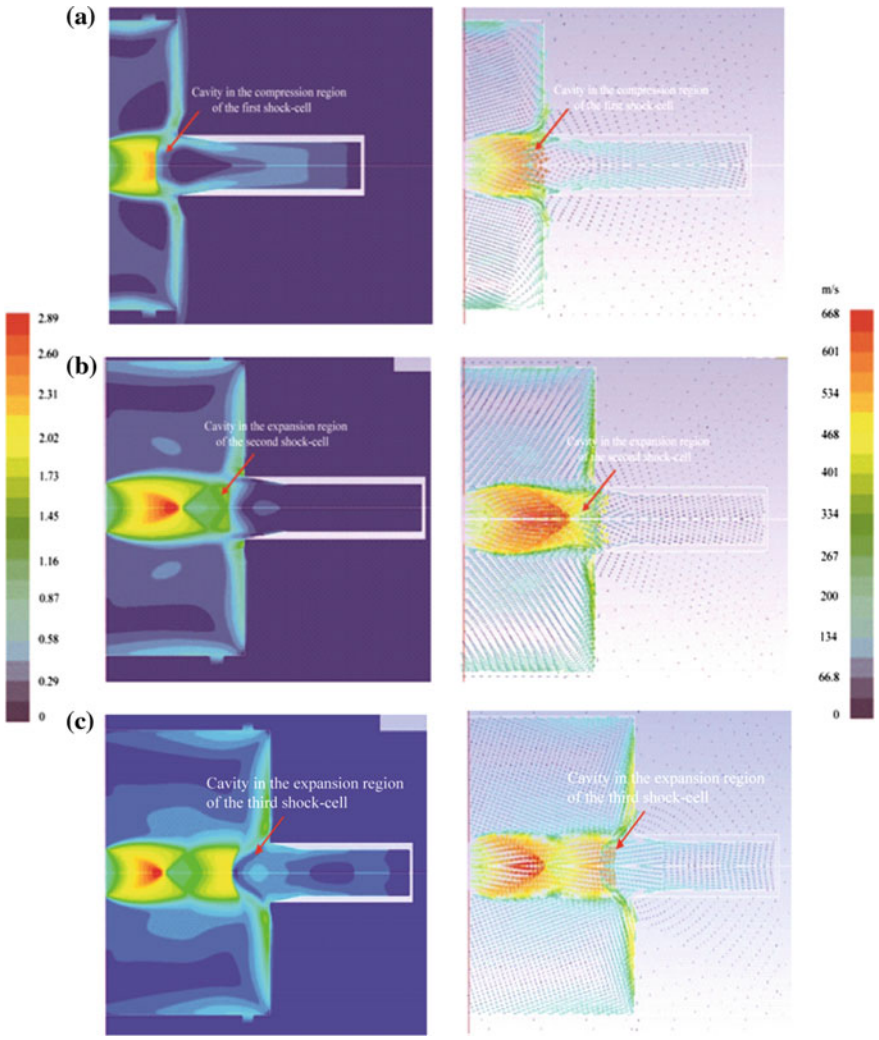

Fig. 6 Comparison of Mach number contours and transient velocity vectors of a partially covered Hartmann whistle (L/D_j = 2.86, R = 5) at S/D_j's of **a** 1.43, **b** 2.86, and **c** 4.28, for the same relative time instance of 7 ms

conical shock near the cavity mouth following the first shock-cell as shown in Fig. 7a, b. This shows that the regurgitant oscillations at small S/D_j (i.e., 1.43) are primarily due to the oscillations of the partially formed first shock-cell structure as shown in Fig. 7a, b, thus diverting most of the jet flow toward the control orifices. At higher S/D_j's of 2.86 and 4.28, the regurgitant oscillations are observed to be solely driven by the conical shock oscillating near the cavity mouth without causing much change in the location of the first shock as shown in Fig. 7a, b.

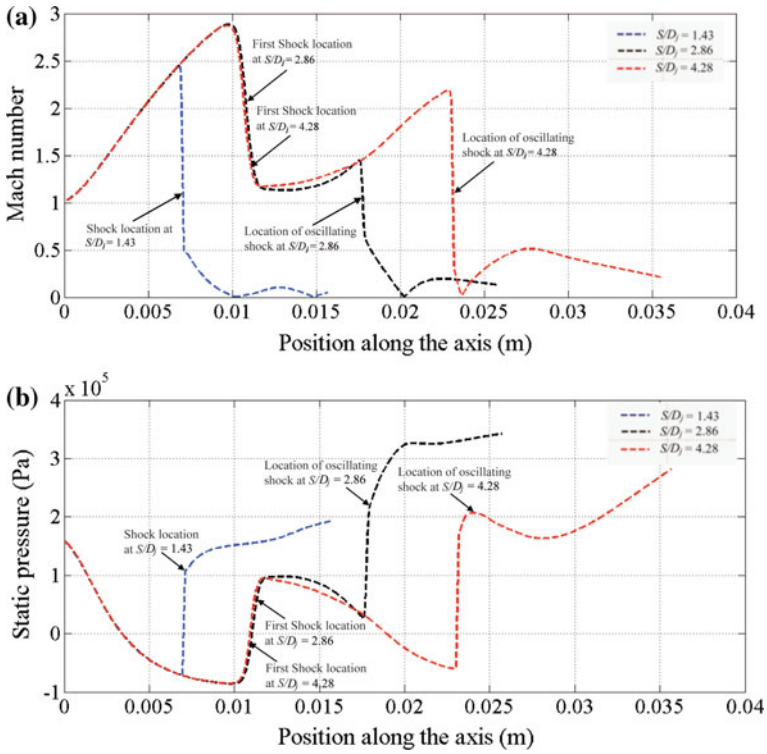

Fig. 7 Variation of Mach number and static pressure with position along the axis of a partially covered Hartmann whistle ($L/D_j = 2.86$, $R = 5$) at S/D_j's of **a** 1.43, **b** 2.86, and **c** 4.28, for the same relative time instance of 7 ms

4 Conclusions

A detailed computation of the interaction of the jet flow with a partially covered cylindrical Hartmann whistle was carried out to understand the shock as well as the regurgitant oscillation characteristics of a partially Hartmann whistle for various normalized standoff distances. The relevant parameters that modify the shock as well as regurgitant oscillations of the Hartmann whistle are the cavity standoff distance, nozzle pressure ratio, cavity length, cavity shield, etc. The computations were done for various values of normalized standoff distances S/D_j's of 1.43, 2.86, and 4.28 with cavity length, cylindrical shield height as well as nozzle pressure ratio as constant. The current study focuses on understanding the shock as well as regurgitant oscillation characteristics of the Hartmann whistle when the pulsating jet exits through the two small openings (i) near the cavity mouth and (ii) away from the cavity mouth by preventing the huge spillover. The modifications imparted to the shock as well as regurgitant oscillation features of partially covered Hartmann whistles are systematically compared using transient velocity vectors, Mach number

contours, etc. for various standoff distances. The velocity vectors show flow diversion features as well as inflow and outflow phases of the jet regurgitant oscillations. The Mach contours of partially shielded Hartmann whistles indicate the underexpanded shock-cell structure as well as the regions of flow deceleration and re-acceleration. It also shows that the resonant oscillations are chiefly driven by jet regurgitance at smaller standoff distances, but at higher standoff distances the resonant oscillations are primarily driven by the fluid column oscillations in the shock-cells, shield as well as in the cavity zones. Thus, the current computations reveal that the standoff distance is a key factor that controls the strength of shock, fluid column as well as regurgitant oscillations in a partially covered Hartmann whistle for achieving effective flow control.

References

Chang SM, Lee S (2001) On the jet regurgitant mode of a resonant tube. J Sound Vibr 246(4): 567–581

Edin M, Narayanan S, Abdul Jaleel H (2015) Numerical simulation of jet flow impinging on a shielded Hartmann whistle. Int J Aeronaut Space Sci 16(2):123–136

Gravitt JC (1959) Frequency response of an acoustic air-jet generator. J Acoust Soc Am 31 (11):1516–1518

Iwamoto J (1990) Experimental study of flow oscillation in a rectangular jet driven tube. Trans ASME J Fluids Eng 112(1):23–27

Spalart PR, Allmaras SR (1992) A one-equation turbulence model for aerodynamic flows, American Institute of Aeronautics and Astronautics, AIAA-92-0439

Tam CKW (1995) Jet noise generated by large-scale coherent motion. In: Hubbard HH (ed) Aeroacoustics of flight vehicles, theory and practice, vol 1. Acoustical Society of America, Melville, p 1095

Tam CKW, Tanna HK (1982) Shock associated noise of supersonic jets from convergent-divergent nozzles. J Sound Vib 81:337–358

Numerical Investigation of Hypersonic Flow Past a Spherically Blunted Nose Cone

Ashish Narayan, Rakesh Kumar and S. Narayanan

Abstract This paper numerically investigates the flow past a spherically blunted nose cone at a hypersonic Mach number of 5.8. The present study focuses in determining the flow/shock characteristics of the nose cone such as pressure coefficient, shock detachment distance and location and shape of bow shock formed ahead of the spherically blunted nose cone etc. The shock detachment distance, pressure coefficient, location and shape of bow shock in spherically blunted cones have numerous applications in the design of high speed aerodynamic vehicles such as space shuttles, missiles, rockets etc. The design of geometric parameters in hypervelocity vehicles are very important and are highly challenging for improving its performance and hence to alleviate the aerodynamic heating. The key parameters that play a significant role in affecting the aerodynamic characteristics of nose cone are semi-cone angle, bluntness ratios etc. Therefore, the present study focuses to investigate the effect of semi-cone angles of 5° and 20° and bluntness ratios of 0.4 and 0.8, in order to understand the aerodynamic performance characteristics of the spherically blunted nose cones. The velocity vector shows the flow direction which indicate clearly the deceleration near the nose, re-acceleration through the sideways of the nose cone as well the formation of recirculation zone behind the cone base. The shape and location of the bow shock formed ahead of the nose as well as the shock detachment distance is shown with the help of the Mach number contour. It is observed that the pressure coefficient decreases rapidly up to a certain distance along the wall and thereafter it remains almost constant for both the bluntness ratios (0.4 and 0.8) and semi cone angles (5° and 20°). It is observed that there is no significant variation in the shock detachment distance observed for both the bluntness ratios (0.4 and 0.8) and semi cone angles (5° and 20°) studied. In general, it is observed that increase in temperature is more for small semi cone angles and bluntness ratios and it decreases for higher bluntness ratios and cone angles. The

A. Narayan · R. Kumar · S. Narayanan (✉)
Department of Mechanical Engineering, IIT (ISM) Dhanbad,
Dhanbad 826004, Jharkhand, India
e-mail: snarayan.1979@gmail.com

A. Narayan
e-mail: ashishnarayan2007@gmail.com

M.K. Singh et al. (eds.), *Applications of Fluid Dynamics*, Lecture Notes
in Mechanical Engineering, https://doi.org/10.1007/978-981-10-5329-0_16

increase in temperature may be due to viscous dissipation which arises due to curved shocks which makes the flow rotational due to the existence of large entropy gradients. A minimum temperature is achieved for a bluntness ratio of 0.8 and 20° semi cone angle. Thus, this paper sufficiently demonstrates the effect of different bluntness ratios and semi cone angles on the aerodynamic as well as heating characteristics of a spherically blunted nose cone.

1 Introduction

The spherically blunted nose cones are amongst the configurations of interest with numerous applications in the design of high speed aerodynamic vehicles (i.e., entry vehicles) such as space shuttles, rockets etc. These configurations have been under investigation for the last few decades in order enhance the performance by reducing the drag and to alleviate the aerodynamic heating Ali et al. (2012). The shape of bow shock formed ahead of the nose cone, shock detachment distance etc. play a significant role in controlling the performance (i.e., drag reduction characteristics) of the nose cones. The generation of high temperature at the cone surfaces in re-entry vehicles due to aerodynamic heating forms one of the major design considerations of nose cone geometries. The prediction of aerodynamic drag and its reduction by making proper nose cone geometry is highly challenging. Some of the relevant literatures of flow past nose cones are given below.

Harris (1967) investigated the aerodynamic characteristics and the pressure distributions for a spherically blunted cone at 25° semi-cone angle and a bluntness ratio of 0.2. He observed that pressure coefficients determined using modified Newtonian theory showed good agreement with those obtained on the nose portion but it showed variance on the conical portion of the body. He also noticed that the results obtained with tangent-cone theory agreed well on the rearward portion of the conical body.

O'Bryant (1956) found that the shock standoff distance between the body and the bow shock formed ahead of a spherically blunted nose cone in hypersonic flow varies linearly with nose radius.

Menezes et al. (2005) experimentally investigated the effect of multi step base on the overall drag characteristics of a missile shaped body with a flat base configuration, at a hypersonic Mach number of 5.75. It was observed that the after body with multi step base showed about 8% reduction in the overall drag as compared to the flat base configuration.

Albeit several researchers have investigated the flow past a spherically blunted nose cone at hypersonic Mach numbers but the detailed computational study to compare the effect of different parameters such as semi-cone angles (5° and 20°) and bluntness ratios (0.4 and 0.8) on the aerodynamic behaviors (i.e., flow/shock) such as drag, pressure coefficient, detachment distance etc. are scarce. Thus, an exhaustive numerical simulation is carried out in the current study to predict the aerodynamic characteristics of spherically blunted nose cones of different configurations, which forms the key objective of the present study.

2 Computational Domain and Grid

The physical geometry, domain of computation, and boundary conditions for the problem are shown in Fig. 1. The computational domain (Fig. 1) is fixed as 600 and 420 mm in the axial and radial directions in order to capture the complex flow/shock structures and the aerodynamic characteristics. The grid is constructed using ANSYS CFD. The computational grid with varying mesh size is shown in Fig. 2. Fine grids were used in the regions of large gradients so as to accurately capture the complex shock structures. A steady axisymmetric simulation is carried out using the commercial software ANSYS FLUENT 15 with an implicit density based solver. The fluid is considered as a compressible (i.e., ideal gas) for the present simulations with no slip boundary condition enforced at the walls. A total of about 150,000 cells are used in the present simulations. The simple one equation Spalart-Allmaras turbulence model with standard values of model constants (σ_v = 2/3, C_{b1} = 0.1355, C_{b2} = 0.622, k = 0.42, C_{w1} = 3.21, C_{w2} = 0.3, C_{w3} = 2.0, C_{v1} = 7.1) are used for modelling turbulence. The Spalart-Allmaras turbulence model is essentially intended for aerodynamic applications generally observed in high speed flows past airfoils, boundary-layers etc. Also, this one equation model has been observed to give good results with reduced computational time for problems involving wall bounded flows as well as boundary layers subjected to adverse pressure gradients Spalart and Allmaras (1992).

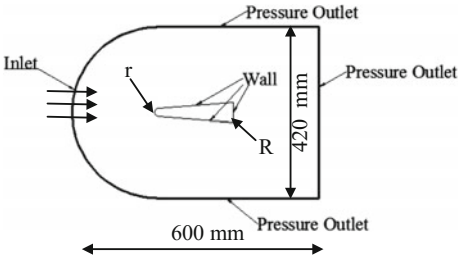

Fig. 1 Computational domain

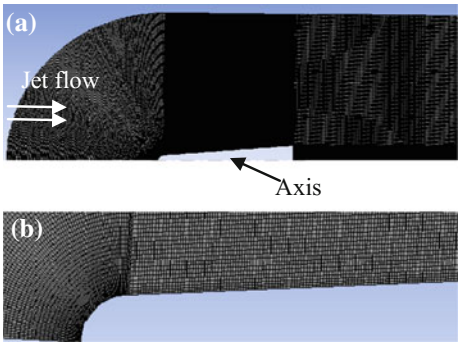

Fig. 2 **a** Computational grid. **b** Enlarged view of the grid near the nose cone

2.1 Governing Equations

The 2D steady axisymmetric governing equations which control the occurrence of the physical phenomena when a hypersonic flow past a nose cone are as follows.

2.1.1 Mass Conservation Equation

$$\frac{\partial}{\partial x}(\rho u_x) + \frac{\partial}{\partial r}(\rho u_r) + \frac{\rho u_r}{r} = 0 \tag{1}$$

where, x is the axial coordinate, r is the radial coordinate, u_x is the axial velocity, u_r is the radial velocity.

2.1.2 Axial Momentum Conservation Equation

$$\begin{aligned}\frac{1}{r}\frac{\partial}{\partial x}(r\rho u_x u_x) + \frac{1}{r}\frac{\partial}{\partial r}(r\rho u_r u_x) = &-\frac{\partial p}{\partial x} + \frac{1}{r}\frac{\partial}{\partial x}\left[r\mu\left(2\frac{\partial u_x}{\partial x} - \frac{2}{3}(\nabla\cdot\vec{u})\right)\right] \\ &+ \frac{1}{r}\frac{\partial}{\partial r}\left[r\mu\left(2\frac{\partial u_x}{\partial r} + \frac{\partial u_r}{\partial x}\right)\right] + F_x\end{aligned} \tag{2}$$

2.1.3 Radial Momentum Conservation Equation

$$\begin{aligned}\frac{1}{r}\frac{\partial}{\partial x}(r\rho u_x u_r) + \frac{1}{r}\frac{\partial}{\partial r}(r\rho u_r u_r) = &-\frac{\partial p}{\partial r} + \frac{1}{r}\frac{\partial}{\partial x}\left[r\mu\left(\frac{\partial u_r}{\partial x} + \frac{\partial u_x}{\partial r}\right]\right. \\ &+ \frac{1}{r}\frac{\partial}{\partial r}\left[r\mu\left(2\frac{\partial u_r}{\partial r} - \frac{2}{3}(\nabla\cdot\vec{u})\right)\right] - 2\mu\frac{u_r}{r^2} + \frac{1}{r}\frac{\partial}{\partial r}\left[r\mu\left(2\frac{\partial u_r}{\partial r} - \frac{2}{3}(\nabla.\vec{u})\right)\right] - 2\mu\frac{u_r}{r^2}\end{aligned} \tag{3}$$

where,

$$\nabla.\vec{u} = \frac{\partial u_x}{\partial x} + \frac{\partial u_r}{\partial r} + \frac{u_r}{r}$$

F_x and F_r comprises external body forces, model-dependent sources terms as well as user-defined sources, u_z is the swirl velocity.

2.1.4 Energy Conservation Equation

$$\frac{\partial}{\partial t}(\rho E) + \nabla.\left(\vec{u}(\rho E + p)\right) = \nabla.\left(k_{\text{eff}}\nabla T - \sum\nolimits_j h_j\vec{J}_j + (\bar{\bar{\tau}}_{\text{eff}}.\vec{u})\right) \tag{4}$$

here, k_{eff} is the effective thermal conductivity ($k_{\text{eff}} = k + k_t$). The first three terms on the right-hand side of Eq. (4) represent energy transfer by conduction, species diffusion ($\vec{J}_j$ represents diffusion flux of species j) and viscous dissipation. In the current study the second term on the right hand side is zero since there is no diffusion of species.

2.1.5 Equation of State

$$p = \rho R_c T. \tag{5}$$

2.2 *Grid-Sensitivity Study*

The type and number of grids used in the simulation significantly influences the accuracy of the numerical predictions and hence it becomes extremely important to do grid-sensitivity test before going for the productive simulations. Therefore, the grid sensitivity studies were carried out by varying the number of cells as: 150,000, 175,000 and 200,000. The variation of Mach number with position along the axis for various grids for $r/R = 0.2$ at 5° is shown in Fig. 3 showing grid sensitivity. The study revealed that the current results obtained with 150,000 cells are almost invariant to further grid refinement. Further, the boundary layer near the wall of the nose cone is resolved by restricting the maximum wall $y+$ value within about 4.

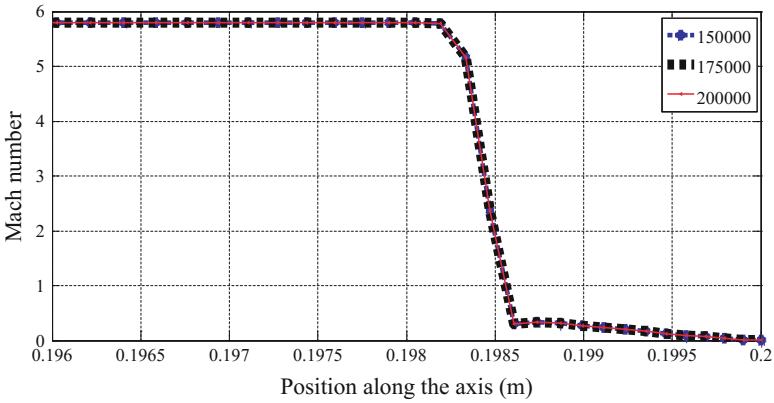

Fig. 3 Axial variation of Mach number with position along the axis for various grids showing grid sensitivity

Table 1 Comparative study of maximum pressure coefficient value for analytical and numerical at 5° semi cone angle for bluntness ratio 0.4 & 0.8

S. No.	*r*/*R* ratio at 5°	Analytical value of pressure coefficient	Numerical value of pressure coefficient	% error
1	0.4	1.81	1.83	1.1
2	0.8	1.81	1.81	–

Table 2 Comparative study of maximum pressure coefficient value for analytical and numerical at 20° semi cone angle for bluntness ratio 0.4 & 0.8

S. No.	*r*/*R* ratio at 20°	Analytical value of pressure coefficient	Numerical value of pressure coefficient	% error
1	0.4	1.81	1.83	1.1
2	0.8	1.81	1.81	–

2.3 Validation

In order to ensure that the predictions are right, the maximum pressure coefficient for (r/R = 0.4 and 0.8) and cone angles (5° and 20°) at M = 5.8, obtained from the present computations is compared with Allen and Eggers (1953), Menezes et al. (2005), and O'Bryant (1956) (Eq. 6) in Tables 1 and 2 for two different cone angles of 5° and 20°. The $C_{p,\max}$ obtained from present computation (r/R = 0.4 and 0.8) and cone angles (5° and 20°) show excellent agreement with those predicted by Harris (1964), Harris (1967), and Wells and Armstrong (1962) (Eq. 6) within about 1%.

$$c_{p,\max} = \frac{\gamma+3}{\gamma+1}\left[1 - \frac{2}{M_\infty^2(\gamma+3)}\right]. \tag{6}$$

3 Results and Discussions

3.1 Variations of Pressure Coefficient and Mach Number with Position Along the Axis for Different Bluntness Ratios and Semi Cone Angles

The variation of pressure coefficient on the wall with distance is shown in Figs. 4 and 5 for different cone angles (5° and 20°) at bluntness ratios of 0.4 and 0.8. It is noticed that pressure coefficient decreases hastily up to a certain distance along the wall and thereafter it remains almost constant, for the bluntness ratios and cone angles studied. Another striking feature observed here is that the maximum pressure coefficient of around 1.8 obtained at the nose is almost independent of bluntness ratios and cone angles. Also it is observed that the large cone angles possess higher value of pressure coefficients as compared to smaller ones for all the bluntness ratios studied even though their maximum pressure coefficients are same Harris (1967).

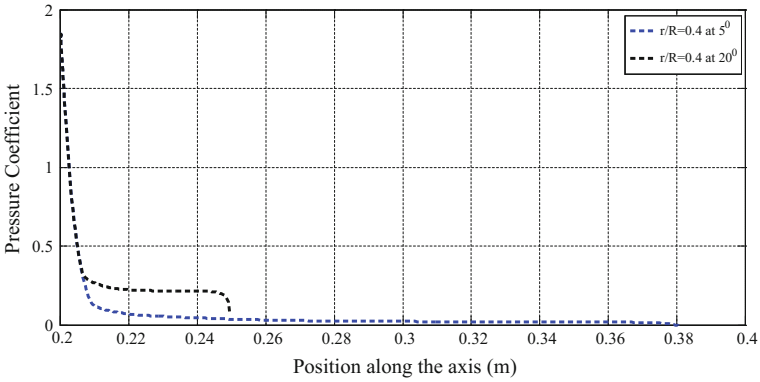

Fig. 4 Variation of pressure coefficient on the wall at 5° and 20° for r/R = 0.4

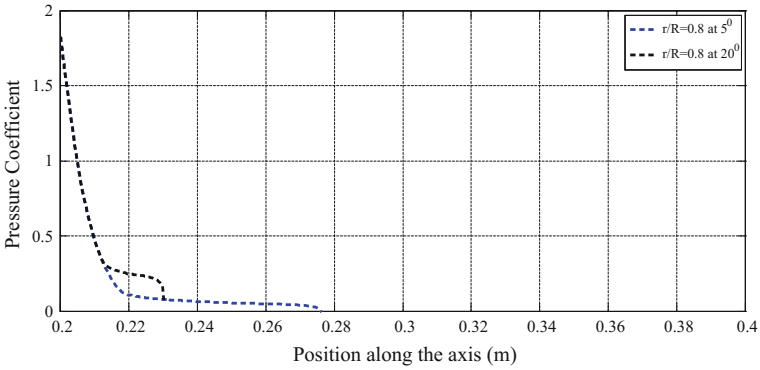

Fig. 5 Variation of pressure coefficient on the wall at 5° and 20° for r/R = 0.8

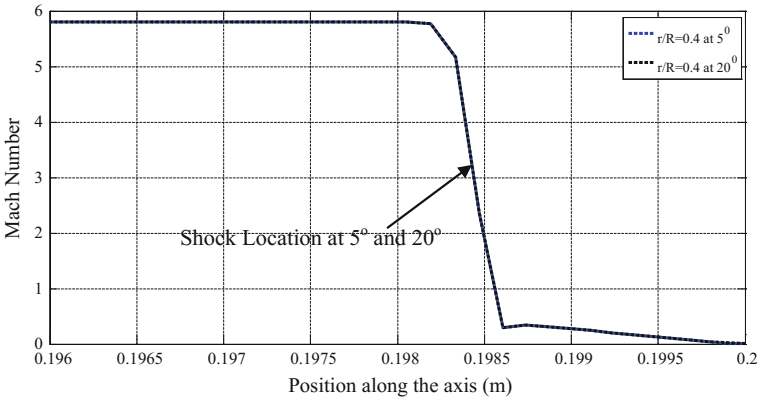

Fig. 6 Variation of Mach number with position along the axis for 5° and 20° at r/R 0.4

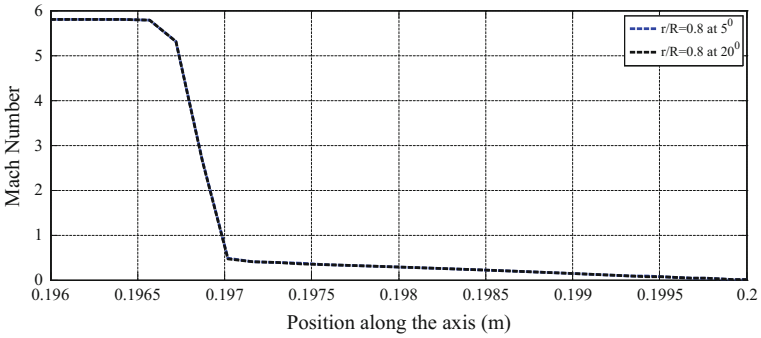

Fig. 7 Variation of Mach number with position along the axis for 5° and 20° at *r*/*R* 0.8

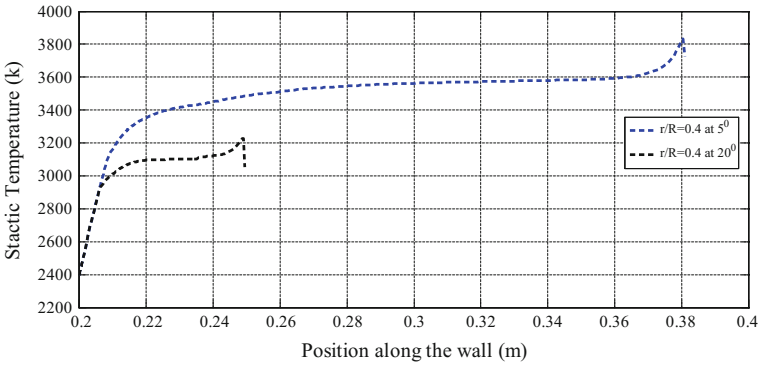

Fig. 8 Variation of static temperature on the wall at 5° and 20° for $r/R = 0.4$

The variation of Mach number with position along the axis for different cone angles (5° and 20°) at bluntness ratios of 0.4 and 0.8 is shown in Figs. 6 and 7. It is observed that the shock detachment distance increases with increase in cone angles for both the bluntness ratios studied. It is seen that for both the *r*/*R* values the shock is steeper at smaller cone angles as compared to larger ones. Thus, the current study reveals that the shock detachment distance is observed to be a strong function of bluntness ratios and cone angles.

3.2 Variations of Temperature with Position Along the Wall of a Spherically Blunted Nose Cone for Different Bluntness Ratios and Semi Cone Angles

The variation of temperature with position along the wall of a spherically blunted cone is shown in Figs. 8 and 9 for various bluntness ratios (a) 0.2 (b) 0.4 at different semi cone angles (θ_c = 5° and 20°). The increase of fluid temperature (due to

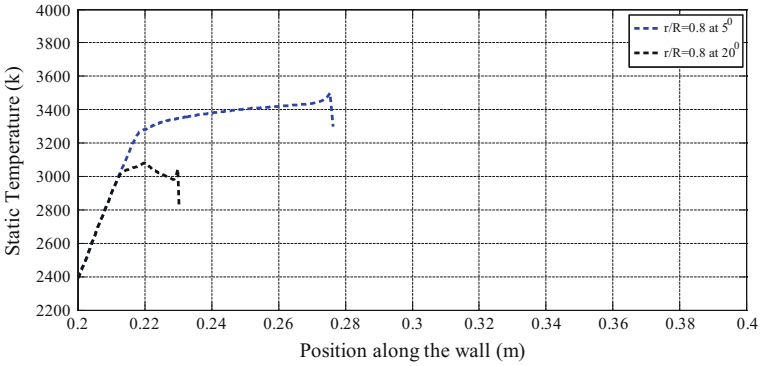

Fig. 9 Variation of static temperature on the wall at 5° and 20° for $r/R = 0.8$

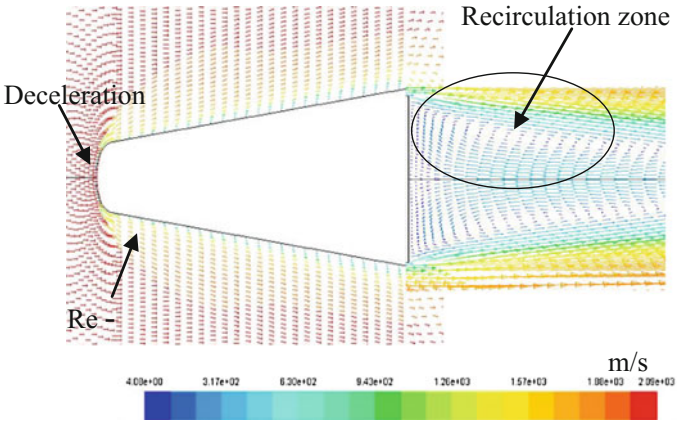

Fig. 10 Velocity vector

friction heat) is due to the conversion of kinetic energy of the flow into thermal energy via a process called viscous dissipation. The static temperature increases hastily and attains a maximum value and thereafter it follows decreasing trend for all bluntness ratios and semi cone angles studied Allen and Eggers (1953).

3.3 Numerical Prediction of Flow/Shock Structures Around a Spherically Blunted Nose Cone

In order to understand flow/shock features clearly the velocity vector and Mach contour for $r/R = 0.2$, semi cone angle 5°, is shown in Figs. 10 and 11. The velocity vector (Fig. 10) clearly depicts the flow features such as deceleration near the nose

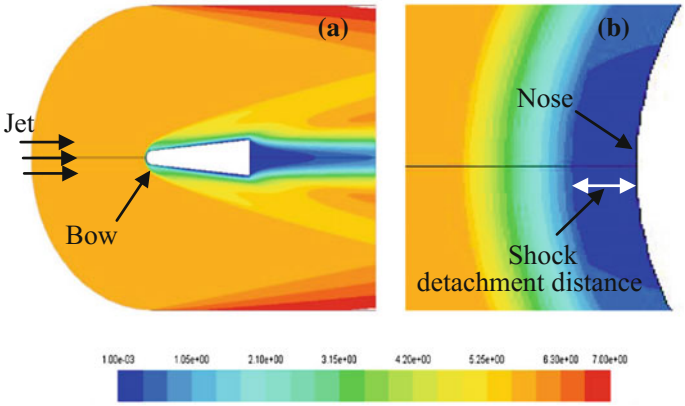

Fig. 11 **a** Mach number contour. **b** Enlarged view of Mach contour showing shock detachment distance

and re-acceleration through the sideways of the spherically blunted nose cone. It also reveals the formation of recirculation zone behind the base of the nose cone. The Mach number contour (Fig. 11) shows the shape and location of bow shock formed ahead of the nose cone. The enlarged view of Mach contour (Fig. 11b) depicts the shock detachment distance.

4 Conclusions

A detailed computational study was conducted to study the influence of different nose cone parameters such as semi-cone angles, bluntness ratios on the aerodynamic characteristics of the spherically blunted nose cones at a mach number of 5.8. the two different bluntness ratios (0.4 and 0.8) and semi-cone angles (5° and 20°) are investigated in the current study to determine the influence of nose cone parameters on the aerodynamic characteristics such as pressure coefficient, shock detachment distance, static temperature, location and shape of bow shock etc., which finds huge applications in the design of entry vehicles such as space shuttles, missiles etc. the velocity vector (Fig. 10) obtained from the preliminary studies represents the flow deceleration ahead of the nose followed by re-acceleration through the sideways. It also portrays the existence of flow recirculation behind the nose cone. The detachment distance as well as the structure of bow shock formed ahead of the nose cone is well represented by the Mach number contour (Fig. 11). The current study reveals that the pressure coefficient shows a sharp decrease up to a certain distance along the wall thereafter it follows a constant behavior. There is no significant variance in the shock detachment distance is observed for the semi cone angles (5° and 20°) and bluntness ratios (0.4 and 0.8) studied. It is observed that the static temperature

increases with increase in distance along the wall. Further, the increase in static temperature is observed to be higher for smaller semi cone angles and bluntness ratios whereas it decreases for higher bluntness ratios and cone angles. The increase in static temperature may be due to viscous dissipation near the wall as well as due to the curved shocks which makes the flow rotational due to the existence of large entropy gradients. Thus, this paper sufficiently demonstrates the effect of different nose cone geometries (semi cone angles and bluntness ratio) on the aerodynamic as well as heating characteristics of a spherically blunted nose cone.

References

Ali AS, Husain M, Qureshi NM (2012) Effects of nose-bluntness ratio on aerodynamic performance for re-entry vehicle. J Space Technol 1(1):38–41

Allen JH, Eggers JA (1953) A study of the motion and aerodynamic heating of ballistic missiles entering the earth's atmosphere at the high supersonic speeds, Report 1381

Harris EJ (1964) Force-coefficient and moment-coefficient correlations and air-helium simulation for spherically blunted cones, NASA TN D-2184

Harris EJ (1967) Aerodynamic characteristics of a spherically blunted 25° cone at a mach number of 20. National aeronautics and space administration. NASA TN D-4098

Menezes V, Kumar S, Maruta K, Reddy KPJ, Takayama K (2005) Hypersonic flow over a multi-step after body. J Shock Waves 14(5/6):421–424

O'Bryant TW (1956) An experimental investigation of hypersonic flow an over blunt nosed cone at Mach number of 5.8

Spalart PR, Allmaras SR (1992) A one-equation Turbulence Model for Aerodynamic Flows, American Institute of Aeronautics and Astronautics, AIAA-92-0439

Wells WR, Armstrong WO (1962) Tables of aerodynamic coefficients obtained from developed newtonian expressions for complete and partial conic and spheric bodies at combined angles of attack and sideslip with some comparisons with hypersonic experimental data. NASA TR R-127

Numerical Investigation of Subsonic Flow Past a Flat Plate Aerofoil

Shailesh Kumar Jha, S. Narayanan and L.A. Kumaraswamidhas

Abstract The present work numerically investigates the effect of two different trailing edge geometries such as sharp as well as blunt on the aerodynamic characteristics of a flat plate aerofoil. The modifications in the flow as well as aerodynamic characteristics of sharp and blunted trailing edge configurations of a flat plate aerofoil are systematically compared using pressure coefficient, lift coefficient, vortex shedding, etc. The study was conducted for a chord-wise Reynolds number of 4.99×10^5 at an angle of attack of 25°. The large difference in the pressure coefficient observed between the top and bottom surface in the case of blunt trailing edge as compared to sharp ones indicates that the blunted trailing edge geometry generates higher lift than the sharp trailing edge ones. It is observed from spectra that the vortex shedding for both the blunted and sharp trailing edge geometries occurs at a Strouhal number of around 0.34. The increase of energy as well as broader wake in the blunted trailing edge geometry indicates higher drag as compared to the sharp trailing edge geometry. Thus, this paper sufficiently demonstrates the effect of sharp and blunted trailing edge geometries on the aerodynamic characteristics of a flat plate aerofoil.

List of Symbols

BS	Bottom surface
BTE	Blunt trailing edge
c	Chord length of the flat plate airfoil (m)
C_d	Coefficient of drag
C_l	Coefficient of lift
St	Strouhal number (fc/U)

S.K. Jha (✉) · S. Narayanan
Department of Mechanical Engineering, Indian Institute of Technology (Indian School of Mines), Dhanbad 826004, Jharkhand, India
e-mail: shailesh26jha@gmail.com

L.A. Kumaraswamidhas
Department of Mining Machinery Engineering, Indian Institute of Technology (Indian School of Mines), Dhanbad, Dhanbad 826004, Jharkhand, India
e-mail: lakdhas1978@gmail.com

M.K. Singh et al. (eds.), *Applications of Fluid Dynamics*, Lecture Notes in Mechanical Engineering, https://doi.org/10.1007/978-981-10-5329-0_17

STE Sharp trailing edge
TS Top surface
U Free stream velocity (m/s)
α Geometric angle of attack (degrees)
X Position along the chord (m)

1 Introduction

The flow past bluff bodies have been investigated by the several researches for the past few decades due to its immense applications in aviation, mechanical, civil, etc., such as flow past an aircraft wing, flow over tube bundles in heat exchangers, and around bridges. From fluid mechanics viewpoint, the flow over bluff body comprises several corporal phenomena such as vortex formation, vortex shedding, flow separation. Lam and Wei (2010) studied the physics behind fluctuating lift and drag of the inclined flat plate aerofoil and developed a correlation between fluctuating aerodynamic forces and vortex shedding. Yang et al. (2012) investigated the asymmetric wake patterns behind the flat plate inclined in the post-stall domain. They found the strengths of the vortices from the trailing and leading edges and determined that the intrinsic instability in a fluid is due to low angle of attack rather than low Reynolds number (Re). Grid-generated turbulence effect on sectional lift force over circular cylinder has been studied by Blackburn and Melbourne (1996). They found that in low-intensity turbulence flow the vortices are disorganised while they found organised vortices in high turbulence intensity flow. Vortex shedding behind a long flat plate at various incidence angles was experimentally studied by Lam and Leung (2005). They found a train of vortices from leading and trailing edges behind the flat plate airfoil. They also observed that trailing edge vortex has higher peak vorticity level at its center and induces more fluid circulation with high Reynolds stress than the leading edge vortex. Even though several studies on flat plate aerofoils are available a detailed comparative study to understand the flow and aerodynamic characteristics such as pressure coefficient, vortex shedding mechanisms, wake profiles on two different flat plate trailing edge configurations such as sharp and blunt to determine the geometry for better performance are scarce which forms the specific objective of the current study.

2 Computational Domain, Boundary Condition, and Grid

The physical geometry, computational domain, and boundary conditions for the present study were shown in Fig. 1. The computational domain (Fig. 1) was kept as −6c and 14c in the stream-wise direction and ±5c normal to the stream-wise direction. The structured grid (Fig. 2) with varying mesh size was constructed using ANSYS CFD. Fine grids were used near flat plate aerofoil where the flow effects are significant in order to resolve the boundary layer properly and grids were made uncouth in those regions where flow effects are absent. The computations were done using pressure-based implicit solver. The fluid was considered as incompressible (i.e., constant density) in the present computation. The one-equation Spalart and Allmaras (1992) turbulence model with standard values of model constants ($\sigma_v = \frac{2}{3}$, $C_{b1} = 0.1355$, $C_{b2} = 0.622$, $k = 0.42$, $C_{w1} = 3.21$, $C_{w2} = 0.3$, $C_{w3} = 2.0$, $C_{v1} = 7.1$) was used for present computation. Spalart and Allmaras (1992) mode is fairly a simple one-equation model and has been shown to give good results for problems involving wall bounded flows as well as boundary layers subjected to unfavorable pressure gradients with reduced computational time.

2.1 Governing Equations

The 2D incompressible flow equations for the flow past a flat plate airfoil is given below.

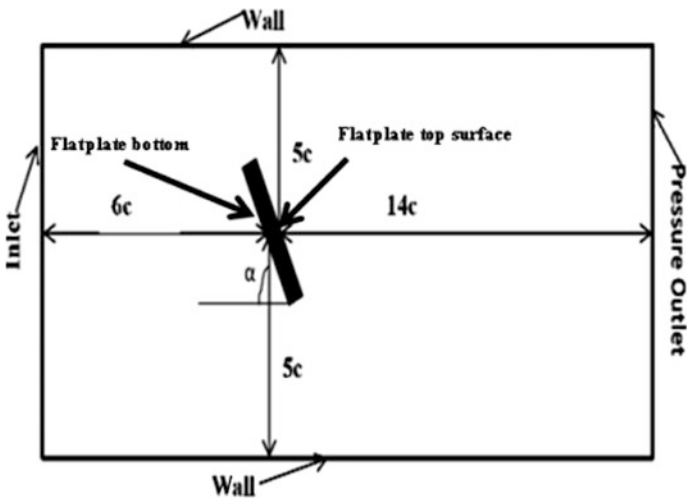

Fig. 1 Computational domain

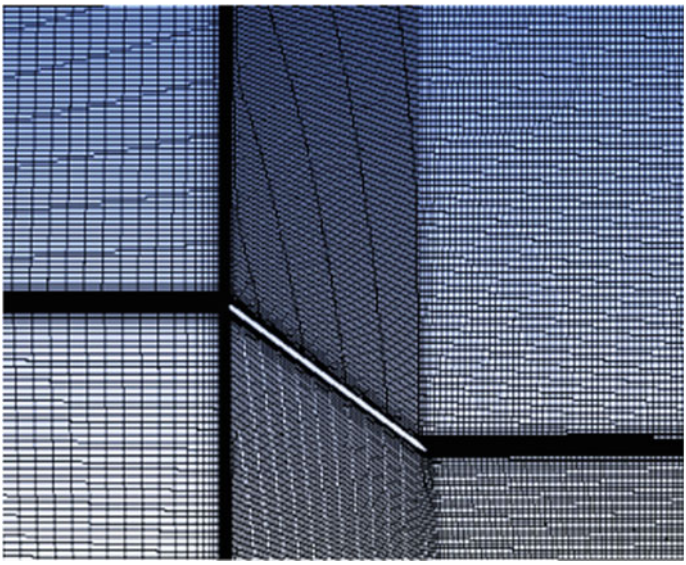

Fig. 2 Computational grid

2.1.1 Mass Conservation Equation

The equation for conservation of mass can be written as follows:

$$\frac{\partial u}{\partial x} + \frac{\partial v}{\partial y} = 0 \tag{1}$$

where, u, v are velocity along x- and y-axis, respectively.

2.1.2 Momentum Conservation Equation

(a) **Along x-axis**

$$\frac{\partial u}{\partial t} + \frac{\partial (u^2)}{\partial x} + \frac{\partial (uv)}{\partial y} = -\frac{1}{\rho}\frac{\partial P}{\partial x} + \upsilon\left(\frac{\partial^2 u}{\partial x^2} + \frac{\partial^2 u}{\partial y^2}\right) \tag{2}$$

(b) **Along y-axis**

$$\frac{\partial v}{\partial t} + \frac{\partial (uv)}{\partial x} + \frac{\partial (v^2)}{\partial y} = -\frac{1}{\rho}\frac{\partial P}{\partial x} + \upsilon\left(\frac{\partial^2 v}{\partial x^2} + \frac{\partial^2 v}{\partial y^2}\right) \tag{3}$$

where, u, v are velocity along x- and y-axis, respectively, P is the pressure, ρ is the fluid density which is constant for the present work since flow is considered as incompressible and υ is the kinematic viscosity of the fluid.

2.2 Validation

The variation of pressure coefficient with position along the wall of the flat plate aerofoil obtained from present computation is compared with those of Yang et al. (2012) in Fig. 3 for the same parametric conditions. It clearly shows the pressure coefficient obtained from the present computation on both the top and bottom surface of the flat plate aerofoil matches very well with those given by Yang et al. (2012). Also the comparison of C_l, C_d values obtained from the present computation for 20° and 30° angles of attack show reasonably good agreement with those given by Lam and Wei (2010) and are compared in Tables 1 and 2.

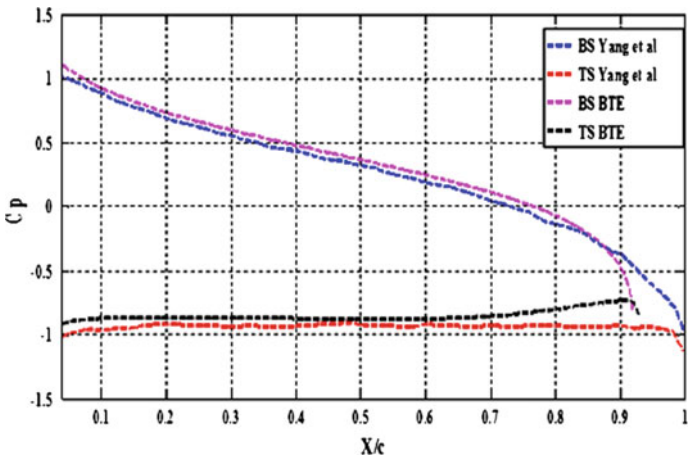

Fig. 3 Distribution of pressure coefficient C_p along the plate surface inclined at $\alpha = 25°$, obtained from two-dimensional simulation of present work and three-dimensional simulation by Yang et al. (2012)

Table 1 Comparison of present study lift coefficient value with the value obtained by Lam and Wei (2010)

α	C_l (present CFD data)	C_l (Lam and Wei)	Error (%)
20°	3.02	3.24	7.28%
30°	2.98	3.02	1.34

Table 2 Comparison of present study drag coefficient value with the value obtained by Lam and Wei (2010)

α	C_d (present CFD data)	C_d (Lam and Wei)	Error (%)
20°	1.17	1.20	3
30°	1.72	1.76	4

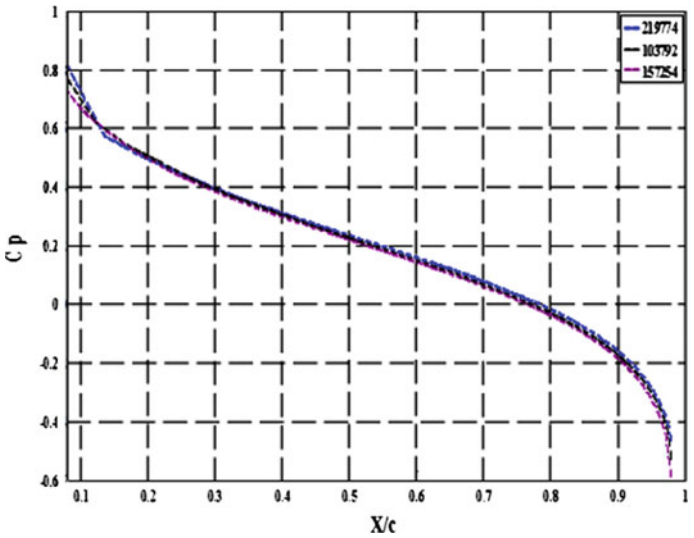

Fig. 4 Variation of pressure coefficient with position along the length of the plate for various grids showing grid sensitivity

2.3 Grid Independence Study

The grid sensitivity test was carried out by varying the number of cells as: 103,792, 157,254, and 219,774 and found that the current results obtained with 103,792 cells are almost invariant to further grid refinement. The variation of pressure coefficient with position along the length of the flat plate is shown in Fig. 4 representing grid sensitivity.

3 Results and Discussions

3.1 Variation of Pressure Coefficient with Position Along the Length of the Flat Plate for Different Trailing Edge Geometry

The variation of pressure coefficient with position along the length for different trailing edge geometry is shown in Fig. 5. The difference in the pressure coefficient of top and bottom surface is higher in the case of blunt trailing edge as compared to sharp ones, and this difference decreases with increase in distance along the chord. Another striking feature observed here is that the C_p at the bottom surface of both sharp and blunt geometries falls rapidly from a maximum value to minimum where it is almost constant for both the trailing edge geometries at the top surface. Thus, it reveals that the lift generation will be more for blunt trailing edge as compared to sharp ones.

3.2 Power Spectral Density

The frequency spectra of the lift coefficient fluctuation over the top surface of the plate for different trailing edge geometry are shown in Fig. 6. For blunt trailing edge, two peaks (a) are observed with low variation while sharp trailing edge has single peak (b). The vortex shedding for both the blunted and sharp trailing edge geometries occurs roughly at a Strouhal number of around 0.34 and is indicated in Fig. 6. Spectra of blunted trailing edge show more energy up to a Strouhal number

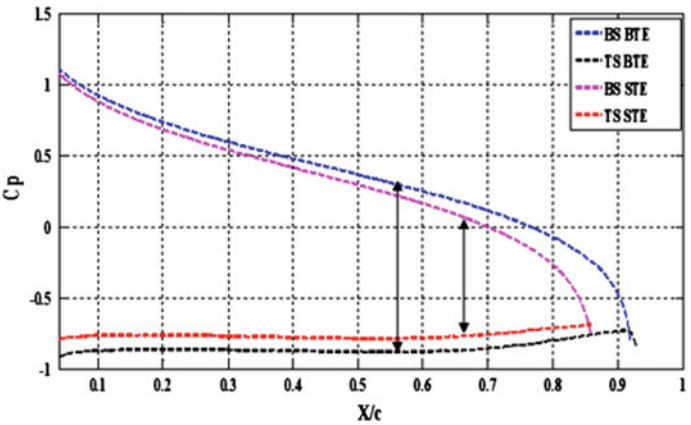

Fig. 5 Variation of pressure coefficient with position along the length of the plate for different trailing edge geometry at 2.281 s

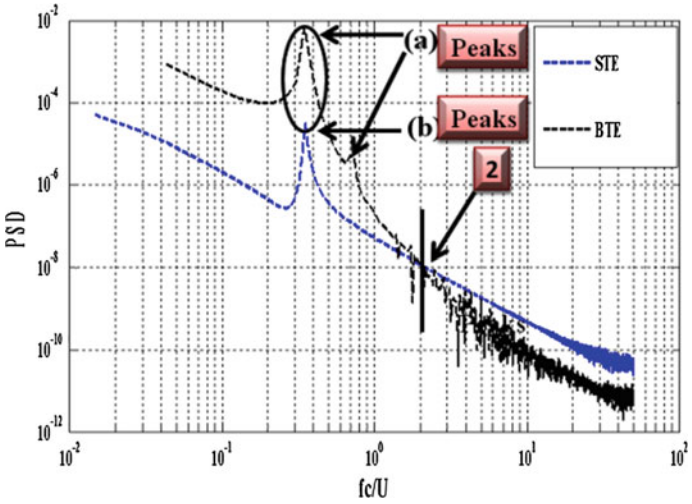

Fig. 6 Spectra of fluctuating lift coefficient at U = 5 m/s, AOA = 25°

of 2 thereafter it falls below the sharp trailing edge geometry. The increase of energy in the blunted geometry as compared to sharp ones represents broader wake and higher drag which is discussed in the following section.

3.3 Velocity Vector for Blunt and Sharp Trailing Edge Geometry

The comparison of velocity vectors between blunted and sharp trailing edge geometries are shown in Fig. 7. It is seen that a set of counter-rotating vortices are formed from leading and trailing edges of the blunt and sharp trailing edge geometries. The size of the vortex generated from the leading edge is large compared to those generated from the trailing edge for both the blunt and sharp geometries as shown in Fig. 7. More vortices are generated from trailing edge of blunt which leads to high drag than the sharp edge.

3.4 Wake Velocity Profiles for Sharp and Blunted Trailing Edge Configurations

The variation of wake profile showing velocity deficit for blunted and sharp trailing edge configuration is shown in Fig. 8. It is observed that the velocity deficit is more for blunted trailing edge than sharp ones which indicates more drag in blunted

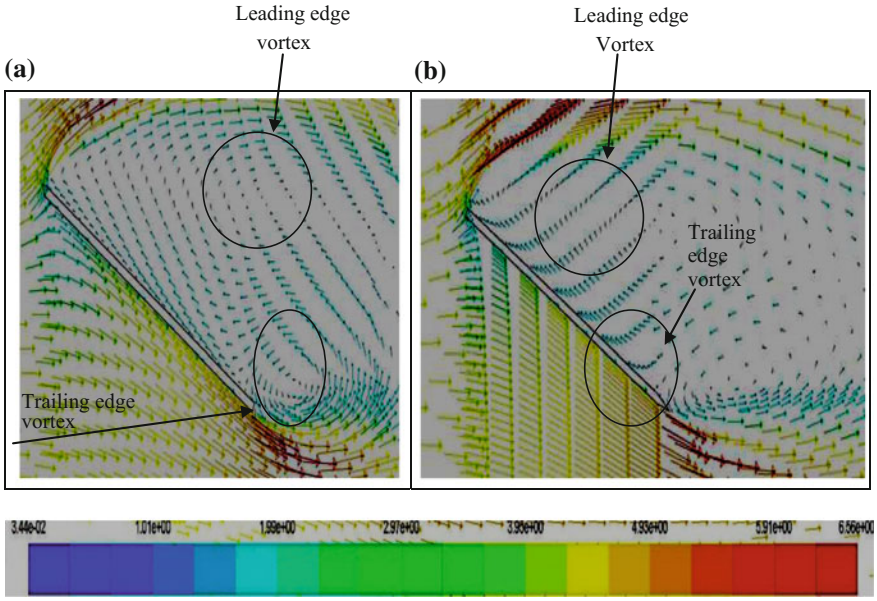

Fig. 7 Velocity vectors showing vortex shedding in **a** BTE, and **b** STE flat plate at 1.37 s

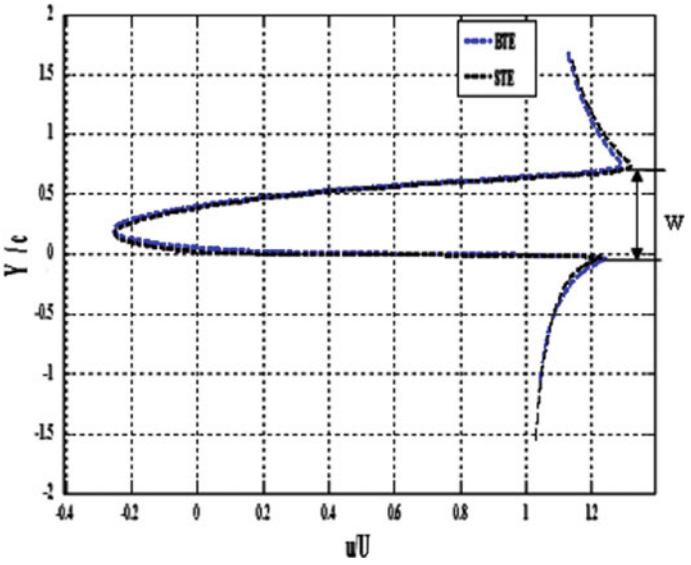

Fig. 8 Wake velocity profile for BTE and STE geometry at 2.281 s

geometry. This is further confirmed by determining the wake width which is given below. The width of the wake (W) for blunted trailing edge geometry is around 0.1185 m, whereas it is about 0.1094 m for sharp ones. The increase of wake width in blunted trailing edge geometry indicates that it generates broader wake than sharp ones. The presence of broader wake in the blunted geometry represents that it generates higher drag as compared to the sharp ones.

4 Conclusions

A detailed numerical study was conducted to understand the effect of different trailing edge geometries such as sharp, blunt on the flow, and aerodynamics characteristics of the flat plate aerofoil at a Reynolds number of (Re) of 4.99×10^4. The pressure coefficient shows the sharp decrease along the length of the bottom surface, while it is almost constant along the top surface for both the sharp and blunted trailing edge geometries. The difference in the pressure coefficient between the top and bottom surface is higher in the case of blunt trailing edge as compared to sharp ones, and this difference decreases with increase in distance along the chord. The spectra show the vortex shedding for both the blunted and sharp trailing edge geometries occurs at a Strouhal number of around 0.34. The existence of broader wake in the blunted geometry reveals that it generates higher drag as compared to the sharp ones. Thus, the current paper adequately exemplifies the effect of different trailing edge geometries such as sharp and blunted profiles on the aerodynamic characteristics of the flat plate aerofoil.

References

Blackburn HM, Melbourne WH (1996) The effects of free-stream turbulence on sectional lift force on a circular cylinder. J Fluid Mech 11:267–292

Lam KM, Leung MYH (2005) Asymmetric vortex shedding flow past an inclined flat plate at high incidence. Eur J Mech B/Fluid 24:33–48

Lam KM, Wei WT (2010) Numerical simulation of vortex shedding from an inclined flat plate. Eng Appl Comput Fluid Mech 4:569–579

Spalart PR, Allmaras SR (1992) A one-equation Turbulence Model for Aerodynamic Flows. AIAA J 92-0439

Yang D, Pettersen B, Anderson HI, Narasimhamurty VD (2012) Vortex shedding in flow past n inclined flat plate at high incidence. Phys Fluids 24:084103

Compare Tornado Force Coefficients on Dome and Prism Building Using Three-Dimensional Computational Fluid Dynamics Model

Majdi A.A. Yousef and R. Panneer Selvam

Abstract Wind loads on structures have been investigated for the last five decades. For straight line (SL) wind, the forces on buildings are available from standards and wind tunnel testing. Few studies have been conducted to investigate tornado forces on cubical buildings and to distinguish between tornadic wind loads and SL wind loads. In the tornado-damaged areas, dome buildings seem to have less damage. However, few studies have been investigated to study a tornado interaction with a dome building. In this work, the forces on a dome are computed using computational fluid dynamics (CFD) for tornadic and SL wind. Then, the interaction of a tornado on a dome and a prism building are compared and analyzed. This work describes the results of the tornado wind effect on a dome building. The conclusions drawn from this study are illustrated by various visualizations. The tornado force coefficients on a dome building are larger than force due to SL wind, about 40% more in x-direction and 120% more in z-direction. The tornado maximum pressure coefficients also are higher than SL wind by 130%. The tornado force coefficients on the prism are larger than the forces on the dome, about 150% more in x-direction and about 110% more in z-direction. The tornado maximum pressure coefficients on prism also are greater, by 200%. Hence, a dome building has less tornadic load than a prism because of its aerodynamic shape.

1 Introduction

Every year in the USA, more than 1,000 tornadoes cause about 65 fatalities, 1,500 injuries, and at least 400 million dollars in economic damage, as reported by the American National Weather Service (NWS 2011). In order to mitigate this

M.A.A. Yousef (✉) · R. Panneer Selvam
Department of Civil Engineering, University of Arkansas, 4190 Bell Engineering, Fayetteville, AR 72701, USA
e-mail: myousef@uark.edu

R. Panneer Selvam
e-mail: rps@uark.edu

M.K. Singh et al. (eds.), *Applications of Fluid Dynamics*, Lecture Notes in Mechanical Engineering, https://doi.org/10.1007/978-981-10-5329-0_18

Fig. 1 **a** Survived concrete dome (Parker 2013) and **b** survived wood dome (Age Dome 2015)

damage, it is necessary to design buildings that are more resistant to tornadoes. The first requirement for accomplishing this goal is a better understanding of tornado–structure interaction and tornado-induced loads on buildings. The development in tornado wind modeling can lead to a better prediction of tornado maximum forces. Then, the outcome can be implemented for improving the design standards. Past research has focused on the influence of tornado forces on different structures, such as gable-roofed, rectangular, and cubic or tall buildings. Selvam and Millett (2003) and Millett (2003) did pioneering work on computer modeling simulations of tornado interaction with a cubic structure. They showed that the tornado produced twice the force coefficient on the roof of a cubic structure compared to the SL wind flow. Iowa State University (ISU) group has investigated in the laboratory the interaction between a translating tornado and a low rise gabled-roofed structure or a tall structure (Sarkar et al. 2006; Yang et al. 2011; Zang and Sarkar 2010; Hann et al. 2010; Hu et al. 2011). Their study has shown that the tornado produced two to three times the force coefficients on the roof compared to the SL flow.

A literature review of tornado damage investigation shows that the structures were partially or completely destroyed by tornadoes, except the dome structures. In one instance, a thin shell concrete dome, in Blanchard, OK was hit by an EF5 tornado (Parker 2013). Although badly damaged by heavy, flying debris, the dome shell survived (Fig. 1a). In another instance, a wood dome house in Texas survived after it was hit by the EF5 tornado as shown in Fig. 1b (Age Dome 2015). From this observation, one can say that the shape may reduce the forces on structure.

2 Objectives

A literature review of tornado–structure interaction shows that the wind effects of tornadoes on dome building has not been sufficiently explored, which justifies the necessity of the research in this study. Therefore, a numerical simulation is conducted to study in detail the interaction of a tornado on a dome structure. Then, the numerical results are compared with those due to SL wind. In addition, the results

are compared with those that are computed for prism building. The detail of the objective is listed below:

1. Use the computer model for making some flow visualizations to understand the flow behavior around the dome and rectangular prism.
2. Use the computer model for computing the forces and pressure coefficients on dome and prism building due to straight-line wind and tornado-type wind.
3. Compare the force and pressure coefficients on dome and prism buildings due to straight line and tornadic wind.

3 Tornado Wind Field Modeling

The Rankine combined vortex model (RCVM) is the simplest model that can satisfy the Navier–Stokes (NS) equations, as reported by Lewellen (1993). This model consists of two different flow fields, which are the force vortex region and free vortex region as shown in Fig. 2. In the force vortex region, the tangential velocity of tornado, V_θ, increases linearly with the distance from the tornado center, r, where $r \leq r_{\max}$. In the free vortex region, the tangential velocity is decreasing inversely to the radius the region where $r > r_{\max}$. In this computational simulation, a translational velocity, V_t, with respect to the building is superimposed onto the RCVM wind field, in addition to a vertical logarithmic variation to account for the boundary layer, as reported by Selvam (1993). More detail about RCVM can be found in Selvam and Millett (2005).

4 Fluid–Structure Interaction Modeling

The flow around the structure is computed by solving the Navier–Stokes (NS) equations. The turbulence is modeled using large eddy simulation (LES). The flow equations are approximated by either finite element method (FEM) or finite

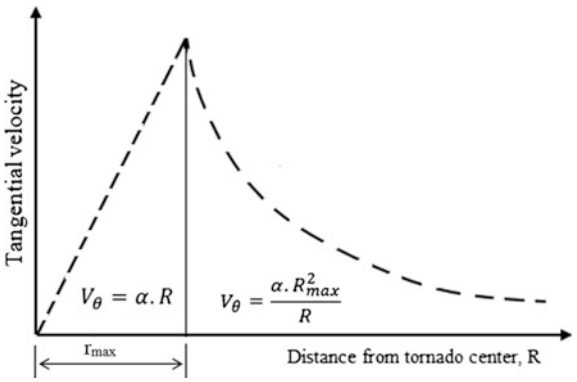

Fig. 2 Rankine combined vortex of tornado velocity

different method (FDM). The FDM code has been used previously by Selvam and Millett (2005) to study flow over cubic prism. This is based on orthogonal grid system, and it is computationally very efficient. The same code is used to compute the forces around the rectangular prism (Alrasheedi and Selvam 2011; Gorecki and Selvam 2015). The FDM code based on body fitted was developed to study flow around a dome, but it had more error in transporting the tornado-like vortex. Hence, the FEM code based on body fitted was developed to study flow around a dome. Ahmad and Selvam (2015) used this numerical model to study the tornado–terrain interaction. They validated this numerical model by comparing the results with experimental. The detail of the equations and methods of solving are documented in the above references. The superiority of FEM to FDM in transporting vortices is reported in Selvam (1998). The FEM code takes more computer time, and hence parallel computing is utilized. More detail about parallel computing can be found in Ahmad and Selvam (2015).

5 Problem Geometry and Boundary Conditions

The structure (the hemispherical dome or rectangular prism) is located on the path of the translating vortex. The counterclockwise rotating vortex travels along x-axis with a constant velocity (V_t) as shown in Fig. 3. The structure is located at reasonable distance from the boundary of the computational domain, to not inhibit the flow-structure. On the surface of the structure either dome or prism, the velocities are considered to be zero, i.e., no-slip condition. At each time step, the interior velocities and pressures are computed by solving the NS equations. More details about the boundary conditions can be found in Selvam and Millet (2005). The parameters of the tornado are presented in Table 1.

Table 2 includes the sizes of the hemispherical dome, rectangular prism, and computational domain, in both the dimensionless and the SI units. The classifications for the dome and prism dimensions are presented in Fig. 4. The height and projected area of the dome and prism are assumed to be same. Instead of taking projected area of the dome and prism same, in future study, the volume of the dome

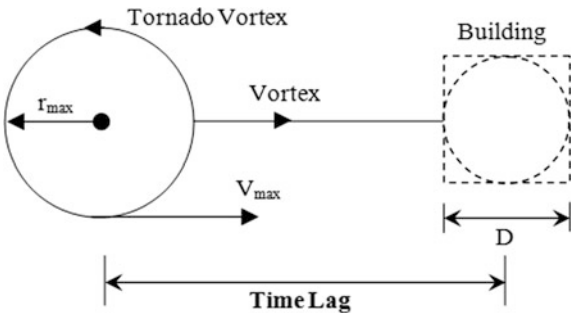

Fig. 3 Schematic of path translating tornado with building

Table 1 Rankine combined vortex parameters and the ground roughness

Units	α	r_{max}	V_t	V_θ	$V_{max} = V_t + V_\theta$	Z_0
Non-dimensional	1.0	3.0	1.0	3.0	4.0	0.045
SI units	1.0 s^{-1}	30 m	10 m s^{-1}	30 m s^{-1}	40 m s^{-1}	0.00375

Where Z_0 is the ground roughness

Table 2 Dome, prism, and domain size

	Dome (model 1)		Prism (model 2)			Domain size		
Units	D	H	L	D	H	L_D	W_D	H_D
SI units (m)	20.0	10.0	17.72	17.72	10.0	600	600	450
Non-dimensional	2.0	1.0	1.772	1.772	1.0	60	60	45

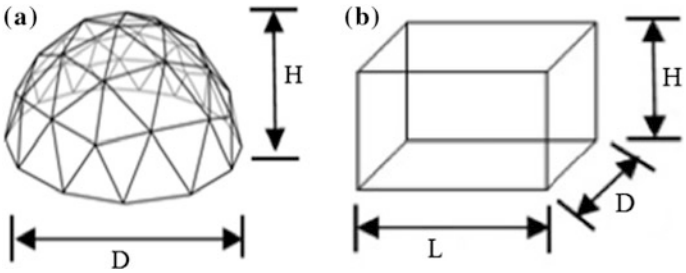

Fig. 4 Nomenclature; **a** dome building dimension; **b** prism building dimension

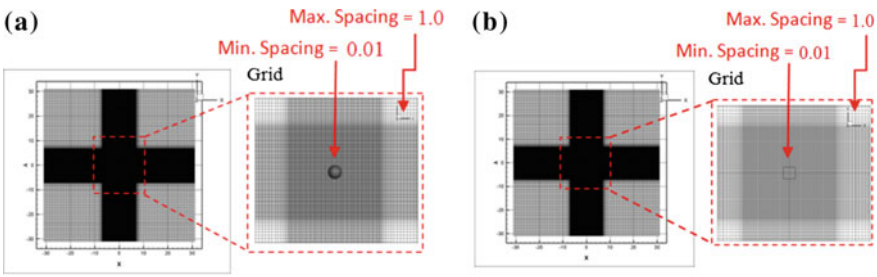

Fig. 5 Computational grid in *xy*-plane; **a** vortex–dome building interaction; **b** vortex–prism building interaction

and prism also will be taken as the same. Here the focus is on same projected area and height. The x and y plane of the used grids, across the dome and prism, are established in Fig. 5. The grid spacing from the building is increased by 1.2 times the previous spacing until it reaches 0.25D spacing. The 0.5 spacing is applied only on the $6 \times r_{max}$ wide lane on the vortex path and around the dome and prism.

Outside the path the grid spacing is equal to $0.5D$ units. The fine grid spacing inside and outside the path is recommended by Gorecki and Selvam (2015). The dome and prism boundary layer is resolved by fine grid refinement. The first grid spacing next or close to the dome and prism buildings is assumed to be 0.005D as suggested by Selvam and Millet (2005), where D is a structure's width. The Reynolds number based on the height of the dome and prism is $Re = 1.2 \times 10^6$.

Nomenclature

The force coefficients are calculated using the following equations:

$$C_X = F_x/\left(0.5\rho V^2 A\right) \tag{1}$$

$$C_y = F_y/\left(0.5\rho V^2 A\right) \tag{2}$$

$$C_z = F_z/\left(0.5\rho V^2 A\right) \tag{3}$$

$$C_p = \Delta_p/\left(0.5\rho V^2\right) \tag{4}$$

where C_x, C_y, and C_z are the computed force coefficients in the x, y, and z, respectively. The F_x, F_y, and F_z are respective forces in x, y, and z directions, ρ is the density of air, V is the reference velocity, and v is the kinematic viscosity of air. Cp is the mean pressure coefficient, Δp is the pressure difference, and $P - Pref.$ ($Pref.$ is equal to 0.0). The reference velocity in the tornado wind field is the maximum velocity, which is equal to $V_\theta + V_t$. By integrating the pressure in each direction on the surface, the forces are computed.

6 Results and Discussion

6.1 Tornado Vortex Interaction with the Dome and the Prism, Described by Contours and Pressure Iso-Surface

The primary advantage of CFD modeling of the tornado–structure interaction is the capability to investigate the wind characteristics for any building shape at any instant in time. Figure 6 displays the interaction of tornado wind with the dome and the prism at various instances of non-dimensional time (t = 10, 24, 45). Before the interaction of the vortex with the structures, the vortex in front of the dome and the prism at time 10 exhibits a regular uninterrupted cylindrical shape as shown in Fig. 6a, b. At time 24, the low-level part of the vortex starts to interact with the building. As the vortex travels ahead: the vortex over the dome transports smoothly until it passes the building, whereas the vortex over the prism starts to separate until it passes the building as illustrated in Fig. 6c, d. Since the prism building has

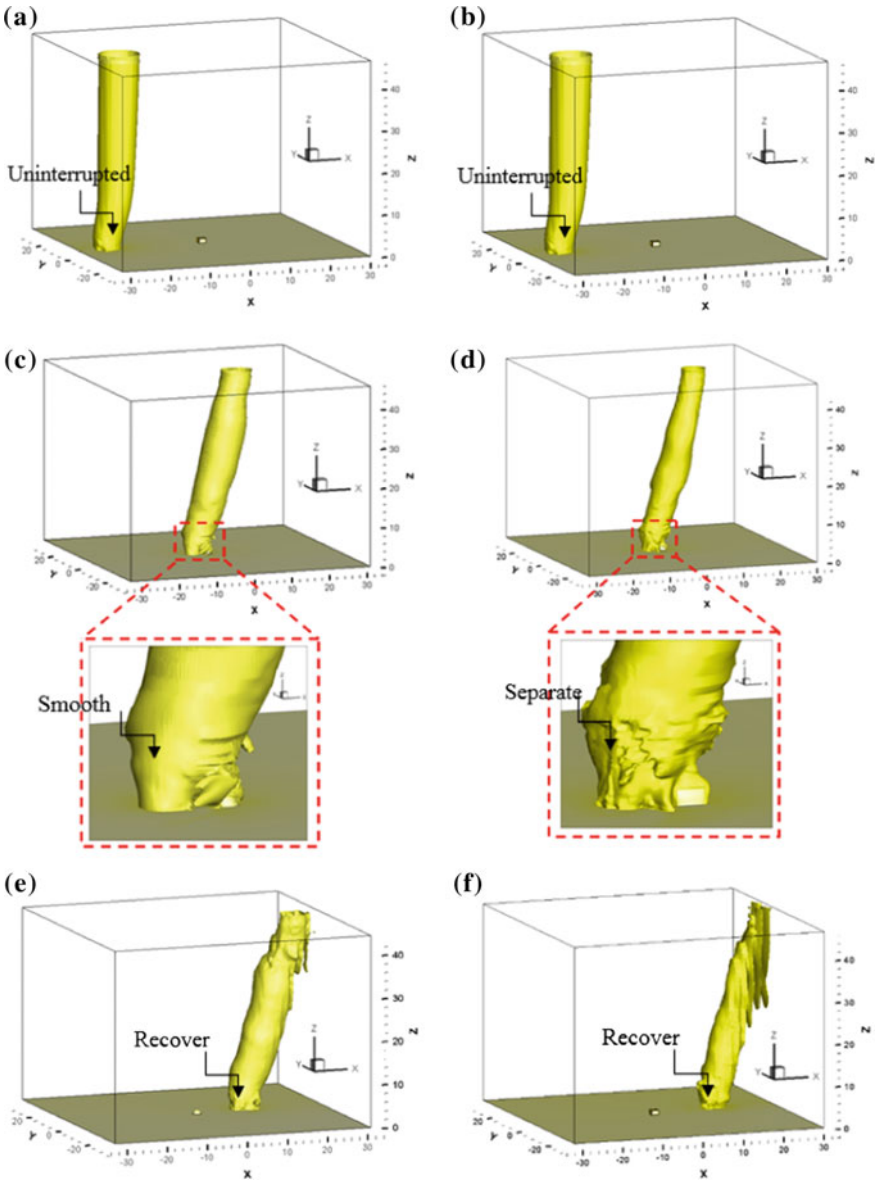

Fig. 6 Isometric view of tornado vortex–dome and prism interaction in pressure iso-surface at various times **a**, **b** 10, **c**, **d** 24, and **e**, **f** 45 unite

angles, sharp corners, and flat surfaces, they give the wind something to lift or push against it. Therefore, the vortex separates when it travels over the prism. However, the dome building does not have those features. The dome has smooth and rounded surfaces that make the vortex transfer smoothly over it. As the vortex moves away

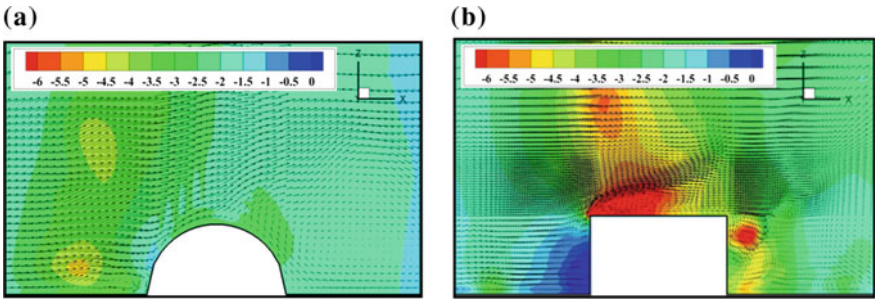

Fig. 7 Close view of *xz*-plane of tornado vortex dome (**a**) and prism (**b**) interaction in pressure contours at time 24 s

from the dome and the prism building at time 45, it straightens up and starts to recover its initial cylindrical shape in Fig. 6e, f.

The *x* and the *z* plane velocities vector in pressure contours for the dome and the prism building at time 24 are illustrated in Fig. 7. The tornado vortex generates large amounts of vertical wind around each building. With the dome and prism building interactions, the wind is changed from horizontal to vertical wind all around the roof of the buildings. As the high-pressure vertical wind flows past the corners of the prism building, flow separation occurs just above the entire roof surface as seen by the turbulent wake above the building. However, with the dome building interaction, the wind travels smoothly over the dome building since the dome does not have multiple sharp corners like the prism building. Therefore, the rotational wind due to tornadoes may create higher forces on the prism than the dome.

6.2 *Tornado Force and Pressure Coefficients over the Dome and the Prism*

The three-dimensional contours of the pressures for the dome and the prism building are illustrated in Fig. 8. The absolute maximum pressure on the dome is—2.0. The maximum effect of the negative pressure is seen close to the top of the dome. The absolute maximum pressure on the prism is—6.0. The maximum effect of the negative pressure is seen on the roof and walls of the prism close to the sharp edge and corners. The prism mode makes higher pressure than the dome model, about 200%. The dome created less pressure since the dome does not have multiple sharp corners like the prism building.

The tornado force coefficients for dome and prism presented in Fig. 9 are calculated by integrating pressure all over the buildings. These tornado forces are compared with forces due to SL wind that are illustrated in Fig. 10. It is found that the force coefficients on dome due to the tornado wind are larger than those due to

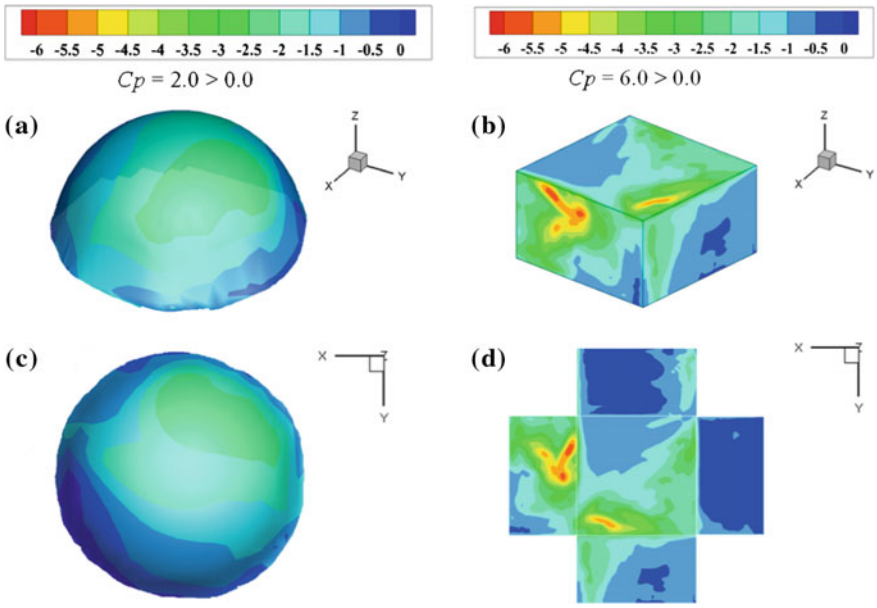

Fig. 8 **a** and **b** Absolute maximum pressure coefficient contour plots under the influence of tornado wind of dome and prism buildings, respectively; **c** *xy*-plane of dome building pressure; **d** exploded faces of the prism building pressure coefficients

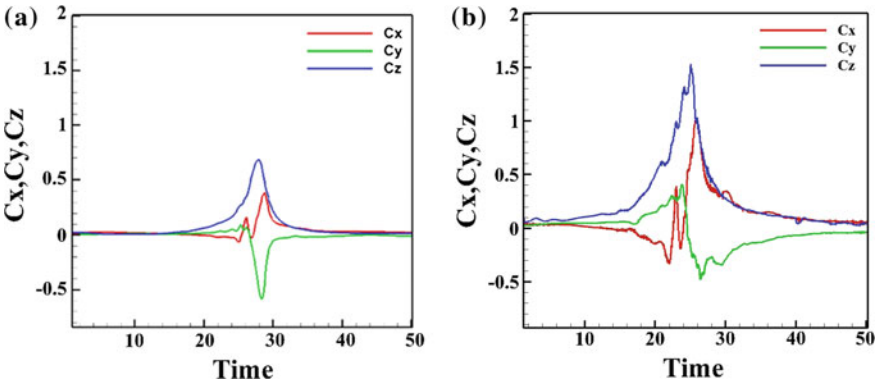

Fig. 9 Maximum force coefficients on prism due to **a** SL wind and **b** tornado wind

the SL wind, about 40% more in *x*-direction and about 120. Also, it is found that the force coefficients on prism due to the tornado wind are larger than those due to the SL wind, about 60% more in *x*-direction and about 130% more in *z*-direction.

The maximum C_x, C_y, C_z values due to tornado for the dome building and prism building are compared. It was found that the prism model makes higher force

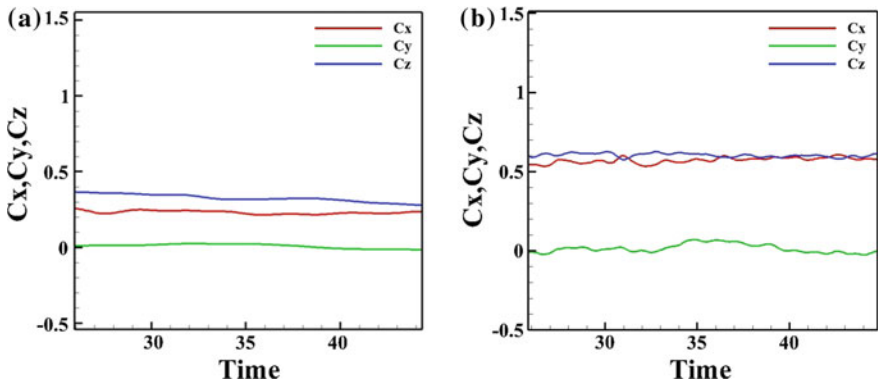

Fig. 10 Maximum force coefficients on dome due to **a** SL wind and **b** tornado wind

coefficients than the dome model, about 150% more in *x*-direction and 110% more in the *z*-direction. In our comparison the coefficients are calculated for the same maximum velocities and hence for the same maximum wind speed of the tornado wind.

7 Conclusions

In this paper, the effect of force and pressure coefficients on dome and rectangular prism building having same height and projected surface area is compared. A three-dimensional CFD simulation, based on large eddy simulation, is applied to numerically simulated tornado–structure interaction using computational fluid dynamics. The conclusions arrived from the accomplished work are listed below.

1. The tornado force coefficients on the dome building are larger than forces due to SL wind, about 40% more in *x*-direction and 120% more in *z*-direction. The tornado pressure coefficients are larger than pressure due to SL wind, about 130% more.
2. The force coefficients on prism due to the tornado wind are larger than those due to the SL wind, about 60% more in *x*-direction and about 130% more in *z*-direction. The tornado pressure coefficients are greater, about 140% more.
3. The translating tornado wind produces higher overall forces coefficients on the prism than dome, about 150% more in *x*-direction and 110% more in *z*-direction. The tornado pressure coefficients on prisms are greater, about 200% more.

References

Age Dome (2015) Tornado shelters/domes in disasters. http://newagedomeconstruction.com/services/tornado-shelters/. Retrieved from 6 Oct 2014

Ahmed N, Selvam RP (2015) Ridge effects on tornado path deviation. Int J Civ Struct Eng Res 3:273–294

Alrasheedi NH, Selvam RP (2011) Computing tornado forces on different building sizes. In: Proceedings of the 13th international conference on wind engineering (ICWE13), Amsterdam, Netherlands

Gorecki PM, Selvam RP (2014) Visualization of tornado-like vortex interacting with wide tornado-break wall. J Vis 1–14

Gorecki MP, Selvam RP (2015) Rankine combined vortex interaction with a rectangular prism. Int J Comput Fluid Dyn 1–13

Haan FL, Balaramudu VK, Sarkar PP (2010) Tornado-induced wind loads on a low-rise building. J Struct Eng 136:106–116

Hu H, Yang Z, Sarkar P, Hann F (2011) Characterization of the wind loads and flow fields around a gable-roof building model in tornado-like winds. Exp Fluids 51:835–851

Lewellen WS (1993) Tornado vortex theory. In: Church C, Burgess D, Doswell C, Davies-Jones R (eds) The Tornado: its structure, dynamics, prediction, and hazards. Geophysical Monograph 79, American Geophysical Union, pp 19–39

Millett PC (2003) Computer modeling of the tornado-structure interaction: investigation of structural loading on a cubic building. Master's Thesis, University of Arkansas, Fayetteville, AR

NWS (2011) Tuscaloosa-Birmingham Tornado. http://www.srh.noaa.gov/bmx/?n=event_04272011-tuscbirm. Retrieved from 7 Oct 2014

Parker F (2013) A testament to the dome shape. http://www.monolithic.org/testimonials/domers-respond-to-moore-oklahoma. Retrieved from 7 Oct 2014

Sarkar PP, Haan FL, Balaramudu V, Sengupta A (2006) Laboratory simulation of tornado and microburst to assess wind loads on buildings. In: Proceedings structures congress, ASCE, Reston, VA

Selvam RP (1993) Computer modeling of tornado forces on buildings. In: Proceedings of the 7th US national conference on wind engineering, Gary C. Hart, Los Angeles, pp 605–613

Selvam RP (1998) Computational procedures in grid based computational bridge aerodynamics. In: Larsen A, Dahl E (eds) Bridge Aerod, Balkema, Rotterdam, pp 327–336

Selvam RP, Millett P (2003) Computer modeling of tornado forces on buildings. Wind Struct 6:209–220

Selvam RP, Millett P (2005) Large eddy simulation of the tornado-structure interaction to determine structural loadings. Wind Struct 8(1):49–60

Yang Z, Sarkar P, Hu H (2011) An experimental study of a high-rise building model in tornado-like flows. J Fluids Struct 27:471–486

Zhang W, Sarkar PP (2010) Influence of surrounding buildings on the flow around a low-rise building in ABL and tornado-like winds. In: 5th international symposium on computational wind engineering (CWE), Chapel Hill, North Carolina, USA

Mathematical Study of Peristalsis in the Presence of Electrokinetic Transport in Parallel Plate Microchannel

D. Tripathi, Shashi Bhushan, Ashu Yadav and Ashish Sharma

Abstract Electrokinetic transport of fluids through microchannel by micropumping and microperistaltic pumping has much interest for many engineering, medical, and industrial applications. Motivated in part by the need of mathematical model to study the electrokinetic transport by peristaltic pumping, an analytical approach is presented. A non-integral number of wave propagation is considered for transportation of fluid bolus along the channel length. Debye-Hückel linearization is employed to find out the potential function. A non-dimensional analysis is employed to simplify the governing equations. Low Reynolds number and large wavelength approximations are taken into account. The effects of characteristic electrical double layer (EDL) thickness and maximum electroosmotic velocity on pumping characteristics are discussed by computational results.

1 Introduction

The recent emerging microfluidic technologies such as microfluidics devices, micropumping, and peristaltic micropumping have been reported in detail by Iverson and Garimella (2008). Without moving mechanical parts, an electroosmotic pump which generates high pressure and flow is intended by Goodson et al. (2005). An electroosmosis modulated microperistaltic pump is engineered by Xie et al. (2004) on the basis of peristalsis phenomenon. Another peristaltic micropump is also engineered by Brettschneider and Dorrer (2013). In same direction, some more microfluidic peristaltic pumps are also fabricated and discussed by Chou et al. (2015) and Zhang et al. (2015). An analytical approach is adopted to study the electromagnetohydrodynamic flow of viscoelastic fluids with Jeffrey model through two parallel microchannels which are presented by Si and Jian (2015). Peristalsis is a physiological mechanism in which the physiological fluids like food bolus, blood,

D. Tripathi (✉) · S. Bhushan · A. Yadav · A. Sharma
Department of Mechanical Engineering, Manipal University Jaipur,
Jaipur 303007, Rajasthan, India
e-mail: dharmtri@gmail.com

M.K. Singh et al. (eds.), *Applications of Fluid Dynamics*, Lecture Notes
in Mechanical Engineering, https://doi.org/10.1007/978-981-10-5329-0_19

urine, bile and sperm are being transported by continuous muscle contractions and relaxation. This mechanism is automatic process. The muscles contract and relax due to chemical mechanism. It was being studied in physiology; however, some interesting fluid mechanical investigations are reported subsequently by Burns and Parkes (1967), Fung and Yih (1968), Jaffrin and Shapiro (1971), Li and Brasseur (1993), Pozrikidis (1987), Shapiro et al. (1969), Shukla et al. (1980), Takabatake and Ayukawa (1982). These studies are limited for Newtonian fluids, so further modifications for non-Newtonian fluids, MHD fluids, heat transfer fluids, and nanofluids are required. Considering these facts, Tripathi and Bég (2014) presented a model for viscoelastic fluids, in another study Tripathi and Bég (2013) for MHD couple stress fluids; Blanchette (2014) discussed the effects of suspended drops on peristaltic transport; Ellahi et al. (2014) reported the heat transfer analysis on peristaltic pumping; Tripathi and Anwar Bég (2014) investigated for nanofluids; Kothandapani and Prakash (2015) extended for MHD nanofluids; and Akbar et al. (2015) further improved for MHD nanofluids through permeable channels.

Nowadays, the interdisciplinary works (mathematical biosciences) and multi-disciplinary works (a mathematical study of electroosmotic flow in physiological systems) have been most demanded and attracted to research communities. Most of the above works present a mathematical model of peristaltic transport in various physical aspects and constraints. However the electrokinetic theory was not introduced in peristaltic transport model, first time Chakraborty (2006) focused the electrokinetic effects on peristaltic transport. He considered thin electric double layer phenomenon where electroosmotic slip boundary condition is taken into account. Electrokinetic is the study of a group of phenomena, i.e., electrophoresis, electroosmosis, diffusiophoresis, capillary osmosis, sedimentation potential, streaming potential/current, colloid vibration current, electric sonic amplitude that occur in particles (solid, liquid or gas) containing fluids due to intrinsic or extrinsic electric field. Inspired from the wide applications of electrokinetic in various fields, an electroosmotic flow in microchannel with electric double layer (EDL) phenomenon is reported by Dey et al. (2012) where external electric field is considered. A dielectrophoresis (H-DC-iDEP) microfluidic blood plasma separation is also analyzed by Mohammadi et al. (2015). However these models are formulated mathematically and ignored the experimental observations of peristaltic/oscillating flow nature of physiological movements.

Considering the huge applications of both peristaltic and electrokinetic mechanisms in fabrication of biomedical devices and peristaltic micropumps, a mathematical model is designed to discuss the effects of Helmholtz-Smoluchowski velocity and Debye length on peristaltic transport of Newtonian fluids through microchannel. We consider the sinusoidal flow regime where the non-integral number of waves is propagating along the microchannel length. This study answers the mechanism of peristaltic pumping under the influence of electrokinetic transport like “How peristaltic pumping can be controlled by electrokinetic mechanisms?” This model is new concept and applicable in the field of microfluidics transport process.

2 Mathematical Formulation

A schematic representation of flow regime with finite length (L) channel is depicted in Fig. 1, and it is mathematically expressed as:

$$\bar{h}(\bar{\xi},\bar{t}) = a - b\cos^2\frac{\pi}{\lambda}(\bar{\xi} - c\bar{t}) \quad \forall x \in [0, L] \tag{1}$$

where a, b, λ, $\bar{\xi}$, c, $\bar{t}$, and L are the half width at the inlet, amplitude, wavelength, axial coordinate, wave velocity, time, and channel length, respectively.

The governing equations for two-dimensional incompressible flow with an axially applied electrokinetic body force are given as:

$$\frac{\partial \bar{u}}{\partial \bar{\xi}} + \frac{\partial \bar{v}}{\partial \bar{\eta}} = 0, \tag{2}$$

$$\rho\left(\frac{\partial}{\partial \bar{t}} + \bar{u}\frac{\partial}{\partial \bar{\xi}} + \bar{v}\frac{\partial}{\partial \bar{\eta}}\right)\bar{u} = -\frac{\partial \bar{p}}{\partial \bar{\xi}} + \mu\left(\frac{\partial^2 \bar{u}}{\partial \bar{\xi}^2} + \frac{\partial^2 \bar{u}}{\partial \bar{\eta}^2}\right) + \bar{\rho}_e E_\xi, \tag{3}$$

$$\rho\left(\frac{\partial}{\partial \bar{t}} + \bar{u}\frac{\partial}{\partial \bar{\xi}} + \bar{v}\frac{\partial}{\partial \bar{\eta}}\right)\bar{v} = -\frac{\partial \bar{p}}{\partial \bar{\eta}} + \mu\left(\frac{\partial^2 \bar{v}}{\partial \bar{\xi}^2} + \frac{\partial^2 \bar{v}}{\partial \bar{\eta}^2}\right), \tag{4}$$

where $\rho, \bar{u}, \bar{v}, \bar{p}, \mu$, and E_ξ denote the fluid density, axial velocity, transverse velocity, pressure, fluid viscosity, and elctrokinetic body force. The Poisson-Boltzmann's equation is defined as:

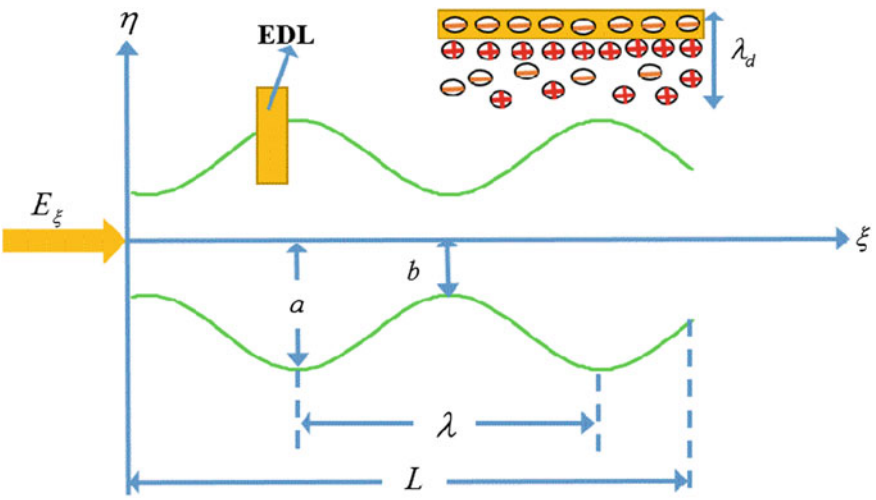

Fig. 1 Geometry of non-integral peristaltic wave propagation induced by electroosmotic flow

$$\nabla^2\bar{\Phi} = -\frac{\bar{\rho}_e}{\varepsilon} \tag{5}$$

in which ρ_e is the density of the total ionic change and ε is the permittivity. For a symmetric (z:z) electrolyte, the density of the total ionic energy, ρ_e, is given by, $\rho_e = ez(n^+ - n^-)$, in which n^+ and n^- are the number of densities of cations and anions, respectively, and are given by Boltzmann distribution (considering no EDL overlap) $n^{\pm} = n_0 \mathrm{Exp}\left[\pm\frac{ez\bar{\Phi}}{K_B T}\right]$, where n_0 represents the concentration of ions at the bulk, which is independent of surface electrochemistry, e is the electronic charge, z is charge balance, K_B is the Boltzmann constant, and T is the average temperature of the electrolytic solution.

Introduce the following non-dimensional parameters;

$$\begin{aligned} &\xi = \frac{\bar{\xi}}{\lambda}, \eta = \frac{\bar{\eta}}{a}, t = \frac{c\bar{t}}{\lambda},\ u = \frac{\bar{u}}{c},\ v = \frac{\bar{v}}{c\delta},\ \delta = \frac{a}{\lambda},\ h = \frac{\bar{h}}{a}, \\ &\varphi = \frac{b}{a}, p = \frac{\bar{p}a^2}{\mu c\lambda},\ \mathrm{Re} = \frac{\rho ca}{\mu}, \Phi = \frac{\bar{\Phi}}{\zeta}, \end{aligned} \tag{6}$$

where δ is wave number, Re is the Reynolds number, and ζ is the zeta potential. Applying long wavelength and low Reynolds number approximations, the above Eqs. (2)–(4) reduce to

$$\frac{\partial u}{\partial \xi} + \frac{\partial v}{\partial \eta} = 0, \tag{7}$$

$$\frac{\partial p}{\partial \xi} = \frac{\partial^2 u}{\partial \eta^2} + m^2 U_{HS}\Phi, \tag{8}$$

$$\frac{\partial p}{\partial \eta} = 0. \tag{9}$$

where $m = aez\sqrt{\frac{2n_0}{\varepsilon K_B T}} = \frac{a}{\lambda_d}$ is known as the electroosmotic parameter and λ_d is Debye length or characteristic thickness of electrical double layer (EDL) and $U_{HS} = -\frac{E_\xi \varepsilon\zeta}{\mu c}$ is the Helmholtz-Smoluchowski velocity or maximum electroosmotic velocity. Applying Debye-Hückel linearization approximation $\sinh\left(\frac{ez\Phi}{K_B T}\right) \approx \frac{ez\Phi}{K_B T}$, Eq. (5) reduces to:

$$\frac{\partial^2 \Phi}{\partial \eta^2} = m^2\Phi \tag{10}$$

The boundary conditions are:

$$\left.\frac{\partial \Phi}{\partial \eta}\right|_{\eta=0} = 0, \Phi|_{\eta=h} = 1, \left.\frac{\partial u}{\partial \eta}\right|_{\eta=0} = 0 u|_{\eta=h} = 0, v|_{\eta=0} = 0,$$
$$v|_{\eta=h} = \frac{\partial h}{\partial t}, p|_{\xi=0} = p_0 \text{ and } p|_{\xi=L} = p_L \tag{11}$$

Integrating twice Eq. (10) and using the boundary conditions, the potential function is obtained as:

$$\Phi = \frac{\cosh(m\eta)}{\cosh(mh)} \tag{12}$$

Integrating Eq. (8) and using boundary conditions (11), the axial velocity is obtained as:

$$u = \frac{1}{2}\frac{\partial p}{\partial \xi}\left(\eta^2 - h^2\right) - U_{HS}\left\{\frac{\cosh(m\eta)}{\cosh(mh)} - 1\right\} \tag{13}$$

Using the Eq. (13) and boundary condition (11), the transverse velocity from continuity equation is obtained as:

$$v = -\frac{1}{6}\frac{\partial^2 p}{\partial \xi^2}\left(\eta^3 - 3\eta h^2\right) + \eta h \frac{\partial p}{\partial \xi}\frac{\partial h}{\partial \xi} - U_{HS}\sinh(m\eta)\frac{\tanh(mh)}{\cosh(mh)}\frac{\partial h}{\partial \xi} \tag{14}$$

Using Eq. (14) and boundary conditions (11), the pressure gradient is obtained as:

$$\frac{\partial p}{\partial \xi} = \frac{1}{h^3}\left[G_0(t) + 3\left\{\int \frac{\partial h}{\partial t} d\xi + U_{HS}\left(h - \frac{\tanh(mh)}{m}\right)\right\}\right] \tag{15}$$

where $G_0(t)$ is arbitrary function of t to be evaluated by using finite length boundary conditions (11). The pressure difference can be computed along the axial length by

$$\Delta p = p(\xi, t) - p(0, t) = \int_0^{\xi} \frac{\partial p}{\partial s} \mathrm{d}s \tag{16}$$

and $G_0(t)$ is expressed as:

$$G_0(t) = \frac{(p_l - p_0) - 3\int_0^L h^{-3}\left\{\int \frac{\partial h}{\partial t}\mathrm{d}\xi + U_{HS}\left(h - \frac{\tanh(mh)}{m}\right)\right\}\mathrm{d}\xi}{\int_0^L h^{-3}\mathrm{d}\xi} \tag{17}$$

The present model can be reduced for a particular case ($U_{HS} = 0$) where peristaltic transport of viscous fluids through finite length channel can be studied. It can also be reduced for another case ($m \to \infty$) where electroosmotic flow of Newtonian fluids in the presence of peristalsis with very thin electric double layer can be discussed.

3 Numerical Results and Discussion

In this section, the numerical results to discuss the effects of characteristic thickness of electric double layer ($\lambda_d \propto 1/m$) and external electric field ($E_\xi \propto U_{HS}$) on potential profile, velocity profile, pressure distribution, local wall shear stress, and trapping are illustrated through Figs. (2, 3, 4, and 5). Figure 1 is drawn for geometry of peristaltic flow regime.

Figure 2a, b shows the potential profile, i.e., potential function versus transverse coordinate. It is seen that the potential profile is parabolic shape, i.e., it is minimum at origin and asymptotes are $\eta = \text{const}$.

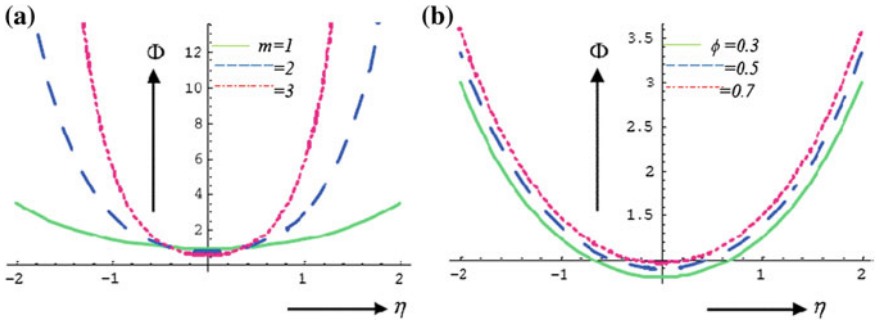

Fig. 2 Potential profile at $\xi = 1.0, t = 0$ for **a** $\varphi = 0.6$, **b** $m = 1$

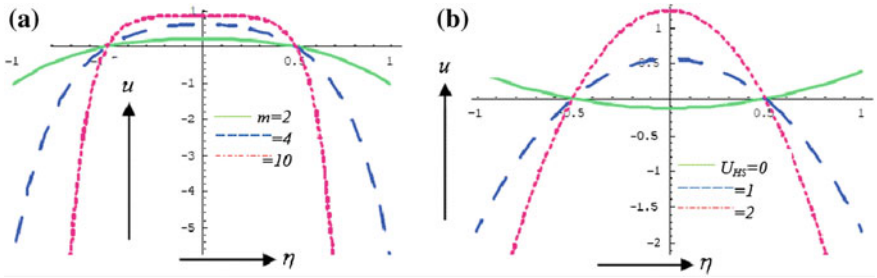

Fig. 3 Velocity profile (axial velocity vs. transverse coordinate) at $\varphi = 0.5, \xi = 1.0, t = 0, \frac{\partial p}{\partial \xi} = 1$

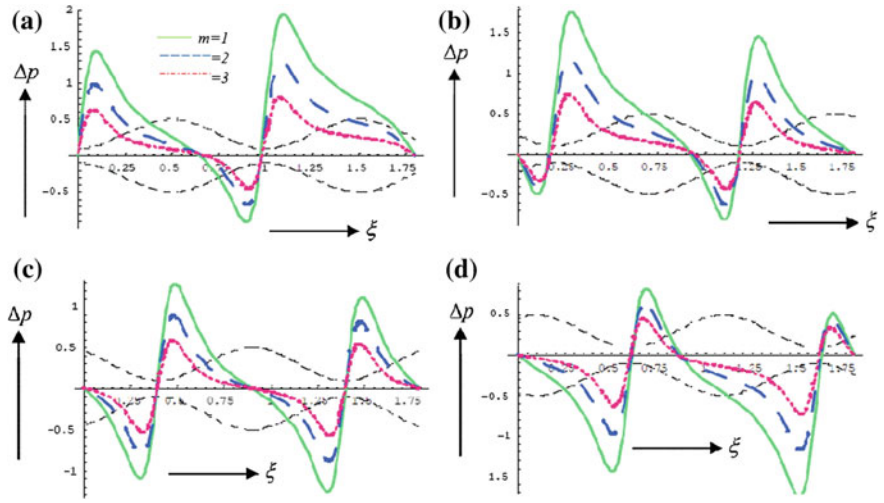

Fig. 4 Pressure difference versus axial channel length at $\varphi = 0.8, l = 1.8, p_l = p_0 = 0, U_{HS} = 1$ for different values of Debye length at **a** $t = 0$, **b** $t = 0.2$, **c** $t = 0.4$, **d** $t = 0.6$

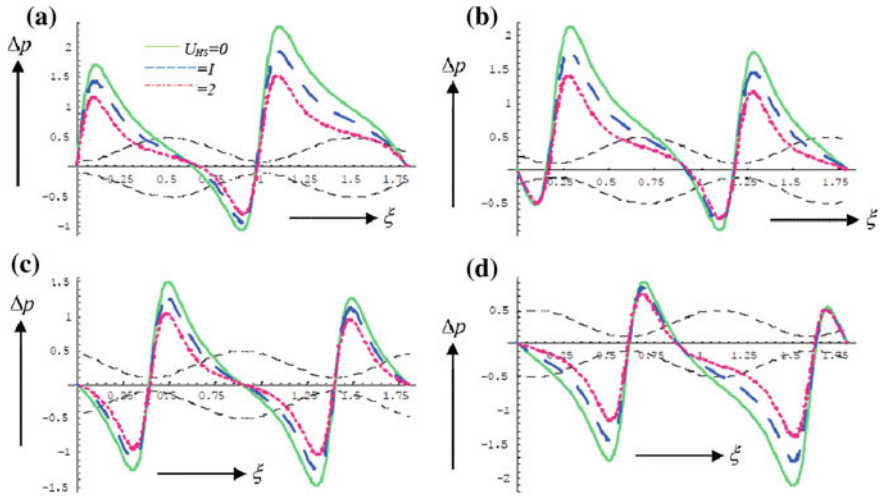

Fig. 5 Pressure difference versus axial channel length at $\varphi = 0.8, l = 1.8, p_l = p_0 = 0, m = 1$ for different values of Helmholtz-Smoluchowski velocity at **a** $t = 0$, **b** $t = 0.2$, **c** $t = 0.4$, **d** $t = 0.6$

Figure 2a shows the effect of thickness of EDL on potential profile, and it is noticed that magnitude of potential function enhances with reducing the thickness of EDL. Figure 2b depicts the influence of amplitude of wave on potential profile. It is pointed out that potential function enhances with increasing the amplitude of the wave.

Figures 3a, b illustrates the effects of EDL thickness and external electric field on velocity profile. It is seen that velocity profiles are in parabolic nature. Figure 3a depicts the effect of EDL thickness on velocity profile, and it is revealed that the velocity profile is shifted from parabolic shape to trapezoid shape when EDL thickness goes down. This shifting tendency explains the effects of electrokinetic in the form of changing the nature from Stokes' flow profile (parabolic) to electroosmotic flow profile (trapezoid). Figure 3b depicts a comparative study for velocity profile with and without external electric field, and it is remarked that the velocity profile is positively parabolic without external electric field, whereas it is negatively parabolic with external electric field. It is further concluded that the vertex of parabolic velocity profile expands with enhancing the external electric field effects.

Figure 4a–d are plotted for pressure difference against the axial length to discuss the effects of EDL thickness and external electric field. Non-integral number of train waves are considered to propagate along the channel length, i.e., length of channel is considered as 1.8 multiple of wavelength of peristaltic wave. The pressures at both end of channel are taken zero, and four different steps of moving fluid bolus are shown at different time instants $t = 0$, $t = 0.2$, $t = 0.4$, $t = 0.6$. From Figures, it is pointed out that the pressure difference is not uniform at fully contracted walls; in Fig. 4a, the pressure at first contracted walls position is less in comparison with pressure at second contracted walls, while it reverse in Fig. 4b; in Fig. 4c, it is uniform along the channel length, but in Fig. 4d, it is similar to Fig. 4a but direction is opposite. It is also revealed that the pressure enlarges for thicker EDL phenomenon

Figure 5a–d are drawn for pressure difference against the axial channel length of channel to compute the effects of external electric field. Same considerations like Fig. 4 have been adopted. It is found that pressure diminishes with enhancing the electric field effects. It is also noticed that the pressure is more for peristaltic pumping without external electric field and vice versa.

4 Concluding Remarks

We analyze the effect of external electric field on peristaltic transport of Newtonian fluids through finite length channel which is studied to discuss how to control the physiological flow by adding and opposing the pressure-driven flow by effect of electric double layer phenomena. On the basis of the computational results, the concluding remarks are:

- Potential function enhances with reducing the thickness of EDL, whereas potential function enhances with increasing the amplitude of the wave.
- Velocity profile increases with increasing the magnitude of external electric field.
- Pressure rises for thicker EDL formation, and the pressure is more with reducing the effect of external electric field.

References

Akbar NS, Raza M, Ellahi R (2015) Influence of induced magnetic field and heat flux with the suspension of carbon nanotubes for the peristaltic flow in a permeable channel. J Magn Magn Mater 381:405–415

Blanchette F (2014) The influence of suspended drops on peristaltic pumping. Phys Fluids (1994-present) 26: 061902

Brettschneider T, Dorrer C (2013) Microfluidic peristaltic pump, method and pumping system: Google Patents

Burns J, Parkes T (1967) Peristaltic motion. J Fluid Mech 29:731–743

Chakraborty S (2006) Augmentation of peristaltic microflows through electro-osmotic mechanisms. J Phys D Appl Phys 39:5356

Chou H-P, Fu AY, Quake SR (2015) Microfluidic devices and methods of use: Google Patents

Dey R, Chakraborty D, Chakraborty S (2012) Extended Graetz problem for combined electroosmotic and pressure-driven flows in narrow confinements with thick electric double layers. Int J Heat Mass Transf 55:4724–4733

Ellahi R, Bhatti MM, Vafai K (2014) Effects of heat and mass transfer on peristaltic flow in a non-uniform rectangular duct. Int J Heat Mass Transf 71:706–719

Fung Y, Yih C (1968) Peristaltic transport. J Appl Mech 35:669–675

Goodson KE, Chen C-H, Huber DE, Jiang L, Kenny TW, Koo J-M et al (2005) Electroosmotic microchannel cooling system: Google Patents

Iverson BD, Garimella SV (2008) Recent advances in microscale pumping technologies: a review and evaluation. Microfluid Nanofluid 5:145–174

Jaffrin M, Shapiro A (1971) Peristaltic pumping. Annu Rev Fluid Mech 3:13–37

Kothandapani M, Prakash J (2015) Effect of radiation and magnetic field on peristaltic transport of nanofluids through a porous space in a tapered asymmetric channel. J Magn Magn Mater 378:152–163

Li M, Brasseur JG (1993) Non-steady peristaltic transport in finite-length tubes. J Fluid Mech 248:129–151

Mohammadi M, Madadi H, Casals-Terré J, Sellarès J (2015) Hydrodynamic and direct-current insulator-based dielectrophoresis (H-DC-iDEP) microfluidic blood plasma separation. Anal Bioanal Chem 407:4733–4744

Pozrikidis C (1987) A study of peristaltic flow. J Fluid Mech 180:515–527

Shapiro AH, Jaffrin MY, Weinberg SL (1969) Peristaltic pumping with long wavelengths at low Reynolds number. J Fluid Mech 37:799–825

Shukla J, Parihar R, Rao B, Gupta S (1980) Effects of peripheral-layer viscosity on peristaltic transport of a bio-fluid. J Fluid Mech 97:225–237

Si D, Jian Y (2015) Electromagnetohydrodynamic (EMHD) micropump of Jeffrey fluids through two parallel microchannels with corrugated walls. J Phys D Appl Phys 48:085501

Takabatake S, Ayukawa K (1982) Numerical study of two-dimensional peristaltic flows. J Fluid Mech 122:439–465

Tripathi D, Bég OA (2013) Transient magneto-peristaltic flow of couple stress biofluids: a magneto-hydro-dynamical study on digestive transport phenomena. Math Biosci 246:72–83

Tripathi D, Bég OA (2014a) Peristaltic propulsion of generalized Burgers' fluids through a non-uniform porous medium: A study of chyme dynamics through the diseased intestine. Math Biosci 248:67–77

Tripathi D, Bég OA (2014b) A study on peristaltic flow of nanofluids: application in drug delivery systems. Int J Heat Mass Transf 70:61–70

Xie J, Shih J, Lin Q, Yang B, Tai Y-C (2004) Surface micromachined electrostatically actuated micro peristaltic pump. Lab Chip 4:495–501

Zhang X, Chen Z, Huang Y (2015) A valve-less microfluidic peristaltic pumping method. Biomicrofluidics 9:014118

Journal Bearing Lubrication of Power Law Fluid with Consistency Variation Including Convection

Dhaneshwar Prasad, Sudam Sekhar Panda and Venkata Subrahmanyam Sajja

Abstract An effort is made to discuss the vital effects of temperature on hydrodynamic lubrication of journal bearing by non-Newtonian power law lubricants. Boundary surfaces are assumed to be rigid and isothermal. It is assumed that the consistency of the lubricant varies with film temperature and pressure, as considered by some researchers. The employed equations of motion and the continuity are solved numerically and analytically. For the numerical solution, Runge–Kutta–Fehlberg method is employed with adequate tolerance. The effects of temperature and pressure are analyzed through various table and graphs as functions of the consistency index of the lubricant velocity and journal velocity.

1 Introduction

In general, in a heavily loaded lubricated bearing, high pressure and temperature plays significant role. The lubricant properties do not remain constant, and it depends on pressure and temperature. However, solving Reynolds and energy equation simultaneously and analytically is a complicated task, and one has to work out numerically. Sometimes the convergence of solution is so poor that getting one

D. Prasad
Department of Mathematics, K.M. Centre for Post Graduate Studies, Lawspet 605008, Puducherry, India

S.S. Panda
Department of Mathematics, Dravidian University, Kuppam, Andhra Pradesh, India

S.S. Panda
Sir C.R.R. College of Engineering, Eluru 534001, Andhra Pradesh, India

V.S. Sajja (✉)
Department of Mathematics, K.L. University, Guntur 522502, Andhra Pradesh, India
e-mail: manyam19@gmail.com

M.K. Singh et al. (eds.), *Applications of Fluid Dynamics*, Lecture Notes in Mechanical Engineering, https://doi.org/10.1007/978-981-10-5329-0_20

feasible solution is difficult. In view of these situations, one may attempt this by making some appropriate assumption to get a feasible solution.

Johnson and Mangkoesoebroto (1993) built up a theory of lubrication for the power law fluid and investigated it intricately. Just the infinite width gap is measured. Here the flow is considered between rigid walls of subjective shape under consolidated coquet and crushing movement with a pressure gradient. A mathematical equation for the pressure gradient is formed by combining these mathematical statements. To show the hypothesis, it is utilized to compute the pressure dispersion for a parabolic slider bearing and the pressure inclination and velocity distribution when the mass flux is recommended. Nessil et al. (2013) studied the lubrication of journal bearings by utilizing non-Newtonian liquids which are depicted by a power law model. The performance qualities of the journal bearings are resolved for different estimations of the non-Newtonian power law index 'n' which lie between 0.9 and 1.1 including Newtonian. The obtained numerical results demonstrate that for the dilatants liquids ($n > 1$), the load conveying limit, the pressure, the temperature, and the frictional power increases while for the pseudoplastic liquids ($n < 1$), the outcome is reversed. The impact of the temperature consequences for these qualities is critical at higher estimations of the flow behavior index 'n'.

Mongkolwongrojn and Aiumpornsin (2010) analyzed the static and dynamic qualities of journal bearing greased up with non-Newtonian oils in view of Carreau viscosity model. The unsteady state modified Reynolds, and the non-adiabatic energy equations have been figured in light of non-Newtonian Carreau liquids to acquire the static and dynamic qualities of journal bearing in thermohydrodynamic oil administration. The Reynolds and energy equations including the heat conduction equation are simultaneously solved together numerically with the given boundary conditions using finite difference method. Khonsari and Brewe (1989) concentrated on the performance parameters for a finite length journal bearing lubricated with micropolar liquids. Results demonstrate that the load conveying limit is significantly higher than the Newtonian liquids which rely upon the size of material characteristic length and the coupling number. It is also explained that in spite of the fact that the frictional force connected with micropolar liquids is higher than that of a Newtonian liquid, the friction coefficient of micropolar liquids has a tendency to be lower than that of the Newtonian. Kango et al. (2014) studied about the impacts of viscous heat dispersal and non-Newtonian rheology of oil on the performance parameters of microtextured journal bearing. The finite difference technique is used to solve this model by the help of mass conservation algorithm (JFO limit conditions) and oil blending temperature ideas. Yang et al. (2014) analyzed the rheological properties of bubbly oil under comparatively low-to-high shear rates using a rheometer. A model equation where cavitation algorithm is applied which includes shear rate and temperature to develop the bubbly lubrication model of journal bearings. Furthermore, results show that as volume fraction increases, maximum pressure, load capacity, friction force, and leak flow increase slightly at lower shear rates, decline obviously at higher shear rates, but increase to a peak and then decrease at intermediate shear rates.

Boncompain et al. (1986) presented a general THD theory and a comparison between theoretical and experimental results. The generalized Reynolds equation, the energy equation in the film, and the heat transfer equation in the bush and the shaft are solved simultaneously. The cavitation in the film, the lubricant recirculation, and the reversed flow at the inlet are taken into account. Along with addition, the thermo-elastic deformations are also calculated in order to define the film thickness. Mongkolwongrojn and Aiumpornsin (1960) investigated the effects of temperature variations within the oil film thickness, and the coming about consistency variation along and over the film which are thought to be in charge of the lift in parallel surface bearing. A numerical solution for a special bearing is acquired for various heat limit conditions, and a result comparison of the traditional analysis is made. Exceptionally impressive contrasts from the traditional analysis are acquired. A few solutions of the heat balance in bearing are likewise displayed. Gao et al. (2014) discussed the impacts of eccentricity ratio by utilizing computational fluid dynamics (CFD) and considering the contrasts between the physical properties of the water and of the oil on pressure distribution of water lubricant film. At that point numerical analysis of journal bearings with various measurements is embraced under various rotational velocities. In view of the analysis, under the given load and rotational velocity, a situation is arised for selecting the initial diameter dimension which is utilized to plan a productive water-greased up plain bearing.

Ahmad et al. (2014) presented an experimental work to determine the effect of oil groove location on the temperature and pressure in hydrodynamic journal bearings. Measurements of temperature and pressure were obtained for speeds of 300, 500, and 800 rpm at different radial loads. Changes in oil groove location were shown to affect the temperature and pressure to some extent.

In light of the above discussion, an effort has been made in this work to include the heat of convection in the energy equation. Solutions are obtained for pressure, temperature, and delta for circular coordinate.

2 Mathematical Model

2.1 Flow Equations

The flow equations of the hydrodynamic lubrication of journal bearing are considered as—Sing et al. (2008a, b):

$$\frac{dp}{dx} = \frac{\partial}{\partial y}\left[m\left|\frac{\partial u}{\partial y}\right|^{n-1}\frac{\partial u}{\partial y}\right] \tag{1}$$

$$\frac{\partial u}{\partial x} + \frac{\partial v}{\partial y} = 0 \tag{2}$$

where

$$m = m_0 e^{\alpha p - \beta(T_m - T_0)} \tag{3}$$

with

$$T_m = \frac{1}{h}\int_0^h T\,dy \tag{4}$$

$$h = c\,(1 - \varepsilon \cos\ \theta) \tag{5}$$

Prescribed boundary conditions are mentioned below for the above equations as:

$$u = U \text{ at } y = h;\ \text{and } u = 0 \text{ at } y = 0 \tag{6}$$

where U is the velocities of the journal

From geometry given in Fig. 1, one may observe that for each θ, $\frac{\partial u}{\partial y} = 0$ at $y = \delta\,(-\pi \le \theta \le \pi)$ in both the regions:

$$\text{I} : -\pi \le \theta < -\theta_1 \quad \text{and} \quad \text{II} : -\theta_1 < \theta \le \pi.$$

Further, four subregions are formed by δ profile having velocities u_1, u_2, u_3, and u_4 from the two regions. The velocity boundary conditions for the undertaken geometry are:

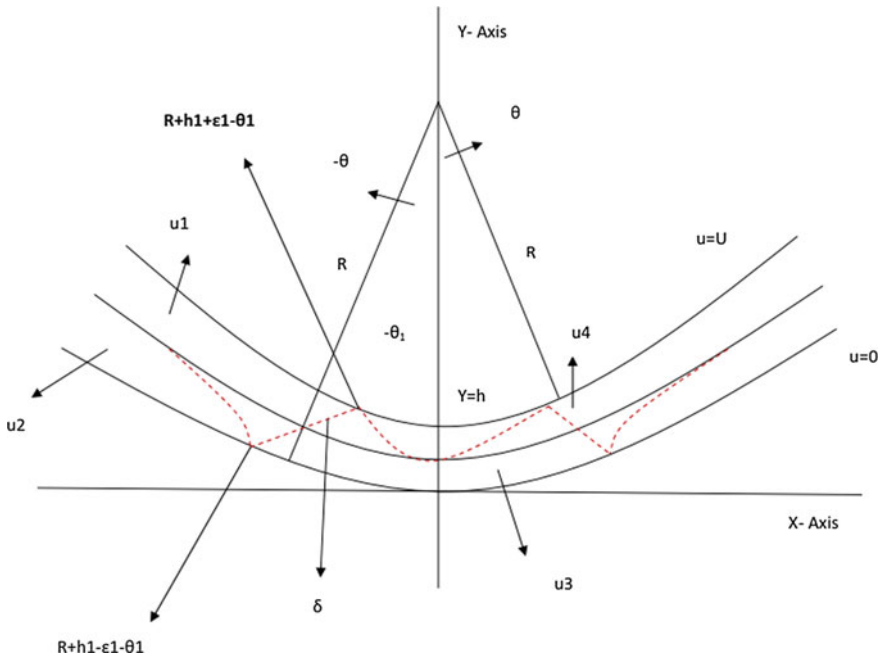

Fig. 1 Journal bearing geometry with delta profile shown in *dotted line*

$$\frac{\partial u_1}{\partial y} \geq 0, \delta \leq y \leq h, \frac{\partial u_2}{\partial y} \leq 0, 0 \leq y \leq \delta, \quad \text{I: } -\pi \leq \theta < -\theta_1 \tag{7}$$

$$\frac{\partial u_3}{\partial y} \geq 0, 0 \leq y \leq \delta, \frac{\partial u_4}{\partial y} \leq 0, \delta \leq y \leq h, \quad \text{II: } -\theta_1 < \theta \leq \pi \tag{8}$$

Integration of Eq. (1) twice for the region: $-\pi \leq \theta < -\theta_1$; leads to,

$$u_1 = U + \left(\frac{n}{n+1}\right)\left(\frac{1}{m_1}\frac{\mathrm{d}p_1}{\mathrm{d}x}\right)^{1/n}\left[(y-\delta)^{\frac{n+1}{n}} - (h-\delta)^{\frac{n+1}{n}}\right]; \quad \delta \leq y \leq h \tag{9}$$

$$u_2 = \left(\frac{n}{n+1}\right)\left(\frac{1}{m_1}\frac{\mathrm{d}p_1}{\mathrm{d}x}\right)^{1/n}\left[(\delta-y)^{\frac{n+1}{n}} - (\delta)^{\frac{n+1}{n}}\right]; \quad 0 \leq y \leq \delta \tag{10}$$

Similarly, for the region $-\theta_1 < \theta \leq \pi$:

$$u_3 = \left(\frac{n}{n+1}\right)\left(-\frac{1}{m_2}\frac{\mathrm{d}p_2}{\mathrm{d}x}\right)^{1/n}\left[(\delta)^{\frac{n+1}{n}} - (\delta-y)^{\frac{n+1}{n}}\right], \quad 0 \leq y \leq \delta \tag{11}$$

$$u_4 = U + \left(\frac{n}{n+1}\right)\left(-\frac{1}{m_2}\frac{\mathrm{d}p_2}{\mathrm{d}x}\right)^{1/n}\left[(h-\delta)^{\frac{n+1}{n}} - (y-\delta)^{\frac{n+1}{n}}\right], \quad \delta \leq y \leq h \tag{12}$$

Again Q, the volume flux which is obtained by solving Eq. (2) for the region: $-\pi \leq \theta < -\theta_1$, as

$$\begin{aligned} &\frac{\partial}{\partial x}\int_0^h u\,dy = 0 \Rightarrow \frac{\mathrm{d}Q}{\mathrm{d}x} = 0 \text{ where } Q = \int_0^h u\,\mathrm{d}y \\ &Q = \int_0^\delta u_2 \mathrm{d}y + \int_\delta^h u_1 \mathrm{d}y \\ &= U(h-\delta) - \left(\frac{n}{2n+1}\right)\left(\frac{1}{m_1}\frac{\mathrm{d}p_1}{\mathrm{d}x}\right)^{1/n}\left[(\delta)^{\frac{2n+1}{n}} + (h-\delta)^{\frac{2n+1}{n}}\right] \end{aligned} \tag{13}$$

The flux Q may be taken at $\theta = -\theta_1$, because it is constant everywhere in the region, where $x = R\theta$,

$$Q = \int_0^h u\mathrm{d}y = c_1, \text{ say}$$

with the condition $\frac{\mathrm{d}p}{\mathrm{d}x} = 0$, at $\theta = -\theta_1, h = h_1$ in (1) and calculate Q where (1) reduces to

$0 = \frac{\partial}{\partial y}\left[m\left|\frac{\partial u}{\partial y}\right|^{n-1}\frac{\partial u}{\partial y}\right]$, We get the volume flux at $\theta = -\theta_1$ is $U\,h_1/2$.

Hence, $Q(-\theta_1) = \int_0^{h1} u\,\mathrm{d}y = \frac{Uh_1}{2} = c_1$ and

$$\frac{\mathrm{d}p_1}{\mathrm{d}x} = m_1\left(\frac{2n+1}{n}\right)^n\left[\frac{U(h-\delta) - U(h_1/2)}{(\delta)^{\frac{2n+1}{n}} + (h-\delta)^{\frac{2n+1}{n}}}\right]^n, \quad -\pi \le \theta < -\theta_1 \tag{14}$$

$$\frac{\mathrm{d}p_2}{\mathrm{d}x} = -m_2\left(\frac{2n+1}{n}\right)^n\left[\frac{U(h_1/2) - U(h-\delta)}{(\delta)^{\frac{2n+1}{n}} + (h-\delta)^{\frac{2n+1}{n}}}\right]^n, \quad -\theta_1 < \theta \le \pi \tag{15}$$

By taking $x = R\theta, \mathrm{d}x = Rd\theta$ we get

$$\frac{\mathrm{d}p_1}{\mathrm{d}\theta} = m_1 R\left(\frac{2n+1}{n}\right)^n\left[\frac{U(h-\delta) - U(h_1/2)}{(\delta)^{\frac{2n+1}{n}} + (h-\delta)^{\frac{2n+1}{n}}}\right]^n, \quad -\pi \le \theta < -\theta_1 \tag{16}$$

In the same way, one can obtained in other region as:

$$\frac{\mathrm{d}p_2}{\mathrm{d}\theta} = -m_2 R\left(\frac{2n+1}{n}\right)^n\left[\frac{U(h_1/2) - U(h-\delta)}{(\delta)^{\frac{2n+1}{n}} + (h-\delta)^{\frac{2n+1}{n}}}\right]^n; \quad -\theta_1 < \theta \le \pi \tag{17}$$

Using the velocity matching conditions: $u_1 = u_2$ and $u_3 = u_4$ at $y = \delta$, one can obtain a single relationship as:

$$\left(\frac{2n+1}{n+1}\right)\left[\frac{[(h-\delta-h_1/2)]\left[(h-\delta)^{\frac{n+1}{n}} - (\delta)^{\frac{n+1}{n}}\right]}{(\delta)^{\frac{2n+1}{n}} + (h-\delta)^{\frac{2n+1}{n}}}\right] = 1 \tag{18}$$

It may be emphasized that Eq. (18) cannot be used to evaluate δ in the region $\theta = -\theta_1 - \varepsilon_1$ and $\theta = -\theta_1 + \varepsilon_1$ since $\frac{\partial u}{\partial y} \neq 0$ at these points at all. Hence it can be calculated using circular coordinate as

$$r - r_1 = \frac{(r_2 - r_1)}{(\theta_2 - \theta_1)}(\theta - \theta_1) \tag{19}$$

2.2 Energy Equation

The temperature equation of the fluid flow with normal assumptions for this problem is taken as Tropea et al. (2007)

$$\begin{aligned} k\frac{\partial^2 T}{\partial y^2} + m\left|\frac{\partial u}{\partial y}\right|^{n-1}\left(\frac{\partial u}{\partial y}\right)^2 &= \rho\, C_s\left(u_m \frac{\mathrm{d}T_m}{\mathrm{d}x}\right) \\ k\frac{\partial^2 T}{\partial y^2} + m\left|\frac{\partial u}{\partial y}\right|^{n-1}\left(\frac{\partial u}{\partial y}\right)^2 &= \phi(x); \text{where } \phi(x) = \rho\, C_s\left(u_m \frac{\mathrm{d}T_m}{\mathrm{d}x}\right) \end{aligned} \tag{20}$$

For this equation, the boundary conditions are taken as

$$T_1 = T_{11} \text{ at } y = h; T_2 = T_{12} \text{ at } y = 0 \tag{21}$$

Applying these above conditions in the region, $-\pi \le \theta < -\theta_1$, T_{11}, and T_{12} are calculated as:

$$\begin{aligned} T_1 = {} & \frac{y^2}{2k}\phi(x) - \left(\frac{m_1}{k}\right)\left(\frac{1}{m_1}\frac{\mathrm{d}p_1}{\mathrm{d}x}\right)^{\frac{n+1}{n}} \frac{n^2}{(2n+1)(3n+1)}(y-\delta)^{\frac{3n+1}{n}} \\ & + c_2 y + d_2, \quad \delta \le y \le h \end{aligned} \tag{22}$$

$$\begin{aligned} T_2 = {} & \frac{y^2}{2k}\phi(x) - \left(\frac{m_1}{k}\right)\left(\frac{1}{m_1}\frac{\mathrm{d}p_1}{\mathrm{d}x}\right)^{\frac{n+1}{n}} \frac{n^2}{(2n+1)(3n+1)}(\delta-y)^{\frac{3n+1}{n}} \\ & + c_3 y + d_3, \quad 0 \le y \le \delta \end{aligned} \tag{23}$$

By using the matching heat flux condition and temperature matching condition $k\frac{\partial T_1}{\partial y} = k\frac{\partial T_2}{\partial y}$ at $y = \delta$, $T_{11} = T_{12}$ at $y = \delta$ and in (22) and (23), one may get $c_1 = c_2 = c$ (say) and $d_1 = d_2 = d$ (say), hence using (21), (22), (23) give

$$\begin{aligned} c = \frac{1}{h}\Bigg[c = T_{11} - T_{12} - \frac{h^2}{2k}\phi(x) + \left(\frac{m_1}{k}\right)\frac{n^2}{(2n+1)(3n+1)}\left(\frac{1}{m_1}\frac{\mathrm{d}p_1}{\mathrm{d}x}\right)^{\frac{n+1}{n}} \\ \left[(h-\delta)^{\frac{3n+1}{n}} - (\delta)^{\frac{3n+1}{n}}\right]\Bigg] \end{aligned} \tag{24}$$

$$d = T_{12} + \left(\frac{m_1}{k}\right)\frac{n^2}{(2n+1)(3n+1)}\left(\frac{1}{m_1}\frac{\mathrm{d}p_1}{\mathrm{d}x}\right)^{\frac{n+1}{n}} \delta^{\frac{3n+1}{n}} \tag{25}$$

In the same way, one can get in the region $-\theta_1 < \theta \le \pi$

$$T_3 = -\left(\frac{m_2}{k}\right)\left(-\frac{1}{m_2}\frac{\mathrm{d}p_2}{\mathrm{d}x}\right)^{\frac{n+1}{n}}\frac{n^2}{(2n+1)(3n+1)}(\delta - y)^{\frac{3n+1}{n}} + a_1 y + b_1 \tag{26}$$

$$T_4 = -\left(\frac{m_2}{k}\right)\left(-\frac{1}{m_2}\frac{\mathrm{d}p_1}{\mathrm{d}x}\right)^{\frac{n+1}{n}}\frac{n^2}{(2n+1)(3n+1)}(y - \delta)^{\frac{3n+1}{n}} + a_2 y + b_2 \tag{27}$$

Use of the matching heat flux condition and temperature matching condition $k\frac{\partial T_3}{\partial y} = k\frac{\partial T_4}{\partial y}$ at $y = \delta$, $T_{11} = T_{12}$ at $y = \delta$, in (26) and (27) with $a_1 = a_2 = a$; and $b_1 = b_2 = b$ one can get

$$a = \frac{1}{h}\left[T_{11} - T_{12} - \frac{h^2}{2k}\phi(x) + \left(\frac{m_2}{k}\right)\frac{n^2}{(2n+1)(3n+1)}\left(-\frac{1}{m_2}\frac{\mathrm{d}p}{\mathrm{d}x}\right)^{\frac{n+1}{n}}\left[(h-\delta)^{\frac{3n+1}{n}} - (\delta)^{\frac{3n+1}{n}}\right]\right] \tag{28}$$

$$b = T_{12} + \left(\frac{m_2}{k}\right)\frac{n^2}{(2n+1)(3n+1)}\left(-\frac{1}{m_1}\frac{\mathrm{d}p_2}{\mathrm{d}x}\right)^{\frac{n+1}{n}}\delta^{\frac{3n+1}{n}} \tag{29}$$

At last as defined in (4), the mean temperatures T_{m1} and T_{m2} are:

$$T_m = \frac{1}{h}\int_0^h T\,\mathrm{d}y = \frac{1}{h}\int_0^\delta T_2\,\mathrm{d}y + \frac{1}{h}\int_\delta^h T_1\,\mathrm{d}y, \quad \text{or}$$

$$T_{m1} = \frac{1}{2}(T_{11} + T_{12}) - \frac{h^2}{12k}\phi(x) - \frac{nA}{(4n+1)}\left[\frac{(h-\delta)^{\frac{4n+1}{n}} + (\delta)^{\frac{4n+1}{n}}}{h}\right] + A\left[\frac{(\delta)^{\frac{3n+1}{n}} + (h-\delta)^{\frac{3n+1}{n}}}{2}\right], \quad -\pi \le \theta < -\theta_1 \tag{30}$$

where $A = -\left(\frac{m_1}{k}\right)\left(\frac{1}{m_1}\frac{\mathrm{d}p_1}{\mathrm{d}x}\right)^{\frac{n+1}{n}}\left(\frac{n^2}{(2n+1)(3n+1)}\right)$, Similarly,

$$T_{m2} = \frac{1}{2}(T_{11} + T_{12}) - \frac{h^2}{12k}\phi(x) - \frac{nB}{(4n+1)}\left[\frac{(h-\delta)^{\frac{4n+1}{n}} + (\delta)^{\frac{4n+1}{n}}}{h}\right] + B\left[\frac{(\delta)^{\frac{3n+1}{n}} + (h-\delta)^{\frac{3n+1}{n}}}{2}\right], \quad -\theta_1 < \theta \le \pi \tag{31}$$

where $B = -\left(\frac{m_2}{k}\right)\left(-\frac{1}{m_2}\frac{dp_2}{dx}\right)^{\frac{n+1}{n}}\left(\frac{n^2}{(2n+1)(3n+1)}\right)$.

2.3 Dimensionless Schemes

Using dimensionless scheme Prasad et al. (2014), the Eqs. (16), (17), (30), and (31) can be written as

$$\frac{\mathrm{d}\overline{p_1}}{\mathrm{d}\theta} = \overline{m}\left(\overline{f}\right)^n; \quad -\pi \le \theta < -\theta_1 \tag{32}$$

$$\frac{\mathrm{d}\overline{p_2}}{\mathrm{d}\theta} = -\overline{m}\left(-\overline{f}\right)^n; \quad -\theta_1 < \theta \le \pi \tag{33}$$

$$\frac{\mathrm{d}\overline{T}_{m1}}{\mathrm{d}\theta} = \left[\overline{T}_A - \overline{T}_{m1} - \left(\frac{n}{3n+1}\right) p_r \overline{m}\left(\overline{f}\right)^{n+1} \overline{g}\right] / (p_e \overline{\gamma}); \quad -\pi \le \theta < -\theta_1 \tag{34}$$

$$\frac{\mathrm{d}\overline{T}_{m2}}{\mathrm{d}\theta} = \left[\overline{T}_A - \overline{T}_{m2} - \left(\frac{n}{3n+1}\right) p_r \overline{m}\left(-\overline{f}\right)^{n+1} \overline{g}\right] / (p_e \overline{\gamma}); \quad -\theta_1 < \theta \le \pi \tag{35}$$

where $\overline{g} = \left[\frac{n}{4n+1}\left(\frac{\left(\overline{h}-\overline{\delta}\right)^{\frac{4n+1}{n}} + \overline{\delta}^{\frac{4n+1}{n}}}{\overline{h}}\right) - \left(\frac{\left(\overline{h}-\overline{\delta}\right)^{\frac{3n+1}{n}} + \overline{\delta}^{\frac{3n+1}{n}}}{2}\right)\right]$, $\overline{m} = mc_n\alpha$ etc.;

$c_n = \left(\frac{U}{c}\right)^n \left(\frac{2n+1}{n}\right)^n \left(\frac{R}{c}\right)$, $\overline{f} = \frac{(\overline{h}-\overline{\delta}) - \overline{h}_1/2}{\left(\overline{h}-\overline{\delta}\right)^{\frac{2n+1}{n}} + \overline{\delta}^{\frac{2n+1}{n}}}$

$$p_e = \frac{\rho\, C_p U c}{K}, \quad p_r = \frac{\beta\, U c}{K\,\alpha}\left(\frac{c}{R}\right), \quad \overline{\gamma} = \frac{\overline{h}\overline{h}_1}{24\overline{R}}, \quad \overline{T}_A = \frac{T_{11} + T_{12}}{2}$$

here P_e and P_r are modified Peclet and Prandtl numbers.

2.4 Load

The load components W is calculated as

$$W = 2\int_0^{\pi} p\,\cos\theta\, R\,\mathrm{d}\theta = -2R\int_0^{\pi} \sin\theta \frac{\mathrm{d}p}{\mathrm{d}\theta}\mathrm{d}\theta$$

$$\overline{W} = 2\int_0^{\pi} \overline{p}\,\cos\theta\,\mathrm{d}\theta, \text{where } \overline{W} = \frac{W\alpha}{R}, \overline{W} = -2\int_0^{\pi} \sin\theta \frac{\mathrm{d}\overline{p}}{\mathrm{d}\theta}\mathrm{d}\theta$$

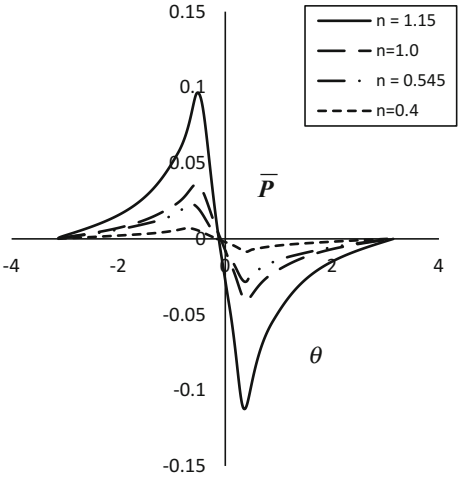

Fig. 2 At different values of n, θ versus pressure profile

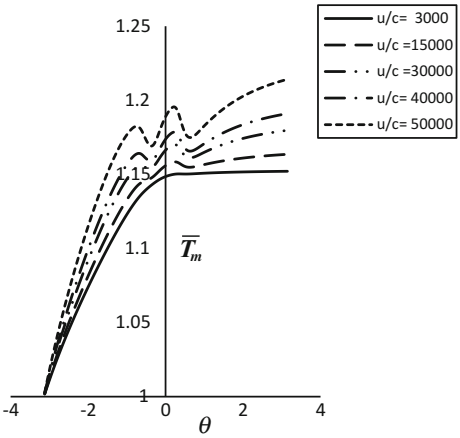

Fig. 3 Temperature at $n = 1.15$, at different velocity

3 Numerical Calculation

Theoretical approach of numerically calculated results for pressure and temperature regarding the flow characteristics index n and the velocity ratio U/c is exhibited through figures and tables. We consider the estimation of n in the middle of 0.4 and 1.15. For computing, the following sets of values are used: $\bar{R} = 12.0$, $\alpha = 1.6 \times 10^{-9}\text{dyne}^{-1}\text{m}^2$, $\varepsilon = 0.701, Pe = 400.9, \overline{U} = 44000/\text{s}$. The simultaneous Eqs. (32, 34) and (33, 35) are numerically solved for dimensionless temperature $\bar{T}_m$ and pressure $\bar{P}$ and by Runge–Kutta–Fehlberg method to analyze the qualitative behavior of lubricants. The difference of $\bar{P}$ and $\bar{T}_m$ is presented, respectively, in Figs. 2 and 3. One can observe that one feature is common in every case that the general shape of the profile does not changed if n varies.

3.1 Pressure Distribution

For various values of n, the pressure distribution $\bar{P}$ versus θ has been shown in Fig. 2. $\bar{P}$ increases constantly when θ increases from $-\pi$ to $-\theta_1$. The pressure profile $\bar{P}$ then decreases from here to $+\theta_1$ then again increases up to $\theta = \pi$ Wang et al. (2001), Thomsen and Klit (2011), and Balasoiu et al. (2013). The increase of pressure with n is similar to that of Peng and Khonsari (2006), Singh et al. (2008a, b), Xiong and Wang (2012), and Chen et al. (2013).

3.2 Temperature Distribution

For various values of U/c, the mean temperature distributions $\bar{T}_m$ are shown in Fig. 3. It is exciting to observe that $\bar{T}_m$ increases with θ except in the neighborhood of zero where the trend is somewhat zigzag. The same feature is seen by Liu et al. (2008). Further, temperature $\bar{T}_m$ is studied for different values of n.

Table 1 Load

U/c	N	Theta1	Load	Traction
44,000	1.15	0.52675	0.092651	0.092906
	1	0.559	0.032125	0.032201
	0.545	0.659	0.020373	0.022046
	0.4	0.7095	0.005891	0.006734
40,000	1.15	0.5268	0.086423	0.086503
	1	0.56	0.029728	0.029742
	0.545	0.659	0.019424	0.021032
	0.4	0.7094	0.005666	0.006492
36,000	1.15	0.528	0.079721	0.079579
	1	0.561	0.027276	0.027166
	0.545	0.66	0.018353	0.019991
	0.4	0.711	0.005453	0.006218
32,000	1.15	0.5293	0.072685	0.072381
	1	0.5616	0.024634	0.024566
	0.545	0.6602	0.017345	0.018863
	0.4	0.7107	0.005193	0.005952
28,000	1.15	0.53094	0.065245	0.064864
	1	0.564	0.016996	0.01685
	0.545	0.66099	0.016222	0.017671
	0.4	0.711	0.004929	0.005644

3.3 *Load*

Load is shown in Table 1. It can be seen from the table that the load increases with *n* and U/c both. Load increases with n shows that dilatant fluid exerts more pressure than that of pseudoplastic fluids (Prasad et al. 2014). Further, increase of load with U/c shows that higher velocity is responsible for higher pressure.

4 Conclusion

An additional effort has been made to include the heat of convection in the energy equation. Solutions are obtained for pressure, the mean temperature, and delta for circular coordinate. The following conclusions may be drawn:

- The pressure $\bar{P}$ increases when the power law index n increases.
- The mean temperature $\bar{T}_m$ increases with n for fixed P_e.
- Temperature $\bar{T}_m$ decreases as P_e increases, for fixed n.
- Load and traction decrease when the values of n decrease for a fixed value of U/c.
- For a fixed value of *n*, load increases with U/c.

References

Ahmad MA, Kasolang S, Dwyer RS (2014) Experimental study on the effects of oil groove location on temperature and pressure profiles in journal bearing lubrication. Tribol Int 74:79–86

Balasoiu AM, Braun MJ, Moldovan SI (2013) A parametric study of porous self-circulating hydrodynamic bearing. Tribol Int 61:176–193

Boncompain R, Fillon M, Frene J (1986) Analysis of thermal effects in hydrodynamic bearings. J Tribol 108(2):219–224

Chen CY, Chen QD, li WL (2013) Characteristics of journal bearings with anisotropic slip. Tribol Int 61:144–155

Gao G, Yin Z, Jiang D, Zhang X (2014) Numerical analysis of plain journal bearing under hydrodynamic lubrication by water. Tribol Int 75:31–38

Hunter WB, Zienkiewicz OC (1960) Effect of temperature variations across the lubricant films in the theory of hydrodynamic lubrication. J Mech Eng Sci 2(1):52–58

Johnson MW, Mangkoesoebroto S (1993) Analysis of lubrication theory for the power law fluid. J Tribol 115(1):71–77

Kango S, Sharma RK, Pandey RK (2014) Thermal analysis of microtextured journal bearing using non-Newtonian rheology of lubricant and JFO boundary conditions. Tribol Int 69:19–29

Khonsari MM, Brewe DE (1989) On the performance of finite journal bearings lubricated with micropolar fluids. Tribol Trans 32(2):155–160

Liu D, Zjang W, Zhang T (2008) A simplified one dimensional thermal model for journal bearing. J Tribol 30

Mongkolwongrojn M,Aiumpornsin C (2010) Theoretical investigation of journal bearings with non-Newtonian fluids included thermal effects. Adv Tribol, 52–53

Nessil A, Larbi S, Belhaneche H, Malki M (2013) Journal bearings lubrication aspect analysis using non-Newtonian fluids. Adv Tribol 212568:9. doi:10.1155/2013/212568

Peng ZC, Khonsari MM (2006) A thermohydrodynamic analysis of foil journal bearing. J Lubr Technol 128

Prasad D, Panda SS, Subrahmanyam SV (2014) Power law fluid film lubrication of journal bearing with squeezing and temperature effects. In: Proceedings of international conference on advances in tribology and engineering systems. Lecture notes on mechanical engineering, Springer, UK, pp 73–84

Sing U, Roy I, Sahu M (2008a) Stedy state THD analysis of cylindrical fluid film journal bearing with an axial groove. Tribol Int 4:1135–1144

Sing U, Roy L, Sahu M (2008b) Steady state THD analysis of cylindrical fluid film journal bearing with an axial groove. Tribol Int 4:1135–1144

Thomsen K, Klit P (2011) A study on complaints layers and its influence on dynamic response of a hydrodynamic Journal bearing. Tribol Int 44:1872–1877

Tropea C, Yarin AL, Foss JF (2007) Springer handbook of experimental fluid mechanics. Springer, Berlin. ISBN:3-540-25141-3, ISBN:978-3-540-25141-5: 661

Wang XL, Zhu K, Wen S (2001) THD analysis of journal bearing lubricated with couple stress fluid. Tribol Int 34:335–343

Xiong S, Wang QJ (2012) A steady state hydrodynamic lubrication model with the Payvar-Salant mass conservation model. J Tribol 134(031703–1):031703–031716

Yang HR, Wang XL, Zhang YY, Du JF (2014) Study on the bubbly lubrication of journal bearings at various shear rates and temperatures. Tribol Int 71:132–139

Numerical Simulation of Flow Around Square Cylinder with an Inlet Shear in a Closed Channel

Atendra Kumar and Rajendra K. Ray

Abstract In this paper, two-dimensional unsteady flow of incompressible fluid past a square cylinder placed in a closed finite domain is studied in the presence of an inlet linear shear velocity profile. The flow has been investigated for Reynolds number $Re = 100$ and shear rate $K = 0.0, 0.05, 0.1$. The governing equations are solved by using the higher order compact (HOC) finite difference scheme. The purpose of the present study is to elaborate the influence of shear rate on the vortex shedding phenomenon behind the square cylinder. The results are presented in terms of streamline pattern, vorticity contours, lift–drag coefficients, and their corresponding power spectra. It is observed that the vortex shedding phenomenon strongly depends on Re as well as K. The strength and size of vortices vary as a function of Re and K, but not significantly for the current values of parameters.

1 Introduction

The subject of flow around solid objects is applicable to many practical as well as industrial applications such as skyscrapers, suspension bridges, towers, tides and currents, offshore structures. In past few years, so many numerical and experimental studies have been declared in the literature with new observations. However, most of the research is done for uniform free-stream flow past circular and square cylinders. However, the fluid–solid interaction is different for shear flow than uniform flow because of embedded vorticity or turbulence in the inlet flow (Cheng et al. 2007; Hawang and Sue 1997; Kumar and Ray 2015). The confined flow past a square cylinder mounted inside a closed channel was investigated by Breuer et al. (2000). The results were computed by two different numerical techniques, a

A. Kumar (✉) · R.K. Ray
School of Basic Sciences, Indian Institute of Technology Mandi, Mandi, 175001 Kamand, Himachal Pradesh, India
e-mail: atendra.iitd@gmail.com

R.K. Ray
e-mail: rajendra@iitmandi.ac.in

M.K. Singh et al. (eds.), *Applications of Fluid Dynamics*, Lecture Notes in Mechanical Engineering, https://doi.org/10.1007/978-981-10-5329-0_21

lattice-Boltzmann automata (LBA) and a finite volume method (FVM) for $Re = 300$ by assuming the flow to be two-dimensional. By comparing the results computed from both techniques, excellent agreement is found between the LBA and FVM.

The higher order compact (HOC) finite difference methods are popularly known for the solution of the problems involving fluid flow because of their high accuracy and compact difference stencil. Kalita et al. (2004) developed this type of HOC scheme on Cartesian non-uniform grids for the steady 2D convection–diffusion equation with variable coefficients without any transformation. As time goes on, this scheme has extended on non-uniform polar grids by (Kalita and Ray 2009; Ray and Kalita 2010) to figure out the flow phenomenon around circular cylinder, lift–drag forces, which can be easily extended for curvilinear coordinates. Later on, Lankadasu and Vengadesan (2010) and Kumar and Ray (2015) apply this scheme to understand the vortex shedding phenomenon for shear flow around square cylinder placed in an infinite physical domain at $Re = 100, 200$. The accuracy and efficiency of HOC scheme have already been confirmed in the case of flow past cylinder problem. Till now, this scheme is not tested for the problem of shear flow around square cylinder placed in a closed finite domain.

2 Mathematical Formulation

2.1 Governing Equations

The problem of unsteady, incompressible shear flow past an impulsively started square cylinder of side length "a" placed in a closed domain is considered in this paper. The schematic flow diagram of the physical problem is shown in Fig. 1.

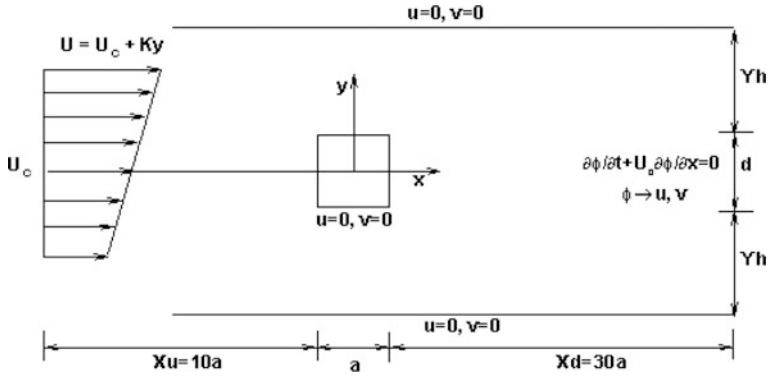

Fig. 1 Schematic diagram of the shear flow past square cylinder

The flow is governed by the incompressible Navier–Stokes equations. The dimensionless stream function-vorticity $(\psi - \omega)$ form of the N–S equations in Cartesian coordinates (x, y) is given by

$$\frac{\partial^2 \omega}{\partial x^2} + \frac{\partial^2 \omega}{\partial y^2} = Re\left(u\frac{\partial \omega}{\partial x} + v\frac{\partial \omega}{\partial y} + \frac{\partial \omega}{\partial t}\right) \tag{1}$$

$$\frac{\partial^2 \psi}{\partial x^2} + \frac{\partial^2 \psi}{\partial y^2} = -\omega \tag{2}$$

Here, ω represents vorticity and ψ for stream function, and u and v represent the x-direction and y-direction velocity components, respectively. The velocity components u, v in terms of stream function ψ can be written as

$$u = \frac{\partial \psi}{\partial y}, \quad v = -\frac{\partial \psi}{\partial x} \tag{3}$$

And vorticity ω is

$$\omega = \frac{\partial v}{\partial x} - \frac{\partial u}{\partial y} \tag{4}$$

For the physical boundary conditions, at inlet, a linear shear velocity profile has been applied,

$$u = U_c + Ky, \quad v = 0 \tag{5}$$

where U_c is the centerline velocity of inflow and K is the shear parameter. For making the problem computationally efficient, the artificial outflow boundaries of the computational domain are considered sufficiently far from the cylinder boundary to minimize their effect on the characteristics of the flow near the surface of square cylinder. In the present study, the outflow is considered $30a$ distant from the cylinder.

No-slip boundary conditions are considered on the surface of the cylinder, and top–bottom boundaries of the domain and convective boundary condition are applied at the outflow (Kumar and Ray 2016).

$$\frac{\partial \phi}{\partial t} + U_c\frac{\partial \phi}{\partial x} = 0 \tag{6}$$

2.2 Numerical Discretization

We discretized the governing equations using higher order compact (HOC) scheme on Cartesian grids. Thus, the HOC discretizations of the governing Eqs. (1 and 2) at $(i,j)^{th}$ grid point of the computational domain are given as

$$\begin{aligned}&\left[Re + A11_{ij}\delta_x^2 + A12_{ij}\delta_y^2 + A13_{ij}\delta_x + A14_{ij}\delta_y + A15_{ij}\delta_x\delta_y\right.\\&\left. + A16_{ij}\delta_x\delta_y^2 + A17_{ij}\delta_x^2\delta_y + A18_{ij}\delta_x^2\delta_y^2\right]\omega_{ij}^{n+1} = \left[Re + A21_{ij}\delta_x^2\right.\\&\left. + A22_{ij}\delta_y^2 + A23_{ij}\delta_x + A24_{ij}\delta_y + A25_{ij}\delta_x\delta_y + A26_{ij}\delta_x\delta_y^2\right.\\&\left. + A27_{ij}\delta_x^2\delta_y + A28_{ij}\delta_x^2\delta_y^2\right]\omega_{ij}^{n}\end{aligned} \tag{7}$$

and

$$\left[\delta_x^2 + \delta_y^2 - (H2 + K2)\delta_x^2\delta_y^2\right]\psi_{ij} = \left[-1 + H2\delta_x^2 + K2\delta_y^2\right]\omega_{ij} \tag{8}$$

respectively, where the coefficients are defined as

$$\begin{aligned}&A11_{ij} = -H12Re - 0.5\Delta tA1_{ij}, A12 = -K12Re - 0.5\Delta tA2_{ij},\\&A13_{ij} = -H11Re - H12u_{ij}Re^2 - 0.5\Delta tA3_{ij},\\&A14_{ij} = -K11Re - K12v_{ij}Re^2 - 0.5\Delta tA4_{ij},\\&A15_{ij} = -0.5\Delta tA5_{ij}, A16_{ij} = -0.5\Delta tA6_{ij},\\&A17_{ij} = -0.5\Delta tA7_{ij}, A18_{ij} = -0.5\Delta tA8_{ij},\end{aligned}$$

where

$$\begin{aligned}A1_{ij} &= 1 + H11Reu_{ij} + H12Re^2u_{ij}^2 + 2H12Re(u_x)_{ij},\\A2_{ij} &= 1 + K11Rev_{ij} + K12Re^2v_{ij}^2 + 2K12Re(v_y)_{ij},\\A3_{ij} &= -Reu_{ij} + H11Re(u_x)_{ij} + K11Re(u_y)_{ij} + H12Re^2u_{ij}(u_x)_{ij}\\&\quad + H12Re(u_{xx})_{ij} + K12Re(u_{yy})_{ij} + K12Re^2v_{ij}(u_y)_{ij},\\A4_{ij} &= -Rev_{ij} + H11Re(v_x)_{ij} + K11Re(v_y)_{ij} + H12Re^2u_{ij}(v_x)_{ij}\\&\quad + H12Re(v_{xx})_{ij} + K12Re(v_{yy})_{ij} + K12Re^2v_{ij}(v_y)_{ij},\\A5_{ij} &= H11Rev_{ij} + K11Reu_{ij} + H12Re^2u_{ij}v_{ij} + 2H12Re(v_x)_{ij}\\&\quad + 2K12Re(u_y)_{ij} + K12Re^2u_{ij}v_{ij},\\A6_{ij} &= -H11 - H12Reu_{ij} + K12Reu_{ij},\\A7_{ij} &= -K11 + H12Rev_{ij} - K12Rev_{ij}, A8_{ij} = -H12 - K12,\end{aligned}$$

The detailed explanation of the discretization leading to Eqs. (7) and (8) and finite difference operators can be found in Kumar and Ray (2015).

3 Results and Discussion

At $Re = 100$, an extensive investigation of the wake flow behind the cylinder at different shear parameter (K) values is presented in this paper. In this study, we consider blockage ratio to be $B = 8d$ (B is domain width) for understanding the domain boundary effect on the flow phenomenon. For the computation, a uniform grid of size 1001×161 is to be used. Figure 2 shows the vorticity contours and the streakline patterns for different K values to describe the flow phenomenon. For $K = 0.0$, vorticity contours shown in Fig. 2a, it is clear that size and strength of the positive and negative vortices developed in this case are same. The vortices shed behind the cylinder in a regular alternating arrangement. This is also clear from the streakline pattern shown in Fig. 2b. For $K = 0.05$, Fig. 2c, d shows the vorticity contours and streakline evolution, respectively. In this case, the sizes of the negative vortices are different than those of positive vortices but not significantly for the current value of K. We have seen this effect significantly with increasing in K value, i.e., $K = 0.1$ in Fig. 2e. The flow becomes asymmetric behind the cylinder; vortices shed from the bottom surface of the cylinder are of slender shape. The fluid layers passing through upper surface have more relative velocity than the bottom surface of the cylinder because of significant shear effect in the incoming flow. The streakline pattern for $K = 0.1$ shown in Fig. 2f describes the similar flow phenomenon.

The fluid flowing past a solid body exerts a force on it. The tangential component of this force is called drag force and normal component is called lift force. In Fig. 3, lift coefficient fluctuation with time and their corresponding power spectra

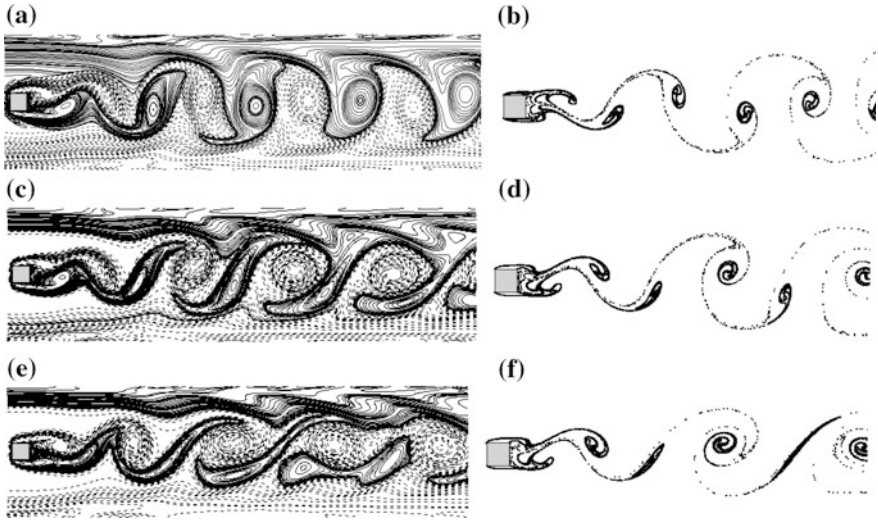

Fig. 2 Vortcity contours (*left*) and streakline pattern (*right*) for $Re = 100$. **a**, **b** $K = 0.0$; **c**, **d** $K = 0.05$; and **e**, **f** $K = 0.1$

for $Re = 100$ are plotted at three different shear parameter values as $K = 0.0, 0.05, 0.1$. For $K = 0.0$, Fig. 3a shows a single peak value in lift coefficient and their corresponding power spectra; this means vortices shed behind the cylinder of the same frequency. When $K = 0.05$, Fig. 3c shows the lift coefficient variation with time, and no significant change occurs from the previous case, and the amplitude of fluctuation is approximately constant. Power spectrum shows a single peak in Fig. 3d. However, increasing the K value to 0.1 shows similar lift coefficient pattern in Fig. 3e with decreasing vortex shedding frequency. It is clear from power spectra plot shown in Fig. 3f, where frequency corresponding to peak value defines vortex shedding frequency (Strouhal number).

Another most important characteristic quantity of the flow past square cylinder is the drag coefficient shown in Fig. 4 for $K = 0.0, 0.05, 0.1$. The periodic fluctuation corresponds to alternate vortex shedding phenomenon. When $K = 0.0$, Fig. 4a

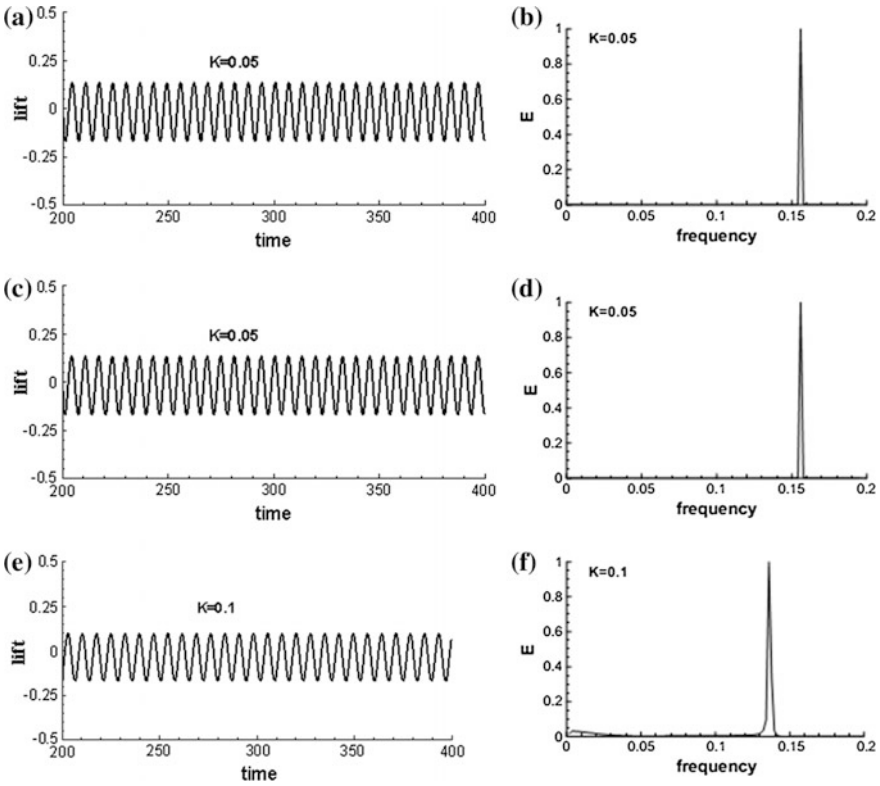

Fig. 3 Lift coefficient fluctuation with time and their corresponding power spectrum for $Re = 100$ at different K values

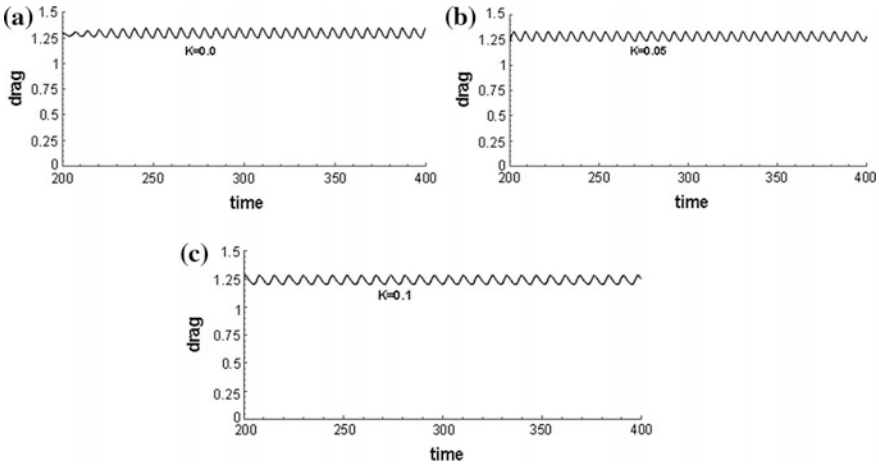

Fig. 4 Drag coefficient fluctuation with time for $Re = 100$ at different K values

shows that drag coefficient fluctuates with approximate constant amplitude. Figure 4b shows no significant change in the drag coefficient fluctuation for $K = 0.05$ except initial stage of the flow. However, mean value of the drag coefficient decreases with increasing K value. For $K = 0.0$, drag coefficient variation with time shown in Fig. 4c, it is observed that mean value of drag coefficient decreases. The amplitude of fluctuation is nearly same with the previous K values.

4 Conclusion

In this paper, a higher order compact numerical simulation of shear flow past square cylinder placed in a closed domain is carried out. The computational results are shown for $Re = 100$ and $K = 0.0, 0.05, 0.1$ in terms of vorticity contours, drag coefficients, lift coefficients, and their corresponding power spectra. It is found that vortex shedding phenomenon depends significantly on K as well as Re value. The frequency of vortex shedding decreases with increasing K values. We have studied the effect of shear rate on the flow phenomenon near the surface of the square cylinder for a long range of shear parameter values, but the full study is not in the scope of this paper.

Acknowledgements The work has been done under a SERB funded project (No.: SERB/F/7046/2013-2014 dated 12.02.2014). The authors kindly acknowledge the financial support of SERB (DST), Govt. of India.

References

Breuer M, Bernsdorf J, Zeiser T, Durst F (2000) Accurate computations of the laminar flow past a square cylinder based on two different methods: lattice-Boltzmann and finite-volume. Int J Heat Fluid Flow 21:186–196

Cheng M, Whyte DS, Lou J (2007) Numerical simulation of flow around a square cylinder in uniform-shear flow. J Fluids Struct 23:207–226

Hwang RR, Sue YC (1997) Numerical simulation of shear effect on vortex shedding behind a square cylinder. Int J Numer Meth Fluids 24:1409–1420

Kalita JC, Ray RK (2009) A transformation-free hoc scheme for incompressible viscous flows past an impulsively started circular cylinder. J Comput Phys 228:5207–5236

Kalita JC, Dass AK, Dalal D (2004) A transformation-free hoc scheme for steady-state convection diffusion on non-uniform grids. Int J Numer Meth Fluids 44:33–53

Kumar A, Ray RK (2015) Numerical study of shear flow past a square cylinder at Reynolds number 100, 200. Procedia Eng 127:102–109

Kumar A, Ray RK (2016) Higher order compact numerical simulation of shear flow past inclined square cylinder. Adv Intell Syst Comput 452:305–313

Lankadasu A, Vengadesan S (2010) Shear effect on square cylinder wake transition characteristics. Int J Numer Meth Fluids 67:1115–1134

Ray RK, Kalita JC (2010) A transformation-free hoc scheme for incompressible viscous flows on non-uniform polar grids. Int J Numer Meth Fluids 62:683–708

Fluidic Logic Element Performance Calculation

V.N. Samsonov, E.I. Kurkin, O.E. Lukyanov and V.G. Shakhov

Abstract The results of gas-dynamic characteristic studies of logic chips jet element are considered. The study carried out by numerical method is based on the integration of the Navier–Stokes equations. For closure of simultaneous equations in this research, the two-region hybrid turbulence model of transfer of tangential stress is used. The model of compressed viscous gas is applied. Its properties correspond to properties of air of standard atmosphere at the height of mean sea level. The main characteristics of the switching logic element output signals, depending on the influence of control signals, were found. It is shown that relative rate in the output channels depends on the relative pressure in the control channels. It is calculated the required values of pressure in control channels of logic element necessary for switching of an output signal. Because of viscous properties of working body, the Coanda effect which is used for sticking of feeding air current to channel walls for purpose of steady work logical device is realized. Zones of flow contraction are installed in channels of device

V.N. Samsonov
Department of Machine Design Principles, Samara National Research University,
34, Moskovskoe Shosse, Samara 443086, Russian Federation
e-mail: samsonov@ssau.ru

E.I. Kurkin (✉) · O.E. Lukyanov · V.G. Shakhov
Department of Aircraft Construction and Design, Samara National Research University,
34, Moskovskoe Shosse, Samara 443086, Russian Federation
e-mail: eugene.kurkin@mail.ru

O.E. Lukyanov
e-mail: lukyanovoe@mail.ru

V.G. Shakhov
e-mail: shakhov@ssau.ru

M.K. Singh et al. (eds.), *Applications of Fluid Dynamics*, Lecture Notes
in Mechanical Engineering, https://doi.org/10.1007/978-981-10-5329-0_22

1 Introduction

Development of automation and its extended application in all industries set a task to create the cheap, reliable and simple control systems capable to carry out difficult functions (Zalmanzon 1969). Some classification and general design of fluidic elements were shown in Olivotto (2010). The possible solution of this task is the use of pneumonic hydro-automatics (Leskiewicz and Zaremba 1980). Development of pneumatic automation led to creation of wide scale of devices (Ferner 1954), carrying out such functions as information acquisition (sensors with pneumatic exit, pneumatic switches, and others) (Prusenko 1965), transformation and information storage (pneumatic regulators, optimizers, analog computing device, relay systems) (Fudim 1973, Slovar' po kibernetike 1989) information presentation (recording devices, indicators) (Berends et al. 1968), embodiment of control action (pneumatic actuating devices). In Russia has been consistently developed the modular pneumatic control system containing a number of blocks, implementing independent automatic control function, united to solve complex logical tasks. The systems known under general name "Fluidics" or "Pneumonic" are not containing moving components (Yeaple 1960) and using the principle of direct interaction of flows. They have the following advantages: they can be much cheaper and reliable in comparison with systems containing moving mechanical components and they can be used under more difficult operating conditions compared to electronic components. The much attention in since and industry of many countries is given to fluidics (Korotkov 1972; Bowles et al. 1960). Development of new logic devices of pneumatic automation is possible not only on the basis of field researches (Wilson et al. 1969), but also with mobilization of resources of computing aero hydrodynamics. The main purpose of this article is to evaluate the possibility of determining the characteristics of fluidic logical elements using the methods of computational aerodynamics.

Research subject in this article is the element of fluidics carrying out logical operation "OR-NOT-OR" presented on Fig. 1. According to (Chaplygin 1989), the similar devices use small working pressure about 0.5 kPa. The device is equipped with channel for air/gas feed, control channels, output channels, and communication channels with atmosphere. To feed channel, the air with a certain pressure is supply. The control channels are designed to giving of air control signals for purpose of deviation of feed channel air jet to the left or to the right to corresponding output channels. At pressure application to the left control channel, the air current directed from feed channel sticks to the right wall of extending internal channel of trigger and, thus, gets to the right output channel of pneumatic device which forms a certain logical signal. For redirection of air current in left output channel for the purpose of change of logic instruction, it is necessary to apply pressure to the right control channel that will entail "exfoliation" gas flow from the right wall of internal channel of device, "sticking" to the left wall of channel and, respectively, giving of air current in left output channel.

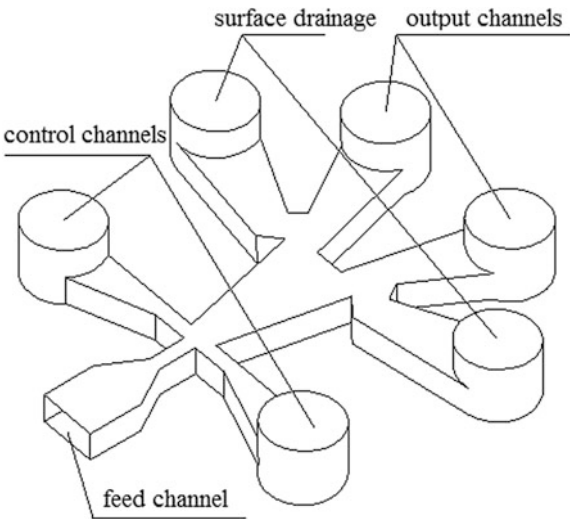

Fig. 1 Scheme of logic element

Computational fluid dynamics approach has been used for numerical study of bistable amplifiers fluidic element (Roger 2003). Main goal of our research is to obtain performance characteristic of fluidic logic element "OR-NOT-OR" type using ANSYS CFX software.

2 Research Technique. Mathematical Models

The mathematical model of finite volume method based on solution of Navier–Stokes equations is applied for theoretical research of operation process of considered device (Wilcox 2006). For closure of simultaneous equations in this research, the turbulence model of transfer of tangential stress (SST) is used (Lantry et al. 2005). On the basis of three-dimensional geometrical model (see Fig. 1), the working area by digitization of working volume of logic element on final volumes forming in total a computational grid (Fig. 2) is generated.

Geometric singularities of considered logic element allow using the structured computational grids for calculation that provides the best grid repeatability, reduces estimation time, and gives big accuracy at smaller quantity of cells. The ordered regular structure of grid has block character (Fig. 3). The similar structure in round channels prevents appearance of acute-angled cells which are badly affecting the process of repeatability and stability of decision.

For modeling of viscous interaction of channels' wall and gas, the gradient growth of thickness of cells from surface of channel is provided. The choice of thickness of first cell on surface of internal channels of device is carried out, relying

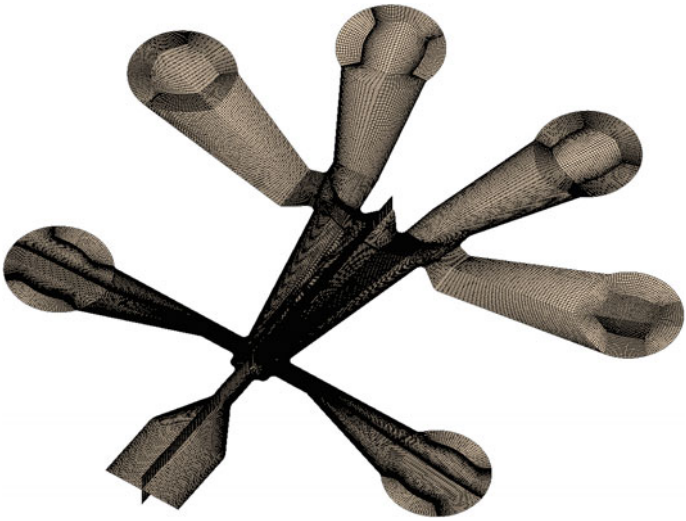

Fig. 2 Computational grid in sectional view

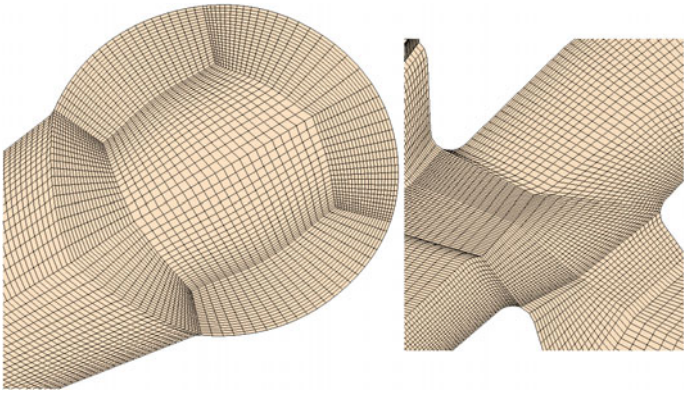

Fig. 3 Computational grid in sectional view of output channel

on ensuring the recommended value of relative thickness of first cell y^+. A number of scoping calculations for analysis of grid repeatability and definition of distribution of value y^+ on walls of element model which value should not exceed five units for chosen turbulence model (Fig. 4) are carried out. The calculation area consists of 2,700,000 cells which provides good convergence and repeatability of the results obtained.

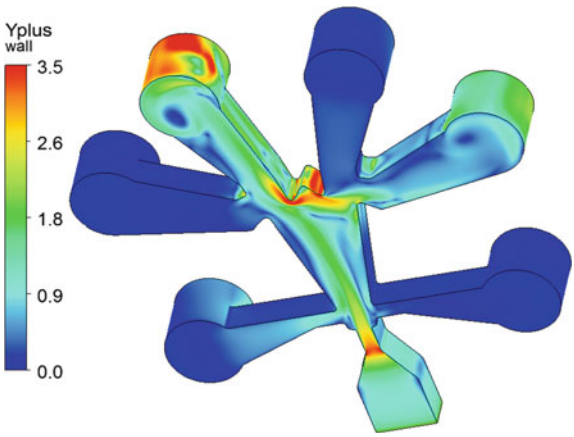

Fig. 4 Distribution of relative thickness of first cell y^+ on surface of walls of model channel

3 Performance Calculation of Control Element

According to technical characteristics of similar devices (Chaplygin 1989), boundary conditions of element model have been set. On feed channel inlet, the velocity of flow was set 18 m/s, and on control channels, the pressure was set from 0 to 400 Pa depending on set element operating mode. On output channels of element, the condition of lack of excessive pressure was set. Drainage channel outputs allow to flow of gas in both directions. The model of compressed viscous gas with constant dynamic viscosity is used. When carrying out numerical experiment, the gas current in channels of logic element for purpose of impact assessment of pressure value of control signals upon deviation of air current of feed channel creating consumption in this or that output channel of element is simulated. The calculation distributed (velocity fields and pressure fields) and integrated (consumption, pressure) gas-dynamic characteristics of considered logic element is carried out for variants of pressure application serially in left and right control channels from 0 to 450 Pa. On Fig. 5, the velocity field in channels of logic element at pressure application of 350 Pa upon the left control channel is presented.

Pressure was distributed on element channels, as shown on Fig. 6. Increase of pressure is observed in place of gas contraction in input channel.

In calculations, the model of compressed gas was used, therefore the gas density which reached 1.24 kg/m^3 (Fig. 7) also grows in zones of an elevated pressure.

After switching off of control signal as Coanda effect is realized, the air current remains stuck to the right wall of the channel. It is well visible on velocity field in element channels presented on Fig. 8.

Switching the jet back requires overcoming the Coanda effect—redirection of the jet from the right side of the element in other output channel needs apply pressure to the right control channel (Figs. 9 and 10). Switching of a signal happens

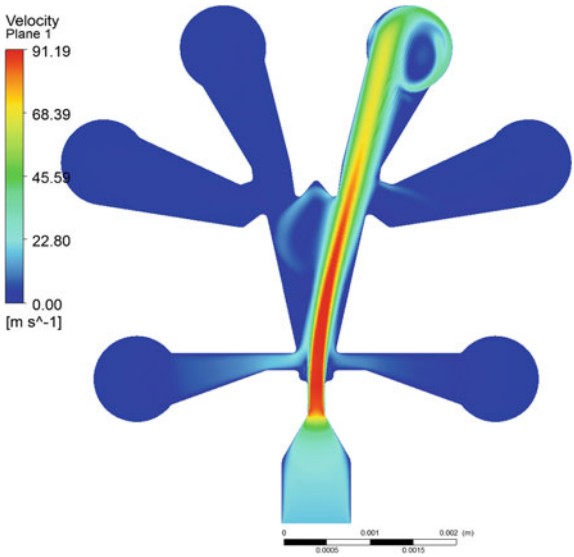

Fig. 5 The velocity field in channels of logic element (pressure in left control channel is 350 Pa), m/s

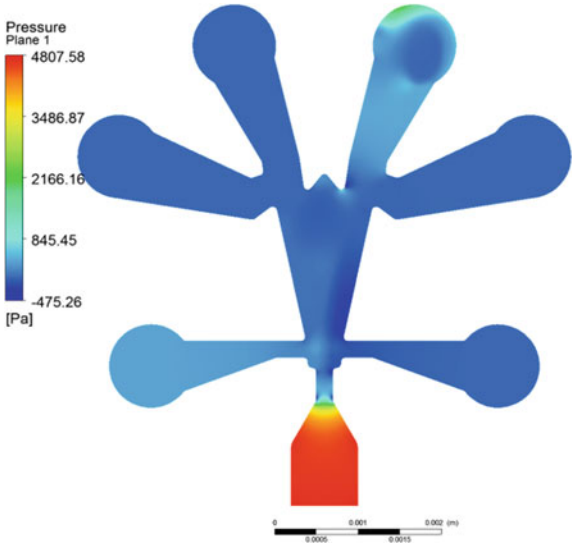

Fig. 6 The pressure field in channels of logic element (pressure in left control channel is 350 Pa), Pa

not at once as for air current separation from the right wall of channel, it is necessary to overcome viscosity forces, having given considerable pressure to the right control channel.

For considered case, it was required apply pressure to the right control channel of 400 Pa to carry out switching of signal, having created an air consumption in the left output channel (see Fig. 11).

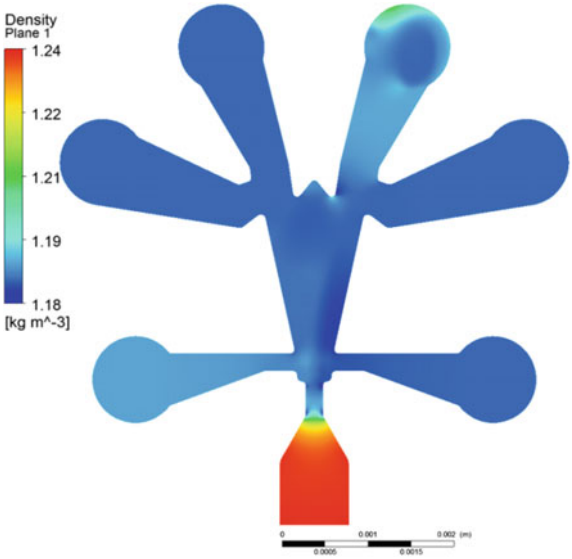

Fig. 7 Distribution of gas density in channels of trigger (the left control signal is 350 Pa), kg/m^3

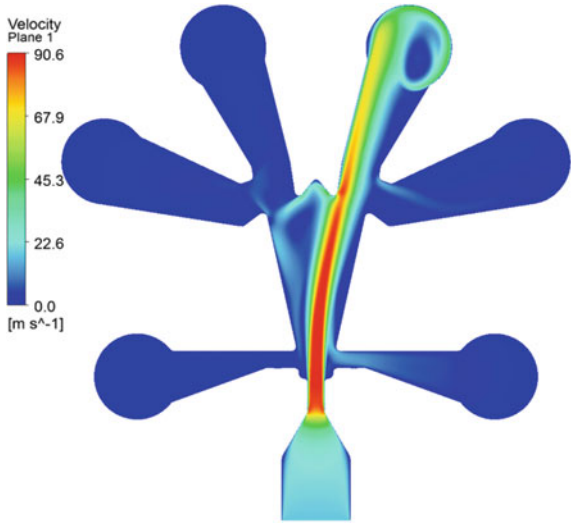

Fig. 8 The velocity field in air channels of trigger (the control signals are disconnected), m/s

Similarly, for switching of a signal back in the right output channel, it is necessary to give to the left control channel the pressure is 400 Pa. At switched-off control signals, the feeding air current steadily provides air consumption in the same output channel.

On Fig. 12, the schedules of dependences of relative consumptions in output channels from relative pressure in control channels are reported. The continuous line corresponds to change of air consumption in the left output channel $W_{вых}$

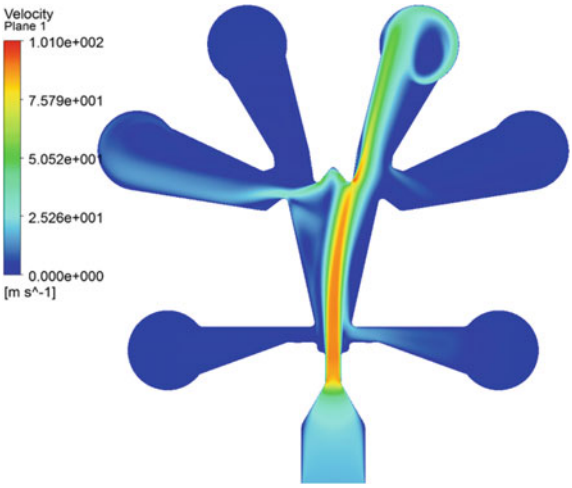

Fig. 9 The velocity field in air channels of trigger (the right control signal is increased to 150 Pa), m/s

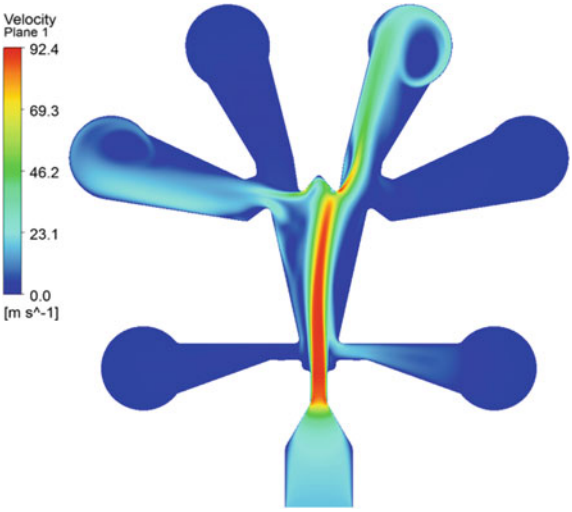

Fig. 10 The velocity field in air channels of trigger (the right control signal is increased to 300 Pa), m/s

depending on pressure of the control channel $P_{упр}$, correlated to consumption in feed channel $W_{пит}$ and to pressure in the feed channel $P_{пит}$. The dot line corresponds to change of air consumption in the right output channel depending on the pressure of control channel. The reduced schedule well reflects the process of switching of signal of a logic element which as a result of properties of viscous gas possesses a hysteresis.

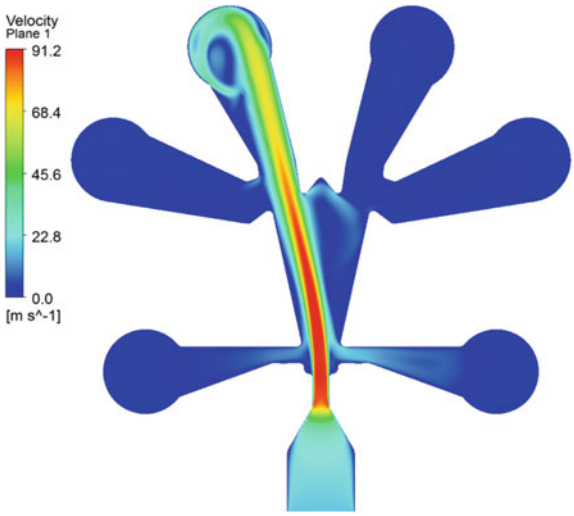

Fig. 11 The velocity field in channel of logic element (pressure in the right control channel is 400 Pa), m/s

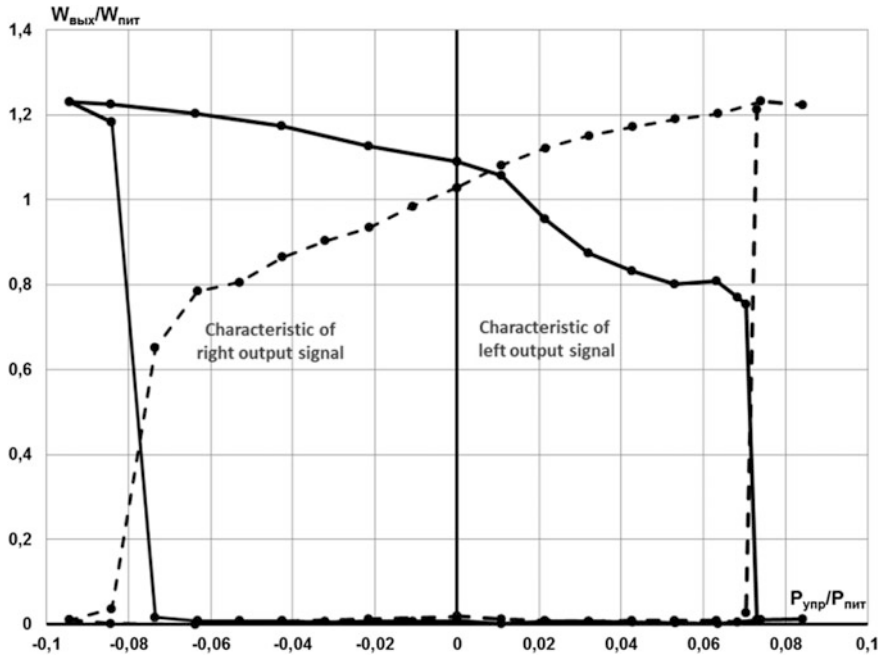

Fig. 12 Schedules of dependences of relative consumptions in output channels from relative pressure in control channels

4 Conclusion

The analysis of results of researches allows to draw conclusion that such property of gas as viscosity, at its current in channels of logic device can realize Coanda effect. Pressure application to one of control channels of element is reason of "sticking" of feeding gas current to opposite wall of central channel of element that creates consumption in one of output channels. Control signal cutoff does not entail no switching of output signal as the current of viscous gas remains stuck to opposite wall of central channel. For switching of output signal, it is necessary to apply pressure to other control channels that will cause sticking of gas current to other wall of central channel and formation of air consumption in other output channel. The process of functioning of element is visible on Fig. 5 in form of schedule forming hysteresis loops.

References

Berends TK, Efremova TK, Tagaevskaya AA (1968) Elementy i skhemy pnevmoavtomatiki, Moscow. 310

Bowles RE, Horton BM, Warren RW (1960) Fluid computing elements open new doors in control. Control Eng 7(5):26–30

Chaplygin EI (1989) Strujnye logicheskie ehlementy i ustrojstva avtomaticheskogo upravleniya tekhnologicheskim oborudovaniem. VNIITEHMR, Moscow, p 64

Ferner V (1954) Neue pneumatische bzw. Hydraulische Elemente in der Meβ- und Regelungstechnik, Technik, 6

Fudim EV (1973) Pnevmaticheskaya vychislitel'naya tekhnika. Teoriya ustrojstv i ehlementov, Slovar' po kibernetike, Moscow, 751

Korotkov FA Elementy i ustrojstvo strujnoj tekhniki (1972) Moscow. Energiya. 96

Lantry RB, Menter FR (2005) Transition modelling for general CFD application in aeronautics. AIAA 2005–522:14

Leskiewicz HJ, Zaremba M (1980) Pneumatic and hydraulic components and instruments in automatic control. In: Proceedings of the IFAC symposium, Warsaw, Poland. 290 (1st edn)

Olivotto C (2010) Fluidic elements based on Coanda effect. INCAS Bull 2(4):163–172

Prusenko VS (1965) Pnevmaticheskie datchiki i vtorichnye pribory, Moscow. 192

Wilson MP, Coogan CH, Southall K (1969) Experimental investigation of a fluidic volume flowmeter. Pap Am Soc Mech Eng 3:4

Roger RP, Chan SC (2003) Numerical study of fluidic bistable amplifiers. In: 33rdAIAA fluid dynamics conference. AIAA 2003-3459, pp. 1–10

Wilcox DC (2006) Turbulence Modeling for CFD: 522

Yeaple F (1960) No moving parts for fluid amplifier. Prod Eng 31(11):17

Zalmanzon LA (1969) Teoriya ehlementov pnevmoniki, Moscow: Nauka. 507

Numerical Investigation of Extremely Viscous Short Fibers-Reinforced Multiphase Anisotropic Fluid Flow in Flat Channel

E.I. Kurkin and V.O. Sadykova

Abstract In this chapter, the parameters of molding of thermoplastics reinforced with short high-strength fibers are considered on the example of plate molding from PEEK 90HMF20 material. Modeling of thermoplastic molding was done in Moldex3D system. The setting of three-dimensional geometrical model of gating area, characteristics of system of heat supply of tool, and also molding process parameters: temperature condition, pressure, and filling time are presented. Hydrodynamic calculation of plate molding is executed. The field of distribution of casting front, temperature, and pressure is obtained. The vector field of orientation of reinforcing fibers is calculated that allows to consider anisotropy of characteristics of composite material when carrying out strength calculations. It is noted that facial layers have more ordered structure in comparison with inside layer because the fibers are turned under the influence of shear flow (so-called main effect) that confirms good agreement with carried-out calculations to theoretically known character of current. The technology of export of data about fiber orientation from Moldex3D in Digimat system is shown. This technology allows calculation of stress-strain state of structures from short-reinforced composite materials in ANSYS Mechanical using Digimat Wizard taking into account the orientation of the reinforcing fibers.

1 Introduction

The composite materials reinforced with short fibers combine high strength and weight efficiency inherent of traditional polymer composite materials and high technological capabilities of production by injection molding. Composite material on the basis of short carbon fibers (PEEK/CF) possesses highest mechanical

E.I. Kurkin (✉) · V.O. Sadykova
Department of Aircraft Construction and Design, Samara National Research University, 34, Moskovskoe Shosse, Samara 443086, Russian Federation
e-mail: eugene.kurkin@mail.ru

V.O. Sadykova
e-mail: sadykova-vlada@rambler.ru

M.K. Singh et al. (eds.), *Applications of Fluid Dynamics*, Lecture Notes in Mechanical Engineering, https://doi.org/10.1007/978-981-10-5329-0_23

characteristics. Such material has the high modulus of elasticity and at the same time big strength limit. This article is devoted to the development of methods of product design from PEEK/CF and calculation of casting parameters.

Stiffness and strength of created material significantly changes according to the change in orientation and concentration of fibers. The formation of products reinforced with short fibers in many cases is made by injection methods during which there is current of material which is inevitably leading to change in orientation of reinforcing fibers. In product, there can be areas in which fibers are located along the direction of casting flow, and areas in which they have accidental orientation. Concentration of reinforcing fibers can also become uneven and requires forecasting. For example, increasing the concentration of reinforcing particles is usually observed near the walls of the mold which the flow reflects, and near injection hole. Properties of the product material from short fiber reinforced composite made by injection molding can change considerably in different areas of the structure. For forecasting mechanical characteristics of the materials reinforced with short fibers, there is the need for mathematical modeling of molding process of non-Newtonian fluids with the subsequent experimental verification of received results.

Modeling of plate molding was carried out in the Moldex3D software, widely applied for simulation of structures molding from short fiber reinforced materials (Advani 1994; Gupta and Wang 1993). The program complex Moldex3D is intended for modeling of hydraulic processes of casting under pressure of the thermoplastic materials reinforced with short fibers. Non-Newtonian character is a feature of these materials. Viscosity of short-reinforced composites is high and depends on the speed of casting. Moldex3D allows to define orientation of short fibers in material in process of casting and after polymerization (Foss 2004). Creation of control technology of melt flow and arrangement of fibers in composite materials allow to achieve the set of mechanical characteristics of product in the required directions. As the thermoflexible composite is used, the products possess possibility of repeated material recovery in case of melting and repeated casting.

Orientation problems in fiber-reinforced thermoplastic composites processing are difficult for solving without simplification. Modeling polymers behavior at completing forms considered in (Wang 2007). The model of fiber orientation is important for accurate forecast of characteristics. The Folgar–Tucker model (Advani and Tucker 1987) is used extensively to definite the state change of fiber orientation. The predicted rate of change of fiber orientation with respect to time is higher than experimentally observed. To eliminate this difference, Wang et al. (2008) developed a new model, which is called the reduced strain closure (RSC) model. This model is an upgraded Folgar–Tucker model in which the scalar factor reduces own velocity of orientation tensor values in absence of changes in own velocity vectors. Phelps and Tucker (2009) proposed the use of two-dimensional diffusion tensor on the surface of spherical coordinate system for anisotropic rotary diffusion orientation equation. The anisotropic rotary diffusion (ARD) model is characterized by a second-order tensor. Phelps and Tucker (2009) suggest ARD-RSC fiber orientation model, consisting of a combination of equations of ARD and RSC models, to improve predictions of fiber orientation in

injection molded long-fiber thermoplastic composites. Tseng et al. (2012) developed a new model of fiber orientation which is called Improved Anisotropic Rotary Diffusion model combined with Retarding Principal Rate model (iARD-RPR). The iARD model describes the anisotropic properties of the fiber orientation, and the RPR model reduces the rate of change of orientation. This model has been used by Moldex3DVR-R11 from CoreTech System Co, Ltd.

2 Tool Construction for Plate Casting

The tool geometry for plate casting consists of drop gate and filled form. On the basis of geometrical characteristics of plate and drop gate (Fig. 1), the three-dimensional geometrical model of gating area is created (Fig. 2). The sizes of plate were chosen on the basis of the requirements for the possibility of cutting samples for mechanical characteristics tests, including tensile tests in longitudinal and transverse direction according to the ISO 527-2:2012 standard. The sizes of plate are chosen proceeding from schemes of pattern cutoff 150 × 200 mm. Graded plate thickness is supposed equal to 4 mm.

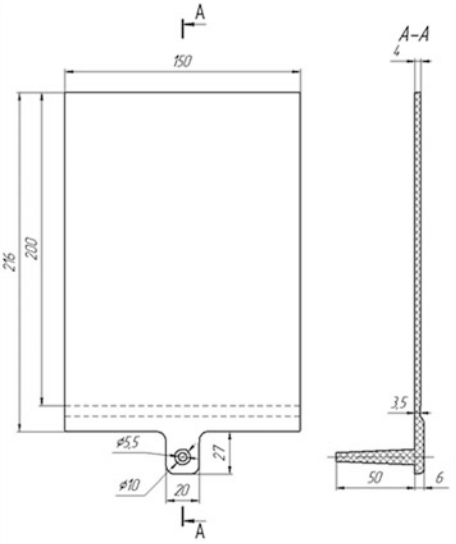

Fig. 1 Main projections of gating area of product (flat plate)

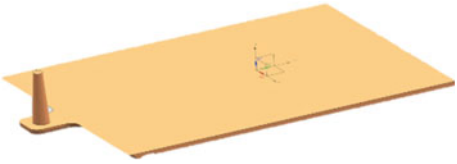

Fig. 2 Three-dimensional geometrical model of gating area of product (flat plate)

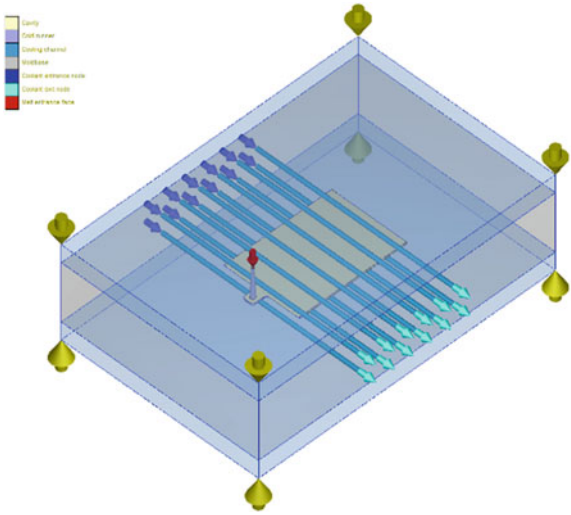

Fig. 3 Assignment of characteristics of heat exchange system of tool in program complex Moldex3D

Three-dimensional geometrical models of product are imported from CAD system to Moldex3D through a data exchange STEP format between systems of CAE (*.stp file).

3 Flow Simulation of Tool in Program Complex Moldex3D

After loading three-dimensional geometrical model of computational area in program Moldex3D eDesign, the characteristics of heat exchange system of designed gating tool are set: quantity of tubes of transfer of heat carrier, their diameter, and arrangement which were optimized on the basis of further modeling (Fig. 3).

The optimum combination of geometrical parameters of tool allows to receive the greatest velocity and completeness of filling of form at molding. It provides the rational distribution of flows preventing the effect of incomplete injection, buildup of weld lines, and minimizing molding cycle time by reducing a buckling and shrinkage loss.

Plate and runner mesh was constructed in Moldex3D Designer system (Fig. 4).

4 Material Characteristics in Program Complex Moldex3D

For research of molding process of material containing reinforcing fibers, the Moldex3D Flow and Fiber modules are used.

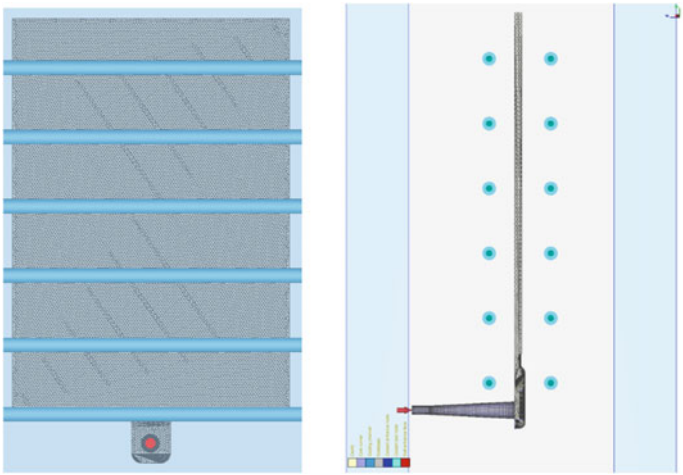

Fig. 4 Plate and runner Moldex3D mesh

Polymer | Grade Name | Producer	PEEK | Victrex 90HMF20 (an) | VICTREX
Mechanical Properties	Fiber-filled polymer - Experimental properties
Poisson's ratio v12	0.4 (-)
Poisson's ratio v23	0.4 (-)
Modulus E1 (fiber direction)	1.19e+011 (dyne/cm^2)
Modulus E2 (transverse direction)	6.4e+010 (dyne/cm^2)
Shear Modulus G	4.25e+010 (dyne/cm^2)
CLTE a1 (fiber direction)	2e-005 (1/K)
CLTE a2 (transverse direction)	5.5e-005 (1/K)
Fiber Length/Diameter (L/D)	20 (-)
Interaction coefficient	0.01 (-)
Fiber weight percentage	30 (%)

Fig. 5 Parameters of reinforcement PEEK 90HMF20

Moldex3D Flow module gives a solution of filling problem. Moldex3D Fiber module provides validated modeling of three-dimensional fiber orientation in the molding process using the Folgar-Tucker model and its modification for long fiber reinforcement. Characteristics of material are submitted in Figs. 5, 6, 7, and 8.

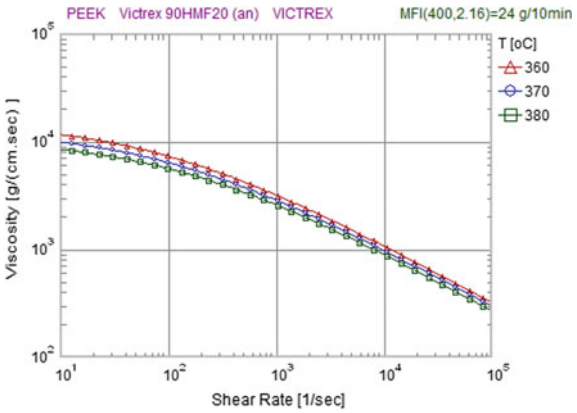

Fig. 6 Viscosity of material PEEK 90HMF20

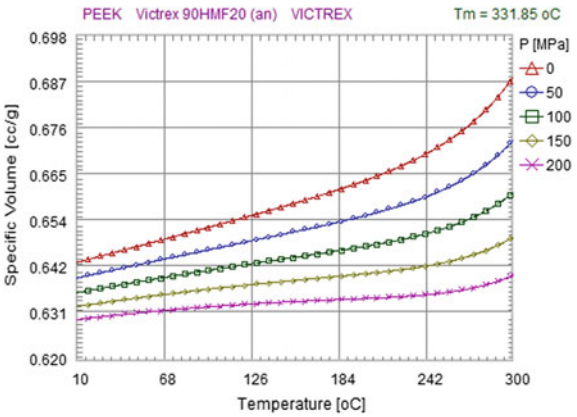

Fig. 7 Parameter of material temperature expansion PEEK 90HMF20

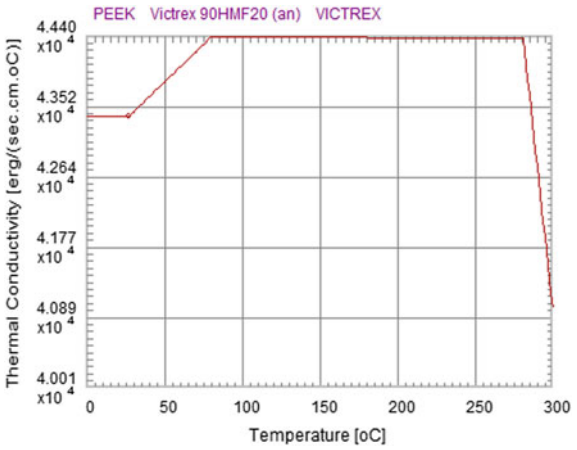

Fig. 8 Specific volume of material PEEK 90HMF20

5 Assignment of Parameters of Molding Technological Process in Program Complex Moldex3D

Technological parameters of molding process are set in Moldex3D by means of master of technological mode. The parameter setting of modeling is most approached to parameter setting of casting in control system of molding machine Negri Bossi—VE 210-1700 (Fig. 9).

For calculation of molding of thermoplastic material in Moldex3D system, molding process parameters are set: temperature condition (Fig. 10), pressure and time of the process (Fig. 11).

6 Hydrodynamic Calculation of Plate Molding in Program Complex Moldex3D

Hydrodynamic calculation of plate molding in Moldex3D showed full passing of casting front (Fig. 12). The filling time of plate is 4.7 s. Results of calculation give detailed information on the process of filling of casting mold. Temperature

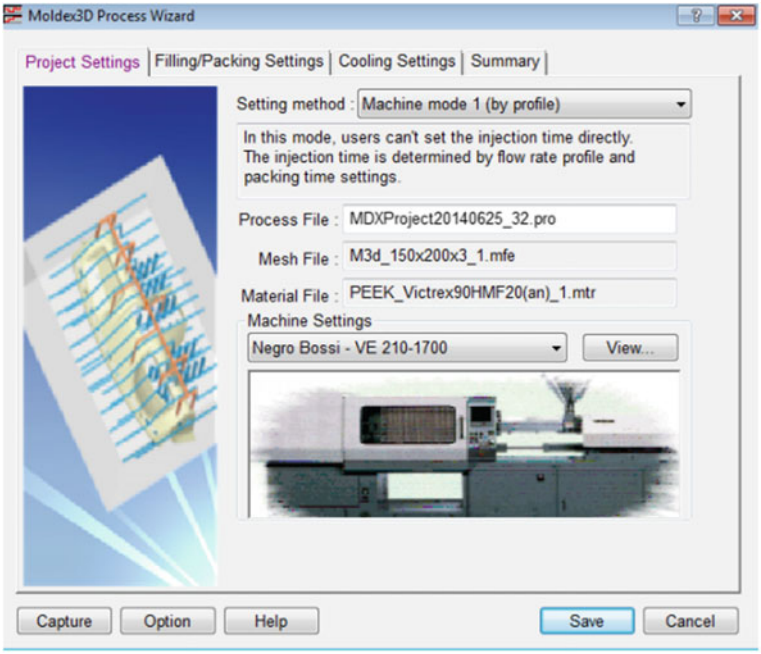

Fig. 9 Assignment of parameters of molding machine

Description	Description
Polymer	PEEK
Grade Name	Victrex 90HMF20 (an)
Producer	VICTREX
Comment	30%GF ,MFI(400,2.16)=24 g/10min ,D=1.52 g/cc
Last modified date	2014/06/25
Process condition	Process condition
Melt temperature (minimum)	360 oC
Melt temperature (normal)	370 oC
Melt temperature (maximum)	380 oC
Mold temperature (minimum)	160 oC
Mold temperature (normal)	170 oC
Mold temperature (maximum)	190 oC
Ejection temperature	285 oC
Freeze temperature	295 oC

Fig. 10 Temperature conditions of molding

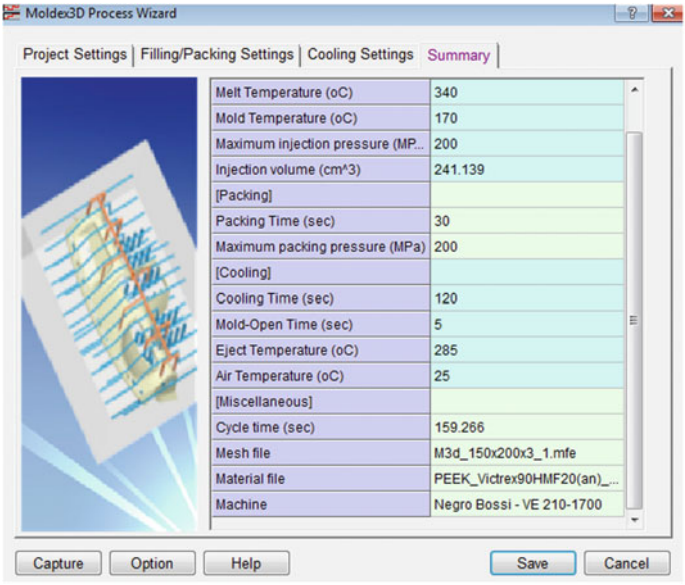

Fig. 11 Parameters of molding: pressure and time of the process

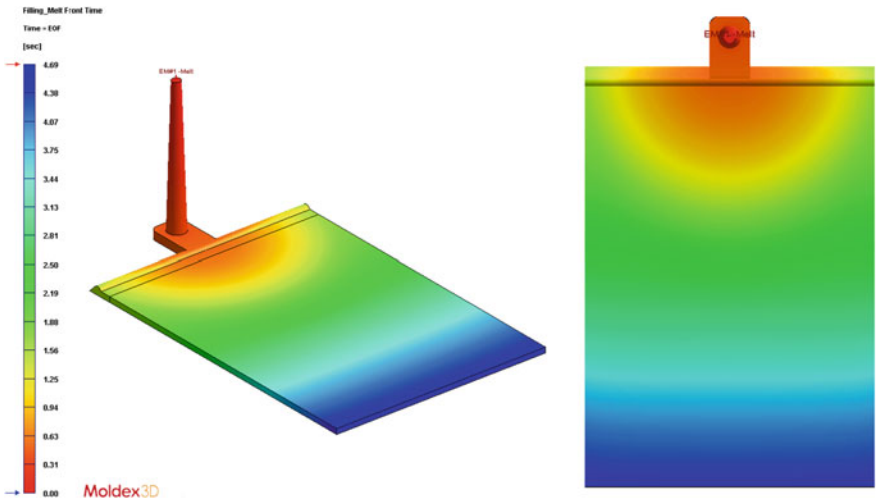

Fig. 12 Casting front of plate

Fig. 13 Temperature distribution of hot-melt

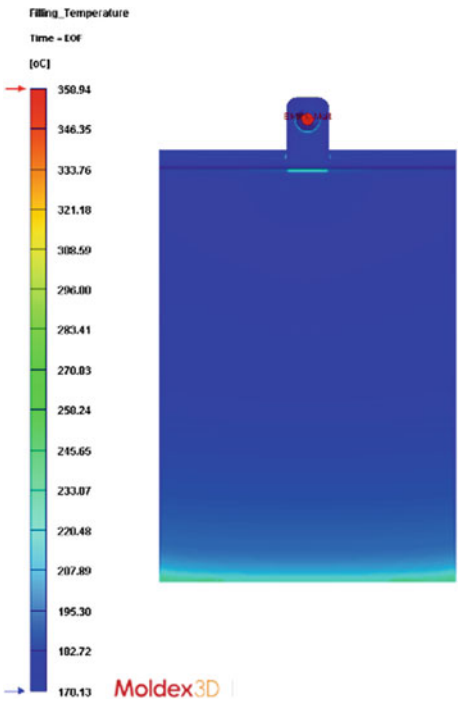

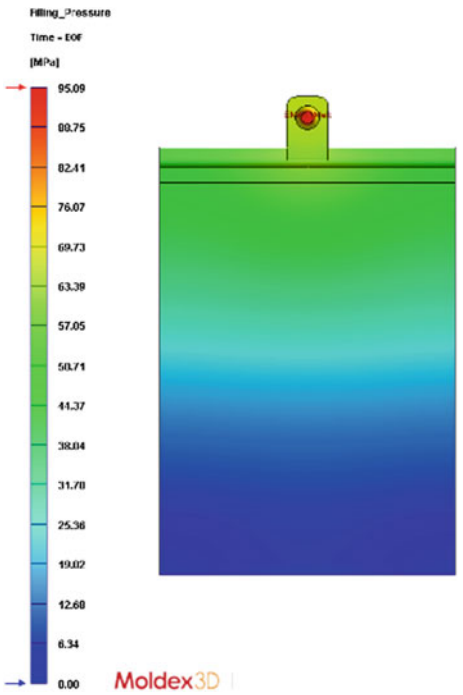

Fig. 14 Pressure distribution of hot-melt

distribution of hot-melt is presented in Fig. 13, and pressure distribution of hot-melt is presented in Fig. 14 The maximum temperature in molding process is 358 °C, and pressure is 96 MPa.

7 Estimation of High-Strength Reinforcement Fiber Orientation in Program Complex Moldex3D

In Fig. 15 is presented the degree of fiber orientation expressed through an orientation tensor in longitudinally upper (Fig. 15a) and bottom surfaces of the plate (Fig. 15b).

In Fig. 16 is presented the degree of fiber orientation in center body section of plate expressed through an orientation tensor.

Facial layers have more ordered structure in comparison with inside layer because the fibers are turned under the influence of shear flow (so-called main effect, as shown in Fig. 17). If the injection velocity is higher, the gradients of velocities on thickness are higher and the difference in orientation of facial and inside layers is stronger. Stiffness and strength of pattern is proportional to degree of order, or degree of fiber orientation. This phenomenon was confirmed with

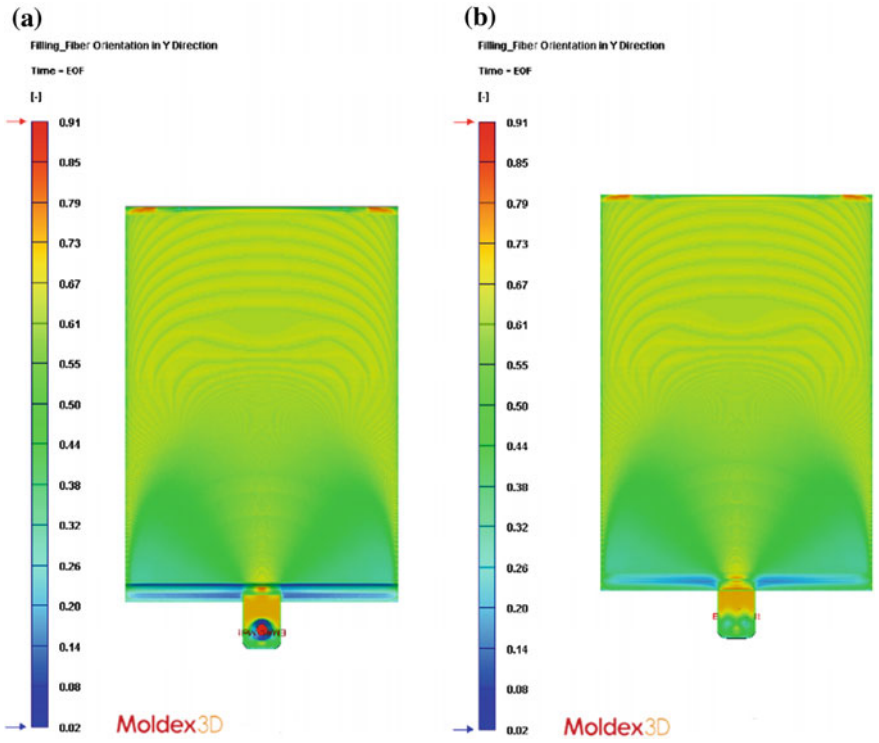

Fig. 15 Degree of fiber orientation in longitudinally upper (**a**) and bottom surfaces of plate (**b**)

computational researches in Moldex3D. The reinforcement structure in center body section of plate, confirming character of such current, is presented in Fig. 18.

The results of calculation of fiber orientation are kept in the file of orientation *. o2d, allowing to consider fiber orientation in strength analysis of products from made material (Fig. 19).

8 Conclusion

The calculation methodology of parameters of casting of thermoplastics reinforced with short high-strength fibers is developed.

Methodology of short fibers-reinforced multiphase anisotropic fluid flow modeling in Moldex3D system is shown in example of plate molding from PEEK 90HMF20 material. The setting of three-dimensional geometrical model of gating area, characteristics of system of heat supply of tool, and also molding process parameters: temperature condition, pressure, and filling time are presented.

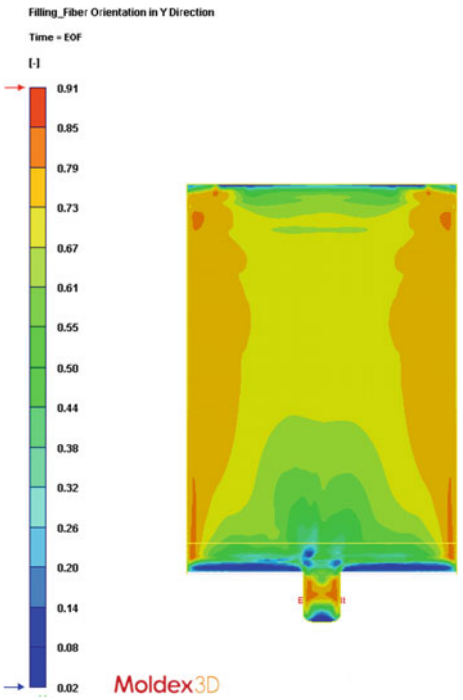

Fig. 16 Degree of fiber orientation in center body section of plate

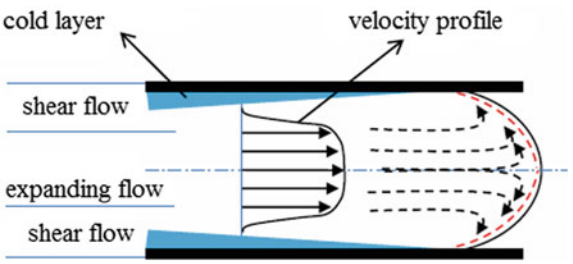

Fig. 17 Pattern of hot-melt flow on through-thickness of plate

Hydrodynamic calculation of plate molding in program complex Moldex3D showed full passing of casting front and allowed to define detailed information about the molding process, including temperature distribution and pressure distribution of hot-melt.

The carried-out hydrodynamic calculation allowed to define the orientation of reinforcing fibers that allow to consider correctly anisotropy of characteristics of composite material when carrying out strength calculations. The technology of export of data about fiber orientation to programs for carrying out strength researches on example of information transfer about reinforcing of plate from Moldex3D in Digimat system is shown.

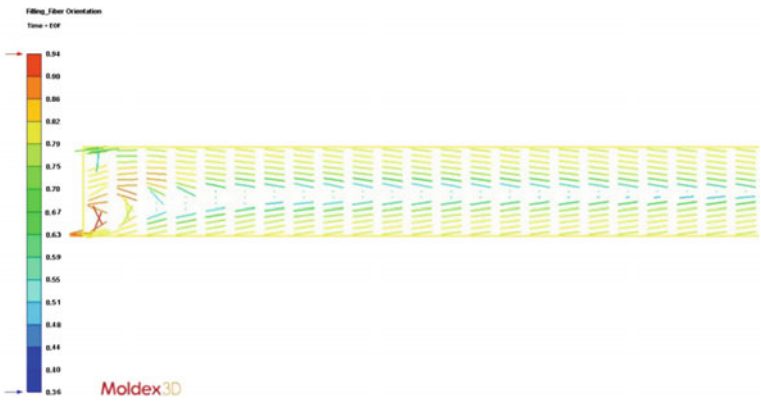

Fig. 18 Reinforcement structure in center body section of plate

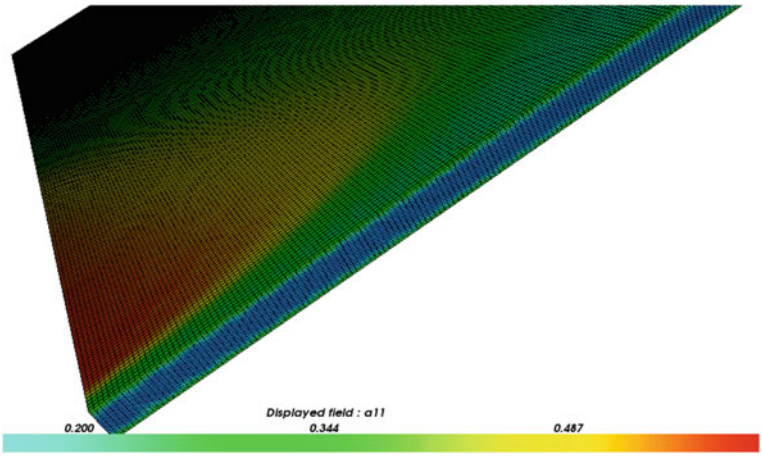

Fig. 19 Export of orientation field of reinforcement fiber in system Digimat for orientation accounting in stiffness and strength analyzes of pattern

It is noted that facial layers have more ordered structure in comparison with inside layer because the fibers are turned under the influence of shear flow (so-called main effect) that confirms good agreement with carried-out calculations to theoretically known character of current.

Acknowledgements The reported study was funded by RFBR according to the research project No. 16-31-60093 mol_a_dk.

References

Advani SG (1994) Flow and rheology in polymer composites manufacturing. Elsevier, New York
Advani SG, Tucker CL III (1987) J Rheol 31:751
Foss (2004) Polym Compos 25:343
Gupta M, Wang KK (1993) Polym Compos 14:5
Phelps JH (2009) Processing-microstructure models for shortand long-fiber thermoplastic composites. University of Illinois at Urbana-Champaign
Phelps JH, Tucker CL III (2009) J Non-Newtonian Fluid Mech 156:165
Tseng HS, Chang RY, Hsu CH (2012) Method and computer readable media for determining orientation of fibers in a fluid. U.S. patent pending in USPTO with publication application number of US-201220330627-A1
Wang J (2007) Improved fiber orientation predictions for injection molded composites. University of Illinois at Urbana, Champaign
Wang J, O'Gara JF, Tucker CL III (2008) J Rheol 52:1179

Hybrid Finite Difference-Finite Volume Schemes on Non-uniform Grid

A. Arun Govind Neelan and Manoj T. Nair

Abstract High aspect ratio, skewness, non-orthogonality, and non-uniformity of grids have been a major issue for mesh developers for a long time. In this present work, we have taken an initial step for a numerical scheme that can handle any kind of mesh. Problems associated with non-uniformity of the grid (that can be related to aspect ratio in higher dimension) and achieving high order accuracy in those grids are discussed. A Hybrid Finite Difference-Finite Volume Method (Hybrid FD-FVM) which can retain high order accuracy on an arbitrary mesh by combining the advantage of higher order convergence property of finite difference method (FDM) and conservativeness property of FVM is presented. Though higher order version of FVM is available, they work well only on uniform meshes or slightly perturbed unstructured grid or gradually stretched grid. Smooth variation in meshes is recommended for CFD packages to obtain good accuracy—the reasons are discussed in the paper. FVM on the arbitrary mesh is at most second order accurate and are generally about first order accurate. Our method ensures higher order convergence on arbitrary non-uniform non-overlapped mesh but does not ensure complete numerical conservativeness on the non-uniform mesh for problems without shocks. The present work does not use volume averaging which is commonly used in FVM. The volume averaging works well in uniform mesh and can severely affect the result on the arbitrary varying non-uniform mesh. That also discussed here.

1 Introduction

Finite difference method, finite volume method, and finite element method (FEM) are popular tools used to solve problems in fluid dynamics. Though they are derived from the family—Method of Weighted Residual, they differ in the

A.A.G. Neelan (✉) · M.T. Nair
Department of Aerospace Engineering, Indian Institute of Space Science and Technology, Thiruvananthapuram 695547, Kerala, India
e-mail: arungovindneelan@gmail.com

M.K. Singh et al. (eds.), *Applications of Fluid Dynamics*, Lecture Notes in Mechanical Engineering, https://doi.org/10.1007/978-981-10-5329-0_24

derivation procedure so they have their unique advantage as well as disadvantage. FDM assumes weight is an impulse function centered at that point. FVM assumes weight is one inside the evaluating cell and zero everywhere else. Petrov Galerkin-Finite Element Method assumes shape functions as its weight. FDM is the simplest method, can be extended to higher order easily. FVM ensures conservativeness at each cell, so they are ideal for fluid dynamics problem. FEM is based on minimizing energy, and they are good for structural mechanics and relatively more accurate than other methods on most of the grids.

Roe (1987), Jureti and Gosman (2010), Diskin and Thomas (2010) and Bouche et al. (2005) have shown that FVM gives lower order convergence on non-uniform meshes. This may be because of averaging process, poor gradient calculation, skewness, etc. Please refer paper by Jureti and Gosman (2010) to get an overall picture of the different source of errors in FVM and various error estimators. Higher order methods are essential to get a high accurate result. One class of high-resolution scheme is WENO. More detailed of this class can be found in paper by Jiang and Wu (1999), Shu (2003), Henrick et al. (2005). Initially, WENO scheme is derived for uniform mesh and then extended to non-uniform mesh. They may not work well on all kind of non-uniform mesh. WENO method in the arbitrary grid using mapping procedure was studied by Dumbser and Kser (2007), Dumbser et al. (2013), but the reliability of those methods to achieve higher order accuracy on any kind of arbitrary grid is limited. Another class of higher order method is compact schemes. They have a good spectral resolution. Lele (1992), Pereira et al. (2001), Gaitonde and Shang (1997) studied compact schemes vigorously but extending that to the arbitrary grid is a challenging task. So FVM on unstructured mesh with higher order accuracy is not a well-developed one.

In this work, we have formulated a hybrid method, which retains the advantage of FDM, that is, it can maintain higher order accuracy on non-uniform grids. Here we have considered non-uniformity in the grid; we have assumed that other essential grid properties like orthogonality and low skewness have been taken into account. Use higher order methods developed for the uniform grid on uniformly stretched grid results in loss of accuracy. More details and examples on uniform and non-uniform grids can be found in a book by Shashkov (1995). Highly stretched grid or non-uniform grid may produce wiggles in solution. Both the issues will be discussed in this work. Spalart and Streett (2001) pointed out that, to improve the accuracy of the solution and reduce computational cost in high gradient zones like boundary layers, high aspect ratio mesh is required.

Another important issue is if Neumann boundary condition is not resolved well that error will propagate inside the domain and reduce or even decay the solution especially for the elliptic equation. This lower order treatment of Neumann boundary condition will also reduce the order of convergence rate of the solution even if we use higher order methods inside the domain. Pirozzoli (2002) stated that using bad numerical schemes, oscillations will also propagate from the boundary as well as initial conditions. Hill and Pullin (2004) has shown that the accuracy of

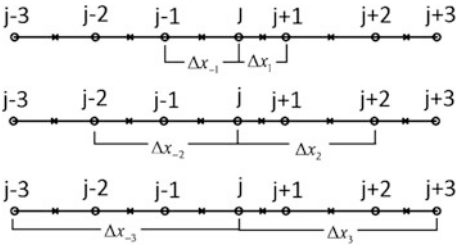

Fig. 1 Grid nomenclature used in this work

large eddy simulation (LES) depends not only on sub-grid stress model but also on how the derivative term is treated. In all those situation high aspect ratio mesh is unavoidable where our method is ideal.

2 Motivation

Basic nomenclature given for non-uniform grid is shown in Fig. 1. Following Diskin and Thomas (2010), non-uniform grid is generated by perturbing a uniform grid with grid spacing Δx by a value that is generated using pseudo-random number in between $\pm 0.4\Delta x$.

2.1 FDM on Uniform and Non-uniform Grid

First derivative representation of FDM on uniform grid with second-order accuracy can be represented as

$$\frac{\mathrm{d}u}{\mathrm{d}x} = \frac{3u_i - 4u_{i-1} + 2u_{i+1}}{2\Delta x} \tag{1}$$

Let us take a simple function and its derivative:

$$u(x) = \cos(kx) \quad -2\pi \leq \mathrm{x} \leq 2\pi \tag{2a}$$

$$\frac{\mathrm{d}u}{\mathrm{d}x} = -k\sin(kx) \tag{2b}$$

The order of convergence for this function using the discretization given in Eq. (1) is approximately two, as shown in Fig. 2. The behavior of Eq. (1) for non-uniform grid is not satisfactory. It gives unwanted oscillations in the result with almost zero order convergence if we use an average Δx of the domain for Δx in Eq. (1). Diffused results are obtained if we use an average of Δx_{-1} and Δx_{-2} for Δx

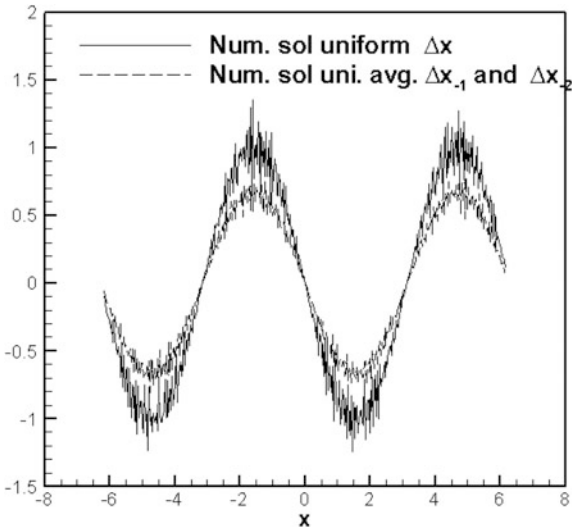

Fig. 2 First derivative of cos (x) using uniform FDM on the non-uniform grid

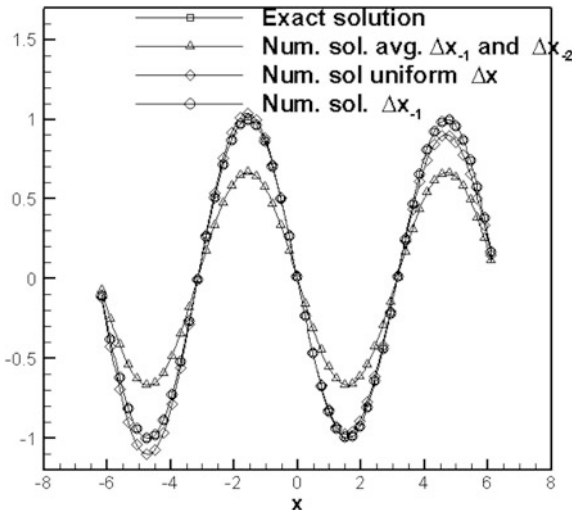

Fig. 3 First derivative of cos (x) using uniform FDM in AP grid

in Eq. (1). It may be because of $\Delta x = \frac{\Delta x_{-1} + \Delta x_{-2}}{2}$ acts like a Laplace operator (diffusive operator).

Now we shall explore the effect of uniformly varying grid. One kind of such grid is arithmetic progression (AP) grid that has grid spacing in AP series. Figure 3 shows the solution of uniform FDM on AP grid. AP grid does not produce unwanted oscillations like in arbitrary non-uniform grids, but it provides interesting results. It gives diffused result if we use average of Δx_{-1} and Δx_{-2} for Δx and also gives diffused result for an average Δx_i of the domain. However, it produces a better

result if we replace Δx in Eq. (1) by Δx_{-1}. Though the scheme is second order accurate it is able to produce more than second-order convergence for Fourier basis ($\sin(ax)$ and $\cos(ax)$) for some value of a in AP series. The optimum value of a for better convergence is about 1.128 Δx. On that optimal grid, Eq. (1) gives a root mean square (rms) error convergence of −2.66, the convergence rate of maximum error (L_∞) is −2.60, and convergence rate of minimum error is −3.64. This kind of higher convergence is observed only for Fourier basis not seen in polynomial basis.

2.2 Issues of FVM on Non-uniform Grid

Let say Q is the variable in the control volume, then the averaged value of Q over the cell is given by

$$\overline{Q} = \frac{1}{V}\int_V Q \mathrm{d}v \tag{3}$$

For more details of this method please refer books by LeVeque and Randall (2002), Lomax et al. (2013). Derivation of third-order dual volume FVM in non-uniform Δx_1, Δx_{-1}, Δx_{-2}, and Δx_{-3} grids as follows where volume averaged term can be written as,

$$u_i = \frac{2}{\Delta x_1 + \Delta x\_1}\int_{\frac{\Delta x_{-1}}{2}}^{\frac{\Delta x_1}{2}} u(\xi)\mathrm{d}\xi \tag{4a}$$

$$u_{i-1} = \frac{2}{\Delta x_{-2}}\int_{-\frac{\Delta x_{-1}+\Delta x_{-2}}{2}}^{-\frac{\Delta x_{-1}}{2}} u(\xi)\mathrm{d}\xi \tag{4b}$$

$$u_{i-2} = \frac{2}{\Delta x_{-3} - \Delta x_{-1}}\int_{-\frac{\Delta x_{-1}+\Delta x_{-2}}{2}}^{-\frac{\Delta x_{-1}+\Delta x_{-2}}{2}} u(\xi)\mathrm{d}\xi \tag{4c}$$

For third-order approximation, numerical flux can be written as

$$u(\xi) = a + b\xi + c\xi^2 \tag{5}$$

Coefficients a, b, and c are determined using Eq. (4a). Here, face fluxes are calculated using following equations.

$$u_{i+0.5} = u(0.5\Delta x_1) \tag{6a}$$

$$u_{i-0.5} = u(0.5\Delta x_{-1}) \tag{6b}$$

Then the derivative for non-uniform mesh can be approximated as

$$\frac{\mathrm{d}u}{\mathrm{d}x} = 2\frac{u_{i+0.5} - u_{i-0.5}}{\Delta x_{-1} + \Delta x_1} \tag{7}$$

Substituting expanded Eq. (6a) in Eq. (7) we get Eq. (8)

Equation (8) gives second-order accuracy on uniform grid and produce wiggles in non-uniform grid. Even if we use higher order polynomial in Eq. (5), this procedure will give at most second-order accuracy on uniform grid. Wiggles observed in non-uniform mesh are due to averaging procedure. If we skip the averaging procedure, it will give wiggle-less result which can go maximum up to second-order convergence. So averaging process that is commonly used in FVM for non-uniform grid is not recommended. Another interesting feature of this method is that it is able to achieve wiggle-less second-order accuracy on gradually stretched grid like AP grid (please see Fig. 4). This may be one of the reasons, why most of the FVM packages give an accurate result on the smooth mesh and poor result in abrupt varying grids.

$$\begin{aligned}
\frac{\mathrm{d}u}{\mathrm{d}x} = {} & \frac{8\Delta x_{-2}^2 u_i - 2\Delta x_{-1}^2 u_i + 4\Delta x_{-3}^2 u_i - 2\Delta x_1^2 u_{i-1} + 2\Delta x_1^2 u_{i-2}}{(\Delta x_1 + \Delta x_{-1} + \Delta x_{-2})(\Delta x_1 + \Delta x_{-3} + \Delta x_{-2})(\Delta x_{-2} - \Delta x_{-1} + \Delta x_{-3})} \\
& + \frac{2\Delta x_{-1}^2 u_{i-2} - 12\Delta x_{-2}^2 u_{i-1} + 4\Delta x_{-2}^2 u_{i-2} - 4\Delta x_{-3}^2 u_{i-1} - 6\Delta x_1 \Delta x_{-1} u_i}{(\Delta x_1 + \Delta x_{-1} + \Delta x_{-2})(\Delta x_1 + \Delta x_{-3} + \Delta x_{-2})(\Delta x_{-2} - \Delta x_{-1} + \Delta x_{-3})} \\
& + \frac{6\Delta x_1 \Delta x_{-2} u_{i-2} + 6\Delta x_1 \Delta x_{-3} u_i - 6\Delta x_{-1} \Delta x_{-2} u_i - 2\Delta x_{-1} \Delta x_{-3} u_{i-1}}{(\Delta x_1 + \Delta x_{-1} + \Delta x_{-2})(\Delta x_1 + \Delta x_{-3} + \Delta x_{-2})(\Delta x_{-2} - \Delta x_{-1} + \Delta x_{-3})} \\
& + \frac{12\Delta x_{-3} \Delta x_{-2} u_i + 2\Delta x_1 \Delta x_{-1} u_{i-1} + 4\Delta x_{-1} \Delta x_1 u_{i-2} - 12\Delta x_1 \Delta x_{-2} u_{i-1}}{(\Delta x_1 + \Delta x_{-1} + \Delta x_{-2})(\Delta x_1 + \Delta x_{-3} + \Delta x_{-2})(\Delta x_{-2} - \Delta x_{-1} + \Delta x_{-3})} \\
& + \frac{6\Delta x_1 \Delta x_{-2} u_{i-2} - 6\Delta x_1 \Delta x_{-3} u_{i-1} + 6\Delta x_{-1} \Delta x_{-2} u_{i-2} - 6\Delta x_1 \Delta x_{-1} u_i}{(\Delta x_1 + \Delta x_{-1} + \Delta x_{-2})(\Delta x_1 + \Delta x_{-3} + \Delta x_{-2})(\Delta x_{-2} - \Delta x_{-1} + \Delta x_{-3})} \\
& + \frac{2\Delta x_{-1} \Delta x_{-3} u_{i-1} - 12\Delta x_{-2} \Delta x_{-3} u_{i-1}}{(\Delta x_1 + \Delta x_{-1} + \Delta x_{-2})(\Delta x_1 + \Delta x_{-3} + \Delta x_{-2})(\Delta x_{-2} - \Delta x_{-1} + \Delta x_{-3})}
\end{aligned} \tag{8}$$

3 Hybrid FD-FVM on Uniform Grid

Fourth-order accurate FD scheme on non-uniform mesh on $i-2$, $i-1$, i, $i+1$ and $i+2$ with grid spacing $\Delta x_{-2}, \Delta x_{-1}, \Delta x_1$ and Δx_2, respectively, is

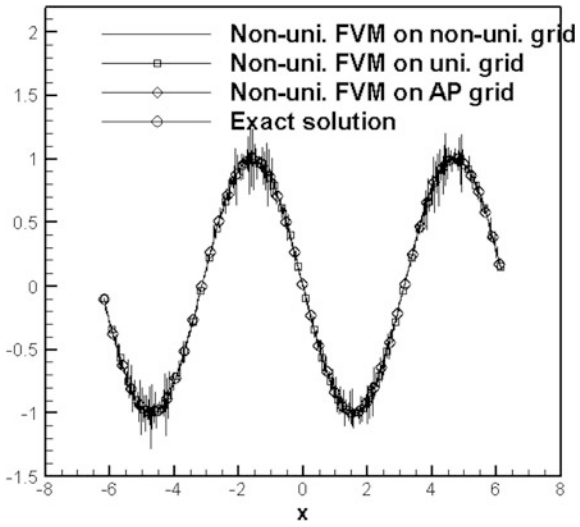

Fig. 4 First derivative of cos (x) using non-uniform FVM on uniform and non-uniform grids

$$\begin{aligned}\frac{\mathrm{d}u}{\mathrm{d}x} = &-\frac{\Delta x_1\Delta x_2\Delta x_{-1}}{\Delta x_{-2}(\Delta x_1+\Delta x_{-2})(\Delta x_2+\Delta x_{-2})(\Delta x_{-1}-\Delta x_{-2})}u_{i-2}\\ &+\frac{\Delta x_1\Delta x_2\Delta x_{-2}}{\Delta x_{-1}(\Delta x_1+\Delta x_{-1})(\Delta x_2+\Delta x_{-1})(\Delta x_{-1}-\Delta x_{-2})}u_{i-1}\\ &+\frac{\Delta x_1\Delta x_2\Delta x_{-1}+\Delta x_1\Delta x_2\Delta x_{-2}-\Delta x_1\Delta x_{-2}\Delta x_{-1}-\Delta x_{-1}\Delta x_2\Delta x_{-2}}{\Delta x_1\Delta x_2\Delta x_{-1}\Delta x_{-2}}u_i\\ &-\frac{\Delta x_2\Delta x_{-1}\Delta x_{-2}}{\Delta x_1(\Delta x_1+\Delta x_{-1})(\Delta x_{-2}+\Delta x_1)(\Delta x_1-\Delta x_2)}u_{i+1}\\ &+\frac{\Delta x_1\Delta x_{-1}\Delta x_{-2}}{\Delta x_2(\Delta x_2+\Delta x_{-1})(\Delta x_{-2}+\Delta x_2)(\Delta x_1-\Delta x_2)}u_{i+2}\end{aligned} \tag{9}$$

In FVM, we write derivative of fluxes as

$$\frac{\mathrm{d}u}{\mathrm{d}x} = 2\frac{u_{i+0.5}-u_{i-0.5}}{\Delta x_{-1}+\Delta x_1} = a_{-2}u_{i-2}+a_{-1}u_{i-1}+a_0u_i+a_1u_{i+1}+a_2u_{i+2} \tag{10}$$

We shall write fluxes as

$$u_{i+0.5} = ar_2u_{i+2}+ar_1u_{i+1}+ar_0u_i+ar_{-1}u_{i-1} \tag{11a}$$

$$u_{i-0.5} = al_1u_{i+1}+al_0u_i+al_{-1}u_{i-1}+al_{-2}u_{i-2} \tag{11b}$$

For shock-free flows, the solutions should be smooth and there should not be any discontinuity in fluxes. Left interface flux of ith cell should equal to right interface flux of $i-1$th cell. To satisfy that, apart from using integral foam of conservative equation, it should satisfy the "telescoping property." Numerical schemes are

expected to satisfy "telescoping property" at least in steady state condition. Conditions required for that is:

$$\begin{aligned} ar_2 &= a_2 \\ al_1 &= ar_2 \\ ar_1 &= a_1 + al_1 \\ al_0 &= ar_1 \\ ar_0 &= a_0 + al_0 \\ al_{-1} &= ar_0 \\ ar_{-1} &= a_{-1} + al_{-1} \\ al_{-2} &= ar_{-1} = -a_{-2} \end{aligned} \tag{12}$$

But in non-uniform mesh to satisfy "telescoping property" ar_i should be function of $\Delta x_2, \Delta x_1$ and Δx_{-1} and al_i should be function of $\Delta x_1, \Delta x_{-1}$ and Δx_{-2} and also

$$ar_i(\Delta x_{i-1}, \Delta x_i, \Delta x_{i+1}, \Delta x_{i+2}) = al_{i-1}(\Delta x_{i-2}, \Delta x_{i-1}, \Delta x_i, \Delta x_{i+1}) \tag{13}$$

The first condition is easy to achieve, but second condition (Eq. 13) is not easy, maybe impossible to achieve. So we use the basic condition of "telescoping property" in uniform mesh (Eq. 12) to ensure our method is free from any unwanted source term in discretization, at least in uniform mesh. Since this will not satisfy Eq. (13) it may have some source term left in non-uniform discretization; however, it will retain the order, unlike other FVM. Comparing Eqs. 9 and 12 gives

$$ar_2 = \frac{\Delta x_1 \Delta x_{-1} \Delta x_{-2}}{\Delta x_2(\Delta x_2 + \Delta x_{-1})(\Delta x_2 + \Delta x_{-2})(\Delta x_1 - \Delta x_2)}$$

$$\begin{aligned} ar_1 = {} & \frac{\Delta x_{-1}\Delta x_{-2}(\Delta x_1 + \Delta x_2^2 + \Delta x_1^2 \Delta x_2 + \Delta x_1^2 \Delta x_{-1} + \Delta x_1^2 \Delta x_{-2})}{\Delta x_1 \Delta x_2(\Delta x_1 + \Delta x_{-1})(\Delta x_1 + \Delta x_{-2})(\Delta x_2 + \Delta x_{-1})(\Delta x_2 + \Delta x_{-2})} \\ & + \frac{\Delta x_{-1}\Delta x_{-2}(\Delta x_2^2 \Delta x_{-2} + \Delta x_1^3 + \Delta x_2^3 + \Delta x_2 \Delta x_1 \Delta x_{-1} + \Delta x_2^2 \Delta x_{-1})}{\Delta x_1 \Delta x_2(\Delta x_1 + \Delta x_{-1})(\Delta x_1 + \Delta x_{-2})(\Delta x_2 + \Delta x_{-1})(\Delta x_2 + \Delta x_{-2})} \\ & + \frac{\Delta x_{-1}\Delta x_{-2}(\Delta x_2 \Delta x_1 \Delta x_{-2} + \Delta x_{-1} \Delta x_1 \Delta x_{-2} + \Delta x_2 \Delta x_{-2} \Delta x_{-1})}{\Delta x_1 \Delta x_2(\Delta x_1 + \Delta x_{-1})(\Delta x_1 + \Delta x_{-2})(\Delta x_2 + \Delta x_{-1})(\Delta x_2 + \Delta x_{-2})} \end{aligned}$$

$$\begin{aligned} ar_0 = {} & \frac{\Delta x_{-1}\Delta x_{-2}(\Delta x_1 + \Delta x_2^2 + \Delta x_1^2 \Delta x_2 + \Delta x_1^2 \Delta x_{-1})}{\Delta x_1 \Delta x_2(\Delta x_1 + \Delta x_{-1})(\Delta x_1 + \Delta x_{-2})(\Delta x_2 + \Delta x_{-1})(\Delta x_2 + \Delta x_{-2})} \\ & + \frac{\Delta x_{-1}\Delta x_{-2}(\Delta x_2 \Delta x_1 \Delta x_{-2} + \Delta x_{-1} \Delta x_1 \Delta x_{-2} + \Delta x_2 \Delta x_{-1} \Delta x_{-2})}{\Delta x_1 \Delta x_2(\Delta x_1 + \Delta x_{-1})(\Delta x_1 + \Delta x_{-2})(\Delta x_2 + \Delta x_{-1})(\Delta x_2 + \Delta x_{-2})} \\ & + \frac{\Delta x_{-1}\Delta x_{-2}(\Delta x_2^2 \Delta x_{-1} + \Delta x_2^2 \Delta x_{-2} + \Delta x_1^3 + \Delta x_2^3)}{\Delta x_1 \Delta x_2(\Delta x_1 + \Delta x_{-1})(\Delta x_1 + \Delta x_{-2})(\Delta x_2 + \Delta x_{-1})(\Delta x_2 + \Delta x_{-2})} \\ & + \frac{\Delta x_{-1}\Delta x_{-2}(\Delta x_1^2 \Delta x_{-2} + \Delta x_2^2 \Delta x_{-1} + \Delta x_1 \Delta x_2 \Delta x_{-1})}{\Delta x_1 \Delta x_2(\Delta x_1 + \Delta x_{-1})(\Delta x_1 + \Delta x_{-2})(\Delta x_2 + \Delta x_{-1})(\Delta x_2 + \Delta x_{-2})} \end{aligned}$$

$$
\begin{aligned}
al_1 &= ar_2 \\
al_0 &= ar_1 \\
al_{-1} &= ar_0 \\
al_{-2} &= \frac{\Delta x_1 \Delta x_2 \Delta x_{-1}}{\Delta x_{-2}(\Delta x_1 + \Delta x_{-2})(\Delta x_2 + \Delta x_{-2})(\Delta x_{-1} - \Delta x_{-2})} \\
ar_{-1} &= \frac{\Delta x_{-2}(\Delta x_1^2 + \Delta x_{-1}^2 + \Delta x_1 \Delta x_{-1}^2 \Delta x_2 + \Delta x_1^2 \Delta x_2^2 - \Delta x_1^2 \Delta x_2 \Delta x_{-1})}{\Delta x_1 \Delta x_2 \Delta x_{-1}(\Delta x_{-2} + \Delta x_1)(\Delta x_{-2} + \Delta x_2)(\Delta x_{-1} + \Delta x_{-2})} \\
&\quad + \frac{\Delta x_{-2}(\Delta x_1^2 \Delta x_{-1} \Delta x_{-2} - \Delta x_1 \Delta x_2^2 \Delta x_{-1} + \Delta x_1 \Delta x_2^2 \Delta x_{-2})}{\Delta x_1 \Delta x_2 \Delta x_{-1}(\Delta x_{-2} + \Delta x_1)(\Delta x_{-2} + \Delta x_2)(\Delta x_{-1} + \Delta x_{-2})} \\
&\quad + \frac{\Delta x_{-2}(-\Delta x_1 \Delta x_{-1} \Delta x_{-2}^2 - 2\Delta x_1 \Delta x_2 \Delta x_{-1} \Delta x_{-2} + \Delta x_1 \Delta x_2 \Delta x_{-2}^2)}{\Delta x_1 \Delta x_2 \Delta x_{-1}(\Delta x_{-2} + \Delta x_1)(\Delta x_{-2} + \Delta x_2)(\Delta x_{-1} + \Delta x_{-2})} \\
&\quad + \frac{\Delta x_{-2}(\Delta x_2^2 \Delta x_{-1}^2 - \Delta x_2^2 \Delta x_{-1} \Delta x_{-2} + \Delta x_2 \Delta x_{-1}^2 \Delta x_{-2})}{\Delta x_1 \Delta x_2 \Delta x_{-1}(\Delta x_{-2} + \Delta x_1)(\Delta x_{-2} + \Delta x_2)(\Delta x_{-1} + \Delta x_{-2})} \\
&\quad + \frac{\Delta x_{-2}(\Delta x_1^2 \Delta x_{-2} \Delta x_2 - \Delta x_2 \Delta x_{-1} \Delta x_{-2}^2 + \Delta x_1 \Delta x_{-1}^2 \Delta x_{-2})}{\Delta x_1 \Delta x_2 \Delta x_{-1}(\Delta x_{-2} + \Delta x_1)(\Delta x_{-2} + \Delta x_2)(\Delta x_{-1} + \Delta x_{-2})}
\end{aligned}
\tag{14}
$$

Equation (10) with coefficient in Eq. (14) is fourth-order accurate Hybrid FD-FV scheme that can ensure conservativeness as well as order on uniform mesh. This kind of scheme can be used in direct numerical simulation (DNS) where all kind of error should be minimized.

4 Result and Discussion

We have tested our schemes on linear advection equation and nonlinear Burgers equation. General form of equation used for test case is

$$\frac{\partial u}{\partial t} + c\frac{\partial u}{\partial x} = \mu \frac{\partial^2 u}{\partial x^2}$$

For wave equation $c = 1$ $\mu = 0$ and for Burgers equation $c = u$ $\mu = 0.1$. Initial condition for 1D wave equation is

$$u(0, x) = \exp(-\ln 2(x/3)^2)$$

Initial condition for 1D Burgers equation is

$$u(0, x) = 1 + \sin(4\pi x)\ 0.5 \leq x \leq 1$$
$$u(0, x) = 1 \text{ else where}$$

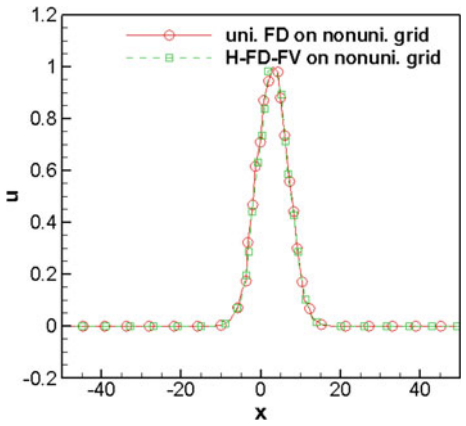

Fig. 5 Numerical results of advection equation in two different grids show oscillations

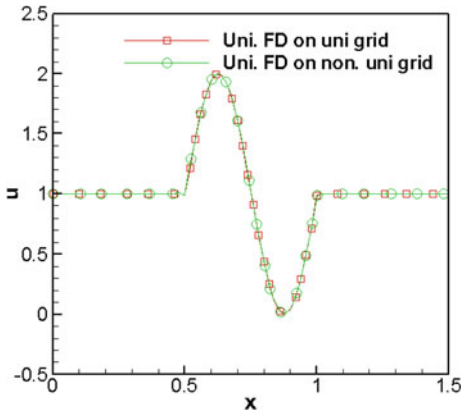

Fig. 6 Numerical results advection equation in two different grids doesn't show oscillations

Figure 5 shows unwanted small oscillations are seen in convection equation when we use FDM developed for the uniform grid on non-uniform grids. That can be rectified using Hybrid FD-FVM. In convection problems, for some high wave number initial condition(IC) because of restriction of grid size due to numerical dispersion or dissipation, we will be working on very fine grids. In those fine grids, those oscillations are negligible that can be seen in Fig. 6. Since our spatial discretization scheme is central, RK method proposed in paper by Neelan and Nair (2016) is used for time discretization. For high wave number problems, RK methods proposed in paper by Neelan et al. (2016) can be used. Similar results are observed in Burgers equation. We refine grid in numerical analysis when oscillations are observed. Figure 7 shows that refining the grid reduces amplitude of oscillation in uniform FDM but Hybrid FD-FVM is oscillation-free (Fig. 8) even on course grid.

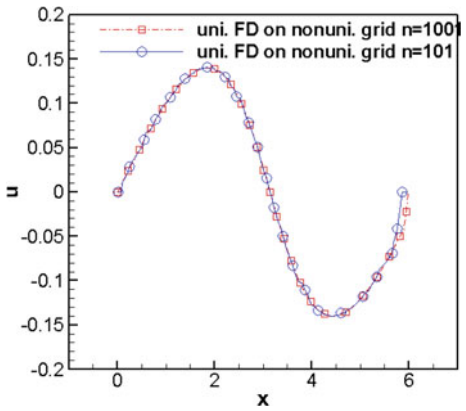

Fig. 7 Effect of grid refining of FDM on non-uniform grids

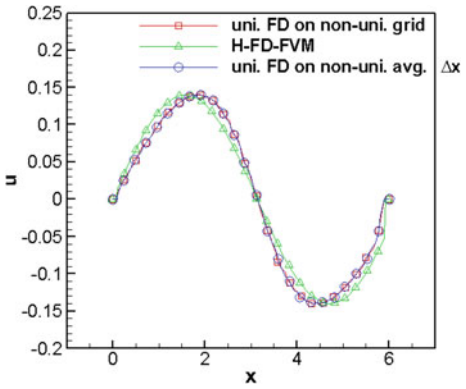

Fig. 8 Numerical results of Burgers equation on uniform FD versus H-FD-FVM

5 Conclusion

Hybrid FD-FVM of fourth-order accuracy on non-uniform mesh is proposed. The advantage of this method is it can retain conservativeness on uniform grid as well as convergence on non-uniform grid. Our method is ideal, if there is abrupt non-uniformity found in mesh especially near boundary layer or high gradient of flow field variable is present. It is not recommended in the smooth area because of computational cost. We have pointed out the limitations of FVM and FDM developed for uniform meshes on non-uniform mesh and some special cases where we can use FVM developed for uniform grid on non-uniform grids like gradually stretched AP grid and very slightly perturbed non-uniform grids. We have also discussed the limitation of higher order FVM on non-uniform grid and drawback of averaging procedure in FVM.

References

Bouche D, Ghidaglia JM, Pascal F (2005) Error estimate and the geometric corrector for the upwind finite volume method applied to the linear advection equation. SIAM J Numer Anal 43(2):578–603

Diskin B, Thomas JL (2010) Notes on accuracy of finite-volume discretization schemes on irregular grids. Appl Numer Math 60(3):224–226

Dumbser M, Kser M (2007) Arbitrary high order non-oscillatory finite volume schemes on unstructured meshes for linear hyperbolic systems. J Comput Phys 221(2):693–723

Dumbser M, Iben U, Munz CD (2013) Efficient implementation of high order unstructured WENO schemes for cavitating flows. Comput Fluids 86:141–168

Gaitonde D, Shang JS (1997) Optimized compact-difference-based finite-volume schemes for linear wave phenomena. J Comput Phys 138(2):617–643

Henrick AK, Aslam TD, Powers JM (2005) Mapped weighted essentially non-oscillatory schemes: achieving optimal order near critical points. J Comput Phys 207(2):542–567

Hill DJ, Pullin DI (2004) Hybrid tuned center-difference-WENO method for large eddy simulations in the presence of strong shocks. J Comput Phys 194(2):435–450

Jiang GS, Wu CC (1999) A high-order WENO finite difference scheme for the equations of ideal magnetohydrodynamics. J Comput Phys 150(2):561–594

Jureti F, Gosman AD (2010) Error analysis of the finite-volume method with respect to mesh type. Numer Heat Transfer Part B Fundam 57(6):414–439

Lele SK (1992) Compact finite difference schemes with spectral-like resolution. J Comput Phys 103(1):16–42

LeVeque RJ (2002) Finite volume methods for hyperbolic problems, vol 31. Cambridge University Press, Cambridge

Lomax H, Pulliam TH, Zingg DW (2013) Fundamentals of computational fluid dynamics. Springer Science and Business Media

Neelan AG, Nair MT (2016) Optimized dispersion relation schemes for spatial and temporal discretization. IJTET 14(01)

Neelan AG, Nair MT, Ashraf S (2016) Stability preserving Runge-Kutta method using genetic algorithm. In: Sixth international congress on computational mechanics and simulation (ICCMS-16), IIT-Bombay, 27th June to 1st July 2016

Pereira JMC, Kobayashi MH, Pereira JCF (2001) A fourth-order-accurate finite volume compact method for the incompressible Navier Stokes solutions. J Comput Phys 167(1):217–243

Pirozzoli S (2002) Conservative hybrid compact-WENO schemes for shock-turbulence interaction. J Comput Phys 178(1):81–117

Roe PL (1987) Error estimates for cell-vertex solutions of the compressible Euler equations

Shashkov M (1995) Conservative finite-difference methods on general grids, vol 6. CRC Press, Boca Raton

Shu CW (2003) High-order finite difference and finite volume WENO schemes and discontinuous Galerkin methods for CFD. Int J Comput Fluid Dyn 17(2):107–118

Spalart PR, Streett C (2001) Young-person's guide to detached-eddy simulation grids

Numerical Solution of Unsteady Free Convective Flow Past a Vertical Plate with Heat and Mass Fluxes Considering Chemical Reaction and Heat Absorption

G.S. Seth, Thirupathi Thumma and M.K. Mishra

Abstract Laminar boundary layer natural convection flow with heat and mass transfer of an optically thick heat-radiating and heat-absorbing fluid along with first-order chemical reaction has been investigated numerically. The partial differential equations (PDEs) governing the flow model are non-dimensionalized and solved using finite element technique. A grid independence analysis is carried out to ensure the convergence of solutions, and the code has been validated by comparing the results obtained via utilized method with those of earlier published results. To gain a better perspective of flow field, the solution of non-dimensional velocity, temperature, and concentration of the fluid is presented in a graphical form. Fluid temperature is observed to decrease through-out the thermal boundary layer on increasing the heat absorption. Chemical reaction has an adverse effect on species concentration.

1 Introduction

In nature, natural convection or free convection flows arise frequently either due to temperature differences or concentration differences, or also due to both. Natural convective flows along with the heat and mass transport arise in many natural and engineering processes such as convection in Earth's mantle, formation of convection cells due to sunlight, evaporation at the surface of a water body, drying, flow in

G.S. Seth · M.K. Mishra (✉)
Department of Applied Mathematics, Indian Institute of Technology (Indian School of Mines), Dhanbad, Dhanbad 826004, Jharkhand, India
e-mail: manojmishra.iitg@gmail.com

G.S. Seth
e-mail: gsseth_ism@yahoo.com

T. Thumma
Department of Mathematics, BV Raju Institute of Technology, Narsapur, Medak 502313, Telangana, India
e-mail: thirupathi.thumma@gmail.com

M.K. Singh et al. (eds.), *Applications of Fluid Dynamics*, Lecture Notes in Mechanical Engineering, https://doi.org/10.1007/978-981-10-5329-0_25

a desert cooler, and energy transfer in a wet cooling tower and have, therefore, attained a considerable attention by researchers in recent years. Owing to its inescapable application in various industries, viz. chemical, petroleum, biological, and agricultural industries, a great deal of importance has been given to study the simultaneous effects of heat and mass transfer due to natural convection by various researchers considering different aspects of flow geometry, thermal and solutal boundary conditions and various parameters affecting the flow. Some of the research articles by Mathers et al. (1957), Soundalgekar and Ganesan (1981), Narahari and Nayan (2011), Narahari and Dutta (2012), Hussanan et al. (2013), Jain (2013) are worth mentioning. A rigorous review of the literature concerning convective flow with heat and mass transfer problems is given in the books of Kays et al. (2012) and Bergman et al. (2011).

Gas turbines, nuclear power plants and numerous propulsion devices such as aircrafts, satellites, space vehicles, and missiles are some of the examples which require a very high temperature, and thus, the role of thermal radiation becomes indispensable (Sparrow and Cess 1978). A considerable amount of interest has been shown in the study of radiation interaction with free convection flow. Some of the relevant studies are due to Cess (1966), Hossain and Takhar (1996), Chamkha (1997), Muthucumaraswamy and Ganesan (2003), Seth et al. (2011), and Das et al. (2015).

Heat absorption phenomena become relevant in a non-isothermal flow domain, and consideration of heat absorption is significant while studying the heat transfer characteristics. Further, the study of chemical reaction phenomenon cannot be ignored while studying the transportation of heat mass with fluid flow due to its immense importance in industries of hydrometallurgical, chemical, polymer production, food processing, etc. Previous investigations dealing with heat absorption/generation and chemical reaction can be found in the works of Das et al. (1994), Takhar et al. (2000), Chamkha and Khaled (2001), Chamkha (2004), Seth et al (2015, 2016), Raju et al. (2016), Srinivasacharya and Reddy (2016).

The present study deals with time-dependent free convective fluid flow along with heat and mass transfer past a vertical flat plate of an infinite length under the influence of radiation, heat absorption (heat sink), and chemical reaction with uniform wall temperature/ uniform heat flux and variable mass flux, which have been investigated numerically. A careful survey of the literature suggests that no attempt has been made to study the above-mentioned fluid flow model.

2 Mathematical Formulation

Consider the time-dependent natural convection flow of a viscous, incompressible, and optically thick heat-radiating and heat-absorbing fluid past an infinite vertical plate in the presence of first-order chemical reaction between the fluid and species concentration. The schematic model of the coordinate system of the problem is depicted in Fig. 1.

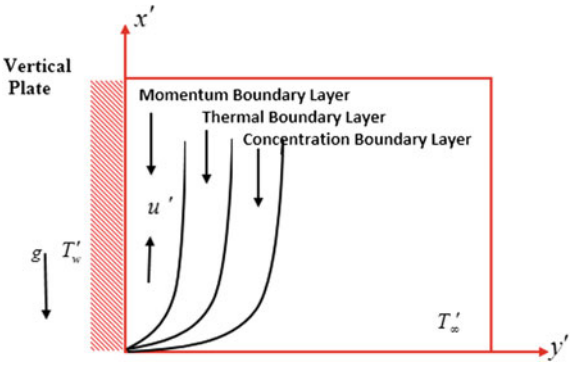

Fig. 1 Schematic diagram of the problem

Initially at time $t' \leq 0$, both the plate and the fluid are maintained at uniform temperature T'_∞ and uniform concentration C'_∞. For $t' > 0$, the plate temperature is raised or lowered to T'_w for uniform wall temperature (UWT) case and heat transfer rate at the surface of plate is considered constant for uniform heat flux (UHF) case. Also, the mass transfer rate at the plate is proportional to the species concentration. The flow is generated solely due to thermal and solutal buoyancy forces. Since plate is assumed to be of an infinite length along x' and z' axes, all the physical quantities are dependent of t' and y' only. The radiative heat flux along x'-axis is considered to be insignificant in comparison to the radiative heat flux along y'-axis (Sparrow and Cess 1978).

By considering the aforementioned assumptions, the dimensional governing Prandtl's boundary layer equations for unsteady natural convective flow of viscous, incompressible, chemically reacting, heat-absorbing, and radiative fluid under Boussinesq approximations are given by:

$$\frac{\partial u'}{\partial t'} = -\frac{1}{\rho}\frac{\partial p}{\partial x'} + \upsilon\frac{\partial^2 u'}{\partial y'^2} + g\beta_T(T' - T'_\infty) + g\beta_C(C' - C'_\infty), \tag{1}$$

$$-\frac{1}{\rho}\frac{\partial p}{\partial y'} = 0, \tag{2}$$

$$\frac{\partial T'}{\partial t'} = \frac{k}{\rho C_p}\frac{\partial^2 T'}{\partial y'^2} - \frac{1}{\rho C_p}\frac{\partial q_r}{\partial y'} - \frac{Q_H}{\rho C_p}(T' - T'_\infty), \tag{3}$$

$$\frac{\partial C'}{\partial t'} = D\frac{\partial^2 C'}{\partial y'^2} - k_r(C' - C'_\infty). \tag{4}$$

where u' represents the fluid velocity along x'-axis, T' is the temperature of the fluid, β_T is the coefficient of thermal expansion, g is the acceleration due to gravitational, β_C is the volumetric expansion coefficient, υ is the kinematic viscosity, ρ is the fluid density, k is the thermal conductivity, C_p is the specific heat at constant pressure,

D is the mass diffusivity, q_r is the radiative heat flux, Q_H is the heat absorption coefficient, and K_r is the first-order chemical reaction coefficient.

The initial and boundary conditions (Das et al. 2015) of the problem as described above are as follows:

$$\begin{aligned} &\text{for} \quad t' \le 0 \;\; \{\forall\, y' \ge 0 \;\; u'(y',t') = 0, \;\; T' = T'_\infty, \;\; C' = C'_\infty \\ &\text{for} \quad t' > 0 \left\{ \begin{array}{c} y' = 0 \;\; u'(0,t') = 0, \;\; \frac{\partial T'}{\partial y'} = -\frac{q'}{k}(\text{UHF}), \\ T' = T'_w(\text{UWT}), \;\; \frac{\partial C'}{\partial y'} = -\frac{q^*}{D^*}C' \\ y' \to \infty \;\; u'(\infty,t') \to 0, \;\; T'(\infty,t') \to T'_\infty, \\ C'(\infty,t') \to C'_\infty \end{array} \right\} \end{aligned} \tag{5}$$

where q and q^* represents the heat and mass fluxes at the surface.

It is concluded from Eq. (1) that pressure p is independent of y', so the value of flow pressure is same throughout the boundary layer and in the free stream. Therefore, from Eq. (1) and initial and boundary conditions (5), we have $-\frac{1}{\rho}\frac{\partial p}{\partial x'} = 0$, and thus Eq. (1) takes the form

$$\frac{\partial u'}{\partial t'} = \upsilon \frac{\partial^2 u'}{\partial y'^2} + g\left[\beta_T(T' - T'_\infty) + \beta_C(C' - C'_\infty)\right]. \tag{6}$$

Applying Rosseland approximation (Raptis 1998), the net radiative heat flux term can be written as follows:

$$q_r = \frac{-4\sigma^*}{3k^*}\frac{\partial T'^4}{\partial y'} \tag{7}$$

where σ^* and k^* are Stefan–Boltzmann constant and Roseland mean absorption coefficient, respectively. One can linearize the nonlinear term T'^4 occurring in Eq. (10) with the help of Taylor series by assuming a small variation between the boundary layer fluid temperature and ambient fluid temperature, retaining terms up to first order only. Thus, T'^4 can be represented as follows:

$$T'^4 \cong 4T'^3_\infty T' - 3T'^4_\infty \tag{8}$$

Using Eqs. (7) and (8), Eq. (3) becomes:

$$\frac{\partial T'}{\partial t'} = \frac{k}{\rho C_p}\frac{\partial^2 T'}{\partial y'^2} + \frac{1}{\rho C_p}\frac{16\sigma^* T'^3_\infty}{k^*}\frac{\partial^2 T'}{\partial y'^2} - \frac{Q_H}{\rho C_p}(T' - T'_\infty). \tag{9}$$

The dimensional partial differential Eqs. (4), (6), and (9) are converted into dimensionless form with the help of following dimensionless variables:

$$y = \frac{q^* y'}{D}, \quad u = \frac{u' D^*}{v q^*}, \quad t = \frac{q^{*2} t' v}{D^2}, \quad \theta = \frac{T' - T'_\infty}{T'_w - T'_\infty} (\text{UWT}),$$
$$\theta = \frac{(T' - T'_\infty) q^* k}{q' D^*} (\text{UHF}), \quad C = \frac{C' - C'_\infty}{C'_\infty} \tag{10}$$

The highly coupled, dimensionless governing partial differential equations are given by:

$$\frac{\partial u}{\partial t} = \frac{\partial^2 u}{\partial y^2} + Gr\theta + GcC, \tag{11}$$

$$\frac{\partial \theta}{\partial t} = \frac{1}{Pr}\left(1 + \frac{4R}{3}\right)\frac{\partial^2 \theta}{\partial y^2} - Q\theta, \tag{12}$$

$$\frac{\partial C}{\partial t} = \frac{1}{Sc}\frac{\partial^2 C}{\partial y^2} - KrC \tag{13}$$

where $R = \frac{4\sigma^* T'^3_\infty}{kk^*}$ is radiation parameter, $Gr = \frac{g\beta_T (T'_w - T'_\infty) D^3}{v^2 q^{*2}}$ (UWT) is the thermal Grashof number for uniform wall temperature case, $Gr = \frac{g\beta_T q D^4}{v^2 k q^{*4}}$ (UHF) is the thermal Grashof number for uniform heat flux case, $Gc = \frac{g\beta_C D^3 C'_\infty}{v^2 q^{*3}}$ is the solutal Grashof number, $Pr = \frac{v\rho C_p}{k}$ is the Prandtl number, $Sc = \frac{v}{D}$ is the Schmidt number, $Kr = \frac{k_r D^2}{v q^{*2}}$ is the chemical reaction parameter, and $Q = \frac{Q_H D^2}{v\rho C_p q^{*2}}$ is the heat absorption parameter.

Corresponding transformed non-dimensional initial and boundary conditions are given as follows:

$$\begin{aligned} &\text{for} \quad t \le 0 \ \{\forall\, y \ge 0 \ \ u(y,t) = 0, \ \ \theta(y,t) = 0, \ \ C(y,t) = 0 \\ &\text{for} \quad t > 0 \begin{cases} \text{at } y = 0 \ \ u(0,t) = 0, \ \ \frac{\partial \theta}{\partial y} = -1 \ (\text{UHF}), \\ \theta(0,t) = 1 \ (\text{UWT}), \ \ \frac{\partial C}{\partial y} = -(1 + C) \\ \text{as } y \to \infty \ \ u(\infty,t) \to 0, \ \ \theta(\infty,t) \to 0, \\ C(\infty,t) \to 0 \end{cases} \end{aligned} \tag{14}$$

3 Solution Methodology

The transformed system of linear, coupled, and dimensionless PDEs (11) to (13) along with the initial and boundary conditions (14) is solved numerically for fluid velocity, fluid temperature, and species concentration with the help of extensively

validated and robust finite element technique. A typical finite element technique involves 5 fundamental steps which are domain discretization, derivation of the element equations, assembly of element equations, imposition of boundary conditions, and solution of the assembled equations. An excellent description of these steps is presented in the textbooks by Reddy (2006).

4 Grid Independence Study

The grid independence analysis is conducted by dividing the entire domain into successively sized grids $131 \times 131, 151 \times 151$ and 171×171, which are presented in Table 1. The free stream boundary conditions are replaced by an appropriate large value where the fluid velocity, fluid temperature, and concentration profiles approach to zero asymptotically. We executed the developed code for different step sizes and found very good agreement between the results for all the profiles. After many trials for computational flexibility, we imposed $y_{\max} = 8$ where $y_{\max} \to \infty$. We adopted for all the computations 150 intervals of equal step size 0.053. At every node, four unknowns are to be found so that, after the assembly of element equations, a set of 453 algebraic equations are formed; consequently, an iterative method is adopted and, by introducing boundary conditions, the system of algebraic equations are solved. The solution is expected to be converged when the difference between two successive iterates satisfies the desired accuracy 10^{-4}. An excellent convergence for all the results is achieved.

Table 1 Grid independence analysis for fluid velocity, fluid temperature (UWT case), and species concentration at distinct points of boundary layer coordinate y

Velocity—u (UWT)			Temperature—T (UWT)			Concentration—C		
No. of grid points								
131	151	171	131	151	171	131	151	171
0	0	0	1	1	1	0.9	0.9	0.9
0.7146	0.7146	0.7146	0.9828	0.9828	0.9828	0.8821	0.8821	0.8821
1.3541	1.3541	1.3541	0.9655	0.9655	0.9655	0.8642	0.8642	0.8642
1.9231	1.9231	1.9231	0.9483	0.9483	0.9483	0.8463	0.8463	0.8463
2.426	2.426	2.426	0.9312	0.9312	0.9312	0.8285	0.8285	0.8285
2.8671	2.8671	2.8671	0.914	0.914	0.914	0.8107	0.8107	0.8107
3.2509	3.2509	3.2509	0.897	0.897	0.897	0.793	0.793	0.793
3.5814	3.5814	3.5814	0.8799	0.8799	0.8799	0.7753	0.7753	0.7753
3.8628	3.8628	3.8628	0.863	0.863	0.863	0.7578	0.7578	0.7578
4.099	4.099	4.099	0.8461	0.8461	0.8461	0.7403	0.7403	0.7403

Table 2 Comparison of shear stress for various parameter values when $t = 0.5$, $R = 2$, $Q = 0$ and $Kr = 0$

Gr	*Gc*	*Sc*	Pr	Das et al. (2015)		Present results	
				UHF	UWT	UHF	UWT
2	3	2.62	0.71	1.5819	1.1376	1.5818780	1.1376051
4	3	2.62	0.71	2.5089	1.6204	2.5089312	1.6203853
6	3	2.62	0.71	3.4360	2.1032	3.4359844	2.1031656
8	3	2.62	0.71	4.3630	2.5859	4.3630375	2.5859459
5	**2**	2.62	0.71	1.9046	0.7940	1.9046495	0.7939672
5	**4**	2.62	0.71	4.0403	2.9296	4.0402661	2.9295838
5	**6**	2.62	0.71	6.1759	5.0652	6.1758827	5.0652004
5	**8**	2.62	0.71	8.3115	7.2008	8.3114993	7.2008170
5	3	**0.24**	0.71	7.5091	6.3984	7.5090717	6.3983894
5	3	**0.45**	0.71	2.8036	1.6929	2.8035536	1.6928713
5	3	**0.62**	0.71	2.3596	1.2490	2.3596397	1.2489574
5	3	**0.78**	0.71	2.2919	1.1813	2.2919329	1.1812506
5	3	2.62	**0.72**	2.9499	1.8584	2.9499460	1.8584397
5	3	2.62	**2**	1.7439	1.6068	1.7439382	1.6067521
5	3	2.62	**5**	1.1831	1.3849	1.1831369	1.3849398
5	3	2.62	**7.1**	1.0501	1.3058	1.0501457	1.3058452

5 Validation of Numerical Results

To establish the correctness of these numerical results which are obtained through MATLAB code, we compared the present results for skin friction with the results obtained through analytical approach. It should be noted that solution approaches to the solution of Das et al. (2015) when $Kr = Q = 0$, which are shown in Table 2. These comparisons confirm that the present results are in agreement with the published reports. Therefore, these favorable comparisons gives us a great confidence and subsequently the developed code can be used in presenting the results graphically.

6 Results and Discussion

The primary aim of this paper is to study the transient chemically reacting and optically thick heat-radiating natural convective boundary layer flow of viscous, incompressible fluid past a vertically upward plate with heat absorption effect by

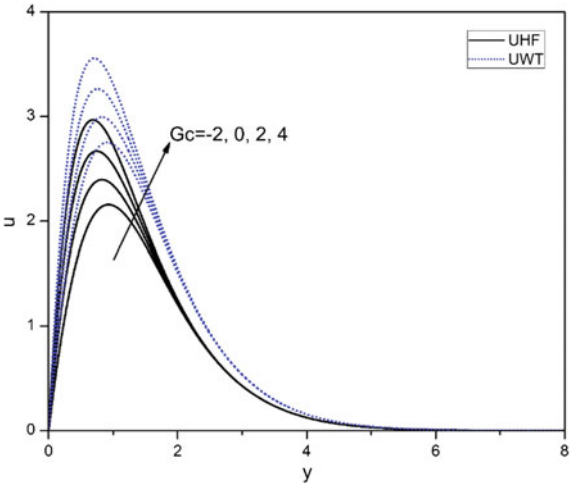

Fig. 2 Velocity profiles against y for different values of Gc

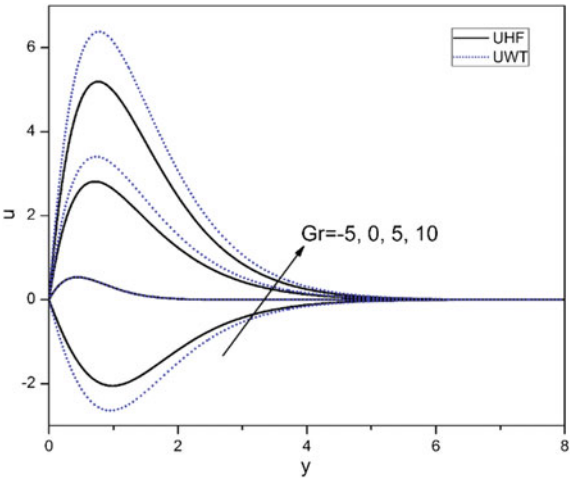

Fig. 3 Velocity profiles against y for different values of Gr

employing finite element method with Galerkin weighted residual scheme. Additionally, the influences of Gc, Gr, R, Q, Sc, and Kr on the flow field variables, viz. fluid velocity, fluid temperature, and species concentration distributions, are discussed and represented graphically in Figs. 2, 3, 4, 5, 6, 7, 8, and 9. In this paper, we present the solutions for the above physical parameters by adopting the default values $Gr = 5, Gc = 3, t = 0.5,\ Pr = 0.71, R = 2, Q = 5, Sc = 2.62,$ and $Kr = 1$ for finite element computation.

All the figures for fluid velocity u and fluid temperature T have been plotted for both cases of thermal boundary condition, i.e., for UHF and UWT conditions. It is seen that for all the flow parameters, the velocity rises from zero and obtains a peak value and then decreases exponentially as non-dimensional coordinate y approaches toward free stream.

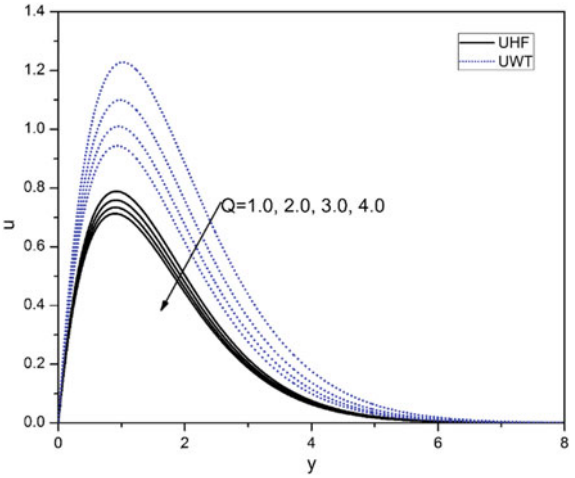

Fig. 4 Velocity profiles against y for different values of Q

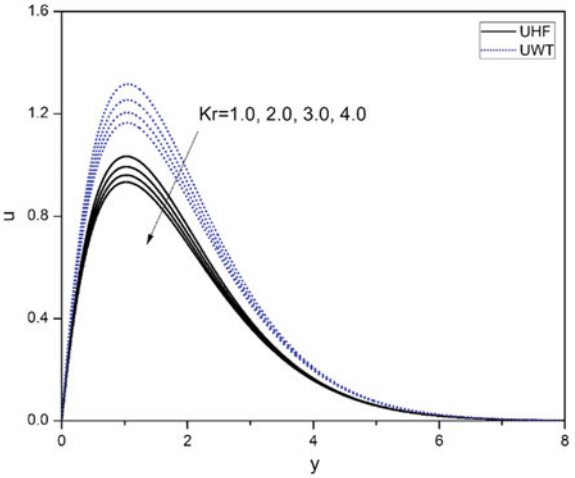

Fig. 5 Velocity profiles against y for different values of Kr

Figure 2 is plotted for dimensionless velocity versus the non-dimensional boundary layer coordinate y for increasing values of Gc. The solutal Grashof number represents the ratio between solutal buoyancy force and viscous force; thus, the strength of buoyancy force gets stronger with the increasing value of Gc. The figure indicates that for both cases of thermal boundary conditions, the fluid velocity starts from zero and approaches to peak values in the proximity of plate and then decreases exponentially to zero as y approaches to the free stream. It is seen from Fig. 2 that the fluid velocity gets accelerated as Gc increases.

Thermal Grashof number, Gr, represents the ratio of thermal bouncy force to viscous force; thus, Gr is directly proportional to the thermal buoyancy force. An increase in Gr leads to a higher buoyancy force which leads the fluid to move with higher velocity. This phenomenon can be seen in the Fig. 3 which is plotted for

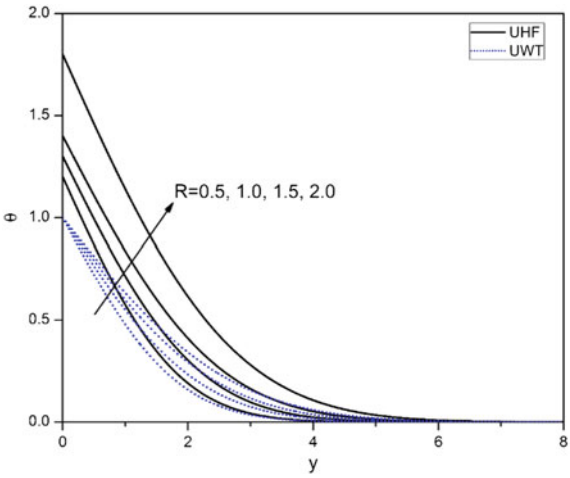

Fig. 6 Temperature profiles against y for different values of R

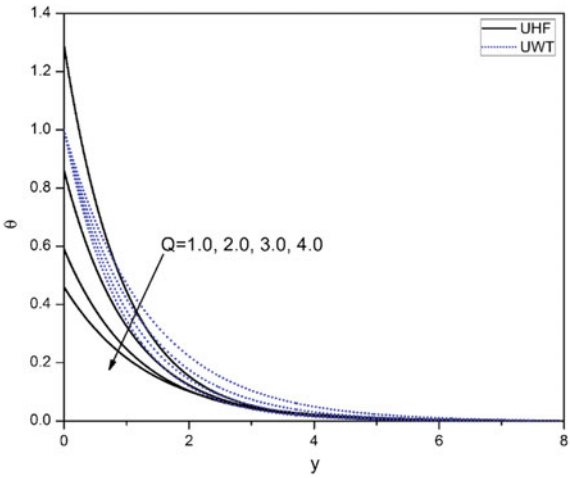

Fig. 7 Temperature profiles against y for different values of Q

both cases of thermal boundary conditions, i.e., for UHF and UWT. It is interesting to see that the flow direction gets reversed for negative values of thermal Grashof number.

Effects of heat absorption Q and chemical reaction Kr over dimensionless fluid velocity have been characterized in Figs. 4 and 5. These figures exhibit that the velocity has a declining nature for increasing value of both chemical reaction and heat absorption parameters. Since chemical reaction and heat absorption act as a destructing force for temperature and species concentration (Figs. 7 and 9), which results in a slow distribution of temperature and species concentration throughout the temperature and concentration boundary layers, respectively. It results in small

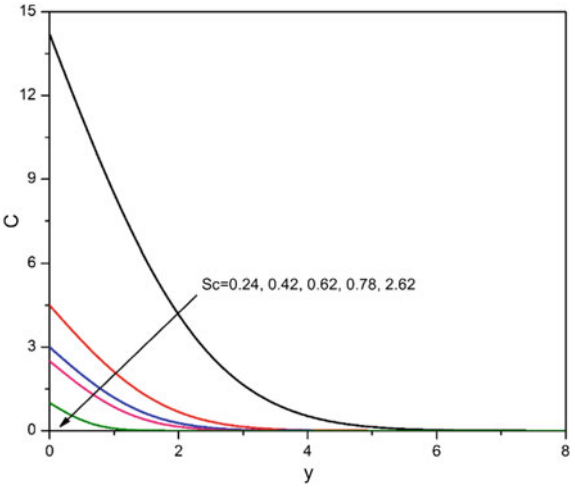

Fig. 8 Concentration profiles against y for different values of Sc

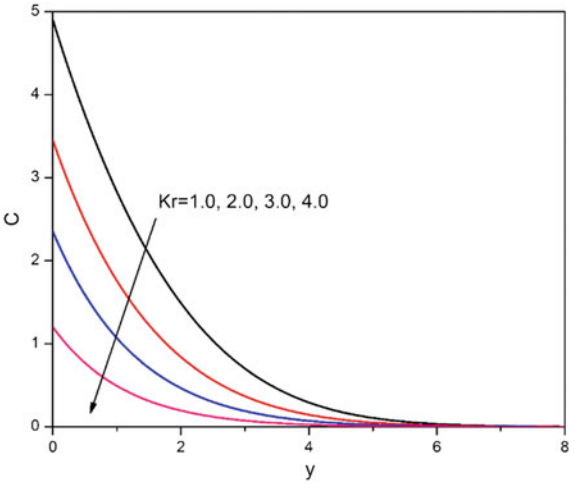

Fig. 9 Concentration profiles against y for different values of Kr

temperature and species concentration differences and consequently a weak buoyancy force, which ultimately reduces the velocity.

Effect of radiation over dimensionless temperature distribution is shown in Fig. 6. The tendency of thermal radiation for optically thick heat-radiating fluid is to increases the temperature which is clearly evident from the figure.

Behavior of temperature corresponding to the heat absorption is shown in Fig. 7. Physically, the tendency of heat absorption effect is to diminish the fluid temperature, which is also evident from the figure.

Figure 8 exhibits that the surface concentration as well as concentration within its boundary layer reduces rapidly with increasing value of Sc. Since Schmidt

number *Sc* is inversely proportional to mass diffusivity, an increase in *Sc* results in a weaker mass diffusion which reduces the concentration within the boundary layer.

Effect of chemical reaction *Kr* over the species concentration *C* has been demonstrated in Fig. 9, and it is clear from the figure that the species concentration falls with the increasing effect of chemical reaction.

It is important to note that the non-dimensional velocity is found to be higher in case of UWT condition than that for the UHF boundary condition for all pertinent flow parameters.

7 Conclusion

The present article investigates the flow characteristics of an unsteady laminar boundary layer free convective flow with heat and mass transfer of a viscous, incompressible, chemically reactive, heat-absorbing, and radiative fluid past a flat plate. The problem is investigated under two cases of thermal boundary conditions, i.e., for UWT and UHF conditions. The noteworthy findings of the investigation reveal that:

The fluid velocity is found higher in case of uniform wall temperature condition than that of uniform heat flux condition for all flow pertinent parameters. The flow is generated solely due to the buoyancy forces, and it found to be increasing with the increasing strength of buoyancy forces. The increasing strength of the heat absorption reduces the temperature as well as the fluid velocity. Optically thick heat-radiating fluids temperature is found to be increasing with the increasing strength of thermal radiation. Tendency of chemical reaction is to lessen the concentration distribution and also the fluid velocity. The concentration distribution within the boundary layer has decreasing tendency corresponding to the increasing strength of mass diffusion and chemical reaction.

Acknowledgements The authors are thankful to unknown reviewers for their insightful comments which helped us to improve the quality of present work.

References

Bergman TL, Incropera FP, Lavine AS (2011) Fundamentals of heat and mass transfer. Wiley, New York

Cess RD (1966) The interaction of thermal radiation with free convection heat transfer. Int J Heat Mass Transf 9:1269–1277

Chamkha AJ (1997) solar radiation assisted natural convection in a uniform porous medium supported by a vertical flat plate. ASME J Heat Transfer 119:89–96

Chamkha AJ (2004) Unsteady MHD convective heat and mass transfer past a semi-infinite vertical permeable moving plate with heat absorption. Int J Eng Sci 42:217–230

Chamkha AJ, Khaled ARA (2001) Similarity solutions for hydromagnetic simultaneous heat and mass transfer by natural convection from an inclined plate with heat generation or absorption. Heat Mass Transf 37:117–123

Das UN, Deka R, Soundalgekar VM (1994) Effects of mass transfer on flow past an impulsively started infinite vertical plate with constant heat flux and chemical reaction. Forschung im Ingenieurwesen 60:284. Doi:10.1007/BF02601318

Das S, Jana RN, Chamkha AJ (2015) Unsteady free convection flow past a vertical plate with heat and mass fluxes in the presence of thermal radiation. J Appl Fluid Mech 8(4):845–854

Hossain MA, Takhar HS (1996) Radiation effects on mixed convection along a vertical plate with uniform surface temperature. Heat Mass Transf 31:243–248

Hussanan A, Khan I, Sharidan S (2013) An exact analysis of heat and mass transfer past a vertical plate with Newtonian heating. J Appl Math. Article ID: 434571, 9 p

Jain A (2013) Radiation and chemical reaction effects on unsteady double diffusive convective flow past an oscillating surface with constant heat flux. ISRN Chem Eng. Article ID: 846826, 8 p

Kays WM, Crawford ME, Weigand B (2012) Convective heat and mass transfer. Tata McGraw-Hill Education

Mathers WG, Madden AJ, Piret EL (1957) Simultaneous heat and mass transfer in free convection. Ind Eng Chem 49:961–968

Muthucumaraswamy R, Ganesan P (2003) Radiation effects on flow past an impulsively started infinite vertical plate with variable temperature. Int J Appl Mech Eng 8:125–129

Narahari M, Dutta BK (2012) Effects of thermal radiation and mass diffusion on free convection flow near a vertical plate with Newtonian heating. Chem Eng Commun 199:628–643

Narahari M, Nayan MY (2011) Free convection flow past an impulsively started infinite vertical plate with Newtonian heating in the presence of thermal radiation and mass diffusion. Turkish J Eng Environ Sci 35:187–198

Raju RS, Reddy GJ, Rao JA, Rashidi MM, Gorla RSR (2016) Analytical and numerical study of unsteady MHD free convection flow over an exponentially moving vertical plate with heat absorption. Int J Thermal Sci 107:303–315

Raptis A (1998) Radiation and free convection flow through a porous medium. Int Comm Heat Mass Transf 25:289–295

Reddy JN (2006) An introduction to the finite element method, 3rd edn. McGraw-Hill Book Company, New York

Seth GS, Ansari MA, Nandkeolyar R (2011) MHD natural convection flow with radiative heat transfer past an impulsively moving plate with ramped wall temperature. Heat Mass Transf 47:551–561

Seth GS, Hussain SM, Sarkar S (2015) Hydromagnetic natural convection flow with heat and mass transfer of a chemically reacting and heat absorbing fluid past an accelerated moving vertical plate with ramped temperature and ramped surface concentration through a porous medium. J Egyptian Math Soc 23:197–207

Seth GS, Sharma R, Kumbhakar B (2016) Heat and mass transfer effects on unsteady MHD natural convection flow of a chemically reactive and radiating fluid through a porous medium past a moving vertical plate with arbitrary ramped temperature. J App Fluid Mech 9:103–117

Soundgelkar VM, Ganesan P (1981) Finite difference analysis of transient free convection on an isothermal vertical flat plate. Int J Eng Sci 19:757–770

Sparrow EM, Cess RD (1978) Radiation heat transfer. Hemisphere, Washington

Srinivasacharya D, Reddy GS (2016) Chemical reaction and radiation effects on mixed convection heat and mass transfer over a vertical plate in power-law fluid saturated porous medium. J Egyptian Math Soc 24:108–115

Takhar HS, Chamkha AJ, Nath G (2000) Flow and mass transfer on a stretching sheet with a magnetic field and chemically reactive species. Int J Eng Sci 38:1303–1314

Numerical Analysis of Unsteady MHD Mixed Convection Flow in a Lid-Driven Square Cavity with Central Heating on Left Vertical Wall

K. Venkatadri, S. Gouse Mohiddin and M. Suryanarayana Reddy

Abstract The article presents a numerical study performed on analysis of unsteady magneto-convective heat transfer in a square enclosure with partial active wall. The thermally insulated top and bottom wall while the left vertical wall is heated at Centre the rest of the left vertical wall is adiabatic and right vertical wall maintained at a lower temperature T_c. MAC (Marker-and-Cell) method is used to solve numerically set of dimensionless governing partial differential equations. The effect of local heat source on left wall is evaluated. The influence of the governing of thermophysical parameters, namely Prandtl number, Rayleigh number (Ra), Hartmann number (Ha), Grashof number (Gr) and Reynolds number (Re), is obtained. The results of streamlines and temperature are presented graphically and discussed.

Nomenclature

Ha	Hartmann number
g	Acceleration due to gravity, m s^{-2}
k	Thermal conductivity, Wm^{-1} K^{-1}
H	Height square cavity, m
K	Permeability, m^2
N	Total number of nodes
Nu	Local Nusselt number
Gr	Grashof number
T	Temperature, K
u	x component of velocity, m s^{-1}
U	x component of dimensionless velocity
U_0	x lid velocity, m s^{-1}

K. Venkatadri (✉) · S. Gouse Mohiddin
Department of Mathematics, Madanapalle Institute of Technology & Science, Madanapalle 517325, AP, India
e-mail: venkatadri.venki@gmail.com

M. Suryanarayana Reddy
Department of Mathematics, JNTUA College of Engineering, Pulivendula 516390, AP, India
e-mail: machireddysnr.maths@jntua.ac.in

M.K. Singh et al. (eds.), *Applications of Fluid Dynamics*, Lecture Notes in Mechanical Engineering, https://doi.org/10.1007/978-981-10-5329-0_26

V y component of dimensionless velocity
X Dimensionless distance along x
Y Dimensionless distance along y
v y component of velocity, m s^{-1}
p Pressure, Pa
P Dimensionless pressure
Pr Prandtl number
Re Reynolds number
Ri Richardson number

Greek symbols

α Thermal diffusivity, m^2s^{-1}
β Volume expansion coefficient, K^{-1}
γ Penalty parameter
T Dimensionless temperature
υ Kinematic viscosity, m^2s^{-1}
ρ Density, kg m^{-3}
Ψ Stream function

1 Introduction

Mixed convection flow and heat transfer in lid-driven cavity is one of the interesting problems for researchers in various thermal boundary conditions. This problem is commonly focused on a variety of wide technical applications. Such applications include lubrication technologies, cooling of electronic devices, food processing, drying technologies, float glass production, flow and heat transfer in solar ponds, dynamics of lakes and thermal hydraulics of nuclear reactors. The magneto-convective heat transfer and the mixed convective flow of the fluid in an enclosure are very important in the field of engineering. Mohamad and Viskanta (1995) examined the influence of a vibrating lid on the fluid flow in a shallow cavity with thermal structures. Several numerical studies on lid-driven enclosure flows are observed by research investigators and few of them can be found from Refs. (Gupta and Manohar 1979; Benjamin and Denny 1979; Ghia et al. 1982; Schreiber and Keller 1983; Barragy and Carey 1997; Aydin and Fener 2001; Peng et al. 2003; Erturk et al. 2005).

The study of cavity flows with an oscillating lid has been done by some research investigators (Soh and Goodrich 1988; Iwatsu et al. 1992; Nishimura and Kunitsugu 1997; Sriram et al. 2006; Khanafer et al. 2007). Davis and Jones (1983) conducted a numerical study on pure natural convection with linearly heated walls; Nguyen and Prudhomme (2001) examined the natural convection flow in a

rectangular lid-driven cavity submitted to a constant heat flux at the top and bottom walls and also in side walls. Prasad and Koseff (1996) conducted an experimental analysis of combined forced and natural convection in a lid-driven rectangle cavity; in this study, the horizontal top wall moves with uniform speed at low temperature, and both vertical walls are adiabatic, with a maintained temperature difference (ΔT) 1–8 °C, thermal parameters $Gr = 10^7 - 5 \times 10^9$, and $Re = 0 - 12 \times 10^3$. Also Ri changes between 10^{-1} and 10^3. The computed Nusselt number was correlated to Re, Ri and depth-wise aspect ratio. They observed that the heat transfer is insensitive to Gr/Re^2, and the flow patterns are observed with various aspect ratios 1:1, 2:1, 3:1 and 4:1. Sharif et al. (2004) studied numerically the combined, forced and free convection in rectangular cavity with different thermal aspect ratios under the effect of heat flux at the bottom wall, in the presence of moving vertical walls. They observed that the maximum dimensionless temperature decreases in different locations of the heat source and the average Nusselt number enhanced as the heat source is moved from left to right wall for various aspect ratios with fixed Reynolds number $(Re = 100)$. Chamkha (2002) analyzed a numerical analysis on internal heat generation or absorption influence with MHD mixed convection in a square cavity and found that the vertically moving lid of cavity flow and heat transfer inside the enclosure is affected with magnetic field strongly. The present study observed the mixed convection in a lid-driven square cavity in the presence of magnetic field with partial heating of left vertical wall for two different positions in the presence of magnetic field parallel to gravity. The heated portion is moved to middle and bottom of the left wall and maintained uniform dimensionless temperature in right wall. The heat transfer rate is maximum for high Hartmann number and minimum for low Ha. The computed results are presented graphically in the form of stream functions and isotherms (temperature), also for dimensionless temperature with the influence of Hartmann number (Ha).

2 Mathematical Modelling and Simulation

The regime under investigation is illustrated in Fig. 1. Consider a two-dimensional square cavity where the walls are thermally insulated except the right and partially active left walls. The left vertical wall is partially heated and rest of the wall is adiabatic. The right vertical wall is maintained uniformly at cold temperature. The lid velocity of the cavity is $u = U_0$. Thermo-physical properties of the fluid such as thermal conductivity, viscosity, specific heat and thermal expansion coefficient are treated as constant. The governing equations for the unsteady two-dimensional natural convection of mass, momentum and energy in the enclosure (cavity) by invoking Boussinesq approximation can be written in non-dimensional form as:

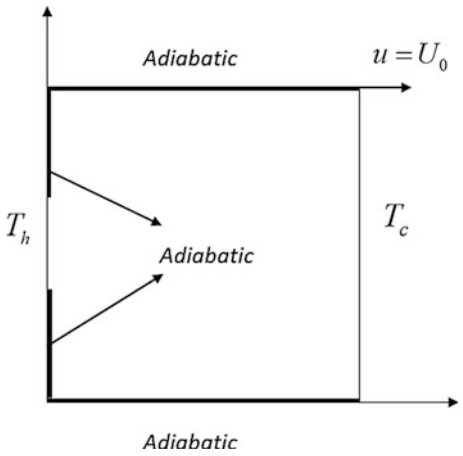

Fig. 1 Schematic diagram of enclosure heat transfer system

$$\frac{\partial u}{\partial x} + \frac{\partial v}{\partial y} = 0 \tag{1}$$

$$\frac{\partial u}{\partial t} + u\frac{\partial u}{\partial x} + v\frac{\partial u}{\partial y} = -\frac{\partial p}{\partial x} + \frac{1}{Re}\left(\frac{\partial^2 u}{\partial x^2} + \frac{\partial^2 u}{\partial y^2}\right) - \frac{Ha^2}{Re}u \tag{2}$$

$$\frac{\partial v}{\partial t} + u\frac{\partial v}{\partial x} + v\frac{\partial v}{\partial y} = -\frac{\partial p}{\partial y} + \frac{1}{Re}\left(\frac{\partial^2 v}{\partial x^2} + \frac{\partial^2 v}{\partial y^2}\right) + Ri \cdot T \tag{3}$$

$$\frac{\partial T}{\partial t} + u\frac{\partial T}{\partial x} + v\frac{\partial T}{\partial y} = \frac{1}{Re\,Pr}\left(\frac{\partial^2 T}{\partial x^2} + \frac{\partial^2 T}{\partial y^2}\right) \tag{4}$$

The initial and boundary conditions in dimensionless form are:

$$\begin{aligned} &t = 0: \quad u = v = 0, \quad 0 \le x \le 1, \quad 0 \le y \le 1, \\ &t > 0: \quad u = v = 0, \quad \frac{\partial T}{\partial y} = 0, \ \text{at} \ x = y = 0 \ \text{and} \ y = 1, \\ &T = 1, \quad \text{Active part} \ \frac{\partial T}{\partial x} = 0, \ x = 0, \ \text{and} \ T = 0 \ \text{for} \ x = 1 \end{aligned} \tag{5}$$

The dimensionless variables and parameters are defined as:

$$\begin{aligned} &x = X/H, \ \ y = Y/H, \ \ u = U/U_o, \ \ u = V/U_o, \ \ \theta = \frac{T - T_c}{T_h - T_c}, \\ &p = \frac{P}{\rho U_0^2}, \ \ Pr = \frac{v}{\alpha}, \ \ Re = \frac{U_o L}{v}, \ \ Gr = \frac{g\beta(T_h - T_c)L^3}{v^2} \end{aligned} \tag{6}$$

Here, X and Y are dimensionless x-coordinates and y-coordinates, respectively, U is dimensionless velocity along the direction of x-coordinates, V is dimensionless velocity along the direction of y-coordinates, θ is dimensionless temperature function, P is pressure (dimensionless), Pr is Prandtl number, Re is Reynolds number, Gr is Grashof number, T_c is cold wall temperature, T_h is hot wall temperature, T is dimensional temperature, p is dimensional pressure, g is gravity, ρ is fluid density, α is thermal diffusivity, ν is kinematic viscosity, H is height of enclosure (cavity wall dimension), and t is dimensional time. We note that the emerging thermal Grashof number encompasses the relative influence of mixed convection forces to viscous forces in the regime.

3 Marker-and-Cell (Mac) Numerical Solution and Validation

The unsteady dimensionless governing partial Eqs. (2)–(4) have been solved by the MAC method (Harlow and Welch 1965). The pressure distribution is obtained by making use of continuity equation (Mohamad and Viskanta 1995); the numerical solutions are carried out in terms of the non-dimensional velocity components (u, v) and stream functions (ψ)(Batchelor 1967). As per the Cauchy–Riemann equations, stream function (ψ) is defined as $u = \frac{\partial \psi}{\partial y}$ and $v = -\frac{\partial \psi}{\partial x}$, where positive and negative signs of ψ denote anticlockwise and clockwise circulations, respectively. In the MAC approach, although we consider viscous flow, viscosity is not actually required for numerical stability (Harlow and Welch 1965). Cell boundaries are labelled with half-integer values in the finite difference discretization. The marker particles do not participate in the calculation. Here, we elaborate on the numerical discretization procedure. Based on the weak conservative form of the unsteady two-dimensional Navier–Stokes equations and heat conservation equation as defined by Eqs. (1)–(4), we implement a grid meshing procedure using the following notation at the centre of a cell:

$$u_{i-1/2,j} = \frac{1}{2}\left[u_{i-1,j} + u_{i,j}\right] \tag{7}$$

From X-momentum conservation Eq. (2), we have:
Advection terms:

$$\frac{\partial(uu)}{\partial x} = \frac{uu1 - uu2}{\Delta x} \tag{8}$$

where

$$uu1 = \left[\frac{1}{2}\left(u_{i,j} + u_{i+1,j}\right)\right]^2$$
$$uu2 = \left[\frac{1}{2}\left(u_{i-1,j} + u_{i,j}\right)\right]^2 \tag{9}$$

Similarly, we have:

$$\frac{\partial(uv)}{\partial y} = \frac{uv1 - uv2}{\Delta y} \tag{10}$$

where

$$uv1 = \frac{1}{2}\left(u_{i,j} + u_{i,j+1}\right).\frac{1}{2}\left(v_{i,j} + v_{i+1,j}\right)$$
$$uv2 = \frac{1}{2}\left(u_{i,j} + u_{i,j-1}\right).\frac{1}{2}\left(v_{i,j-1} + v_{i+1,j-1}\right) \tag{11}$$

The following central difference formula is used for the second-order derivatives:

$$\nabla^2 u = \frac{\partial^2 u}{\partial x^2} + \frac{\partial^2 u}{\partial y^2}$$

$$\nabla^2 u = \frac{u_{i-1,j} - 2u_{i,j} + u_{i+1,j}}{\Delta x^2} + \frac{u_{i,j-1} - 2u_{i,j} + u_{i,j+1}}{\Delta y^2} \tag{12}$$

Applying to the y-direction momentum conservation Eq. (3), we have:
Advection term:

$$\frac{\partial(vu)}{\partial x} = \frac{vu1 - vu2}{\Delta x} \tag{13}$$

Here, the following notation applies for convection term:

$$uv1 = \frac{1}{2}\left(u_{i,j+1} + u_{i,j}\right) \cdot \frac{1}{2}\left(v_{i,j} + v_{i+1,j}\right)$$
$$uv2 = \frac{1}{2}\left(u_{i-1,j+1} + u_{i-1,j}\right) \cdot \frac{1}{2}\left(v_{i,j} + v_{i-1,j}\right)$$

$$\frac{\partial(vv)}{\partial y} = \frac{vv1 - vv2}{\Delta y}$$

$$\begin{aligned} vv1 &= \left[\frac{1}{2}\left(v_{i,j+1} + v_{i,j}\right)\right]^2 \\ vv2 &= \left[\frac{1}{2}\left(v_{i,j-1} + v_{i,j}\right)\right]^2 \end{aligned} \tag{14}$$

The central difference formula for the Laplacian operator is given by:

$$\begin{aligned} \nabla^2 v &= \frac{\partial^2 v}{\partial x^2} + \frac{\partial^2 v}{\partial y^2} \\ \nabla^2 v &= \frac{v_{i-1,j} - 2v_{i,j} + v_{i+1,j}}{\Delta x^2} + \frac{v_{i,j-1} - 2v_{i,j} + v_{i,j+1}}{\Delta y^2} \end{aligned} \tag{15}$$

Effectively, the x-momentum equation discretization technique can be summarized as:

$$u^{n+1} = u^n + \Delta t\left(-u\frac{\partial u}{\partial x} - v\frac{\partial u}{\partial y} + \frac{1}{Re}\left(\frac{\partial^2 u}{\partial x^2} + \frac{\partial^2 u}{\partial y^2}\right) - \frac{Ha^2}{Re}u\right) \tag{16}$$

There is a slight modification needed in the y-momentum equation due to the addition of a new term. Therefore, this term must be included in the discretized equation and we have:

$$v^{n+1} = v^n + \Delta t \cdot \left(-u\frac{\partial v}{\partial x} - v\frac{\partial v}{\partial y} + \frac{1}{Re}\left(\frac{\partial^2 v}{\partial x^2} + \frac{\partial^2 v}{\partial y^2}\right) + Ri \cdot T\right) \tag{17}$$

Pressure is calculated with elliptical pressure Poisson's equation:

$$\frac{\nabla \cdot u^{n+1}}{\Delta t} = \nabla^2 p^{n+1}$$

Updated velocities with pressure are:

$$\begin{aligned} u &= u^{n+1} - \frac{\Delta t}{\Delta x}\left(p_{i+1,j}^{n+1} - p_{i,j}^{n+1}\right) \\ v &= v^{n+1} - \frac{\Delta t}{\Delta x}\left(p_{i+1,j}^{n+1} - p_{i,j}^{n+1}\right) \end{aligned}$$

It is further noteworthy that the temperature term T is co-located such that it coincides with velocity before using it in the above equation to account for the staggered grid. After u^{n+1} and v^{n+1} are projected to get u and v, we can use the discretized temperature equation to get T at next time level (T^{n+1}) via the algorithm:

$$T^{n+1} = T^n + \Delta t \cdot \left(-u\frac{\partial T}{\partial x} - v\frac{\partial T}{\partial y} + \frac{1}{Re\,Pr}\left(\frac{\partial^2 T}{\partial x^2} + \frac{\partial^2 T}{\partial y^2}\right)\right) \tag{18}$$

Now, integrate in time by an incremental time step Δt in every iteration, and this cycle continues until the final time $t = 1.0$ reached. The variables are co-located and plotted. Modern variants of the MAC method utilize the conjugate gradient schemes which solve the Poisson equation. Further details are provided in Harlow and Welch (1965). To confirm mesh independence, a grid-independence study is

Table 1 Grid independent study

Grid size	Average Nusselt number (Nu)
51 × 51	0.17437
61 × 61	0.17798
71 × 71	0.17319
81 × 81	0.17562

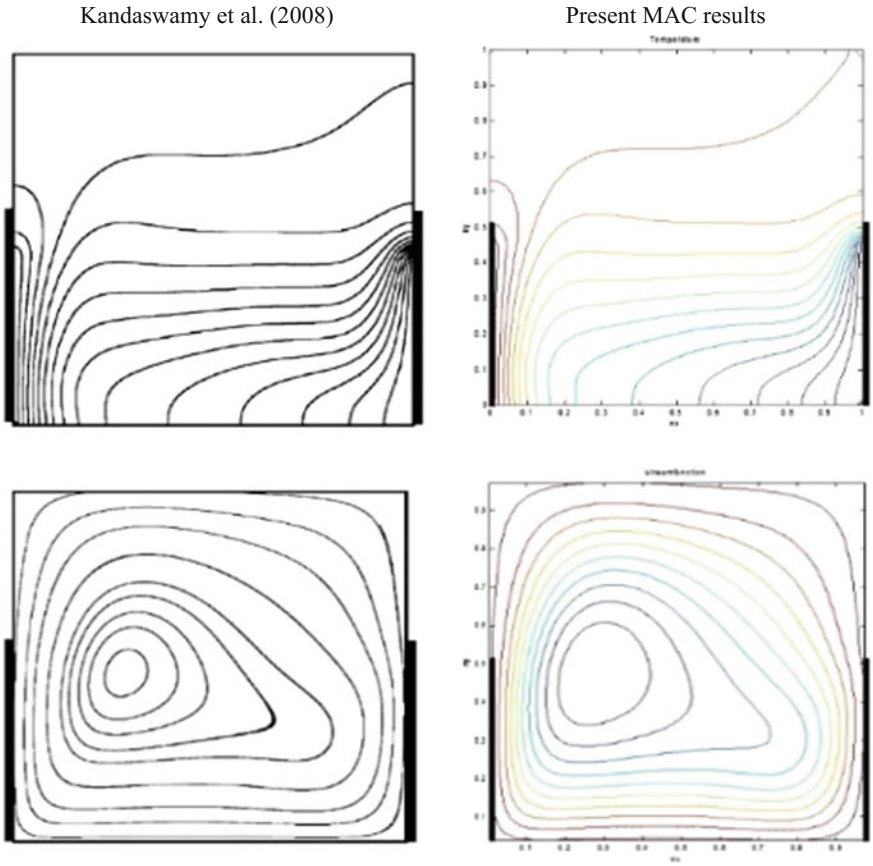

Fig. 2 Comparison of contour plots for bottom–bottom vertical walls with $Pr = 0.71$, $Gr = 10^5$, $Ha = 10$

conducted. In computational fluid dynamics, of which finite difference simulation is merely one methodology, once a mesh provides a solution which is invariant with the finer meshes, the coarser mesh can be adopted. This reduces computational cost but retains the necessary accuracy. Table 1 shows that accuracy to three decimal places is achieved for computed Nusselt number at the horizontal bottom wall with a mesh of 61 × 61 which is sufficient for heat transfer computations, and therefore, this is adopted for all subsequent simulations.

Furthermore to validate the present computations, visualizations of the temperature (isotherm) and stream function distributions are provided. These replicate the solutions of Kandaswamy et al. (2008). The results are in very close correlation, as observed in Fig. 2 and confidence in the present MAC computational code is therefore justifiably high.

4 MAC Numerical Results and Discussion

The computational simulation studies are performed based on 51 × 51 grids. The numerical solutions are obtained for $Gr = 10^4 - 10^5$, $Pr = 0.71$ and $Re = 10 - 10^2$. Top and bottom walls of the cavity are thermally insulated while the left vertical wall is partially heated and right vertical wall is maintained uniformly at cold temperature. Also the horizontal top wall has uniform velocity $U = 1$. In the current investigation, the MAC method gives the smooth solutions at the interior domain including magnetic effect. Figure 3a–c shows the contours of stream function and isotherms for the active portion (centre of the left wall) for $Pr = 0.71, Gr = 10^5, Re = 10$ and different values of magnetic field, $Ha = 10 - 10^2$. In case of heat portion on centre of the left wall with magnetic effect, $Ha = 10$, the stream function forms two fully rotating vertices. The mixed convective force which arises with the particles of fluid are heated close to the hot portion acts equally to the hot portion to move diagonally and descend towards the isothermal wall, the corresponding temperature patterns are almost parallel to the horizontal walls at middle of the enclosure as the flow is stagnant at the core. To increase the $Ha = 50$. The stream function is symmetric of stream function Fig. 3a. The corresponding isotherms in Fig. 3b shows that the convective heat transfer is less at top corner of heat portion wall and bottom corner of cold wall. The stream function contours are decrease for $Ha = 10^2$ the isotherms are spread equally to the cavity.

In Figs. 4a–c and 5a–d, the stream function and isotherms contours are more at the bottom active portion of left side wall with the increase in the magnetic fields with $Ha = 10, 15, 20, 30, 40, 50, 70$ and 100. The influence of active portion of left wall and magnetic field effects is depicted. Two convective circulations are formed in the core with a large cell around them with flow all over the cavity, and the

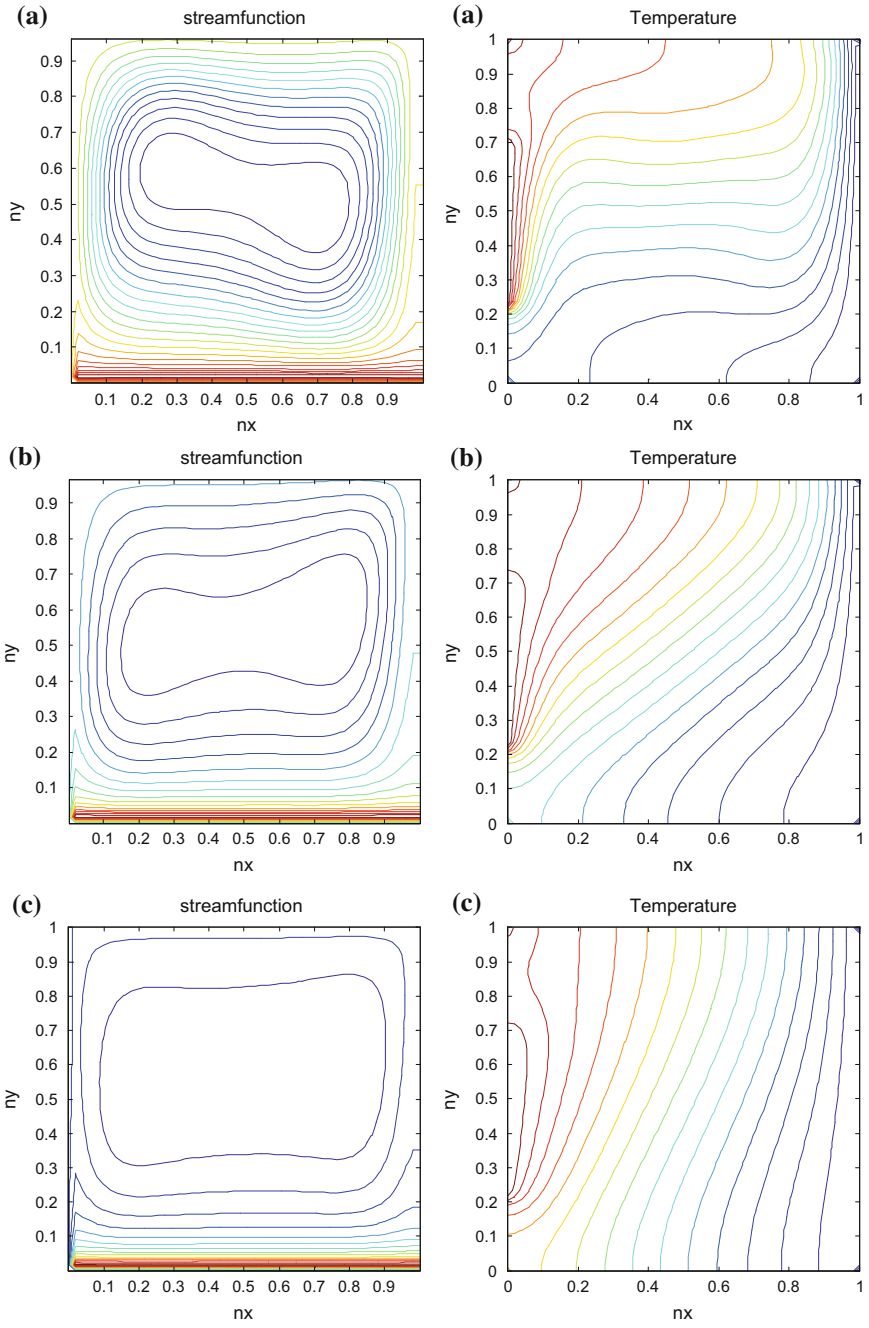

Fig. 3 Stream functions (*left side*) and isotherms (*right side*) for $Pr = 0.7, Re = 10, Gr = 10^5$. **a** $Ha = 10$, **b** $Ha = 50$, **c** $Ha = 100$

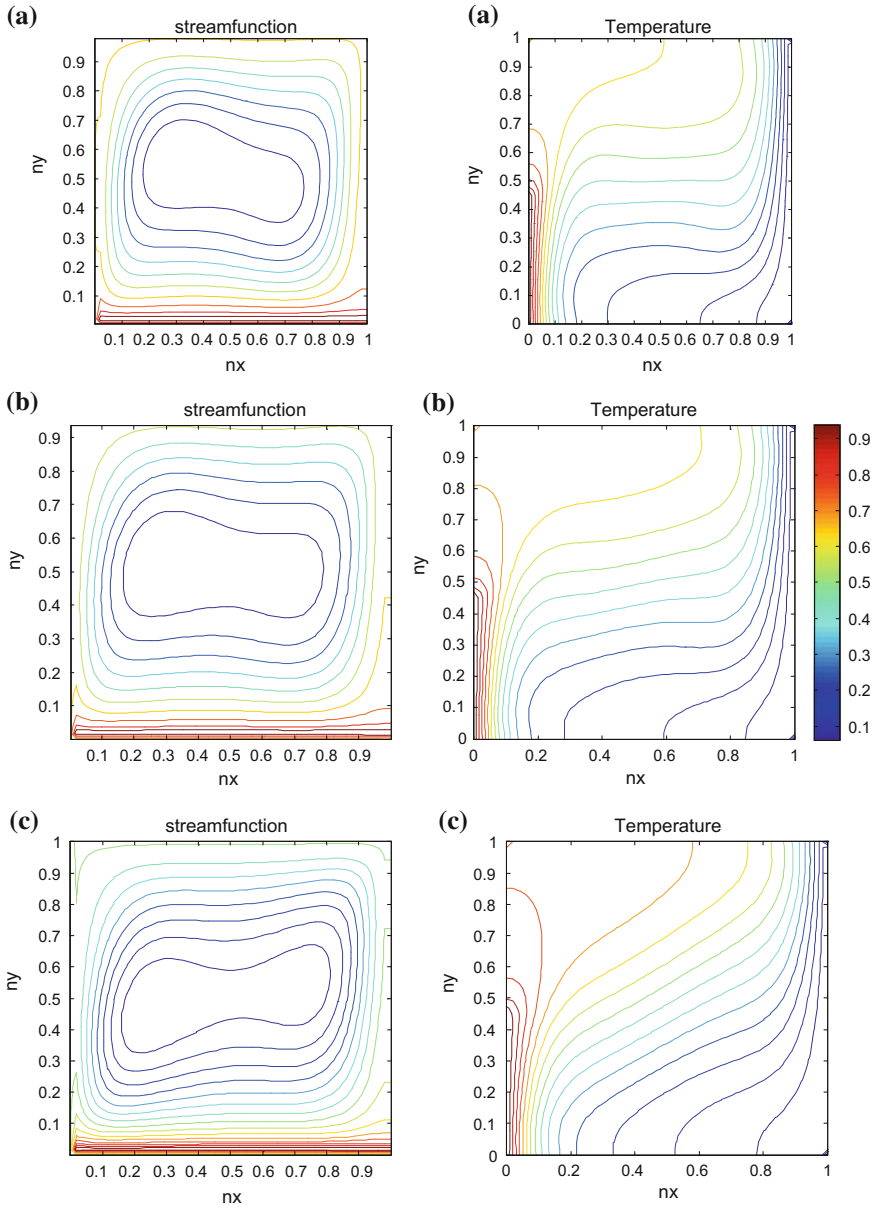

Fig. 4 Stream functions and isotherms for $Pr = 0.71, Re = 10, Gr = 10^5$. **a** $Ha = 10$, **b** $Ha = 15$, **c** $Ha = 30$

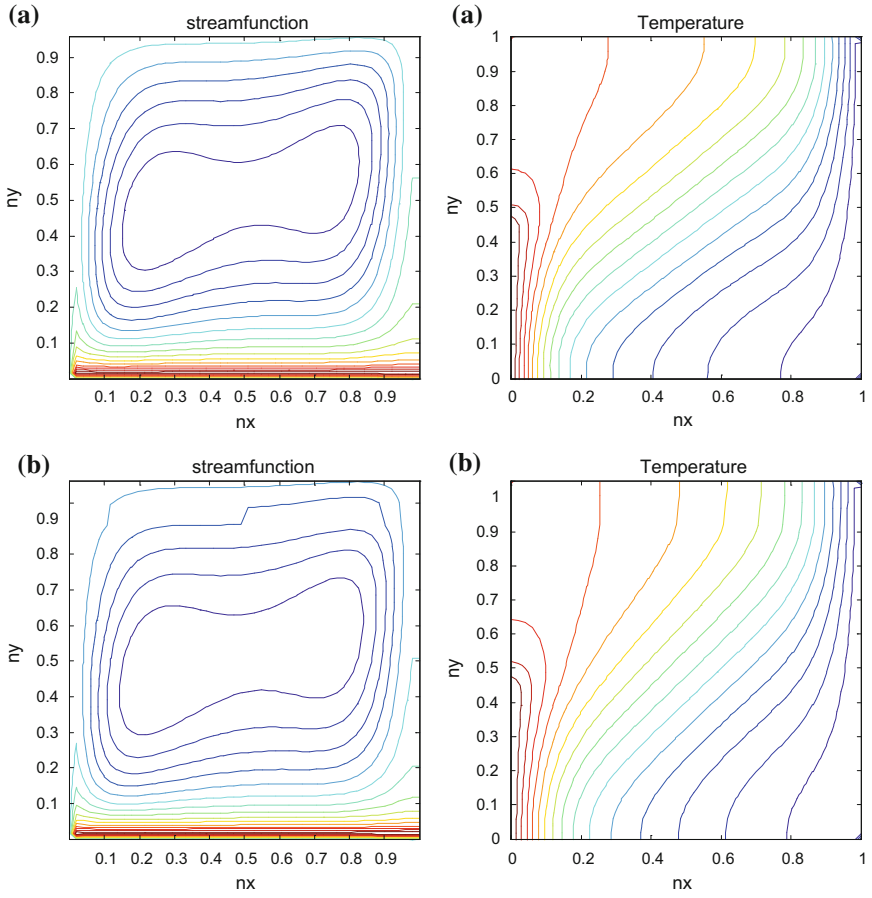

Fig. 5 Stream functions and isotherms for $Pr = 0.71, Re = 10, Gr = 10^5$. **a** $Ha = 40$, **b** $Ha = 50$, **c** $Ha = 70$, **d** $Ha = 100$

convective cells move (rotate anticlockwise) to active portion with the increase in Hartmann number. Streamline contours decrease with high magnetic effect $(Ha = 100)$. From the isotherm contours (see Fig. 4), it is observed that the isotherm lines are nearly same for different Ha numbers with fixed Ri; the formation of thermal boundary layer at heating portion reduces for increasing the magnetic field (see Figs. 4 and 5); the temperature gradient reduces as low magnetic field. Figure 5d indicates that the isotherms are low concentrated at active region the hot particles transport same energy in all regions of the cavity.

In bottom active region of left wall in Fig. 6a shows the effect of magnetic field $(Ha = 100)$ and the Reynolds number $(Re = 100)$ on isotherms concentration. The left wall of top corner in Fig. 6b indicates the effect of Hartmann number $(Ha = 50)$ and fixed Re the heat transfer made with convection in the hot portion (bottom)

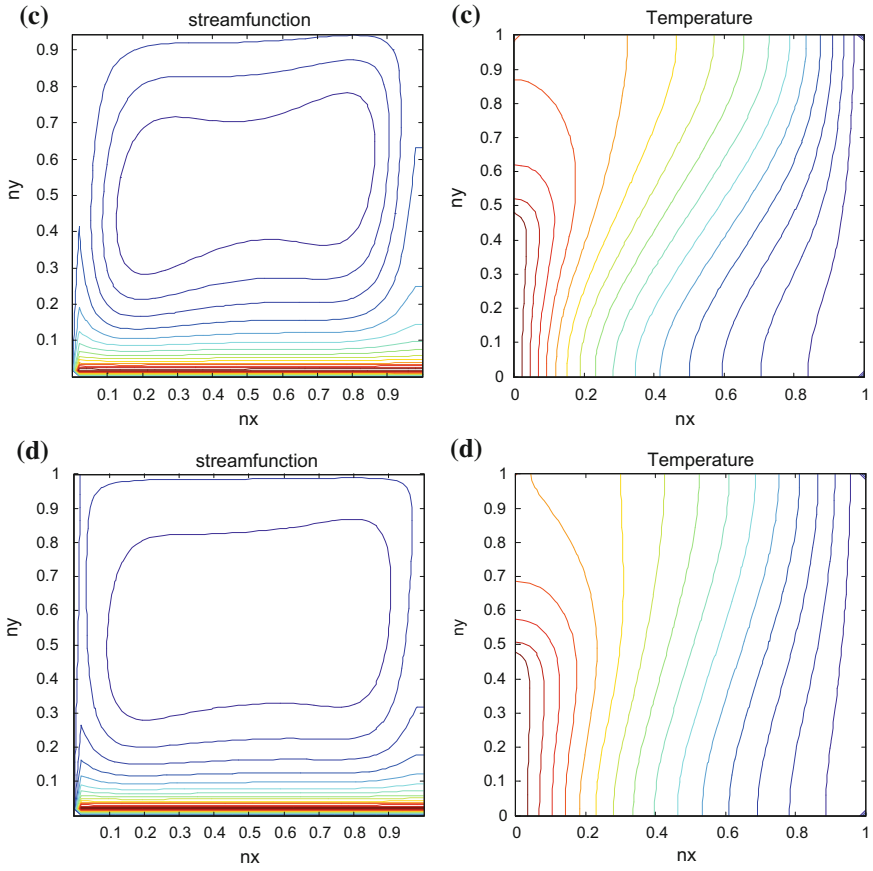

Fig. 5 (continued)

and cold wall of the cavity is thermally active. The boundary layer formation at close to active part and cold wall of the cavity is observed in Fig. 6c and d with $Ha = 10$, and the convective heat transfer in active regions in top (left side) of the lid-driven cavity is thermally inactive. The isotherms for different values of Ha with $Ri = 1$ are depicted in Fig. 7 in the isotherms pattern are almost equal for all values of Hartmann number except in Fig. 7a.

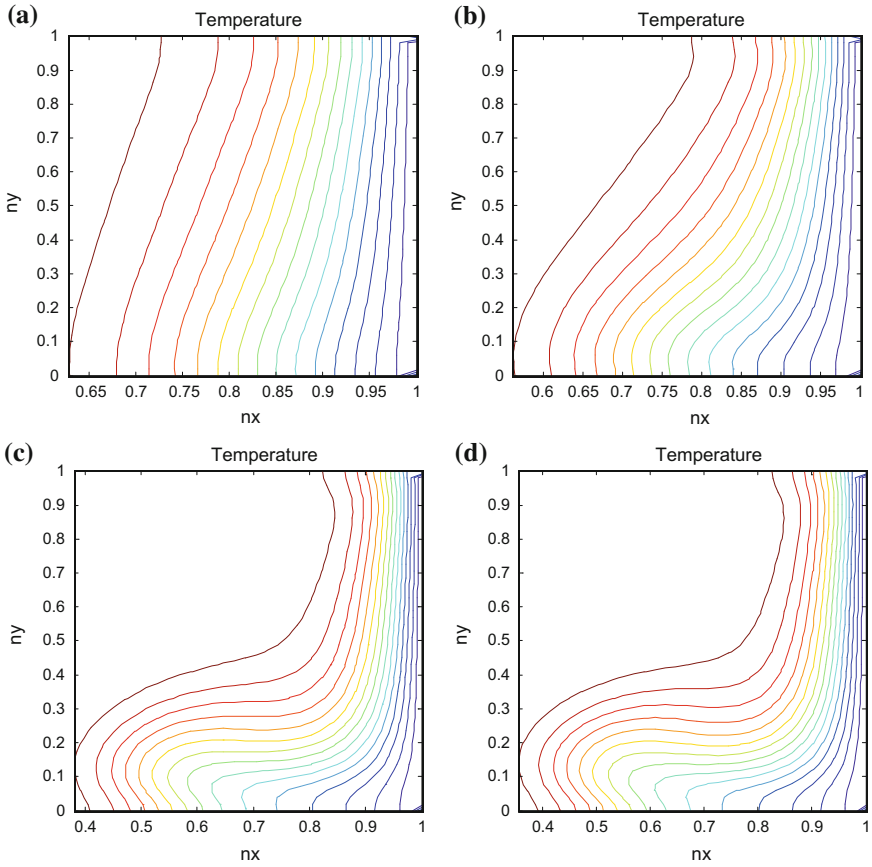

Fig. 6 Isotherms for $Pr = 0.71, Gr = 10^5, Re = 100, Ri = 10$. **a** $Ha = 100$, **b** $Ha = 50$, **c** $Ha = 10$, **d** $Ha = 0$

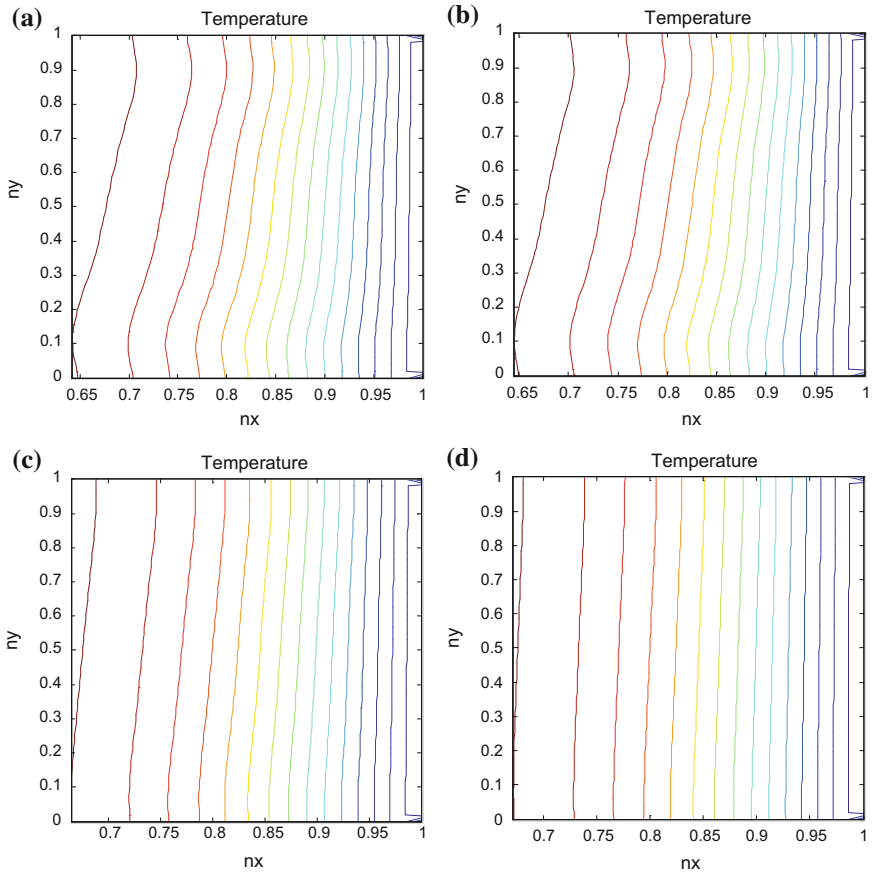

Fig. 7 Isotherms for $Pr = 0.71, Gr = 10^4, Re = 100, Ri = 1$. **a** Ha = 0, **b** Ha = 10, **c** Ha = 50, **d** Ha = 100

5 Conclusions

A numerical investigation of unsteady heat transfer in a Newtonian fluid occupying a square cavity has been conducted. The governing dimensionless equations have been solved numerically with the Marked and Cell (MAC) finite difference approach. The magneto-convective fluid flow in a cavity has been simulated with a partial heating on vertical side (left) wall and thermal insulation of top and bottom walls in presence of magnetic field. It is found that the heat transfer rate is enhanced in the centre thermally active region for high Ha. The rate of flow also increases for low Ha. The isotherm patterns are unchanged for $Re = 100, Gr = 10^4$ with fixed Pr for different Hartmann numbers. The MAC numerical scheme apparently achieves efficient and accurate solutions for transient enclosure of thermal mixed convection.

References

Aydin M, Fener RT (2001) Boundary element analysis of driven cavity flow for low and moderate Reynolds numbers. Int J Numer Methods Fluids 37:45–64

Barragy E, Carey GF (1997) Stream function-vorticity driven cavity solutions using p finite elements. Comput Fluids 26:453–468

Batchelor GK (1967) An introduction to fluid dynamics. Cambridge University Press, UK

Benjamin AS, Denny VE (1979) On the convergence of numerical solutions for 2-D flows in a cavity at large Re. J Comput Phys 33:340–358

Chamkha AJ (2002) Hydromagnetic mixed convection flow with vertical lid driven cavity in presence of internal heat generation or absorption. Numer Heat Transfer A 41:529–546

Davis GD, Jones IP (1983) Natural convection in a square cavity: a comparison exercise. Int J Numer Methods Fluids 3:227–248

Erturk E, Corke TC, GÄokcÄol C (2005) Numerical solutions of 2-D steady incompressible driven cavity flow at high Reynolds numbers. Int J Numer Methods Fluids 48:747–774

Ghia U, Ghia KN, Shin CT (1982) High-Re solutions for incompressible flow using the Navier-Stokes equations and a multigrid method. J Comput Phys 48:387–411

Guo Guanghong, Sharif Muhammad AR (2004) The study of mixed convection in rectangular cavity moving cold vertical walls with various aspect ratios in presence of linear flux heat source on the bottom wall. Int J Therm Sci 43:465–475

Gupta MM, Manohar RP (1979) Boundary approximations and accuracy in viscous flow computations. J Comput Phys 31:265–288

Harlow FH, Welch JE (1965) Numerical calculation of time-dependent viscous incompressible flow of fluid with free surface. Phys Fluids 8:2182–2190

Iwatsu R, Hyun JM, Kuwahara K (1992) Numerical simulation of flows driven by a torsionally-oscillating lid. J Fluid Eng 114:143–151

Kandaswamy P, Muthtamilselvan M, Lee J (2008) Prandtl number effects on mixed Convection in a lid-driven porous cavity. J Porous Media 11:791–801

Khanafer KM, Al-Amiri AM, Pop I (2007) Numerical simulation of unsteady convection in a driven cavity using an externally exited sliding lid. Eur J Mech B/Fluids 26:669–687

Mohamad AA, Viskanta R (1995) Flow and heat transfer in a lid-driven cavity filled with a stably stratified fluid. Appl Math Model 19:465–472

Nguyen TH, Prudhomme M (2001) Bifurcation of convection flows in a rectangular cavity subjected to uniform heat fluxes. Int Comm Heat Mass Transfer 28:23–30

Nishimura T, Kunitsugu K (1997) Fluid mixing and mass transfer in two-dimensional cavities with time-periodic lid velocity. Int J Heat Fluid Flow 18:497–506

Peng YF, Shiau YH, Hwang RR (2003) Transition in a 2-D lid-driven cavity flow. Comput Fluids 32:337–352

Prasad AK, Koseff JR (1996) Mixed convection heat transfer in a deep lid-driven cavity flow with cold top wall moving constant velocity. Int J Heat Fluid Flow 17:460–467

Schreiber R, Keller HB (1983) Driven cavity flows by efficient numerical techniques. J Comput Phys 49:310–333

Soh WH, Goodrich JW (1988) Unsteady solution of incompressible Navier-Stokes equations. J Comput Phys 79:113–134

Sriram S, Deshpande AP, Pushpavanam S (2006) Analysis of spatiotemporal variations and flow structures in a periodically driven cavity. J Fluid Eng 128:413–420

Numerical Simulation of Dynamics of the Drop Formation at a Vertical Capillary Tube

Pardeep, Mayank Srivastava and M.K. Sinha

Abstract The objective of this work is to study the parametric effects on the drop formation. For this, an experimentally verified computational domain that gives an accurate result is developed in the commercial software, FLUENT version 14.0. The numerical simulation of the Navier–Stokes equation has been obtained by combining the volume of fluid model with the finite volume method. To obtain the precise results in the finite volume technique, fine meshing is developed to track the movement of droplet in the air interface. The shape of drop formation obtained through the computational method is being verified with the experimental results available in the literature. The effect of parameters, i.e., viscosity and flow rate, is investigated in detail and also validated with the previous research works. The effect of viscosity on the development of satellite drop formation is also studied. This work is quite good agreement with the experimental work.

1 Introduction

A drop is a little section of fluid, limited totally or just about totally by free surfaces. A drop may frame when fluid collects at the lower end of a tube or other surface limit, creating a hanging drop called a pendant drop. Drops might likewise be framed by the buildup of a vapor or by atomization of a bigger mass of fluid. During the drop formation, the primary droplet is the largest drop that is ejected from the capillary tube. Along with primary droplets, some extra droplets (known as satellite droplet) are occasionally generated due to the collapse of the liquid column by surface tension. These satellite droplets are usually smaller than intended primary

Pardeep (✉) · M. Srivastava · M.K. Sinha
Department of Mechanical Engineering, NIT Jamshedpur, Jamshedpur 831014, India
e-mail: mail2pardeepbishnoi@gmail.com

M.K. Sinha
e-mail: mksinha.me@nitjsr.ac.in

M.K. Singh et al. (eds.), *Applications of Fluid Dynamics*, Lecture Notes in Mechanical Engineering, https://doi.org/10.1007/978-981-10-5329-0_27

Fig. 1 Drop formation in Savort's experiment

droplet. Dynamic of drop depends upon various factors such as viscosity of the liquid, surface tension between the liquid and atmospheric medium, density of the liquid, flow rate of the liquid in the capillary tube. Drop formation is widely used in chemical processing, printing technology, medical application, soldering, metallurgical work, and spraying.

The source of drop formation was recognized about 200 years ago by Felix Savart in Paris. In 1833, he observed experimentally about the drop formation during flow of water through a nozzle as shown in Fig. 1. Small drops in between the two bigger drops are named as 'satellite drop'. Basaran (2002) and Bhat (2008) explained different methods of drop formation and its application. Many researchers uncovered the various characteristics of drop before detachment and after detachment through experimental and numerical techniques. Different aspects of dripping, jetting, liquid bridge, and various stability factors that occur in the drop formation were explained by Egger (1997, 2006).

Viscosity is the most important parameter considered for drop formation. According to Zhang and Basaran (1995), viscosity plays a great role in stabilizing the pendant drop. Due to this reason, for high viscous liquid, the pendant drop's thread length (L_d) increases, and this was similar to Zhang and Stone (1997). They studied the dynamics of drop formation for low Reynolds number (Re) by using boundary integral method. According to them, satellite drop formation depends on the thread length of the pendant drop. At low value of viscosity ratio, thread length is low, and hence, there is no satellite drop formation. As stated by Zhang (1998, 1999), the value of thread length increases with respect to an increase in the viscosity ratio. He analyzed the dynamics of 2-ethyl 1-hexagonal drop by continuum surface method. Rothert et al. (2003) and Wehking (2014) experimentally proved that pinch-off process slows down with increasing viscosity. Drop formation is the outcome of stability between the viscosity and surface tension stated by Vladimir and Marko (2005). According to Zhang and Basaran (1995), for the stagnant value of viscosity ratio (λ) and variable value of capillary ratio, breakoff length faintly depends on gravitational bond number (β). Varieties of analytical and numerical methods were applied for the determination of dynamic of methods by Dravid (2008), Joseph et al. (1999), Pan and Suga (2003), Renardy and Renardy (2002), and Tirtaatmadja et al. (2006). Nowadays, the most commonly used method is volume of fluid for the simulation of the dynamics of drop formation.

A large number of experimental works are available on this topic but still more investigation is required. The objective of this paper is to validate the volume of fluid with the numerical analysis of Wilkes (1999). This paper presents the effects of different parameters on the dynamics of drop formation.

2 CFD Analysis of Drop Formation

2.1 Physical Description of the Problem

The domain consists of two regions: a 85% glycerin chamber (capillary tube) and an air chamber with coordinate system as shown in Fig. 2. The surface inside the capillary is neutrally wettable, while the surface surrounding the capillary orifice is non-wettable. We consider different compositions of glycerin as our base fluid which is being incompressible and Newtonian fluid as shown in Table 1.

To analyze the drop formation process from capillary tube into ambient air, we use 'volume of fluid model,' i.e., VOF model in FLUENT version 14.0.

At time zero, 85% glycerin fills the capillary tube, while the rest of the domain is filled with the air. Both fluids are assumed to be at rest. To initiate the ejection, the

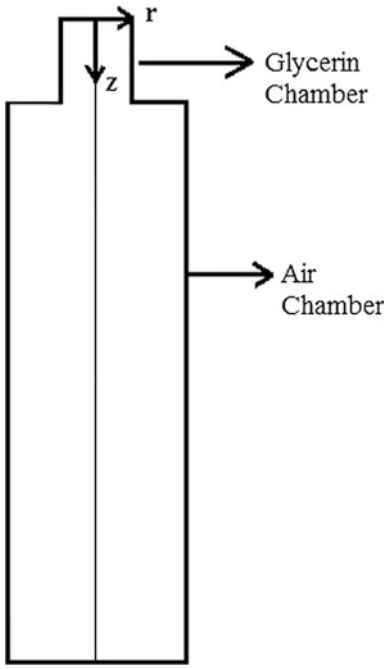

Fig. 2 Physical diagram of nozzle

Table 1 Physical properties of glycerin (Wilkes 1999)

Liquid	Density (g/cm^3)	Viscosity (poise)	Surface tension (dyne/cm)
85% glycerin	1.223	1.129	66.0
70% glycerin	1.182	0.229	68.5
50% glycerin	1.272	0.061	70.0
20% glycerin	1.048	0.018	72.4

85% glycerin velocity at the inlet boundary suddenly rises from 0 to 1 ml/min with fully developed profile. Gravity force which acts toward z direction is also included in the simulation. Due to the axial symmetry of the problem, a 2D geometry is used.

2.2 Mathematical Modeling

For free surface flow, the detachment process of a drop depends upon a lot of factors which include the flow rate through the capillary, viscosity of liquid phase (μ), density of both phases (ρ), surface tension between liquid and air (σ), and the diameter of capillary tube.

The assumptions made in the mathematical formulation and the solution process are the following based on which the governing equations are written.

1. The fluid flows are laminar and Newtonian.
2. The model is axisymmetric.
3. The surrounding air can be considered as incompressible.
4. The liquid properties are known and constant.
5. The evaporation of the liquid is neglected.
6. At the inlet of the capillary tube, fluid flow is assumed to be fully developed flow.
7. The thickness of the nozzle is neglected.

With the above assumptions, the Navier–Stokes equation in non-dimensional form for the transient motion of the liquid is given as

$$\nabla \cdot \boldsymbol{v} = 0, \tag{1}$$

$$Re\left(\frac{\partial \boldsymbol{v}}{\partial t} + \boldsymbol{v} \cdot \nabla \boldsymbol{v}\right) = \nabla \cdot \boldsymbol{\tau} + \left(\frac{G}{Ca}\right)\boldsymbol{j} \tag{2}$$

$$\tau = -p\boldsymbol{I} + [\nabla \boldsymbol{v} + (\nabla \boldsymbol{v})^{\mathrm{T}}] \tag{3}$$

The variable in Eq. (1), i.e., ∇, is the gradient operator; $\boldsymbol{v}$ is the resultant velocity vector. Similarly, in Eq. (2), τ is the stress tensor; $\mathbf{j}$ is the unit vector in z direction. In Eq. (3), p represents the dimensionless pressure, and $\boldsymbol{I}$ is the identity tensor.

Also during the non-dimensionalization process, three-dimensionless numbers are introduced in Eq. (2),
Reynolds number, $Re = \rho UD/\mu$, gravitational bond number, $G = \rho g R^2/\sigma$,
Capillary number, $Ca = \mu U/\sigma$.

The flow is consider as fully developed, so its velocity profile becomes

$$v_z = \frac{2Q}{\pi R^2}\left\{1 - \left(\frac{r}{R}\right)^2\right\}, \quad 0 \le r \le R \tag{4}$$

where r is the radial coordinate of drop phase, and v_z is the flow velocity in z direction.

The maximum velocity of liquid-phase flow for the fully developed flow is given as

$$U = \frac{2Q}{\pi R^2} \tag{5}$$

2.3 Initial and Boundary Conditions

The boundary conditions for the solution of Eqs. (1) and (2) are shown in Fig. 3, which is stated as:

1. Inlet of the domain is velocity inlet.
2. Flow rate is 1 ml/min.
3. The fluid must obey conditions of no slip and no penetration along the inner wall of the capillary.
4. Outlet of the computational domain is pressure outlet.

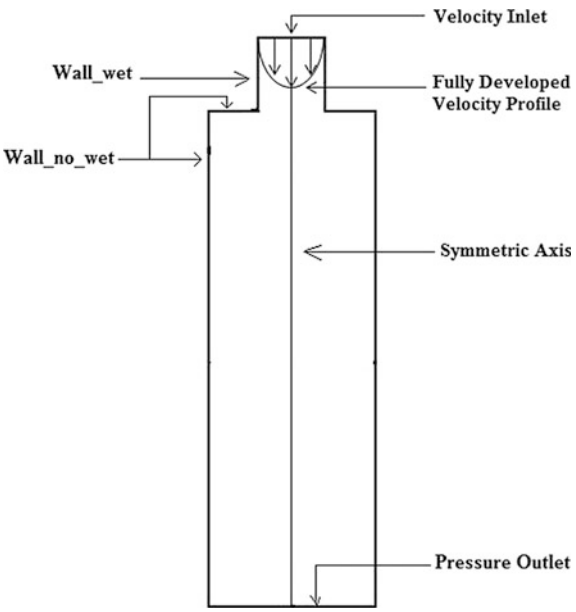

Fig. 3 Physical domain with boundary conditions

3 Results and Discussion

3.1 Grid Sensitivity Test

Grid sensitivity test is performed to check the effect of meshing on the computation results. In the grid sensitivity test, we change the number of cells for the same computational domain as shown in Table 2. After the number of cells reaches 7000, the thread length increases quite slowly, but increases the time period of the computational process relatively more. Therefore, for the numerical analysis, we have chosen the total number of cells around 7000 which gives accurate thread length as compared to the experimental result reported by Wilkes (1999) and Zhang and Basaran (1995).

3.2 A Comparison of Drop Detachment Profile with Experimental

Wilkes (1999) reported a sequence of drop formation of 85% glycerin from a nozzle which is fed from an Orion Sage Model M361 pump. This pump has the capability of producing flow rate from 0.03 ml/h to 60 ml/min. Data are collected with the help of Kodak EktaPro-intensified imager which can record 12,000 frames per second. Kodak EktaProHi-Sec processor is used to save the images. Further, for the extraction of data, Kodak EktaPro system or Sigma Scan Pro 4.0 image analyzer software is being used.

Figure 4 shows the comparison of different sequences of drop formation obtained from experimental method and VOF numerical method. The actual detachment time of the 85% glycerin drop in air is 5.07 s (from initial) and 2.29 s (after previous drop's detachment), which is within 3% error as compared with the Wilkes (1999) and Zhang and Basaran (1995). Furthermore, the above image proves that the VOF method also provides the precise information regarding the motion of drop during the detachment process.

Figure 5 shows the variation of the thread length with various composition of glycerin. It shows that the thread length variation is quite similar to the experimental work. It also proves the validation of CFD work with the experimental work.

Table 2 Variation of thread length with the number of cells

S. No.	No. of cells	Thread length (mm)
1	2000	7.12
2	7000	7.39
3	15,000	7.43

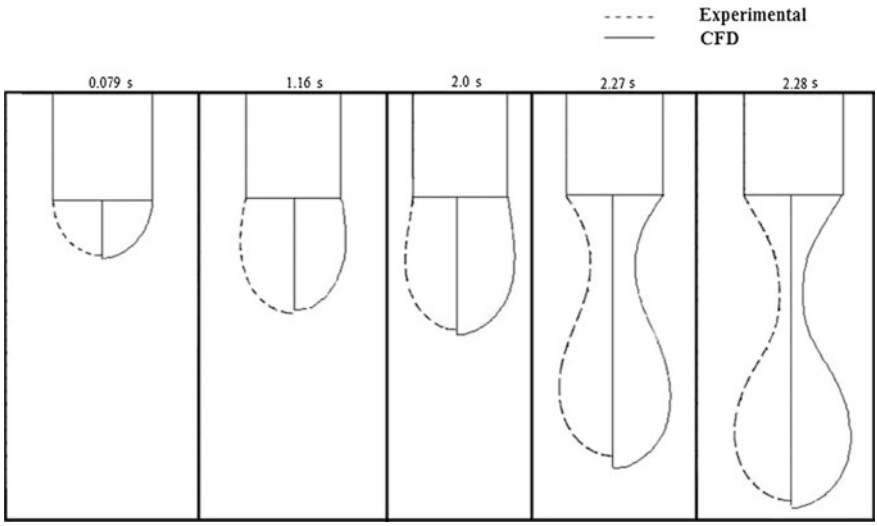

Fig. 4 Comparison of detachment profile of pendant drop at various time sequences

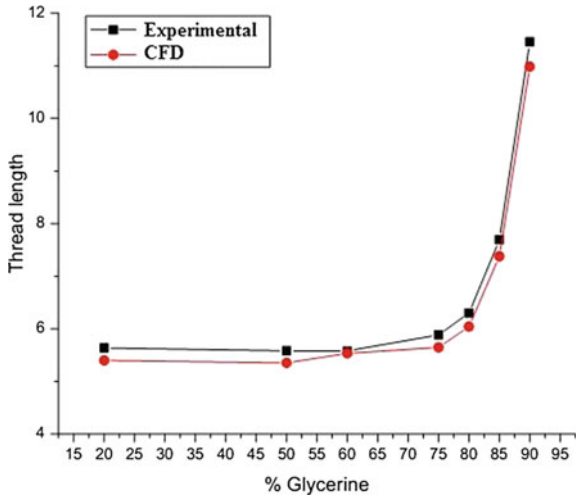

Fig. 5 Variation of thread lengths as a function of various glycerin compositions

3.3 Drop Elongation and Breakup

After the validation of the present computation with the experimental results, we are screening the variation of the dimensionless thread length at various flow rates regarding the detachment time, i.e., $t_d - t$ is shown in Fig. 6.

Figure 6 shows that the lower the flow rate, more time is spent by the droplet during the detachment process. The value of dimensionless drop elongation just

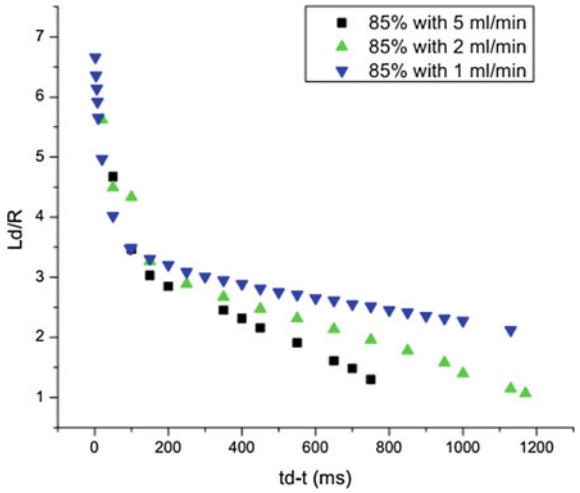

Fig. 6 Dimensionless length of drop growing out of a tube of radius $R = 1.6$ mm with detachment time at various flow rates

before the detachment is more with low flow rate as compared to higher flow rate. The reason behind this is that at high flow rate pendant drop loses its equilibrium prior to low flow rate. The liquid flow rate also toughens the occurrence of drop fabrication. Similar development is also reported by Zhang and Basaran (1995).

3.4 Effect of Viscosity

According to Kumar and Kuloor (1970), there is a very little effect of viscosity variation on the volume of detached drop. However, it actively influences the drop formation process especially during necking and detachment period.

To safeguard the damping interfacial oscillations of the detaching drop, viscosity of the liquid drop plays a great role. The interface variation developed in the drop just before breaking becomes smooth. When the value of viscosity increases, the thread length of the drop also increases as shown in Fig. 7.

When drop dynamic system is compared with spring balance system, we can say that the damping force of spring balance system is similar to the viscosity of drop formation. It means that if we increase the viscosity in the list of various properties of liquid droplet, it will eliminate the oscillation that rises during the drop formation process. It will also increase the detachment process of the drop. Also, the viscosity leads to the process of satellite drop formation. Satellite drop is formed only due to viscosity of the liquid drop. It can be said that a high value of viscosity liquid drop has long thread before the breakoff. So when this long thread breaks, a large shrinking force is generated in the thread which in turn will generate the small satellite drops as shown in Fig. 8. Hence, liquid bridge is the only source of satellite drop formation.

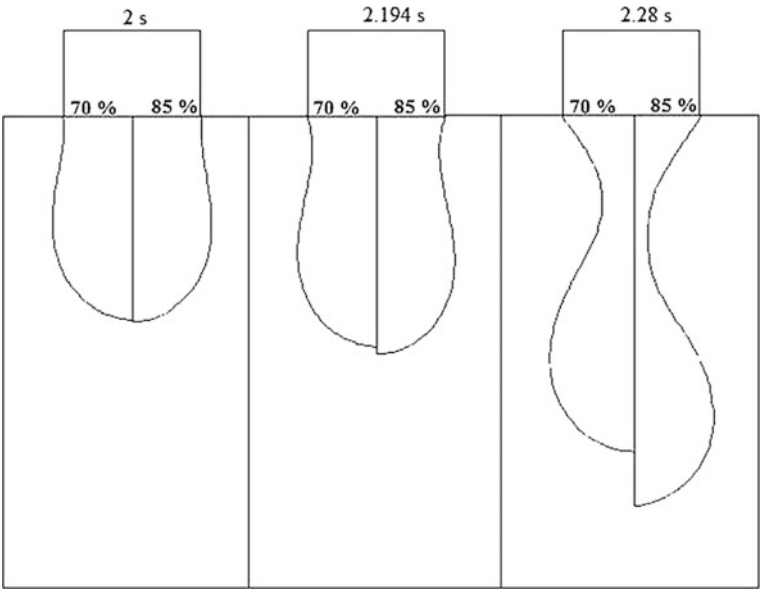

Fig. 7 Comparison of 70 and 85% glycerin at various time steps

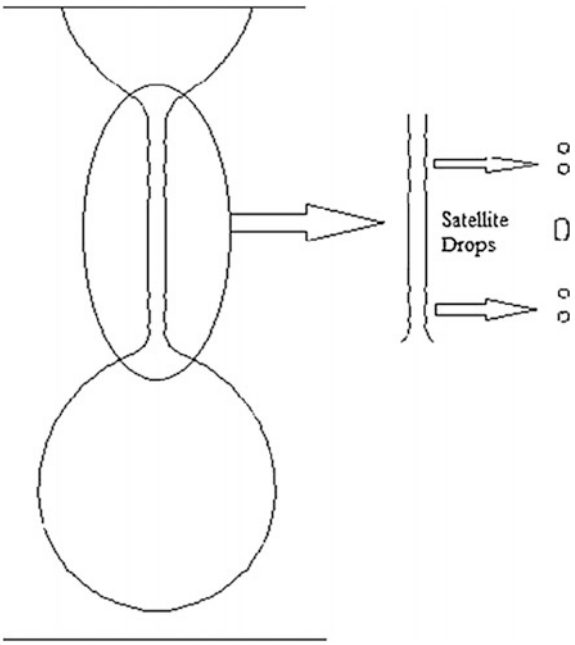

Fig. 8 Formation of satellite drops after breakoff for 85% glycerin

Due to the high recoil force on both ends of the thread, both upper part and lower part of the thread shrink and convert it into small droplets. The conversion is shown in Fig. 8.

4 Conclusion

In the present work, an experimentally verified computational model is being developed to study the various parameter effects on the dynamics of drop formation. The volume of fluid (VOF) method is used for the numerical simulation of the computational domain. VOF method is one of the best methods for studying the free surface problems.

Through numerical analysis, the sequences of detachment profile of drop formation for various viscosities are compared with the experimental source. It is found that for low viscosity liquid, thread length variation is negligible. While for higher viscosity liquids, thread length variation is exponentially increased. Also, as the viscosity of the liquid increases, the thread length is also increased which further disintegrates into small droplets, i.e., satellite droplets of the high recoil force developed in the liquid thread. Similarly, when the flow rate of the dripping increases, dimensionless thread length starts decreasing because at higher flow rate, thread length is less as compared to the lower flow rate.

This investigation also proves that the CFD tools are quite efficient and accurate for the free surface flow problems.

References

Basaran OA (2002) Small-Scale free surface flows with breakup: drop formation and emerging applications. AIChE J 48(9):1842–1848

Bhat P (2008) Drop formation methods and applications. Purdue University, IN 47907. https://pharmahub.org/resources/268

Dravid V (2008) Drop formation in non-Newtonian jets at low Reynolds. J Fluids Eng ASME 130:081504(1)–081504(8)

Eggers J (1997) Non linear dynamics and breakup of frees surface flows. Rev Mod Phys 69 (3):865–929

Eggers J (2006) A brief history of drop formation. Non-Smooth Mech Anal 14:163–172

Joseph DD, Belanger J, Beavers GS (1999) Breakup of a liquid drop suddenly exposed to a high-speed airstream. Int J Multiph Flow 25:1263–1303

Kumar R, Kuloor NR (1970) Bubble formation in viscous liquids under constant flow conditions. Canad J Chem Eng 48(4):383–388

Pan Y, Suga K (2003) Capturing the pinch off of liquid jets by the level set method. ASME J Fluids Eng 125:922–930

Renardy Y, Renardy M (2002) PROST: a parabolic reconstruction of surface tension for the volume of fluid method. J Comput Phys 183:400–421

Rothert A, Richter R, Rehberg I (2003) Formation of a drop: viscosity dependence of three flow regimes. New J Phys 5:59.1–59.13

Tirtaatmadja V, MecKinley GH, Cooper JJ (2006) White, drop formation and breakup of low viscosity elastic fluids: effects of molecular weight and concentration. HML report, Department of Mechanical Engineering, MIT, USA

Vladimir G, Marko M (2005) Drop formation in a falling stream of liquid. Am J Phys 73(5): 415–419

Wehking JD (2014) Effects of viscosity, interfacial tension, and flow geometry on droplet formation in a microfluidic T-junction. Microfluid Nanofluid 16:441–453

Wilkes ED (1999) Computational and experimental analysis of dynamics of drop formation. Phys Fluids 11(12):3577–3598

Zhang X (1998) Dynamics of drop formation in viscous flows. Chem Eng Sci 54:1759–1774

Zhang X (1999) Dynamics of growth & breakup of viscous pendant drops into air. J Colloid Interface Sci 212(1):107–122

Zhang X, Basaran OA (1995) An experimental study of dynamics of drop formation. Phys Fluid 7 (6):1184–1203

Zhang DF, Stone HA (1997) Drop formation in viscous flows at a vertical capillary tube. Phys Fluid 9(8):2234–2242

Part V
Magneto Hydrodynamics

Squeezing of Bingham Fluid Between Two Plane Annuli

Singeetham Pavan Kumar and Kadaba Puttanna Vishwanath

Abstract In this study, the presence of Bingham fluid between two parallel plane annuli with constant squeeze motion is theoretically analyzed. The effect of radius of separation on core thickness, pressure distribution, and squeeze force for different values of Bingham number has been investigated. By considering equilibrium of an element of the core in the fluid, thickness of the rigid plug core has been calculated numerically. The properties of the squeeze film are investigated through the non-Newtonian effects on the squeeze force of the plane for various annular spaces.

Nomenclature

h^*	Squeeze film thickness
$H = h^*/h^* = 1$	Dimensionless squeeze film thickness
r^*	Radial coordinate
$r = r^*/r_2^*$	Dimensionless radial coordinate
z^*	Axial coordinate
$z = z^*/h^*$	Dimensionless axial coordinate
r_1^*	Inner radius
r_2^*	Outer radius
v_r^*	Radial velocity component
v_z^*	Axial velocity component
p^*	Pressure
p	Dimensionless pressure
$\dot{h}^* = -v_s$	Squeeze velocity
r_0^*	Radius of separation
$\lambda = r_0^*/r_2^*$	Dimensionless radius of separation
$k = r_1^*/r_2^*$	Ratio of inner and outer radius
p_a^*	Ambient pressure

S. Pavan Kumar (✉) · K.P. Vishwanath
Department of Mathematical and Computational Sciences, National Institute of Technology Karnataka, Mangalore 575025, Karnataka, India
e-mail: singeetham.pavan@gmail.com

M.K. Singh et al. (eds.), *Applications of Fluid Dynamics*, Lecture Notes in Mechanical Engineering, https://doi.org/10.1007/978-981-10-5329-0_28

p_a	Dimensionless ambient pressure
τ_{rz}	Dimensionless shear stress
τ_0	Yield stress
μ	Newtonian viscosity
$B = \frac{\tau_0 (h^*)^2}{\mu v_s r_2^*}$	Bingham number
$h_{1_1}^*, h_{2_1}^*$	Boundaries of core thickness in $r_1^* \le r^* \le r_0^*$
$h_{1_2}^*, h_{2_2}^*$	Boundaries of core thickness in $r_0^* \le r^* \le r_2^*$
$h_{c_1}^*$	Core thickness in the region $r_1^* \le r^* \le r_0^*$
$h_{c_2}^*$	Core thickness in the region $r_0^* \le r^* \le r_2^*$
H_1, H_2	Dimensionless boundaries of the core thickness
H_{1_1}, H_{2_1}	Dimensionless boundaries of the core thickness in $k \le r \le \lambda$
H_{1_2}, H_{2_2}	Dimensionless boundaries of the core thickness in $\lambda \le r \le 1$
$H_c = H_{c_1}$	Dimensionless core thickness in the region $k \le r \le \lambda$
$H_c = H_{c_2}$	Dimensionless core thickness in the region $\lambda \le r \le 1$
w^*	Squeeze force
w	Dimensionless squeeze force
$w(k, N)$	Dimensionless squeeze force of Newtonian fluid

1 Introduction

Recent studies of squeezing flows are considered as an important role due to its practical applications in physical, biophysical, chemical engineering, polymer processing, and food industry, among many others. Further, there has been an increasing interest in the usage of non-Newtonian viscoplastic fluid as lubricants.

In general, viscoplastic fluid behavior is differentiated by the existence of yield stress τ_y, which must be applied for the fluid to deform or flow. Three commonly used mathematical models for viscoplastic fluids are Bingham, Herschel–Bulkley, and Casson model. In the present work, we characterize the rheological properties of viscoplastic fluid considering Bingham model. The constitutive equation for a Bingham model in three-dimensional form is as follows:

$$\begin{aligned} \bar{\bar{\tau}} &= \left[\mu + \frac{\tau_y}{|\dot{\gamma}|}\right] \bar{\bar{\dot{\gamma}}} \quad \text{for} \quad |\tau| > \tau_y, \\ \bar{\bar{\dot{\gamma}}} &= 0 \qquad\qquad\quad \text{for} \quad |\tau| \le \tau_y, \end{aligned}$$

where $\left|\dot{\gamma}\right| = \left[\frac{1}{2}\left(\bar{\bar{\dot{\gamma}}} : \bar{\bar{\dot{\gamma}}}\right)\right]^{\frac{1}{2}}$ is the magnitude of the symmetric rate-of-strain tensor $\bar{\bar{\dot{\gamma}}} = \nabla \bar{v} + (\nabla \bar{v})^T$.

Earlier some of the researchers (Turns 1983; Singh et al. 1990; Lin 1996; Usha and Vimala 2003) analyzed flow of Newtonian fluid in squeeze film between circular plane annuli. Some of the examiners (Archibald 1956; Shukla 1964; Elkouh et al. 1982; Lin and Hung 2008) considered the power law fluid model to observe the squeeze film performance in circular or annular disks with couple stress. Several investigators (Wilson 1993; Balmforth and Craster 1999; Alexandrou et al. 2001; Smyrnaios and Tsamopoulos 2001; Walicka 2011) examined the flow of viscoplastic Bingham fluid in squeeze film bearing in the presence of rigid plug core.

In the present work, the problem of squeezing Bingham fluid between two parallel plane annuli with constant squeeze has been analyzed. Viscoplastic is characterized by the existence of yield value, which leads to the formation of rigid plug core in the flow region (Vishwanath and Kandasamy 2010). The effects of radius of separation on core thickness, pressure distribution, and squeeze force have been investigated. By considering equilibrium of an element of the core in the fluid, the thickness of rigid plug core has been calculated numerically for various values of Bingham number. Expressions for core thickness, pressure distribution, and squeeze force are presented. Numerical solutions have been obtained for the characteristics of squeeze motion such as pressure distribution, squeeze force for different values of Bingham number, and annular space. The properties of the squeeze motion are investigated through the non-Newtonian effects of Bingham fluid on the squeeze force for various annuli.

2 Mathematical Formulation of the Problem

The schematics of the problem are as shown in Figs. 1 and 2. We consider an isothermal, incompressible, steady flow of a time-independent viscoplastic fluid squeezed between parallel plane annulus separated by a distance h^*. Let r_1^* and r_2^* be the two inner and outer radii of the plane annulus. The planes are approaching each other with a constant squeeze velocity v_s under a squeeze force w^*.

We consider cylindrical polar coordinates (r^*, θ^*, z^*) with axial symmetry and the origin fixed at the center of the lower plane. Here r^* represents the distance measured along the radial direction and z^* along the axis normal to the parallel plane. Let v_r^* and v_z^* be the velocity components in the radial (r^*) and axial directions (z^*), respectively. Let p^* denote the pressure which is a function of r^* only and p_a^* is the ambient pressure. It is assumed that there is no sliding motion of the two planes. Let the boundaries of the core be given by $z = h_1^*(r^*)$ and $z = h_2^*(r^*)$ as shown in Fig. 3.

Under the assumptions of the theory of lubrication, neglecting inertia terms, one gets the following governing equations in non-dimensional form for the flow system as shown in Fig. 1:

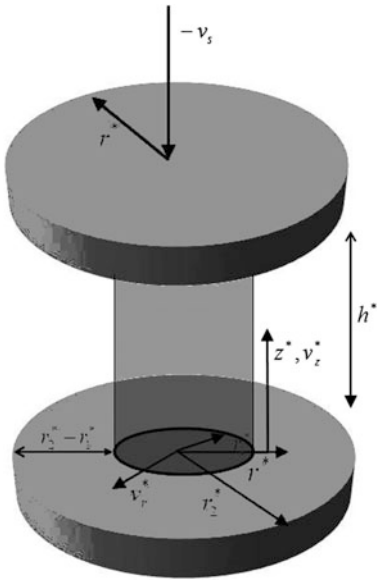

Fig. 1 Schematic representation of annular squeeze film

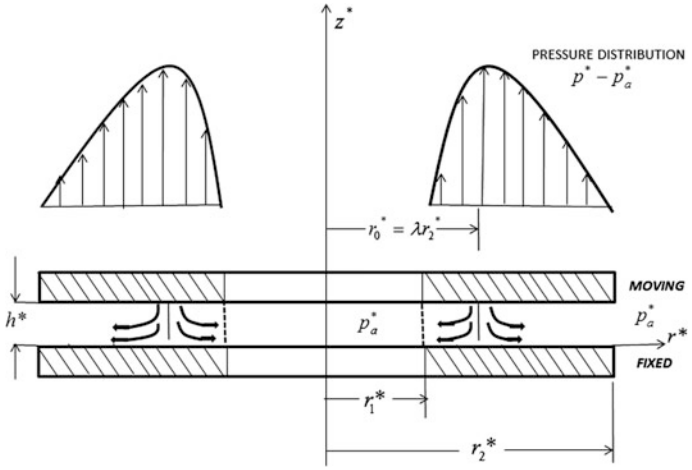

Fig. 2 Schematic representation of pressure distribution

$$0 = -\frac{\partial p}{\partial r} + \frac{\partial \tau_{rz}}{\partial z} \tag{1}$$

$$0 = \frac{\partial p}{\partial z} \tag{2}$$

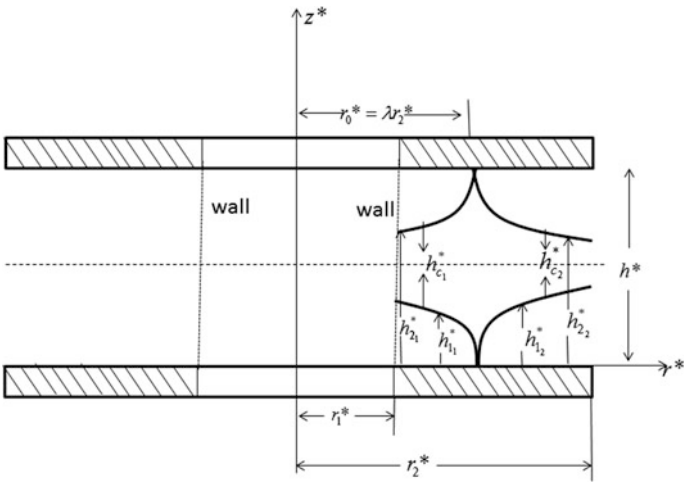

Fig. 3 Schematic representation of core thickness

$$0 = \frac{1}{r}\frac{\partial}{\partial r}(rv_{\mathrm{r}}) + \frac{\partial v_{\mathrm{z}}}{\partial z} \tag{3}$$

where τ_{rz} is the shear stress, $\frac{\partial p}{\partial r}$ is the pressure gradient.

The non-dimensional form of constitutive equation for Bingham fluid is given by

$$\tau_{rz} = B + \frac{\partial v_{\mathrm{r}}}{\partial z} \tag{4}$$

where $\frac{\partial v_{\mathrm{r}}}{\partial z}$ is the rate of deformation and $B = \frac{\tau_0 (h^*)^2}{\mu v_{\mathrm{s}} r_2^*}$ is the Bingham number.

The boundary conditions are

$$\begin{aligned} &v_{\mathrm{r}}(r,0) = v_{\mathrm{r}}(r,1) = 0, \\ &v_{\mathrm{z}}(r,0) = 0, \\ &v_{\mathrm{z}}(r,1) = -v_{\mathrm{s}}, \end{aligned}$$

and

$$p(k) = p(1) = p_{\mathrm{a}} = 1,$$

where $k = r_1^*/r_2^*$, $H = h^*/h^* = 1$.

3 Solution to the Problem

The distribution of the radial component of velocity obtained by integrating Eq. (1), using boundary conditions on v_r and assuming v_r and $\frac{\partial v_r}{\partial z}$ are continuous at $z = H_1$ and $z = H_2$, is given by

$$v_r = \frac{1}{2}\frac{\partial p}{\partial r}\left((z - H_1)^2 - H_1^2\right) \quad \text{in} \quad 0 \le z \le H_1 \tag{5}$$

$$v_r = \frac{1}{2}\frac{\partial p}{\partial r}\left((z - H_2)^2 - (1 - H_2)^2\right) \quad \text{in} \quad H_2 \le z \le 1 \tag{6}$$

and the core velocity as,

$$v_c = \frac{1}{2}\frac{\partial p}{\partial r}\left(-H_1^2\right) = \frac{1}{2}\frac{\partial p}{\partial r}\left(-(1 - H_2)^2\right) \quad \text{in} \quad H_1 \le z \le H_2 \tag{7}$$

The integral form of continuity equation, obtained from Eq. (3) and applying the boundary conditions on v_z, is

$$(r^2 - \lambda^2) = 4\int_0^{1/2} r v_r \mathrm{d}z \tag{8}$$

where $\lambda = r_0^*/r_2^*$ is the radius of separation which is a function of k and B. In this study r_0^* represents the radius of a fixed cylindrical stream surface that divides the flow into two regions whose radial velocity components are of opposite signs.

Substituting v_r from Eqs. (5) and (7) in (8), by taking $H_1 = \frac{1-H_c}{2}$ from Fig. 3, yields the expressions for pressure gradient:

$$\frac{\partial p}{\partial r} = \frac{12\left(\frac{\lambda^2}{r} - r\right)}{(1 - H_{c_1})^2(2 + H_{c_1})} \quad \text{in} \quad k \le r \le \lambda \tag{9}$$

and

$$\frac{\partial p}{\partial r} = \frac{-12\left(r - \frac{\lambda^2}{r}\right)}{(1 - H_{c_2})^2(2 + H_{c_2})} \quad \text{in} \quad \lambda \le r \le 1 \tag{10}$$

The above equations show that the pressure gradient is continuous at $r = \lambda$ and the values are equal to zero.

Considering the equilibrium of an element of the core in the fluid, we get

$$\frac{\partial p}{\partial r} = \frac{2B}{H_{c_1}} \quad \text{in} \quad k \le r \le \lambda \tag{11}$$

and

$$\frac{\partial p}{\partial r} = -\frac{2B}{H_{c_2}} \quad \text{in} \quad \lambda \le r \le 1 \tag{12}$$

Eliminating $\frac{\partial p}{\partial r}$ from Eqs. (9) and (11), rearranging the equation, we get

$$H_{c_1}^3 - \left(\frac{6}{B}\left(\frac{\lambda^2}{r} - r\right) + 3\right)H_{c_1} + 2 = 0 \quad \text{in} \quad k \le r \le \lambda \tag{13}$$

Doing the same process for Eqs. (10) and (12), we get

$$H_{c_2}^3 - \left(\frac{6}{B}\left(r - \frac{\lambda^2}{r}\right) + 3\right)H_{c_2} + 2 = 0 \quad \text{in} \quad \lambda \le r \le 1 \tag{14}$$

The above two Eqs. (13) and (14) are called equations of core thickness, where $H_{c_1} = H_{c_1}(r, B)$ and $H_{c_{21}} = H_{c_2}(r, B)$ can be evaluated by using any numerical iterative technique.

Integrating Eqs. (9) and (10) with respect to r and applying the boundary conditions on p, we get the following expressions for pressure distribution:

$$p(r) - 1 = 12 \times \int_k^r \frac{\left(\frac{\lambda^2}{r} - r\right)}{(1 - H_{c_1})^2(2 + H_{c_1})} \mathrm{d}r \quad \text{in} \quad k \le r \le \lambda \tag{15}$$

and

$$p(r) - 1 = 12 \times \int_r^1 \frac{\left(r - \frac{\lambda^2}{r}\right)}{(1 - H_{c_2})^2(2 + H_{c_2})} \mathrm{d}r \quad \text{in} \quad \lambda \le r \le 1 \tag{16}$$

Since the pressure distribution is continuous at '$r = \lambda$', one can obtain the dimensionless radius of separation 'λ' using Eqs. (15) and (16).

$$\int_k^\lambda \frac{\left(\frac{\lambda^2}{r} - r\right)}{(1 - H_{c_1})^2(2 + H_{c_1})} \mathrm{d}r - \int_\lambda^1 \frac{\left(r - \frac{\lambda^2}{r}\right)}{(1 - H_{c_2})^2(2 + H_{c_2})} \mathrm{d}r = 0 \tag{17}$$

The root of above equation, 'λ', is only a function of k and B. Equation (17) has been solved numerically by using Newton–Raphson iterative technique and Simpson's rule of integration.

Substituting Eqs. (9) and (10) in Eqs. (5) and (7) respectively, we get
In $k \le r \le \lambda$, $0 \le z \le H_{1_1}$

$$v_r = \frac{6\left(\frac{\lambda^2}{r} - r\right)}{(1 - H_{c_1})^2(2 + H_{c_1})}\left(\left(z - \frac{1 - H_{c_1}}{2}\right)^2 - \left(\frac{1 - H_{c_1}}{2}\right)^2\right) \tag{18}$$

In $k \le r \le \lambda$, $H_{1_1} \le z \le H/2$

$$v_c = \frac{6\left(\frac{\lambda^2}{r} - r\right)}{(1 - H_{c_1})^2(2 + H_{c_1})}\left(-\left(\frac{1 - H_{c_1}}{2}\right)^2\right), \tag{19}$$

In $\lambda \le r \le 1, 0 \le z \le H_{1_2}$

$$v_r = \frac{-6\left(r - \frac{\lambda^2}{r}\right)}{(1 - H_{c_2})^2(2 + H_{c_2})}\left(\left(z - \frac{1 - H_{c_2}}{2}\right)^2 - \left(\frac{1 - H_{c_2}}{2}\right)^2\right) \tag{20}$$

In $\lambda \le r \le 1$, $H_{1_2} \le z \le H/2$

$$v_c = \frac{-6\left(r - \frac{\lambda^2}{r}\right)}{(1 - H_{c_2})^2(2 + H_{c_2})}\left(-\left(\frac{1 - H_{c_2}}{2}\right)^2\right) \tag{21}$$

where H_{1_1}, H_{1_2} are core heights in both regions. The above Eqs. (18)–(21) show that $v_r = 0$ at $r = \lambda$, the surface of separation.

The squeeze force is obtained by integrating the pressure difference over the area of the plane annulus, that is,

$$w = 2\pi \int_k^1 (p - 1) r \, dr \tag{22}$$

Substituting for $(p - 1)$ from Eqs. (15) and (16), we get

$$w = 24\pi\left[\int_k^\lambda r\left(\int_k^r \frac{\left(\frac{\lambda^2}{r} - r\right)}{(1 - H_{c_1})^2(2 + H_{c_1})} dr\right) dr + \int_\lambda^1 r\left(\int_r^1 \frac{\left(r - \frac{\lambda^2}{r}\right)}{(1 - H_{c_2})^2(2 + H_{c_2})} dr\right) dr\right]$$

One can find these squeeze force values by using any of the numerical techniques.

4 Results and Discussion

The core thickness for different values of inner wall radius (k) and Bingham number (B) have been computed, and the results are shown in Figs. 4 and 5. From these figures, we can observe that, firstly, core thickness for different values of Bingham number increases from the inner wall to the point of separation and further decreases along the radius to the periphery. The rate of change of core thickness for different values of Bingham number decreases along the radius from the wall to the point of separation and further again increases up to the periphery with increase in inner wall radius. Hence, the core thickness in general for fluids with higher Bingham numbers is more than the fluids with lower Bingham numbers. Further, core thickness increases with the increase in the inner wall radius and the point of separation shifts slightly toward the periphery.

The pressure distribution for different values of inner wall radius (k) and Bingham number have been computed, and the results are depicted in Figs. 6 and 7. From these figures, we can observe that pressure distribution for different values of

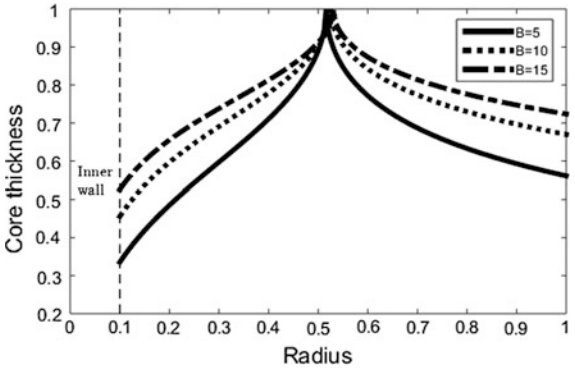

Fig. 4 Core thickness distribution for inner radius $k = 0.1$

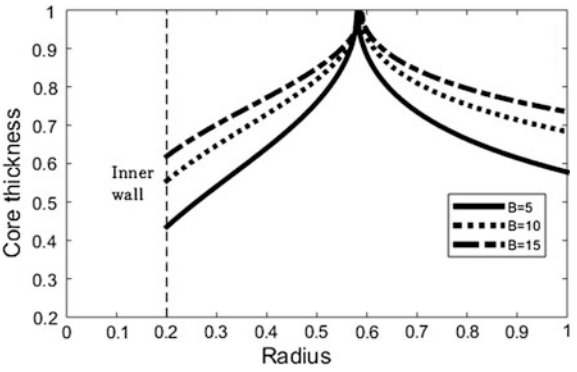

Fig. 5 Core thickness distribution for inner radius $k = 0.2$

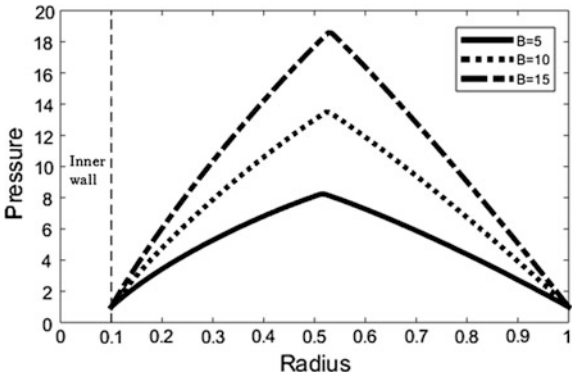

Fig. 6 Pressure distribution for inner radius $k = 0.1$

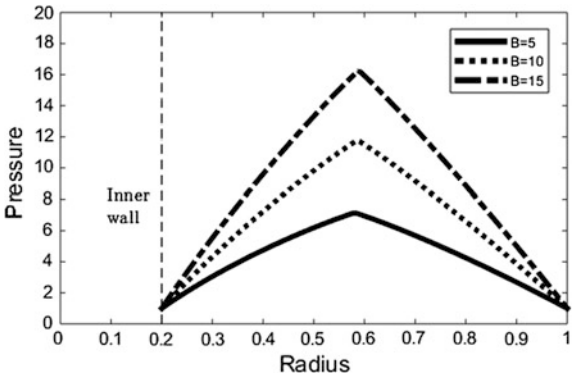

Fig. 7 Pressure distribution for inner radius $k = 0.2$

Bingham number increases from the inner wall to the point of separation and further decreases along the radius to the periphery.

Further, the rate of change of pressure distribution for different values of Bingham number increases along the radius from the wall to the point of separation and further again decreases up to the periphery with increase in inner wall radius. Further, pressure distribution decreases with the increase in the inner wall radius.

The squeeze force distribution for different values of inner wall radius (k) and Bingham number have been calculated, and values are shown in Table 1. Further, squeeze force decreases with the increase in the inner wall radius. It can be noticed that the rate of change of the squeeze force of different values of Bingham number increases with increase in inner wall radius. Hence, the squeeze force in general for fluids with higher Bingham numbers is more than the fluids with lower Bingham numbers.

Table 1 Squeeze force values for B and k

Bingham number (B)	Inner radius (k)		
	$k = 0.1$	$k = 0.2$	$k = 0.3$
$B = 0$	2.699307	2.001127	1.429114
$B = 5$	12.092450	9.948654	7.929672
$B = 10$	20.495248	17.093872	13.789590
$B = 15$	28.593208	23.996830	19.461669

5 Conclusion

The shape of the rigid core formation along the radial direction is determined numerically for various values of Bingham number and inner wall radius. It is found that core thickness reaches maximum value at the point of separation. Pressure distribution for different values of Bingham number and inner wall radius has been calculated. It is observed that pressure increases along the radius from the wall to the radius of separation and further again decreases up to the periphery. It is noticed that core thickness and pressure distribution are not symmetric about radius of separation. The rate of change of the squeeze force for different values of Bingham number increases with increase in inner wall radius. Further, squeeze force increases with increase in Bingham number.

References

Alexandrou N, Duc E, Entov V (2001) Inertial viscous and yield stress effects in Bingham fluid filling of a 2-d cavity. J Non-Newton Fluid Mech 96:383–403

Archibald FR (1956) Load capacity and time relations for squeeze films. Trans ASME 78:29–35

Balmforth NJ, Craster RV (1999) A consistent thin-layer theory for Bingham plastics. J Nonnewton Fluid Mech 84:65–81

Elkouh AF, Nigro NJ, Liou YS (1982) Non-newtonian squeeze film between two plane annuli. J Tribol 104:275–278

Lin JR (1996) Viscous shear effects on the squeeze-film behavior in porous circular disks. Int J Mech Sci 38:373–384

Lin JR, Hung CR (2008) Combined effects of non-Newtonian rheology and rotational inertia on the squeeze film characteristics of parallel circular discs. Proc Inst Mech Eng J Eng Tribol 222:629–636

Shukla JB (1964) Theory for the squeeze film for power law fluid lubricants. ASME 64:1–4

Singh P, Radhakrishnan V, Narayan KA (1990) Squeezing flow between parallel plates. Ingenieur-Archiv 60:274–281

Smyrnaios DN, Tsamopoulos JA (2001) Squeeze flow of Bingham plastics. J Non-Newton Fluid Mech 100:165–189

Turns SR (1983) Annular squeeze films with inertial effects. J Tribol 105:361–363

Usha R, Vimala P (2003) Squeeze film force using an elliptical velocity profile. J Appl Mech 70:137–142

Vishwanath KP, Kandasamy A (2010) Inertia effects in circular squeeze film bearing using Herschel-Bulkley lubricants. Appl Math Model 34:219–227
Walicka A (2011) Pressure distribution in a porous curvilinear squeeze film bearing lubricated by a Bingham fluid. Int J Appl Mech Eng 16:1215–1224
Wilson SDR (1993) Squeezing flow of a Bingham material. J Nonnewton Fluid Mech 47:211–219

Capturing the Transient Behaviour of MHD Double-Diffusive Free Convection in Vertical Channel with Adiabatic and Isothermal Walls and Mass Inflow at Adiabatic Wall

G.S. Seth, S. Sarkar and A.K. Singha

Abstract An investigation has been undertaken to capture the transient behaviour of MHD heat and mass transfer double-diffusive free convection flow of a viscous, incompressible and electrically conducting fluid in vertical channel with adiabatic and isothermal walls amid mass inflow at the adiabatic wall. Semi-analytical solutions to the governing equations representing the flow are found by first applying Laplace transformation and then inverting by INVLAP routine of MATLAB. The numerical solution for fluid temperature, species concentration, fluid velocity, Nusselt number, Sherwood number and skin friction are represented by figures for a range of pertinent flow parameters. Behavioural changes on the flow profiles occurring due to change in physical entities during transition from unsteady to steady state are captured and discussed. Formation of boundary layers near the channel walls for small values of time and their transition into main flow due to large values of time are depicted.

1 Introduction

Study of hydrodynamic free convection flows within a vertical channel has drawn attention of several researchers for the duration of past few decades due to its diversified applications in natural phenomena and in a number of industrial

G.S. Seth · A.K. Singha
Department of Applied Mathematics, Indian Institute of Technology (Indian School of Mines) Dhanbad, Dhanbad 826004, Jharkhand, India
e-mail: gsseth_ism@yahoo.com

A.K. Singha
e-mail: adityakumarsingha@gmail.com

S. Sarkar (✉)
Department of Mathematics, School of Applied Sciences, KIIT University, Bhubaneshwar 751024, India
e-mail: sarkar.ism@gmail.com

M.K. Singh et al. (eds.), *Applications of Fluid Dynamics*, Lecture Notes in Mechanical Engineering, https://doi.org/10.1007/978-981-10-5329-0_29

processes such as cross-hatching on ablative surfaces, transpiration, heat pipes in thermal conduction of spacecrafts and rocket boosters, film vaporization in incineration chambers, etc. Due to its wide applications, numerous investigations have been done towards the understanding of hydrodynamic flows in a vertical channel. One of the earliest studies on hydrodynamic convective flow was reported by Tao (1960). Aung and Worku (1985) presented a numerical study dealing with mixed convection in a vertical channel through asymmetric wall heating with uniform heat flux. Hamadah and Wirtz (1991) studied the laminar fully developed mixed convective flow in a vertical channel where direction of buoyancy force is opposite to that of main flow. Guria and Jana (2006) analyzed two-dimensional mixed convective flow and heat transfer in a vertical curly channel subjected to passing heat waves. Lin et al. (2009) simulated the flow of fluids inside a vertical microchannel. Recently, Adesanya (2015) investigated the unsteady natural convection flow of heat breeding fluid through a porous vertical channel with temperature jump and velocity slip.

Investigation of magnetohydrodynamic (MHD) flow of an electrically conducting fluid within a channel is of massive curiosity because it has innumerable practical applications in astrophysical and geophysical fluid dynamics, plasma aerodynamics, nuclear engineering, MHD power generator and manufacturing process in industry. Motivated by such applications, Bathaiah (1980) analyzed the unsteady two-dimensional flow through a straight channel with porous flat walls under uniform transverse magnetic field. Hernandez and Zamora (2005) discussed different aspects of laminar air flow induced by free convection in a vertical channel under non-uniform heating. Umavathi and Malashetty (2005) investigated MHD mixed convection in a vertical channel using perturbation technique and considering Ohmic and viscous dissipations. Barletta and Celli (2008) studied forced and free convective flow in a vertical channel with isothermal and adiabatic walls. Seth and Ansari (2009) studied the effects of Hall current and rotation on magnetohydrodynamic convective flow in a channel. Seth et al. (2010) examined unsteady MHD convection flow within two parallel plates rotating about a vertical axis including heat source/sink, porous medium and slip boundary conditions. Srinivas and Muthuraj (2010) analyzed MHD mixed convection radiative flow in a vertical channel implanted in a porous medium using HAM. Das et al. (2015) studied mixed convective MHD nanofluid flow in a vertical channel. Seth et al. (2016) investigated the effects of Hall current and rotation on unsteady magnetohydrodynamic convective flow of a heat absorbing fluid embedded in a fluid-saturated porous medium. Seth et al. (2016) also investigated joint forced and free convection Couette–Hartmann flow inside a rotating channel incorporating Hall effects and finitely conducting walls.

The goal of the present work is directed to study the transient behaviour of hydromagnetic double-diffusive free convection flow of a viscous, incompressible and electrically conducting fluid in a vertical channel with adiabatic and isothermal walls, taking mass inflow at adiabatic wall into account. The main feature of this research is to capture the time-bound effects of different essential parameters on boundary layer formation, fluid flow, heat transfer and mass transfer.

2 Problem Formulation and Its Solution

Consider transient hydromagnetic free convection flow with heat and mass transfer of an electrically conducting, viscous and incompressible fluid within an infinite vertical channel of width L. Coordinate system is opted in such a way that x'-axis is directed upward along the walls and y'-axis at right angles to plane of the walls in the fluid. Externally, an uniform transverse magnetic field B_0 (parallel to y'-axis) is applied across the walls. Initially, i.e. at time $t' \leq 0$, fluid is at rest and the walls of the channel are maintained at uniform temperature T'_0 and uniform species concentration C'_0. When $t' > 0$, the temperature of the wall at $y' = L$ is raised to uniform temperature T'_w and maintained thereafter (isothermal), whereas no heat is allowed to escape to surrounding at the wall $y' = 0$, i.e. $\frac{\partial T'}{\partial y'} = 0$ (adiabatic). Also, at time $t' > 0$, there is uniform mass inflow at the adiabatic wall $y' = 0$ which increases species concentration at the surface of the wall $y' = 0$ to regular species concentration C'_w and is maintained subsequently while the species concentration at the surface of the wall $y' = L$ is maintained at C'_0. A schematic diagram of the problem is illustrated in Fig. 1.

Taking into consideration all the aforementioned suppositions, the governing equations for transient hydromagnetic free convection double-diffusive flow of an electrically conducting, viscous and incompressible fluid are given by

$$\frac{\partial u'}{\partial t'} = \nu \frac{\partial^2 u'}{\partial y'^2} - \frac{\sigma B_0^2}{\rho} u' + g\beta_1 \left(T' - T'_0\right) + g\beta_2 \left(C' - C'_0\right), \tag{1}$$

$$\rho c_p \frac{\partial T'}{\partial t'} = k \frac{\partial^2 T'}{\partial y'^2}, \tag{2}$$

$$\frac{\partial C'}{\partial t'} = D \frac{\partial^2 C'}{\partial y'^2}, \tag{3}$$

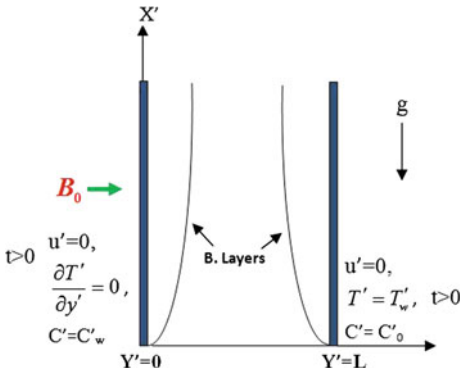

Fig. 1 Geometry of the problem

where $u', T', C', c_p, D, g, k, \beta_1, \beta_2, v, \rho$ and σ are, respectively, fluid velocity in x'-direction, fluid temperature, species concentration, specific heat at constant pressure, chemical molecular diffusivity, acceleration due to gravity, thermal conductivity of the fluid, volumetric coefficient of thermal expansion, volumetric coefficient of expansion for species concentration, kinematic coefficient of viscosity, fluid density and electrical conductivity.

Initial and boundary conditions for the problem describing the fluid flow are delineated underneath

$$u' = 0, \quad T' = T'_0, \quad C' = C'_0 \text{ for } 0 \le y' \le L \text{ and } t' \le 0, \tag{4a}$$

$$u' = 0, \quad \frac{\partial T'}{\partial y'} = 0, \quad C' = C'_w \text{ at } y' = 0 \text{ and } t' > 0, \tag{4b}$$

$$u' = 0, \quad T' = T'_w, \quad C' = C'_0 \text{ at } y' = L \text{ and } t' > 0, \tag{4c}$$

Equations (1)–(3), in non-dimensional form, could be outlined as

$$\frac{\partial u}{\partial t} = \frac{\partial^2 u}{\partial \eta^2} - M^2 u + Gr\, T + Gc\, C, \tag{5}$$

$$\frac{\partial T}{\partial t} = \frac{1}{Pr}\frac{\partial^2 T}{\partial \eta^2}, \tag{6}$$

$$\frac{\partial C}{\partial t} = \frac{1}{S_c}\frac{\partial^2 C}{\partial \eta^2}, \tag{7}$$

where

$$\eta = y'/L, \quad u = u'L/v, \quad t = t'v/L^2, \quad T = \left(T' - T'_0\right)/\left(T'_w - T'_0\right), \quad C = \left(C' - C'_0\right)/\left(C'_w - C'_0\right),$$
$$Gr = g\beta_1 L^3\left(T'_w - T'_0\right)/v^2, \quad Gc = g\beta_2 L^3\left(C'_w - C'_0\right)/v^2, \quad M^2 = \sigma B_0^2 L^2/\rho v$$

where M^2, Gr, Gc, Pr and Sc are, respectively, magnetic parameter, thermal Grashof number, solutal Grashof number, Prandtl number and Schmidt number.

Initial and boundary conditions (4a)–(4c), in dimensionless form, could be scripted as

$$u = 0, \quad T = 0, \quad C = 0 \text{ for } 0 \le \eta \le 1 \text{ and } t \le 0, \tag{8a}$$

$$u = 0, \quad \frac{\partial T}{\partial \eta} = 0, \quad C = 1 \text{ at } \eta = 0 \text{ and } t > 0, \tag{8b}$$

$$u = 0, \quad T = 1, \quad C = 0 \text{ at } \eta = 1 \text{ and } t > 0, \tag{8c}$$

Equations (5)–(7), after taking Laplace transform and using initial conditions (8a), become

$$\frac{\mathrm{d}^2\bar{u}}{\mathrm{d}\eta^2} - \left(s + M^2\right)\bar{u} + Gr\,\overline{T} + Gc\,\overline{C} = 0, \tag{9}$$

$$\frac{\mathrm{d}^2\overline{T}}{\mathrm{d}\eta^2} - Pr\,s\overline{T} = 0, \tag{10}$$

$$\frac{\mathrm{d}^2\bar{C}}{\mathrm{d}\eta^2} - Sc\,s\,\bar{C} = 0, \tag{11}$$

where $\bar{u}(\eta, s) = \int_0^\infty u(\eta, t)\mathrm{e}^{-st}\mathrm{d}t$, $\overline{T}(\eta, s) = \int_0^\infty T(\eta, t)\mathrm{e}^{-st}\mathrm{d}t$, $\overline{C}(\eta, s) = \int_0^\infty C(\eta, t)\mathrm{e}^{-st}\mathrm{d}t$ and $s > 0$ (s being Laplace transform parameter).

Boundary conditions (8b) and (8c), upon the application of Laplace transformation, take the following shape

$$\bar{u} = 0, \quad \frac{\partial\overline{T}}{\partial\eta} = 0, \quad \overline{C} = 1/s \ \text{ at } \ \eta = 0 \tag{12a}$$

$$\bar{u} = 0, \quad \overline{T} = 1/s, \quad \overline{C} = 0 \ \text{ at } \ \eta = 1 \tag{12b}$$

Solution of Eqs. (9)–(11) put through the boundary conditions (12a) and (12b) is given by

$$\bar{u}(\eta, s) = \bar{u}_1(\eta, s) + \bar{u}_2(\eta, s) + \bar{u}_3(\eta, s), \tag{13}$$

$$\overline{T}(\eta, s) = \frac{\cosh\left(\sqrt{s\,Pr}(\eta)\right)}{s\cosh\left(\sqrt{s\,Pr}\right)}, \tag{14}$$

$$\overline{C}(\eta, s) = \frac{\sinh\left(\sqrt{s\,Sc}(1-\eta)\right)}{s\,\sinh\left(\sqrt{s\,Sc}\right)}, \tag{15}$$

where

$$\bar{u}_1(\eta, s) = -G_1\sinh\left(\sqrt{s+M^2}(1-\eta)\right)/\left(\cosh\left(\sqrt{Pr\,s}\right)\sinh\left(\sqrt{s+M^2}\right)\right),$$
$$\bar{u}_2(\eta, s) = -G_1\sinh\left(\sqrt{s+M^2}(\eta)\right)/\sinh\left(\sqrt{s+M^2}\right) + G_1\cosh\left(\sqrt{s\,Pr}(\eta)\right)/\cosh\left(\sqrt{s\,Pr}\right),$$
$$\bar{u}_3(\eta, s) = -G_2\sinh\left(\sqrt{s+M^2}(1-\eta)\right)/\sinh\left(\sqrt{s+M^2}\right) + G_2\sinh\left(\sqrt{s\,Sc}(1-\eta)\right)/\sinh\left(\sqrt{s\,Sc}\right),$$

$$G_1 = \frac{Gr}{s(s(1-Pr)+M^2)}, \quad G_2 = \frac{Gc}{s(s(1-Sc)+M^2)}$$

The Laplace inverse of solutions (13)–(15) cannot be obtained analytically in terms of known elementary functions. Therefore, we have resorted to the most popular tool for evaluating the inverse of Laplace transformation—the INVLAP subroutine of MATLAB to find the inverse Laplace of solutions (13)–(15) numerically. Now, skin friction (τ) and rate of heat transfer (Nu) and rate of mass transfer (Sh) are given by:

$$\tau_0 = \left.\frac{\partial u}{\partial \eta}\right|_{\eta=0}, \quad \tau_1 = \left.\frac{\partial u}{\partial \eta}\right|_{\eta=1}, \tag{16}$$

$$Nu = Nu_1 = \left.\frac{\partial T}{\partial \eta}\right|_{\eta=1} \quad \text{and} \quad Nu_0 = 0, \quad (\text{Since wall } \eta = 0 \text{ is a diabatic}) \tag{17}$$

$$Sh_0 = \left.\frac{\partial C}{\partial \eta}\right|_{\eta=0}, \quad Sh_1 = \left.\frac{\partial C}{\partial \eta}\right|_{\eta=1} \tag{18}$$

In order to find τ_0, τ_1, Nu, Sh_0 and Sh_1, the solutions (13)–(15) are first differentiated analytically w.r.t. η and then inverted using INVLAP.

3 Discussion of Results

With the purpose of examining behavioural changes on the flow profiles occurring due to change in physical entities during unsteady state to steady state transition, numerical values of fluid velocity u, fluid temperature T, species concentration C, rate of mass transfer (Sh), rate of heat transfer (Nu) and skin friction (τ) are computed using INVLAP subroutine of MATLAB and are illustrated in Figs. 2, 3, 4, 5,

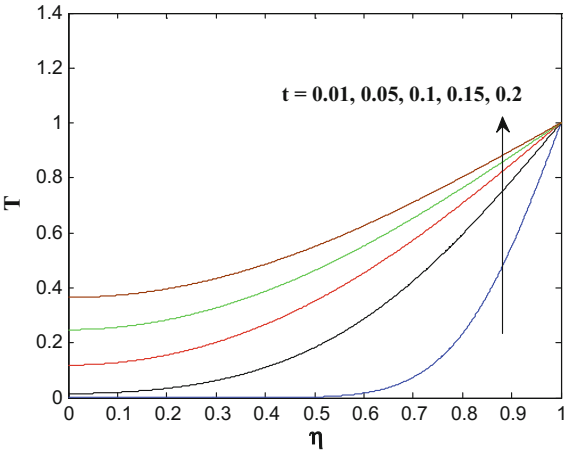

Fig. 2 Temperature profiles when $Pr = 0.71$

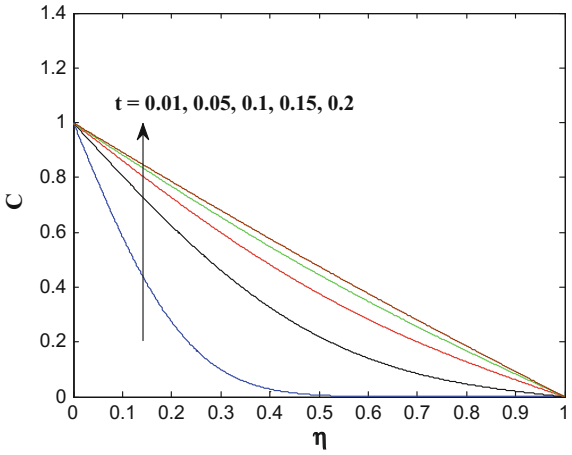

Fig. 3 Concentration profiles when $Sc = 0.6$

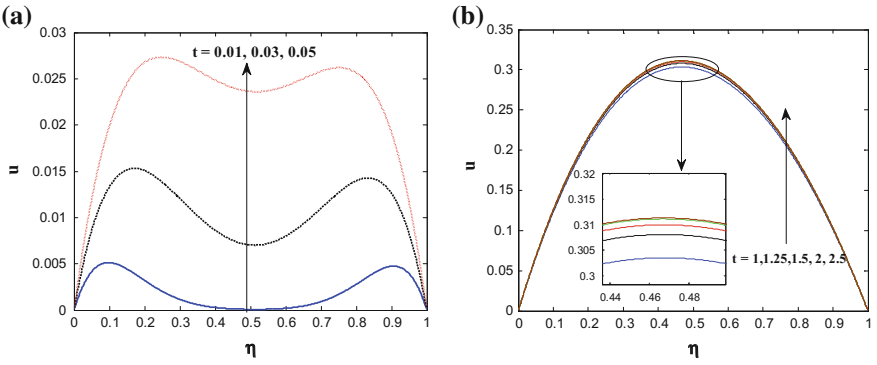

Fig. 4 Velocity profiles when $Gr = 2$, $Gc = 2$, $M^2 = 4$, $Pr = 0.71$, $Sc = 0.6$, **a** velocity profiles for small time, **b** velocity profiles for large time

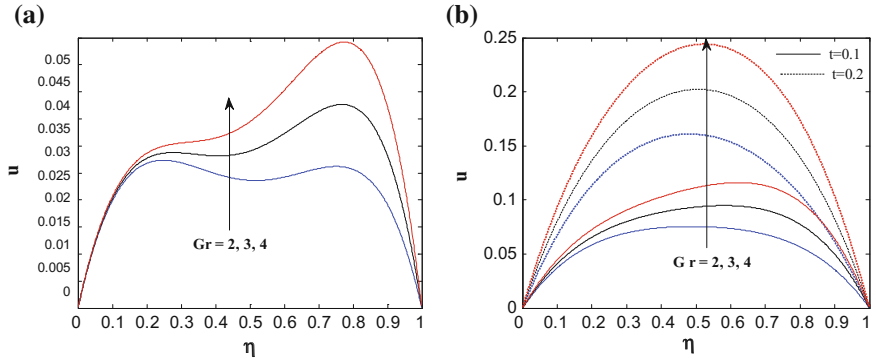

Fig. 5 Velocity profiles when $Gc = 2$, $M^2 = 4$, $Pr = 0.71$, $Sc = 0.6$, **a** velocity profiles when $t = 0.05$, **b** velocity profiles when $t = 0.1, 0.2$

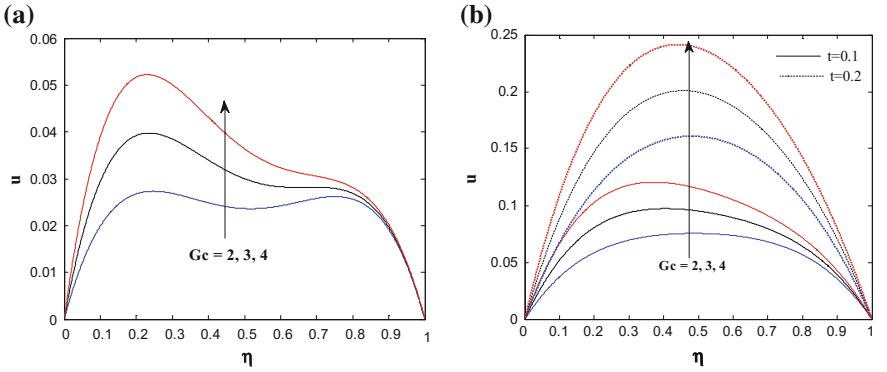

Fig. 6 Velocity profiles when $Gr = 2$, $M^2 = 4$, $Pr = 0.71$, $Sc = 0.6$, **a** velocity profiles when $t = 0.05$, **b** velocity profiles when $t = 0.1, 0.2$

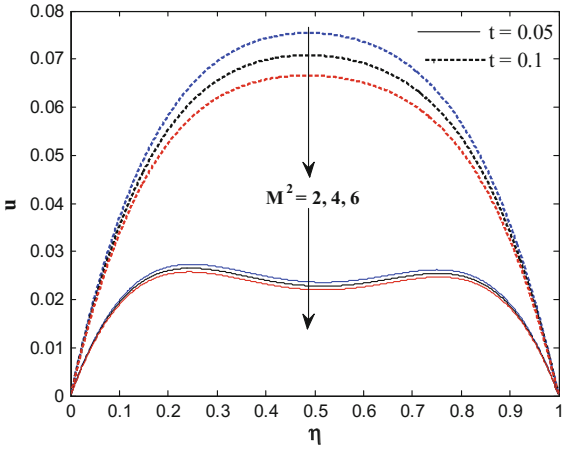

Fig. 7 Velocity profiles when $Gr = 2$, $Gc = 2$, $Pr = 0.71$, $Sc = 0.6$

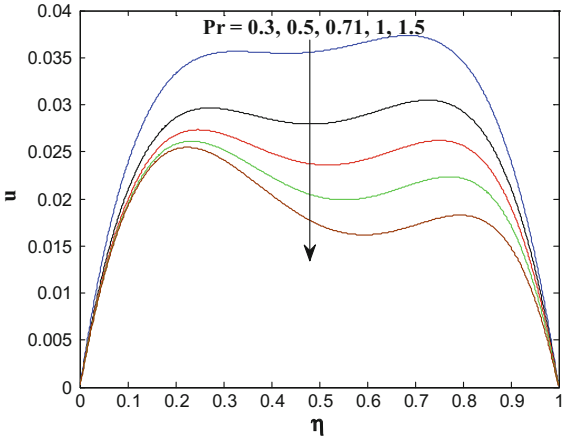

Fig. 8 Velocity profiles when $Gr = 2$, $Gc = 2$, $M^2 = 4$, $Sc = 0.6$, $t = 0.05$

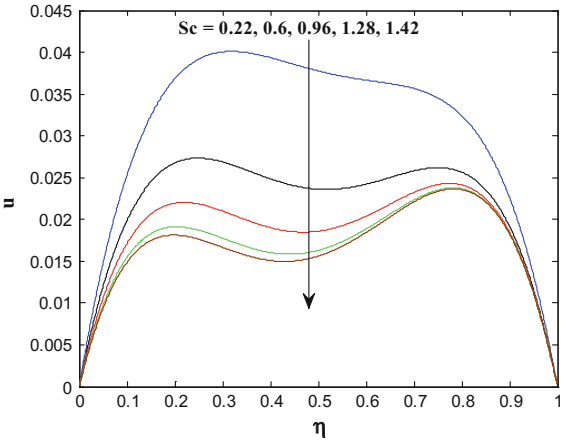

Fig. 9 Velocity profiles when $Gr = 2$, $Gc = 2$, $M^2 = 4$, $Pr = 0.71$, $t = 0.05$

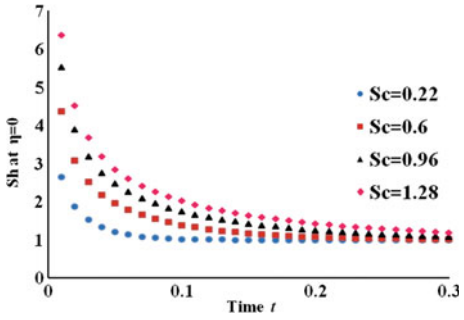

Fig. 10 Rate of mass transfer (Sh) versus time (t) at $\eta = 0$

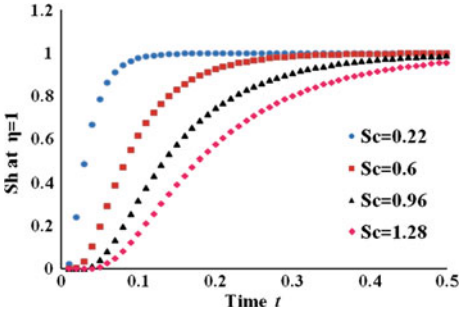

Fig. 11 Rate of mass transfer (Sh) versus time (t) at $\eta = 1$

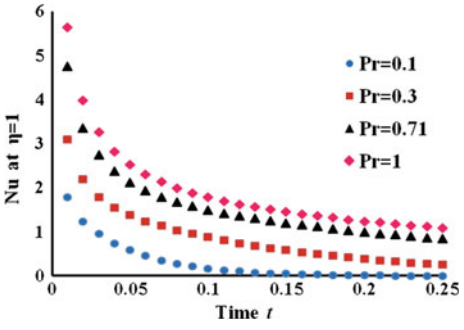

Fig. 12 Rate of heat transfer (Nu) versus time (t) at $\eta = 1$

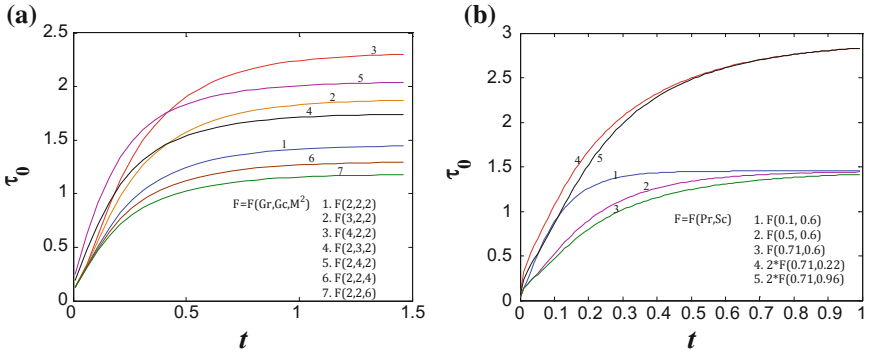

Fig. 13 Skin friction at $\eta = 0$, **a** skin friction at $\eta = 0$ when $Pr = 0.71$, $Sc = 0.6$, **b** skin friction at $\eta = 0$ when $Gr = 2$, $Gc = 2$, $M^2 = 4$

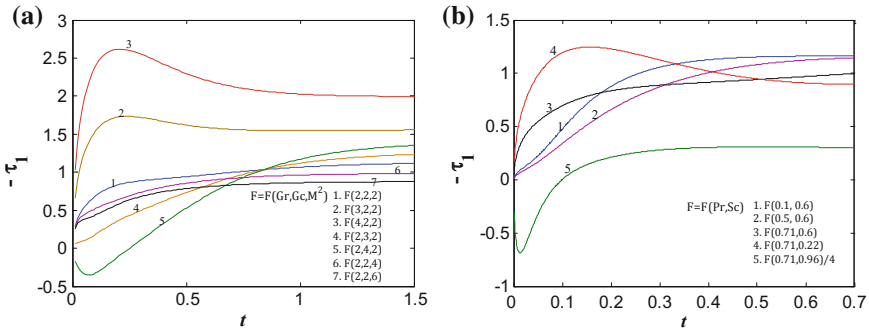

Fig. 14 Skin friction at $\eta = 1$, **a** skin friction at $\eta = 1$ when $Pr = 0.71$, $Sc = 0.6$, **b** skin friction at $\eta = 1$ when $Gr = 2$, $Gc = 2$, $M^2 = 4$

6, 7, 8, 9, 10, 11, 12, 13 and 14 for a supposed range of values of pertinent flow parameters.

Indeed, Figs. 2, 3 and 4 offer a luminous sight into the formation of thermal, solutal and hydrodynamic boundary layers near the channel walls for small values of time. It is evident from Fig. 2 that as t increases, T increases throughout the channel. It is also perceived that temperature profiles show a gradual rise in temperature with time near the adiabatic wall ($\eta = 0$) while it falls uniformly from its maximum value at the isothermal wall ($\eta = 1$). It is noted from Fig. 3 that C increases as t increases. Due to uniform species inflow at $\eta = 0$ for $t > 0$, species concentration is maximum at $\eta = 0$ and it uniformly decreases to its minimum value at $\eta = 1$. The steepness of concentration profiles from $\eta = 0$ to $\eta = 1$ decreases with the increase in time.

Figure 4a, b depicts velocity profiles for small values and large values of time t correspondingly. It is perceived from Fig. 4a that as t increases there is a sharp rise

in u near the walls of the channel which induces a gradual rise in u in rest of the region of the channel. This is due to the fact that adiabatic and isothermal wall conditions at $\eta = 0$ and $\eta = 1$ cause a rise in temperature at the walls, and there is a rise in species concentration due to species inflow at $\eta = 0$. This pilots a significant thrust in fluid velocity as time progresses. The rise in fluid velocity happens gradually which leads to the formation of beautiful hydrodynamic boundary layers near the walls of the channel for small values of time t which then continuously transfer their velocity gradients to the rest of the channel and finally merge to form the main flow (Fig. 4b). Figure 4a, b candidly explains the phenomena of the transition of boundary layer flow to main flow, where it is perceived from Fig. 4b that fluid velocity has reached steady state where there is negligible increase in fluid velocity for increase in time and flow within the channel is symmetric and in equilibrium.

Figure 5a, b illustrates the effect of thermal buoyancy force on fluid velocity for small and large values of time. Perceivably, u increases on increasing Gr throughout the channel as fluid flow is assisted by the thermal buoyancy force. However, for small values of time t, higher velocity peaks are observed near the isothermal wall ($\eta = 1$) (when $Gr > 2$) since temperature rises gradually at the adiabatic wall ($\eta = 0$). This leads to the formation of boundary layers near the walls of the channel for small values of time. Moreover, at $Gr = 2$ (and $Gc = 2$ fixed) the thermal and solutal diffusions are of equal strength so comparable velocity peaks at both walls $\eta = 0$ and $\eta = 1$ are expected but adiabatic wall condition at $\eta = 0$ gives impetus to fluid velocity near $\eta = 0$, so a higher velocity peak is observed. As time increases (see Fig. 5b), the effect of thermal buoyancy force becomes uniform throughout the channel and velocity peaks which were titled towards isothermal wall gradually tend to assume a uniform peak when approaching steady state.

Figure 6a, b demonstrates the consequences of solutal buoyancy force on fluid velocity for small and large values of time. It is noticed that u increases on increasing Gc throughout the channel as fluid flow is assisted by the solutal buoyancy force. However, for small values of time t, higher velocity peaks are observed near the adiabatic wall ($\eta = 0$) (when $Gc > 2$) due to uniform species inflow and boundary layers are noted. As time increases (see Fig. 6b), velocity peaks which were titled towards adiabatic wall gradually tend to assume a uniform peak in order to approach steady state. This feature is comparable with the earlier result as effect of solutal buoyancy force like thermal buoyancy force becomes uniform throughout the channel along with the passing of time.

Figure 7 describes the effect of magnetic field on fluid velocity for small and large values of time. It is evident that u decreases on increasing M^2 throughout the channel. Therefore, it is implicative that magnetic field tends to reduce fluid velocity throughout the channel which is due to the action of Lorentz force. It is also seen that velocity profiles are flattened in the most of the region of the channel for higher values of magnetic field which supports the popular notion that magnetic field helps in controlling undulations in boundary layer flow by making the fluid flow laminar.

Figures 8 and 9 portray the effects of thermal and solutal diffusions on fluid velocity for small time. It is apparent that u decreases throughout the channel on increasing Pr and Sc, respectively. Pr is the quotient of the viscosity to thermal diffusivity, and Sc is the quotient of viscosity to solutal (molecular) diffusivity. This implies that thermal and solutal diffusions step up fluid velocity throughout the channel. Figures 10 and 11 present the rate of mass transfer (Sh) at the adiabatic ($\eta = 0$) and isothermal ($\eta = 1$) walls of the channel w.r.t. time t for various values of Sc. It is perceived from Fig. 10 that for small values of time t, Sh is lower for lower values of Sc at $\eta = 0$, but it is seen from Fig. 11 that Sh is elevated for lower values of Sc at $\eta = 1$. However, for large values of time t, Sh at both the walls reaches steady state earlier for lesser values of Sc than for greater values of Sc. This observation is in concurrence with the fact that fluids with higher solutal diffusivity (low Sc) will transfer mass more rapidly than fluids with lower solutal diffusivity (higher Sc).

Figure 12 presents the rate of heat transfer (Nu) at the isothermal wall ($\eta = 1$) w.r.t. time t for different values of Pr. It is observed from Fig. 12 that for small values of time t, Nu is higher for higher values of Pr. It is also illustrious that for higher values of time t, Nu for lower values of Pr, tends to zero earlier than that for higher values of Pr. This observation is in concurrence with the fact that fluids with higher thermal diffusivity (low Pr) will loose (transfer) heat at a greater rate than fluids with lower thermal diffusivity (higher Pr).

Figures 13 and 14 present skin friction at the adiabatic ($\eta = 0$) and isothermal ($\eta = 1$) walls with respect to time t for a given choice of pertinent flow parametric vales. It is evident from Figs. 13a to 14b that τ_0 and τ_1 increase in magnitude as Gr and Gc increase, whereas it decreases in magnitude as M^2, Pr and Sc increase. This implies that thermal and solutal buoyancy force and thermal and solutal diffusivities enrich skin friction, whereas magnetic field decreases it. Such kind of an outcome could be easily deciphered by the fact that buoyancy forces be it thermal or solutal and diffusivities related to thermal and mass are albeit excellent boosters for fluid velocity. The more the velocity, the more is the friction with the walls and, therefore, skin friction is more. For a higher magnetic field, the value of skin friction reaches steady state at a faster rate which is in concurrence with the fact that magnetic field resists the flow by virtue of Lorentz force.

4 Conclusions

Transient behaviour of MHD heat and mass transfer double-diffusive free convection flow of a viscous, incompressible and electrically conducting fluid in vertical channel with adiabatic and isothermal walls amid mass inflow at the adiabatic wall is captured. A marvellous insight into the formation of thermal, solutal and hydrodynamic boundary layers near the channel walls for small values of time is provided through figures, and their behavioural changes with respect to pertinent flow parameters is recorded. The rise in fluid velocity happens gradually which leads to the formation of beautiful hydrodynamic boundary layers near the walls of

the channel for small values of time t which then continuously transfer their velocity gradients to the rest of the channel and finally merge to form the main flow. Thermal and solutal buoyancy forces and thermal and solutal diffusivities tend to enhance fluid velocity, whereas magnetic field has a reverse effect on it. Higher magnetic field suppresses velocity and aids in reaching steady state.

References

Adesanya SO (2015) Free convective flow of heat generating fluid through a porous vertical channel with velocity slip and temperature jump. Ain Shams Eng J 6:1045–1052

Aung W, Worku G (1985) Mixed convection in ducts with asymmetric wall heat fluxes. J Heat Transf 109:947–951

Barletta A, Celli M (2008) Mixed convection MHD flow in vertical channel: effects of joule heating and viscous dissipation. Int J Heat Mass Transf 51:6110–6117

Bathaiah D (1980) MHD flow through a porous straight channel. Acta Mech 3:223–229

Das S, Jana RN, Makinde OD (2015) Mixed convective magnetohydrodynamic flow in a vertical channel filled with nanofluids. Int J Eng Sci Technol 18:244–255

Guria M, Jana RN (2006) Hydrodynamic flows through vertical wavy channel with travelling thermal waves embedded in porous medium. Int J Appl Mech Eng 11(3):609–621

Hamadah TT, Wirtz RA (1991) Analysis of laminar fully developed mixed convection in a vertical channel with opposing buoyancy. J Heat Transf 113:507–510

Hernandez J, Zamora B (2005) Effects of variable properties and non-uniform heating on natural convection flows in vertical channels. Int J Heat Mass Transf 48:793–807

Lin TA, Hosoi AE, Ehrlich DJ (2009) Vertical hydrodynamic focusing in glass micro-channels. Biomicrofluidics 3(1):014101. doi:10.1063/1.3055278

Seth GS, Ansari MS (2009) Magnetohydrodynamic convective flow in a rotation channel with Hall effects. Int J Theor Appl Mech 4(2):205–222

Seth GS, Nandkeolyar R, Md Ansari S (2010) Unsteady MHD convective flow within a parallel plate rotating channel with thermal source/sink in a porous medium under slip boundary conditions. Int J Eng Sci Technol 2(11):1–16

Seth GS, Sharma R, Kumbhakar B (2016a) Effects of hall current on unsteady MHD convective Couette flow of heat absorbing fluid due to accelerated movement of one of the plates of the channel in a porous medium. J Porous Media 19(1):13–30

Seth GS, Sarkar S, Makinde OD (2016b) Combined free and forced convection Couette-Hartmann flow in a rotating channel with arbitrary conducting walls and hall effects. J Mech 32(5): 613–629

Srinivas S, Muthuraj R (2010) Effects of thermal radiation and space porosity on MHD mixed convection flow in a vertical channel using homotopy analysis method. Commun Nonlinear Sci Numer Simulat 15:2098–2108

Tao LN (1960) On combined free and forced convection in channels. J Heat Transf 8(3):233–238

Umavathi JC, Malashetty MS (2005) Magnetohydrodynamic mixed convection in a vertical channel. Int J Non-Linear Mech 40:91–101

Effect of Newtonian Cooling/Heating on MHD Free Convective Flow Between Vertical Walls with Induced Magnetic Field

Sarveshanand and A.K. Singh

Abstract An analysis is performed for the steady MHD free convective flow between two vertical walls assuming that the fluid is viscous, incompressible, and electrically conducting. The impacts of the Newtonian cooling/heating and induced magnetic field have been considered in the mathematical formulation of the problem. The nondimensionalized simultaneous differential equations, governing the problem, have been solved analytically for the temperature, the velocity, and the induced magnetic field. The manifestations have been made for the induced current density, the skin-friction, and the mass flux. The impact of the Hartmann number, the Biot number, and the magnetic Prandtl number on the velocity, the induced magnetic field, and the induced current density diagrams have been presented by considering a temperature-dependent source/sink. It is inspected that the velocity, the induced magnetic field, and the induced current density diagrams have decreasing tendency with rise in the value of the Hartmann number. Further, it is also noticed that with enhancement in the magnetic Prandtl number the velocity diagram decreases, but the induced magnetic field and the induced current density diagrams have increasing nature. It is beheld that the impression of Newtonian cooling/heating is to reduce/raise the velocity as well as the induced magnetic field and the induced current density. The impacts of the governing parameters on the skin-friction and mass flux have also been concluded dealing with their numerical values given in the tables.

Sarveshanand (✉)
Department of Mathematics, K.N. Government P.G. College,
Gyanpur, Bhadohi, UP, India
e-mail: sarveshda@gmail.com

A.K. Singh
Department of Mathematics, Institute of Science, Banaras Hindu University,
Varanasi 221005, UP, India
e-mail: ashok@bhu.ac.in

M.K. Singh et al. (eds.), *Applications of Fluid Dynamics*, Lecture Notes
in Mechanical Engineering, https://doi.org/10.1007/978-981-10-5329-0_30

1 Introduction

A substantial meditation has been obtained in explications on the natural convective flows of electrically conducting, viscous, and incompressible fluids in the existence of external magnetic fields. Such flows in the literature attracted many researchers because of their enterprising utilities in varied subdivisions of the science and technology. Branches having practical applications of such specious flows are geophysics, nuclear science, medical science, combustion modeling, etc. By enforcing an external magnetic field on such type of fluid motions, the heat transfer and the skin-friction can be reduced. Falling under the complexity of the problems, the free convection studies have been handled theoretically as well numerically and thus studied repeatedly due to its industrial and geophysical applications. These analyses have frequently focused on the flow geometry and the dynamical processes. Further, many good considerations in the literature have been received in the studies of free convective flows of electrically conducting fluids in the presence of external magnetic field. Such coupled flows, deals with the governing equations, which carry more complexity than the nonmagnetic fluid flow equations. In one of the earlier finding in MHD, Hartmann et al. (1937) deliberated theoretical as well as an experimental description by considering the hydromagnetic flow between parallel plates. This work provided an underlying intellectuality for flourish of various hydromagnetic devices. Further, Ostrach (1952) analyzed the steady laminar convection between two vertical walls of a viscous incompressible fluid. There are other related earlier fabrications in free convective deliberations of the flow between vertical walls by paying attention on the impact of a uniform external magnetic field (Osterle and Young 1961; Nath 1974; Mishra and Mohapatra 1975; Jha 1991; Singh and Singh 1991; Paul et al. 1996). Sacheti et al. (1994) focused on an unsteady hydromagnetic natural convective flow with stationary heat flux and deliberated a precise solution. A unified view to the analytical solutions of a magnetohydrodynamic free convective flow has been described by Chandran et al. (2001).

In most of the discussed explorations related to the magnetohydrodynamic natural convective flows, the authors have ignored the impact of induced magnetic field for simple mathematical analysis of the problem. However, the induced electric current develops a magnetic field in the fluid due to which its motion alters the actual magnetic field; simultaneously their flow in the magnetic field develops mechanical forces which are responsible to change the motion of fluid. So, it is required to include, in various physical circumstances, the impact of induced magnetic field while formulating magnetohydrodynamic equations. Various analysis of MHD natural convective flows between vertical walls with the induced magnetic field have been presented by taking into account different aspects of the flow formation (Ghosh et al. 2010; Singh et al. 2010; Kwanza and Balakiyema 2012; Kumar and Singh 2013; Sarveshanand and Singh 2015). Recently, the impact of induced magnetic field on the free convection with the Newtonian heating/cooling in vertical concentric annuli has been explored by Kumar and Singh (2015).

The present paper analyzes the steady magnetohydrodynamic natural convective flow between two vertical walls of a viscous, incompressible, and electrically conducting fluid by considering the impacts induced magnetic field as well as the Newtonian cooling/heating in the visitation of a temperature-dependent source/sink. The expressions for the velocity field, the induced magnetic field, the temperature field, the induced current density, the skin-friction, and the mass flux in dimensionless form have been obtained by solving the governing equations analytically. The impact of the Hartmann number, the Biot number, and the magnetic Prandtl number on alteration of the velocity, the induced magnetic field, and the induced current density profiles have been demonstrated in the graphs. The influences of various parameters on the numerical values of the skin-friction and mass flux have been discussed by means of the tabulated values.

2 Mathematical Formulation

We are paying attention the steady two-dimensional natural convective flow of a viscous, incompressible, and electrically conducting fluid between two vertical walls separated by a distance h, by considering the impact of the Newtonian cooling/heating as well as the induced magnetic field in the presence of source/sink. The x'-axis is taken along the left wall, vertically in the upward direction and perpendicular to this direction into the fluid, the y'-axis is taken. In the y'-direction, a uniform magnetic field has employed of with strength B_0'. At the wall $y' = 0$, the impact of the Newtonian cooling/heating and at the wall $y' = h$, a constant temperature T_h' have been considered. The dependency of the variables representing the flow has considered only on the co-ordinate y', as the walls are assumed to be of infinite length. Let u' be the velocity component along x'-direction. Thus, the velocity and magnetic fields are decomposed as $(u', 0, 0)$ and $\left(B_{x'}, B_0', 0\right)$, respectively.

The Physical model is shown in Fig. 1. Under these considerations and with the boundary layer and the Boussinesq approximations, the governing equations for the model are given by

$$\vartheta \frac{\mathrm{d}^2 u'}{\mathrm{d}y'^2} + g\beta\left(T' - T_0'\right) + \frac{\mu_e B_0'}{\rho}\frac{\mathrm{d}B_{x'}}{\mathrm{d}y'} = 0, \tag{1}$$

$$B_0' \frac{\mathrm{d}u'}{\mathrm{d}y'} + \frac{1}{\sigma\mu_e}\frac{\mathrm{d}^2 B_{x'}}{\mathrm{d}y'^2} = 0, \tag{2}$$

$$\frac{\mathrm{d}^2 T'}{\mathrm{d}y'^2} + \frac{s'}{\rho c_p}\left(T' - T_0'\right) = 0, \tag{3}$$

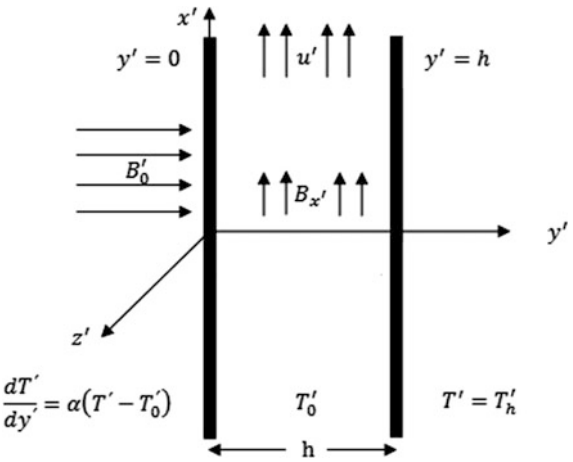

Fig. 1 Physical model

and the boundary conditions are given by

$$\begin{cases} u' = B_{x'} = 0, & \frac{dT'}{dy'} = \alpha(T' - T'_0), & \text{at } y' = 0, \\ u' = B_{x'} = 0, & T' = T'_h, & \text{at } y' = h. \end{cases} \tag{4}$$

To obtain the governing equations in dimensionless form, we use the nondimensional parameters given as

$$y = \frac{y'}{h}, \quad u = \frac{\vartheta u'}{g\beta h^2(T' - T'_0)}, \quad T = \frac{T' - T'_0}{T'_h - T'_0}, \quad B = \frac{\vartheta^2 Bx'}{g\beta h^3 B'_0(T' - T'_0)}, \tag{5}$$

The dimensionless forms of the governing equations are obtained as

$$\frac{d^2u}{dy^2} + Ha^2\frac{dB}{dy} + T = 0, \tag{6}$$

$$\frac{d^2B}{dy^2} + Pm\frac{du}{dy} = 0, \tag{7}$$

$$\frac{d^2T}{dy^2} + ST = 0, \tag{8}$$

with nondimensionalized form of the boundary conditions as

$$\begin{cases} u = B = 0, & \frac{dT}{dy} = BiT, & \text{at } y = 0, \\ u = B = 0, & T = 1, & \text{at } y = 1 \end{cases} \tag{9}$$

In the above equations, the physical parameters in dimensionless form are

$$S = \frac{s'L^2}{\rho C_P}, \quad Ha^2 = \frac{\mu_e h^2 B_0'^2}{\vartheta^2 \rho}, \quad Pm = \vartheta \sigma \mu_e, \quad Bi = \alpha h. \tag{10}$$

Serially the source/sink parameter, the Hartmann number, the magnetic Prandtl number, and the Biot number.

3 Method of Solution

Equations (6)–(9) have been solved analytically by the theory of simultaneous ODE. Due to the dependency, the solution of Eq. (8) on the value of the source/sink parameter S, according as it takes positive or negative values, we have considered the cases when there is a temperature-dependent source or sink.

3.1 Case I—When Temperature-Dependent-Source is Present ($S > 0$)

The demonstrations for u, B, and T in dimensionless form are as

$$u = E_{26}\exp(E_3 y) + E_{25}\exp(-E_3 y) + E_4\cos(\sqrt{S}y) + E_5\sin\left(\sqrt{S}y\right) + E_{27}, \tag{11}$$

$$B = E_{28}\exp(E_3 y) + E_{29}\exp(-E_3 y) + E_8\cos(\sqrt{S}y) + E_9\sin\left(\sqrt{S}y\right) + E_{24}, \tag{12}$$

$$T = E_1\cos(\sqrt{S}y) + E_2\sin\left(\sqrt{S}y\right). \tag{13}$$

The induced current density is demonstrated as

$$J = -\frac{\mathrm{d}B}{\mathrm{d}y} = -E_3E_{28}\exp(E_3 y) + E_3E_{29}\exp(-E_3 y) + E_8\sqrt{S}\sin(\sqrt{S}y) + E_9\sqrt{S}. \tag{14}$$

The expressions for the skin-friction on both the walls are given by

$$\tau_1 = \left(\frac{\mathrm{d}u}{\mathrm{d}y}\right)_{y=0} = E_3(E_{26} - E_{25}) + E_5\sqrt{S}, \tag{15}$$

$$\begin{aligned}\tau_2 = -\left(\frac{\mathrm{d}u}{\mathrm{d}y}\right)_{y=1} &= E_3\{E_{25}\exp(-E_3) - E_{26}\exp(E_3)\} \\ &+ \sqrt{S}\left\{E_4\sin\left(\sqrt{S}\right) - E_5\cos(\sqrt{S})\right\}.\end{aligned} \tag{16}$$

The expression for the mass flux is given by

$$\begin{aligned}Q = \int_0^1 u\mathrm{d}y &= \frac{E_{26}\{\exp(E_3) - 1\}}{E_3} + \frac{E_{25}\{1 - \exp(-E_3)\}}{E_3} + \frac{E_5\{1 - \cos(\sqrt{S})\}}{\sqrt{S}} \\ &+ \frac{E_4\sin(\sqrt{S})}{\sqrt{S}} + E_{27}.\end{aligned} \tag{17}$$

3.2 *Case II—When Temperature-Dependent Sink is Present ($S<0$)*

If $S<0$, then $S = -F$, where $F > 0$. So in nondimensional form, the expressions for u, B, T, and the induced current density are given by

$$\begin{aligned}u = {} & F_{24}\exp(F_3 y) + F_{23}\exp(-F_3 y) + F_4\cosh(\sqrt{F}y) \\ & + F_5\sinh\left(\sqrt{F}y\right) + F_{25},\end{aligned} \tag{18}$$

$$\begin{aligned}B = {} & F_{26}\exp(F_3 y) + F_{27}\exp(-F_3 y) + F_7\cosh(\sqrt{F}y) \\ & + F_8\sinh\left(\sqrt{F}y\right) + F_{22},\end{aligned} \tag{19}$$

$$T = F_1\cosh(\sqrt{F}y) + F_2\sinh\left(\sqrt{F}y\right), \tag{20}$$

$$\begin{aligned}J = {} & -F_3F_{26}\exp(F_3 y) + F_3F_{27}\exp(-F_3 y) - F_7\sqrt{F}\sinh(\sqrt{F}y) \\ & - F_8\sqrt{F}\cosh\left(\sqrt{F}y\right).\end{aligned} \tag{21}$$

Further, the skin-friction and mass flux in this case are given by

$$\tau_1 = F_3(F_{24} - F_{23}) + F_5\sqrt{F}, \tag{22}$$

$$\begin{aligned}\tau_2 = {} & F_3\{F_{23}\exp(-F_3) - F_{24}\exp(F_3)\} \\ & - \sqrt{F}\left\{F_4\sinh\left(\sqrt{F}\right) + F_5\cosh(\sqrt{F})\right\},\end{aligned} \tag{23}$$

$$\begin{aligned}Q = {} & \frac{F_{24}\{\exp(F_3) - 1\}}{F_3} + \frac{F_{23}\{1 - \exp(-F_3)\}}{F_3} + \frac{F_5\left\{\cosh\left(\sqrt{F}\right) - 1\right\}}{\sqrt{F}} \\ & + \frac{F_4\sinh\left(\sqrt{F}\right)}{\sqrt{F}} + F_{25}.\end{aligned} \tag{24}$$

Here the constant used are given in the appendix.

4 Results and Discussion

The considered MHD natural convective model is characterized by a number of physical parameters. We restrict us by considering two cases and taking two simple numerical values of the source/sink parameter as $S = 1$ and $S = -1$, respectively, showing that there is source or sink. This leads simply to analyze the effect of most significant parameters of the problem such as the Hartmann number, the Biot number, and the magnetic Prandtl number.

Figure 2 shows the variation of velocity profile with the Hartmann number for varied values of the Biot number by considering the temperature-dependent source. The graph clearly shows that the velocity profile decreases with rise in the value of Hartmann number. It is also noticed that with rise in the positive value of the Biot number the velocity profile is found to be a deceasing nature showing that the velocity profile has diminishing character in case of Newtonian cooling. With enhancement in the negative value of Biot number, the velocity profile is found to be growing nature showing that the velocity profile rises in case of Newtonian heating.

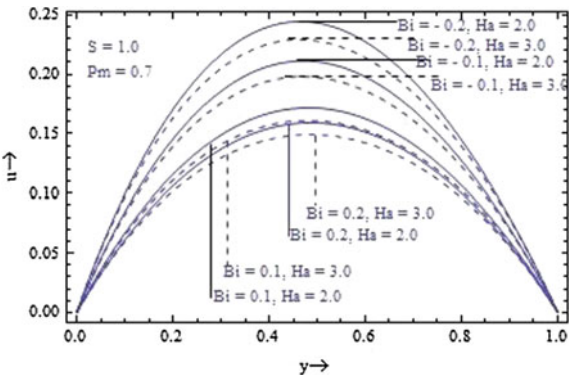

Fig. 2 Velocity profile for *Bi* and *Ha* ($S > 0$)

A similar behavior from the velocity diagram is noticed with the Hartmann number and Biot number as plotted in Fig. 3 showing the case when there is a temperature-dependent sink. It is observed that in this case also the velocity profile has a decreasing tendency with the rise in the value of Hartmann number as well as the positive value of the Biot number while has a reverse aptitude with the rise in the negative value of the Biot number.

Figures 4 and 5 exhibit the alteration of velocity profile with the magnetic Prandtl number for multiple values of the Biot number by considering the presence of source/sink. For these cases, it is apparent from the graphs that the velocity reduces with growth in the magnetic Prandtl number.

Figures 6 and 7 show the nature of the velocity profile for the higher positive values of the Biot number. In both the cases, when there is a source or sink, the graphs display that the Newtonian cooling at higher level gives almost same velocity profiles.

Figures 8 and 9 show a similar behavior of the velocity profile at the very low negative values of the Biot number. These graphs clearly also show that the velocity profile follows the nearly the same curves in case of Newtonian heating to a higher level.

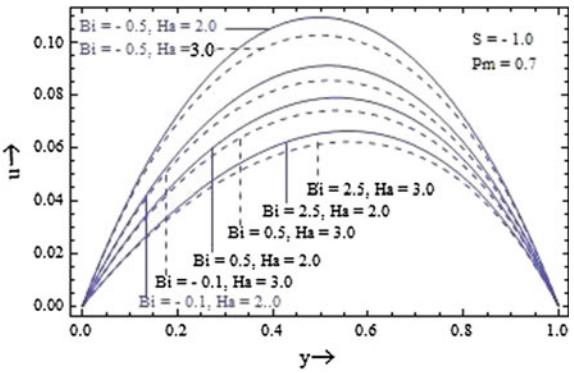

Fig. 3 Velocity profile for *Bi* and *Ha* ($S<0$)

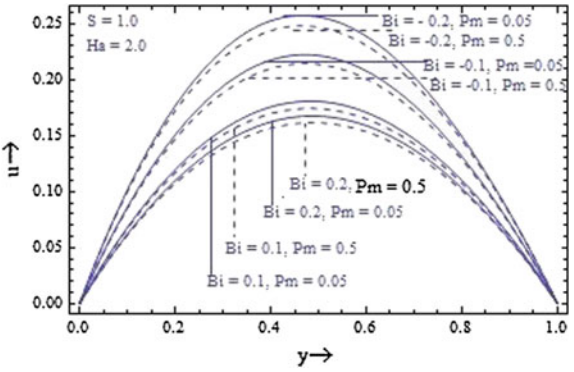

Fig. 4 Velocity profile for *Bi* and *Pm* ($S>0$)

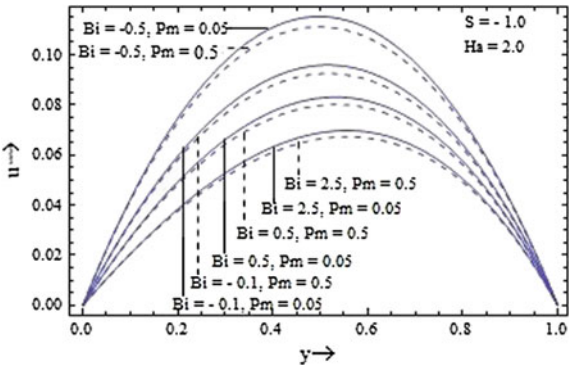

Fig. 5 Velocity profile for *Bi* and *Pm* ($S<0$)

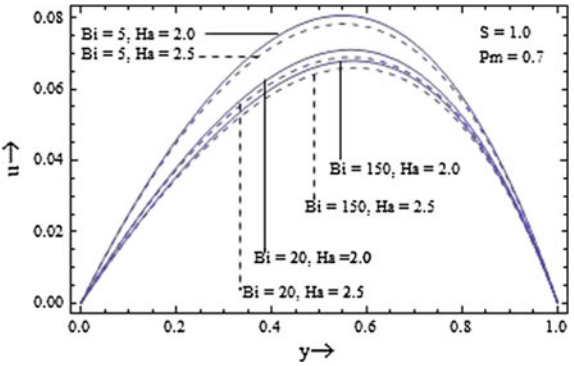

Fig. 6 Velocity profile at high *Bi* ($S > 0$)

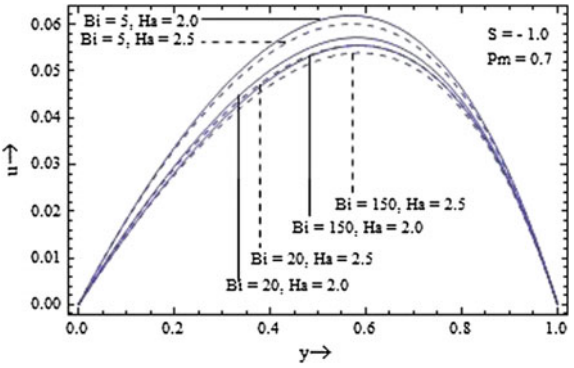

Fig. 7 Velocity profile at high *Bi* ($S<0$)

Figures 10 and 11 display the change in the magnetic field diagram with Hartmann number and the Biot number having, respectively, the existence of source and sink. It is seen from the graphs that with expansion in the value of Hartmann number, the induced magnetic field profile decreases. Also, with rise in the negative value of Biot number, the induced magnetic field profile is found to be an

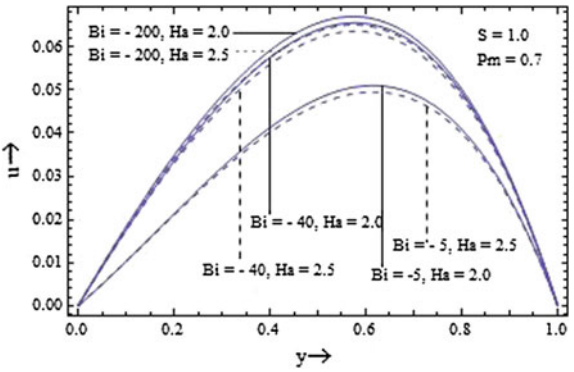

Fig. 8 Velocity profile at low *Bi* $(S > 0)$

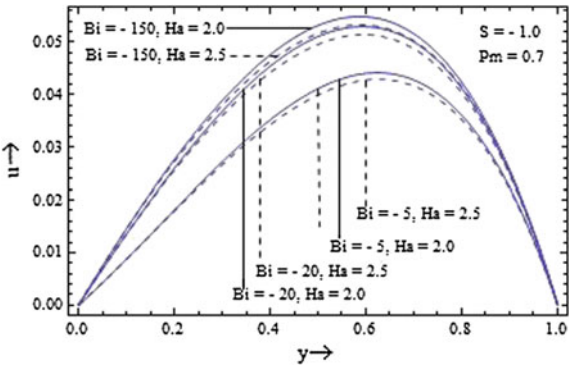

Fig. 9 Velocity profile at low *Bi* $(S < 0)$

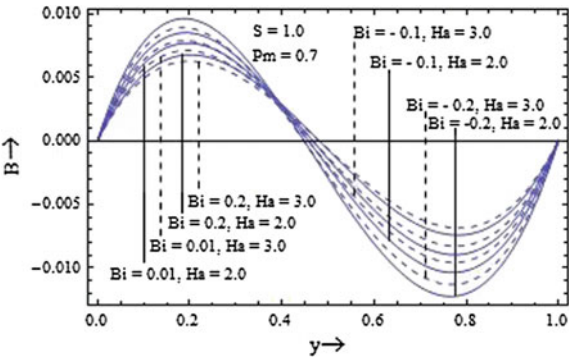

Fig. 10 Induced magnetic field profile for *Bi* and *Ha* $(S > 0)$

increasing nature showing that induced magnetic field profile increases in case of heating. But with the growth in the positive value of Biot number, the induced magnetic field profile is found to be a diminishing nature which shows that the cooling leads to decrease the induced magnetic field profile.

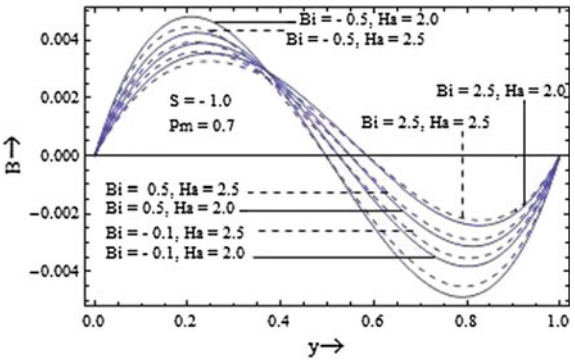

Fig. 11 Induced magnetic field profile for *Bi* and *Ha* ($S<0$)

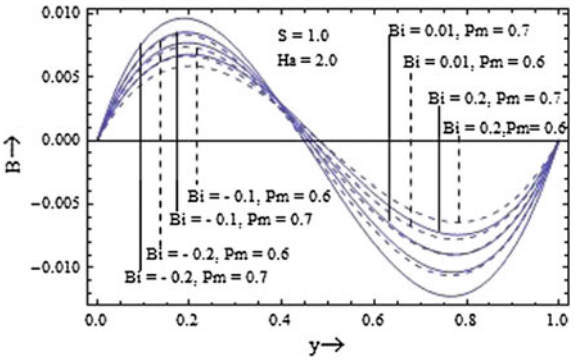

Fig. 12 Induced magnetic field profile for *Bi* and *Pm* ($S>0$)

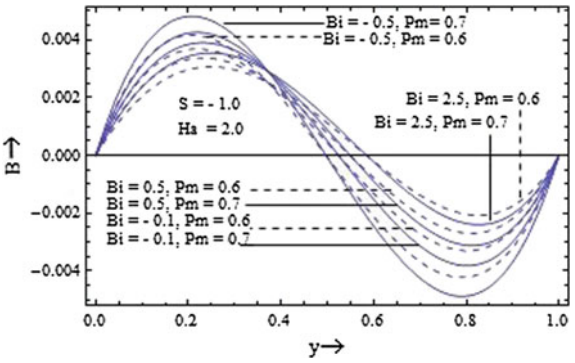

Fig. 13 Induced magnetic field profile for *Bi* and *Pm* ($S<0$)

Figures 12 and 13 specify the alteration of magnetic field diagram with the magnetic Prandtl number having a source/sink. When there is a source or sink, it is inspected that the induced magnetic profile decreases with rise in the value of magnetic Prandtl number. The character of the induced magnetic profile for the higher positive values of the Biot number has been demonstrated in Figs. 14 and 15. The presence of source or sink shows that the Newtonian cooling at higher level

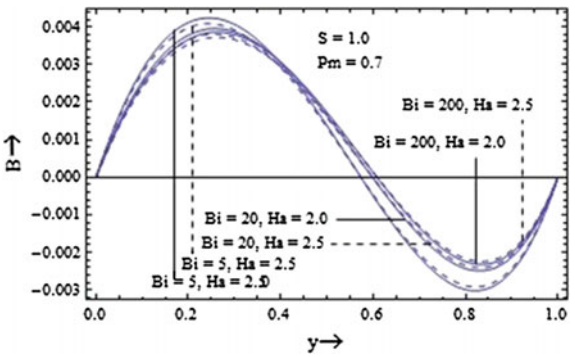

Fig. 14 Induced magnetic field profile at high Bi $(S > 0)$

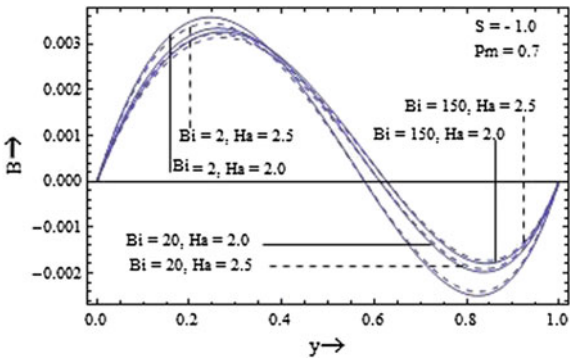

Fig. 15 Induced magnetic field profile at high Bi $(S<0)$

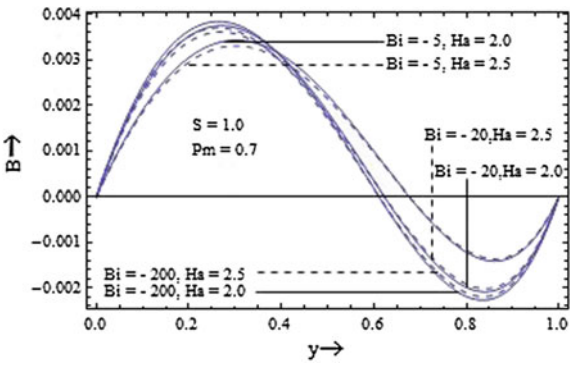

Fig. 16 Induced magnetic field profile at low Bi $(S > 0)$

leads the nearly the same induced magnetic profile. Figures 16 and 17 show an identical behavior of the magnetic field profile at the very low negative values of the Biot number. The graphs clearly gesture that the induced magnetic field profile approaches the nearly same curves with Newtonian heating at higher level. The appearance of the induced magnetic field profile near the wall at $y = 0$ is parabolic in upward direction, but near the wall at $y = 1$ it is parabolic downward exposing that the direction of the induced magnetic field has changed.

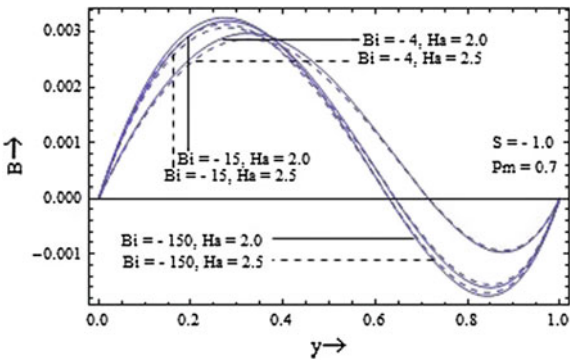

Fig. 17 Induced magnetic field profile at low *Bi* $(S<0)$

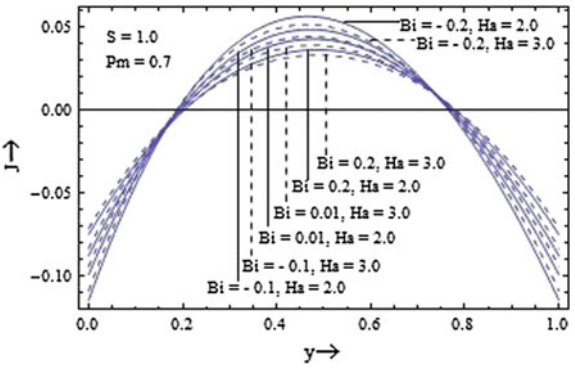

Fig. 18 Induced current density profile for *Bi* and *Ha* $(S>0)$

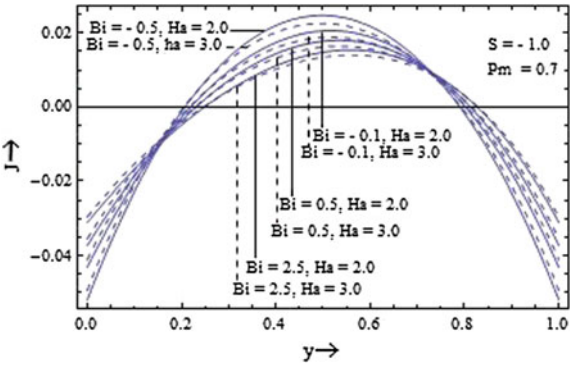

Fig. 19 Induced current density profile for *Bi* and *Ha* $(S<0)$

Figures 18 and 19 point out the change of induced current density profile with varied values of the Biot number and the Hartmann number keeping a source/sink. It is noticed that the current density diagram reduces with rise in the value of Hartmann number. With magnification in the negative value of Biot number, the current density diagram is found to be an increasing character showing that heating leads to enhance the induced current density profile.

Further, it is observed that with rise in the positive value of the Biot number, the current density diagram is found to be of a diminishing character which shows that with cooling current density diagram decreases. Figures 20 and 21 show the change of current density graphs with the magnetic Prandtl number having a source/sink. It is found that as the value of magnetic Prandtl number rises, the current density diagram increases not only in the presence of source but also in the presence of sink.

Figures 22 and 23 show the nature of the induced current density diagram for the Newtonian cooling at higher level. The graphs notify that with cooling at higher level there is no difference in the behavior of the induced current density profile in the existence of source/sink. A very similar behavior of the induced current density diagram at the very low negative values of the Biot number is shown in Figs. 24 and 25.

Figures 24 and 25 clearly show that the current density diagram is almost same for higher level heating. It is also noticed from the induced current density profile that positive value of the current density founded maximum nearly in the middle of the two walls and the nearly identical negative value is attended on left as well as on the right wall.

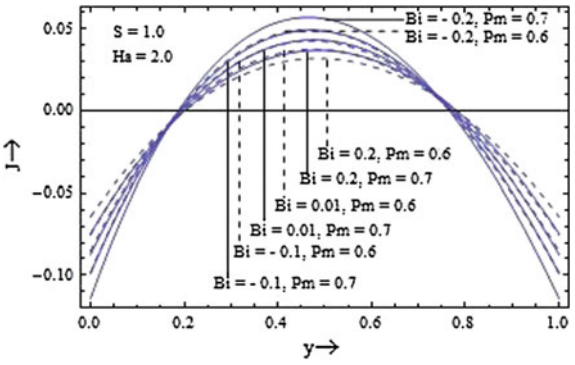

Fig. 20 Induced current density profile for *Bi* and *Pm* ($S > 0$)

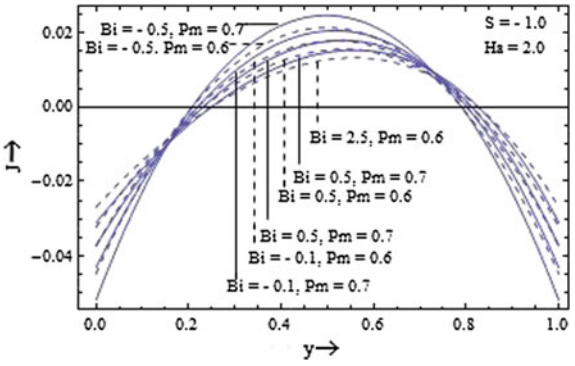

Fig. 21 Induced current density profile for *Bi* and *Pm* ($S > 0$)

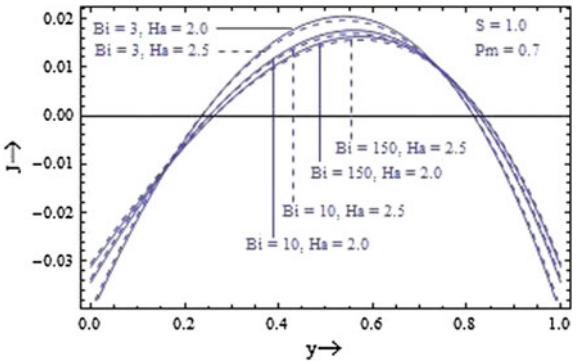

Fig. 22 Induced current density profile at high *Bi* ($S > 0$)

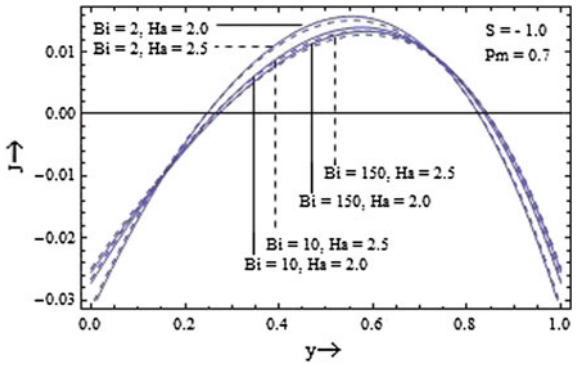

Fig. 23 Induced current density profile at high *Bi* ($S < 0$)

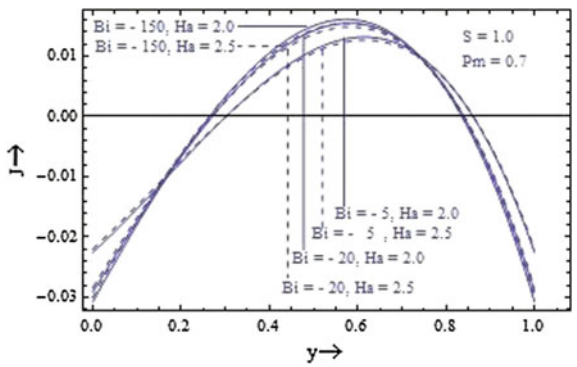

Fig. 24 Induced current density profile at low *Bi* ($S > 0$)

For various values the parameters, the skin-friction on the walls and mass flux have represented in Table 1. When there is a temperature-dependent source, table clearly demonstrates that the skin-friction on the left wall reduces with rise in the values of the Hartmann number but on the right wall, it raises with Hartmann

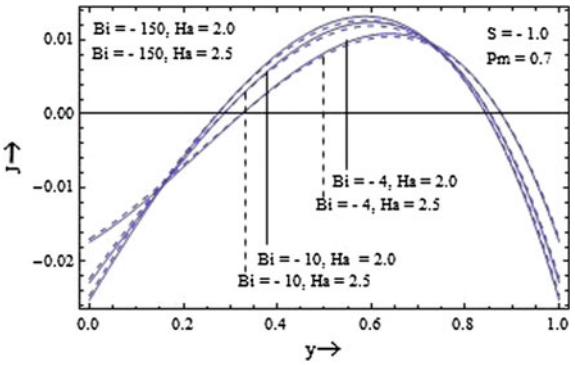

Fig. 25 Induced current density profile at low *Bi* ($S<0$)

Table 1 Numerical values of skin-friction and mass flux ($s>0$)

Bi	*Pm*	*Ha*	$S = 1$		
			τ_1	τ_2	Q
0.1	0.6	2	0.759609	0.661548	0.115861
		3	0.757455	0.663702	0.110771
		5	0.752057	0.669100	0.098016
	0.7	2	0.759305	0.661852	0.115143
		3	0.756861	0.664297	0.109366
		5	0.750928	0.670229	0.095347
0.5	0.6	2	0.560682	0.554071	0.090881
		3	0.560537	0.554217	0.086889
		5	0.560173	0.554580	0.076883
	0.7	2	0.560661	0.554092	0.090318
		3	0.560490	0.554257	0.085786
		5	0.560097	0.554657	0.074790
−0.1	0.6	2	0.969161	0.774765	0.141294
		3	0.964892	0.779035	0.135929
		5	0.954191	0.789736	0.120277
	0.7	2	0.968559	0.775367	0.142175
		3	0.963713	0.780214	0.134205
		5	0.951952	0.791975	0.117002
−0.5	0.6	2	3.157980	1.957340	0.417030
		3	3.131600	1.983710	0.398711
		5	3.065510	2.049800	0.352798
	0.7	2	3.154260	1.96106	0.414447
		3	3.124320	1.99099	0.393653
		5	3.051680	2.06363	0.343191

Table 2 Numerical values of skin-friction and mass flux ($s<0$)

Bi	*Pm*	*Ha*	$S = -1$		
			τ_1	τ_1	τ_1
0.1	0.6	2	0.338815	0.338815	0.338815
		3	0.340174	0.340174	0.340174
		5	0.343582	0.343582	0.343582
	0.7	2	0.339006	0.339006	0.339006
		3	0.340549	0.340549	0.340549
		5	0.344296	0.344296	0.344296
0.5	0.6	2	0.297635	0.297635	0.297635
		3	0.299447	0.299447	0.299447
		5	0.303994	0.303994	0.303994
	0.7	2	0.297890	0.297890	0.297890
		3	0.299480	0.299480	0.299480
		5	0.304946	0.304946	0.304946
−0.1	0.6	2	0.369589	0.369589	0.369589
		3	0.370609	0.370609	0.370609
		5	0.373167	0.373167	0.373167
	0.7	2	0.369733	0.369733	0.369733
		3	0.370890	0.370890	0.370890
		5	0.373702	0.373702	0.373702
−0.5	0.6	2	0.476559	0.476559	0.476559
		3	0.476400	0.476400	0.476400
		5	0.476001	0.476001	0.476001
	0.7	2	0.476537	0.476537	0.476537
		3	0.476356	0.476356	0.476356
		5	0.475917	0.475917	0.475917

number. On the left wall, the skin-friction reduces with growth in the value of the magnetic Prandtl number, whereas it raises on the right wall. Whenever the positive values of the Biot number get raised, the skin-friction decreases on both the walls show that cooling leads to decrement in the skin-friction. Further, it is noticed that the rise in the negative values of the Biot number leads to rise in value of the skin-friction on both the walls which shows that heating leads to enhance the skin-friction.

Table 2 shows that the skin-friction on the wall at $y = 0$ get enhanced with rise in the values of the Hartmann number while it reduces with Hartmann number on the wall at $y = 1$. Further, on the wall at $y = 0$ the skin-friction rises with rise in the

magnetic Prandtl number but opposite nature is noticed on the wall at $y = 1$. In the existence of a temperature-dependent sink also, cooling leads to decrease the skin-friction and heating leads to magnify the skin-friction. It is also clear from the table that the value of mass flux has diminishing nature with growth in the value of Hartmann number and the magnetic Prandtl number. In case when there is source/sink the mass flux decreases by cooling, while it increases by the heating.

5 Conclusions

It is found that the velocity profile has a diminishing nature with rise in the value of Hartmann number. With Newtonian heating the velocity profile increases, while it has a decreasing nature with Newtonian cooling. The induced magnetic field graph as well as the induced current density graph has diminishing tendency with rise in the value of the Hartmann number. The impact of the magnetic Prandtl number is to reduce the velocity profile but to enhance the induced magnetic field and the induced current density profiles. The influence of Newtonian cooling/heating is to reduce/raise the velocity, the induced magnetic field, and the induced current density diagrams. The skin-friction at one wall reduces, while rises on the other with rise in the value of the Hartmann number in the existence of source, but there is a reverse nature when there is a sink. With the Magnetic Prandtl number, a similar behavior is noticed. It is noticed that skin-friction decreases/increases with Newtonian cooling/heating. The mass flux reduces with rise in the value of the Hartmann number as well as the value of the magnetic Prandtl number. Newtonian cooling leads to decrease the mass flux, while effect of heating is to increase the mass flux.

Symbols:

u'—the velocity along x'-direction, u—the velocity dimensionless form, $B_{x'}$—the induced magnetic field along x'-direction, B'_0—the applied external magnetic field in the y'-direction, B—dimensionless induced magnetic field, T'_0—the ambient temperature, T'—the temperature of the fluid, T—the temperature of the fluid in dimensionless form, ϑ—the kinematic viscosity, μ_e—the magnetic permeability, g—the acceleration due to gravity, β—the coefficient of volume expansion, ρ—the density of the fluid, c_p—the specific heat at constant pressure, k—the thermal conductivity of the fluid, σ—conductivity of the fluid, s'—the source/sink variable, S—the source/sink parameter, α—constant, h—the characteristic length, Bi—the Biot number, Ha—the Hartmann number, Pm—the magnetic Prandtl number.

Appendix

$$E_1 = \frac{\sqrt{S}}{Bi\,\sin\sqrt{S}+\sqrt{S}\,\cos\sqrt{S}},\quad E_3 = Ha\sqrt{Pm},\quad E_{15} = \frac{1}{2E_7},$$
$$E_2 = \frac{Bi}{Bi\,\sin\sqrt{S}+\sqrt{S}\,\cos\sqrt{S}},\quad E_4 = \frac{E_1}{S+E_3^2},\quad E_5 = \frac{E_2}{S+E_3^2},$$
$$E_{16} = \frac{E_6}{2},\quad E_{11} = \frac{E_6}{\exp(E_3)},\quad E_{12} = -\frac{E_4\cos\left(\sqrt{S}\right)+E_5\sin\left(\sqrt{S}\right)}{\exp(E_3)},$$
$$E_{13} = -\frac{1}{E_7\exp(E_3)},\quad E_{17} = -\frac{E_4E_7+E_8}{2E_7},\quad E_{18} = \frac{E_6}{2}-\frac{E_6-E_{11}}{1-E_{10}},$$
$$E_{14} = \frac{E_8\cos\left(\sqrt{S}\right)+E_9\sin\left(\sqrt{S}\right)}{E_7\exp(E_3)},\quad E_{19} = \frac{E_4+E_{12}}{1-E_{10}}-\frac{E_4E_7+E_8}{2E_7},$$
$$E_{20} = E_{15}+\frac{E_{13}}{1+E_{10}},\quad E_{21} = \frac{E_6}{2}-\frac{E_6}{1+E_{10}},\quad E_{22} = \frac{E_4+E_{14}}{1+E_{10}}-\frac{E_4E_7+E_8}{2E_7},$$
$$E_{23} = \frac{E_{19}E_{20}-E_{15}E_{22}}{E_{18}E_{20}-E_{15}E_{21}},\quad E_{24} = \frac{E_{19}-E_{18}E_{23}}{E_{15}},\quad E_{25} = E_{17}-E_{15}E_{24}-E_{16}E_{23},$$
$$E_{26} = -E_4-E_{25}-E_6E_{23},\quad E_{27} = E_6E_{23},\quad E_{28} = -E_7E_{26},\quad E_{29} = E_7E_{25}$$
$$F = -S,\quad F_3 = Ha\sqrt{Pm},\quad F_1 = \frac{\sqrt{F}}{Bi\,\sinh\sqrt{F}+\sqrt{F}\,\cosh\sqrt{F}},$$
$$F_2 = \frac{Bi}{Bi\,\sinh\sqrt{F}+\sqrt{F}\,\cosh\sqrt{F}},\quad F_4 = -\frac{F_1}{F-F_3^2},\quad F_5 = -\frac{F_2}{F-F_3^2},$$
$$F_6 = -\frac{Pm}{F_3},\quad F_7 = -\frac{F_5Pm}{\sqrt{F}},\quad F_8 = -\frac{F_4Pm}{\sqrt{F}},\quad F_9 = \exp(-2F_3),$$
$$F_{10} = \frac{1}{Pm\,\exp(F_3)},\quad F_{14} = -\frac{1}{2F_6},\quad F_{11} = -\frac{F_4\cosh\sqrt{F}+F_5\sinh\sqrt{F}}{\exp(F_3)},$$
$$F_{12} = \frac{1}{F_6\exp(F_3)},\quad F_{17} = \frac{2F_{12}F_6-F_9-1}{2F_6(1+F_9)},\quad F_{18} = \frac{F_9-1}{2Pm(1+F_9)},$$
$$F_{13} = -\frac{F_7\cosh\sqrt{F}+F_8\sinh\sqrt{F}}{F_6\exp(F_3)},\quad F_{25} = \frac{F_{21}}{Pm},\quad F_{15} = \frac{2F_{10}Pm-F_9-1}{2Pm(1-F_9)},$$
$$F_{16} = \frac{2F_{11}F_6+F_4F_6F_9+F_4F_6+F_7-F_7F_9}{2F_6(1-F_9)},\quad F_{24} = -\frac{F_{21}}{Pm}-F_{23}-F_4,$$
$$F_{19} = \frac{2F_{13}F_6+F_4F_6+F_7F_9+F_7-F_4F_6F_9}{2F_6(1+F_9)},\quad F_{21} = \frac{F_{16}F_{17}-F_{14}F_{19}}{F_{15}F_{17}-F_{14}F_{18}},$$
$$F_{22} = \frac{F_{16}-F_{15}F_{21}}{F_{14}},\quad F_{20} = \frac{F_7-F_4F_6}{2F_6},\quad F_{23} = F_{20}-F_{14}F_{19}-\frac{F_{21}}{2Pm},$$
$$F_{26} = F_{24}F_6,\quad F_{27} = -F_{23}F_6.$$

References

Chandran P, Sacheti NC, Singh AK (2001) An unified approach to analytical solution of a hydromagnetic free convection flow. Scientiae Mathematicae Japonicae 53:467–476

Ghosh SK, Beg OA, Zueco J (2010) Hydromagnetic free convection flow with induced magnetic field effects. Meccanica 14:175–185

Hartmann J, Lazarus F, Hg-Dynamics II (1937) Experimental investigations on the flow of Mercury in homogenous magnetic field. DetKgl. Danske Videnskabernes Selskab. Mathematisk-fysiske Meddelelser XV: 7

Jha BK (1991) MHD free and forced convection flow past an infinite vertical plate with heat source. Astrophys Space Sci 183:169–175

Kumar A, Singh AK (2013) Unsteady MHD free convective flow past a semi-infinite vertical wall with induced magnetic field. Appl Math Comput 222:462–471

Kumar D, Singh AK (2015) Effect of induced magnetic field on natural convection with Newtonian heating/cooling in vertical concentric annuli. Procedia Eng 127:568–574

Kwanza JK, Balakiyema JA (2012) Magnetohydrodynamic free convective flow past an infinite vertical porous plate with magnetic induction. J Fusion Energy 31:352–356

Mishra SP, Mohapatra P (1975) Unsteady free convection flow from a vertical plate in the presence of a uniform magnetic field. Zeitschriftfür Angewandte Mathematik und Mechanik 55:759–762

Nath G (1974) Solutions of boundary layer equations governing free convective and magneto-hydrodynamic flows through parametric differentiation. Zeitschriftfür Angewandte Mathematik und Mechanik 54:685–693

Osterle JF, Young FJ (1961) Natural convection between heated vertical plates in horizontal magnetic field. J Fluid Mech 11:512–518

Ostrach S (1952) Laminar natural convection flow and heat transfer of the fluids with and without heat sources in channels with constant wall temperature. NASA Technical Note No. 2863

Paul T, Jha BK, Singh AK (1996) Transient free convective flow in a vertical channel with constant heat flux on the walls. Heat Mass Transf 32:61–63

Sacheti NC, Chandran P, Singh AK (1994) An exact solution for unsteady magnetohydrodynamic free convection flow with constant heat flux. Int Commun Heat Mass Transf 21:131–142

Sarveshanand, Singh AK (2015) Magnetohydrodynamic free convection between vertical parallel porous plates in the presence of induced magnetic field. SprigerPlus 4:333

Singh AK, Singh JN (1991) Transient hydromagnetic free-convection flow past an impulsively started vertical plat. Astrophys Space Sci 176:523–529

Singh RK, Singh AK, Sacheti NC, Chandran P (2010) On hydromagnetic free convection in the presence of induced magnetic field. Heat Mass Transf 46:523–529

Radial Vibrations in Unbounded Micropolar Elastic Solid with Fluid Loaded Spherical Cavity

R. Srinivas and K. Somaiah

Abstract In this paper, the radial vibrations in unbounded micropolar elastic solid with fluid loaded spherical cavity have been investigated. The micropolar elastic solid is homogeneous and isotropic, while the loaded fluid is homogenous, isotropic, and inviscid. The frequency equation for radial vibrations of macro-displacements is derived and which is influenced by the loaded fluid, while the vibrations for micro-rotations are not influenced by the loaded fluid and these have been coinciding with the results of Somaiah (Comput Sci Math Biol 47–50, 2016). The dispersion relation for macro-displacements is obtained as particular case of this investigation. Further, numerical computations have been performed and have also been shown graphically to understand the behavior of phase speed and dispersion equations in the medium.

1 Introduction

The study of radial vibrations is most important generalization of theoretical and practical applications in several fields like geophysics, seismology, and synthetic porous materials. Ghosh (1975) discussed the radial vibrations of isotropic elastic sphere and hollow sphere. Love (1944) treatise contains an account of the forced vibrations of a sphere due to body forces derivable from a potential. Sphere problem in connection with the problems of geodynamics was considered by Love (1926). The complete solution of sphere subject to dynamic surface tractions and computed natural frequencies of the free oscillations by Grey and Eringen (1955).

R. Srinivas (✉)
Department of Mathematics, Vardhaman College of Engineering, Shamshabad, Hyderabad 501218, Telangana, India
e-mail: remidi_srinivas@yahoo.co.in

K. Somaiah
Department of Mathematics, Kakatiya University, Warangal 506009, Telangana, India
e-mail: somaiahkamidi@gmail.com

M.K. Singh et al. (eds.), *Applications of Fluid Dynamics*, Lecture Notes in Mechanical Engineering, https://doi.org/10.1007/978-981-10-5329-0_31

Many authors like Blake (1952) and Eringen (1957) have discussed the problems of elastic waves from a spherical cavity situated in an unbounded elastic medium. The vibrations of fluid filled elastic spherical and spheroidal shells were discussed by Rang and Dimaggio (1967). Radial vibrations due to a spherical cavity in micropolar elastic solid were studied by Tomar and Singh (2003). Recently, Somaiah (2016) studied the effect of rotation and micropolarity on radial vibrations.

In this paper, we derived the dispersion equation for the radial vibrations in unbounded micropolar elastic solid with fluid loaded spherical cavity. It is observed that the dispersion equation is not encountered in classical theory of elasticity. Further, the results of classical case are obtained as particular case of it.

2 Basic Equations

The basic governing equations of homogeneous isotropic micropolar elastic solid are given by Eringen and Suhubi (1964).

The balance of momentum equation is

$$(\lambda+\mu)u_{l,lk}+(\mu+\kappa)u_{k,ll}+\kappa\varepsilon_{klm}\phi_{m,l}+\rho(f_k-\ddot{u}_k)=0 \tag{1}$$

The balance of the stress moment equation is

$$(\alpha+\beta)\phi_{l,lk}+\gamma\phi_{k,ll}+\kappa\varepsilon_{klm}u_{m.l}-2\kappa\phi_k+\rho\left(l_k-j\ddot{\phi}_k\right)=0 \tag{2}$$

The stress tensor t_{kl} and couple stress tensor m_{kl} are given by

$$t_{kl}=\lambda u_{r,r}\delta_{kl}+\mu\left(u_{k,l}+u_{l.k}\right)+\kappa\left(u_{l,k}-\varepsilon_{klr}\phi_r\right) \tag{3}$$

$$m_{kl}=\alpha\phi_{r,r}\delta_{kl}+\beta\phi_{k,l}+\gamma\phi_{l,k} \tag{4}$$

In the above equations, $\bar{u}$ is displacement vector, $\bar{f}$ is the body force, $\bar{l}$ is the body couple vector, ρ is the density, j is the micro-inertia, δ_{kl} is the Kronecker delta, ε_{klr} is the permutation symbol, an index (say k) following a comma indicates partial differentiation with respect to the coordinate (x_k), dot superposed on a symbol denotes partial differentiation with respect to the time t, and $\lambda,\mu,\kappa,\alpha,\beta,\gamma$ are the material coefficients which satisfy the following inequalities.

$$3\lambda+2\mu+\kappa\geq 0,\quad 2\mu+\kappa\geq 0,\quad \kappa\geq 0$$
$$3\alpha+\beta+\gamma\geq 0,\quad -\gamma\leq\beta\leq\gamma,\quad \gamma\geq 0$$

3 Formulation and Solution of the Problem

We consider a spherical cavity of radius a in a uniform micropolar elastic solid of infinite extent. We are interested only in radial vibrations. The radial displacement $\vec{u}$ and the radial micro-rotation $\vec{\phi}$ depend only on the radial distance r from the origin and time, and the other components $u_\theta, u_q, \phi_\theta$ and ϕ_q are zero. Hence, we take

$$\vec{u} = u(r,t)e_r \tag{5}$$

$$\vec{\phi} = \phi(r,t)e_r \tag{6}$$

where e_r is the unit vector at the position vector in the direction of the tangent to the r-curve.

In view of Eqs. (5) and (6) and under the absence of body forces and body couples, the equations of motion (1)–(4) would reduce to

$$\frac{\partial^2 u}{\partial r^2} + \frac{2}{r}\frac{\partial u}{\partial r} - \frac{2}{r^2}u = \frac{\rho}{(\lambda+2\mu+\kappa)}\frac{\partial^2 u}{\partial t^2} \tag{7}$$

$$\frac{\partial^2 \phi}{\partial r^2} + \frac{2}{r}\frac{\partial \phi}{\partial r} - \frac{2}{r^2}\phi - \frac{2\kappa}{(\alpha+\beta+\gamma)}\phi = \frac{\rho j}{(\alpha+\beta+\gamma)}\frac{\partial^2 \phi}{\partial t^2} \tag{8}$$

$$t_{rr} = (\lambda+2\mu+\kappa)\frac{\partial u}{\partial r} + \frac{2\lambda}{r}u \tag{9}$$

$$m_{rr} = (\alpha+\beta+\gamma)\frac{\partial \phi}{\partial r} + \frac{2\alpha}{r}\phi \tag{10}$$

Now, we shall derive the dispersive equation for the radial vibrations in an unbounded micropolar elastic solid having a spherical cavity filled with homogeneous inviscid fluid of density $\rho^{(f)}$. The field equations and the constitutive relations for homogeneous inviscid fluid are given by Kumar et al. (2013).

$$\nabla\left(\nabla \cdot u^{(f)}\right) = \frac{\rho^{(f)}}{\xi^{(f)}}\frac{\partial^2 u^{(f)}}{\partial t^2} \tag{11}$$

and

$$t_{rr}^{(f)} = \xi^{(f)}\left(\nabla \cdot u^{(f)}\right)\delta_{rr} \tag{12}$$

where $u^{(f)}$ is displacement vector of the medium corresponding the fluid in the medium, $\xi^{(f)}$ and $\rho^{(f)}$ are the bulk modulus and density of the fluid, respectively.

For the radial vibrations, we take

$$u^{(f)} = \left(u^{(f)}, 0, 0\right)$$

with

$$u^{(f)} = \frac{\partial \psi^{(f)}}{\partial r} \tag{13}$$

where $\psi^{(f)}$ is the potential of the fluid. Making use of Eq. (13) in Eqs. (11) and (12), the displacement potential $\psi^{(f)}$ in the liquid medium satisfies the equation

$$\nabla^2 \psi^{(f)} = \frac{\rho^{(f)}}{\xi^{(f)}} \frac{\partial^2 \psi^{(f)}}{\partial t^2} \tag{14}$$

and

$$t_{rr}^{(f)} = \xi^{(f)} \nabla^2 \psi^{(f)} \tag{15}$$

where $\nabla^2 = \frac{\partial^2}{\partial r^2} + \frac{2}{r}\frac{\partial}{\partial r}$.

We seek the solution of Eq. (14) in the form of

$$\psi^{(f)}(r,t) = \Psi(r) e^{i\omega t} \tag{16}$$

where ω is the angular frequency. Substituting Eq. (16) in Eq. (14), we obtain

$$\nabla^2 \Psi + l^2 \Psi = 0 \tag{17}$$

where

$$l = \omega \sqrt{\frac{\rho^{(f)}}{\xi^{(f)}}} \tag{18}$$

Let

$$\Psi(r) = \frac{1}{\sqrt{r}} T(r) \tag{19}$$

Inserting Eq. (19) in Eq. (17), we get

$$r^2 T''(r) + rT'(r) + \left((lr)^2 - \left(\frac{1}{2}\right)^2\right) T(r) = 0 \tag{20}$$

which is a Bessel equation, and the solution of Eq. (20) is

$$T(r) = B' J_{\frac{1}{2}}(lr) + B Y_{\frac{1}{2}}(lr) \tag{21}$$

where B', B are arbitrary constants, $J_{\frac{1}{2}}$ and $Y_{\frac{1}{2}}$ are modified Bessel functions of order $\frac{1}{2}$.

Substituting Eqs. (19) and (21) in Eq. (16), we get

$$\psi^{(f)}(r,t) = \frac{1}{\sqrt{r}}\left[B' J_{\frac{1}{2}}(lr) + B Y_{\frac{1}{2}}(lr)\right] \mathrm{e}^{i\omega t} \tag{22}$$

Since $\psi^{(f)} \to 0$ as $r \to \infty$ and it is possible only if $B' = 0$.
For large values of z, we have $Y_{\frac{1}{2}}(z) = \sqrt{\frac{\pi}{2z}}\mathrm{e}^{-z}$
So,

$$Y_{\frac{1}{2}}(lr) = \sqrt{\frac{\pi}{2lr}}\mathrm{e}^{-lr} \tag{23}$$

Substituting Eq. (23) in Eq. (22), we get

$$\psi^{(f)}(r,t) = B\sqrt{\frac{\pi}{2l}}\mathrm{e}^{-lr}\frac{1}{r}\mathrm{e}^{i\omega t} \tag{24}$$

The presence of liquid $P^{(f)}$ and radial displacements are given by

$$P^{(f)} = -t_{rr}^{(f)} = B\sqrt{\frac{\pi}{2l}}\rho^{(f)}\frac{\omega^2}{r}\mathrm{e}^{i\omega t - lr} \tag{25}$$

$$u^{(f)} = \frac{\partial \psi^{(f)}}{\partial r} = -B\sqrt{\frac{\pi}{2l}}\frac{\rho^{(f)}}{r^2}\mathrm{e}^{i\omega t - lr} \tag{26}$$

The appropriate boundary condition is

$$t_{rr} = -P^{(f)} \quad \text{at} \quad r = a \tag{27}$$

Now, we seek the solution of Eq. (7) of the form

$$u(r,t) = R(r)\,\mathrm{e}^{i\omega t} \tag{28}$$

On using Eq. (28) in Eq. (7), we obtain

$$\frac{\mathrm{d}^2 R}{\mathrm{d}r^2} + \frac{2}{r}\frac{\mathrm{d}R}{\mathrm{d}r} - \frac{2}{r^2}R + \frac{\omega^2\rho}{\lambda + 2\mu + \kappa}R = 0 \tag{29}$$

Suppose

$$x = hr \tag{30}$$

where

$$h^2 = \frac{\omega^2 \rho}{\lambda + 2\mu + \kappa} \tag{31}$$

Using Eqs. (30) and (31), Eq. (29) can be expressed as

$$\frac{\mathrm{d}^2 R}{\mathrm{d}x^2} + \frac{2}{x}\frac{\mathrm{d}R}{\mathrm{d}x} - \frac{2}{x^2}R + R = 0 \tag{32}$$

The general solution of Eq. (32) is

$$R(x) = A\frac{\mathrm{d}}{\mathrm{d}x}\left(\frac{\mathrm{e}^{ix}}{x}\right)$$

Hence,

$$u(r,t) = A\left[\frac{i}{hr} - \frac{1}{(hr)^2}\right]\mathrm{e}^{i(\omega t + hr)} \tag{33}$$

where x in terms of r is given by Eq. (30) and A is an arbitrary constant.

Substituting Eqs. (33) and (25) in the boundary condition (27), we obtain

$$A(\lambda + 2\mu + \kappa)\left[\frac{2i\lambda}{ha^2} + \frac{2(1-\lambda)}{h^2 a^3} - \left(\frac{1}{a} + \frac{2i}{ha^2}\right)\right]\mathrm{e}^{i(h-il)a} + B\sqrt{\frac{\pi}{2la}}\rho^{(f)}\omega^2 = 0 \tag{34}$$

which is the dispersive equation for radial macro-displacements of the solid and it depends on the loaded fluid in the cavity. The frequency of classical case can be obtained as a particular case of it by allowing κ tending to zero in Eq. (32). All these results coincide with the results of Somaiah (2016) in empty non-rotating solid. Also, the additional dispersive equation for radial micro-rotations coincides with the result obtained by Somaiah (2016).

4 Numerical Results and Discussion

In order to study numerically the dispersive Eq. (34) and square phase speed $v^2 = \frac{\omega^2 a^2}{\pi^2}$ of radial displacement for $h = \sqrt{\frac{\rho}{\lambda + 2\mu + \kappa}}\omega_0$ with non-dimensional value $\omega_0 = 0.8$ and for non-dimensional amplitude ratios of $\frac{A}{B}$, we have taken the relevant values of

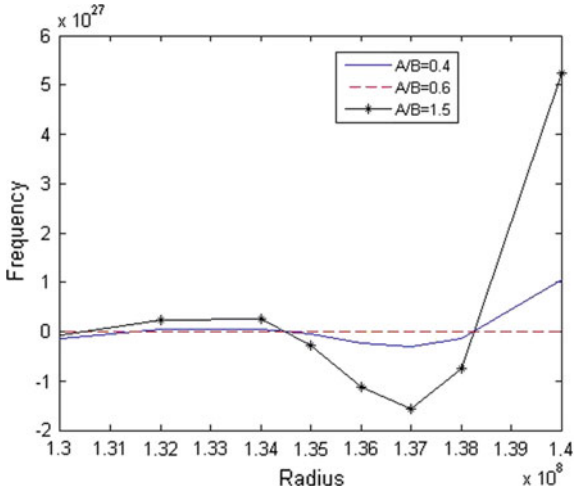

Fig. 1 Frequency versus Radius

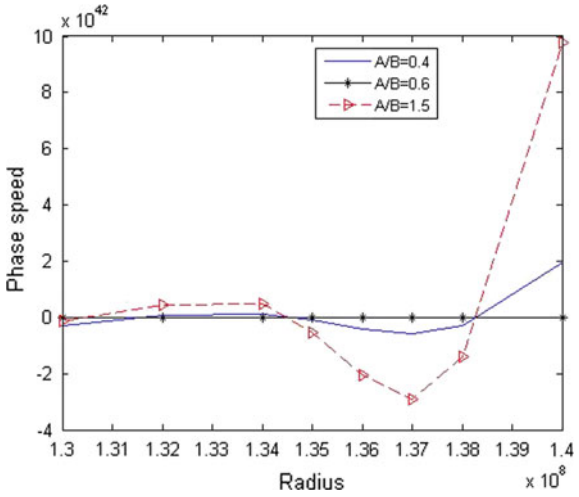

Fig. 2 Phase speed versus Radius

aluminum epoxy as solid material from Deswal and Kumar (2010) and liquid values from Ewing et al. (1957) as follows:

$$\frac{A}{B} = 0.4, 0.6, 1.5, \quad \lambda = 7.59 \times 10^9\,\mathrm{N/m^2}, \quad \mu = 1.89 \times 10^9\,\mathrm{N/m^2},$$
$$\kappa = 0.015 \times 10^9\,\mathrm{N/m^2}, \quad \rho = 2.192 \times 10^3\,\mathrm{kg/m^3}, \quad j = 0.196 \times 10^{-6}\,\mathrm{m^2},$$
$$\xi^{(f)} = 2.14 \times 10^9\,\mathrm{N/m^2} \quad \text{and} \quad \rho^{(f)} = 1.0 \times 10^3\,\mathrm{kg/m^3}.$$

We study the variation of frequency, square phase speed versus non-dimensional radius a with $13 \times 10^7 \leq a \leq 14 \times 10^7$. The variation of frequency versus radius

a for non-dimensional amplitude ratios of $\frac{A}{B}$ is shown in Fig. 1, and the phase speed curves for non-dimensional amplitude ratios of $\frac{A}{B}$ and radius $a = 13.55 \times 10^7$ are shown in Fig. 2. From Figs. 1 and 2, we observed that phase speed and frequency are zero for non-dimensional amplitude ratio is $\frac{A}{B} = 0.6$.

5 Conclusions

This paper considers an unbounded micropolar elastic solid having a fluid loaded spherical cavity of measurable radius. In the study of radial vibrations, it is observed that

(i) The frequency equation for radial macro-displacements is derived which depends on the loaded fluid in the cavity.
(ii) An additional frequency equation for radial micro-rotations coincides with the results of Somaiah (2016), and comparative results are shown in graphically.

References

Blake FG (1952) Spherial wave propagation in solid media. J Acoust Soc Am 24:211–215
Deswal S, Kumar R (2010) Wave motion in a viscous fluid filled bore in a micropolar elastic medium with voids. Proc Natl Acad Sci India A80:223–234
Eringen AC (1957) Elasto-dynamic problem concerning the spherical cavity. Q J Mech Appl Mech 10:257–270
Eringen AC, Suhubi ES (1964) Non-linear theory of simple micro-elastic solids-I. Int J Eng Sci 2:189–203
Ewing WM, Jardetzky WS, Press F (1957) Elastic waves in layered media. The Mac-Graw Hill Company, New York
Ghosh PK (1975) The mathematics of waves and vibration. The Mac-Million Company of India Limited, India
Grey RM, Eringen AC (1955) The elastic sphere under dynamic and impact loads, ONR Technical Report Number 8. Purdue University, Lafayette, Indiana
Kumar R, Divya, Kumar K (2013) Propagation of wave through cylindrical bore in a swelling porous elastic media. Mater Phys Mech 16:135–143
Love AEH (1926) Some problems of geodynamics. Cambridge University Press, London
Love AEH (1944) A treatise on mathematical theory of elasticity, 4th edn. Dover Publications, New York
Rang R, Dimaggio F (1967) Vibrations of fluid filled spherical and spheroidal shells. J Acoust Soc Am 42:1278–1286
Somaiah K (2016) Effect of rotation and micropolarity in an unbounded micropolar elastic solid having a spherical cavity. Comput Sci Math Biol (Special issue) 47–50
Tomar SK, Singh H (2003) Radial vibrations due to a spherical cavity in micropolar elastic solid. Indian J Pure Appl Math 34(12):1785–1796

Unsteady Mixed Convective Flow in a Porous Lid-Driven Cavity with Constant Heat Flux

B. Md. Hidayathulla Khan, V. Ramachandra Prasad and R. Bhuvana Vijaya

Abstract In this paper, we present the numerical analysis of mixed convection in a square cavity filled with porous medium. The left wall of the enclosure is kept at a constant heat flux, and the dimensionless governing equations are solved numerically with Marker and Cell (MAC) method. The numerical results are discussed graphically with the effect of Darcy number, Prandtl number, Rayleigh number, Grashof number, Reynolds number, temperature and streamlines.

Nomenclature

Da	Darcy number
g	Acceleration due to gravity, m s^{-2}
k	Thermal conductivity, Wm^{-1} K^{-1}
L	Length of the square cavity, m
K	Permeability, m^2
N	Total number of nodes
Nu	Local Nusselt number
Gr	Grashof number
T	Temperature, K
U	x component of velocity, m s^{-1}
U	x component of dimensionless velocity
U_0	x lid velocity, m s^{-1}
V	y component of dimensionless velocity
X	Dimensionless distance along x-coordinate
Y	Dimensionless distance along y-coordinate

B. Md. Hidayathulla Khan (✉) · R. Bhuvana Vijaya
Department of Mathematics, JNTU Ananthapur, Anantapuramu 515002, India
e-mail: bmdhkh@gmail.com

V. Ramachandra Prasad
Department of Mathematics, Madanapalle Institute of Technology and Science, Madanapalle 517325, India
e-mail: rcpmaths@gmail.com

M.K. Singh et al. (eds.), *Applications of Fluid Dynamics*, Lecture Notes in Mechanical Engineering, https://doi.org/10.1007/978-981-10-5329-0_32

V y component of velocity, m s^{-1}
p Pressure, Pa
P Dimensionless pressure
Pr Prandtl number
Re Reynolds number
Ri Richardson number

Greek symbols

α Thermal diffusivity, m^2 s^{-1}
β Volume expansion coefficient, K^{-1}
γ Penalty parameter
θ Dimensionless temperature
υ Kinematic viscosity, m^2 s^{-1}
ρ Density, kg m^{-3}
Φ Basis functions
Ψ Stream function

1 Introduction

Mixed convection is generally the combination of free convection and forced convection. Mixed convection, in permeable medium flowing within enclosures, is found in a variety of applications in engineering and geophysical systems like lubrication technologies, cooling of electronic gadgets, drying technologies. The flow and heat transmission caused by shear and buoyancy forces in cavities have been investigated in the literature. An analysis reveals that there are two kinds of studies: the first one is horizontally sliding lid at the upper wall (Iwatsu and Hyun 1995; Mohamad and Viskanta 1991; Prasad and koseff 1996; Freitas and Street 1988; Mohamad and Viskanta 1995; Khanafer and Chamkha 1999; Sharif 2007), and the second one is horizontally sliding lid at the bottom wall (Chen et al. 1981) or oscillating lid (Iwatsu et al. 1992a, b; Nield and Bejan 2006). The bounding case $Ri \to 0$ and $Ri \to \infty$ relates to the forced and natural convection flows separately. The details of Ri in convective stream with permeable medium are discussed well in the books by Pop and Ingham (2001), Bejan et al. (2004), Ingham and Pop (2005), Nield and Bejan (2006) and Vafai (2000, 2005).

Al-Amiri (2000) numerically investigated the energy transfer in a lid-driven square enclosure filled with permeable medium. Stable thermal stratification structure has been observed by introducing a temperature gradient. Nusselt number is correlated within the parameter ranges $Da = 10^{-3} - 10^{0}$ and $Ri = 10^{-2} - 10^{1}$

for fixed value of $Gr = 10^5$. A numerical study has been conducted by Khanafer and Vafai (2002) on mixed convection heat and mass transfer in a lid-driven square enclosure filled with a non-Darcian fluid-saturated permeable medium. Finite-volume technique as well as alternating direction implicit (ADI) method has been used for solving the governing equations numerically. Chin et al. (2007) examined the mixed convection flow past a vertical surface inserted in a permeable medium when the viscosity of the fluid changes with temperature conversely. The influence of oscillating lid temperature on transient mixed convection heat exchange from a permeable vertical surface inserted in a saturated permeable medium with internal heat generation or absorption is studied by Duwairi et al. (2007), and Galerkin finite element method is used to solve the Navier–Stokes equations. Kandaswamy et al. (2008a, b) performed a numerical investigation on mixed convection heat exchange in a square enclosure filled with a fluid-saturated permeable medium. The vertical walls of the cavity are insulated when the top and bottom walls are kept at constant with distinct temperatures. The walls of the lid-driven enclosure are fixed except the top horizontal wall which is moving at a constant speed.

2 Mathematical Modelling and Simulation

The regime under investigation is illustrated in Fig. 1. Consider a two-dimensional square cavity where the walls are thermally insulated except the left wall which is maintained at constant heat flux. The upper wall of the cavity is assumed to move from left to right with uniform velocity, U_0. Thermo-physical properties of the fluid

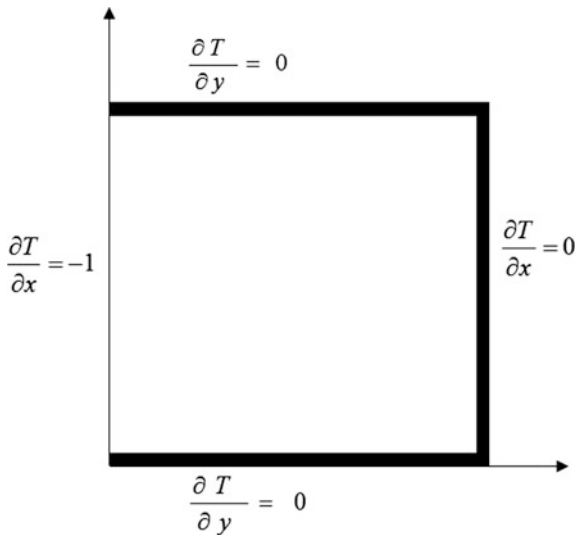

Fig. 1 Schematic diagram of enclosure heat transfer system

such as thermal conductivity, viscosity, specific heat and thermal expansion coefficient are treated as constant. The governing equations for the unsteady two-dimensional natural convection of mass, momentum and energy in the enclosure (cavity) by invoking Boussinesq approximation can be written in non-dimensional form as:

$$\frac{\partial u}{\partial x}+\frac{\partial v}{\partial y}=0. \tag{1}$$

$$\frac{\partial u}{\partial t}+u\frac{\partial u}{\partial x}+v\frac{\partial u}{\partial y}=-\frac{\partial p}{\partial x}+\frac{1}{Re}\left(\frac{\partial^2 u}{\partial x^2}+\frac{\partial^2 u}{\partial y^2}\right)-\frac{1}{Re.Da}u. \tag{2}$$

$$\frac{\partial v}{\partial t}+u\frac{\partial v}{\partial x}+v\frac{\partial v}{\partial y}=-\frac{\partial p}{\partial y}+\frac{1}{Re}\left(\frac{\partial^2 v}{\partial x^2}+\frac{\partial^2 v}{\partial y^2}\right)-\frac{1}{Re.Da}v+Ri.T. \tag{3}$$

$$\frac{\partial T}{\partial t}+u\frac{\partial T}{\partial x}+v\frac{\partial T}{\partial y}=\frac{1}{Re\,Pr}\left(\frac{\partial^2 T}{\partial x^2}+\frac{\partial^2 T}{\partial y^2}\right). \tag{4}$$

The transformed primary and secondary velocity and also thermal boundary conditions are:

$$\begin{aligned}&u(x,1)=1, u(x,0)=u=u(0,y)=u(1,y)=0,\\&v(x,1)=v(x,0)=v(0,y)=v(1,y)=0,\\&\tfrac{\partial T}{\partial x}(0,y)=-1,\ \ \tfrac{\partial T}{\partial x}(1,y)=0,\ \ \tfrac{\partial T}{\partial y}(x,0)=\tfrac{\partial T}{\partial y}(x,1)=0\end{aligned} \tag{5}$$

The dimensionless variables and parameters are defined as:

$$\begin{aligned}&x=X/H,\ \ y=Y/H,\ \ u=U/U_0,\ \ u=V/U_0,\ \ \theta=\frac{T-T_c}{T_h-T_c},\\&p=\frac{P}{\rho U_0^2},\ \ Pr=\frac{v}{\alpha},\ \ Re=\frac{U_0 L}{v},\ \ Ri=\frac{Gr}{Re^2},\ \ Gr=\frac{g\beta(T_h-T_c)L^3}{v^2}.\end{aligned} \tag{6}$$

Here X is dimensionless x-coordinate, Y is dimensionless y-coordinate, U is dimensionless x-direction velocity, V is dimensionless y-direction velocity, θ is dimensionless temperature function, P is dimensionless pressure, Pr is Prandtl number, Re is Reynolds number, Ri is Richardson number, Gr is Grashof number, T is dimensional temperature, p is dimensional pressure, g is gravity, ρ is fluid density, α is thermal diffusivity, v is kinematic viscosity, H is height of enclosure (cavity wall dimension), and t is dimensional time. We note that the emerging thermal Grashof number encompasses the relative influence of gravity (buoyancy) forces to viscous forces in the regime.

3 MAC Numerical Solution and Validation

The momentum and energy balance Eqs. (2)–(4) have been solved using the Marker and Cell (MAC) method (Amsden and Harlow 1970). The pressure distribution is obtained by making use of continuity Eq. (1). The numerical solutions are carried out in terms of the velocity components (u, v) and stream functions (ψ). As per the Cauchy–Riemann equations, stream function (ψ) is defined as $u = \frac{\partial \psi}{\partial y}$ and $v = -\frac{\partial \psi}{\partial x}$, where positive and negative signs of ψ denote anticlockwise and clockwise circulations, respectively. In the MAC approach, although we consider viscous flow, viscosity is not actually required for numerical stability (Amsden and Harlow 1970). Cell boundaries are labelled with half-integer values in the finite difference discretization. The marker particles do not participate in the calculation. Here we elaborate on the numerical discretization procedure. Based on the weak conservative form of the unsteady two-dimensional Navier–Stokes equations and heat conservation equation as defined by Eqs. (1)–(4), we implement a grid meshing procedure using the following notation at the centre of a cell:

$$u_{i-1/2,j} = \frac{1}{2}\left[u_{i-1,j} + u_{i,j}\right]. \tag{7}$$

Applying to the x-direction momentum conservation Eq. (2) we have:

Discretized advection terms:

$$\frac{\partial(uu)}{\partial x} = \frac{uu1 - uu2}{\Delta x} \tag{8}$$

where

$$\begin{aligned} uu1 &= \left[\frac{1}{2}\left(u_{i,j} + u_{i+1,j}\right)\right]^2 \\ uu2 &= \left[\frac{1}{2}\left(u_{i-1,j} + u_{i,j}\right)\right]^2 \end{aligned} \tag{9}$$

Similarly, we have:

$$\frac{\partial(uv)}{\partial y} = \frac{uv1 - uv2}{\Delta y} \tag{10}$$

where

$$\begin{aligned} uv1 &= \frac{1}{2}\left(u_{i,j} + u_{i,j+1}\right).\frac{1}{2}\left(v_{i,j} + v_{i+1,j}\right) \\ uv2 &= \frac{1}{2}\left(u_{i,j} + u_{i,j-1}\right).\frac{1}{2}\left(v_{i,j-1} + v_{i+1,j-1}\right) \end{aligned} \tag{11}$$

The following central difference formula is used for the second-order derivatives:

$$\begin{aligned}\nabla^2 u &= \frac{\partial^2 u}{\partial x^2} + \frac{\partial^2 u}{\partial y^2} \\ \nabla^2 u &= \frac{u_{i-1,j} - 2u_{i,j} + u_{i+1,j}}{\Delta x^2} + \frac{u_{i,j-1} - 2u_{i,j} + u_{i,j+1}}{\Delta y^2}\end{aligned} \tag{12}$$

Applying to the y-direction momentum conservation Eq. (3) we have:

Advection term:

$$\frac{\partial(vu)}{\partial x} = \frac{vu1 - vu2}{\Delta x} \tag{13}$$

Here the following notation applies:

$$\begin{aligned} uv1 &= \frac{1}{2}\left(u_{i,j+1} + u_{i,j}\right).\frac{1}{2}\left(v_{i,j} + v_{i+1,j}\right) \\ uv2 &= \frac{1}{2}\left(u_{i-1,j+1} + u_{i-1,j}\right).\frac{1}{2}\left(v_{i,j} + v_{i-1,j}\right) \\ \frac{\partial(vv)}{\partial y} &= \frac{vv1 - vv2}{\Delta y} \\ vv1 &= \left[\frac{1}{2}\left(v_{i,j+1} + v_{i,j}\right)\right]^2. \\ vv2 &= \left[\frac{1}{2}\left(v_{i,j-1} + v_{i,j}\right)\right]^2 \end{aligned} \tag{14}$$

The central difference formula for the Laplacian operator is given by:

$$\begin{aligned}\nabla^2 v &= \frac{\partial^2 v}{\partial x^2} + \frac{\partial^2 v}{\partial y^2} \\ \nabla^2 v &= \frac{v_{i-1,j} - 2v_{i,j} + v_{i+1,j}}{\Delta x^2} + \frac{v_{i,j-1} - 2v_{i,j} + v_{i,j+1}}{\Delta y^2}\end{aligned} \tag{15}$$

Effectively, the x-momentum equation discretization technique can be summarized as:

$$\tilde{u} = u^n + \mathrm{d}t.\left[-\left(u\frac{\partial u}{\partial x} + v\frac{\partial u}{\partial y}\right) + \alpha_1\left(\frac{\partial^2 u}{\partial x^2} + \frac{\partial^2 u}{\partial y^2}\right) - \alpha_2 u\right] \tag{16}$$

where $\alpha_1 = 1/Re$ and $\alpha_2 = 1/Re.Da$. There is a slight modification needed in the y-momentum equation due to the addition of a new term. Therefore, this term must be included in the discretized equation, and we have:

$$\tilde{v} = v^n + \mathrm{d}t.\left(-\left[u\frac{\partial v}{\partial x} + v\frac{\partial v}{\partial y}\right] + \alpha_1\left(\frac{\partial^2 v}{\partial x^2} + \frac{\partial^2 v}{\partial y^2}\right) - \alpha_2 v + \beta.T\right) \tag{17}$$

where $\alpha_1 = 1/Re$, $\alpha_2 = 1/Re.Da$, and $\beta = Gr/Re^2$. It is further noteworthy that the temperature term T is co-located such that it coincides with velocity before using it in the above equation to account for the staggered grid. After $\tilde{u}$ and $\tilde{v}$ are projected to get u and v by Poisson pressure equation.

$$\frac{\nabla.u^*}{dt} = \nabla^2 p$$

We can use the discretized temperature equation to get T at next time level (T^{n+1}) via the algorithm:

$$T^{n+1} = T^n + \Delta t.\left[-\left(u\frac{\partial T}{\partial x} + v\frac{\partial T}{\partial y}\right) + \chi\left(\frac{\partial^2 T}{\partial x^2} + \frac{\partial^2 T}{\partial y^2}\right)\right] \tag{18}$$

where $\chi = \frac{1}{Re\,Pr}$. Next, we integrate in time by an incremental step dt in each iteration until the final time $t = 1.0$ is reached. The variables are co-located and plotted. Modern variants of the MAC method utilize the conjugate gradient schemes which solve the Poisson equation. Further details are provided in Amsden and Harlow (1970). To confirm mesh independence, a Grid Independence Study is conducted. In computational fluid dynamics, of which finite difference simulation is merely one methodology, once a mesh provides a solution which is invariant with the finer meshes, the coarser mesh can be adopted. This reduces computational cost but retains the necessary accuracy. Table 1 shows that accuracy to three decimal places is achieved for Nusselt number at the left wall with a mesh of 61 × 61 which is sufficient for heat transfer computations, and therefore, this is adopted for all subsequent simulations.

Furthermore to corroborate the present computations, visualizations of the temperature (isotherm) and streamline distributions for two special cases have been provided. These replicate the solutions of Kandaswamy et al. (2008a, b). The equivalent Rayleigh number used in Kandaswamy et al. (2008a, b) is merely the product of the thermal Grashof number and Prandtl number used in the present model (i.e. $Ra = Gr\,Pr$). Generally, very close correlation is attained as observed in Figs. 2 and 3, and confidence in the present MAC computational code is therefore justifiably high.

Table 1 Grid Independence Study

Grid size	Average Nusselt number (Nu)
21 × 21	0.1500
31 × 31	0.1525
41 × 41	0.1554
51 × 51	0.1587
61 × 61	0.1592

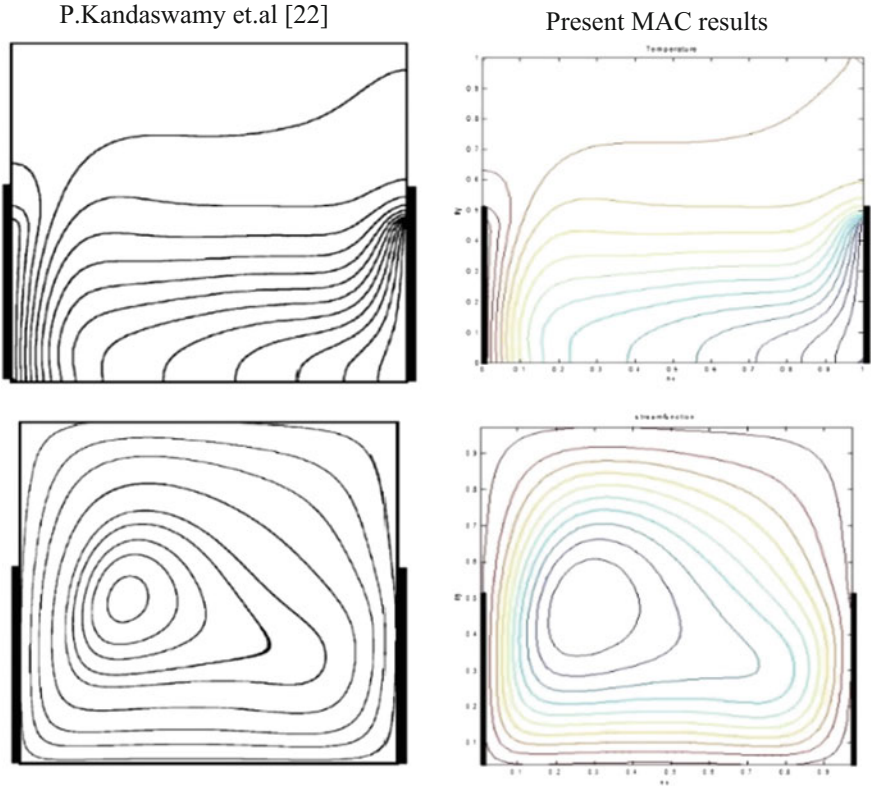

Fig. 2 Comparison contour plots, for bottom–bottom thermal condition vertical walls with $Pr = 0.71, Gr = 10^5, Ha = 10$

4 MAC Numerical Results and Discussion

In this present investigation, the Reynolds number is kept constant at Re = 100. Numerical solutions of flow and temperature fields are obtained for various values of $Da(Da = 10^{-3} - 10^{0})$, $Pr(Pr = 0.71)$, and $Ri(Ri = 0.01 - 10)$ within a lid-driven permeable square cavity. The heat transfer in the lid-driven porous cavity is convection for values of parameters (Re, Pr, Gr) for any Da. Figures 4, 5 and 6a–d show the streamlines and temperature contours for heat flux of left wall, and remaining walls are thermally insulated with different Ri. Figure 3 shows the effect of Darcy number for $Pr = 0.71, Re = 100$ and $Gr = 10^2$. At low Richardson Number $Ri(Ri = 10^{-3})$, the effect of mixed convection seems to be dominant. Figure 3a indicates the primary streamline circulation occupies the cavity fully; however, the strength of the circulation is weak at $Da = 10^{-3}$. The corresponding isotherms are parallel to the vertical wall at the left-side portion of the driven cavity as the flow is stagnant. Figure 3b shows that the primary streamline cell moves to

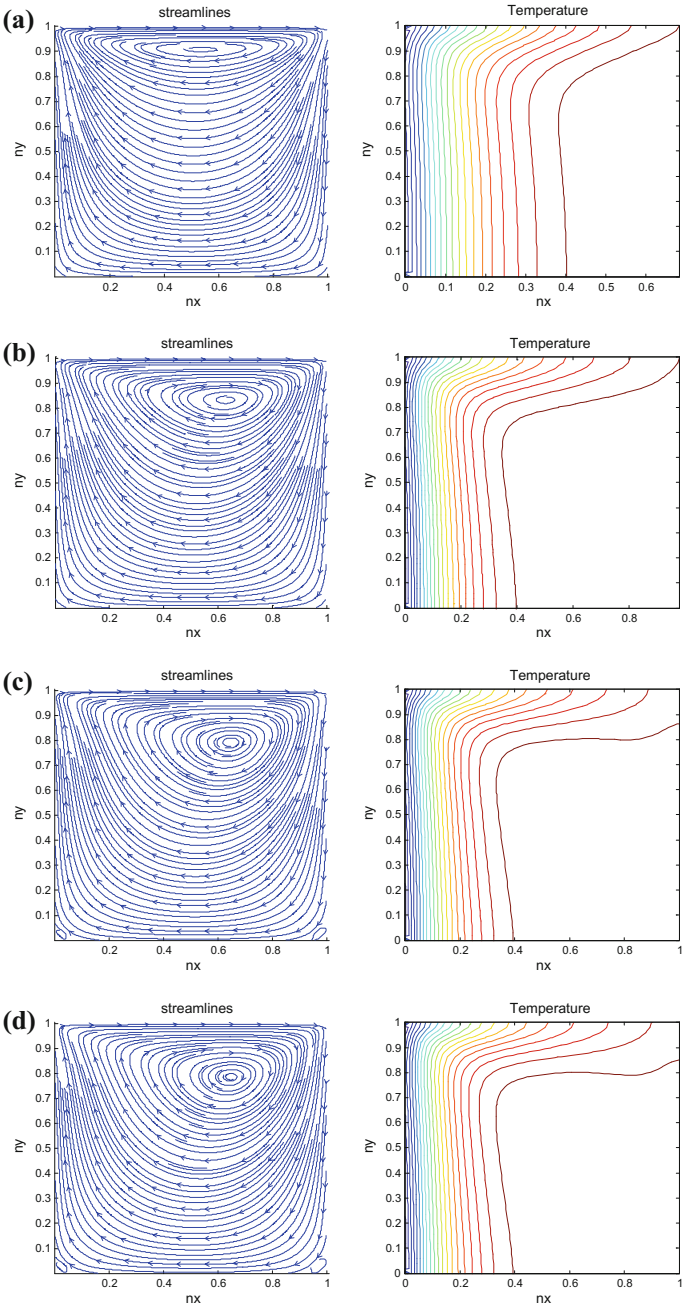

Fig. 3 Streamlines and isotherms for $Re = 100, Ri = 0.01$, **a** $Da = 0.001$, **b** $Da = 0.01$, **c** $Da = 0.1$, **d** $Da = 1$

the right wall of top corner under the effect of Darcy number $Da = 10^{-2}$. The corresponding isotherms are more concentrated at the left vertical wall. Figure 3c shows the streamlines for the effect of Darcy number $Da = 10^{-1}$. The single enlarged cell moves towards the right vertical wall, and the corresponding isotherms indicate that the convective heat transfer is zero at the bottom right vertical wall. The nature of streamlines is same in Fig. 3c, and the corresponding isotherms in Fig. 3d reveal the convective mode of heat transfer at the bottom region of the right wall of the enclosure is thermally inactive.

Figure 4 shows the effect for various Darcy numbers for $Pr = 0.71$ and fixed $Ri(Ri = 0.1)$. It will repeat same contours.

Figure 5 shows the effect for various Darcy numbers for $Pr = 0.71$, $Re = 100$ and fixed $Ri(Ri = 1)$. Two developed clockwise-rotating vortices are seen inside the cavity in Fig. 5a: first one is the fully formed vortex on top wall, and second one is very small vortex formed at the left side of the bottom wall. The corresponding isotherms are parallel to the left wall of the cavity by the effect of Darcy number $Da = 0.001$. Figure 5b–d shows the effect of Darcy numbers $Da = 0.01, 0.1, 1$. The streamlines are formed as two rotating vortices: fully formed vortex cell is located near top wall, and a small vortex cell is formed at left-side corner of bottom wall of the cavity, the size of the small vortex increases as the Darcy number is increased. The corresponding isotherms are more concentrated near the heat flux wall with the formation of thermal boundary layer, the energy is transferred in right corner of bottom wall, and right vertical wall of lid-driven cavity is thermally inactive.

Figure 6 shows the effect for various Darcy numbers for $Pr = 0.71$, $Re = 100$ and fixed $Ri(Ri = 10)$. The mirror image effect is shown in Fig. 6a for streamline contours with Darcy number $Da = 0.001$. The corresponding isotherms indicate the heat transfer is decreased at the right side of the vertical wall and the rate of heat transfer is high at the left wall and top moving lid. Figure 6b–c, shows that two fully developed clockwise circulations are formed in the cavity, the primary circulation is formed at the right side of the corner top wall and top corner right side walls, and also secondary circulation is formed at the bottom of left vertical wall and left side of bottom wall. The corresponding isotherms indicate that the isotherms occupy only left and moving top wall. The convective heat transfer is zero at the right wall and right side of the bottom wall of lid-driven porous cavity by the effect of Darcy number $Da = 0.01, Da = 0.1$. The influence of Darcy number $Da = 1$ on porous cavity shows that the streamlines are formed in two circulations diagonally as shown in Fig. 6d. Mixed convection is lesser due to less thermal gradient induced by thermal mixing.

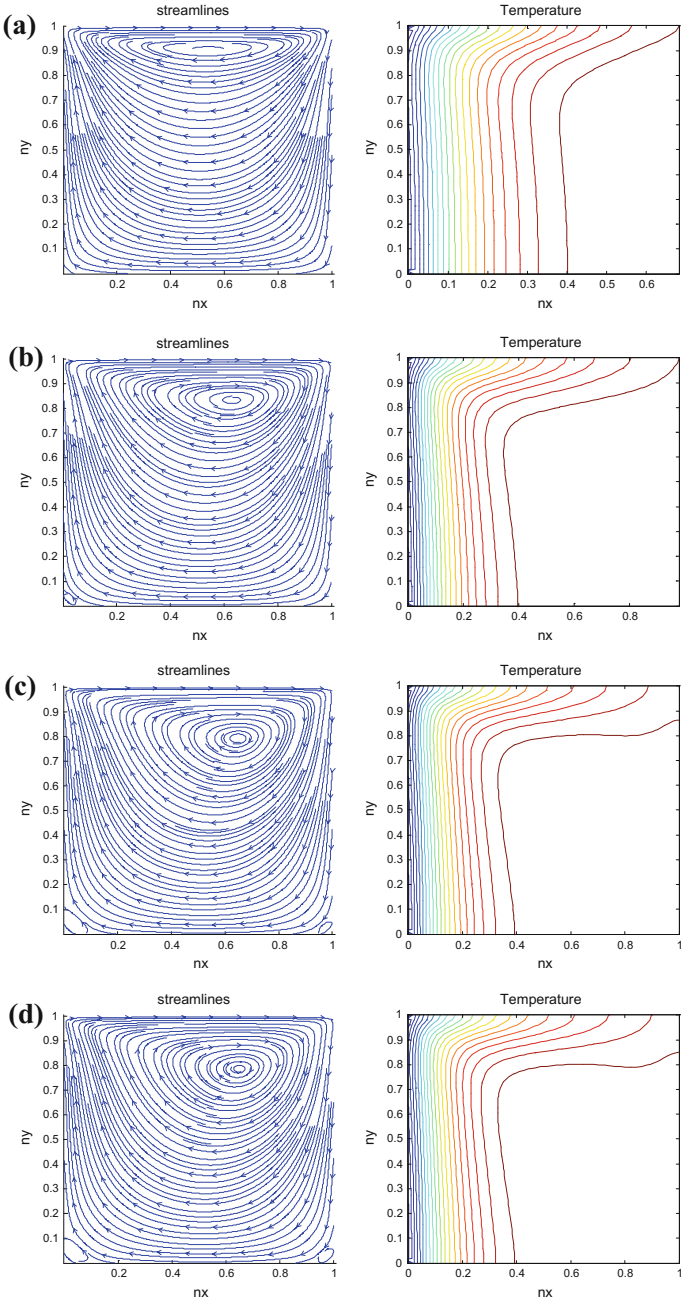

Fig. 4 Streamlines and isotherms for $Re = 100, Ri = 0.1$, **a** $Da = 0.001$, **b** $Da = 0.01$, **c** $Da = 0.1$, **d** $Da = 1$

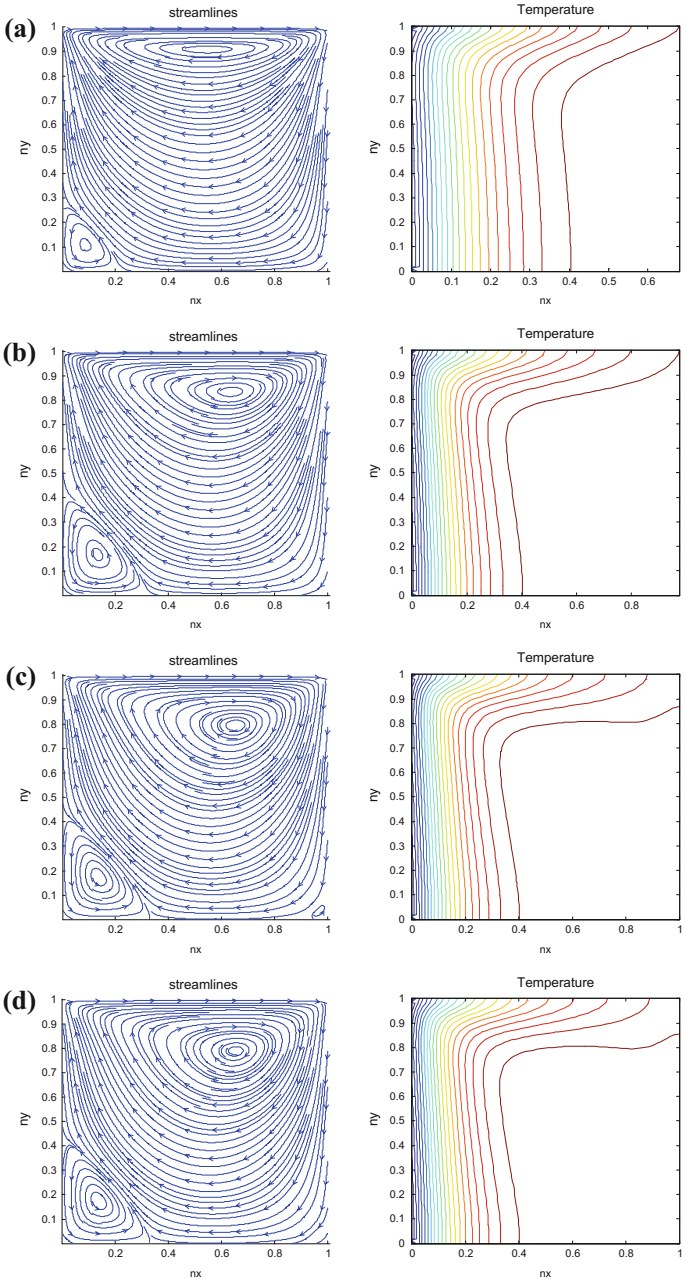

Fig. 5 Streamlines and isotherms for $Re = 100, Ri = 1$, **a** $Da = 0.001$, **b** $Da = 0.01$, **c** $Da = 0.1$, **d** $Da = 1$

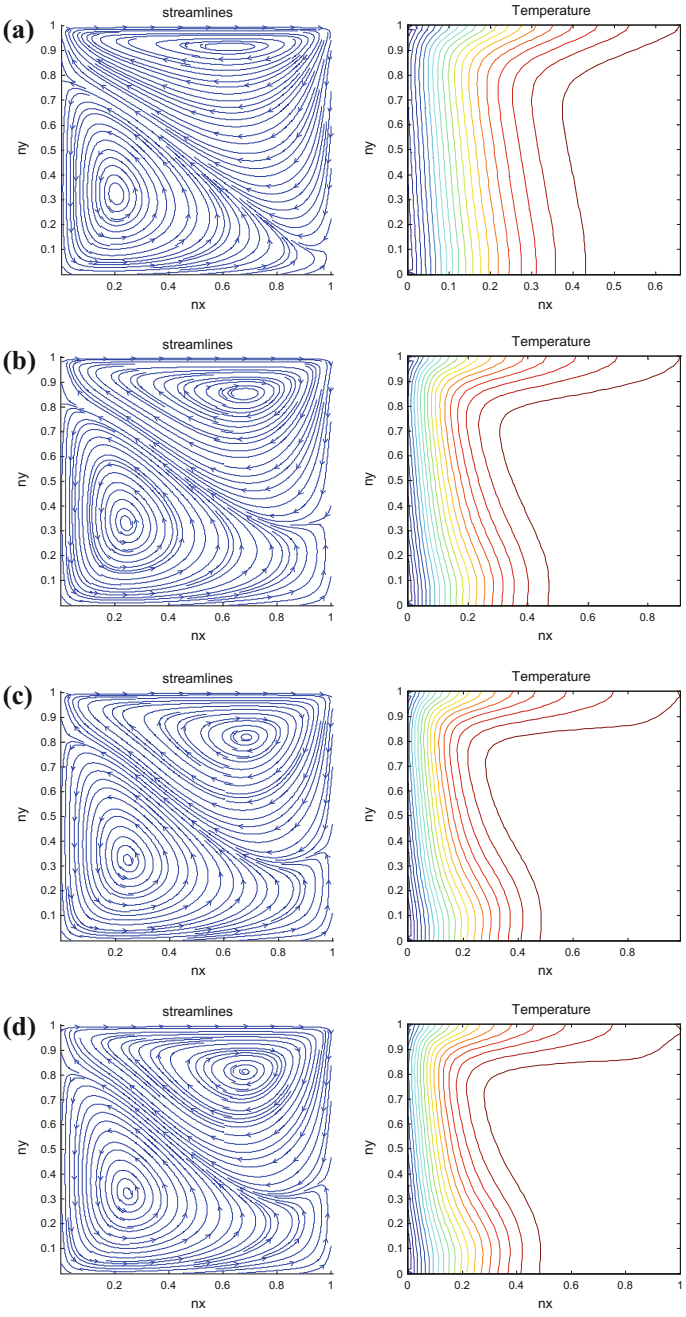

Fig. 6 Streamlines and isotherms for $Re = 100, Ri = 10$, **a** $Da = 0.001$, **b** $Da = 0.01$, **c** $Da = 0.1$, **d** $Da = 1$

5 Conclusions

The influence of heat flux on the left wall and the remaining walls is adiabatic on the flow, and heat exchange characteristics due to lid-driven mixed convection flow within a permeable square cavity have been studied in the present investigation. It is observed that the heat exchange rate is decreased for high Ri with Darcy number $Da = 1$. Heat transfer rate is enhanced for low $Ri(Ri = 0.01)$ and Darcy number $Da(Da = 0.001)$. The flow rate is increased for decrease in Darcy number. For increase in the Richardson number Ri in all cases, the flow rate is also enhanced.

References

Al-Amiri AM (2000) Analysis of momentum and energy transfer in a lid-driven cavity filled with a porous medium. Int J Heat Mass Transf 43:3513–3527

Amsden AA, Harlow FH (1970) A simplified MAC technique for incompressible fluid flow calculations. J Comp Phys 6:322–325

Bejan A, Dincer I, Lorente S, Miguel AF, Reis AH (2004) Porous and complex flow structures in modern technologies. Springer, New York

Chen CJ, Neshat HN, Ho KS (1981) Finite-analytical numerical solution of heat transfer in two-dimensional cavity flow. Numer Heat Transf 4:179–197

Chin KE, Nazar R, Arifin NM, Pop I (2007) Effect of variable viscosity on mixed convection boundary layer flow over a vertical surface embedded in a porous medium. Int Commun Heat Mass Transf 34:464–473

Duwairi HM, Damseh RA, Tashtoush (2007) Transient mixed convection along a vertical plate embedded in porous media with internal heat generation and oscillating temperature. Chem Eng Commun 194:1516–1530

Freitas CF, Street RL (1988) Non-linear transient phenomena in a complex recirculating flow: a numerical investigation. Int J Num Methods Fluids 8:769–802

Ingham DB, Pop I (eds) (2005) Transport phenomena in porous media, vol 3. Elsevier, Oxford

Iwatsu R, Hyun JM (1995) Three-dimensional driven-cavity flows with a vertical temperature gradient. Int J Heat Mass Transf 38:19–28

Iwatsu R, Hyun JM, Kuwahara K (1992a) Convection in a differentially heated square cavity with a torsionally-oscillating lid. Int J Heat Mass Transf 35:1069–1076

Iwatsu R, Hyun JM, Kuwahara K (1992b) Numerical simulation of flows driven by a torsionally-oscillating lid in a square cavity. J Fluids Eng 114:143–149

Kandaswamy P et al (2008a) Magnetoconvection in an enclosure with partially active vertical walls. Int J Heat Mass Transf 51:1946–1954

Kandaswamy P, Muthtamilselvan M, Lee J (2008b) Prandtl number effects on mixed convection in a lid-driven porous cavity. J Porous Media 11:791–801

Khanafer KM, Chamkha AJ (1999) Mixed convection flow in a lid-driven enclosure with a fluid-saturated porous medium. Int J Heat Mass Transf 42:2465–2481

Khanafer K, Vafai K (2002) Double-diffusive mixed convection in a lid-driven enclosure filled with a fluid-saturated porous medium. Numer Heat Transf A 42:465–486

Mohamad AA, Viskanta R (1991) Transient low Prandtl number fluid convection in a liddriven cavity. Numer Heat Transf Part A 19:187–205

Mohamad AA, Viskanta R (1995) Flow and heat transfer in a lid-driven cavity with stably stratified fluid. Appl Math Model 19:465–472

Nield DA, Bejan A (2006) Convection in porous media, 3rd edn. Springer, Berlin

Pop I, Ingham DB (2001) Convective heat transfer: mathematical and computational modelling of viscous fluids and porous media. Pergamon Press, Oxford
Prasad AK, Koseff JR (1996) Combined forced and natural convection heat transfer in a deep lid-driven cavity flow. Int J Heat Fluid Flow 17:460–467
Sharif MAR (2007) Laminar mixed convection in shallow inclined driven cavities with hot moving lid on top and cooled from bottom. Appl Therm Eng 27:1036–1042
Vafai K (ed) (2000) Handbook of porous media. Marcel Dekker, New York
Vafai K (ed) (2005) Handbook of porous media, 2nd edn. Taylor & Francis, New York

Chemically Reactive-Free Convective MHD Flow of Rivlin-Ericksen Fluid Past a Movable Vertical Plate Enriched in Porous Material

Pooja Sharma and Ruchi Saboo

Abstract The chemically reactive viscous incompressible electrically conducting free convective flow of Rivlin-Ericksen fluid along a vertical semi-infinite moving permeable plate enriched in the porous material with existence of crosswise magnetic field and pressure gradient in the presence of variable suction has been considered. The study of heat transfer due to magnetic field is also done. The heat, continuity, and mass equations are solved, and their respective results are shown through graphs. In addition to that, Nusselt number, skin friction coefficient, and Sherwood number are also measured and depicted through tables. It was concluded from the actual study that highly chemically reacting Rivlin-Ericksen fluid flow becomes slow, but it can be accelerated for the values of high mass buoyancy.

Nomenclature

$\overline{C}$	Species concentration
$\bar{t}$	Time
$\bar{u}$	Fluid velocity along the plate
y	Non-dimensional distance along y-axis
β	Volumetric coefficient of expansion with species concentration
M	Hartmann number
K_1	Chemical reaction parameter
α	Thermal diffusivity
K_p	Porosity parameter
g	Acceleration due to gravity
γ	Chemical reaction coefficient
$\in$	A small positive constant
ρ	Fluid density

P. Sharma (✉) · R. Saboo
Department of Mathematics & Statistics, Manipal University Jaipur, Jaipur 303007, India
e-mail: pooja_2383@yahoo.co.in

R. Saboo
e-mail: ruchipsaboo@gmail.com

M.K. Singh et al. (eds.), *Applications of Fluid Dynamics*, Lecture Notes in Mechanical Engineering, https://doi.org/10.1007/978-981-10-5329-0_33

B_0 Magnetic field of even strength
υ Kinematic viscosity
Sc Schmidt number
τ Skin friction
v Non-dimensional velocity normal the plate
$\overline{C}_w$ Species concentration at wall
$\overline{T}_\infty$ Fluid temperature far from the surface
$\overline{T}_w$ Wall temperature
$\overline{K}p$ Permeability of the medium
$\overline{T}$ Temperature of the fluid
$\bar{y}$ Distance along y-axis
θ Dimensionless fluid temperature
Rc Dimensionless viscoelastic parameter of the Rivlin-Ericksen fluid
t Non-dimensional time
u Non-dimensional velocity along the plate
Ec Eckert number
$\overline{U}_\infty$ Free stream velocity
D Mass diffusivity
U_p Constant velocity of moving plate
$\bar{v}$ Velocity of the fluid in y direction
Nu Nusselt number
Gc Grashof number for mass transfer
Sh Sherwood number
Pr Prandtl number
C_f Skin friction coefficient
σ Electrical conductivity
C Non-dimensional species of concentration
$\overline{C}_\infty$ Species concentration far from the surface
K_0 Kinematic viscoelasticity

1 Introduction

The study of energy and mass transfer in the fluid flow through various geometries entrenched in porous medium has numerous industrial and geophysical usages like dehydrating of porous solids, thermal insulations, cooling of electronics system, nuclear reactors, abstraction of crude oil, many chemical processes, filtration of ground water, granular insulation.

Chamkha (1996) discussed the natural convection past a vertical surface immersed in a porous medium with magnetic effects. In the same external conditions, Eldabe and Mohamed (2002) analyzed the flow of the non-Newtonian fluid in the presence of heat source.

The flow of chemically reactive fluid with many external environmental conditions has the significance in process industries and has consequently a substantial extent of attraction in last decays. MHD boundary layer flow is of extensive attention in MHD power generation systems and liquid metal fluids. Due to its wide range of submissions, many researchers have explored the magnetic field effect on the fluid problems.

Ananda et al. (2009) examined the ohmic heated flow with hydromagnetic conditions. Sharma et al. (2011) also discussed the chemically reactive and radiative flow along the vertical porous wall with the same environments. Sahin and Zueco (2010) analyzed the problem of flow in vertically upward direction with the impact of external heat source and chemical reaction. Then, Sharma et al. (2015) extended the same study for viscoelastic fluid (Walter's liquid model-B).

Darcy's law represents the gross effect, when a porous material permeated by a fluid. Therefore, the general viscous term in Rivlin-Ericksen fluid equation is presented by $\left[-\frac{1}{\bar{k}}\left(\bar{\mu}+\bar{\mu}^{*}\frac{\partial q^{*}}{\partial t^{*}}\right)\right]$, where $\bar{\mu}$ is the viscosity of the fluid, $\bar{\mu}^{*}$ is viscoelasticity of Rivlin-Ericksen fluid, q^{*} is the fluid velocity due to Darcy effect, and $\bar{\kappa}$ is the permeability of medium. In the physical world, the study of the Rivlin-Ericksen fluid flow through a porous medium has become a major application recapture of crude oil from the pores of reservoir rocks.

In view of that, Daleep and Ajaib (2012) discussed the rate of complex growth in the flow of Rivlin-Ericksen viscoelastic fluid in porous medium. Rana (2012) extended his work to demonstrate the thermal instability in rotating fluid saturated with suspended dust particles. Kumar et al. (2013) discussed the Rivlin-Ericksen viscoelastic flow past an impulsively started vertical plate with variable temperature and concentration. Then, Rana and Chand (2013) further studied the Rivlin-Ericksen double-diffusive convection fluid flow in a Brinkman porous medium.

In recent years, Popoola et al. (2016) analyzed the effect of MHD viscoelastic fluid flow in the presence of heat and mass transfers with chemical reaction. Then, Ravikumar et al. (2014) extend the work of Kumar et al. (2013) by considering the same flow with MHD and variable suction.

In above of the mentioned work, the chemical reaction effect on mass transfer has not been analyzed in Rivlin-Ericksen fluid flow. In the present paper, the impact of chemical reaction and variable temperature has been studied in unsteady fluid flow along a semi-infinite vertical moving permeable plate entrenched in the porous medium with uniform transverse magnetic field and suction.

2 Mathematical Formulation

Unsteady flow of viscous immiscible incompressible electrically conducting Rivlin-Ericksen fluid flow along a moveable vertical semi-infinite porous plate enriched is considered in a uniform porous medium subjected to constant transverse magnetic field (Fig. 1).

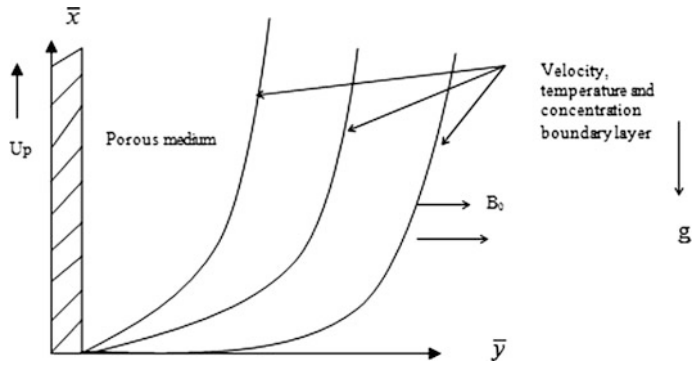

Fig. 1 Geomaterical configuration

Let $\bar{x}$-axis be vertically upward along the plate and in the direction of flow, and $\bar{y}$-axis is existing in its crosswise direction. In the beginning of the fluid flow, we are presuming that the vertical surface and existing fluid have the equal temperature T and concentration C throughout the fluid flow region. When time increases ($t > 0$), $\overline{T}_w$ and $\overline{C}_w$ are the new temperature and mass concentration, respectively, of the fluid nearby the plate.

The following postulation is made throughout the fluid flow:

(i) The applied magnetic field is perpendicular to the direction of flow, and induced magnetic field is supposed to be insignificant in comparison with the applied magnetic field; therefore, the Reynolds number becomes negligible.
(ii) The vertical permeable plate is supposed to move by a persistent rate of speed in the fluid flow way from downward to upward direction in positive x-axis. Free stream velocity, wall temperature, and species concentration at plate are following the small perturbation law in terms of the exponentially increasing order.
(iii) Dissipation due to viscosity and magnetic field is supposed to be neglected in the study.

By using these statements, the fluid flow regulating differential equations are as follows:

$$\frac{\partial \bar{v}}{\partial \bar{y}} = 0, \tag{1}$$

$$\frac{\partial \bar{u}}{\partial \bar{t}} + \bar{v}\frac{\partial \bar{u}}{\partial \bar{y}} = -\frac{1}{\rho}\frac{\partial \bar{p}}{\partial \bar{x}} + \upsilon\frac{\partial^2 \bar{u}}{\partial \bar{y}^2} + g\beta\left(\overline{C} - \overline{C}_\infty\right) - \upsilon\frac{\bar{u}}{\overline{K}p} - \frac{\sigma B_0^2}{\rho}\bar{u} - \frac{K_0}{\rho}\left(\frac{\partial^3 \bar{u}}{\partial \bar{t}\partial \bar{y}^2} + \bar{v}\frac{\partial^3 \bar{u}}{\partial \bar{y}^3}\right), \tag{2}$$

$$\frac{\partial \overline{T}}{\partial \bar{t}} + \bar{v}\frac{\partial \overline{T}}{\partial \bar{y}} = \frac{\kappa}{\rho Cp}\frac{\partial^2 \overline{T}}{\partial \bar{y}^2} + \frac{\sigma B_0^2}{\rho Cp}\bar{u}^2 + \frac{\mu}{\overline{K}p\rho Cp}\bar{u}^2, \tag{3}$$

$$\frac{\partial \overline{C}}{\partial \bar{t}} + \bar{v}\frac{\partial \overline{C}}{\partial \bar{y}} = D\frac{\partial^2 \overline{C}}{\partial \bar{y}^2} - K_l\left(\overline{C} - \overline{C}_\infty\right), \tag{4}$$

Then, the boundary conditions are shown as follows:

$$\begin{aligned} &\bar{y} \to \infty : \ \bar{u} \to \overline{U}_\infty = U_0\left(1 + \in \mathrm{e}^{\bar{n}\bar{t}}\right), \ \ \overline{T} \to T_\infty, \ \ \overline{C} \to C_\infty, \\ &\bar{y} = 0 : \ \bar{u} = \bar{u}_p, \ \ \overline{T} = \overline{T}_w + \in \left(\overline{T}_w - \overline{T}_\infty\right)\mathrm{e}^{\bar{n}\bar{t}}, \ \ \overline{C} = \overline{C}_w + \in \left(\overline{C}_w - \overline{C}_\infty\right)\mathrm{e}^{\bar{n}\bar{t}}, \end{aligned} \tag{5}$$

The suction velocity at the plate surface is time dependent and given as

$$\bar{v} = -V_0\left(1 + \in A\mathrm{e}^{\bar{n}\,\bar{t}}\right), \tag{6}$$

where V_0 is the mean suction velocity, A real constant, and $\in A \ll 1$. For the outside region of the boundary layer, Eq. (2) follows

$$-\frac{1}{\rho}\frac{\partial \bar{p}}{\partial \bar{x}} = \frac{\mathrm{d}\overline{U}_\infty}{\mathrm{d}\bar{t}} + \frac{\nu}{\overline{K}p}\overline{U}_\infty + \frac{\sigma}{\rho}B_0^2\overline{U}_\infty. \tag{7}$$

3 Method of Solution

By taking the subsequent dimensionless quantities

$$\begin{aligned} &u = \frac{\bar{u}}{U_0}, \ \ v = \frac{\bar{v}}{V_0}, \ \ y = \frac{V_0\bar{y}}{\nu}, \ \ U_\infty = \frac{\overline{U}_\infty}{U_0}, \ \ U_p = \frac{\bar{u}_p}{U_0}, \\ &\theta = \frac{\overline{T} - \overline{T}_\infty}{\overline{T}_w - \overline{T}_\infty}, \ \ K_p = \frac{\overline{K}pV_0^2}{\nu^2}, \ \ Pr = \frac{\nu}{\alpha}, \ \ M = \frac{\sigma B_0^2\nu}{\rho V_0^2}, \\ &Rc = \frac{K_0V_0^2}{\nu^2}, \ \ \gamma = \frac{K_l\upsilon}{V_0^2}, \ \ Ec = \frac{U_0^2}{Cp\left(\overline{T}_w - \overline{T}_\infty\right)}, \ \ N = M + \frac{1}{K_p}, \\ &C = \frac{\overline{C} - \overline{C}_\infty}{\overline{C}_w - \overline{C}_\infty}, \ \ t = \frac{\bar{t}V_0^2}{\nu}, \ \ Sc = \frac{\nu}{D}, \ \ Gc = \frac{\nu g\beta\left(\overline{C}_w - \overline{C}_\infty\right)}{U_0V_0^2}, \ \ n = \frac{\bar{n}\nu}{V_0^2}, \end{aligned} \tag{8}$$

into Eqs. (1)–(4) with Eqs. (6) and (7), we get

$$\frac{\partial u}{\partial t} - (1 + \in Ae^{nt})\frac{\partial u}{\partial y} = \frac{dU_\infty}{dt} + \frac{\partial^2 u}{\partial y^2} + Gc\,C + N(U_\infty - u) - Rc\left[\frac{\partial^3 u}{\partial t \partial y^2} - (1 + \in Ae^{nt})\frac{\partial^3 u}{\partial y^3}\right], \tag{9}$$

$$\frac{\partial \theta}{\partial t} - (1 + \in Ae^{nt})\frac{\partial \theta}{\partial y} = \frac{1}{Pr}\frac{\partial^2 \theta}{\partial y^2} + MEcu^2 + \frac{Ec}{K_p}u^2, \tag{10}$$

$$\frac{\partial C}{\partial t} - (1 + \in Ae^{nt})\frac{\partial C}{\partial y} = \frac{1}{Sc}\frac{\partial^2 C}{\partial y^2} - \gamma C, \tag{11}$$

The boundary conditions (5) are changed into

$$\begin{aligned} &y = 0: \; u = U_p, \;\; \theta = 1 + \in e^{nt}, \;\; C = 1 + \in e^{nt}, \\ &y \to \infty: \; u \to U_\infty, \;\; \theta \to 0, \;\; C \to 0, \end{aligned} \tag{12}$$

The Eqs. (9)–(11) are the non-linear partial differential equations and to solve them we separate the steady and unsteady parts of velocity field, temperature field and concentration field by using the following expressions.

$$u(y,t) = u_0(y) + \in u_1(y)e^{nt} + O(\in^2) + \cdots, \tag{13}$$

$$\theta(y,t) = \theta_0(y) + \in \theta_1(y)e^{nt} + O(\in^2) + \cdots, \tag{14}$$

$$C(y,t) = C_0(y) + \in C_1(y)e^{nt} + O(\in^2) + \cdots, \tag{15}$$

where u_0, θ_0, C_0 denote steady parts and u_1, θ_1, C_1 denote unsteady parts. Equations (13)–(15) are substituted into the Eqs. (9)–(11), and then, harmonic and non-harmonic terms are equated. Here, we are assuming to neglect the higher order term of $\in$.

Zeroth-order equations

$$Rc\,u_0^{***} + u_0^{**} + u_0^{*} - N\,u_0 = -Gc\,C_0 - N, \tag{16}$$

$$\theta_0^{**} + \theta_0^{*} Pr = -MEcPr\,u_0^2 - \frac{Ec}{K_p}Pru_0^2, \tag{17}$$

$$C_0^{**} + C_0^{*} Sc - \gamma Sc\,C_0 = 0, \tag{18}$$

First-order equations

$$Rc\,u_1^{***} + (1 - Rc\,n)u_1^{**} + u_1^{*} - N\,u_1 - n\,u_1 = n - Gc\,C_1 - N - Rc\,u_0^{***} - A\,u_0^{*}, \tag{19}$$

$$\theta_1^{**} + Pr\,\theta_1^{*} - n\,Pr\,\theta_1 = -A\,Pr\,\theta_0^{*} - 2MEcPru_0u_1 - 2\frac{Ec\,Pr}{K_p}u_0u_1, \tag{20}$$

$$C_1^{**} + C_1^{*}Sc - (n+\gamma)Sc\,C_1 = -A\,C_0^{*}, \tag{21}$$

where star (*) refers the rate of change in reference of y.
The followed boundary conditions are given as

$$\begin{aligned} &y = 0: \; u_0 = U_p, \;\; u_1 = 0, \;\; \theta_0 = 1, \;\; \theta_1 = 1, \;\; C_0 = 1, \;\; C_1 = 1, \\ &y \to \infty: \; u_0 = 1, \;\; u_1 = 1, \;\; \theta_0 \to 0, \;\; \theta_1 \to 0, \;\; C_0 \to 0, \;\; C_1 \to 0, \end{aligned} \tag{22}$$

Equations (18) and (21) are solvable with (22). Through straightforward calculations, the solution of C_0 and C_1 is known but not given here due the sake of brevity.

Equations (16) and (19) are still third-order coupled differential equations; however, only two boundary conditions are available. Assuming $Rc \neq 0$, then u_0 and u_1 can be expanded in the powers of Rc as given below:

$$u_0 = u_{01} + Rc\,u_{02} + O\left(Rc^2\right), \tag{23}$$

$$u_1 = u_{11} + Rc\,u_{12} + O\left(Rc^2\right). \tag{24}$$

Using Eqs. (23) and (24) into Eqs. (16) and (19), the zeroth-order and first-order equations are given as

Zeroth-order equations

$$u_{01}^{**} + u_{01}^{*} - N\,u_{01} = -Gc\,C_0 - N, \tag{25}$$

$$u_{02}^{**} + u_{02}^{*} - N\,u_{02} = -u_{01}^{***}, \tag{26}$$

First-order equations

$$u_{11}^{**} + u_{11}^{*} - (N+n)u_{11} = -A\,u_{01}^{*} - n - N - Gc\,C_1, \tag{27}$$

$$u_{12}^{**} + u_{12}^{*} - (N+n)u_{12} = -u_{11}^{***} + n\,u_{11}^{**} - u_{01}^{***} - A\,u_{02}^{*}, \tag{28}$$

And the boundary condition is as follows:

$$\begin{aligned} y = 0 :\ & u_{01} = U_p,\ \ u_{02} = 0,\ \ u_{11} = 0,\ \ u_{12} = 0, \\ y \to \infty :\ & u_{01} = 1,\ \ u_{02} = 0,\ \ u_{11} = 1,\ \ u_{12} = 0. \end{aligned} \tag{29}$$

The differential Eqs. (25)–(28) are solvable through straight forward calculation and their results are shown through the graphs.

4 Coefficient of Skin Friction

The rate of velocity field in terms of skin friction coefficient at the plate is expressed by

$$C_f = \left[\frac{\tau_w}{\rho v_0^2}\right]_{y=0} = \left(\frac{\partial u}{\partial y}\right)_{y=0} = \left(\frac{\partial u_0}{\partial y}\right)_{y=0} + \in \mathrm{e}^{nt}\left(\frac{\partial u_1}{\partial y}\right)_{y=0}. \tag{30}$$

5 Nusselt Number

The rate of heat transfer in terms of Nusselt number at the plate is expressed by

$$Nu = -\left(\frac{\partial \theta}{\partial y}\right)_{y=0} = -\left(\frac{\partial \theta_0}{\partial y} + \in \mathrm{e}^{nt}\frac{\partial \theta_1}{\partial y}\right)_{y=0}. \tag{31}$$

6 Sherwood Number

The Sherwood number at the plate is referred by

$$Sh = -\left(\frac{\partial C}{\partial y}\right)_{y=0} = \left(\frac{\partial C_0}{\partial y} + \in \mathrm{e}^{nt}\frac{\partial C_1}{\partial y}\right)_{y=0}. \tag{32}$$

7 Result and Discussion

The numerical computation followed to carry out the study of velocity field, temperature field, and concentration field governs the fluid flow, and their results are expressed through the graph.

In order to study the of velocity, temperature, and concentration fields, numerical computations are carried out for various values of porosity parameter, Hartman

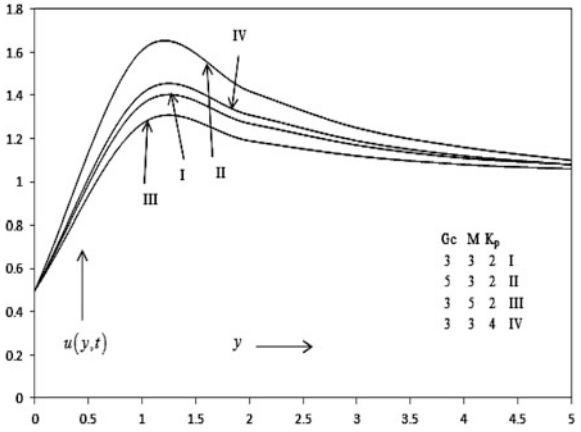

Fig. 2 Velocity distribution along direction y when $Rc = 1.5$, $A = 0.5$, $\kappa = 0.5$, $Sc = 0.22$, $\varepsilon = 0.25$, and $\gamma = 1$

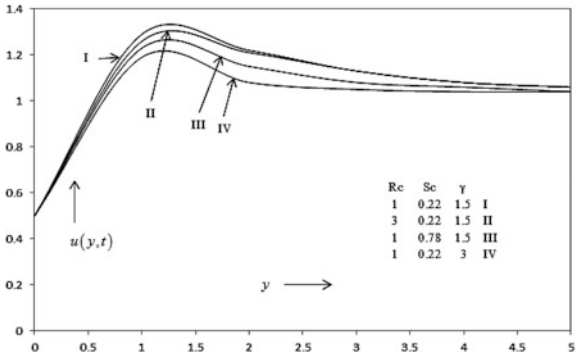

Fig. 3 Velocity distribution along direction y when $Gc = 3$, $A = 0.5$, $\kappa = 0.5$, $Kp = 1.5$, $M = 2$ and $\varepsilon = 0.25$

number, mass buoyancy, Schmidt number, Eckert number, Prandtl number, and chemical reaction parameters which describe the flow characteristics and the results are reported in terms of graphs.

Figure 2 shows the effects of Grashof number for mass transfer, magnetic field parameter, and permeability on the velocity field. It is seen that velocity diminishes with the upsurge of Hartman number through the boundary layer. Opposite characteristic is observed in the case of Grashof number for mass transfer and permeability parameter.

Figure 3 exhibits the effetcs of visco-elastic parameter, chemical reaction parameter and Schmidt number on the fluid velocity. It is seen that their presence reduce the velocity at all the points of flow region. The same result of this agreement is found by Ravikumar et al. (2014).

We observed from Fig. 4 mass buoyancy and permeability parameter enhancing the fluid temperature. For the free stream, it is approaching to zero which is a representation of cooling effect in the fluid flow. Besides this due to the increase of intensity of magnetic field, fluid temperature is reducing rapidly throughout the flow region.

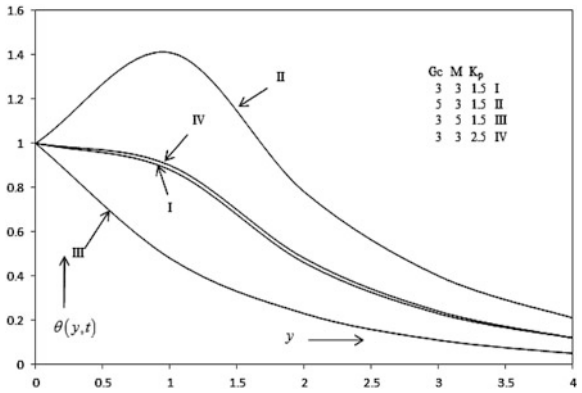

Fig. 4 Temperature distribution along direction y when $Rc = 1.5$, $A = 0.5$, $\kappa = 0.5$, $Sc = 0.22$, $\gamma = 1$, $Ec = 1$, $\varepsilon = 0.25$ and $Pr = 10$

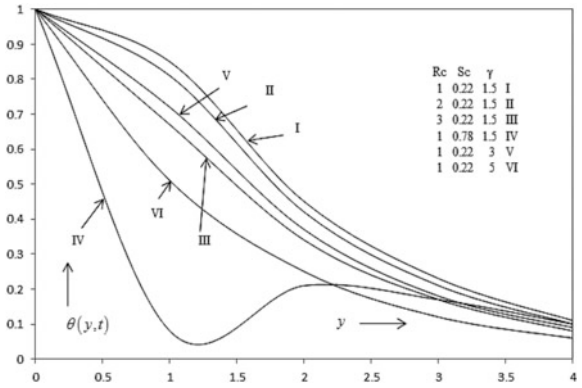

Fig. 5 Temperature distribution along direction y when $Gc = 3$, $M = 2$, $A = 0.5$, $\kappa = 0.5$, $Kp = 1.5$, $Ec = 1$, $\varepsilon = 0.25$ and $Pr = 10$

The consequence of chemical reaction parameter, viscoelastic parameter, and Schmidt number is expressed from Fig. 5. Due to upsurging in the elastic parameter of the fluid, the fluid temperature is declining continuously in the flow region. Similarly when Schmidt number and chemical reaction parameter rises then the fluid temperature become less.

From Fig. 6 it is seen that small growth in Prandtl number and Eckert number decreases the fluid temperature. Eckert number, which is the characteristic of heat dissipation enhances the fluid temperature throughout the fluid region.

Figures 7 and 8 demonstrate the rate of mass transfer. We see that the fluid species become less concentrate with the rising values of Sc and γ.

The impact of all physical parameters on skin friction coefficient, Nusselt number, and Sherwood number for various values of the pertinent parameters is displayed in Tables 1, 2, and 3. It can be noted that from Table 1, the effects of Gc are to increase the magnitude of skin friction. But we get quite opposite results for other parameters.

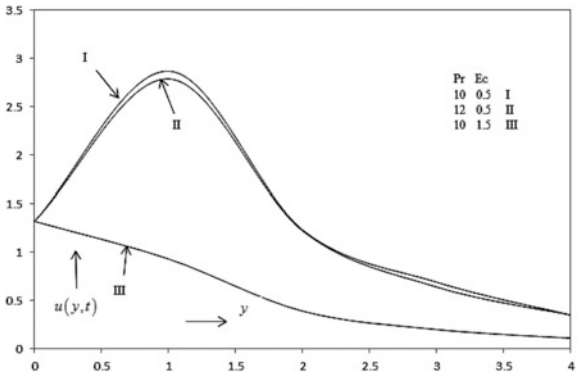

Fig. 6 Temperature distribution along direction y when $Rc = 1.5$, $A = 0.5$, $\kappa = 0.5$, $Sc = 0.22$, $\gamma = 1$, $Gc = 3$, $M = 3$ and $Kp = 1.5$

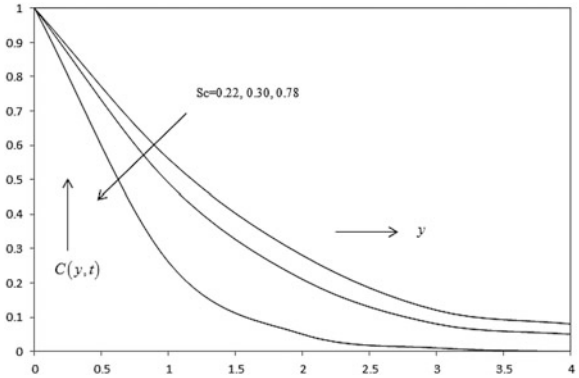

Fig. 7 Concentration distribution along direction y when $A = 0.5$, $\gamma = 1$ and $\varepsilon = 0.25$

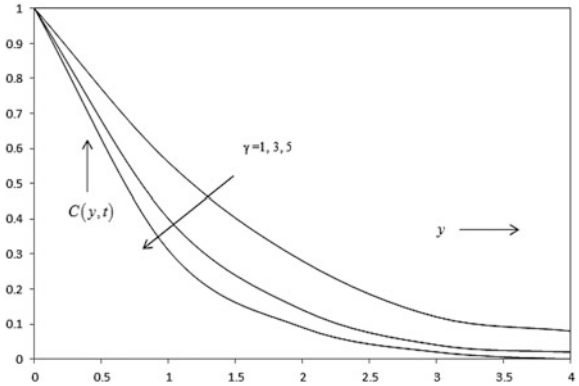

Fig. 8 Concentration distribution along direction y when $A = 0.5$, $Sc = 0.22$ and $\varepsilon = 0.25$

Table 1 Skin friction coefficient at the plate for various parameters as $n = 1$ and $t = 1$

S. No.	*Rc*	*Sc*	*M*	*Kp*	*Gc*	Γ	C_f
1.	1	0.22	3	1.5	3	1.5	2.6758
2.	3	0.22	3	1.5	3	1.5	0.2681
3.	1	0.30	3	1.5	3	1.5	1.334
4.	1	0.22	5	1.5	3	1.5	0.5831
5.	1	0.22	3	2.5	3	1.5	1.5495
6.	1	0.22	3	1.5	5	1.5	6.0408
7.	1	0.22	3	1.5	3	3	0.9839

Table 2 Coefficient of Nusselt number at the plate for various parameters as $n = 1$ and $t = 1$

S. No.	*Rc*	*Sc*	*M*	*Kp*	*Gc*	Γ	*Ec*	*Pr*	*Nu*
1.	1	0.22	3	1.5	3	1.5	0.5	0.71	−67.98
2.	3	0.22	3	1.5	3	1.5	0.5	0.71	−211.67
3.	1	0.30	3	1.5	3	1.5	0.5	0.71	−70.21
4.	1	0.22	5	1.5	3	1.5	0.5	0.71	−127.41
5.	1	0.22	3	2.5	3	1.5	0.5	0.71	−67.00
6.	1	0.22	3	1.5	5	1.5	0.5	0.71	−132.33
7.	1	0.22	3	1.5	3	3	0.5	0.71	−72.29
8.	1	0.22	3	1.5	3	1.5	1	0.71	−68.52
10.	1	0.22	3	1.5	3	1.5	0.5	7.0	109.64

Table 3 Coefficient of Sherwood number at the plate for various parameters as $n = 1$ and $t = 1$

S. No	*Sc*	γ	*Sh*
1.	0.22	1.5	1.0440
2.	0.30	1.5	1.2405
3.	0.78	1.5	2.2031
4.	0.22	3	1.3476

On careful study of Table 2, it is observed that the Nusselt number rises with upsurge values of permeability parameter while decreases for other parameters.

From Table 3, it is depicted that the Sherwood number, which determines the rate of solute concentration at the plate surface, is reaching to its high values with upsurged values of Schmidt number and parameter due to chemical reaction.

8 Conclusions

In this research article, the effects of chemical reaction on the MHD free convective flow of Rivlin-Ericksen fluid along a vertical porous plate have been considered. The resultant nonlinear differential equations are solved with suitable boundary conditions. The impacts of various physical parameters which are regulating the

fluid flow are discussed under results and discussion. By using the obtained results, the following conclusions are made:

(i) The flow of Rivlin-Ericksen fluid is highly effected by elasticity parameter and mass buoyancy. The high elastic fluid flow is slow under the other stable environment. Beside this, mass buoyancy accelerates the fluid flow and fluid temperature but extremely chemically reactive Rivlin-Ericksen fluid flow is comparatively slow throughout flow region.
(ii) The permeability of the porous region supports the fluid velocity as well as fluid temperature which is caused by less obstacles in fluid flow.
(iii) In highly chemically reactive Rivlin-Ericksen fluid flow, the fluid temperature is reduced rapidly. Similarly, intensity of the applied magnetic field precisely regulates the fluid flow and temperature field. This is a better cause for reducing both of them.
(iv) The species concentration is reduced by high chemically reactive fluids.

References

Ananda RN, Varma SVK, Raju MC (2009) Thermo diffusion and chemicals effects with simultaneous thermal and mass diffusion in MHD mixed convection flow with ohmic heating. J. Nav Archit Mar Eng 6:84–93

Chamkha AJ (1996) MHD free convection from a vertical plate embedded in a thermally stratified porous medium. Fluid/Part Sep J 3:195–206

Daleep KS, Ajaib SB (2012) Bounds for complex growth rate in thermosolutal convection in Rivlin-Ericksen viscoelastic fluid in a porous medium. Int J Eng Sci Adv Technol 2(6): 1564–1571

Eldabe NTM, Mohamed MAA (2002) Heat and mass transfer in hydromagnetic flow of the non-Newtonian fluid with heat source over an accelerating surface through porous medium. Chaos Solitons Fractals 13(4):907–917

Kumar R, Abbas AI, Sharma V (2013) Anumnerical study of free convection heat and mass transfer in a Rivlin-Ericksen viscoela stic flow past an impulsively started vertical plate with variable temperature and concentration. Int J Heat Fluid Flow 44:258–264

Popoola AO, Baoku IG, Olajuwon BI (2016) Heat and mass transfer on MHD viscoelastic fluid flow in the presence of viscous dissipation and chemical reaction. Int J Heat Technol 34:15–26

Rana GC (2012) Thermal instability of compressible Rivlin-Ericksen rotating fluid permeated with suspended dust particles in porous medium. Int J Appl Math Mech 8(4):97–110

Rana GC, Chand R (2013) Double-diffusive convection in compressible Rivlin-Ericksen fluid permeated with suspended particles in a Brinkman porous medium. Int J Appl Math Mech 9 (10):58–73

Ravikumar V, Raju MC, Raju GSS (2014) Combined effects of heat absorption and MHD on convective Rivlin-Ericksen flow past a semi-infinite vertical porous plate with variable temperature and suction. Ain Shams Eng J 5:867–875

Sharma PR, Sharma P, Kumar N (2011) Influence of chemical reaction and radiation on unsteady MHD free convection flow and mass transfer through viscous incompressible fluids past a heated vertical plate immersed in porous medium in the presence of heat source. Appl Math Sci 5:2249–2260

Sharma PR, Sharma P, Saboo R (2015) MHD free convection radiative flow of visco-elastic fluid (Walter's liquid model-B) in the presence of chemical reaction. Acta Technica 60:359–373
Sahin A, Zueco J (2010) Combined heat and mass transfer by mixed convection MHD flow along a porous plate with chemical reaction in presence of heat source. Appl Math Mech 31(10): 1217–1230

A Three-Dimensional CFD Simulation for the Nonlinear Parallel Flow Phenomena Through Coarse Granular Porous Media

Ashes Banerjee, Srinivas Pasupuleti, G.N. Pradeep Kumar and Sekhar Chandra Dutta

Abstract Among many of the nonlinear equations presented throughout the decade, Forchheimer equation is the most widely experimented and investigated. In this study, a simple CFD model created using ANSYS Fluent 15.0 has been used in order to predict the flow through a parallel flow permeameter packed with crushed stone of three different sizes. The results obtained were compared with the experimental results obtained from a similar kind of experimental set under similar type of field and media conditions. Furthermore, the statistical validation of the simulation results with the experimentally obtained results suggests that this type of model can be used for analysing the flow though porous media as a substitute of the complex laboratory experiments with a reasonable precision.

1 Introduction

The relationship between the hydraulic gradient and velocity in the porous media has not been defined properly when flow exceeds the laminar regime. The studies of post laminar flow conditions through porous media are very important in order to predict the flow in aquifer, flow through filter media, flow through rock fill dam and in the case of oil and gas well etc. As flow passes the laminar regime in all these cases, the actual head loss often exceeds the value of the same obtained by the Darcy's law, proposed by Henry Darcy in the year 1856 as

$$V = ki \tag{1}$$

A. Banerjee (✉) · S. Pasupuleti · S.C. Dutta
Department of Civil Engineering, Indian Institute of Technology (Indian School of Mines), Dhanbad, Dhanbad 826004, Jharkhand, India
e-mail: ashes742@gmail.com

G.N. Pradeep Kumar
Department of Civil Engineering, SVU College of Engineering, Sri Venkateswara University, Tirupati 517502, Andhra Pradesh, India
e-mail: saignp@gmail.com

M.K. Singh et al. (eds.), *Applications of Fluid Dynamics*, Lecture Notes in Mechanical Engineering, https://doi.org/10.1007/978-981-10-5329-0_34

where 'k' is the coefficient of permeability, V is the superficial velocity of flow, and i is the hydraulic gradient. However, this linear relationship is not applicable when the Reynolds number exceeds the value of 10 which has been described as the post-laminar regime Kovacs (1971, 1981). Hence, number of nonlinear forms of equations has been proposed by various researchers such as Forchheimer (1901), Blake (1923), Ergun (1952), Wilkins (1955), Scheidegger (1958), Barr (2001) considering the effect of inertia for flow at higher Reynolds number. Among all these equations, the Forchheimer equation is the mostly studied and debated. The equation is in a form of simple quadratic equation, i.e.

$$i = aV + bV^2 \tag{2}$$

where a and b are Darcy and non-Darcy coefficients, V = superficial velocity of flow through the porous media, and i = hydraulic gradient. Later, Eq. (2) has been modified by Forchheimer (Scheidegger 1958) adding a third term to account for transitional conditions as

$$i = aV + bV^2 + cV^3 \tag{3}$$

This equation was further modified in order to take into account the effect of transitional conditions of seepage flow as

$$i = aV + bV^2 + cV^{1.5} \tag{4}$$

where c is a coefficient.

Equation (4) was again generalized by Polubarinova-Kochina (Scheidegger 1958) to contain a time-dependent term as

$$i = aV + bV^2 + c\frac{\mathrm{d}V}{\mathrm{d}t} \tag{5}$$

Equation (5) has been used in case of oscillatory flows through porous media (Andersen and Burcharth 1995; Hall et al. 1995; Van Gent 1995). For steady flow condition, Eq. (5) reduces to Eq. (2). Although Eqs. (3) and (4) contain all three of linear, turbulent, and transitional regimes, according to McCorquodale, these equations are slightly better than Eq. (2). As per him, Eq. (3) yields almost same value of 'i' for Reynolds number 600–4000. But for its simplicity and reliability, Eq. (2) is mostly used in computation (Pasupuleti et al. 2014).

With the development of the computational technology, the flow through porous media can now be calculated very easily by solving the Navier–Stokes equation using computational fluid mechanics (CFD) even in the turbulent regime. A very detailed solution can be capitulated containing the local values of variables such as pressure, velocity, temperature, viscosity, shear stress. Such detailed solutions can be of great importance in understanding the phenomena as an alternative of the experimental process.

In this paper, a numerical model has been created in order to check the applicability of the Forchheimer equation for non linear parallel flow through porous media. Furthermore, the simulation results have been compared with the experimental results statistically in order to validate the simulation results.

2 Numerical Modelling

In order to simulate the flow through porous media in a parallel flow permeameter, a simple CFD model has been created using the ANSYS Fluent 15.0. Using CFD approach means numerically solving the continuity equation (Eq. 6) and momentum conservation equation or the Navier–Stokes equation (Eq. 7) using the desired boundary conditions.

$$\frac{\partial u_i}{\partial x_i} = 0 \tag{6}$$

u_i is the velocity in the x_i direction.

$$\rho u_j \frac{\partial u_i}{\partial x_j} = -\frac{\partial P}{\partial x_i} + \frac{\partial}{\partial x_i}\left(\mu \frac{\partial u_i}{\partial x_i}\right) + \rho g_i \tag{7}$$

With P = total pressure, ρ = fluid density, μ = molecular viscosity, and g = gravitational acceleration (Versteeg and Malalasekera 2007).

Turbulence modelling has been used in the present study as the Reynolds number of flow lies within the range of 1736–7194 which represents the turbulent flow as per the definition of Kovacs (1971, 1981). In order to model turbulence, the Reynolds-averaged Navier–Stokes (RANS) equation has been used where Eqs. (6) and (7) have been averaged assuming that the turbulent quantities generate averaged quantities amplified by fluctuant ones described as Eqs. (8) and (9).

$$u_j = \overline{u_j} + u_j' \tag{8}$$

$$p = \bar{p} + p' \tag{9}$$

where u_j and p are the turbulent velocity and pressure and $\overline{u_j}$, $\bar{p}$ and u_j', p' are the average and fluctuant components of velocity and pressure, respectively. However, it does not close the equation, generating a new term named 'Reynolds Stresses' $\left(\overline{-\rho u_i' u_j'}\right)$, which can be again defined by the Boussinesq hypothesis, i.e.

$$-\rho\overline{u_i' u_j'} = \mu_t\left(\frac{\partial u_i}{\partial x_j} + \frac{\partial u_j}{\partial x_i}\right) - \frac{2}{3}\left(\rho k + u_t \frac{\partial u_i}{\partial x_i}\right)\delta_{ij} \tag{10}$$

where μ_t is the turbulent viscosity, k is the turbulent kinetic energy, and δ_{ij} is the Kronecker symbol. The value of μ_t can be calculated using Eq. (11).

$$\mu_t = \rho . C_\mu \frac{k^2}{\varepsilon} \tag{11}$$

with $C_\mu = 0.09$ for standard k-ε model.

In order to close the equation system, two new equations were introduced defining the values of turbulent kinetic energy (k) and turbulent dissipation rate (ε) named as k-ε model. The 'realizable k-ε model' (Shih et al. 1995) is a revised version of the standard k-ε model (Jones and Launder 1972) containing a new formulation for dissipation rate ε and has been used in this study in order to close the equation system because of its superior performance over a large variety of conditions such as flows involving rotation, boundary layers under strong adverse pressure gradients, separation, recirculation, and its applicability over a wide range of flow (Shih et al. 1995; ANSYS 2013).

3 Model Description

The geometric model was created with ANSYS Fluent 15.0 software containing a tank, a cylindrical parallel flow permeameter, and an inlet pipe using geometry option. The different selections such as inlet, wall, outlet, and the contact regimes were selected carefully. The permeameter has been created as porous media. A homogeneous porous media has been created in order to reduce the complicacy and the time taken for the calculation; however, the porosity has been given as it was obtained during the experimentation. The porous media have been characterized by two coefficients, the viscous resistance factor $(1/\alpha)$ and inertial resistance factor (C_2) which were calculated (ANSYS 2013) as

$$\Delta P = aV + bV^2 \tag{12}$$

where

$$a = \frac{\mu}{\alpha} \quad \text{and} \quad b = \frac{1}{2}\rho C_2 \tag{13}$$

Table 1 Values of the viscous and inertial resistance for different media sizes

Media size (mm)	Porosity (%)	Darcy coefficient	Non-Darcy coefficient	Viscous resistance	Inertial resistance
29.8	44.84	1078	68,510	1778261.659	226.4793388
34.78	43.1	1871	61,912	3086389.205	204.6677686
41.59	43.62	2125	58,343	3505385.922	192.8694215

where ΔP and V are the average pressure drop and velocity through the porous medium calculated from the experimental results. Values of the viscous and inertial resistance factors are presented in Table 1.

4 Boundary Conditions

The boundary conditions have been selected carefully as it influences the result significantly. The inlet velocity was calculated by dividing the discharge measured during the experimentation by the area of the inlet pipe. As described earlier, the turbulent kinetic energy (k) and turbulent dissipation rate (ε) are required to inject in order to close the equation system. Equations (14) and (15) have been used to calculate the value of the same based on the turbulent intensity I (depending on the Reynolds number Re), the turbulence length scale l (depending on the hydraulic diameter D_h), and the inlet velocity V (ANSYS 2013).

$$k = \frac{3}{2}(V.I)^2 \quad \text{with} \quad I = 0.16(Re)^{-(1/8)} \tag{14}$$

where Re is the Reynolds number for pipe flow defined as $\frac{\rho V d}{\mu}$

$$\varepsilon = C_\mu^{3/4} \frac{k^{3/2}}{l} \quad \text{with} \quad l = 0.07 D_h \tag{15}$$

The outlet has been designed as an outflow boundary assuming that the flow is completely developed and where the diffusion flux for all the flow variables in the exit direction is zero.

5 Meshing

The continuous domain has been discretized using structured mesh in order to substitute it with the finite number of volumes (meshes). The size of the mesh has a great influence on the simulation results; therefore, in order to finalize the

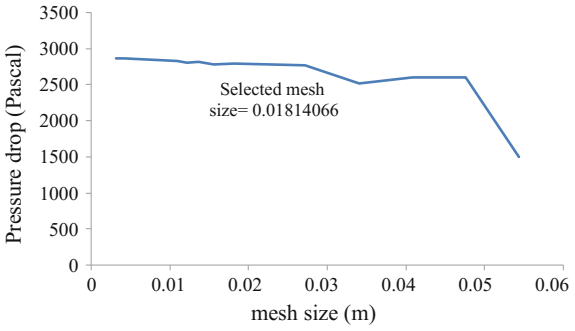

Fig. 1 Value of pressure drop for different mesh sizes

Table 2 Detail of the mesh used for simulation

Mesh size	Nodes	Elements	Skewness			Orthogonal quality		
0.0181406	37,683	32,998	Max.	Min.	Average	Max.	Min	Average
			0.55	5.79×10^{-4}	9.06×10^{-2}	0.99	0.71	0.982

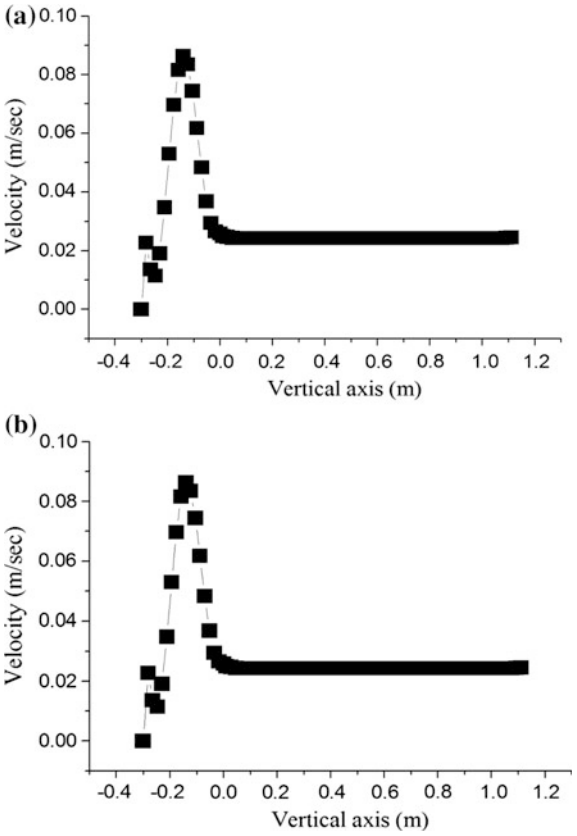

Fig. 2 **a** Variation of total pressure with vertical axis for 29.8-mm crushed stones. **b** Variation of velocity with vertical axis for 29.8-mm crushed stones

appropriate mesh size, a mesh convergence study has been performed with 15 different mesh sizes and the result has been presented in Fig. 1. Based on the effect of the simulation results and time taken for the simulation, a mesh size of 0.01814066 m has been selected. Table 2 provides the detail of the created mesh. Values of the parameters such as skewness and orthogonal quality were checked for the selected mesh size, and all the values were found to be within acceptable range.

6 Results

The value of the pressure loss through the porous media and the velocity through the porous media has been simulated. The pressure drop and the velocity distribution obtained from the simulation are shown in Figs. 2a, b, 3a, b, and Fig. 4a, b

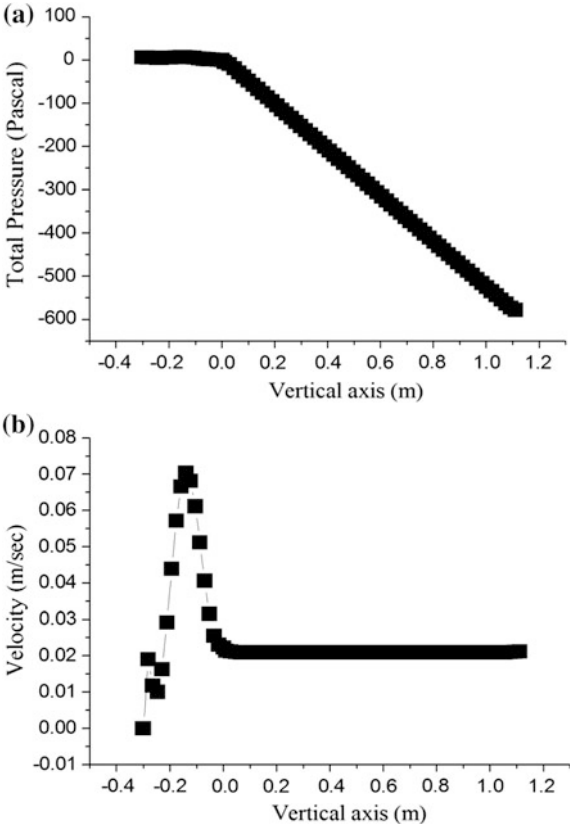

Fig. 3 **a** Variation of total pressure with vertical axis for 34.78-mm crushed stones. **b** Variation of velocity with vertical axis for 34.78-mm crushed stones

for media size of 29.8, 34.78, and 41.59 mm with a porosity of 44.48, 43.10, and 43.62% and for a discharge of 399.3919, 420.4125, and 350.4688 cc/sec, respectively. Same type of plot has been obtained for other discharges. The pressure plots clearly show the loss in head as the flow advances through porous media The negative sign in the total pressure appears because the operating pressure has been set to 0 Pa (to cut down rounding errors) and flow is assumed to be incompressible. As Navier–Stokes equations contain the pressure gradient hence pressure differences drive the flow therefore, in regions of separated flow, the low pressure inside that region will be relative to the lowest fixed pressure in the system and may go negative. The velocity plots represent a fluctuating velocity in the tank section and an average superficial velocity in the permeameter section.

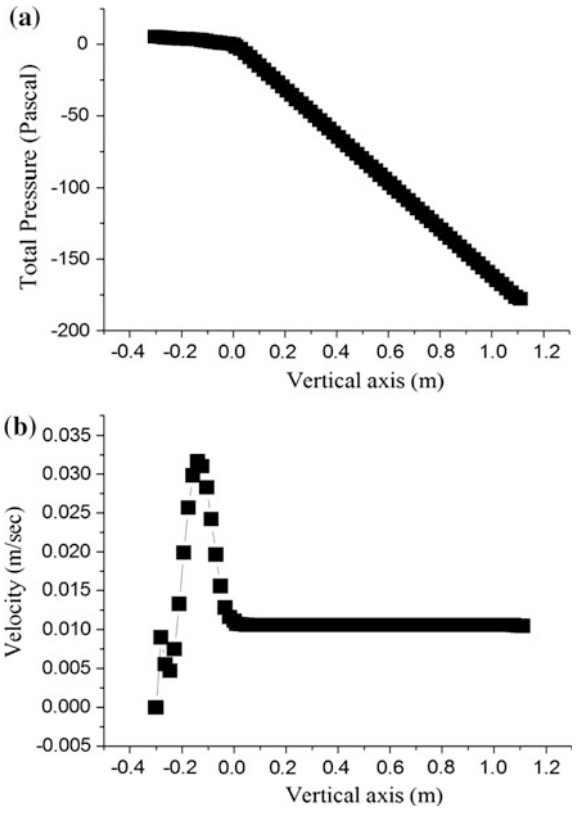

Fig. 4 **a** Value of total pressure with *z*-axis for 41.59-mm crushed stones. **b** Value of velocity with *z*-axis for 41.59-mm crushed stones

7 Experimental Set-up

Experimentation has been performed in a parallel flow permeameter of 250 mm dia. with three different media sizes 29.8, 34.78, and 41.59 mm. The accessories such as a header tank (1000 mm × 300 mm × 300 mm) and centrifugal pump have been attached with the permeameter. The velocity of the flow has been calculated after measuring the discharge using a triangular notch. A manometer board has been attached in order to measure the head loss with tapings at an interval of every 50 mm. The water is allowed to flow under a constant head. Temperature has been recorded after every run to calculate the viscosity of the fluid.

8 Comparison Between Experimental and Simulation Result

Obtained experimental and the simulation results have been plotted in Figs. 5, 6, and 7. The results obtained from the CFD simulation are found to be in a good agreement with the experimental results for all three media sizes. Finally, the results were validated statistically using the standard '*z*-test' for all three samples.

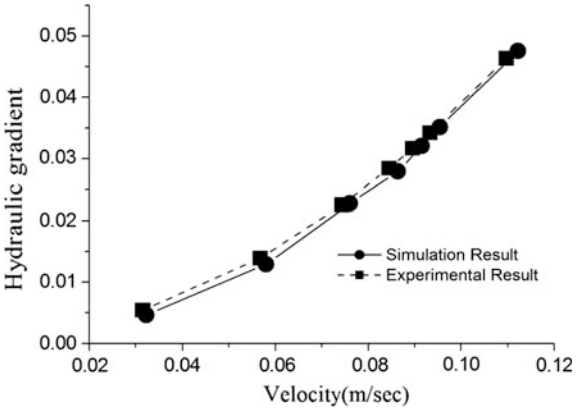

Fig. 5 Comparison of simulation and experimental results for 29.8-mm crushed stones

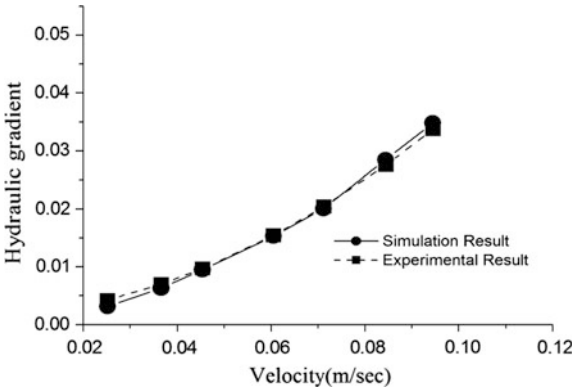

Fig. 6 Comparison of simulation and experimental results for 34.78-mm crushed stones

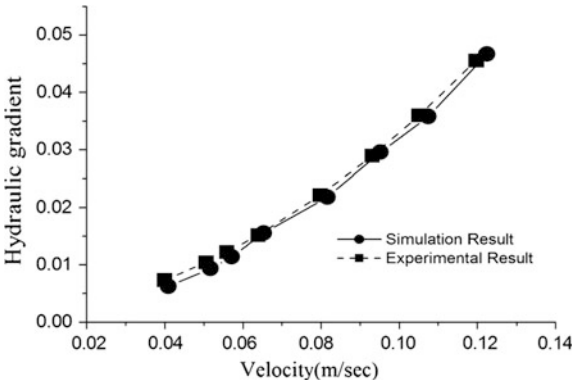

Fig. 7 Comparison of simulation and experimental results for 41.59-mm crushed stones

9 Statistical Validation

The agreement between the experimental and simulated results has been investigated using the standard 'z-test' (Mann and Lacke 2010; Chen and Nadarajah 2014; Camblor 2014). The hypothesis was introduced in order to check the validity as presented in Eq. (16).

$$\begin{aligned} H_0 &: \mu_1 = \mu_2 \\ H_1 &: \mu_1 \neq \mu_2 \end{aligned} \tag{16}$$

where μ_1 and μ_2 are the population mean of the experimental and simulation results. To validate the result, the null hypothesis H_0 must be accepted at a level of significance (α) of 5% or at a considered confidence level of 95% (Mann and Lacke 2010). The present study deals with a two tailed hypothesis, and therefore, $\alpha = \frac{0.05}{2} = 0.025$. The corresponding value Z_{critical} is ± 1.96 (from z table). So the value of $Z_{\text{calculated}}$ should be within this range [−1.96, 1.96]. The $Z_{\text{calculated}}$ can be calculated from Eq. (17).

$$Z_{\text{calculated}} = \frac{(\overline{x_1} - \overline{x_2}) - (\mu_1 - \mu_2)}{\sqrt{\frac{\sigma_1^2}{N_D} + \frac{\sigma_2^2}{N_D}}} \tag{17}$$

where $\overline{x_1}$, $\overline{x_2}$ and μ_1, μ_2 are the sample and population mean for the experimental and simulation result, N_D is the total number of data points (sample) σ_1, σ_2 are the standard deviation for the experimental and simulation result.

Table 3 Values from the z-test for different media size

Media size (mm)	$\overline{x_1}$	$\overline{x_2}$	σ_1	σ_2	N_D	Z value
29.80	0.081	0.081242	0.071453432	0.070066613	250	0.051
34.78	0.077	0.077295	0.06677038	0.065459479	250	0.0445
41.59	12	12.95693	10.66377842	11.49681807	250	0.964135

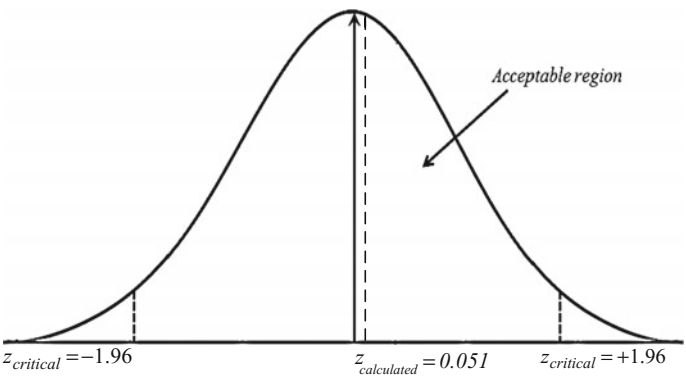

Fig. 8 Binomial distribution curve for z-test of 29.8-mm crushed stones

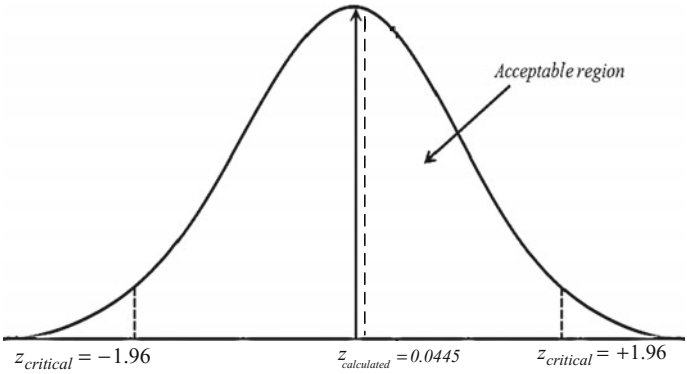

Fig. 9 Binomial distribution curve for z-test of 34.78-mm crushed stones

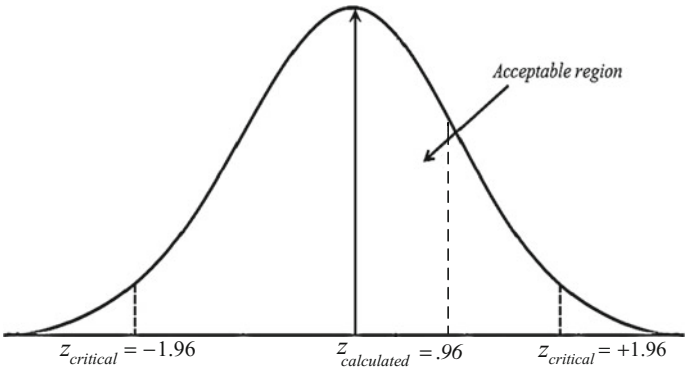

Fig. 10 Binomial distribution curve for z-test of 41.59-mm crushed stones

The result of the z-test for three different media sizes are presented in Table 3 which shows that the value of $Z_{\text{calculated}}$ is within the acceptable range [−1.96, 1.96] for all three media sizes; therefore, the null hypothesis is accepted, and the simulation results can be accepted. Furthermore, the results have been plotted in the binomial distribution diagram (Tian et al. 2015; Liu and Hong 2015) and presented in Figs. 8, 9, and 10.

10 Conclusions

The present study shows a simple a nonlinear CFD model created using commercial software ANSYS Fluent 15.0 to predict the velocity and pressure drop for parallel flow through a coarse granular media. The results obtained from the simulation were compared with the experimental results, and finally, they were validated using

the standard z-test statistically. The values of the $Z_{calculated}$ for all three media sizes were found to be within the acceptable limit [−1.96, 1.96] validating the acceptability of the simulation results. This type of model can be very useful in order to simulate the flow for different field and media conditions and therefore to investigate the effect of those conditions on the pressure drop velocity relation. Furthermore, this type of model can be useful to predict the head loss and to visualize the flow for different conditions instead of performing complex experiments in the laboratory.

Acknowledgements The authors would like to thank the faculty of Civil and Mechanical Engineering for their support, in utilizing the facilities in the department. The authors would also acknowledge the funding from IIT (ISM), Dhanbad, for RPS (Research Promotion Scheme) vide no: FRS (62)/2013–2014/CE for the fabrication of the permeameter experimental set-up.

References

Andersen O, Burcharth HF (1995) On the one-dimensional steady and unsteady porous flow equation. Coast Eng 24:233–257

ANSYS, Inc. (2013) Ansys Fluent 15.0: Users Guide, U.S.A

Barr DW (2001) Turbulent flow through porous media. Ground Water 39(5):646–650

Blake F (1923) The resistance of packing to fluid flow. Trans. Am. Soc. Chem Eng 14:415–522

Camblor PM (2014) On correlated z-values distribution in hypothesis testing. Comput Stat Data Anal 79:30–43

Chen Z, Nadarajah S (2014) On the optimally weighted z-test for combining probabilities from independent studies. Comput Stat Data Anal 70:387–394

Ergun S (1952) Fluid flow through packed columns. Chem Eng Prog 48:89–94

Forchheimer P (1901) Wasserbewegung durch boden. Z Ver Deutsch Ing 45:1782–1788

Hall R, Smith GM, Turcke D (1995) Comparison of oscillatory and stationary flow through porous media. Coast Eng 24(3):217–232

Jones WP, Launder B (1972) The prediction of laminarization with a two-equation model of turbulence. Int J Heat Mass Transf 15(2):301–314

Kovacs G (1971) Seepage through saturated and unsaturated layers. Hydrol Sci J 16(2):27–40

Kovacs G (1981) Seepage Hydraulics. ESPC, New york

Liu X, Hong Y (2015) Analysis of railroad tank car releases using a generalized binomial model. Accid Anal Prev 84:20–26

Mann PS, Lacke CJ (2010) Introductory statistics. Wiley, Delhi

Pasupuleti S, Kumar G, Jayachandra K (2014) Quantification of effect of convergence in porous media flow. In 5th international conference on porous media and their applications in science, engineering and industry, Hawaii, 2014

Scheidegger AE (1958) The physics of flow through porous media. Soil Sci 86(6):355

Shih TH, Liou WW, Shabbir A, Yang Z, Zhu J (1995) A new k-ϵ eddy viscosity model for high reynolds number turbulent flows. Comput Fluids 24(3):227–238

Tian GL, Ma H, Zhou Y, Deng D (2015) Generalized endpoint-inflated binomial model. Comput Stat Data Anal 89:97–114

Van Gent MRA (1995) Porous flow through rubble-mound material. J Waterw Port Coast Ocean Eng 121(3):176–181

Versteeg HK, Malalasekera W (2007) An introduction to computational fluid dynamics: the finite volume method. Pearson Education, New Jersey

Wilkins JK (1955) Flow of water through rock fill and its application to the design of dams. NZ Eng 10(11):382–387

Part VI
Solute Transport Modeling and Water Jet

Dust Ion Acoustic Solitary Waves in Quantum Dusty Plasmas: A New Approach to Obtain Sagdeev Potential

Gadadhar Banerjee and Sarit Maitra

Abstract Quantum hydrodynamic model is used to study the existence and propagation of dust ion acoustic solitary waves (DIASWs). Here, Sagdeev's non-perturbative method is used, and the Sagdeev potential is obtained numerically by using fourth-order Runge–Kutta method. A critical Mach number is observed for the existence of DIASWs. The numerical simulation results indicate that the dust grains may influence not only the amplitude and width but also the existence domain of the soliton. The quantum effects on the solitary waves are also mentioned.

1 Introduction

For the past few decades, a great involvement has been seen in studying quantum transport models in dusty plasmas. The classical plasmas are often associated with high temperature and low particle density modes. But in some situations like superdense astrophysical bodies (Jung 2001; Chabrier et al. 2002), nonlinear quantum optics (Gloge and Marcuse 1969), ultra small electronics devices (Marklund and Shukla 2006), metallic nanostructures (Manfredi 2005), the existence of low temperature and high particle number density has been observed, where the de Broglie wavelength of the plasma particles is comparable to the dimension of the system and so the quantum effects cannot be ignored. Quantum plasmas are studied mainly by two approaches, viz. quantum kinetic approach and quantum hydrodynamic (QHD) approach. The kinetic approach is needed to discuss the Landau damping (Suh et al. 1991) of waves in quantum plasmas. The most widely used approach for studying quantum plasmas is QHD approach. Madelung (1926) was the first to give the mathematical derivation of QHD model. The hydrodynamic equations can be derived by using the Schrödinger–Poisson system

G. Banerjee (✉) · S. Maitra
Department of Mathematics, National Institute of Technology, Durgapur, Durgapur 713209, West Bengal, India
e-mail: gban.iitkgp@gmail.com

M.K. Singh et al. (eds.), *Applications of Fluid Dynamics*, Lecture Notes in Mechanical Engineering, https://doi.org/10.1007/978-981-10-5329-0_35

of equations (Haas 2011). Due to the quantum tunneling effects, a new force in terms of the gradient of Bohm potential (Gardner and Ringhofer 1996) appears in the momentum equation. As the plasma particles obey Fermi–Dirac distribution, the pressure term in the momentum equation is described by the Fermi pressure law, which includes the quantum statistical effects. Thus, mathematical formulation for classical plasmas is suitably modified by including these two quantum characteristics.

QHD model has been used by several authors for studying quantum plasmas. The existence of quantum ion acoustic (QIA) wave was first studied by Haas et al. (2003) in unmagnetized quantum plasmas by using the one-dimensional QHD model. Later, the QHD model has been applied on studying various linear and nonlinear features of QIA (Ali et al. 2007; Haas 2005), quantum electron acoustic (Sah and Manta 2009; Mahmood and Masood 2008; Misra et al. 2007) and quantum positron acoustic (Metref and Tribeche 2014) solitary waves (SWs) in different plasma regimes. Quantum ion acoustic waves have been investigated also in carbon nanostructures (Wei and Wang 2007) and metallic nanowires (Moradi 2015) by using the QHD model. However, due to contamination, dust impurities may exist in quantum plasmas like the microelectronic devices or metallic nanostructures. The various linear and nonlinear phenomena of quantum dust acoustic (DA) (Ali and Shukla 2006; Misra and Chowdhury 2006; El-Taibany and Wadati 2007; Wang et al. 2012) and dust ion acoustic (DIA) (Masood et al. 2007; Khan and Mushtaq 2007) waves have been investigated by several authors. Treating the charged carbon nanotubes as the charged dust which is surrounded by electron and ion, Shukla (2009) derived the dispersion relation of DA waves. The existence of DIA wave has been theoretically reported in metallic multiwalled carbon nanotubes (Fathalian and Nikjo 2010).

Most of these studies in quantum plasmas have been made by applying the reductive perturbation technique. Recently, Hanif et al. (2014) employed a numerical technique to study ion acoustic (IA) shock waves in dense quantum plasmas. Sagdeev's method is applied in order to observe the existence of arbitrary amplitude solitary wave. The inclusion of Bohm potential term in the momentum equation makes the task of finding the closed-form analytical expression of pseudopotential difficult. However, Mahmood and Mushtaq (2008) studied IA wave propagation in an unmagnetized quantum plasma by using Sagdeev's pseudopotential approach under quasi-neutrality condition. Later, Mahmood (2008) employed the same method to study the DIA waves in dense Fermi plasmas.

In this work, pseudopotential method has been employed to study arbitrary amplitude quantum DIA waves together with the Poisson equation. In order to find pseudopotential function, a different technique is being used. Different sections of this article are organized as follows: In Sect. 2, basic equations are given, and in Sect. 3, expression for pseudopotential is derived. The results and discussion are presented in Sects. 4 and 5 presents conclusions.

2 Basic Equations

Here, a quantum plasma with electrons, ions, and dust particles is considered. The dust grains are negatively charged and do not move as they are highly massive. Owing to small mass, the electrons are supposed to be inertialess. The system of equations describing the dynamics is as follows:

$$\frac{\partial n_i}{\partial t} + \frac{\partial}{\partial x}(n_i v_i) = 0, \tag{1a}$$

$$\frac{\partial v_i}{\partial t} + v_i \frac{\partial v_i}{\partial x} + \frac{e}{m_i}\frac{\partial \phi}{\partial x} = 0, \tag{1b}$$

$$0 = e\frac{\partial \phi}{\partial x} - \frac{1}{n_e}\frac{\partial p_e}{\partial x} + \frac{\hbar^2}{2m_e}\frac{\partial}{\partial x}\left[\frac{1}{\sqrt{n_e}}\frac{\partial^2}{\partial x^2}(\sqrt{n_e})\right], \tag{1c}$$

$$\frac{\partial^2 \phi}{\partial x^2} = 4\pi e(n_e + Z_{d0}n_{d0} - n_i), \tag{1d}$$

where n_s, v_s, m_s are the number density, velocity, and mass of electron $(s = e)$ and ion $(s = i)$, respectively. ϕ is the electrostatic potential. n_{d0} and Z_{d0} are the number densities and charge numbers of dust grains at equilibrium, respectively. $\hbar$ is the Planck's constant and $-e(e)$ is the electron (ion) charge. Here, the electrons are assumed to follow the one-dimensional zero-temperature Fermi gas pressure law (Haas et al. 2003).

$$p_e = \frac{m_e v_{\mathrm{Fe}}^2}{3n_{e0}^2} n_e^3, \tag{2}$$

where the Fermi electron velocity is given by $v_{Fe} = \sqrt{2K_B T_{\mathrm{Fe}}/m_e}$, K_B and T_{Fe} are the Boltzmann constant and Fermi temperature, respectively. The charge neutrality condition at equilibrium is given by

$$n_{i0} = n_{e0} + Z_{d0}n_{d0}. \tag{3}$$

Equations (1a)–(1d) are written in the normalized form as follows:

$$\frac{\partial n_i}{\partial t} + \frac{\partial}{\partial x}(n_i v_i) = 0, \tag{4a}$$

$$\frac{\partial v_i}{\partial t} + v_i \frac{\partial v_i}{\partial x} = -\frac{\partial \phi}{\partial x}, \tag{4b}$$

$$0 = \frac{\partial \phi}{\partial x} - n_e \frac{\partial n_e}{\partial x} + \frac{H^2}{2\delta} \frac{\partial}{\partial x} \left[\frac{1}{\sqrt{n_e}} \frac{\partial^2}{\partial x^2} (\sqrt{n_e}) \right], \tag{4c}$$

$$\frac{\partial^2 \phi}{\partial x^2} = \delta n_e + d - n_i, \tag{4d}$$

where the potential ϕ is normalized by $\frac{2K_B T_{Fe}}{e}$, v_i and n_s are normalized by $C_0 = \left(\frac{2K_B T_{Fe}}{m_i}\right)^{\frac{1}{2}}$ and n_{s0} $(s = e, i)$, respectively. The space and time coordinates are normalized by the ion Fermi wave length $\lambda = \left(\frac{2K_B T_{Fe}}{4\pi n_{i0} e^2}\right)^{\frac{1}{2}}$ and ion plasma period $\omega_{pi}^{-1} = \left(\frac{m_i}{4\pi n_{i0} e^2}\right)^{\frac{1}{2}}$, respectively. Here, the dust density parameter $d = \frac{Z_{d0} n_{d0}}{n_{i0}}$, $\delta = \frac{n_{e0}}{n_{i0}}$, electron plasma period $\omega_{pe} = \left(\frac{4\pi n_{e0} e^2}{m_e}\right)^{\frac{1}{2}}$, and the nondimensional quantum parameter H is defined as $H = \frac{\hbar \omega_{pe}}{2K_B T_{Fe}}$. The charge neutrality condition (3) implies $\delta = 1 - d$.

3 Arbitrary Amplitude Solitons

To obtain the traveling wave solutions of the Eqs. (4a)–(4d) that are stationary in a frame moving with a velocity M, it is considered that all the dependent variables depend on $\xi = x - Mt$, M being the Mach number normalized to the quantum ion acoustic speed C_0. Then, Eqs. (4a) and (4b) reduce to

$$n_i = \frac{M}{M - v_i}, \tag{5a}$$

$$(v_i - M)^2 = M^2 - 2\phi, \tag{5b}$$

where the boundary conditions as $\xi \to \pm\infty$, $n_i \to 1, v_i \to 0$, and $\phi \to 0$ are used. Then, Eqs. (5a) and (5b) imply that

$$n_i = \frac{1}{\sqrt{1 - \frac{2\phi}{M^2}}}, \tag{6}$$

Equation (4c) reduces to

$$n_e^2 = 1 + 2\phi + \frac{H^2}{\delta} \left[\frac{1}{\sqrt{n_e}} \frac{\partial^2}{\partial \xi^2} (\sqrt{n_e}) \right], \tag{7}$$

imposing the boundary conditions $\phi \to 0, n_e \to 1$, and $\frac{\partial^2}{\partial \xi^2}\left(\sqrt{n_e}\right) \to 0$ as $\xi \to \pm\infty$. Then, first neglecting the quantum diffraction effect (i.e., $H = 0$) from Eq. (7), we get $n_e = (1+2\phi)^{\frac{1}{2}}$, which when plugged again in the Bohm potential term of Eq. (7), the following density expression for electron is obtained (Misra and Chowdhury 2006).

$$n_e^2 = 1 + 2\phi + \frac{H^2}{\delta}\left[(1+2\phi)^{-\frac{1}{4}}\frac{\partial^2}{\partial \xi^2}(1+2\phi)^{\frac{1}{4}}\right]. \tag{8}$$

Equation (8), which expresses the electron density as a function of the electrostatic potential, is derived on the basis of semiclassical limit for the small value of H.

Now substituting the density expressions from Eqs. (6) and (8) in Poisson equation, we obtain

$$\frac{\mathrm{d}^2\phi}{\mathrm{d}\xi^2} = \delta\sqrt{1 + 2\phi + \frac{H^2}{\delta}\left[(1+2\phi)^{-\frac{1}{4}}\frac{\partial^2}{\partial \xi^2}(1+2\phi)^{\frac{1}{4}}\right]} + d - \frac{1}{\sqrt{1-\frac{2\phi}{M^2}}}. \tag{9}$$

Using the boundary condition $\phi \to 0, \frac{\mathrm{d}\phi}{\mathrm{d}\xi} \to 0$ and $\frac{\mathrm{d}^2\phi}{\mathrm{d}\xi^2} \to 0$ as $\xi \to \pm\infty$, we obtain pseudopotential $V(\phi)$ as

$$V(\phi) = -\frac{1}{2}\left(\frac{\mathrm{d}\phi}{\mathrm{d}\xi}\right)^2 \tag{10a}$$

where the charge neutrality condition gives

$$V(0) = V'(0) = 0. \tag{10b}$$

Equation (10a) implies

$$V'(\phi) = -\frac{\mathrm{d}^2\phi}{\mathrm{d}\xi^2}. \tag{11}$$

Making use of Eqs. (11) and (10a), Eq. (9) reduces to

$$V'(\phi) = -\delta\sqrt{(1+2\phi) + \frac{H^2}{\delta}\left[\frac{3V(\phi)}{2(1+2\phi)^2} - \frac{V'(\phi)}{2(1+2\phi)}\right]} - d + \frac{1}{\sqrt{1-\frac{2\phi}{M^2}}}. \tag{12}$$

Equation (12) implies

$$\frac{dV}{d\phi} = \left(A - \frac{D}{2}\right) \pm \sqrt{B + CV + \frac{D^2}{4} - AD} \tag{13}$$

where

$$\begin{aligned} A &= \frac{1}{\sqrt{1 - \frac{2\phi}{M^2}}} - d, \quad B = \delta^2(1 + 2\phi), \\ C &= \frac{3H^2\delta}{2(1 + 2\phi)^2} \quad \text{and} \quad D = \frac{H^2\delta}{2(1 + 2\phi)}. \end{aligned} \tag{14}$$

Here, making use of the charge neutrality condition (10b) in Eq. (12), we have

$$\frac{dV}{d\phi} = \left(A - \frac{D}{2}\right) - \sqrt{B + CV + \frac{D^2}{4} - AD}. \tag{15}$$

Equation (15) represents a first-order ordinary differential equation in ϕ with initial condition $V(0) = 0$ which has been solved by using fourth-order Runge–Kutta method to obtain $V(\phi)$. It is observed from the density expressions (6) and (8) that in order to prevent wave braking, there are limitations on ϕ that $-\frac{1}{2} < \phi < \frac{M^2}{2}$. For the existence of SWs, $V(\phi)$ need to satisfy the following Sagdeev's conditions:

(i) $V''(\phi) < 0$ at $\phi = 0$, so that the fixed point at the origin is unstable.
(ii) $\exists$ a nonzero ϕ_m, the maximum (or minimum) value of ϕ, at which $V(\phi) = 0$.
(iii) $V(\phi) < 0$, for $0 < |\phi| < |\phi_m|$.

Condition (i) gives the lower limit of M for the existence of SWs as $M > M_c$, where

$$M_c = \frac{1}{\sqrt{1 - d}}. \tag{16}$$

Now here for $d \to 0$, $M_c \to 1$ which is same as obtained for simple electron-ion plasmas.

4 Results and Discussion

In this section, the obtained numerical results have been discussed. The values of the parameter are taken as (Misra and Chowdhury 2006; Masood et al. 2007) $n_{e0} \sim 5 \times 10^{29}$, $n_{i0} \sim 2 \times 10^{30}$, $Z_{d0} \sim 10^3$, and $T_{\mathrm{Fe}} \sim 10^2 K$. It is observed from the Eq. (16) that the critical Mach number M_c for the existence of a solitary wave depends upon the dust density parameter d. The variation M_c with the dust concentration d is plotted in Fig. 1. It is observed that M_c increases with an increase in d. It should be pointed here that as the value of M depends upon a specific normalization, some care should be taken to interpret the results physically. The true Mach number is defined by the ratio M/M_c. From this ratio, the reference speed C_0 used in normalization of M disappears (Baluku et al. 2010; Baluku and Hellberg 2012). Thus, the existence condition, $M > M_c$ for solitary waves, implies that the true Mach number $M/M_c > 1$. In Fig. 2a, the pseudopotential $V(\phi)s$ are plotted for three values of d, where $H = 0.4$ and $M/M_c = 1.2$, and corresponding potential profiles are plotted in Fig. 2b. It is found that as d increases, both the amplitude and width of the SWs increase which is in agreement with what has been reported by Khan and Mushtaq (2007). $V(\phi)s$ are plotted in Fig. 3a for different values of the quantum diffraction parameter H, and corresponding potential profiles are plotted in Fig. 3b. The small effect of H is observed on the width of the solitary wave. However, Haas (2005) pointed out that for moderate H, quantum diffraction effects can be negligible if the density is slowly varying in comparison with typical length scale. Here also the small effect of the quantum diffraction parameter is found. It is found that for a small increase in the parameter H, the amplitude does not differ but the width decreases. Next in Fig. 4a, $V(\phi)$s are plotted for different values of M/M_c and respective potential profiles are plotted in Fig. 4b. It is seen that both the amplitude and width of the soliton increase as the true Mach number increases.

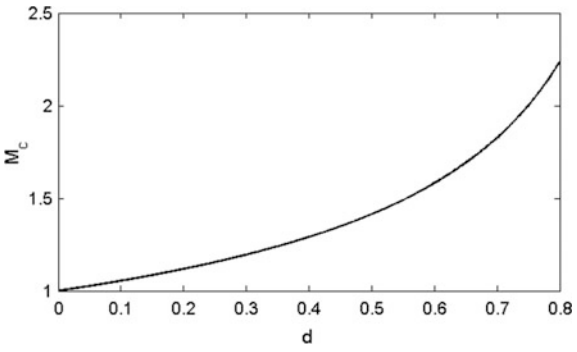

Fig. 1 Plot of M_c against d

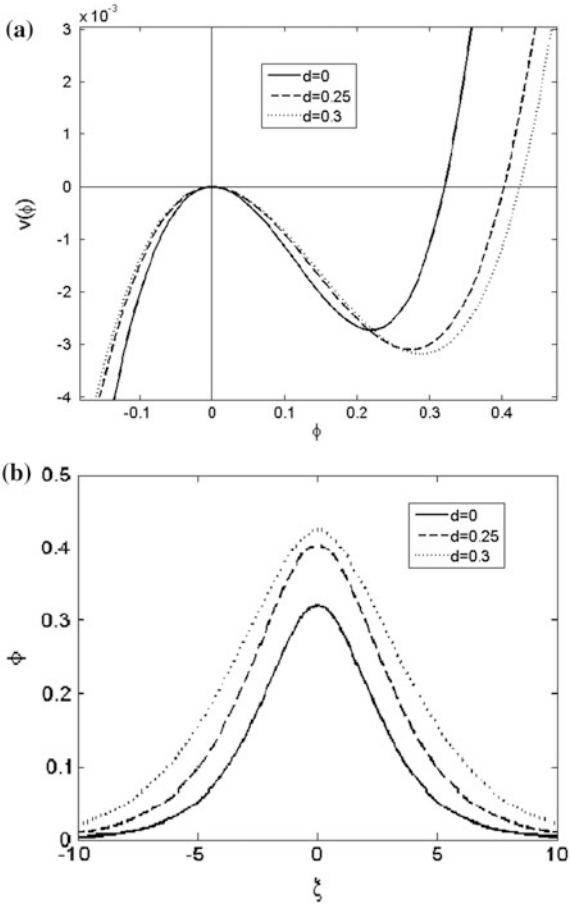

Fig. 2 **a** Plot of $V(\phi)$ for different values of d. **b** Plot of corresponding potential profiles. Here, $= 0.4$, $M/M_c = 1.2$

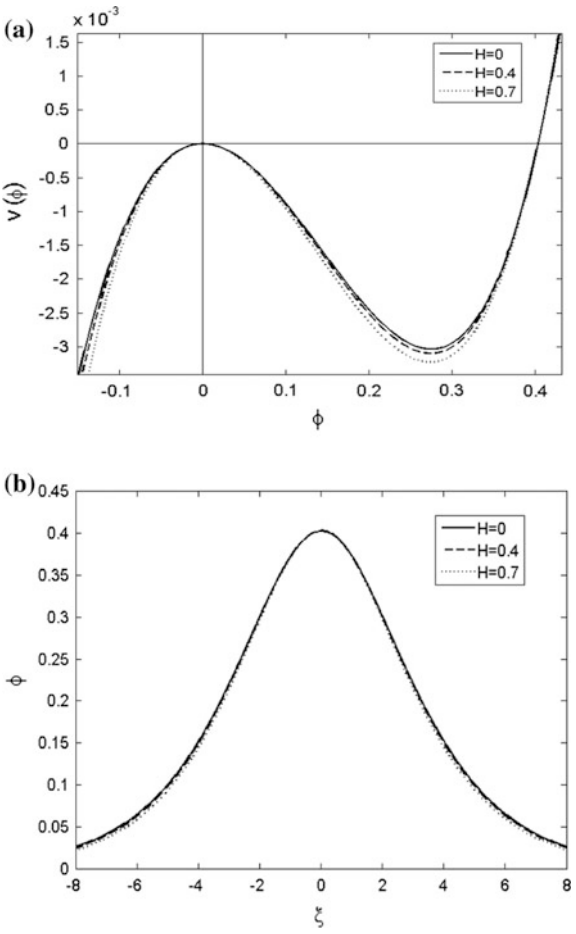

Fig. 3 **a** Plot of $V(\phi)$ for different values of H. **b** Plot of corresponding potential profiles. Here, $d = 0.25$ and $M/M_c = 1.2$

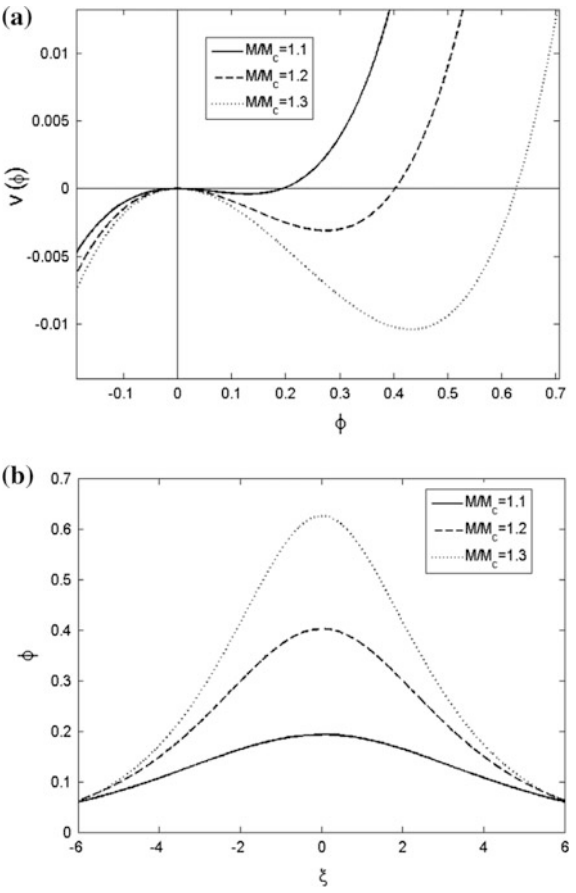

Fig. 4 **a** Plot of $V(\phi)$ for different values of M/M_c. **b** Plot of corresponding potential profiles. Here, $d = 0.25$ and $H = 0.4$

5 Conclusion

In this article, the propagation of DIASWs has been studied by applying Sagdeev's pseudopotential approach in an unmagnetized quantum dusty plasma together with the Poisson equation. The pseudopotential function is obtained numerically by using fourth-order Runge–Kutta method. A numerical investigation is carried out to observe the effects of different parameters. It is observed that the amplitude and width of the DIA waves are modified due to the presence of dust particles, which is in agreement with what has been reported by Khan and Mushtaq (2007). It is also found that the width of the solitary wave decreases due to increase in quantum diffraction parameter but amplitude does not differ.

References

Ali S, Shukla PK (2006) Dust acoustic solitary waves in a quantum plasma. Phys Plasmas 13:022313
Ali S, Moslem WM, Shukla PK, Schlickeiser R (2007) Linear and nonlinear ion-acoustic waves in an unmagnetized electron-positron-ion quantum plasma. Phys Plasmas 14:082307
Baluku TK, Hellberg MA (2012) Ion acoustic solitons in a plasma with two-temperature kappa-distributed electrons. Phys Plasmas 19:012106
Baluku TK, Hellberg MA, Kourakis I, Saini NS (2010) Dust ion acoustic solitons in a plasma with kappa-distributed electrons. Phys Plasmas 17:053702
Chabrier G, Douchin E, Potekhin Y (2002) Dense astrophysical plasmas. J Phys: Condens Matter 14:9133–9139
El-Taibany WF, Wadati Miki (2007) Nonlinear quantum dust acoustic waves in nonuniform complex quantum dusty plasma. Phys Plasmas 14:042302
Fathalian A, Nikjo S (2010) Dust-ion-acoustic wave oscillation in metallic multiwalled carbon nanotubes. Phys Plasmas 17:103710
Gardner CL, Ringhofer C (1996) Smooth quantum potential for the hydrodynamic model. Phys Rev E 53:157–168
Gloge D, Marcuse D (1969) Formal quantum theory of light rays. J Opt Soc Am 59:1629–1631
Haas F (2005) A magnetohydrodynamic model for quantum plasmas. Phys Plasmas 12:062117
Haas F (2011) Quantum plasmas: an hydrodynamic approach. Atomic, optical, and plasma physics, vol 65. Springer, Berlin
Haas F, Garcia LG, Goedert J, Manfredi G (2003) Quantum ion-acoustic waves. Phys Plasmas 10:3858–3866
Hanif M, Ali S, Mukhtar Q, Mirza AM (2014) Numerical study of ion acoustic shock waves in dense quantum plasma. Phys Plasmas 21:032705
Jung YD (2001) Quantum-mechanical effects on electron–electron scattering in dense high-temperature plasmas. Phys Plasmas 8:3842–3844
Khan SA, Mushtaq A (2007) Linear and nonlinear dust ion acoustic waves in ultracold quantum dusty plasmas. Phys Plasmas 14:083703
Madelung E (1926) Quantum theory in hydrodynamical form. Z Phys 40:332–336
Mahmood S (2008) Arbitrary amplitude dust ion acoustic solitary waves in dense Fermi plasmas. Phys Plasmas 15:014502
Mahmood S, Masood W (2008) Electron acoustic solitary waves in unmagnetized two electron population dense plasmas. Phys Plasmas 15:122302
Mahmood S, Mushtaq A (2008) Electron acoustic solitary waves in unmagnetized two electron population dense plasmas. Phys Lett A 372:3467–3470
Manfredi G (2005) How to model quantum plasmas. Fields Inst Commun 46:263–287
Marklund M, Shukla PK (2006) Nonlinear collective effects in photon-photon and photon-plasma interactions. Rev Mod Phys 78:591–640
Masood W, Mushtaq A, Khan R (2007) Linear and nonlinear dust ion acoustic waves using the two-fluid quantum hydrodynamic model. Phys Plasmas 14:123702
Metref H, Tribeche M (2014) Quantum positron acoustic waves. Phys Plasmas 21:122117
Misra AP, Chowdhury AR (2006) Modulation of dust acoustic waves with a quantum correction. Phys Plasmas 13:072305
Misra AP, Shukla PK, Bhowmik C (2007) Electron-acoustic solitary waves in dense quantum electron-ion plasmas. Phys Plasmas 14:082309
Moradi A (2015) Quantum ion-acoustic wave oscillations in metallic nanowires. Phys Plasmas 22:054502
Sah OP, Manta J (2009) Nonlinear electron-acoustic waves in quantum plasma. Phys Plasmas 16:032304

Shukla PK (2009) Dispersion properties of low-frequency electrostatic oscillations in metallic carbon nanotubes. Phys Lett A 373:256–257

Suh N, Feix MR, Bertrand P (1991) Numerical simulation of the quantum Liouville-Poisson system. J Comput Phys 94:403–418

Wang Y, Zhou Z, Qiu H, Wang F, Lu Y (2012) The quantum dusty magnetosonic solitary wave in magnetized plasma. Phys Plasmas 19:013704

Wei L, Wang YN (2007) Quantum ion-acoustic waves in single-walled carbon nanotubes studied with a quantum hydrodynamic model. Phys Rev B 75:193407

Influence of Abrasive Water Jet Turning Parameters on Variation of Diameter of Hybrid Metal Matrix Composite

Akash Nag, Ashish Kumar Srivastava, Amit Rai Dixit, Somnath Chattopadhyaya, Amitava Mandal, Dagmar Klichová, Petr Hlaváček, Michal Zeleňák and Sergej Hloch

Abstract Abrasive water jet turning is one of the recently developed manufacturing technologies. It has gained its importance due to its capability to machine difficult-to-cut material with advantages such as absence of thermal effects, high machining flexibility and little cutting force. In this study, the influence of water jet turning parameters such as abrasive type and abrasive mass flow rate has been analysed on the variation of diameter with the target diameter of metal matrix composite. Composite material A359/Al_2O_3/B_4C fabricated by electromagnetic stir casting process was used in the experiment. To select the level of parameter, one-variable-at-a-time analysis was used. The results revealed that the abrasive type had a greater influence on the deviation of diameter from the target diameter as compared to mass flow rate.

A. Nag (✉) · A.K. Srivastava · A.R. Dixit · S. Chattopadhyaya · A. Mandal
Department of Mechanical Engineering, Indian Institute of Technology (Indian School of Mines), Dhanbad, Dhanbad 826004, Jharkhand, India
e-mail: akashnag1992@gmail.com

A.K. Srivastava
e-mail: ashish7185@gmail.com

A.K. Srivastava
Noida Institute of Engineering and Technology, Noida, India

D. Klichová · P. Hlaváček · M. Zeleňák · S. Hloch
Department of Material Disintegration, Institute of Geonics Academy of Science of Czech Republic, Studentska, Ostrava, Poruba 708 00, Czech Republic
e-mail: dagmar.klichova@ugn.cas.cz

M. Zeleňák
e-mail: Michal.zelenak@ugn.cas.cz

S. Hloch
e-mail: hloch.sergej@gmail.com

S. Hloch
Faculty of Manufacturing Technologies, TU of Košice with the seat in Prešov, Bayerova 1, 080 01 Prešov, Slovak Republic

M.K. Singh et al. (eds.), *Applications of Fluid Dynamics*, Lecture Notes in Mechanical Engineering, https://doi.org/10.1007/978-981-10-5329-0_36

List of Symbols and Abbreviations

MMC	Metal matrix composite
AWJM	Abrasive water jet machining
AWJ	Abrasive water jet
AJWT	Abrasive water jet turning
OVAT	One variable at a time

1 Introduction

A metal matrix composite (MMC) consist of at least two constituents, one being necessarily a metal and the other material may be a different metal or another material, such as ceramic or organic compound. When three or more materials are present, it is called a hybrid composite (Clyne 2000). MMCs offer higher specific strength and stiffness, higher working temperature and higher wear resistance. Aluminium composites are used in various engineering applications for its high strength-to-weight ratio particularly in aircraft and automobile parts such as cylinder blocks and cylinder liners. Miller et al. (2000), Dinwoodie (1987), Rohatgi (1991). However, MMCs also have some disadvantages compared with metals. Chief among these are high abrasiveness of the reinforcing fibres, its heterogeneity and heat sensitiveness Kök (2009), Abrate and Walton (1992), Sahin et al. (2002). Conventional tool material cannot be used for machining MMC's due to high tool wear rate and long machining time Santhanakrishnan et al. (1989), Sakuma and Seto (1983, 1981), Ramulu et al. (1991). However, non conventional methods such as abrasive water jet machining (AWJM), electrical discharge machining (EDM), laser beam machining (LBM) and plasma beam machining (PBM) are successful in machining these materials because the process machinability does not depend upon material hardness and strength. Abrasive water jet machining is a process in which material removal is done by impact erosion of concentrated high-velocity stream of abrasive particle entrained in high-velocity water stream. In abrasive water jet, turning the abrasive water jet is fed by the nozzle, along specific distance and axis, and the workpiece rotates around an axis. The schematic diagram of turning setup is shown in Fig. 1. This paper investigates the machinability of B_4C- and Al_2O_3-reinforced aluminium alloy matrix composite using abrasive water jet turning and the influence of process parameters such as abrasive grain type and abrasive mass flow rate on the final diameter of the machined surface.

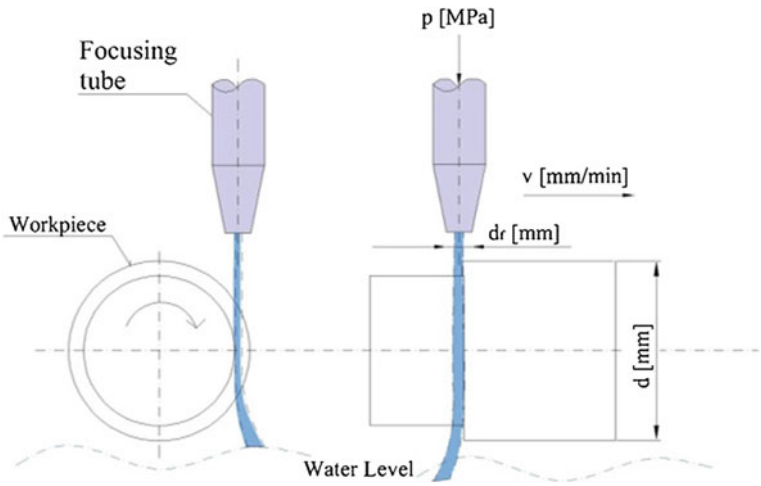

Fig. 1 Schematic diagram of abrasive water jet turning

2 State-of-the-Art Analysis

Hashish (1987) was first to develop abrasive water jet turning. He studied the influence of traverse speed, water pressure, rotational speed, abrasive size, type of abrasive, jet angle, abrasive flow rate and lateral feed increment on surface waviness. He reported that there was a decline in the performance with very high mass flow rate due to overloading of the water jet with abrasives and the dimensional tolerances can be improved by steadiness of process parameters. Machined surface with abrasive water jet (AWJ) did not showed any change in microstructure of the specimen, and tensile test of AWJ-turned sample also stated that the process did not affected the tensile characteristic of the material.

Finnie (1960) investigated erosion of surfaces by solid particles. He predicted a model for angle of impact which leads to maximum erosion and showed velocity dependence on erosion for ductile material.

Manu and Babu (2009) developed a mathematical model based on erosion model of Finnie for predicting final diameter of the machined workpiece. They considered impact angle, traverse speed and nozzle diameter as a function of the decreased diameter. They found out that most of the prediction based on the model was matched by experimental results.

Zohourkari and Zohoor (2010) developed a mathematical model to estimate the final diameter of the cylindrical workpiece machined by abrasive water jet turning (AWJT). They stated that MRR achieved according to Hashish model is less as compared to Finnie. The proposed model by them predicted desired geometry with high correlation with the experimental geometry.

Yue et al. (2014) worked on optimizing machining parameters such as water pressure, jet feed speed, abrasive flow rate, surface speed and nozzle tilt angle over surface roughness and MRR. He observed that in offset radial mode of turning, the actual depth of cut achieved was less than desired.

Kumar et al. (2016) used AWJM to cut friction stir welding joints. They concluded that AWJ cutting generated regular cut surface topography and did not generate any heat-affected zone (HAZ). It was also observed that the cut surface by AWJ was not affected by the rotational speed of the tool.

3 Material and Method

The material used in this paper is hybrid metal matrix composite (MMC) which consist of A359 aluminium alloy as base metal matrix, 2% B_4C and 2% Al_2O_3 as reinforce components. It was fabricated using electromagnetic stir casting process (Srivastava et al. 2016a, b). A359 aluminium alloy was used for its good casting and wettability properties. Composition of the alloy is shown in Table 1. B_4C is the third hardest material and has low specific gravity and impact resistance. Al_2O_3 have a high dielectric properties and good conductivity. The properties of the constituents of the hybrid MMC are shown in Table 2.

The experimental turning was performed on a 2D X–Y cutting table, which had a cutting head specially designed for the AWJ cutting. The water pressure was generated by a PTV pump with two pressure intensifiers. The MMC workpiece was fixed in the 3-jaw-mounted chuck device, which enabled the rotation of the workpiece. Water is pumped at a sufficiently high pressure and is passed through orifice which converts the potential energy of water into kinetic energy. This yields high-velocity jet of water. Abrasive particles are added to the water jet to enhance its cutting ability.

Table 1 Composition of A359 aluminium alloy

Elements	Si	Cu	Mg	Mn	Fe	Zn	Ti	Al
Percentage (%)	8.5–9.5	0.2	0.5–0.7	0.1	0.2	0.1	0.2	Remaining

Table 2 Basic properties of constituents of hybrid MMC Srivastava et al. (2016a, b)

Constituents	A359 (Base metal)	2% Al_2O_3	2% B_4C
Density (g/cm^3)	2.66	3.2	2.52
Thermal conductivity (W/mK)	152	100	30–42
Specific gravity (g/cm^3)	2.68	3.7	2.51
Melting point (°C)	600	2072	2445

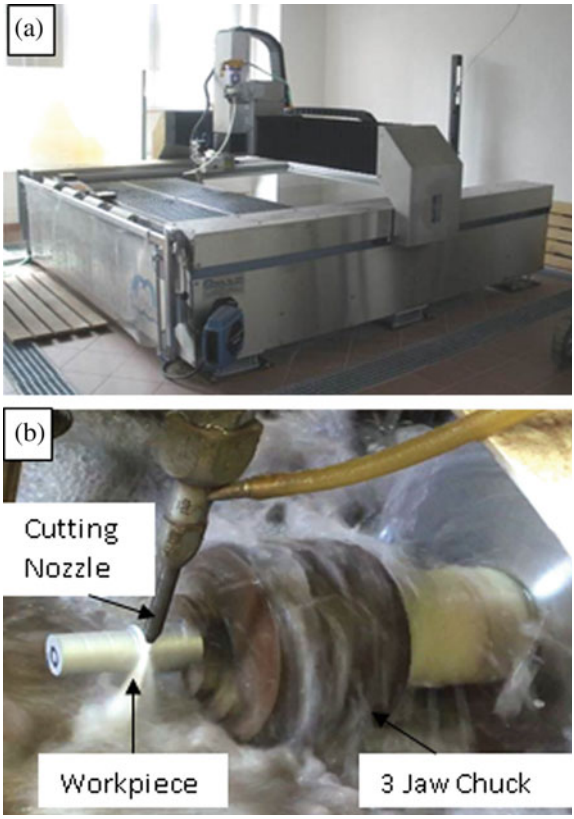

Fig. 2 **a** AWJ setup. **b** AWJ machining zone of MMC material

The abrasive particles are allowed to entrain in water jet to form abrasive water jet with sufficient high velocity. Such high-velocity abrasive jet can machine almost all material. The nozzle was first given the desired depth of cut and then was made to travel along the length of the workpiece. The machine had to be calibrated each time when new abrasive grains were used for machining. AWJ setup and machining zone is shown in Fig. 2a, b.

One-variable-at-a-time analysis (OVAT) was used in this experiment. In OVAT analysis, one process parameter is varied at a time from lower to higher value by keeping all other process parameter constant, and we measure the effect of parameter change on the final diameter. In this work, we took abrasive type and mass flow rate as input machining parameters to see its effect on the final diameter of the workpiece. Two types of abrasives were selected, and four levels of mass flow rates were used. The experimental conditions used during the experiment are shown in the Table 3.

Table 3 Experimental conditions

Factors	Values
Cutting head type	Slice II by PTV
Pressure p (MPa)	300
MESH	80
Angle of attack ϕ (°)	90
Standoff distance z (mm)	15
Depth of cut a_p (mm)	2
Revolution rpm (r/min)	400
Traverse speed v (mm min^{-1})	10
Abrasive type	Barton garnet, Olivine
Abrasive mass flow rate m_a (g/min)	100, 200, 300, 400

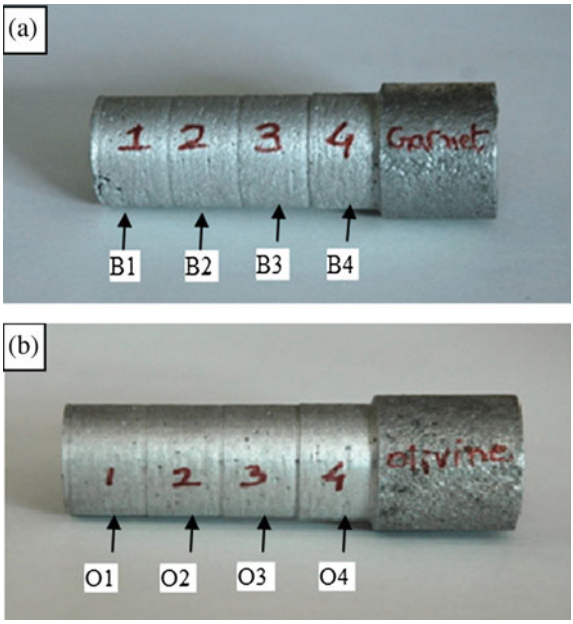

Fig. 3 **a** Machined workpiece using Barton garnet grains, **b** machined workpiece using olivine grains

4 Results and Discussion

The machined surface image is shown in Fig. 3a, b. The final diameter of the machined surface was measured at 4 different places for every experiment by using vernier calliper to avoid any error in the measurement. Mean values of the diameter were taken to calculate the deviation between desired and actual final diameter. The observation table is shown in Table 4.

Table 4 Observation table of abrasive water jet turning

Abrasive	Exp. No.	Abrasive mass flow rate (g/min)	Initial diameter	Final diameter (desired)	Final diameter (actual)	Final diameter (mean)	ΔD	ΔD (%)
Barton garnet (1)	B1	400	25.45	21.45	20.73	20.69	0.76	3.54
					20.67			
					20.66			
					20.71			
	B2	300	25.45	21.45	20.88	20.88	0.57	2.66
					20.86			
					20.90			
					20.87			
	B3	200	25.45	21.45	21.10	21.10	0.36	1.63
					21.06			
					21.09			
					21.13			
	B4	100	25.45	21.45	21.63	21.60	−0.15	−0.70
					21.57			
					21.59			
					21.62			
Olivine (2)	O1	400	25.45	21.45	20.87	20.91	0.54	2.52
					20.89			
					20.92			
					20.96			
	O2	300	25.45	21.45	20.95	20.98	0.47	2.19
					20.98			
					21.00			
					20.99			
	O3	200	25.45	21.45	21.15	21.16	0.29	1.35
					21.16			
					21.14			
					21.18			
	O4	100	25.45	21.45	21.73	21.74	−0.29	−1.35
					21.75			
					21.77			
					21.72			

$$\Delta D = \text{Mean Final Diameter (Actual)} - \text{Final Diameter (Desired)}$$
$$\Delta D\% = \Delta D \div \text{Final Diameter (Desired)}$$

It was observed that the final diameter reduced as we increased the abrasive mass flow rate for both the abrasive grains while the depth of cut was kept constant throughout the experiment. It may be due to the fact that by increasing the abrasive mass flow rate, amount of abrasive interacting or involving in cutting process

increases. Due to which more amount of material erosion takes place for same machining length and time. It was also observed from the results that the final diameter was less than the desired diameter for higher values of abrasive flow rate. The deviation of actual final diameter from desired diameter followed an inversely linear trend with the abrasive mass flow rate. The result also highlighted an observation that while turning with olivine abrasive, the difference in diameters obtained was not large and was similar for high flow rates, but for Barton garnet abrasive, it varied evenly with the abrasive mass flow rates. Moreover, Barton garnet gave a larger range of diameter deviation than that obtained by olivine grains. It may be due to the change in their crystalline structure which generates coarser and smoother cuts. The graph of the actual diameter obtained and desired diameter with different abrasive grain and different abrasive mass flow rate has been plot and shown in Fig. 4a, b.

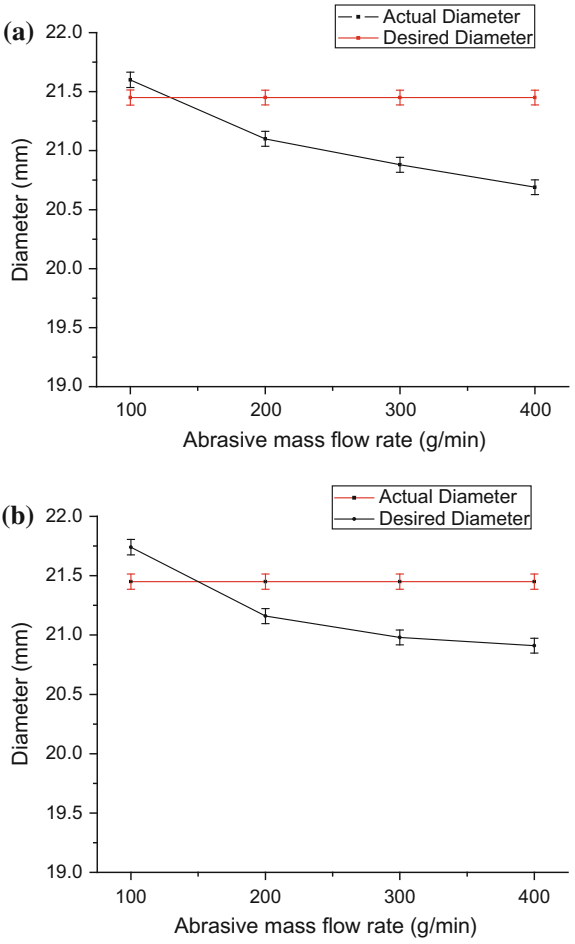

Fig. 4 Desired and actual diameter obtained using **a** Barton garnet abrasive grains, **b** olivine abrasive grains

5 Conclusion and Future Scope

Based on the experiments, it can be concluded that

- AWJT can be used successfully to turn hybrid metal matrix composite by eliminating the problem of tool wear which occurs during conventional turning.
- Due to the absence of any temperature rise in the machining area, no change in the microstructure or physical properties of the machined surface takes place.
- Proper control of the required dimension can be obtained by setting appropriate machining parameters.
- Increase in abrasive flow rate increases the interaction of abrasive with the material leading to higher material removal.
- Use of different abrasive grains makes the surface smoother or coarser depending on their shape and physical properties.
- Olivine abrasive grains give better dimensional control than Barton garnet grains.

Further investigation on the machined surface finish and study of surface topography of the machined surface obtained by varying the machining parameters can be done. Moreover, influence of other machining parameters on the machinability of difficult-to-machine material like Hybrid MMC's can be investigated.

Acknowledgements This work was supported by the Slovak Research and Development Agency under Contract No. APVV-207-12. Experiments were carried out with the support of the Institute of Clean Technologies for Mining and Utilization of Raw Materials for Energy Use—Sustainability Program, reg. no. LO1406 financed by Ministry of Education, Youth and Sports of the Czech Republic—and with support for the long-term conceptual development of the research institution RVO: 68145535.

References

Abrate S, Walton DA (1992) Machining of composite materials Part I: Traditional methods. Compos Manufact 3(2):75–83

Clyne TW (2000) An introductory overview of MMC systems, types, and developments. Compr Compos Mater 3:1–26

Dinwoodie J (1987) Automotive applications for MMC's based on short staple alumina fibres (No. 870437). SAE Technical Paper

Finnie I (1960) Erosion of surfaces by solid particles. Wear 3(2):87–103

Hashish M (1987) Turning with abrasive-waterjets—a first investigation. J Eng Ind 109(4): 281–290

Kök M (2009) A study on the machinability of Al_2O_3 particle reinforced aluminium alloy composite. Pract Metall 46(11):580–597

Kumar R, Chattopadhyaya S, Dixit AR, Bora B, Zelenak M, Foldyna J, Hloch S, Hlavacek P, Scucka J, Klich J, Sitek L (2016) Surface integrity analysis of abrasive water jet-cut surfaces of friction stir welded joints. Int J Adv Manuf Technol 1–15

Manu R, Babu NR (2009) An erosion-based model for abrasive waterjet turning of ductile materials. Wear 266(11):1091–1097

Miller WS, Zhuang L, Bottema J, Wittebrood A, De Smet P, Haszler A, Vieregge A (2000) Recent development in aluminium alloys for the automotive industry. Mater Sci Eng: A 280(1):37–49

Ramulu M, Faridnia M, Garbini JL, Jorgensen JE (1991) Machining of graphite/epoxy composite materials with polycrystalline diamond (PCD) tools. J Eng Mater Technol 113(4):430–436

Rohatgi P (1991) Cast aluminum-matrix composites for automotive applications. JOM 43(4): 10–15

Sahin Y, Kok M, Celik H (2002) Tool wear and surface roughness of Al_2O_3 particle-reinforced aluminium alloy composites. J Mater Process Technol 128(1):280–291

Sakuma K, Seto M (1981) Tool wear in cutting glass-fiber-reinforced-plastics: the relation between cutting temperature and tool wear. Bull JSME 24(190):748–755

Sakuma K, Seto M (1983) Tool wear in cutting glass-fiber-reinforced plastics: the relation between fiber orientation and tool wear. Bull JSME 26(218):1420–1427

Santhanakrishnan G, Krishnamurthy R, Malhotra SK (1989) High speed steel tool wear studies in machining of glass-fibre-reinforced plastics. Wear 132(2):327–336

Srivastava AK, Dixit AR, Tiwari S (2016a) A review on the intensification of metal matrix composites and its nonconventional machining. Sci Eng Compos Mater. https://doi.org/10.1515/secm-2015-0287

Srivastava AK, Dixit AR, Tiwari S (2016b) Investigation of micro-structural and mechanical properties of metal matrix composite A359/B 4 C through electromagnetic stir casting. Indian J Eng Mater Sci 23(2&3):171–180

Yue Z, Huang C, Zhu H, Wang J, Yao P, Liu Z (2014) Optimization of machining parameters in the abrasive waterjet turning of alumina ceramic based on the response surface methodology. Int J Adv Manuf Technol 71(9–12):2107–2114

Zohourkari I, Zohoor M (2010 January) Mathematical modeling of abrasive waterjet turning of ductile materials. In: ASME 2010 10th biennial conference on engineering systems design and analysis. American Society of Mechanical Engineers, pp 825–830

Peristaltic Flow of a Bingham Fluid in Contact with a Jeffrey Fluid

R. Saravana, P. Hariprabakaran, R. Hemadri Reddy and S. Sreenadh

Abstract The article concerns the peristaltic transport of two-layered fluid, consisting of a Bingham fluid in the core region and a Jeffrey fluid in the peripheral region through a channel. The flow is analyzed in the wave of reference under the assumptions of long wavelength and low Reynolds number. The analytical expressions for stream function, pressure rise, and the frictional force per wavelength in both the regions are obtained. The effect of physical parameters namely yield stress, Jeffrey parameter associated with the flow are presented graphically. This model helps to understand the behavior of two immiscible physiological fluids in living structures and in modeling the biomechanical instruments.

1 Introduction

The mechanism of peristalsis takes place in the food bolus transport through esophagus, chyme movement in the gastrointestinal tract, lymph transport in the lymphatic vessels, urine transport from kidney to bladder through the ureter, and in the vasomotion of small blood vessels. In mechanical aspects, the peristaltic pumps are modeled to transport the corrosive liquids in nuclear industries and to filter blood in dialysis machine. A few investigations on the peristaltic flow of physiological

R. Saravana (✉)
Department of Mathematics, Madanapalle Institute of Technology and Science, Madanapalle 517325, Andhra Pradesh, India
e-mail: saravanasvu@gmail.com

P. Hariprabakaran
Department of Mathematics, Thiruvalluvar University College of Arts and Science, Gajalnaickanpatti, Tirupattur 635901, Tamil Nadu, India

R. Hemadri Reddy
Department of Mathematics, School of Advanced Science, VIT University, Vellore 632014, Tamil Nadu, India

S. Sreenadh
Department of Mathematics, Sri Venkateswara University, Tirupati 517502, Andhra Pradesh, India

M.K. Singh et al. (eds.), *Applications of Fluid Dynamics*, Lecture Notes in Mechanical Engineering, https://doi.org/10.1007/978-981-10-5329-0_37

fluids have been reported in the literature (Nadeem and Akram 2009; Saravana et al. 2011; Vajravelu et al. 2013). The behavior of blood flow through small vessels represents two-layered flow which includes plasma peripheral layer and suspension of all erythrocytes in core region. Brasseur et al. (1987) reported the influence of Newtonian peripheral layer of different viscosities on the peristaltic pumping. Usha and Ramachandra Rao (1997) investigated the two-layered peristaltic flows with long wavelength and low Reynolds number assumptions. Narahari and Sreenadh (2010) analyzed the peristaltic pumping of a Bingham fluid with Newtonian peripheral region, and Hari Prabakaran et al. (2013) extended this work through an inclined channel. Very recently, Kavitha et al. (2015) addressed the peristaltic pumping of a Jeffrey fluid in contact with a Newtonian fluid in an inclined channel.

Keeping all these aspects in mind, we investigated the peristaltic flow of a Bingham fluid in the core region in contact with a Jeffrey fluid in the peripheral region. The analytical expressions for two-layered flow are obtained under the long wavelength and low Reynolds number assumptions. The effect of yield stress parameter and Jeffrey parameter on the flow and the shape of interface is presented graphically.

2 Mathematical Formulation

Consider the two-layered peristaltic flow of an incompressible Bingham fluid occupying core region and an incompressible Jeffrey fluid occupying peripheral region through a two-dimensional channel. For simplicity and without loss of symmetricity, we restrict our analysis to the half width of the channel and it is shown in Fig. 1. In the Cartesian coordinate system (X, Y), the flexible channel walls are modeled as

$$Y = H(X,t) = a + b\sin\frac{2\pi}{\lambda}(X - ct) \tag{1}$$

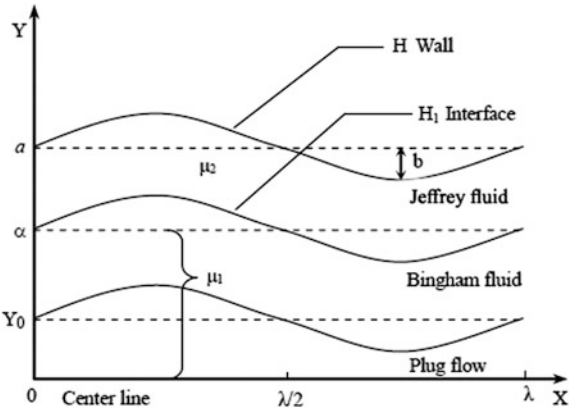

Fig. 1 Physical model

The letters a, b, c, and t denote half width of the channel, amplitude, speed of the wave, and time, respectively. The Greek letter λ represents wavelength.

The deformation separating the core and peripheral layers is represented by $H_1(X,t)$.

The stress tensor model for Bingham fluid in core region following (Chen et al. 2004; Frigaard and Ryan 2004) are

$$\tau_1 = \mu_1 \frac{\mathrm{d}u_1}{\mathrm{d}y} + \tau_0 \mathrm{sign}\left(\frac{\mathrm{d}u_1}{\mathrm{d}y}\right), \quad |\tau_1| > \tau_0, \tag{2}$$

$$\frac{\mathrm{d}u_1}{\mathrm{d}y} = 0, \quad |\tau_1| < \tau_0 \tag{3}$$

and the corresponding stress tensor for Jeffrey fluid in peripheral region following Hayat and Ali (2008) are

$$\tau_2 = \frac{\mu_2}{1+\lambda_1}(\dot{\gamma} + \lambda_2 \ddot{\gamma}), \tag{4}$$

where $\tau_i (i = 1, 2)$ and $\mu_i (i = 1, 2)$ represent the stress tensors and viscosities in the core and peripheral regions, respectively, u_1 denotes the velocity in the central region, τ_0 is the yield stress, λ_1 is the ratio of relaxation to retardation times, λ_2 is the delay time, $\dot{\gamma}$ is shear rate, and dots over the quantity indicate differentiation with respect to time.

The transformation between the laboratory frame (X, Y) and wave frame (x, y) is given by

$$\left.\begin{array}{l} x = X - ct,\ y = Y,\ u(x,y) = U(X - ct, Y) - c, \\ v(x,y) = V(X - ct, Y),\ p(x) = P(X,t),\ \psi = \Psi - Y \end{array}\right\} \tag{5}$$

where ψ and Ψ are the stream functions in the wave frame and laboratory frame, respectively.

We define the non-dimensional quantities as follows:

$$\begin{aligned} &\bar{x} = \frac{x}{\lambda},\ \bar{y} = \frac{y}{a},\ \bar{h} = \frac{h}{a},\ \bar{h}_1 = \frac{h_1}{a},\ \bar{t} = \frac{ct}{\lambda},\ \bar{P} = \frac{Pa^2}{\mu_1 \lambda c}, \\ &\quad \phi = \frac{b}{a},\ \bar{\tau}_i = \frac{a}{\mu_1 c}\tau_i,\ \bar{\psi}_i = \frac{\psi_i}{ac}, \\ &\bar{\tau}_0 = \frac{a}{\mu_1 c}\tau_0,\ \bar{q} = \frac{q}{ac},\ \bar{F} = \frac{Fa}{\mu_1 \lambda c},\ \bar{u}_i = \frac{u_i}{c} = \frac{\partial \psi_i}{\partial \bar{y}},\ \bar{v}_i = \frac{v_i \lambda}{ac} = \frac{-\partial \psi_i}{\partial \bar{x}} (i = 1, 2), \\ &\bar{\mu} = \begin{cases} 1, & 0 \le \bar{y} \le \bar{h}_1 \\ \mu\left(= \frac{\mu_2}{\mu_1}\right), & \bar{h}_1 \le \bar{y} \le \bar{h} \end{cases} \end{aligned} \tag{6}$$

Here $\bar{u}_i$ and $\bar{v}_i$ are the velocity components in the wave frame along $\bar{x}$ and $\bar{y}$ directions.

The governing equations of motion of immiscible flow in both the core and peripheral layer, under the assumptions of long wavelength and low Reynolds number (dropping bars), are

$$\frac{\partial}{\partial y}\left[-\tau_0 + \frac{\partial^2 \psi_1}{\partial y^2}\right] = \frac{\partial p}{\partial x}, \quad 0 \le y \le h_1 \tag{7}$$

$$0 = \frac{\partial p}{\partial y}, \tag{8}$$

$$\frac{\partial}{\partial y}\left[\frac{\mu}{1+\lambda_1}\frac{\partial^2 \psi_2}{\partial y^2}\right] = \frac{\partial p}{\partial x}, \quad h_1 \le y \le h \tag{9}$$

The corresponding boundary conditions are

$$\psi_1 = 0 \quad \text{at} \quad y = 0 \tag{10}$$

$$(\psi_1)_{yy} = \tau_0 \quad \text{at} \quad y = 0 \tag{11}$$

$$\psi_2 = q = \text{constant} \quad \text{at} \quad y = h \tag{12}$$

$$\psi_1 = \psi_2 = q_1 = \text{constant} \quad \text{at} \quad y = h_1 \tag{13}$$

$$(\psi_2)_y = -1 \quad \text{at} \quad y = h \tag{14}$$

The letters q and q_1 indicate the total and the core fluxes across any cross section in the wave frame, respectively. In addition, shear stress and velocity are continuous across the interface. The peripheral layer flux is given by $q_2 = q - q_1$. The incompressibility of the fluids follows that q, q_1 and q_2 are independent of x. The dimensionless average volume flow rate $\overline{Q}$ over one period $T\left(=\frac{\lambda}{c}\right)$ of the peristaltic wave is defined as

$$\overline{Q} = q + 1. \tag{15}$$

3 Solution of the Two-Fluid System

Solve Eqs. (7)–(9) together with the boundary conditions (10)–(14) and

$$\psi_1 = (\psi_1)_p \quad \text{at} \quad y = y_0 \tag{16}$$

$$(\psi_1)_p = 0 \quad \text{at} \quad y = 0 \tag{17}$$

where y_0 is the upper limit of the plug flow region and $(\psi_1)_p$ is the plug flow region stream function.

The stream functions in the core (plug flow and non-plug flow regions) and peripheral region are obtained as

$$(\psi_1)_p = y\left[-1 - \tau_0(h_1 - y_0) + \left((1+\lambda_1)F_2 - \mu y_0^2\right)\left[\frac{6(q+h) + 3\tau_0\left(h_1^2 - y_0^2\right)}{4\left((1+\lambda_1)F_3 - \mu y_0^3\right)}\right]\right] \quad \text{for} \quad 0 \le y \le y_0 \tag{18}$$

$$\psi_1 = -y - \tau_0 h_1 y + \frac{\tau_0}{2}\left(y^2 + y_0^2\right) + \left[\frac{2(q+h) + \tau_0\left(h_1^2 - y_0^2\right)}{8\left((1+\lambda_1)F_3 - \mu y_0^3\right)}\right] \left[6(1+\lambda_1)F_2 y - 2\mu\left(y^3 + 2y_0^3\right)\right] \quad \text{for} \quad y_0 \le y \le h_1 \tag{19}$$

$$\psi_2 = -y + (q+h) + \frac{\left[6(q+h) + 3\tau_0\left(h_1^2 - y_0^2\right)\right]\left[3yh^2 - y^3 - 2h^3\right]}{12\left(F_3 - \mu y_0^3\right)} \quad \text{for} \quad h_1 \le y \le h \tag{20}$$

where

$$(1+\lambda_1)F_j = (1+\lambda_1)h^j + (\mu - (1+\lambda_1))h_1^j \quad (j = 2, 3)$$

The axial pressure gradient is given by

$$\frac{\mathrm{d}p}{\mathrm{d}x} = -\left[\frac{6\mu(q+h) + 3\mu\tau_0\left(h_1^2 - y_0^2\right)}{2\left((1+\lambda_1)F_3 - \mu y_0^3\right)}\right] \tag{21}$$

3.1 Interface Equation

The unknown interface $h_1(x)$ is solved from (19) using the boundary condition (10). Thus, we get the algebraic equation governing the interface $h_1(x)$ as

$$\begin{aligned}
&\tau_0(1+\lambda_1)h_1^5 + 4(\mu - (1+\lambda_1))h_1^4 - (2(q+h)(2\mu - 3(1+\lambda_1)) \\
&\quad -4q_1(\mu - (1+\lambda_1)) + \tau_0(1+\lambda_1)\left(3h^2 + y_0^2\right))h_1^3 \\
&\quad + \left(2\tau_0(1+\lambda_1)h^3\right)h_1^2 - \left(\left(6qh^2 + 2h^3 - 3\tau_0 y_0^2 h^2\right)(1+\lambda_1) + 4\mu y_0^3\right)h_1 \\
&\quad + \left(4q_1 - 2\tau_0 y_0^2\right)h^3(1+\lambda_1) - 4q_1\mu y_0^3 + 4(q+h)\mu y_0^3 = 0
\end{aligned} \tag{22}$$

where q and q_1 are independent of x.

Using the condition $h_1 = \alpha,\ \ y_0 = \alpha_1$ at $x = 0$ in Eq. (22), we get

$$q_1 = \frac{\begin{pmatrix} \tau_0(1+\lambda_1)\alpha^5 + 4(\mu-(1+\lambda_1))\alpha^4 \\ -\big(2(q+1)(2\mu-3(1+\lambda_1)) + \tau_0(1+\lambda_1)\big(\alpha_1^2+3\big)\big)\alpha^3 \\ +2\tau_0(1+\lambda_1)\big(\alpha^2-\alpha_1^2\big) + 4(q+1)\mu\alpha_1^3 \\ -\big(6q(1+\lambda_1) + 4\mu\alpha_1^2 - 3\tau_0(1+\lambda_1)\alpha_1^2 + 2(1+\lambda_1)\big)\alpha \end{pmatrix}}{4\mu\alpha_1^3 - 4(\mu-(1+\lambda_1))\alpha^3 - 4(1+\lambda_1)} \tag{23}$$

3.2 The Pumping Characteristics

Integrating Eq. (21) with respect to x over one cycle of the wavelength, we get the pressure rise (drop) as

$$\Delta P = -3\mu\big(\overline{Q}-1\big)I_1 - 3\mu I_2 - \frac{3}{2}\mu\tau_0 I_3 \tag{24}$$

where

$$I_1 = \int_0^1 \frac{1}{F_3(1+\lambda_1) - \mu y_0^3}\,\mathrm{d}x; \quad I_2 = \int_0^1 \frac{h}{F_3(1+\lambda_1) - \mu y_0^3}\,\mathrm{d}x;$$

$$I_3 = \int_0^1 \frac{h_1^2 - y_0^2}{F_3(1+\lambda_1) - \mu y_0^3}\,\mathrm{d}x$$

4 Graphical Results and Discussion

In wave frame analysis, the interface is also known as streamline and is calculated by using Eq. (22). The variations in interface shape for yield stress, Jeffrey parameter, and the ratio of viscosity are plotted in Figs. 2, 3, and 4. From Fig. 2, we notice that the decrease in yield stress results the thinner peripheral layer in the dilated region. Figure 3 shows that an increase in Jeffrey parameter yields the thicker peripheral layer in the dilated region. The streamlines for viscosity ratio are shown in Fig. 4. From the figure, we have seen that the high viscosity ratio gives rise in the thinner peripheral layer in the dilated region. Also, we find that the shape

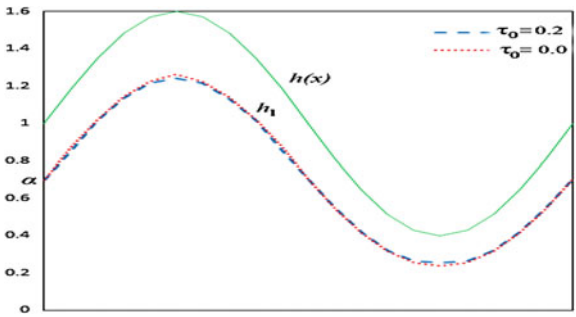

Fig. 2 Interface shape for yield stress with $\phi = 0.6$, $\mu = 0.9$, $\overline{Q} = 0.1$, $\alpha = 0.7$, $\lambda_1 = 1$

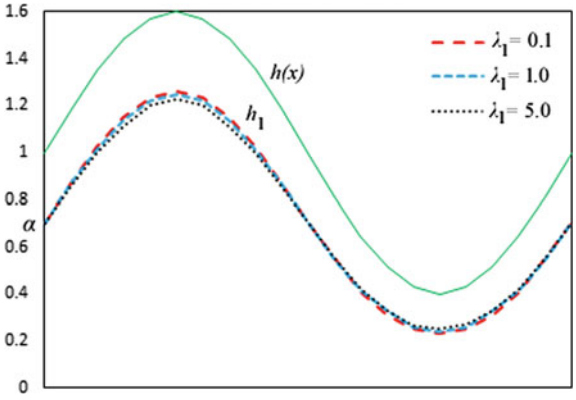

Fig. 3 Interface shape for Jeffrey parameter with $\phi = 0.6$, $\mu = 0.9$, $\overline{Q} = 0.1$, $\alpha = 0.7$, $\tau_0 = 0.1$

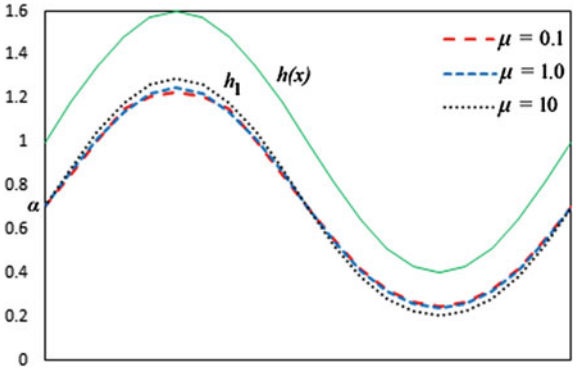

Fig. 4 Interface shape for ratio of viscosity with $\phi = 0.6$, $\lambda_1 = 1$, $\overline{Q} = 0.1$, $\alpha = 0.7$, $\tau_0 = 0.1$

of interface between the two fluids is not unique. The relation between pressure rise and volume flow rate is determined from Eq. (24). The effect of yield stress and Jeffrey parameter on the pumping characteristics is presented graphically in Figs. 5 and 6. Figure 5 depicts that for a given flux $\overline{Q}$, the pressure rise decreases with increasing yield stress. Figure 6 illustrates that for a given flux $\overline{Q}$, the pressure rise increases with increasing the Jeffrey parameter. In addition, we observe that the relation between pressure rise and volume flow rate is linear. In the absence of yield stress and Jeffrey parameter, the equations and the corresponding results of present study were found to be good in agreement with those of Brasseur et al. (1987).

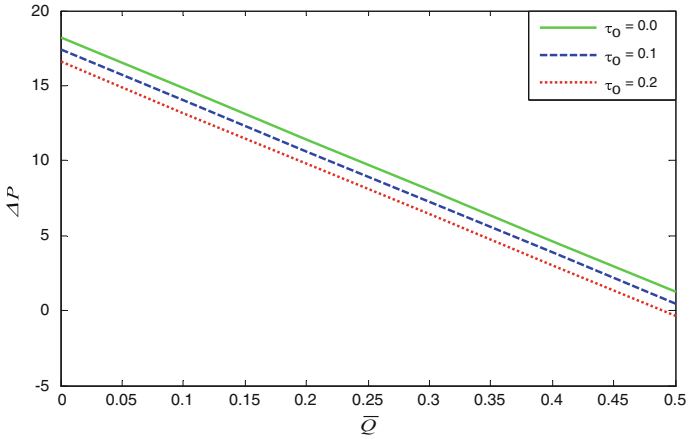

Fig. 5 ΔP versus $\overline{Q}$ for different yield stress parameters with $\phi = 0.6$, $\mu = 0.9$, $\lambda_1 = 0.1$, $\alpha = 0.7$

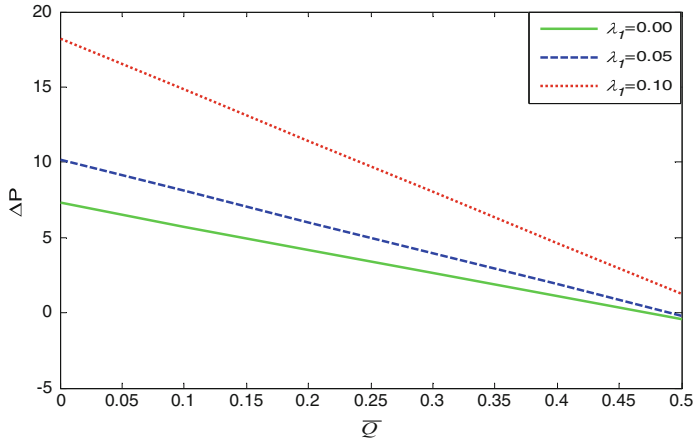

Fig. 6 ΔP versus $\overline{Q}$ for different Jeffrey parameters with $\phi = 0.6$, $\mu = 0.9$, $\tau_0 = 0.1$, $\alpha = 0.7$

5 Conclusion

The analytical solution for the peristaltic pumping of a Bingham fluid in contact with a Jeffrey fluid has been derived. The numerical computed results are presented graphically. The results of present study reveal that the decrease in yield stress results the thinner peripheral layer and an increase in Jeffrey parameter yields the thicker peripheral layer in the dilated region. The study shows that for pumping region $(\Delta P > 0)$, the flow rate and pressure difference are lowered for higher values of yield stress, whereas the flow rate and pressure difference increase by increasing the Jeffrey parameter.

References

Brasseur JG, Corrsin S, Lu Nan Q (1987) The influence of a peripheral layer of different viscosity on peristaltic pumping with Newtonian fluids. J Fluid Mech 174:495–519

Chen CI, Chen CK, Yang YT (2004) Unsteady unidirectional flow of Bingham fluid between parallel plates with different given volume flow rate conditions. Appl Math Model 28:697–709

Frigaard IA, Ryan DP (2004) Flow of a visco-plastic fluid in a channel of slowly varying width. J Non-newton Fluid Mech 123:67–83

Hari Prabakaran P, Hemadri Reddy R, Sreenadh S, Saravana R, Kavitha A (2013) Peristaltic pumping of a Bingham fluid in contact with a Newtonian fluid in an inclined channel under long wave length approximation. Adv Appl Fluid Mech 13(2):127–139

Kavitha A, Hemadri Reddy R, Saravana R, Sreenadh S (2015) Peristaltic transport of a Jeffrey fluid in contact with a Newtonian fluid in an inclined channel. Ain Shams Eng J. doi:10.1016/j.asej.2015.10.014

Nadeem S, Akram S (2009) Peristaltic transport of a hyperbolic tangent fluid model in an asymmetric channel. Zeitschrift fur Naturforschung 64a:559–567

Narahari M, Sreenadh S (2010) Peristaltic transport of a Bingham fluid in contact with a Newtonian fluid. Int J Applied Math Mech 6(11):41–54

Saravana R, Sreenadh S, Venkataramana S, Hemadri Reddy R, Kavitha A (2011) Influence of slip conditions, wall properties and heat transfer on MHD peristaltic transport of a Jeffrey fluid in a non-uniform porous channel. Int J Innov Technol Creative Eng 1(11):10–24

Hayat T, Ali N (2008) Peristaltic motion of a Jeffrey fluid under the effect of a magnetic field in a tube. Commun Nonlinear Sci Numer Simul 13:1343–1352

Usha S, Ramachandra Rao AR (1997) Peristaltic transport of two-layered power-law fluids. J Biomech Eng 119:483–488

Vajravelu K, Sreenadh S, Saravana R (2013) Combined influence of velocity slip, temperature and concentration jump conditions on MHD peristaltic transport of a Carreau fluid in a non-uniform channel. Appl Math Comput 225:656–676

Performance Analysis of Pulsating Water Jet Machining During Disintegration of Rocks by Means of Acoustic Emission

Rupam Tripathi, Madhulika Srivastava, Sergej Hloch, Somnath Chattopadhyaya, Alok Kumar Das, Alokesh Pramanik, Dagmar Klichová and Pavel Adamcik

Abstract Over the decades, water jet cutting has been widely used for rock disintegration in mining operations and quarrying purposes. The impact of high-pressure water jet on hard material like rock, coal ruins the original structure of the material; therefore, low-pressure water jet comes into the existence. In recent year, pulsating water jet has been applied in numerous ways such as surface cleaning, exclusion of damaged material layers, preparation of surfaces, and disintegration of materials. It has also a great potential for application in hard rock breakage as conventional methods are cumbersome, not readily accessible and have economical limitations. The performance of the jet increases significantly by the generation of pulses causing disintegration of material at a relatively lower energy and costs. This paper focuses on the study of the disintegration processes of marble and granite by pulsating water jet subjected to erosion via acoustic emission. The experiments are performed by using pulsating water jet with modulation frequency of 20.20 kHz. The MVT circular nozzle with an orifice diameter of 0.9 mm, standoff distance from the target material 6 mm, traverse speed varied from 2 to

R. Tripathi (✉) · M. Srivastava · S. Chattopadhyaya · A.K. Das
Department of Mechanical Engineering, Indian Institute of Technology (Indian School of Mines), Dhanbad, Dhanbad 826004, Jharkhand, India
e-mail: rupam.tripathi10@gmail.com

S. Hloch
Faculty of Manufacturing Technologies, TU of Košice with the seat in Prešov, Bayerova 1, 080 01 Presov, Slovak Republic
e-mail: hloch.sergej@gmail.com

S. Hloch · D. Klichová
Department of Material Disintegration, Institute of Geonics Academy of Science of Czech Republic, Studentska, Ostrava, Poruba 708 00, Czech Republic
e-mail: dagmar.klich@ugn.cas.cz

A. Pramanik
Department of Mechanical Engineering, Curtin University, Perth, Australia
e-mail: Alokesh.Pramanik@curtin.edu.au

P. Adamcik
Technická Diagnostika, Ltd., Jilemnického 4, 080 01 Prešov, Slovak Republic
e-mail: tdg@diagnostika.sk

M.K. Singh et al. (eds.), *Applications of Fluid Dynamics*, Lecture Notes in Mechanical Engineering, https://doi.org/10.1007/978-981-10-5329-0_38

16 mm/s, and pump pressure 60 MPa was used for water jetting. The topography of granites and marble on the cut depth and surface quality were investigated by the optical profile meter. Moreover, dependable relations between some physical and mechanical properties of the rocks and the depth of cut were observed. The online monitoring of acoustic emission shows the change in response to the pulse frequency at different time intervals.

Abbreviations

PWJ	Pulsating water jet
AE	Acoustic emission
WJ	Water jet
FFT	Fast fourier transform
Ra	Mean arithmetic deviation of roughness
Rq	Root-mean-square deviation of the profile
Rz	Maximum height of the roughness profile
Sq	Root-mean-square roughness
f	Frequency (kHz)
d	Diameter of the nozzle (mm)
v	Traverse speed (mm/s)
p	Pressure (MPa)
z	Standoff distance (mm)

1 Introduction

Water jet offers wide range of solutions in rock cutting and has greatly been used for disintegration of rocks. Manipulation of large volume of water at low pressure as a tool can be done efficiently and effectively (Knill et al. 1968).

Over several decades, granite is being actively used as a building material due to its exceptional properties like resistance to aesthetic properties and environmental effects (Zelenak et al. 2015). Though granite is compatible with the environmental conditions, it has limited industrial application. Since 1960, rock breakage technology is using high-pressure, low volume jet-gained popularity in scientific research and industrial applications and pulsed water jet provided new direction for hard rock breakage (Karakurt et al. 2012). Various studies has been reported related to the design of nozzle but only few are concerned with the parametric study like traverse speed, pressure etc. The present study focus on studying the variation of traverse speed of nozzle during disintegration of rocks.

In the past two decades, the use of natural stone has been made more significant. The growing commercial market and competition for natural stone have resulted in increased demand for innovative manufacturing process (Tripathi et al. 2016).

Due to the composition of natural stone (granite, shale, concrete), especially granite machining and processing with traditional system have some difficulties. Therefore, new technology comes in the picture that is pulsating water jet machining. Due to this, increase machining efficiency by minimizing production time and cost required. Among the innovative manufacturing process, water jet has developed broad application (Knill et al. 1968).

WJ has been widely used in exclusion of damaged material layers, surface cleaning, breakage of biological material, and many other applications (Srivastava et al. 2016; Foldyna et al. 2012). The formation of pulses in pulsating water jet is based upon the generation of acoustic waves using a transducer which acts on the pressurized liquid and transmits it to the actuators in acoustic chamber filled with pressurized liquid. These acoustic waves are then amplified using a mechanical amplifier and transferred to the nozzle with the help of a liquid waveguide (Zelenak et al. 2015; Lehocka et al. 2016).

The impact of the highly energized liquid mass stream on the solid surface causes the disintegration of the surface due to the formation of short pressure transients.

This phenomenon of disintegration consists of two main stages: (a) Initially, the water hammer pressures are generated due to the compressive nature of the liquid. These pressures cause the most serious damages to the surface. (b) As this impact pressure releases, liquid starts flowing away from the point of impact. The velocity with which the liquid flows tangentially is five times the impact velocity (Foldyna et al. 2012).

Nowaday's acoustic emission phenomenon is one of the best phenomena. It is nondestructive testing of highly stressed material as a result of internal deformation mechanism may be used to examine the deformation and failure of rocks under load. Therefore, it has been used in laboratory on the material such as gold crystal and wooden beams. It has been also found many applications in model studies of the earthquake and testing of the missiles casings. This method can be used in material research which is metal or nonmetal (Knill et al. 1968). The method and inspection of surface quality by continuous control (online) still remain the issue (Hloch et al. 2013a, b; Delijaicov et al. 2010; Fowler et al. 2005; Hassan et al. 2004; Hloch et al. 2011). In accordance with the performed measurements, we are searching for the dependence between acoustic emission and its factors of the WJ factor.

Hloch et al. (2013a, b) investigated during the analysis of acoustic emission hydroabrasive cutting for indirect control that the behavior with the exactly scheduled change of the cutting condition and cutting head transverse and analysis and comparison of the examined section of the experimentation through FFT spectral analysis. They performed the experimental procedure on the single variable factor of the AWJ, to be analyzed the C sample monitored as solely i.e., the represent part of the large experiment. Application of the remaining sample A, B, D shows dependency on the variable factor changing speed, abrasive mass flow rate ma, and focusing tube diameter d_f. These dependency or regulation equations are monitored through the online control process. Zelenak et al. (2015) investigated to

visualize of the high-speed pulsating and continuous water jet structures and velocity flow vector field to test the applicability of the shadowgraph technique combined with PIV processing algorithms.

The main aim of this work is to study the erosion effects caused during the disintegration of rock or mining material by pulsating water jet. The acoustic emission was measured during the experimentation using the LabVIEW to describe the surface phenomena and studying the effects of parameters. In addition to this, the surface roughness of the obtained traces was evaluated using non-contact type optical profile meter Microprof FTR and to determine the effects of parameters on the depth of cut.

2 Experimental Study

The experiment was conducted at Institute of Geonics of the CAS, Ostrava-Poruba. In order to study the disintegration processes of marble and granite by pulsating water jet via acoustic emission and vibration, we used Software National Instruments (NI), LabVIEW 2012 SP1 f5 ver. 12.0.1, Sound and Vibration Measurement Suite 12.0.0, Spectral Measurements Toolkit 2.6.3, Advanced Signal Processing Toolkit 12.0.0, and hardware (NI) accelerometer WR712F-M4 up to 65 kHz. The technological setup includes: (a) plunger pump Hammelmann HDP 253 (b) Robot ABB IRB 6640-180 for handling the pulsating water head (Fig. 1).

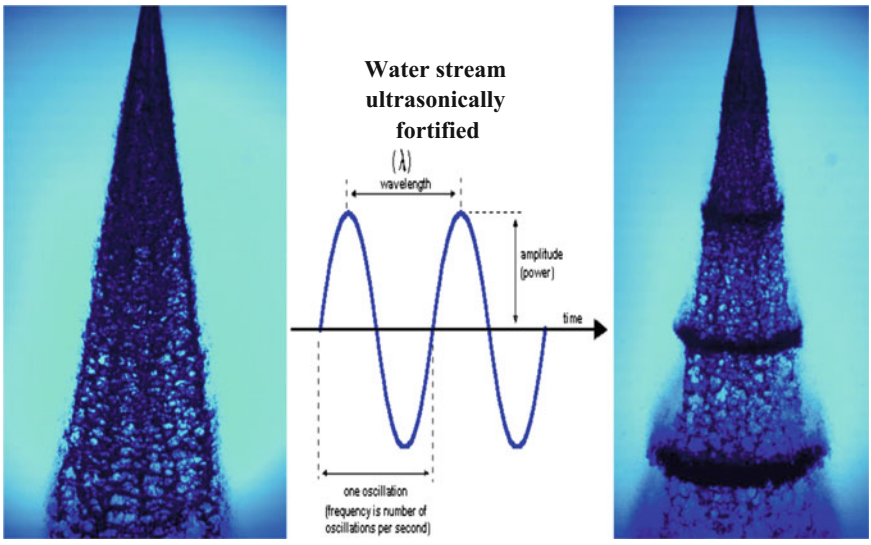

Fig. 1 Water stream ultrasonically fortified on the *left*—without pulsation, on the *right*—with pulsation 20 kHz (Zelenak et al. 2015)

Table 1 shows the experimental condition. An Ecoson WJ-UG_630-40 generator was used as a source of acoustic waves for the generation of pulsating water jet.

The experiments were performed with the modulation frequency of 20.2 kHz (Fig. 2).

Table 1 Experimental condition (Tripathi et al. 2016)

f (kHz)	*p* (MPa)	*d* (mm)	*z* (mm)	*v* (mm/s)	Material	A (mm)	P (W)	Liquid
20.2	60	0.9	30	2, 4, 6, 8, 10, 12, 14, 16	marble	6	380	H_2O
20.2	60	0.9	30	2, 4, 6, 8, 10, 12, 14, 16	granite	6	380	H_2O

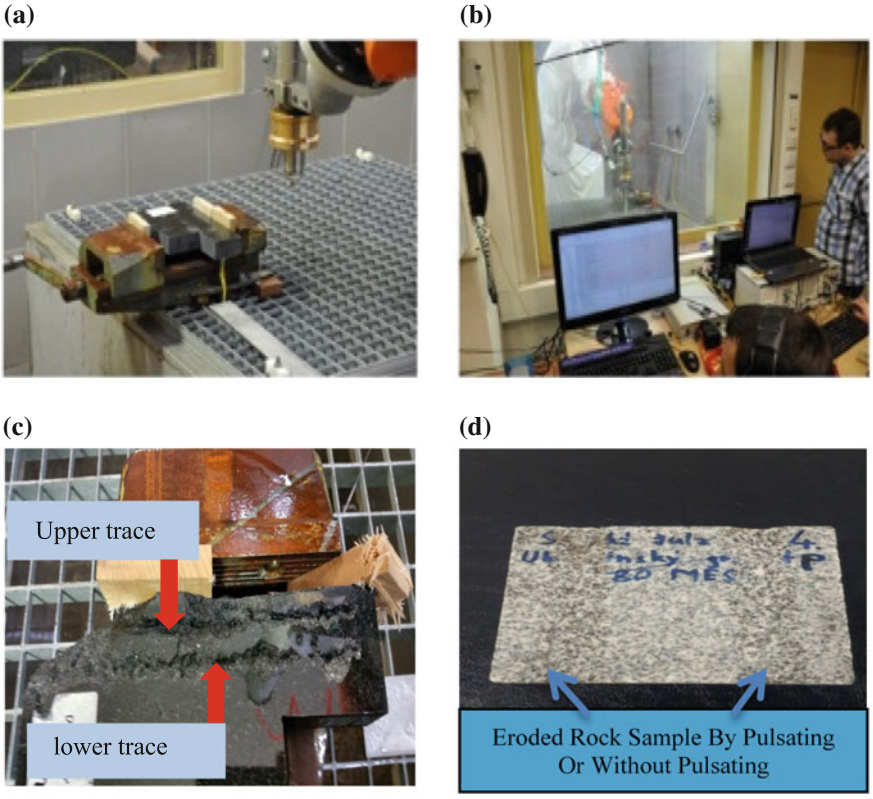

Fig. 2 **a** Experimental setup. **b** Monitoring the process. **c** Rock sample with black granite. **d** White marble (Tripathi et al. 2016)

3 Result and Discussion

The surface roughness of the disintegrated samples of granite was measured using optical MicroProf FRT profilometer at the Institute of Geonics AS CR, v.v.i. Ostrava. The 3D plots of the surface were evaluated for samples disintegrated under following conditions: two grooves were performed by continuous water jet using circular nozzle orifice diameter d = 0.9 mm at pressure levels p = 60 MPa visible traces were observed only in case of PWJ.

Figure 3 shows the setup of the optical profilometer using which 3D and 2D profiles of the granite and marble samples are traced also, the depth and width of cut during disintegration were evaluated.

A high level of isotropy was observed from the parameter analysis of the disintegrated samples. From the topographical analysis of the surface of the grooves, it was observed that a lower value of surface roughness *Ra*, *Rq,* and *Rz* was achieved at v = 2 mm/s and v = 4 mm/s. In Fig. 3, uneven values of surface roughness were observed in the form of peaks and valleys. It was observed that as the feed rate was increased, the values of the surface roughness were increased.

On comparing the traces of the pulsating and continuous water jet, it was observed that the traces created by the pulsating water jet were much deeper than continuous water jet. These depths generated by the circular nozzle during disintegration are shown in the Fig. 4a–d. It is observed that the material is squeezed out

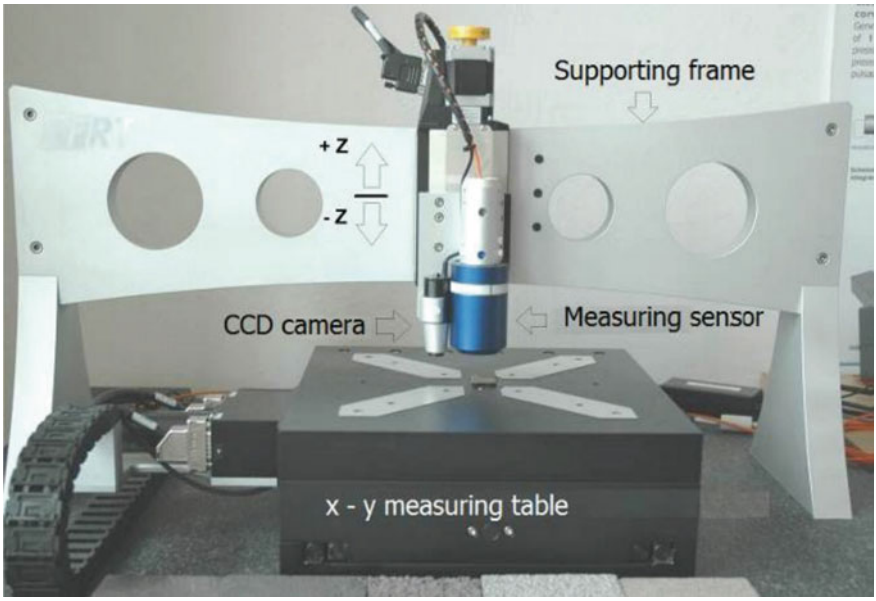

Fig. 3 Optical Profilometer

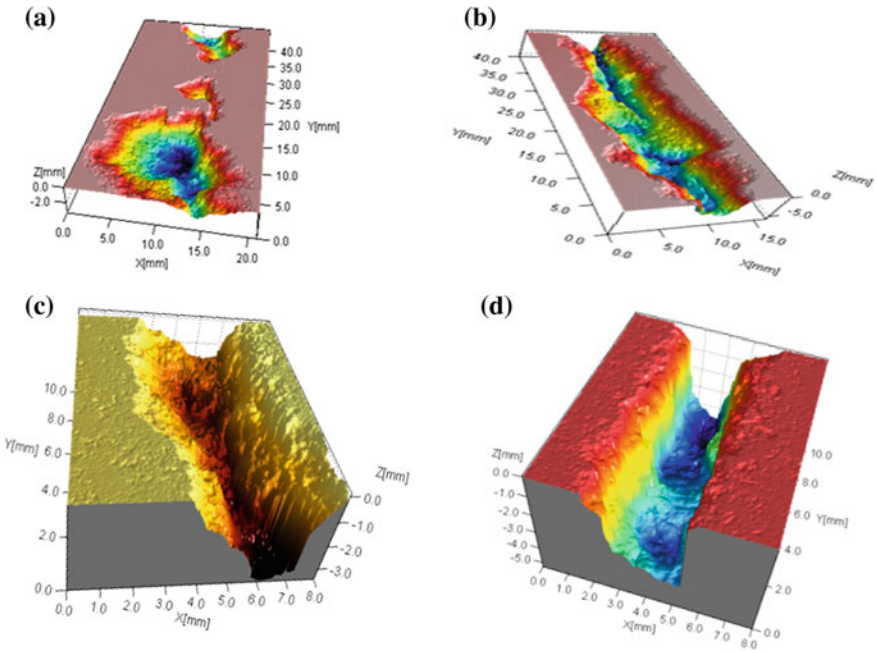

Fig. 4 Non-contact type Profilometer. **a** 3D profile record during granite disintegration by pulsating water jet, **b** 3D profile record during granite disintegration by continuous water jet, **c** 3D profile record during marble disintegration by pulsating water jet, **d** 3D profile record during marble disintegration by continuous water jet

above the edge of groove of the sample. Figure 4c, d shows the maximum depth of the groove.

The average value of roughness was calculated in the SPIP 6.6.1 program. The final average values of surface roughness are stated above in the Fig. 5a, b. It follows from the aforementioned case that a lower surface roughness can be achieved by the pulsating water jet with the higher transverse speed.

The figure below shows the frequency pulse versus time graph of marble and granite samples disintegrated by pulsating and continuous water jet. From the experimental data, the difference during the time course of disintegration of granite by water jet and pulsating water jet by vibration can be seen in Figs. 6, 7, and 8. During the disintegration of rock by pulsating water jet, the link between the material being cut and the optimum frequency of the pulse for different materials can show the change in response to the pulse frequency.

The above graphs show that a more stable region was observed in case of samples treated with PWJ than continuous water jet.

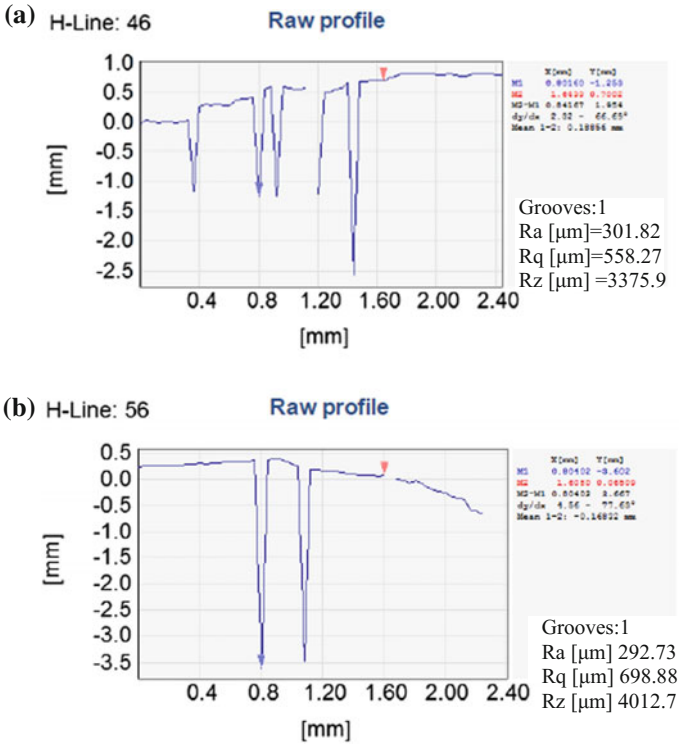

Fig. 5 **a** Graphical illustration of disintegrated grooves with pulsating water jet. **b** Graphical illustration of disintegrated grooves without pulsating water jet

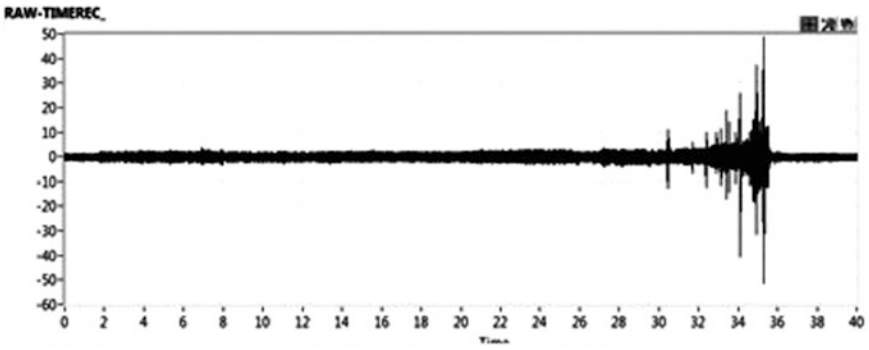

Fig. 6 Time course of disintegration of marble by pulsating water jet by vibration

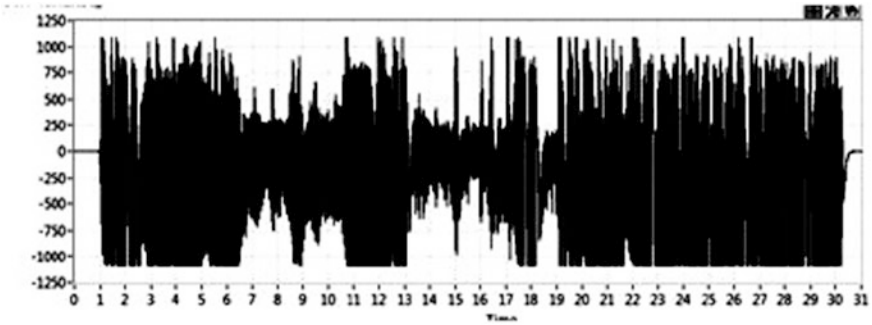

Fig. 7 Time course of disintegration of granite by pulsating water jet

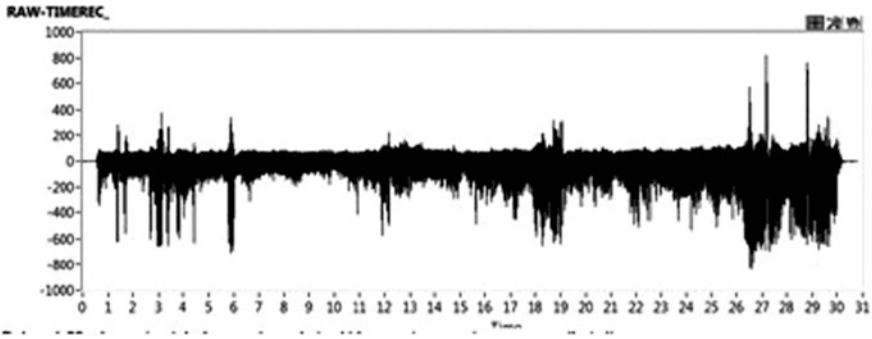

Fig. 8 Time course of disintegration of granite by water jet

4 Conclusion and Future Scope

This technology has been increasingly used in manufacturing field as well as the material is disintegrated by the shock impact waves (Tripathi et al. 2016, Srivastava et al. 2016). The capacity of the pulsating water jet in rocks was experimentally investigated. The main conclusion of the study can be summarized as follows:

- From the preliminary experimental data, the difference during the time course of disintegration of granite and marble by water jet and pulsating water jet by vibration can be seen in Figs. 6, 7 and 8.
- Deeper traces were observed in pulsating water jet as compare to the continuos water jet with the help of the SPIP 6.6.0 software.
- Additionally, the effect of the acoustic emission is used to relate the technological conditions with the other control parameters to disintegrate in the materials.

Over the years, WJ and AWJ have shown some technological and economical limitations in industrial application of rock and coal cutting (Sharma et al. 2011).

Therefore, the technology is trending toward the disintegration of these materials at lower pressures for which pulsating WJ is the solution. This technology has potential to be used in wide variety of applications like stone carving, 3D printing, biomedical application, and architectures with much more efficiency as compare to other WJ machining process.

Acknowledgements This work was supported by the Slovak Research and Development Agency under contract no. APVV-207-12. Experiments were conducted with the support of the project of the Institute of Clean Technologies for Mining and Utilization of Raw Materials for Energy Use—Sustainability Program, reg. no. LO1406 financed by the Ministry of Education, Youth and Sports of the Czech Republic, and Institute of Geonics with support for the long-term conceptual development of the research institution RVO: 68145535.

References

Delijaicov S (2010) Improved model to predict machined surface roughness based on the cutting vibrations signal during hard turning. Arch Mater Sci Eng 45:102–107

Foldyna J, Klich J, Hlavacek P, Zelenak M, Scucka J (2012) Erosion of metals by pulsating water jet. Tehnicki vjesnik-Technical Gazette 19:381–386

Fowler G, Shipway PH, Pashby IR (2005) Abrasive water-jet controlled depth milling of Ti6A14 V alloy—an investigation of the role of jet—workpiece traverse speed and abrasive grit size on the characteristics of the milled material. J Mater Process Tech 161:407–414

Hassan AI, Chen C, Kovacevic R (2004) On-line monitoring of depth of cut in AWJ cutting. Int J Mach Tool Manuf 44:595–605

Hloch S, Tozan H, Yagimli M (2011) Using waterjet in reverse logistic operations in discarded munitions processing. Tehnicki vjesnik-Technical Gazette 18:267–271

Hloch S, Foldyna J, Sitek L, Zelenak M, Hlavacek P, Hvizdos P, Kloc J, Monka P, Monkova K, Kozak D, Magurova D (2013a) Disintegration of bone cement by continuous and pulsating water jet. Tehnicki vjesnik-Technical Gazette 20(4):593–598

Hloch S, Valicek J, Kozak D, Tozan H, Chattopadhyaya S, Pavel A (2013b) Analysis of acoustic emission emerging during hydroabrasive cutting and options for indirect quality control. Int J Adv Manuf Technol 66:45–58

Karakurt I, Gokhan A, Kerim A (2012) An experimental study on the depth of cut of granit in abrasive. Waterjet Cutting Mater Manuf Processes 27:538–544

Knill JL, Franklin JA, Malone AW (1968) A study of acoustic emission from stressed rock. Int J Rock Mech Min Sci 5:87–121

Lehocka D, Klich J, Foldyna J, Hloch S, Krolczyk JB, Carach J, Krolczyk GM (2016) Copper alloys disintegration using pulsating water jet. Measurement 82:375–383

Sharma V, Chattopadhyaya S, Hloch S (2011) Multi response optimization of process parameters based on Taguchi-Fuzzy model for coal cutting by water jet technology. Int J Adv Manuf Tech 56:1019–1025

Srivastava M, Tripathi R, Hloch S, Chattopadhyaya S, Dixit AR (2016) Potential of using water jet peening as a surface treatment process for welded joints. Procedia Eng 149:472–480

Tripathi R, Srivastava M, Hloch S, Adamcik Pavel, Chattopadhyaya S, Das AK (2016) Monitoring of acoustic emission during the disintegration of rock. Procedia Eng 149:481–488

Zelenak M, Foldyna J, Scucka J, Hloch S, Riha SZ (2015) Visualisation and measurement of high-speed pulsating and continuous water jets. Measurement 72:1–8

Three-Dimensional Solute Transport Problems in an Aquifer: Numerical Approaches

Mritunjay Kumar Singh, Rakesh Kumar Singh and Vijay P. Singh

Abstract The solution of solute transport problem in an aquifer with suitable boundary conditions has been dealt by various analytical methods in the past. But, the analytical approach becomes more difficult to apply when either dealing with complex boundary conditions or higher order solute transport problems. The difficulty may be reduced by handling the problem by numerical approaches as in the present paper, forward in time centered in space (FTCS) finite-difference scheme is used to solve the three-dimensional advection-dispersion equation (ADE) with Dirichlet and Neumann boundary conditions. The Dirichlet boundary conditions are taken temporally dependent. The numerical solution is obtained graphically with the help of MATLAB software package, and further under a special case, the numerical solution obtained by FTCS scheme is validated with the solution obtained by PDEtool which is based on the finite-element method.

1 Introduction

By various ways, the solutes or pollutants enter into the groundwater system through porous formation. Once these solutes or pollutants enter into the groundwater system, these pollutants will be transported by flowing groundwater and may degrade water quality at nearby wells and streams (Wexler 1992). The solute transport problem has been described by advection-dispersion equation (ADE) with initial and boundary

M.K. Singh · R.K. Singh (✉)
Department of Applied Mathematics, Indian Institute of Technology (Indian School of Mines), Dhanbad 826004, Jharkhand, India
e-mail: rakeshsingh5725@gmail.com

M.K. Singh
e-mail: drmks29@rediffmail.com

V.P. Singh
Department of Biological and Agricultural Engineering & Zachry Department of Civil Engineering, Texas A and M University, College Station, TX 77843-2117, USA
e-mail: vsingh@tamu.edu

M.K. Singh et al. (eds.), *Applications of Fluid Dynamics*, Lecture Notes in Mechanical Engineering, https://doi.org/10.1007/978-981-10-5329-0_39

conditions. The difficulty level of solute transport problem depends on the various factors affecting during the solute transportation in an aquifer, the dimension of the ADE describing solute transport problem, and type of initial and boundary conditions taken. A large number of papers, based on the analytical solution of ADEs, have been published in the past. But, due to the large variability of flow and transport properties in the medium and the nonideal nature of applicable initial and boundary conditions, the usefulness of analytical solution is often limited and, therefore, numerical method may be needed (Leij et al. 1991). The analytical solute transport models are not capable of handling all kinds of solute transport problems that come across in practice due to the fact that almost all analytical solute transport models in the literature are based on unidirectional flow fields as well as other restrictive assumptions (Batu 2005). Hence, numerical approach may be applicable in those cases.

Leij et al. (1991) presented the several analytical solutions for three-dimensional solute transport in semi-infinite porous medium with unidirectional flow using first-type and third-type boundary conditions. Many papers have been published which discuss the analytical solution of one-, two-, and three-dimensional solute transport in groundwater system with finite and infinite aquifer length (Wexler 1992; Park and Zhan 2001; Yeh 1981). Dehghan (2004) discussed the various explicit and implicit finite-difference approximations for the numerical solution of three-dimensional advection-diffusion equation with Dirichlet boundary condition and also discussed the stability condition in each case for the corresponding finite-difference equations by using Von Neumann stability method. Tamsir et al. (2016) solved the three-dimensional ADE by using modified cubic B-spline differential quadrature method that converted the ADE into a system of first-order ODEs. Yadav et al. (2012) presented the analytical solution of three-dimensional model for nonreactive solute transport in semi-infinite homogeneous porous media. They have considered the concentration in liquid and solid phase and taken the dispersion coefficient as temporally dependent. Sankarnaraynan et al. (1998) have solved the three-dimensional convective-dispersive equation by using higher order upwind scheme for convective term to minimize the numerical diffusion.

The main objective of this paper is to derive numerical solution for the three-dimensional ADE during two-dimensional flow in a three-dimensional finite medium using finite-difference method.

2 Numerical Solution of Solute Transport Problem

The three-dimensional solute transport problem for homogeneous and isotropic medium with time-dependent boundary conditions is as follows:

$$\frac{\partial c}{\partial t} = -v_1 \frac{\partial c}{\partial x} - v_2 \frac{\partial c}{\partial y} + D_x \frac{\partial^2 c}{\partial x^2} + D_y \frac{\partial^2 c}{\partial y^2} + D_z \frac{\partial^2 c}{\partial z^2}, \tag{1}$$

where c is solute concentration [M L^{-3}], v_1 and v_2 are average linear velocities [L T^{-1}], D_x, D_x and D_x are constant dispersion coefficients [L^2 T^{-1}], t is time [T], and x, y, and z are spatial variables [L].

Initial condition:

$$c(x, y, z, t) = 0; \quad 0 \le x, y, z \le L, \quad t = 0 \tag{2}$$

Boundary conditions:

$$c(x, y, z, t) = \exp(-m_1 t); \quad 0 \le y, z \le L, \quad x = 0, \quad t > 0 \tag{3}$$

$$c(x, y, z, t) = \exp(-m_2 t); \quad 0 \le x, z \le L, \quad y = 0, \quad t > 0 \tag{4}$$

$$c(x, y, z, t) = 0; \quad 0 \le x, y \le L, \quad z = 0, \quad t > 0 \tag{5}$$

$$\frac{\partial c}{\partial x} = \frac{\partial c}{\partial y} = \frac{\partial c}{\partial z} = 0; \quad x = y = z = L, \quad t > 0, \tag{6}$$

where m_1 and m_2 are parameters called flow resistance coefficient [T^{-1}].

Here, we solve the three-dimensional advection-dispersion Eq. (1) by using forward in time centered in space (FTCS) scheme which is based on finite-difference method.

Let the domain of three-dimensional space be divided into a network of cubes of sides $\Delta x = \Delta y = \Delta z = h$, by drawing the set of lines $x = ih, i = 0, 1, 2, \ldots$; $y = jh, j = 0, 1, 2, \ldots$ and $z = kh, k = 0, 1, 2, \ldots$. The points of intersection of these lines are called grid points, or we may call block corner points. The diagram of three-dimensional space with finite-difference grids is shown in Fig. 1. Let the

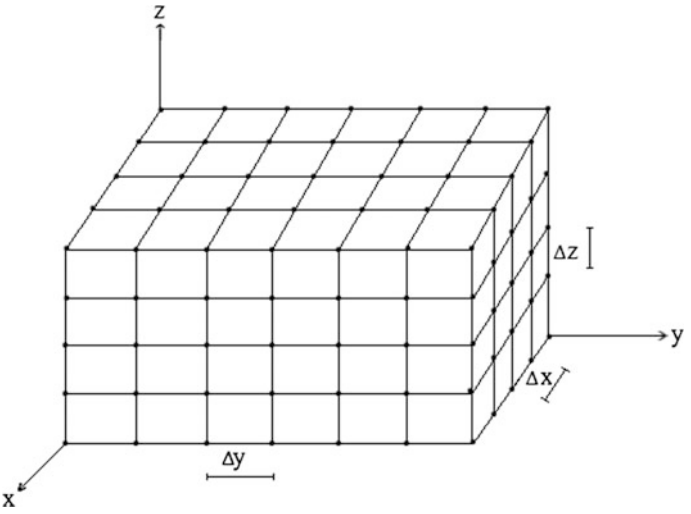

Fig. 1 Three-dimensional space with finite-difference grid points

coordinates of an intersecting point (x, y, z) are represented as (i, j, k). Similarly the points say $(x+h, y, z)$, $(x, y+h, z)$, and $(x, y, z+h)$ are represented as $(i+1, j, k)$, $(i, j+1, k)$, and $(i, j, k+1)$, respectively.

Now, let the time domain for the problem is $0 \le t \le T$ covered by a plane of blocks of uniformly spaced with interval Δt along vertical axis. Again let Δx, Δy, and Δz be the space intervals in x-, y-, and z-directions, respectively. Let M, N, and Q are the total number of intervals in x-, y-, and z-directions, respectively, and L is the space length along x-, y-, and z-directions, then we have $\Delta x = L/M$, $\Delta y = L/N$, and $\Delta z = L/Q$.

Now approximating Eq. (1), by using first-order forward-difference in time and second-order central-difference in space at the intersecting point (i, j, k, n), we get

$$\frac{c_{i,j,k}^{n+1} - c_{i,j,k}^{n}}{\Delta t} = -v_1\left[\frac{c_{i+1,j,k}^{n} - c_{i-1,j,k}^{n}}{2\Delta x}\right] - v_2\left[\frac{c_{i,j+1,k}^{n} - c_{i,j-1,k}^{n}}{2\Delta y}\right] + D_x\left[\frac{c_{i+1,j,k}^{n} - 2c_{i,j,k}^{n} + c_{i-1,j,k}^{n}}{(\Delta x)^2}\right] + D_y\left[\frac{c_{i,j+1,k}^{n} - 2c_{i,j,k}^{n} + c_{i,j-1,k}^{n}}{(\Delta y)^2}\right] + D_z\left[\frac{c_{i,j,k+1}^{n} - 2c_{i,j,k}^{n} + c_{i,j,k-1}^{n}}{(\Delta z)^2}\right]. \tag{7}$$

After rearrangement, Eq. (7) takes the form

$$c_{i,j,k}^{n+1} = \left(r_1 + \frac{r_4}{2}\right)c_{i-1,j,k}^{n} + \left(r_2 + \frac{r_5}{2}\right)c_{i,j-1,k}^{n} + r_3 c_{i,j,k-1}^{n} - (2r_1 + 2r_2 + 2r_3 - 1)c_{i,j,k}^{n} + \left(r_1 - \frac{r_4}{2}\right)c_{i+1,j,k}^{n} + \left(r_2 - \frac{r_5}{2}\right)c_{i,j+1,k}^{n} + r_3 c_{i,j,k+1}^{n},$$

$$i = 1, 2, \ldots, M-1; \quad j = 1, 2, \ldots, N-1; \quad k = 1, 2, \ldots, Q-1, \tag{8}$$

where $r_1 = \frac{D_x \Delta t}{(\Delta x)^2}$, $r_2 = \frac{D_y \Delta t}{(\Delta y)^2}$, $r_3 = \frac{D_z \Delta t}{(\Delta z)^2}$, $r_4 = \frac{v_1 \Delta t}{\Delta x}$, and $r_5 = \frac{v_2 \Delta t}{\Delta y}$.

Approximating the given three derivative boundary conditions in Eq. (6) at the boundary points $i = M, j = N$ and $k = Q$, respectively, we have

$$c_{i+1,j,k}^{n} = c_{i-1,j,k}^{n}, \quad i = M \tag{9}$$

$$c_{i,j+1,k}^{n} = c_{i,j-1,k}^{n}, \quad j = N \tag{10}$$

and

$$c_{i,j,k+1}^{n} = c_{i,j,k-1}^{n}, \quad k = Q \tag{11}$$

Using relation (11) in Eq. (8) gives

$$c_{i,j,k}^{n+1} = \left(r_1 + \frac{r_4}{2}\right)c_{i-1,j,k}^{n} + \left(r_2 + \frac{r_5}{2}\right)c_{i,j-1,k}^{n} + 2r_3 c_{i,j,k-1}^{n} - (2r_1 + 2r_2 + 2r_3 - 1)c_{i,j,k}^{n} + \left(r_1 - \frac{r_4}{2}\right)c_{i+1,j,k}^{n} + \left(r_2 - \frac{r_5}{2}\right)c_{i,j+1,k}^{n},$$

$$i = 1, 2, \ldots, M-1; \quad j = 1, 2, \ldots, N-1; \quad k = Q \tag{12}$$

Using relations (10) and (11) in Eq. (8) gives

$$c_{i,j,k}^{n+1} = \left(r_1 + \frac{r_4}{2}\right)c_{i-1,j,k}^{n} + 2r_2 c_{i,j-1,k}^{n} + 2r_3 c_{i,j,k-1}^{n} - (2r_1 + 2r_2 + 2r_3 - 1)c_{i,j,k}^{n} + \left(r_1 - \frac{r_4}{2}\right)c_{i+1,j,k}^{n},$$

$$i = 1, 2, \ldots, M-1; \quad j = N; \quad k = Q \tag{13}$$

Using (9) and (11) in Eq. (8) gives

$$c_{i,j,k}^{n+1} = 2r_1 c_{i-1,j,k}^{n} + \left(r_2 + \frac{r_5}{2}\right)c_{i,j-1,k}^{n} + 2r_3 c_{i,j,k-1}^{n} - (2r_1 + 2r_2 + 2r_3 - 1)c_{i,j,k}^{n} + \left(r_2 - \frac{r_5}{2}\right)c_{i,j+1,k}^{n},$$

$$i = M; \quad j = 1, 2, \ldots, N-1; \quad k = Q \tag{14}$$

Using (10) in Eq. (8) gives

$$c_{i,j,k}^{n+1} = \left(r_1 + \frac{r_4}{2}\right)c_{i-1,j,k}^{n} + 2r_2 c_{i,j-1,k}^{n} + r_3 c_{i,j,k-1}^{n} - (2r_1 + 2r_2 + 2r_3 - 1)c_{i,j,k}^{n} + \left(r_1 - \frac{r_4}{2}\right)c_{i+1,j,k}^{n} + r_3 c_{i,j,k+1}^{n},$$

$$i = 1, 2, \ldots, M-1; \quad j = N; \quad k = 1, 2, \ldots, Q-1 \tag{15}$$

Using (9) in Eq. (8) gives

$$c_{i,j,k}^{n+1} = 2r_1 c_{i-1,j,k}^{n} + \left(r_2 + \frac{r_5}{2}\right)c_{i,j-1,k}^{n} + r_3 c_{i,j,k-1}^{n} - (2r_1 + 2r_2 + 2r_3 - 1)c_{i,j,k}^{n} + \left(r_2 - \frac{r_5}{2}\right)c_{i,j+1,k}^{n} + r_3 c_{i,j,k+1}^{n},$$

$$i = M; \quad j = 1, 2, \ldots, N-1; \quad k = 1, 2, \ldots, Q-1 \tag{16}$$

Using (9) and (10) in Eq. (8) gives

$$c_{i,j,k}^{n+1} = 2r_1 c_{i-1,j,k}^{n} + 2r_2 c_{i,j-1,k}^{n} + r_3 c_{i,j,k-1}^{n} - (2r_1 + 2r_2 + 2r_3 - 1)c_{i,j,k}^{n} + r_3 c_{i,j,k+1}^{n},$$

$$i = M; \quad j = N; \quad k = 1, 2, \ldots, Q-1 \tag{17}$$

And at the last, using (9), (10), and (11) in Eq. (8) gives

$$c_{i,j,k}^{n+1} = 2r_1 c_{i-1,j,k}^{n} + 2r_2 c_{i,j-1,k}^{n} + 2r_3 c_{i,j,k-1}^{n} - (2r_1 + 2r_2 + 2r_3 - 1)c_{i,j,k}^{n},$$

$$i = M; \quad j = N; \quad k = Q \tag{18}$$

All the eight explicit Eqs. (8), (12)–(18) together will give the solution of the three-dimensional ADE (1).

Now to solve the ADE (1), consider $v_1 = 0.3$ km/year, $v_2 = 0.4$ km/year, $d_1 = 0.01$ km^2/year, $d_2 = 0.02$ km^2/year, $d_3 = 0.03$ km^2/year, $M = 20$, $N = 20$, $Q = 20$, $T = 1$ year, $L = 1$ km, $\Delta t = 0.02$ year, $m_1 = 0.0006$ year^{-1}, $m_2 = 0.0003$ year^{-1}.

It should be noted that the above all eight explicit equations must satisfy the stability criteria (Hoffman 1992; Mehdi 2004). Here, the spatial and temporal steps have been taken carefully so that the stability condition should not vanish.

Numerical solution of the above eight explicit equations manually will take too much time and will be tedious when higher degree of accuracy required. Therefore,

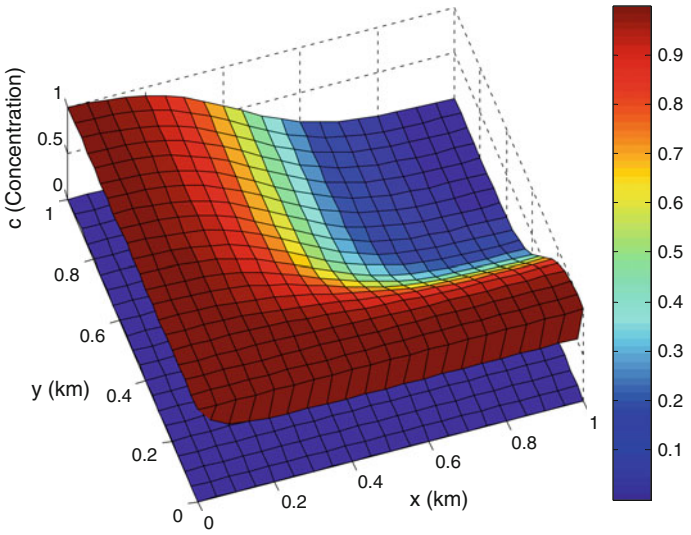

Fig. 2 Numerical solution of the three-dimensional ADE (1)

Table 1 Numerical results for the solution of ADE (1) at the time $t = 1$ year

Value of solute concentration $c(x, y, z, t)$ in 3D space at $t = 1$ year corresponding to x-, y-, and z-coordinates										
0.9994	0.9997	0.9997	0.9997	0.9997	0.9997	0.9997	0.9997	0.9997	0.9997	0.9997
0.9994	0.9995	0.9995	0.9995	0.9993	0.9990	0.9986	0.9980	0.9974	0.9967	0.9960
0.9994	0.9994	0.9992	0.9987	0.9979	0.9966	0.9948	0.9925	0.9898	0.9868	0.9838
0.9994	0.9991	0.9984	0.9970	0.9946	0.9909	0.9859	0.9796	0.9722	0.9641	0.9559
0.9994	0.9987	0.9970	0.9939	0.9886	0.9807	0.9698	0.9562	0.9402	0.9230	0.9057
0.9994	0.9980	0.9950	0.9892	0.9796	0.9652	0.9457	0.9213	0.8928	0.8623	0.8316
0.9994	0.9972	0.9923	0.9832	0.9681	0.9457	0.9154	0.8774	0.8336	0.7867	0.7400
0.9994	0.9963	0.9894	0.9767	0.9557	0.9246	0.8826	0.8303	0.7702	0.7062	0.6429
0.9994	0.9955	0.9867	0.9705	0.9439	0.9047	0.8518	0.7863	0.7113	0.6319	0.5536
0.9994	0.9947	0.9844	0.9653	0.9341	0.8882	0.8264	0.7502	0.6633	0.5716	0.4818
0.9994	0.9942	0.9827	0.9615	0.9269	0.8761	0.8079	0.7240	0.6287	0.5284	0.4306
0.9994	0.9939	0.9816	0.9590	0.9222	0.8682	0.7959	0.7071	0.6064	0.5008	0.3981
0.9994	0.9936	0.9810	0.9575	0.9194	0.8635	0.7889	0.6973	0.5936	0.4850	0.3796
0.9994	0.9935	0.9806	0.9567	0.9179	0.8610	0.7851	0.6921	0.5869	0.4769	0.3701
0.9994	0.9935	0.9804	0.9563	0.9172	0.8599	0.7834	0.6897	0.5838	0.4731	0.3658
0.9994	0.9934	0.9803	0.9562	0.9169	0.8593	0.7826	0.6886	0.5824	0.4715	0.3639
0.9994	0.9934	0.9803	0.9561	0.9167	0.8591	0.7823	0.6882	0.5819	0.4708	0.3632
0.9994	0.9934	0.9803	0.9561	0.9167	0.8591	0.7822	0.6880	0.5817	0.4706	0.3629
0.9994	0.9934	0.9803	0.9561	0.9167	0.8590	0.7821	0.6880	0.5817	0.4705	0.3629
0.9994	0.9934	0.9803	0.9561	0.9167	0.8590	0.7821	0.6880	0.5816	0.4705	0.3628
0.9994	0.9934	0.9803	0.9561	0.9167	0.8590	0.7821	0.6880	0.5816	0.4705	0.3628
0.9997	0.9997	0.9997	0.9997	0.9997	0.9997	0.9997	0.9997	0.9997	0.9997	
0.9953	0.9947	0.9942	0.9938	0.9935	0.9933	0.9932	0.9931	0.9931	0.9931	
0.9810	0.9785	0.9764	0.9748	0.9736	0.9728	0.9723	0.9720	0.9719	0.9718	
0.9482	0.9414	0.9358	0.9315	0.9284	0.9263	0.9250	0.9242	0.9238	0.9236	
0.8894	0.8751	0.8635	0.8546	0.8482	0.8439	0.8413	0.8397	0.8389	0.8385	
0.8031	0.7782	0.7581	0.7428	0.7320	0.7248	0.7203	0.7178	0.7164	0.7159	
0.6967	0.6593	0.6292	0.6066	0.5907	0.5803	0.5739	0.5702	0.5683	0.5675	
0.5845	0.5346	0.4946	0.4648	0.4440	0.4306	0.4224	0.4177	0.4153	0.4143	
0.4821	0.4211	0.3727	0.3369	0.3121	0.2962	0.2866	0.2812	0.2784	0.2773	
0.4000	0.3307	0.2760	0.2358	0.2082	0.1905	0.1799	0.1740	0.1710	0.1698	
0.3419	0.2671	0.2083	0.1652	0.1358	0.1170	0.1059	0.0997	0.0965	0.0953	
0.3052	0.2271	0.1659	0.1213	0.0909	0.0715	0.0601	0.0538	0.0505	0.0492	
0.2845	0.2047	0.1422	0.0968	0.0659	0.0463	0.0347	0.0283	0.0250	0.0237	
0.2739	0.1933	0.1303	0.0845	0.0534	0.0337	0.0220	0.0156	0.0123	0.0110	
0.2691	0.1881	0.1249	0.0789	0.0477	0.0279	0.0163	0.0098	0.0065	0.0052	
0.2670	0.1859	0.1226	0.0766	0.0453	0.0256	0.0139	0.0075	0.0042	0.0029	
0.2663	0.1851	0.1217	0.0757	0.0445	0.0247	0.0130	0.0066	0.0033	0.0020	
0.2660	0.1848	0.1215	0.0754	0.0442	0.0244	0.0127	0.0063	0.0030	0.0017	
0.2659	0.1847	0.1214	0.0753	0.0441	0.0243	0.0126	0.0062	0.0029	0.0016	
0.2659	0.1847	0.1213	0.0753	0.0440	0.0243	0.0126	0.0061	0.0029	0.0016	
0.2659	0.1847	0.1213	0.0753	0.0440	0.0243	0.0126	0.0061	0.0029	0.0016	

the solution has been obtained graphically with the help of MATLAB software as shown in Fig. 2.

In Fig. 2, the solute concentration is distributed in the three-dimensional space from the initial planes *xz* and *yz* toward the final boundary planes *xz* and *yz* due to advection in x- and y-directions and dispersion in *x*-, *y*-, and *z*-directions. The solute concentration has been taken zero on the initial plane *xy* as showing dark blue color at the bottom of the space.

The numerical results obtained for the solution of the ADE (1) have been shown in Table 1.

In Table 1, the 21 columns and 21 rows are representing the values of solute concentration distributed in the three-dimensional space at the time $t = 1$ year corresponding to *x*-, *y*-, and *z*-coordinates.

2.1 Special Case

When there is only diffusion in the *x*- and *y*- directions and no advection in any direction, then the obtained graphical solutions of the ADE (1) by FTCS scheme and finite element method (PDEtool), have been shown in Figs. 3 and 4, respectively.

From Figs. 3 and 4, we observed that there is good agreement between the numerical solutions obtained by FTCS scheme and PDEtool.

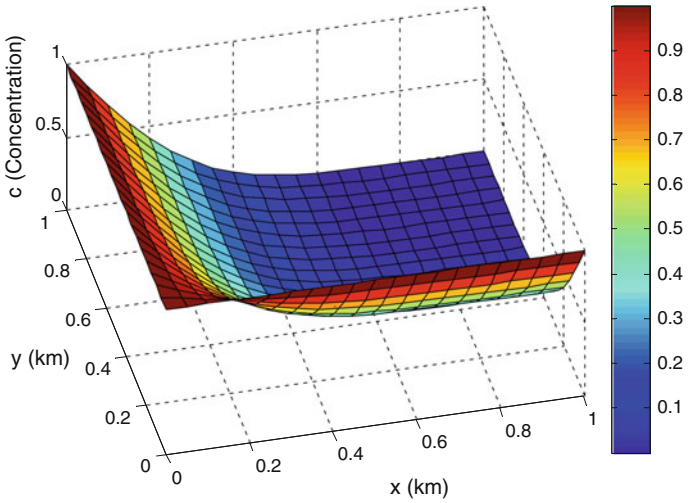

Fig. 3 Numerical solution of the three-dimensional ADE (1) by FTCS scheme when there is no advection

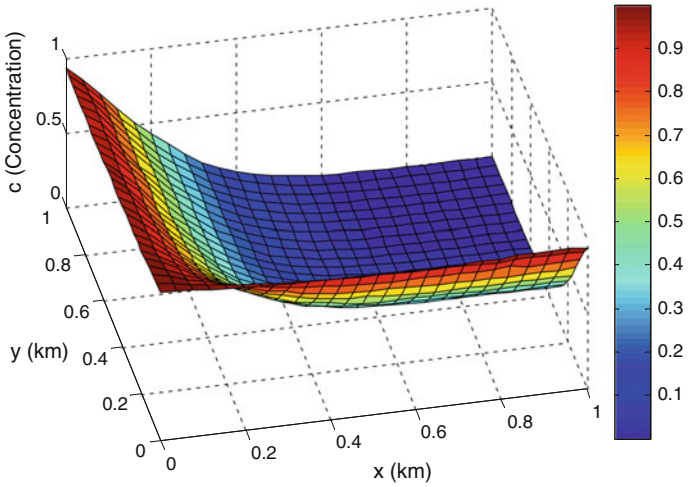

Fig. 4 Numerical solution of the three-dimensional ADE (1) by PDEtool when there is no advection

3 Conclusions

Three-dimensional ADE has been solved by using FTCS explicit method, and its numerical solution has been obtained successfully by MATLAB software. Also under a special case when diffusion coefficient in the z-direction supposed as zero and taken no advection in any direction, the numerical solution obtained by FTCS method has been found with good agreement to the solution obtained by finite element method. The numerical solutions obtained in this work may be helpful for researchers to understand the solute transport phenomenon in the three-dimensional space.

Acknowledgements Authors are thankful to the Indian Institute of Technology (Indian School of Mines), Dhanbad for providing financial assistance through JRF scheme.

References

Batu V (2005) Applied flow and solute transport modeling in aquifers: fundamental principles and analytical and numerical methods. CRC Press

Dehghan M (2004) Numerical solution of the three-dimensional advection–diffusion equation. Appl Math Comput 150(1):5–19

Hoffman JD (1992) Numerical methods for engineering and scientists. Purdo University, West Lafayette

Leij FJ, Skaggs TH, van Genuchten MT (1991) Analytical solutions for solute transport in three-dimensional semi-infinite porous media. Water Resour Res 27(10):2719–2733

Park E, Zhan H (2001) Analytical solutions of contaminant transport from finite one-, two-, and three-dimensional sources in a finite-thickness aquifer. J Contam Hydrol 53(1):41–61

Sankaranarayanan S, Shankar NJ, Cheong HF (1998) Three-dimensional finite difference model for transport of conservative pollutants. Ocean Eng 25(6):425–442

Tamsir M, Srivastava VK, Mishra PD (2016) Numerical simulation of three dimensional advection-diffusion equations by using modified cubic B-spline differential quadrature method. Asia Pacific J Eng Sci Tech 2(7):1–13

Wexler EJ (1992) Analytical solutions for one-, two-, and three-dimensional solute transport in ground-water systems with uniform flow. US Government Printing Office

Yadav RR, Jaiswal DK, Yadav HK (2012) Three-dimensional temporally dependent dispersion through porous media: analytical solution. Environl Earth Sci 65(3):849–859

Yeh GT (1981) AT123D: analytical transient one-, two-, and three-dimensional simulation of waste transport in the aquifer system (No. ORNL-5602). Oak Ridge National Lab., TN (USA)

Surface Treatment of AISI 304 Using Pulsating Water Jet Peening

Madhulika Srivastava, Rupam Tripathi, Sergej Hloch, Ayush Rajput, Drupad Khublani, Somnath Chattopadhyaya, Amit Rai Dixit, Josef Foldyna, Pavel Adamčík, Jiri Klich, Michal Zelenak and Dagmar Klichová

Abstract Water jet peening has gained attention as a potential surface treatment process for improving the fatigue life of a component. The tensile residual stress in the component initiates the stress corrosion cracking and reduces its fatigue life. The mitigation of this tensile residual stress can be effectively achieved by water jet peening process due to its resistance to corrosion, flexibility in treating complex areas and capability to maintain the eco-friendly environment. In the present work, the AISI 304 plates were treated with pulsating water jet (actuator frequency $f = 20.19$ Hz) at the pressure of $p = 20$ MPa with traverse speed of $v = 0.5$ mm/s and $v = 2.5$ mm/s using two different types of nozzles; flat nozzle of diameter

M. Srivastava (✉) · R. Tripathi · A. Rajput · D. Khublani · S. Chattopadhyaya · A.R. Dixit
Department of Mechanical Engineering, Indian Institute of Technology (Indian School of Mines), Dhanbad 826004, Jharkhand, India
e-mail: madhulikamech3003@gmail.com

R. Tripathi
e-mail: rupam.tripathi10@gmail.com

A. Rajput
e-mail: ayushrajput49@gmail.com

D. Khublani
e-mail: khublani@gmail.com

S. Chattopadhyaya
e-mail: somuismu@gmail.com

A.R. Dixit
e-mail: ar.dixit@mece.ism.ac.in

S. Hloch
Faculty of Manufacturing Technologies, TU of Košice with the seat in Prešov, Bayerova 1, Presov 080 01, Slovak Republic
e-mail: hloch.sergej@gmail.com

S. Hloch · J. Foldyna · J. Klich · M. Zelenak · D. Klichová
Department of Material Disintegration, Institute of Geonics Academy of Science of Czech Republic, Studentska, Ostrava, Poruba 708 00, Czech Republic
e-mail: josef.foldyna@ugn.cas.cz

M.K. Singh et al. (eds.), *Applications of Fluid Dynamics*, Lecture Notes in Mechanical Engineering, https://doi.org/10.1007/978-981-10-5329-0_40

d = 1 mm (HAMMELMANN) and circular nozzle of diameter d = 1.9 mm (STONEAGE). The microstructural analysis of the treated and untreated region was conducted to analyse the effect of traverse speed and the type of nozzle on the erosion process. The study revealed that more erosion occurs at lower traverse speed; however, fewer surface depressions were observed in the case of flat nozzles. The X-ray diffraction technique was also used to analyse the effect of traverse speed and the type of nozzle on the residual stress of the samples. In addition to this, the acoustic emission during the ongoing process was monitored using LabView 2012 SP1 f5 ver. 12.0.1. The results indicate that acoustically monitored pulsating water jet peening process can be used as tool for the controlled local treatment process arising from the impact of the pulsed water jet on the surface of sample.

Abbreviations and Symbols

WJP	Water jet peening
PWJ	Pulsating water jet
XRD	X-ray diffraction
FESEM	Field emission scanning electron microscope
AE	Acoustic emission
f	Frequency (kHz)
d	Diameter of the nozzle (mm)
v	Traverse speed (mm/s)
p	Pressure (MPa)
z	Stand-off distance (mm)

1 Introduction

Austenitic stainless steel (AISI 304) has wide mechanical, automotive and nuclear applications as it inherits magnificent properties such as high toughness, better corrosion resistance, high ductility, drawability and formability. These components possess residual stress, which has the tendency to improve or deteriorate the

J. Klich
e-mail: jiri.klich@ugn.cas.cz

M. Zelenak
e-mail: michal.zelenak@ugn.cas.cz

D. Klichová
e-mail: dagmar.klichova@ugn.cas.cz

P. Adamčík
Technická Diagnostika, Ltd., Jilemnického 4, Prešov 080 01, Slovak Republic
e-mail: tdg@diagnostika.sk

component depending on their magnitude and nature. The positive effect of compressive residual stress is widely used in industries. Over the years, possible methods are being adopted to improve the adverse effect of the residual stresses such as shot peening, laser shock peening and water jet peening (Meguid et al. 1999). Water jet peening has emerged as a promising technique for mitigating the stress corrosion cracking which results into the improvement of the residual stresses and the fatigue life of the component (Srivastava et al. 2016). The possible drawbacks associated with shot peening, i.e. defects and rough surface, which has pernicious effects to fatigue crack initiation have been eliminated in the water jet peening process (Eftekhari et al. 1995). In addition to this, WJP method does not involve any thermal effects as in laser peening (Ding and Ye 2006). In the WJP process, the droplets of water are impinged against the surface being treated. The impact of the droplets generates a surface pressure distribution that exceeds the yield strength of the material. A localized plastic deformation is induced by the peak loads that are constrained by the surrounding material thereby inducing high compressive residual stress (Hashimoto et al. 2013) (Fig. 1).

Water jet technology in recent times is being used in varieties of applications such as cleaning, cutting, paint removal, surface textures and increasing fatigue life of the component by imposing positive effects compressive residual stress in the subsurface layer (Mochizuki et al. 1993). Water jet as a tool for surface treatment refers to any process that is used to modify, enhance or remove the exposed surfaces of a component or structure. The applications that require surface treatment range from low-precision process like rust removal from ship hulls to control processes such as texture automotive cylinder bores to promote the adhesion of thermal spray coatings. A continuous water jet has several modifications like AWJ and PWJ (Foldyna et al. 2004, 2009, 2012). WJ and AWJ are presently being used in industries and have some economic and technological limitations. The current

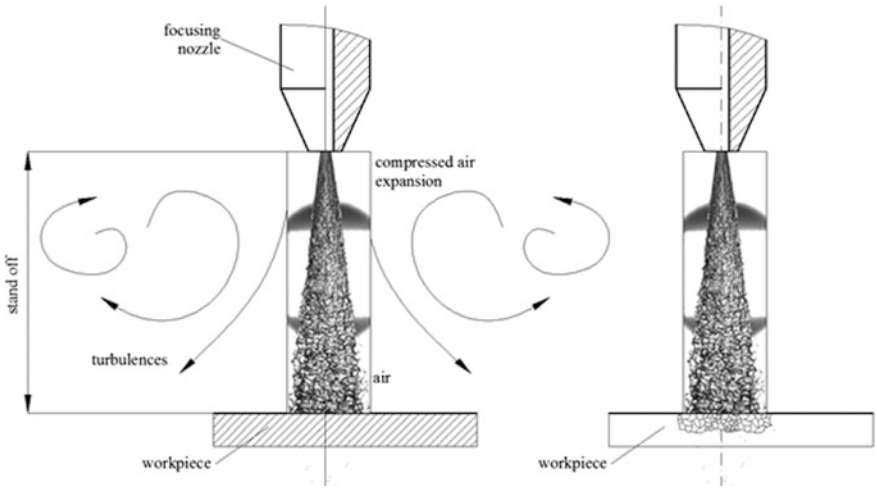

Fig. 1 Mechanism of water jet peening

industry is trending towards erosion of materials at lower pressures for different applications. This could be achieved by using pulsating water jet (Lehocka et al. 2016; Zelenak et al. 2015). Pulsating water jet involves initially a continuous jet exiting from the nozzle which later turns into individual clusters of fluid. Eventually, the material is then treated with high-energy droplets. Over the years, attempts are being made to attain the discontinuity of the jet, but the modification of continuous jet in form of pulses is found to be most advantageous (Lehocka et al. 2016). The pulsating water jet is practically being investigated for disintegration of rocks (Vijay and Foldyna 1994; Tripathi et al. 2016), redevelopment of concrete structures (Foldyna 2011), scale removal from steels (Hnizdil and Raudensky 2010), erosion of metals (Foldyna et al. 2012) and in medicine for dental hygiene (Sharma et al. 2008), orthopaedics and traumatology (Hloch et al. 2013a, b) and dermal medicine (Akbari and Shafii 2002). In this study, an attempt has been made to utilize the effectiveness of PWJ for the surface treatment process.

In the past decades, possible attempts had been made to analyse the effect of various process parameters such as jet pressure p (MPa) and traverse speed v (mm/min) on the residual stress, the roughness and the erosion of the component. Colosimo et al. (2000) explained the empirical relation between the peening parameters, residual stress and surface roughness of the material. Ramulu et al. (2000) evaluated the effect of high-pressure water jet on the surface integrity and texture of the metal through an experimental study. The residual stress fields obtained after the treatment were analysed to distinguish the influence of material properties. Arola et al. (2001) observed that the residual stress on the surface of titanium alloy after water jet peening increased with increasing pressure, and also negligible change in roughness was observed. The experimental study of water jet peening at 600 MPa (Hashish et al. 2005) revealed that plastic deformation was achieved at much deeper layers in case of water jet peening than laser peening. The degree of the deformation was found to be dependent on the peening parameters and the desired surface roughness. Also, a comparative study between water jet peening and shot peening on aluminium alloy depicted that the compressive stress induced near the strengthened surface by water jet peening was higher than shot peening, thereby more increase in the fatigue life was observed in case of water-jet-peened surface. Though many works had been reported regarding the effect of residual stress on the surface treated by water jet, efforts are required to cover the large range of materials and to analyse the variation of the changing process parameters.

Online monitoring of acoustic emission in the recent years has been used effectively for defect analysis during the ongoing process (Hloch et al. 2013a, b). Valicek and Hloch (2010) utilized the negative characteristic of noise as a source of information to describe the ongoing process. The appropriate application of sensors monitors the AE generated during the process for the fault detection. For instance, in the case of abrasive water jet cutting insufficient cutting depth, choked orifice, etc. was detected by using acoustic emission as an indirect monitoring tool (Hassan et al. 2004). Hreha et al. (2012) attempted to monitor the vibrations generated during the hydro-abrasive cutting of stainless steel and observed that fault

conditions like broken focussing tube, fractured water nozzle can be detected and controlled during the online monitoring of acoustic emission. Similarly, Hreha et al. (2015) during the online monitoring of AWJ cutting of AISI 309 analysed the dependency of the surface topography of the material being cut on the emission spectrum arising during the process. The online monitoring of AE involves measurement and evaluation of the ongoing phenomenon which helps in the characterization of the processes accurately. It involves the collection and evaluation of the AE (Tripathi et al. 2016). The data evaluated from the acoustic emission spectra helps to predict the ongoing process and determine the state of PWJ during the time of its exposure to the material. This information can be applied to any position during the ongoing experiment on the surface of the material. The solution is highly influenced by the input parameters of the technological process in order to achieve the optimal parameters for preventing the disintegration of the material (Chen 2008; Natarajan et al. 2011; Chen et al. 2011; Salak et al. 2006; Sharma 2011).

In this work, the surface of AISI 304 is treated using pulsating water jet using two different types of nozzles; flat nozzle and circular nozzle. The microstructural analysis was conducted to evaluate the effect of plastic deformation on the treated surface. In order to analyse the effect of type of nozzle on the residual stress improvement, the surface residual stresses will be measured using X-ray diffraction method. Also, during the treatment of AISI 304 samples, indirect monitoring of acoustic emission using LabView 2012 SP1 f5 ver. 12.0.1 was performed. The aim of using the acoustic emission as an indirect monitoring tool is to use it as a source of information during the ongoing process for a better control over the treatment process.

2 Material and Experimentation

The water jet peening was performed on the surface of AISI 304 plate having mechanical properties and composition given in Tables 1 and 2, respectively. The AISI 304 plate (350 mm × 50 mm × 5 mm) was clamped on the fixture which was attached to the frame of the machine (Fig. 3). The technological set-up (Fig. 2) includes—plunger pump HAMMELMANN HDP 253 (maximum operating pressure—150 MPa, maximum flow rate 67 l min^{-1}) and robot ABB IRB 6640-180 for handling the pulsating water head. The acoustic waves are generated by ultrasonic generator Ecoson WO-UG_630-20 specially designed for pulsating water jetting. The treatment process was performed in a linear direction along the width of the sample using two types of nozzles: flat (HAMMELMANN) (Fig. 2a) and circular (STONEAGE) (Fig. 2b) with the experimental conditions stated in Table 3. Sufficient gap was maintained between the consecutive treatments in order to avoid the overlap of the treated surface (Fig. 4). As the flat nozzle exit is

Table 1 Composition of AISI 304

Element	C (%)	Mn (%)	S (%)	Si (%)	P (%)	Ni (%)	Cr (%)
SS (AISI 304)	0.08	2.00	0.03	1.0	0.04	8–10.5	18–20

Table 2 Mechanical properties of AISI 304

STN	W. Nr.	Grade	Tensile strength Rm (N-mm^{-2})	Yield strength		Elongation (%)	HR Bmax.	Structure
				$Rp_{0,2}$	Rp_1			
17.240	1.4301	304	500/900	175	210	45	88	Austenitic

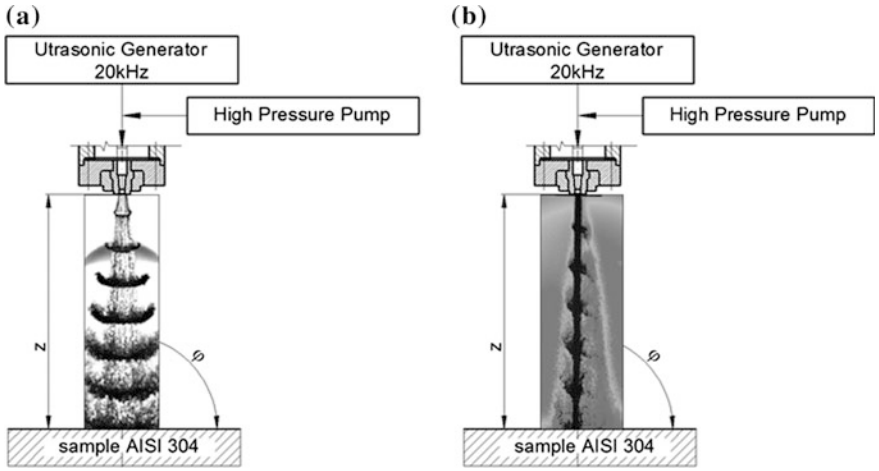

Fig. 2 Principle of technological set-up: **a** flat nozzle, **b** circular nozzle

elliptical in shape, it forms a wider jet at a spray angle of 10° and resulted in rectangular cross section on the surface of the workpiece after the treatment process. In contrast to this, the circular nozzle exit is circular in shape and resulted in circular cross section on the surface of the workpiece.

The acoustic emission generated during the peening process was measured using Spectral Measurements Toolkit 2.6.3 with accelerometer WR712F-M4 capable of measuring up to 65 kHz. The AE parameters were obtained by processing the raw AE signal using Advanced Signal Processing Toolkit 12.0.0 by LabView 2012 SP1 f5 ver. 12.0.1 (National Instrument). A piezoelectric accelerometer was fixed at the back side of the workpiece before clamping. The two other accelerometer sensors were also fixed for sensing the pressure in the chamber at the time of impact.

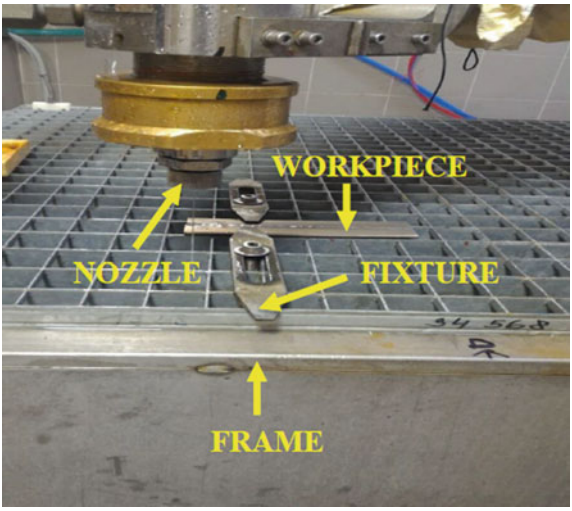

Fig. 3 Experimental set-up

Table 3 Experimental conditions

S. No.	Type of nozzle	d (mm)	f (kHz)	Z (mm)	p (MPa)	v (mm/s)
1.	Flat	1	20	30	20	0.5 2.5
2.	Circular	1.9	20	30	20	0.5 2.5

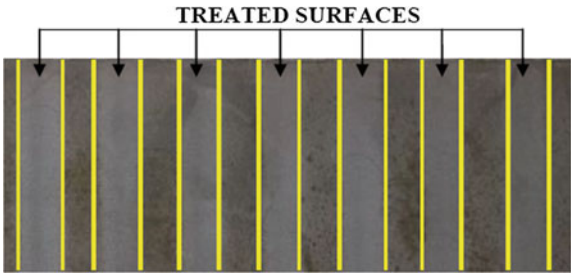

Fig. 4 Treated AISI 304 samples by pulsating water jet using flat nozzle d = 1 mm 10° and round nozzle d = 1.9 mm

3 Results and Discussion

3.1 AE Analysis

The acoustic emission was recorded during the peening process caused by the impact of the pulsed water jet with the surface of the sample. These signals were

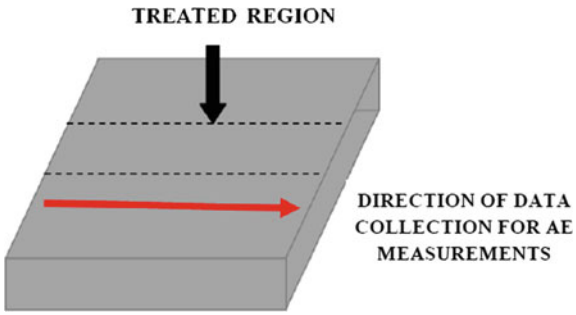

Fig. 5 Position on the sample for AE analysis

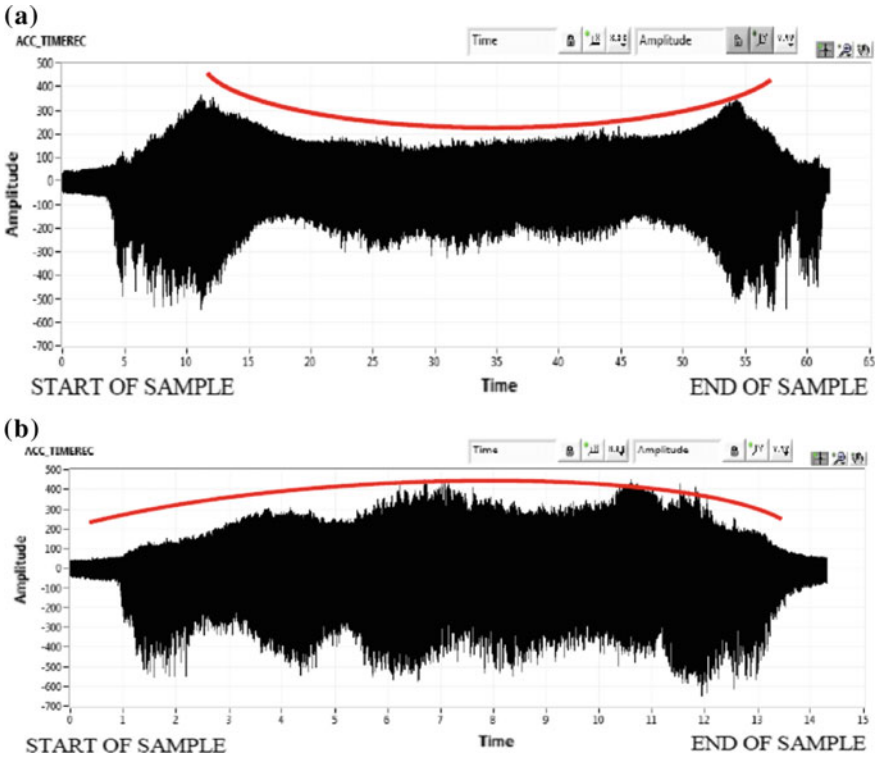

Fig. 6 Acoustic emission signal behaviour: (**a**) flat nozzle, v = 0.5 mm/s; (**b**) flat nozzle, v = 2.5 mm/s; (**c**) circular nozzle, v = 0.5 mm/s; (**d**) circular nozzle, v = 2.5 mm/s

recorded from the commencement of the peening process till the width of the sample was covered (Fig. 5).

Figure 6a–d shows the acoustic emission signals recorded at different traverse speed at pressure of 20 MPa using flat and circular nozzles. According to the

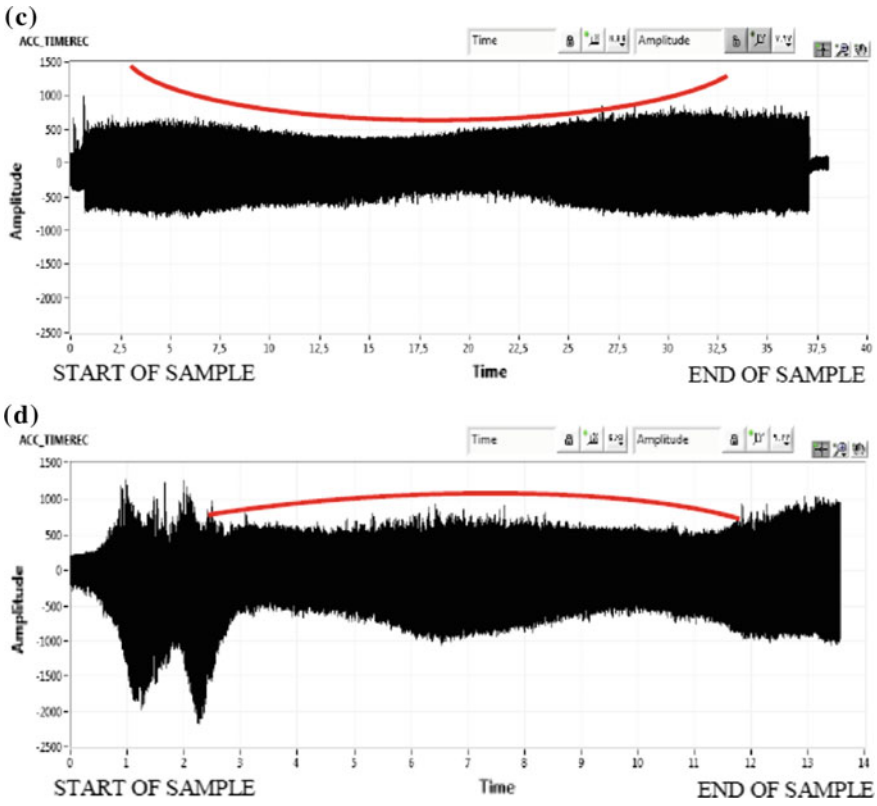

Fig. 6 (continued)

analysis of measured acoustic emission, it is possible to conclude that the signal intensity measurement during peening with the circular nozzle is two times bigger than using flat nozzle due to water dispersion under angle 10° of flat nozzle. As shown in Fig. 6, the peak values of amplitude are achieved after few seconds of the beginning of the peening process due to the commencement of the repeated impact of the pulsed water jet on the surface of sample. The traverse speed has shown influential behaviour in the waveform, i.e. the signal obtained using traverse speed $v = 0.5$ mm/s has convex shape, while at higher traverse speed $v = 2.5$ mm/s it showed a concave behaviour. At higher traverse speed $v = 2.5$ mm/s, the signal intensity increases abruptly in the case of flat nozzle. However, the circular nozzle showed a significant change in which the low traverse speed $v = 0.5$ mm/s causes low actuation particular in the middle part of the sample and high traverse speed $v = 2.5$ mm/s actuates middle part of the sample to the edge of the sample more. The possible reason behind this variation could be the plastic deformation that occurs more at lower traverse speed. The present results show the important difference in the shape of the signals with the variation in the traverse speed.

Therefore, these acoustic emission results can be used as important source information about the ongoing plastic deformation during the surface treatment process.

3.2 Surface Erosion

After the treatment of AISI 304 by pulsating water jet, the microstructural analysis of the surface was examined using FESEM (FESEM Supra 55 having resolution of 0.8 nm at 15 kV, and 1.6 nm at 1 kV; 12-1000000X magnification; 100 V to 30 kV acceleration voltage; and Schottky field emission electron gun.). These micrographs were taken at 500× magnification as shown in Fig. 7a–e. The microstructure of AISI 304 surface indicates noticeable erosion in the treated region in form of small depressions. These depressions are more visible for the treatments subjected to lower traverse speed (Fig. 7b, c). Therefore, it can be interpreted that the erosion mechanism is dependent upon the duration of the impact of pulsed water jet with the target material which, in turn, is dependent upon the traverse speed. From Fig. 7a (original surface) and Fig. 7b–e (treated surface), it can be noted that substantial amount of erosion occurs on the surface after the treatment process. For the same parameter, the treatments carried out with flat nozzle (Fig. 7b, d) showed fewer surface depressions or less severe erosions as compared to treatments carried out using circular nozzle (Fig. 7c, e). In Fig. 7c, it was observed that disintegration of material occurs in case of circular nozzles when treated at traverse speed of 0.5 mm/s; however, under same parameter, the micrograph of flat nozzle showed the occurrence of surface depressions Fig. 7b.

Figure 7f was observed at 1000× magnification which shows the main impact zone and cavities created after the treatment process. These cavities are the result of peening mechanism in which the droplets impact the surface being treated and lead to plastic deformation which is constraint by the surrounding material.

3.3 Residual Stress Measurement

The residual stress measurements are conducted using X-ray diffraction method by Panalytical High Resolution XRD-I, PW 3040/60 (Fig. 8). The measurements will be conducted on the surface of samples treated with round and flat nozzles as shown in Fig. 9.

The residual stresses will be measured on the surface of the untreated and treated regions to evaluate the changes before and after the treatment process and also to evaluate the influence of geometry of nozzle on the residual stress improvement. Due to certain limitations, these tests could not be conducted at present, but in future the results will be evaluated and reported.

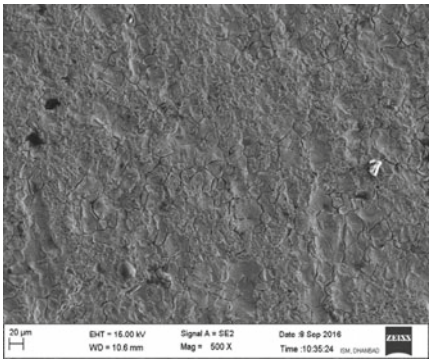

(a) Untreated surface

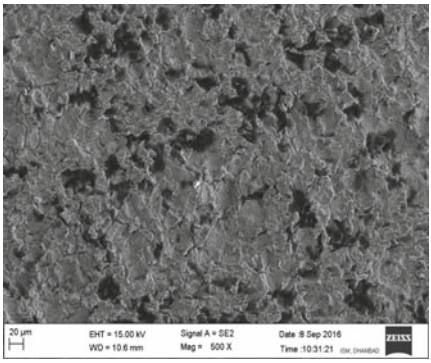

(b) Flat nozzle (v=0.5m/s, P=20MPa)

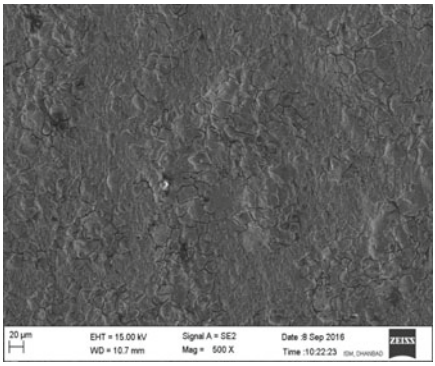

(c) Circula rnozzle (v=0.5m/s, P=20MPa)

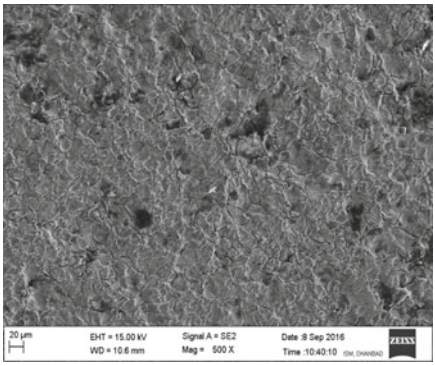

(d) Flat nozzle (v=2.5m/s, P=20MPa)

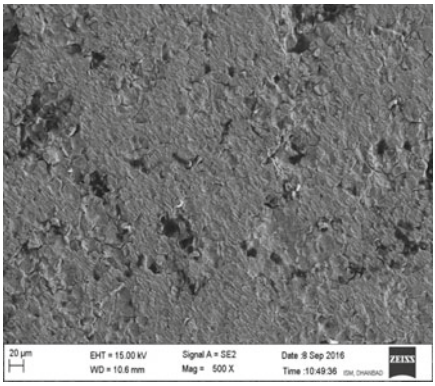

(e) Circular nozzle (v=2.5m/s, P=20MPa)

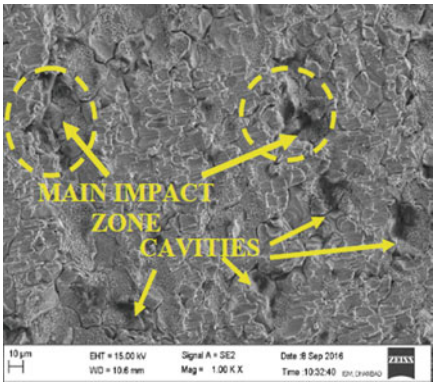

(f) Circular nozzle (v=2.5m/s, P=20MPa)

Fig. 7 FESEM images of treated and untreated AISI 304 samples

Fig. 8 X-ray diffraction machine

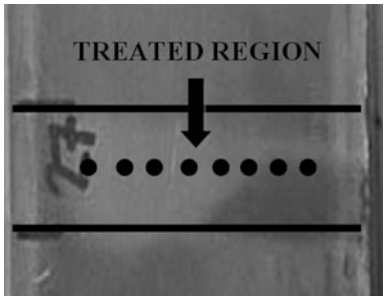

Fig. 9 Sample for residual stress measurement

4 Conclusion and Future Scope

This experimental investigation presents a new and effective method for the surface treatment process. The AISI 304 plates are treated using pulsating water jet using two different types of nozzles, flat and circular, at different set of parameters. From the present study, the following conclusions can be made:

(i) The microstructural analysis of the treated samples revealed that more erosion or surface depressions were observed on the surface of the samples that are treated at lower traverse speed.
(ii) Considering the effect of geometry of the nozzle on the surface erosion, it was observed the flat nozzle leads to less surface erosions as compared to circular nozzle when treated under same conditions.
(iii) The acoustic emission signals recorded during the peening process showed a influential behaviour on the traverse speed. The waveform showed convex behaviour for low traverse speed and concave behaviour for high traverse speed.

(iv) The signal intensity obtained for circular nozzle was more than the flat nozzle due to water dispersion at an angle of 10°.
(v) These acoustic emission results can be used as important source information for performing a controlled treatment process on the surface of the specimen.

Further, in the future, the effect of treatment on the residual stress will be evaluated to check the effectiveness of the process as a surface treatment technique. Also, the acoustic emission recorded during the peening process is interpreted according to the residual stress results obtained in order to present an effective way to control the parameters hence, maintaining the surface integrity.

Acknowledgements This work was supported by the Slovak Research and Development Agency under Contract No. APVV-207-12 and Indian Institute of Technology (Indian School of Mines), Dhanbad, India. Experiments were carried out with the support of the Institute of Clean Technologies for Mining and Utilization of Raw Materials for Energy Use—Sustainability Program, reg. no. LO1406 financed by Ministry of Education, Youth and Sports of the Czech Republic, and with support for the long-term conceptual development of the research institution RVO: 68145535.

References

Akbari P, Shafii MB (2002) Numerical simulation of an impinging water jet applied to cooling human skin. In: Proceedings of 21st international congress on applications of laser and electro-optics (ICALEO), 11 p

Arola D, McCain ML, Kunaporn S (2001) Waterjet and abrasive waterjet surface treatment of titanium: a comparison of surface texture and residual stress. Wear 249(10–11):943–950

Chen L (2008) Study on prediction of surface quality in machining process. J Mater Process Technol 205:439–450

Chen CC, Chiang KT, Chou CC, Liao YC (2011) The use of D-optimal design for modelling and analysing the vibration and surface roughness in the precision turning with a diamond cutting tool. Int J Adv Manuf Technol 54:465–478

Colosimo BM, Monno M, Semeraro Q (2000) Process parameters control in water jet peening. Intern J Mater Product Technol 15(1–2):10–19

Ding K, Ye L (2006) Simulation of multiple laser shock peening of a 35CD4 steel alloy. J Mater Process Technol 178:162–169

Eftekhari A, Talia JE, Mazumdar PK (1995) Influence of surface condition on the fatigue of an aluminium-lithium alloy (2090-T3). Mater Sci Engg A 199:L3–L6

Foldyna J (2011) Use of acoustic waves for pulsating water jet generation. In: Beghi MG (ed) Acoustic waves—from microdevicse to helioseisomology. Intech, pp 323–342

Foldyna J, Sitek L, Svehla B, Svehla S (2004) Utilization of ultrasound to enhance high-speed water jet effects. Ultrason Sonochem 11 3(4):131–137

Foldyna J, Sitek L, Scucka J, Martinec P, Valicek J, Palenikova K (2009) Effects of pulsating water jet impact on aluminium surface. J Mater Process Technol 209(20):6174–6180

Foldyna J, Klich J, Hlavacek P, Zelenak M, Scucka J (2012) Erosion of metals by pulsating water jet. Tehnički vjesnik 19(2):381–386

Hashimoto T, Osawa Y, Itoh S, Mochizuki M, Nishimoto K (2013) Long-term stability of residual stress improvement by water jet peening considering working processes. J Press Vessel Technol 135:1–8

Hashish M, Chillman A, Ramulu M (2005) Waterjet peening at 600 MPa: a first Investigation. In: Fluids engineering division, vol 261. The American Society of Mechanical Engineers, pp 45–52

Hassan AI, Chen C, Kovacevic R (2004) On-line monitoring of depth of cut in AWJ cutting. Int J Mach Tool Manuf 44:595–605

Hloch S, Folydna J, Sitek L, Zelenak M, Hlavacek P, Hvizdos P, Kloc J, Monka P, Monkova K, Kozak D, Magurova D (2013a) Disintegration of bone cement by continuous and pulsating water jet. Tehnički vjesnik 20(4):593–598

Hloch S, Valicek J, Kozak D (2013b) Analysis of acoustic emission emerging during hydroabrasive cutting and options for indirect quality control. Int J Adv Manuf Technol 66 (1–4):45–58

Hnizdil M, Raudensky M (2010) Descaling by pulsating water jet. In: Proceedings of metal 19th international conference metallurgy and materials, pp 209–213

Hreha P, Hloch S, Peržel V (2012) Analysis of acoustic emission recorded during monitoring of abrasive waterjet cutting of stainless steel AISI 309. Tehnički vjesnik 19(2):355–359

Hreha P, Radvanska A, Hloch S, Perzel V, Krolczyk G, Monkova K (2015) Determination of vibration frequency depending on abrasive mass flow rate during abrasive water jet cutting. Int J Adv Manuf Technol 77:763–774

Lehocka D, Klich J, Foldyna J, Hloch S, Krolczyk JB, Carach J, Krolczyk GM (2016) Copper alloys disintegration using pulsating water jet. Measurement 82:375–383

Mahmoudi AH, Salahi F, Ghasemi A (2016) Comparison between residual stress induced by waterjet peening and shot peening. In: International conference on surface modification technologies

Meguid SA, Shagal G, Stranart JC (1999) Finite element modelling of shot-peening residual stresses. J Mater Process Technol 92–93:401–404

Mochizuki M, Enomoto K, Sakata S, Kurosawa K, Saito H, Tsujimura H, Ichie K (1993) A study on residual stress improvement by water jet peening. In: Proceedings of the 5th international conference on shot peening. Oxford, pp 247–256

Natarajan C, Muthu S, Karuppuswamy P (2011) Prediction and analysis of surface roughness characteristics of a non-ferrous material using ANN in CNC turning. Int J Adv Manuf Technol 57(9):1043–1051

Ramulu M, Kunaporn S, Arola D (2000) Water jet machining and peening of metals. J Press Vessel Technol-Trans ASME 122(1):90–95

Salak A, Vasilko K, Selecka M (2006) New short time face turning method for testing the machinability of PM steels. J Mater Process Technol 176:62–69

Sharma V (2011) Multi response optimization of process parameters based on Taguchi-Fuzzy model for coal cutting by water jet technology. Int J Adv Manuf Technol 56:1019–1025

Sharma NC, Lyle DM, Qaqish JG, Galustians J, Schuller R (2008) The effect of a dental water jet with orthodontic tip on plaque and bleeding in adolescent patients with fixed orthodontic appliances. Am J Orthod Dentofac Orthop 133(4):565–571

Srivastava M, Tripathi R, Hloch S, Chattopadhyaya S, Dixit AR (2016) Potential of using water jet peening as a surface treatment process for welded joints. Procedia Eng 149:472–480

Tripathi R, Srivastava M, Hloch S, Adamčík P, Chattopadhyaya S, Das AK (2016) Monitoring of acoustic emission during the disintegration of rock. Procedia Eng 149:481–488

Valicek J, Hloch S (2010) Using the acoustic sound pressure level for quality prediction of surfaces created by abrasive waterjet. Int J Adv Manuf Technol 48:193–203

Vijay MM, Foldyna J (1994) Ultrasonically modulated pulsed jets: basic study. In: Proceeding of the 12th international conference on jet cutting technology. Rouen, France

Zelenak M, Foldyna J, Scucka J, Hloch S, Riha Z (2015) Visualisation and measurement of high-speed pulsating and continuous water jets. Measurement 72:1–8

Pollutant Transport in a Semi-infinite Heterogeneous Porous Media

S. Begam, S. Ahamad and Chandan Kumar Thakur

Abstract This study proposed an analytical model of contaminant solute transport with an impact of elemental recharge rate of aquifer. The domain of study is considered as a heterogeneous porous media. Dispersion is directly proportional to the square of the seepage velocity, whereas the velocity is a function of both time and distance variables. Initially, the aquifer is not pollutant free; some background concentration is present there. Temporally dependent exponentially decreasing input source is considered, and the concentration gradient is assumed to be zero at the exit boundary. Laplace transform technique (LTT) is used to obtain the analytical solution and is validated with the numerical solution which is obtained using explicit finite difference method.

1 Introduction

To describe the contaminant transport in porous media, advection–dispersion equation (ADE) is generally used in which dispersion coefficient plays an important role. Generally, while ADE is solved, the dispersion is assumed to be constant, but according to the results of some field studies (Taylor and Howard 1987; Domenico and Robbins 1984; Toride et al. 1995), dispersion is distance-dependent; i.e., it increases with distance 'x' from the source of contamination. Sposito et al. (1986) showed that dispersion coefficient increases with distance or travel time. Wang et al. (1998) suggested that to have a good model of solute transport, it was necessary to

S. Begam (✉) · C.K. Thakur
Department of Applied Mathematics, Indian Institute of Technology (Indian School of Mines), Dhanbad 826004, Jharkhand, India
e-mail: sultanabegam26@gmail.com

C.K. Thakur
e-mail: Chandan.ism.2014@gmail.com

S. Ahamad
Department of Mathematics, CIT, Ranchi 835103, Jharkhand, India
e-mail: shafique.ism@gmail.com

M.K. Singh et al. (eds.), *Applications of Fluid Dynamics*, Lecture Notes in Mechanical Engineering, https://doi.org/10.1007/978-981-10-5329-0_41

consider scale-dependent dispersion coefficient. Watson et al. (2002) pointed out that the hydrodynamic dispersion coefficient was a nonlinear function of the seepage velocity.

A large number of analytical and numerical solutions have been developed for ADE with scale-dependent dispersion in heterogeneous medium (Khan and Jury 1990; Zhang et al. 1994; Logan 1996; Pang and Hunt 2001; Gao et al. 2010; Natarajan and Suresh Kumar 2014). A semi-analytical solution was derived by You and Zhan (2013) for contaminant transport in a finite aquifer with linear asymptotic or exponential scale-dependent dispersion and time-dependent sources. Sharma et al. (2014) proposed a reactive solute transport model used in heterogeneous porous media with time-dependent and distance-dependent dispersion using finite-volume method. Natarajan (2015) presented a numerical model using implicit finite difference method in which the effect of nonlinear sorption and time-dependent as well as distance-dependent dispersion was shown.

In this paper, an analytical solution for ADE with the impact of an extra source term is derived and is compared with the numerical solution. A source of contamination such as an ash pond, dump site, or industrial disposal site lies above the aquifer; there could be a possibility of pollution reaching the underlying aquifer (Rastogi 2007). To represent that physical situation, an extra source term $\frac{c'w}{\theta}$ is added with the regular advection–dispersion equation (Rastogi 2007). Here, w is elemental recharge rate with solute concentration c', and θ is the effective porosity of the aquifer. The ADE is solved with Dirichlet-type boundary condition and distance-dependent dispersion. It is considered that the aquifer is not solute-free initially, and it is represented by a linear expression of the initial source with an exponentially deceasing function of distance variable x. One end of the domain, the time-dependent decreasing source is injected, and solute mass is ejected from the other end of the domain, and so, flux is supposed to be zero. Dispersion is directly proportional to the square of the seepage velocity. To analyse the impact of the added source term with AD equation is one of the objective of this paper.

2 Mathematical Model

The models for predicting solute transport in porous media are generally based on the advection–dispersion-type transport equations. For one-dimensional solute transport process in an isotropic semi-infinite heterogeneous aquifer with an external source of contamination, the transport equation may be written as follows

$$\frac{\partial C}{\partial t} = \frac{\partial}{\partial x}\left[D(x,t)\frac{\partial C}{\partial x} - u(x,t)C\right] + \frac{c'w}{\theta} \tag{1}$$

where $C(x,t)$ $[ML^{-3}]$ is the contaminant concentration, u $[LT^{-1}]$ is the groundwater velocity or seepage velocity, D $[L^2T^{-1}]$ is the dispersion coefficient, t $[T]$ is time, and x $[L]$ is distance variable.

The suitable initial and boundary conditions are

$$C(x,t) = c' + c_i \exp(-\gamma x); \quad x \geq 0, \quad t = 0 \tag{2}$$

$$C(x,t) = c' + c_0 \exp(-\lambda_s t); \quad x = 0, \quad t > 0 \tag{3}$$

$$\frac{\partial C}{\partial x} = 0; \quad x \to \infty, \quad t > 0 \tag{4}$$

where c_i $[MT^{-3}]$ is initial background solute concentration, γ $[L^{-1}]$ is a constant decay parameter with space, and λ_s $[T^{-1}]$ is decay constant parameter with time.

3 Analytical Solution

As we considered the seepage velocity is a time- and distance-dependent function and dispersion is directly proportional to square of the velocity, the expressions for dispersion and seepage velocity are written as follows

$$u(x,t) = u_0 f(mt)(1+ax) \quad \text{and} \quad D(x,t) = D_0 f(mt)^2 (1+ax)^2 \tag{5}$$

where u_0 $[LT^{-1}]$ is initial groundwater velocity, D_0 $[L^2T^{-1}]$ is initial dispersion coefficient, m $[T^{-1}]$ is flow resistance coefficient, a $[L^{-1}]$ is inhomogeneity parameter along the longitudinal direction, and $f(mt)$ is an arbitrary function.

Using Eq. (5) in Eq. (1), one can get

$$\frac{\partial C}{\partial t} = D_0 f(mt)^2 \frac{\partial^2 C}{\partial x^2} - u_0 f(mt) \frac{\partial C}{\partial x} + \frac{c'w}{\theta} \tag{6}$$

Introduce one new space variable Z with the following transformation:

$$Z = \frac{1}{a} \log(1+ax) \tag{7}$$

$$\frac{\partial C}{\partial t} = D_0 f(mt)^2 \frac{\partial^2 C}{\partial Z^2} - u_0 f(mt) f_1(mt) \frac{\partial C}{\partial Z} - a u_0 f(mt) C + \frac{c'w}{\theta} \tag{8}$$

where, $f_1(mt) = 1 - \frac{aD_0}{u_0} f(mt)$

Again, after using the following transformation

$$X = \frac{f_1(mt)}{f(mt)} Z \tag{9}$$

Equation (8) becomes

$$\frac{1}{f_1(mt)^2}\frac{\partial C}{\partial t} = D_0\frac{\partial^2 C}{\partial X^2} - u_0\frac{\partial C}{\partial X} - au_0\frac{f(mt)}{f_1(mt)^2}C + \frac{c'w}{\theta}\frac{1}{f_1(mt)^2} \tag{10}$$

Introducing a new time variable T using the following transformation

$$T = \int_0^t f_1(mt)^2 \mathrm{d}t \tag{11}$$

we reduce Eq. (10) into

$$\frac{\partial C}{\partial T} = D_0\frac{\partial^2 C}{\partial X^2} - u_0\frac{\partial C}{\partial X} - au_0\frac{f(mt)}{f_1(mt)^2}C + \frac{c'w}{\theta}\frac{1}{f_1(mt)^2} \tag{12}$$

Corresponding initial and boundary conditions are

$$C(X,T) = c' + c_i\exp(-\gamma X); \quad X \geq 0, \quad T = 0 \tag{13}$$

$$C(X,T) = c' + c_0\exp(-\lambda_s T); \quad X = 0, \quad T > 0 \tag{14}$$

$$\frac{\partial C}{\partial X} = 0; \quad X \to \infty, \quad T > 0 \tag{15}$$

Now, to remove the convective term from Eq. (12), we use the following transformation

$$C(X,T) = K(X,T)\exp\left[\frac{u_0}{2D_0}X - \left\{\frac{u_0^2}{4D_0} + \frac{af(mt)}{f_1(mt)^2}u_0\right\}T\right] + \frac{c'w}{au_0\theta}\frac{1}{f(mt)} \tag{16}$$

Equation (12) becomes

$$\frac{\partial C}{\partial T} = D_0\frac{\partial^2 C}{\partial X^2} \tag{17}$$

The corresponding initial and boundary conditions in Eqs. (13)–(15) become

$$K(X,T) = \left\{c' + c_i\exp(-\gamma X) - \frac{c'w}{au_0\theta}\right\}\exp\left(-\frac{u_0}{2D_0}X\right); \quad X \geq 0, \quad T = 0 \tag{18}$$

$$K(X,T) = \{c' + c_i\exp(-\lambda_s T) - q\}\exp(\phi); \quad X = 0, \quad T > 0 \tag{19}$$

$$\frac{\partial K}{\partial X} + \frac{u_0}{2D_0}K = 0; \quad X \to \infty, \ \ t > 0 \tag{20}$$

where,

$$q = \frac{c'w}{au_0\theta}\frac{1}{f(mt)} \quad \text{and} \quad \phi = \left\{ \left(\frac{u_0^2}{4D_0} + \frac{af(mt)}{f_1(mt)^2}u_0 \right) T \right\}$$

Using Laplace transform and inverse Laplace transform, we obtain the solution for above model which is as follows:

$$C(X,T) = [E(X,T) + F(X,T) - G(X,T) - H(X,T) + J(X,T)] \tag{21}$$

where

$$\begin{aligned} E(X,T) = \frac{(c'-q)}{2}\Bigg[&\exp\left\{ \left(\frac{u_0}{2D_0} - \sqrt{\frac{\phi}{D_0}} \right) X \right\} \operatorname{erfc}\left(\frac{X}{2\sqrt{D_0 T}} - \sqrt{\phi T} \right) \\ &+ \exp\left\{ \left(\frac{u_0}{2D_0} + \sqrt{\frac{\phi}{D_0}} \right) X \right\} \operatorname{erfc}\left(\frac{X}{2\sqrt{D_0 T}} + \sqrt{\phi T} \right) \Bigg] \end{aligned} \tag{22a}$$

$$\begin{aligned} F(X,T) = \frac{c_0}{2}\Bigg[&\exp\left\{ (\lambda_0 - \phi)T + \left(\frac{u_0}{2D_0} - \sqrt{\frac{\lambda_0}{D_0}} \right) X \right\} \operatorname{erfc}\left(\frac{X}{2\sqrt{D_0 T}} - \sqrt{\lambda_0 T} \right) \\ &+ \exp\left\{ (\lambda_0 - \phi)T + \left(\frac{u_0}{2D_0} + \sqrt{\frac{\lambda_0}{D_0}} \right) X \right\} \operatorname{erfc}\left(\frac{X}{2\sqrt{D_0 T}} + \sqrt{\lambda_0 T} \right) \Bigg] \end{aligned} \tag{22b}$$

$$\begin{aligned} G(X,T) = \frac{b}{2}\Bigg[&\exp\left\{ \left(\frac{u_0^2}{4D_0} - \phi \right) T \right\} \operatorname{erfc}\left(\frac{X}{2\sqrt{D_0 T}} - \frac{u_0}{2}\sqrt{\frac{T}{D_0}} \right) \\ &+ \exp\left\{ \frac{u_0}{D_0}X + \left(\frac{u_0^2}{4D_0} - \phi \right) T \right\} \operatorname{erfc}\left(\frac{X}{2\sqrt{D_0 T}} + \frac{u_0}{2}\sqrt{\frac{T}{D_0}} \right) \Bigg] \end{aligned} \tag{22c}$$

$$\begin{aligned} H(X,T) = \frac{c_i}{2}\Bigg[&\exp\left\{ \left(\frac{u_0}{2D_0} - \frac{\alpha}{\sqrt{D_0}} \right) X + (\alpha^2 - \phi) T \right\} \operatorname{erfc}\left(\frac{X}{2\sqrt{D_0 T}} - \alpha\sqrt{T} \right) \\ &+ \exp\left\{ \left(\frac{u_0}{2D_0} + \frac{\alpha}{\sqrt{D_0}} \right) X + (\alpha^2 - \phi) T \right\} \operatorname{erfc}\left(\frac{X}{2\sqrt{D_0 T}} + \alpha\sqrt{T} \right) \Bigg] \end{aligned} \tag{22d}$$

and

$$J(X,T) = b\exp\left\{\left(\frac{u_0^2}{4D_0} - \phi\right)T\right\} + c_i\exp\left\{(\alpha-\phi)T - \left(\gamma + \frac{u_0}{D_0}\right)X\right\} + \frac{c'w}{au_0\theta}\frac{1}{f(mt)} \tag{22e}$$

Here,

$$\alpha^2 = D_0\left(\gamma + \frac{u_0}{2D_0}\right)^2; \quad b = \left(c' - \frac{c'w}{au_0\theta}\right); \quad \lambda_0 = (\phi - \lambda_s).$$

4 Numerical Solution

Explicit finite difference method is used to obtain the numerical solution of the problem. For that, the semi-infinite domain needs to convert into a finite one. The following transformation is used to convert the domain

$$Y = 1 - \exp(-X) \tag{23}$$

Apply Eq. (23) in the ADE Eq. (12) and corresponding initial and boundary conditions in Eqs. (13)–(15), Eqs. (12)–(15) reduced to

$$\frac{\partial C}{\partial T} = D_0(1-Y)^2\frac{\partial^2 C}{\partial Y^2} - (u_0 + D_0)(1-Y)\frac{\partial C}{\partial Y} - \rho C + \sigma \tag{24}$$

$$C(Y,T) = c' + c_i\psi(1-Y); \quad Y \geq 0, \quad T = 0 \tag{25}$$

$$C(Y,T) = c' + c_0\exp(-\lambda_s T); \quad Y = 0, \quad T > 0 \tag{26}$$

$$\frac{\partial C}{\partial Y} = 0; \quad Y \to \infty, \quad T > 0 \tag{27}$$

where $\rho = au_0\frac{f(mt)}{f_1(mt)^2}$; $\sigma = \frac{c'w}{\theta}\frac{1}{f(mt)}$.

The domains Y and t are divided into equal number of subintervals and represented as follows:

$$Y_i = Y_{i-1} + \Delta Y, \quad i = 1,2,\ldots,M; \quad \Delta Y = 0.04 \tag{28}$$

$$T_j = T_{j-1} + \Delta T, \quad j = 1,2,\ldots,N; \quad \Delta T = 0.0001 \tag{29}$$

Here, i and j represent the distance and time, respectively. ΔY is the step of distance, and ΔT is the time step. The contaminant concentration at a point Y_i at jth subinterval of time T is denoted as $C_{i,j}$. The first- and second-order space derivative in Eq. (24) is approximated by central difference approximation, and first-order

time derivative is approximated by forward difference approximation, respectively. Using two-level explicit finite difference method in Eqs. (24)–(27), one can get

$$C_{i,j+1} = C_{i,j} - \rho C_{i,j}\Delta T + \sigma \Delta T + D_0(1 - Y_i)^2\left(C_{i+1,j} - 2C_{i,j} + C_{i-1,j}\right)\frac{\Delta T}{\Delta Y'^2} - (u_0 + D_0)(1 - Y_i)\left(C_{i+1,j} - C_{i-1,j}\right)\frac{\Delta T}{2\Delta Y'} \tag{30}$$

$$C_{i,0} = c' + \psi c_i(1 - Y_i); \quad i > 0 \tag{31}$$

$$C_{0,j} = c' + c_0 \exp\left(-\lambda_s T_j\right); \quad j > 0 \tag{32}$$

$$C_{M,j} = C_{M-1,j}; \quad j > 0 \tag{33}$$

5 Result and Discussion

The contaminant concentration values are computed for the analytical solution described by Eq. (21) in a finite domain $0 \leq x \leq 1$ km of semi-infinite region. The input values are taken as follows $c_i = 0.0001$, $c' = 0.01$, $c_0 = 0.9$, $D_0 = 0.05\ \left(\text{km}^2/\text{year}\right)$, $u_0 = 0.5$ (km/year), $m = 0.6$ (/year), $\lambda_s = 0.01$ (/year), $\gamma = 0.01$ (/km), $w = 0.0002$, $\theta = 0.32$, $a = 1.3$, $f(mt) = \exp(-mt)$. The numerical approximation is done using explicit finite difference method (forward time centre space—FTCS), and for the numerical approximations, we take $\Delta Y = 0.04$ and $\Delta T = 0.0001$.

In Fig. 1, contaminant concentration is predicted for three different time duration $t = 2, 3, 4$ years and it is observed that as time increases concentration decreases.

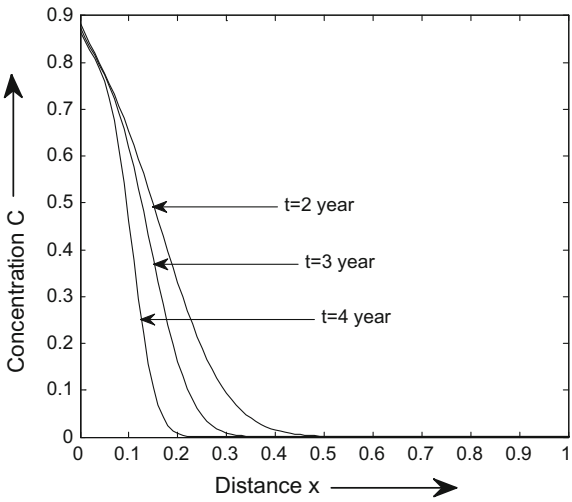

Fig. 1 Contaminant concentration pattern for three different duration $t = 2, 3, 4$ years

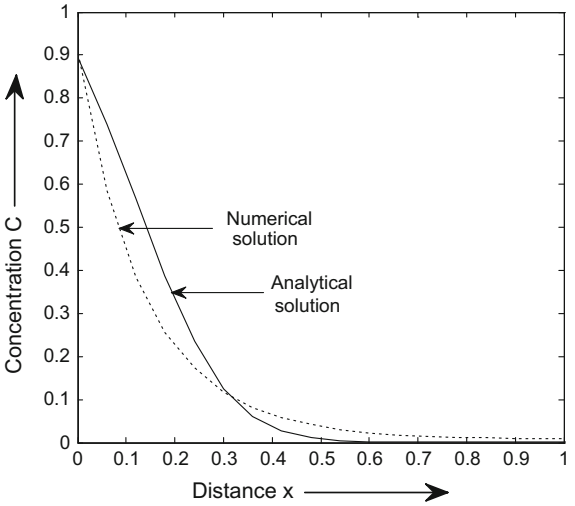

Fig. 2 Comparison of analytical and numerical results of concentration for $t = 1$ year

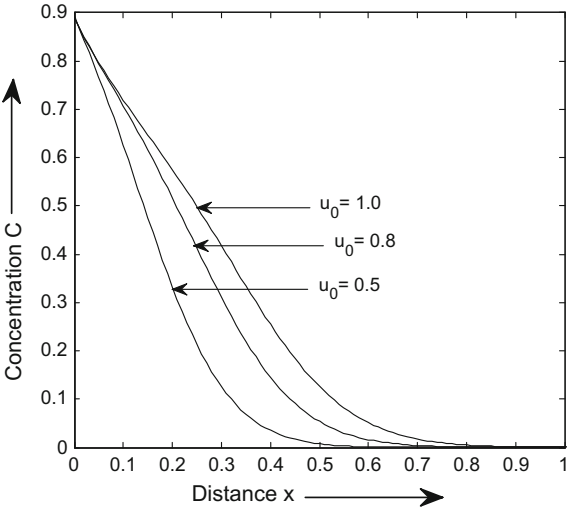

Fig. 3 Contaminant concentration patterns for varying initial seepage velocity u_0 for $t = 1$ year

Maybe this is happened because of the external source term which has been added with the ADE. The contaminant concentration values decrease with distance too and become zero after travelling a long distance. So, we can say that as solute travels away from the source of contamination, it becomes harmless. The comparison between analytical and numerical results of concentration is shown in Fig. 2. It is observed that the patterns of both graphs are same, but they deviate from each other with some numerical values. Initially, numerical values are higher than the analytical values, but after $x = 0.3$ (km), they get the reverse pattern.

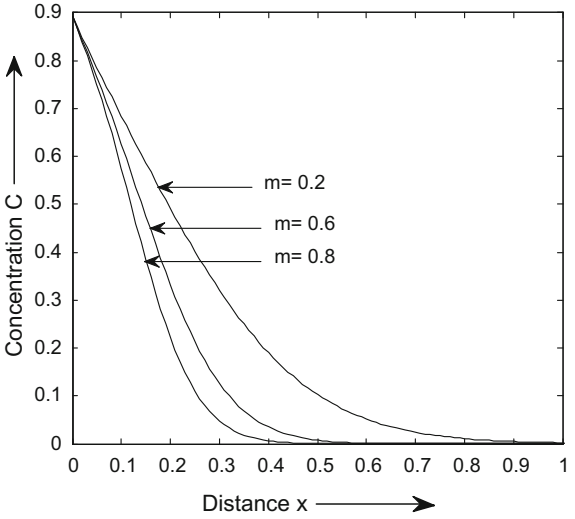

Fig. 4 Contaminant concentration patterns for different values of flow resistance coefficient m for $t = 1$ year

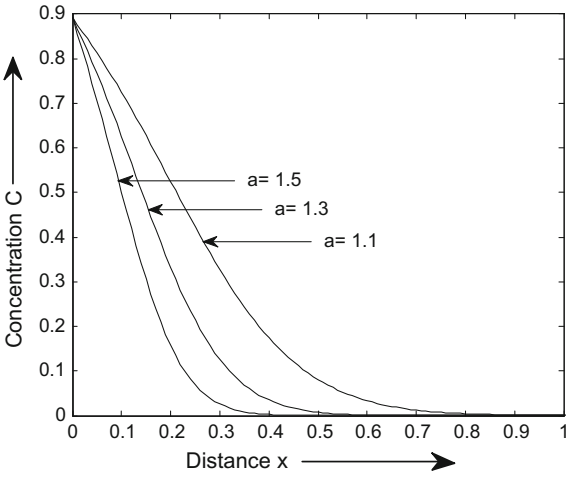

Fig. 5 Contaminant concentration patterns for different values of inhomogeneity parameter a for $t = 1$ year

Concentration values for varying seepage velocity $u_0 = 0.5, 0.8, 1.0$ are predicted for $t = 1$ year in Fig. 3. It is observed that as the seepage velocity increases, contaminant concentration increases. Figure 4 depicts the concentration behaviour for varying flow resistance coefficient $m = 0.2, 0.6, 0.8$ during $t = 1$ year. It can be seen from the figure that as m increases, concentration decreases. Inhomogeneity parameter a plays an important role for solute transport model in heterogeneous medium. So, the impact of a is shown in Fig. 5. Concentration values are predicted for $a = 1.1, 1.3, 1.5$. It can be seen from the figure that as the values of inhomogeneity parameter a increase, concentration decreases.

6 Summary and Conclusions

An analytical study of scale-dependent solute dispersion in heterogeneous porous media is discussed through this work. An external source term is included with the regular ADE. The solute transport is studied for Dirichlet-type boundary condition and is compared with the analytical solution obtained by using explicit finite difference method. It is observed from this study that contaminant concentration decreases with time as well as with distance. So, we can say as the solute travels far away from the source of contamination, it becomes harmless.

References

Domenico PA, Robbins GA (1984) A dispersion scale effect in model calibrations and field tracer experiments. J Hydrol 70:123–132

Gao G, Zhan H, Feng S, Fu B, Ma Y, Huang G (2010) A new mobile-immobile model for reactive solute transport with scale-dependent dispersion. Water Resour Res 46:W08533

Khan AUH, Jury WA (1990) A laboratory study of the dispersion scale effect in column outflow experiments. J Contam Hydrol 5:19–131

Logan JD (1996) Solute transport through porous media with scale dependent dispersion and periodic boundary conditions. Adv Water Resour 184(3–4):261–276

Natarajan N (2015) Effect of distance-dependent and time-dependent dispersion on non-linearly sorbed multispecies contaminants in porous media. ISH J Hydraul Eng. doi:10.1080/09715010.2015.1043597

Natarajan N, Suresh Kumar G (2014) Effect of fracture skin formation in clay fractured porous media. ISH J Hydraul Eng 20(3):263–273

Pang L, Hunt B (2001) Solutions and verification of a scale-dependent dispersion model. J Contam Hydrol 53:21–39

Rastogi AK (2007) Numerical groundwater hydrology. Penram International Publishing Pvt. Ltd., India, pp 781–783

Sharma PK, Ojha CSP, Joshi N (2014) Finite volume model for reactive transport in fractured porous media with distance and time dependent dispersion. Hydrol Sci J 59(8):1582–1592

Sposito G, White RE, Darrah PR, Jury WA (1986) A transfer function model of solute transport through soil, the convection-dispersion equation. Water Resour Res 22:255–262

Taylor SR, Howard KWF (1987) A field study of scale-dependent dispersion in a sandy aquifer. J Hydrol 90:11–17

Toride N, Leij F, van Genuchten MT (1995) The CXTFIT code for estimating transport parameters from laboratory or field tracer experiments, Version 2. Research Report 137, US Salinity Lab, Riverside, CA

Wang JC, Booker JR, Carter JP (1998) Experimental investigation of contaminant transport in porous media. Research Report No. R776, Centre for Geotechnical Engineering, Department of Civil Engineering, The University of Sydney

Watson SJ, Barry DA, Schotting RJ, Hassanizadeh SM (2002) Validation of classical density-dependent solute transport theory for stable high concentration-gradient brine displacements in coarse and medium sands. Adv Water Resour 25:611–635

You K, Zhan H (2013) New solutions for solute transport in a finite column with distance-dependent dispersivities and time-dependent solute sources. J Hydrol 487:87–97

Zhang R, Huang K, Xiang J (1994) Solute movement through homogeneous and heterogeneous soil columns. Adv Water Resour 17(5):317–324

Solution to Advection–Dispersion Equation for the Heterogeneous Medium Using Duhamel's Principle

Amit Kumar Pandey, Rohit Kumar and Mritunjay Kumar Singh

Abstract This work dealt with advection–dispersion problem in heterogeneous medium while the medium is initially considered to be polluted as a functional combination of source term and zero-order production term with distance. Further, Dirichlet-type boundary condition is employed to get insight to the realistic situation for achieving practical solution to the problem. Duhamel's integration technique has been applied to solve the system. Non-dimensional numbers responsible for the domination of advection and dispersion in the transport of solute have been explored through appropriate graphs. Variability of velocity field and dispersion of the solute due to heterogeneity of the medium has also been taken into consideration while solving the system. The comparison has been made between the different outcomes significantly using graphical approach.

1 Introduction

Due to increasing human activities on the surface and subsurface of earth, it has been proved important to get deep insight into the flow problems concerned with pollutant concentration distribution due to atmospheric dispersion. People from the field of hydrology, civil engineering, and mathematical modeling have been showing significantly great interest in the problems related to solute transport. Behavior of concentration distribution through an open medium such as lakes and

A.K. Pandey
Department of Applied Science, KIET Group of Institution,
Ghaziabad 201206, India
e-mail: pandeyamit286@gmail.com

R. Kumar · M.K. Singh (✉)
Department of Applied Mathematics, Indian Institute of Technology
(Indian School of Mines), Dhanbad 826004, Jharkhand, India
e-mail: drmks29@rediffmail.com

R. Kumar
e-mail: rohitmaheshwari001@gmail.com

M.K. Singh et al. (eds.), *Applications of Fluid Dynamics*, Lecture Notes
in Mechanical Engineering, https://doi.org/10.1007/978-981-10-5329-0_42

rivers and porous medium like aquifer can be well predicted using a mathematical model containing advection–dispersion term to provide more realistic picture of solute transport and on the basis of which remedial processes may be imposed to reduce or eliminate the damages. It also has broad applications in the disciplines such as soil physics, chemical engineering, biosciences, and petroleum engineering. To explore the effect of dispersion, the sequence of study and research, narrowed the work to the problem of longitudinal dispersion for a periodically varying input. Ogata and Banks (1961) discussed advection–dispersion with constant initial concentration for different boundary conditions. Harleman and Rumer (1963) worked on the effect of longitudinal and lateral dispersion in an isotropic porous medium. Marino (1974) studied distribution of contaminants in porous medium. Niamiand and Rushton (1977) studied flow analysis against dispersion in porous media for different initial and boundary conditions. Kumar (1983) obtained solution to advection–dispersion problem for unsteady flow against dispersion in finite porous media with linear isotherm. Genuchten and Parker (1984) focused their work on the boundary conditions for displacement experiments through short laboratory soil columns, and Barry and Sposito (1989) presented analytical solution of a convection–dispersion model with time-dependent transport coefficients. Yates obtained analytical solutions for describing the transport of dissolved substances in heterogeneous semi-infinite porous medium with the dispersion dependent on distance and of exponential nature along the uniform flow (Yates 1990, 1992). Leij et al. (1991) obtained analytical solution for three-dimensional semi-infinite medium. Batu and van Genuchten (1993) presented analytical solutions for non-equilibrium solute transport with first-order decay and zero-order production term. Fry et al. (1993) obtained analytical solutions to the solute transport with rate-limited desorption and decay. Fred (1995) obtained analytical solutions of unsaturated flow in groundwater in one-, two- and three-dimensions. Huang et al. (1996) narrowed their work to the exact solutions for one-dimensional transport equation with asymptotic scale-dependent dispersion. Zoppou and Knight (1997) focused their work on analytical solutions for advection–diffusion equation with spatially variable coefficients. Singh et al. (2008) studied longitudinal dispersion with time-dependent source concentration in semi-infinite medium. Singh et al. (2009) studied conservative solute transport in one-dimensional homogeneous porous media with velocity varying with respect to time. Singh et al. (2010) worked to obtain analytical solution for two-dimensional solute transport in finite aquifer with time-dependent boundary conditions. Guerrero and Skaggs (2010) focused their work on analytical solutions of the one-dimensional advection–dispersion solute transport equation with time-dependent boundary conditions coefficients in a finite domain. The objective of present study is to extend Duhamel's theorem to one-dimensional advection–dispersion solute transport problems for a heterogeneous medium where spatial variable and time variable are taken into consideration with time-dependent boundary conditions. The equations developed in this paper hence may be used to extend existing solutions to situations where the boundary conditions are time-dependent.

2 Problem Formulation and Solution

As far as the heterogeneous porous medium is concerned, the transport equation for solute is formulated by considering spatial as well as temporal variability of seepage velocity and solute dispersion. The partial differential equation describing advection–dispersion effects in a heterogeneous semi-infinite medium can be expressed as

$$\frac{\partial C}{\partial t} + \frac{1-n}{n}\frac{\partial F}{\partial t} = \frac{\partial}{\partial x}\left(D\frac{\partial C}{\partial x} - uC\right) + \gamma \tag{1}$$

where D [L^2 T^{-1}] is the longitudinal dispersion coefficient, C [M L^{-3}] is the volume averaged dispersing solute concentration (liquid phase), u [L T^{-1}] is the unsteady pore seepage velocity, F [M L^{-3}] is the solute concentration (solid phase), γ [M L^{-3} T^{-1}] is the zero-order production rate coefficient for solute production in the liquid phase, n is the porosity of different geological formations, t and x are temporal and distance variables, respectively.

Let us consider linear isotherm $F = K_d c$ where F is the solid-phase solute concentration, C is the liquid-phase solute concentration, and K_d is isotherm constant $\left(\frac{mg}{g}\right)(dm^3/g)^n$ related to adsorption capacity.

Equation (1) is considered with the following initial and boundary conditions.

$$c(x,0) = c_i f(\alpha x) + \frac{\gamma x g(\alpha x)}{u} \tag{2}$$

Considering

$$f(\alpha x) = 1, \quad g(\alpha x) = 0 \tag{3}$$

Equation (2) becomes

$$c(x,0) = c_i \tag{4}$$

$$c(0,t) = c_i + c_0 e^{-\delta t}, \quad t > 0 \tag{5}$$

$$\frac{\partial c}{\partial x} = 0; \quad x \to \infty \tag{6}$$

where dimension of α is L^{-1}, and λ [t^{-1}] is decay constant.

Using the relation $F = K_d C$ in Eq. (1), we get

$$\left(1 + \frac{1-n}{n}K_d\right)\frac{\partial C}{\partial t} = \frac{\partial}{\partial x}\left(D\frac{\partial c}{\partial x} - uC\right) + \gamma \tag{7}$$

$$r\frac{\partial c}{\partial t} = \frac{\partial}{\partial x}\left[D_0(f(pt))^2(1+\beta x)^2\frac{\partial c}{\partial x} - u_0 f(pt)(1+\beta x)c\right] + \gamma \tag{8}$$

where

$$r = 1 + \frac{1-n}{n}K_d \tag{9}$$

Now, if the velocity field varies linearly with distance and the dispersion coefficient is proportional to the square of the velocity is employed with modified form as (Zoppou and Knight, 1997; Kumar, 2009)

$$u = u_0 f(pt)(1+\beta x) \tag{10}$$

Relation between dispersion parameter and the seepage velocity (due to heterogeneity of the medium) is

$$D = D_0(f(pt))^2(1+\beta x)^2 \tag{11}$$

Now, Eq. (6) can be written as

$$r\frac{\partial c}{\partial t^*} = \frac{\partial}{\partial x}\left[D_0 f(pt)(1+\beta x)^2\frac{\partial c}{\partial x} - u_0(1+\beta x)c\right] + \gamma^* \tag{12}$$

where

$$t^* = \int_0^t f(pt)\mathrm{d}t, \quad \frac{\gamma}{f(pt)} = \gamma^* \tag{13}$$

By using the transformation $y = \log(1+\beta x)^2$ and proceeding, we get.

$$r\frac{\partial c}{\partial t^*} = \left[4D_0\beta^2 f(pt)\frac{\partial^2 c}{\partial y^2} - 2u_0 g(pt)\frac{\partial c}{\partial y} - u_0\beta c + \gamma^*\right] \tag{14}$$

where

$$g(pt) = \left(1 - \frac{D_0\beta f(pt)}{u_0}\right) \tag{15}$$

Consider

$$z = \frac{1}{2}\int \frac{g(pt)}{f(pt)}\mathrm{d}y \tag{16}$$

Equation (14) turns to

$$r\frac{f(pt)}{g^2(pt)}\frac{\partial c}{\partial t^*} = \left[D_0\beta\frac{\partial^2 c}{\partial z^2} - u_0\frac{\partial c}{\partial z} - u_0\beta c\frac{f(pt)}{(g(pt))^2} + \gamma^*\frac{f(pt)}{(g(pt))^2}\right] \tag{17}$$

$$t^{**} = \int_0^t \frac{g^2(pt)}{f(pt)}\mathrm{d}t^* \tag{18}$$

Equation (17) becomes

$$r\frac{\partial c}{\partial t^{**}} = \left[D_0\frac{\partial^2 c}{\partial z^2} - u_0\frac{\partial c}{\partial z} - u_0 c\frac{f(pt)}{g(pt)^2} + \gamma^*\frac{f(pt)}{g(pt)^2}\right] \tag{19}$$

Using the transformation

$$c(z,t^{**}) = k(z,t^{**})\exp\left[\frac{u_0}{2D_0}z - \frac{1}{r}\left\{\frac{u_0^2}{4D_0} + \frac{f(pt)u_0\beta}{g^2(pt)}\right\}t^{**}\right] + \frac{\gamma^*}{\beta u_0} \tag{20}$$

Equation (19) turns to be

$$r\frac{\partial k}{\partial t^{**}} = D_0\frac{\partial^2 k}{\partial z^2} + \phi_1 k \tag{21}$$

where

$$\phi = \frac{1}{r}\left\{\frac{u_0^2}{4D_0} + \frac{f(pt)u_0\beta}{g^2(pt)}\right\} \tag{22}$$

and corresponding initial and boundary conditions

$$\frac{\gamma^* f(pt)u_0}{g^2(pt)}(1-b^*) = \phi_1 \tag{23}$$

$$k(0,t^{**}) = \left[c_i - \frac{\gamma^*}{u_0} + c_0 e^{-\delta t^{**}}\right]\exp(\phi t^{**}), \quad t^{**} > 0 \tag{24}$$

$$\frac{\partial k}{\partial z} = -\frac{ku_0}{2D_0}, \quad z \to \infty \tag{25}$$

To solve Eq. (23), we use Duhamel's theorem.

Let $\varphi(x, t^{**}; \sigma)$ [M L^{-3}] be the auxiliary solution of Eq. (23) where σ is a parameter. Therefore, Eq. (23) takes the form

$$r\frac{\partial\varphi(z,t^{**};\sigma)}{\partial t^{**}} = L\varphi(z,t^{**};\sigma) \tag{26}$$

where

$$L = D_0\frac{\partial^2}{\partial z^2} \tag{27}$$

$$\varphi(z,0;\sigma) = \left(c_i - \frac{\gamma^*}{u_0}\right)\mathrm{e}^{-\frac{u_0}{2D_0}z} \tag{28}$$

$$\varphi(0,t^{**};\sigma) = \left(c_i - \frac{\gamma^*}{u_0} + c_0\mathrm{e}^{-\delta\sigma}\right)\exp(\phi\sigma) \tag{29}$$

Now

$$k(z,t^{**}) = \frac{\partial}{\partial t^{**}}\int_0^{t^{**}}\varphi(z,t^{**}-\sigma,\sigma)\mathrm{d}\sigma \tag{30}$$

Using condition (28), we can write

$$k(z,t^{**}) = \int_0^{t^{**}}\frac{\partial}{\partial t^{**}}\varphi(z,t^{**}-\sigma,\sigma)\mathrm{d}\sigma + \left(c_i - \frac{\gamma^*}{u_0}\right)\mathrm{e}^{-\frac{u_0}{2D_0}z} \tag{31}$$

Consider the transformation

$$\varphi(z,t^{**},\sigma) = \psi(z,t^{**})\left(c_i - \frac{\gamma^*}{u_0} + c_0\mathrm{e}^{-\delta\sigma}\right)\exp(\phi\sigma) \tag{32}$$

where $\psi(Z,t^{**})$ is dimensionless. Now, Eq. (32) together with Eqs. from (26) to (29) turns to be

$$r\frac{\partial\psi(z,t^{**})}{\partial t^{**}} = L\psi(z,t^{**}) \tag{33}$$

and the initial and boundary conditions be

$$\psi(z,0) = \left(c_i - \frac{\gamma^*}{u_0}\right)\mathrm{e}^{-\frac{u_0}{2D_0}z}\left(c_i - \frac{\gamma^*}{u_0} + c_0\mathrm{e}^{-\delta\sigma}\right)^{-1}\exp(-\phi\sigma) \tag{34}$$

$$\psi(0,t^{**}) = 1 \tag{35}$$

$$\frac{\partial \psi(z,t^{**})}{\partial z} = -\frac{u_0 \psi(z,t^{**})}{2D_0}, \quad z \to \infty \tag{36}$$

And Eq. (30) becomes

$$k(z,t^{**}) = \int_0^{t^{**}} \frac{\partial}{\partial t^{**}} \psi(z,t^{**}-\sigma)\left(c_i - \frac{\gamma^*}{u_0} + c_0 \mathrm{e}^{-\delta\sigma}\right)\exp(\phi\sigma)\mathrm{d}\sigma + \left(c_i - \frac{\gamma^*}{u_0}\right)\mathrm{e}^{-\frac{u_0}{2D_0}z} \tag{37}$$

Solving Eq. (33) gives

$$\begin{aligned}\psi(z,t^{**}) = {} & \frac{1}{2}\sqrt{\frac{r}{D_0}}z\frac{1}{\sqrt{\pi t^{**3}}}\mathrm{e}^{-\frac{rz^2}{4D_0 t^{**}}} \\ & + \frac{1}{2}\frac{D_0\alpha}{r}\mathrm{e}^{\frac{u_0^2}{4rD_0}t^{**}}\left[\mathrm{e}^{\frac{u_0}{2D_0}z}\mathrm{erfc}\left(\frac{z}{2}\sqrt{\frac{r}{D_0 t^{**}}} + \frac{u_0}{2}\sqrt{\frac{1}{rD_0}t^{**}}\right)\right. \\ & \left. + \mathrm{e}^{-\frac{u_0}{2D_0}z}\mathrm{erfc}\left(\frac{z}{2}\sqrt{\frac{r}{D_0 t^{**}}} - \frac{u_0}{2}\sqrt{\frac{1}{rD_0}t^{**}}\right)\right] + \alpha\mathrm{e}^{\left(\frac{u_0^2}{4rD_0}t^{**} - \frac{u_0}{2D_0}z\right)}\end{aligned} \tag{38}$$

and subsequently, we obtain the following.

$$\begin{aligned}k(z,t^{**}) = {} & \frac{1}{2}\left(c_i - \frac{\gamma^*}{u_0}\right)\left[\mathrm{e}^{\sqrt{\frac{r}{D_0}}z + \phi t^{**}}\mathrm{erfc}\left(\frac{1}{2}\sqrt{\frac{r}{D_0 t^{**}}}z + \sqrt{\phi t^{**}}\right)\right. \\ & \left. + \mathrm{e}^{-\sqrt{\frac{r}{D_0}}z + \phi t^{**}}\mathrm{erfc}\left(\frac{1}{2}\sqrt{\frac{r}{D_0 t^{**}}}z - \sqrt{\phi t^{**}}\right)\right] \\ & + \frac{1}{2}\left[\mathrm{e}^{\sqrt{\frac{r}{D_0}}z + (\phi-\delta)t^{**}}\mathrm{erfc}\left(\frac{1}{2}\sqrt{\frac{r}{D_0 t^{**}}}z + \sqrt{(\phi-\delta)t^{**}}\right)\right. \\ & \left. + \mathrm{e}^{-\sqrt{\frac{r}{D_0}}z + (\phi-\delta)t^{**}}\mathrm{erfc}\left(\frac{1}{2}\sqrt{\frac{r}{D_0 t^{**}}}z - \sqrt{(\phi-\delta)t^{**}}\right)\right] \\ & - \frac{\alpha D_0}{r}\mathrm{e}^{-\frac{u_0}{2D_0}z + \frac{u_0^2}{4rD_0}t^{**}}\end{aligned} \tag{39}$$

$$\alpha = \frac{r}{D_0}\left(-c_i + \frac{\gamma^*}{u_0}\right) \tag{40}$$

and therefore the required solution is obtained and given in Eq. (41) and shown below in Table 1.

Table 1 Comparison of concentration for velocity pattern in the negative direction of flow using Laplace transform technique and Duhamel's principle for different values of space variable

X	$C(x, 1)$, $r = 6.3125$, $f = -1$, Eq. (41)	$C(x, 1)$, $r = 5.25675$, $f = -1$, Eq. (41)	$C(x, 1)$, $r = 3.04545$, $f = -1$, Eq. (41)
0	1.320080555740326	1.2736769897326	1.0857943622641613
2	0.0110904	0.011325949907992358	0.012425118205856196
3	0.011089	0.011322709937820844	0.012400864027169393
4	0.01108896739561866	0.011322618852877005	0.012399677809392965
5	0.01108896575312241	0.011322613244237546	0.012399565804943084

$$c(z,t^{**}) = k(z,t^{**}) \exp\left[\frac{u_0}{2D_0} z - \phi t^{**}\right] + \frac{\gamma^*}{\beta u_0} \tag{41}$$

3 Results and Discussion

The input values available in the hydrological literature are reported by Singh and Kumari (2014). $C_i = 0.01$, $C_0 = 1.0$, $u_0 = 0.7$ (km/year), $D_0 = 0.1$ (km^2/year), $\gamma_0 = 0.0005$ (km), $\lambda = 0.002$ (/year), $K_d = 2.5$, $n = 0.32$ (gravel), $n = 0.35$ (sand), $n = 0.55$, $m = 0.001$ (/year) have been used to compute the analytical solution given in Eq. (41); (1), (2), and (3) represents concentration distribution for sand, gravel, and clay medium for the time period $t = 2$ years, $t = 3$ years, and $t = 4$ years; and it has been observed that for the velocity pattern of fluid flow in the negative direction of x-axis, concentration decreases smoothly with increasing time period as well as with increasing spatial variable at each position, and it further reduces to a saturated level tending to zero. It has also been observed that at each position corresponding value of concentration in gravel medium is more than that in sand medium and in clay medium as well. It indicates that concentration of solute for the clay medium is most sensitive than that for the sand medium and gravel medium (Figs. 1, 2 and 3).

Figure 4 represents concentration profile for different values of Peclet number for gravel, sand, and clay medium for the time period of $t = 1$ year, and it has been observed that the curves are normal curves with different values of flatness. Up to a certain distance, it has been observed that concentration at each position increases with increasing value of Peclet number (i.e., with increasing value of advection). High Peclet number denotes highly advective system, and low Peclet number denotes highly dispersive system (low advective system). Therefore, it is observed that concentration increases with increasing value of dispersivity and with decreasing value of advection at each position and that approaches to a saturated level tending to zero.

Figure 5 represents concentration distribution for different values of Courant numbers for the gravel, sand, and clay mediums for the time period of $t = 2$ years;

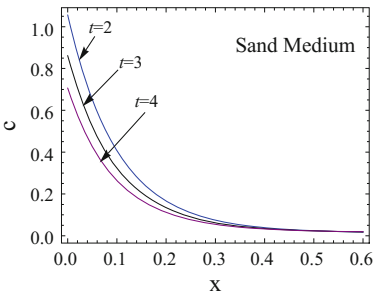

Fig. 1 Concentration distributions for velocity in the direction opposite to the direction of flow for sand medium

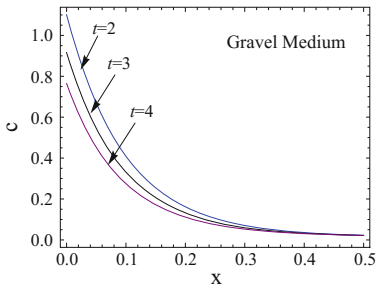

Fig. 2 Concentration distributions for velocity in the direction opposite to the direction of flow for gravel medium

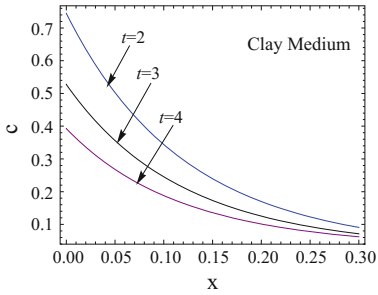

Fig. 3 Concentration distributions for velocity in the direction opposite to the direction of flow for clay medium

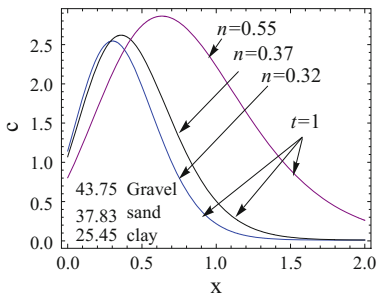

Fig. 4 Concentration distribution for different mediums with different values of Peclet number at $t = 1$ year

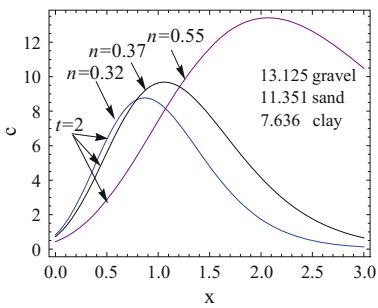

Fig. 5 Concentration distribution for different mediums with different values of Courant number at $t = 2$ year

it has been observed that up to a certain distance concentration increases at each position with increasing value of Courant number, and then, it reverses its behavior and starts increasing with decreasing value of Courant number at each position and that further approaches to a saturated level tending to zero. This change in the behavior may be due to different porosities of the mediums as well as the velocity pattern of solute transport.

Figure 6 represents concentration distribution for different values of Courant numbers for the gravel, sand, and clay mediums for the time period of $t = 1$ year, it has been observed that the concentration for gravel, sand, and clay mediums for $t = 2$ year is more than that for $t = 1$ year at each position, and it tends to a saturated level that further tends to zero for the value of spatial variable less than that for $t = 2$ years.

Figure 7 represents concentration distribution for gravel, sand, and clay mediums for different values of Peclet number for the time period of $t = 1$ year and for velocity pattern in the negative direction of x-axis; it is observed that up to a distance concentration at each position increases with increasing value of Peclet number and after that it starts decreasing with increasing value of Peclet number, concentration further settles to a saturated level tending to zero; and it can be said that up to a distance advection dominates the concentration and after that its dispersion dominates the concentration of solute.

Figure 8 represents concentration profile for gravel, sand, and clay mediums with corresponding values of Courant number for the time period of $t = 2$ years. It

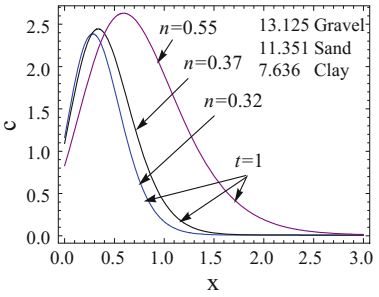

Fig. 6 Concentration distribution for different mediums with different values of Courant number at $t = 1$ year

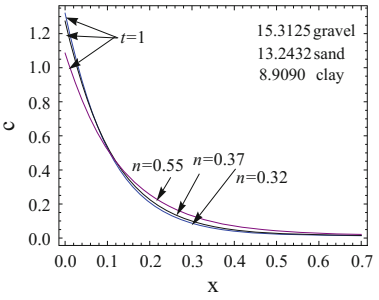

Fig. 7 Concentration distribution for velocity in the direction opposite to the direction of flow for different mediums with different values of Peclet number at $t = 1$ year

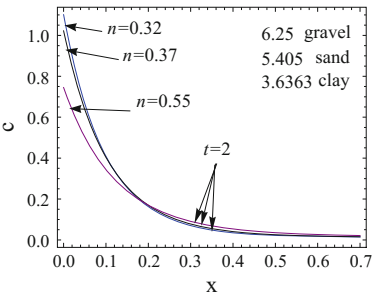

Fig. 8 Concentration distribution for velocity in the direction opposite to the direction of flow for different mediums with different values of Courant number at $t = 2$ year

has been observed that concentration increases with increasing value of Courant number at each position up to a certain distance, and then, it starts decreasing with increasing value of Courant number. This is due to the negative velocity pattern and the porosity of the mediums. The concentration further reduces to a saturated level tending to zero.

4 Conclusions

(1) Application of Duhamel's theorem was extended for advection–dispersion transport problem for time-dependent boundary conditions, and concentration values at a distance $x = 1$ unit have been obtained for different velocity patterns and for velocity in the negative direction of the distance.
(2) Concentration distribution for different values of Peclet numbers and Courant numbers has been shown by suitable graphs for the gravel, sand, and clay mediums and for exponentially increasing/decreasing velocity patterns as well as for the velocity in the negative direction of x-axis.
(3) A good agreement between the concentration values obtained by Duhamel's principle and that obtained by Laplace transform technique for gravel sand and clay mediums has been observed.
(4) The kinetic nature of the solute transport into the groundwater predicted for gravel, sand, and clay type geological formation with a good comparison set by appropriate graphs.

References

Al-Niami ANS, Rushton KR (1977) Analysis of flow against dispersion in porous media. J Hydrol 33:87–97

Barry DA, Sposito G (1989) Analytical solution of a convection—dispersion model with time dependent transport coefficients. Water Resour Res 25(12):2407–2416

Batu V, van Genuchten MT (1993) A comprehensive set of analytics solutions for non-equilibrium solute transport with first-order decay and zero-order production. Water Resour Res 29:2167–2182

Fry VA, Istok JD, Guenther RB (1993) Analytical solutions to the solute transport equation with rate-limited desorption and decay. Water Resour Res 29(9):3201–3208

Guerrero JSP, Skaggs TH (2010) Analytical solution for one-dimensional advection-dispersion transport equation with space-dependent coefficients. J Hydrol 390:57–65

Harleman DRF, Rumer RR (1963) Longitudinal and lateral dispersion in an isotropic porous medium. J Fluid Mech 385–394

Huang K, van Genuchten MT, Zhang R (1996) Exact solutions for one dimensional transport with asymptotic scale dependent dispersion. Appl Math Model 20:297–308

Kumar N (1983) Unsteady flow against dispersion in finite porous media. J Hydrol 63:345–358

Kumar A, Jaiswal DK, Kumar N (2009) Analytical solutions of one-dimensional advection-diffusion equation with variable coefficients in a finite domain. J Earth Syst Sc 118:539–549

Leij FJ, Skaggs TH, van Genuchten MT (1991) Analytical solutions for solute transport in three-dimensional semi-infinite porous medium. Water Resour Res 27:2719–2733

Marino MA (1974) Distribution of contaminants in porous media flow. Water Resour Res 10:1013–1018

Ogata A, Banks RB (1961) A solution of the differential equation of longitudinal dispersion in porous media. United States Government Printing Office, Washington

Singh MK, Kumari P (2014) Contaminant concentration prediction along unsteady groundwater flow. Modelling and Simulation of Diffusive Processes vol XII, pp 257–276

Singh MK, Mahto NK, Singh P (2008) Longitudinal dispersion with time dependent source concentration in semi infinite aquifer. J Earth Syst Sci 117(6):945–949

Singh MK, Singh VP, Singh P, Shukla D (2009) Analytical solution for conservative solute transport in one dimensional homogeneous porous formations with time dependent velocity. J Eng Mech 135(9):1015–1021

Singh MK, Singh P, Singh VP (2010) Analytical solution for two dimensional solute transport in finite aquifer with time dependent source concentration. J Eng Mech 136(1):1309–1315

Fred T (1995) 1-D, 2-D, 3-D analytical solutions of unsaturated flow in groundwater. J Hydrol 170:199–214

van Genuchten MT, Parker JC (1984) Boundry conditions for displacement experiments through short laboratory soil columns. Soil Sci Soc Am J 48:703–708

Yates SR (1990) An analytical solution for one-dimensional transport in heterogeneous porous media. Water Resour Res 26:2331–2338

Yates SR (1992) An analytical solution for one-dimensional transport in porous media with an exponential dispersion function. Water Resour Res 28:2149–2154

Zoppou C, Knight JH (1997) Analytical solutions for advection and advection diffusion equation with spatially variable coefficients. J Hydraul Eng 123:144–148

Two-Dimensional Solute Transports with Periodic Input Source in Semi-infinite Aquifer

Affreen Akhter, Chandan Kumar Thakur and Mritunjay Kumar Singh

Abstract The present study deals with two-dimensional solute transport equation with time-dependent source in homogeneous semi-infinite aquifer. Linear isotherm is taken into consideration due to interaction between solid and liquid phases. Initially, the domain is not solute-free. Initially, space-dependent exponentially increasing form with initial concentration is taken into consideration. At the one end of the domain, time-dependent source concentration is taken into account. Due to no mass flux at the other end of the domain concentration gradient is assumed to be zero. Laplace integral transform technique (LITT) is used for analytical solution, whereas explicit finite difference (EFD) scheme is used for numerical approximation. The exponentially decreasing and asymptotic form velocity function is taken into consideration for the graphical representation of the solutions.

1 Introduction

Ordinary resources and waste production in modern society often pose a threat to the groundwater quality and already have resulted in many incidents of groundwater pollutants. The groundwater contaminants can originate from point source or nonpoint sources. Contaminants are dissolved in groundwater due to complex physical and chemical processes such as advection, diffusion, chemical reactions, adsorption, and biodegradation and decay. The prediction of contaminants is described in mathematical form which is represented as advection-dispersion equation (ADE).

A. Akhter (✉) · C.K. Thakur · M.K. Singh
Department of Applied Mathematics, Indian Institute of Technology (Indian School of Mines), Dhanbad 826004, Jharkhand, India
e-mail: affreen92@gmail.com

C.K. Thakur
e-mail: chandan@am.ism.ac.in

M.K. Singh
e-mail: drmks29@rediffmail.com

M.K. Singh et al. (eds.), *Applications of Fluid Dynamics*, Lecture Notes in Mechanical Engineering, https://doi.org/10.1007/978-981-10-5329-0_43

Analytical solutions of one-dimensional solute transport problems, subject to different initial and boundary conditions, infinite, semi-finite domain have been reported in the literature (e.g., vanGenuchten and Alves 1982; Lindstorm and Boersma 1989; Fry et al. 1993; Singh and Das 2015). Ogata and Banks (1961) discussed the solution of ADE equation for the constant input concentration with moving boundary coordinate. Banks and Ali (1964) discussed dispersion and adsorption in solute transport modeling through porous media flow. Kumar (1983) discussed an analytical solution of advection-dispersion equation in finite nonadsorbing and adsorbing porous media. Crank (1975) established a moving boundary problems for the transport modeling in groundwater. Putti et al. (1990) developed the triangular finite volume technique for solving the solute transport equation. Yates (1992) explored the linear growth of the dispersion process in heterogeneous porous media with the effect of scale-dependent dispersivity in solute transport modeling. Zoppou and Knight (1997) proposed analytical solutions for advection-diffusion equation with spatially variable coefficients. Lin and Ball (1998) proposed an analytical solution for solute transport in a multi-layered porous medium by using Green's function technique with the help of arbitrary boundary condition and initial condition. Kartha and Srivastava (2008) discussed the comparison between numerical and analytical solution with the effect of immobile water content on advection-dispersion equation in unsaturated zone. Singh et al. (2008) introduced an analytical solution with time-dependent source in semi-infinite aquifer. Kaya (2010) developed a numerical solution of the advection-diffusion equation solved using the differential quadrature method with the help of explicit and implicit finite difference method. Chen et al. (2012) introduced a novel method for analytical solution of multi-species advective-dispersive transport equation. They showed the effect of sequentially coupled first-order decay reactions. Jiao and Zhang (2014) developed two-dimensional physical-based inverse method in confined and unconfined aquifers under unknown boundary conditions. Majdalani et al. (2015) discussed solute transport in periodical heterogeneous porous medium with scale-dependent dispersion at high degree of heterogeneity variation.

This paper describes two-dimensional advection-dispersion equation solved with the effect of linear isotherm and zero-order production term in semi-infinite domain. Initially, the domain is not solute-free. Initially, exponentially increasing source with initial concentration is taken into consideration. At one end of the domain, linear expression of periodic source concentration is taken into consideration. Laplace integral transform technique (LITT) is used for analytical solution, whereas explicit finite difference (EFD) approximation is used for numerical solution. The dispersion directly proportional to the seepage velocity concept is used for the solutions. Time-dependent velocity pattern is used for graphical representation of the solutions.

2 Mathematical Modeling

During the past decades, solute transport model is used for predicting the fate and transport of contaminant constituents in surface, subsurface, and groundwater flow system due to accidental spills and municipal, industrial, and hazardous waste materials. Solute transport modeling frequently relies on analytical and numerical solutions of advection-dispersion (AD) equation. The governing two-dimensional advection-dispersion (AD) equation is as follows

$$\frac{\partial c}{\partial t} + b\left(\frac{1-\phi}{\phi}\right)\frac{\partial c^*}{\partial t} = D_x\frac{\partial^2 c}{\partial x^2} + D_y\frac{\partial^2 c}{\partial y^2} - u(t)\frac{\partial c}{\partial x} - v(t)\frac{\partial c}{\partial y} - \frac{\rho}{\phi}c - \frac{b}{\phi}c^* + q \tag{1}$$

where $D_x[L^2T^{-1}]$ and $D_y[L^2T^{-1}]$ are the dispersion coefficient along longitudinal and transverse direction of the flow. $c[ML^{-3}]$ is the solute concentration in the liquid phase. $c^*[ML^{-3}]$ is the solute concentration in the solid phases. $u[LT^{-1}]$ and $v[LT^{-1}]$ are the groundwater velocity along longitudinal and transverse direction of the flow. $q[MLT^{-1}]$ is the zero-order production which represents the frequent growth of the solute. $b[ML^{-3}]$ is the bulk density of the solid matrix. ρ is the volumetric flux, and $x[L]$ and $y[L]$ are the length. $t[T]$ is the time, and ϕ is the porosity of the aquifer.

The solid–liquid phases are interconnected as

$$c^* = k_d c \tag{2}$$

Initially, the domain is not solute-free, i.e., some initial background concentration exists in the domain in the form of exponentially increasing space-dependent function.

$$c(x,0) = c_i e^{(x+y)} \quad x > 0, t = 0 \tag{3}$$

At the origin, the input point source concentration is taken as a periodic function in the form of Dirichlet-type boundary conditions. At the other end of the domain, concentration gradient is assumed to be zero.

$$c(0,t) = \frac{c_0}{2}(1 + \cos(mt))\, x = 0, t > 0 \tag{4}$$

$$\frac{\partial c}{\partial x} = 0 \quad \frac{\partial c}{\partial y} = 0 \quad x \to \infty, y \to \infty \tag{5}$$

In this study, u and v can be expressed as

$$u = u_0 f(mt)\, v = v_0 f(mt) \tag{6a}$$

where u_0 and v_0 are the initial value of u and v.

It is assumed that dispersion coefficient is directly proportional to the initial seepage velocity

$$D_x = D_{x_0} f(mt)\, D_y = D_{y_0} f(mt) \tag{6b}$$

Again using the transformation

$$T = \int_0^t f(mt)\mathrm{d}t \tag{7a}$$

$$z = x + y \tag{7b}$$

Using Eqs. (2), (6a),(6b),(7a), and (7b) in Eq. (1), we can write

$$R\frac{\partial c}{\partial T} = D\frac{\partial^2 c}{\partial z^2} - u\frac{\partial c}{\partial z} - w_0 c - q_0 \tag{8a}$$

and

$$R = 1 + \left(\frac{1-\phi}{\phi}\right) b k_d, w_0 = \frac{1}{f(mt)}\left(\frac{\rho}{\phi} + \frac{b}{\phi}\mu k_d\right) \text{ and } q_0 = \frac{b}{f(mt)} \tag{8b}$$

where k_d is distribution coefficient and R is the retardation factor.

According to the transformations, our initial and boundary conditions can be written as

$$c(z,0) = c_i(1+z), z > 0\, T = 0 \tag{9}$$

$$c(0,T) = \frac{c_0}{4}\left(4 - m^2T^2\right) \quad z = 0, T > 0 \tag{10}$$

$$\frac{\partial c}{\partial z} = 0, \quad z \to \infty, T > 0 \tag{11}$$

Further using new transformation

$$c(z,T) = k(z,T)\mathrm{e}^{\left(\frac{uz}{2D} - \frac{1}{R}\left(\frac{u^2}{4D} + w_0\right)T\right)} + \frac{q_0}{w_0} \tag{12}$$

In Eq. (8a), corresponding initial and boundary conditions in Eqs. (9)–(11) and solve by Laplace transformation technique (LTT); we obtain the final result as follows:

$$\begin{aligned} c(z,T) = &\left[\left(c_0 - \frac{q_0}{w_0}\right)F_1(z,T) + \frac{c_0 m^2}{2}F_2(z,T)\right. \\ &\left. -\left(c_0 - \frac{q_0}{w_0}\right)F_3(z,T) + \frac{c_i u}{R}F_4(z,T)\right] \\ &\exp\left(\frac{uz}{2D} - \frac{1}{R}\left(\frac{u^2}{4D} + w_0\right)T\right) + \left[\left(c_0 - \frac{q_0}{w_0}\right)\right. \\ &\exp\left(\beta^2 T - \frac{uz}{2D}\right) + zc_i \exp\left(\beta^2 T - \frac{uz}{2D}\right) - \frac{c_i u}{R}T \\ &\left.\exp\left(\beta^2 T - \frac{uz}{2D}\right)\right] \exp\left(\frac{uz}{2D} - \frac{1}{R}\left(\frac{u^2}{4D} + w_0\right)T\right) + \frac{q_0}{w_0} \end{aligned} \tag{13}$$

where

$$\begin{aligned} F_1(z,T) = &\frac{1}{2}\exp\left(\alpha^2 T - \alpha z\sqrt{\frac{R}{D}}\right) erfc\left(\frac{z}{2}\sqrt{\frac{R}{DT}} - \alpha\sqrt{T}\right) \\ &+ \frac{1}{2}\exp\left(\alpha^2 T + \alpha z\sqrt{\frac{R}{D}}\right) erfc\left(\frac{z}{2}\sqrt{\frac{R}{DT}} + \alpha\sqrt{T}\right) \end{aligned} \tag{14}$$

$$\begin{aligned} F_2(z,T) = &\left(\alpha T^2 - \frac{zT}{2}\sqrt{\frac{R}{D}} + \frac{z}{4\alpha^2} - \frac{zT}{2} + \frac{z^2}{4\alpha}\sqrt{\frac{R}{D}}\right) \\ &\times \exp\left(\alpha^2 T - \alpha z\sqrt{\frac{R}{D}}\right) erfc\left(\frac{z}{2}\sqrt{\frac{R}{DT}} - \alpha\sqrt{T}\right) \\ &+ \left(\alpha T^2 + \frac{zT}{2}\sqrt{\frac{R}{D}} - \frac{z}{4\alpha^2} + \frac{zT}{2} - \frac{z^2}{4\alpha}\sqrt{\frac{R}{D}}\right) \\ &\times \exp\left(\alpha^2 T + \alpha z\sqrt{\frac{R}{D}}\right) erfc\left(\frac{z}{2}\sqrt{\frac{R}{DT}} + \alpha\sqrt{T}\right) \\ &- \frac{z}{\alpha}\sqrt{\frac{T}{\pi}}\exp\left(\frac{-z^2 R}{4DT}\right) \end{aligned} \tag{15}$$

$$\begin{aligned} F_3(z,T) = &\frac{1}{2}\exp\left(\beta^2 T - \beta z\sqrt{\frac{R}{D}}\right) erfc\left(\frac{z}{2}\sqrt{\frac{R}{DT}} - \beta\sqrt{T}\right) \\ &+ \frac{1}{2}\exp\left(\beta^2 T + \beta z\sqrt{\frac{R}{D}}\right) erfc\left(\frac{z}{2}\sqrt{\frac{R}{DT}} + \beta\sqrt{T}\right) \end{aligned} \tag{16}$$

$$F_4(z,T) = \frac{1}{4\beta}\left(2\beta T - z\sqrt{\frac{R}{D}}\right)\exp\left(\alpha^2 T - \alpha z\sqrt{\frac{R}{D}}\right) \times erfc\left(\frac{z}{2}\sqrt{\frac{R}{DT}} - \alpha\sqrt{T}\right) + \frac{1}{4\beta}\left(2\beta T + z\sqrt{\frac{R}{D}}\right) \times \exp\left(\alpha^2 T + \alpha z\sqrt{\frac{R}{D}}\right) erfc\left(\frac{z}{2}\sqrt{\frac{R}{DT}} + \alpha\sqrt{T}\right) \tag{17}$$

$$\alpha = \frac{1}{R}\left(\frac{u^2}{4D} + w_0\right) \tag{18}$$

$$\beta = \frac{u^2}{4DR} \tag{19}$$

3 Numerical Solution

Numerical solution of solute transport modeling is used for prediction of transport of contaminants in nonhomogeneous and anisotropic media under different conditions. Ataie-Ashtiani et al. (1999) developed the truncation error through the Taylor series expansion of the one-dimensional advection-dispersion equation. Bakker (1999) has established analytical and numerical solution for groundwater flow in a multi-aquifer system.

The numerical solution of advection-dispersion equation in Eq. (8a) with the initial and boundary condition (9)–(11) in semi-infinite domain is obtained by changing into finite domain. In order to solve numerically, the domain is changed into the finite domain by using the transformation

$$X = 1 - \mathrm{e}^{-x} \tag{20}$$

and

$$Y = 1 - \mathrm{e}^{-y} \tag{21}$$

Using Eqs. (20) and (21), Eq. (8a) can be written as

$$R\frac{\partial c}{\partial T} = (1-X)^2 D_{x_0}\frac{\partial^2 c}{\partial X^2} + (1-Y)^2 D_{y_0}\frac{\partial^2 c}{\partial Y^2} - \xi(1-X)\frac{\partial c}{\partial X} - \eta(1-Y)\frac{\partial c}{\partial Y} - w_0 c + q_0 \tag{22}$$

where; $\xi = D_{x_0} + u_0$ and $\eta = D_{y_0} + v_0$

The corresponding initial and boundary conditions in Eqs. (9)–(11) can be written as

$$c(X,Y,0) = \frac{c_i}{(1-X)(1-Y)} \quad X > 0, Y > 0, T = 0 \tag{23}$$

$$c(0,0,T) = \frac{c_0}{4}\left(4 - m^2T^2\right) \quad X = 0, Y = 0, T > 0 \tag{24}$$

$$\frac{\partial c}{\partial X} = 0, \frac{\partial c}{\partial Y} = 0 \quad X \to 1, Y \to 1, T > 0 \tag{25}$$

The finite difference method is derived by using Taylor expansion. In the present work, we used the general form of explicit finite difference approximation with a forward time and central space forward difference scheme, and then Eqs. (22)–(25) can be written as

$$\begin{aligned} c_{i,j,k+1} = &\left(1 - \frac{1-\omega_0}{R}\right)c_{i,j,k} + \frac{D_{x_0}(1-X_i)}{R}\left[c_{i+1,j,k} - 2c_{i,j,k} + c_{i-1,j,k}\right] \\ &\times \frac{\Delta T}{\Delta X^2} + \frac{D_{y_0}(1-Y_i)}{R}\left[c_{i,j+1,k} - 2c_{i,j,k} + c_{i,j-1,k}\right] \\ &\times \frac{\Delta T}{\Delta Y^2} - \frac{\varepsilon(1-X_i)}{R}\left[c_{i+1,j,k} - c_{i-1,j,k}\right] \\ &\times \frac{\Delta T}{2\Delta X} - \frac{\eta(1-Y_i)}{R}\left[c_{i,j+1,k} - c_{i,j-1,k}\right]\frac{\Delta T}{2\Delta Y} + q_0 \end{aligned} \tag{26}$$

Initial and boundary conditions can be written as

$$c_{i,j,k} = \frac{c_i}{(1-X_i)(1-Y_j)} \quad i > 0, j > 0, T = 0 \tag{27}$$

$$c_{0,0,j} = \frac{c_0}{4}\left(4 - m^2T_k^2\right) \quad k > 0 \tag{28}$$

$$c_{M,j,k} = c_{M-1,j,k} \text{ and } c_{i,N,k} = c_{i,N-1,k} \tag{29}$$

where the subscripts i, j, and k refers to space and time variables respectively. Also, ΔT is the time increment whereas ΔX and ΔY are space increments in Eq. (26).

The space variables (X, Y) and time domain T are discretized by a rectangular grid points $\left(X_i, Y_j, T_k\right)$ with mesh size as follows

$$X_i = X_{i-1} + \Delta X \quad i = 1, 2, 3 \ldots M. \quad X_0 = 0, \quad \Delta X = 0.005$$

$$Y_j = Y_{j-1} + \Delta Y \quad j = 1, 2, 3 \ldots N. \quad Y_0 = 0, \quad \Delta Y = 0.005$$

$$T_k = T_{k-1} + \Delta T \quad k = 1, 2, 3 \ldots I \quad T_0 = 0, \quad \Delta T = 0.001$$

where M, N, and I are integers.

$c_{i,j,k}$ be the contaminant concentration at a point for the space domain X_i and Y_j with time domain T_k.

4 Stability Condition

The numerical solution using finite difference scheme is said to be convergent if the stability condition is satisfied. In finite difference technique, we used the forward difference in time for the first-order derivative with respect to time which contains the first-order accuracy. With the help of finite difference scheme, our governing Eq. (8a) can be written as

$$\begin{aligned} c_{i,j,k+1} =& (\alpha_1 + \beta_1)c_{i-1,j,k} + (\gamma_1 + \delta_1)c_{i,j-1,k} \\ &+ (1 - \zeta - 2\alpha_1 - 2\gamma_1)c_{i,j,k} + (\alpha_1 - \beta_1)c_{i+1,j,k} \\ &+ (\gamma_1 - \delta_1)c_{i,j+1,k} + \frac{q_0 \Delta T}{R} \end{aligned} \tag{30}$$

where

$$\alpha_1 = \frac{D_{x_0}\Delta T}{R\Delta X^2}, \beta_1 = \frac{u_0 \Delta T}{2R\Delta X}, \gamma_1 = \frac{D_{y_0}\Delta T}{R\Delta Y^2}, \delta_1 = \frac{v_0 \Delta T}{2R\Delta Y} \text{ and } \zeta = \frac{\omega_0 \Delta T}{R}$$

Equation (30) can be written in matrix form as

$$[c]^{k+1} = A[c]^k \tag{31}$$

where A is the matrix that contains all the constraints. The finite difference scheme is stable if the eigenvalues of A must have modulus values less than or equal to unity.

After using the Gerschgorin circle method, the time step can be written as

$$\Delta T \leq \frac{1}{\left(\frac{D_{x_0}}{R\Delta X^2} + \frac{D_{x_0}}{R\Delta X^2} + \frac{D_{y_0}}{R\Delta Y^2} + \frac{u_0}{2R\Delta X} + \frac{v_0}{2R\Delta Y}\right)} \tag{32}$$

5 Numerical Result and Discussion

The analytical and numerical solutions for the two-dimensional advection-dispersion equation are computed for the given set of input data:

$c_0 = 1.0$, $c_i = 0.1$, $q_0 = 0.0002$, $u_0 = 0.002$, $v_0 = 0.002$, $D_{x_0} = 0.005$, $D_{y_0} = 0.005$, $n = 0.25$, $k_d = 0.02$.

The contaminant concentration distribution pattern has been predicted for temporally dependent velocity pattern such as exponentially increasing and asymptotic form of velocity pattern. Mathematically, these velocity patterns can be written as:

$$\text{(a)} \quad f(mt) = 1 - \exp(-mt), \quad T = \frac{1}{m}(\exp(-mt) - 1) + t \tag{33}$$

$$\text{(b)} \quad f(mt) = 1 + \frac{mt}{(1 + m^2t^2)}, \quad T = \frac{1}{2m}\left(\log(1 + m^2t^2)\right) + t \tag{34}$$

where m is the flow resistance coefficient.

The contaminant concentration distribution pattern has been predicted for the finite domain $0 \le x \le 0.5$ and $0 \le y \le 0.5$.

Figure 1 is predicted for the concentration distribution pattern of clay medium with exponentially decreasing velocity pattern. As time increases, the concentration pattern increases, but with respect to space the concentration pattern follows its minimum value of harmless concentration. The entire concentration pattern for the different time interval 1, 2, and 3 years, respectively, attains the same value at the end of the domain. Similarly, type concentration pattern is predicted in Fig. 2 for the asymptotic form of the velocity pattern with clay medium. The concentration

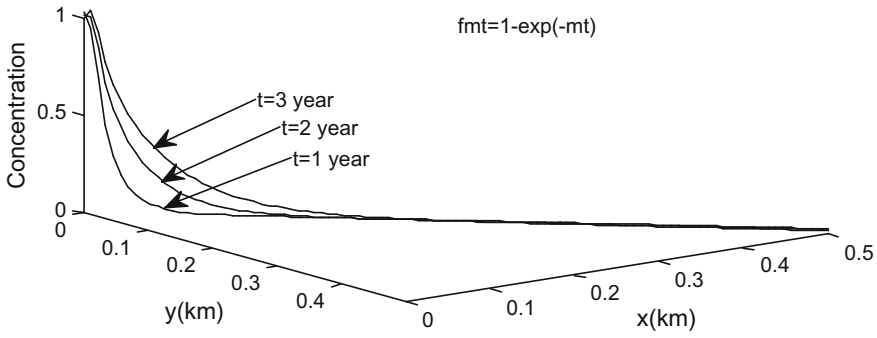

Fig. 1 Concentration distribution pattern for exponentially decreasing velocity patterns with clay medium

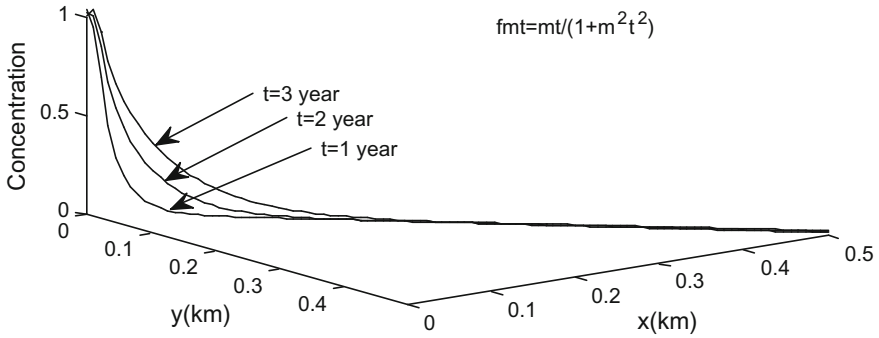

Fig. 2 Concentration distribution pattern for asymptotic velocity patterns with clay medium

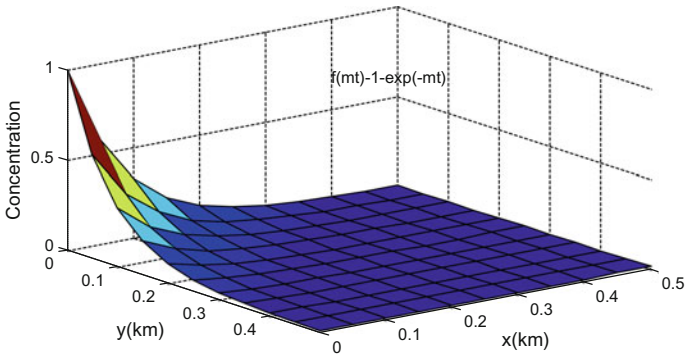

Fig. 3 Surface contaminant concentration for exponentially decreasing velocity pattern at time $t = 3$ year

pattern follows the increasing nature with respect to time, but it attains its minimum harmless concentration with respect to distance.

The surface concentration graph is predicted in Figs. 3 and 4 for the different velocity patterns with particular time period of 3 years. Figure 3 is predicted for the exponentially decreasing velocity pattern in which concentration pattern follows the decreasing nature with respect to space. Initially, it attains the maximum level of concentration, but it follows the minimum harmless concentration level after covering some distance in the region $0 \leq x \leq 0.5$ and $0 \leq y \leq 0.5$. Similarly, Fig. 4 is predicted for the asymptotic form of the velocity pattern with particular time period of 3 years. Initially, it attains its maximum level of concentration values, but it decreases with respect to the longitudinal as well as transversal direction of the flow.

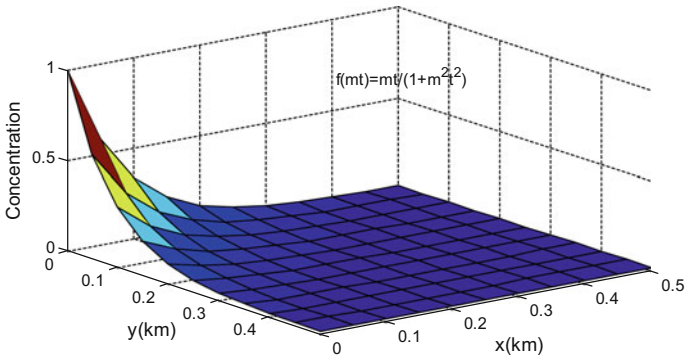

Fig. 4 Surface contaminant concentration for asymptotic velocity pattern at time t = 3 year

Table 1 Concentration values at time t = 3 year for zero-order production $q_0 = 0.002$

X (km)	0.0	0.05	0.10	0.15	0.20
Exponentially decreasing	1.0015	0.3723	0.1278	0.0495	0.0250
Asymptotic	1.0007	0.3774	0.1314	0.0512	0.0258

Table 2 Concentration values at time t = 3 year zero-order production $q_0 = 0.003$

X (km)	0.0	0.05	0.10	0.15	0.20
Exponentially decreasing	1.0025	0.3680	0.1235	0.0452	0.0208
Asymptotic	1.0018	0.3731	0.1271	0.0470	0.0216

Tables 1 and 2 provide the concentration values at different zero-order production terms for the different velocity patterns. In Table 1, initially concentration values attain higher in exponentially decreasing velocity pattern as compared to the asymptotic form velocity pattern. It follows the reverse pattern for distance 0.05 to 0.2. Similar trend is attained in Table 2 for $q_0 = 0.003$. In Table 1 less concentration values are attained at each of the points for the different velocity pattern as compared to Table 2, but for every value of q_0 concentration value decreases with respect to space.

6 Summary and Conclusions

Two-dimensional advection-dispersion equation (ADE) is solved analytically and numerically by using the Laplace transform technique and explicit finite difference approximation, respectively. The effect of the zero-order production term has been explored. Solute concentration pattern is predicted for the clay medium, in which

concentration pattern increases with respect to time and decreases with respect to space. Exponentially decreasing and asymptotic form temporally dependent velocity pattern has been used.

References

Ataie-Ashtiani B, Lockington DA, Volker RE (1999) Truncation errors in finite difference models for solute transport equation with first-order reaction. J Contam Hydrol 35(4):409–428

Bakker M (1999) Simulating groundwater flow in multi-aquifer systems with analytical and numerical Dupuit-models. J Hydrol 222(1):55–64

Banks RB, Ali J (1964) Dispersion and adsorption in porous media flow. J Hydraul Div 90:13–31

Chen JS, Lai KH, Liu CW, Ni CF (2012) A novel method for analytically solving multi-species advective-dispersive transport equations sequentially coupled with first-order decay reactions. J Hydrol 420:191–204

Crank J (1975) The mathematics of diffusion. Oxford University Press, London (2nd edn)

Fry VA, Istok JD, Guenther RB (1993) An analytical solution to the solute transport equation with rate-limited desorption and decay. Water Resour Res 29(9):3201–3208

Jiao J, Zhang Y (2014) Two-dimensional physical-based inversion of confined and unconfined aquifers under unknown boundary conditions. Adv Water Resour 65:43–57

Kartha SA, Srivastava R (2008) Effect of immobile water content on contaminant transport in unsaturated zone. J Hydro-Env Res 1(3):206–215

Kaya B (2010) Solution of the advection-diffusion equation using the differential quadrature method. KSCE J Civil Eng 14(1):69–75

Kumar N (1983) Unsteady flow against dispersion in finite porous media. J Hydrol 63(3):345–358

Lindstrom FT, Boersma L (1989) Analytical solutions for convective-dispersive transport in confined aquifers with different initial and boundary conditions. Water Resour Res 25(2): 241–256

Liu C, Ball WP (1998) Analytical modeling of diffusion-limited contamination and decontamination in a two-layer porous medium. Adv Water Resour 21:297–313

Majdalani S, Chazarin JP, Delenne C, Guinot V (2015) Solute transport in periodical heterogeneous porous media: importance of observation scale and experimental sampling. J Hydrol 520:52–60

Ogata A, Banks RB (1961) A solution of the differential equation of longitudinal dispersion in porous media (No. 411-A)

Putti M, Yeh WWG, Mulder WA (1990) A triangular finite volume approach with high-resolution upwind terms for the solution of groundwater transport equations. Water Resour Res 26(12): 2865–2880

Singh MK, Das P (2015) Scale dependent solute dispersion with linear isotherm in heterogeneous medium. J Hydrol 520:289–299

Singh MK, Singh P, Mahato NK (2008) Longitudinal dispersion with time dependent source concentration in semi-infinite aquifer. J Earth Syst Sci 6:945–949

Van Genuchten MT, Alves WJ (1982) Analytical solutions of the one-dimensional convective-dispersive solute transport equation (No. 157268). United States Department of Agriculture Economic Research Service

Yates SR (1992) An analytical solution for one dimensional transport in porous media with an experimental dispersion function. Water Resour Res 28(8):2149–2154

Zoppou C, Knight JH (1997) Analytical solutions for advection-diffusion equation with spatially variable coeffiecients. J Hydraul Eng 123:144–148

Mathematical Modeling of One-Dimensional Advection Dispersion Equation in Groundwater Contamination Using Different Velocity and Dispersion for Different Zones

Mritunjay Kumar Singh, Ayan Chatterjee and Priyanka Kumari

Abstract Groundwater contamination problem is modeled using advection dispersion equation with different phase velocity and dispersion. This type of flow problem can be occurred or visualized depending upon the geometry as the surface of the aquifer is made of various soil materials. We consider different velocity and dispersion for different zones. Initially, the aquifer is contamination free, and advection dispersion equation is used to model the system subject to the condition that the source is acting at origin and contaminant concentration flux is zero at the semi-infinite part of the boundary. Laplace transform technique is used to solve the system analytically, and graphs are plotted to show the effect in the aquifer with multiphase.

1 Introduction

Groundwater is one of the most useful resources for the most of the people of rural India. But day by day groundwater is contaminated and becomes useless for daily purposes. From last few decades, advection dispersion equation is used to model the contaminant concentration flow in the aquifer system. Kaluarachchi and Parker (1989) discussed an efficient finite element method for modeling multiphase flow in groundwater contamination problem. Logan (1996) presented an extension of the work of Yates (1992) for solute transport in porous media with scale-dependent

M.K. Singh (✉) · A. Chatterjee
Department of Applied Mathematics, Indian Institute of Technology (Indian School of Mines), Dhanbad 826004, Jharkhand, India
e-mail: drmks29@rediffmail.com

A. Chatterjee
e-mail: ayan@am.ism.ac.in

P. Kumari
Department of Mathematics, K.K. College of Engineering and Management, Dhanbad 828109, Jharkhand, India
e-mail: sinki_burnwal@yahoo.com

M.K. Singh et al. (eds.), *Applications of Fluid Dynamics*, Lecture Notes in Mechanical Engineering, https://doi.org/10.1007/978-981-10-5329-0_44

dispersion and periodic boundary conditions. Huyakorn et al. (1994) explored formulation of three-dimensional multiphase flow model for assessing NAPL contamination in porous and fractured media. Aral and Liao (1996) obtained a general analytical solution for an infinite domain aquifer, where two-dimensional solute transport equation with time-dependent dispersion coefficient was used. Batu (1996) explored multiple sources for generalized three-dimensional solute transport model. Arbogast et al. (1996) derived mathematical formulation and some numerical approximation techniques for a system of coupled partial differential and algebraic equations to describe multiphase flow in groundwater contamination problem. Lewis and Ghafouri (1997) developed a novel finite element double porosity model for multiphase flow through deformable fractured porous media. Rahman and Lewis (1999) used finite element modeling of multiphase immiscible flow in deforming porous media for subsurface systems. One-dimensional simulation of solute transfer in saturated–unsaturated porous media using the discontinuous finite element method was discussed by Diwa et al.(2001). Rubin and Atkinson (2001) explored various properties of environmental fluid flow modeling in environmental fluid mechanics. Lewis and Pao (2002) described numerical simulation of three-phase flow in deforming fractured reservoirs. Younes (2003) presented multidimensional fluid flow and heat or mass transport in porous media. Klubertanz et al. (2003) developed a miscible and immiscible multiphase flow in deformable porous media. Wortmann et al. (2005) and Moreira et al. (2005) used the generalized integral Laplace transform technique for the simulation of pollutant dispersion in the atmosphere and solved the advection dispersion equation analytically. Sander and Braddock (2005) explored analytical solution to the transient, unsaturated transport of water and contaminants through horizontal porous media. Oliaei et al. (2009) described some numerical issues using element-free Galerkin meshless method for coupled hydromechanical problems. Khoei and Mohammadnejad (2011) described numerical modeling of multiphase fluid flow in deforming porous media, in which they compared between two- and three-phase models for seismic analysis of earth and rockfill dams. Ngien et al. (2011) explored numerical modeling of multiphase immiscible flow in double porosity featured groundwater systems. Zamani and Bombardelli (2013) presented analytical solutions of nonlinear and variable-parameter transport equations to verify the numerical solver. Singh and Kumari (2014) and Singh et al. (2014) discussed longitudinal dispersion with time-dependent source concentration along unsteady groundwater flow in a semi-infinite aquifer with time-dependent velocity and dispersion.

In most of the available literature, authors used space dependency directly in the problems to model the system. Actually, if we carefully observe the space-time-dependent velocity and dispersion in groundwater system, then we see that it can only be happen when the geometry of the system changes with distance, i.e., the space dependency is zonal. It is well known that the boundary of the aquifer is made of various soil materials like clay, gravel. We are also well aware of the fact that velocity and dispersion differ from medium to medium. So we solve advection dispersion equation in semi-infinite medium with constant source acting at the origin in an initially contamination-free aquifer. As we are going to discuss the flow

problem using space-time-dependent dispersion and velocity, then we solve the ADE with source acting at any point in the domain, and using this solution, we may be able to find the contaminant concentration for each phase. Laplace transform technique is used to solve the problem analytically, and MATLAB is used to draw the graphs.

2 Mathematical Formulation

We consider one-dimensional advection dispersion equation (ADE) to model the multiphase contamination flow in the aquifer system, where the single source is acting at the origin of the system. To ensure the space dependency in the groundwater flow, we have to consider the dispersion and velocity profile in such a way that when the formation of the medium changes like rock, clay, then velocity and dispersion also vary. We want to solve the ADE with single source acting at any point in the domain. We consider that the concentration gradient tends to zero at semi-infinite part of the boundary. So the modeled system can be written as (Fig. 1)

$$\frac{\partial C}{\partial T} = D(T)\frac{\partial^2 C}{\partial x^2} - u(T)\frac{\partial C}{\partial x} \tag{1}$$

with the following conditions:

$$C(x,T) = 0, \quad T = 0, \quad x \geq 0, \tag{2}$$

$$C(x,T) = c_0, \quad x = a, \quad T \geq 0, \tag{3}$$

$$\frac{\partial C}{\partial x} = 0, \quad \text{as} \quad x \to \infty. \tag{4}$$

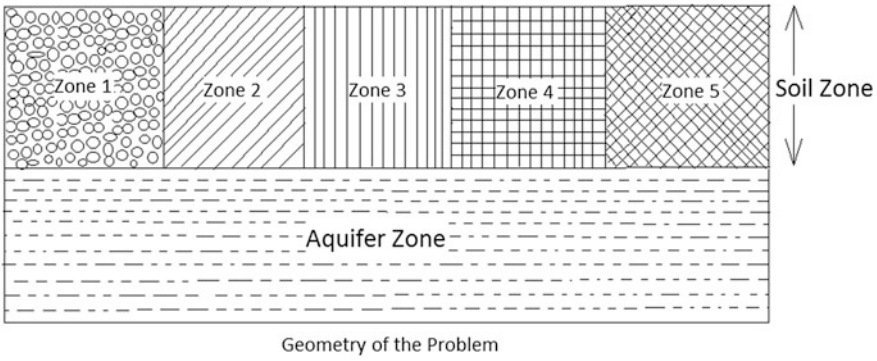

Fig. 1 Geometry of the problem

where $C(x,T)$ is the contaminant concentration, c_0 are the constant concentrations, $D(T)$ is the dispersion along positive x direction, and $u(T)$ is the velocity profile of groundwater.

By using the solution of advection dispersion equation of single model system, we can predict the contaminant concentration in aquifer through different zones of soil. For that we have considered different velocity and dispersion coefficiennts in soil zones.

3 Analytical Solution

We assume that $u = u_0 f(T)$ and $D = D_0 f(T)$. Here, $f(T)$ is either exponentially decreasing or sinusoidal or constant.

Consider $t = \int_0^T f(T)\mathrm{d}T$

$$\frac{\partial C}{\partial t} = D_0 \frac{\partial^2 C}{\partial x^2} - u_0 \frac{\partial C}{\partial x}. \tag{5}$$

The corresponding initial and boundary conditions given by Eqs. (2), (3), and (4) can also be written as follows:

$$C(x,t) = 0, \quad x \geq 0; t = 0 \tag{6}$$

$$C(x,t) = c_0, \quad t \geq 0, x = a \tag{7}$$

$$\frac{\partial C}{\partial x} = 0, \quad x \to \infty \tag{8}$$

Now, we consider that $C(x,t) = K(x,t)\mathrm{e}^{\left(\frac{u_0 x}{2D_0} - \frac{u_0^2 t}{4D_0}\right)}$, and by substituting in Eqs. (5)–(8), one can get the transform equation as follows:

$$\frac{1}{D_0}\frac{\partial K}{\partial t} = \frac{\partial^2 K}{\partial x^2} \tag{9}$$

Also, the corresponding initial and boundary condition changes to

$$K(x,t) = 0, \quad t = 0, \quad x \geq 0 \tag{10}$$

$$K(x,t) = c_0 \exp\left(-\frac{u_0 x}{2D_0} + \frac{u_0^2 t}{4D_0}\right), \quad x = a, \quad t > 0 \tag{11}$$

$$\frac{\partial K}{\partial x} + \frac{u_0 K}{2D_0} = 0, \quad \text{when} \quad x \to \infty \tag{12}$$

Using the Laplace transform technique, we get the solution of Eq. (9) with initial and boundary conditions (10–12) as follows:

$$K(X,T) = \frac{c_0}{2}\exp\left(-\frac{u_0 a}{2D_0}\right)\left[\exp\left(\frac{u_0^2 t}{4D_0} - \frac{u_0(x-a)}{2D_0}\right) erfc\left(\frac{x-a}{2\sqrt{tD_0}} - \frac{u_0\sqrt{t}}{2\sqrt{D_0}}\right) + \exp\left(\frac{u_0^2 t}{4D_0} + \frac{u_0(x-a)}{2D_0}\right) erfc\left(\frac{x-a}{2\sqrt{tD_0}} + \frac{u_0\sqrt{t}}{2\sqrt{D_0}}\right)\right] \tag{13}$$

Now using the transformation, we get the solution as follows:

$$C(x,t) = \frac{c_0}{2}\exp\left(\frac{u_0(x-a)}{2D_0} - \frac{u_0^2 t}{4D_0}\right)\left[\exp\left(\frac{u_0^2 t}{4D_0} - \frac{u_0(x-a)}{2D_0}\right) erfc\left(\frac{x-a}{2\sqrt{tD_0}} - \frac{u_0\sqrt{t}}{2\sqrt{D_0}}\right) + \exp\left(\frac{u_0^2 t}{4D_0} + \frac{u_0(x-a)}{2D_0}\right) erfc\left(\frac{x-a}{2\sqrt{tD_0}} + \frac{u_0\sqrt{t}}{2\sqrt{D_0}}\right)\right] \tag{14}$$

4 Discussion

Using the solution (14), we want to interoperate multizone flow in one dimension. If the geometry of the system changes, then velocity and dispersion become spatially dependent. It is a well-known fact that in gravel medium, the velocity and dispersion differ from clay and other mediums. Boundary surfaces of an aquifer can be made of using various medium with different materials and that can create a zonal flow problem. Suppose one source of contamination occurs at the origin of the aquifer, then the flow of the contaminant goes through the various material zones, where dispersion and velocity coefficients are different from the previous one. So if we come to know the effect of contaminant concentration at the end of one zone then we can also find the impact of the same in the next zone.

Five equal size zones of various materials are considered and studied with various dispersion and velocity coefficients. The single source is acting at the origin of the aquifer with constant contaminant concentration one. We consider that the length of the each zone as 0.1 km, and dispersion and velocity of the five zones are as follows: $u_0 = 0.11, D_0 = 0.0022$, $u_0 = 0.10, D_0 = 0.002$, $u_0 = 0.12, D_0 = 0.0024$, $u_0 = 0.09, D_0 = 0.0018$, and $u_0 = 0.07, D_0 = 0.0014$. It is clear from Fig. 2 that the contaminant concentration decreases slowly with distance depending upon the phases.

In Fig. 3, we have shown the comparison between multizone and single-zone contaminant flow problem. It is clear from the study that in single-zone flow, the contaminant concentration decreases more rapidly than multizone flow problem. So we can say that in the case of the multizone flow contaminant shows more effect

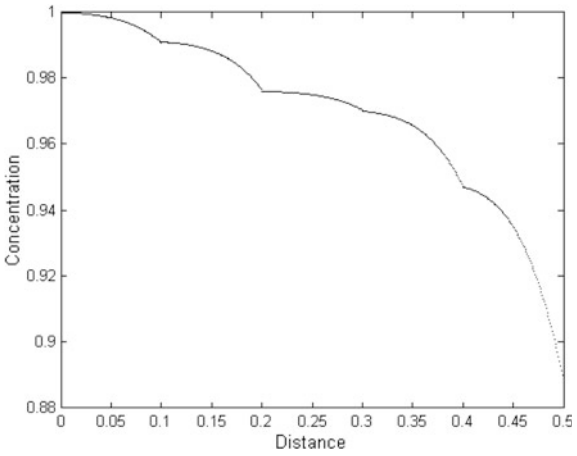

Fig. 2 Multizone flow modeling: concentration with distance at fixed time $t = 3$

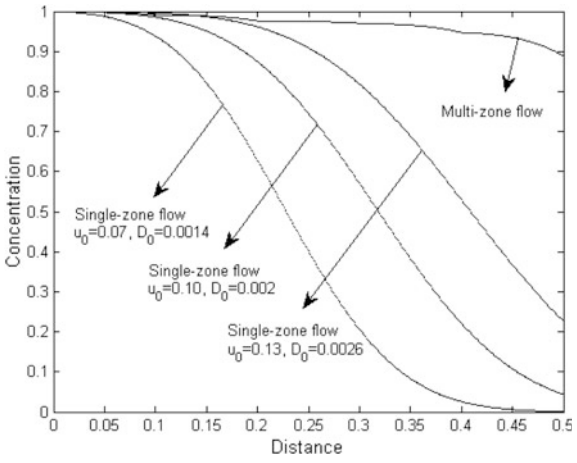

Fig. 3 Comparison of single-zone and multizone concentration with distance at fixed time $t = 3$

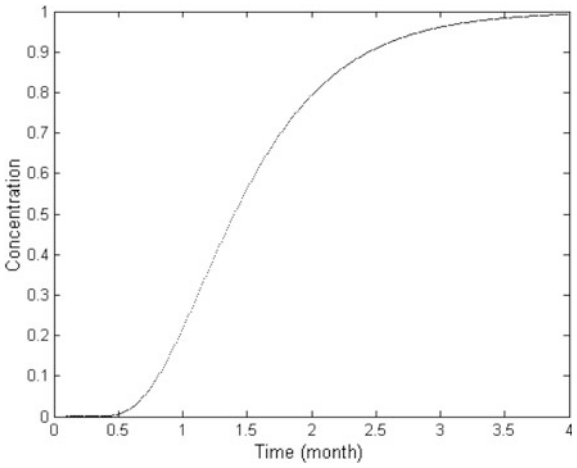

Fig. 4 Concentration with time for a fixed distance $x = 0.2$

than single-zone flow and causes more casualties as it shows its effect for a longer distance.

From Fig. 4, it is clear that the contaminant concentration increases for a fixed point ($x = 0.2$ km) with time and achieves its maximum concentration level when $t = 4$. The same velocity and dispersion coefficients are considered ($u_0 = 0.10, D_0 = 0.002$) according to the position of the point.

5 Conclusion

One new type of multizone flow model is derived and solved analytically using Laplace transform technique. Multizone contaminant flow solution shows more impact than single-phase contaminant flow solution in the aquifer, as it covers more distance than single-zone contaminant flow. Space dependency is incorporated using different zones. Using analytical solution, we can get a closed form of the solution, and we may be able to use it to consider some remedial measure to eliminate the contaminant concentration from the aquifer system.

References

Aral MM, Liao B (1996) Analytical solutions for two-dimensional transport equation with time-dependent dispersion coefficients. J Hydrol Eng 1:20–32

Arbogast T, Wheeler MF, Zhang NY (1996) A nonlinear mixed finite element method for a degenerate parabolic equation arising in flow in porous media. SIAM J Numer Anal 33: 1669–1687

Batu V (1996) A generalized three dimensional analytic solute transport model for multiple rectangular first type sources. J Hydrol 174(1–2):57–82

Diwa EB, Lehmann F, Ackerer Ph (2001) One dimensional simulation of solute transfer in saturated-unsaturated porous media using the discontinuous finite element method. J Contam Hydrol 51(3–4):197–213

Huyakorn PS, Panday S, Wu YS (1994) A three-dimensional multiphase flow model for assesing NAPL contamination in porous and fractured media, 1. Formulation. J Contam Hydrol 16 (2):109–130

Kaluarachchi JJ, Parker JC (1989) An efficient finite element method for modeling multiphase flow. Water Resour Res 25(1):43–54

Khoei AR, Mohammadnejad T (2011) Numerical modeling of multiphase fluid flow in deforming porous media: a comparison between two- and three-phase models for seismic analysis of earth and rockfill dams. Comput Geotech 38:142–166

Klubertanz G, Bouchelaghem F, Laloui L, Vulliet L (2003) Miscible and immiscible multiphase flow in deformable porous media. Math Comput Model 37:571–582

Lewis RW, Ghafouri HR (1997) A novel finite element double porosity model for multiphase flow through deformable fractured porous media. Int J Numer Anal Methods Geomech 21:789–816

Lewis RW, Pao WKS (2002) Numerical simulation of three-phase flow in deforming fractured reservoirs. Oil Gas Sci Technol 57:499–514

Logan JD (1996) Solute transport in porous media with scale-dependent dispersion and periodic boundary conditions. J Hydrol 184(3–4):261–276

Moreira DM, Vilhena MT, Tirabassi T, Buske D, Cotta RM (2005) Near-source atmospheric pollutant dispersion using the new GILTT method. Atmos Environ 39:6289–6294

Ngien SK, Rahman NA, Lewis RW, Ahmad K (2011) Numerical modeling of multiphase immiscible flow in double-porosity featured groundwater systems. Int J Numer Anal Methods Geomech

Oliaei MN, Soga K, Pak A (2009) Some numerical issues using element-free Galerkin meshless method for coupled hydro-mechanical problems. Int J Numer Anal Methods Geomech 33: 915–938

Rahman NA, Lewis RW (1999) Finite element modeling of multiphase immiscible flow in deforming porous media for subsurface systems. Comput Geotech 24:41–63

Rubin H, Atkinson J (2001) Environmental Fluid Mechanics. Mar-353 cel Dekker New York

Sander GC, Braddock RD (2005) Analytical solutions to the transient, unsaturated transport of water and contaminants through horizontal porous media. Adv Water Resour 28:1102–1111

Singh MK, Kumari P (2014) Contaminant concentration prediction along unsteady groundwater flow, modeling and simulation of diffusive processes. Series: Simulation Foundations, Methods and Applications, Springer, pp. 257–276

Singh MK, Ahamad S, Singh VP (2014) One-dimensional uniform and time varying solute dispersion along transient groundwater flow in a semi-infinite aquifer. Acta Geophys 62 (4):872–892. doi:10.2478/s11600-014-0208-7

Wortmann S, Vilhena MT, Moreira DM, Buske D (2005) A new analytical approach to simulate the pollutant dispersion in the PBL. Atmos Environ 39:2171–2178

Yates SR (1992) An analytical solution for one-dimensional transport in porous media with an exponential dispersion function. Water Resour Res 28:49–54

Younes A (2003) On modeling the multidimensional coupled fluid flow and heat or mass transport in porous media. Inter J Heat Mass Transfer 46(2):367–379

Zamani K, Bombardelli FA (2013) Analytical solutions of nonlinear and variable-parameter transport equations for verification of numerical solvers. Fluid Mech, Environ. doi:10.1007/s10652-013-9325-0

Solute Dispersion Along Unsteady Groundwater Flow in a Semi-infinite Homogeneous Aquifer Using Linguistic Hedge by Mamdani Model

Abhijit Debnath, Umesh Prasad and Mritunjay Kumar Singh

Abstract In the present study, the analytical solutions for dispersion of contaminants along unsteady flow of groundwater through semi-infinite aquifer are represented by fuzzy linguistic hedges. The sources of pollution are both a point input at origin and a spatially distributed background source. The analytical solutions thus obtained are put into Mamdani model with different linguistic variables, and the model thus formed gives the result of solute concentration in literal sense in different point of time and space. The MATLAB code has been generated to simulate the Mamdani Model and to find the fuzziness of the solution of AD equation (Advection-Dispersion Equation) along unsteady flow.

1 Introduction

It has been investigated that, in India, the groundwater flow and the level varies seasonally. We know the groundwater velocity and level remains maximum after the rainy season and becomes minimum at summer. In tropical region such as India, groundwater flow shows a sinusoidal nature throughout the year. There are a considerable body of literature available on solute transport which may be enlisted and are related with AD equation since last four or five decades. The AD equation represents a standard model to predict the solute movement in groundwater based on conservation of mass and Fick's law of diffusion Fried and Combarnous (1971),

A. Debnath (✉)
Department of Mathematics, Asansol Engineering College, Vivekananda Sarani, Kanyapur, Asansol 713305, India
e-mail: a13deb13@gmail.com

U. Prasad
RIT, Koderma, Koderma 825409, Jharkhand, India
e-mail: umeshpd5u@gmail.com

M.K. Singh
Department of Applied Mathematics, Indian Institute of Technology (Indian school of Mines), Dhanbad, Dhanbad 826004, Jharkhand, India
e-mail: drmks29@rediffmail.com

M.K. Singh et al. (eds.), *Applications of Fluid Dynamics*, Lecture Notes in Mechanical Engineering, https://doi.org/10.1007/978-981-10-5329-0_45

Bear (1972), Chrysikopoulos et al. (1990) conducted a series of experiments to investigate longitudinal dispersion of reactive contaminants through natural channels. Van Genuchten (1981) solved a 1D advection-dispersion equation with adsorption, zero-order production and first-order decay. Van Genuchten and Alves (1982) obtained analytical solution by Laplace transform method with third-type boundary condition. Using Fourier transform and superposition method, Valocchi and Roberts (1983) obtained a solution of 1D advection-dispersion equation in semi-infinite and infinite domains for continuous input of periodically fluctuating concentration and finite duration input of pulse-type concentration.

In the present study, one-dimensional solute dispersion along unsteady groundwater flow in a homogeneous aquifer is considered. Sinusoidal time-dependent expression for groundwater velocity is considered separately. Rumer (1962) found that a relationship for steady flow was also valid for unsteady flow with sinusoidally varying velocity through porous media. Earlier, all the analytical solution or the numerical solution of AD equation gives the numeral value of concentration at certain space and time. In this study, the decision in language for the solute concentration is obtained by the application of fuzzy inference. This study deals with the amount of solute concentration (high or medium or low) in linguistic terms. The solution obtained for the one-dimensional AD equation is put into fuzzy inference engine to get the solution in terms of linguistic variables.

2 Dispersion in Homogeneous Aquifer

The contaminants from instantaneous point source (spills), such as septic tanks, cemeteries, mine spoils over the ground, infiltrate to groundwater and spread along the flow. The solute concentration distribution in one-dimensional space with zero-order liquid phase source is defined by Scheidegger (1961), Bachmat and Bear (1964)

$$\frac{\partial c^*}{\partial t} = \frac{\partial}{\partial x}\left[D\frac{\partial c^*}{\partial x} - uc^*\right] + \gamma^* \tag{1}$$

An appropriate initial condition has been chosen as

$$c^*(x,0) = C_1 + \frac{\gamma^* x}{u}; \quad x \geq 0 \tag{2}$$

The first boundary condition is taken as at $x = 0$,

$$-(1-\delta)\frac{D}{u}\frac{\partial c^*}{\partial x} + c^* = C_0 f(t); \quad 0 < t \leq t_0 \tag{3a}$$

$$= 0; \quad t > t_0 \tag{3b}$$

another boundary condition is taken as

$$\frac{\partial c^*}{\partial x} = \text{finite as} \, x \to \infty \tag{4}$$

where c^* is solute concentration in liquid phase, D is the dispersion coefficient and u is the groundwater velocity at position x and time t. γ^* is the zero-order production. The unsteady flow of groundwater is taken as

$$u(t) = u_0(1 - \sin mt) \tag{5}$$

Here, m is flow resistance coefficient and u_0 is the initial velocity. As D and u are independent of x, for a homogeneous aquifer Eq. (1) may be written as

$$\frac{\partial c^*}{\partial t} = D\frac{\delta^2 c^*}{\partial x^2} - u\frac{\partial c^*}{\partial x} + \gamma^* \tag{6}$$

3 Mamdani Model for Fuzzy Inference

When the input variables are mapped into output space by using the fuzzy logic deduction mechanism which includes IF-THEN rules, fuzzy logical operators and variables, then the total process is called fuzzy inference. As the human reasoning is quite compatible with IF-THEN rules and human language may be approximated with fuzzy logic, the inference process converts the crisp values onto human language resulting to the huge acceptance to any people who does not know the mathematics behind it. Mamdani-type fuzzy inference process contains following steps:

Step 1. Input variables are to be fuzzified
Step 2. Application of fuzzy operators
Step 3. Different implication methods
Step 4. Suitable method of aggregation
Step 5. Suitable method of defuzzification.

Here, the input variables are considered to be mt and x. The solute concentration is considered to be the output variable. In this study, the most common logical operators such as AND operator and OR operator are used, and to formulate the logical operations, the function min and max are taken into consideration. A fuzzy output set has been generated after application of IF-THEN Rules. Then, the method of aggregation is being implemented for combination of these fuzzy sets which represent the outputs as a single result so that decision can be made upon the result. The final combined fuzzy set is the output of aggregation process. In the final step, the defuzzification process is done where the combined fuzzy set from

aggregation process will output a single scalar quantity. In this study the centroid method of defuzzification has been taken.

In this study, TISO (Two-input single-output) model of Mamdani is being applied. For simplification, the input variable x (space) has been classified with 3 membership functions "source", "midway" and "far"; the output variable has 3 membership functions "low", "medium" and "high". The time input variable (mt) has been divided into two parts of any year "(A) before rainy season" and "(B) after rainy season" taken as input variables, and each of them are classified with 3 membership functions "early", "mid" and "late". The output variable C (Solute concentration variable) whose range in universe of discourse is taken to be [0.1, 0.3] w.r.t variable A and range w.r.t variable B is [0.1, 0.4].

The fuzzification of the input variable x (space) has been taken in the interval [0, 10] and for both the input variables (A) and (B) are taken in the interval of [0, 6]. The fuzzification is done under the Gaussian membership function (Figs. 1, 2, 3, 4 and 5).

Month of June is considered to be the initial of "after rainy season", and month of January will be considered as initial of "before rainy season". From the analytical

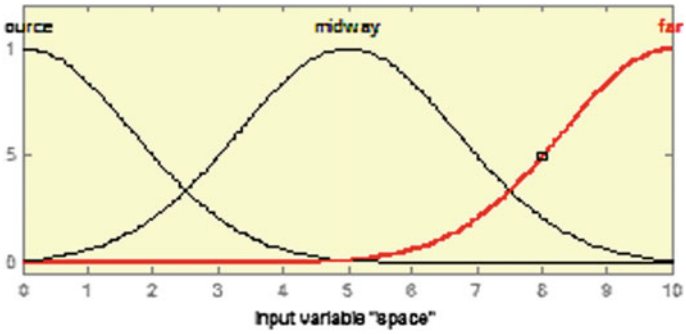

Fig. 1 Fuzzification of space (x) input variable

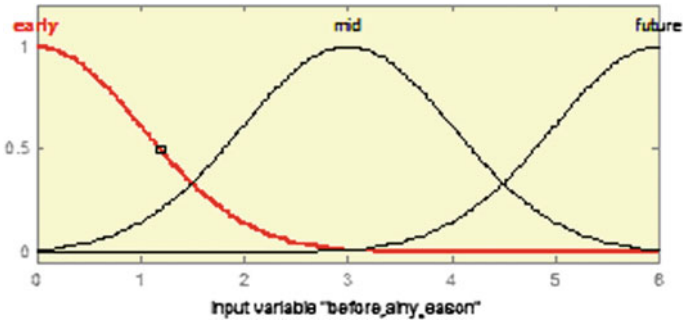

Fig. 2 Membership function of input variable A

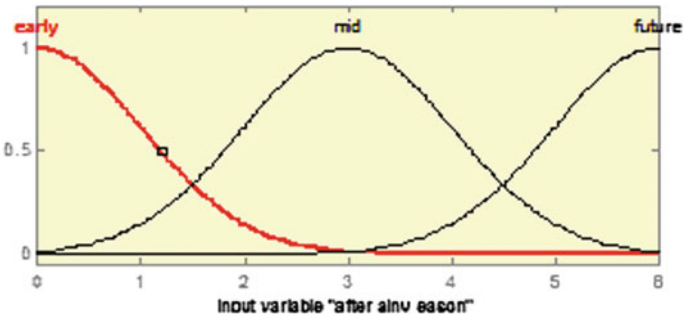

Fig. 3 Membership function of input variable *B*

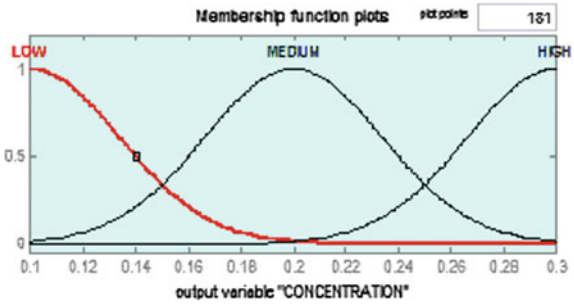

Fig. 4 Fuzzification of output variable *C* (After rainy season)

Fig. 5 Fuzzification of output variable *C* (Before rainy season)

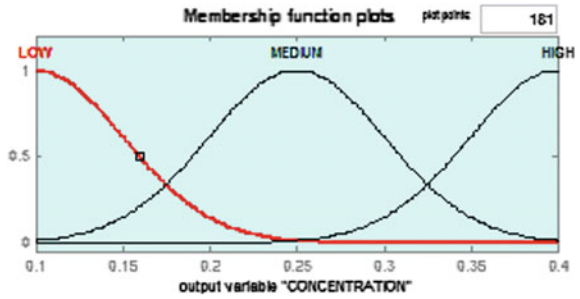

solution of Eq. (1) under (2), (3a, b), (4) and (5), a sample of concentration is derived from MATLAB given in the following Table 1 and initial velocity is taken as 0.01 km/per day. Table 1 contains the data for solute concentration in "after rainy season".

Table 1 Solute concentration with spatial variable

mt (time)	Space (s)	Conc (c)	*mt* (time)	Space (s)	Conc (c)	*mt* (time)	Space (s)	Conc (c)	*mt* (time)	Space (s)	Conc (c)
2	0	0.1753	3	0	0.1984	4	0	0.2478	5	0	0.2967
2	0.05	0.1414	3	0.05	0.1635	4	0.05	0.2131	5	0.05	0.2633
2	0.1	0.1217	3	0.1	0.1392	4	0.1	0.1845	5	0.1	0.2338
2	0.15	0.1131	3	0.15	0.1245	4	0.15	0.1621	5	0.15	0.2083
2	0.2	0.1115	3	0.2	0.1173	4	0.2	0.1456	5	0.2	0.1869
2	0.25	0.1128	3	0.25	0.1152	4	0.25	0.1344	5	0.25	0.1696
2	0.3	0.115	3	0.3	0.1158	4	0.3	0.1277	5	0.3	0.1561
2	0.35	0.1175	3	0.35	0.1177	4	0.35	0.1243	5	0.35	0.1461
2	0.4	0.12	3	0.4	0.12	4	0.4	0.1234	5	0.4	0.1392
2	0.45	0.1225	3	0.45	0.1225	4	0.45	0.1241	5	0.45	0.135
2	0.5	0.125	3	0.5	0.125	4	0.5	0.1257	5	0.5	0.1328
2	0.55	0.1275	3	0.55	0.1275	4	0.55	0.1278	5	0.55	0.1322
2	0.6	0.13	3	0.6	0.13	4	0.6	0.1301	5	0.6	0.1327
2	0.65	0.1325	3	0.65	0.1325	4	0.65	0.1325	5	0.65	0.134
2	0.7	0.135	3	0.7	0.135	4	0.7	0.135	5	0.7	0.1358
2	0.75	0.1375	3	0.75	0.1375	4	0.75	0.1375	5	0.75	0.1379
2	0.8	0.14	3	0.8	0.14	4	0.8	0.14	5	0.8	0.1402
2	0.85	0.1425	3	0.85	0.1425	4	0.85	0.1425	5	0.85	0.1426
2	0.9	0.145	3	0.9	0.145	4	0.9	0.145	5	0.9	0.145
2	0.95	0.1475	3	0.95	0.1475	4	0.95	0.1475	5	0.95	0.1475
2	1	0.15	3	1	0.15	4	1	0.15	5	1	0.15

Model I

First, we set up inference rule between B, x and C. We set up a logic flow for the TISO Mamdani model where two input "space (x)" and "after rainy season (B)" gives output "solute concentration (C)".
Rule 1. If x is source or B is early, then C is high.
Rule 2. If x is midway or B is early, then C is medium.
Rule 3. If x is far or B is early, then C is Low.
Rule 4. If x is source and B is mid, then C is medium.
Rule 5. If x is midway or B is mid, then C is low.
Rule 6. If x is far or B is mid, then C is low.
Rule 7. X is source and B is future, then C is high.
Rule 8. If x is midway or B is future, then C is medium.
Rule 9. If x is far or B is future, then C is low.
The logic flow of TISO inference system is given in Fig. 6:

.

Using fuzzy toolbox of MATLAB by Mamdani model, Figs. 7 and 8 have been drawn. Figure 7 shows the solute concentration "after rainy season" in first year in different space, and Fig. 8 shows the relationship in fuzzy model between solute concentration and space in first year (Fig. 9).

Model II

Next, we consider the input variable "before rainy season (A)", space (x) and the output variable "solute concentration (C)". In the universe of discourse, the intervals for A, x and C are considered to be [0, 6], [0, 10] and [0.1, 0.4], respectively. Table 2 shows the analytical solution of Eq. (1) for solute concentration in first year for "before rainy season".

The inference rule for the variables x, A and C are given as follows:

1. If x is source and A is early, then C is high
2. If x is source and A is mid, then C is high
3. If x is source and A is future, then C is high
4. If x is midway and A is early, then C is low
5. If x is midway and A is mid, then C is low
6. If x is midway and A is future, then C is medium
7. If x is far and A is early, then C is medium
8. If x is far and A is mid, then C is low
9. If x is far and A is future, then C is low

Figure 11 shows the defuzzified value of solute concentration in the first year of "before rainy season" in the space of 10-km span. Figure 10 shows a relationship between the solute concentration and space in defuzzified form in the span of mt [6, 8]. All the defuzzification occurs in centroid method (Fig. 12).

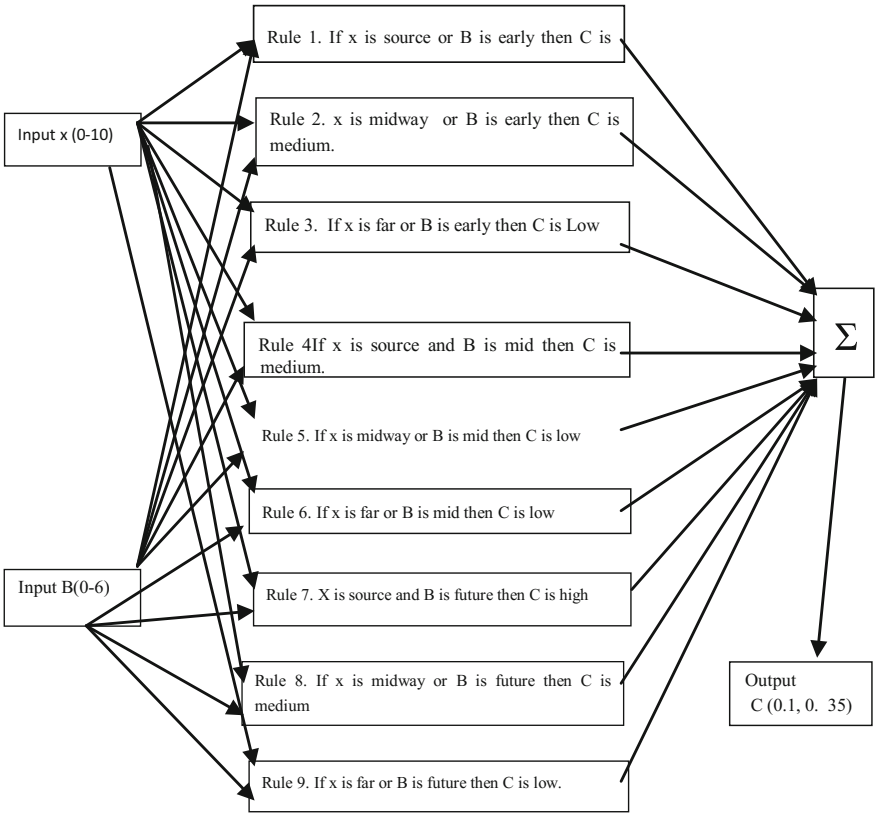

Fig. 6 Logic flow chart of TISO inference model I

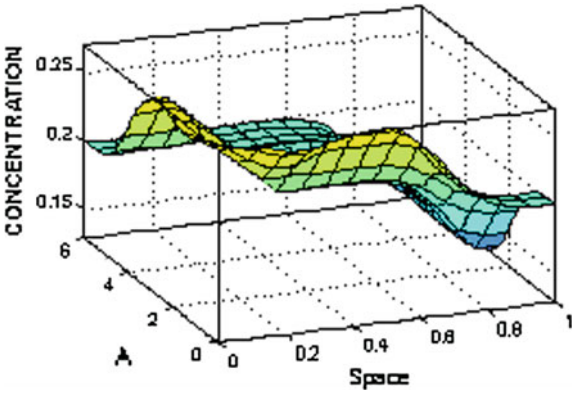

Fig. 7 Solute concentration for first year "after rainy season"

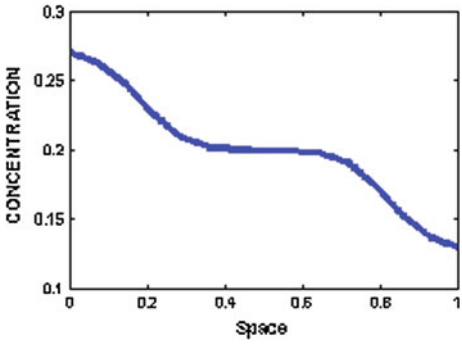

Fig. 8 Solute concentration with space

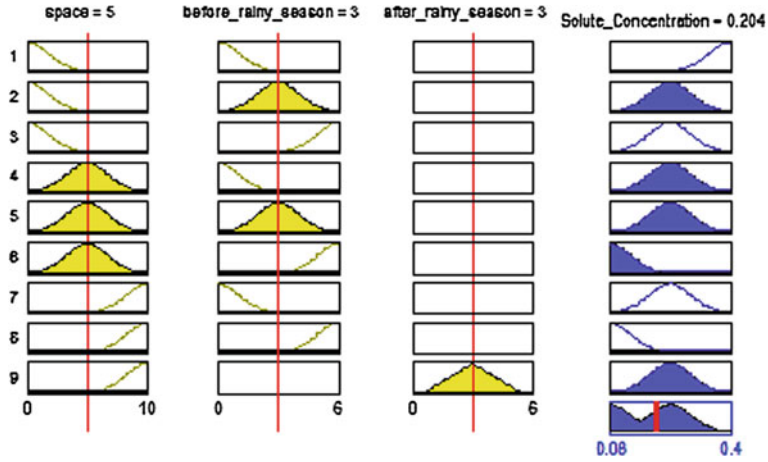

Fig. 9 Rule viewer for Mamdani model I

Fig. 10 Concentratrion with space

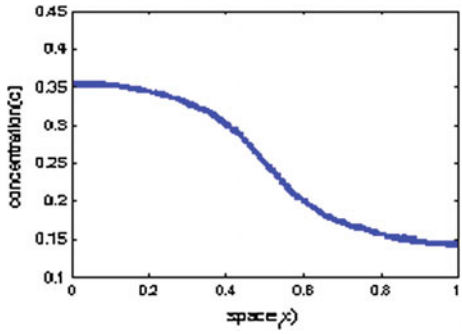

Table 2 Solute concentration in first year for "before rainy season"

Space (s)	*mt* (time)	Conc (c)	Space (s)	*mt* (time)	Conc (c)	Space (s)	*mt* (time)	Conc (c)
0	6	0.3296	0	7	0.3433	0	8	0.345
0.05	6	0.2974	0.05	7	0.3117	0.05	8	0.3134
0.1	6	0.2681	0.1	7	0.2825	0.1	8	0.2843
0.15	6	0.2418	0.15	7	0.2562	0.15	8	0.2579
0.2	6	0.2187	0.2	7	0.2326	0.2	8	0.2343
0.25	6	0.1989	0.25	7	0.212	0.25	8	0.2136
0.3	6	0.1822	0.3	7	0.1943	0.3	8	0.1959
0.35	6	0.1687	0.35	7	0.1796	0.35	8	0.181
0.4	6	0.1581	0.4	7	0.1676	0.4	8	0.1688
0.45	6	0.1501	0.45	7	0.1583	0.45	8	0.1593
0.5	6	0.1445	0.5	7	0.1512	0.5	8	0.1521
0.55	6	0.1409	0.55	7	0.1463	0.55	8	0.147
0.6	6	0.139	0.6	7	0.1432	0.6	8	0.1438
0.65	6	0.1383	0.65	7	0.1415	0.65	8	0.1419
0.7	6	0.1387	0.7	7	0.141	0.7	8	0.1413
0.75	6	0.1397	0.75	7	0.1414	0.75	8	0.1416
0.8	6	0.1413	0.8	7	0.1424	0.8	8	0.1426
0.85	6	0.1433	0.85	7	0.144	0.85	8	0.1441
0.9	6	0.1454	0.9	7	0.1459	0.9	8	0.146
0.95	6	0.1477	0.95	7	0.148	0.95	8	0.1481
1	6	0.1501	1	7	0.1503	1	8	0.1503

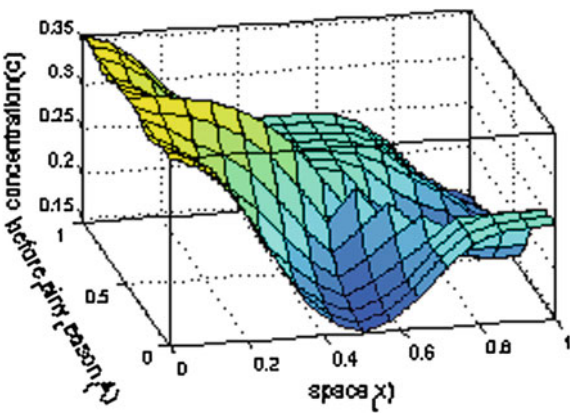

Fig. 11 Solute concentration for first year "before rainy season"

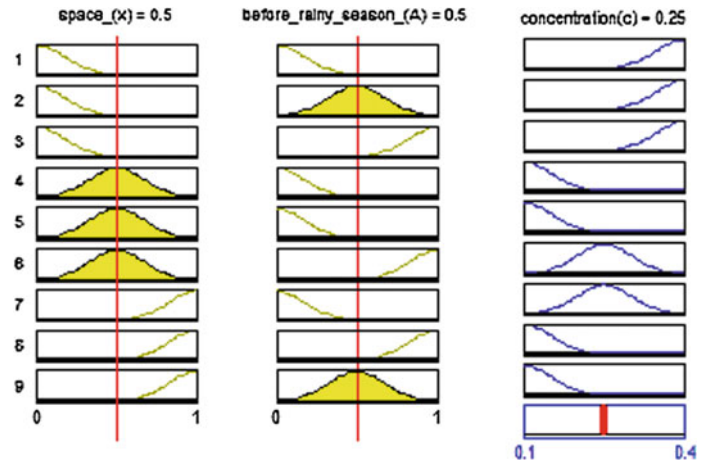

Fig. 12 Rule editor of Mamdani model II

4 Conclusion

The present study considers two variable input space and time, although the groundwater velocity is considered to be time dependent. Kumar and Kumar (1997) derived numerical and analytical solution of the AD equation with appropriate initial and boundary condition by using suitable nondimensionalisation of parameters. The concentration pattern for the solution of Kumar and Kumar (1997) showed the seasonal behaviour with respect to time as well as space. The solution shows that for a concentrated point input at the origin with time-dependent velocity in sinusoidal nature in homogeneous porous media, the solute concentration follows a seasonal pattern over a year in tropical region. But the amount of solute concentration in linguistic terms could not be defined there. The present study forms a linguistic model of solute concentration in seasonal pattern. The results in crisp values are at par with the analytical solution of the AD equation under third-type boundary condition with time-dependent velocity. This model could be further modified to a MISO (multi-input single-output) model of Mamdani inference rule so that in practical field of heterogeneous medium, the solute concentration could be defined in linguistic terms.

References

Bachmat Y, Bear J (1964) The general equations of hydrodynamic dispersion. J Geophys Res 69:2562–2567

Bear J (1972) Dynamics of fluids in porous media. Elsevier, New York, pp 134–135

Chrysikopoulos CV, Roberts PV, Kitanidis PK (1990) One-dimensional solute transport in porous media with partial well-to-well recirculation: application to field experiment. Water Resour Res 26(6):1189–1195

Fried JJ, Combarnous MA (1971) Dispersion in porous media. Adv Hydro Sci 7:169–281

Kumar N, Kumar M (1997) Solute dispersion along unsteady groundwater flow in a semi-infinite aquifer. Hydrol Earth Syst Sci 2(1):93–100

Rumer RR (1962) Longitudinal dispersion in steady and unsteady flow. J Hydraul Div 88:147–173

Scheidegger AE (1961) General theory of dispersion in porous media. J Geophys Res 66:10

Valocchi AJ, Roberts PV (1983) Attenuation of groundwater contaminant pulses. J Hydraul Eng 109(12):1665–1682

Van Genuchten MTh (1981) Analytical solution for chemical transport with simultaneous adsorption, zero order production and first order decay. J Hydrol 49:213–233

Van Genuchten MTh, Alves WJ (1982) Analytical solutions of the one dimensional convective-dispersive solute transport equation. U.S. Department of agriculture technical Bulletin No 1661:151 Washington, DC

Effect of Water Pressure During Abrasive Waterjet Machining of Mg-Based Nanocomposite

Kumari Bimla Mardi, Amit Rai Dixit, Ashish Kumar Srivastava, Ashish Mallick, Jiri Scucka, Petr Hlaváček, Sergej Hloch and Michal Zeleňák

Abstract The pressure of the waterjet influences the overall performance of the abrasive waterjet cutting system through operational and phenomenological effects. In this study, the effect of water pressure in surface quality of Mg-based nanocomposite was investigated. The as-machined surfaces were examined by field emission scanning electron microscope to determine the surface morphology. The surface topography of selected nanocomposite was examined and compared. The results show that the surface quality is better at higher pressure. However, at lower water pressure, there is too much interaction among the low-energy abrasive particles and this may cause insufficient material removal. Abrasive waterjet cutting seems to be promising tool for machining metal matrix composites in terms of no thermal damages, no micro-structural changes and negligible sub-surface damages on the machined surface.

K.B. Mardi (✉) · A.R. Dixit · A.K. Srivastava · A. Mallick
Department of Mechanical Engineering, Indian Institute of Technology (Indian School of Mines), Dhanbad, Dhanbad 826004, Jharkhand, India
e-mail: kbmardi@gmail.com

A.R. Dixit
e-mail: ar.dixit@mece.ism.ac.in

A.K. Srivastava
e-mail: ashish7185@gmail.com

A.K. Srivastava
Noida Institute of Engineering and Technology, Greater Noida, India

J. Scucka · P. Hlaváček · S. Hloch · M. Zeleňák
Department of Material Disintegration, Institute of Geonics Academy of Science of Czech Republic, Studentska, Ostrava, Poruba 708 00, Czech Republic
e-mail: jiri.scucka@ugn.cas.cz

S. Hloch
e-mail: hloch.sergej@gmail.com

M. Zeleňák
e-mail: michal.zelenak@ugn.cas.cz

M.K. Singh et al. (eds.), *Applications of Fluid Dynamics*, Lecture Notes in Mechanical Engineering, https://doi.org/10.1007/978-981-10-5329-0_46

1 Introduction

Abrasive waterjets (AWJs) are mainly formed by high-velocity waterjet, operated at pressure of up to 400 MPa to produce a water stream travelling in a speed of 915 m/s. A stream of abrasive particles is introduced and entrained in the waterjet in such a manner that the waterjet's momentum is transferred to the abrasives. The coherent, abrasive waterjet is produced for propulsion of abrasive particle with high velocity (Benedict 1987). This jet is then directed towards the working area to do the cutting.

The abrasive waterjet machining (AWJM) is an advanced technique that was successfully used for processing wide range of materials such as AA5083-H32 aluminium alloy (Yuvaraja and Kumar 2015), brass-360 (Babu and Muthukrishnan 2014), nickel-based superalloy (Uthayakumar et al. 2016), stainless steel AISI 304 (Singh and Chaturvedi 2014). However, very few literatures are available on AWJM of metal matrix composite materials. Kumar and Kumaresan (2015) presented the investigation on machinability of SiC particle reinforced metal matrix composite during AWJ cutting. They studied the influence of water pressure, traverse rate and standoff distance on surface roughness (SR). They applied the Taguchi's design of experiments to collect surface roughness values. Selvan and Raju (2012) experimented AWJ machining of grey cast iron, to examine the influence of water pressure, traverse speed, nozzle standoff distance and abrasive mass flow rate on surface roughness. They used Taguchi method to find out optimum process parameters. The main observation was all the operational parameters have direct effect on SR but water pressure has the most effect on SR. They discussed that SR values decrease with the increase in pressure due to number of impacting particles increases in machining zone. Hashish (1989) presented the exhaustive review on pressure effects of AWJM. He discussed the influence of pressure on the parameters of cutting performances (depth of cut, specific area generation, maximum cutting traverse rate, surface waviness and cost of cutting) and nozzle operational characteristics (jet spreading characteristics, abrasive particle fragmentation, suction capability, wear of mixing tubes and mixing efficiency). He reported that increasing the pressure will allow the suction of more abrasive flow, with an associated increase in cutting capability. Liu et al. (2003) attempted a computational fluid dynamics (CFD) simulation study on the dynamic characteristics of the abrasive waterjet. They calculated the abrasive particle velocities and trajectories based on the three-phase turbulent flow. They also discussed the distribution of pressure and velocity in the jet axial as well as radial direction. They found that the cutting performance is independent for a typical nozzle standoff distance from 2 to 5 mm, and variation in velocity and dynamic pressure is not significant for 80–90% of the jet diameter. Caydas and Hascalik (2008) developed artificial neural network (ANN) and regression model to predict surface roughness in AWJ machining. The traverse speed, waterjet pressure, standoff distance, abrasive grit size and abrasive flow rate were used as machining parameters. They also conducted the Taguchi's design of experiments for collecting the roughness values.

The main finding was the waterjet pressure found as most dominant parameter on SR followed by traverse speed. They reported that the surface waviness and surface roughness increase with jet pressure.

2 Materials and Methods

In this study, the 6% Al (99.9% purity) balanced by Mg (99.9% purity) supplied by Alfa Aesar (Massachusetts, USA) was taken as matrix material and 0.66 wt% Al_2O_3 nanoparticles supplied by Baikowski (Japan) was taken as reinforcement material. The material was processed by novel manufacturing method, i.e. disintegrated melt deposition method followed by hot extrusion (Hassan et al. 2008). The present method brings together the advantages of both conventional casting and spray deposition to produce bulk material. The benefits of using this method are uniform distribution of particles, fine equiaxed grains and low porosity due to the rapid solidification of the atomized melt leading to improved properties (Gupta and Wong 2015). The basic physical and mechanical property of the constituents of selected nanocomposite is shown in Table 1. The density of the material was measured by Archimedes principle. The hardness and elastic modulus of the mirror-polished samples were measured by nanoindentation testing using XP-nanoindenter (Agilent, USA) in continuous stiffness mode (CSM).

Table 1 Physical and mechanical properties of Mg-6Al/0.66% Al_2O_3 nanocomposite

Material	Density (g/cm^3)	Hardness (GPa)	Elastic modulus (GPa)
Mg-6Al/0.66 Al_2O_3	1.751204	0.8–1.2	47–51

Table 2 Machining condition of AWJ cutting

AWJ device for cutting by PTV: CNC WJ2020B-1Z-D			
Material: Mg-6Al/0.66% Al_2O_3			
Parameters	Symbols	Unit	Value
Pressure of water	P	MPa	400, 100
Traverse speed	v_t	mm/min	40, 20
Thickness of sample	H	mm	8
Abrasive mass flow rate	m_a	g/min	300, 200
Abrasive size	–	mesh	80
Water nozzle diameter	$\varnothing d_o$	mm	0.33
Focusing tube diameter	$\varnothing d_f$	mm	0.9
Standoff distance	Z	mm	2
Position of cutting head	φ	°	90
Abrasives used	–	–	Australian garnet

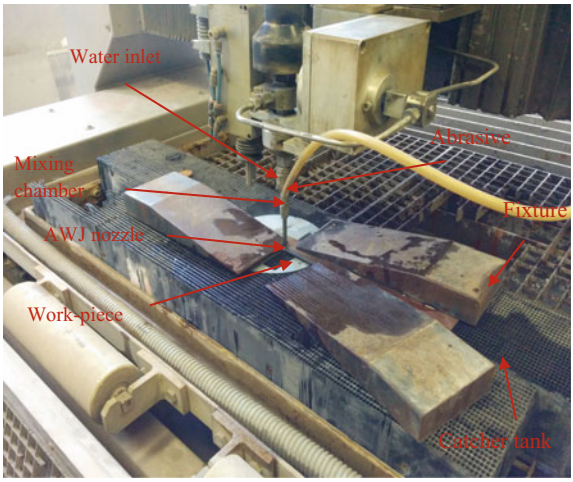

Fig. 1 Experimental set-up for AWJ cutting

2.1 Abrasive Waterjet Machining

The AWJM process was performed on PTV: CNC WJ2020B-1Z-D machine. The machining condition during AWJ cutting is shown in Table 2. Figure 1 illustrates the experimental set-up of AWJ machine. After machining, the machined surfaces were examined by Olympus LEXT OLS 3100 laser confocal microscope and field emission scanning electron microscope (FESEM) for better resolution.

3 Results and Discussion

The AWJ surfaces were examined in terms of topography and surface roughness. Surface topography of AWJ surfaces was examined by Olympus LEXT OLS 3100 laser confocal microscope, and for better resolution surfaces were further investigated by field emission scanning electron microscope (FESEM).

3.1 Surface Topography

Figure 2a, b shows the as-machined AWJ surfaces generated at different pressures. From figure, the cutting traces are apparent and abrasive scooping and ploughing action can also be seen. The surfaces are full of irregular depressions, valleys and peaks. The cutting traces are sometimes interrupted or overlapped by other traces due to collision occurs between abrasives. During high pressure in Fig. 2a, traces are comparatively longer, narrower and approximately parallel than the traces at

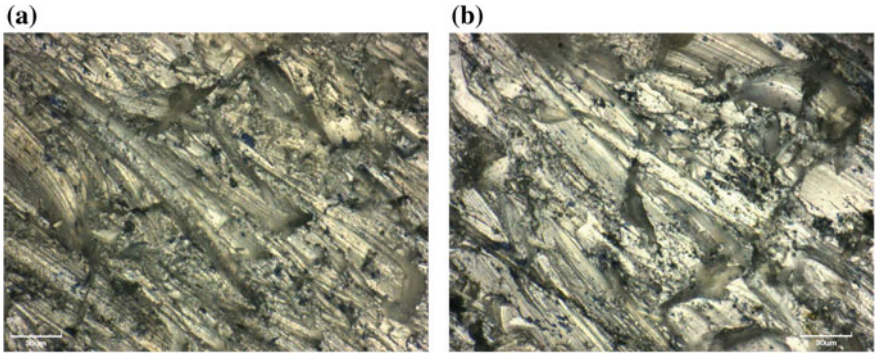

Fig. 2 2D surface detail of as-machined AWJ cutting surface **a** p = 400 MPa, m_a = 300 g/min, v_t = 20 mm/min, **b** p = 100 MPa, m_a = 200 g/min, v_t = 40 mm/min

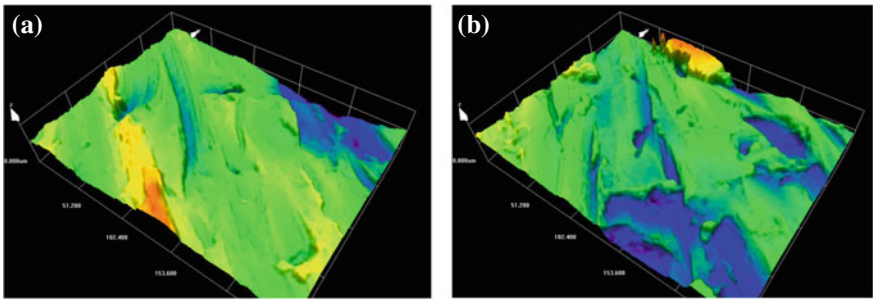

p= 400 MPa, m_a= 300 g/min, v_t= 20 mm/min

p= 100 MPa, m_a= 200 g/min, v_t= 40 mm/min

Fig. 3 3D surface detail (Olympus LEXT OLS 3100 laser confocal microscope)

low pressure. Since, higher jet pressure results into the continuous stream of the abrasive particles with higher kinetic energy. The 3D surface detail of AWJ machined surface was illustrated in Fig. 3. The FESEM micrographs (Fig. 5) clearly show the regular surface generated with high jet pressure compared to the surface at low pressure. The possible reason behind this fact is at increased water pressure the fragmentation of brittle abrasive particles takes place. Therefore, the smaller abrasive particles along with high kinetic energy produce smoother surface. In Fig. 4b, topography shows some deep cutting traces at lower jet pressure, and this may be due to the too much interaction between low-energy abrasive particles which was not observed in surface generated at higher pressure Fig. 4a. The surfaces were also characterized in terms of surface finish that has been discussed in next section.

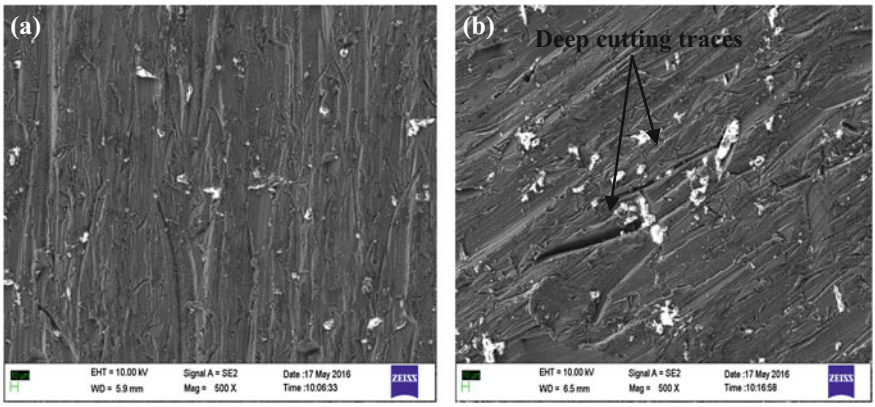

Fig. 4 FESEM micrograph of AWJ machined surface **a** p = 400 MPa, m_a = 300 g/min, v_t = 20 mm/min, **b** p = 100 MPa, m_a = 200 g/min, v_t = 40 mm/min

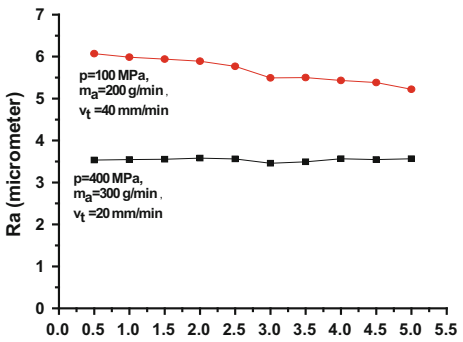

Fig. 5 Effect of water pressure as a function of surface roughness values

3.2 *Surface Roughness*

The surface finish of selected material machined with abrasive waterjet cutting was characterized in terms of average surface roughness (*Ra*). Surface roughness is one of the important response parameters which helps us to determine the micro-effects of each impacting particles. *Ra* was measured using an optical profilometer MicroProf FRT at the Institute of Geonics AS CR, v.v.i. On the machined surface, response value was measured by 10 numbers of lines spaced by 0.5 mm. The effect of water pressure on surface roughness is shown in Fig. 5. It is evident from the figure that there is big difference in *Ra* values as the water pressure changes from 100 to 400 MPa. The values are around 3.4 µm when the water pressure is 400 MPa whereas at 100 MPa pressure, it varies between 5 and 6 µm. The higher value of *Ra* at low pressure indicates insufficient material removal due to low kinetic energy of the abrasive particles. On the other hand, more kinetic energy during 400 MPa waterjet pressure removes maximum amount of material providing

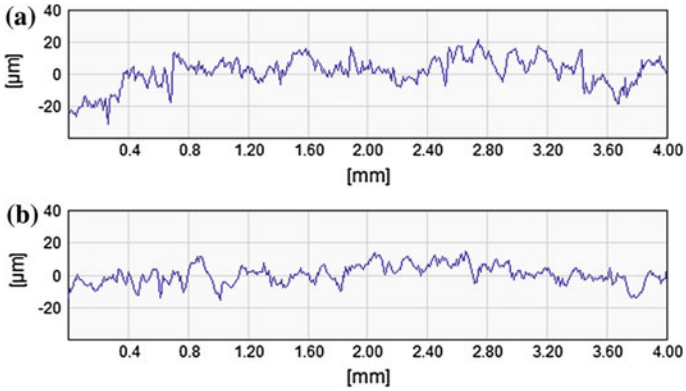

Fig. 6 Profile height (µm) versus transverse length (mm): **a** surface profile for setting parameter, p = 100 MPa, m_a = 200 g/min, v_t = 40 mm/min, **b** surface profile for setting parameter, p = 400 MPa, m_a = 300 g/min, v_t = 20 mm/min

a smooth finish and thus reducing the roughness value. These results can also be correlated with the FESEM micrograph. Since the size of abrasive particle (177 µm) is much bigger than size of reinforcement particle (50 nm), therefore no noticeable effect of nanoparticles on surface roughness was seen.

The surface quality was evaluated using the surface profiles obtained from optical profilometry. Figure 6 shows typical surface profiles obtained under two different experimental conditions. As shown in Fig. 6a, the surface profile for the low pressure AWJM specimen demonstrates irregularly spaced, non-uniform peaks and valleys relative to Fig. 6b. Moreover, the surface profile seems as more random than periodic and this higher degree of randomness indicates a high degree of roughness. Whereas, the surface profile obtained for the 400 MPa waterjet pressure, shown in Fig. 6b, was much more uniform and the variance in peak to valley height is smaller. That indicates comparatively good surface finish.

4 Conclusions and Future Scope

Experimental investigations have been carried out on the surface topography and surface roughness in abrasive waterjet machining of Mg-based nanocomposite. The effects of water pressure on surface roughness have been investigated.

As a result of this study, it is observed that irregular surface finish, deep cutting traces, insufficient cutting and material removal result from low water pressure. On the contrary, the high waterjet pressure leads to increase in kinetic energy of the abrasive particles at maximum level. That results into higher removal of material from the surface. The surface roughness measurement also shows the higher value of *Ra* at lower waterjet pressure, and the decreased value of *Ra* was seen during

machining at high waterjet pressure. This indicates that high waterjet pressure is recommended for good surface finish.

Further investigation regarding plastic deformation of this material due to high pressure waterjet machining can be done. The change in residual stress due to variation in water pressure can also be investigated.

Acknowledgements The authors would like to acknowledge to the Institute of Geonics, Ostrava, 70800, the Czech Republic and the Institute of Materials Research, Slovak Academy of Science, Watsonova 47, 04001 Kosice, Slovakia for their support in some experimental work to carry out. This article was written in connection with the project of the Institute of Clean Technologies for Mining and the Utilization of Raw Materials for Energy Use—Sustainability program, reg. no. LO1406 financed by the Ministry of Education, Youth and Sports of the Czech Republic, and with support for the long-term conceptual development of the research institution RVO: 68145535.

References

Babu MN, Muthukrishnan N (2014) Investigation on surface roughness in abrasive water jet machining by the response surface method. Mater Manuf Process 29(11–12):1422–1428

Benedict GF (1987) Non-traditional manufacturing processes. Manufacturing engineering and material processing, vol 19. Marcel dekker, Inc.

Caydas U, Hascalik A (2008) A study on surface roughness in abrasive waterjet machining process using artificial neural networks and regression analysis method. J Mater Process Technol 202:574–582

Gupta M, Wong WLE (2015) Magnesium-based nanocomposites: lightweight materials of the future. Mater Charact 105:30–46

Hashish M (1989) Pressure effects in abrasive waterjet (AWJ) machining. J Eng Mater Technol 111:221–228

Hassan SF, Tan MJ, Gupta M (2008) High-temperature tensile properties of Mg/Al_2O_3 nanocomposite. Mater Sci Eng A 486:56–62

Kumar BA, Kumaresan G (2015) Abrasive water jet machining of aluminum-silicon carbide particulate metal matrix composites. Mater Sci Forum 830–831:83–86

Liu H, Wang J, Brown RJ, Kelson N (2003) Computational fluid dynamics (CFD) simulation of ultrahigh velocity abrasive waterjet. Key Eng Mater 233–236:477–482

Selvan MCP, Raju NMS (2012) Analysis of surface roughness in abrasive water jet cutting of cast iron. Int J Sci Environ Technol 1(3):174–182

Singh D, Chaturvedi V (2014) Investigation of optimal processing condition for abrasive water jet machining for stainless steel AISI 304 using grey relational analysis coupled with S/N ratio. Appl Mech Mater 592–594:438–443

Uthayakumar M, Khan MA, Kumaran ST, Slota A, Zajac J (2016) Machinability of nickel based superalloy by abrasive water jet machining. Mater Manuf Process 31(13):1733–1739

Yuvaraja N, Kumar MP (2015) Multiresponse optimization of abrasive water jet cutting process parameters using TOPSIS approach. Mater Manuf Process 30(7):882–889

Analytical Solution for Solute Transport Influenced by Spatially Dependent Dispersion Along Spatiotemporally Dependent Porous Media Flow

Abhishek Sanskrityayn and Vinod Kumar Bharati

Abstract One-dimensional pollutant's solute transport originating from the instantaneous source and the continuous point source is studied in aquifer through the analytical solutions of the advection–diffusion equation (ADE). Dispersion coefficient is considered spatially dependent, and flow velocity is considered spatially and temporally dependent. The solution is obtained in infinite domain using Green's Function Method (GFM). To use this method, the variable coefficients of the ADE are reduced into constant coefficients through a pertinently developed coordinate transformation equation. The analytical solutions are validated through previously existing analytical solutions.

1 Introduction

Pollutants originating from continuous or instantaneous sources in the form of industrial and municipal wastes are being discharged into the nearby water bodies of rivers and lakes. Pollutants get infiltrated from rivers and lakes and from dumping garbage sites, mines, etc., into the adjoining groundwater aquifer system. One way to study the transport of such pollutant's mass down the stream of such water bodies and its attenuation with position and time is being studied through analytical and numerical solutions of linear advection diffusion equation (ADE) based on Fick's first and second laws of diffusion.

The heterogeneity of the natural porous media such as aquifer and oil reservoir has been delineated by spatially dependent or temporally dependent dispersion coefficient in the linear ADE. Pickens and Grisak (1981) modeled the heterogeneity of the medium by time-dependent dispersion coefficient of arbitrary forms. Basha and El-Habel (1993) obtained the analytical solution of the one-dimensional advection–diffusion equation (ADE) with time-dependent dispersion coefficient

A. Sanskrityayn (✉) · V.K. Bharati
Department of Mathematics, Institute of Science, Banaras Hindu University, Varanasi 221005, India
e-mail: abhi.bhu2008@gmail.com

M.K. Singh et al. (eds.), *Applications of Fluid Dynamics*, Lecture Notes in Mechanical Engineering, https://doi.org/10.1007/978-981-10-5329-0_47

using GFM (Green's Function Method). Later, this work was extended by Aral and Liao (1996) in two dimensions, and the analytical solutions were obtained using the same method. Some analytical solutions of the ADE have been obtained using linear expressions in position variable for the velocity (Zoppou and Knight 1997; Kumar et al. 2010). Chen et al. (2008) have used an asymptotic function for the dispersion and have solved one- and two-dimensional ADEs using extended power series method coupled with Laplace transform. They have cited a long list of references of the papers using scale-dependent or time-dependent dispersion coefficient. Singh et al. (2009) have obtained the analytical solution of the one-dimensional ADE with sinusoidally varying and exponentially decreasing time-dependent velocity. Guerrero and Skaggs (2010) presented a general analytical solution of one-dimensional ADE using GITT (generalized integral transform technique) with distance-dependent coefficients. Suk (2013) have presented semi-analytical solution for multispecies transport coupled with a sequential first-order reaction network under variable flow velocities and dispersion coefficients by employing GITT and general linear transformation method. You and Zhan (2013) derived solutions for solute transport in one-dimensional finite domains with distance-dependent dispersion coefficient and time-dependent source and compared them with the corresponding solutions for semi-infinite domain to investigate the effects of outer boundary conditions. A significant contribution has been made through a recent paper (Zamani and Bombardelli 2014) by getting analytical solutions of nonlinear advection–diffusion equation with spatiotemporal variability of the velocity and dispersion coefficient.

In an earlier pioneer work using GFM, Yeh (1981) developed a generalized analytical transient, one-, two-, and/or three-dimensional (AT 123D) computer code for estimating the transport of wastes in the groundwater aquifer system. Sternberg et al. (1996) have suggested that the heterogeneity of the porous media along with the effects of velocity fluctuations on dispersive mixing may be modeled more effectively through a dispersion coefficient parameter of the ADE as a function of both space and time. On the basis of this paper, Su et al. (2005) have obtained the analytical solutions of one-dimensional ADE by taking the dispersivity in the form of separable power—law dependence on both time and scale. Selvadurai (2004) has obtained the analytical solution of the ADE with uniform dispersion coefficient and exponentially decaying time-dependent flow velocity, suggesting that if either the porous medium is deformable or the pore fluid is compressible, then flow velocity will be both space- and time-dependent. Jia et al. (2013) presented the semi-analytical solution of the two novel ADE model: one model considered a uniform diffusion coefficient and a linearly increasing flow velocity with position, and the other one considered both transport coefficients linearly increasing with position variable. Sanskrityayn and Kumar (2016) described the heterogeneity of the medium through the temporally dependent dispersion coefficient and spatially and temporally dependent flow velocity and have obtained the analytical solutions using GFM.

In the present study, dispersion coefficient is considered spatially dependent and velocity is considered spatially and temporally dependent. The spatial dependence

delineates the heterogeneity of the medium, and the temporal dependence is considered in the unsteady flow domain. Spatial dependence of dispersion coefficient is considered proportional to the square of that of velocity (Scheidegger 1957). The analytical solutions of the ADE with such parameters as its coefficients are obtained for instantaneous and continuous type sources using GFM. To use this method, ADE is reduced into diffusion equation with source term and constant coefficient through pertinently developed coordinate transformation equation.

2 Mathematical Formulation and Analytical Solution

The transport of solutes in porous media has generally been considered a Fickian diffusive process that is a mechanism governed by the advection–diffusion equation (ADE). The linear ADE in 1D infinite medium in the general form (Scheidegger 1954; Bear and Bachmat 1967; Fried 1975; Matheron and de Marsily 1980) may be written as:

$$\frac{\partial c}{\partial t} = \frac{\partial}{\partial x}\left[D(x,t)\frac{\partial c}{\partial x} - u(x,t)c\right] + q(x,t), \quad -\infty < x < \infty, \quad t > 0 \tag{1}$$

where c is the solute concentration in the domain (x,t) of position and time variables, $q(x,t)$ represents an instantaneous source or continuous source of the dispersing mass introduced in the infinite porous domain. Dispersion coefficient is considered to be spatially dependent and velocity to be spatially and temporally dependent. The spatial dependence owes to heterogeneity of the medium (Pickens and Grisak 1981), and temporal dependence is due to transient flow. Hence, both may be written as $D(x,t) = D_0 f_1(x)$ and $u(x,t) = u_0 f_2(x,t)$, where D_0 and u_0 may be referred to as dispersion coefficient and velocity, respectively, in the homogeneous medium. ADE in Eq. (1) is reduced into a solvable form in a new domain of position and time variables, (X,t'), through appropriate transformation equations

$$X = X(x,t), \quad t' = t \tag{2}$$

In that case ADE in Eq. (1) in terms of new dependent variable $C(X,t')$ may be obtained as

$$\frac{\partial C}{\partial t'} = D_0 f_1 \left(\frac{\partial X}{\partial x}\right)^2 \frac{\partial^2 C}{\partial X^2} - \left[u_0 f_2 \frac{\partial X}{\partial x} + \frac{\partial X}{\partial t'} - D_0 \frac{\partial}{\partial x}\left(f_1 \frac{\partial X}{\partial x}\right)\right]\frac{\partial C}{\partial X} - u_0 \frac{\partial f_2}{\partial x} C + q_1(X,t') \tag{3}$$

As this partial differential equation contains both $f_1(x)$ and $f_2(x,t)$ so to get it in a solvable form we have to proceed with assuming an expression for one of the two

and get another one in the process. Let the expression for the dispersion coefficient be considered as

$$D(x,t) = D_0 f_1(x) = D_0(1+ax)^2, \tag{4}$$

In the process of getting a suitable transformation X in terms of (x,t), an expression for the velocity is introduced as follows (see the Appendix)

$$u(x,t) = u_0 f_2(x,t) = u_0(1+ax)\psi(mt) \tag{5}$$

The constants a and m occurring in the above expressions are referred to as spatial parameter and temporal parameter, respectively, of dimensions so that ax and mt are dimensionless. Using the expressions in Eqs. (4) and (5), the ADE in the domain $-\infty < x < \infty$ and $t > 0$ may be written as

$$\frac{\partial c}{\partial t} = \frac{\partial}{\partial x}\left[D_0(1+ax)^2\frac{\partial c}{\partial x} - u_0(1+ax)\psi(mt)c\right] + q(x,t) \tag{6}$$

To get its analytical solution, an initial condition is assumed as

$$c(x, t=0) = C_i\omega(x) \tag{7}$$

The ADE in Eq. (6) is reduced into a solvable form

$$\frac{\partial C}{\partial t'} = D_0\frac{\partial^2 C}{\partial X^2} - u_0\frac{\partial C}{\partial X} - au_0\psi(mt')C + q_1(X,t'), \tag{8}$$

by developing a coordinate transformation equations (see the Appendix)

$$X = \frac{1}{a}\log|1+ax| + \int_0^t (u_0 + aD_0 - u_0\psi)\mathrm{d}v; \quad t' = t \tag{9}$$

Further using following transformations (now onwards t' is written as t simply for convenience)

$$\eta = X - u_0 t, \tag{10}$$

$$K(\eta,t) = C(\eta,t)\beta(t), \tag{11}$$

where

$$\beta(t) = \exp\left(au_0\int_0^t \psi(mv)\mathrm{d}v\right), \tag{12}$$

one by one, ADE in Eq. (8) may be reduced in a diffusion equation with constant coefficient

$$\frac{\partial K}{\partial T} = D_0 \frac{\partial^2 K}{\partial \eta^2} + Q(\eta, T)\beta(t), \tag{13}$$

where the non-homogeneous term $Q(\eta, T)$ is the source term in the new domain of position and time. The initial condition may be written as

$$K(\eta, T = 0) = C_i \omega_1(\eta) \quad -\infty < \eta < \infty, \quad T > 0 \tag{14}$$

Now, the solution of the problem comprising of Eqs. (13) and (14) in the infinite domain may be obtained by using the Green's Function Method (Haberman 1987; Basha and El-Habel 1993) as

$$\begin{aligned} K(\eta, T) = &\int_0^t \int_{-\infty}^{\infty} \frac{1}{\sqrt{4\pi D_0 (t - t_0)}} \exp\left\{ -\frac{(\eta - \chi)^2}{4D_0(t - t_0)} \right\} Q(\chi, \zeta)\beta(\zeta) \mathrm{d}\chi \mathrm{d}\zeta \\ &+ C_i \int_{-\infty}^{\infty} \frac{1}{\sqrt{4\pi D_0 t}} \exp\left\{ -\frac{(\eta - \chi)^2}{4D_0 t} \right\} \omega_1(\chi) \mathrm{d}\chi \end{aligned} \tag{15}$$

where χ and ζ are the dummy variables.

Using back the transformations used above, the desired solution $c(x, t)$ may be written as

$$\begin{aligned} c(x,t) = &\int_0^t \int_{-\infty}^{\infty} \frac{1}{\sqrt{4\pi D_0 (t - t_0)}} \exp\left[-\frac{1}{4D_0(t - t_0)} \left\{ \begin{array}{l} \frac{1}{a}\log\frac{1 + ax}{a\xi} \\ + \int_{t_0}^{t} (aD_0 - u_0\psi)\mathrm{d}v \end{array} \right\}^2 \right] \frac{Q_1(\xi, t_0)\beta(t_0)}{a\xi\beta(t)} \mathrm{d}\xi \mathrm{d}t_0 \\ &+ \frac{C_i}{\sqrt{4\pi D_0 t}} \int_{-\infty}^{\infty} \exp\left\{ -\frac{(\eta - \chi)^2}{4D_0 t} \right\} \frac{\omega_1(\chi)}{\beta(t)} \mathrm{d}\chi; \end{aligned} \tag{16}$$

where

$$Q_1(\xi, t_0) = q\left[\xi - \frac{1}{a}, t_0 \right], \tag{17}$$

$$\omega_1(\chi) = \omega\left[\exp(a\chi) - \frac{1}{a} \right] \tag{18}$$

The injected source may be instantaneous, pulse type, or continuous. In the first type of point source, the time of injection is very small; in the second type of

source, it is for a finite period of time; and in the last type, the source exists continuously. Solutions are obtained for the instantaneous source and the continuous source, respectively. For discussion and illustration of the solutions in different cases, the domain is considered initially solute-free that is $C_i = 0$ is considered in Eq. (7).

2.1 Instantaneous Point Injection

The instantaneous source introduced at the origin is defined as

$$q(x,t) = M\delta(x)\delta(t) \tag{19}$$

where M is the injected pollutant mass in the water body, $\delta(x)$ is the Dirac delta function. In the present study, $\delta(x)$ is considered. From analytical solution (16), we may have

$$c(x,t) = \frac{1}{\beta(t)}\frac{1}{\sqrt{4\pi D_0 t}}\exp\left[-\frac{1}{4D_0 t}\left\{\frac{1}{a}\log(1+ax) + \int_0^t (aD_0 - u_0\psi)\mathrm{d}v\right\}^2\right] \tag{20}$$

2.2 Continuous Point Injection

Continuous source introduced at the origin of the temporally dependent flow domain may be defined as

$$q(x,t) = C_0 u(0,t)\delta(x), \quad t > 0 \tag{21}$$

where $u(x,t)$ is the velocity at each position x at a time t. The solution for the solute transport from continuous source may be obtained from that in Eq. (16) as

$$c(x,t) = C_0 \int_0^t \frac{u(0,t_0)}{\sqrt{4\pi D_0(t-t_0)}}\exp\left[-\frac{1}{4D_0(t-t_0)}\left\{\frac{1}{a}\log(1+ax) + \int_{t_0}^t (aD_0 - u_0\psi)\mathrm{d}v\right\}^2\right] \times \frac{\beta(t_0)}{\beta(t)}\mathrm{d}t_0 \tag{22}$$

As $a \to 0$ (spatially independent velocity and dispersion coefficient), the two solutions in Eqs. (20) and (22) reduce to those in Eqs. (30) and (32) of

Sanskrityayn and Kumar (2016) under the limit $\alpha = 0$ and temporally independent dispersion coefficient, for instantaneous and continuous sources, respectively. Four expressions of $\psi(mt)$ are considered and the respective solutions are obtained as follows:

(i) $\psi(mt) = 1$. Using Eqs. (20) and (22), the respective solutions for instantaneous and continuous injection sources may be obtained as

$$c(x,t) = \frac{\exp(-au_0 t)}{\sqrt{4\pi D_0 t}} \exp\left[-\frac{1}{4D_0 t}\left\{\frac{1}{a}\log(1+ax) + (aD_0 - u_0)t\right\}^2\right] \tag{23}$$

and

$$c(x,t) = C_0 \int_0^t \frac{u_0}{\sqrt{4\pi D_0 (t-t_0)}} \exp\left[-\frac{1}{4D_0(t-t_0)}\left\{\frac{1}{a}\log(1+ax) + (aD_0 - u_0)(t-t_0)\right\}^2\right] \times \frac{\exp(au_0 t_0)}{\exp(au_0 t)} \mathrm{d}t_0 \tag{24}$$

(ii) $\psi(mt) = \exp(-mt)$. It is an exponentially decelerating function. This expression is also considered by Selvadurai (2004) to describe the solute transport from a continuous source of uniform dispersion coefficient in the temporally dependent porous medium flow. Using Eqs. (20) and (22), the respective solutions for instantaneous and continuous injection sources may be obtained as

$$c(x,t) = \frac{1}{\beta(t)\sqrt{4\pi D_0 t}} \exp\left[-\frac{1}{4D_0 t}\left\{\frac{1}{a}\log(1+ax) + aD_0 t - \frac{u_0}{m}(1-\exp(-mt))\right\}^2\right] \tag{25}$$

and

$$c(x,t) = \frac{C_0 u_0}{\beta(t)} \int_0^t \frac{\exp(-mt_0)}{\sqrt{4\pi D_0 (t-t_0)}} \exp\left[-\frac{1}{4D_0(t-t_0)}\left\{\frac{1}{a}\log(1+ax) + aD_0(t-t_0) - \frac{u_0}{m}(\exp(-mt_0) - \exp(-mt))\right\}^2\right] \times \beta(t_0)\mathrm{d}t_0, \tag{26}$$

where $\beta(t) = \exp\{au_0(1 - e^{-mt})/m\}$ and m represents the temporally dependent parameter. As $a \to 0$, the solution in Eq. (26) reduces to the solution obtained by Selvadurai (2004).

(iii) $\psi(mt) = \exp(mt)$. It is an exponentially accelerating function. Using Eqs. (20) and (22), the respective solutions for instantaneous and continuous injection sources may be obtained as

$$c(x,t) = \frac{1}{\beta(t)\sqrt{4\pi D_0 t}} \exp\left[-\frac{1}{4D_0 t} \left\{ \frac{1}{a}\log(1+ax) + aD_0 t + \frac{u_0}{m}(1 - \exp(mt)) \right\}^2 \right] \tag{27}$$

and

$$c(x,t) = \frac{C_0 u_0}{\beta(t)} \int_0^t \frac{\exp(mt_0)}{\sqrt{4\pi D_0 (t-t_0)}} \exp\left[-\frac{1}{4D_0(t-t_0)} \left\{ \frac{1}{a}\log(1+ax) + aD_0(t-t_0) + \frac{u_0}{m}(\exp(mt_0) - \exp(mt)) \right\}^2 \right] \beta(t_0)\mathrm{d}t_0, \tag{28}$$

where $\beta(t) = \exp\{au_0(e^{mt} - 1)/m\}$.

(iv) $\psi(mt) = (1+mt)^{-1}$. It is decelerating asymptotically from 1 at $t = 0$ to 0 as $t \to \infty$. Using Eqs. (20) and (22), we obtain the respective solutions for instantaneous and continuous injection sources as

$$c(x,t) = \frac{1}{\beta(t)\sqrt{4\pi D_0 t}} \exp\left[-\frac{1}{4D_0 t} \left\{ \frac{1}{a}\log(ax+1) + aD_0 t - \frac{u_0}{m}\log(1+mt) \right\}^2 \right] \tag{29}$$

and

$$c(x,t) = \frac{C_0 u_0}{\beta(t)} \int_0^t \frac{(1+mt_0)^{-1}}{\sqrt{4\pi D_0 (t-t_0)}} \exp\left[-\frac{1}{4D_0(t-t_0)} \left\{ \frac{1}{a}\log(1+ax) + aD_0(t-t_0) - \frac{u_0}{m}\log\left(\frac{1+mt}{1+mt_0}\right) \right\}^2 \right] \beta(t_0)\mathrm{d}t_0 \tag{30}$$

where $\beta(t) = (1+mt)^{\frac{au_0}{m}}$.

In all the above solution as $a \to 0$, the dispersion coefficient becomes uniform and velocity becomes temporally dependent.

3 Results and Discussion

To illustrate the analytical solutions obtained in the different cases, the values of dispersion coefficient and velocity in homogeneous medium are considered to be $D_0 = 0.2$ m^2/day and $u_0 = 0.25$ m/day, respectively. The domain for illustration is considered to be $0 \leq x(m) \leq 100$. To describe the heterogeneous medium and homogeneous medium, two values of the spatial-dependent parameter are considered to be $a(\mathrm{m}^{-1}) = 0.1, 0.0001)$, respectively, while for representing transient and steady flow, two values of temporally dependent parameter $m(\mathrm{day}^{-1}) = 0.05, 0.0001$, respectively, are considered. The former value of a means the pollutant has spatially dependent dispersion coefficient and the flow has spatially and temporally dependent velocity. The latter value of a represents the uniform dispersion coefficient and temporally dependent velocity. In all the figures, the solid curves represent the solute transport through heterogeneous medium along spatially and temporally dependent flow, and the dashed curves represent the same through the homogeneous medium along the transient flow. These curves describe the solution in Eq. (20) for instantaneous source or Eq. (22) for continuous source, obtained in the present study in the general form. The dotted curves in all the figures represent the solute transport through homogenous medium along the uniform flow, obtained from the two solutions in Eqs. (20) and (22) for the smaller values of the spatial and temporal parameters, given at the outset of this section. These solutions are validated by comparing the proposed solutions with the existing solutions (obtained from the proposed ones as special cases) for instantaneous source and continuous source.

Figure 1 exhibits the solution for the instantaneous source given in Eq. (25) for exponentially decelerating function. The solid and dashed curves, drawn at the time $t(\mathrm{days}) = 25$ and $t(\mathrm{days}) = 50$, represent the concentration level in both heterogeneous $(a = 0.1)$ and homogeneous medium $(a = 0.0001)$, respectively. As evident from the figure, the input concentration (concentration at the origin) decreases very fast with time. The peak value of a concentration curve lowers down with time, but the curve acquires longer domain. This trend of a curve shows that the pollutant is originating from an instantaneous source. These curves reflect that the pollutant transport is faster in heterogeneous medium $(a = 0.1)$ characterized by the lower peak concentration than that in the homogeneous medium $(a = 0.0001)$ characterized by the higher peak. It is due to increased value of dispersion coefficient and the velocity at each position in the former medium than in the latter medium.

Figure 2 illustrates the solutions given in Eqs. (23), (27), and (29) discussed for instantaneous source for three expressions of $\psi(mt)$: uniform function, exponentially accelerating function, and asymptotically decelerating function, respectively,

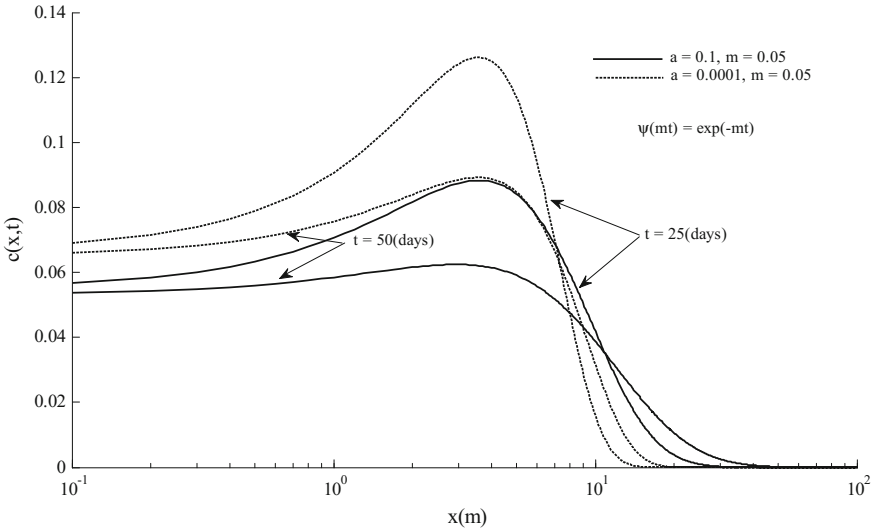

Fig. 1 Concentration level evaluated from the solution (25) due to instantaneous source along unsteady flow in the heterogeneous medium (*solid curves*) and homogeneous medium (*dashed curves*)

at $t = 25$ days. As evident from the figure, the peak concentration values are equal for the two latter expressions of $\psi(mt)$ in the homogeneous medium (dashed curves) due to uniform dispersion coefficient. Also the solute transport is faster in case velocity is exponentially accelerating than that in case of asymptotically decelerating flow due to temporally dependent flow velocity in the homogeneous medium $(a = 0.0001)$. It may further be observed that in the heterogeneous medium $(a = 0.1)$, the concentration peak values are lower than the homogeneous medium due to increased value of dispersion coefficient and velocity at each position of the former medium than those in the latter medium. Hence, the concentration peak values for $\psi(mt) = 1$ is lying between the peak values for other two expressions of $\psi(mt)$. Under the limit $a \to 0$, the proposed analytical solution in Eq. (20) becomes the solution of Sanskrityayn and Kumar (2016). Both the solutions are illustrated in this figure for the same three temporal functions stated above. The proposed solutions represented by dashed curves match perfectly with the respective solutions of Sanskrityayn and Kumar (2016) represented by curves marked with circles.

Figure 3 exhibits the solutions for the continuous source given in Eqs. (24), (26), and (28) for the three expressions of $\psi(mt)$, uniform function, exponentially decelerating function, and exponentially accelerating function, respectively, at $t = 25$ days. The dotted curves represent these solutions describing the solute transport due to uniform dispersion coefficient along steady flow in the homogeneous medium, and the dashed curves represent the solute transport due to uniform dispersion along unsteady flow through the same medium. As evident from the

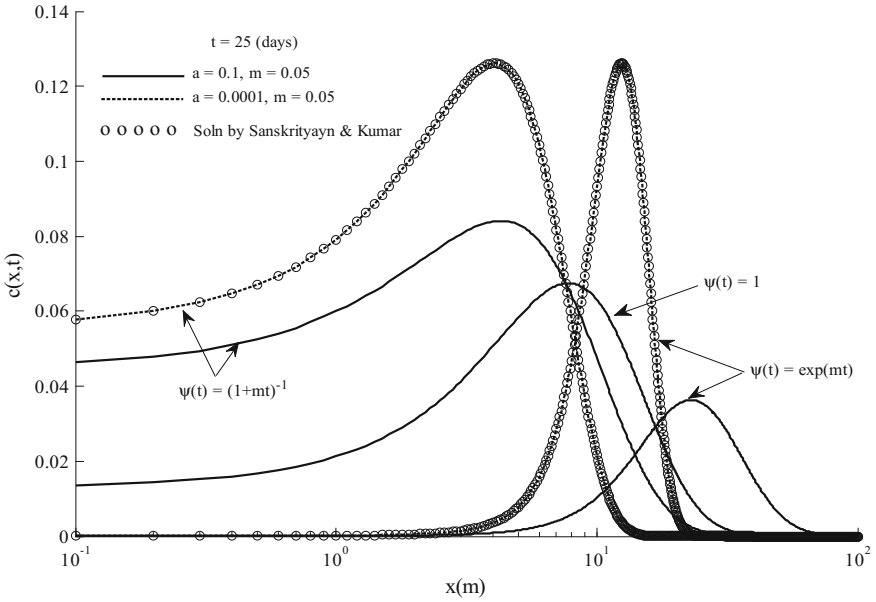

Fig. 2 Effect of heterogeneity on the solute transport from the instantaneous source shown by *solid* and *dashed curves* representing proposed solutions in Eqs. (23), (27), and (29) for two values of spatial parameter *a*, respectively, along with comparison of proposed solution with an existing solution (Sanskrityayn and Kumar 2016)

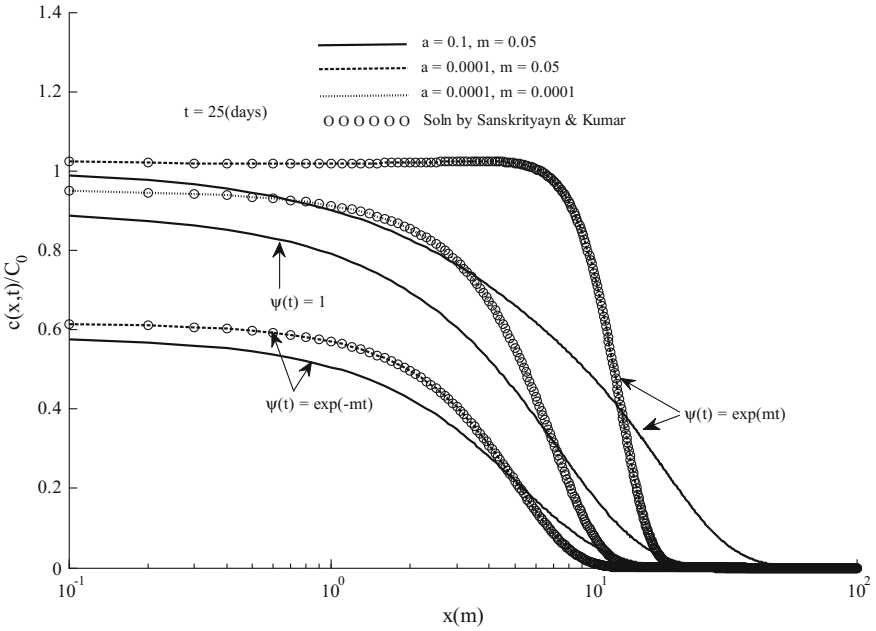

Fig. 3 Effect of heterogeneity on the solute transport due to continuous source demonstrated by the proposed solutions in Eqs. (24), (26), and (28) for two values of *a*, respectively, along with comparison of proposed solution with an existing solution (Sanskrityayn and Kumar 2016)

figure, in the homogeneous medium, the solute transport along exponentially decelerating flow is slower than that along the steady flow, but it is faster along the exponentially accelerating flow. It is due to temporal dependence of flow velocity. The solid curves represent these solutions describing the solute transport due to spatially dependent dispersion coefficient along spatially and temporally dependent steady flow in the heterogeneous medium. Due to increasing spatial dependence, the values of dispersion coefficient and velocity at each position in the heterogeneous medium will be higher than those in the homogeneous medium. Hence, the solute transport is faster in the heterogeneous medium (solid curves) than that in the homogeneous medium (dashed and dotted curves). The concentration values decreases in the vicinity of the origin (source location) in heterogeneous medium than that in the homogeneous medium. As $a \rightarrow 0$, the proposed analytical solution in Eq. (22) becomes the solution of Sanskrityayn and Kumar (2016). Both the solutions are illustrated in this figure for the same three temporal functions stated above. The proposed solutions represented by dashed curves match perfectly with the respective solutions of Sanskrityayn and Kumar (2016) represented by curves marked with circles. Figure 4 verifies the proposed analytical solution in Eq. (26) with previous existing solution of Selvadurai (2004). To draw the present figure, the value of dispersion coefficient and velocity in the homogeneous medium are considered to be $D_0 = 0.005$ m^2/day and $u_0 = 0.25$ m/day, respectively. The solid curves and curves marked with circles drawn, at the time $t(\text{days}) = 5, t(\text{days}) = 25$ and $t(\text{days}) = 50$, represent the proposed solution and the solution of Selvadurai (2004) in the homogeneous medium, respectively. As evident from the figure, both

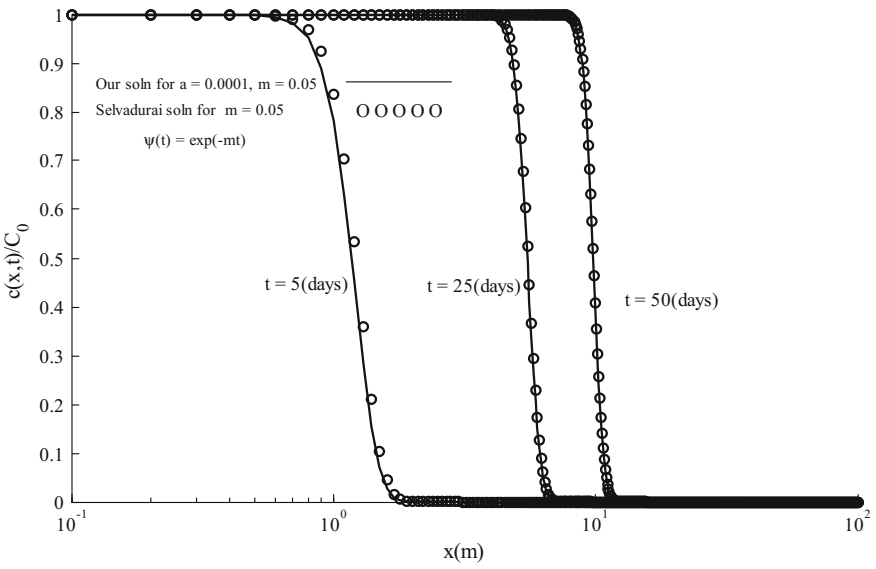

Fig. 4 Comparison of the solution of Selvadurai (2004) shown by curves marked with circles with the proposed solution in Eq. (26) shown by solid curves for a continuous source

the solution curves perfectly match with each other. Hence, the analytical solutions developed in the present study are apropos to more general hydrological conditions influencing the solute transport in groundwater originating from instantaneous and continuous sources.

4 Conclusion

Green's Function Method (GFM) is used to solve a one-dimensional ADE with the source term and with the variable coefficients. The variability of the coefficients describes the heterogeneity of the medium of particulate type in more general way apropos to the theories and experimental field observations (Pickens and Grisak 1981; Scheidegger 1957; Sternberg et al. 1996). The ADE with such coefficients is reduced into a solvable form through a pertinently developed transformation equation defining a new space variable. How the variability of dispersion coefficient with position and velocity with position and time is influencing the solute transport pattern is assimilated through figures. The analytical solutions of the present paper are verified with the previous existing analytical solution. Some known solutions are derived as particular cases from the solutions of the present paper. It accomplishes the validation of the mathematical formulations and analytical procedures obtaining the solutions. Though an ADE with such variable coefficients may be solved using Fourier and Laplace integral transformations in a combined way, in the present study it is not possible due to the fact that it is possible to apply Laplace integral transform on the non-homogeneous source term of the ADE in the transformed independent variables. Hence, GFM is the only option to get the analytical solution.

Acknowledgements The first author acknowledges his gratitude to University Grants Commission, Government of India for financial and academic assistance in the form of Senior Research Fellowship.

Appendix

If the ADEs in Eqs. (3) and (8) are same, then we have

$$f_1\left(\frac{\partial X}{\partial x}\right)^2 = 1, \tag{31}$$

$$u_0 f_2 \frac{\partial X}{\partial x} + \frac{\partial X}{\partial t} - D_0 \frac{\partial}{\partial x}\left(f_1 \frac{\partial X}{\partial x}\right) = u_0, \tag{32}$$

and

$$\frac{\partial f_2}{\partial x} = a\psi(t) \tag{33}$$

Solving (33), we get $f_2(x,t)$; hence, we have

$$u(x,t) = u_0 f_2(x,t) = au_0\psi(t)x + u_0\phi(t) \tag{34}$$

Using Eqs. (31) and (34), Eq. (32) will become

$$\frac{D_0}{2\sqrt{f_1}}\frac{\partial f_1}{\partial x} - (au_0\psi(t)x + u_0\phi(t))\frac{1}{\sqrt{f_1}} - \frac{\partial X}{\partial t} = -u_0 \tag{35}$$

Integrating Eq. (31) with respect to x, we have

$$X = \int \frac{\mathrm{d}x}{\sqrt{f_1}} + \phi_1(t) \tag{36}$$

Using it in Eq. (35), we get

$$u_0 + \frac{D_0}{2\sqrt{f_1}}\frac{\partial f_1}{\partial x} - (au_0\psi(t)x + u_0\phi(t))\frac{1}{\sqrt{f_1}} = \frac{\partial}{\partial t}\left(\int \frac{\mathrm{d}x}{\sqrt{f_1}} + \phi_1(t)\right) \tag{37}$$

For the expression of $f_1(x,t)$ in Eq. (2), above Eq. (37) will become

$$(u_0 + aD_0)(1 + ax) - (au_0\psi(t)x + u_0\phi) = \frac{\mathrm{d}\phi_1}{\mathrm{d}t}(1 + ax) \tag{38}$$

Above equation holds good for

$$a(u_0 + aD_0) - au_0\psi = a\frac{\mathrm{d}\phi_1}{\mathrm{d}t}, \tag{39}$$

and

$$(u_0 + aD_0) - u_0\phi = \frac{\mathrm{d}\phi_1}{\mathrm{d}t} \tag{40}$$

From Eq. (39), we have

$$\phi_1(t) = \int_0^t (u_0 + aD_0 - u_0\psi)\mathrm{d}v \tag{41}$$

Using above equation in (40), we get

$$u_0\phi = u_0\psi \tag{42}$$

So using Eqs. (34) and (42), we have the expression for velocity as in Eq. (5). Also, we may get the transformation equation being used as given in Eq. (9) by using Eq. (2) and Eq. (41) in Eq. (36).

References

Aral MM, Liao B (1996) Analytical solutions for two-dimensional transport equations with time-dependent dispersion coefficients. J Hydrol Eng 1:20–32

Basha HA, El-Habel FS (1993) Analytical solution of the one-dimensional time dependent transport equation. Water Resour Res 29(9):3209–3214

Bear J, Bachmat Y (1967) A generalized theory on hydrodynamic dispersion inporous media. In: IASH symposium on artificial recharge and management of aquifers, vol 72. IASH Publications, pp 7–16. Inter Union Geodynemics. Geophys, Haifa, Israel

Chen JS, Ni CF, Liang CP, Chiang CC (2008) Analytical power series solution for contaminant transport with hyperbolic asymptotic distance-dependent dispersivity. J Hydrol 362(1): 142–149

Fried JJ (1975) Groundwater Pollution. Elsevier, New York

Guerrero JSP, Skaggs TH (2010) Analytical solution for one-dimensional advection-dispersion transport equation with distance-dependent coefficients. J Hydrol 390(1–2):57–65

Haberman R (1987) Elementary applied partial differential equations. Prentice-Hall, Englewood Cliffs

Jia X, Zeng F, Gu Y (2013) Semi-analytical solutions to one-dimensional advection-diffusion equations with variable diffusion coefficient and variable flow velocity. Appl Math Comput 221:268–281

Kumar A, Jaiswal DK, Kumar N (2010) Analytical solutions to one-dimensional advection-diffusion equation with variable coefficients in semi-infinite media. J Hydrol 380:330–337

Matheron G, De Marsily G (1980) Is transport in porous media always diffusive? A counter example. Water Resour Res 16(5):901–917

Pickens JF, Grisak GE (1981) Scale-dependent dispersion in stratified granular aquifer. Water Resour Res 17(4):1191–1211

Sanskrityayn A, Kumar N (2016) Analytical solution of the advection-diffusion equation in heterogeneous infinite medium using Green's function method. J Earth Syst Sci 125(8): 1713–1723

Scheidegger AE (1954) Statistical hydrodynamics in porous media. J Appl Phys 25

Scheidegger AE (1957) The physics of flow through porous media, 3rd edn. University of Toronto Press, Toronto

Selvadurai APS (2004) On the advective-diffusive transport in porous media in the presence of time-dependent velocities. Geophys Res Lett 31:1–5

Singh MK, Singh VP, Singh P, Shukla D (2009) Analytical solution for conservative solute transport in one-dimensional homogeneous porous formations with time-dependent velocity. J Eng Mech 135(9):1015–1021

Sternberg SPK, Cushman JH, Greenkorn RA (1996) Laboratory observation of nonlocal dispersion. Transp Porous Media 13:23–151

Su N, Sander GC, Liu F, Anh V, Barry DA (2005) Similarity solutions for solute transport in fractal porous media using a time- and scale dependent dispersivity. Appl Math Model 29 (9):852–870

Suk H (2013) Developing semi-analytical solutions for multispecies transport coupled with a sequential first-order reaction network under variable flow velocities and dispersion coefficients. Water Resour Res 49:3044–3048

Yeh GT (1981) AT123D: analytical transient one-, two-, and three-dimensional simulation of waste transport in the aquifer system. Environmental Science Division 1439 Report ORNL-5602, Oak Ridge, Tennessee, USA

You K, Zhan H (2013) New solutions for solute transport in a finite column with distance-dependent dispersivities and time-dependent solute sources. J Hydrol 487:87–97

Zamani K, Bombardelli FA (2014) Analytical solutions of nonlinear and variable parameter transport equations for verifications of numerical solvers. Environ Fluid Mech 14:711–742

Zoppou C, Knight JH (1997) Analytical solutions for advection and advection-diffusion equations with spatially variable coefficients. J Hydraul Eng 123:144–148

Part VII
Miscellaneous

Surface Wave Propagation in Inhomogeneous Liquid Layer over a Heterogeneous Anisotropic Elastic Half Space

Pasupati Paul, Santimoy Kundu and Dinbandhu Mandal

Abstract The effect of the inhomogeneity and homogeneity on the dispersion of the Rayleigh-type surface waves in an inhomogeneous liquid layer over a heterogeneous transversely isotopic elastic half space has been discussed. The frequency equation is obtained. The dispersion curve of variation of phase velocity with the wave number is observed and depicted graphically. Also various particular cases have been considered.

1 Introduction

The earth surface structure is not always uniform; one portion of the crust is land, and other three portions are filled by liquid (mainly water). Oceans, rivers contain homogeneous or inhomogeneous liquid. Many researchers have central interest to investigate surface wave propagation in shallow and deep ocean. The study of surface waves has always attracted the interest of the scientific community because of the importance and complexity of the waves that propagate in liquid–solid interfaces.

At earlier, Stoneley (1926), Biot (1952), and Tolstoy (1954) discussed the propagation of elastic waves in an oceanic model consisting of a liquid layer of finite depth lying over an isotropic homogeneous half space. Abubakar and Hudson (1961) studied the dispersive property of liquid overlying a semi-infinite

P. Paul (✉) · S. Kundu
Department of Applied Mathematics, Indian Institute of Technology (Indian School of Mines), Dhanbad, Dhanbad 826004, Jharkhand, India
e-mail: pasupati753@gmail.com

S. Kundu
e-mail: kundu_santi@yahoo.co.in

D. Mandal
Department of Mathematics, Chaibasa Engineering College (Estd. by Govt. of Jharkhand & Run by Techno India under PPP), Chaibasa, Jhinkpani 833215, Jharkhand, India
e-mail: dinbandhumandal@gmail.com

M.K. Singh et al. (eds.), *Applications of Fluid Dynamics*, Lecture Notes in Mechanical Engineering, https://doi.org/10.1007/978-981-10-5329-0_48

homogeneous anisotropic layer. Scholte (1961, 1962), Scott (1970) analyzed the elastic wave propagation in inhomogeneous layer. Gogna (1979), Sharma et al. (1990, 1991), Kaushik and Tomar (1994), Saini and Tomar (1995) studied the surface wave propagation in uniform liquid layer overlying two solid elastic layers. Sharma et al. (1990, 1991), Samal and Chattaraj (2011), Pal and Mandal (2012) investigated surface propagation in the combination of a porous layer and an elastic solid layer under uniform liquid layer. Kumar and Hundal (2007) solved the surface wave propagation by considering incompressible porous half space under a homogeneous finite liquid layer. Kumar et al. (2002), Kumar and Hundal (2007) gave the discussion on inhomogeneous liquid layer over a homogeneous liquid layer and liquid saturated porous half space. Dong and Hovem (2011) studied the interface wave as like fluid–solid interface wave (Scholte wave).

In the present work, we have considered the problem of surface wave propagation (two-dimensional) in an inhomogeneous liquid layer lying over a semi-infinite heterogeneous anisotropic (transversely isotropic) elastic half space. This appears in realistic model of the structure of ocean or river. Here, the waves are termed as Rayleigh-type waves which are propagated in the bottom of ocean. For deep ocean, this interface wave is called Scholte wave. We have assumed the vertically heterogeneity of both layers in which the elastic constants of solid space vary exponentially with the depth.

2 Formulation of the Problem

Here, we have considered an inhomogeneous liquid layer (M_1) of thickness h (ocean) over a heterogeneous anisotropic elastic solid half space (M_2). In the

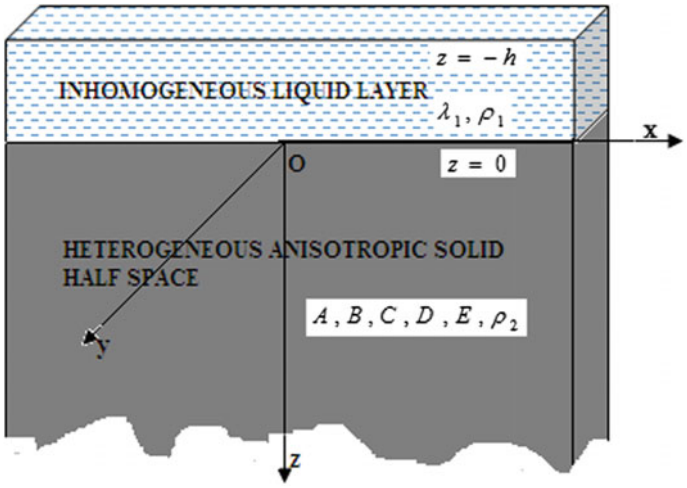

Fig. 1 Geometry of the problem

rectangular Cartesian coordinate system, we have taken the z-axis vertically downwards and x-axis along the interface between two layers. The origin O is chosen on the interface (Fig. 1). Therefore, the media M_1 and M_2 occupy the regions $-h \leq z < 0, 0 \leq z$, respectively.

Since we are discussing the Rayleigh-type surface wave with wave fronts parallel to yz-plane, the components of displacement along the x and z directions are independent of the y coordinate and the displacement components along the y direction are zero.

2.1 Inhomogeneous Liquid Layer (M_1)

For the liquid layer, following Gogna (1969), we consider inhomogeneity varying with depth as

$$\lambda_1 = \lambda_0(1+\alpha z), \quad \rho_1 = \rho_0(1+\alpha z), \tag{1}$$

where λ_0 and ρ_0 are bulk modulus and density at the interface respectively,α is inhomogeneity factor. Let $u_1(x,z,t), w_1(x,z,t)$ are the displacement components of liquid particle along the direction of x,z-axis, respectively.

The Equations of motion of liquid are given by

$$\frac{\partial}{\partial x}(\lambda_1\theta) = \rho_1 \frac{\partial^2 u_1}{\partial t^2}, \quad \frac{\partial}{\partial z}(\lambda_1\theta) = \rho_1 \frac{\partial^2 w_1}{\partial t^2} \tag{2}$$

where $\theta = \frac{\partial u_1}{\partial x} + \frac{\partial w_1}{\partial z}$.

Equation (2) reduces as

$$\left.\begin{aligned} &\frac{\partial^2 u_1}{\partial x^2} + \frac{\partial^2 w_1}{\partial x \partial z} = \frac{1}{c_1^2}\frac{\partial^2 u_1}{\partial t^2} \\ &\frac{\partial^2 u_1}{\partial x \partial z} + \frac{\partial^2 w_1}{\partial z^2} + \left(\frac{\partial u_1}{\partial x} + \frac{\partial w_1}{\partial z}\right)\left(\frac{\alpha}{1+\alpha z}\right) = \frac{1}{c_1^2}\frac{\partial^2 w_1}{\partial t^2} \end{aligned}\right\} \tag{3}$$

where $c_1^2 = \frac{\lambda_0}{\rho_0}$ and since the direction of surface waves propagation is in positive direction of x-axis with a phase velocity c and wave number k, we assume the solutions of Eq. (3) are

$$u_1 = U_1(z)e^{ik(x-ct)}, \quad w_1 = W_1(z)e^{ik(x-ct)} \tag{4}$$

Using (4) in the first equation of (3), we have

$$\frac{dW_1}{dz} + \frac{ia^2}{k}U_1 = 0 \tag{5}$$

where $a^2 = k^2(1 - \frac{c^2}{c_1^2})$.

Again using second equation of (3), (4), and (5), we get

$$\frac{\mathrm{d}^2 W_1}{\mathrm{d}z^2} + \left(\frac{\alpha}{1+\alpha z}\right)\frac{\mathrm{d}W_1}{\mathrm{d}z} - a^2 W_1 = 0 \tag{6}$$

We take transformation as $p = a\frac{1+\alpha z}{\alpha}$, and then Eq. (6) reduces to

$$\frac{\mathrm{d}^2 W_1}{\mathrm{d}p^2} + \frac{1}{p}\frac{\mathrm{d}W_1}{\mathrm{d}z} - W_1 = 0 \tag{7}$$

This is Modified Bessel's equation of order zero.

Then using the solutions of (7) and (5), we get displacement components of (4) as following

$$\left.\begin{aligned} u_1 &= \frac{ik}{a}\left[L_1 I_1\left(a\frac{1+\alpha z}{\alpha}\right) - L_2 K_1\left(a\frac{1+\alpha z}{\alpha}\right)\right]\mathrm{e}^{ik(x-ct)} \\ w_1 &= \left[L_1 I_0\left(a\frac{1+\alpha z}{\alpha}\right) + L_2 K_0\left(a\frac{1+\alpha z}{\alpha}\right)\right]\mathrm{e}^{ik(x-ct)} \end{aligned}\right\} \tag{8}$$

Here L_1, L_2 are arbitrary constants. $I_0(z), K_0(z)$ are modified Bessel's functions first and second kind of order zero and $I_1(z), K_1(z)$ are modified Bessel's functions first and second kind of order one.

2.2 *Heterogeneous Anisotropic Elastic Solid Half Space (M_2)*

The strain energy function for transversely isotropic elastic medium is given by Love (1944).

$$\begin{aligned} 2W^* = {} & A(e_{xx}^2 + e_{yy}^2) + Be_{zz}^2 + 2C(e_{xx} + e_{yy})e_{zz} + 2(A - 2E)e_{xx}e_{yy} \\ & + D(e_{yz}^2 + e_{zx}^2) + Ee_{xy}^2 \end{aligned} \tag{9}$$

where A, B, C, D and E are real and positive elastic parameters, e_{xx}, e_{yy}, etc., are the components of strain. Then the components of stress at any point are given by

$$\tau_{ij} = \frac{\partial W^*}{\partial e_{ij}}, \quad (i, j = x, y, z) \tag{10}$$

Let the displacement components in this media are $u_2 = u_2(x, z, t)$, $v_2 = 0$, $w_2 = w_2(x, z, t)$.

We assume the elastic property of heterogeneous half space varying exponentially, so

$$\{A, B, C, D, \rho_2\} = \{A_0, B_0, C_0, D_0, \rho_{02}\}\mathrm{e}^{bz} \tag{11}$$

and A, B>D

Then the equation of motion for the surface waves without body forces is given by

$$\frac{\partial \tau_{xx}}{\partial x} + \frac{\partial \tau_{xz}}{\partial z} = \rho_2 \frac{\partial^2 u_2}{\partial t^2}, \quad \frac{\partial \tau_{xz}}{\partial x} + \frac{\partial \tau_{zz}}{\partial z} = \rho_2 \frac{\partial^2 w_2}{\partial t^2} \tag{12}$$

Using (9), (10), and (11) in Eqs. (12), we get

$$\left.\begin{aligned} A_0 \frac{\partial^2 u_2}{\partial x^2} + D_0 \frac{\partial^2 u_2}{\partial z^2} + (C_0 + D_0) \frac{\partial^2 w_2}{\partial x \partial z} + bD_0 \left(\frac{\partial u_2}{\partial z} + \frac{\partial w_2}{\partial x} \right) = \rho_{02} \frac{\partial^2 u_2}{\partial t^2} \\ D_0 \frac{\partial^2 w_2}{\partial x^2} + B_0 \frac{\partial^2 w_2}{\partial z^2} + (C_0 + D_0) \frac{\partial^2 u_2}{\partial x \partial z} + b \left(C_0 \frac{\partial u_2}{\partial x} + B_0 \frac{\partial w_2}{\partial z} \right) = \rho_{02} \frac{\partial^2 w_2}{\partial t^2} \end{aligned}\right\} \tag{13}$$

For the propagation of surface wave in the positive x direction, we have

$$u_2 = Me^{-kmz}\mathrm{e}^{ik(x-ct)}, \quad w_2 = Ne^{-kmz}\mathrm{e}^{ik(x-ct)} \tag{14}$$

where M, N are constants, m is real and positive.

From (13) and (14), we get

$$\left.\begin{aligned} Mk[D_0(km^2 - bm) + (\rho_{02}c^2 - A_0)k] - Nik[km(C_0 + D_0) - bD_0] = 0 \\ Mik[(C_0 + D_0)km - bC_0] - Nk[B_0(km^2 - bm) + (\rho_{02}c^2 - D_0)k] = 0 \end{aligned}\right\} \tag{15}$$

Eliminating M, N, we have

$$\begin{vmatrix} D_0(km^2 - bm) + (\rho_{02}c^2 - A_0)k & -i[km(C_0 + D_0) - bD_0] \\ -i[(C_0 + D_0)km - bC_0] & B_0(km^2 - bm) + (\rho_{02}c^2 - D_0)k \end{vmatrix} = 0 \tag{16}$$

or

$$B_0 D_0 \left(km^2 - bm\right)^2 + kG_0\left(km^2 - bm\right) + H_0 = 0 \tag{17}$$

which is the quadratic equation of $km^2 - bm$, where $G_0 = \rho_{02}c^2(B_0 + D_0) + 2C_0D_0 - A_0B_0 + C_0^2$ and $H_0 = (\rho_{02}c^2 - A_0)(\rho_{02}c^2 - D_0)k^2 + b^2C_0D_0$.

Hence $km^2 - bm = \frac{-kG_0 \pm \sqrt{k^2 G_0^2 - 4B_0 D_0 H_0}}{2B_0 D_0} = R_{1,2}$ where upper sign corresponds to R_1 and the lower one corresponds to R_2.

Then we have

$$\left.\begin{aligned} km^2 - bm - R_1 &= 0 \\ km^2 - bm - R_2 &= 0 \end{aligned}\right\} \tag{18}$$

Let m_1, m_2 be two positive and real roots of above two equations.

Then

$$m_1 = \frac{b + \sqrt{b^2 + 4kR_1}}{2k}, \quad m_2 = \frac{b + \sqrt{b^2 + 4kR_2}}{2k}$$

So following (14), we get

$$\left.\begin{aligned} u_2 &= \left(M_1 e^{-km_1 z} + M_2 e^{-km_2 z}\right) e^{ik(x-ct)} \\ w_2 &= \left(n_1 M_1 e^{-km_1 z} + n_2 M_2 e^{-km_2 z}\right) e^{ik(x-ct)} \end{aligned}\right\} \tag{19}$$

where $\frac{N}{M} = \frac{N_j}{M_j} = \frac{D_0(km_j^2 - bm_j) + (\rho_{02} c^2 - A_0)k}{i\left[km_j(C_0 + D_0) - bD_0\right]} = n_j, \quad (j = 1, 2).$

3 Boundary Conditions

The relative boundary conditions are as follows

(a) Vanishing of normal stress component at the free surface of the liquid layer, $z = -h$

i.e., $(\tau_{zz})_1 = \lambda_1 \theta = 0$

(b) Continuity of normal displacement and stress components, vanishing of shear stress at the interface $z = 0$

i.e., $(w_1)_1 = (w_2)_2, \quad (\tau_{zz})_1 = (\tau_{zz})_2, \quad (\tau_{xz})_2 = 0$

Here, the indexes 1, 2 indicate the liquid layer and solid half space, respectively.

4 Dispersion Relation

Using Eqs. (8) and (19) in the above boundary conditions and eliminating L_1, L_2, M_1, M_2, we get a 4×4 determinant equation as follows

$$\begin{vmatrix} I_1(p_1) & -K_1(p_1) & 0 & 0 \\ I_0\left(\frac{a}{\alpha}\right) & K_0\left(\frac{a}{\alpha}\right) & -n_1 & -n_2 \\ \lambda_0 I_1\left(\frac{a}{\alpha}\right) & -\lambda_0 K_1\left(\frac{a}{\alpha}\right) & 2k(B_0 n_1 m_1 - iC_0) & 2k(B_0 n_2 m_2 - iC_0) \\ 0 & 0 & ikn_1 - m_1 & ikn_2 - m_2 \end{vmatrix} = 0 \quad (20)$$

i.e.,

$$S_1\left[I_1(p_1)K_1\left(\frac{a}{\alpha}\right) - K_1(p_1)I_1\left(\frac{a}{\alpha}\right)\right] + 2S_2 ik\left[I_1(p_1)K_0\left(\frac{a}{\alpha}\right) + K_1(p_1)I_0\left(\frac{a}{\alpha}\right)\right] = 0 \quad (21)$$

where

$$p_1 = a\frac{1-\alpha h}{\alpha}, S_1 = \lambda_0(n_1 m_2 - n_2 m_1),$$
$$S_2 = (m_1 - m_2)(B_0 k n_1 n_2 - C_0) + i(n_1 - n_2)(B_0 m_1 m_2 - C_0 k)$$

Equation (21) is called dispersion equation of surface wave propagation in the present model. It is the relation of phase velocity of surface wave to its wave number, multivalued function of phase velocity.

5 Particular Cases

I. If $h = 0$, in the absence of liquid layer, the boundary conditions are reduced to $(\tau_{zz})_2 = 0$, $(\tau_{xz})_2 = 0$ at $z = 0$. Then the simplest form of Eq. (21) is

$$S_2 = 0. \quad (22)$$

This equation is the frequency equation of Rayleigh waves on the free surface of heterogeneous anisotropic elastic half space.

II. If $\alpha = 0$, $b = 0$, then the model will represent the propagation of surface wave in homogeneous liquid overlying a homogeneous anisotropic elastic half space.

III. If $\alpha = 0$, $b \neq 0$, the frequency equation will represent the model consisting uniform liquid layer overlying inhomogeneous transversely isotropic elastic half space.

IV. If $\alpha \neq 0$, $b = 0$, the structure of the oceanic crust layer will be of inhomogeneous liquid layer overlying homogeneous transversely isotropic elastic half space.

V. If $h = \infty$ i.e., for deep liquid layer (in deep ocean), then the Rayleigh-type wave termed as Scholte wave, because it propagates at an interface between a fluid and an elastic solid medium.

6 Numerical Result and Discussion

Here, we have investigated the possibility of the propagation of surface waves discussed above along the x-direction for the present model and some particular cases. We have drawn the graph of the ratio of phase velocity (c) of the surface waves to the velocity (c_1) of the dilatation wave in liquid versus the wave number (kh), which are showing that the surface wave is dispersive.

For liquid layer, we have followed Ewing et al. (1957), the following values

$$\lambda_0 = 0.214 \times 10^{11}\text{dyn/cm}^2, \quad \rho_0 = 1.01\text{g/cm}^3$$

For heterogeneous anisotropic layer, following Love (1944), the values are

$$\begin{aligned} A_0 &= 26.94 \times 10^{11}\ \text{dyn/cm}^2, \\ B_0 &= 23.63 \times 10^{11}\ \text{dyn/cm}^2, \\ C_0 &= 6.53 \times 10^{11}\ \text{dyn/cm}^2, \\ D_0 &= 6.61 \times 10^{11}\ \text{dyn/cm}^2, \\ \rho_{02} &= 2.7\, g/\text{cm}^3 \end{aligned}$$

Gogna (1979), Sharma et al. (1990), Kaushik and Tomar (1994), Saini and Tomar (1995) have also considered the same values in their research paper.

In Figs. 2, 3, and 4, we see that the variation of phase velocity has changed for smaller value of kh and negligible for large value of kh with the different depth of

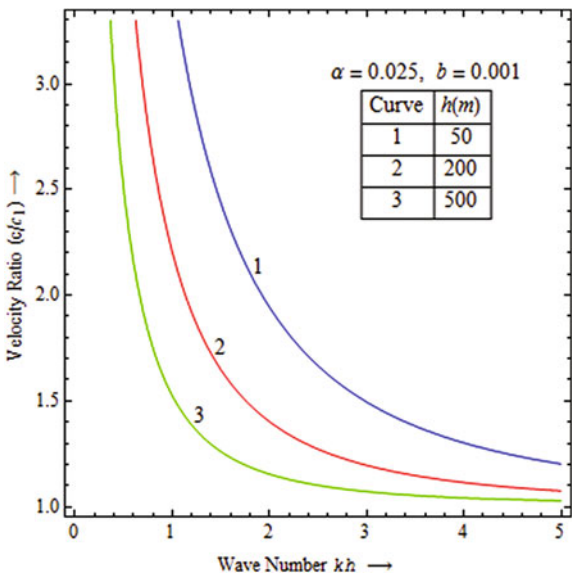

Fig. 2 Variation of phase velocity with wave number ($\alpha = 0.025, \quad b = 0.001$)

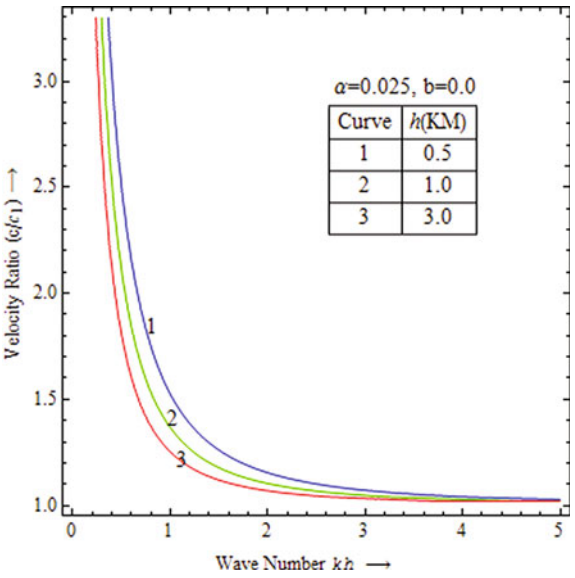

Fig. 3 Variation of phase velocity with wave number ($\alpha = 0.025, \quad b = 0.0$)

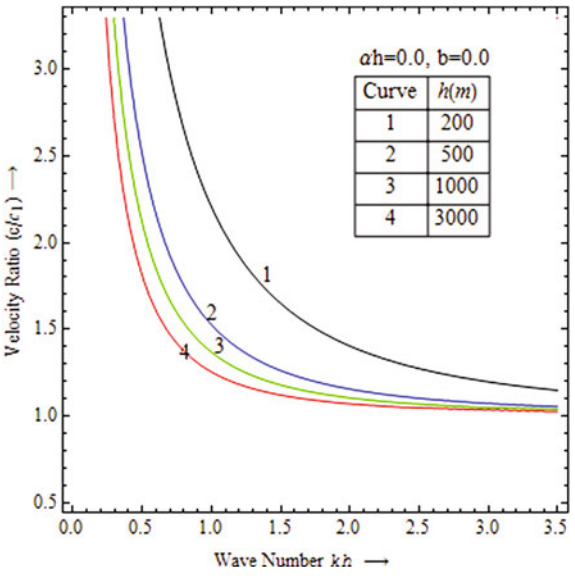

Fig. 4 Variation of phase velocity with wave number ($\alpha h = 0.0, \quad b = 0.0$)

liquid layer by the effect of inhomogeneity of both layers ($\alpha = 0.025, \quad b = 0.001$), inhomogeneity of liquid layer and homogeneity of half space ($\alpha = 0.025, \quad b = 0.0$) and homogeneity of both layers ($\alpha h = 0.0, \quad b = 0.0$), respectively. Figures 5 and 6 show that when one of the medium is homogeneous ($\alpha = 0.0$ or $b = 0.0$), the phase velocity is greater than when same medium is inhomogeneous (($\alpha = 0.5$ *or* $b = 0.005$) for fixed value of kh.

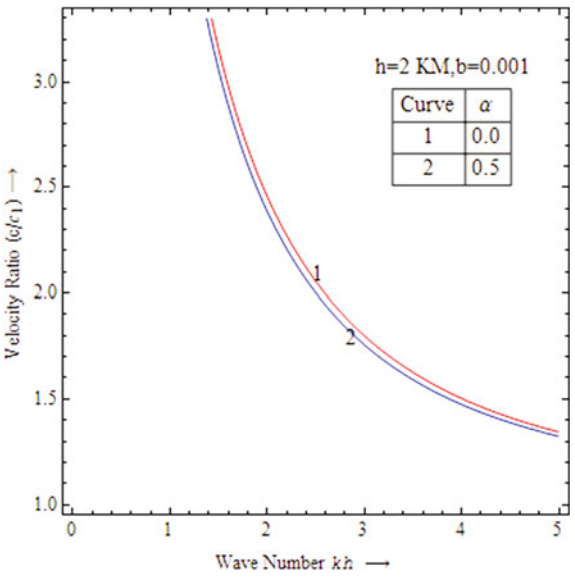

Fig. 5 Variation of phase velocity with wave number ($h = 2$ KM, $b = 0.001$)

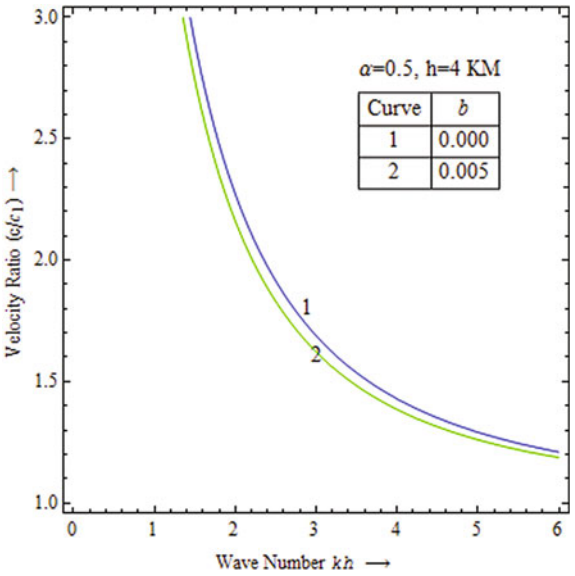

Fig. 6 Variation of phase velocity with wave number ($h = 4$ KM, $\alpha = 0.5$)

7 Conclusion

We conclude that effect of inhomogeneity, homogeneity of both layer and the variation of depth of liquid layer has changed the phase velocity for different frequencies. Thus, using such experiment, we could calculate the dispersion curves and compare them with observed values.

The surface wave propagation in an oceanic crust model has important possible applications in the field of oceanography, seismology, civil engineering, and geosciences aspects. The effect of these waves in shallow or deep ocean on this inhomogeneous structure during earthquakes is a very interesting field of study and research in theoretical seismology. This work can be extended for another structure of oceanic crust model.

References

Abubakar I, Hudson JA (1961) Dispersive properties of liquid overlying an aelotropic half space. Geophys. J Roy Astr Soc 5:217–229

Biot MA (1952) The interaction of Rayleigh and Stoneley waves in the ocean bottom. Bull Seismol Soc Am 42:81–93

Dong H, Hovem JM (2011) Interface waves. In: Vila RP (ed) Waves in fluids and solids. InTech. ISBN: 978-953-307-285-2. Available from: http://www.intechopen.com/books/waves-in-fluids-and-solids/interface-waves

Ewing M, Jardetzky W, Press F (1957) Elastic waves in layered media. McGraw Hill, New York

Gogna ML (1969) Analysis of seismological data. Ph.D. thesis, Cambridge University, Cambridge

Gogna ML (1979) Surface wave propagation in a homogeneous anisotropic layer lying over a homogeneous semi-infinite isotropic half space and under a uniform layer of liquid. Bull Indian Soc Earthq Technol 16:1–12

Kaushik VP, Tomar SK (1994) Surface waves in vertically heterogeneous and transversely isotropic layer overlying a homogeneous isotropic half space and under a uniform layer of liquid. J Phys Earth 42:399–409

Kumar R, Miglani A, Garg NR (2002) Surface wave propagation in a double liquid layer over a liquid-saturated porous half space. Sadhana 27:643–655

Kumar R, Hundal BS (2007a) Surface wave propagation in a fluid-saturated incompressible porous medium. Sadhana 32:155–166

Kumar R, Hundal BS (2007b) Surface wave propagation in a fluid-saturated incompressible porous half space lying under two layers of different liquids. Earth Planets Space 59:926–936

Love AEH (1944) A Treatise on the mathematical theory of elasticity. Dover Publications, New York

Pal PC, Mandal D (2012) Surface waves in fluid-saturated porous layer bounded by a liquid layer and an orthotropic elastic half space. J Info Math Sci 4:39–49

Saini SL, Tomar SK (1995) Surface wave propagation in anisotropic elastic layer sandwiched between a uniform layer of liquid and heterogeneous solid elastic half space. India J Pure Appl Math 26:1021–1033

Samal SK, Chattaraj R (2011) Surface wave propagation in fiber-reinforced anisotropic elastic layer between liquid saturated porous half space and uniform liquid layer. Acta Geo 59:470–482. doi:10.2478/s11600-01100002-8

Scholte JGJ (1961) Propagation of waves in inhomogeneous media. Geophys Prospect 9:87–116

Scholte JGJ (1962) Oblique propagation of waves in inhomogeneous media. Geophys J R Astron Soc 7:244–261

Scott RA (1970) Transient elastic waves in an inhomogeneous layer. Bull Seismol Soc Am 60:383–392

Sharma MD, Kumar R, Gogna ML (1990) Surface wave propagation in a transversely isotropic elastic layer overlying a liquid-saturated porous solid half-space and lying under a uniform layer of liquid. Pure Appl Geophys 133:523–540

Sharma MD, Kumar R, Gogna ML (1991) Surface wave propagation in a liquid-saturated porous layer overlying a homogeneous transversely isotropic half-space and lying under a uniform layer of liquid. Int J Solids Struct 27:1255–1267

Stoneley R (1926) The effect of the ocean on Rayleigh waves. Mon Not R Astron Soc Geophys Suppl 1:349–356

Tolstoy I (1954) Dispersive properties of a fluid layer overlying a semi-infinite elastic solid. Bull Seismol Soc Am 44:493–512

Qualitative Analysis of a Three Species Predator–Prey Model with Stochastic Fluctuation

Soumen Kundu and Sarit Maitra

Abstract In this paper, a multi-team predator–prey model, with two preys and one predator species, has been considered within stochastically fluctuating environment. In the first part, we have studied the stability of the model around the equilibrium points and later, introducing white noise terms to the deterministic model, the effects of stochastic fluctuating environment are studied. Numerical simulations have been performed to examine the stability and other properties of the stochastic model.

1 Introduction

Predator–prey interactions are one of the most important issues of ecology. It can determine the distributions of different species as well as the stability of an ecosystem. Lotka–Volterra model gives a simple mathematical description of the predator–prey interaction. The generalized Lotka–Volterra model involving k preys and k predators is:

$$\frac{\mathrm{d}x_i}{\mathrm{d}t} = x_i\left(a_i - \sum_{j=1}^{k} b_{ij}y_j\right)$$

$$\frac{\mathrm{d}y_i}{\mathrm{d}t} = y_i\left(\sum_{j=1}^{k} c_{ij}y_j - d_i\right) \quad i = 1, 2, \ldots, k \tag{1.1}$$

where constants a_i, d_i are growth rate for the preys and natural death rate for the predators respectively, and b_{ij}, c_{ij} $(i, j = 1, 2, \ldots, k)$ are interaction constants. Though the two species prey–predator model $(k = 2)$ has been studied a lot in

S. Kundu (✉) · S. Maitra
Department of Mathematics, National Institute of Technology, Durgapur, Durgapur 713209, West Bengal, India
e-mail: soumenkundu75@gmail.com

M.K. Singh et al. (eds.), *Applications of Fluid Dynamics*, Lecture Notes in Mechanical Engineering, https://doi.org/10.1007/978-981-10-5329-0_49

different contexts, the investigation of the system with three or more species are rather less in number. Freedman and Waltman (1984) considered the case with predator-mediated coexistence in Lotka–Volterra ordinary differential equation model for two competing species that are preyed by a common predator and showed that the addition of a predator can lead to persistence of the system. Zhang and Zhang (2011) have discussed the dynamical behavior of a stage-structured population model involving gestation delay within stochastically fluctuating environment and harvesting. Saha and Bandyopadhyay (2008) presented the dynamical analysis of a delayed ratio-dependent prey–predator model in fluctuating environment. They pointed out that the gestation delay with large magnitude has the ability to drive the system from a stable to an unstable one. Elettreby (2009) studied the local stability of the predator–prey model in which the prey teams help each other and also studied the global stability and persistence in the absence of cooperation. A lot of literature have discussed the predator-prey interaction in both deterministic and stochastic environment (Choudhury 1992; Kot 2001; Carletti et al. 2004; Bandyopadhyay et al. 2008). Bandyopadhyay and Chattopadhyay (2005) gave a detailed discussion about the stability of a ratio-dependent predator–prey model and the effect of the environmental fluctuation on the stability of the model. Here, in this work we have considered a three species population with two teams of preys with densities $x(t)$ and $y(t)$ interacting with a team of predator with density $z(t)$. Now assume the model as follows:

$$\begin{aligned}
\frac{\mathrm{d}x(t)}{\mathrm{d}t} &= a_1x(t)(1-x(t)) - a_2x(t)z(t) + a_3x(t)y(t)z(t)\\
\frac{\mathrm{d}y(t)}{\mathrm{d}t} &= b_1y(t)(1-y(t)) - b_2y(t)z(t) + a_3x(t)y(t)z(t)\\
\frac{\mathrm{d}z(t)}{\mathrm{d}t} &= -c_1z^2(t) + c_2x(t)z(t) + c_3y(t)z(t)
\end{aligned} \tag{1.2}$$

where $a_1, a_2, a_3, b_1, b_2, c_1, c_2, c_3$ are positive constants and $x(0) > 0, y(0) > 0$, $z(0) > 0$. The terms $a_1x(t)(1-x(t))$ and $b_1y(t)(1-y(t))$ denote the logistic growth of prey species in the absence of predation. The effect of the predation is to reduce the prey growth rate by a term proportional to the prey and predator populations; so the terms $-a_2x(t)z(t)$ and $-b_2y(t)z(t)$ exist. The term $a_3x(t)y(t)z(t)$ represents the cooperation due to presence of the predation. In the absence of any prey, the predator's death rate results in inverse decay which is given by the term $-c_1z^2(t)$. Now the terms $c_2x(t)z(t)$ and $c_3y(t)z(t)$ are the prey's contribution to the predator's growth rate. All the parameter values are measured in units of per day.

In this paper, firstly, in the absence of stochastic fluctuation we have studied the stability of the equilibrium points of the model and then incorporating white noise to the model (1.2), the effects of stochastic fluctuating environment are studied.

2 Deterministic Model and Its Stability Analysis

Linear stability implies that a system is stable over small short-lived disturbances. To check the linear stability, consider the Jacobian matrix of the system (1.2) as follows:

$$J(x,y,z)=\begin{pmatrix} a_1(1-2x)-z(a_2-a_3y) & a_3xz & -x(a_1-a_3y) \\ a_3yz & b_1(1-2y)-z(b_2-a_3x) & -y(b_2-a_3x) \\ c_2z & c_3z & -2c_1z+c_2x+c_3y \end{pmatrix} \tag{2.1}$$

The characteristic equation for the model (1.2) is given by-

$$|J(x,y,z)-\lambda I|=0 \tag{2.2}$$

For the system (1.2), we get several equilibrium points like:

$$E^0(0,0,0), E^1(1,0,0), E^2(0,1,0), E^3(1,1,0), E^4\left(0,\frac{c_1b_1}{b_2c_3+c_1b_1},\frac{c_3b_1}{b_2c_3+c_1b_1}\right),$$

$E^5\left(\frac{c_1a_1}{a_2c_2+a_1c_1},0,\frac{a_1c_2}{a_2c_2+a_1c_1}\right)$ and the interior equilibrium point $E^6(x^*,y^*,z^*)$ where

$$x^*=\frac{\left(\frac{b_1\sqrt{a_1b_1}c_1c_2}{a_2}+\frac{a_1b_1c_1c_3}{a_2}+c_2^2\sqrt{a_1b_1}+b_1c_2c_3+a_1c_3^2+c_3^2\sqrt{a_1b_1}\right)}{a_1c_3^2-b_1c_2^2},$$

$$y^*=\frac{\frac{a_1b_1c_1c_2}{a_2}+\sqrt{a_1b_1}c_2^2+b_1c_2^2+\frac{a_1\sqrt{a_1b_1}c_1c_3}{a_2}+a_1c_2c_3+\sqrt{a_1b_1}c_2c_3}{b_1c_2^2-a_1c_3^2},$$

$$z^*=\frac{\sqrt{a_1b_1}}{a_2}$$

Now we calculate the eigen value of (2.2) at the equilibrium points. For the point $E^0(0,0,0)$ the eigen values are

$$\lambda=0,a_1,b_1. \tag{2.3}$$

Since $a_1,b_1>0$, it is an unstable equilibrium point. Similarly, for

$E^1(1,0,0)$ we get the eigen values,

$$\lambda=-a_1,b_1,c_2 \tag{2.4}$$

Due to $b_1, c_2 > 0$, E^1 is an unstable equilibrium point. Now for $E^2(0,1,0)$ we get

$$\lambda = a_1, -b_1, c_3 \tag{2.5}$$

As $a_1, c_3 > 0$, it is an unstable equilibrium point. Now for $E^3(1,1,0)$ we get

$$\lambda = -a_1, -b_1, c_2 + c_3. \tag{2.6}$$

As $c_2 + c_3 > 0$, it is an unstable equilibrium point. Thus, all of the equilibrium points E^0, E^1, E^2, E^3 are unstable equilibrium points. Now $E^4\left(0, \frac{c_1 b_1}{b_2 c_3 + c_1 b_1}, \frac{c_3 b_1}{b_2 c_3 + c_1 b_1}\right)$ will be locally asymptotically stable if $\left|J\left(0, \frac{c_1 b_1}{b_2 c_3 + c_1 b_1}, \frac{c_3 b_1}{b_2 c_3 + c_1 b_1}\right)\right| < 0$, i.e., if

$$a_1 < \frac{c_3 b_1 (a_2 b_2 c_3 + a_2 c_1 b_1 - a_3 c_1 b_1)}{(b_2 c_3 + c_1 b_1)^2}. \tag{2.7}$$

Similarly, $E^5\left(\frac{a_1 c_1}{a_1 c_1 + a_2 c_2}, 0, \frac{a_1 c_3}{a_1 c_1 + a_2 c_2}\right)$ will be locally asymptotically stable if

$$b_1 < \frac{c_2 a_1 (a_2 b_2 c_2 + b_2 c_1 a_1 - a_3 c_1 a_1)}{(a_1 c_1 + a_2 c_2)^2}. \tag{2.8}$$

and $E^6(x^*, y^*, z^*)$ will be locally asymptotically stable if

$$\begin{aligned} a_1 b_1 > \frac{1}{c_1^3} \big(& -a_2 a_3 c_2 c_3 c_1 - a_2 a_3 c_3^2 c_1 - b_2 a_3 c_2^2 c_1 - a_2 a_3 c_2 c_3 c_1 \\ & + 2 b_2 a_3 c_3^2 c_1 + 4 b_2 a_3 c_1 c_2 c_3 - 2 a_2 b_2 c_2^2 c_1 + 2 a_2 a_3 c_3^2 c_1 \\ & + 2 b_2 a_3 c_2^2 c_1 - 4 a_2 b_2 c_1 c_2 c_3 + 4 a_2 a_3 c_1 c_2 c_3 - 2 a_2 b_2 c_2^2 c_1 \\ & + 2 a_2 a_3 c_2^2 c_1 + b_2 c_2 c_1^2 a_1 - a_3 c_1^2 a_1 - 2 b_2 c_3 c_1^2 a_1 + 2 a_3 c_3 c_1^2 a_1 \\ & - 2 b_2 c_2 c_1^2 a_1 + 2 a_3 c_2 c_1^2 a_1 - a_3 c_3 c_1^2 b_1 + a_2 c_3 c_1^2 b_1 + 2 a_3 c_3 c_1^2 b_1 \\ & + 2 a_3 c_2 c_1^2 b_1 - 2 a_2 c_3 c_1^2 b_1 - 2 a_2 c_2 c_1^2 b_1 \big). \end{aligned} \tag{2.9}$$

Now if $a_3 = 0$, i.e., no mutual help among the preys are occurring against the predator, then E^6 will be locally asymptotically stable if

$$\begin{aligned} a_1 b_1 > \frac{1}{c_1^3} \big(& -2 a_2 b_2 c_2^2 c_1 - 4 a_2 b_2 c_1 c_2 c_3 - 2 a_2 b_2 c_2^2 c_1 + b_2 c_2 c_1^2 a_1 \\ & - 2 b_2 c_3 c_1^2 a_1 - 2 b_2 c_2 c_1^2 a_1 + a_2 c_3 c_1^2 b_1 - 2 a_2 c_3 c_1^2 b_1 - 2 a_2 c_2 c_1^2 b_1 \big) \end{aligned} \tag{2.10}$$

a_1, b_1 are the logistic growth rates of species $x(t), y(t)$, respectively.

3 Effects of Fluctuating Environment on the System

In this section, the effects of the presence of stochastic fluctuation are studied. We introduce white noises in each of the equations of the system (1.2) to take into account the effect of randomly fluctuating environment. Here the effect of the fluctuating environment is manifested due to the variations for the cooperation, predation terms. The stochastic version corresponding to the deterministic model (1.2) with random environment fluctuation takes the following form:

$$\begin{aligned}\frac{dx(t)}{dt} &= a_1x(t)(1-x(t)) - a_2x(t)z(t) + a_3x(t)y(t)z(t) + \sigma_1\xi_1(t)\\ \frac{dy(t)}{dt} &= b_1y(t)(1-y(t)) - b_2y(t)z(t) + a_3x(t)y(t)z(t) + \sigma_2\xi_2(t)\\ \frac{dz(t)}{dt} &= -c_1z^2(t) + c_2x(t)z(t) + c_3y(t)z(t) + \sigma_3\xi_3(t)\end{aligned} \tag{3.1}$$

where σ_i, $i = 1, 2, 3$ are real constants expressing the environmental driving forces and the so-called perturbed terms $\xi_i(t)$, $i = 1, 2, 3$ are mutually independent Gaussian white noises with $\langle\xi_i(t)\rangle = 0$ and $\langle\xi_i(t)\xi_j(t_1)\rangle = \delta_{ij}\delta(t - t_1)$, $i, j = 1, 2, 3.\langle\cdot\rangle$. represents the ensemble average due to the effect of the environmental fluctuation, δ_{ij} is the Kronecker delta expressing the spectral density of the white noise, and δ is the Dirac delta function with t and t_1 being the distinct time. Now we study the dynamic behavior around the interior equilibrium point $E^6(x^*, y^*, z^*)$.

Introducing a transformation of the form $\bar{x} = x - x^*, \bar{y} = y - y^*, \bar{z} = z - z^*$ in Eq. (3.1), we get the following linearized system:

$$\begin{aligned}\frac{d\bar{x}}{dt} &= a_{11}\bar{x} + a_{12}\bar{y} + a_{13}\bar{z} + \sigma_1\xi_1(t)\\ \frac{d\bar{y}}{dt} &= a_{21}\bar{x} + a_{22}\bar{y} + a_{23}\bar{z} + \sigma_2\xi_2(t)\\ \frac{d\bar{z}}{dt} &= a_{31}\bar{x} + a_{32}\bar{y} + a_{33}\bar{z} + \sigma_3\xi_3(t)\end{aligned} \tag{3.2}$$

where $a_{11} = a_1 - 2a_1x^* - a_2z^* + a_3y^*z^*$, $a_{12} = a_3x^*z^*$, $a_{13} = a_3x^*y^* - a_2x^*$, $a_{21} = a_3y^*z^*$, $a_{22} = b_1 - 2b_1y^* - b_2z^* + a_3x^*z^*$, $a_{23} = a_3x^*y^* - b_2y^*$, $a_{31} = c_2z^*$, $a_{32} = c_3z^*$, and $a_{33} = c_3y^* + c_2x^* - 2c_1z^*$

The system of Langevin equations in (3.2) can be written into the matrix form as:

$$\frac{d}{dt}X(t) = AX(t) + C\xi(t) \tag{3.3}$$

where

$$X(t) = \begin{pmatrix} \bar{x}(t) \\ \bar{y}(t) \\ \bar{z}(t) \end{pmatrix} \quad A = \begin{pmatrix} a_{11} & a_{12} & a_{13} \\ a_{21} & a_{22} & a_{23} \\ a_{31} & a_{32} & a_{33} \end{pmatrix},$$

$$C = \begin{pmatrix} \sigma_1 & 0 & 0 \\ 0 & \sigma_2 & 0 \\ 0 & 0 & \sigma_3 \end{pmatrix} \quad \text{and} \quad \xi(t) = \begin{pmatrix} \xi_1(t) \\ \xi_2(t) \\ \xi_3(t) \end{pmatrix}.$$

The solution of (3.3) with the nonnegative initial condition $X(0) = \begin{pmatrix} \bar{x}_0 \\ \bar{y}_0 \\ \bar{z}_0 \end{pmatrix}$, $(\bar{x}_0, \bar{y}_0, \bar{z}_0) > 0$ is given by

$$X(t) = \mathrm{e}^{At} X(0) + \int_0^t \mathrm{e}^{A(t-t_1)} C\xi(t_1) \mathrm{d}t_1 \tag{3.4}$$

Here

$$\mathrm{e}^{At} = \frac{1}{\Delta} \begin{pmatrix} K_{11} & K_{12} & K_{13} \\ K_{21} & K_{22} & K_{23} \\ K_{31} & K_{32} & K_{33} \end{pmatrix} \tag{3.5}$$

where

$$\Delta = \frac{(\lambda_1 - \lambda_2)(\lambda_2 - \lambda_3)(\lambda_3 - \lambda_1)\left[a_{13}^2 a_{21} + a_{13}a_{23}(a_{22} - a_{11}) - a_{12}a_{23}^2\right]}{[a_{12}a_{21} + (a_{11} - \lambda_1)(\lambda_1 - a_{22})][a_{12}a_{21} + (a_{11} - \lambda_2)(\lambda_2 - a_{22})][a_{12}a_{21} + (a_{11} - \lambda_3)(\lambda_3 - a_{22})]}$$

$\lambda_1, \lambda_2, \lambda_3$ are the eigen values for the matrix A, and $K_{11}, K_{12}, K_{13}, K_{21}, K_{22}, K_{23}, K_{31}, K_{32}, K_{33}$ are given by

$$
\begin{aligned}
K_{11} &= [a_{12}a_{23} + a_{13}(\lambda_1 - a_{22})]T_{11}\mathrm{e}^{\lambda_1 t} - [a_{12}a_{23} + a_{13}(\lambda_2 \\
&\quad - a_{22})]T_{12}\mathrm{e}^{\lambda_2 t} + [a_{12}a_{23} + a_{13}(\lambda_3 - a_{22})]T_{13}\mathrm{e}^{\lambda_3 t} \\
K_{12} &= -[a_{12}a_{23} + a_{13}(\lambda_1 - a_{22})]T_{21}\mathrm{e}^{\lambda_1 t} + [a_{12}a_{23} \\
&\quad + a_{13}(\lambda_2 - a_{22})]T_{22}\mathrm{e}^{\lambda_2 t} - [a_{12}a_{23} + a_{13}(\lambda_3 - a_{22})]T_{23}\mathrm{e}^{\lambda_3 t} \\
K_{13} &= -[a_{12}a_{23} + a_{13}(\lambda_1 - a_{22})]T_{31}\mathrm{e}^{\lambda_1 t} + [a_{12}a_{23} \\
&\quad + a_{13}(\lambda_2 - a_{22})]T_{32}\mathrm{e}^{\lambda_2 t} - [a_{12}a_{23} + a_{13}(\lambda_3 - a_{22})]T_{33}\mathrm{e}^{\lambda_3 t} \\
K_{21} &= [a_{13}a_{21} + a_{23}(\lambda_1 - a_{11})]T_{11}\mathrm{e}^{\lambda_1 t} - [a_{13}a_{21} + a_{23} \\
&\quad (\lambda_2 - a_{11})]T_{12}\mathrm{e}^{\lambda_2 t} + [a_{13}a_{21} + a_{23}(\lambda_3 - a_{11})]T_{13}\mathrm{e}^{\lambda_3 t} \\
K_{22} &= -[a_{13}a_{21} + a_{23}(\lambda_1 - a_{11})]T_{21}\mathrm{e}^{\lambda_1 t} + [a_{13}a_{21} \\
&\quad + a_{23}(\lambda_2 - a_{11})]T_{22}\mathrm{e}^{\lambda_2 t} - [a_{13}a_{21} + (\lambda_3 - a_{11})]T_{23}\mathrm{e}^{\lambda_3 t} \\
K_{23} &= -[a_{13}a_{21} + a_{23}(\lambda_1 - a_{11})]T_{31}\mathrm{e}^{\lambda_1 t} + [a_{13}a_{21} \\
&\quad + a_{23}(\lambda_2 - a_{11})T_{32}\mathrm{e}^{\lambda_2 t} - [a_{13}a_{21} + a_{23}(\lambda_3 - a_{11})]T_{33}\mathrm{e}^{\lambda_3 t} \\
K_{31} &= -T_{11}\mathrm{e}^{\lambda_1 t} + T_{12}\mathrm{e}^{\lambda_2 t} - T_{13}\mathrm{e}^{\lambda_3 t} \\
K_{32} &= T_{21}\mathrm{e}^{\lambda_1 t} - T_{22}\mathrm{e}^{\lambda_2 t} + T_{23}\mathrm{e}^{\lambda_3 t} \\
K_{33} &= T_{31}e^{\lambda_1 t} - T_{32}e^{\lambda_2 t} + T_{33}e^{\lambda_3 t}
\end{aligned}
$$

and

$$
\begin{aligned}
T_{11} &= \frac{(\lambda_2 - \lambda_3)\left[a_{11}^2 a_{23} + a_{13}a_{21}(\lambda_2 + \lambda_3 - a_{22}) + a_{23}(\lambda_2\lambda_3 + a_{12}a_{21}) - a_{11}\{a_{13}a_{21} + a_{23}(\lambda_2 + \lambda_3)\}\right]}{[a_{12}a_{21} - (\lambda_1 - a_{11})(\lambda_1 - a_{22})][a_{12}a_{21} - (\lambda_2 - a_{11})(\lambda_2 - a_{22})][a_{12}a_{21} - (\lambda_3 - a_{11})(\lambda_3 - a_{22})]} \\
T_{12} &= \frac{(\lambda_1 - \lambda_3)\left[a_{11}^2 a_{23} + a_{13}a_{21}(\lambda_1 + \lambda_3 - a_{22}) + a_{23}(\lambda_1\lambda_3 + a_{12}a_{21}) - a_{11}\{a_{13}a_{21} + a_{23}(\lambda_1 + \lambda_3)\}\right]}{[a_{12}a_{21} - (\lambda_1 - a_{11})(\lambda_1 - a_{22})][a_{12}a_{21} - (\lambda_2 - a_{11})(\lambda_2 - a_{22})][a_{12}a_{21} - (\lambda_3 - a_{11})(\lambda_3 - a_{22})]} \\
T_{13} &= \frac{(\lambda_1 - \lambda_2)\left[a_{11}^2 a_{23} + a_{13}a_{21}(\lambda_2 + \lambda_1 - a_{22}) + a_{23}(\lambda_2\lambda_1 + a_{12}a_{21}) - a_{11}\{a_{13}a_{21} + a_{23}(\lambda_2 + \lambda_1)\}\right]}{[a_{12}a_{21} - (\lambda_1 - a_{11})(\lambda_1 - a_{22})][a_{12}a_{21} - (\lambda_2 - a_{11})(\lambda_2 - a_{22})][a_{12}a_{21} - (\lambda_3 - a_{11})(\lambda_3 - a_{22})]} \\
T_{21} &= \frac{(\lambda_2 - \lambda_3)[a_{13}(\lambda_2 - a_{22})(\lambda_3 - a_{22}) + a_{12}\{a_{13}a_{21} + a_{23}(\lambda_2 + \lambda_3 - a_{11} - a_{22})\}]}{[a_{12}a_{21} - (\lambda_1 - a_{11})(\lambda_1 - a_{22})][a_{12}a_{21} - (\lambda_2 - a_{11})(\lambda_2 - a_{22})][a_{12}a_{21} - (\lambda_3 - a_{11})(\lambda_3 - a_{22})]} \\
T_{22} &= \frac{(\lambda_1 - \lambda_3)[a_{13}(\lambda_1 - a_{22})(\lambda_3 - a_{22}) + a_{12}\{a_{13}a_{21} + a_{23}(\lambda_1 + \lambda_3 - a_{11} - a_{22})\}]}{[a_{12}a_{21} - (\lambda_1 - a_{11})(\lambda_1 - a_{22})][a_{12}a_{21} - (\lambda_2 - a_{11})(\lambda_2 - a_{22})][a_{12}a_{21} - (\lambda_3 - a_{11})(\lambda_3 - a_{22})]} \\
T_{23} &= \frac{(\lambda_1 - \lambda_2)[a_{13}(\lambda_2 - a_{22})(\lambda_1 - a_{22}) + a_{12}\{a_{13}a_{21} + a_{23}(\lambda_2 + \lambda_1 - a_{11} - a_{22})\}]}{[a_{12}a_{21} - (\lambda_1 - a_{11})(\lambda_1 - a_{22})][a_{12}a_{21} - (\lambda_2 - a_{11})(\lambda_2 - a_{22})][a_{12}a_{21} - (\lambda_3 - a_{11})(\lambda_3 - a_{22})]} \\
T_{31} &= \frac{(\lambda_2 - \lambda_3)\left[a_{13}^2 a_{21} + a_{13}a_{23}(a_{22} - a_{11}) - a_{12}a_{23}^2\right]}{[a_{12}a_{21} - (\lambda_1 - a_{11})(\lambda_1 - a_{22})][a_{12}a_{21} - (\lambda_2 - a_{11})(\lambda_2 - a_{22})][a_{12}a_{21} - (\lambda_3 - a_{11})(\lambda_3 - a_{22})]} \\
T_{32} &= \frac{(\lambda_1 - \lambda_3)\left[a_{13}^2 a_{21} + a_{13}a_{23}(a_{22} - a_{11}) - a_{12}a_{23}^2\right]}{[a_{12}a_{21} - (\lambda_1 - a_{11})(\lambda_1 - a_{22})][a_{12}a_{21} - (\lambda_2 - a_{11})(\lambda_2 - a_{22})][a_{12}a_{21} - (\lambda_3 - a_{11})(\lambda_3 - a_{22})]} \\
T_{33} &= \frac{(\lambda_1 - \lambda_2)\left[a_{13}^2 a_{21} + a_{13}a_{23}(a_{22} - a_{11}) - a_{12}a_{23}^2\right]}{[a_{12}a_{21} - (\lambda_1 - a_{11})(\lambda_1 - a_{22})][a_{12}a_{21} - (\lambda_2 - a_{11})(\lambda_2 - a_{22})][a_{12}a_{21} - (\lambda_3 - a_{11})(\lambda_3 - a_{22})]}
\end{aligned}
$$

Thus we can write the solution of Eq. (3.3) in the form

$$\begin{pmatrix} \bar{x}(t) \\ \bar{y}(t) \\ \bar{z}(t) \end{pmatrix} = \frac{1}{\Delta} \begin{pmatrix} K_{11} & K_{12} & K_{13} \\ K_{21} & K_{22} & K_{23} \\ K_{31} & K_{32} & K_{33} \end{pmatrix} \begin{pmatrix} \bar{x}_0 \\ \bar{y}_0 \\ \bar{z}_0 \end{pmatrix} + \int_0^t \mathrm{e}^{A(t-t_1)} C\xi(t_1)\mathrm{d}t_1. \tag{3.6}$$

where $\mathrm{e}^{A(t-t_1)}$ can be obtained by putting $t = t - t_1$ in the expression of e^{At}. Now using the condition of Gaussian white noises $\langle \xi_i(t) \rangle = 0, i = 1, 2, 3,$ we get $\langle X(t) \rangle = \mathrm{e}^{At} X(0)$. Considering another result $\langle \xi_i(t)\xi_j(t_1) \rangle = \delta_{ij}\delta(t - t_1)$, and using the property of Dirac delta function $\int_{t_1}^{t_2} f(t)\delta(t - a)\mathrm{d}t = f(a)$, for $\mathrm{t}_1 < t < \mathrm{t}_2$, we get the population variances as:

$$\begin{aligned}
\sigma_{\bar{x}}^2 &= \langle \bar{x}^2(t) \rangle - \langle \bar{x}(t) \rangle^2 \\
&= -\frac{1}{\Delta^2} \Bigg[P_{11}^2 \left\{ \frac{T_{11}^2 \left(1 - \mathrm{e}^{2\lambda_1 t}\right) + T_{21}^2 \left(1 - \mathrm{e}^{2\lambda_1 t}\right) + T_{31}^2 \left(1 - \mathrm{e}^{2\lambda_1 t}\right)}{2\lambda_1} \right\} \\
&\quad + P_{12}^2 \left\{ \frac{T_{12}^2 \left(1 - \mathrm{e}^{2\lambda_2 t}\right) + T_{22}^2 \left(1 - \mathrm{e}^{2\lambda_2 t}\right) + T_{32}^2 \left(1 - \mathrm{e}^{2\lambda_2 t}\right)}{2\lambda_2} \right\} \\
&\quad + P_{13}^2 \left\{ \frac{T_{13}^2 \left(1 - \mathrm{e}^{2\lambda_3 t}\right) + T_{23}^2 \left(1 - \mathrm{e}^{2\lambda_3 t}\right) + T_{33}^2 \left(1 - \mathrm{e}^{2\lambda_3 t}\right)}{2\lambda_3} \right\} \\
&\quad + 2P_{11}P_{12} \left\{ \frac{T_{11}T_{12} \left(1 - \mathrm{e}^{(\lambda_1 + \lambda_2)t}\right) + T_{21}T_{22} \left(1 - \mathrm{e}^{(\lambda_1 + \lambda_2)t}\right) + T_{31}T_{32} \left(1 - \mathrm{e}^{(\lambda_1 + \lambda_2)t}\right)}{\lambda_1 + \lambda_2} \right\} \\
&\quad + 2P_{11}P_{13} \left\{ \frac{T_{11}T_{13} \left(1 - \mathrm{e}^{(\lambda_1 + \lambda_3)t}\right) + T_{21}T_{23} \left(1 - \mathrm{e}^{(\lambda_1 + \lambda_3)t}\right) + T_{31}T_{33} \left(1 - \mathrm{e}^{(\lambda_1 + \lambda_3)t}\right)}{\lambda_1 + \lambda_3} \right\} \\
&\quad + 2P_{12}P_{13} \left\{ \frac{T_{12}T_{13} \left(1 - \mathrm{e}^{(\lambda_2 + \lambda_3)t}\right) + T_{23}T_{22} \left(1 - \mathrm{e}^{(\lambda_3 + \lambda_2)t}\right) + T_{33}T_{32} \left(1 - \mathrm{e}^{(\lambda_3 + \lambda_2)t}\right)}{\lambda_3 + \lambda_2} \right\} \Bigg]
\end{aligned} \tag{3.7a}$$

$$\begin{aligned}\sigma_{\bar{y}}^2 &= \langle \bar{y}^2(t)\rangle - \langle \bar{y}(t)\rangle^2 \\ &= -\frac{1}{\Delta^2}\left[Q_{11}^2\left\{\frac{T_{11}^2\left(1-e^{2\lambda_1 t}\right)+T_{21}^2\left(1-e^{2\lambda_1 t}\right)+T_{31}^2\left(1-e^{2\lambda_1 t}\right)}{2\lambda_1}\right\}\right. \\ &\quad + Q_{12}^2\left\{\frac{T_{12}^2\left(1-e^{2\lambda_2 t}\right)+T_{22}^2\left(1-e^{2\lambda_2 t}\right)+T_{32}^2\left(1-e^{2\lambda_2 t}\right)}{2\lambda_2}\right\} \\ &\quad + Q_{13}^2\left\{\frac{T_{13}^2\left(1-e^{2\lambda_3 t}\right)+T_{23}^2\left(1-e^{2\lambda_3 t}\right)+T_{33}^2\left(1-e^{2\lambda_3 t}\right)}{2\lambda_3}\right\} \\ &\quad + 2Q_{11}Q_{12}\left\{\frac{T_{11}T_{12}\left(1-e^{(\lambda_1+\lambda_2)t}\right)+T_{21}T_{22}\left(1-e^{(\lambda_1+\lambda_2)t}\right)+T_{31}T_{32}\left(1-e^{(\lambda_1+\lambda_2)t}\right)}{\lambda_1+\lambda_2}\right\} \\ &\quad + 2Q_{11}Q_{13}\left\{\frac{T_{11}T_{13}\left(1-e^{(\lambda_1+\lambda_3)t}\right)+T_{21}T_{23}\left(1-e^{(\lambda_1+\lambda_3)t}\right)+T_{31}T_{33}\left(1-e^{(\lambda_1+\lambda_3)t}\right)}{\lambda_1+\lambda_3}\right\} \\ &\quad \left. + 2Q_{12}Q_{13}\left\{\frac{T_{12}T_{13}\left(1-e^{(\lambda_2+\lambda_3)t}\right)+T_{23}T_{22}\left(1-e^{(\lambda_3+\lambda_2)t}\right)+T_{33}T_{32}\left(1-e^{(\lambda_3+\lambda_2)t}\right)}{\lambda_3+\lambda_2}\right\}\right]\end{aligned} \tag{3.7b}$$

$$\begin{aligned}\sigma_{\bar{z}}^2 &= \langle \bar{z}^2(t)\rangle - \langle \bar{z}(t)\rangle^2 \\ &= -\frac{1}{\Delta^2}\left[R_{11}^2\left\{\frac{T_{11}^2\left(1-e^{2\lambda_1 t}\right)+T_{21}^2\left(1-e^{2\lambda_1 t}\right)+T_{31}^2\left(1-e^{2\lambda_1 t}\right)}{2\lambda_1}\right\}\right. \\ &\quad + R_{12}^2\left\{\frac{T_{12}^2\left(1-e^{2\lambda_2 t}\right)+T_{22}^2\left(1-e^{2\lambda_2 t}\right)+T_{32}^2\left(1-e^{2\lambda_2 t}\right)}{2\lambda_2}\right\} \\ &\quad + R_{13}^2\left\{\frac{T_{13}^2\left(1-e^{2\lambda_3 t}\right)+T_{23}^2\left(1-e^{2\lambda_3 t}\right)+T_{33}^2\left(1-e^{2\lambda_3 t}\right)}{2\lambda_3}\right\} \\ &\quad + 2R_{11}R_{12}\left\{\frac{T_{11}T_{12}\left(1-e^{(\lambda_1+\lambda_2)t}\right)+T_{21}T_{22}\left(1-e^{(\lambda_1+\lambda_2)t}\right)+T_{31}T_{32}\left(1-e^{(\lambda_1+\lambda_2)t}\right)}{\lambda_1+\lambda_2}\right\} \\ &\quad + 2R_{11}R_{13}\left\{\frac{T_{11}T_{13}\left(1-e^{(\lambda_1+\lambda_3)t}\right)+T_{21}T_{23}\left(1-e^{(\lambda_1+\lambda_3)t}\right)+T_{31}T_{33}\left(1-e^{(\lambda_1+\lambda_3)t}\right)}{\lambda_1+\lambda_3}\right\} \\ &\quad \left. + 2R_{12}R_{13}\left\{\frac{T_{12}T_{13}\left(1-e^{(\lambda_2+\lambda_3)t}\right)+T_{23}T_{22}\left(1-e^{(\lambda_3+\lambda_2)t}\right)+T_{33}T_{32}\left(1-e^{(\lambda_3+\lambda_2)t}\right)}{\lambda_3+\lambda_2}\right\}\right]\end{aligned} \tag{3.7c}$$

where $P_{11} = a_{12}a_{23} + a_{13}(\lambda_1 - a_{22})$, $P_{12} = a_{12}a_{23} + a_{13}(\lambda_2 - a_{22})$, $P_{13} = a_{12}a_{23} + a_{13}(\lambda_3 - a_{22})$, $Q_{11} = a_{13}a_{21} + a_{23}(\lambda_1 - a_{11})$, $Q_{12} = a_{13}a_{21} + a_{23}(\lambda_2 - a_{11})$, $Q_{13} = a_{13}a_{21} + a_{23}(\lambda_3 - a_{11})$, $R_{11} = 1$, $R_{12} = 1$, $R_{13} = 1$.

Relations (3.7a), (3.7b), (3.7c) show that environmental noises $\sigma_i, i = 1, 2, 3$ affect the fluctuation strength of the populations. Due to the increase of environmental noises, the amplitude of oscillations for the population densities also increase, which can be exhibited through Figs. 10 and 12. The numerical solutions for both the deterministic and stochastic models are presented in the next section with the suitable set of parameter values.

4 Numerical Simulations

In the previous sections, we have discussed analytically the stability of the nonlinear differential equation models in the absence and then in the presence of the environmental noises. We now present some simulation work for better understanding of our analytical results. Here we have considered different values of the environmental noises $(\sigma_i, i = 1, 2, 3)$ to observe biologically different dynamical scenarios of the model. Here the parameter values are taken from Elettreby (2009), and a_2, b_2, a_3 are chosen in such a way that they satisfy condition (2.7), (2.8), and (2.9).

In Figs. 1 and 2, $x(t), y(t), z(t)$ have been plotted with time 't' using the set of differential equations (3.1) with the set of parameter values $a_1 = 1, b_1 = 2, c_1 = 0.1, c_2 = 1.0, c_3 = 1.4, a_2 = 1.1, b_2 = 1.5, a_3 = 0.8$. Here the equilibrium point E^4 is seen to be locally asymptotically stable. Figure 3 shows the phase portrait near E^4.

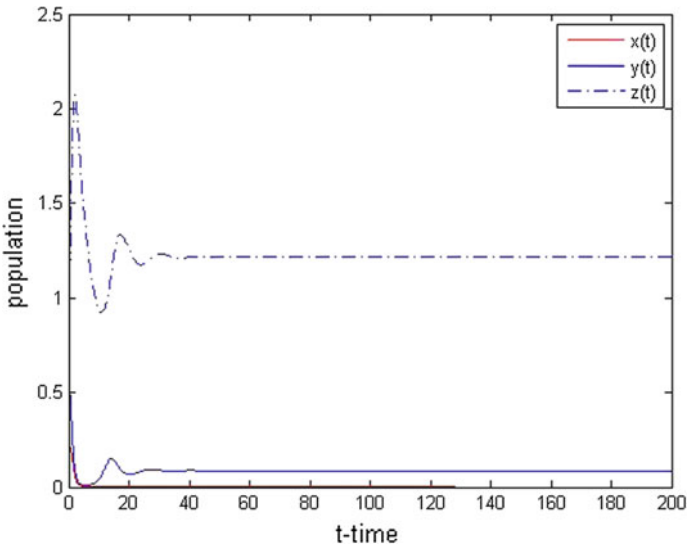

Fig. 1 Time series plot of $x(t), y(t), z(t)$ for the model (3.1), when $\sigma_i = 0, i = 1, 2, 3$ and E^4 is the equilibrium point, which is stable

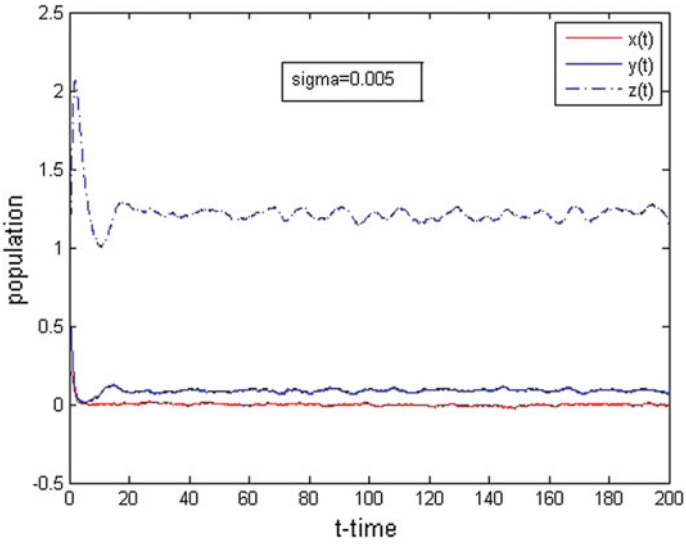

Fig. 2 Time series plot of $x(t), y(t), z(t)$ for the model (3.1), when $\sigma_i = 0.005, i = 1, 2, 3$ and E^4 as the equilibrium point, which is stochastically stable

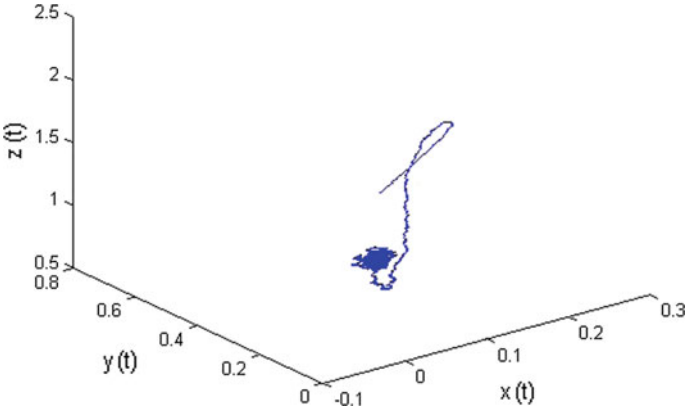

Fig. 3 Phase portrait of the model system (3.1) when $\sigma_i = 0.005, i = 1, 2, 3$

Also using the set of differential equations (3.1) the point E^5 with the set of parameter values $a_1 = 1, b_1 = 0.4, c_1 = 0.3, c_2 = 1.0, c_3 = 1.4, a_2 = 1.1, b_2 = 1.5, a_3 = 0.8$ is seen to be locally asymptotically stable (see Figs. 4, 5 and 7), and Figs. 6 and 8 are the phase portraits around E^5.

Now in Figs. 9, 10 and 12, $x(t), y(t), z(t)$ have been plotted with time 't' using the set of differential Eq. (3.1) with the set of parameter value $a_1 = 1, b_1 = 2,$

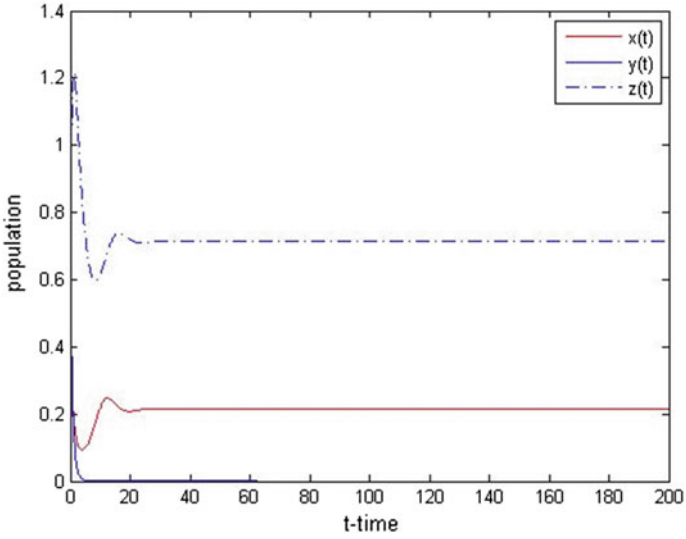

Fig. 4 Stable solution of $x(t), y(t), z(t)$ for the model (3.1) when $\sigma_i = 0, i = 1, 2, 3$

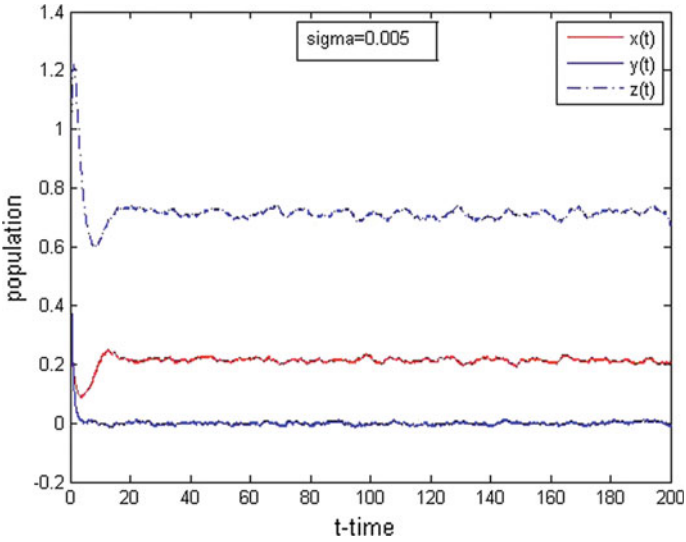

Fig. 5 Stochastically stable solution of $x(t), y(t), z(t)$ for the model (3.1), when $\sigma_i = 0.005, i = 1, 2, 3$

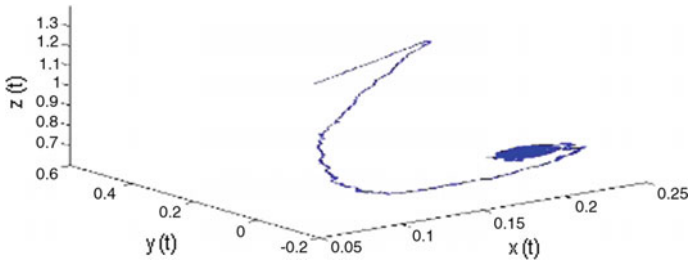

Fig. 6 Phase portrait of the model system (3.1) when $\sigma_i = 0.005, i = 1, 2, 3$

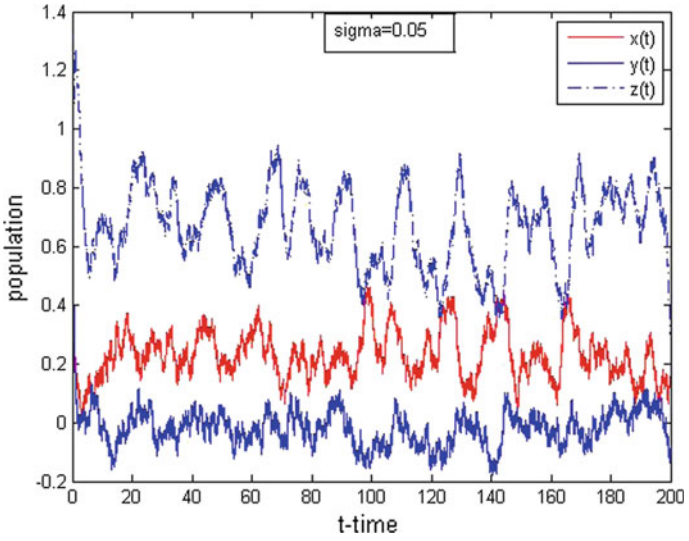

Fig. 7 Large amount of fluctuations in $x(t), y(t), z(t)$ for the model (3.1), when $\sigma_i = 0.05, i = 1, 2, 3$

$c_1 = 2.0, c_2 = 1.0, c_3 = 1.6, a_2 = 1.1, b_2 = 1.5, a_3 = 0.8$. Here the equilibrium point E^6 is seen to be locally asymptotically stable. Figures 11 and 13 show the phase portraits around E^6.

5 Conclusion

In this paper, we have shown the effect of environmental fluctuations on a three species predator–prey model. This work is an extension of the work by Elettreby (2009), by introducing white noise terms in each of the equations. In natural

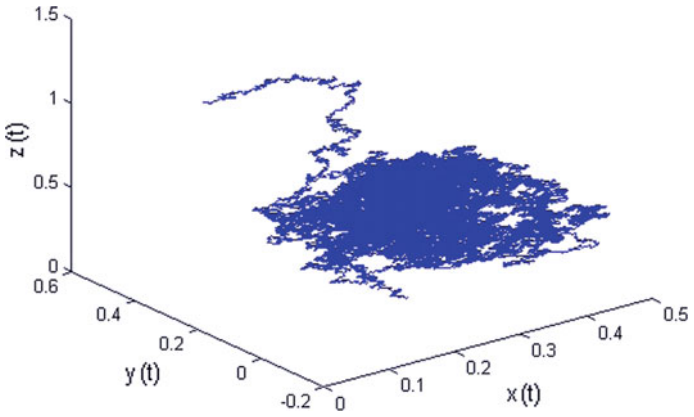

Fig. 8 Phase portrait of the model system (3.1) when $\sigma_i = 0.05, i = 1, 2, 3$

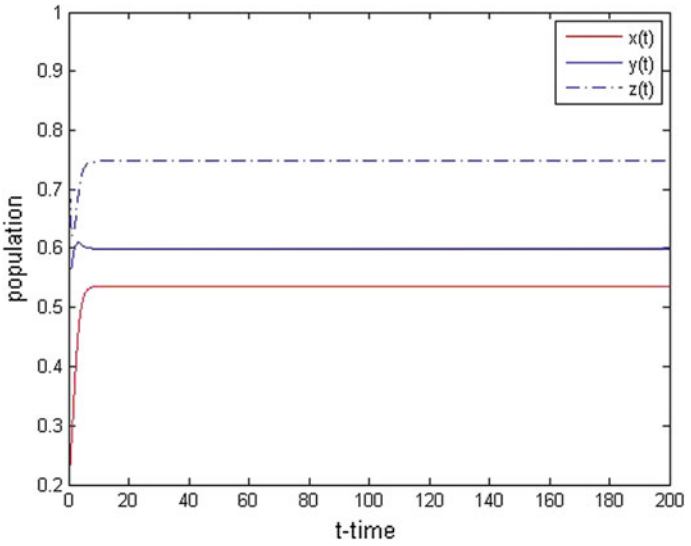

Fig. 9 Time series plot of $x(t), y(t), z(t)$ for the model (3.1), when $\sigma_{\mathrm{i}} = 0, \mathrm{i} = 1, 2, 3$ and E^6, which is stable

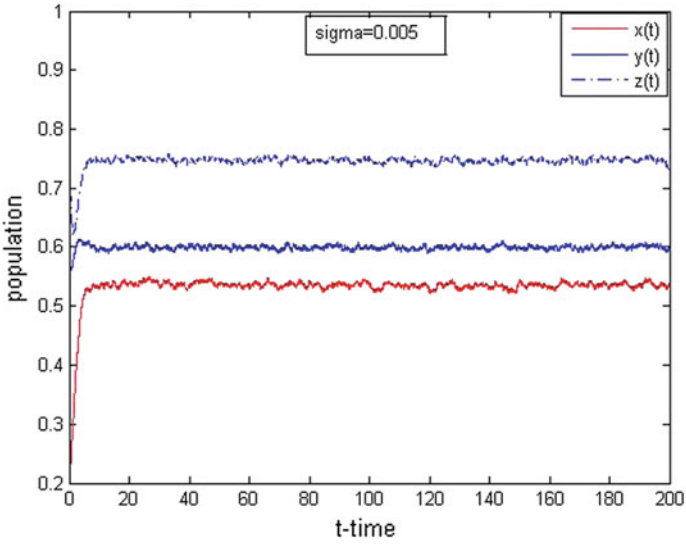

Fig. 10 Stochastically stable solution of $x(t), y(t), z(t)$ for the model (3.1), when $\sigma_i = 0.005, i = 1, 2, 3$

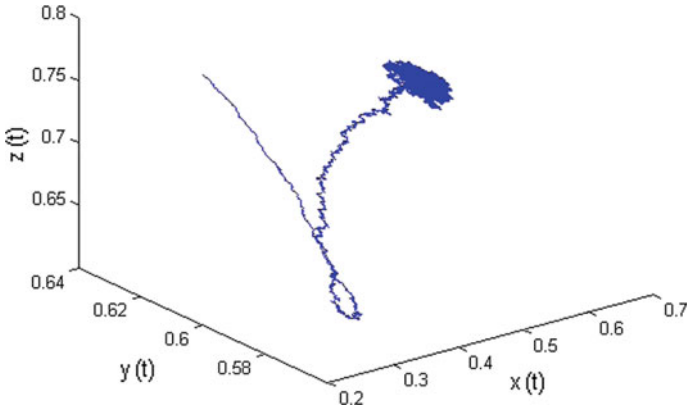

Fig. 11 Phase portrait of the model system (3.1) when $\sigma_i = 0.005, i = 1, 2, 3$

environment, the environmental fluctuation is one of the important components for ecological systems. First in the absence of environmental fluctuation, we have obtained the conditions for local asymptotical stability. Next we have studied the local stability behavior around E^6 for the three species predator–prey model within deterministic environment. Finally by the numerical method, we have discussed the stochastic model by introducing Gaussian white noise terms to each of the deterministic equations. For the stochastic model, numerical results indicate that the

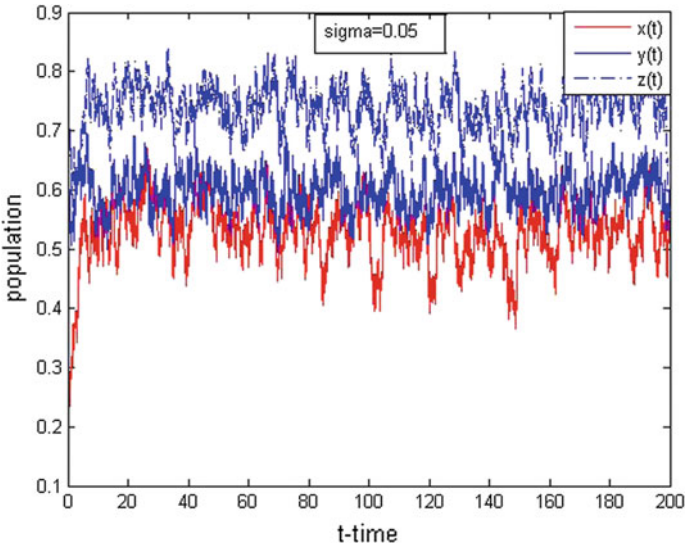

Fig. 12 Large amount of fluctuation in $x(t), y(t), z(t)$ for the model (3.1), when $\sigma_i = 0.05, i = 1, 2, 3$

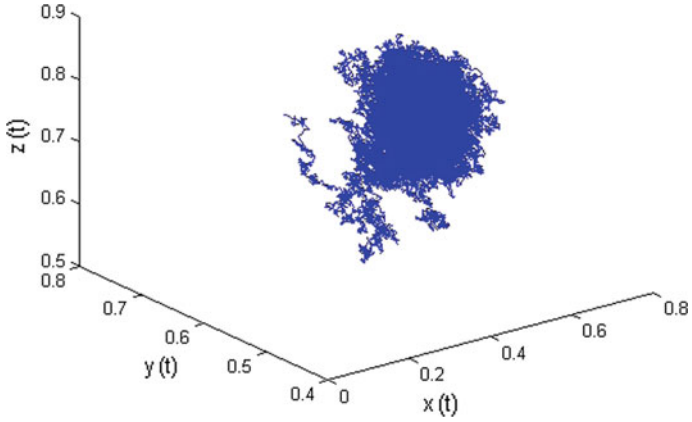

Fig. 13 Phase portrait of the model system (3.1) when $\sigma_i = 0.05, i = 1, 2, 3$

system is asymptotically stable. With the increase of the environmental forces, the frequency and amplitude of oscillation for the population density are also increased. These indicate that the magnitude of environmental forces play an important role to determine the magnitude of oscillation of the three species predator–prey model within a fluctuating environment.

Acknowledgements The first author is thankful to DST, New Delhi, India, for its financial support under INSPIRE fellowship.

References

Bandyopadhyay M, Chattopadhyay J (2005) Ratio-dependent predator-prey model, effect of environmental fluctuation and stability. Nonlinearity 8:913–936

Bandyopadhyay M, Saha M, Pal T (2008) Deterministic and stochastic analysis of a delayed allelopathic phytoplankton model within fluctuating environment. Nonlinear Anal Hybrid Syst 2:958–970

Carletti M, Burrage K, Burrage PM (2004) Numerical simulation of stochastic ordinary differential equations in bio-mathematical modelling. Math Comp Simul 64:271–277

Choudhury R (1992) On bifurcations and chaos in predator-prey models with delay. Chaos Solitons Fractals 2:393–409

Elettreby MF (2009) Two-prey one-predator model. Chaos Solitons Fractals 39:2018–2027

Freedman HI, Waltman P (1984) Persistence in models of three interacting predator-prey population. Math Biosci 68:213–231

Kot M (2001) Elememts of mathematical ecology. Cambridge University Press, New York

Saha T, Bandyopadhyay M (2008) Dynamical analysis of a delayed ratio-dependent prey-predator model within fluctuating environment. Appl Math Comput 196:458–478

Zhang Y, Zhang Q (2011) Dynamic behaviour in a delayed stage-structure population model with stochastic fluctuation and harvesting. Nonlinear Dyn 66:231–245

Plane Wave Propagation in a Rotating Micropolar Microstretch Elastic Solid in Special Case

K. Somaiah

Abstract The present work investigates the propagation of plane waves in a rotating micropolar microstretch elastic solid in a case of irrotational macro-displacements and zero micro-rotations. Three types of basic waves consisting of transverse microstretch waves, transverse micropolar waves, and coupled longitudinal waves are propagated. All these waves are frequency-dependent and hence, dispersive in nature. Except microstretch waves, all these waves are effected by angular rotation of the solid. The variation of these waves with angular frequency and angular rotations has also been depicted graphically for specific models.

1 Introduction

The generalization theory of micropolar elasticity (1966) is called microstretch elasticity, and this theory was introduced by Eringen (1971). The material points of microstretch solids can stretch and can contract independently of their translations and rotations. In these solids, the motion is characterized by seven degrees of freedom, namely three for translation, three for rotation, and one for stretch. The theory of microstretch elastic solid differs from the theory of micropolar elasticity in the sense that there is an additional degree of freedom called stretch and there is an additional kind of stress called microstretch vector. The microstretch elastic solids are asphalt, composite fibers, porous elastic material filled with gas or in viscid fluid, etc.

Singh (2002) studied the reflection of plane waves from free surface of microstretch elastic solid. Gravitational effect on plane waves in a generalized thermo-microstretch elastic solid was studied by Othman et al. (2013). Recently, Somaiah and Srinivas (2015) studied plane longitudinal waves in a micropolar elastic solid. Effect of rotation on longitudinal wave propagation was studied by

K. Somaiah (✉)
Department of Mathematics, Kakatiya University, Warangal 506009, Telangana, India
e-mail: somaiahkamidi@gmail.com

M.K. Singh et al. (eds.), *Applications of Fluid Dynamics*, Lecture Notes in Mechanical Engineering, https://doi.org/10.1007/978-981-10-5329-0_50

Sreelakshmi et al. (2015). The present investigations are the plane longitudinal and plane transverse waves in case of irrotational macro-displacements and vanishing micro-rotations in a rotating micropolar microstretch elastic solid.

2 Basic Equations

The equations of motion in a rotating homogeneous isotropic generalized micropolar microstretch elastic solid in the absence of body forces, body couples, and stretch free are given by Eringen (1999), Green and Lindsay (1972) as follows:

$$\begin{aligned}(\lambda+2\mu+K)\nabla\left(\nabla.\vec{u}\right)-(\mu+K)\nabla\times\nabla\times\vec{u}+K\nabla\times\vec{\phi}+\lambda_o\nabla\phi^*\\ =\rho\left[\frac{\partial^2\vec{u}}{\partial t^2}+\vec{\Omega}\times\left(\vec{\Omega}\times\vec{u}\right)\right]\end{aligned} \tag{1}$$

$$(\alpha+\beta+\gamma)\nabla\left(\nabla\cdot\vec{\phi}\right)-\gamma\nabla\times(\nabla\times\vec{\varphi})+K\nabla\times\vec{u}-2K\vec{\phi}=\rho J\frac{\partial^2\vec{\phi}}{\partial t^2} \tag{2}$$

$$\alpha_0\nabla^2\phi^*-\lambda_1\phi^*-\lambda_0\nabla\cdot\vec{u}=\frac{\rho J_0}{2}\frac{\partial^2\phi^*}{\partial t^2} \tag{3}$$

where λ,μ Lame's constants, K is the elastic constant, α,β,γ are micro-rotational parameter, $\alpha_0,\lambda_0,\lambda_1$ are microstretch elastic constants, ρ is density, J is the micro inertia, J_0 is the micro inertia of micro element, $\vec{u}$ is macro displacement vector, $\vec{\phi}$ is the micro-rotation vector, ϕ^* is the microstretch scalar which are satisfy the following inequalities: $3\lambda+2\mu+K\geq 0$; $2\mu+K\geq 0$; $K\geq 0$; $3\alpha+\beta+\gamma\geq 0$; $-\gamma\leq\beta\leq\gamma$; $\gamma\geq 0$; and $\vec{\Omega}\times\left(\vec{\Omega}\times\vec{u}\right)$ is the time dependent part of centripetal acceleration.

3 Formulation of the Problem

We use the rectangular coordinate system (x, y, z), and medium is assumed to be rotating about z-axis with a constant rate with constant angular velocity $\vec{\Omega}=(0,0,\Omega)$, where Ω is the component of rotation. The displacement vector $\vec{u}$ and micro-rotation vector $\vec{\phi}$ are taken as $\vec{u}=(u_1,u_2,0)$, $\vec{\phi}=(0,0,\phi)$. We write Eqs. (1) and (2) in terms of dilation Δ and micro-rotation dilation Δ' with

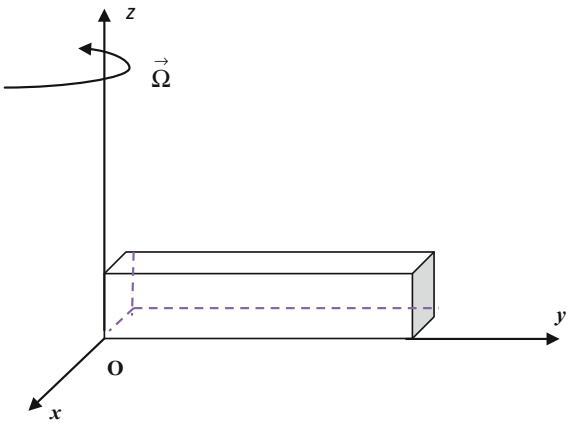

Fig. 1 Geometry of the problem

$$\Delta = \frac{\partial u_1}{\partial x} + \frac{\partial u_2}{\partial y} \tag{4}$$

$$\Delta' = \frac{\partial \phi}{\partial z} \tag{5}$$

are given by

$$(\lambda + 2\mu + K)\frac{\partial}{\partial x}\Delta - (\mu + K)\nabla^2 u_1 - K\frac{\partial \phi}{\partial y} + \lambda_0 \frac{\partial \phi^*}{\partial x} = \rho\left[\frac{\partial^2 u_1}{\partial t^2} - \Omega^2 u_1\right] \tag{6}$$

$$(\lambda + 2\mu + K)\frac{\partial}{\partial y}\Delta - (\mu + K)\nabla^2 u_2 + K\frac{\partial \phi}{\partial x} + \lambda_0 \frac{\partial \phi^*}{\partial y} = \rho\left[\frac{\partial^2 u_2}{\partial t^2} - \Omega^2 u_2\right] \tag{7}$$

$$(\alpha + \beta + \gamma)\nabla^2 \phi - \gamma\frac{\partial}{\partial z}\Delta' + K\left(u_{2,1} - u_{1,2}\right) - K\phi = \rho J\frac{\partial^2 \phi}{\partial t^2} \tag{8}$$

where $\nabla^2 = \frac{\partial^2}{\partial x^2} + \frac{\partial^2}{\partial y^2}$ (Fig. 1).

4 Propagation of Waves in Case of Irrotational Macro-displacements and Zero Micro-rotation

We consider the propagation of waves in micropolar microstretch elastic solid, in which irrotational macro-displacements and zero micro-rotation. This means

$$\vec{\phi} = (0, 0, \phi) = 0 \tag{9}$$

and $\nabla \times \vec{u} = \vec{0}$ becomes

$$\frac{\partial u_2}{\partial x} = \frac{\partial u_1}{\partial y} \tag{10}$$

The condition (10) satisfied if the displacements u_1, u_2 are derivable and

$$\frac{\partial \Delta}{\partial x} = \nabla^2 u_1 \tag{11}$$

$$\frac{\partial \Delta}{\partial y} = \nabla^2 u_2 \tag{12}$$

On using conditions (9)–(12), Eqs. (6)–(8) leads to

$$(\lambda + \mu)\nabla^2 u_1 + \lambda_0 \frac{\partial \phi^*}{\partial x} = \rho \left[\frac{\partial^2 u_1}{\partial t^2} - \Omega^2 u_1 \right] \tag{13}$$

$$(\lambda + \mu)\nabla^2 u_2 + \lambda_0 \frac{\partial \phi^*}{\partial y} = \rho \left[\frac{\partial^2 u_2}{\partial t^2} - \Omega^2 u_2 \right] \tag{14}$$

Adding Eqs. (13) and (14), we obtain

$$c_1 \nabla^2 \vec{u} + c_2 e \phi^* = \frac{\partial^2 \vec{u}}{\partial t^2} - \Omega^2 \vec{u} \tag{15}$$

Equation (3) may be written as

$$a_1 \nabla^2 \phi^* - a_2 \phi^* - a_3 \nabla \cdot \vec{u} = \frac{\partial^2 \phi^*}{\partial t^2} \tag{16}$$

where

$$c_1 = \frac{\lambda + \mu}{\rho}; \quad c_2 = \frac{\lambda_0}{\rho}; \quad a_1 = \frac{2\alpha_0}{\rho J_0}; \quad a_2 = \frac{2\lambda_1}{\rho J_0}; \quad a_3 = \frac{2\lambda_0}{\rho J_0};$$

and

$$e = \frac{\partial}{\partial x} + \frac{\partial}{\partial y}. \tag{17}$$

We observe that Eqs. (15) and (16) are coupled in $\vec{u}, \phi^*$.

Plane waves advancing in the positive direction of unit vector $\hat{n}$ may be expressed as

$$\left[\vec{u}, \phi^*\right] = \left[\vec{A}, B\right] \exp\left[ik\left(\hat{n} \cdot \vec{r} - vt\right)\right] \tag{18}$$

where $\vec{A}, B$ are amplitudes, k is the wave number, and $\vec{r}$ is the position vector. Thus,

$$k = \frac{2\pi}{l} \tag{19}$$

and

$$\vec{r} = x_k i_k \tag{20}$$

where l is the wavelength and x_k is the component of $\vec{r}$. Inserting Eq. (18) in Eqs. (15) and (16) we obtain,

$$\left[k^2\left(v^2 - c_1\right) + \Omega^2\right]\vec{A} + c_2 ik(n_1 + n_2)B = 0 \tag{21}$$

and

$$-a_3 ik\vec{A} \cdot \hat{n} + \left[k^2\left(v^2 - a_1\right) + a_2\right]B = 0 \tag{22}$$

where n_1, n_2 are unit vector components of normal $\hat{n}$ in xy-plane, so we take $n_1 = n_2 = \frac{1}{\sqrt{2}}$ in Eq. (21), we obtain

$$\left[k^2\left(v^2 - c_1\right) + \Omega^2\right]\vec{A} + \sqrt{2}c_2 ikB = 0 \tag{23}$$

Solving Eq. (23) for B we obtain,

$$B = -\left[\frac{k^2(v^2 - c_1) + \Omega^2}{\sqrt{2}c_2 ik}\right]\vec{A} \tag{24}$$

After inserting Eq. (24) in Eq. (22) leads to

$$\sqrt{2}a_3 c_2 k^2\left(\vec{A} \cdot \hat{n}\right) + \left[k^2\left(v^2 - a_1\right) + a_2\right]\left[k^2\left(c_1 - v^2\right) - \Omega^2\right]\vec{A} = 0 \tag{25}$$

4.1 Plane Transverse Waves

For plane transverse waves take $\vec{A} \cdot \hat{n} = 0$ in Eq. (25) we obtain the speed of transverse waves are:

$$v_{T_1}^2 = \frac{a_1\omega^2}{\omega^2 + a_2} \tag{26}$$

and

$$v_{T_2}^2 = \frac{c_1\omega^2}{\omega^2 + \Omega^2} \tag{27}$$

where $v = \frac{\omega}{k}$.

Equation (26) is the phase velocity of transverse microstretch wave and Eq. (27) is the phase velocity of transverse micropolar wave.

4.2 Plane Longitudinal Waves

For plane longitudinal waves, we have $\left|\vec{A}\cdot\hat{n}\right| = \left|\vec{A}\right| = A$ in Eq. (25) we obtain the following quadratic equation in v^2;

$$\left(v^2\right)^2 + Bv^2 + C = 0 \tag{28}$$

where

$$B = -\omega^2\left[a_1\left(\omega^2 + a_2\right)^{-1} + c_1\left(\omega^2 + \Omega^2\right)^{-1}\right]$$

and

$$C = \omega^2\left[a_1c_1\omega^2 - \sqrt{2}a_3c_2\right]\left(\omega^2 + a_2\right)^{-1}\left(\omega^2 + \Omega^2\right)^{-1}. \tag{29}$$

The speed of coupled longitudinal waves are

$$v_{L_{1,2}}^2 = \frac{-B \pm \sqrt{B^2 - 4C}}{2} \tag{30}$$

where + sign for $v_{L_1}^2$ and − sign for $v_{L_2}^2$.

Particular case

(i) On neglecting of microstretch parameters (that means $a_1 = a_2 = 0$), Eq. (28) reduces to

$$v^2 = \frac{c_1\omega^2}{\omega^2 + \Omega^2} = v_{T_2}^2.$$

(ii) On neglecting of micropolar parameters (that means $c_1 = c_2 = 0$), Eq. (28) reduces to

$$v^2 = \frac{a_1\omega^2}{\omega^2 + a_2} = v_{T_1}^2.$$

5 Numerical Results and Discussion

To study the effect of angular rotation on coupled longitudinal waves and effect of angular frequency on transverse microstretch waves, transverse micropolar waves, we consider two material values. Material-I values (2013) and material-II values (2016) as follows:

Material-I:

$$\lambda = 9 \cdot 4 \times 10^{10}\,\text{N/m}^2; \quad \mu = 4 \cdot 0 \times 10^{10}\,\text{N/m}^2; \quad \rho = 1 \cdot 74 \times 10^3\,\text{kg/m}^3;$$
$$J = 2 \times 10^{-2}\,\text{m}^2; \quad J_0 = 0.19 \times 10^{-17}\,\text{m}^2; \quad \alpha_0 = 0.00008 \times 10^{-5}\text{N};$$
$$\lambda_0 = 0.21 \times 10^{11}\text{N/m}^2; \quad \lambda_1 = 0.007 \times 10^{12}\,\text{N/m}^2$$

Material-II:

$$\lambda = 7.59 \times 10^9\,\text{N/m}^2; \quad \mu = 1.90 \times 10^9\text{N/m}^2; \quad \rho = 2.192 \times 10^3\,\text{kg/m}^3;$$
$$j = 0.196 \times 10^{-6}\,\text{m}^2; \quad J_0 = 0.196 \times 10^{-6}\,\text{m}^2; \quad \alpha_0 = 15.947 \times 10^3\,\text{N};$$
$$\lambda = 0.57702 \times 10^3\,\text{N/m}^2; \quad \lambda_1 = 34.650 \times 10^3\,\text{N}.$$

The effect of angular rotation on coupled longitudinal phase speeds $v_{L_{1,2}}^2$ for material-I are shown in Figs. 2 and 3, respectively, and Fig. 4 shows that effect of angular rotation on both phase speeds. The phase speeds $v_{L_1}^2$ are inverse proportional, while $v_{L_2}^2$ are proportional to angular rotations.

The variation of non-dimensional angular frequency ω with range $0.5 \leq \omega \leq 5$ versus phase speed ($v_{T_2}^2$) of transverse micropolar wave for material-I for angular rotation $\Omega = 5$ and 20 are shown in Figs. 5 and 6 respectively. From Fig 7, we observe that micropolar transverse waves propagate slowly under the effect of high

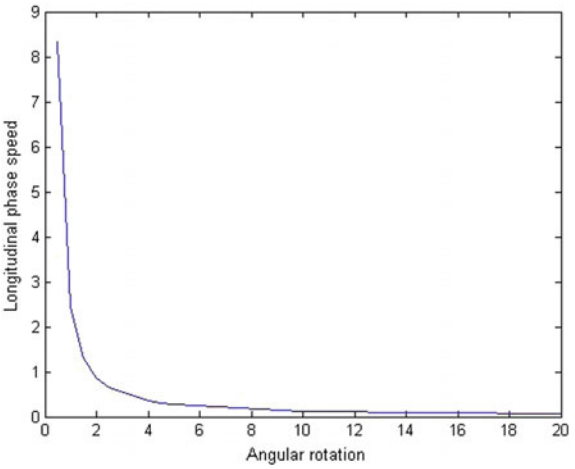

Fig. 2 Variation of coupled longitudinal phase speed $v_{L_1}^2$ versus angular rotation

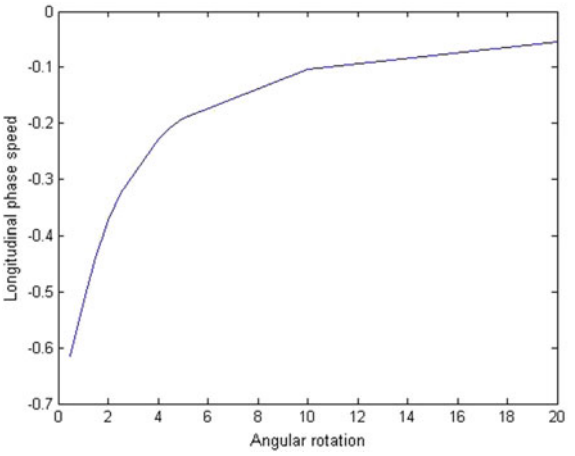

Fig. 3 Variation of coupled longitudinal phase speed $v_{L_2}^2$ versus angular rotation

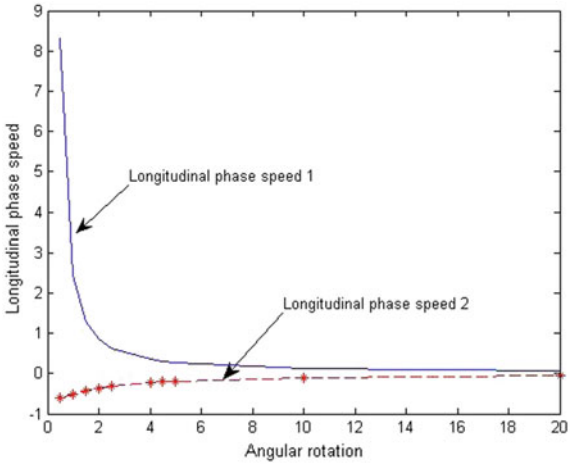

Fig. 4 Variation of coupled longitudinal phase speeds $v_{L_{1,2}}^2$ versus angular rotation

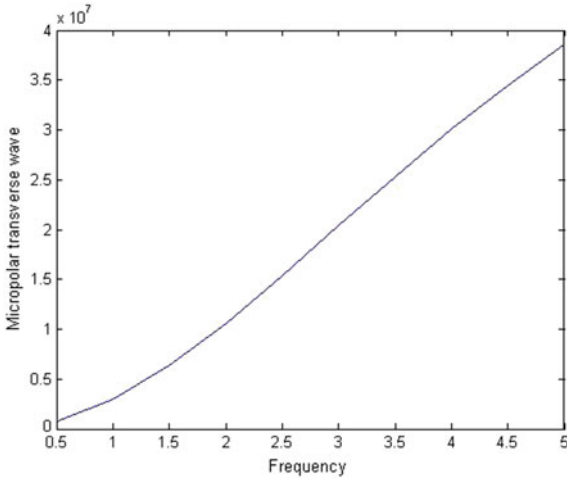

Fig. 5 Variation of micropolar transverse phase speed versus non-dimensional frequency for $\Omega = 5$

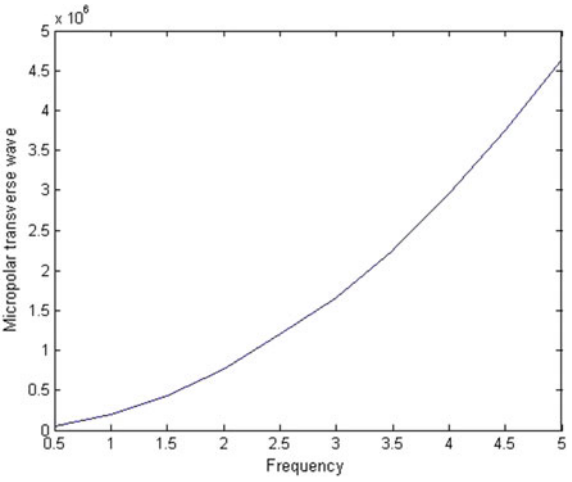

Fig. 6 Variation of micropolar transverse phase speed versus non-dimensional frequency for $\Omega = 20$

angular rotation in the given range of angular frequency. The variation of non-dimensional angular frequency ω for the same range versus phase speed ($v_{T_1}^2$) of transverse microstretch waves for microstretch materials I and II are shown in Figs. 8 and 9, respectively. From Fig. 10, we observed that transverse microstretch waves propagate slowly in low density material-I than high density material-II.

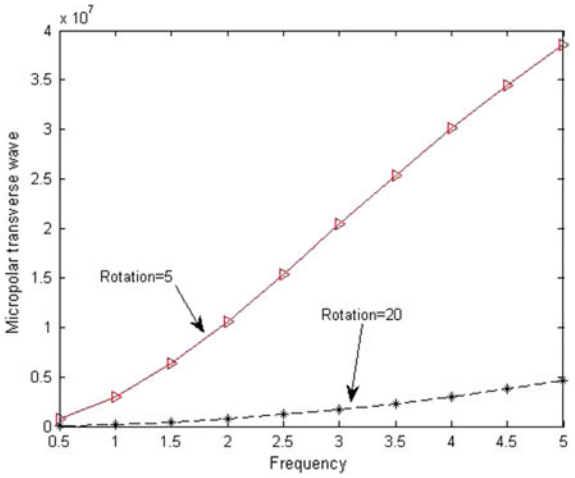

Fig. 7 Variation of micropolar transverse phase speed versus non-dimensional frequency for $\Omega = 5, 20$

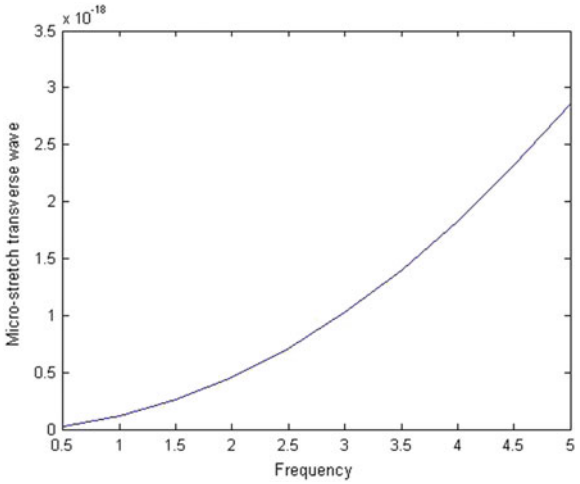

Fig. 8 Variation of microstretch transverse phase speed versus non-dimensional frequency for material-I

6 Conclusions

The plane wave propagation in a rotating micropolar microstretch elastic solid with a special case has been studied in this present paper. In these investigations, we conclude that:

(i) Three sets of waves, namely transverse microstretch, transverse micropolar, and coupled longitudinal plane waves are propagated in a solid.
(ii) The angular rotation is not effected on the transverse microstretch waves.

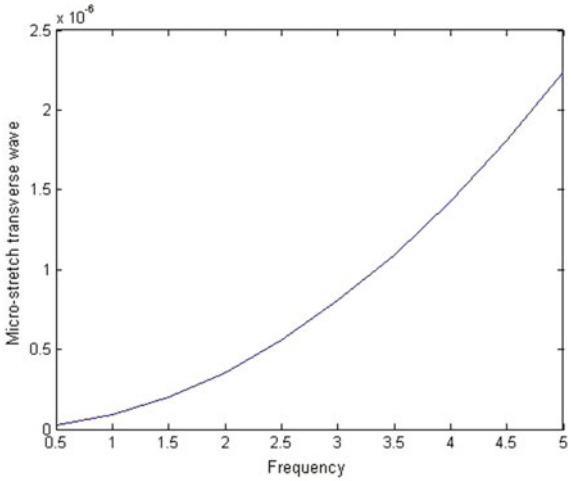

Fig. 9 Variation of microstretch transverse phase speed versus non-dimensional frequency for material-II

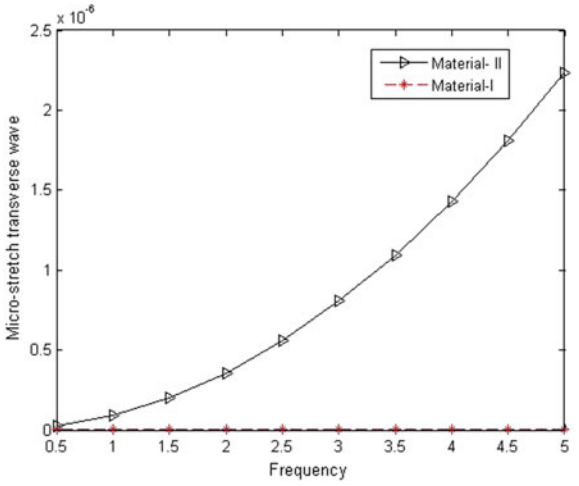

Fig. 10 Variation of microstretch transverse phase speed versus non-dimensional frequency for material-I and II

(iii) All these waves are dependent on the angular frequency, so they are dispersive in nature.

(iv) From numerical discussion, we say that micropolar transverse waves propagate with high speed under low angular rotation in any model, and microstretch transverse waves propagate with high speed in high density model.

References

Eringen AC (1971) Micropolar elastic solids with stretch. Ari Kitabevi Matbassi, Istanbul 24:1–18
Eringen AC (1966) J Math Mech 15:909
Eringen AC (1999) Micro-continuum field theories I. Foundation and solids. Springer, New York
Green AE, Lindsay KA (1972) Thermoelasticity. J Elast 2(1):1–7
Khurana A, Tomar SK (2016) Wave propagation in nonlocal microstretch solid. Appl Math Model 000:1–18
Kumar R, Kaur M, Rajvanshi SC (2013) Wave propagation at an interface of elastic and microstretch thermo-elastic solids with micro-temperatures. J Solid Mech 5:226–244
Othman MIA, Atwa SY, Jahangir A, Khan A (2013) Gravitational effect on plane waves in a generalized thermo-microstretch elastic solid under Green Naghdi theory. Appl Math Inf Sci Lett 1(2):25–38
Singh B (2002) Proceedings of Indian Academic Science (Earth Planet Science)
Somaiah K, Srinivas R (2015) Propagation of plane longitudinal waves in a micropolar elastic solid with voids. Math Sci Int Res J 4(2):61–64
Sreelakshmi T, Rama E, Somaiah K (2015) Effect of rotation on longitudinal wave propagation in an elastic solid with a cylindrical hole. Proceedia Eng 127:660–664

Possibility and Causes of Backward Bifurcation in a Cholera Model

Sandeep Sharma and Nitu Kumari

Abstract Backward bifurcation in an epidemiological model is a phenomenon in which the model possesses stable endemic equilibria together with a stable disease-free equilibrium. Till now, this phenomenon has been observed in a number of epidemic models. In this work, we investigate the possibility of backward bifurcation in a cholera model. We also explore the role of various factors, which induce backward bifurcation in other epidemic models. We believe the present work provides an insight of the dynamics of a cholera model and possible causes of backward bifurcation in the same.

1 Introduction

Occurrence of various infectious diseases (like dengue, tuberculosis, cholera) posed a major challenge in front of the modern society. The event of infectious disease results in huge loss of lives and other resources. Despite our increased understanding of infectious diseases and development of medical sciences, the infectious diseases caused millions of deaths and disabilities across the globe. Hence, people from different corners of science and medicine are working to find some robust mechanism to prevent the spread of infectious diseases. Compartmental mathematical models have emerged as a useful tool in this direction. The information provided by these models helps in reducing or eliminating the epidemics. However, the success of an epidemic model to predict the future course of the epidemic lies in the assumptions involved in the formulation of the model.

Waterborne diseases (e.g., cholera, typhoid, hepatitis) are outcome of scarcity of safe drinking water. The possibility of multiple transmission of disease makes the study of waterborne disease more challenging. Among all the diseases which belong to the class of waterborne diseases, cholera attracts more attention. This

S. Sharma · N. Kumari (✉)
School of Basic Sciences, Indian Institute of Technology Mandi,
Mandi 175001 Himachal Pradesh, India
e-mail: nitu@iitmandi.ac.in

M.K. Singh et al. (eds.), *Applications of Fluid Dynamics*, Lecture Notes
in Mechanical Engineering, https://doi.org/10.1007/978-981-10-5329-0_51

accounts to 3–5 million cholera cases and 100,000–120,000 deaths around the globe.

Cholera is caused by the bacterium Vibrio cholera. The bacteria enter into the human body through ingestion of contaminated water and food. Cholera can transmit directly, from human to human, and also indirectly, from environment to human. At primary stage, there may be no symptoms of the infection but in long term, it may turn fatal and cause leg cramps, vomiting, and watery diarrhea (Mwasa and Tchuenche 2011). In the absence of proper treatment, the infection results in circulatory collapse, rapid dehydration, and death within 12–24 h (Sanchez et al. 1994). Despite several efforts, cholera is still an endemic in many parts of the world (Safi et al. 2013). Accounts to this, a number of mathematical models are proposed and analyzed to comprehend the dynamics of cholera. To study the spread of 1973 cholera in Mediterranean, a mathematical model was proposed and analyzed by Capasso and Fontana (1979). In Codeço (2001), an extension of the general SIR epidemic model is proposed by incorporating environmental component to understand the dynamics of cholera. Hartley et al. (2005) extended the model proposed in Codeço (2001) by introducing the concept of hyperinfectivity. The mathematical model proposed in Mukandavire et al. (2011) considers both human-to-human and environment-to-human transmission of cholera to study the patterns of disease transmission in Zimbabwe. The model proposed in Mwasa and Tchuenche (2011), and Posny et al. (2015) investigate the role of public health interventions to prevent the spread of epidemics. As vaccination is a significant tool to reduce the size of the epidemic, therefore a number of models pertaining to cholera address the role of vaccination on the spread of cholera (Safi et al. 2013; Zhou et al. 2012; Zhou and Cui 2011). The use of disinfectants is another potential method to prevent the spread of cholera. Hence, mathematical models are also used to study the impact of disinfectants on the dynamics of cholera (Misra and Singh 2012; Misra et al. 2012).

The manuscript is organized in four sections. A survey on possible causes of backward bifurcation in epidemic models is performed in Sect. 2. The existence of backward bifurcation is explored in Sect. 3. The manuscript ends with a conclusion of our study in Sect. 4.

2 Backward Bifurcation

The basic reproduction number helps us to comprehend the dynamics of a compartmental epidemic model. In general, the diseases can be eliminated (or disease-free equilibrium will be stable) by making $R_0 < 1.$, while disease persists in the population (or endemic equilibrium will be stable) if $R_0 > 1$. But for some model, the dynamics will be more complicated. In such models, an stable endemic equilibrium exists even when $R_0 < 1$. This phenomenon is termed as backward bifurcation. In other words, in case of backward bifurcation, making $R_0 < 1$ does not ascertain that the disease will eliminate. An extensive detail on backward bifurcation can be found in Brauer (2004, 2011) and Dushoff et al. (1998).

The schematic diagram of forward bifurcation and backward bifurcation is given in Figs. 1 and 2, respectively. In short, we can conclude that the study of backward bifurcation is necessary due to the following two facts:

(i) The control of disease requires more efforts whenever the backward bifurcation occurs. This particular reason relates it directly to the health management programs implemented by the authorities.
(ii) The backward bifurcation gives rise to more complicated dynamics and thus requires more mathematical efforts to deal with the particular model.

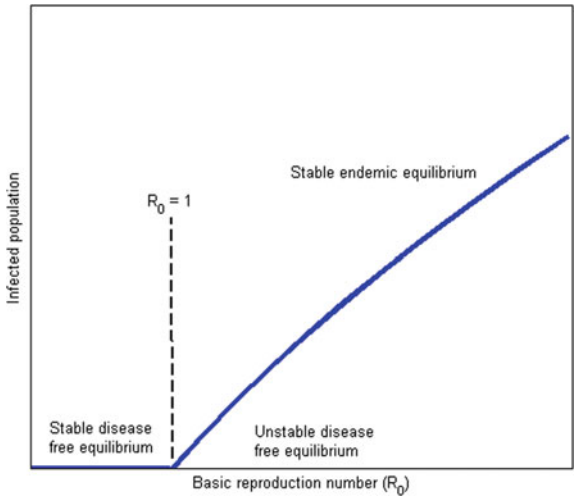

Fig. 1 Forward bifurcation

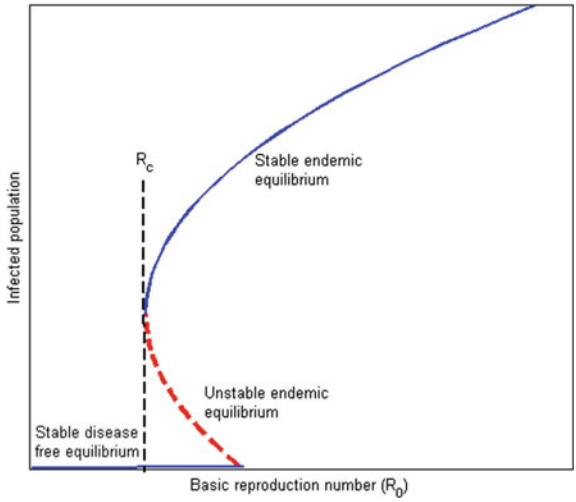

Fig. 2 Backward bifurcation

Due to the above-mentioned reasons, the possibility of backward bifurcation have been explored in different epidemic models of tuberculosis (Gerberry 2016; Chavez and Song 2004; Buonomo and Lacitignola 2010), malaria (Chitnis et al. 2006; Buonomo and Vargas-De-León 2013; Mukandavire et al. 2009), Chlamydia trachomatis (Sharomi and Gumel 2011a, b, 2009), and dengue (Garba et al. 2008). Apart from this, the backward bifurcation also exists for model with different epidemiological phenomena such as vaccination (Arino et al. 2003; Buonomo and Lacitignola 2011; Zaleta and Hernandez 2000; Sharomi et al. 2007), types of transmission rate (Buonomo and Lacitignola 2012; Alexander and Moghadas 2004), and types of treatment functions (Wang 2006; Zhang and Liu 2008).

3 Backward Bifurcation in Cholera Model

As we have discussed in Sect. 1, the dynamics of cholera is complicated due to the possibility of multiple transmission pathways. To inculcate this, a number of mathematical models are proposed to capture the dynamics of cholera. Despite this, backward bifurcation is generally absent in the cholera model. A number of vaccination models exhibit backward bifurcation. But, the same is not true for cholera models with vaccination (discussed in 1).

In particular, the model studied in Zhou et al. (2012) seems a suitable candidate for backward bifurcation, as it consists of both saturation transmission rate and imperfect vaccination.

$$\begin{aligned}
\frac{dS}{dt} &= (1-\rho)A - \frac{\beta SB}{(K+B)} - \phi S + \theta V - \mu_1 S \\
\frac{dV}{dt} &= \rho A - \frac{\sigma\beta VB}{(K+B)} + \phi S - \theta V - \mu_1 V \\
\frac{dI}{dt} &= \frac{\beta SB}{(K+B)} + \frac{\sigma\beta VB}{(K+B)} - (d+\alpha+\mu_1) \\
\frac{dB}{dt} &= \eta I - \mu_2 B
\end{aligned} \tag{1}$$

The details of assumptions and parameters of the model can be find in Zhou et al. (2012).

The model possesses two equilibrium points, namely disease free and endemic. The disease-free equilibrium point is given as $E_0 = (S^0, V^0, 0, 0)$ where,

$$S^0 = \frac{A[\theta + (1-\rho)\mu_1]}{\mu_1(\mu_1 + \theta + \phi)} \quad \text{and} \quad V^0 = \frac{A(\phi + \rho\mu_1)}{\mu_1(\mu_1 + \theta + \phi)}.$$

For the model (1), the basic reproduction number is obtained as

$$R_v = \frac{\eta\beta A[\theta + (1-\rho)\mu_1 + \sigma\phi + \sigma\mu_1\rho]}{K\mu_1\mu_2(\mu_1+\theta+\phi)(\mu_1+\alpha+d)}$$

Moreover, the existence of endemic equilibrium has been established by the following quadratic equation

$$A_1 I^2 + A_2 I + A_3 = 0$$

where,

$$\begin{aligned}
A_1 &= \mu_2(\mu_1+d+\alpha)\left(\mu_1^2+\mu_1\theta+\mu_1\phi+\mu_1\beta+\mu_1\beta\sigma+\beta^2\sigma+\beta\theta+\beta\phi\sigma\right)\\
A_2 &= K\mu_1\left(2\mu_1^2+2\mu_1\theta+2\mu_1\phi+\beta\mu_1+\beta\phi\sigma+\beta\theta+\mu_1\sigma\beta\right)\\
&\quad - A\beta\sigma(\sigma\beta+\mu_1\sigma\rho+\mu_1+\theta+\phi\sigma-\rho\mu_1)\\
A_3 &= K\mu_1\mu_2(\mu_1+d+\alpha)(\mu_1+\theta+\phi)(1-R_v)
\end{aligned}$$

There is possibility of backward bifurcation when $A_2 < 0$ and $R_v < 1$. But, in Sect. 5 of Zhou et al. (2012), it is shown that both conditions are not satisfied simultaneously. This is probably due the absence of the reinfection.

Similarly, the other vaccination models proposed in Safi et al. (2013) and Cui et al. (2014) do not exhibit backward bifurcation, while the other analogous generic vaccination models (e.g., Brauer 2004; Arino et al. 2003; Buonomo and Lacitignola 2011) depict the existence of backward bifurcation. From this discussion, it appears that the backward bifurcation may not be possible in cholera model. But, the cholera model with saturated recovery proposed in Zhou et al. (2017) shows the existence of backward bifurcation.

We proceed with a short discussion of the model presented in Zhou et al. (2017). The model is;

$$\begin{aligned}
\frac{dS}{dt} &= A - \frac{\beta SB}{K+B} - \mu_1 S + rI + \frac{cI}{b+I}\\
\frac{dI}{dt} &= \frac{\beta SB}{K+B} - (r+\mu_1+\delta)I - \frac{cI}{b+I}\\
\frac{dB}{dt} &= \eta I - \mu_2 B
\end{aligned} \tag{2}$$

The existence of endemic equilibrium has been established by the following quadratic equation

$$P_1 I^2 + P_2 I + P_3 = 0$$

Here,

$$
\begin{aligned}
P_1 &= \eta\left(\mu_1 r + \mu_1^2 + \beta\delta + \beta\mu_1 + \mu_1\delta\right) \\
P_2 &= K\mu_1\mu_2 r + K\mu_1\mu_2\delta + K\mu_1^2\mu_2 + \eta\mu_1\beta b + \eta\delta\beta b + b\eta r\mu_1 \\
&\quad + \mu_1^2 b\eta + \mu_1\delta\eta b + A\beta\eta \\
P_3 &= K\mu_1\mu_2(b\mu_1 + c + rb + \delta b)(1 - R_0)
\end{aligned}
$$

Motivated from this, we propose a new model with saturated removal rate $\frac{cI}{b+I}$ as follows

$$
\begin{aligned}
\frac{\mathrm{d}S}{\mathrm{d}t} &= A - \frac{\beta SB}{K+B} - \mathrm{d}S \\
\frac{\mathrm{d}I}{\mathrm{d}t} &= \frac{\beta SB}{K+B} - (r+d+\delta)I - \frac{cI}{b+I} \\
\frac{\mathrm{d}R}{\mathrm{d}t} &= \frac{cI}{b+I} + rI - \mathrm{d}R \\
\frac{\mathrm{d}B}{\mathrm{d}t} &= \eta I - \mu B
\end{aligned}
\tag{3}
$$

In the model (3), A represents the total recruitment rate (including immigrants and newborns). $\frac{\beta SB}{K+B}$ is the disease transmission rate, where K is the concentration of the bacteria that yields 50% chance of catching infection. The model also involves natural recovery rate r. The natural death rate d is same for individuals of each compartment, while the disease-related death rate is δ. η is the rate at which infected population contribute to the concentration of bacteria. The natural decay rate of the bacteria is μ.

The basic difference between models (2) and (3) is movement of the recovered individuals. In model (2), the recovered individuals join the susceptible class and may again get infected, while in model (3) recovered individuals join the removed class and do not become infected, once recovered. Similar studies are available in literature on generic compartmental models (Wang 2006, 2009).

Now, we obtain the disease-free equilibrium point as $E^0 = \left(\frac{A}{d}, 0, 0\right)$. Next, we calculate the basic reproduction number of the model using the next-generation matrix method given by Van den Driessche and Watmough (2002) as

$$
R_0 = \frac{A\eta\beta b}{K\mu d(rb + bd + \delta b + c)}
$$

The existence of endemic equilibrium is established by the following quadratic equation

$$
AI^2 + BI + C = 0
$$

where,

$$A = \eta\left(dr + d^2 + \beta\delta + \beta d + d\delta + \beta r\right)$$
$$B = \eta\beta bd + \eta\beta b\delta + \eta\beta br + \eta\beta c + \mu Kd^2 + \mu Kd\delta + \mu Kdr + \eta\beta d^2 + \eta\beta d\delta + \eta bdr + \eta cd - A\beta\eta$$
$$C = K\mu d(bd + c + rb + \delta b)(1 - R_0)$$

Here, we state the following result for the existence of endemic equilibrium

Theorem 3.1 *The proposed model system* (3) *has*

(i) *a unique endemic equilibrium whenever* $R_0 > 1$;
(ii) *a unique endemic equilibrium whenever* $R_0 = 1$ *and* $B < 0$;
(iii) *two endemic equilibriums if* $R_0 < 1$, $B < 0$ *and* $B^2 - 4AC > 0$;
(iv) *no endemic equilibrium otherwise*.

Now, we discuss graphically the possibility of the backward bifurcation in Fig. 3.

The infectious population at equilibria versus R_0 shows a backward bifurcation when $R_c < R_0 < 1$, leading to the existence of multiple endemic equilibria. The saddle-node bifurcation occurs at $R_0 = R_c$, where the stable endemic equilibria collide with other unstable endemic equilibria.

Although reinfection is not involved here, still the model shows the possibility of the backward bifurcation.

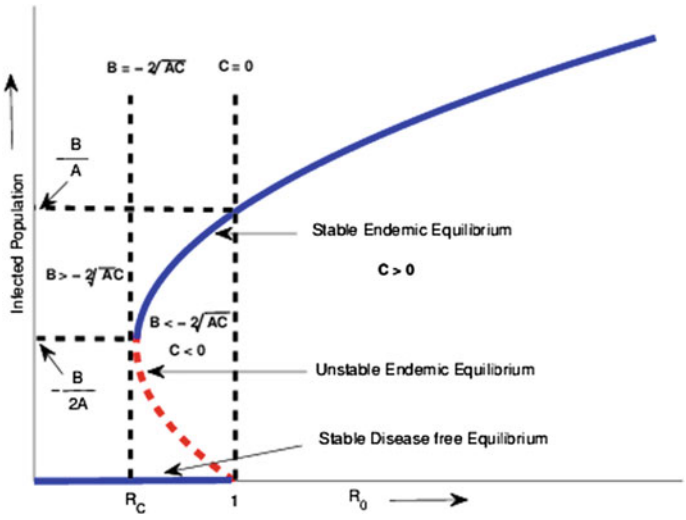

Fig. 3 Bifurcation diagram of the model system (3)

4 Conclusion

The phenomena of backward bifurcation poses a serious health challenge as bringing R_0 below unity is not enough to eradicate the disease. Due to this, it is a general tendency to avoid the backward bifurcation while modeling the disease, if possible. But, the study performed in Gerberry (2016) made some contradictory remarks to this general belief. The study observes that the factors (e.g., vaccination) implemented to eliminate the disease increase the size of the region where the backward bifurcation occurs. However, the number of infected individuals reduces significantly in the presence of such interventions. The discussion on backward bifurcation on cholera model yields that saturated recovery/treatment cause backward bifurcation. This makes the scenario worse whenever the spread of cholera takes place. Given the situation of the complicated dynamics and rapid spread of cholera, efforts should be made to prevent the existence of backward bifurcation. Moreover, the factors which induce the backward bifurcation in cholera model are limited treatment capacity which in no case reduces the size of the epidemic as discussed in Gerberry (2016).

Thus, present study brought forth an important fact that whenever the cholera outbreak occurs, we should enforce maximum possible medical arrangements to reduce the size of the epidemics. Such actions preclude the existence of backward bifurcation and will also reduce the mortalities.

References

Alexander ME, Moghadas SM (2004) Periodicity in an epidemic model with a generalized non-linear incidence. Math Biosci 189(1):75–96

Arino J, McCluskey CC, Van den Driessche P (2003) Global results for an epidemic model with vaccination that exhibits backward bifurcation. SIAM J Appl Math 64(1):260–276

Brauer F (2004) Backward bifurcations in simple vaccination models. J Math Anal Appl 298(2): 418–431

Brauer F (2011) Backward bifurcations in simple vaccination/treatment models. J Biol Dyn 5(5): 410–418

Buonomo B, Lacitignola D (2011) On the backward bifurcation of a vaccination model with nonlinear incidence. Nonlinear Anal: Model Control 16(1):30–46

Buonomo B, Lacitignola D (2010) Analysis of a tuberculosis model with a case study in Uganda. J Biol Dyn 4(6):571–593

Buonomo B, Lacitignola D (2012) Forces of infection allowing for backward bifurcation in an epidemic model with vaccination and treatment. Acta Applicandae Mathematicae 122(1): 283–293

Buonomo B, De-León CV (2013) Stability and bifurcation analysis of a vector-bias model of malaria transmission. Math Biosci 242(1):59–67

Capasso V, Fontana PSL (1979) A mathematical model for the 1973 cholera epidemic in the European mediterranean region. Revued'épid émiologie et de Santé Publiqué 27(2):121–132

Chavez CC, Song B (2004) Dynamical models of tuberculosis and their applications. Math Biosci Eng 1(2):361–404

Chitnis N, Cushing JM, Hyman JM (2006) Bifurcation analysis of a mathematical model for malaria transmission. SIAM J Appl Math 67(1):24–45
Codeço CT (2001) Endemic and epidemic dynamics of cholera: the role of the aquatic reservoir. BMC Infect Dis 1(1):1
Cui J, Wu Z, Zhou X (2014) Mathematical analysis of a cholera model with vaccination. J Appl Math article ID324767, 16 pp
Dushoff J, Huang W, Chavez CC (1998) Backwards bifurcations and catastrophe in simple models of fatal diseases. J Math Biol 36(3):227–248
Garba SM, Gumel AB, Abu Bakar MR (2008) Backward bifurcations in dengue transmission dynamics. Math Biosci 215(1):11–25
Gerberry DJ (2016) Practical aspects of backward bifurcation in a mathematical model for tuberculosis. J Theor Biol 388:15–36
Hartley DM, Morris JG Jr, Smith DL (2005) Hyperinfectivity: a critical element in the ability of v. cholerae to cause epidemics? PLoS Med 3(1):e7
Kribs-Zaleta CM, Velasco-Hernandez JX (2000) A simple vaccination model with multiple endemic states. Math Biosci 164(2):183–201
Misra AK, Mishra SN, Pathak AL, Misra P, Naresh R (2012) Modeling the effect of time delay in controlling the carrier dependent infectious disease–cholera. Appl Math Comput 218(23): 11547–11557
Misra AK, Singh V (2012) A delay mathematical model for the spread and control of water borne diseases. J Theor Biol 301:49–56
Mukandavire Z, Gumel AB, Garira W, Tchuenche JM (2009) Mathematical analysis of a model for HIV-malaria co-infection. Math Biosci Eng 6(2):333–362
Mukandavire Z, Liao S, Wang J, Gaff H, Smith DL, Morris JG (2011) Estimating the reproductive numbers for the 2008–2009 cholera outbreaks in Zimbabwe. Proc Natl Acad Sci 108 (21):8767–8772
Mwasa A, Tchuenche JM (2011) Mathematical analysis of a cholera model with public health interventions. Biosystems 105(3):190–200
Posny D, Wang J, Mukandavire Z, Modnak C (2015) Analyzing transmission dynamics of cholera with public health interventions. Math Biosci 264:38–53
Safi MA, Melesse DY, Gumel AB (2013) Dynamics analysis of a multi-strain cholera model with an imperfect vaccine. Bull Math Biol 75(7):1104–1137
Sanchez JL, Vasquez B, Begue RE, Meza R, Castellares G, Cabezas C, Watts DM, Svennerholm AM, Sadoff JC, Taylor DN (1994) Protective efficacy of oral whole-cell/ recombinant-b-subunit cholera vaccine in Peruvian military recruits. Lancet 344(8932): 1273–1276
Sharomi O, Gumel AB (2009) Re-infection-induced backward bifurcation in the transmission dynamics of chlamydia trachomatis. J Math Anal Appl 356(1):96–118
Sharomi O, Gumel AB (2011a) Dynamical analysis of a sex-structured chlamydia trachomatis transmission model with time delay. Nonlinear Anal: Real World Appl 12(2):837–866
Sharomi O, Gumel AB (2011b) Mathematical study of a risk-structured two group model for chlamydia transmission dynamics. Appl Math Model 35(8):3653–3673
Sharomi O, Podder CN, Gumel AB, Elbasha EH, Watmough J (2007) Role of incidence function in vaccine-induced backward bifurcation in some HIV models. Math Biosci 210(2):436–463
Van den Driessche P, Watmough J (2002) Reproduction numbers and sub-threshold endemic equilibria for compartmental models of disease transmission. Math Biosci 180(1):29–48
Wang W (2006) Backward bifurcation of an epidemic model with treatment. Math Biosci 201(1):58–71
Wang ZW (2009) Backward bifurcation in simple SIS model. Acta Mathematicae Applicatae Sinica, English Series 25(1):127–136
Zhang X, Liu X (2008) Backward bifurcation of an epidemic model with saturated treatment function. J Math Anal Appl 348(1):433–443

Zhou XY, Cui J, Zhang ZH (2012) Global results for a cholera model with imperfect vaccination. J Franklin Inst 349(3):770–791

Zhou X, Cui J (2011) Modeling and stability analysis for a cholera model with vaccination. Math Methods Appl Sci 34(14):1711–1724

Zhou X, Shi X, Cui J (2017) Stability and backward bifurcation on a cholera epidemic model with saturated recovery rate. Math Methods Appl Sci 40(4):1288–1306

Insights into Ventilation Demand Estimation for High-Speed Supercavitating Underwater Vehicles

Ashish Karn, Vishal Narula, Roger E.A. Arndt and Jiarong Hong

Abstract The difference between the typical peak speeds of an aerial and an underwater vehicle is enormous. Evidently, the reason behind this huge disparity lies in the tremendous skin friction drag experienced by an underwater vehicle. However, this difference can be bridged if the underwater vehicles were somehow engulfed by elongated gas/vapor bubbles or cavities as these vehicles travel underwater. Such huge cavities or 'supercavities' can be generated via two different approaches—cavitation or ventilation. Among the two, the generation of a supercavity through ventilation is more interesting, since it can be accomplished at much lower speeds. For the operation of such underwater vehicles in the ventilation mode, it is imperative to determine the ventilation demand, or the amount of gas to be carried on board. The present study reports some interesting insights into the factors that determine the estimation of this ventilation demand. Two most important factors governing the estimation of ventilation demand are the ventilation requirement for the formation and sustenance of a supercavity. These two factors, in turn, are dependent upon the operational conditions of a vehicle, as well as unsteady state conditions prevailing under the ocean. The current work explores the dependence of the formation and sustenance air entrainment rates of a supercavity at different operational conditions of the supercavitating vehicle.

A. Karn (✉)
Department of Mechanical Engineering, University of Petroleum and Energy Studies, Dehradun, Uttarakhand 248007, India
e-mail: karn@umn.edu

A. Karn · R.E.A. Arndt · J. Hong
St. Anthony Falls Laboratory, University of Minnesota Twin Cities, Minneapolis 55414, MN, USA

V. Narula
Department of Mechanical Engineering, College of Engineering Roorkee, Roorkee 247667, Uttarakhand, India

M.K. Singh et al. (eds.), *Applications of Fluid Dynamics*, Lecture Notes in Mechanical Engineering, https://doi.org/10.1007/978-981-10-5329-0_52

Nomenclature

P_∞	Ambient pressure
P_c	Internal cavity pressure
Fr	Froude number
U	Flow velocity
d_c	Cavitator size
g	Gravitational acceleration
C_Q	Gas entrainment coefficient
$\dot{Q}$	Gas ventilation rate
$C_{Q\text{form}}$	Formation air entrainment coefficient
$C_{Q\text{sust}}$	Collapse gas entrainment coefficient
P_{in}	Pressure inside at the supercavity rear portion
P_{out}	Pressure outside at the supercavity rear portion
$\Delta\tilde{P}$	Nondimensional pressure difference
$\Delta\tilde{P}_{\text{est}}$	Estimated nondimensional pressure difference
D_T	Diameter of the water tunnel
C_D	Drag coefficient

Greek Symbols

σ	Cavitation number
ρ	Water density

1 Introduction

The difference between the typical peak speeds of an aerial and an underwater vehicle is enormous. Evidently, the reason behind this huge disparity lies in the tremendous skin friction drag experienced by an underwater vehicle (Karn et al. 2015a). However, this difference can be bridged if the underwater vehicles were somehow engulfed by elongated gas/vapor bubbles or cavities as these vehicles travel underwater. Such huge cavities or 'supercavities' (shown in Fig. 1) can be

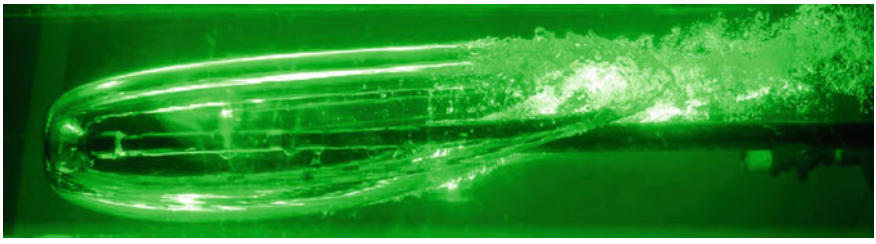

Fig. 1 Laser-illuminated supercavity formed around a disk cavitator with a body present inside the supercavity

generated via two different approaches—cavitation or ventilation. Supercavitation is a special case of cavitation which can be employed to create a bubble of gas/vapor inside water, large enough to encompass a vehicle traveling through the water. The phenomenon of supercavitation is generally characterized by nondimensional parameters like cavitation number, $\sigma = 2(P_\infty - P_c)/\rho U^2$ and Froude number $(Fr = U/\sqrt{gd_c})$ where P_∞, P_c, ρ, U, g, and d_c denote the ambient pressure, the internal cavity pressure, water density, flow velocity, gravitational acceleration, and cavitator size, respectively. A ventilated supercavity is generated by blowing noncondensable gas into the low-pressure region near the nose of the vehicle. Ventilated supercavitation has numerous advantages over natural supercavitation including the requirement of low speed, greater adaptability for vehicle maneuvering and control. Further, it also avoids the problems associated with attainment of high speed that is required for supercavity formation through cavitation, such as surface damage, buffeting, and vibrations (Kinzel et al. 2009). The ventilation requirements for a supercavity are characterized by the gas entrainment coefficient, $C_Q = \dot{Q}/Ud_c^2$, where $\dot{Q}$ denotes the gas ventilation rate. The determination of the gas storage requirements for a ventilated supercavitating vehicle requires information on gas supply rate to form and sustain a steady supercavity at different flow conditions.

A question may be raised here, as to what causes the difference between the air entrainment rates required to form and sustain a supercavity. The answer to this intriguing question lies in the fundamental physics of the process, in particular, the hysteresis behavior shown by the ventilation process. Ventilation hysteresis refers

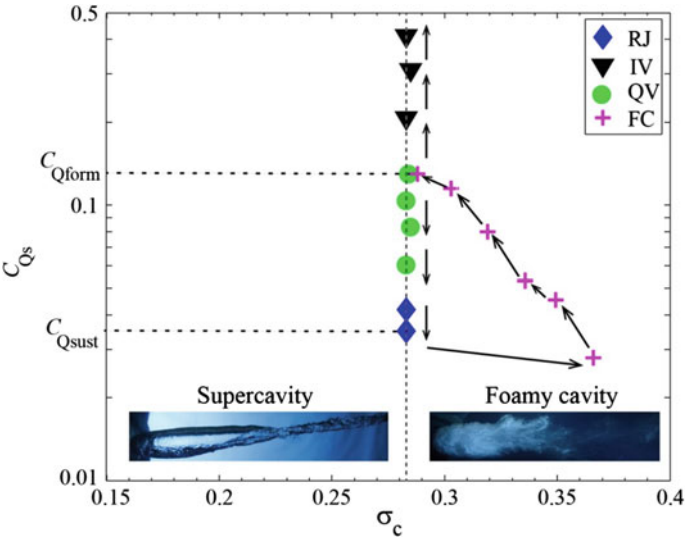

Fig. 2 Typical ventilation hysteresis curve observed in our experiments for a cavitator of 20 mm in diameter (adapted from Karn et al. 2016a). RJ, IV and QV refer to reentrant jet, interacting vortex, quad vortex, and FC denotes a foamy cavity

to a phenomenon, whereby the supercavity can be sustained at much lower values of gas entrainment than required for its formation, as shown in Fig. 2. Ventilation hysteresis is closely related to the formation and collapse gas entrainments, and studies on ventilation hysteresis have been reported before (Karn et al. 2016a).

As Fig. 2 shows, a foamy cavity shows a decrement in σ and an increase in length when C_Q is increased. This process continues till a supercavity is established (C_Q equals $C_{Q\text{form}}$, formation air entrainment coefficient), after which no further reduction in σ is possible upon change in C_Q. However, the supercavity is maintained even as C_Q drops down to very low values. Eventually, when C_Q drops below $C_{Q\text{sust}}$ (collapse gas entrainment coefficient), the supercavity transitions back into a foamy cavity. Recently, Karn et al. (2016a) discussed the phenomenon of ventilation hysteresis, particularly focusing on the transition of closure modes of a supercavity and relating ventilation hysteresis to the internal flows in a supercavity. However, the gas entrainment rate at the formation and collapse of a supercavity has not yet been examined in detail, and thus, is the subject of the current study.

2 Experimental Setup and Procedures

Experiments are conducted to measure ventilation flow rates and formation and collapse processes of a ventilated supercavity under different flow conditions. The experiments are carried out in the high-speed water tunnel at the Saint Anthony Falls Laboratory. This water tunnel is a closed recirculating facility with a

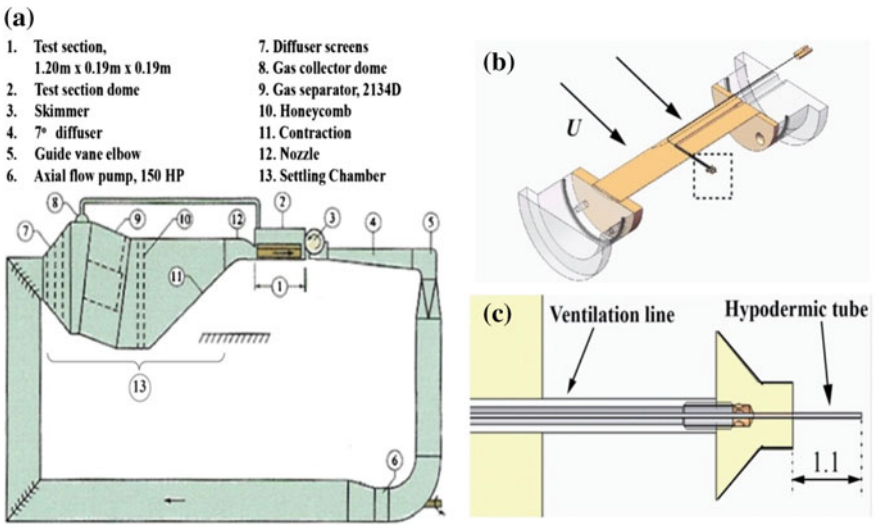

Fig. 3 Schematic of **a** SAFL water tunnel facility, **b** backward-facing model, **c** a close view of the backward-facing model showing the ventilation line and hypodermic tube for pressure measurement

horizontal test section of 1.20 m (length) × 0.19 m (width) × 0.19 m (height). This tunnel is specifically designed for cavitation and gas ventilation studies and is capable of operating at a maximum velocity of 20 m/s.

Figure 3 shows a schematic of the experimental facility. A disk cavitator with its back surface facing the incoming flow and mounted downstream of a hydrofoil-shaped strut (referred to as 'backward-facing model' in Kawakami and Arndt 2011) is employed in the current experiments. Figure 3 illustrates the backward-facing model within the test section. The gas flow rate is controlled by a mass flow controller and is kept steady during the experiments. During the experiments, the ventilation flow rates for the process of supercavity formation and collapse are measured, and the corresponding high-speed videos of this process are recorded to obtain physical insights into the phenomena. The measurements of $C_{Q\text{form}}$ and $C_{Q\text{sust}}$ are repeated for different cavitator sizes and flow conditions. A cavitator of 20 mm in diameter is used, and $C_{Q\text{form}}$ and $C_{Q\text{sust}}$ are measured at a fixed Fr.

3 Results and Discussion

The gas entrainment behaviors at steady state are studied first for the 20 mm cavitator by varying Fr in the range of 5–25. Figure 4 shows a typical variation of $C_{Q\text{form}}$ with Fr. As Fig. 4 shows, $C_{Q\text{form}}$ initially increases, attains a maximum, and then decreases, as Fr is increased. Two separate regimes can be identified around the maximum obtained in this curve, which are related to the concentration of individual bubbles in the flow. Fr less than nine corresponds to a low bubble concentration regime, whereas higher Fr characterizes a high bubble concentration zone. This trend can be explained based on the assertion that the supercavity formation process is driven by bubble coalescence, as suggested by previous studies (Karn et al. 2016a). For a fixed cavitator size, an increase in Fr implies an increase in flow turbulence. This increased turbulence generally breaks up the individual

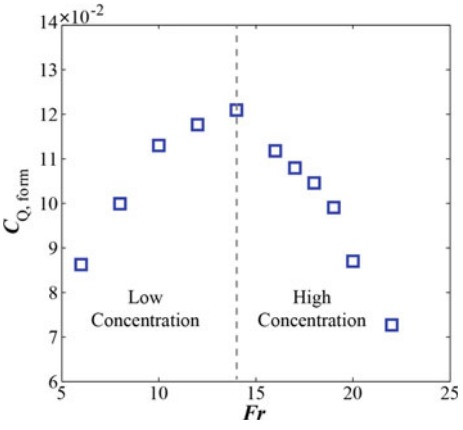

Fig. 4 Dependence of $C_{Q\text{form}}$ upon Fr for the 20 mm cavitator

bubbles into smaller sizes as reported by previous wake studies. Our previous observations have shown that there are lesser number of bubbles at low *Fr* and an increase in *Fr* results in smaller individual bubbles, and an increase in the number of bubbles (Karn et al. 2015b, 2016b). With increasing *Fr*, the formation of a supercavity necessitates the coalescence of these resulting smaller individual bubbles. Thus, there is an increased ventilation requirement to increase the size and number of bubbles to form a coalesced supercavity. Previous studies have reported that an increase in C_Q results in an increment in both number and size of bubbles (Karn et al. 2015b, 2016b). However, in the high-concentration regime, this effect of increased number of bubbles offsets the reduction in the size of individual bubbles. In this regime, the bubble concentration becomes so high that bubbles are closely packed together in the bubble cloud. Due to the restricted free space for bubble movement and the concomitant increase in bubble collision frequency, the coalescence process is favored, resulting in decreased gas entrainment requirement for supercavity formation with increasing *Fr*.

The dependence of $C_{Q\text{sust}}$ upon *Fr* is presented in Fig. 5. As Fig. 5 shows, $C_{Q\text{sust}}$ initially decreases sharply with *Fr* and then stays constant. This trend of supercavity collapse can be explained using the postulated framework of supercavity closure presented in Karn et al. (2016a). According to them, the supercavity closure is determined by a balance of pressure inside (P_{in}) and outside (P_{out}) at the supercavity rear portion. The nondimensional pressure difference defined as, $\Delta\tilde{P} = 2(P_{\text{out}} - P_{\text{in}})/\rho U^2$, characterizes different supercavity closure modes (e.g., twin-vortex, reentrant jet) as well as the foamy state of a cavity. Their data suggested that $\Delta\tilde{P}$ for a foamy cavity is significantly larger than for a supercavity. In other words, when P_{out} far exceeds P_{in},, the high pressure difference forces water jet to gush inside the supercavity, causing it collapse. Thus, at a high $\Delta\tilde{P}$,, larger gas entrainment is required to inhibit the growth of reentrant jet and maintain a stable supercavity. Further, based on their results, $\Delta\tilde{P}$ can be estimated from the momentum balance for the supercavity as (neglecting the pressure drop due to

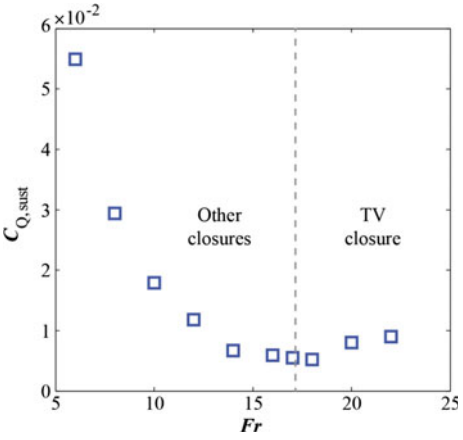

Fig. 5 Dependence of $C_{Q\text{sust}}$ upon *Fr* for the 20 mm cavitator

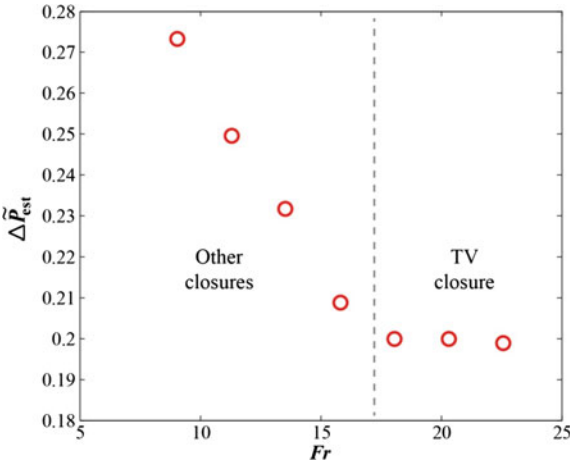

Fig. 6 Dependence of $\Delta\tilde{P}_{est}$ upon Fr for the 20 mm cavitator

viscosity) $\Delta\tilde{P}_{est} = \sigma - C_D(d/D_T)^2$, where D_T represents the diameter of the water tunnel. As shown in Fig. 6, $\Delta\tilde{P}_{est}$ exhibits a similar trend with respect to Fr as that of C_{Qsust}. Thus, larger the $\Delta\tilde{P}_{est}$, the more the supercavity is susceptible to collapse, and consequently a greater gas entrainment is required to prevent such a collapse. It is noteworthy that similar to formation gas entrainment curve, the collapse gas entrainment curve can also be divided into two separate regimes. Our experiments have shown that the regime in which $\Delta\tilde{P}_{est}$ does not change significantly with Fr corresponds to supercavities with stable twin-vortex closure at C_{Qsust}. On the other hand, the region in which $\Delta\tilde{P}$ decreases sharply with Fr is characterized by other closure modes at C_{Qsust}, including reentrant jet, quad-vortex, or unstable closure modes as reported by Karn et al. (2016a).

4 Conclusions

In the current study, some interesting insights into the gas entrainment behaviors in the formation and collapse of a ventilated supercavity are presented for steady flows. Our experiments have shown that the gas entrainment required to establish a supercavity is much greater than the minimum gas entrainment required to sustain it. Further, these gas entrainment values depend on Fr. Specifically, the measurements of the formation gas entrainment coefficients under different Fr numbers indicate that it does not monotonically increase with Fr but displays increasing and decreasing trends in different regimes of Fr. These trends can be attributed to the variation in coalescence efficiency with bubble concentration at different flow conditions. On the other hand, the collapse air entrainment coefficient initially decreases with Fr and then approaches a constant. This trend has been shown to be related to the change in the nondimensional pressure inside and outside the cavity at the supercavity rear portion.

References

Karn A, Arndt REA, Hong J (2015a) Dependence of supercavity closure upon flow unsteadiness. Exp Therm Fluid Sci 68:493–498

Karn A, Ellis C, Hong J, Arndt REA (2015b) Investigation into the turbulent bubbly wake of a vented hydrofoil: moving towards improved turbine aeration techniques. Exp Therm Fluid Sci 64:186–195

Karn A, Arndt REA, Hong J (2016a) An experimental investigation into supercavity closure mechanisms. J Fluid Mech 789:259–284

Karn A, Shao S, Arndt R, Hong J (2016b) Bubble coalescence and breakup in turbulent bubbly wake of a ventilated hydrofoil. Exp Therm Fluid Sci 70:397–407

Kawakami E, Arndt REA (2011) Investigation of the behavior of ventilated supercavities. J Fluids Eng 133(9):091305-1–091305-11

Kinzel MP, Lindau JW, Kunz RF (2009) Air entrainment mechanisms from artificial supercavities: insight based on numerical simulations. In: Proceedings of the 7th international symposium on cavitation, CAV, 136, Ann Arbor, Michigan, USA

Author Index

M.K. Singh et al. (eds.), *Applications of Fluid Dynamics*, Lecture Notes in Mechanical Engineering, https://doi.org/10.1007/978-981-10-5329-0